GSI Report 2008-1
July 2008

SCIENTIFIC REPORT 2007

Gesellschaft für Schwerionenforschung mbH Darmstadt
Member of the Helmholtz Association

FAIR Start event on November 7, 2007: The photo shows the Federal Minister for Education and Research, Annette Schavan (center right), and the Prime Minister of Hessen, Roland Koch (center left), together with delegates and representatives from Austria, Finland, France, Germany, Poland, Romania, Russia, Spain, Sweden and the UK after signing a communiqué on the joint construction and operation of the FAIR facility, thereby giving the official 'starting shot' for FAIR.
Cover photo by G. Otto, GSI.

GSI Scientific Report 2007

GSI Report 2008-1
<http://www.gsi.de/library/GSI-Report-2008-1/>

ISSN: 0174-0814
and GSI Report 2008-1

Publisher: Gesellschaft für Schwerionenforschung mbH, GSI
Planckstr. 1, 64291 Darmstadt, Germany, <http://www.gsi.de>
GSI is a member of the Helmholtz association of national research centres <http://www.helmholtz.de>.

Publication date: July 2008
E-only-edition: <http://www.gsi.de/library/GSI-Report-2008-1/>

Editor: Katrin Große,
Contact: gsilibrary@gsi.de, phone: +496159 712610, fax: +496159 713049.
Technical Team at GSI for the printed and the Internet versions: T. Badura, I. Giese, K. Große, U. Meyer, V. Schaa and K. Schiebel.

For the production of this report templates and scripts of the JACoW collaboration (Joint Accelerator Conferences on Web <http://www.jacow.org>) were used.

Foreword

2007 was a very important year for GSI and its long-term future. The FAIR project passed significant milestones with regard to technical, administrative and political preparations for its realization. The highlight was undoubtedly the official launch event for the FAIR project on November 7, 2007, celebrated in the presence of more than 1400 guests from Science and Politics – amongst them the Federal Minister for Education and Research, Dr. Annette Schavan, the Prime Minister of the State of Hessen, Roland Koch and many high ranking representatives from the FAIR partner countries (see Cover Photo). Minister Schavan and Prime Minister Koch, together with delegates from Austria, Finland, France, Poland, Romania, Russia, Spain, Sweden and the UK, signed a communiqué on the joint construction and operation of the FAIR facility, thereby giving the official 'starting shot' for FAIR. In the meantime, all administrative preparations have been successfully completed, and GSI as well as the FAIR community are looking forward to the next most important event - the official founding of the FAIR GmbH - which is scheduled for autumn 2008.

In 2007, there were also significant advancements in the technical preparations for FAIR – impressive progress was achieved in developing and implementing solutions to technical challenges such as the dynamic vacuum problem, the realization of fast cycling super-conducting magnets or the production of very short intense bunches. Technical Design Reports (TDRs) for the FAIR synchrotrons and storage rings are presently under preparation and shall be submitted by late summer 2008. TDRs are also being prepared for selected FAIR experiments. For a number of key components such as the super-conducting magnets, design and prototyping has progressed to a state that allows first orders to be placed in 2009 – after the establishment of the FAIR GmbH.

Not only does the present Annual Report refer to the advances achieved in the planning and preparation of FAIR, it also provides an impressive summary of the results and achievements made in the ongoing research program at the existing UNILAC-SIS-ESR facility. Despite considerable upgrading work ongoing at the accelerators in order to prepare for their role as FAIR injector, it was possible once again to deliver more than 11,000 beam hours to the users (integral target time). The beam availability amounted to about 90 %, as in the years before.

Major research highlights from nuclear and hadron physics include the production of element 112 via 'warm fusion' reaction $^{48}Ca + ^{238}U$ (as a preparatory step for the long-term experimental runs, scheduled in the course of this year, for hunting element 120), detailed nuclear structure studies of neutron-rich isotopes exploiting the RISING detector and the R^3B set-up, new high-statistics data obtained at HADES on enhanced di-electron emission in C+C collisions at relativistic energies as well as corresponding data on elementary pp and pn reactions giving experimental evidence for a strong isospin dependence of the dilepton production in the mass range above the pion-Dalitz region.

In the fields of atomic physics, plasma physics and materials research, first experiments with the newly installed ESR reaction-microscope to study atoms in extremely high dynamical fields are to be mentioned as well as the successful double-pass operation of the complete PHELIX system with the projected output energy of 500 Joule, and the observation of structural phase transitions under simultaneous influence of high pressure and ion irradiation.

Significant progress was achieved with regard to the mid-term projects. The ALICE TPC, the FOPI upgrade, and the TASCA separator were completed and successfully commissioned with first experiments being scheduled at CERN and GSI, respectively, in 2008. The HADES upgrade as well as the setting up of HITRAP behind the ESR and the new material research area at the UNILAC HITRAP progressed according to schedule and will be completed by autumn 2008. A breakthrough was achieved with regard to PHELIX, where a first experiment exploiting both the PHELIX laser beam together with a UNILAC ion beam was carried out very recently (in May 2008).

Remarkable headway was also made in the field of radiobiology and cancer therapy. Prominent research results include radiobiological studies aiming at an extension of ion beam therapy to other indications such as prostate cancer, the development of new beam control systems allowing the irradiation of moving tumors, and the optimization of algorithms for biological treatment planning. Within the HIT project (Heidelberg Ion beam Therapy), the accelerator systems were successfully commissioned and the required beam specifications at the horizontal therapy achieved. Moreover, the assembly of the gantry was completed and first commissioning runs with beam performed in early 2008.

In total, the Annual Report comprises over 300 articles; more than 1500 authors, mainly from outside GSI, contributed to the report, which reflects the strong attraction of the existing GSI facility and the future prospects of FAIR.

The progress achieved and described in the Annual Report is the result of the work and dedication of many - the in-house staff, scientific, technical and administrative, and the many, many outside users including, most importantly, post-docs and doctoral students from universities in Germany, Europe and worldwide. To all of them my sincere 'thanks' and the strong wish for a continuation and – where possible – extension of the successful cooperation.

Indeed the continuation and extension of scientific-technical cooperation with research partners from at home and abroad will be at the heart of GSI's future strategy in order to meet the challenges ahead: realizing major contributions to FAIR on the one hand, and maintaining a top-rate albeit reduced and focused research program on the other. Important cornerstones within this future strategy are the newly established Helmholtz Alliance on ExtreMe Matter physIcs (EMMI), approved in November 2007, the LOEWE – Helmholtz International Centre for FAIR, approved in June 2008, and the Helmholtz Graduate School on Hadron and Ion Research, approved in May 2008. Moreover, an agreement on strategic partnership between GSI and the universities at Darmstadt, Frankfurt, Gießen, Heidelberg and Mainz is presently under preparation, aiming at major extensions of the existing cooperation with regard to FAIR. All in all, the above mentioned new initiatives will provide extra funds over the next 6-8 years of more than 60 million € for GSI/FAIR-related cooperative research activities, including about 35 new professorships as well as a large number of additional young investigator, postdoc and doctoral student positions.

Finally, as new Director of GSI - since August 2007 - I would like to state the probably obvious: the basis for the impressive progress described in the Annual Report, in particular with regard to FAIR, was provided under the guidance of my predecessor, Walter Henning, and, regarding the administrative preparations for FAIR, also of the former Administrative Director, Alexander Kurz. GSI and I personally are very much obliged to both, and we would like to express once more our gratitude for their dedication and seminal contributions towards paving the way for FAIR.

Scientific Director, GSI

Contents

The FAIR project

Status of the FAIR Project

FAIR Joint Core Team
GSI, Darmstadt, Germany

The year 2007 saw tremendous progress in the realisation of the FAIR facility. During the year the FAIR member states have been joined by Austria and Slovenia. The Republic of Georgia has been granted observer status.

The FAIR project was officially started at 7th November 2007 with a start version based on declared funding of 940 million € at that time). With more than 1400 people attending, delegates of the member states signed a communiqué reaffirming their commitment to build the full FAIR project.

Figure 1: More than 1400 people attended the start of the FAIR project on 7th November 2007

The celebration was followed-up the next day by a symposium with gave a concise overview of the physics at FAIR and its significance in the international research environment. It was attend by more than 500 physicists.

FAIR is unique in its attempt to build an entire accelerator facility via its member states, something which is common in experiment collaborations. It is planned that sub-systems will be built by institutes within the various member countries and installed at the FAIR site. This concept relies on the expertise, infrastructure and willingness of the laboratories of the member states. In autumn 2007 this was put to test: In a first call for expression of interests 22 laboratories from 9 member states answered. This response exceeded all expectations, already covering the majority of the work-packages that have to be executed. The needed consolidation and organisation of these work-packages will be addressed during 2008.

The 14 experiment collaborations with more than 2500 scientists have consolidated their attempts to acquire the necessary funding for a successful realization of their plans. In parallel, significant progress of the research and development of the various detectors has been achieved. This is reflected in the following 44 contributions.

The first technical design reports (TDR) are expected for 2008. They are the final detailed description of the experiment, its detectors or important parts. The TDRs will be evaluated by expert panels who can recommend the start of construction of the particular sub-detectors, e.g. the PANDA electro-magnetic calorimeter.

The progress on the R&D for the accelerators is covered in a dedicated section of this report. Altogether more than 70 reports of working groups and collaboration have been gathered in this years report, showing the ongoing efforts to realize the FAIR project.

In parallel the necessary steps for the civil construction are being taken. It is intended to officially found the FAIR GmbH in autumn 2008.

The creation of the FAIR GmbH and its first year of operation will be supported by a FP7 grant of the European Commission.

The CBM experiment at FAIR*

V. Friese, W.F.J. Müller, P. Senger, GSI Darmstadt, and the CBM Collaboration

Compressed Baryonic Matter: physics case and detector setup

The mission of the Compressed Baryonic Matter (CBM) experiment at FAIR is to explore the QCD phase diagram in the region of high baryon densities. The physics of dense baryonic matter and the relevant observables in nucleus-nucleus collisions have been worked out in detail in the CBM Physics Book which will appear in 2008. The detailed understanding of the evolution of the partonic/hadronic fireball requires new measurements which have not yet been performed at FAIR energies. The most promising observables are rare probes which carry information on the matter properties, such as particles containing charm quarks (D-mesons and charmonia), low-mass vector mesons decaying into dilepton pairs (ρ, ω and ϕ mesons), or Ω hyperons (consisting of 3 strange quarks). The measurement of event-by-event fluctuations, correlations, and of the collective flow of hadrons (including the flow of rare probes) will provide important information on the dynamics of the fireball.

The goal of the CBM research program is to determine the equation-of-state of strongly interacting matter, to discover the phase transition from hadronic to partonic matter and the QCD critical endpoint, and to investigate the in-medium properties of hadrons as a signature for the onset of chiral symmetry restoration. This program requires the systematic and comprehensive investigation of the above mentioned observables as function of beam energy, system size and collision centrality.

The experimental task is to identify hadrons and leptons in collisions with up to 1000 charged particles at event rates of up to 10 MHz. These measurements require fast self-triggered read-out electronics, a high-speed data acquisition (DAQ) architecture, and an appropriate high-level event-selection concept. A particular experimental challenge is the measurement of D-mesons which is based on the real-time selection of displaced vertices with an accuracy of 50 μm.

A schematic view of the proposed CBM detector concept is shown in figure 1. Inside a large aperture dipole magnet there is a Silicon Tracking and Vertexing System which consists of two parts: a Micro-Vertex Detector (MVD, 2 silicon pixel layers) and the Silicon Tracking System (STS, several layers of silicon microstrip detectors). The Silicon detector array has to provide the capabilities for track reconstruction, determination of primary and secondary vertices, and momentum determination. For the lepton measurements two options are under investigation. One possibility is to identify electron-positron pairs from the decay of low mass vector mesons using a Ring Imaging Cherenkov (RICH) detector. High-energetic electrons and positrons from charmonium decays can be identified efficiently with a Transition Radiation Detector (TRD).

The alternative option is to measure muon pairs with a detection system consisting of hadron absorber layers (made of iron) sandwiched by large area tracking detector layers. If the RICH will be replaced by a muon detector the TRD will be converted into a tracking detector for hadron measurements together with the timing RPC. The TOF-RPC detector serves for two purposes: for background suppression during muon measurements with absorbers, and for hadron identification with muon absorbers removed. The ECAL will be used for the identification of photons.

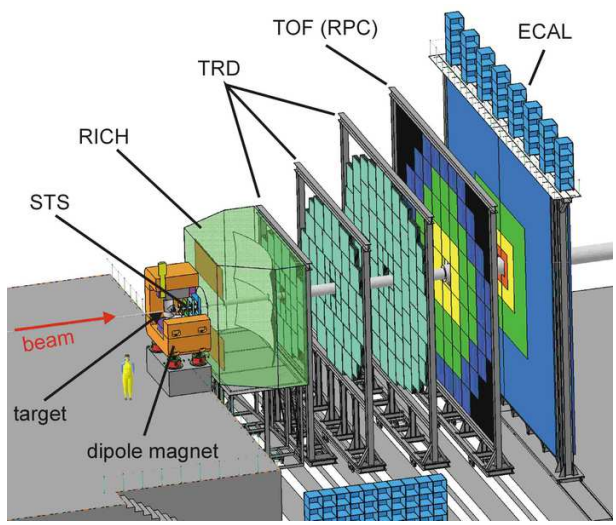

Figure 1: The Compressed Baryonic Matter (CBM) experiment planned at FAIR. The setup consists of a high resolution Silicon Tracking System (STS), a Ring Imaging Cherenkov detector (RICH), three stations of Transition Radiation Detectors (TRD) with 3-4 radiator/detector layers each, a time-of-flight (TOF) system made of Resistive Plate Chambers (RPC), and an Electromagnetic Calorimeter (ECAL) based on lead/scintillator "Shashlik" technology.

In the following we briefly review the status of the feasibility studies and the detector R&D for CBM. The simulations have been performed within the FAIRroot software framework. The routines for track and vertex reconstruction have been improved in speed by a factor of 1000 which allows to perform sophisticated high-statistics simulations for detector layout optimization (see I. Kisel et al., this report).

* Work supported by EU/FP6 HADRONPHYSICS (see Annex) and by INTAS

The Silicon Tracking System

In order to reduce the number of detector technologies (hybrid pixel and micro-strips) we designed a detector system consisting of 8 double-sided micro-strip sensor layers only. This tracking system has been optimized with respect to track reconstruction efficiency, momentum resolution and redundancy (see R. Karabowicz et al., this report). In addition, details of the detector including a realistic sensor layout, micro-cables and support structure have been implemented in the simulation software. First prototype double-sided micro-strip sensors with different sizes have been produced and tested. The next step is to produce a demonstrator consisting of a double-sided sensor connected to a self-triggered read-out chip (n-XYTER), and to perform test measurements with proton beams at GSI (see J.M. Heuser et al. and C. Schmidt et al., this report).

D meson identification and vertex detector

The Micro-Vertex Detector (MVD) - which is close to the target and has limitations in radiation hardness and read-out speed - will be installed only for open charm measurements which requires high-precision vertexing. The MVD consists of two layers of Monolithic Active Pixel Sensors (MAPS) which can be made very thin in order to reduce multiple scattering. Feasibility studies demonstrate that particles with open charm ($D^0, D^{\pm}, D_s$, and Λ_c) can be measured with good efficiency and excellent signal/background ratio using a detector setup consisting of 2 MAPS and 6 double-sided micro-strip stations (see I. Vassiliev et al., this report). The R&D on the MVD concentrates on the improvement of radiation hardness and readout speed of the MAPS, and on the development of a demonstrator (see S. Amar-Youcef et al., this report).

Hadron Identification by Time-of-Flight

The study of event-by-event fluctuations and particle correlations is based on the measurement of pions, kaons and protons. Hadron identification in CBM requires track reconstruction using the STS and the TRD, and TOF determination with the timing RPC wall. The total reconstruction efficiency for hadrons (STS-TRD-RPC) is well above 80 %. This result is based on realistic detector layouts and performances. The R&D on prototype timing RPCs concentrates on high rate capability, low resistivity material, long term stability and the realization of large arrays with overall excellent timing performance.

Electron identification with RICH and TRD

The simulations on electron identification are based on reconstructed tracks in STS and TRD, on ring recognition in the RICH photon detector, on ring-track matching, and on the statistical analysis of the energy loss signal in the TRD (see C. Höhne et al., this report). The combined information from RICH and TRD is sufficient to suppress the pion contamination in the electron sample. Low-mass vector mesons can be identified using elaborated background rejection strategies (see T. Galatyuk et al., this report). The J/ψ meson yield is well visible above the combinatorial background (see A. Maevskaya et al., this report). The TRD-R&D activities are focused on the development of highly granular and fast gaseous detectors which can stand the high-rate environment of CBM. Prototype gas detectors (based on MWPC and GEM technology) have been built and tested with particle rates of up to 200 kHz/cm^2 without deterioration of performance (see M. Petrovici et al. and A. Andronic et al., this report). Moreover, test measurements of RICH mirror and photon detector performances have started.

Muon measurements with hadron absorbers

The CBM muon detection system consists of active hadron absorbers located just behind the Silicon Tracking System. The idea is to continuously track all charged particles through the whole absorber, starting with the tracks measured by the Silicon tracker (which defines the momentum). This concept requires highly granulated and fast tracking detectors which are located in each gap between the absorber layers. The muon detection system is shown in figure 2.

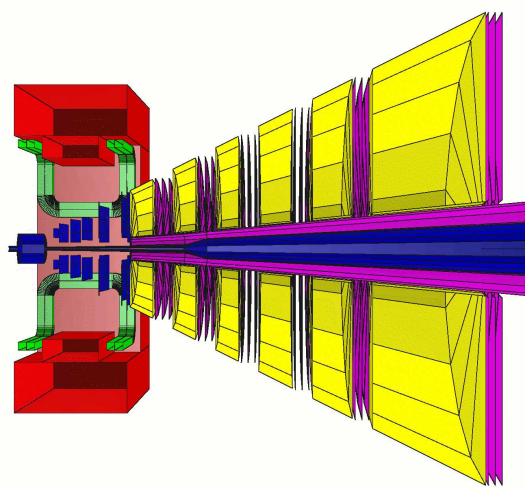

Figure 2: Sketch of the CBM muon detection system consisting of alternating layers of iron hadron absorbers and detectors

The simulations are based on track reconstruction algorithms taking into account a realistic pad layout of the muon chambers according to an occupancy of 5%. The studies demonstrate that both low-mass vector mesons and charmonia can be identified above the combinatorial background which is dominated by muons from weak pion decays (see A. Kiseleva et al., this report). The challenge for the muon chambers and for the track reconstruction algorithms is the huge particle density of up to 1 hit/cm^2 per event in the first detector layers. Therefore, the current detector R&D concentrates on the design of fast and highly granulated gaseous detectors based on GEM technology.

R&D for the demonstrator of the CBM-Micro-Vertex Detector (MVD) *

S. Amar-Youcef[1,2], M. Deveaux[1,4], D. Doering[1], J. Heuser[3], I. Fröhlich[1], J. Michel[1], C. Müntz[1], C. Schrader[1], J. Stroth[1], T. Tischler[1], and B. Wiedemann[1]

[1]IKF, University Frankfurt; [2]Helmholtz Research School, Frankfurt; [3]GSI, Darmstadt; [4]IPHC, Strasbourg

Status of the MVD-Demonstrator

The MVD of the future CBM-experiment at FAIR is needed to identify open charm particles by reconstructing their secondary decay vertex (SV). To reach the required SV resolution, the detector will be installed in beam vacuum and its material budget (MB) has to stay below $\sim 0.5\% X_0$ per layer. Monolithic Active Pixel Sensors (MAPS) [1] are the currently preferred sensing elements and provide the necessary spatial resolution of few μm.

To study their integration to a detector, a demonstrator is being built in the IKF technology lab of University Frankfurt. This project addresses open questions regarding the design of an ultra thin cooling support for the sensor chips, their handling and their integration into a central data aquisition system. The latter includes the design of particular hardware and algorithms for readout and data sparsification [2]. Our concept for a demonstrator module is depicted in

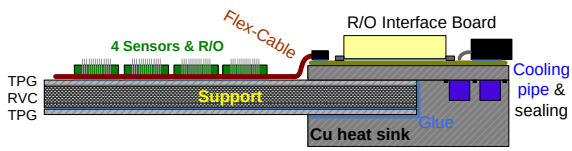

Figure 1: Side view of demonstrator layout: Support sandwich structure applied to a cooling and connecting entity

Figure 1. A cooling support based on the very heat conductive and stiff Thermal Pyrolytic Graphite (TPG) hosts the sensors and evacuates their power (up to ~ 1 W/cm^2). Additional stiffness is reached by adding the very light RVC (Reticulated Vitreous Carbon) between two layers of TPG. "MIMOTEL" MAPS ($\sim 1\ cm^2$, $\sim 1\ ms$ readout time) can be mounted on each side of the support. These sensors, which are provided by IPHC Strasbourg, are biased and read out with flexprint cables connecting them with a small PCB hosting signal buffers.

The trade off between low MB, efficient heat evacuation and mechanical stability is being optimized with thermal and mechanical simulations. We assume today that the thickness of the cooling support will be $\sim 0.2\% X_0$. The multilayer flexprint cables required will add $\sim 0.3\% X_0$ if being installed on both sides. After mounting sensors being thinned to $\sim 100\ \mu m$ by conventional industrial means, we will reach a MB of $\sim 0.4\% X_0$ ($\sim 0.7\% X_0$) for a MVD station with a single (a double) layer of MAPS. This value is not yet satisfactory for CBM but the experiences obtained with this demonstrator will guide further optimisation steps. Lower MB may be reached by using thinner sensors [3] with digital output. This output requires fewer pins and allows using lighter flexprint cables.

* In collaboration with IPHC. Work supported by BMBF (06FY173I), GSI Darmstadt (F&E) and Helmholtz Research School Frankfurt

Radiation Tolerance

A second important issue for the CBM MVD is its radiation tolerance. Intense studies were performed in the context of a common R&D activity of IKF and IPHC. Measurements with ^{55}Fe-photons on neutron irradiated sensors highlighted that the radiation induced drop of the charge collection efficiency (CCE) is substantially reduced for small pixels (see figure 2). As this drop forms the dominant radiation damage, the radiation tolerance of MAPS increases substantially with smaller pixel pitch. This was cross checked and confirmed with beam tests [3]. However, using small pixels comes with draw backs in terms of lower time resolution and higher power dissipation.

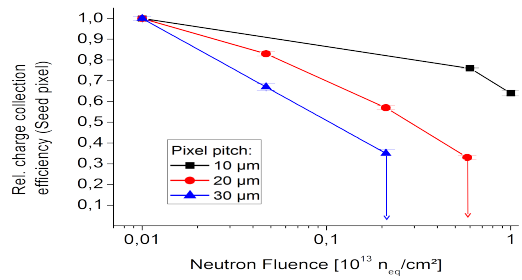

Figure 2: The CCE of pixels as function of the pixel pitch. CCEs below 0.4 are considered as upper limits.

A second potential way of improving the radiation tolerance of MAPS is to operate them at LN_2-temperatures. The CERN-RD39 collaboration recently demonstrated that the CCE of heavily irradiated, n-doped silicon detectors is partly restored at this temperature [4]. Substantial improvements in the radiation tolerance might be reached, if those promising results could be reproduced with the p-doped sensors of MAPS. An experiment for testing this approach and to establish the radiation tolerance of cryogenic MAPS is currently under preparation.

References

[1] R. Turchetta et al., NIM-A Vol. 458, Iss. 3, P. 677-689

[2] C. Schrader et al., 'A Readout System for the CBM-MVD Demonstrator', this report

[3] A. Besson et al., 'Achievements of CMOS Pixel Sensors for the CBM Micro-Vertex Detector', this report

[4] CERN-RD 39, NIM-A Vol. 440, Iss. 1, P. 5-16

A Readout System for the CBM-MVD Demonstrator*

C. Schrader[1], S. Amar-Youcef[1], N. Bialas[1], M. Deveaux[1], D. Doering[1], J. Heuser[2], I. Fröhlich[1], J. Michel[1], C. Müntz[1], S. Schreiber[1], J. Stroth[1], T. Tischler[1], B. Wiedemann[1]

[1]IKF, University Frankfurt, Germany, [2]GSI, Darmstadt, Germany

A micro-vertex detector for track reconstruction, consisting of two layers of monolithic active pixel sensors (MAPS [1]) is planned for the CBM experiment. Here, the readout of the MAPS detector stations, which will deliver a raw data rate of up to ~100 Gbit/s/cm² [2], is challenging.

To study the electronic and mechanical integration of these sensors into a detector system, a so-called "demonstrator" is being constructed at the IKF Technology Lab.

The sensor planned to be used in the demonstrator (MIMOTEL, with 4 matrices of 64 x 256 pixel array, 30 µm pixel pitches and a readout speed of ~1 ms/frame) delivers a data rate up to 100 MB/s, which places high demands on the readout electronics. A fast readout add-on board for the TRBv2 [2] standard was developed with on-board functionality for data reduction in order to replace an existing USB board as provided by IPHC, Strasbourg.

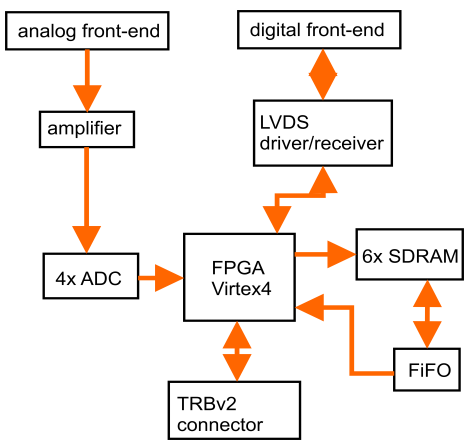

Figure 1: Components of the MAPS readout board.

The new board comprises 4 analog input signal channels which receive the analog signals from the 4 matrices of each MAPS chip via an RJ45 connector. A differential-to-differential amplifier helps to balance the input for the differential ADCs, so that the 4 ADCs provide maximum performance.

The ADCs with sampling frequences of up to 50 MHz, convert the analog signals to 12-bit digital signals. The digital front-end with low voltage differential drivers and receivers (LVDS) is mainly used to control the sensor.

The data is further processed online using a VIRTEX IV LX40 FPGA with internal FIFO and 512 MB external SDRAM organized in 6 memory banks.

To process the MAPS data on-line the system has to work with pipelined algorithms for correlated double sampling (CDS) and hit discrimination until the identified hits are transmitted externally via the optical link (2Gbit/s) of the TRBv2. Since the data is continuously delivered by every MIMOTEL chip the algorithms have to work in real-time.

The interface between the TRBv2 board and the add-on board is established with two high-speed LVDS connectors (15Gbit/s), which also provide power for the add-on board (+5V, 10A), converted on the add-on board to supply the voltages for the individual units (between ±12V). The digital and analog components have separate power supplies and ground planes to reduce electrical cross talk.

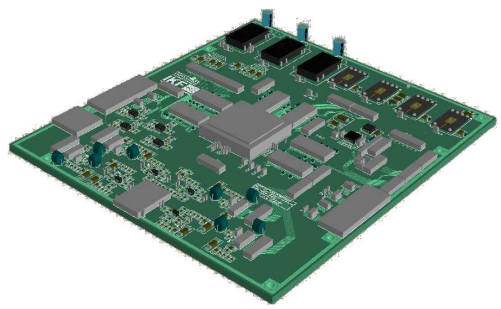

Figure 2: Layout of the MAPS add-on prototype board.

The schematics and the layouts of the 12 layer board were designed in collaboration with the electronic workshop of IKF, using the design software Altium©. The board was submitted for production and will be assembled and tested early 2008. In parallel to the hardware developments, data acquisition algorithms for the FPGA (including CDS, bit reduction and hit finding) were developed and successfully simulated in VHDL.

REFERENCES

[1] R. Turchetta et al., Volume 458, Issue 3, Pages 677-689.
[2] S. Amar-Youcef, Diploma Thesis (2007).
[3] I. Fröhlich et al., A General Purpose Trigger and Readout Board (TRB), IEEE Trans. Nucl. Sci, in print

* Work supported by the BMBF (06FY 173I)

Achievements of CMOS Pixel Sensors for the CBM Micro-Vertex Detector [1]

A.Besson[1], G.Claus[1], M.Deveaux[1,2], A.Dorokhov[1], G.Dozière[1], W.Dulinski[1], Ch.Hu-Guo[1], A.Himmi[1], K.Jaaskelainen[1], F.Morel[1], I.Valin[1], and M.Winter[1]

[1]IPHC and Université L.Pasteur, Strasbourg; [2]J.W.Goethe Universität, Frankfurt

CMOS pixel sensors are being developed for the CBM Micro-Vertex Detector (MVD). They provide the high resolution required to reconstruct efficiently decay vertices of short-lived particles, such as charmed mesons. The present R&D is mainly driven by the severe running conditions expected in the vicinity of the experimental target. The most significant outcome obtained in 2007 is summarised hereafter. Prominent results include performances of a fast sensor architecture with discriminated outputs, the tolerance to non-ionising radiation, the design of a zero-suppression micro-circuit and industrial thinning. The report also gives an overview of the R&D plans for 2008.

Fast read-out architecture

The fast read-out architecture developped for the MVD was already presented in previous reports [1]. The most recent sensor featuring this architecture (called MIMOSA-16) is composed of 32 columns of pixels read out in parallel. Each pixel includes correlated double sampling micro-circuits. 24 columns are ended with a discriminator (the remaining 8 columns have analog outputs for test purposes).

The sensor was mounted on a Si-strip telescope and its detection performances were assessed as a function of the discriminator threshold with a 180 GeV π^- beam at the CERN-SPS. A detection efficiency of $\sim$ 99.9 % was observed for fake hit rates in the order of a few 10^{-5}. The single point resolution was found to be $\lesssim 5\ \mu m$, i.e. substantially better than the binary resolution ($\sim 7.2\ \mu m$) reflecting the pixel pitch (25 μm). This value satisfies the MVD requirements, aleviating the need for ADCs.

The MIMOSA-16 architecture is foreseen to evolve towards a sensor incorporating integrated zero-suppression micro-circuits. A prototype zero-suppression chip (called SUZE-01) was designed and fabricated in 2007. It features a 2-step logic encoding the compactified address of pixels delivering a charge above the discriminator threshold, and is equipped with output memories. Preliminary test results indicate that the zero-suppression logic performs according to the specifications.

The next major objectives consist in fabricating 2 full scale sensors: a first one, without integrated zero-suppression, for the STAR Heavy Flavour Tracker, and a second one for the beam telescope of the FP-6 project EUDET, which incorporates zero-suppression. To bridge the gap with these final sensors, a medium size prototype (MIMOSA-22) was designed in 2007 and submitted to fabrication in Octobre. It features 128 columns of 576 pixels (18.4 μm pitch), each ended with a discriminator. It adds to the MIMOSA-16 design integrated JTAG steering micro-circuits and improved testability. The chip characterisation should start in February 2008.

Radiation tolerance

The tolerance of the sensors to non-ionising radiation, already studied in previous years, was assessed with a sensor expected to withstand higher fluencies than chips tested previously. The sensor (called MIMOSA-18) is composed of 4 matrices of 256×256 pixels. The pixel pitch amounts to only 10 μm, a value which reinforces the charge collection efficiency. Several chips were exposed to low energy neutrons at the Llubjana irradiation facility. The highest integrated doses amounted to $\sim 6{\cdot}10^{12}$ and 10^{13} n_{eq}/cm^2. In the latter case, the photon gas accompanying the neutrons and irradiating the sensor translated into a integrated ionising dose of 100–200 kRad. Irradiated sensors were subsequently mounted on a Si-strip telescope and exposed to a 120 GeV π^- beam at the CERN-SPS. The detection performances observed for a coolant temperature of -20°C and a read-out time of 3 ms are summarised in the table below. The latter displays the sensor noise, the cluster charge, the signal-to-noise ratio and the detection efficiency for the two values of the fluence and before irradiation.

Fluence (n_{eq}/cm^2)	**0**	**$6{\cdot}10^{12}$**	**$1{\cdot}10^{13}$**
Noise ($e^- ENC$)	10.8±0.3	12.2±0.3	14.3±0.3
Q_{clust} (e^-)	1026	680	560
S/N (MPV)	28.5±0.2	20.4±0.2	14.7±0.2
Det. Eff. (%)	99.93±0.03	99.85±0.05	99.5±0.1

The major outcome of the study is that MIMOSA sensors can tolerate fluences of O(10^{13} n_{eq}/cm^2), provided the pixel design is adapted to this issue. The R&D next steps aim to adapt the design to the other MVD specifications.

Thinning

Several different MIMOSA sensors were thinned individually to $\sim$ 50 μm in industry. Thinned MIMOSA-18 sensors (5.5×7.5 mm^2 large) were mounted on their interface board and consecutively characterised at the CERN-SPS. No performance loss was observed, demonstrating that 50 μm thin sensors constitute a valid baseline assumption for the MVD geometry.

References

[1] S. Amar-Youcef et al., GSI Report 2007-1 18.

[1] *This work was supported by BMBF (06FY173I) and GSI (F&E).*

Layout studies of the Silicon Tracking System for the CBM experiment*

R. Karabowicz, J. M. Heuser, and the CBM Collaboration
GSI, Darmstadt, Germany

The Silicon Tracking System (STS) serves the CBM experiment as a track reconstruction and momentum measurement detector. It is designed to provide high tracking efficiency and good momentum resolution for the charged particles produced in nuclear interactions in the target. As the multiplicities in central Au + Au collisions at FAIR energies reach 1000 charged particles a high granularity and low mass detector device is required. The major change in the STS layout compared to the previous versions [1] is an increased number of stations fully based on micro-strip detectors. Other changes include segmentation of the stations according to the prototype designs and introduction of passive material.

Detector Layout

The current STS detector concept comprises 8 detector stations schematically shown in Fig. 1. The stations are build of 300μm thick double-sided silicon micro-strip sensors arranged in vertical modules with fixed horizontal size of 6cm. The vertical size of the sensors varies from 2 to 16cm to ascertain a maximum occupancy of less than 5% and to minimize the number of channels. For the radiation studies and occupancy results, see [2]. The arrangement of sensors and modules in a single station is presented in Fig. 2.

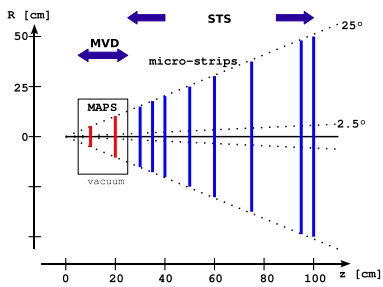

Figure 1: Schematics of the STS + MVD detector systems.

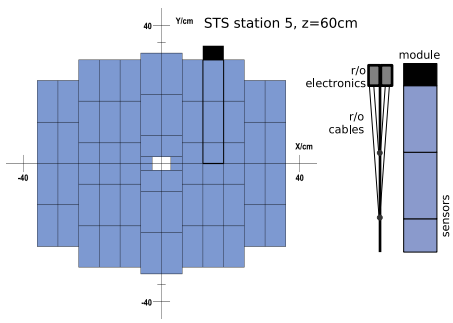

Figure 2: Silicon micro-strip sensors arranged into modules of different lenghts building up a tracking station.

In order to achieve a low-mass detector we have decided to place the read-out electronics at the perimeter of the STS. Signals from the sensors will be read outby thin capton micro-cables. The silicon detector will be mounted on an ultralight carbon fiber skeleton. These additional materials are already present in the GEANT simulations of the CBM experiment, as indicated in Fig. 2. The double-sided silicon sensors have active strips with a pitch of 60μm (initially 50μm) on both sides, oriented vertically in the front layer and rotated by a stereo angle of 15° in the back plane. Please refer to [3] for more details on the detector R&D. For high-resolution vertex measurements, e. g. open charm detection, the STS is supported with a Micro-Vertex Detector (MVD) consisting of two very thin and fine-pitch MAPS pixel detector stations close to the target.

Performance studies

The performance of the STS detector was evaluated on various levels. The tracking routines are based on a Cellular Automaton for track finding and a Kalman filter for track fitting [4]. The tracking efficiencies vary from 99.7% for single track events to ca. 95% in central Au + Au events at 25 AGeV (for tracks with momenta exceeding 1 GeV/c). The momentum resolution depends stronly on the detector's radiation length and changes from 1.2 % in case of standalone silicon sensors to 1.6 % for the full STS setup with readout cables and carbon support structure. Although the tracking results depend only weakly and linearly on the strip pitch or the stereo angle, the small deterioration of the track reconstruction performance leads to rather strong decrease in the full physics analysis, e. g. of the light vector meson muon decay channel.

Conclusions and plans

A rather detailed STS detector layout has been implemented in the simulation of the CBM experiment.The dependence of the reconstruction results on several important parameters has been studied. Future plans include the development of realistic detector response functions that include signal sharing between strips and hit clusters. Another urgent topic being studied at the moment is a possible conceptual change of the STS detector and replacement of the double-sided detectors with single-sided ones.

References

[1] J. M. Heuser et al., *Layout studies and sensor prototypes for the CBM Silicon Tracking System*, GSI Report 2007-1 19

[2] R. Karabowicz et al., *Radiation environment in the CBM experiment*, this report

[3] J. M. Heuser et al., *First microstrip detector prototypes for the CBM Silicon Tracking System*, this report

[4] I. Kisel et al., *Fast SIMDized Kalman filter based track fit*, this report

* Supported by EU/FP6 HADRONPHYSICS (see Annex) and INTAS

First microstrip detector prototypes for the CBM Silicon Tracking System*

J. M. Heuser[1], Chr. J. Schmidt[1], A. Lymanets[2], R. Röder[3], and L. Long[3]
[1]GSI, Darmstadt, Germany; [2]FIAS, J. W. Goethe University, Frankfurt, Germany; [3]CIS, Erfurt, Germany

The first prototypes of a double-sided silicon microstrip detector for the CBM Silicon Tracking System (STS) have been produced in cooperation of GSI and the CIS Institute for Micro Sensors in Erfurt.

Low mass silicon tracking stations

The STS plays a central role in the CBM experiment as it will exclusively perform track and momentum measurements of the charged particles created at the target. One of its key requirements is an especially low-mass construction, essential for achieving momentum resolution down to about 1%. This is particularly challenging because the high charged-particle densities (up to 30 per cm^2) and the high interaction rates (up to 10 MHz) require a large number of detector channels equipped with fast power dissipating front-end electronics. The necessary cooling system introduces an excessive material budget. We have started to explore an STS concept that avoids the readout electronics and its cooling infrastructure in the aperture [1]. The building block of the STS tracking stations is a ladder structure made from double-sided microstrip detectors. It comprises several sectors of different strip lengths, realized with single or multiple chained sensors, that are individually read out at the periphery of the stations through very thin flat cables with high line density.

Microstrip detector prototype CBM01

A double-sided microstrip detector compatible with this STS concept has been designed in 2006 [2]. It addresses specific connectivity issues of the module. The prototype features a 15 degree stereo angle between the p and the n side strips. Their readout is performed in AC mode. Punch-through biasing structures are applied. On both detector sides, 1024 contact pads are arranged near the top and bottom edges. Their pitch of 50.7 μm matches the input of the n-XYTER chip that will be used during the initial prototyping phase. On the stereo (p-implanted) side, unconnected corner regions are avoided by linking the metal of every short strip with its matching partner in the opposite corner through a line on a second metal layer.

Production and first test results

In Summer 2007, a first batch of 24 4-inch wafers has been produced with 285 μm thick polished 5 kΩcm float zone material. The production involved a set of 17 masks. A wafer, seen on the photograph in Fig. 1, fits the 5.5 cm wide CBM01 detector, five test sensors with 256 by 256 orthogonal strips of 50.7 μm and 80 μm pitch, and several other test structures. Current-voltage and capacity-voltage characterizations have been performed. The requested specifications were achieved with high yield. Detailed measurements of other quantities, e.g. inter-strip capacitances, and in-beam tests are being prepared.

Next steps

For the next design iteration, systematic simulations of the detector technology have been performed. A technology wafer with various test structures has been submitted for production, now addressing improved radiation tolerance with poly-silicon bias structures, measures to increase the breakdown voltage, as well as several insolation technologies of n-strips.

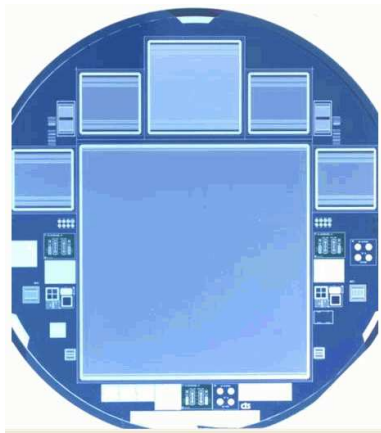

Figure 1: The CBM01 detector (center), five test detectors, and various test structures on a silicon wafer of 4" diameter.

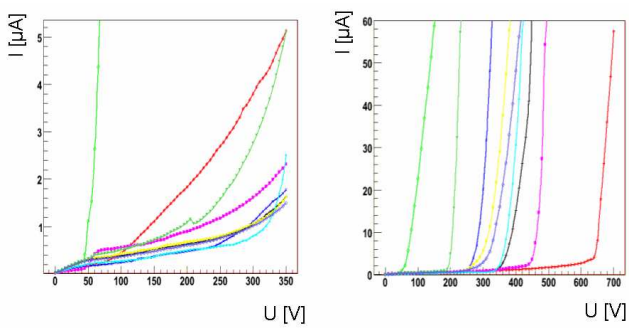

Figure 2: Current-voltage behaviour of 9 CBM01 sensors: Low voltage region (left) and breakthrough region (right).

References

[1] J. M. Heuser, Nucl. Instr. Meth. Res. A582 (2007) 910-915
[2] J. M. Heuser et al., GSI Report 2007-1 19

* Supported by EU/FP6 HADRONPHYSICS (see annex) and INTAS

Fast SIMDized Kalman filter based track fit*

I. Kisel† [1,2], S. Gorbunov[2], U. Kebschull[2], V. Lindenstruth[2], and W.F.J. Müller[1]
[1]GSI, Darmstadt, Germany; [2]KIP, University of Heidelberg, Germany

The core of data reconstruction in high energy physics is the Kalman filter. Therefore, the development of fast Kalman filter based reconstruction algorithms, making maximal use of the available processors power, is of utmost importance. A powerful feature supported by almost all up-to-date PC processors is a SIMD instruction set, which allows to pack several data items in one register and operate on all of them in one go, thus achieving more operations per clock cycle. A novel Cell processor extends the parallelization further combining a general-purpose PowerPC processor core with 8 streamlined coprocessing elements (SPEs) which greatly accelerate vector-processing applications.

In our investigation, after a significant memory optimization and a comprehensive numerical analysis, the Kalman filter based track fitting algorithm of the CBM experiment has been vectorized using inline operator overloading [1]. Thus the algorithm continues to be flexible with respect to any CPU family used for data reconstruction.

Stage	Time/track	Speedup
Initial scalar version	12 ms	—
Approximation of the field	240 μs	50
Optimization of the algorithm	7.2 μs	35
Vectorization	1.6 μs	4.5
Porting to SPE	1.1 μs	1.5
Parallelization on 2 Cells	0.1 μs	10
Final simdized version	0.1 μs	120000

Table 1: Summarized stages of the porting procedure

Table 1 summarizes all stages of the investigation. The elimination of the magnetic field map and, as a result, the possibility to avoid access to the main memory increases the speed of the algorithm by up to 50 times. Optimization of the algorithm results in a 35 times faster performance. The vectorization stage, requiring both software and hardware changes, gives a speedup by a factor of 4.5. Porting to SPE resulted in 1.5 increase of the speed with respect to a Pentium 4 processor used at the previous stages. The last stage is another hardware improvement making use of all 16 SPEs of the Cell Blade computer and gives another 10 times speedup. In total the speed of the algorithm has been increased by a factor of 120,000.

* Work supported by the European Community-Research Infrastructure Activity under the FP6 "Structuring the European Research Area" programme (HadronPhysics, contract number RII3-CT-2004-506078) and by the BMBF Project "FAIR-CBM: Entwicklung von schnellen und leistungsfähigen Methoden für Ereignisselektion"

† I.Kisel@gsi.de

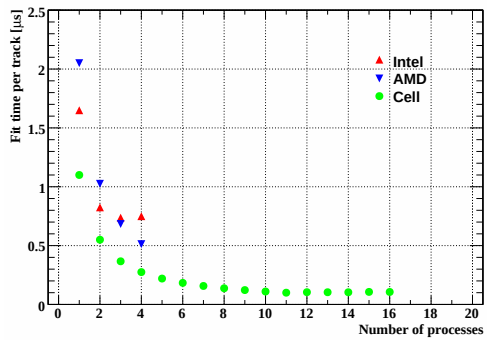

Figure 1: Fit time per track for the Intel, AMD and Cell based computers running different number of processes in parallel

We have compared the timing performance of the simdized version of the Kalman filter based track fitting routine running on three different CPU architectures: Intel[1], AMD[2] and Cell[3]. Both the Intel and the AMD based personal computers are treated by the operating system as having 4 processors each. Figure 1 shows that the hyper-threading of the Intel Xeon processor does not improve the performance in this particular case of the fitting procedure. In contrast, the dual core technology of the AMD Opteron processor shows stability of the timing performance due to its NUMA architecture. In the Cell Blade computer all 16 SPEs work completely independently and in parallel. They show a constant speed of the algorithm per processing unit up to 11 processes. For more processes, the speed is slightly reduced, presumably due to the large data flow through the element interconnect bus. In general, despite of having significant differences in architecture and clock rate, all computers have shown a similar speed of the algorithm per processing unit.

The SIMDized Kalman filter based fitting routines have been also included into the cellular automaton track finder of the CBM experiment, resulting in an increase of the reconstruction speed by a factor of 1,000 with respect to the initial scalar version running on the same Pentium 4 based computer.

References

[1] S. Gorbunov, U. Kebschull, I. Kisel, V. Lindenstruth and W.F.J. Müller, *Fast SIMDized Kalman filter based track fit*. Comp. Phys. Commun., 2008, in press.

[1] `lxg1411` (2 Intel Xeon with HT, 2.66 GHz) at GSI.
[2] `eh102` (2 Dual Core AMD Opteron 265, 1.8 GHz) at KIP.
[3] `blade11bc4` (2 Cell Broadband Engines, 2.4 GHz) at the IBM Laboratory Böblingen.

Implementation of a Hough Tracker for CBM*

C. Steinle[1], A. Kugel[1], and R. Männer[1]

[1]University of Mannheim, Department of Computer Engineering V, 68131 Mannheim, Germany

Abstract:In this report we describe the ongoing process on the Hough Transform which can be used for the tracking of particles in the CBM STS detector.

Hough Transform

The Hough transform is a global method for track finding. All STS detector hits have to be transformed into a parameter space according to the components of the track momentum p (θ, $-\frac{q}{p_{xz}}$, γ).This leads to our 3D Hough transform [1].

The hardware algorithm structure and the block diagram of the data path in front of the histogram can be found in [2]. The strategy for the histogram usage can be found in [1]. The implementation of the final parts is not developed yet in hardware. All investigated concepts are at first suitable for a single chip FPGA implementation. But because of the limited resources of such a chip and the huge algorithm resource requirements, we adapted the algorithm to be also suitable for a multi chip system. This system is depicted in figure 1. Within this concept it is now possible to balance the hardware resources with regard to the necessary system speed which is defined by the data input and the number of parallel used tracking systems. In this case, we can use also the flexibility of the Hough tracking algorithm to implement the different units on different platforms like FPGA or CELL BEs, because we can use different parallelism levels.

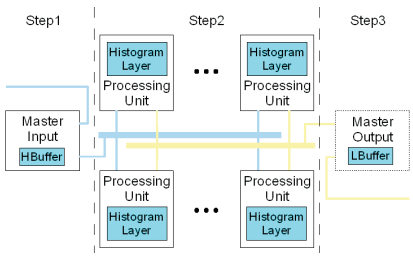

Figure 1: System design

If we think about such a FPGA system we can use all the single FPGA strategies just on different chips connected with a network. A common CELL BE has, except of the final LBuffer, resources for all mentioned units on a single chip. Further on with the usage of a CELL BE, it is easy to develop and proof the networking concept. So a cheap and rapid prototyping system is found by the Playstation3 system. It is obvious that the possible parallelism level on such a system is different compared to the FPGA. Here the major used parallelism is given by the fact that the histogram entry for one transformed hit is a plane in consecutive layers. So as we have 128 bits ALU width, we can insert a plane in at the utmost 16 consecutive layers in parallel. So our next step belonging to the hardware is the implementation of the developed concepts on a Playstation3 system to proof them. Further on the algorithm's final stage has to be developed and implemented in a HDL for a FPGA.

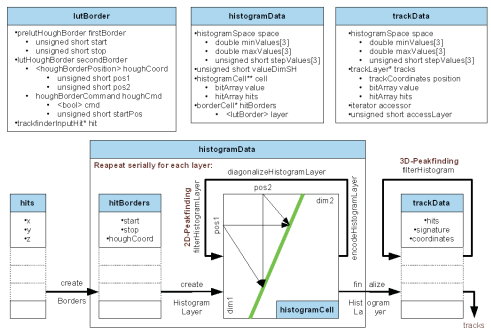

Figure 2: Software design

The software simulation of the Hough tracking algorithm is setup and ready for use in the CBMROOT framework. Figure 2 depicts the software design of the algorithm. The CBMROOT module 'htrack' contains the Hough tracking algorithm and many analyses to help adopting the parameters of the algorithm. Further on there are internal analyses to check and verify each step of processing. A summary of all implemented analyses can be found in the manual of the module which is actually in a reviewing state. Additionally the external interfaces are illustrated in a separate how-to which is also in a reviewing state. Our next step in software is to use an automatic analysis to produce an optimal peak finding geometry. Further on these two transformation formulas should be exchangeable to use the 4^{th} order Runge-Kutta method for improving the track model as mentioned in [2].

References

[1] J. Gläss, C. Steinle, R. Männer, "Tracking in the Silicon Tracker System of the CBM Experiment using Hough Transform", RT2005, June 2005, Stockholm, http://www.sysf.physto.se/RT2005/.

[2] C. Steinle, A. Kugel, R. Männer, "Implementation of a Hough Tracker for CBM", CBM Progress Report 2006, February 2007.

* Work supported by EU/FP6 HADRONPHYSICS

D^+, D_s^+ and Λ_c decay feasibility study in the CBM experiment

I. Vassiliev[1], S. Gorbunov[2], I. Kisel[1,2], S. Seddiki[1,3], I. Sevastiuk[4], and the CBM Collaboration

[1]GSI, Darmstadt, Germany; [2]KIP, Ruprecht-Karls University, Heidelberg, Germany; [3]IPHC, Institut Pluridisciplinaire Hubert Curien, Strasbourg, France; [4]NTSU, National Taras Shevchenko University, Kiev, Ukraine

A measurement of the different charmed mesons, but also the Λ_c would be important for getting a solid estimate on the total charm production cross section at threshold. The $D^{\pm}$-mesons, the $D_s^{\pm}$ and the Λ_c-barions have lifetimes of 312 μm, 123μm and 59μm respectively. Therefore, the most important ingredient in their identification is a precise detection of the secondary decay vertex. For this purpose the high resolution Micro-Vertex Detector (two MAPS detectors of 150 μm) is used in order to suppress the background of kaons and pions emitted from the primary vertex. No kaon or pion identification with TOF is applied, however, it is important to use the time-of-flight measurement in order to reject or select (for Λ_c signal) the proton tracks from the sample.

In order to reconstruct the charmed hadrons with a reasonable signal-to-background ratio, a set of mainly topological cuts is placed on single tracks as well as on reconstructed vertices. As example, figure 1 presents the resulting background suppression of such cuts for the 3-particle decay of the D^+ meson. Single track χ^2_{prim} cuts mainly rely on the back-extrapolation of the tracks to the primary vertex requiring them to miss it. For the reconstructed charmed mesons on the other hand, the back-extrapolation is required to stem from the primary vertex which allows to reduce strongly the geometrically reconstructed 3-particle vertices.

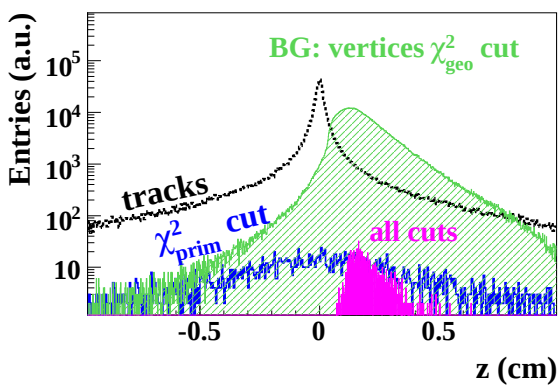

Figure 1: Distribution of single tracks and secondary vertices along the beam line for $D^+ \to K^-\pi^+\pi^+$ reconstruction: All primary tracks (black line) and those selected by χ^2_{prim} cuts as single track candidates for D^+ daugthers (blue). 3-particle secondary vertices after first geometrical cuts (light green), and finally selected D^+ candidates including more stringent topological cuts (magenta).

The reconstructed invariant mass spectra of all investigated charmed hadrons and decay channels in central Au+Au collisions at 25 AGeV beam energy are shown in figure 2. Numbers for efficiency and acceptance are presented in table 1. Multiplicities have been taken from HSD or/and Statistical models.

	D^+	D_s^+	Λ_c
decay channel	$K^-\pi^+\pi^+$	$K^-K^+\pi^+$	$pK^-\pi^+$
multiplicity HSD	$4.2 \cdot 10^{-5}$	$5.4 \cdot 10^{-6}$	-
multiplicity SM	$8.4 \cdot 10^{-5}$	$1.4 \cdot 10^{-4}$	$4.9 \cdot 10^{-4}$
branching ratio	9.5%	5.3%	5.0%
geom. acceptance	39.6%	29.6%	53.0%
reconst. efficiency	97.5%	97.5%	97.6%
z-resolution	60 μm	67 μm	70 μm
total efficiency	4.2%	1.0%	0.5%
$\sigma_m[MeV/c^2]$	11.0	12.0	12.0
$S/B_{2\sigma}$ ratio	9.0	0.3	0.25
yield (10^{12}central)	162K	72(2.9)K	107K

Table 1: Acceptance and efficiencies, mass resolution, and signal-to-background ratio (S/B) in a $2\sigma_m$ region around the peak for open charm reconstruction in central Au+Au collisions at 25 AGeV beam energy. The total efficiency is calculated from the product of geometrical acceptance, reconstruction and cut efficiencies.

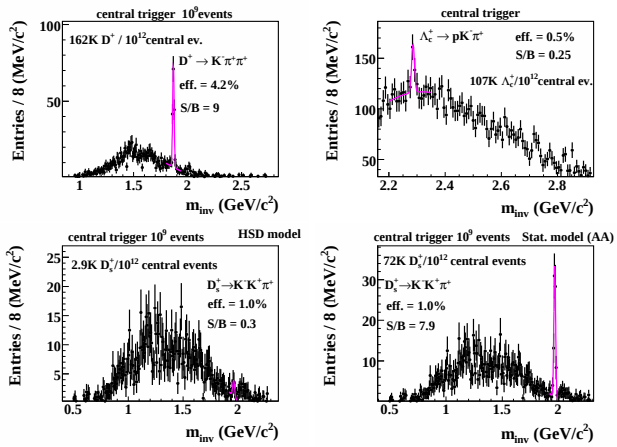

Figure 2: Reconstructed charmed hadrons in 10^9 central $Au + Au$ collision at 25 AGeV. $D^+ \to K^-\pi^+\pi^+$ (upper left), $\Lambda_c \to pK^-\pi^+$ (upper right) and $D_s^+ \to K^-K^+\pi^+$ HSD-model prediction (lower left) and Statistical model (lower right)

D^0 decay feasibility study in the CBM experiment

I. Vassiliev[1], S. Gorbunov[2], I. Kisel[1,2], and the CBM Collaboration
[1]GSI, Darmstadt, Germany; [2]KIP, Ruprecht-Karls University, Heidelberg, Germany

One of the major experimental challenges of the CBM experiment is to trigger on the displaced vertex of the D-meson via hadronic decay modes $D^0 \rightarrow K^-\pi^+$ and $D^0 \rightarrow K^-\pi^+\pi^+\pi^-$ in the environment of a heavy-ion collision. This task requires fast and efficient track reconstruction algorithms and high resolution secondary vertex determination. Particular difficulties in recognizing the displaced vertex of the rare D meson decays are caused by weak K^0_S, Λ- and Σ-barion and hyperon decays which produce displaced vertices 1 cm downstream the target (the mean life time of the D^0 mesons is $c\tau = 122.9$ μm), very low multiplicity of the D meson production, low branching ratios and multiple scattering in the beam pipe and detectors.

To study the feasibility of D^0 mesons measurement in the CBM experiment a set of 10^4 central Au+Au UrQMD events at 25 AGeV have been simulated. Two main branches of D^0 decay $K^-\pi^+$ or $K^-\pi^+\pi^+\pi^-$ have been added to each event in order to simulate a signal in the environment of background hadrons. Simultaneous measurement of two decay channels of the same particle give the CBM experiment a unique opportunity to reduce systematic uncertainties. The STS geometry with 2 MAPS and 6 double-sided strip detectors has been used. The first MAPS detector have been placed at 10 cm downstream the target in order to reduce radiation damage. The primary vertex was reconstructed with high accuracy (5.7 μm in z direction, 1.0 μm in x and y) from about 450 tracks fitted in the STS with a non-homogeneous magnetic field by the Kalman filter procedure similar described in [1].

A novel algorithm has been developed to reconstruct the D^0's life time and the decay length together with their corresponding errors. The algorithm first finds the primary vertex using all reconstructed tracks, and then the D^0 meson is reconstructed from its two daughter particles in case of $D^0 \rightarrow K^-\pi^+$ or from its four daughter particles in case of $D^0 \rightarrow K^-\pi^+\pi^+\pi^-$ using the primary vertex as the production point. Because of originating from a displaced decay vertex, the D^0 meson daughter tracks have a non-vanishing impact parameter at the target plane. Since the majority of the primary tracks have very small impact parameter, a significant part (99%) of the background tracks was rejected using a cut on their χ^2 distance to the primary vertex. The combinatorial background is suppressed mainly by the vertex χ^2_{geo} and χ^2_{topo} cut for good quality detached vertices. Numbers for multiplicity, cut efficiencies, acceptance, z-vertex resolution, mass resolution, signal to background ratios and yields per 10^{12} central interactions are presented in the table 1.

After applying all cuts the $D^0 \rightarrow K^-\pi^+$ reconstruction efficiency is 3.25% and $D^0 \rightarrow K^-\pi^+\pi^+\pi^-$ is only 0.37% due to lower geometrical acceptance and applying χ^2 distance to the primary vertex cut for all four daughter particles. From the other hand, requirement of good quality detached vertices created by 4 particles significantly decrease combinatorial background as one can see in Figure 1. The shape of the background in the signal IM region has been estimated using the event mixing technique. The resulting background plus D^0 and $\bar{D}^0$ signal spectrums are shown. The signal to background ratio is about 4.4 for $D^0 \rightarrow K^-\pi^+$ and about 7.1 for $D^0 \rightarrow K^-\pi^+\pi^+\pi^-$ decay modes.

	$D^0 + D^0$	D^0
decay channel	$K^-\pi^+$	$K^-\pi^+\pi^+\pi^-$
multiplicity	$1.5 \cdot 10^{-4}$	$4.0 \cdot 10^{-5}$
branching ratio	3.8%	7.7%
geom. acceptance	55.7%	19.3%
reconst. efficiency	98%	97.7%
z-resolution	54 μm	82 μm
total efficiency	3.25%	0.37%
$\sigma_m[MeV/c^2]$	11.0	12.0
$S/B_{2\sigma}$ ratio	4.4	7.1
yield	52KD^0+174K$\bar{D}^0$	10KD^0+32K$\bar{D}^0$

Table 1: Acceptance and efficiencies, mass resolution, and signal-to-background ratio (S/B) in a $2\sigma_m$ region around the peak for open charm reconstruction in central Au+Au collisions at 25 AGeV beam energy. The total efficiency is calculated from the product of geometrical acceptance, reconstruction and cut efficiencies.

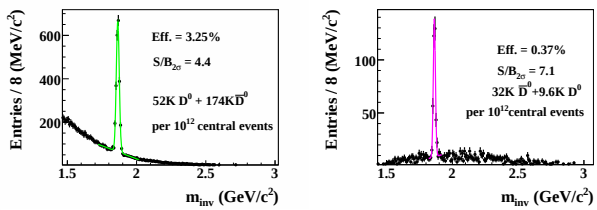

Figure 1: The D^0+$\bar{D}^0$ (left) and $D^0 \rightarrow K^-\pi^+\pi^+\pi^-$ (right) signal and combinatorial background invariant mass spectra. The estimated signal and combinatorial background corresponds to 10^9 central events.

References

[1] S. Gorbunov, I. Kisel and Iouri Vassiliev, Analysis of D^0 Meson Detection in Au+Au Collisions at 25 AGeV, CBM-PHYS-note-2005-001, June 2005.

Open charm trigger feasibility study in the CBM experiment

I. Vassiliev[1], I. Kisel[1,2], and the CBM Collaboration
[1]GSI, Darmstadt, Germany; [2]KIP, Ruprecht-Karls University, Heidelberg, Germany

One of the most important experimental task of the CBM experiment is to identify D-mesons and Λ_c-barions at event rates up to 10 MHz. Therefore, open charm trigger for the CBM experiment is required to effectively reject background events. Events containing very rare D-mesons decay or Λ_c decay should be accepted by the trigger with a maximal efficiency. Open charm particles decays are supposed to be detected via hadronic decay modes $D^0, \bar{D}^0 \rightarrow K^{\mp}\pi^{\pm}$, $D^{\pm} \rightarrow K^{\mp}\pi^{\pm}\pi^{\pm}$, $D_s^{\pm} \rightarrow K^{\mp}K^{\pm}\pi^{\pm}$ and $\Lambda_c \rightarrow pK^{-}\pi^{+}$. Lifetimes of the open charm particles are in the range between 60 μm and 312 μm, therefore the most prominent characteristic of their identification is a precise detection of the secondary decay vertex several mm downstream the target. The presence of a detached kaon in any of the shown decay modes is another important feature. Two open charm trigger configurations have been proposed: Detached Kaon Trigger requirering STS, TOF, and global tracking; Detached Vertex Trigger based on the STS detector only. To study feasibility of the open charm trigger a set of 10^4 central and minimum bias Au+Au UrQMD events at 25 AGeV have been simulated. The STS geometry with 2 MAPS and 6 double-sided strip detectors has been used.

Detached Kaon Trigger is the simplest one. On the other hand central UrQMD event at 25 AGeV contains about 40 K^+ and 13 K^-. Some of the tracks, identified as a $K^{\pm}$ by the TOF and the STS have large impact parameter χ^2_{prim} distance to the primary vertex due to multiple scattering effect in the target and STS detector. Even relatively strong $\chi^2_{prim} > 3\sigma$ trigger cut doesn't permit to reject more than 32% (rejection factor 1.47) of the central events.

In order to achieve a rejection factor of at least 5 for central events the Detached Vertex Trigger (DVT) has been proposed. The DVT algorithm is shown on the Figure 1.

The first part of the DVT algorithm includes four stages: track finder, track fitter, primary vertex finder and charm track candidates selection where about 15 tracks per central UrQMD event are selected. The next two stages are decision making part of the algorithm. They include the open charm vertex candidate creation from the selected negative and positive tracks. Then the pairing is done to create if possible the particles with a good quality geometrical vertex $\chi^2_{2geo} < 3\sigma$ along the z-axis between 250 μm and 1 cm downstream the primary vertex. The selected tracks (about 5 per central UrQMD event) are marked at this stage. Analysis shows that majority of the selected tracks are multiple scattered primary tracks and the ones providing from K^0_S or Λ decays. Figure 2 shows the invariant mass of the selected particles with clearly seen peaks from K^0_S or Λ decays.

Event is rejected by the trigger if no good quality geometrical vertex is found. In order to keep D^+, D_s-mesons and Λ_c-barions 3-prong vertices are analyzed at the last stage. If at least one 3-prong vertex with $\chi^2_{3geo+topo} < 3\sigma$ is found, then the event is accepted. Otherwise the algorithm makes a step backward and checks if the event contains D^0. This decision is based on the invariant mass (IM) check (IM of the selected particles are above 1.3 GeV/c) and 2-prong topological constrain vertex with $\chi^2_{2topo} < 3\sigma$. Event is accepted if these two conditions are fulfilled. Currently the DVT gives the rejection factor of 5.2 for central and about 40 for minimum bias Au+Au UrQMD events at 25 AGeV.

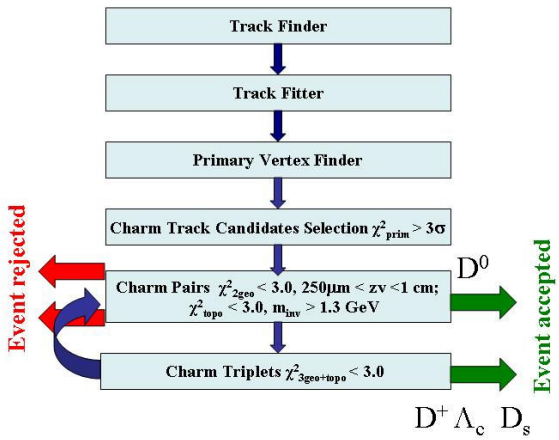

Figure 1: Block-diagram of the Detached Vertex Trigger.

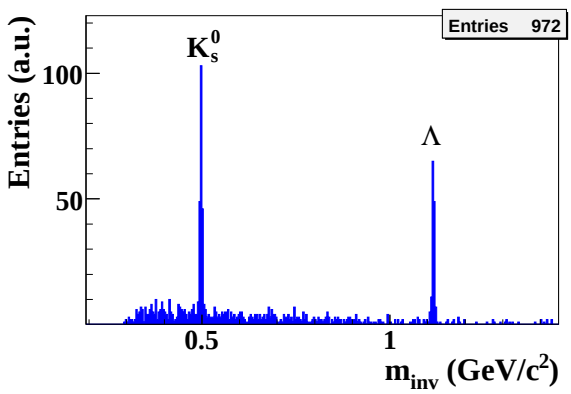

Figure 2: Invariant mass of the selected particles. K^0_S and Λ decays up to few mm downstream the target are the main sources of the background.

Open charm reconstruction with the CBM Micro Vertex Detector*

C.Dritsa[1,2] , M.Deveaux[2,3] and F. Rami[2]
[1]GSI, Darmstadt, Germany ; [2]IPHC, Strasbourg, France; [3]IKF, Frankfurt, Germany

The study of open charm production in nucleus-nucleus collisions is one of the major physics issues of the CBM experiment planned at the future FAIR facility. A Micro Vertex Detector (MVD) based on Monolithic Active Pixel Sensors (MAPS) [1] has been proposed to reconstruct open charm hadrons by identifying their secondary decay vertex. Simulations studies were undertaken in the past to demonstrate the feasibility of this approach for $D^0 \rightarrow K^- \pi^+$ reconstruction in central Au+Au collisions [2, 3]. However, the statistics used in those early studies was limited due to technical constraints. Moreover, only one beam energy (25 AGeV) was addressed so far.

Within this work, a new software architecture allowing for massive parallel simulation based on event mixing was developed. This allowed us to improve the statistics reached by more than one order of magnitude. Moreover, the expected performance of D^0 reconstruction was also investigated at both the lower and higher ends of the FAIR energy range (respectively, 15 and 35 AGeV)

The detector geometry used for this study consists of 3 MAPS stations at 10-15-20cm distance from the target, 1 hybrid station at 30cm and 5 strip detectors at 50-62.5-75-87.5-100cm. The thickness of MAPS stations was assumed to be 200µm silicon equivalent. Hybrid pixels and strip detectors had a thickness of 750µm and 400µm silicon respectively. The spatial resolution of MAPS was set to 5µm, which corresponds to a detector with small pixels and digital readout. By using an event mixing technique we reached an equivalent background of a few hundreds of millions of central Au+Au collisions. 10^4 $D^0 \rightarrow K^- \pi^+$, each one being embedded in a central event, provided the signal statistics used as input of the simulation. The daughter particles were identified as originating from a decay vertex displaced from the primary vertex. Several selection cuts were applied [3] to reject the combinatorial background and to increase the Signal-to-Background ratio. The values of those cuts were set using an iterative algorithm that aims to maximize the significance of the signal [3]. The reconstructed invariant mass distributions of signal and background were normalised to match the D^0 production multiplicity and the branching ratio for $D^0 \rightarrow K^- \pi^+$ (3.8 %). The results, expressed in terms of the Signal-to-Background ratio (S/B) and the number of reconstructed D^0-mesons (N_{D0}) within the MAPS detector lifetime, are summarized in Table 1 for all 3 beam energies (15, 25 and 35 AGeV).

The secondary vertex resolution of the MVD depends strongly on multiple scattering. In consequence, the thickness of the MVD stations is a crucial parameter for the measurement of D^0 particles with CBM. This effect was also investigated in the present work. A dedicated simulation study was performed at 25 AGeV, assuming an upper limit for the thickness (500 µm silicon-equivalent) of the MVD stations. In this study, an updated geometry composed of 2 MAPS stations and 6 strip detector stations was used. The results show a S/B ≈ 0,3, with a D^0 detection efficiency of 0,7% and about 3000 D^0–mesons being reconstructed during the detector's lifetime.

Table 1: Expected performances of the CBM experiment for $D^0 \rightarrow K^- \pi+$ reconstruction in central Au+Au at different beam energies. The MAPS detector lifetime is expressed in terms of central Au+Au collisions.

Beam Energy (AGeV)	D^0 Multiplicity	MAPS detector lifetime	S/B	N_{D0}
15	$1{,}2\times10^{-5}$	$\sim1{,}4\times10^{11}$	0,2	1.000
25	$1{,}2\times10^{-4}$	$\sim1{,}2\times10^{11}$	0,9	13.000
35	$1{,}2\times10^{-3}$	$\sim1{,}1\times10^{11}$	8	77.000

Substantial uncertainties of about an order of magnitude remain for the above mentioned results. This is mainly because the production multiplicities for D^0-mesons are poorly known (the values assumed here are listed in Table 1). However, it is justified to state that CBM may measure D^0-mesons with reasonable statistics at the highest beam energy (35 AGeV). This holds also for 25 AGeV, provided that the D^0 multiplicity is not significantly lower than the one assumed in the present simulations. At the lowest energy (15 AGeV), D^0 detection seems feasible but the number of reconstructed particles may be insufficient for detailed physics studies.

The present study underlines also the importance of using thin (~200µm silicon equivalent) MVD stations. A significant drop in performances (about a factor of 4 in the number of reconstructed D^0-particles and a factor of 3 in the S/B-ratio) is observed when assuming the more conservative material budget of 500µm silicon equivalent. A minimized material budget of the MVD appears therefore as a crucial point for the success of open charm physics in the CBM experiment.

References

[1] CBM Collaboration, Technical Status Report, 2005.
[2] I. Vassiliev et al, GSI Scientific Report, 2005.
[3] M. Deveaux, PhD, University Strasbourg/Frankfurt (2008), submitted.

*This work was supported by BMBF (06FY1731) and GSI (F&E)

Systematic investigations on the di-electron setup of CBM*

K. Antipin[1], C. Höhne[2], and H. Appelshäuser[1]

[1]Institut für Kernphysik, University of Frankfurt, Germany; [2]GSI Darmstadt, Germany

Di-leptons are considered an important observable for the understanding and characterization of high density baryon matter created in A+A collisions. Since leptons leave the fireball without further interaction, their study provides information on in-medium properties of vector mesons or on the restoration of chiral symmetry.

In this report we focus on the electron decay channel of the low-mass vector mesons and will report on systematic investigations on an optimization of the di-electron setup of CBM and establish a limit on the pion misidentification. The main challenge in di-electron spectroscopy is the efficient reduction of background electrons which dominantly stem from π^0 - Dalitz decays and γ conversions in the target. This study is fully based on a MC study of central Pb-Pb collisions at 25 AGeV.

In the currently applied background suppression strategy [1] first a cut of $M_{\rm inv} < 0.025\,{\rm GeV}/c^2$ is placed in order to reject tracks from reconstructed γ-conversion pairs. Afterwards a topological cut on the distance of identified tracks to the closest hit of not accepted tracks in the first tracking station (MAPS, 10 cm behind the target) is applied. In order to increase the power of this cut the following modifications were investigated: The magnetic field between target and first MVD station was systematically reduced and electron identification (e-ID) in the first MVD was assumed. In Figure 1 is shown the distance of identified electron tracks to the nearest hit of not accepted tracks for different sources of electron tracks. Two cases are presented: 0 Tm field integral in the first 10 cm (solid line) and e-ID in the 1^{st} MVD with the standard field of CBM reduced to 70% corresponding to a field integral of 0.07 Tm (dashed line). As the mean distances of electrons from π^0 or γ conversion differ from the ρ-meson a cut can be placed to reject background. The field integral in the first 10 cm was varied from 0% to 100% of 0.07 Tm and for each field value a specific cut was established. In Figure 2 is shown the resulting fraction of rejected electrons from π^0 and γ conversion. Electrons from the ρ meson are rejected on a constant 20% level for the configuration with e-ID in the first MAPS detector and with a larger and further increasing fraction without.

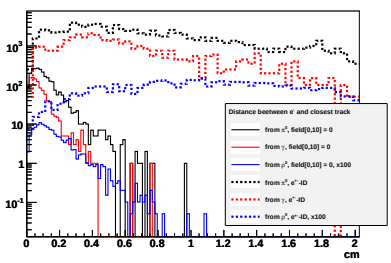

Figure 1: Distance to hits from the closest not accepted track with e-ID and with a field integral of 0 Tm in the first 10 cm.

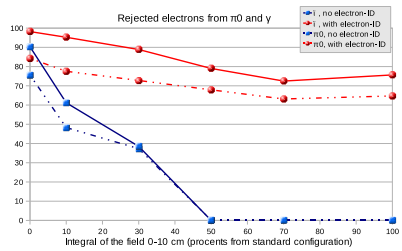

Figure 2: Rejected electrons from π^0 and γ conversion with and without e-ID versus a given field integral in the first 10 cm (100% correspond to 0.07 Tm).

However, the signal to background ratio in the e^+e^- invariant mass range from 0.2-0.9 GeV/c^2 is increased only by a factor of 2 under these conditions, i.e. with e-ID and field integral less then 0.02 Tm, and remains nearly unaffected without e-ID but reduced field.

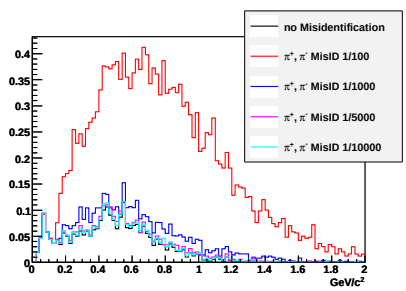

Figure 3: Combinatorial background assuming different levels of pion misidentification.

In a second study, a limit on the pion rejection power was established. The combinatorial background was calculated applying all cuts as established in [1] and assuming different pion misidentification levels, see Figure 3. The fraction of misidentified pions in the background amounts to 85%, 37%, 11.2%, 6.8% respectively. At a π-misidentification of $1/5000$ or better the combinatorial background is dominated by physical sources (88.8%).

References

[1] T. Galatyuk et al., GSI report 2005, FAIR-QCD-CBM-06.

* Work supported by BMBF, GSI, and the Helmholtz Research School H-QM

CBM-RICH layout optimization *

C. Höhne[1]
[1]GSI, Darmstadt, Germany

The RICH detector in CBM shall provide electron identification together with the TRD detectors for the measurement of low-mass vector mesons and charmonium in the di-electron decay channel. Both observables are considered key probes for the study of compressed baryonic matter in heavy ion collisions. A RICH design based on first general considerations has been developed and studied in detector simulations and feasibility studies [1, 2]. These studies include full event reconstruction and electron identification in the proposed CBM setup. Current results clearly demonstrate the feasibility of these measurements [2]. Combining RICH, TRD and TOF information a pion suppression of 10^{-4} at an electron identification efficiency of 80% is reached for 2 GeV/c $< p <$ 8 GeV/c. Efficiencies and signal-to-background ratios for reconstructed low-mass vector mesons and charmonium are very promising [3, 4]. However, the layout of the RICH detector was only implemented based on a first, educated guess. An optimization of the RICH in particular with respect to minimizing its dimensions is awaiting. This process has been started and first results will be presented in this report.

In order to keep the number of detected photoelectrons per electron ring when reducing the overall length of the detector a radiator gas with larger refractive index has to be chosen to compensate the lower yield of Cherenkov photons. We investigated CO_2 instead of N_2, see table 1. The larger refractive index of CO_2 slightly lowers the threshold of Cherenkov light production for pions; otherwise both gases have similar, convenient properties. With mirrors of 3 m radius this allows to reduce the detector length by 30% resulting in an overall reduction of the RICH dimensions by a factor 2-3 (table 1, compact RICH) while keeping the same geometrical acceptance. The number of channels in the photodetector plane has been calculated based on the H8500 MAPMT from Hamamatsu. Considering the fact that the RICH acceptance so far has been kept rather large and has not yet been optimized with respect to the physics analysis, a total number of 64k channels corresponding to 1000 MAPMTs is realistic. A first design of a compact RICH detector based on the parameters given in table 1 was implemented in the CBM simulation framework in order to study its characteristics. The layout is not yet optimized as rings still show strong distortions in the photodetector plane. Currently this reduces the efficiency of ring reconstruction from 90% to 75% and increases the ring radius resolution from 2% to 6%. With an optimized position of the photodetector plane we expect to reach the same performance as before. However, even with this reduced RICH performance a pion suppression factor of nearly 10^{-4} is again reached in combination with TRD and TOF information. Based on this first promising results we will continue developing an optimized, reduced RICH layout for CBM.

* Supported by EU/FP6 HADRONPHYSICS (see Annex)

	large RICH	compact RICH
radiator gas	N_2	CO_2
γ_{th}	41	33.3
p^{π}_{th} [GeV/c]	5.6	4.65
λ_{th} [nm]	< 160	~ 175
radiator length	2.5 m	1.76 m
full length	2.9 m	2.1 m
mirror radius	4.5 m	3 m
mirror size	$2(5.7 \cdot 2)$ m^2	$2(4.2 \cdot 1.4)$ m^2
	~ 22.8 m^2	~ 11.8 m^2
photodetector size	$2(3.2 \cdot 1.4)$ m^2	$2(2.4 \cdot 0.78)$ m^2
	~ 9 m^2	~ 3.7 m^2
No. of channels	$\sim$ 200k	$\sim$ 85k

Table 1: Comparison of layout parameters for the large and compact RICH detector. The size of the photodetector can be further reduced on account of the acceptance, the mirror would be reduced accordingly.

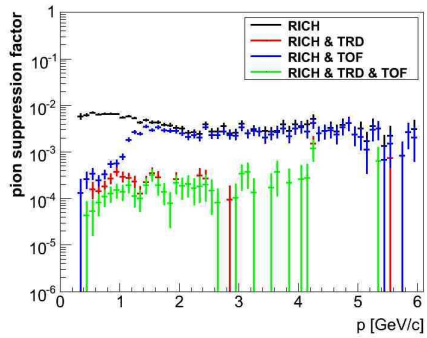

Figure 1: Pion suppression factor for central Au+Au collisions at 25 AGeV with the small RICH layout.

References

[1] C. Höhne et al., Nucl. Instr. Meth. A 553 (2005) 91.

[2] C. Höhne et al., Proceedings of 6th International workshop on RICH counters 2007, to be published in Nucl. Instr. Meth. A.

[3] T. Galatyuk et al., *Di-electron spectroscopy in CBM*, GSI Scientific Report 2007 and CBM Progress Report 2007.

[4] A. Maevskaya et al., *Charmonium reconstruction in CBM*, CBM Progress Report 2007.

Electron Identification in the Compressed Baryonic Matter (CBM) experiment

S. Das*[1] and C. Höhne[1]

[1]Gesellschaft für Schwerionenforschung mbH (GSI), Darmstadt, Germany

One of the key physics programs of CBM is to study the spectroscopy of both low and high mass vector mesons (namely ρ, ω, ϕ, J/Ψ, Ψ') through their di-electron decay channels. The first step towards this is the identification of electrons. In the current CBM set up, electron identification involves the Ring Imaging CHerenkov counter (RICH), the Transition Radiation Detector (TRD) and the Time Of Flight (TOF) detector. The information from RICH and TRD are used to identify the electrons and those from TOF help to suppress the pions in the identified electron sample. A software package has been developed to perform the electron identification. The methods and performance of electron identification after full event reconstruction will be presented in this report.

In the event reconstruction, particles are first tracked by the tracking detectors placed inside a dipole magnetic field providing the momentum of the tracks. The information from RICH, TRD and TOF is then associated to these tracks to form a global track.

RICH rings are found using ring reconstruction algorithms[1]. Next, the tracks are extrapolated from the last STS plane to the photodetector plane. Rings are associated to tracks choosing pairs with closest distance between track and ring centre. Rings with ring-track distance more than 1 cm are rejected as wrong matches. A set of ring quality cuts is also applied in order to reject fake rings. Finally, the electrons are identified choosing a range of radii of $\langle R \rangle \pm 3\sigma$, with $\langle R \rangle$ = 6.17 cm and σ = 0.14 cm. Pion rings leak into this band and are identified as electrons only from momenta of 8-10 GeV/c on.

While passing through the TRD planes, pions have only the specific energy loss (dE/dx) whereas electrons have additional energy loss by emission of transition radiation. The CBM electron identification framework provides three different methods to discriminate electrons from pions, based on their total energy loss, namely the Likelihood, the Wkn[2] and Artificial Neural Network methods.

In addition to the RICH and TRD, the information from TOF is also used to reject pions from the identified electron sample. The mass of charged particles is calculated from the length traversed by the particle and the time required to do that. A momentum dependent cut on m^2 is used to reject hadrons from the identified electron sample.

After the electron identification each of the identified tracks is associated to its available Monte Carlo information for quality assessment of the electron identification. The relevant quantities are defined as

$$\text{efficiency} = \frac{\text{identified true electrons}}{\text{electrons in RICH acceptance}} \qquad (1)$$

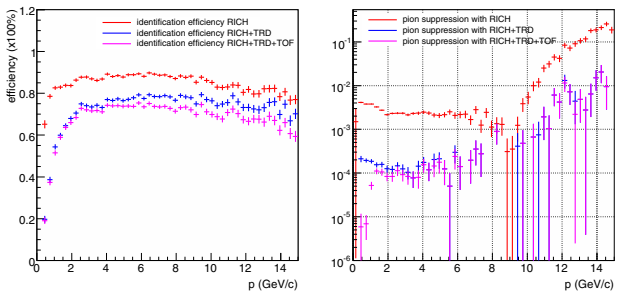

Figure 1: Efficiency of electron identification (left) and pion suppression factor (right) as function of momentum for central Au+Au collisions at 25 AGeV beam energy.

and

$$\text{pion suppression} = \frac{\text{pions identified as electrons}}{\text{pions in RICH acceptance}} \qquad (2)$$

The performance of the detectors as well as the electron identification software were studied with central Au+Au collisions at 25 AGeV beam energy, generated by UrQMD[3]. These events were tracked through the CBM detector system using GEANT3[4] and reconstructed afterwards. The electron identification efficiency as well as the π-suppression factor as function of momentum are shown in Fig. 1. With the combined information from all detectors we achieve an efficiency of 70% for momenta $>$ 2 GeV/c. The drop in efficiency towards low momentum results from tracking, ring finding efficiencies and TRD and TOF acceptance losses compared to RICH. Using the RICH alone, a π-suppression factor of 500 is achieved whereas after combining information from TRD and TOF, the π-suppression factor reaches up to $\sim 10^{-5}$ for low momentum. From these results it is clear that the use of TRD helps significantly to discard the wrongly identified pions as electrons from the identified electron sample and in addition to that the TOF brings down the π-suppression factor by an order of magnitude for momenta $<$ 2 GeV/c. The set of cuts for different detectors are being optimized to obtain the best values of these two quantities. The electron identification is expected to be further improved by an optimized combination of various detector information.

References

[1] S. Lebedev *et.al*, this report.

[2] P. Zrelov and V. Ivanov, NIM **A 310**, 623 (1991).

[3] S.A. Bass *et. al*, Prog. Part. Nucl. Phys. **41**, 255 (1998).

[4] http://wwwasd.web.cern.ch/wwwasd/geant/

* S.Das@gsi.de (Supported by EU/FP6 HADRONPHYSICS)

Di-electron spectroscopy in CBM*

T. Galatyuk[1], S. Das[1], and C. Höhne[1]
[1]GSI, Darmstadt, Germany

The emission of lepton pairs out of the hot and dense collision zone of heavy ion reactions is a promising probe to study the electromagnetic structure of hadrons under extreme conditions. The reconstruction of low-mass vector mesons (ρ^0, ω, ϕ) is one of the prime tasks of the CBM experiment. In this report, we present the status of simulations of the electron pair measurement in CBM and compare the expected performance to that of previous or existing dilepton experiments.

The general challenge of di-electron measurements in heavy-ion collisions is to cope with the large background of electrons originating from other than the desired sources. This is in particular difficult in the CBM spectrometer since electron identification is not provided in front of the magnetic field required for tracking. This leads to a considerable material budget in front of the RICH detector.

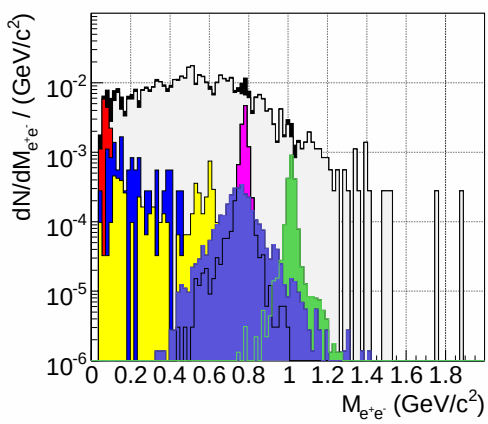

Figure 1: Di-electron invariant mass spectra for central $Au + Au$ collisions at a beam energy of 25 AGeV. Black area: unlikesign combinations of e^+ and e^-, grey: combinatorial background. Red: π^0, dark blue: η, yellow: ω-Dalitz, magenta: ω, green: ϕ, violet: ρ^0. The simulated data sample (200 k events) corresponds to 10 seconds of beam time.

An important requirement for efficient background rejection is electron identification with high efficiency and purity. In CBM, the RICH detector in combination with TRD and TOF provides a π-suppression factor of 10^4 at 50 electron efficiency for momenta below 2 GeV [1]. With such high a purity of the identified electron sample, the dominant background sources are random combinations of e^- and e^+ from π^0-Dalitz decay and γ conversion, the latter mostly in the target. Several topological cuts have been developed to reduce the background [2]. The invariant mass spectrum of dielectron pairs including full event reconstruction and electron identification after applying all cuts is shown in Figure 1. The signal-to-background (S/B) ratio in a ± 2 σ_m range around the ω pole mass is 0.3 at a signal efficiency of 6.7%. For the invariant mass region above 200 MeV/c^2 a S/B ratio of 1/16 is obtained.

A strong excess of di-lepton pairs over the yield expected from neutral meson decays was observed by hitherto existing dilepton experiments [3, 4, 5]. From a parametrisation of the published enhancement factors as function of $\sqrt{s}$ and $dN_{ch}/d\eta$, we expect this factor to be not smaller than 6 in central Au+Au collisions at 25 AGeV. For CBM, we thus deduce a S/B ratio of $6 \times 1/16$ for $m_{inv} > 200\,\mathrm{MeV}/c^2$. As Figure 2 demonstrates, this performance is well competitive with previous experiments measuring di-leptons in heavy-ion collisions at similar charged track densities.

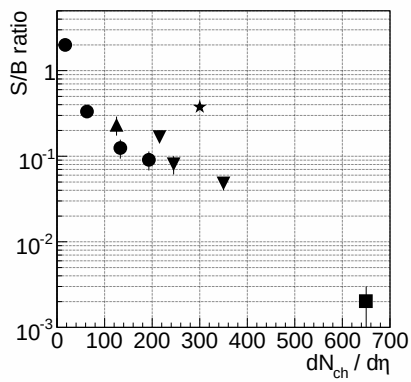

Figure 2: Signal-to-background ratio for m_{inv} larger than 200 MeV$/c^2$ as function of $dN_{ch}/d\eta$. Circle: NA60 data; triangle: CERES data, square: PHENIX data; star: CBM assuming an enhancement factor of 6.

References

[1] S. Das et al., *Electron identification with RICH and TRD in CBM*, this report

[2] T. Galatyuk et al., *Strategies for electron pair reconstruction in CBM*, GSI Scientific Report 2005/FAIR-QCD-CBM-06

[3] D. Adamova et al. (CERES collaboration), *Enhanced Production of Low-Mass Electron-Positron Pairs in 40-AGeV Pb-Au Collisions at the CERN SPS*, Phys. Rev. 91 (2003) 042301

[4] S. Damjanovic for the NA60 collaboration., *First measurement of the ρ spectral function in nuclear collisions*, arXiv:nucl-ex/0609026 v1, 16 Sep 2006

[5] S. Afanasiev et al., (PHENIX collaboration), *Enhancement of the dielectron continuum in Au+Au collisions at $\sqrt{s_{NN}}$=200 GeV*, atXiv:0706.3034v1[nucl-ex], 20 Jun 2007

* Work supported by EU-FP6 HADRONPHYSICS and INTAS

J/ψ and Ψ' detection in the di-electron decay channel in CBM

A.Maevskaya[2], A.Kurepin[2], and C.Höhne[1]
[1]GSI, Darmstadt, Germany; [2]INR RAS, Moscow, Russia

The study of the energy dependence of charmonium production in heavy ion collisions got new interest recently due to the new measurements at RHIC showing that the anomalous J/ψ suppression for central events is about the same as for NA50 at much lower energies [1]. So far this effect is difficult to explain in theoretical models. A measurements of charmonium states at CBM energies (15-35 AGeV) could thus contribute to an understanding of charonium production. New results from the NA50 experiment on Ψ' production in Pb-Pb collisions at different centralities [2] show that the anomalous suppression is much stronger than for J/ψ. The deviation from normal suppression starts at less central collisions than for J/ψ and is similar for S-U and Pb-Pb systems. Hence Ψ' production at CBM is desirable in spite of the lower BR compared to J/ψ. In this report the feasibility of Ψ' measurements is studied for the first time. Multiplicities of J/ψ and Ψ' production were taken from the HSD model[3].

The simulations were perfomed with an implemetaion of the standard CBM detector layout. Decay electrons from J/ψ and Ψ' (simulated by PLUTO) were embedded in central Au+Au collisions generated by UrQMD. Due to the very low J/ψ and even more rare Ψ' rate the so called "superevent" technique was used for background simulations [5]: all electrons were mixed together producing all possible unlike sign pairs. Background studies show that the most importand background source are dieletrons from γ conversion in the gold target. For reducing this effect the target thickness was set to 25μm. The STS detector was implemented using Si strip detectors only. Full event reconstruction in CBM was done using the currently available rather realistic detector responses. All reconstructed tracks from the main vertex crossing at least 4 STS stations and being identified as electrion in RICH and TRD were used for the invariant mass spectra. Electron identification in CBM is described in [4]: an elliptic "ring" fit and neural network ring quality cuts were applied, and a maximum distance of 1cm was allowed for ring-track matching. Tracks were identified as electron if the ring radius was between 5.3 and 7 cm. Electron identification in TRD was performed using 3 different statistical analysis methods: neural network, likelyhood and goodness-to-fit criterion [6]. For all 3 methods cuts were chosen to provide an electrons efficiency of 90%. Electrons were selected if they were identified by all 3 methods. The combined RICH & TRD identification suppressed pions to a level of 10^{-4} for momenta from 1 to 13 AGeV/c. In order to suppress the physical electron background a transverse momentum cut was applied for each track.

Table 1 shows multiplicity, signal-background ratio, the reconstruction efficiency and mass resolution of J/ψ and Ψ' mesons. A cut of $P_t > 1.2 GeV/c$ was applied to each electron track.

	mult.	branch. ratio	S/B	eff	σ_m
J/ψ	$1.92 \cdot 10^{-5}$	0.06	13	0.14	27 MeV
Ψ'	$2.56 \cdot 10^{-7}$	0.0088	0.3	0.19	29 MeV

Table 1: Characteristic numbers for J/ψ and Ψ' for central Au+Au collisions at 25 AGeV .

The full J/ψ and Ψ' phase space is covered with those settings. The next important step in the feasibility studies is the investigation of a J/ψ trigger.

Figure 1 shows the resulting invariant mass spectra of J/ψ and Ψ' mesons and the combinatorial background for $4 \cdot 10^{10}$ central Au+Au collisions at 25AGeV.

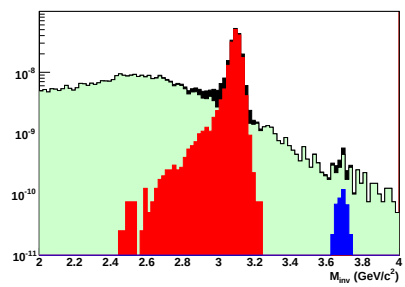

Figure 1: Invariant mass spectra for J/ψ and Ψ' mesons after a lower P_t cut of 1.2 GeV/c and an upper momentum cut of 13 GeV/c on the electrons.

These feasibility studies show that J/ψ and even Ψ' reconstruction is very promising using a target thickness of 25μm.

References

[1] A.Adare et al., PHENIX coll., nucl-ex/0611020
[2] B.Alessandro et al., Eur.Phys.J.C49:559-567,2007.
[3] W.Cassing, E.I.Bratkovskaya, S.Juchem, Nucl. Phys. A674(2000)249.
[4] S.Das et al., this report
[5] A.B. Kurepin et al., CBM-PHYS-note-2007-001
[6] V.Ivanov et al., this report

Ring Reconstruction in the CBM RICH detector*

S. Lebedev† [1,2] and G. Ososkov[2]

[1]GSI, Darmstadt, Germany; [2]JINR LIT, Dubna, Russia

In this contribution we will present innovations and improvements which have been developed for ring reconstruction in the CBM RICH detector.

A RICH ring recognition algorithm based on the Hough Transform (HT) [1, 2] was rewritten improving the speed and ring finding efficiency. The HT is now optimized for the Hamamatsu PMT H8500-03 (22 hits per electron ring). Using the Hamamatsu PMT did not result in an efficiency drop in comparison to the PMT proposal from Protvino (40 hits per electron ring).

In systematic studies for both, the standard and the compact RICH layout [3] the following parameters were varied: Hamamatsu or Protvino PMTs were used, different beam energies, number of noise hits in the PMT plane, magnetic fields from an Active Shielding magnet and a standard dipole magnet with a larger stray field in RICH. In dependence on those conditions ring finding and ring-track matching efficiencies and fake ring rejection in dependence on momentum, radial position and hit density were investigated. It was found that due to an increasing hit density with higher beam energies the ring finding efficiency drops slightly, the fake ring rate and ring-track mismatches increase at the same time. As long as less then 1% of the PMTs have noise hits in one event the ring finding efficiency is not effected. Integrated ring finding and ring-track matching efficiencies for the two magnetic fields are the same.

As the rings in the photodetector plane have a slight elliptic shape a fitting method was developed based on ellipses. With this we expect to extract more precise ”ring” parameters, a better determination of the ”ring” centre and therefore an improved ring track matching. It will also be investigated whether these parameters can be used in order to separate primary and secondary electrons as many of the latter cross the RICH detector with very different angles thus showing different ring distortions in the photodetector plane.

An algorithm for handling ellipse-like rings was developed and implemented in the CBM software framework. We use Kepler’s ellipse definition to build the fitting functional. MINUIT is used for the minimization of this functional. This algorithm was tested on simulated data and has shown good and interesting results. It was obtained that in the current CBM-RICH setup most of the rings have an elliptic shape with a mean eccentricity of 0.43. For electrons from the main vertex a clear dependence of the ellipse rotation angle on the azimuthal angle of the electrons is observed.

The values of the major and minor axes of the ellipse are strongly dependent on the position on the PMT plane. The mean value of the major axes varies from 5.8 cm in the outer part of the PMT to 6.6 cm in the inner part, for the minor axes it varies from 5.2 cm to 5.9 cm. Therefore a radius (axes) correction algorithm was introduced for an improved radius resolution and thus pion suppression. Our algorithm is based on a radius correction map, obtained from large simulated statistics. This improves the resolution by a factor of two.

The existing fake ring rejection algorithm was improved after studying distributions of 10 parameters related to the fitted ellipses: major half axes, minor half axes, rotation angle etc. These parameters are used as input to a trained artificial neural network (ANN), reducing strongly the contribution of fake rings.

The current performance after all improvments is presented in Figure 1. The results were obtained for electrons embedded into central Au+Au collisions at 25 AGeV. The integrated ring finding efficiency for primary electrons is 93.6 % and the average number of fake rings is 4.0 per event. After applying the fake rejection routine based on the ANN we got 90.92 % efficiency and a number of fake rings of only 0.29 per event.

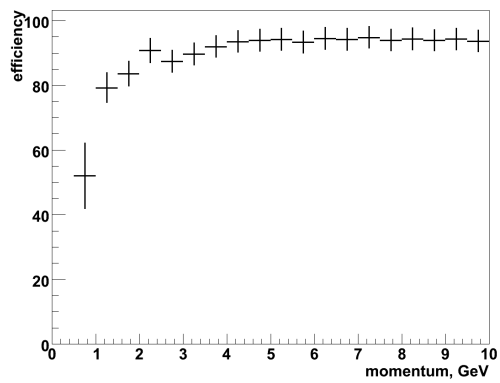

Figure 1: Ring finding efficiency vs. momentum (HT ring finder and fake rejection by use of neural net).

References

[1] Hough P.V. C., “Method and Means for Recognizing Complex Patterns”, U.S. Patent 3,069,654 1962.

[2] S. Lebedev, G. Ososkov, C. Hoehne, “Ring Recognition in the CBM RICH detector”, JINR Communication E10-2007-88. Dubna, 2007.

[3] C. Hoehne, this report.

* Work supported by FP6 Hadron Physics (see Annex.)

† s.lebedev@gsi.de

TRD layout studies and energy loss simulations

F. Uhlig[1] and the CBM Collaboration
[1]GSI, Darmstadt, Germany

The main tasks of the Transition Radiation Detector (TRD) [1] in the CBM experiment are on one hand the electron identification and on the other hand the tracking capabilities, which have to be fulfilled in an environment with a count rate of the order of 100 kHz/cm^2. Prototypes of single TRD layers which could fulfill the experimental requirements were developed by several groups [2,3,4].

Geometries

Geometries of two of these prototypes were also implemented in the simulation of the CBM experiment, a single gap MWPC with a gas layer of 6 mm and a double-sided MWPC with two gas layers of 6 mm described in detail in another report of this book [5]. To study general properties of the TRD like energy loss, electron identification or tracking performance an idealized version of the geometries is used which is sensitive in the complete detector plane. These idealized geometries are also used to compare the simulation with the data from the beam test.
To study a more realistic detector performance a TRD built up from single detector chambers is used. The layout is optimized in such a way that the complete detector with several layers can be built with only three different detector modules.

Energy Loss

To get realistic information about the electron identification capabilities of the TRD in the simulation it is important to verify that the ionization energy loss of the detector is described correctly. Since it is not possible to simulate the transition radiation this part of the energy loss is modeled by ourselves and also checked with the experimental data. The comparison with experimental data was done for the GEANT3 simulation and will be done for the GEANT4 simulation in near future. By choosing the correct model to calculate the ionization energy loss in thin materials it was possible to describe the energy loss quite well as can be seen in fig. 1.

Electron ID

The electron identification is based on the energy loss information of all twelve layers of the TRD. In the simulation three different methods to perform the task of electron identification are implemented. The first method is a maximum likelihood method which uses the normalized energy loss spectrum of electrons and pions. These spectra are created with the simulation knowing the particle ID. Using the normalized energy loss spectrum for electrons and pions one gets the probability P($E|e$) that an electron and the probability P($E|\pi$) a pion deposits this energy E in the detector. Adding the information of all twelve layers and assuming that the layers are identical one gets the probability to be an electron or a pion, which is then used to define the Likelihood to be an electron in the following way

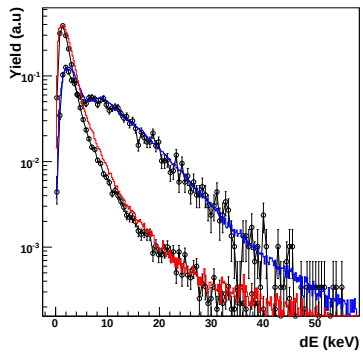

Figure 1: Measured energy losses for pions and electrons (black) are shown together with results of the simulation for pions (red) and electrons (blue).

$$L_e = \frac{P_e(E)}{P_e(E) + P_\pi(E)}. \quad (1)$$

The value ranges between 0 and 1 and is used to discriminate between electrons and pions. The second method is also a probability approach which is described in detail at [6]. The third method uses a neural network which was trained with a pure electron (signal) and a pure pion (background) sample [7].

References

[1] B. Dolgoshein, “Transition radiation detectors.”, Nucl. Instrum. Meth., A326(434-469), 1993

[2] M. Klein-Bösing et al., “Position resolution of a high efficiency transition radiation detector for high counting rate environments”, Nucl. Instrum. Meth. Phys. Res., A585(83-87), 2008

[3] M. Petris et al., “High counting rate transition radiation detector”, Nucl. Instrum. Meth. Phys. Res., A581(406-409), 2007

[4] A. Andronic et al., “Electron/pion identification with fast TRD prototypes”, GSI Jahresbericht, 2006

[5] M. Klein-Bösing et al., “High efficiency TRD for CBM in test beam and simulation”, GSI Jahresbericht, 2007

[6] V.V. Ivanov and P.V. Zrelov, Int. J. Comput. & Math. with Appl., vol. 34, No. 7/8, (1997)703-726

[7] E.P. Akishina et al., “Electron/Pion Identification in the CBM TRD Using a Multilayer Perceptron”. JINR Communication E10-2007-17. Dubna, 2007.

Systematic studies on MWPCs for TR detection at high rates

D. Gonzalez-Diaz[1], A. Andronic[1], C. Garabatos[1], A. Kalweit[1], and F. Uhlig[1]
[1]GSI, Darmstadt, Germany

In a series of measurements conducted at GSI ([1], [2]), the possibility of using MWPCs based on Xe/CO_2 for TR detection at the anticipated CBM fluxes of 100 kHz/cm^2 was explored. Here, the already existing data are enhanced by including additional measurements on Ne mixtures, together with the characteristic 'gain vs voltage' curves for a number of chamber configurations, focusing on the maximum achievable gain. Furthermore, the theoretical formalism of [3] is used in its full extent by resorting to only two free parameters for each noble gas mixture, according to $1/\mu = f/\mu_{Xe(Ar,Ne)} + (1-f)/\mu_{CO_2}$ with f being the fraction of noble gas and μ_i the mobility of the drifting ion on gas i (Blanc's law [4]). Following [3], the functional dependence of the gain vs rate can be readily obtained as:

$$M = M_o \exp(-a^2 \frac{q_e n_o}{2\mu} \frac{sh^2}{C_l} \frac{Mr}{\ln M - b}) \qquad (1)$$

where M stands for the detector gain at a given rate r, M_o is the gain at zero rate, q_e the electron charge, n_o the primary ionization, s the wire pitch, h the gap, C_l the capacity per unit length, and the gain is described by an exponential law such that $\log_{10} M = aV - b$. After numerical evaluation, the transcendental equation 1 can be used for fitting the data for all the mixtures in the spirit of [1], [2], yielding μ_{Xe}, μ_{Ar}, μ_{Ne} and 3 values for μ_{CO_2} (assuming the nature of the drifting ion to be uncertain). By defining the gain drop $F = 1 - M/M_o$, the maximum affordable rate at operating gain M_o if a maximum gain drop F is allowed in the chamber will be given by:

$$r = \frac{\ln[(1-F)M_o] - b}{(1-F)M_o} \frac{1}{a^2} \frac{2\mu}{q_e n_o} \frac{C_l}{sh^2} \ln(1-F) \qquad (2)$$

and it is shown in Fig. 1 for the case where $F = 5\%$ and $M_o = 10^4$ under X-ray illumination at an average energy $E = 6.7$ keV (approximately 2 times more than mips).

The effect of the finite beam size was evaluated from measurements at 10 times bigger illumination area ($A \sim 6$ cm^2) and estimated to be less than a factor 2, nevertheless a more precise determination will be pursued in the future. Fig. 1 indicates that operation of the chamber at $M_o = 10^4$ and fluxes up to 100 kHz/cm^2 is feasible in Xe mixtures and can be pushed higher roughly proportionally to F/M_o.

A very fundamental issue for operation of MWPCs is the maximum achievable gain before photon or ion feedback results in self-sustained currents that make impossible the chamber operation. For $s = 3$ and $s = 4$ mm pitch, Xe/CO_2 based mixtures could be operated up to $M_o = 10^5$, being the maximum gain slightly higher for Ne and Ar based mixtures (Fig. 2). Operation at gains lower than $M_o = 10^4$ ensures therefore a safe margin for dealing with a wide range of primary ionizations, providing at the same time the rate capability required by CBM.

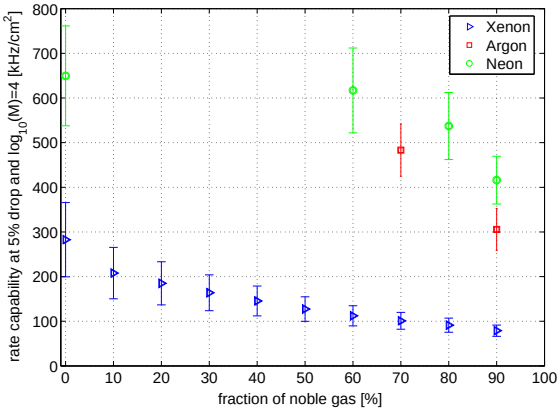

Figure 1: Rate capability at 5% drop and $M = 10^4$ for $s = 4$, $h = 3$ mm chamber.

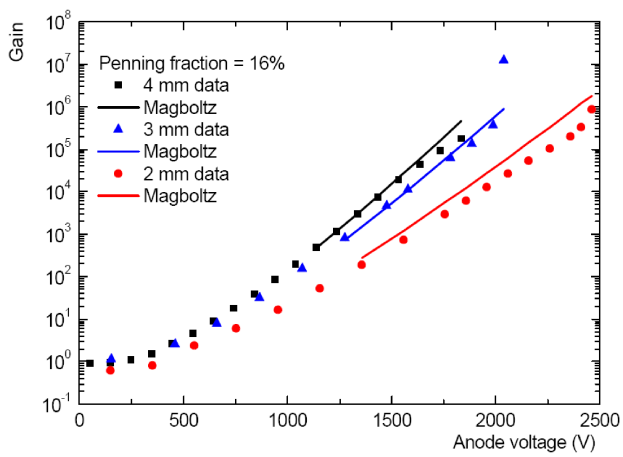

Figure 2: Gain vs voltage curve for $s = 2, 3, 4$ mm chambers, together with a preliminary Magboltz description assuming 16% Penning fraction.

With the still on-going measurements we plan to systematically explore a broad set geometries and gas mixtures that will be of interest for CBM, providing valuable information for making a sound choice of the final detector.

References

[1] A. Kalweit, Bachelorarbeit, Darmstadt TU, May 2006.

[2] C. Garabatos, F. Uhlig, G. Hamar, GSI-report 2006-02-28.

[3] G. C. Smith and E. Mathieson, IEEE Trans. Nucl. Sci. 34(1987)420.

[4] F. Sauli, CERN 77-09, 1977.

The muon detection system for the CBM experiment*

A. Kiseleva[1], S. Gorbunov[2], I. Kisel[1, 2], E. Kryshen[3], V. Nikulin[3], M. Ryzhinskiy[4], and P. Senger[1]

[1]GSI, Darmstadt, Germany; [2]University, Heidelberg, Germany; [3]PNPI, Gatchina, Russia; [4]SPbSPU, St.Petersburg, Russia

The layout of the CBM muon detection system has been improved and optimized in 2007 with respect to background suppression and a more realistic detector response. The modifications include:

- compact absorber system in order to reduce the number of muons from weak pion decays;
- realistic detector segmentation according to an occupancy of 5%;
- additional shielding in order to reduce the background of secondary electrons produced in the beam pipe;
- additional ToF detector to suppress the background due to punch-through kaons and protons.

The present design of the muon detection system consists of several hadron absorber layers (iron with variable thickness) and 15-18 tracking detectors based on GEM technology. For the measurement of muons from low mass vector mesons (ρ, ω, ϕ) the total iron absorber thickness is 125 cm (corresponding 7.5 λ_I) whereas for muons from charmonia 1m of iron is added (corresponding total thickness of 13.4 λ_I). For Au+Au collisions at 25 AGeV about 0.3 background tracks per event are reconstructed. These background tracks consist of muons (60%), kaons (25%), pions (7%), protons (3%), and ghosts (5%). About 80% of the muons originate from weak pion decays which happen inside the absorber, 20% of the muons originate from weak pion decays in front of the absorbers. These numbers refer to the iron absorber of 125 cm thickness.

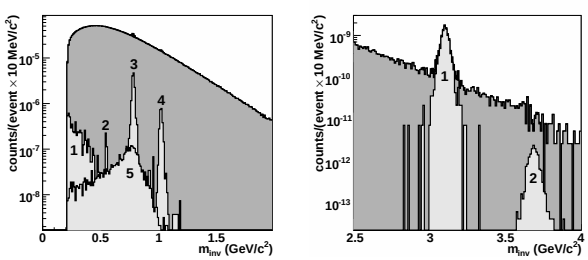

Figure 1: Muon pair invariant mass spectra. Left panel — η_{Dalitz} (1), η (2), ω (3), ϕ (4), ρ (5), and combinatorial background (grey area). Right panel — J/ψ (1), ψ‘ (2), and combinatorial background (grey area) for muons with $p_t >$ 1 GeV/c.

The vector meson decays were simulated with the PLUTO generator assuming a thermal source with a temperature of 130 MeV. The multiplicity for central Au+Au collisions 25 AGeV beam energies is taken from the HSD transport code [1]. The background was calculated with the UrQMD event generator. Both signal and background are transported through the detector setup using the transport code GEANT3 within the cbmroot simulation framework. The L1 tracking procedure [2] has been used for the track finding in the STS and muon system, and for momentum reconstruction in the STS. For the track reconstruction we assume that the detector layers are segmented into pads according to a occupancy of 5%.

The resulting invariant mass spectra are shown in figure 1 (left panel — low mass and right panel — high mass regions). The efficiency for vector meson detection and the signal-to-background ratio, calculated in a $\pm 2\sigma$ window around the signal peaks, are presented in the table 1. A transverse momentum cutoff more than 1 GeV/c was used for tracks in the charmonium region.

observables	ρ	ω	ϕ	J/ψ	ψ‘
S/B ratio	0.002	0.11	0.06	7	0.09
efficiency (%)	2.8	4	7	7.7	8.2
mass resolution (MeV/c^2)		10	12	22	31

Table 1: Signal-to-background ratio and efficiency for vector mesons from Au+Au collisions at 25 AGeV.

In the ongoing simulations we have started to take into account detector inefficiencies and clustering of pads. Moreover, we have removed one out of three detector station after each absorber layer, and reduced such the total number of tracking detectors from 15 to 10. It turned out that a detector efficiency of 95% can be tolerated without losses of track reconstruction efficiency which is very similar for the setup with 15 and 10 detector stations. In order to optimize the muon detection system further we will improve the track propagation algorithm for thick absorbers. Moreover, we will investigate the possibility to generate a hardware dimuon trigger both for charmonium and low-mass vector mesons.

References

[1] W. Cassing, et al., Nucl. Phys. A 691 (2001) 74.

[2] S. Gorbunov, I. Kisel and Iou. Vassiliev, CBM-PHYS-note-2005-001.

* Work supported by EU/FP6 HADRONPHYSICS (see Annex) and by INTAS.

Track reconstruction in the TRD and MuCh detectors*

A. Lebedev† [1,2] and G. Ososkov[2]
[1]GSI, Darmstadt, Germany; [2]JINR LIT, Dubna, Russia

The successful application of the TRD tracking algorithms [1] lead to the idea to generalize and optimize those algorithms in a flexible way in order to make them applicable for other, similar detectors. In this contribution we present how this idea was realized and applied for the TRD layout optimization and for track finding in the MuCh detector.

Since both tracking detector setups (TRD and MuCh) are analogous in many details, the same approach can be used for tracking in these detectors. Therefore, a generalized algorithm of track finding in the CBM tracking detectors has been developed. It is based on the Kalman Filter and track following methods where the next track point is searched in an area surrounding a predicted point. The main idea is to apply a general algorithm of track finding to different detectors and only adopt it to a specific one by changing the tracking routine parameters. This helps to decrease code duplication, thus significantly easing the software support.

In our implementation, tracking is accomplished in an iterative way. In each iteration, tracking parameters have to be specified, and hits belonging to tracks found in the current iteration are deleted from the hit array. In order to use the tracking routine, one has to specify the number of tracking iterations, the maximum number of allowed missing hits in a detector station, start and end station for the tracking, the sigma coefficient determining the searching region, and other parameters of the tracking. The searching region can be determined in two different ways: (1) using the covariance matrix of the predicted track parameters and position errors of the hits; (2) calculating the maximal deviation between the predicted position and a hit on the basis of a look-up table obtained from a simulation with large statistics.

For the TRD, two different approaches have been used: a standalone TRD track finder (using only TRD information), and an algorithm based on the information from tracks found in preceding detectors (STS-based or MuCh-based). For the MuCh detector, which consists of a sequence of several absorber and detector layers, vertex tracks reconstructed in the STS have been used as seeds for track reconstruction.

The software was embedded into the CbmRoot framework and tested on central Au+Au collisions at 25 AGeV beam energy from UrQMD.

Using the TRD track finder, a detector layout study has been performed in order to optimize the detector setup while keeping high reconstruction efficiency. The aim of this study is to minimize the costs of the detector. The standard detector setup for the TRD consists of 3 stations and 4 layers in each station (4-4-4), 12 layers in total. To minimize the number of stations, several TRD geometries with 3 layers in each station (25% savings) and with 2 layers in each station (50% savings) have been studied. For the standalone TRD track finder, two additional geometries have been studied, with 4 layers in the first station and 2 or 3 layers in the others (4-3-3 and 4-2-2). The tracking performance for the different TRD layouts looks surprisingly similar. An efficiency of 95-96% for the STS-track based TRD track finder and of 89% for the standalone TRD track finder has been achieved. However, this conclusion on the layout relates to tracking performance only without considering the task of electron-pion separation and should be completed by that consideration. The STS-track based TRD track finding efficiency for the standard TRD geometry (4-4-4) is shown in Figure 1 as function of momentum.

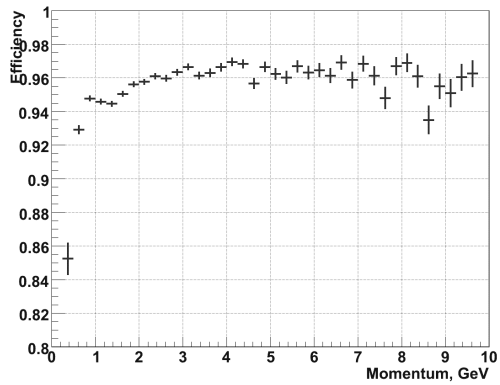

Figure 1: TRD tracking efficiency as function of momentum for tracks found in the STS

Similar to the scheme introduced above, track finding routines for the so called "compact" MuCh geometry [2] have been developed and tested. Decay muons from the omega meson were embedded into UrQMD events in order to simulate interesting track candidates. First results are rather promising. An efficiency at the level of 1.9-2.6% for signal pairs was achieved. This efficiency includes acceptance and full track reconstruction. The performance depends on the tracking parameters; typically, an increase of the signal finding efficiency also increases the background.

References

[1] A. Lebedev, G. Ososkov, *TRD and Global tracking*, X. CBM collaboration meeting, Dresden, 27 September 2007, [http://www.gsi.de/documents/DOC-2007-Oct-97.html]

[2] A. Kiseleva et al., *The muon detection system for the CBM experiment*, this report

* Work supported by FP6 Hadron Physics (see Annex.)
† andrey.lebedev@gsi.de

Radiation environment in the CBM experiment*

R. Karabowicz, D. Bertini, and the CBM Collaboration
GSI, Darmstadt, Germany

The CBM experiment focuses on detecting extreme conditions produced in heavy ion collisions by observing rare probes such as light vector mesons or charmonium particles [1]. Achievement of the goal depends crucially on collecting high statistics data which requires running of the experiment at high collision rates. At present, we expect the collision rates to reach 10^7 minimum bias Au + Au collisions per second on 1% radiation length target.

Such running conditions produce a high radiation environment, which has to be studied to identify both hot spots and regions in the experimental cave with low radiation limits.

Radiation in the CBM cave

Radiation simulations were run in the FLUKA package [2]. 50 UrQMD minimum bias Au + Au collisions at 25 AGeV were injected into FLUKA which transported the produced particles in the simplified geometry of the CBM experimental cave. Result is shown in the left part of Fig. 1 as a scatter plot of the particle fluence converted to 1 MeV neutron equivalent units in a Y-Z projection of the CBM cave. It shows rather uniform distribution of radiation level in the CBM cave except of the region close to the target, where radiation is much higher. To estimate the background of the beam particles that do not collide in the target single gold ions were also shooted through the experimental hall and the results can be seen in the right part of Fig. 1. One sees that the back scattering of the beam in the dump produces a cone of heavy radiation comparable to the background from target interractions.

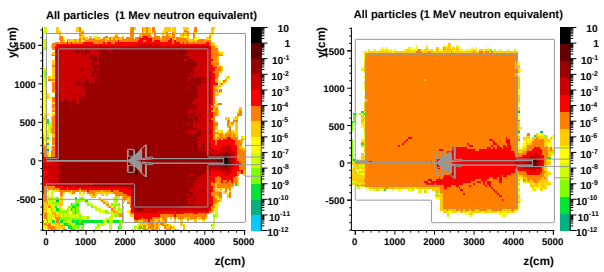

Figure 1: Y-Z scatter plot of particle fluence in CBM cave for gold nuclei colliding with the gold target at 25 AGeV (left-hand side) and the gold nuclei interacting in the beam dump (right-hand side).

Radiation in STS

In the course of performing the FLUKA simulations it appeared necessary to compare the results obtained with this transport code with the default transport code of the CBM experiment, i.e. GEANT [3]. We have chosen the charged particle energy loss in the silicon stations as the value to compare the two codes. The energy loss predicted by GEANT was found to be about 20% higher than that produced by FLUKA. The results proved to be relatively stable against changing GEANT or FLUKA settings. The only visible difference was observed when increasing the number of tracking steps in the silion material - energy loss produced by GEANT increased threefold.

The above comparison blossomed in a possibility of performing radiation studies in the demanding environment of the STS. Assuming CBM experiment lifetime of about $3 \cdot 10^{14}$ minimum bias Au + Au interactions at 25 AGeV (which corresponds to about 6 years of running) estimated total integrated dose in the silicon detector reaches 20 megarads, see Fig. 2.

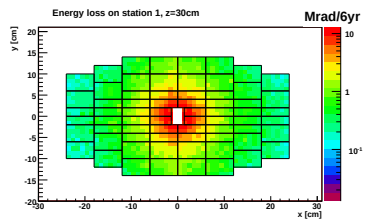

Figure 2: Radiation dose on first STS station in 6 years of running

Conclusions and plans

Preliminary studies of the radiation environment in the CBM experiment performed in the last year pronounce the challenging aspects of the detector setup and running conditions. Rough estimates predict radiation doses on levels comparable to that expected for the LHC experiments. It appears that the present construction of the beam dump is far too simplistic and is crucial to keep the radiation doses low in the CBM cave. Future efforts will focus on optimizing the cave geometry to reduce the radiation limits and on performing radiation tests of most exposed detectors.

References

[1] P. Senger, *The CBM experiment at FAIR*, this report

[2] A. Fassó, A. Ferrari, J. Ranft and P. R. Sala, *FLUKA, a multi-particle transport code*, CERN-2005-10(2005),INFN/TC_05/11,SLAC-R-773, and references therein

[3] R. Brun, et al., *GEANT 3 User Guide*, CERN, 1985

* Supported by EU/FP6 HADRONPHYSICS (see Annex) and INTAS

Data Communication Tests on Active Buffer Board*

J. Adamczewski[2], W. Gao[† 1], A. Kugel[1], R. Männer[1], G. Marcus[1], and A. Wurz[1]
[1]Informatik V, University of Mannheim, Germany; [2]GSI, Darmstadt, Germany

Abstract: The Active Buffer Board (ABB) was re-designed and equipped with a larger FPGA, Virtex-4FX60. A test infrastructure, based on the embedded PowerPC processor, was developed and applied to verify memory controllers and high-speed serial links. A protoype integration into a PCIe based DAQ system was started, employing partial reconfiguration, interrupt handling and dual-channel DMA.

ABB hardware

In order to test the re-designed ABB cards and to test memory and interconnection modules a number of IP-cores have been developed.

Test Infrastructure

The infrastructure module is based on the embedded PowerPC processor in the Virtex-4 FPGA. Specialised IP-cores to access the serial links and memory interface via the processor bus (PLB) enable to build a complete system using the XILINX EDK software, together with the default modules, like timer and UART.

Serial Link (MGT) Test

This module consists of a pseudo random number generator to generate the bits pattern and the corresponding comparison logic for the error rate statistics. Test patterns and run paramters are software programmable via the PLB interface, which attaches to the infrastructure module. MGT paramters can be controlled likewise, using the MGT ICAP interface. The serial links have been successfully tested with data-rates of 5 Gbps over coaxial cable and PCB traces. 2.5 Gbps have been tested with optical transceiver modules and differential flat cables. Multiple MGTs can be tested simultaneously.

Memory Controller

High-speed dual-ported memory controller are required for a data-acquisition purpose of the ABB. With today's high capacity SRAMs and DRAMs this can become a non-trivial task, due to the asymetric read/write behaviour of DDR-2 SRAMs and the inherent complexity of dynamic memory (page structure, refresh, precharge times etc.). The ABB memory controller provides independent, FIFO buffered fast read and write paths with data transfer on every clock edge. In addition, a PLB interface is available to exercise the memory under software control. Memory interface are available for DDR-2 SRAM and DDR-1 DRAM. DDR-2 DRAM has been tested as well but becomes very inefficient on random access.

PCIe DMA Project

PCI Express DMA Engine Improvement

Two DMA channels, upstream and downstream, are built to transfer data between the Active Buffer Board and the host through PCI Express bus. External memory is currently emulated using internal block RAM (BRAM). FIFOs are used to emulate external I/O to/from DCB/BNet via MGTs. The two channels can run simultaneously. The maximum transfer per DMA command size is 4GB. DMA descriptors for scatter-gather DMA reside in host memory. The DMA DONE status is acknowledged through interrupt messages. The driver and the test programs have been well improved and modified both in Mannheim and GSI targeting Intel and AMD machines. For large transfersize, we achieve around 700MB/s downstream (to peripheral) and 800 MB/s upstream (to host) with a 4-lane PCIe interface.

Partial Reconfiguration Experiment

In order to resolve licensing issues an attempt was made to employ the partial reconfiguration technique to combine developments from different project partners (PCIe core and user logic respectively) into a single FPGA device. Unfortuately the XILINX software tools are not fully mature in this respect and several work-arounds have been neccessary. A stable design, however only with 1 PCIe lane, was successfully generated finally.

PCI Express Interrupt Generator

A programmable interrupt generator was developed and used to measure the latency of the driver and the system. Basic tests show that the system we are using can stand an interrupts arrival rate of 60 000 Hz.

References

[1] W. Gao, A. Kugel, R. Männer and G. Marcus, "PCI Express DMA Engine Design", CBM Progress Report 2006, February 2007.

* Work supported by EU, EURONS contract No. 506065.
† wgao@rumms.uni-mannheim.de

Improved Setup of the PANDA Detector*

L. Schmitt† for the PANDA Collaboration

Introduction

PANDA is a next generation hadron physics detector [1] planned for the future Facility for Antiproton and Ion Research (FAIR) at Darmstadt, Germany [2]. It will use cooled antiproton beams with an energy between 1.5 GeV and 15 GeV interacting with various internal targets.
Main topics of the experiment are hadron spectroscopy, in particular the search for exotic states in the charmonium region, the study of charm hadrons in the nuclear medium, spectroscopy of double-hypernuclei and nucleon structure. From these a list of physics benchmarks can be derived defining the requirements for the PANDA detector system. These comprise 4π acceptance, vertex detection, particle identification of Kaons, muons and $e^{\pm}$, electromagnetic calorimetry from a few MeV to several GeV and a good momentum resolution in the order of $\delta p/p \sim 1\%$. The detector has to operate at high rates of up to 20 MHz and employ efficient event selection algorithms.

Forward Tracking

The setup described in the PANDA Technical Progress Report [1] contained drift chambers with 1 cm cell size for all forward trackers. Inside the solenoid magnet only two stations were planned at a rather close distance to each other. Simulations showed that pattern recognition cannot proceed well with the short lever arm and only two stations. In addition the position of the drift chambers was in a region with low transverse field giving a bad momentum resolution. Finally the particle fluxes obtained from the simulation indicate that the chambers would operate at their design limits.

To improve this situation a completely different detector type had to be implemented. In the new setup three thin large area GEM detector stations with 6 planes and 12 coordinates are proposed. The basic design is in accordance with the COMPASS triple GEM small area tracker [3]. However for PANDA larger GEM foils are required which are currently in development at CERN. GEM detectors are very thin and have low mass. The compact built allow positioning further upstream freeing space for further optimisation of the densely packed forward endcap.

In addition a lack of acceptance for hyperon decays in the forward direction was observed. Having fairly long lifetimes they decay frequently beyond the micro vertex detector but are nevertheless forward peaked so that they often also miss the central tracker. Their acceptance was increased by adding two more disks of silicon strip detectors in the bore of the central tracker.

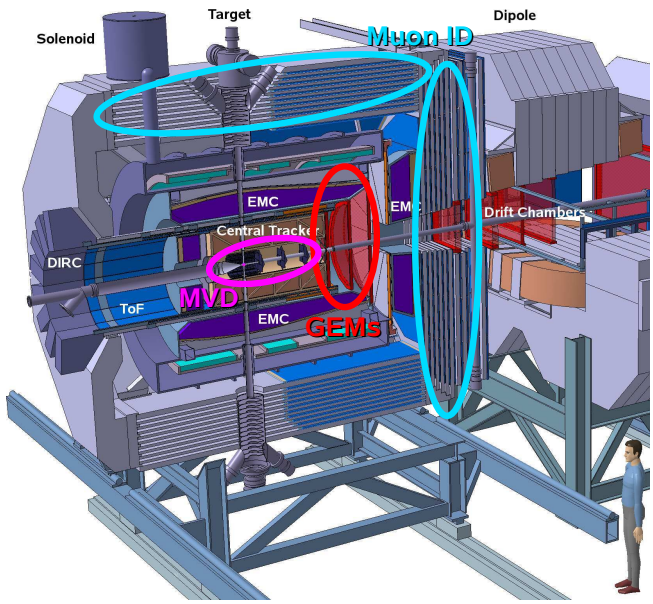

Figure 1: Improved PANDA setup. Forward tracking (MVD and GEMs) and muon identification were enhanced.

Muon Detection

The system for muon identification as outlined in [1] needed improvement, since it would only work well for muons at higher momenta. The relatively low momentum muons in PANDA have high straggling and absorption in the iron absorbers. Therefore a more appropriate range tracking system has to be introduced by means of fine layers in the solenoid yoke and additional absorber/detector layers between the solenoid and the dipole magnet.

Now, 11 detection layers in the barrel yoke, 6 detection layers inside the downstream endcap and further 6 detection layers in the gap between the two magnets are planned. The total absorber thickness is 39 cm of iron in the barrel, 32 cm in the endcap and 30 cm between the magnets.

References

[1] M. Kotulla et al. [PANDA Collaboration], *Strong Interaction Studies with Antiprotons*, Darmstadt, February 2005, Technical Progress Report.

[2] L. Äystö et al., *An International Accelerator Facility for Beams of Ions and Antiprotons*, GSI, Darmstadt, 2001, Conceptual Design Report.

[3] B. Ketzer et al., *Triple GEM tracking detectors for COMPASS*, IEEE Trans. Nucl. Sc. 49, 2403 (2002)

* Work supported by EU, Contracts Nos. 506078, 515873, 211382.
† GSI, Darmstadt, Germany

Performance of PWO-II Prototype Arrays for the EMC of PANDA*

R. W. Novotny[1], W. Döring[1], V. Dormenev[2], P. Drexler[1], W. Erni[3], R. Schubert[1], M. Steinacher[3], M. Thiel[1], A. Thomas[4] and for the PANDA collaboration

[1]2nd Physics Institute, JLU, Giessen, Germany; [2]RINP, Belarus State University, Minsk, Belarus; [3]Physik Department, University Basel, Switzerland; [4]Nuclear Physics Institute, University Mainz, Germany

The electromagnetic calorimeter (EMC) of the target spectrometer of PANDA is one of the major components to provide high-resolution photon and meson spectroscopy. The calorimeter has to cope with photons in the energy range starting at a few tens of MeV up to several GeVs. The operation within a superconducting solenoid excludes read-out with fast photomultipliers. Therefore, large area avalanche photo diodes (LAAPDs) have been selected as the appropriate sensor and are presently under development.

Irrespective of the finally collected scintillation light, cooling of the scintillator reduces the thermal quenching of the scintillation processes and improves the energy resolution. For an operating temperature of t=-25°C an increase of the light yield by a factor >4 can be considered compared to room temperature.

The design of the detector concept, read-out and operating conditions depend on the response function to high-energy photons of prototypes. As part of an extensive program the response function to energy marked photons between 40MeV and 675MeV, respectively, was performed at the tagged photon facility MAMI at Mainz [1].

A 3x3 PWO-II-array, comprising 200mm long straight crystals of 20x20mm^2 cross section, was exposed to a collimated photon beam with a diameter of d < 8mm at the front face of the crystals. The matrix was cooled down and well stabilized at a temperature of t = 0°C. It could be moved remote controlled in two dimensions perpendicular to the axis of the collimated photon beam to perform a relative calibration of each detector element under beam conditions.

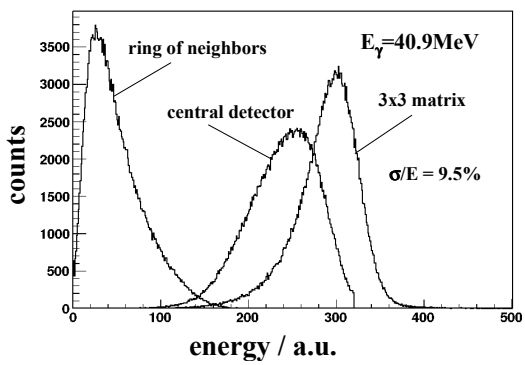

Figure 1. Experimental line shape of the 3x3 PWO-II matrix measured at 40.9MeV.

Each crystal was coupled to one LAAPD of prototype-2 version (S8664-1010SPL) with an active area of 1cm^2, a quantum efficiency of 70% (at 420nm) and a capacitance of 270pF at a gain of 50. The charge signal of the LAAPD was amplified with a low noise and low power charge sensitive pre-amplifier (LNPP) with a sensitivity of 0.5V/pC and a small feedback time constant of 25µs [2].The output signal was fed into a 16-fold multi-functional NIM-module (*MESYTEC,* MSCF-16), which contained spectroscopic (1µs Gaussian shaping) and timing-filter amplifiers (INT=DIFF=50ns), as well as CFDs for analogue and logic circuits. The energy response was digitized in a peak-sensing ADC (*CAEN* V785N). The energy and time information of each scintillator together with the timing response of the relevant tagger channels were recorded event-by-event for an off-line analysis.

The distribution of the electromagnetic shower within the 3x3 matrix was obtained after a relative calibration of the individual modules. Figs. 1 and 2 illustrate the line shape as well as the energy resolution over the entire photon energy range.

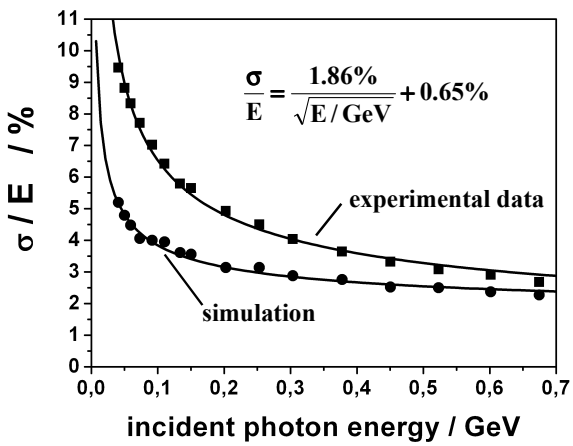

Figure 2. Experimental energy resolution as a function of incident photon energy measured for a 3x3 PWO-II matrix read-out with LAAPDs. The result of a GEANT4 simulation is shown for comparison.

The obtained results not even exploiting an additional gain factor of 2 for the light output in case of an operation at t=-25°C ensure the applicability of PWO for em-calorimetry down to energies of 10-20MeV. In addition, in the present experiment only 25% of the crystal end face was covered by the LAAPD. Therefore, adding a second sensor will further improve the performance.

References

[1] I. Anthony, et al., "Design of a Tagged Photon Spectrometer for Use with the Mainz 840 MeV Microtron," *Nucl. Instr. and Meth.*, A 301 (1991) 230-240.

[2] R. W. Novotny et al., "High Resolution Calorimetry With PWO-II," 2005 *IEEE Nuclear Science Symposium*, Puerto Rico, Conference Record, ISBN: 0-7803-9222-1, N12-4.

* Work supported by BMBF, GSI and EU (I3HP HadronPhysics).

Advancement of a low noise preamplifier ASIC for the PANDA EMC*

Peter Wieczorek[1] and Holger Flemming[1]
[1]Gesellschaft für Schwerionenforschung

Introduction

For the electromagnetic calorimeter of the PANDA experiment an advanced version of the existing preamplifier and shaper ASIC [1] was produced and specificied.

The measured results of this second iteration realized in a 350 nm CMOS process show an excellent noise performance and full agreement to simulation results.

Concept

Based on the results of the first prototype a second iteration has been developed with the goal to fulfill all the given requirements. A picture of the ASIC containing two equivalent channels is shown in figure 1.

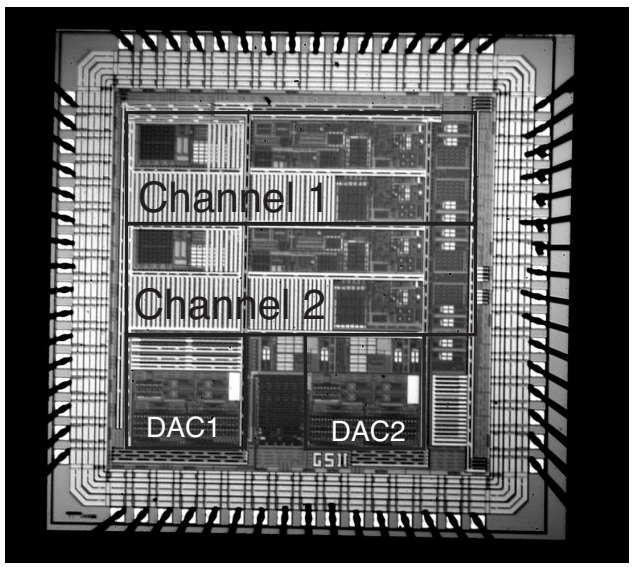

Figure 1: Picture of the preamplifier shaper ASIC

The outstanding achievement of this ASIC is the huge dynamic range of 10.000. Therefore the maximum input charge the premplifier can cope with was increased from 2 pC to 6 pC. Additionally the equivalent noise charge was decreased from 1 fC to 0.6 fC. To handle this dynamic range at the output the readout path is splitted in two output parts with different amplifications. This technique allows to arrange one path for the low and the second path for the high energy region.

Also the shapers were upgraded from a second into third order semigausian shapers with a constant shaping time of 250 ns. The third stage has been build up with a differential amplifier.

The measurements with the fixed voltage reference of the first iteration have shown a demand for more flexible references to guarantee the huge dynamic range at different temperatures. Programmable references have been implemented to solve this.

The differential output amplifiers can cope with a load of up to 10 pF and 20 kΩ.

Measurement

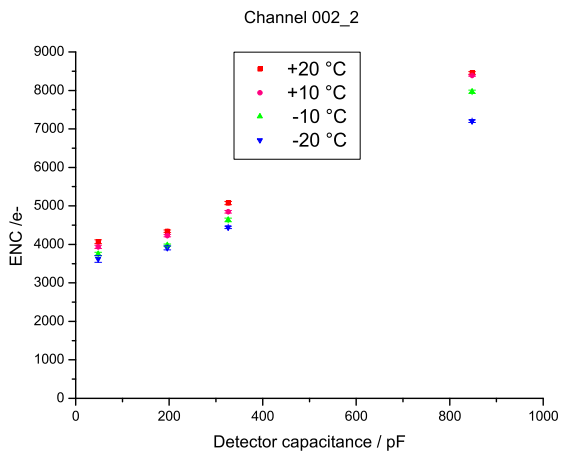

Figure 2: Results of the noise measurements

In particular noise and dynamic range are measured at different temperatures and detector capacities. The noise results for one channel are summerized in figure 2. At the forseen operation temperature of T=-20°C and a detector capacitance of 300 pF an equivalent noise charge (ENC) of 4334 e^- $\pm$ 28 e^- was measured. The power consumption is 49 mW / channel.

Conclusion

The measured results of the second iteration is in excellent agreement to simulations and fulfill the given requirements. In spring 2008 tests with avalanche photo diodes (APD) are designated.

References

[1] P. Wieczorek and H. Flemming, “Low noise preamplifier ASIC for the PANDA EMC”, GSI Scientific Report 2006, June 2007 p. 4.

* Work supported by EU (contact number: RII3-CT-2004-506078)

Comparison of PANDA calorimeter designs using Monte Carlo simulations

J. Zhong, B. Kopf, M. Pelizäus, M. Steinke, and U. Wiedner
Institut für Experimentalphysik I, Ruhr-Universität Bochum

The detection of photons with high efficiency, good energy and position resolution is crucial for the feasibility of most of the PANDA physics program. Therefore PANDA plans to use a high resolution electromagnetic calorimeter, which covers nearly the full solid angle with about 16000 lead tungstate crystals. In order to optimize the properties of the calorimeter, Monte Carlo simulations using the GEANT4 package have been done.

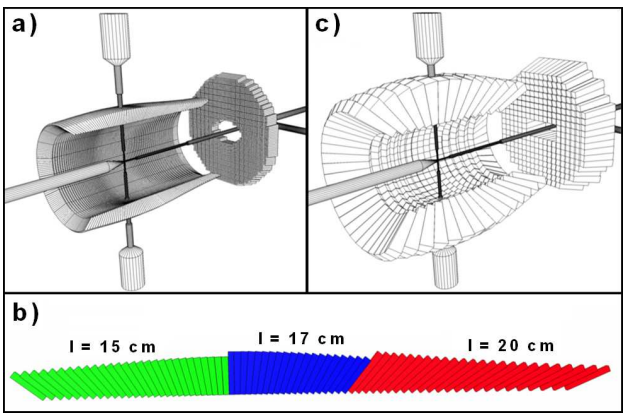

Figure 1: Detector setups, used in the simulations

Figure 1 shows the 3 different calorimeter setups, which have been studied. Setup a) uses $2.2 \times 2.2 \times 20\ \mathrm{cm}^3$ PWO-crystals in the barrel and $2.4 \times 2.4 \times 20\ \mathrm{cm}^3$ crystals in the forward endcap. Because the photon energies in the backward region are one order of magnitude lower than in forward direction (Figure 2), shorter crystals in the backward part of the barrel are under consideration for cost saving reasons. In setup b) crystals with 15 cm, 17 cm and 20 cm length are used. In addition a shashlyk calorimeter of KOPIO type has also been implemented and tested (setup c). It consists of $11 \times 11 \times 59\ \mathrm{cm}^3$ modules. Each module has 330 lead (0.275 mm) and scintillator (1.5 mm) tiles.

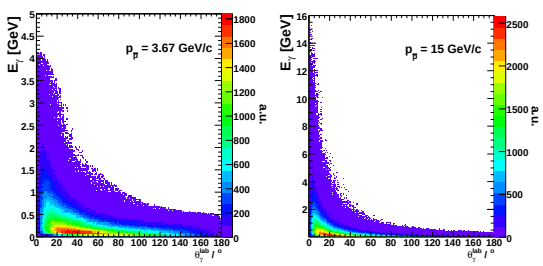

Figure 2: Energy vs. polar angle distribution of photons from $\bar{\mathrm{p}}\mathrm{p}$ collisions, using the Dual Parton Model based event generator (DPM)

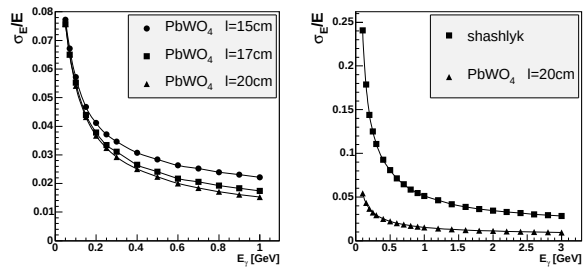

Figure 3: Energy resolutions for photons

The energy resolutions for photons are shown in Figure 3. At very low energies the resolutions for 15 cm, 17 cm and 20 cm PWO crystals are comparable, while at energies above 300 MeV the advantage of longer crystals becomes visible. But even for 1 GeV photons simulation results for 15 cm crystal length are still reasonably good ($\sigma_\mathrm{E}/\mathrm{E}$ = 2.2 %). With the shashlyk setup moderate energy resolution is possible for photons with energy larger than 1 GeV. But at 100 MeV, resolution deteriorates to about 25%. So one of the main requirements of the PANDA calorimeter, namely to detect photons down to 10 MeV, can not be achieved with the shashlyk. Figure 4 shows the reconstructed invariant mass of photon pairs for 200K $\bar{\mathrm{p}}\mathrm{p}$ collisions. Also from these plots one can clearly see the benefits of a PWO calorimeter with good energy resolution and high granularity.

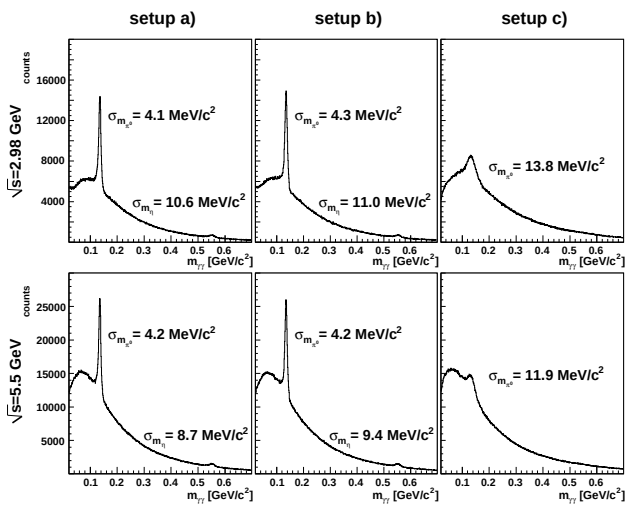

Figure 4: Invariant mass distributions of photon pairs for 200K $\bar{\mathrm{p}}\mathrm{p}$ collisions at $\sqrt{\mathrm{s}}$ = 2.98 GeV and $\sqrt{\mathrm{s}}$ = 5.5 GeV

Tracking fibre detectors based on solid state photomultipliers for $\overline{\mathrm{P}}$ANDA

S. Sánchez Majos*, P. Achenbach†, A. Sanchez Lorente, and J. Pochodzalla
Inst. für Kernphysik, Joh. Gutenberg-Universität, Mainz, Germany

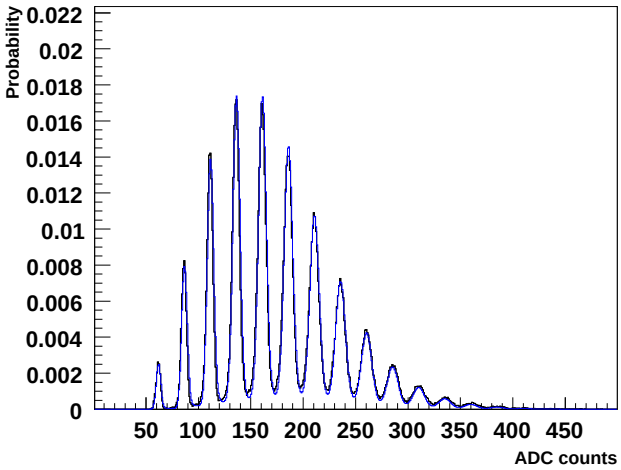

Figure 1: ADC spectrum for a fibre detector with SSPM read-out fitted by physical model to determine the basic SSPM operation parameters.

Solid state photomultipliers (SSPM) consist of a pixelised array of micrometric avalanche photodiodes connected in parallel. Despite the digital character of the signals from the individual pixels the device as a whole behaves analogically as long as the number of incoming photons remains small compared to the quantity of pixels.

SSPM technology reduces even further the complexity and price of fibre tracking detectors by getting rid of voluminous high voltage power supplies and stiff cables used for conventional photomultipliers. In addition, such a detector will be insensitive to magnetic fields. The price to pay is a MHz dark count rate at room temperature. These events are generated by thermal electrons. Internal cross-talk between adjacent pixels can bring that noise to high amplitudes competing with real signals generated by a small number of photons.

A small fibre barrel read-out by SSPM has been discussed as an option for a time-of-flight start detector in $\overline{\mathrm{P}}$ANDA and as an active target for the hypernuclear physics programme in $\overline{\mathrm{P}}$ANDA. Such a detector can be used for the particle identification, for a time reference for the DIRC detector, and for track deconvolution of the TP chamber [1]. The main purpose of the active hypernuclear target is the tracking and stopping of the produced Ξ hyperons and their decay products [1].

The detection efficiency has been measured using a Sr radioactive source for a two metres long cylindrical fibre, 0.89 mm in diameter and double cladding read out in both extremes by two SSPMs (SSPM-0701BG-TO18) manufactured by Photonique as a function of discriminator threshold. The method used was based on the coincidences of two neighbouring fibres (to define trajectories crossing the fibre under study) and a third 2 cm thick detector used to select minimum ionising particles by their energy deposition. High detection efficiencies (93 %) are possible but only for thresholds below one pixel signal amplitude. It seems necessary to use thicker fibres if a low noise detector is desired. A 2 mm square double cladding fibre read out by the SSPM-0606BG4MM-PCB has been suggested as an optimum combination for such a detector which is currently under study in Mainz.

For $\overline{\mathrm{P}}$ANDA the time resolution is a main issue. A SSPM is intrinsically a very fast detector and its single photoelectron time resolution is about 100 ps (FWHM). When coupled to thin and short scintillating fibres the timing properties are fully dominated by the scintillation time constants and depend only on the average number of detected photons. A Monte Carlo simulation for a possible $\overline{\mathrm{P}}$ANDA detector based on 10 cm long double cladding fibres results in a time resolution of 0.9 ns (rms). When dealing with long fibres to the path length dispersion contributes to some extend. Time resolution has been measured for the two metres long fibre mentioned above when excited by minimum ionising particles crossing its centre giving a FWHM= 1.4 ns.

Fig. 1 shows an ADC spectrum measured with one of the SSPMs and induced by a short pulsed UV laser. A physical model for the SSPM was developed whose parameters can be fitted to the data using a Monte Carlo for the random processes of thermal noise rate (4.5 MHz), internal cross-talk (7.7 % probability) and after-pulses (15 % probability).

Radiation hardness is also an important issue due to the relatively small distance from the target area to the detector position. In order to quantify the radiation hardness 14 MeV electrons were used to irradiate a sample of SSPM-0701BG-TO18 diodes. A significant increase in the dark count rate has been observed [2] and the annealing of damaged diodes will be studied.

Considering the requirements for a $\overline{\mathrm{P}}$ANDA start detector of a small target distance, a high granularity and a precise timing, the use of presently available SSPMs seems hindered.

References

[1] Technical progress report for Panda: strong interaction studies with antiprotons, Jan. 2005.

[2] P. Achenbach, S. Sanchez Majos *et al.*, Characterisation of radiation damage in silicon photomultiplier, submitted to Nucl. Instr. and Meth. in Phys. Res. A, Jan. 2008.

* sanchez@kph.uni-mainz.de
† patrick@kph.uni-mainz.de

Optical tests of the DIRC-barrel for the PANDA Experiment*

R. Hohler[1,2], D. Lehmann[1], K. Peters[1,2], G. Schepers[1], C. Schwarz[1], and C. Sfienti[1]
[1]GSI, Darmstadt, Germany; [2]JWG Universität Frankfurt, Germany

The PANDA detector will contain two Cherenkov counters around the interaction point — one as a barrel and the other in forward direction as a disk. The former is mainly developed at GSI. This Cherenkov counter is based on the DIRC-concept (Detection of Internally Reflected Cherenkov photons) and provides particle identification by measuring the Cherenkov-cone angle of relativistic charged particles. Our task is the determination of the radiator surface quality by measuring the internal reflection loss with a laser which simulates the Cherenkov light.

A schematic illustration of the current setup is shown in Figure 1. A beamsplitter cube, composed of two prism, splits the beam from a laser diode. One of both beams measures the optical properties of the radiator and the other beam is used as a reference to reduce temperature effects or laser intensity fluctuations. Diffusors were mounted in front of the photodiodes to minimize the influence of spatial shifts in the laserprofile and of the laser spot.

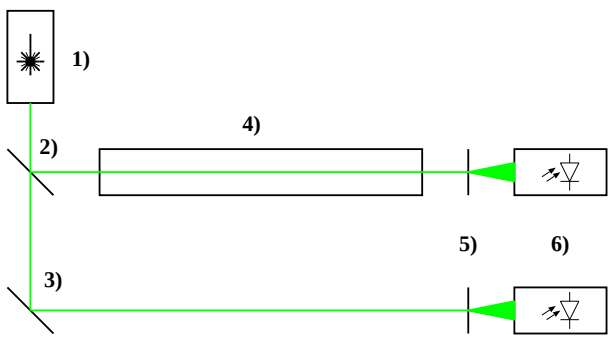

Figure 1: Schematic experiment setup:
1) Laser, 2) beamsplitter, 3) mirror, 4) quartz bar, 5) diffusors, 6) photodiodes.

It is not possible to adjust the quartz bar exactly parallel to the laser beam. Therefore the beam, after traversing the bar, does not hit the diffusor on the same position and with an different incident angle. Because of this fact we measured the radiation characteristic of the diffusor by rotating it. The diffusor plate consists of a regular glass plate with one rough surface. In the perfect case the diffusor is hence a lambertian beamer. Figure 2 shows the radiation characteristic with a step size of 1°. Especially in the high intensity region of both sides of the diffusor a zick-zack-shape is observed. Since previous measurements showed that the sensitive area of the photodiodes are quite homogenous, this zick-zack-shape is probably produced by the surface structure of the diffusor. A difference of 1° of the incident angle can produce an intensity difference of up to $1\ \%$. After the beam traversed the "aligned" quartz bar a shift in the order of $1\ \mathrm{mm}$ could occure. This shift change the incident angle on the diffusor of about 0.5°. We expect a difference in the intensity of about 5 permille, but our goal is a precision of a permille. Therefore the diffusors were removed from the setup.

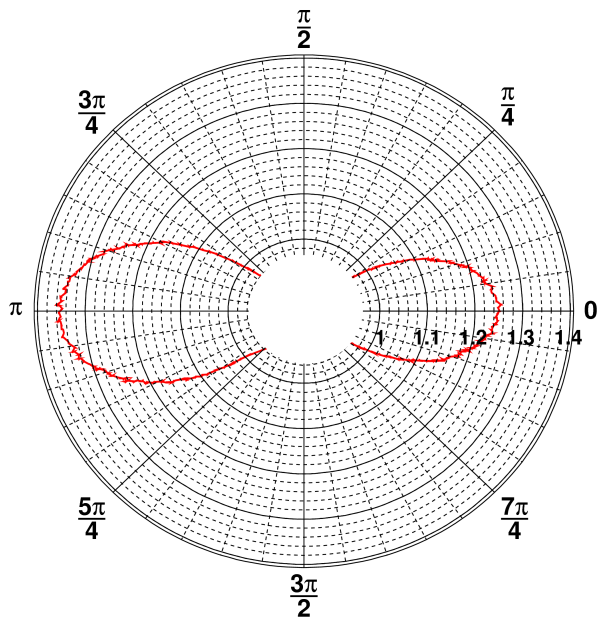

Figure 2: Diffusor radiation characteristic: At zero angle the beam hits first the rough surface of the diffusor and then the regular glass layer and at π the other way around.

Furthermore the transmission of a single glass plate was also measured to extract the bulk absorption of the radiator from the total loss, i.e. bulk and reflection loss. The result of the transmission is $\mathrm{T} = 0.9252 \pm 0.0005$, but newer results show that all used glass plates are very inhomogenous produced by scratches on the glass surface or the roughness of the glass plate. So we have an additional systematic uncertainty to the transmission in the order of some percent. With better glass plates this uncertainty can reduce to 1 permille. This accuracy is necessary to measure in a next step the internal reflection loss of photons in the quartz bar, which depends on its surface quality.

* Work supported by the European Community RESEARCH INFRASTRUCTURES ACTION under the FP6 program: Structuring the European Research Area - Specific Support Action - DESIGN STUDY (contract 515873 - DIRACsecondary-Beams)

References

[1] G. Schepers et al., Scientific Report 2006, "DIRC-Radiator tests for the PANDA Experiment at GSI", 2006

Design of a Disc DIRC Endcap Detector for PANDA at FAIR*

M. Düren† [1], I. Brodski[1], M. Ehrenfried[1], P. Koch[1], S. Lu[1], O. Merle[1], R. Schmidt [1], P. Schönmeier[1], H. Stenzel[1], J. Streit-Lehmann[1], A. Weidenfelder[1], and M. Zühlsdorf[1]

[1]II. Phys. Inst., Univ. Giessen, Heinrich-Buff-Ring 16, 35392 Giessen, Germany

The endcap DIRC

An efficient and capable particle identification (PID) system is crucial for the physics objectives pursued by the PANDA experiment at FAIR [1]. In the endcap region a clear separation of pions and kaons up to momenta of 4 GeV/c is required. A very compact PID detector has been designed that is based on the DIRC (Detection of Internally Reflected Cherenkov light) principle [2, 3, 4].

The main component of the DIRC is an octagonal, 2 cm thick radiator disc of fused silica. Charged particles penetrating the disc emit Cherenkov photons. Some of the photons undergo total reflection and propagate to the rim of the disc where they are detected. In collaboration with the PANDA groups from Edinburgh and Glasgow two different designs are studied. The first design uses focussing lightguides to project the Cherenkov angle on a multi-pixel PMT matrix [5], the second design (Fig. 1) uses the time of propagation (TOP) to extract the Cherenkov angle [6, 7].

The TOP disc DIRC design

The time of propagation of a totally reflected Cherenkov photon in the radiator disc depends on the Cherenkov angle and, due to dispersion, on the wavelength of the photon. 960 multi-channel plate PMTs at the rim of the disc measure the relative arrival times of the Cherenkov photons with a resolution of ~ 30 ps and allow to reconstruct the Cherenkov angle. To minimize the effect of dispersion, two types of dicroic mirrors are placed in front of the PMTs in alternating sequence. The mirrors split the wavelength range of 400-700 nm into two ranges ('blue' and 'green'). Due to the dicroic filters every second channel is sensitive to 'blue' or 'green' photons respectively. Photons which are reflected by a dichroic mirror will travel longer distances, which improves the relative time resolution and the separation power of the detector.

A software package has been developed that simulates the generation and propagation of the Cherenkov photons in the disc and reconstructs the Cherenkov angle. The implemented algorithm is able to identify pions/kaons based on relative time differences alone and does not rely on any external absolute timing information. As the antiproton beam does not have any bunch structure and PANDA uses a triggerless data acquisition this feature of the reconstruction algorithm is especially important. As a result, a 4σ separation between pions and kaons up to about 4 GeV/c is obtained [8].

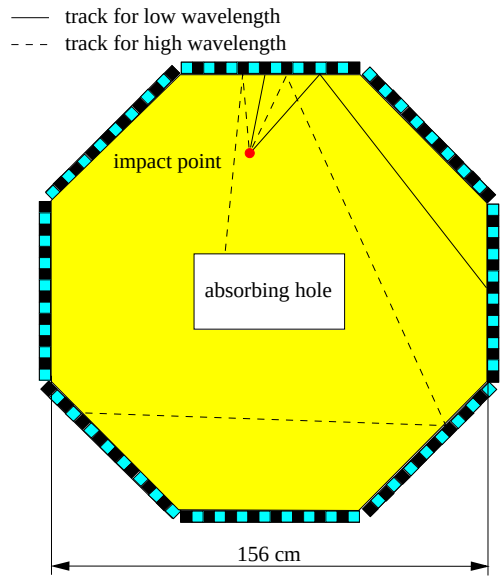

Figure 1: Octagonal radiator disc with tracks of photons of different wavelengths. Dichroic mirrors in front of the photon detectors allow to separate two wavelength ranges and to reduce dispersion effects.

References

[1] PANDA Collaboration, Technical Progress Report, FAIR-ESAC/Pbar 2005

[2] R. Aleksan et al., Nucl. Inst. Meth. A397, 261 (1997)

[3] B. Ratcliff, Nucl. Inst. Meth. A502, 211 (2003)

[4] Y. Enari et al., Nucl. Inst. Meth. A494, 430 (2002)

[5] K. Föhl et al., "The DIRC detectors of the PANDA experiment at FAIR", Proceedings of RICH 2007 conference in Trieste/Italy, 15-20 October 2007, to be published in Nucl. Instrum. Meth. A.

[6] M. Düren et al., "Conceptual Design of a Multi-Chromatic Time-of-Propagation Endcap DIRC for PANDA", Panda internal report, June 2, 2006, http://www.physik.uni-giessen.de/dueren/giessendirc1.pdf.

[7] P. Schönmeier et al., "Disc DIRC Endcap detector for PANDA at FAIR", Proceedings of RICH 2007 conference in Trieste/Italy, 15-20 October 2007, to be published in Nucl. Instrum. Meth. A.

[8] M. Düren et al., "Resolution Studies for a Multi-chromatic Time-of-Propagation Endcap DIRC for PANDA", Panda internal report, October 31, 2007, http://www.physik.uni-giessen.de/dueren/giessendirc2.pdf.

* Work supported by GSI and BMBF

† michael.dueren@uni-giessen.de

Studies of Microchannel Plate PMTs for the PANDA DIRC*

A. Lehmann†[1], A. Britting[1], W. Eyrich[1], C. Pizzolotto[1], A. Teufel[1], and PANDA Cherenkov group
[1]Physikalisches Institut IV, Universität Erlangen-Nürnberg, Erwin-Rommel-Str. 1, D-91058 Erlangen

Introduction

The charged particle identification in PANDA over a wide range of momenta will be done by novel Cherenkov detectors using the DIRC (Detection of Internally Reflected Cherenkov light) principle. Due to space limitations these detectors must be very compact and the photon sensors will be placed inside the PANDA solenoid. A high precision measurement of the Time-of-Propagation (ToP) of the Cherenkov photons from their point of creation to the readout plane is foreseen to allow either the reconstruction of the Cherenkov angle or the correction of dispersive effects in the radiator material. Currently the envisaged time resolution of $\sigma < 50$ ps for single photons (SPh) can only be achieved with microchannel plate (MCP) PMTs.

Response in Magnetic Fields

The photon sensors of the PANDA DIRC have to operate in a magnetic field of possibly up to 2 Tesla. To investigate the response of MCP-PMTs in such an environment we performed measurements at a dipole magnet at the FZ Juelich which delivers magnetic fields of up to 2.05 Tesla. Three different types of MCP-PMTs were investigated: two 8x8 pixel multi-anode MCP-PMTs of Photonis-Burle with 25 and 10 μm pore diameter, respectively, and a single anode MCP-PMT from BINP in Novosibirsk, Russia, with 6 μm pores. In the following, mainly the results of the latter device will be discussed.

The MCP-PMTs were illuminated with ultrafast light pulses of $\sigma = 14$ ps width at a wavelength of 372 nm. The gain and the time resolution of the MCP-PMTs were measured as a function of the magnetic field. We find that a pore diameter of 10 μm or less is needed in a 2 Tesla magnetic field in order to maintain a gain high enough for an efficient single photon detection. Also the effects of the angle between the MCP-axis and the field orientation were studied. In Fig. 1 the results for the BINP MCP-PMT are shown. For angles $\geq 30°$ the gain drops significantly at high magnetic fields. However, by operating the MCP-PMT at an increased high voltage single photon detection inside the PANDA solenoid would be possible even at a field of 2 T and $45°$. The time resolution does not seem to depend a lot upon the magnetic field.

Time Resolution

The time resolution without a magnetic field was precisely measured using a 3 GHz / 20 Gs oscilloscope. For the BINP MCP-PMT the results for combinations of different amplifiers and discriminators were compared. The best performance for SPh was obtained with an Ortec VT120A amplifier which has the highest amplification factor (x200) of the investigated devices, but only a moderate bandwidth (350 MHz). This indicates that for a good time resolution measurement of SPh a high amplification factor is more important than a high bandwidth.

In Fig. 2 the time resolution measured for the Photonis-Burle with 25 μm pores is compared to that of the BINP MCP-PMT with 6 μm pores. Clearly, a smaller pore size results in a better time resolution. For the BINP MCP-PMT a resolution of 27 ps was measured. By unfolding blurring effects caused by the light pulse and electronics devices a net transit time resolution for SPh of $\sigma_t \approx 20$ ps was obtained. This is the best value determined for SPh so far.

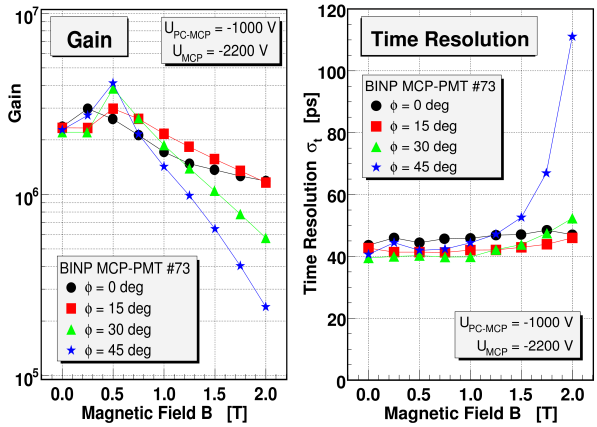

Figure 1: Gain (left) and time resolution (right) for SPh as a function of the magnetic field for different angles ϕ between the MCP axis and the field orientation.

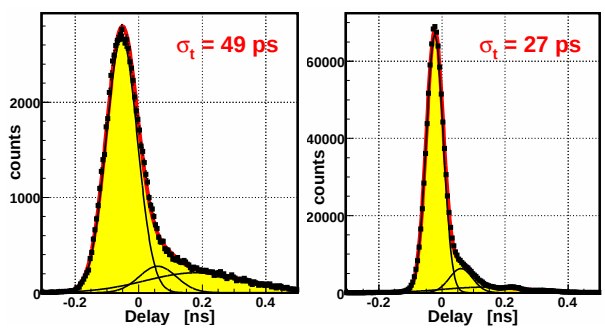

Figure 2: Single photon time resolution for the Photonis-Burle MCP-PMT (left) and the BINP device (right) measured with a fast oscilloscope.

* Work supported by BMBF and GSI
† lehmann@physik.uni-erlangen.de

Particle Background simulation for a triple Germanium Cluster detectors at PANDA*

A. Sanchez Lorente[†1], P. Achenbach[1], A. Botvina[1], M. Kavatsyuk[2], J. Pochodzalla[1], and T.R. Saito[2]
[1]U Mainz, Germany; [2]GSI, Darmstadt, Germany

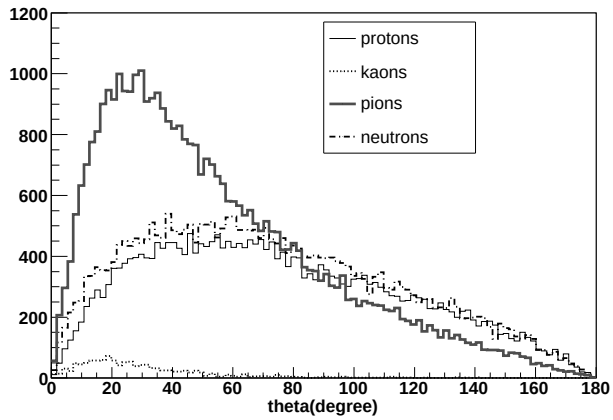

Figure 1: Distribution of produced particles from background reactions. The Germanium detectors will be affected mainly by particles emitted at backward axial angle

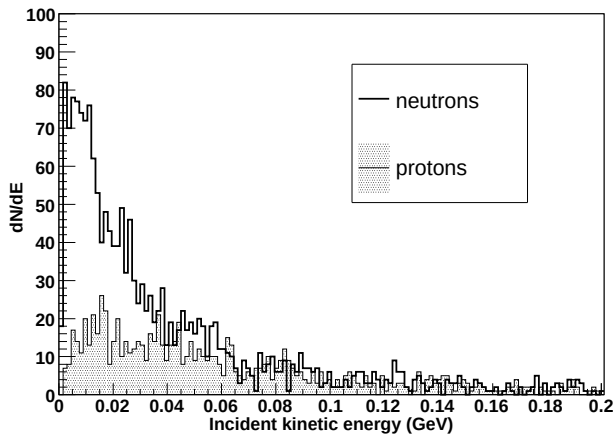

Figure 2: Incident kinetic energy of protons and neutrons entering the Germanium detector surface. The main contribution to a possible radiation damage of the detector is provided by neutrons.

For the high resolution spectroscopy of excited hypernuclear states a position sensitive Germanium γ–array [1] [2] has been implemented in the standard PANDA framework PANDAroot. In the simulation encapsulated n–type Germanium crystals are arranged asymmetrically to form a triple cluster [3]. The total γ–array set-up consists of 15 triple Germanium cluster detectors positioned at backward axial angle around the target region. [4] Hereby the main limitation is the load of high particles rate from background reactions. The influence of this particle background has been simulated to investigate the feasibility of operating this kind of detectors under these condictions.

Background reactions have been calculated by using the UrQMD+Smm [5] event Generator to produce 10000 $\overline{p} + ^{12}C$ interactions at 3 GeV/c (see fig. 1). Most of the produced charged and neutrals particles are emitted into the forward region not covered by the Germanium array. Those charged particles emitted into backward axial angles are very low in kinetic energy, and will be absorved in a large fraction in the material surrounding the target. More critical are nevertheless neutrons emitted into the backward direction which can contribute to the radiation damage of the detector.

Fig. 2 shows the kinetic energy distribution of protons and neutrons entering the surface of the Germanium detectors. As one observes, neutrons are the main contribution in comparison to protons, with a typical kinetic energy of approximatly 20 MeV. At a distance of 30 cm between the primary target and an interaction rate of $5 \cdot 10^6 \mathrm{s}^{-1}$, the load of fast neutrons on the detector array is about 700 particles $\mathrm{cm}^{-2}\mathrm{s}^{-1}$.

Asumming that a n–type Germanium detector [4] is expected to withstand a fast neutrons fluence of about $4 \cdot 10^9$particles cm^{-2}, the results obtained by the simulation suggests that the operation of these Germanium detector will be feasible under the experimental conditions at PANDA.

Hypernuclear Physics is currently attracting renewed attention. Thanks to the use of stored $\overline{\mathrm{p}}$ beams, copious production of double Λ hypernuclei is expected at the PANDA experiment which will enable high precision γ spectroscopy of such nuclei for the first time.

The simultaneous production and implementation of two Λ particles into a nucleus is not feasible. The conversion of a Ξ^- and a proton into two Λ particles releases – ignoring binding energy effects – only 28 MeV/c^2. Accordingly, there is a chance of typically a few percent that both Λ hyperons stick to the same nucleus. Because of this two-step process, spectroscopic studies, based on the analysis of two-body reactions like in single hypernuclei reactions, cannot be performed and spectroscopic information on double hypernuclei can only be obtained via their de-

*This research is part of the EU integrated infrastructure initiative Hadronphysics project under contract number RII3-CT-2004-506078 and by the BMBF under contract number 06MZ225I.
† lorente@kph.uni-mainz.de

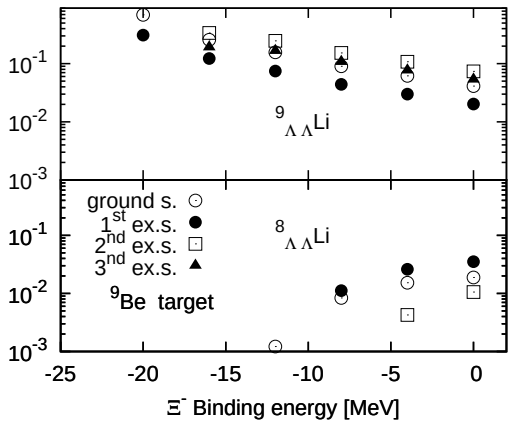

Figure 3: Production of individual ground and excited states of double hypernuclei using a ^{9}Be secondary target.

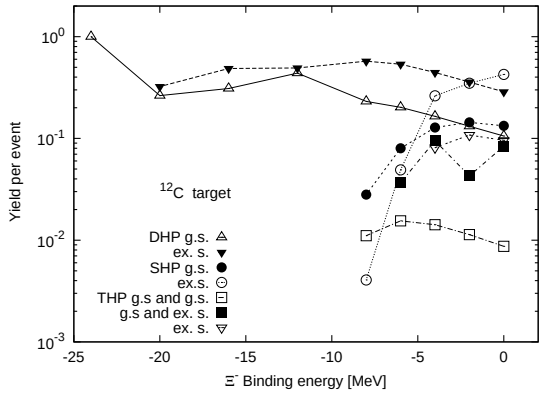

Figure 4: Predicted relative yield for ground states (g.s.) and excited states (ex.s.) in double (DH), single (SH), and and twin hypernuclei (TH) as a function of the Ξ binding energy for a secondary target of ^{12}C .

cay products. Except for the case of very light hypernuclei also neutral particles are emitted unfortunately. Therefore, a unique identification of the double hypernuclei can only be reached via the emitted γ-rays from excited, particle stable states.

For light nuclei with mass numbers $A_0 \leq 13$ even a relatively small excitation energy may be comparable to their binding energy. In the following we therefore assume that the principal mechanism of de-excitation is the explosive decay of the excited nucleus into several smaller clusters. To describe this break-up process and in order to estimate the population of individual excited states in double hyper nuclei after the conversion of the Ξ^-, we have developed a statistical decay model which is reminiscent of the famous Fermi model for particle production in nuclear reactions [6]. We assume that the nucleus break-ups simultaneously into cold and slightly excited fragments [7]. In the case of conventional nuclear fragments, we adopt their experimental masses in ground states, and take into account their excited states, which are stable respective to emission of nucleons. For hypernuclei with single Λ particle, we use the experimental masses and excited states also. For double hypernuclei we adopt theoretically predicted masses and excited states [8, 9].

In the model we consider all possible break-up channels, which satisfy the mass number, hyperon number (i.e. strangeness), charge, energy and momenta conservations, and take into account the competition between these channels. Since the excitation energy of the initially produced double hypernuclei is not exactly known, we performed the calculations as a function of the binding energy of the captured Ξ^-. Calculations were performed for all stable secondary targets (^{9}Be, ^{10}B, ^{11}B, ^{12}C, and ^{13}C) which lead to the production of excited states in double hypernuclei. As an example Fig. 3 shows this excitation function for a ^{9}Be target nucleus. This example as well as Fig. 4 suggests that a significant fraction of the converted Ξ^- lead to the production of a γ-unstable double hypernuclei. Comparing the expected yields for various target nuclei we are presently developing a strategy to uniquely assign observable transition to the corresponding hypernuclei.

References

[1] A. Sanchez Lorente et al., Performance of germanium detectors in high magnetic fields, in GSI Sci. Rep. 2004, p.32 and A. Sanchez Lorente *et al.*, in: GSI Sci. Report 2005, GSI, Darmstadt, 2006, p. 79, FAIR-QCD-PANDA-07

[2] A. Sanchez Lorente et al., Performance of HPGe in high magnetic fields, Nucl. Inst. Meth A 573(2007)410–417.

[3] A. Sanchez Lorente. PhD thesis, U Mainz.

[4] Technical Progress Report for PANDA

[5] A. Galoyan. Private Comunication.

[6] E. Fermi, Progr. Theor. Phys. **5** (1950) 570.

[7] J.P. Bondorf *et al.*, Phys. Rep. **257** (1995) 133.

[8] E. Hiyama *et al.*, Phys. Rev. **66** (2002) 024007.

[9] T. Yamada and K. Ikeda, Phys. Rev. **C56** (1997) 3216.

Development of a High-Rate GEM-Based TPC for PANDA

B. Ketzer*[1], F. Böhmer[1], Q. Weitzel[1], C. Höppner[1], T. Huber[1], I. Konorov[1], A. Mann[1], S. Neubert[1], S. Paul[1], and C. Simonetto[1]

[1]Technische Universität München, Physik Department, 85748 Garching, Germany

Introduction

High-precision spectroscopy of hadrons in the strange and charm sector, as envisaged in the PANDA experiment [1], requires an excellent charged particle tracking system with a very low material budget in order not to spoil the energy and mass resolution of the apparatus. One option for the central tracker is a time projection chamber (TPC), located inside the 2 T solenoid magnetic field between the microvertex detector and the electromagnetic calorimeter. In addition to its excellent tracking properties, a TPC would strongly contribute to particle identification (PID) in the sub-GeV region, which is otherwise not covered by any other detector in PANDA. Owing to the beam properties at the High Energy Storage Ring (HESR), the TPC has to operate at interaction rates up to $2 \cdot 10^7$ in a continuous mode. The use of GEM (Gas Electron Multiplier) foils as amplification stage [2] opens the possibility to bypass the necessity of gating, as the backdrift of ions into the drift volume is suppressed due to the asymmetric field configuration.

Ion Backflow and Space Charge Build-up

To study this suppression, a $10 \times 10\,\mathrm{cm}^2$ dedicated triple-GEM test detector has been built, which allows an easy exchange of the GEM foils and an independent setting of all voltages. The currents on all electrodes under irradiation with Cu X-rays were measured with custom-made high-voltage current meters with a resolution of a few tens of pA. All measurements were carried out without magnetic field and in an Ar/CO_2 (70/30) gas mixture. A minimum ion backflow (ion current on the cathode divided by electron current on the anode) of 0.8% has been achieved.

In order to study the build-up of space charge in the PANDA TPC and the resulting distortions to the drift of electrons, Monte-Carlo simulations of $\bar{p}p$ annihilation events at a rate of $2 \cdot 10^7$/s were carried out, assuming an ion backflow of 0.25%, which seems feasible taking into account the presence of a magnetic field in PANDA. The resulting charge distribution was translated into a 3-D electrical field map using a finite element program. Taking into account both the electric and realistic magnetic fields, radial displacements of up to 6 mm are observed, depending on the rz start position of the electrons (Fig. 1). Such displacements have already been corrected for in other experiments like ALEPH and the STAR.

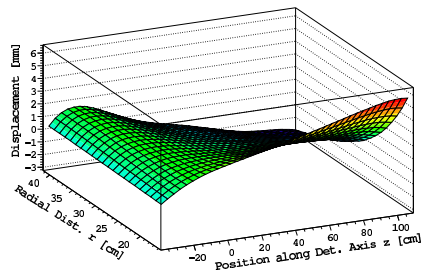

Figure 1: Radial displacement of drifting electrons in realistic electric and magnetic fields, depending on their rz start position. The GEM stack is located at $z = -40\,\mathrm{cm}$.

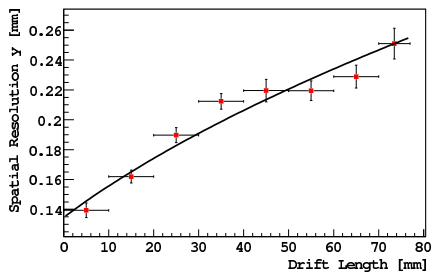

Figure 2: Residual width in y vs. drift distance z. The black curve is the result of a fit taking into account the diffusion.

Measurements with a GEM-TPC

First measurements with cosmic muons have been carried out using a triple-GEM TPC with $7.7\,\mathrm{cm}$ drift length and $10 \times 10\,\mathrm{cm}^2$ active area. The ALICE TPC front-end electronics was used to read 128 of the $1 \times 6\,\mathrm{mm}^2$ pads. The focus during these measurements was on the detection of tracks crossing the TPC almost perpendicularly to the pad plane. The resolution of the TPC was estimated from the residual distribution of clusters from reconstructed tracks. Figure 2 shows the r.m.s. width of the residuals in the y coordinate (1 mm pad width) as a function of the drift distance z. The resolution is limited in this case both by the finite pad width and the noise of the ALICE electronics, which has not been optimized for GEM detectors.

References

[1] PANDA, M. Kotulla, et al., Technical progress report for PANDA: Strong interaction studies with antiprotons, FAIR-ESAC/Pbar/Technical Progress Report (February 2005).

[2] F. Sauli, Nucl. Instr. Meth. A 386 (1997) 531.

* Bernhard.Ketzer@cern.ch

Prototype drift chamber for PANDA experiment

P. Hawranek, A. Heczko, M. Kajetanowicz, K. Korcyl, W. Krzemień, A. Misiak, P. Salabura, J. Smyrski, J. Trębacz, A. Wrońska
Institute of Physics, Jagiellonian University, Cracow, Poland

Introduction

We proposed to use two planar drift chambers for tracking in the Target Spectrometer of the PANDA detector at forward angles ($\theta < 22^o$) which are not covered fully by the straw tube tracker. The chambers have to stand a high counting rate of particles peaked at the most forward angles due to the relativistic boost as well as due to the small angle $\overline{p} - p$ elastic scattering. With the envisaged maximum $\overline{p} - p$ interaction rate of 20 MHz and at the maximum momentum of the antiproton beam of 15 GeV/c, the expected particle flux in the chambers in the vicinity of the 5 cm diameter beam pipe is about 20 kHz/cm^2.

Chamber construction

In order to test the mechanical construction of the proposed drift chambers and to investigate their high rate behavior we constructed a prototype chamber [1]. The chamber contains 1 cm x 1 cm quadratic drift cells arranged in double-layers as it is shown in Fig. 1. The sense wires are made of 20 μm thick gold-plated tungsten, whereas for the 110 μm field and cathode wires gold–plated molybdenum was used. The prototype chamber contains two double layers with vertical wires. This arrangement is sufficient for testing the reconstruction of tracks in the horizontal plane. The diameter of the active area of the chamber is equal to 120 cm. The most central wires in each double layer are mounted on insulating rings which will surround the beam pipe in the PANDA experiment. As a chamber gas we use 90% Ar + 10% CO_2 mixture at atmospheric pressure.

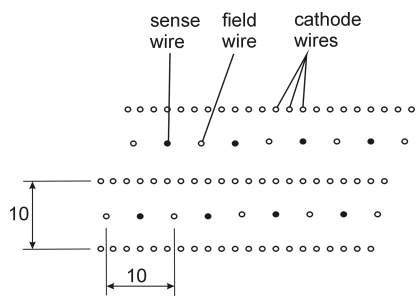

Figure 1: Double layer of drift cells.

The chamber is equipped with 16 channel preamplifier-discriminator cards based on the Fujitsu MB13468 amplifier chip and the LeCroy MVL407S comparator chip. For the drift time measurements we use the TRB-boards developed for the HADES experiment. A photograph of the chamber is shown in Fig. 2.

High rate tests

The prototype drift chamber was tested using the external proton beam of the COSY accelerator in the Research Center - Jülich. The beam momentum was 2.9 GeV/c and the maximum intensity in the spill was $5 \cdot 10^6$ protons per second. The width of the beam intensity profile (FWHM) at the chamber position was about 4 cm horizontally and 8 cm vertically. For the particle fluxes of 20 kHz/cm^2 - as expected at PANDA - the detection efficiency was 96%. We observed a drop of the efficiency when increasing the flux to 200 kHz/cm^2. Tests of the chamber will be continued with respect to the aging effects. Results of the present and planned tests will allow to make a final choice between the drift detectors and the GEM detectors which are considered as an alternative solution for the forward tracking in the Target Spectrometer of the PANDA detector.

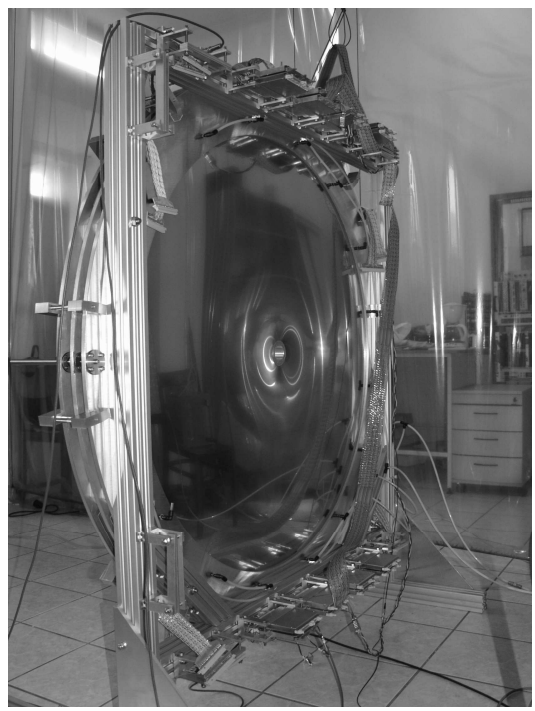

Figure 2: Prototype drift chamber for PANDA.

References

[1] J. Smyrski et al., "Prototype drift chamber for tracking at small angles in the PANDA experiment", Proceedings of the 10th ICATPP Conference on Astroparticle, Particle, Space Physics, Detectors and Medical Physics Application, Como, 8-12 Oct. 2007.

Status of the PandaRoot simulation and analysis framework

PANDA Computing Group[1]

[1] FZJ, Jülich, Germany; GSI, Darmstadt, Germany; Jagellonian University, Cracow, Poland; JLU, Gießen, Germany; KVI/University of Groningen, Groningen, The Netherlands; LPP, Dubna, Russia; Ruhr-University, Bochum, Germany; Soltan Institute for Nuclear Studies, Warsaw, Poland; Technical University of Dresden, Dresden, Germany; Technische Universität München, Garching, Germany; University of Basel, Basel, Switzerland; University of Ferrara and INFN, Ferrara, Italy; University of Frankfurt, Frankfurt, Germany; University of Glasgow, Glasgow, United Kingdom; University of Pavia and INFN, Pavia, Italy; University of Torino and INFN, Torino, Italy

In preparation for experiments with the PANDA detector at FAIR, the FairRoot framework [1] has been employed and evaluated. The FairRoot framework provides the core services for detector simulation and offline analysis. PandaRoot is one of the branches of FairRoot and is designed specifically for the PANDA detector, its reconstruction, and physics analysis.

In 2007, a nearly-complete implementation of the different detector elements and their digitization and reconstruction has been achieved. In addition, advanced tracking algorithms, a track follower based on the GEANE package and a generic Kalman filter have been employed. The PandaRoot framework has meanwhile been used for various design studies of detector components and physics benchmark studies. An example is depicted in Fig. 1, which shows the successful reconstruction of the photon-rich decay of the h_c with a mass of $M(h_c)$=3.526 GeV/c^2 into seven photons via $\bar{p}p \rightarrow h_c \rightarrow \eta_c\gamma$ with $\eta_c \rightarrow \pi^\circ\pi^\circ\gamma$ and $\pi^\circ \rightarrow \gamma\gamma$, $\eta \rightarrow \gamma\gamma$.

A package for performing fast simulations has recently been implemented. With this package one is able to perform very fast a complete simulation. It is based on an parameterization of the individual detector responses without the need for a full Monte-Carlo modeling of the interactions of particles with the detector materials. The parameterization is obtained by a comparison with the results from experimental data or from simulations using a full transport code, such as Geant3, Geant4, or Fluka. In particular, the fast simulation package will be used to generate large numbers of background events within an acceptable period of time.

In addition, part of the Rho analysis tool set [2] has been migrated within the PandaRoot framework. This package contains userfriendly higher-level analysis tools. An example application is shown in Fig. 2. The figure depicts the reconstructed invariant mass of the $D_{s0}(2317)^\pm$ from 10.000 $\bar{p}p \rightarrow D_s^\pm D_{s0}(2317)^\mp$ reactions using the fast simulation package and using the Rho analysis framework.

The PandaRoot framework is designed to run on a large variety of computing platforms. This has the advantage that the software can be employed easily on a GRID environment. The PANDA collaboration is presently expanding and maintaining an AliEN2 GRID network in synergy with the PandaRoot developments. A complete simulation and analysis chain has been successfully tested on the GRID which presently consists of about 10 sites. In addition, advanced monitoring tools, based on MonALISA, are being used in connection to the GRID and framework developments. Furthermore, a physics analysis model has been drafted describing the computing needs to address the variety of physics channels which will be measured with PANDA. This model will be used as input for a more complete computing model for PANDA.

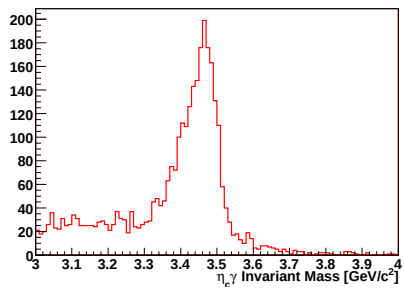

Figure 1: An example of a full reconstruction of the neutral h_c decay into seven photons (see the text). The invariant mass distribution of reconstructed $\eta_c\gamma$ pairs is shown.

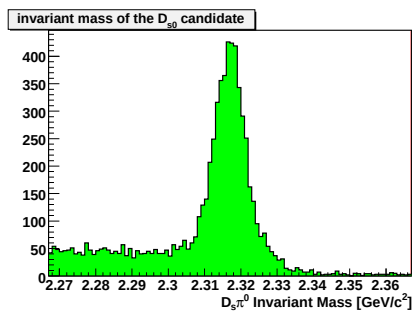

Figure 2: The reconstructed invariant mass of the $D_{s0}(2317)^\pm$ for the reaction $\bar{p}p \rightarrow D_s^\pm D_{s0}(2317)^\mp$, by using the fast simulation and the Rho analysis tool set.

References

[1] M. Al-Turany *et. al.*, GSI scientific report 2006, INSTRUMENTS-METHODS-16, p 211.

[2] http://savannah.fzk.de/websites/hep/rho/

Ramp Compression of Matter Using Intense Heavy Ion Beams at FAIR: The HEDgeHOB Collaboration*

N.A. Tahir[1], A. Ng[2], A. Shutov[3], A.R. Piriz[4], I.V. Lomonosov[3], D.H.H. Hoffmann[5], and C. Deutsch[6]
[1]GSI, Darmstadt, Germany; [2]LLNL, Livermore, USA; [3]IPCP, Chernogolovka, Russia; [4]UCLM, Ciudad Real, Spain; [5]TU Darmstadt, Germany; [6]LPGP, Orsay, France

Laser-driven shockless compression of matter to study material properties under dynamic conditions has been reported elsewhere [1]. In this case the process consists of three distinct phases: First a strong laser driven shock is launched into a reservoir which turns the material into a weakly ionized plasma. After the shock breaks through the rear side of the sample, the plasma moves towards a sample situated some distance away across a vacuum.gap.In the final phase, the plasma piles up slowly against the sample that generates a smoothly increasing applied pressure as it converts its kinetic energy into thermal pressure (ramp shaped profile) that drives a shockless compression of the sample material. This scheme is very useful to study the material properties under dynamic conditions.

We propose that using an intense ion beam one can design a similar experiment which will have numerous advantages over the laser-driven scheme.

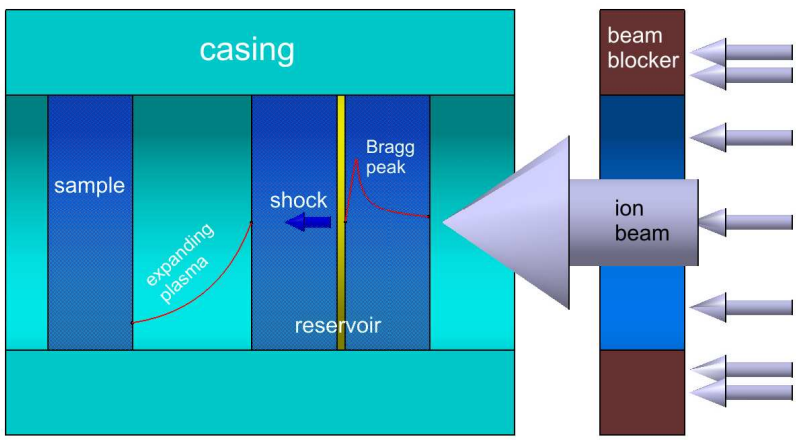

Figure 1: A schematic diagram of proposed ramp compression experiment for the HEDgeHOB Collaboration to study material properties under dynamic conditions.

Figure 1 shows a schematic diagram of this proposed experiment which consists of a cylindrical disc of high-Z reservoir followed by the sample material and the two are enclosed in a strong cylindrical casing. The ion beam is incident on the reservoir and the ions are completely stopped in the material. The high pressure due to the Bragg peak launches a shock in the longitudinal direction that releases material when it arrives at the reservoir boundary. The expanding material piles up against the sample and pressure builds up slowly that drives a shockless compression of the sample material. Simulation carried out using a two-dimensional hydrodynamic computer code show a **60** % compression of an Al sample while the temperature and pressure are of the order of **800 K** and **1 Mbar** respectively.

It is to be noted that an ion beam driven scheme is much more efficient compared to the one driven by laser. Moreover the driving pressure produced by a laser is limited by the the fact that too high laser intensity will cause radiative preheat of the reservoir and the sample material. In case of ion beam heating, on the other hand, preheat can not be a problem as the temperature in the absorption region is a few tens of eV.

Finally one may use a larger sample in case of ion beams with longer time scales for experimental measurements.

References

[1] J. Edwards et al., Phys. Rev. Lett. 92 (2004) 075002.

* Work supported by BMBF

Richtmyer-Meshkov instability in elastic-plastic media*

A. R. Piriz[1,#],J. J. López Cela[1], N. A. Tahir[2], and D. H. H. Hoffmann[2,3]
[1]Univ. de Castilla-La Mancha, Spain; [2]GSI, Darmstadt, Germany, [2]Technische Universität of Darmstadt, Germany

A sort of Richtmyer-Meshkov (RM) instability occurs when a shock wave is launched into the bulk of continuous medium from its boundary surface. Such is the situation in the LAPLAS (Laboratory of Planetary Sciences) experiment planned at GSI to be performed on the future FAIR facility for the study of high energy density states of matter. It happens when the absorber region expands driving the implosion of the pusher layers. Since the pusher remains in solid state during the implosion, it retains elastic-plastic properties that will affect the evolution of the hydrodynamic instabilities. We have studied the RM dynamics of a vacuum/solid interface by means of an analytical model and by two-dimensional numerical simulations with the code ABAQUS [1-3]. The typical behaviour of the perturbation amplitude is shown in Fig.1 for different values of the yield strength Y (5, 10, 20, 40, ∞ MPa) and for a shear modulus $G = 13$ GPa. For reference we also show the classical growth rate ($G = 0$, $Y = \infty$).

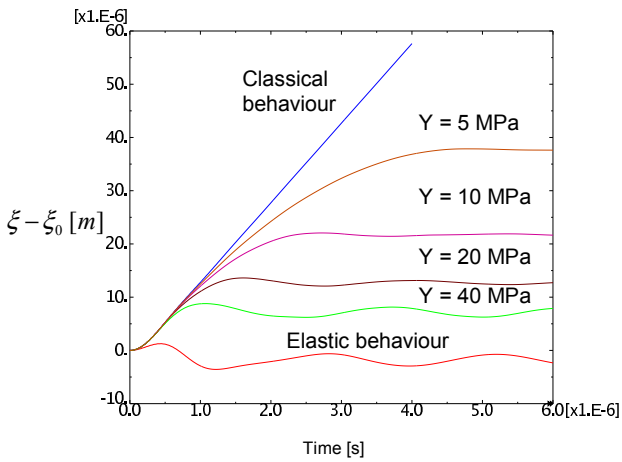

Figure 1: Amplitude evolution for different values of the yield strength and for the classical case.

As we can see, the perturbation grows up to a maximum value ξ_m determined by the yield strength and then it oscillates elastically with an amplitude that is much less than ξ_m ($\xi_0 = 20\ \mu m$ is the initial perturbation amplitude of the interface).

In Fig.2 we have represented the results of extensive numerical simulations for the relative amplitude $\xi_m - \xi_p$, where ξ_p is taken as the amplitude at the time when the interface is free of stresses (the inflexion point in Fig.1). We find that this magnitude is only a function of the parameters combination $\rho\dot{\xi}_p^2 / kY$, where k is the perturbation wavenumber, ρ is the density of the shocked phase and it is determined by the Mie-Grüneisen equation of state, and $\dot{\xi}_p = k\xi_0 u_p$ is the classical growth rate (u_p is the fluid velocity behind the shock).

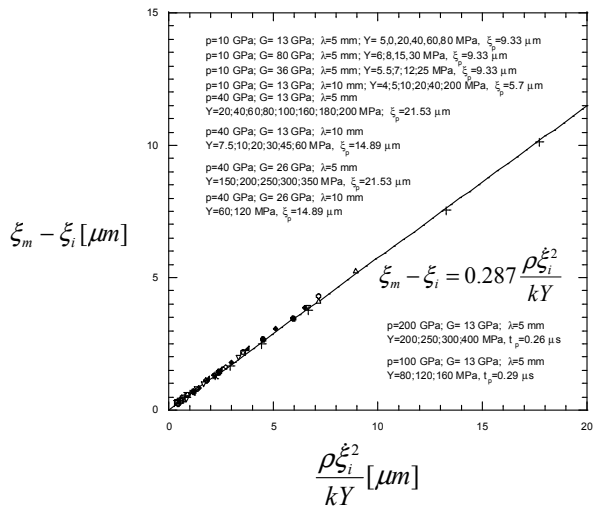

Figure 2: Relative maximum amplitude for different cases.

The previous results suggest a new method to measure the yield strength under dynamic conditions as alternative to the experiments that use the Rayleigh-Taylor (RT) instability [4]. In fact, using RM instability would require determine the perturbation amplitude at any time $t \geq t_m[\xi(t_m) = \xi_m]$. This one measurement experiment would be advantageous in comparison with the RT based experiments that require the experimental determination of the growth rate.

References

[1] A. R. Piriz et al. Phys. Rev. E **72**, 056313 (2005).
[2] A. R. Piriz et al. Am. J. Phys. **74**, 1095 (2006).
[3] A. R. Piriz et al. Phys. Rev. E. **74**, 037301 (2006).
[4] K. T. Ruden et al. Phys. Plasmas **12**, 056309 (2005).

* Work supported by MEC (Spain) contract No. FIS2006-05389 and by BMBF (Germany).
# roberto.piriz@uclm.es

Mote-Carlo simulation of electron spectrometer for the ELISe experiment *

L.V. Chulkov[1,2], H. Simon [1], and the ELISe collaboration[1]
[1]GSI, Darmstadt, Germany; [2]RRC KI, Moscow, Russia

The use of electron as a probe particle provides a powerful tool for examining nuclear structure. The ELectron-Ion Scattering experiment (ELISe) aims at an extension of this method to nuclei beyond the valley of stability. A cooled beam of radioactive ions stored at NESR will collide with an intense electron beam circulating in the electron ring at the interaction zone (IZ). Here, a magnetic spectrometer for the detection of the scattered electrons is to be installed. The technological challenge for the electron spectrometer results from the simultaneous requirement for large acceptance and high momentum resolution.

In one of the versions, an electron spectrometer consists from a deflection chicane magnet (DM) with a vertical dipole magnet (VM) (Fig. 1) [1]. The DM acceptance in azimuthal angle is ± 150 mrad. The specific shape of DM provides the deflection of the scattered electron in the horizontal plane by $\approx \pi/2 - \theta_{e'}$. Electrons elastically scattered to the same polar angle ($\theta_{e'}$) after VM are localized in a small spot at the focal plane. This can be seen in Fig. 1 where trajectories for 500 MeV electrons elastically scattered from 0.74 GeV/nucleon $A = 100$ ions to $\theta_{e'} = 43.9°$ and $\theta_{e'} = 62.8°$ are shown. The 2D coordinate detectors are placed at the focal plane.

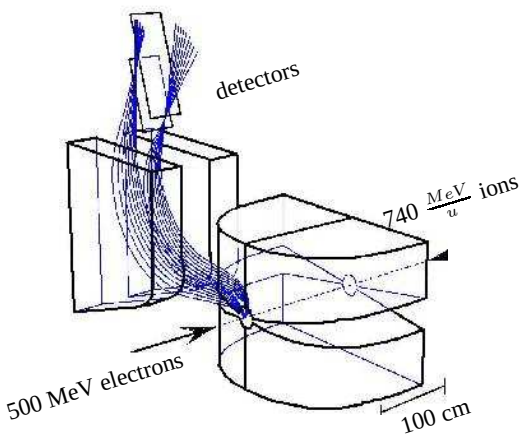

Figure 1: Schematic view of the electron spectrometer.

Full 3D Monte-Carlo simulations have been made to estimate achievable resolution of the proposed spectrometer. These calculations were made in two steps. During the first stage, the electron trajectories were calculated taking into account momentum spread in the electron beam, finite beam size and extended IZ $\sigma_Z \approx 5$ cm. The coordinates of electron hits in detectors were determined. These coordinates were then changed randomly by using the response

* Work supported by INTAS programme, grant No. 05-1000008-8272

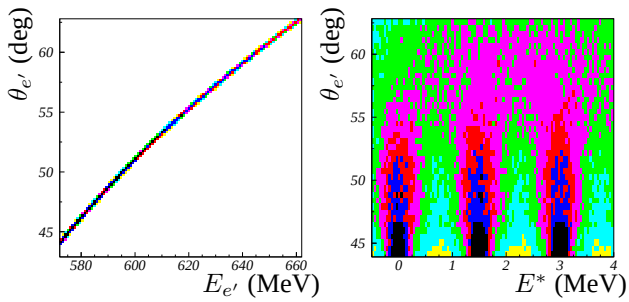

Figure 2: (1). Angle ($\theta_{e'}$) and energy ($E_{e'}$) range covered by one setting of the vertical dipole. The dependence on E^* is so week that elastic and inelastic ($E^* = 1.5, 3.0$ and 4.5 MeV) scattering fuse into one line. Here $E_e = 500$ MeV, $E_I = 0.74$ GeV/nucleon, $A = 100$. (2). Dependence of excitation energy reconstructed via a back-tracing procedure on scattering angle.

function of the detectors and then stored as sequential vectors. The response function of the first detector was assumed to be a Gaussian with $\sigma = 50$ μm. For the second plane detector $\sigma = 100$ μm.

These vectors were used as input for the second stage where a back-tracing routine was applied to reconstruct electron energy $E_{e'}$, polar angle $\theta_{e'}$, azimuthal angle $\phi_{e'}$ and position of the interaction point along the z-axis Z_e. All parameters $E_{e'}$, $\theta_{e'}$, $\phi_{e'}$ and Z_e can be reconstructed by using four coordinates of the hits in the two planes of detectors. The results of simulations are shown in Fig. 2 for the case of a large momentum transfer (in between 400 MeV/c and 600 MeV/c) where the kinematics of the colliding beams is most unfavorable.

The experimental condition for the disentanglement between elastic and inelastic scattering are is shown in the left panel of Fig. 2. The $\theta_{e'}$ range of electrons passing through the VM is about 20° while $E_{e'}$ varies from 560 to 660 MeV. The task is the disentanglement between peaks separated by few hundred keV. The difficulty of this task is illustrated in Fig. 2 (panel 1). The thickness of line is determined by the difference in energies of electrons scattered elastically or inelastically with $E^* = 1.5, 3.0, 4.5$ MeV. The calculations shown in Fig. 2 (panel 2) demonstrate that it is possible to satisfy the experimental requirements with this spectrometer setup.

References

[1] ELISe collaboration, Technical Proposal for the Design, Construction, Commissioning, and Operation of the ELISe setup, 2005. *The scheme of the electron spectrometer was proposed by I. Koop.*

Test of a CCD based bremsstrahlung luminosity monitor prototype for the ELISe experiment*

A.D. Belyaev[1], S.M. Ignatov[1], V.M. Ionov[1], V.G. Nedorezov[1], A.A.Turinge[1], and H. Simon[2]
[1]Institute for Nuclear Research RAS, Moscow, Russia, [2]GSI, Darmstadt, Germany

Coordinate gamma monitors are widely required to measure characteristics of gamma beams or radioactive gamma sources with high accuracy. During many years the most popular detector for such applications was based on the gas filled multiwire proportional chamber (MWPC) (see for example [1]). The advent of modern instruments like charged coupled devices (CCD) allow for solving this problem in a much more effective and convenient manner [2]. CCDs provide coordinate measurements with high accuracy and the opportunity to implement a fully digital readout chain.

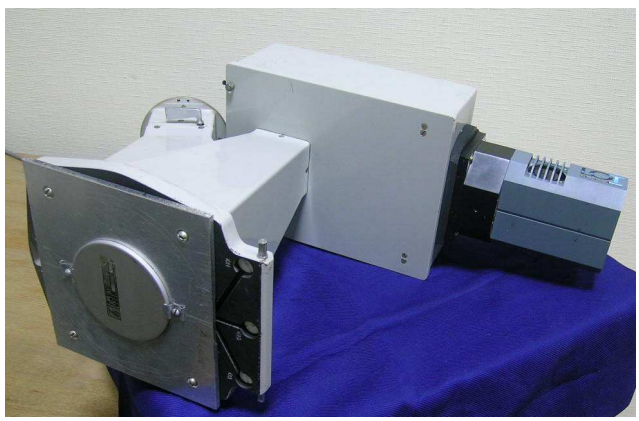

Figure 1: Photograph of the readily assembled prototype gamma imaging system showing the ANDOR CCD system (right), being coupled at 90° using an optical system, to a CsI screen (front).

In the present work we introduce a digital imaging system based on a CCD (shown in Figure 1), for hard gamma radiation. The system is proposed in order to measure the bremsstrahlung quanta being emitted from electrons being scattered off circulating ions at the interaction zone of the ELISe experiment [3]. Thanks to its position sensitivity the system will provide luminosity information together with spatial information on the overlap between the two intersecting beams, and thus, enables to perform a directed optimization by providing the necessary offset information. Already now one can see various other applications for such a detector system.

A first test of functionality was performed using an electron beam with a total energy of 8.5 MeV from the linear accelerator LUE-8.5 being directed to a tungsten bremsstrahlung radiator of 0.5 mm thickness. A lead collimator (13.9 mm diameter, 50 mm thickness) was placed 80 cm downstream of the radiator onto the beam axis. The collimator was covered for this test by an aluminium converter of 100 mm thickness in order to produce secondary electrons and decrease the low energy background.

* Work supported via the INTAS programme of the EC, Open Call, grant No. 05-1000008-8272.

The detection system consists of a scintillation screen made from a 10 mm thick CsI(Tl) crystal with 80 mm diameter, a glass mirror of 1 mm thickness, and an optical lens “Gelios” coupled to the CCD “Andor”. The full system is mounted in a light tight chamber, the distance between the mirror and lens equals to 97 mm.

The CCD chamber view is shown in Figure 1. The scale can be deduced from the size of the scintillation screen that has a diameter of 80 mm. It is important to mention that the total material thickness on the beam axis (scintillator + mirror) is small, so that this device can easily be used as transmission detector, and thus could be coupled with a total absorption gamma detector being installed downstream of the CCD chamber. This detector is foreseen in order to measure the energy spectrum of the emitted bremsstrahlung.

Using a design with a 90° deflection mirror is not only governed by the need to reduce the material budget along the optical axis along the straight section of the two intersecting storage rings, but also in order to protect the CCD camera and optics.

The taken picture shown in Figure 2 demonstrates the systems capability of providing an excellent resolution at sufficiently large sensitivity. Further test experiments are planned – e.g. at the S-DALINAC in Darmstadt – making use of the available higher electron energies.

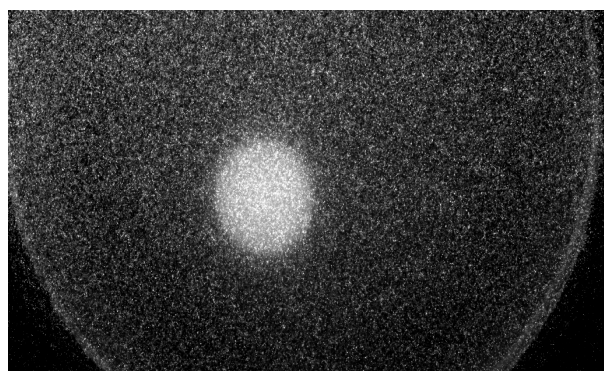

Figure 2: Image of bremsstrahlung being emitted from a tungsten converter irradiated with electrons of 8 MeV energy at a beam current of 400 nA. The boundaries of the beam spot are determined by a lead collimator with an diameter of 13.9 mm in front of the imaging system.

[1] V.A. Zapevalov, D.I. Ivanov, G.Ya. Kezersashvili, V.G. Nedorezov, “Proportional chambers for tracking of fission fragments”, PTE 1 (1980) 80.
[2] N. Kononov, S. Ignatov, V. Nedorezov, V. Potapov. “Digital system for X-Ray imaging with high resolution”. PTE 5 (2006) 156.
[3] FAIR Baseline Technical Report (2006), **4.8** ELISe, http://www.gsi.de/fair/reports/btr.html.

Ion-optical simulations for the FLAIR facility

A. Bräuning-Demian[1], M. Yavor[2]
[1]GSI, Darmstadt, Germany, [2]Institute of Analytical Instrumentation, RAS, St. Petersburg, Russia
for the FLAIR collaboration

Introduction

The FLAIR facility was planned around more then 10 different experiments on atomic and nuclear physics which require antiprotons and highly charged ions with low and ultra low-energies. The gap between the lowest available energy delivered by the New Experimental Storage Ring NESR and the highest energies required by the FLAIR experiments will be bridged by three different decelerators: the Low-energy Storage Ring LSR, the Ultra low-energy Storage Ring USR and the HITRAP. Due to different beam parameters required by the different experiments [1] the beam manipulation and transport inside the FLAIR facility became highly intricate. Therefore, a careful investigation of the transport beam line connecting the decelerators and the experiments is needed.

Layout of the beam transport system

Figure 1 shows the layout of the beam transport system at FLAIR. Beams of 30 MeV antiprotons delivered from the NSER will be cooled and decelerated in LSR at energies between 10 MeV and 0.3 MeV and transported further either for the second deceleration step in USR and HITRAP or directly to the experimental area pbar-Exp. For Biophysical experiments antiprotons of 200-300 Mev will be delivered directly from the NESR.

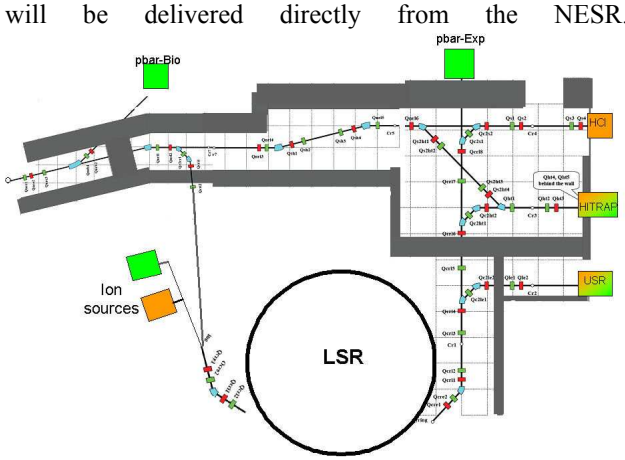

Figure 1: Layout of the FLAIR beam transport system.

The experiments with highly charged ions will get cooled, decelerated beams with energies between 120 MeV/u and 4 MeV/u direct from the NESR. For tests and commissioning purposes ion beams from a local ECR source will be available via LSR. The transfer between the different decelerators and the experiments will be done via fast and slow extraction.

Ion-optical design

For this study the code GICOSY [2] was used. Each beam transport section is an achromatic system. The maximal transversal phase space is 10 π mm mrad but is expected that the value of 1 π mm mrad required by the experiments will be the most probable one due to the fact that all beams will be electron cooled in the storage rings.

The space charge limit of the LSR is known to be $5x10^8$ protons at 0.3 MeV and 1 π mm mrad. It is expected that NESR will deliver $1x\ 10^8$ antiprotons per cycle which could be transferred to USR at energy of 0.3 keV in one bunch. For this case an investigation of possible space charge effects on the ion optics was also performed with the program GIOS [3]. A preliminary estimation indicates that at currents higher then 10^8 charges in 500 nsec such effects became possible. This aspect will be further investigated in close connexion with the transfer scheme of the antiprotons from NESR to USR via LSR.

Figure 2, representative for the whole system, presents the beam envelopes for an antiproton beam at 4 MeV transferred from the LSR, after deceleration and cooling, to HITRAP.

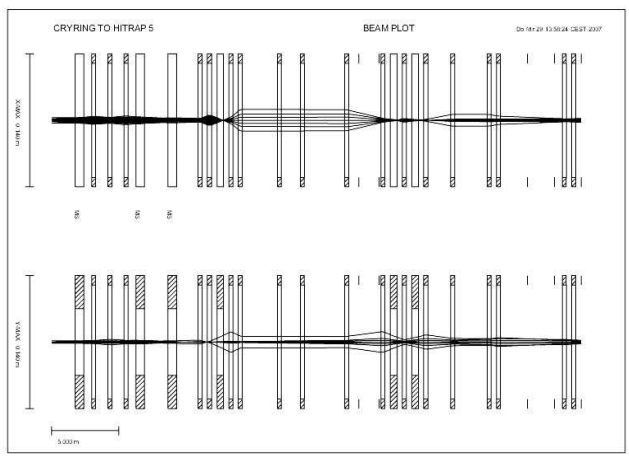

Figure 2: Beam envelopes for the LSR-HITRAP transfer system.

In order to reduce the construction cost all but three magnets have been design with the same specifications, independent of the maximal rigidity required for the different sections of the transport system. This differentiation will be done later at the design of the power supply for each magnet.

References

[1] A. Braeuning-Demian et al., GSI Report 2006-1, p. 4.
[2] http://www-linux.gsi.de/~weick/gicosy/
[3] H. Wollnik et al., AIP Conference Proceedings; ed. C. Eminhizer, 177(1988)74-85.

Measurement of the (anti)proton *g*-factor - Status of the experiment*

S. Ulmer†[1,2], K. Blaum[1,3], S. Kreim[1], H. Kracke[1], C.C. Rodegheri[1], W. Quint[2,3], S. Stahl[4], J. Walz[1]

[1]Institut für Physik, Johannes Gutenberg-Universität, 55099 Mainz, Germany, [2]Ruprecht-Karls-Universität, 69047 Heidelberg, Germany,
[3]GSI, Planckstraße 1, 64291, Darmstadt, Germany [4]www.Stahl-Electronics.com, 67582 Mettenheim, Germany

The precise determination of the *g*-factor of the proton and the antiproton together with their comparison is a stringent test of the CPT invariance theorem on the baryonic sector [1]. In our experiment, which is part of the FLAIR collaboration, the *g*-factor of a single, isolated (anti)proton will be determined by utilizing the continuous Stern-Gerlach effect [2] in a hybrid double Penning trap setup [3]. Measuring the free cyclotron frequency ω_c and the Larmor frequency ω_L the *g*-factor can be determined via the relation

$$g = 2\frac{\omega_L}{\omega_c} \quad . \tag{1}$$

The free cyclotron frequency can be calculated by means of the invariance theorem $\omega_c^2 = \omega_+^2 + \omega_-^2 + \omega_z^2$ where ω_i are the eigenfrequencies of the particle inside the trap [4]. These eigenmotions can be measured via detection of image currents induced in the electrodes by the moving particle in the trap.

Single particle detection needs highly sensitive electronics. The two key pieces of such a detection system are a helical resonator with a high quality factor *Q* and a low-noise amplifier. To achieve a high signal-to-noise ratio (SNR) of the detector, a high *Q*-value of the resonator should be reached. In case of the axial detector at $\nu_z = 680\,\mathrm{kHz}$, coil and shield are made of type II superconducting NbTi with a critical temperature of 9.5 K. The use of a type II superconductor allows us to place the resonator in the high magnetic field near the trap, thus parasitic capacitances can be avoided, resulting in a higher SNR. Systematic rf loss mechanism studies were performed and the tank circuit was optimized. Finally a free *Q*-value >40000 at 1.6 MHz was reached. With the parasitic capacitance of the trap the system will be tuned to the axial resonance frequency.

This resonator was used to investigate the effect of an externally applied magnetic field on the superconducting ac resistance. With the possibility to move our cryostat along the axis of the horizontal bore of a superconducting 1.9 T magnet the *Q*-value could be measured as a function of the magnetic field (see fig.1). These data are of high interest and may have impact on the design of future trap experiments as planned e.g. at the HITRAP facility.

As second key piece of the single-particle detector a low-noise cryogenic field effect transistor (FET) amplifier was designed and tested. Electronic feedback would heat the amplitudes of the trapped particle, leading to linewidth broadening. Thus, care was taken to assemble a feedback-free low-noise amplifier. Finally, at the axial frequency a voltage noise of $1.4\,\mathrm{nV}/\sqrt{\mathrm{Hz}}$ and a current noise of $\approx 3\,\mathrm{fA}/\sqrt{\mathrm{Hz}}$ was reached. With the complete detection system a *Q*-value of 6500 was measured. In case of the cyclotron detection system driven at 29 MHz we proceeded in the same way. With a copper resonator a cryogenic *Q*-value of 1100 and a voltage noise of $0.6\,\mathrm{nV}/\sqrt{\mathrm{Hz}}$ were obtained. In addition to the single-particle detection systems further electronic components as filter boards and room temperature amplifiers were designed and tested. To flip the particle's spin a standard NMR method will be used. In case of the Penning trap the difficulty of the copper electrodes acting as efficient rf shields exists. Thus, a resonant rf coil assembly at a frequency of 80 MHz was developed to drive the required radial magnetic field component.

The whole experimental setup including trap and electronics is mounted and the cryostat is tested to achieve trap temperatures $< 4\,\mathrm{K}$. The next step will be the preparation of a single proton, afterwards a spin-flip should be induced and detected.

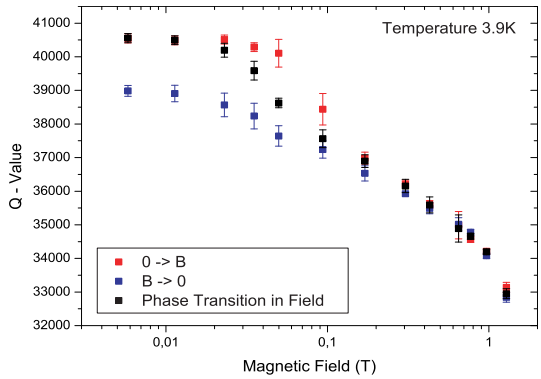

Figure 1: Variation of the Q value of a 1.6 MHz helical resonator as a function of an externally applied magnetic field. Red points: Superconducting phase transition (SCPT) outside the magnet; blue points: SCPT in high magnetic field of 1.1 T; black points: SCPT in position dependent field.

References

[1] R. Bluhm et al., Phys. Rev. Lett. **79**, 1432 (1997).

[2] R.S. Van Dyck et al., Phys. Rev. Lett. **59**, 26 (1987).

[3] J. Verdu, AIP Conf. Proc. LEAP **796**, 260 (2005).

[4] L. S. Brown, G. Gabrielse, Rev. Mod. Phys. **58**, 233 (1986)

* work supported by BMBF under contact number 06MZ227I, HGF under contract number VH-NG-037 and DFG under contract number QU122/3-1-2

† ulmers@uni-mainz.de

Deceleration efficiency for protons at CRYRING

H. Danared, A. Källberg and A. Simonsson
Manne Siegbahn Laboratory, Stockholm, Sweden.

Abstract

The Manne Siegbahn Laboratory is planning for the transfer of the CRYRING synchrotron and storage ring to the future FAIR facility, where it will be used for deceleration of antiprotons and heavy ions at FLAIR. The efficiency of the deceleration process, i.e. the minimization of particle losses, is important, and we show here a strong correlation between losses during the start of the deceleration process and the bunch length of the particle beam, giving criteria for the beam transfer between the NESR and LSR rings.

Introduction

The Manne Siegbahn Laboratory continues the planning for a transfer of the CRYRING synchrotron and storage ring to FLAIR, the facility for low-energy antiproton and ion research at FAIR, where it would be used as the LSR ring for deceleration of antiprotons and ions. In the LSR, antiprotons will be decelerated from 30 MeV kinetic energy down to a minimum of 300 keV and ions will be decelerated through a similar range of magnetic rigidities. The LSR ring must be able to decelerate a sufficient number of particles in a sufficiently short time and with low losses. Therefore, tests with proton beams have been performed at CRYRING in order to investigate these parameters. The protons differ from antiprotons only by the sign of the charge and for the present purpose, a change of polarity of the ring magnets was necessary.

In earlier reports [1, 2], it has been shown that 1.8×10^8 protons could be decelerated from 30 MeV to 300 keV with particle losses not exceeding 10%. This was an improvement with respect to initial results where losses at the start of the deceleration were in the order of 60%.

Deceleration

Since the injection of protons at CRYRING presently takes place at 300 keV, the deceleration studies are made after the beam has first been accelerated to 30 MeV. Thus, the basic machine cycle for the deceleration studies starts with intensity accumulation and cooling at 300 keV, acceleration to 30 MeV, storage at 30 MeV for a short time, and finally deceleration back to 300 keV. The difference between the two results with less than 10% and 60% losses respectively was due to the introduction of an additional beam cooling at an intermediate energy during the acceleration.

Although the beam in both cases is cooled at the injection energy of 300 keV, this cooling is not so strong because of the low energy and it is also counteracted by a high intrabeam-scattering rate. Cooling at 3 MeV during the acceleration phase is more efficient and leads to a smaller transverse beam emittance and, as seen in Fig. 1, shorter bunches in longitudinal phase space.

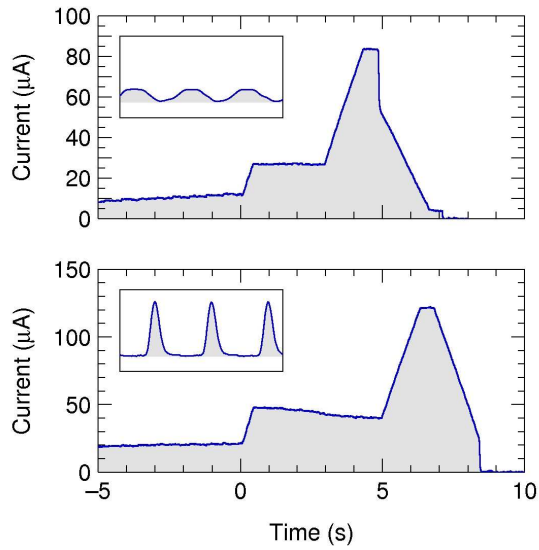

F

Figure 1: Beam currents during acceleration and decelerations and (insets) bunch shape at flat top. In the upper figure no cooling at intermediate energy (0.5–3 s) is applied, but applied in the lower figure (0.5–5 s).

From the upper part of the figure it is seen that there are significant beam losses when deceleration starts at 5 s in the case of no cooling at the intermediate energy of 3 MeV. As seen in the inset, where the timescale is in the microsecond range, no intermediate cooling means that the bunches fill more or less the entire ring circumference. In the lower part of the figure the bunches are shorter because of cooling at 3 MeV, and there is no visible beam loss when deceleration starts at 7 s. In the lower figure there is an intensity loss during cooling and at the end of the deceleration due to poorly adjusted magnet ramps, but this is not related to the present case of study which is the start of the deceleration.

Although the cooling also changes the transverse emittance of the beam, it was verified that moderate transverse displacements of the beam did not have the same effect on beam losses as changing the bunch length, confirming that it is the longitudinal phase space that is important for the deceleration efficiency in our case.

From this study it can be concluded that particles injected from the NESR to the LSR ring can be decelerated with small losses if the transfer is made with bunches that are sufficiently short to be well separated in longitudinal phase space.

References

[1] H. Danared *et al.*, GSI Annual Report 2006, p. 5.
[2] H. Danared *et al.*, Proc. COOL07, p. 234.

Investigations of the Beam Dynamics in the USR*

C.P. Welsch[1,2], M. Grieser[2], A. Papash[3], P. Schmid[2]
[1]Kirchhoff Institute for Physics, University of Heidelberg, Germany; [2]Max-Planck Institute for Nuclear Physics, Heidelberg, Germany; [3]Joint Institute for Nuclear Research, Dubna, Russia

The Ultra-low Energy Storage Ring

The ultra-low energy storage ring (USR) is one of the central elements of FLAIR [1]. It will decelerate antiprotons and possibly highly charged ions in a final step from 300 keV/q to only 20 keV/q.

For the USR to fulfil its role in the FLAIR project, the development of novel and challenging methods and technologies is necessary: the combination of the electrostatic storage mode with a deceleration of the stored ions from 300 keV to 20 keV, electron cooling at all energies in both longitudinal and transverse phase-space, bunching of the stored beam to ultra-short pulses in the nanosecond regime and the development of an in-ring reaction microscope for antiproton-matter rearrangement experiments.

A preliminary layout of the machine lattice was already worked out [2] and more in-detail studies were started in 2007. A particular focus was put on the question of how shortest bunches with a duration of only a few nanoseconds may be realized in an electrostatic machine, where the particle motion is inherently coupled in the transverse and longitudinal phase space, as well as on the design of a highly-flexible beam extraction scheme.

Nanosecond Bunches

For the envisaged in-ring experiments in the USR [3] such short bunches are required for use in collision studies with atomic or molecular gas jet targets. In this case the time structure of the circulating ion bunches can be used as a trigger signal for the experiments. The short duration of the pulses guarantees a high experimental resolution. In this respect, an efficient control of the longitudinal time structure of the stored ion beam is of central importance since it directly determines the quality of the envisaged experiments.

Since many years, it has been a significant challenge for the storage ring accelerator-physics community to develop techniques to reduce the duration of bunches. Up to now, all methods that have been developed go along with various difficulties, which can include reduced stored-beam lifetimes.

This is partially due to the strong space charge limitations that were found in existing electrostatic machines; probably linked to non-linear fields that cannot be avoided in such storage rings. The nature of these effects is not at all understood and it is a part of the ongoing studies to simulate the motion of a stored ion beam in an electrostatic cooler synchrotron under consideration of non-linear fields as well as space charge effects, together with a particular focus on the needs of both internal and external experiments. Thus, novel and innovative concepts for the manipulation and control of the longitudinal beam structure will have to be developed.

Two different concepts are presently under investigation: First, a special operation mode of the storage ring with an optics setting where the phase slippage factor η is negative is being studied. In such a setting the space charge effect would no longer counteract the applied HF voltage. The aim of this work is to develop a thorough understanding of the beam motion and to perform tests with beam in the TSR at the MPI-K. Second, a scheme where different rf frequencies are subsequently applied to the beam to generate shortest bunches is being investigated.

Beam Extraction Scheme

In order to be usable as a true multi-user, multi-purpose facility, the extracted beams from the USR need to be highly flexible in terms of both time structure and intensity. The required longitudinal profiles range from short single pulses with up to 10^7 ions in some 100 ns pulse duration to quasi continuous beams with low intensities where the ions will be used as a nuclear probe by external users.

A combined slow and fast extraction scheme is presently worked out with emphasis on the final beam quality. Different concepts are studied and first results are expected in 2008.

Acknowledgements

The generous support of the Helmholtz Association of National Research Centres (HGF) under contract number VH-NG-328 and of the Gesellschaft für Schwerionenforschung (GSI) Darmstadt is acknowledged.

References

[1] C.P. Welsch, H. Danared,"FLAIR: A Facility for Low-energy Antiproton and Ion Research", Proc. Europ. Part. Acc. Conf., Edinburgh, Scotland (2006)
[2] C.P. Welsch, M. Grieser, J. Ullrich, A. Wolf,"An ultra-low-energy storage ring at FLAIR", NIM A 546 (2005) 405–417
[3] C.P. Welsch, M. Grieser, A. Dorn, R. Moshammer, J. Ullrich,"Exploring Sub-Femtosecond Correlated Dynamics with an Ultra-low Energy Electrostatic Storage Ring", AIP Conf. Proc. 796 (2005) p. 266-271

Status of the FAIR Project

D. Krämer*[1]
[1]GSI, Darmstadt, Germany

The FAIR project has passed most important milestones with respect to political as well as to technical realization during the year 2007. On November 7th, 2007 officials from FAIR partner countries celebrated the Launch of the FAIR Start Version. Delegates from Austria, Germany, Spain, Finland, France, Poland, Romania, Russia, Sweden, Great Britain and the State of Hessen jointly announced the beginning of the realization of the FAIR project in Darmstadt. Furthermore, the design of accelerators and technical systems was reviewed and approved by the Technical Advisory Committee (TAC); in seven dedicated reviews on lattice design, civil construction, magnets, power converters, RF, proton linac, diagnostics and controls, key issues for FAIR were discussed with world leading experts and finally reported to the TAC.

Officials from the FAIR partner states celebrating the Launch of the Start Version on November 7th, 2007: Austria, Germany, Spain, Finland, France, Poland, Romania, Russia, Sweden, Great Britain and State of Hessen

In parallel, the technical detailing of the FAIR accelerators was carried on. Due to the TAC recommendation the lattices of the machines were frozen and a consistent set of parameters was put together. This parameter list specifies relevant technical data of FAIR components. Compared to earlier designs the use of superconducting magnets is with the synchrotrons and the fragment separator. Hybrid solutions, as in the high energy beam transport lines and the collector ring were abandoned to optimize reliability, availability and reduce maintenance during operation. System design of HESR by the collaborators from FZ Jülich has shown that the required field tolerances for the superconducting baseline magnet design needs revision. A conventional room temperature solution is under investigation at present. Prototyping of fast cycled SIS100 dipoles is commencing well. BNG Würzburg produced a straight superconducting magnet that successfully passed the factory acceptance test in December. BINP (Novosibirsk) is planning to deliver a curved full scale SIS100 magnet in early 2008, while JINR (Dubna) is expected to deliver prototypes of bending and focussing magnets up to mid 2008 for final tests at the GSI teststand. Major progress in the R&D of SIS300 magnet system was achieved as INFN (Genoa) agreed on the development of a low loss 4.5 T curved $\cos\Theta$-bending magnet. Present work is realized in close contact to industry and it is expected that the later SIS300 series magnets will be an Italian in-kind contribution to FAIR. Design work on RF systems for the FAIR accelerators is advanced such that specifications and contracts on pre-series cavities and high power generators were prepared for CR and other machines. After successful simulations, tests with a low power model of the new CH-structures confirmed the demonstration of the favourable parameters of the recently proposed accelerator structures by IAP Frankfurt that will be used for the high intensity proton linac. A high power 325 MHz klystron for the teststand planned to be built up was ordered to prepare quality assurance during project execution.

Major advances towards the realization of buildings for FAIR were achieved as the official procedure according to "ZBau"-procedure started. Within EU-wide tender Drees & Sommer was awarded as external steering comp., while tenders for architect and engineering companies are in progress. Activities are focused to receive required building permits by end of 2008.

In the following contributions dedicated aspects of the work on FAIR during the past 12 month are presented.

* d.kraemer@gsi.de

Design Status of the FAIR Synchrotrons SIS100/300 and the HEBT System

P. Spiller, U. Blell, O. Boine-Frankenheim, E. Fischer, E. Floch, G. Franchetti, F. Hagenbuck, I. Hofmann, J. Kaugerts, M. Kirk, A. Krämer, D. Krämer, H. Klingbeil, A. Saa-Hernandez, S. Ratschow, H. Ramakers, H. Welker, C. Omet, N. Pyka, M. Schwickert, J. Stadlmann
GSI, Darmstadt, Germany

SIS100/300

System Layout

The system design of the FAIR [1] synchrotrons SIS100/300 [2] and the HEBT system has been further detailed. However, especially those open issues have been addressed where a technical solution was not obvious and a confirmation of the principle layout was still outstanding, e.g. the strength and cooling of the extraction septum magnets, the deposition of high beam power in a cryogenic quadrupole module of the extraction system and the switching cryostat modules at injection, extraction and transfer. For these technical systems suitable methods of resolution have been developed. According to the successfully completed verifications no reason to change any system layout has been identified.

To accommodate for the FAIR start version an initial, reduced equipment of Rf systems has been defined.

Beam Dynamics

For a better and precise prediction of beam loss during the acceleration cycle the development of high current beam physics models have been enforced. New beam dynamics simulations have been performed including the nonlinear longitudinal and transverse beam dynamics under the influence of space charge and collective effects. Especially during the long accumulation and extraction plateaus, beam loss must be controlled in order to localize machine activation or prevent residual gas pressure bumps. The following items have been addressed:

- Space charge and cavity beam loading effects during several parts of the RF cycle.
- Long-term beam loss during accumulation due to the combined effect of magnet errors, synchrotron motion and 'frozen' space charge at selected working points.
- The SIS100 resistive wall and SIS18 kicker impedances.
- The transverse impedance budget with space charge for coasting beams (Octupoles are proposed in order to stabilize the beam) [3].

Tracking, ripple and synchronisation tolerances of the synchrotrons have been studied for:

- Synchronization requirements for the quadrupoles with the dipoles
- Power supply ripple requirements for the quadrupoles
- Synchronization and ripple requirements for the dipoles with the Rf

Based on the loss predictions, life time and activation have been estimated for those technical devices which face unavoidably heavy beam load. Special protection measures have been derived for the low radiation hard but close components in the ring tunnel.

Investigations have been launched on the influence of the persistent currents and transient field errors of the SIS300 superconducting magnets on the beam dynamics. Although the specific coil layout and the methods applied for reducing the AC loss during fast ramping help to restrict the persistent current flow, a fast feed back system for an online correction of the multipole errors is assumed to be required. Especially under the assumption of a very flexible operation with independent and arbitrary machine cycles, in connection with the stability requirements for slow extraction, the linear and nonlinear machine properties must be carefully controlled.

Ionization Beam Loss

New cross sections for ionization, showing a faster decrease with beam energy, generated by improved atomic physics models for the relativistic energy range of SIS100 have been implemented in the STRAHLSIM calculations [4]. Furthermore, a new energy loss scaling for gas desorption according to $(dE/dx)^2$ has been considered. However, this scaling has only been proven by experiments in a low energy regime. In order to determine the desorption rate in the energy range of SIS100, fast pressure measurements have been performed in the AGS (BNL, Brookhaven). The ionization beam loss in SIS100 has been recalculated based on the new data and the tolerance with respect to a stable residual gas pressure was checked with and without charge scraper system (figure 1) [5].

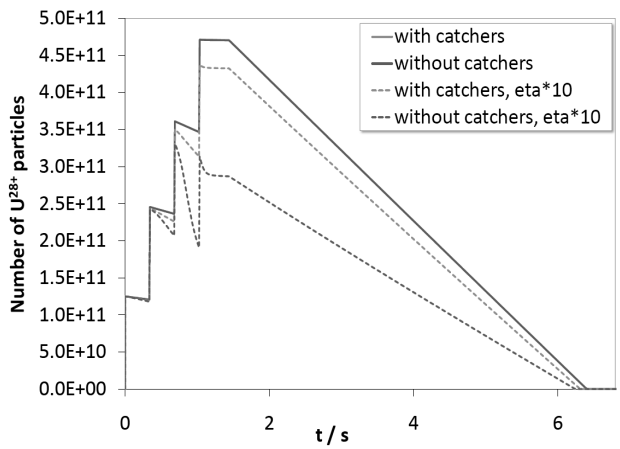

Figure 1: Beam intensity profile in a SIS100 cycle including stacking, acceleration and slow extraction for an expected and increased desorption rate.

Main Magnets

Based on the achieved R&D results of the project pre-phase, manufacturing of a series of SIS100 full length model magnets has been launched [6].

- Straight full length dipole magnets are manufactured at BNG (Würzburg) (figure 2) and at JINR (Dubna)
- A curved dipole magnet is under production at BINP in Novosibirsk.
- A prototype quadrupole magnet is under production at JINR (Dubna).

The production of both full length magnets at JINR is supported by the EU FP6 DIRAC program.

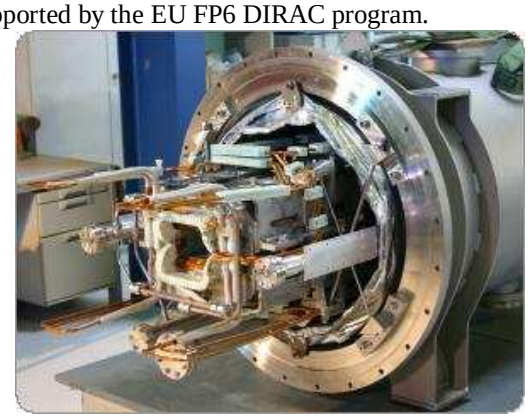

Figure 2: Straight SIS100 prototype dipole magnet manufactured at BNG.

For SIS300, the design and R&D of a fast ramped curved 4.5 T dipole magnet has been continued at INFN, Italy. In parallel, the tooling production for a straight s.c. 6 T dipole magnet has been completed at IHEP, Protvino. The manufacturing of the 1 m long magnet and cold testing shall be finished until May 2008. Both magnets are optimized for a low AC loss and make use of a cable with the bare cable geometry of the LHC dipole outer layer conductor, but with a stainless steel core inside.

RF Systems

The design study performed by BINP, Novosibirsk for the SIS100 acceleration cavity has been completed (figure 3) [7]. The cavity design is close to the existing SIS18 system and the BINP cavity for HIRFL-CSR, Lanzhou, China.

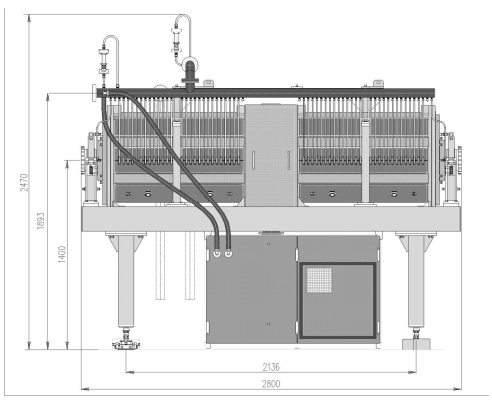

Figure 3: Design study for the ferrite loaded SIS100 acceleration cavity.

Each cavity provides an acceleration voltage of 20 kV in the frequency range of 1.1-2.7 MHz. Twenty cavities are needed to generate the acceleration voltage of 400 kV.

In general especially those systems have been studied in detail which were supposed to be crucial: The high power normal conducting extraction septa of SIS100 and SIS300 are supposed to be technically feasible if the pressure drop and the heat exchange in the water cooling system may be enhanced. The beam loss induced energy, deposited in the quadrupole cryomodule of the extraction system may be removed by means of a local temperature increase and nitrogen cooling. For the switch cryostats a support system structure for the two interleaving doublets has been developed. The planning for all other technical system has been continued and will be summarized in the technical design report TDR.

HEBT

The ion optical revision of the beam transport system for normal- instead of superconducting SIS100 beam line magnets has been completed. The new overall topology is to a large extent consistent with the original layout for superconducting magnets – no significant change in the overall size has resulted from the change in magnet technology. The design of the main warm beam line magnets has been optimized with respect to energy efficiency and operation modes.

The layout for the beam diagnostics and correction system has been fixed and integrated into the beam transport structure. The charge stripper system between SIS18 and SIS100 could be integrated into the existing layout of the 90 degree bend behind SIS18 without major modifications. By means of a fast linear induction motor the stripper foil will be moved into the beam path in a shot-by-shot mode.

The supply buildings, so far matched for the supply of a superconducting HEBT system have been modified for the supply systems of the normal conducting beam lines.

DOCUMENTATION

Documents summarizing the actual status of planning are continuously updated. In order to assure a proper design of the synchrotron and beam transport components, all devices have been sketch as 3D contour drawings and assembled to the complete beam line sections.

REFERENCES

[1] FAIR Baseline Technical Report (FBTR), GSI, (2006)
[2] P. Spiller et.al., Proc. of PAC07, (2007)
[3] V. Kornilov et. al, Phys. Rev. St. Accel, Beams 11, (2008) 014201
[4] S. Shevelkov et.al, private communication
[5] C. Omet et. al, Proc. of PAC07, (2007)
[6] E. Fischer et al, IEEE Transactions On Applied Supercond., Vol 17. No2 June 2007, pp 1078- 1082
[7] V.S. Arbuzov et. al, "Design Study of RF System for SIS100 Accelerating Facility – Final Report".

3D Calculation of the Eddy-Current Losses in the Beam Tube of the SIS100 Dipole Magnet*

S. Koch[1], H. De Gersem[2], and T. Weiland[1]

[1]Technische Universität Darmstadt, Institut für Theorie Elektromagnetischer Felder, Darmstadt, Germany; [2]Katholieke Universiteit Leuven, Campus Kortrijk, Kortrijk, Belgium

Introduction

The eddy-current losses in a simplified model of the SIS100 dipole magnet (Fig. 1a) comprising the elliptical beam tube are calculated. The standard 3D Finite Element (FE) formulation is augmented by a shell element representation of the thin beam tube. Using this approach, the mesh construction can be restricted to the beam tube surface and the outer parts, avoiding the construction of elements inside the beam-tube volume. Therefore the number of unknowns of the overall numerical model is reduced. Furthermore the aspect ratio of the tetrahedra used for the discretization is improved, which leads to a better condition number of the system matrix. Therefore, the simulation time can be reduced significantly without loosing accuracy.

Modelling of the thin beam tube

Even though the SIS100 magnet (Fig. 1a) is long when compared to its cross-section, 2D FE simulations in general are not sufficient to capture all relevant phenomena such as, e.g., the eddy-current losses which appear mainly at the end parts of the yoke. Therefore, 3D FE simulations are applied here. Already for simulations omitting the beam tube, large numerical models are required to resolve the skin-depth of the eddy currents [1]. Therefore, it is not recommended to apply additional mesh refinement in the aperture region accounting for additional geometrical details present there. As the thickness δ of the beam tube (Fig. 1b) is very small compared to the other measures of this magnet, 2D shell elements [2] aligned with the beam-tube surface are applicable to account for the eddy-current losses.

In order to include the shell elements in the numerical model, mesh generation is carried out such that only the surface of the beam tube is represented by mesh faces corresponding to zero thickness. As, therefore, no actual volume mesh is present for this part, the discrete representation is obtained by extruding the surface triangulation (Fig. 1c) perpendicularly by $\pm\delta/2$ during the setup of the discrete model. Hence, the resulting losses during the triangular excitation cycle lasting $1\mathrm{s}$ can be evaluated without the neccessity of geometrically resolving the beam tube in the mesh.

Numerical Results and Discussion

The excitation current in the coils is set to $48\mathrm{kA}$ resulting in a peak aperture field of $2\mathrm{T}$ at $t = 0.5\mathrm{s}$. For two simulation runs using either the shell element representation or the full 3D model the integrated eddy-current losses are listed in Table 1. The computational effort in terms of the iteration count is significantly smaller when using the shell element representation. The remaining difference between the two simulations is due to the fact that the mesh can not be chosen identical. Note that the iteration count is independent of the thickness of the beam tube in the latter case. However, the accuracy and the agreement to the full 3D model deteriorates for increasing values of δ. Hence, the proposed method is well suited if a large contrast in the geometrical measures is present, as it is the case here for values of δ not exceeding $1\mathrm{mm}$.

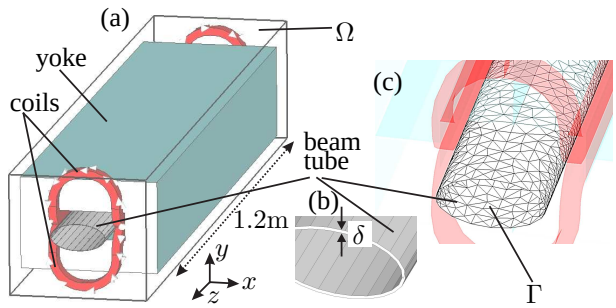

Figure 1: (a) Magnet model, computational domain Ω, (b) thin conductive beam tube, (c) surface mesh representation Γ of the beam tube.

Table 1: Eddy-current losses integrated over one excitation cycle for $\delta = 0.5\mathrm{mm}$ and a beam pipe length of $1.414\mathrm{m}$; performance using shell elements and full 3D modelling: approximately 40,000 d.o.f. on a $1/8$-model of the magnet.

model	losses beam tube (W/m)	# amgcg it.
3D FE + shell	2.57	20
3D FE	2.26	59

References

[1] S. Koch, H. De Gersem, T. Weiland, E. Fischer and G. Moritz, "Transient 3D Finite Element Simulations of the SIS100 Magnet Considering Anisotropic, Nonlinear Material Models for the Ferromagnetic Yoke", Proceedings of the 20th International Conference on Magnet Technology (MT20), 2007.

[2] Z. Ren, "Degenerated whitney prism elements - general nodal and edge shell elements for field computation in thin structures," *IEEE Trans. Magn.*, vol. 34, no. 5, pp. 2547–2550, Sep. 1998.

* Work supported GSI, Darmstadt.

A Longitudinal Feedback System for SIS100*

M. Mehler[1], H. Klingbeil[1], K.P. Ningel[1], B. Zipfel[2]
[1]GSI, Darmstadt, Germany; [2]University of Applied Sciences Fulda, Germany

High intensity operation as planned for the synchrotron SIS100 is expected to lead to ion bunch oscillations in longitudinal phase space that must actively be damped [1]. Therefore a longitudinal feedback system has to be designed that is faster than Landau damping and copes with the expected growth rates of instabilities. One task of this feedback system is the damping of quadrupole oscillation modes. A more detailed description about the damping of these modes can be found in [2, 3].

Simulations [2, 4] with ESME [5] and a machine development experiment at SIS12/18 [6] have shown that quadrupole oscillations which are detectable by beam current amplitude measurements in time domain can be excited and damped by RF voltage amplitude modulations. Based on these specific results, a general closed-loop control system was designed. The principle layout can be seen in Figure 1.

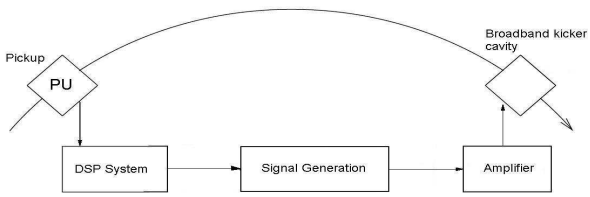

Figure 1: Block diagram of the longitudinal feedback system consisting of pickup, signal processing and kicker.

It is assumed that the SIS100 BPMs can be used as pickup probes because their bandwidth and dynamic range will be sufficiently high as Spice simulations have shown.

The DSP System described in [8] is used to detect phase and amplitude variations of bunched beam currents. Signal processing (e.g., filtering) is done by the software of the DSP system as well. To damp quadrupole oscillations the amplitude of the bunched beam current variations has to be evaluated and fed back to the RF voltage with a phase shift of 90°. This results in an RF voltage amplitude modulation.

A broadband kicker cavity with a bandwidth of about 5...6 MHz to apply the amplitude modulation to the beam is being designed. A modular system is planned using individual cavities with a maximum voltage of 5 kV each. Since such a cavity is not available yet the experiments were performed with the standard SIS12/18 ferrite cavities.

The design described above was simulated with a tool developed at GSI [9] to show its effectiveness. Afterwards a machine development experiment has been carried out in the synchrotron SIS12/18 which is described in detail in [7]. First measurements showed that the developed electronic system damps quadrupole oscillation faster than Landau damping (Figure 2). The system is expected to be fast enough to damp higher-order mode oscillations during high intensity operation decreasing the emittance growth.

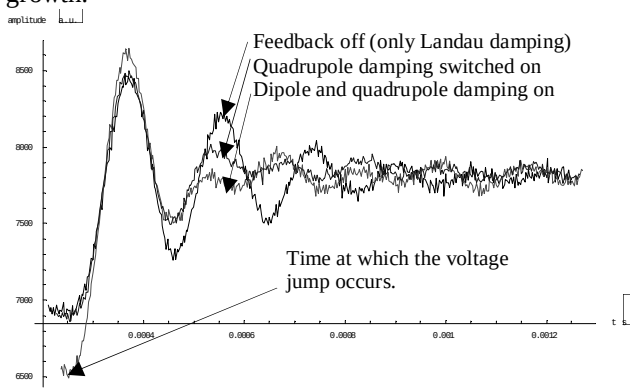

Figure 2: Measured quadrupole oscillation (amplitude data) of the DSP acquisition system in time domain. A voltage jump excites the quadrupole oscillation.

Special thanks go to H. Damerau, H.-G. König, M. Kumm, U. Laier, M. Paoluzzi, C. Rossi, and G. Schreiber.

References

[1] O. Boine-Frankenheim et al., 'Stability of coherent synchrotron oscillations with space charge', PhysRevSTAB.10.104202 (2007)
[2] M. Mehler et al., 'Longitudinal Feedback Systems for FAIR', Version 2.01, GSI Sept. 07
[3] F. Pedersen et al., 'Theory and Performance of the Longitudinal Active Damping System for the CERN PS Booster', IEEE Trans. On Nuclear Science, Vol.NS-24, No.3, June 1977
[4] M. Mehler et al., http://cas.web.cern.ch/cas/Zakopane-2006/Mehler.ppt
[5] J. MacLachlan et al., http://www-ap.fnal.gov/ESME/
[6] M. Mehler et al., http://www.gsi.de/beschleuniger/sis18/pdf/excitation_open_loop_damping.pdf
[7] M. Mehler et al., http://www.gsi.de/beschleuniger/sis18/pdf/Damping_of_Quadrupole.pdf
[8] H. Klingbeil, 'A Fast DSP-Based Phase-Detector for Closed-Loop RF Control in Synchrotrons', IEEE Trans. on Instrumentation and Measurement, Vol.54, No.3, June 2005
[9] B. Zipfel et al., 'Analysis of a Digital Beam Phase Control System', Workshop LLRF05, CERN, (2005)

* Work supported by EU, SIS100 contract No. 515873.
Collaboration partner CERN.

Characterization of cryosorption panels for SIS100/300

M. Wengenroth[1,*], H. Kollmus[1], A. Krämer[1], and St. Wilfert[1]
[1]GSI, Darmstadt, Germany

Abstract

To reach the required vacuum in the 10^{-12} mbar range in SIS100 and SIS300 it is necessary to provide additional pumping speed, beside the cold vacuum chamber walls, for the hardly condensable gases helium and hydrogen. Therefore cryosorption pumps have to be implemented. The pumps will consist of cryopanels coated with micropourous activated charcoal SC2 made by CHEMVIRON and directly cooled with liquid helium. The coating of the cryopanels will be done by FZ Karlsruhe Germany [1,2,3]. In the framework of a diploma thesis [4] similar cryopanels, provided by FZ Karlsruhe, were investigated concerning their pumping speed and capacity.

Experimental Setup

The prototype cryopanels (aluminium substrate) are mounted on the second stage of a Gifford-McMahon cold head, which is equipped with a resistive heater to control the temperature in the range of 8 – 50K. The cryopanels are placed inside the thermal shield and oriented towards the cold head to prevent condensation of easy condensable gases, which would result in a blocking of the micro pores of the charcoal thus inhibiting helium and hydrogen adsorption. A schematic drawing of the setup is shown in figure 1.

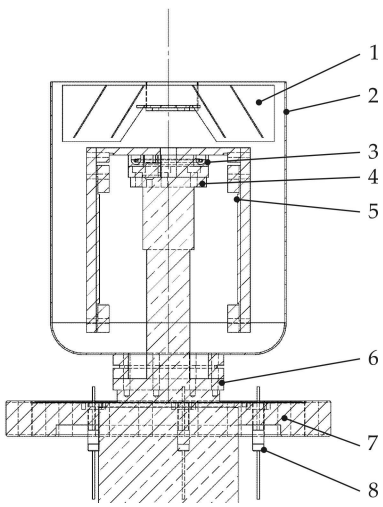

Figure 1: Schematic drawing of the cold head assembly. 1 Baffle, 2 70K thermal shield, 3 resistive heater, 4 second stage, 5 cryopanels, 6 first stage, 7 CF flange, 8 electrical feedthroughs for heater and temperature measurement.

The assembly of the cold head with cryopanles was mounted on a Fischer-Mommsen Dome to measure the pumping speed and adsorption capacity.

Measurements

The pumping speed of the panels was measured for hydrogen and for helium as a function of the temperature. Figure 2 shows the pumping speed per cm^2 panel surface for hydrogen versus the temperature of the panels.

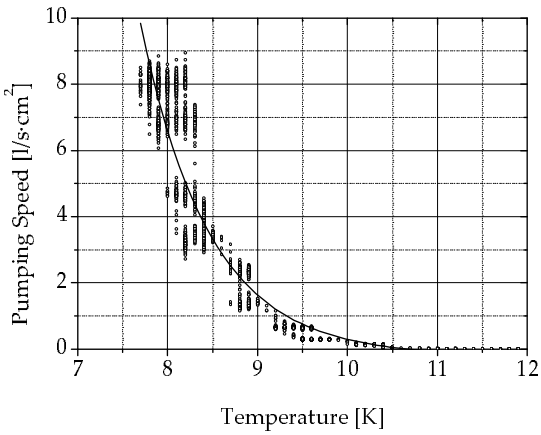

Figure 2: Pumping speed of the panels per cm^2 coated surface in dependence of the temperature. Circles are measured points with a temperature resolution of 0.1 K. The solid line shows an exponential fit.

The values of the pumping speed were 7.5 l/s·cm^2 at 8 K for hydrogen and 0.23 l/s·cm^2 at 7.9 K for helium. The capacity for helium, integrated up to 50 % of the initial pumping speed, was found to be 1.4 mbar·l/cm^2.

Conclusion

The usability of the cryopanels for the pumping of helium and hydrogen has been shown. An important matter is that no useable pumping speed for helium and hydrogen was observed at temperatures above 9 K. Therefore it will be necessary to include the cryosorption pump into the LHe circuit at the proposed SIS 100 setup, since the indirectly cooled beam pipe temperature will be above 10 K [5]. While at the SIS 300 setup the housing of the pump will be submerged directly into the LHe cryostat, the temperature will be sufficiently low (~ 4.2 K).

References

[1] Day, C., Colloids and Surfaces A 187-188, 187 (2001)
[2] Day, C., Schwenk-Ferrero, A., Vacuum 53, 253 (1999)
[3] Day, C. et al., Vacuum 81, 738 (2007)
[4] Wengenroth, M., Diploma Thesis, University of Applied Science Wiesbaden (2008)
[5] FAIR Baseline Technical Report 2006

* Email address: m.wengenroth@gsi.de

Settings Generation for the FAIR/GSI Ring Accelerators

R. Hellmich, A. Redelbach, J. Struckmeier, R. Bär, P. Spiller

GSI, Darmstadt, Germany

FAIR OPERATING SOFTWARE

Based on the basic ideas outlined in chapter *Accelerator Controls (2.14.10, page 699ff)* of the FAIR Baseline Technical Report [1] we continued to developed fundamental concepts for the control programs of the new FAIR ring accelerators [2, 3]. Main focus has been put on the accelerator physics aspects. Principles for the new operating software have been developed:

- The design of the ring operating software should be *generic*. This means that a *single* core program must be designed, capable of adapting itself to the considered ring structure after reading its lattice structure from an external description (XML file or database) [4].

It is planned to design a new *general standard cycle*. Each particular FAIR ring will be operated by specifying a cycle that represents a subset of features of the general standard cycle. In this way it is achieved, that all accelerators can be described and treated in the same manner as viewed by the (generic) control program. As a result, bunches of different operating programs for the calculation of the device ramps like "SIS18-MODI", "SIS100-MODI", "NESR-MODI" etc. may be avoided and replaced by a *single generic* "RING-MODI" operating program.

Intensive discussions reveal that the following development principles are important:

- The general format for data exchange should be XML. Using this format leads to a strict decoupling of the development of different software applications.
- We suggest, that also the lattice structure of the rings and transfer channels should be described with XML. At CERN, a discussion is under way to design a AML (Accelerator Markup Language), which constitutes an XML language that is particularly adapted to the needs of accelerator operation.
- One should follow a modern object oriented approach using JAVA as programming language and Eclipse as a development tool.
- The principles of service oriented architecture (SOA) should be applied, in order to establish a strict decoupling of applications. Thereby it will become possible to delegate the coding of software packages to external firms.
- Legacy software like programs for ion optics can be 'wrapped' and provided as a special service.
- Multi tier architecture with a conceptual separation of layers for data storage (persistence of objects), control and view is a standard demand.
- Duplex operation with hot or cold standby is not required since all physics calculations are performed "off-line".
- It must be foreseen that beam diagnostics data are taken into account for the settings generation.

With the goal of defining the fundamental properties of the controls and machine setting software, a project group has been established under the leadership of 'Accelerator Controls and Electronics'.

SIS18 UPGRADE

Ongoing projects of settings generation are an essential part of the SIS18 upgrade programme in particular. Related activities include:

- Modifications of the set values for fast ramping of SIS18 with 4 T/s or 10 T/s to accomplish a significant reduction of cycle time as a requirement for the booster operation.
- A quasi-automatic correction of the closed orbit has been implemented and successfully tested in machine experiments. This procedure is expected to improve the closed orbit in the horizontal plane after the installation of four additional power supplies for the correction coils.
- The algorithms for the settings generation at the planned dual harmonic operation with a new h=2 cavity have been implemented. In order to specify RF ramps for the new cavity operating at h=2, longitudinal space charge have been considered.
- The set values generation for the upgrade of the injection systems has been modified for the new hardware.

REFERENCES

[1] H.H. Gutbrod et al., FAIR Baseline Technical Report, GSI Darmstadt, ISBN 3-9811298-0-6A, Sep 2006

[2] R. Hellmich, A. Redelbach, P. Spiller, J. Struckmeier, "Konzept zur Neuentwicklung der Betriebsprogramme und deren Strukturierung für die zukünftigen FAIR Kreisbeschleuniger", GSI internal report, (2007)

[3] R. Hellmich, A. Redelbach, J. Struckmeier, "Orientierungspapier zur Entwicklung und Strukturierung der zukünftigen GSI-Betriebsprogramme", GSI internal report, (2007)

[4] R. Hellmich, A. Redelbach, J. Struckmeier, "Vorschlag zur Entwicklung der zukünftigen Software zur Ring-Datenversorgung (GSI/FAIR), GSI internal paper, (2007)

Design and Planning of the FAIR Storage Rings

C. Dimopoulou, A. Dolinskii, B. Franzke, S. El Hanoui, O. Gorda, V. Gostishchev, U. Jandewerth, K. Knie, A. Krämer, H. Leibrock, U. Laier, S. Litvinov, C. Mühle, I. Nesmiyan, F. Nolden, C. Peschke, P. Petri, G. Schreiber, I. Schurig, M. Schwickert, M. Steck

GSI Darmstadt

The concept of the storage rings in the FAIR project has made further progress. Details of the ion optical lattice for the Collector Ring (CR), the accumulator ring (RESR) and the New Experimental Storage Ring (NESR) have been investigated, resulting in a sound layout. This advanced layout is based on a maximum magnetic bending power for all three rings of 13 Tm which will be implemented by the use of normal conducting magnets. The basic ring size and structure of all rings is fixed, higher order corrections as well as a scheme for the correction of orbit errors have been worked out for all rings.

After fixing the main ring dimensions the size of the ring tunnels and the area for all technical systems have been defined. The interior space of the rings, CR/RESR and NESR, will be filled with two-story buildings. The upper floor of these buildings will mainly accommodate the power converters, while the the lower floor will house most other technical systems, such as rf systems, beam diagnostics, injection and extraction supplies, and beam cooling systems. As a typical example Fig. 1 shows the ring tunnel and the lower floor of the CR/RESR building.

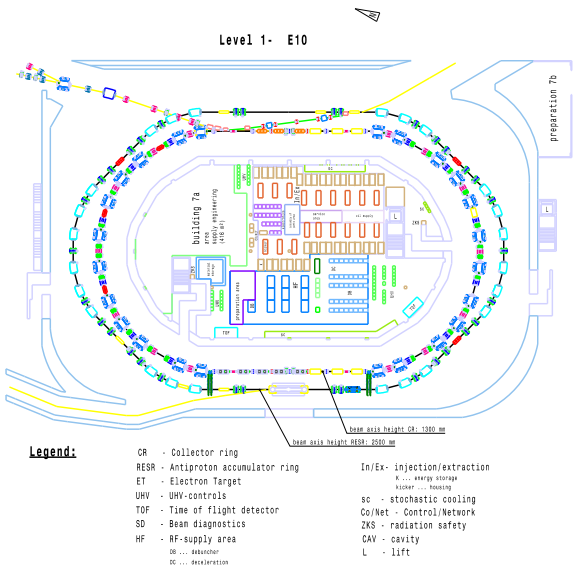

Figure 1: Floor plan of the CR/RESR ring tunnel and the inner area for technical systems.

The R&D for the stochastic pre-cooling system for cooling of ions and antiprotons at different beam velocities has been continued. A dedicated report describes the progress of the stochastic cooling systems for CR and RESR [1].

1 The Collector Ring CR

The main task of the collector ring CR is fast stochastic precooling of secondary beams. Secondary beams can be either antiprotons at an energy of 3 GeV emerging from the antiproton production target and transported through the antiproton separator or Rare Isotope Beams (RIBs) at an energy of 740 MeV/u delivered through the new fragment separator SuperFRS.

The lattice is designed for large flexibility in the choice of the transition energy γ_t to an optimal value. The lattice layout has a racetrack shape consisting of two 180 degrees arc sections connected by two long straight sections. One straight section will be occupied by the injection/extraction devices and three pick-up tanks for stochastic cooling. The other straight section will accommodate five rf cavities for bunch rotation of the incoming short bunch and three kicker tanks for stochastic cooling. Pick-up and kicker tanks for the stochastic cooling are located close to one of the arcs.

The CR has the following characteristics: a) dispersion-free long straight sections; b) betatron phase advance between pick-ups and kickers for stochastic cooling are $\Delta\mu_{h,v} = 7.85$ rad in the RIB mode and $\Delta\mu_{h,v} = 11$ rad in the pbar mode; c) the transition energy γ_t is 2.7 in the RIB mode, 3.6 in the pbar mode and 1.84 in the isochronous mode. All three CR modes will be operated at constant magnetic field level close to the maximum bending power of $B\rho = 13$ Tm. The different optics of the CR can be performed by tuning 12 independent power supplies for the quadrupole magnets. The CR lattice requires strong sextupole magnets for chromaticity correction. In the present layout of the CR 6 families of sextupole magnets are foreseen.

The influence of various magnetic field errors on the mass resolving power in the isochronous mode has been studied. The analytical and numerical simulations show that a resolving power of more than 10^6 can be achieved, if the CR ring acceptance is limited to less than 1 mm mrad and a nonlinear correction scheme is applied. This would allow to determine mass values with the required precision of 10^{-6} [2].

2 The Accumulator and Decelerator Ring RESR

The ion optical concept of the RESR has been completely revised recently. In the new layout the RESR has a hexagonal shape with a circumference of 239.9 m. The layout of the ring is dominated mainly by the requirements of the stochastic cooling system in combination with momentum stacking. The magnetic structure consists of 24 dipole, 34 quadrupole and 8 sextupole magnets. The acceptances of the ring are 25 mm mrad in the horizontal and vertical plane. The lattice is also suitable for fast deceleration of rare isotopes. The ion optical mode of the RESR for deceleration is the same as for the accumulation of antiprotons.

The RESR lattice structure (Fig. 2) has been chosen aiming at the achievement of good properties for the stochastic cooling and at the same time a maximum dynamic aperture [3]. Drift spaces with large dispersion function at the longitudinal stochastic pick-up provide a good separation between injection

and stacking orbit in the arc. These drift spaces have a small vertical beta function at the longitudinal pick-up position. The dispersion function at the stochastic momentum pick-up is as large as 13 m, whereas the vertical beta function is only 3 m.

The beam is injected on an inner orbit at a momentum offset of approximately $\Delta p/p$ = -0.8 % with respect to the central orbit, while the stacked beam circulates on an outer orbit with $\Delta p/p$ = +0.8 %. Although no stacking for rare isotopes is foreseen, the injection scheme is the same as for antiprotons.

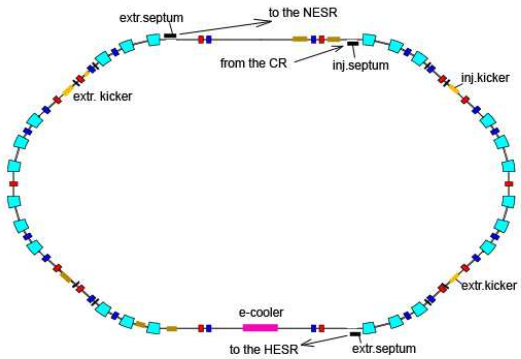

Figure 2: New layout of the RESR storage ring.

The chromaticity correction is done by two families of sextupole magnets. Each family consists of 4 sextupole magnets. The lattice functions have a basic super-periodicity of 2. The adjustment of the transition energy γ_t is obtained by tuning the quadrupoles, which are located between injection and extraction kickers. Using 6 independently powered quadrupole families in the arc a local dispersion bump in six of the dipole magnets can be created such that γ_t can be chosen in the range between 2.5 and 6.4 and the betatron tunes remain unchanged. Closed orbit simulations showed that the remaining orbit distortion in both planes can be reduced to less than 1 mm, if 12 horizontal and 8 vertical dipole correctors are installed in the ring in combination with 20 beam position monitors.

3 The New Experimental Storage Ring NESR

The ion optical structure of the NESR has been modified. By adding a large aperture quadrupole magnet of the CR-type in the middle of the bending section replacing a doublet lens, the number of quadrupole magnets was reduced from 32 to 28 and additional space is now available for sextupole magnets. Transverse acceptances of 150 mm mrad horizontally and 40 mm mrad vertically and a momentum acceptance of ± 1.5 % have been achieved in simulations. The location and strength of sextupole magnets for optimized chromaticity correction have been defined. Dynamic aperture calculations were performed to determine the available ring acceptance. A proper correction scheme for errors of individual magnets and misalignment has been worked out. The required strength and position of injection and extraction elements, both for fast and slow extraction, have been determined in ion optical calculations.

A modified layout of the NESR has been chosen, where the doublet structure is recalculated to a FODO-Doublet structure. The ring circumference of 222.8 m is basically unchanged with four 18 m long straight sections. The maximum strength of the main magnetic ring elements up to a bending power of 13 Tm is readily achievable using normal conducting iron dominated magnets. The magnetic structure consists of 24 dipole, 28 quadrupole and 12 sextupole magnets. 4 quadrupole and 4 sextupole magnets have a wide horizontal aperture up to 400 mm in order to provide transverse acceptances of 150 mm mrad in the horizontal and 40 mm mrad in the vertical plane. These large emittance beams can be accepted for a maximum momentum spread of ± 1.5 %. This is in accordance with the requirements for direct injection and storage of hot secondary beams from the SuperFRS.

In the new NESR arcs the horizontal beta function is as low as 5 m and the dispersion is 6.8 m, that provides a momentum acceptance of the ring of ± 2.5 % for a particle with a zero emittance. Fast and slow extraction from the NESR have been studied. For the fast injection and extraction three full aperture kicker magnets are foreseen. One of them will be used both for the injection and extraction. The NESR is designed for two kinds of slow extraction: charge exchange and resonant extraction. Both methods will use the same extraction elements. Since only decelerated beams will be extracted, the bending power of the extraction components is limited to 4 Tm and the required field strengths are moderate.

The dynamic aperture has been calculated including all kinds of errors and nonlinearities in the magnets. The results of such calculations with the PTC code confirmed that the dynamic aperture exceeds the size of a beam filling the full acceptance. Detailed closed obit correction schemes have been investigated. To provide closed orbit distortions of less than 1 mm one needs to install 16 vertical correctors and 18 beam position monitors. The horizontal orbit corrector coils are integrated in the 24 main dipole magnets and therefore inductively coupled to the dipole coils.

As electron cooling has major importance for the operation of the NESR, both for internal experiments and for the deceleration of ions and antiprotons, the parameters of electron cooled beams have investigated in beams dynamics calculations [4]. The simulations confirmed that, due to the small momentum spread of the cooled beams, the planned voltage of 15 kV of the rf system will be sufficient for all manipulations required in the NESR operation, both with ions and with antiprotons.

The feasibility of a longitudinal stacking scheme to increase the intensity of RIBs has been confirmed both by simulations [5] and by an experimental demonstration at the ESR [6]. According to the simulations, it can be expected that the rf and the electric cooling system in the NESR are powerful enough to fully profit from the fast acceleration cycle of SIS100, i.e. pre-cooled RIBS from the CR can be injected and cooled with a rate of nearly 1 s^{-1}.

References

[1] F. Nolden et al., contribution to this report.
[2] A. Dolinskii et al., NIM A574 (2007) 207.
[3] A. Dolinskii, et al., COOL 07 , Bad Kreuznach, September 2007.
[4] C. Dimopoulou et al., contribution to this report.
[5] T. Katayama et al., GSI Scientific Report 2006, GSI 2007-1, p. 56.
[6] C. Dimopoulou et al., contribution to this report

Developments for Stochastic Cooling at FAIR*

F. Nolden[1], A. Dolinskii[1], S. El Hanaoui[1], U. Jandewerth[1], P. Petri[1], C. Peschke[1], and M. Steck[1]
[1]GSI, Darmstadt, Germany

Electrode and Tank Design

Slotline structures will be used both as pick-ups and kickers in the stochastic cooling system of the CR. A test device was measured by means of the field mapper with the aim of deriving an equivalent circuit with discrete elements [1]. This model circuit was taken as a base for deriving optimized geometrical parameters of the slotline. The new device is now integrated into a first mechanical prototype of a complete module containing 8 slotlines.

As a final step the integration into a prototype vacuum tank with cooled, movable pick-up plates is foreseen.

Microwave Components

A prototype of a power amplifier (two times 100 W cw) in the band 1-2 GHz was specified, ordered, manufactured and measured. S parameters inside and outside the frequency band as well as nonlinearity parameters were tested. The amplifier is close to fulfilling our specifications and has been returned to the manufacturing company for final modifications.

In order to get an optimum signal to noise performance for the precious antiproton beams, cryogenic preamplifiers operated at 30 K will be installed after each slotline [2]. They are assembled inside the vacuum tank. Their electrical, mechanical and vacuum properties were specified. A call for tenders is published. The unconditional stability of the amplifiers at frequencies up to 12 GHz will be tested by means of a broad-band network analyzer.

Optical Notch Filter

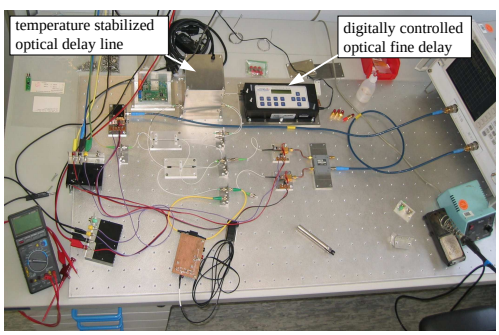

Figure 1: Laboratory model of optical notch filter

Optical notch filters are devices which can lead to a very low longitudinal emitttance at the end of the stochastic cooling cycle. A new layout is developed for FAIR. All components were mounted on a temperature stabilized aluminum plate. The optical delay cable is housed in a casing kept at constant temperature by means of Peltier cooling or heating. A dispersion matching equalizer still has to be designed.

RESR Stochastic Accumulation

The RESR is the accumulation ring for antiprotons in the FAIR project. After a redesign of its ion optical layout a stochastic accumulation scheme was elaborated [3], [4], which is similar to the former AA ring at CERN. Transverse cooling is applied only to the stack core. At the momentum pick-up there is a large dispersion (13 m) and a small vertical beta function (< 3 m), leading to a rapidly decreasing electrode sensitivity towards the stack core. Because of the limited ratio of antiproton density between stack core and tail ($10^{11}/10^{8}$) it is envisaged to try a system design without notch filters. It will be sufficient to use Faltin type pick-ups (at room temperature) and kickers in the RESR. Detailed simulation calculations are under way.

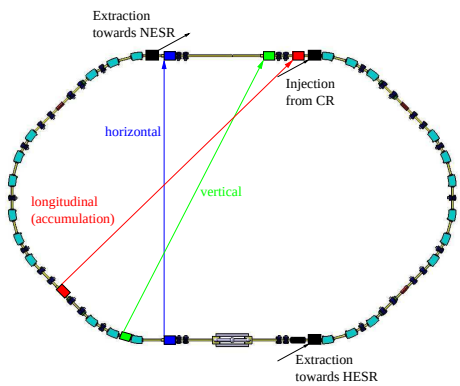

Figure 2: New RESR layout with stochastic cooling lines

References

[1] C. Peschke and F. Nolden, “Pick-up Electrode System for the CR Stochastic Cooling System”, Cool’07, September 2007, p. 194, http://www.JACoW.org.

[2] C. Peschke, F. Nolden, L. Thorndahl, “Pick-up and Kicker Electrodes for the CR”, AIP Conf. Proc 821 (2006), p. 221

[3] A. Dolinskii, F. Nolden, M. Steck “Lattice Considerations for the Collector and Accumulator Rings of the FAIR Project”, Cool’07, September 2007, p. 106, http://www.JACoW.org.

[4] F. Nolden, A. Dolinskii, C. Peschke, “Stochastic Cooling for the FAIR Project”, Cool’07, September 2007, p. 35, http://www.JACoW.org.

* Work supported by EU, EUFP6 contract No. 515873

The Concept of the Antiproton Production and Separation

K. Knie[1], A. Dolinskii[1], B. Franzke[1], and P. Sievers[2]
[1]GSI, Darmstadt, Germany; [2]CERN, Geneva, Switzerland

Due to very similar beam parameters the former Antiproton Accumulation Complex (AAC) at CERN [1] can serve as an archetype for the FAIR source. At FAIR, antiprotons (pbars) will be produced on a metal target bombarded with single short bunch of 29 GeV protons coming from SIS100. Right after the target, the pbar beam is highly divergent with an angular distribution peaking at nearly 100 mrad. Therefore, a pulsed magnetic horn will be situated immediately (≈ 20 cm) behind the target. It can focus pbars with angles up to about 80 mrad. The results of a MARS [2] simulation are depicted in fig. 1. Those pbars, which are within the separator acceptance ($\varepsilon_x = \varepsilon_y = 240\ \pi$ mm mrad, $\Delta p/p = 6$ %), will be transferred to the CR with almost 100% transmission.

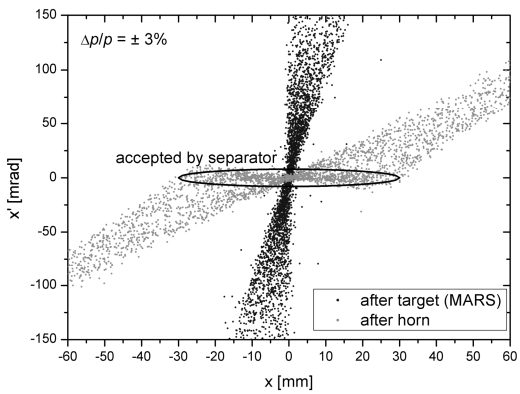

Figure 1: Phase space diagram of the pbars after the target (dark dots) and the horn (light dots).

Ion optical simulations result in further losses of about 20% during the first 200 turns in the collector ring (CR). Fig. 2 shows the present layout of the separator.

The production yield for pbars increases with the target thickness until the absorption of the protons and pbars in the target becomes dominant. Therefore, there is an optimum target length. Obviously, this length depends on the target's density. Because of a more point-like geometry, the collection efficiency is higher for a short target, thus high density materials like iridium (ρ = 22.56 g cm^{-3}) should be favored from this point of view.

On the other hand, all high density (i.e. high Z) materials have a low heat capacity. In addition, the cascade of secondaries cannot spread out as much as in materials with lower density. As a consequence, there will be a large temperature increase in high Z materials after an intense proton pulse as can bee seen in fig. 3. To avoid a melting of the target, relatively large beam diameters have to be chosen, which, however, results in reduced collection efficiencies.

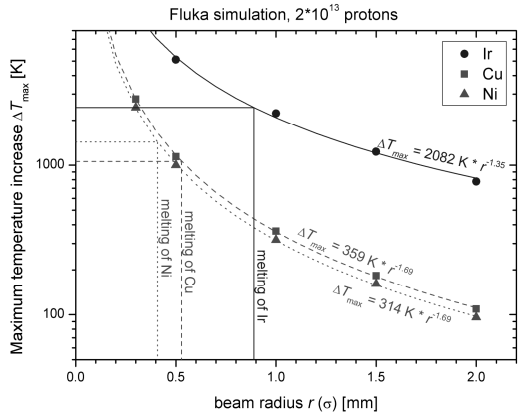

Figure 3: Maximum temperature increase after a pulse of 2×10^{13} primary protons versus the proton beam radius. The calculations were performed with FLUKA [3].

In summary, the highest yields (without melting the target with 2×10^{13} protons per pulse) can be expected for an about 11 cm long nickel target. With about 2×10^{-5} pbars (in the ellipse in fig. 1 and with $\Delta p/p$ = 6 %) per primary proton this yield is more than 10 % higher than that of an 8 cm iridium target.

References

[1] J.V. Allaby, CAS lectures, CERN/PS-AA/83-46, (1983) p. 63.
[2] N.V. Mokhov, Fermilab-FN-628 (1995).
[3] A. Ferrari et al., CERN 2005-10 (2005), INFN/TC_05/11, SLAC-R-773.

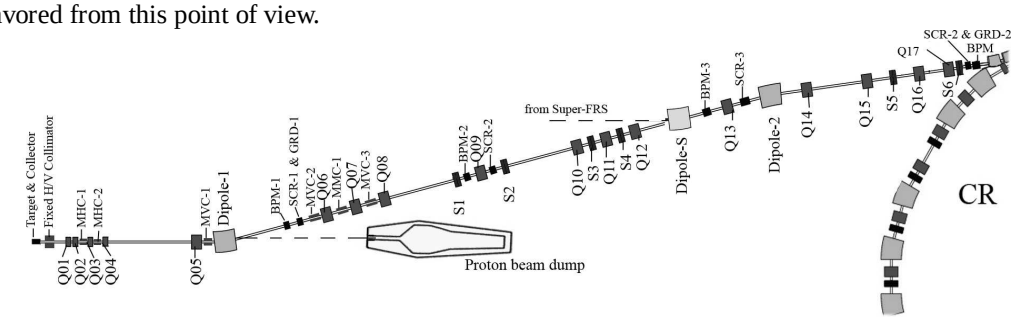

Figure 2: Layout of the FAIR pbar separator (Q, S - Quadrupole and Sextupole magnets, BPM-Beam Position Monitor).

Parameters of Electron Cooled Ion and Antiproton Beams in the NESR

C. Dimopoulou[1], P. Beller[1], F. Nolden[1], and M. Steck[1]
[1]GSI, Darmstadt, Germany

The NESR ring of the FAIR project [1] will store highly charged radioactive and stable ion beams for internal experiments and decelerate ions and antiprotons for transfer to FLAIR. A powerful electron cooling system has been designed [2], covering the full energy range (740-4 MeV/u) for ions and allowing intermediate cooling in the range 800-30 MeV during the deceleration of antiprotons. It will provide highest phase space density of the stored beams, compensate the diffusion of the beams during deceleration and support the accumulation of RIBs in order to achieve maximum luminosity for the collider mode [3].

Beam dynamics studies have been performed to estimate cooling times and beam parameters in the NESR, which are needed (i) for ring design studies e.g. optimization of deceleration and accumulation schemes, definition of RF systems and cycle times, (ii) by the experiments and (iii) by the users of extracted beams. The BETACOOL code [4] was used to investigate the dependence of the cooling time and the equilibrium parameters (transverse emittances and momentum spread) of the electron cooled beams on the initial beam parameters, for realistic operation parameters of the electron cooler [5]. Parkhomchuk's formula [6] with an effective electron velocity corresponding to magnetic field misalignments of 5×10^{-5} is used for the cooling force and the Martini model [7] for Intrabeam Scattering. A magnetic field strength of 0.2 T in the cooling section was assumed.

For ion beams at the maximum injection energy of 740 MeV/u, cooling times of less than 0.5 s were calculated, if the pre-cooled beam from the Collector Ring (CR) is cooled with an electron beam of 1 A. An example is shown in Fig. 1. Even if momentum spread and emittance are twice as large as the design value of the CR, the cooling time does not exceed 1.5 s. Thus, the experiments can fully benefit from the planned cycle time of 1.5 s of SIS100. For the deceleration mode, similar calculations were made at the intermediate and lowest energies at which electron cooling is applied [5]. Due to space charge limitations for highly charged ions at the lowest energy of 4 MeV/u, a maximum intensity of 5×10^7 cooled ions is estimated. This intensity limit is further reduced, if the beam is compressed into a short bunch for transfer to FLAIR.

The conditions for electron cooling are less favorable for antiprotons which are injected at 3 GeV, at larger momentum spread and emittance [1]. Due to their low charge the cooling time can be of the order of minutes as shown in Fig. 2. An adiabatic growth of the beam parameters is assumed during the deceleration from 3 GeV to 800 MeV. The cooling time for antiprotons with a deviation of 1σ of the distribution after stochastic pre-cooling in the CR is 150 s, even with an electron beam current of 2 A. If the experiments request deceleration cycles below 1 minute, better pre-cooling must be achieved. This should be possible by additional stochastic cooling in the RESR.

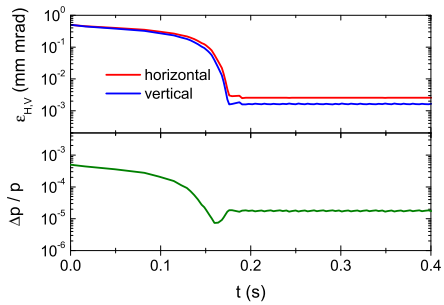

Figure 1: Simulation of electron cooling of a coasting beam of 10^8 $^{132}Sn^{50+}$ ions at 740 MeV/u. The initial beam parameters correspond to the pre-cooled beam from CR. Electron beam current: 1 A.

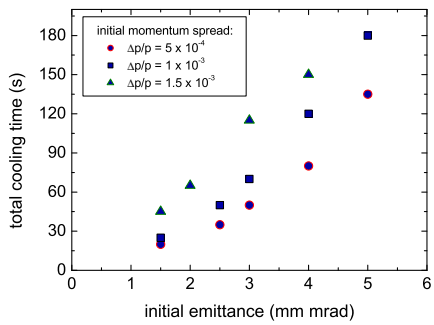

Figure 2: Total cooling time for antiprotons at 800 MeV as a function of transverse emittance and for different initial momentum spreads. Electron beam current: 2 A.

This study also confirmed the necessity of a high-quality magnet system and of electron currents of up to 2 A for fast cooling of short-lived isotopes. However, short cooling times crucially depend on the beam parameters after pre-cooling in the CR and RESR.

References

[1] FAIR Baseline Technical Design Report, GSI (2006).
[2] V.V. Parkhomchuk et al., GSI-Acc-Report-2005-04-001.
[3] T. Katayama et al., Contribution to this Report.
[4] A.O. Sidorin et al., Nucl. Instr. Meth A 558 (2006) 325.
[5] C. Dimopoulou et al., PRST-AB (2007) submitted.
[6] V.V. Parkhomchuk, Nucl. Instr. Meth A 441 (2000) 9.
[7] M. Martini, CERN-PS-84-9 (1984).

Experimental Investigation of Longitudinal Stacking Schemes in the ESR

C. Dimopoulou[1], B. Franzke[1], T. Katayama[1], D. Möhl[1,2], F. Nolden[1], G. Schreiber[1], and M. Steck[1]
[1]GSI, Darmstadt, Germany; [2]CERN, Geneva, Switzerland

Fast longitudinal stacking of RIBs is foreseen in the NESR [1] in order to reach the high intensities required by internal experiments. The stacking is supported by electron cooling. Two schemes were investigated by dedicated beam dynamics simulations. The first uses a broadband Barrier Bucket (BB) rf system, the second makes use of multiple injections on the unstable fixed point of a sinusoidal rf bucket at h=1 [2].

As a proof of principle, both methods were tested in the ESR, with a $^{40}Ar^{18+}$ beam at 65.3 MeV/u injected from SIS [3]. The revolution period T_{rev}=1.02 μs was long enough for stacking with sine-shaped BB pulses of T_B=200 ns period. The SIS and ESR rf systems were synchronised at h=2 and h=1, respectively, since the SIS has the double circumference of the ESR. One of the two SIS bunches (FWHM bunch length: 300-350 ns) is fast extracted to the ESR. The ESR injection kicker pulse was typically 500 ns long (100 ns rise/fall time, 300 ns flat top), which restricted the flexibility in manipulations with BB. The height (in momentum spread) of the rf barrier (defined so that $\pm\delta_B$ is the maximum height of the separatrix) for a sinusoidal pulse is $\delta_B = (2QeV_{rf}/\pi\beta^2\eta h E_{0,tot})^{1/2}$ where $E_{0,tot} = \gamma A m_u c^2$ is the total energy ($m_u c^2$=931.5 MeV is the nucleon mass) and Q the charge state of the ion. For the BB pulses a "harmonic" number $h = T_{rev}/T_B \approx 5$ is defined. Hence, at the same V_{rf} the confining potential of the BB system is $\sqrt{5}$ lower than for the h=1 rf. For operation of the electron cooler with an electron beam density of 3×10^6 cm^{-3} and a magnetic field strength of 0.07 T, the injected beam was cooled down to the equilibrium within about 13 s. At the equilibrium between electron cooling and intrabeam scattering, the measured momentum spread $\Delta p/p$ of the stored beam scaled with the particle number N_i - generally with the beam linear density N_i/B, where $B = T_{stack}/T_{rev}$ is the bunching factor- and cooling current I_e as $(\Delta p/p) \sim (N_i/B)^{0.36} I_e^{-0.3}$.

The increase of beam intensity during the stacking was monitored with the dc current transformer as shown in Fig. 1. For stacking by BB, the $\Delta p/p$ of the stacked beam was estimated by applying the above scaling law, where N_i is the measured saturation intenstity and the stack length T_{stack}=400 ns includes 75% of the uniform distribution as measured in the pickup. The results plotted in Fig. 2 were used to benchmark beam dynamics simulations [4]. For stacking at h=1, at saturation intensity, the stacked bunch length was measured in the pickup and the corresponding $\Delta p/p$ was calculated from the rf bucket formula $(\sigma_t/T_{rev}) = (\beta^2\eta E_{0,tot}/2\pi QehV_{rf})^{1/2}(\Delta p/p)$ and compared with δ_B. The conclusion is that the stacked bunch occupied about 20% of the ring circumference and filled

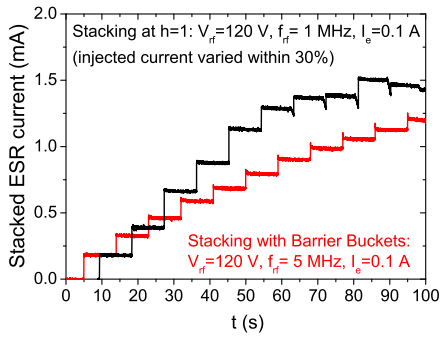

Figure 1: Demonstration of the two accumulation methods with a $^{40}Ar^{18+}$ beam at 65.3 MeV/u in the ESR. The stacking cycle was 9 s, the electron cooling current 0.1 A. A beam current of 0.3 mA corresponds to 10^8 ions.

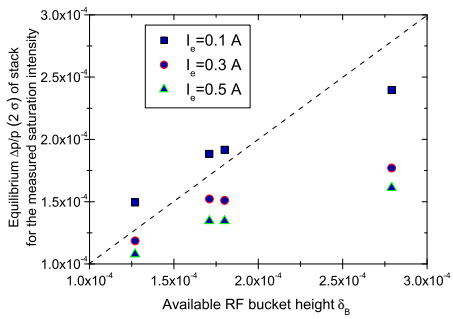

Figure 2: Stacking with BB pulses in the ESR. Momentum spread of the accumulated $^{40}Ar^{18+}$ beam compared with the rf bucket height for different electron cooling currents.

50-60% of the bucket height, for all applied voltages in the range 30-120 V. The measured relative phase of the stacked bunch with respect to the freshly injected bunch indicated that the kicker pulse overlapped with the tail of the stack, causing particle losses at every injection. Therefore, a new stacking experiment at h=1 at a higher beam energy, higher rf voltage, e.g., 1 kV, and improved synchronization between the rf and kicker pules is planned within 2008.

These results confirm the requirements for the NESR systems, namely, faster electron cooling, a BB system with 2 kV peak voltage, adjustable injection kicker pulse and appropriate beam diagnostics.

References

[1] C. Dimopoulou et al., PR-ST AB 10 (2007) 020101.

[2] T. Katayama et al., GSI Annual Report 2006.

[3] C. Dimopoulou et al.,COOL07 Proceedings, JACoW, 2007.

[4] T. Katayama et al., COOL07 Proceedings, JACoW, 2007.

Design of Antiproton Target for FAIR *

N.A. Tahir[1], V. Kim[2], A. Matveichev[2], A. Shutov[2], A. Ostrik[2], I.V. Lomonosov[2], R. Schmidt[3], M. Brugger[3], K. Knie[1], B. Franzke[1], S. Richter[1], and D. Kraemer[1]

[1]GSI, Darmstadt, Germany; [2]IPCP, Chernogolovka, Russia; [3]CERN, Geneva, Switzerland

Production and collection of antiprotons will be one of the many important experiments that will be done at the FAIR. The SIS100 will deliver a bunched proton beam with, intensity = 2 $\times$ 10^{11} protons, bunch length = 25 ns and particle energy = 29 GeV. The design of a production target that will survive over an extended period of time is a very important and difficult problem.

Figure 1 shows the proposed target geometry which is the same as used previously in the CERN antiproton production experiments. It consists of 6 iridium cylinders, each 1 cm long and having a radius of 2 mm with a small gap of 50 μm between two neighboring pieces. This avoids bending of the target as a result of expansion due to heating. The iridium part is enclosed in a solid graphite casing that is followed by an aluminum cover. The advantage of using graphite is that it has much lower absorption cross section for antiprotons. The dimensions of the different parts of the target are shown in the figure. The proton beam is incident at the left face of the target, the protons generate a shower of secondary particles that deposit their energy in the target. The energy deposition is calculated using the FLUKA code and the results are plotted in Fig. 2. The focal spot size of the beam is characterized with a σ = 1.5 mm in this case. The antiprotons generated in the target will be collected on the right side of the target using a magnetic horn.

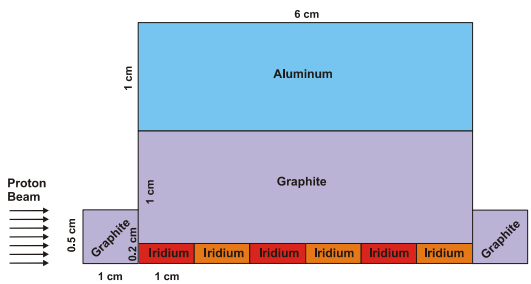

Figure 1: Target initial conditions

Hydrodynamic and thermodynamic response of the target shown in Fig. 1 has been calculated using a a 3D computer code, PIC3D, that includes a semi-empirical equation of state model and elastic-plastic effects. The energy deposition profile shown in Figure 2 is coupled to the 3D code that leads to a maximum energy deposition of 0.17 kJ/g along the beam axis which generates a maximum temperature of 1560 K that is well below the melting temperature of iridium (2700 K). A corresponding maximum pressure of about 9 GPa is generated along the beam axis. The high pressure generates acoustic waves in radial direction that are partly reflected at the graphite–iridium boundary and partly transmitted into the graphite region. This process is repeated when the transmitted wave arrives at the aluminum–graphite boundary. First calculations indicate that the target will survive with the above beam parameters. Since the repetition rate of this experiment will be 0.2 Hz, heat conduction will lead to a substantial cooling of the target during this interval that will avoid heat accumulation.

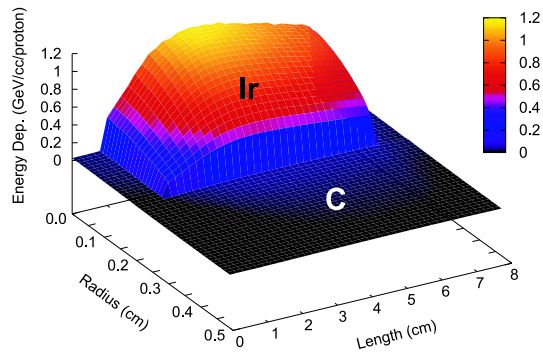

Figure 2: Specific energy deposition by 29 GeV protons in solid graphite and iridium as calculated by FLUKA code.

Figure 3 shows FLUKA calculations of proton energy deposition in a nickel cylinder. It is seen that the level of energy deposition in nickel is significantly lower that in iridium that will lead to a lower temperature and a lower pressure. We are therefore also considering nickel as material for the antiproton production target. A detailed report will be prepared when the final calculations are done.

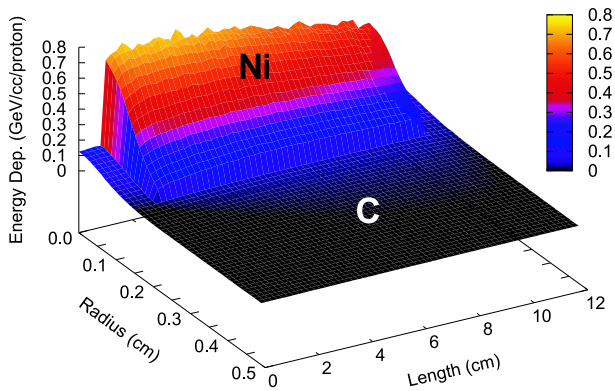

Figure 3: Specific energy deposition by 29 GeV protons in solid graphite and nickel as calculated by FLUKA code.

* Work supported by BMBF

Super-FRS Design Status Report*

M. Winkler[1,#], B. Achenbach[1], D. Acker[1], K.-H. Behr[1], D. Boutin[2], A. Brünle[1], H. Geissel[1,2], M. Gleim[1], W. Hüller[1], C. Karagiannis[1], A. Kelic[1], B. Kindler[1], E. Kozlova[1], A. Kratz[1], H. Leibrock[1], Y. Litvinov[1], B. Lommel[1], J.A. Maruhn[3], G. Moritz[1], C. Mühle[1], G. Münzenberg[1], C. Nociforo[1], W.R. Plaß[2], A. Prochazka[1], C. Scheidenberger[1,2], H. Simon[1], R. Stieglitz[4], K. Sümmerer[1], N. Tahir[1], An. Tauschwitz[3], M. Tomut[1], P. Vobly[5], H. Weick[1], J. Winfield[1], and M. Yavor[6]

[1]GSI, Darmstadt, Germany; [2]JLU Giessen, Germany; [3]JWGU Frankfurt, Germany; [4]FZ Karlsruhe, Germany; [5]BINP, Novosibirsk, Russia; [6]IAI RAS, St. Petersburg, Russia;

Layout of the Super-FRS

The present layout of the Super-FRS is shown in Figure 1 indicating also the related buildings. It consists of the Pre-Separator including the production target and the beam catchers, and the Main-Separator serving the three experimental branches i.e. the High-Energy Branch (HEB), the Low-Energy Branch (LEB), and the Ring Branch (RB).

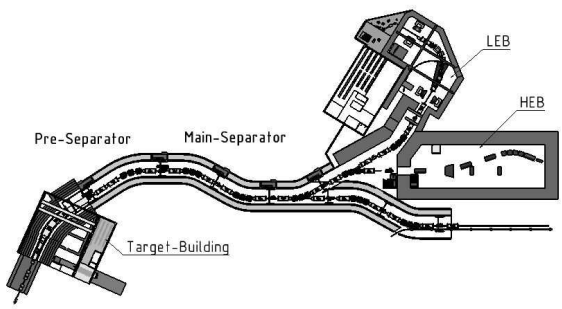

Figure 1: Present layout of the Super-FRS including the target building (left), the tunnel which houses the two separator stages, and the experimental areas for the Low-Energy Branch as well as the High-Energy Branch and the exit to the Ring Branch.

The lattice of one single dipole stage within the Pre- and the Main-Separator is based on 3 super conducting dipole units deflecting the beam by approximately 10° each. For synergy reasons it was intended to use exactly the same dipole magnet as it was assigned for the CR. After taking the decision to decouple the design of these two dipole magnets we investigated once more the possibility to optimize the layout of the Super-FRS, both in respect of scientific/technical and cost-saving criteria. However, these efforts indicate only minor possible improvements, which seem not to be appropriate considering the negative influence elsewhere at FAIR. For this reason we continued to advance the ion-optical and technical design of the Super-FRS based on the existing system as described in the FBTR [1].

High-Power Targets

The target development for Super-FRS has to consider both, the slow and fast extraction mode of the synchrotrons SIS100/300. We envisage to use a rotating graphite wheel as the standard target. In addition a feasibility study on liquid metal targets is worked out, which may serve as a future production target in case of highest energy deposition.

Rotating graphite wheel target

A prototype of the rotating-wheel target has been designed (see Figure 2) and will be fabricated in collaboration with an industrial partner. This prototype considers all necessary features of the future Super-FRS production target but the media supply and handling system was adapted to the present FRS system. This will allow us to test the rotating-wheel concept extensively under realistic conditions at the FRS using SIS18 beams.

It is of high importance for target stability to take into account the impact of short pulses (≈50ns) of high-intensity uranium beams on graphite. In collaboration with GSI plasma physics and CERN, we performed an experiment using a Laser-Doppler-Vibrometer (LDV) set-up to follow the stress waves generated in various materials by the impact of fast-extracted SIS18 beams for ^{238}U pulses of up to $4 \cdot 10^9$ ions/pulse [2]. As a next step, the measured velocity- and displacement-profiles will be compared to calculated ones.

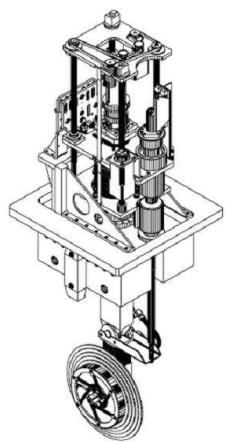

Figure 2: Prototype of the rotating graphite wheel target to be tested with SIS18 beams at the present FRS.

Collaborative efforts with the GSI Materials-Research department were undertaken to investigate the radiation damage of intense uranium beams in graphite. To this end, large fluences of low-energy uranium ions were ac-

* Work supported by the European Community under the FP6 DESIGN STUDY (contract 515873 - DIRACsecondary-Beams).
#m.winkler@gsi.de

cumulated in thin graphite layers. Diagnostic tools involved both Raman spectroscopy to investigate the internal structure of the material and dimensional measurements to follow its swelling as a function of fluence [3].

Liquid-metal target development

The feasibility study of a windowless liquid-Li jet target, has been continued by the KALLA group at FZ Karlsruhe [4]. In 2007, progress has been achieved in the following fields:

- Tests with a **water loop** have been completed. With a novel technique for measuring velocity fields and jet shapes, the calculated jet properties for several nozzles have been measured and compared to continuous-flow dynamics (CFD) calculations. The same numerical models are now being used to calculate liquid-metal jet properties.
- A **liquid-Na test loop** (Figure 3) has been constructed. Again, a novel method for detecting the shapes of totally-reflecting surfaces had to be developed (Double-Layer Projection, DLP). After loading the Na loop in early 2008, a nozzle will be inserted in the test section and the jet shapes will be investigated.
- Boundary conditions to run the loop with **liquid lithium** have been investigated. This concerns mainly the chemical stability of liquid Li in the presence of traces of contaminant elements.

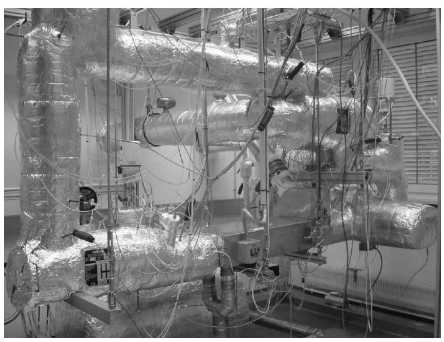

Figure 3: Photograph of the ALINA liquid-Na test loop at the KALLA laboratory at FZ Karlsruhe. The straight vertical tube on the left-hand side will be replaced by the nozzle test section in the next step.

As a third step, the liquid-Na loop can be converted to liquid Li. Important information can, however, be obtained already from the liquid-Na loop since its key flow parameters can be chosen to simulate the liquid-Li ones.

Beam catchers

In the production target approximately 10-20% of the primary beam will react while the non-reacting primary beam has to be stopped localized in beam catchers. These beam catchers will be installed at dedicated positions in the Pre-Separator. The beam catcher has not only to stop the primary beam but also to shield the subsequent parts of the separator from a high level of secondary radiation. Consequently the design of the beam catcher consists of two parts. The front part is made of a ≈40 cm long V-shaped graphite block (Figure 4) which absorbs the energy while a subsequent iron block of ≈60 cm length reduces the neutron radiation on the following magnets.

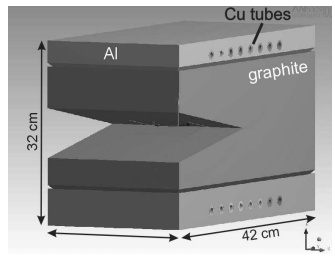

Figure 4: The front part of the beam catcher is made of graphite to absorb efficiently the beam energy. The cooling water runs in copper tubes inside of an aluminium block in close thermal contact to the graphite.

Magnet developments

The magnet R&D for the Super-FRS includes the design and prototype production of normal conducting radiation resistant magnets and super conducting magnets, respectively.

Radiation resistant magnets

Radiation resistant magnets must be used in the very first dipole stage where the production target and the beam dump will cause high radiation levels. A prototype of the dipole magnet has been designed and will be fabricated in collaboration with BINP. The project is in detail presented in [5].

Superferric magnets

All other dipole stages of the Super-FRS will be equipped with superferric magnets. These are iron dominated magnets but using super conducting coils. Thus they unify the advantages of both techniques, i.e. achieving a high field quality by iron shaping and high magnetic field gradients by applying high Ampere-turns. The main R&D activity was the continuation of the prototype development of a dipole magnet (see Figure 5) together with the Chinese FAIR Group. Main components of this magnet are fabricated and it will be assembled and commissioned in 2008.

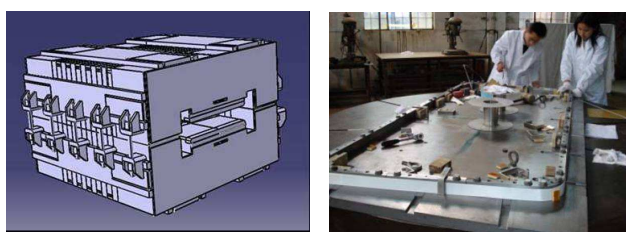

Figure 5: 3D yoke design of the superferric dipole magnet (left) and winding of a test coil (right).

[1] http://www.gsi.de/fair/reports/btr.html
[2] R. Wilfinger *et al.*, this report.
[3] M. Tomut *et al.*, this report
[4] http://www.kalla.fzk.de/gsi
[5] C. Mühle *et al.*, this report

Radiation Resistant Dipole for Super-FRS*

C. Muehle[1#], K.H. Behr[1],H. Geissel[1], A. Marbs[3], G. Moritz[1], I. Pschorn[1], P. Vobly[2] C. Will[1], M. Winkler[1]

[1]GSI, Darmstadt, Germany; [2]Budker Institute of Nuclear Physics, Novosibirsk, Russia; [3]FH Mainz, Germany

Introduction

In the first stage of Super-FRS normal conducting radiation resistant magnets are mandatory due to the high radiation level [1,2,3].

Radiation Resistant Conductor

The use of mineral insulated cables (MIC) is foreseen. The internal copper conductor is surrounded by a MgO insulation layer which is copper-clad. There are MICs available with and w/o internal cooling channels (Figure 1). The internal cooling has on the one side the advantage of a more effective cooling, but on the other side the disadvantages of a more complicated end sealing and the danger of radiolysis in a high radiation field. Commercial available MICs are rated up to 3000 A.

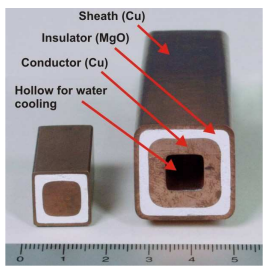

Figure 1: Mineral Insulated Cable (MIC) without a cooling channel (left) and with (right).

Radiation resistant dipole

Besides the radiation resistance the dipole is special due to its pure size. Its main parameters are: Bending angle 11°, bending radius 12.5 m, maximum field 1.6 T, vertical pole gap height ±90 mm, useable vertical gap ±70 mm, useable horizontal aperture ±190 mm, field quality in the useable gap $\pm 3 \cdot 10^{-4}$. The free horizontal aperture must be as wide as ±500 mm for damping the non-stopped primary beam into the beam catchers behind the magnet. A prototype of such a dipole is under production right now.

Dipole Yoke

For enabling the use of beam catchers just behind the magnets an H-type structure with pole shims and an approximated Rogowski end-profile was chosen. Magnetic field calculations show, that a radial end profile optimisation is necessary to reach the requested field quality. As the standard method of gluing thin laminations to rigid blocks is not possible, 150 mm thick milled blocks will be assembled to form the yoke. They are insulated to each other by blue steamed, 0.27 mm thick, laser-cut laminations. Some of the blocks are wedge shaped, to form a curved magnet. The complete yoke weighs 78 tons.

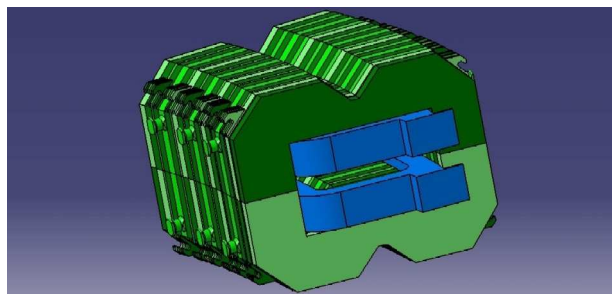

Figure 2: Artists view of the dipole.

Dipole Coil

A solid MIC with a cross section of (19 x 19) mm^2 was chosen. One coil (384 turns) consists of 16 double pancakes operated at 671 A. The total power consumption of the magnet will be 144 kW. The cooling is done by means of 4 copper radiators per coil. Each radiator has 6 parallel cooling channels made from stainless tubes which gives the advantage of a high water flux (240 l/min for both coils) at a low pressure drop (1 bar).

Remote assembly and alignment

During magnet operation the materials will be activated to a high level which does not allow hand on maintenance. In case of a failure a remote controlled disassembly and replacement of the affected parts must be possible. The same applies to survey and alignment.

The remote assembly concept is based on crane handling of the following units: girder with alignment feet, lower half yoke with lower coil, upper half yoke with upper coil. A concept of remote connectors for current, water and interlocks is under development.

A concept for remote survey and alignment, based on a photogrammetric solution, was developed [4].

References

[1] M. Winkler et al., IEEE Trans. on Appl. Supercond. Vol. 16 (2006) 415

[2] A. Zeller et al., IEEE Trans. on Appl. Supercond. Vol. 16 (2006) 164

[3] K.H. Tanaka et al., IEEE Trans. on Appl. Supercond. Vol. 12 (2002) 278

[4] Marbs, A. et al: Final Report on Surveying and Alignment systems for high-radiation areas, Aug. 2007 (Design study: DIRAC secondary beams, NUSTAR 2-Task 7)

* Work supported by the European Community under the FP6 DESIGN STUDY (contract 515873 - DIRACsecondary-Beams).

C.Muehle@gsi.de

Large Aperture Hexapole Magnets for the Super-FRS LEB Spectrometer*

J.S. Winfield[1#], D. Ackermann[1], D. Boutin[2], H. Geissel[1,2], J. Gerl[1], M. Górska[1], C. Nociforo[1], J. Sarén[3], H. Weick[1], M. Winkler[1], and M. Yavor[4]

[1]GSI, Darmstadt, Germany; [2]Justus-Liebig Univ., Gießen, Germany; [3]Univ. of Jyväskylä, Finland; [4]Inst. of Analytical Instrumentation, RAS, St. Petersburg, Russia.

It is proposed to use a magnetic spectrometer [1,2], located behind the Super-FRS [3] in the LEB cave, for experiments with exotic beams at low and intermediate energies (5 to 200 MeV/A) and stopped beams. For the HISPEC/DESPEC [4] experiments where exotic ions are measured in coincidence with gamma spectroscopy at the secondary target MF10, a good mass identification is necessary. This requires a spectrometer with high momentum-acceptance for particle identification via magnetic rigidity analysis and tracking.

A first-order ion-optic design for the spectrometer was presented in Ref. [2]. Higher-order optic calculations have suggested the need for large-aperture hexapole magnets to correct 2nd-order aberrations. With no hexapole correcting magnet, the focal plane of the spectrometer is extremely inclined: at 73° from the perpendicular to the central trajectory. This is typical for large-acceptance spectrometers [5]. Such an inclined focal plane might cause difficulties for certain experiments. A hexapole magnet placed after the dipole can be used to correct the focal plane angle back to the perpendicular by cancelling the matrix element ($x|ap$). However, this has the effect of introducing other aberrations. In particular, the geometrical aberration ($x|aa$) becomes large and has to be corrected by another hexapole *before* the dipole where the dispersion is still zero. The layout and 2nd-order ion optics of the spectrometer, as presently considered, are shown in Fig. 1.

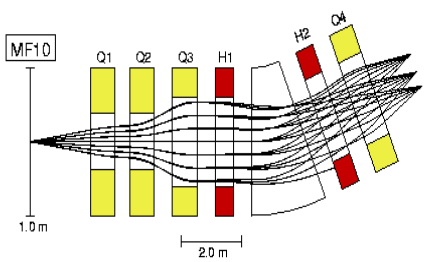

Figure 1: Layout and 2nd-order ion-optics of the magnetic spectrometer with hexapole correction.

The hexapole magnets would need to have a usable aperture of about 600 × 400 mm^2 and an effective length of about 0.6 m. The required hexapole field strengths are about 16 Tm^{-2}. Since it is intended to use superferric quadrupoles for the spectrometer, the hexapole magnets should also be superferric, i.e. iron-dominated lenses, yet with superconducting coils. They could be integrated in a common cryostat together with the quadrupoles.

* Work supported by the EU under the FP6 DESIGN STUDY (contract No. 515873 – DIRACsecondary beams).
#j.winfield@gsi.de

Simulated Knock-out Experiment

A knock-out reaction, where a 160 MeV/u ^{132}Sn secondary beam impinges on a carbon target at MF10 and produces ^{129,130,131}Sn^{50+} fragments which are measured in coincidence with gamma-ray spectroscopy, has been simulated with MOCADI [6]. Particle-tracking detectors are used before and after the spectrometer, assuming spatial and time-of-flight resolutions of 1 mm and 80 ps over a 13-m path length, respectively. The reconstructed mass distributions at the exit of the spectrometer, with a cut on the central rigidity of the ^{132}Sn beam, and as a function of the scattering angle, are shown in Fig. 2.

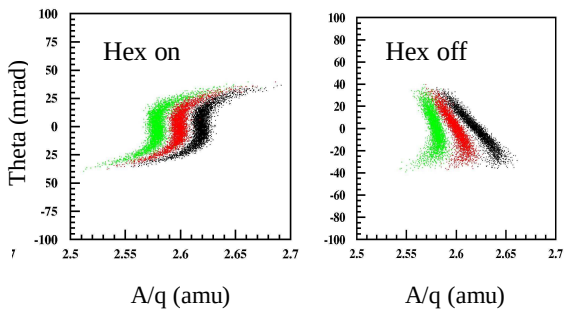

Figure 2: Simulated scattering angle *vs.* mass/charge distributions of ^{129,130,131}Sn at the exit of the spectrometer with (left) and without (right) hexapole correction.

The use of hexapole magnets reduces second-order effects, but at the same time introduces higher-order aberrations which may deteriorate the mass resolution at extreme scattering angles. Therefore we are continuing our ion-optical efforts and extending the simulations to other types of experiments which use the LEB spectrometer.

References

[1] C. Brandau et al., RNB7 conference, Cortina D'Ampezzo, Italy, July 2006; Eur. Phys. J. Special Topics **150** (2007) 225.
[2] D. Boutin et al., GSI Report (2007-1) 55.
[3] http://www.gsi.de/fair/reports/btr.html
[4] HISPEC, DESPEC, NuSTAR Letters of Intent, GSI, 2004.
[5] A. Cunsolo et al., Nucl. Instr. Meth. A **484** (2002) 56.
[6] N. Iwasa et al., Nucl. Instr. Meth. B **126** (1997) 284.

Beam Profile Detector for the Super-FRS*

A. Prochazka[1], K.-H. Behr[1], A. Brünle[1], F. Farinon[1], H. Geissel[1], R. Janik[2], C. Karagiannis[1], J. Kurcewicz[1], C. Nociforo[1], C. Scheidenberger[1], H. Simon[1], B. Sitar[2], P. Strmen[2], I. Szarka[2], H. Weick[1], J. S. Winfield[1], and M. Winkler[1]

[1]GSI, Darmstadt, Germany; [2]Comenius University, Bratislava, Slovakia

Abstract: A new Beam Profile Detectors has been tested at the FRS with fast-extracted carbon beam.

Introduction

The Beam Profile Detectors (BPD) for intense slow and fast-extracted beam have been proposed and designed by the Bratislava group for the future Super-FRS facility [1] within the NUSTAR 3 task of the FP6 EU Design Study.

In order to handle a wide range of intensities, ions and a large amount of charge deposited in the detector as foreseen in the FAIR experiments at the Super-FRS, a gas detector with variable gas pressure and delay line read-out was chosen.

BPD design and test

The first BPD prototype, constructed as a low pressure gas ionization wire chamber with an active area of (10x10)cm^2, was already tested [2]. A new BPD prototype (see Figure 1) having a larger area of (24x12)cm^2 has been tested in October 2007 with a fast-extracted beam. The BPD is modular detector with the basic module of (12x12)cm^2. It is possible to build a BPD with larger dimensions. Cathode wires with 2mm pitch are directly connected to the integrated passive delay lines (total length of the delay is 700ns). In order to obtain a faster read-out time the number of delay lines was increased. Thus the prototype has in total two delay lines for reading the x position and one for the y position. Signals from the anodes can be used for monitoring the spill structure.

The integrated electronics coupled to the detector consisted of charge-sensitive preamplifiers with gain of 30mV/pC and main amplifiers operating with gain 2. The detector test was performed at the FRS by using fast extracted ^{12}C beam delivered at 200 and 400 MeV/u. The beam profile in x and y direction was reconstructed using a Flash ADC SIS 3301 with 100 MHz sampling rate, read by VME under the Multi Branch System of GSI [3]. Signals from the anodes were used for the read-out trigger. During the test a gas mixture Ar+20%CO_2 was used with pressure variation form 1 bar to 5 mbar. The responce of the detector was measured at different beam intensities from 10^4 up to 10^9 ions/spill. The spill length was 300 ns.

An example of measured beam profile in the x and y directions at an intensity of 10^9 ions/spill is given in Figure 2. The data analysis of the collected data is currently in progress.

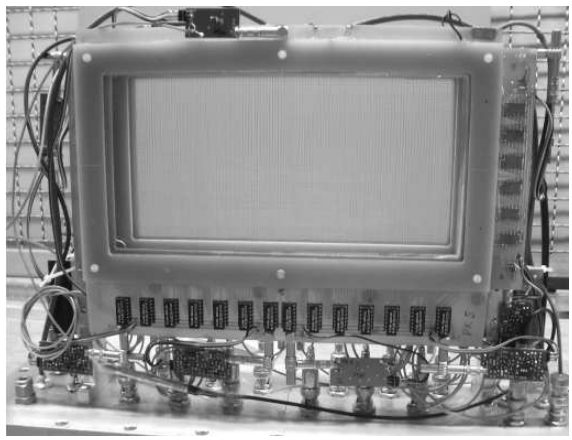

Figure 1: photograph of BPD prototype.

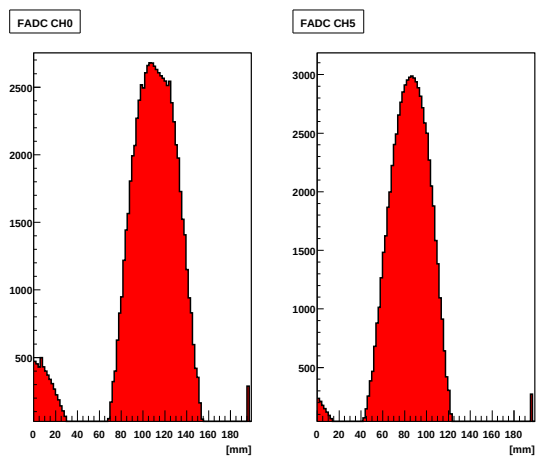

Figure 2: Beam profile in x(CH 0) and y(CH5) directions containing 1.6*10^9 ions per spill.

References

[1] H. Geissel et al., NIM B204 (2003) 71.

[2] C. Nociforo et al., A Beam Profile Detector for the Super-FRS,GSI Scientific report 2006, page 41.

[3] http://www-win.gsi.de/daq/.

* Work supported by European Community under the FP6 DESIGN STUDY (contract 515873 - DIRAC secondary-Beams)

Integrity of Liquid Lithium Production Target for the Super-FRS at FAIR

An. Tauschwitz [1], J.A. Maruhn[1], V. Efremov[2], H. Geissel[3], A. Kelic[3], K. Sümmerer[3], H. Weick[3], and M. Winkler[3]

[1]University of Frankfurt am Main, Germany; [2]JIHT, Moscow, Russia; [3]GSI, Darmstadt, Germany

The use of a windowless liquid-lithium jet as a production target at Super-FRS is currently being discussed. We investigate the stability of a liquid-metal target after irradiation with a pulsed intense energetic ion beam at FAIR. The SIS-100 synchrotron will deliver up to $5 \cdot 10^{11}$ ions of U^{28+} at 1 GeV/u energy for experiments at the Super-FRS. The ion beam will be bunched to a single pulse of 60 ns length. The radial profile of the beam can be well approximated by a Gaussian distribution. According to ion-optical calculations, reasonable characteristics of the secondary beams can be obtained with $\sigma_x = 0.4$ cm, $\sigma_y = 0.8$ cm. The direction of the jet flow corresponds to the y-axis.

Using the above ion-beam parameters, 3-dimensional hydrodynamic calculations were performed to analyze the pressure evolution in the liquid-lithium jet. To calculate the hydrodynamic response of the heated liquid lithium target, an analytical equation of state model suitable for the considered target regime was chosen. The above FAIR ion beam parameters lead to an energy deposition of 0.7 kJ/g in the center of the Gaussian energy profile, producing a pressure of 2.9 kbar. Since the pressure of several kbar launches a weak shock wave in the liquid metal, the process can be analyzed by using the acoustic approach. A linear Mie-Grüneisen equation of state was used for the calculations

$$p(\rho, T) = c_0^2(\rho - \rho_0) + \Gamma \rho c_v (T - T_0)\,, \qquad (1)$$

where $c_0 = 4.5 \cdot 10^5$ cm/s is the bulk sound speed at normal density $\rho_0 = 0.51$ g/cm^3 and at the initial temperature $T_0 = 460$ K; $\Gamma = 0.85$ is the Grüneisen parameter, $c_v = 4.1 \cdot 10^7$ erg/g/K is the specific heat at constant volume.

The energy deposition of the FAIR ion beam with the above parameters is short on the hydrodynamic time scale of the target response and can be considered as instantaneous. After the ion beam energy is deposited, the pressure gradient gives rise to a compression wave, propagating in the xy-plane. At the same time the free surface of the heated region moves outwards and a rarefaction wave runs along the z-axis to the target center. The pressure distribution at $t = 2.2\,\mu$s showing the propagation of shock and rarefaction waves is shown in fig. 1. The center of the target is placed at the origin of the coordinate system. Due to the Gaussian radial profile of the ion beam, the pressure at the target axis starts to drop immediately after the energy deposition. This effect overlaps with an expansion of the free surface, producing at the axis a negative pressure of -2.55 kbar.

The performed calculations assume that the target material can bear such tension without failure. In reality spall, or internal failure, occurs in the condensed media

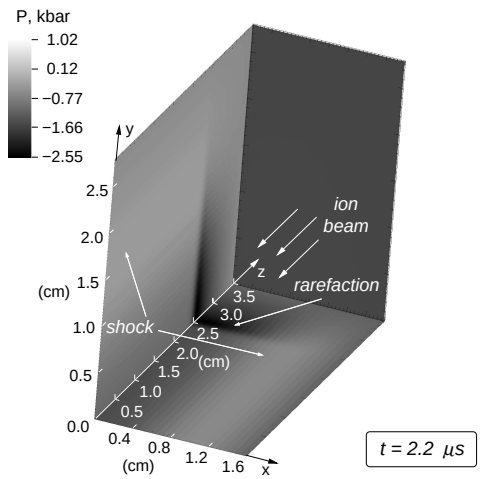

Figure 1: Pressure distribution at $t = 2.2\,\mu$s. The ion beam is directed along the z-axis.

if the magnitude of negative pressure exceeds the tensile (spall) strength of the material. For liquid lithium experimental data on the spall strength are not available at any temperatures. According to the approach of Grady [1], the theoretical spall strength in liquid lithium results in $P_s = -0.09$ kbar, which is achieved in the target already after $t = 210$ ns as shown in fig. 2. Spallation is expected to occur at a distance $s = 0.08$ cm from the target surface. It is expected that the jet will be destroyed due to the following fragmentation of the heated matter [2].

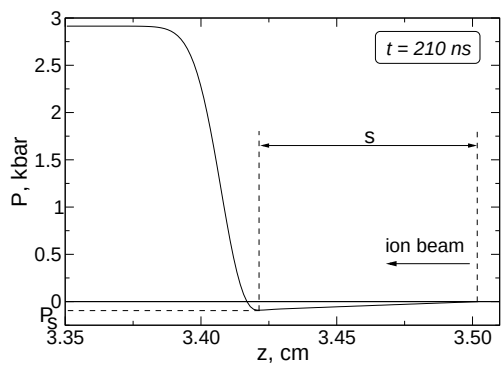

Figure 2: Pressure profile along the z-axis at $t = 210$ ns.

References

[1] D.E. Grady, J. Mech. Phys. Solids **36**, 353 (1988).

[2] An. Tauschwitz et al., NIM A, submitted for publication.

Experimental Investigations on Heavy-Ion Induced Radiation Damage of Graphite for the Super-FRS Target and Beam Catchers *

M. Tomut[1,2,#], B. Achenbach[1], K.H. Behr[1], W. Ensinger[3], H. Geissel[1], A. Hübner[1], A. Kelić[1], B. Kindler[1], M. Krause[3], B. Lommel[1], I. Manika[4], R. Neumann[1], C. Scheidenberger[1], K. Schwartz[1], K. Sümmerer[1], C. Trautmann[1], H. Weick[1], M. Winkler[1]

[1]GSI, Darmstadt, Germany, [2]NIMP, Bucharest, Romania, [3]TU Darmstadt, Germany, [4]University of Latvia, Riga, Latvia

Fine-grained isotropic graphite R6650 (SGL Carbon) has been selected for manufacturing the production target and the beam catchers at the planned Super-FRS fragment separator [1] at FAIR. Failure criteria due to irreversible ion-beam induced damage of these components are related to dimensional changes, degradation of the mechanical strength due to defect accumulation, and/or degradation of the favourable thermo-mechanical properties required to minimize the thermal stresses and fatigue. To get an estimate for the critical doses, both simulations and experiments are needed. This report presents the first results of an experimental study on R6650 polycrystalline graphite exposed to Pb and U ions, showing evidence of dimensional changes, induced stress and hardening. We used 11.1 MeV/nucleon ^{238}U ion beams, which have an energy loss above the threshold for a efficiency for the formation of cylindrical damage trails equal to unity [2].

We investigated dimensional changes of the irradiated material with profilometry. Previous studies have shown that this technique allows a relatively simple, non-destructive test of the sensitivity of a given material to ion-induced damage. The samples were polished to optical quality and partially covered during the irradiation using a thick Al mask. The mean height of the step between pristine and irradiated area has been determined by averaging several individual scans. Microhardness tests were done using an indentation technique.

Our isotropic graphite shows a remarkable resistance to defect production as shown by the low values of dimensional changes at fluences of up to 10^{12} U ions/cm^2. In the range of 10^{12} to 10^{13} U ions/cm^2, the swelling increases steeply. At fluences of 10^{13} U ions/cm^2, the ion tracks having a diameter of about 3 nm start to overlap. At this fluence the measured out-of-plane swelling is 1.3 ± 0.1 μm, 1% of the range (120 μm) of the ions (Fig.1). We also observe a significant bending of this sample due to a strong in-plane stress which develops at the interface between the damaged layer and the non-irradiated substrate.

Profilometer mapping of the surface of samples irradiated with 10^{13} U ions/cm^2 reveals crack formation. Microhardness tests on the surface of this sample show also a hardening of 100-400%.

* Work supported by the European Community under the FP6 DESIGN STUDY (contract 515873 - DIRACsecondary-Beams).

m.tomut@gsi.de

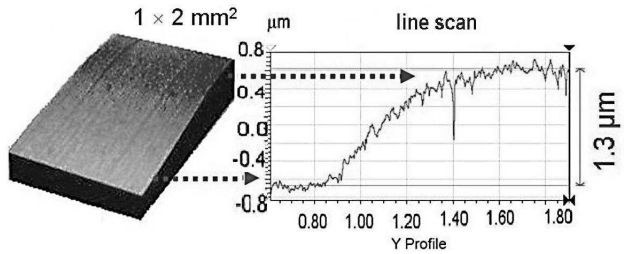

Fig.1 Profilometer mapping at the transition from non-irradiated (front) to irradiated (back) area of the masked polycrystalline graphite sample exposed to 10^{13} U ions/cm^2 (11.1 MeV/u). The selected scan displays a step height of 1.3 μm.

At high energies (low dE/dx) and high operation target temperatures (defect annealing), we expect that the damage is highly reduced. We tried to estimate a scaling factor for efficiency of track formation in isotropic graphite, at Super-FRS energies and target temperatures (calculated previously with ANSYS^{TM}), based on the scanning tunnelling microscopy studies of Liu at al. on highly oriented pyrolytic graphite (HOPG) [2,3]. Assuming an extreme situation, with 10^7 beam pulses/year, a 1s pulse with an intensity of 10^{12} U particles and taking into account a 1 Hz rotation frequency of the wheel, the Super-FRS target could accumulate 10^{17} ions/cm^2 within one year of service. At the planned beam energy (and corresponding energy loss) the track formation efficiency in HOPG would be less than 10^{-3} [2]. This is further reduced by a 10^{-3} factor at temperatures above 800 K, due to track annealing [3]. Extrapolating this efficiency scaling to polycrystalline graphite, the resulting track density/year of Super-FRS target operation would be less than 10^{11} tracks/cm^2 which is well below the critical fluence discussed above.

In the case of graphite as beam catcher, the ion-induced damage might become a more severe problem due to the fact that ions are stopped in the graphite and thus the Bragg peak and the elastic collision cascade close to the ion stopping are inside the bulk material. The large predicted values of swelling will require an elastic interface to the cooling system.

References

[1] H. Geissel et al., Nucl. Instr. Meth. B 204 (2003) 71.
[2] J. Liu et al., Phys. Rev. B 64 (2001) 184115.
[3] J. Liu et al., Nucl. Instr. and Meth. B 245 (2006) 126.

Design Status of the FAIR Proton Linac*

L. Groening[1#], W. Barth[1], G. Clemente[1], H.-L. Dambowy[1], S. Minaev[2], H. Podlech[3], U. Ratzinger[3], A. Schempp[3], W. Vinzenz[1]

[1]GSI, Darmstadt, Germany; [2]ITEP, Moscow, Russia, [3]IAP, University of Frankfurt a.M., Germany.

Introduction

The FAIR proton linac has to provide the primary proton beam for the production of antiprotons [1]. It will deliver a 70 MeV beam to the SIS18 with a repetition rate of 4 Hz. The room temperature linac will be located north of the existing UNILAC complex. Its conceptual layout is shown in Fig. 1 and its main beam parameters are listed in Tab. 1.

Tab. 1: Main parameters of the proton linac for FAIR.

Final energy	70 MeV
Pulse current	35 mA
Protons per pulse	$7 \cdot 10^{12}$
Repetition rate	4 Hz
Trans. beam emittance	2.1 µm (tot. norm.)
Rf-frequency	325.224 MHz

RF-Cavity Development

The availability of 3.0 MW klystrons triggered the development of rf-Coupled Crossed-bar H-cavities (CCH). Two single CH-cavities are merged to one CCH representing a single load to a single klystron. Figure 2 draws a CCH.

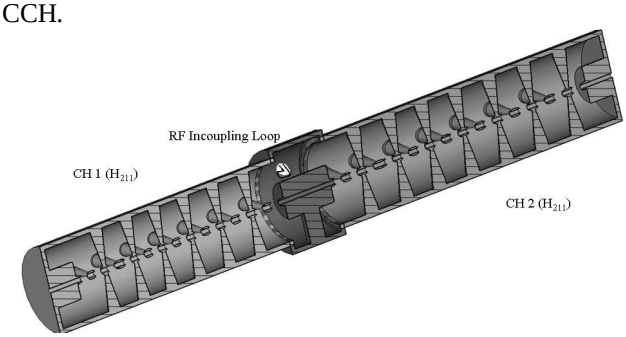

Figure 2: Two rf-coupled CH-cavities.

Although simulations on the rf-properties of CCH are promising, such a cavity never has been built so far. In order to test the production and rf-tuning steps, a scaled 1:2 cold model was successfully built at Frankfurt University. Measurements of the models rf-properties confirmed the simulations. A dedicated report on the rf-properties of the model is given in [2]. As a next step the construction of a fully operating CCH prototype was launched in 2007. Completion is expected in 2009 followed by extensive rf-testing at GSI. It is planned to use this prototype in the FAIR proton linac.

Beam Dynamics Error Studies

Dedicated error studies were started in order to spot eventual locations of increased beam loss. These studies are needed for an advanced radiation shielding layout as well as to obtain limits for tolerable jitter in rf-controls and quadrupole alignment. Gaussian distributed errors on rf-phases and amplitudes as well as on transverse quadrupole positioning were assumed along the whole linac. It was shown that 1 σ rf-errors of ±0.1% in amplitude and ± 1° in phase are not harmful. However, quadrupoles must be aligned to a precision of at least ± 0.1 mm in order to avoid significant beam loss (Fig. 3). The extended beam diagnostic section in the middle of the DTL was identified as a major location of losses.

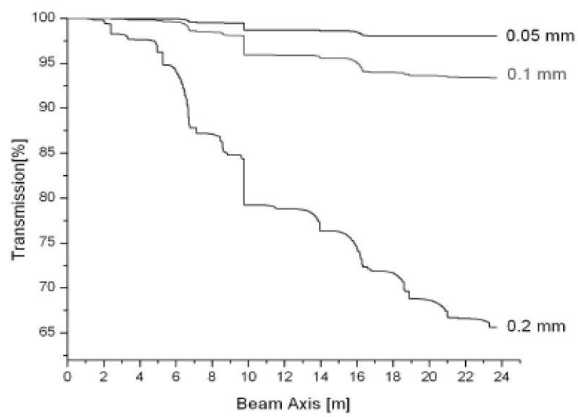

Figure 3: Beam losses along the DTL for different quadrupole alignment errors.

References

[1] *FAIR Baseline Technical Report*, Vol. 2, GSI Darmstadt, Germany, p. 335, (2006).

[2] G. Clemente et al., this report.

* Work supported by EU, CARE contract No. RII3-CT-2003-506395.

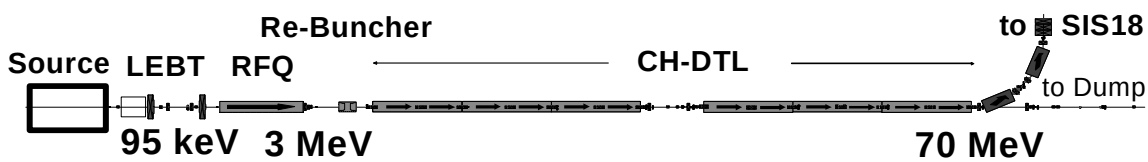

Figure 1: Conceptual layout of the FAIR proton linac.

#la.groening@gsi.de

Fast Chopper and 1 ns Bunch Compressor for Intense Proton Beams

C. Wiesner* , L.P. Chau , M. Droba , O. Meusel , and U. Ratzinger
Institut für Angewandte Physik, Frankfurt/Main, Germany

High intense proton beams are needed for many projects [1, 2]. To develop LINACs operating at the 200 *mA* level is a quite challenging task. Therefore new techniques, concepts and simulation tools have to be carefully developed.

Within "Frankfurter Neutronen Quelle am Stern-Gerlach-Zentrum" FRANZ, shown in Fig.1, a neutron flux will be created by a high intense proton beam hitting a Lithium 7 target [3].

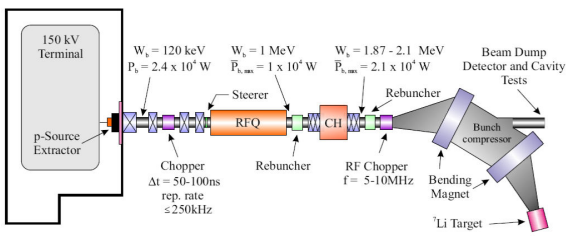

Figure 1: Scheme of the "Frankfurter Neutronen Quelle am Stern-Gerlach-Zentrum".

Intensity and time structure of the neutron pulses depend on the characteristics of the proton beam. Therefore the 200 *mA* dc proton beam delivered by an ion source of the volume type will be transformed into a pulsed beam with the required repetition rate of 250 *kHz*. Pulsing of the ion source is limited by plasma rise time while pulsing of the extraction system might cause destructive high power deposition. Therefore a chopper system in the Low Energy Beam Transport (LEBT) section will be installed to produce proton pulses of 50 to 100 *ns* length. An electric deflection system and a magnetic chopper system are currently investigated. The LEBT section consists of four solenoids already installed at the FRANZ experiment site. The first two solenoids will match the proton beam into the chopper system while the last two magnets are necessary to inject the beam into the RFQ. A schematic layout is shown in Fig.2.

At the high intensities needed for the neutron experiments the issue of space charge becomes fundamental. Preliminary multi-particle simulations show that it is possible to transport the beam through the LEBT section without significant losses assuming a space charge compensation of 85% in the LEBT section before the chopper and no compensation for the pulsed beam.

Accelerating up to 2.1 *MeV* by a RFQ-IH combination the 100 *ns* macro bunches gain a 175 *MHz* micro structure. Deflected by a rf-kicker into a magnetic bending system about 10 micro bunches arrive at the same time at the n-production target (see Fig.3). Micro bunches passing the

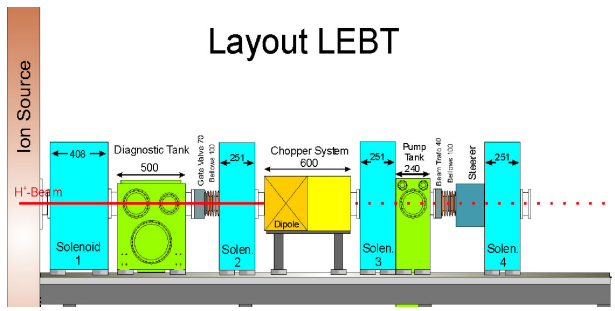

Figure 2: Schematic Layout of the LEBT Section for FRANZ.

bending system approach each other ($\beta\lambda = 0.114\ m$) due to the path differences of the trajectories. Multi-particle simulations with LORASR for a single bunch lead to the efficient transport and transversal bunch focusing. These simulations also show the necessity of a rebuncher within the dipole system in order to reach the 1 *ns* pulse length at the target.

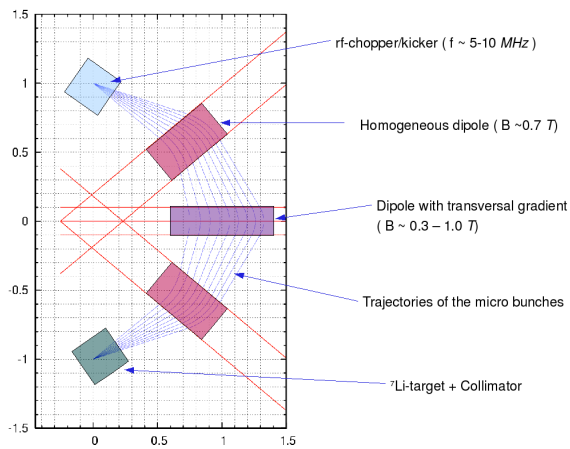

Figure 3: Scheme of the 1 *ns* bunch compressor. The tics in this picture are in distances of 0.1 *m*.

References

[1] O. Meusel et al., Proc. of the Lin. Acc. Conf., Knoxville (2006), MOPO51, 159-161.

[2] G. Aliberti et al., Nucl. Sci. Eng. 146, 13-50 (2001).

[3] M. Heil et al., Nucl. Inst. Meth. A 459, 229-246 (2001).

* wiesner@iap.uni-frankfurt.de

The Development of Coupled CH Structure for FAIR*

G. Clemente[1,2], H. Podlech[1], and U. Ratzinger[2,#]
[1]J.W.Goethe University, Frankfurt am Main, Germany; [2] GSI, Darmstadt, Germany.

Abstract

The primary proton beam for the production of the intense antiproton beam required by FAIR will be provided by a dedicated 70 MeV, 35 mA, 325 MHz Injector. This will be the first linac based on coupled H-mode cavities [1].

A half scale model of the coupled CH modules 3 and 4 of the FAIR proton injector has been constructed and tested. Fabrication of a full scale high power cavity is scheduled for 2009.

The Scaled Model of Resonator II

The second resonator of the FAIR proton injector, i.e. the coupled third and fourth tanks, consists of 29 gaps in total, 13 in the first CH resonator and 14 in the second one resulting in a total inner lenght of around 2.9 meters. The coupling is ensured by an intertank section housing the magnetic triplet needed for the beam focusing. The main properties are summerized in Tab.1.

Tab. 1: The main properties of the second resonator of the FAIR proton injector.

Energy Range [MeV]	11.7-24.3
Frequency [MHz]	325.244
Q-value	15300
Kilpatrick	2.0
Effective Shunt Impedance [MΩ/m]	60
Length [m]	2.9

The complexity of such a cavity requires a deeper experimental investigation on the mode behaviour and, for that reason, a 1:2 scaled model has been built at IAP [2] to test the main RF parameters such as resonance frequency, Q-value, shunt impedance, field distribution and coupling strength. Fig.1 shows the model: the outer cylinder is made of aluminum while the stems and the drift tubes are produced in braze. Eleven plungers are mounted along the cavity (45° with respect to the stem planes) to control the resonance frequency and to adjust the field distribution along the cavity axis.

Experimental Results

The cavity production has been finished in summer 2007 and was followed by several experimental tests.

The resonance frequency was 652.64 MHz with an error of 0.3% with respect the design value of 650.444 MHz: minor adjstuments of the plunger position were required in order to opmitimize the field distribution along the cavity. An example of a rather flat field distribution is shown in Fig.2.

* Work supported by EU, CARE contract No. RII3-CT-2003-506395
#u.ratzinger@iap.uni-frankfurt.de

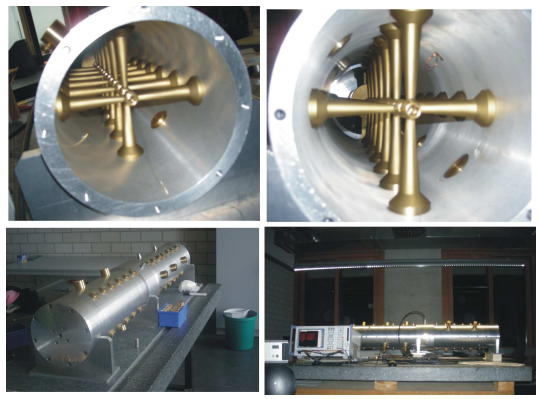

Fig.1: On top, a view of the cavity; bottom, the cavity on the test bench assembled at Frankfurt University.

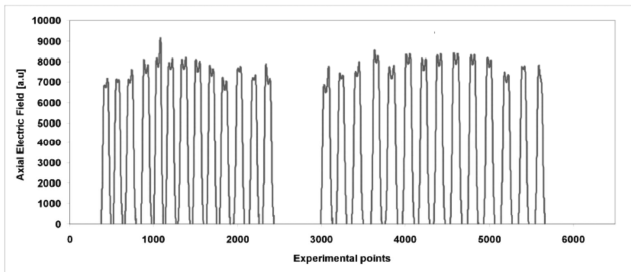

Fig.2: Measured electric field distribution on the beam axis

In correspondance of that optimized configuration for the plungers, the measured shunt impedance reached around 95 % of the ideal value obtained with ideal copper conductivity. This confirms the validity of the simulation method used to investigate the structure.

Conclusions

The development of the coupled CH for the FAIR proton injector is well advanced and the preliminary test on a scaled model confirmed the validity of the coupling concept. A full scale prototype will be constructed and tested with a 2.5 MW Toshiba klystron in order to investigate the RF properties and behaviour under the power condition required during beam operation

References

[1] U. Ratzinger et al, “A 70-MeV Proton Linac for the FAIR Facility Based on CH – Cavities”, LINAC'06, August 2006, Knoxville, pp.526-528.

[2] G. Clemente et al. “Coupled CH-Cavity Development for the FAIR Proton Injector”, GSI Annual Report 2007 p.50.

Numerical calculation of Coupling Impedance for Circular Accelerators*

L. Hänichen[1], A. Al-khateeb[2], O. Boine-Frankenheim[2], W.F.O. Müller[1], and T. Weiland[1]

[1]Technische Universität Darmstadt, Institut für Theorie Elektromagnetischer Felder (TEMF), Schlossgartenstrassse 8, 64289 Darmstadt, Germany; [2]GSI, Darmstadt, Germany

Background

Coupling Impedances present a convenient measure for the quantitative description of the interaction of a particle beam with its immediate environment through beam-induced fields. In order to determine the influence of any accelerator component on beam stability, knowledge about the different impedance contributions is needed. In the present case, the relevant part of the electromagnetic spectrum lies beneath the cutoff frequency of the component, thus no wave propagation or resonance has to be expected.

Preceeding work

The preceeding work was focused on the computation of impedance contributions caused by kicker magnets requiring suited solving techniques for complex-valued problems. The most recent considerations for the planned SIS100 synchrotron accelerator at FAIR include corrugated beampipes for reasons of cryogenic pumping and the related mechanical stability issues. It is clear that this will lead to additional impedance contributions which have to be determined. Common to both applications is the use of an excitation in frequency domain and adapted boundaries at the beam entry and exit plane. The necessary extensions for available EM CAD Software (CST Studio Suite) have been introduced by B. Doliwa for the above mentioned kicker magnets. This approach solves a full frequency domain problem for a predefined number of samples within a given frequency range. Subsequently the impedance curve is computed from the stored solutions.

Goals and current work

The goal is to test, use and modify these routines for impedance calculation of beam pipes. Starting point is the case of a perfect conducting circular pipe. This model will be extended step by step taking finite conductivity and transmissive effects into account. Due to the simplicity of the geometry these results can be compared with the corresponding analytical approaches. By this means we gain knowledge about the reliability of the method. After having finished this procedure the method will be applied to more complicated structures. When studying beam bipe segments with periodically varying cross section (feature period length is still small compared to the wavelengths in the relevant frequency range) it has to be shown how this requires modifications of the boundary conditions. After getting familiar with the existing software modules, trial calculations for simple beam pipe structures are now in progress. The upcoming results are to be reviewed in one of the EPAC 2008 papers.

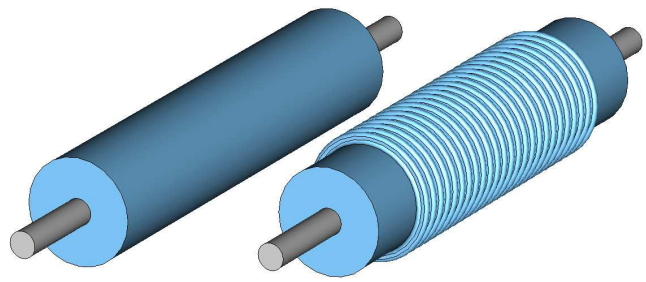

Figure 1: Models for straight beampipe and beampipe with corrugated section including beam current paths.

References

[1] B. Doliwa, H. De Gersem and T. Weiland, “Numerical calculation of coupling impedances for kicker modules.”, FAIR report, March 2006, Darmstadt.

[2] B. W. Zotter and S. A. Kheifets, “Impedances and Wakes in High-Energy Particle Accelerators.”, World Scientific, 1998.

[3] R. L. Gluckstern, “Analytic methods for calculating coupling impedances”, CERN report 2000.

[4] A. M. Al-Khateeb, O. Boine-Frankenheim, R.W. Hasse and I. Hofmann, “Longitudinal impedance and shielding effectiveness of a resistive beam pipe for arbitrary energy and frequency.”, Physical Review E71, 2005.

* Work supported by GSI under contract DAWEI2.

Residual Activity Induced by High-Energy Heavy Ions

I. Strasik[1, 4], E. Kozlova[1], E. Mustafin[1], A. Smolyakov[1, 2], N. Sobolevskiy[3], L. Latysheva[3], M. Pavlovic[4]

[1]GSI, Darmstadt, Germany; [2]ITEP, Moscow, Russia; [3]INR RAS, Moscow, Russia; [4]FEI STU, Bratislava, Slovakia

Introduction

Quantification of the residual activity of accelerator structures due to beam-losses during normal operation is an important issue for existing (SNS or RHIC) and planned (LHC or FAIR) high-energy accelerator facilities. The activation of accelerator structures is already an intensity limiting problem. While beam-losses of 1 W/m for proton machines is presently recognized as tolerable level for insuring the "hands-on" maintenance, the beam-loss tolerances for high-energy heavy-ion accelerators have not yet been quantified.

Experiment

Copper and stainless steel targets were irradiated by 120 MeV/u, 500 MeV/u [1] and 950 MeV/u [2, 3] ^{238}U beams. Copper and stainless steel were chosen for experiment as common materials of accelerator structures. The beams from SIS-18 at the GSI Darmstadt were used to irradiate the targets. The main task of the study was: (1) to identify the isotopes with dominating contribution to the residual activity, (2) to measure depth-profiles of residual activity of induced isotopes, (3) to determine the contribution of individual isotopes to the residual activity and (4) to convert the measured residual activities to dose-rate. Gamma-ray spectroscopy was used as the main analytical technique to identify the isotopes as well as to determine the residual activities and their depth-profiles. The samples were irradiated in the stacked-foil geometry.

Simulations

Monte Carlo particle transport simulation codes like FLUKA and SHIELD can also be used for the study of the residual activity of accelerator structures but it is always necessary to verify validity of physical models and data-libraries implemented in those codes by comparing simulations with experimental data (Fig. 1). It can be seen that the discrepancies between calculated and measured values vary from factor of 1 up to factor of 4.

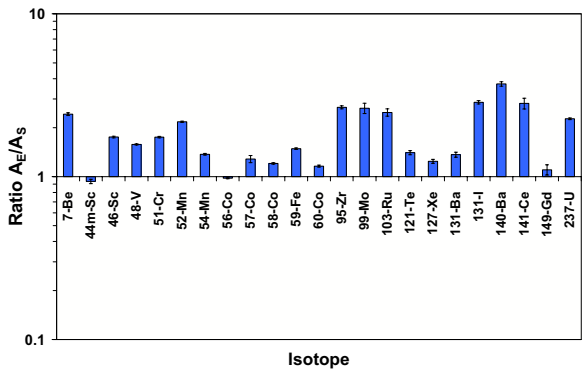

Fig. 1. Ratio A_E/A_S for the isotopes with dominating contribution to residual activity. A_E is the experimentally measured activity and A_S is the activity calculated by FLUKA.

Beam-loss criteria

FLUKA and SHIELD were used to simulate the irradiation of bulk copper and stainless steel targets by different projectiles ^{1}H, ^{4}He, ^{12}C, ^{20}Ne, ^{40}Ar, ^{84}Kr, ^{132}Xe, ^{197}Au, ^{238}U with energies typical for FAIR machines.

It was found that the isotope inventory contributing over 90% to the total activity does not depend on the projectile species, but it depends on the target material and projectile energy. This allowed establishing a scaling law for induced activity as a function of primary ion mass. The activity per nucleon induced by an ion scales down with increasing ion mass. Heavy-ion beam loss of 1 W/m induces lower level of residual activity per nucleon compared to 1 W/m losses of proton beam. For example, 1 GeV/u uranium ion induces 5-times less activity per nucleon compared to 1 GeV proton (Fig. 2).

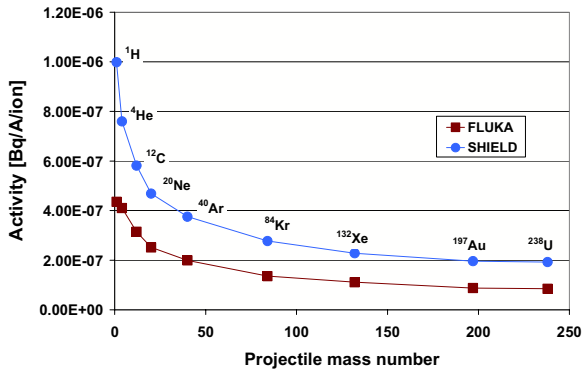

Fig. 2. Total activity per nucleon induced by primary ion (^{1}H, ^{4}He, ^{12}C, ^{20}Ne, ^{40}Ar, ^{84}Kr, ^{132}Xe, ^{197}Au, ^{238}U) in stainless steel target after 1 day of cooling time as a function of primary ion mass.

Conclusions

The data collected in this work can serve as an input for the assessment of tolerable beam-loss levels at high-energy heavy-ion accelerators, which is important to evaluate radiation hazards to personnel.

References

[1] A. Fertman et al., First Results of an Experimental Study of the Residual Activity Induced by High-energy Uranium Ions in Steel and Copper, Nucl. Instr. and Meth. in Phys. Res. **B260/2** (2007) 579.

[2] I. Strasik et al., Depth-profiling of the Residual Activity Induced by 950 MeV/u Uranium Ions in Copper, GSI-Acc-Note-2006-11-002 (2006).

[3] I. Strasik et al., Experimental Study of the Residual Activity Induced by 950 MeV/u Uranium Ions in Stainless Steel Target, GSI-Acc-Note-2007-12-001 (2007).

Study of Thermal Stress Waves Induced by Relativistic Heavy-Ion Beams

R. Wilfinger *[2], A. Kelić †[1], B. Achenbach[1], K. H. Behr[1], A. Bruenle[1], R. Catherall[2], F. Cerutti[2], H. Geissel[1], D. H. H. Hoffmann[3], A. Hug[3], Ch. Karagiannis[1], B. Kindler[1], K. Knie[1], M. Krause[1], M. Kulish[4], J. Lettry[2], B. Lommel[1], J. Menzel[3], N. Müller[3], H. Richter[2], K. Suemmerer[1], N. Tahir[1], M. Tomut[1], Ch. Trautmann[1], S. Udrea[3], D. Varentsov[1], H. Weick[1], M. Winkler[1], and Y. Zhao[5]

[1]GSI, Darmstadt, Germany; [2]CERN, Geneva, Switzerland; [3]TUD, University of Technology, Darmstadt, Germany; [4]IPCP-Chernogolovka, Institute of Problems of Chemical Physics RAS, Chernogolovka, Russia; [5]Institute of Modern Physics, Chinese Academy of Science; Lanzhou, China (730000)

As part of a feasibility study of the use of graphite as the target material for the FAIR Super-FRS in the fast-extraction regime, the response of graphite samples to the impact of fast-extracted uranium beams from SIS18 has been investigated. To this end, the instantaneous velocities and displacements of vibrating target surfaces were measured. The data obtained will serve as an important benchmark for existing theoretical models, in particular those that can handle the region above the elastic domain up to evaporation (like e.g. AUTODYN^{TM}).

The experiment was performed at the HHT experimental area at GSI, using a ^{238}U beam at 350 A MeV. A Laser Doppler vibrometer (LDV) [1], a VISAR [2], and an advanced, custom made interferometer (with two independent light paths to obtain also directly the displacement direction) [3] were employed in order to study radial thermal stresses induced by relativistic heavy-ion beams in cylindrically-shaped targets of various materials: carbon, tungsten, tantalum, copper, and lead.

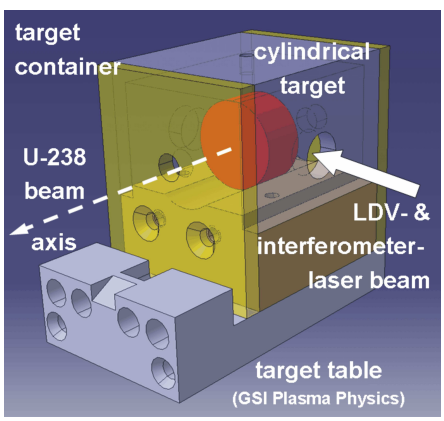

Figure 1: Schematic illustration of a cylindrical target (10 mm diameter, 5 mm length) inside a target container.

The cylindrical targets (Figure 1 schematically indicates a cylinder with 10 mm diameter and 5 mm length) were mounted inside a target container on a standard target table from the GSI Plasma Physics group. The interferometer and LDV laser beams entered through a hole (3 mm diameter) on the side of the container and the VISAR laser beam from the opposite side.

Figure 2 shows the response of a carbon cylinder of 10 mm diameter recorded with the LDV after a ^{238}U pulse impact with a total intensity of 2.25×10^9 ions, 0.9 mm (FWHM) beam diameter, and $\sim$1 μs (FWHM) pulse length. The kicker ejection trigger signal starts at the zero point on the horizontal time-axis.

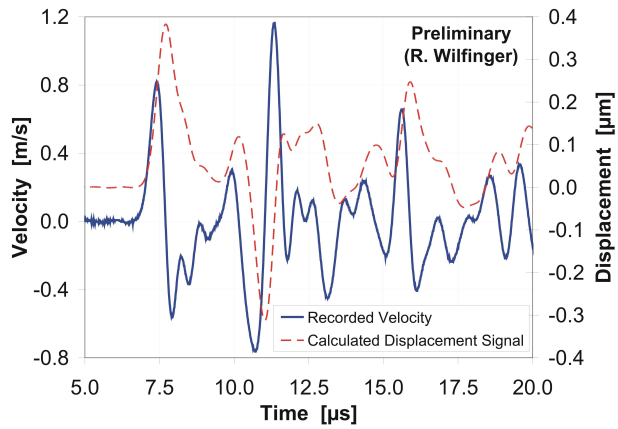

Figure 2: Recorded velocity signal (full line) and the corresponding calculated displacement signal (dashed line) after the impact of 2.25×10^9 uranium ions on a carbon cylinder of 10 mm diameter.

The compressive wave front causes a radial movement (dashed line in Fig. 2) of the cylindrical surface with a maximum amplitude of about 400 nm followed by a contraction of about 300 nm 3 μs later. The next step of the analysis will involve comparisons of these data to theoretical calculations. The experiment was also supported by BMBF 06DA118.

References

[1] R. Wilfinger, et al., "Proton induced thermal stress-wave measurements using a Laser Doppler Vibrometer", RNB7 Proceedings, EPJ — Special Topics, Vol. 150, 2007, p. 379–382.

[2] J. Menzel, "Interferometrische Geschwindigkeitsmessungen an schwerionengetriebenen Targets", Diploma Thesis, TU Darmstadt, 2006.

[3] M. Kulish, private communication, kulishm@ficp.ac.ru, 2007.

* Roman.Wilfinger@cern.ch (S334 spokesperson)
† A.Kelic@gsi.de (S334 contact person)

Development of FAIR superconducting magnets and cryogenic system*

G. Moritz#, K.H. Behr, E. Fischer, E. Floch, G.. Hess, O. Gumenyuk, H. Leibrock, J. Kaugerts, M. Kauschke, J. Macavei, J. P. Meier, C. Muehle, H. Mueller, P. Schnizer, C. Schroeder, S. Y. Shim, A. Stafiniak, K. Sugita, F. Walter, B. Weckenmann, Y. Xiang,
GSI, Darmstadt, Germany

Introduction

R&D continued during 2007 for FAIR superconducting magnets, for the main dipoles, quadrupoles, the correctors, and the corresponding cryogenic distribution / cryostat system as well. Design of cryostat components, such as interconnections and cold-warm transitions of beam tubes, continued as well. R&D was conducted by GSI employees, in collaborations, or by contracts, funded by GSI or the European Union (EU FP6 Design study). Most of the results will be documented in the FAIR Technical Design Report (TDR).

Superconducting Magnets

Rapidly- Cycling Synchrotron Magnets

A good overview of the status of the R&D is given in [1].

SIS 100

- *Main dipole*

Three full length dipole prototype magnets[2], including cryostats, are under construction at BNG (Würzburg), JINR (Dubna) (both straight) and at BINP (Novosibirsk) (curved). Field quality[3] and thermal behaviour[4] was analyzed carefully. The technical designs were checked in several design review meetings. The Factory Acceptance Test of the BNG magnet was passed in December. The magnet will be tested at GSI in April 2008.

At FZK, tests of mechanical properties of coil mockups continued.

A requirement for continuous triangular cycling led to a redesign of the dipole, from a two layer to a one layer coil (providing the required reduction of the hydraulic resistance). At the same time, the coil structure was optimized and the cooling was recalculated.

As baseline, a standard elliptical beam pipe with rib reinforcement will be used. However, for cryogenic pumping, beam pipe cooling is required. Cooling schemes were developed[5].

- *Main Quadrupole*

It is under construction at JINR (Dubna).

- *Correctors*

The design criteria of: 1) low current (to minimize the lead losses of the individually powered magnets) and 2) same cooling scheme as for the main magnets, imposed restrictions on the design. Two options are under investigation: one, based on the Nuclotron-type cable (but with insulated strands), and one with an indirectly cooled bobbin.*

SIS 300

Work on the 6T dipole at IHEP (Protvino) continues. The magnet tooling was accepted. A test coil is under construction. Cable was heat treated according to test results for Minimum Quench Energy at CERN[6] and resistivity measurements at BNL and shipped to IHEP.

R&D for the curved 4.5 T dipole is presently under way at the Italian National Institute of Nuclear Physics (INFN) in the framework of a project called DISCORAP ("DIpoli Super COnduttori RApidamente Pulsati")[7]. Low loss wire (small filament, Cu-Mn interfilamentary matrix) and cable (316L stainless steel core) were ordered. 2D magnetic field design was finished, including the effects of persistent and eddy currents. The prestress of the collared coil was optimized. The AC temperature margin was calculated to be 0.8K. Magnet cryogenic losses are around 5.4 W/m for a cycle between 1.5 and 3 T and a ramp rate of 1 T/s. The machined mandrel of the test coil is ready and the first winding trials have started.

Magnets for Storage rings and the Super-FRS

A cost comparison for nc and sc-versions of the NESR/RESR dipole was in favour of the resistive solution. Also, for the CR dipole the decision for a resistive version was made. As a consequence, only the Super-FRS magnets are superconducting. The dipole prototype is under construction in China. The yoke is partly completed and a practise coil has been tested. The whole magnet should be tested before June 2008. BINP took over now the technical design of the Super-FRS multiplet magnets.

Quench and Electrical Systems

The detection and protection schemes for SIS 100, SIS 300, Super-FRS and the 300Tm beamline were refined. Busbar concepts were developed[8]. Irradiation R&D of insulators has started. A study of a flexible cold electrical link between the power supplies and the machine feed boxes, done in cooperation with industry, showed promising results.

Test Facility for model and prototype magnets

Meanwhile, a SIS 100 dipole model was tested with 2 phase forced-flow-cooling. The results were in good agreement with data previously measured at Dubna.

* Work supported by the European Community under the FP6 DESIGN STUDY (contract 515873 - DIRACsecondary-Beams).
# G.Moritz@gsi.de

Losses were measured with the calorimetric and the VI-method. The facility showed the expected performance and is now waiting for the test of the first SIS 100 dipole prototype[9][10]. 'Mole' and 'stretched wire' are ready for magnetic measurements[11]. Software development for the measurement tasks continues.

Cryogenics

The number of cryogenic consumers within FAIR was reduced during the last year. Now the cryogenic system of FAIR will supply SIS100, SIS300, Super-FRS, small parts of the HEBT (300 Tm), and some experiments with refrigeration power. Therefore, the load list for the cryogenic system was revised and the cryogenic distribution system was adjusted for the new topology of cryogenic consumers in FAIR. The location and size of the building for the cryogenic infrastructure, i.e. compressor buildings and refrigerators was settled. The refrigerator for the test facility and the liquefier for some small experiments are now separated from the main FAIR refrigerators. With this positioning, the new layout of the cryogenic distribution system was started and first steps for a more detailed layout for the cryogenic pipelines could be started.

In addition to the global distribution system, the local distribution system of Super-FRS and HEBT (300 Tm) was discussed. For Super-FRS different cooling schemes were compared and the thermo-siphon scheme, with a common header for a group of magnets, was chosen. Given these new designs, especially with the mentioned cold electrical link, the space requirements for the buildings were revised

Cryostats

SIS 100 Cryostats

Two full length straight dipole cryostats, following the NUCLOTRON suspension concept, were designed. One was designed and built at BNG. A second one comes from BINP, where the commissioning is planned in the 2nd quarter of 2008. The relevant adaptation equipment for test bench operation of the model types was designed and ordered. The development of the beam pipe cold-warm transition was finalised with a prototype specification[12]. Two prototypes for testing were procured. A design study for the transfer cryostats was carried out by ACCEL. The eddy current losses in the dipole thermal shield were investigated and found to be negligible. The development of the special feed-in cryostats was advanced and a detailed installation space study was performed for the cryogenic and current feed-boxes[13].

SIS 300 Cryostats

The cryogenic and beam line interconnection and compensation concept was developed in details by Cracow University of Technology (CUT)[14]. INFN performed the first design studies for the short curved dipole cryostat. An installation space study for the 300 Tm HEBT bypass line was performed. For a closer cooperation with the CUT a contract was placed, covering preliminary design and further optimization of the SIS300 interconnections, including the beam-vacuum, bus-bar, helium flow and thermal shield interconnects, as well as the design of magnet support system.

References

[1] G. Moritz, Proceedings of PAC07, Albuquerque, New Mexiko, USA, June 2007

[2] E. Fischer, H. Khodzhibagiyan, A. Kovalenko, Proceedings of MT20, Philadelphia, Pennsylvania, August 2007

[3] P. Schnizer, B. Schnizer, P. Akishin, E. Fischer, Proceedings of MT20, Philadelphia, Pennsylvania, USA, August 2007

[4] E. Fischer, R. Kurnyshov, P. Scherbakov, Proceedings of EUCAS 2007, Brussels, Belgium, September 2007

[5] S.Y. Shim, GSI F-MT internal note MT-INT-SYS-2007-02_SIS100_Eddy_Cooling, GSI, Darmstadt, Germany, 2007

[6] G.P. Willering, A.P. Verweij, J. Kaugerts, H.H.J. ten Kate, Proceedings of MT20, Philadelphia, Pennsylvania, USA, August 2007

[7] P. Fabbricatore, S, Farinon, F. Alessandria, G. Bellomo, M. Sorbi, G. Volpini, U. Gambardella, J. Kaugerts, G. Moritz, Proceedings of MT20, Philadelphia, Pennsylvania, USA, August 2007

[8] E. Floch, GSI F-MT internal note MT-INT-ErF-2007-009_SIS300_HEBT, GSI, Darmstadt, Germany, 2007

[9] A. Stafiniak, E. Floch, P. Hahne, G. Hess, M. Kauschke, F. Klos, F. Marzouki, G. Moritz, H. Mueller, M. Rebscher, P. Schnizer, C. Schroeder, G. Walter, F. Walter, H. Welker, Proceedings of MT20, Philadelphia, Pennsylvania, August 2007

[10] C. Schroeder, M. Kauschke, Proceedings DKV-Tagung, Hannover, Germany, Nov. 2007

[11] P. Schnizer, H.R. Kiesewetter, T. Mack, T. Knapp, F. Klos, M. Manderla, S. Rauch, M. Schönecker, R. Werkmann, Proceedings of MT20, Philadelphia, Pennsylvania, USA, August 2007

[12] J.P. Meier, GSI Specification, GSI, Darmstadt, Germany, 2007

[13] J.P. Meier, O. Gumenyuk, GSI F-MT internal note MT-INT-JPM-2007-001_Feedbox_space_allocation, GSI, Darmstadt, Germany, 2007

[14] B. Skoczen, A. Wroblewski, Final Report 2007 on the Design of Interconnections for the SIS300 Synchrotron, Cracow University of Technology, Cracow, Poland, 2007

Developments for the FAIR Beam Position Monitors

P. Kowina, P. Forck, M. Freimuth, A. Galatis, W. Kaufmann, K. Lang, and U. Rauch
GSI, Darmstadt, Germany

Introduction

The beam Position Monitor (BPM) system that will be used in the superconducting heavy ion synchrotron SIS100 consists of the following components: i) pick-up (PU) installed in the cryostat with the chassis being a part of the beam pipe ii) signal feed–throughs that are leading the signal out of cryostat iii) impedance matching transformers (described later on in the text) iv) low noise low input–impedance amplifiers [1] and v) *Libera* digitizer that consist of four channel ADC (with 14 bit resolution and 125 MSa/s) and integrated FPGA [2]. The requirements for the BPM system are specified in Ref. [3]. The development of the BPM system was focused on the further investigation of electrical and mechanical features of the PU and the test of the impedance matching components. In parallel an optimization of the position evaluation algorithm was performed and tested on signals stored during one run of SIS18. The results of optimization of the PU are reported in Ref. [4]. The mechanical test of the most crucial PU components interconnections will be carried out in the liquid helium in the new test bench under construction. The first operation of the test bench is foreseen in spring 2008.

This paper presents the results of the tests performed for the coupling transformers and optimization of the position algorithm.

Investigation of the coupling transformers

The amplifiers with high input impedance mounted directly on the PU (like e.g. at SIS18) are the best solution concerning the signal amplitude and its proportionality to the bunch shape [1]. The possible reflections caused by discontinuity of line impedances for such short lines are negligible. However, in SIS 100, due to the heat deposit raised by amplifier power losses, the amplifiers have to be installed outside the cryostat. The length of the signal lead inside the vacuum vessel has to be about one meter to keep the heat flow through all four feeds below 0.5 W per single BPM. In addition, the expected radiation level in the PU neighborhood can reach the level of some ten kGy per year, thus exceeding the maximal radiation dose for the head electronics by almost two orders of magnitude. Therefore, the cable lengths have to be extended by additional four meters to move the amplifiers away from the beam pipe. For reflection free signal transport in such long signal lines the use of $50\ \Omega$ cables with low input impedance amplifier is mandatory. To fulfill all these almost contradicting requirements the coupling transformers have been proposed [1]. The ratio of impedances is proportional to the square of the windings ratio $Z_p/Z_s = (N_p/N_s)^2$. This allows to use a low noise amplifier with 50Ω input impedance without loading the PU with the 50Ω. The most important feature of the coupling transformers is its transfer function expressed as a frequency dependence of the S21 parameter. The bandwidth of the transformers has to cover the frequency range from ~ 0.1 MHz to 100 MHz [3]. Since the transfer function can be extended toward the lower frequencies by using ring materials with high relative permeability Vitroperm 500 F was chosen [5]. Great advantage of this material is its high saturation induction $B_s = 1.2T$. This is extremely important with regard to the dynamic range of the signal amplitude of over 120 dB [3]. Tests were performed for a winding ration of 18:3 on a toroidal core with external/internal diameter of 8.6 mm / 5.9 mm and a thickness of 7.4 mm. The saturation effects were studied using a Network Analyzer whereas the primary winding was biased with DC current. The transfer functions measured for the different currents in the single winding and magnetic field strength are shown in Fig. 1. For the bias current of 3.6 A the deviation of the transfer function is smaller than 5 dB in the interesting frequency range. To cover the whole signal range it might be necessary to use cores either with larger cross sections or with smaller primary winding numbers. Since the expected peak voltage of PU signals reaches 1.8 kV [3] the transformers were tested using pulsed high voltage power supplies up to 4 kV.

The matching transformers have to be installed as close as possible to the PU electrodes i.e. inside the cryostat. Therfore, the features of transformers were tested in the more than 50 thermal cycles using liquid nitrogen. No material degradation was observed. At 77 K the transfer function remains unchanged in the interesting frequency range. The small increase of 0.2 dB can be observed only for fre-

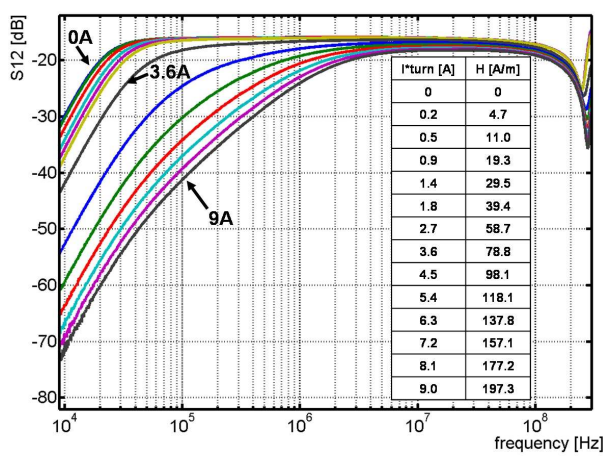

Figure 1: Transfer functions for 18:3 transformer measured at different saturating DC current.

temp.	100 Hz	120 Hz	1 kHz	10 kHz	100 kHz	1 MHz
300K	47.1×10^3	46.9×10^3	46.9×10^3	45.1×10^3	35.8×10^3	6.8×10^3
77K	97.4×10^3	94.7×10^3	72.6×10^3	60.4×10^3	34.7×10^3	6.8×10^3

Table 1: Permeability of the Vitroperm 500 F rings measured at room temperature and in liquid nitrogen.

quencies smaller than 20 kHz. This is an effect of changes in the relative permeability that are more pronounced at the lower frequencies, see table 1.

The permeability of 40 commercial transformers of the same type was compared. The maximum deviation from the mean value was below $\pm 1.5\%$. Only three transformers had systematically 10% larger permeability. To minimize an offset of the position measurement both channels of the same BPM have to be calibrated with an accuracy better than ± 0.1 dB. Therefore the transformers have to be carefully selected.

Optimizations of the window generation algorithm

The position determination in the BPM is based on the comparison of the bunch integrals calculated from the digitized signal of the two opposite electrodes [6]. Most important for position evaluation is a correct window generation in which the individual bunch signal is integrated. For synchrotrons with fast changing accelerating frequency (RF) and strong varying beam parameters, like beam intensity or the bunch lengths, the window generation algorithms using an external trigger information and controlled in a PLL loop circuit [7] are difficult to implement. In this case algorithms are favored that generate the gating signal from the structure of the digitized signal itself [6], because here no additional timing parameters are needed. Moreover, these algorithms are less sensitive on bunch phase instability within the RF bucket which is typical for extremely short acceleration cycles.

An algorithm based on the window triggering on the accumulated and median–filtered signal [6] has been implemented in a FPGA and successfully tested in the online measurements performed on SIS18 and on CERN Proton Synchrotron (PS) [8]. Its stability has been proven also for signals with low signal–to–noise ratio. However, this method is sensitive on distortion of the signal shape. For instance, the double–peak bunch structure that is usually

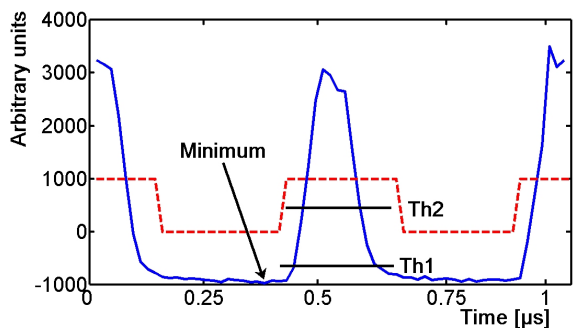

Figure 2: Window generated using a new algorithm. Solid line – original PU signal; dashed line – generated window.

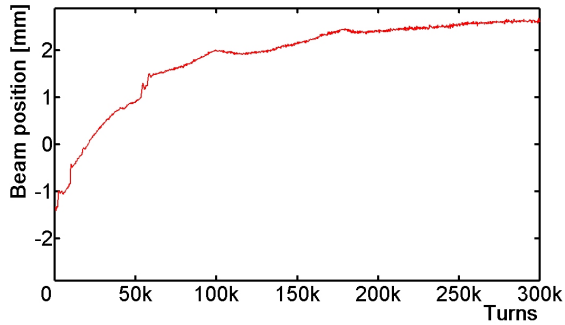

Figure 3: Beam position calculated using new algorithm.

observed for the electron–cooled beam would be recognized by this algorithm as a two separate bunches. Moreover, since this method requires minimum five subsequent samples with monotonic increasing values [6], the window generation fails for the extremely short bunches like e.g. foreseen for the proton beam at SIS100.

The alternative method under investigation is very similar to the method used in the double threshold discriminators, see Fig. 2. The window is opened (dashed line) when the signal is crossing sequentially threshold ($Th1$) and threshold ($Th2$) and is closed when the thresholds are crossed in the opposite order. Both thresholds are dynamically adjusted in respect to the minimum signal value that is recorded in the region in between two subsequent bunches. The values of the thresholds are given by minimum signal value multiplied by arbitrary factors. The factors were experimentally determined in the offline analysis of bunches along a complete acceleration ramp performed for several beam types.

The new algorithm was tested offline with data recorded during the machine development beam time in December 2007. It has been proven that no bunch was lost over the whole acceleration cycle (i.e. over more than 10^6 bunches). The reconstructed beam position over one complete acceleration cycle is shown in Fig. 3. By averaging over 10^3 bunches a resolution of the position determination better than 0.05 mm was achieved. The implementation of this algorithm in the FPGA of the Libera modules connected to the SIS18 BPMs is planned for the first half of 2008.

References

[1] J. Schölles et al., DIPAC'05, Lyon, June 2005, p. 190.
[2] www.i-tech.si
[3] P. Kowina et al., EPAC'06, Edinburgh, June 2006, p. 1022.
[4] P. Kowina et al., DIPAC'07, Venice, May 2007.
[5] www.vacuumschmelze.de
[6] A. Galatis et al., EPAC'06, Edinburgh, June 2006, p. 1019.
[7] J. Belleman et al., DIPAC'05, Lyon, June 2005, p. 137.
[8] A. Galatis et al., DIPAC'07, Venice, May 2007.

A cryogenic current comparator for beam diagnostics in the FAIR project *

A. Steppke[1], R. Geithner[1], R. Neubert[1], W. Vodel[1], H. Reeg[2], and M. Schwickert[2]
[1]Institut für Festkörperphysik, Friedrich-Schiller-Universität Jena, Germany; [2]GSI, Darmstadt, Germany

The non-destructive measurement of beam currents has been successfully achieved using DC beam transformers[1]. A much higher resolution for the FAIR project can only be achieved using cryogenic current comparators (CCC) with superconducting technologies.

Principle of a CCC

A cryogenic current comparator(CCC) is based on the properties of ideal superconductors to expel magnetic flux from the bulk material through shielding currents on the surface of the material. As this effect is only dependent on the magnetic field, the CCC allows measuring the magnetic field, e.g. generated by a passing ion beam, they can be measured non-destructively with a high precision.

In figure 1 the main components of a CCC are shown. The magnetic field of the beam current creates shielding currents on the superconducting magnetic ring structure, which are transformed with a torodial single turn pick-up coil and its ferromagnetic core. The signal from the pick-up coil is feed to a LTS DC SQUID and measured via the external electronics.

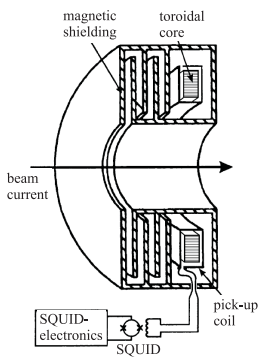

Figure 1: Principle of a cryogenic current comparator

Noise contributions

The design of a CCC requires a thorough knowledge of several noise contributions to achieve a high beam current resolution. As the SQUID and the pick-up coil are very sensitive to external magnetic fields it is necessary to shield both sufficiently against any field sources other than the magnetic field of the ion beam. Grohmann et al.[4, 5] analyzed coaxial cavity structures to suppress unwanted field components. Using this knowledge the current CCC uses a superconducting niobium shield to attenuate non-azimuthal field components by a factor of 120 dB [6].

Because external disturbances can be effectively reduced we studied the influence of thermal noise and the ferromagnetic core material to the overall system resolution. The thermal noise generates a noise current $\sqrt{\langle I^2 \rangle}$, which in conjunction with the inductance L generates a magnetic flux noise $\Phi_{thermal}$ which cannot exceed the magnetic flux due to the beam current for a signal to noise level of unity.

$$\Phi_{beam} = \int_A \vec{B} \cdot \mathrm{d}\vec{f} \geq \Phi_{thermal} = L \cdot \sqrt{\langle I^2 \rangle} \quad (1)$$

For a given pick-up coil the minimum detectable current I_s is dependent on the geometry of the coil ($f(R_a,R_i,b)$), the temperature T, the geometric inductance L and the relative permeability μ_r of the ferromagnetic core material according to:

$$I_s = \frac{2\pi\sqrt{k_b T L}}{\mu_0 \mu_r f(R_a,R_i,b)}. \quad (2)$$

Figure 2 shows the calculated minimum current, which can be detected for different temperatures and relative permeabilities with the currently used single turn toroidal pick-up coil.

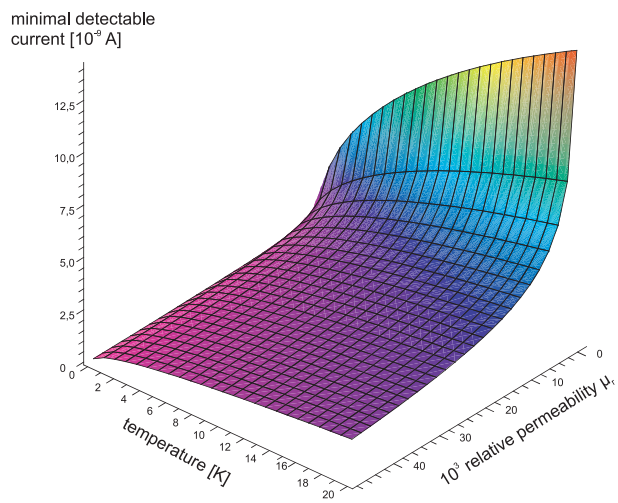

Figure 2: Minimum detectable current as a function of temperature and relative permeability of the core material

Measurements of ferromagnetic materials

The basic analysis of the detectable current shows a strong dependency on the relative permeability of the core material. As the pick-up coil is fully enclosed within the

* Supported by GSI Darmstadt under contract name JVODEL

superconducting shield, the core material has to operate at temperatures in the range of 4.2 K. In standard ferromagnetic materials the permeability decreases by about two orders of magnitude from room temperature to these low temperatures. Preliminary measurements showed a reduction of inductance of coils using Amidon[1] iron powder cores from 450 μH to 4 μH at 4,2 K. Using this knowledge it is necessary to investigate a wide range of ferromagnetic materials at low temperatures in respect to their permeability.

The measurement setup includes a high-precision inductance bridge (Agilent E4980A LCR-Meter) connected to our dipstick in a helium cryostat. A temperature sweep can be achieved with a computer controlled stepper motor, which adjusts the level of the dipstick in respect to the surface of the helium bath. With this setup the material Vitrovac VC6025[2], was measured over a temperature range from 290 K to 1,9 K(figure 3). The inductance of the test coil decreases by 52% over the whole temperature range which shows that the currently used material is already a large improvement over sintered iron powder cores. The high permeability of CoFe-based amorphous alloys is highly dependend on the field annealing. For the

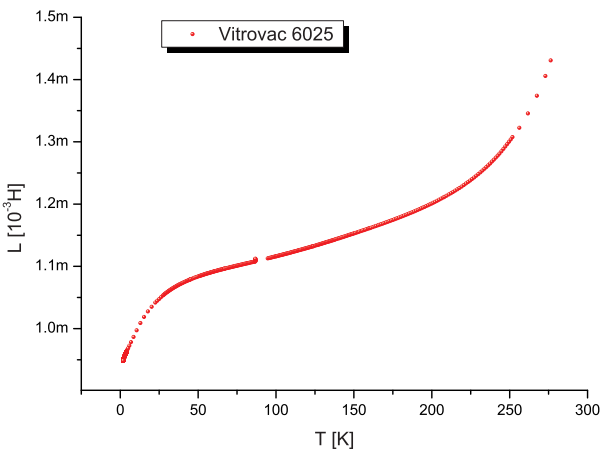

Figure 3: Inductance of a test coil with Vitrovac VC6025 (F, thickness 25μm) as the core material in dependence on temperature

application of a specific ferromagnetic material not only the relative permeability at low temperatures but also the frequency dependence needs to be investigated. Materials like Cryoperm-10[2] exhibit a high permeability which decreases rapidly with increasing frequencies[7].

In the new class of nanocrystalline ferromagnetic materials we measured the temperature- and the frequency-dependence of Vitroperm 500F[2]. While the temperature stability is improved compared to formerly used materials, the measurements presented in figure 4 show a significant drop of permeability for frequencies above 1 kHz. Similar frequency dependencies have also been measured in other nanocrystalline materials, e.g. Magneperm[3]. These results

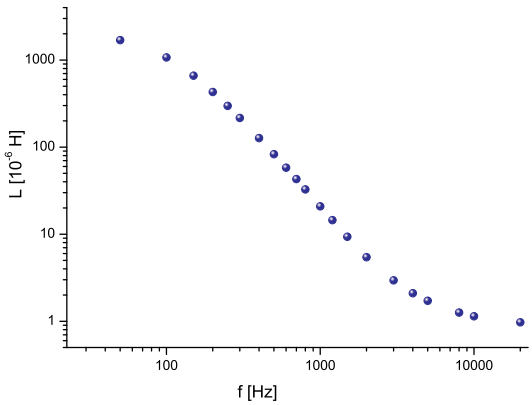

Figure 4: Inductance of a test coil with Vitroperm 500F, thickness 25μm, as the core material at different frequencies at room temperature

show that the different ferromagnetic materials exhibit significant temperature- and frequency dependencies, which have to be evaluated to achieve a high accuracy of the CCC in the final application.

Summary and Outlook

The theoretical investigations showed that with a strong attenuation of external noise sources an improvement of the sensor performance is dependent on the ferromagnetic core material. The current approximation for the minimum detectable current needs to be further extended with the fluctuation-dissipation theorem to analyse the frequency dependence of the thermal noise. With the first measurements of different core materials we could characterize the inductance over a wide temperature range and show first frequency dependencies. Future measurements will include a direct noise measurement using a DC SQUID for the readout of thermal noise signals at low temperatures.

References

[1] K. B. Unser, "The parametric current transformer", *AIP Conf. Proc.*, **252**, April 5, 1992, pp. 266-275

[2] I. K. Harvey, "A precise low temperature dc ratio transformer", *Rev. Sci. Instrum.*, **43**, 1972, p. 1626.

[3] P. Gutmann and H. Bachmair; in V. Kose, *Superconducting Quantum Electronics*, Springer Verlag, 1989, pp. 255-259.

[4] K. Grohmann, et. al., *Cryogenics* **16**, July 1976, pp. 423-429.

[5] K. Grohmann, et. al., *Cryogenics* **16**, October 1976, pp. 601-605.

[6] W. Vodel, R. Neubert, S. Nietzsche, K. Knaack, K. Wittenburg and A. Peters, *IEEE Trans. Appl. Superconductivity*, Vol. 17, 2007, pp. 621-624

[7] H. P. Quach and T. C. P. Chui, *Cryogenics* **44**, 6-8, August 2004, pp. 445-449

[1] Amidon Inc, 240 Briggs Ave Costa Mesa, CA 92626, USA

[2] VACUUMSCHMELZE GmbH & Co. KG, Grüner Weg 37, D-63450 Hanau

[3] MAGNETEC GmbH, Industriestraße 7, D-63505 Langenselbold

Research programme hadrons and nuclei

Ion Source Development and Operation

P. Spädtke, M. Galonska, B. Gutermuth, F. Heymach, R. Hollinger, R. Lang, K. D. Leible, J. Mäder, K. Ochs, J. Roßbach, P. Schäffer, S. Schäffer, M. Stork, K. Tinschert, and C. Vierheller
GSI, Darmstadt, Germany

Two injector beam lines with up to three different ion sources (IS) are used to feed the accelerator simultaneously: the high-charge state injector HLI and the high-current injector HSI.

Ion Sources at the HLI

Regular operation at the High Charge State Injector (HLI) was performed for the following elements:

Table 1: Delivered ion beams in 2007.

Ion	Aux. gas	duration (days)	intensity in front of RFQ [eμA]
$^{7}Li^{+}$	He	13	40 - 60
$^{12}C^{2+}$	O_2	95	60 - 70
$^{34}S^{5+}$	O_2	8	60
$^{36}Ar^{7+}$	O_2	12	70
$^{48}Ca^{10+}$	He	48	70 - 80
$^{64}Ni^{9+}$	He	40	40
$^{112}Sn^{15+}$	O_2	4	20
$^{112}Sn^{17+}$	O_2	6	10
$^{136}Xe^{18+}$	O_2	2	20

The community working on the production and chemical characterization of super heavy elements (SHE) imposed a strong interest for primary ion beams of ^{34}S and ^{36}S. In both cases it is obvious that enriched material has to be used in combination with an ECRIS to take advantage of its low material consumption and high efficiency. According to good experiences with natural material of SO_2 the same procedure for the enriched isotopes was applied. Nevertheless it was essential to do a test run of the ECRIS with ^{34}S to check for the available intensity, beam stability and material consumption. Due to its very low natural abundance the material is not commercially available. Finally A. Yakushev [1] could develop a procedure to convert 2500 mg of highly enriched elementary ^{34}S to $^{34}SO_2$ with an enrichment of 80 %. A test run with the ECRIS was done at the HLI during the last shut down period, which showed that the sample material is well suited for operation. As Fig. 1 shows 60 eμA of $^{34}S^{5+}$ could be obtained, which is the required charge state for acceleration. The long time stability of about $\pm$ 3 % with only a few deviations was demonstrated in a continuous run of 8 days. Afterwards the average material consumption could be determined to be only 1.5 mg SO_2 per hour.

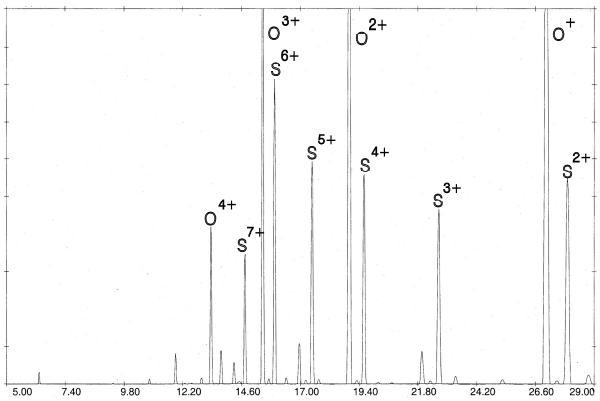

Figure 1: Charge state spectrum of the analyzed ion beam (^{34}S with mixing gas ^{16}O); full vertical scale: 100 eμA, horizontal scale: dipole current in A.

The last experiments with the CAPRICE at the test bench (EIS) before dismounting and preparation for the 28 GHz–project were dedicated to the investigation of variable microwave frequency input. A ramping of the RF frequency in a narrow range ($\pm$ 40 MHz) around the klystron center frequency of 14.5 GHz was performed while measuring the ion output and the beam shape. Remarkable changes in beam intensity have been observed keeping constant all other parameters of IS and beam optics. Furthermore, forward and reflected power were measured precisely to evaluate the reflection coefficient and to study its variation with the IS parameters. As the present frequency sweep range is only $\pm$ 0.28 % and due to the linear dependence of $B_{ecr} \propto \omega_{ecr}$, the variations of the ECR surface are negligible. So the variation in the field pattern is the reason for the observed effects on the source performances. Moreover, the change of the plasma properties consequently affect the frequency response of the whole system also changing the beam conditions. Further details can be found in [2]. The results confirm that an optimization of the microwave coupling by simple frequency tuning can significantly increase the performance of an ECRIS.

Ion Sources at the HSI

Two IS platforms arranged as a "Y" deliver ion beams for the UNILAC. One of it is equipped with a PENNING [3] IS, delivering beam with a high duty cycle up to a

maximum mass to charge ratio of 25, the other is dedicated to low duty cycle operation with one of the high-current IS MUCIS [4], CHORDIS [5], MEVVA [6], or VARIS [7]. The velocity for the injection into the RFQ is 2.2 keV/u with a space charge limit of 0.25 × A/q [emA] where A/q is the mass to charge ratio in atomic units. Because we restricted the extraction voltage for a safe operation, the extracted ion beam from the IS has to be post accelerated with a dc acceleration gap. Due to the fact that experiments at GSI request a wide range of beam intensity: from single particle up to 10^{11} per spill, obtained intensities do not assign necessarily the physical limit, even when the IS operates with natural material.

A very important issue is the beam quality in terms of beam brightness, pulse stability, noise, and beam fluctuations. The following figures show a selection of these topics for the high current IS.

The value of the emittance of the high current IS is given by the geometry of the multi-aperture extraction system (13 × ∅3 mm). For all high current IS the same extraction system is used. As a result the value of the emittance is only defined by the divergence angle of the extracted beam. The explosive ion generation process in vacuum arc IS results in a higher transverse energy of the ions and therefore in a larger divergence angle, as shown in Fig. 3, right. The minimum divergence angle for multi cusp sources is always the same because of the low temperature ion generation process and in a range of 40-50 mrad. This results in a total emittance of 500 π mm mrad . For the vacuum arc IS the minimum divergence angle is 90 mrad resulting in 1000 π mm mrad for the total emittance. The explosive plasma generation process defines the transverse ion energy, which strongly depends on the material. However, the relation between longitudinal and transversal energy is for all materials the same. Therefore, the emittance (divergence angle) is not a function of the material.

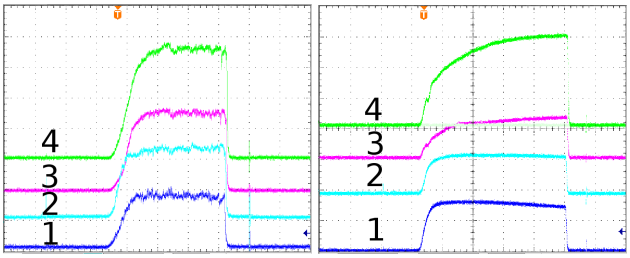

Figure 2: Comparison of beam pulses (200μs/div) along the LEBT for a multi cusp source (right, N_2^+) and for a vacuum arc ion source (left, Ni^{2+}). CH 1: full beam current behind dc post acceleration (left:10 mA/div, right 20 mA/div), CH 2: full beam current in front of bending magnet (left:5 mA/div, right 20 mA/div), CH 3: separated beam behind bending magnet (left:2 mA/div, right 5 mA/div), CH 4: beam current in front of RFQ (left:1 mA/div, right 2 mA/div).

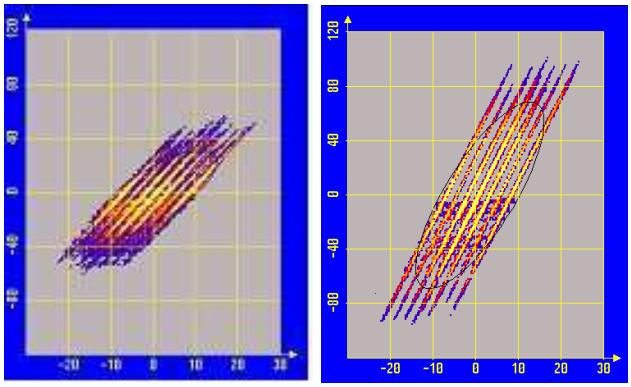

Figure 3: Emittance pattern of a 60 mA at 18 kV argon beam (left, CHORDIS), and 60 mA at 18 kV nickel beam (right, VARIS) y (horizontal) in mm, y' (vertical) in mrad.

Table 2: Typical currents for selected elements in front of the RFQ.

Ion	I_{ex}/U_{ex} [emA/kV]	I_{RFQ} [emA]	duty cycle [Hz/ms]	source
$^{1}H_3^+$	40/6.6	1	5/1	CHORDIS
$^{2}H_3^+$	90/13.2	2	5/1	CHORDIS
$^{14}N_2^+$	40/14	4	5/1	CHORDIS
$^{40}Ar^+$	65/20	20	5/1	MUCIS
$^{181}Ta^{3+}$	75/24	7	5/1	MUCIS
$^{197}Au^{4+}$	60/24	1	1/1	MEVVA
$^{208}Pb^{4+}$	17/12	0.1	15/2	MEVVA
$^{208}Pb^{9+}$	50/5	0.02	50/5	PENNING
$^{238}U^{4+}$	150/35	20	0.25/0.6	MEVVA
$^{238}U^{10+}$		0.05	50/3	PENNING

References

[1] A. Yakushev, TU München, private communication

[2] L. Celona et al., accepted for publication in Rev. Sci. Instrum. (2008)

[3] H. Schulte, W. Jacoby, B. H. Wolf, IEEE Trans. Nucl. Sci. 23, 1042, 1976

[4] R. Keller, K.-N. Leung, GSI Sientific Report 1987, GSI 88-1, 360

[5] R. Keller, P. Spädtke, H. Emig, Vacuum 36, 833(1986)

[6] B. H. Wolf, H. Emig, D. Rck, P. Spädtke, Rev. Sci. Instrum. 65 (10), (1994), 3091

[7] R. Hollinger, M. Galonska, P. Spädtke, Rev. Sci. Instrum. 75 (5), (2004), 1595

[8] U. Ratzinger, Nucl. Instrum. and Meth. in Phys. Res. A (2001) 636-645

[9] L. Dahl, P. Spädtke, Proceedings of the 20th LINAC Conference, Monterey, 2000

Status of the 28 GHz Superconducting ECR Ion Source Project ISIBHI–MSECRIS*

K. Tinschert, GSI, Darmstadt for the ISIBHI collaboration [1]

Superconducting Magnets and Cryostat

The fabrication of the magnet system at ACCEL Instruments [2] started with the winding of the coils. While the manufacturing of the solenoid coils proceeded straightforward, the fabrication of the hexapole coils required a sophisticated winding process which exhibited unexpected problems due to defects of the insulation during pressing and curing of the coils into the cos(3Θ)-shape. Several development steps led to a new manufacturing procedure establishing a reliable coil production, but caused a delay of several months.

In the preparation of the first cold test of the coil system all operation modes and the corresponding forces between coils, ferromagnetic collar and the liquid helium vessel were analyzed. This showed that full energization of only a single solenoidal coil can lead to excessive forces between components of the cold mass. Several structure mechanical changes had to be designed and implemented for safe operation leading to a further delay.

The basic function of the coil system was verified during a first short cold test in an external cryostat in May 2007. The hexapole coil reached nearly 80 % of the nominal current before quenching. Simultaneous operation of the complete coil system was achieved up to 40 % of the nominal hexapole current. This performance was in good agreement with expected values. After application of the mechanical changes to the cold mass, the LHe vessel, radiation shield and thermal insulation were mounted before the system was installed inside its dedicated cryostat. The mechanical adjustment of the coil system, connections through the supply turret and the mounting of the cryocooler cold heads could be finished until October 2007. After the successful leak test of the cryostat vacuum the system was cooled down. The quench training and the first part of the commissioning and acceptance tests were performed in December 2007. The nominal field was obtained for the hexapole alone and for the 3 solenoids without hexapole. While ramping all magnets simultaneously 40 % of the nominal field of the hexapole could be achieved. The quench training will be continued in the beginning of 2008.

RF system and mechanical design

The refurbishment of the 28 GHz gyrotron system has been achieved. After successful factory acceptance of its new high voltage power supply it has been transferred to GSI. The system can be operated up to a power of 10 kW in CW mode and in pulsed mode. The corresponding rise and fall times are 10 ms with a maximum repetition rate of 25 Hz. This will enable normal pulsed mode operation, but afterglow mode will not be accessible.

Another gyrotron system [3] working at the same frequency was procured by GSI and is dedicated to be used with the source at the accelerator facility. Its characteristics are mostly identical to the other system. In addition it will be adequate to operate the ion source in afterglow mode with a pulse fall time of less than 30 μs.

The manufacturing of all components of the plasma chamber, extraction system, injection flange and corresponding vacuum boxes has been achieved. Some changes with respect to the original design have been carried out in order to optimize RF-injection into the plasma chamber and to chose a position for the oven port which is not affected by plasma deposition. More details can be found in [4].

Experimental Setup

All mechanical components for the upgrade of the test stand have been manufactured and have been mostly installed. All infrastructural work for electricity and water cooling has been achieved. The gyrotron system has been put in place for operation with MSECRIS. Some upgrades of beam diagnostics and beam transport line have been done to enable the safe handling of higher beam intensities to be obtained with MSECRIS. After construction and manufacturing of the versatile pepperpot emittance meter it could prove its functionality in various tests.

References

[1] K. Tinschert, P. Spädtke, R. Lang, J. Mäder, J. Roßbach, GSI, Darmstadt, Germany; G. Ciavola, S. Gammino, L. Celona, F. Consoli, G. Gallo, D. Mascali S. Passarello, F. Maimone, S. Barbarino, INFN-LNS, Catania, Italy; A. Galatà, INFN-LNL, Legnaro, Italy; H. Koivisto, M. Savonen, T. Koponen, P. Suominen, T. Ropponen, JYFL, Jyväskylä, Finland; C. Barué, M. Lechartier, GANIL, Caen, France; J. P. M. Beijers, S. Brandenburg, H. R. Kremers, KVI, Groningen, Netherlands; D. Vanrooyen, TSL, Uppsala, Sweden; D. Küchler, R. Scrivens, CERN, Geneva, Switzerland; L. Schachter, S. Dobrescu, NIPNE Bucharest, Romania; K. Stiebing, IKF Frankfurt, Germany

[2] ACCEL Instruments GmbH, Friedrich–Ebert–Str. 1, D–51429 Bergisch Gladbach

[3] GYCOM, 46 Ulyanov Street, 603155 Nizhny Novgorod, Russia

[4] G. Ciavola et al.; Rev. Sci. Instrum., (2007) in print

* Work supported by EU, EURONS contract No. 506065.

UNILAC Status and Developments

W. Barth, L. Dahl, P. Gerhard, L. Groening, M. Kaiser, S. Yaramishev, GSI, Darmstadt, Germany

Status of Operation

In 2007 a carbon beam from the Electron Cyclotron Resonance (ECR) ion source was mainly accelerated via the high charge state injector (HLI) in the UNILAC for the SIS-injection (12 weeks) [1]. Additionally several UNILAC experiments used the beam with a duty factor of up to 30 %. Furthermore the ECR source was in operation for the production of various isotopes (^{7}Li, ^{36}Ar, ^{48}Ca, ^{64}Ni, ^{112}Sn, ^{114}Sn) as well. During a four weeks block of calcium beam and a five weeks block of a nickel beam, experiments for the Super Heavy Element synthesis (SHE) were supplied. Ion beams from the ECR (^{7}Li, ^{36}Ar, ^{48}Ca, ^{64}Ni) were also injected into the SIS 18 (ESR-experiments). The Penning (PIG) ion source provided ^{40}Ar, ^{56}Fe, ^{116}Sn, ^{124}Sn, ^{152}Sm and ^{208}Pb beams with medium intensity, especially while the ECR was used for the irradiation of patients. Heavy ion beams (^{152}Sm, ^{208}Pb) from the PIG source were accelerated via HSI in the UNILAC with short pulses for the injection into the SIS 18; samarium experiments were performed in a three weeks run in the ESR. Additionally, the beams were delivered especially for material research experiments in the experimental hall. The MUlti Cusp Ion Source (MUCIS) provided high-current beams for different high-energy experiments with high intensities (H_2, ^{20}Ne, ^{40}Ar, ^{78}Kr). The Metal Vapour Vacuum Arc (MEVVA) ion source delivered ^{58}Ni for SIS-injection.

After 3½ years without any uranium beam from the MeVVa ion source the UNILAC was in operation for uranium machine studies as well as for regular uranium beam experiments. In general the UNILAC operated with high reliability, even when "multi-beam operation" was accomplished during the treatment of patients. [1]

Machine Experiments

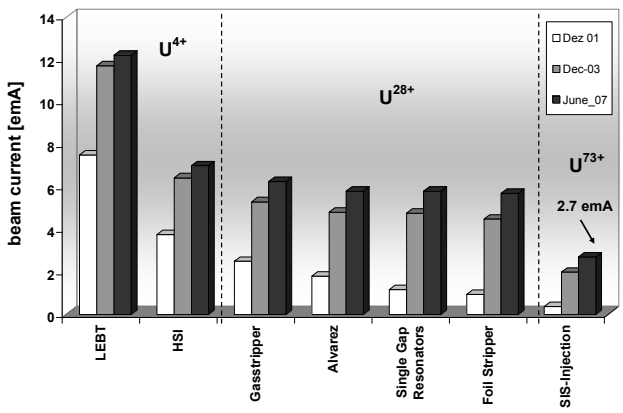

Fig. 1: Uranium beam intensities

For advanced beam tests at the UNILAC a high current argon beam (7.1 emA of Ar^{10+}) was injected into the Alvarez-DTL. With an improved matching procedure a significant reduction of emittance growth rates (20 %) for a zero current phase advance of about 60° was achieved. [2]

Fig. 1 shows the measured maximum uranium beam intensities along the UNILAC and the transfer line to the SIS 18. The results of the first measurement campaign in 2007 is included as well as the data from 2001 and 2003. While the primary U^{4+}-beam intensity was more or less constant, the uranium intensities in the poststripper and in the transfer line could be increased significantly. This is attributed to the different measures performed in the frame of the UNILAC-upgrade program for FAIR (HSI-RFQ, gasstripper, U^{27+}-operation, increased phase advance, high current matching).

Installation of a new charge separator system

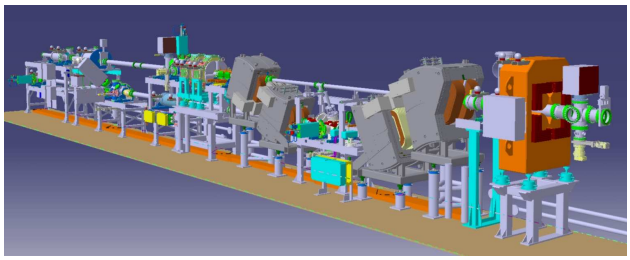

Fig. 2: Technical design of the new charge separator

With the new compact charge separator system emittance blow up and unwanted beam losses for high intensity beam operation could be avoided. A new beam diagnostics test bench is integrated. In parallel to the routine operation in the transfer line beam parameters as ion current, beam profile, beam position, transversal emittance, and beam energy will be measured. [3]

Meanwhile all components are installed. After the final alignment, the commissioning of the different technical systems (power supplies, beam diagnostics, vacuum system, cooling, controls system, interlocks) will start in January 2008, followed by two weeks of beam commissioning.

References

[1] U. Scheeler and D. Wilms, Accelerator Operation Report, (this report)

[2] L. Groening, et. al., Reduction of transverse emittance growth along the UNILAC, (this report)

[3] W. Barth, 2nd Annual Report SIS18_6 "Construction of new infrastructure", (October 2007)

Reduction of Transverse Emittance Growth along the UNILAC*

L. Groening[1], W. Barth[1], W. Bayer[1], L. Dahl[1], P. Forck[1]
[1]GSI, Darmstadt, Germany

Introduction

The preservation of beam quality along the UNILAC Alvarez DTL section is a major concern with respect to the availability of the design beam parameters for FAIR. The DTL comprises 177 accelerating gaps and 184 quadrupoles for transverse beam focusing. They form a periodic structure of linear elements. The high beam currents needed for FAIR arise non-linear space forces leading to emittance growth. The growth depends on the beam envelope shape inside the DTL which can be varied by the quadrupole strengths. Integrating the focusing strength over one period gives the transverse phase advance σ. In case of low currents the so-called zero current phase advance σ_o is calculated analytically.

The beam envelope also depends on the focusing prior to DTL injection, i.e. the matching. A beam is matched if its envelope inhabits the same periodicity as the focusing structure. Mismatched beam envelopes "breath" around the periodic (i.e. matched) solution with a mismatch M, quantifying the mismatch. Experimental campaigns aimed for the dependency of emittance growth on σ_o and M for the Alvarez DTL [1]. The design beam for FAIR is 15 emA of $^{238}U^{28+}$ being space charge equivalent to 7.1 emA of $^{40}Ar^{10+}$. Since $^{40}Ar^{10+}$ is available with higher intensity and allows for a larger spectrum of focusing strengths, $^{40}Ar^{10+}$ was used.

Variation of Focusing Strength

Phase space distributions were measured in front of the DTL. From the transverse measurements the rms-emittances were extracted. The DTL was set to different values of σ_o. From the measurement in front of the DTL M was calculated for each value of σ_o and corresponding emittances were measured behind the DTL. The values for M and for the growth rates as function of σ_o are plotted in Fig. 1 and Fig. 2.

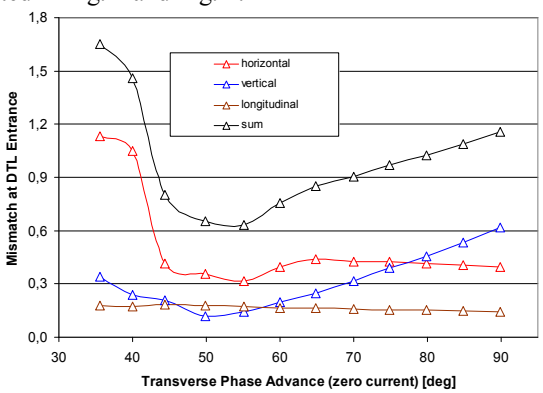

Figure 1: Mismatch parameter as function of the phase advance during the 2006 measurement campaign.

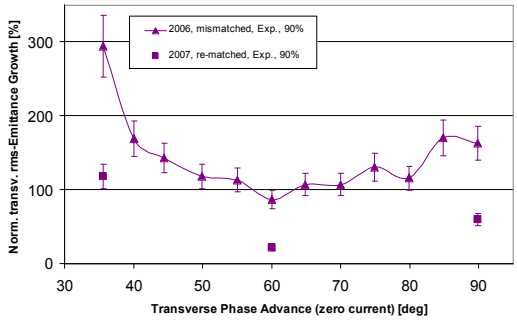

Figure 2: Measured transverse emittance growth as function of the phase advance.

The mismatch was large for low and for high phase advances. Smallest mismatch occurred at $\sigma_o \approx 55°$. A similar behavior was observed for the emittance growth. Highest growth rates of 300% were measured at $\sigma_o = 35°$. It decreases down to 100% at about 60° and increases again to almost 200% for highest σ_o.

Reduction of Mismatch

It was shown that to minimize the emittance growth, σ_o of about 55° must be chosen and M is to be minimized. After the 2006 campaign tools were developed to control the mismatch. These tools were tested in 2007.

Emittance growths and mismatches were measured for three values of σ_o. The mismatches are shown in Fig. 3. Compared to 2006 they were reduced for all phase advances. The corresponding emittance growth rates are shown in Fig. 2. It was demonstrated that by reducing M, emittance growth rates of just 20% can be achieved. It is expected that the demonstrated gain in DTL beam brilliance could be transferred up to injection into SIS18 hence improving the synchrotron injection efficiency.

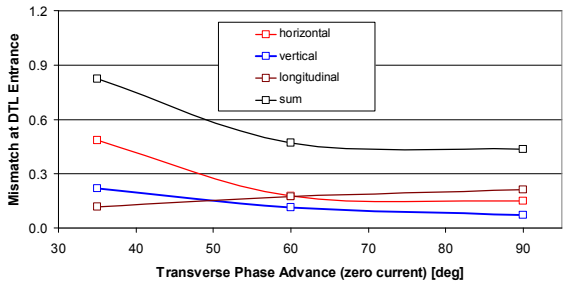

Figure 3: Mismatch parameter as function of the phase advance during the 2007 measurement campaign.

References

[1] www.dania.cea.fr/Phocea/file.php?class=std&&file=Doc/Care/care-report-07-030.pdf

* Work supported by EU, CARE contract No. RII3-CT-2003-506395

SIS18 Status Report of Machine Modifications and Machine Experiments

P. Spiller, U. Blell, H. Eickhoff, G. Franchetti, P. Hülsmann, M. Kirk, H. Kollmus, H. Klingbeil, H. Ramakers, H. Reich-Sprenger, H. Welker, C. Omet, A. Parfenova, N. Pyka, P. Schütt, M. Schwickert, J. Stadlmann
GSI, Darmstadt, Germany

FAIR BOOSTER OPERATION

U^{28+} Beam Intensity

In the frame of machine experiments, the maximum accelerated number of U^{28+}-ions (FAIR reference ion) could be increased to $7x10^9$ ions per cycle. In parallel, the relative amount of beam loss during the cycle has been reduced to about 30% of the injected ions (figure 1). Essentially, this progress has been enabled by a careful machine setting with an optimized vertical closed orbit correction in each lattice cell. Thereby scraping of beam tails at aperture limitations has been minimized and the amount of desorbed gas and correspondingly the ionization loss reduced.

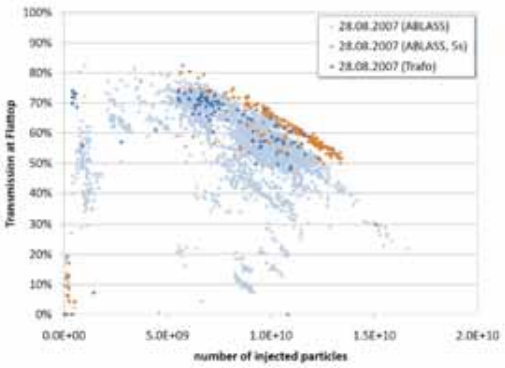

Figure 1: Relative amount of accelerated U^{28+}-ions as a function of the number of injected ions for several machine settings and cycle.

Ion Catcher System

For the stabilization of the pressure at higher beam intensities, the effective gas desorption as seen by the revolving beam has to be minimized. For this purpose, a dedicated ion catcher system will be installed in each lattice cell [1]. Two prototypes (figure 2) of the finally eleven catchers have been built and installed in the synchrotron. Dynamic pressure measurements in the primary and secondary chamber of the scraper will be performed to conclude on the final scraper geometry.

NEG Coated Vacuum Chambers

As an important UHV system upgrade measure, the replacement of the existing main magnet chambers, by new NEG coated chambers has been started. The average pressure in the SIS18 UHV system is determined by the distribution of the pumps and the conductivity of the beam pipe. The aim of NEG coated chambers is to build-up a system which provides strong distributed pumping especially to reduce the pressure peaks and to provide strong pumping at potential loss positions. During the shut downs of 2007, most of the dipole chambers were replaced by new NEG coated chambers. The replacement of the quadrupole chambers will start in 2008.

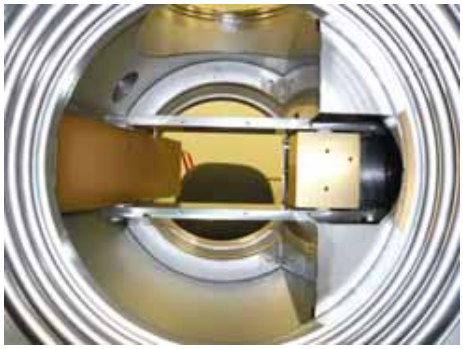

Figure 2: Front view of the scraper chamber with the wedge shaped scraper on the left side (gracing incidence) and the block scraper on the right side (perpendicular incidence).

NEG Coated Vacuum Chambers

As an important UHV system upgrade measure, the replacement of the existing main magnet chambers, by new NEG coated chambers has been started.

Figure 3: NEG coating of a dipole chamber at GSI

The average pressure in the SIS18 UHV system is determined by the distribution of the pumps and the conductivity of the beam pipe. The aim of NEG coated

chambers is to build-up a system which provides strong distributed pumping especially to reduce the pressure peaks and to provide strong pumping at potential loss positions. During the shut downs of 2007, most of the dipole chambers were replaced by new NEG coated chambers (figure 3). The replacement of the quadrupole chambers will start in 2008.

Injection System

The preparations for the exchange of the injection system have been continued. Both, the magnetic inflector system and the electrostatic septum (figure 4) have been redesign and rebuild. The new devices enable an injection of U^{28+}-beams at the standard energy of 11.4MeV/u [2]. However, a reliable operation at the maximum desired septum voltage of 240 kV has not yet been demonstrated. Therefore, the installation of the new injection system has been shifted to the shut down in June 2008 and further tests are conducted in the HV test stand. To achieve a better matching in vertical direction, the installation of an additional vertical steerer magnet at the end of the transfer channel, in front of the new injection system has been prepared.

Power converters

The correction coils in the main dipole magnets are used for two different purposes: a) correction of closed orbit distortions and b) fast displacement of the orbit to prepare for re-injection and extraction. The closed orbit correction in each lattice cell shall be independent from the needs of fast beam displacements and must therefore be realized by two dedicated technical systems. So far, not all horizontal correction coils for the closed orbit correction were equipped with own power converters. In order to decouple the issues mentioned above, new bipolar power converters for the horizontal correction coils have been purchased and installed. The new power converters will enable a precise control of the closed orbit.

Figure 4: HV test of the new 300 kV electrostatic septum.

Projects partly funded by the European Community
DIRAC-PHASE-1 / Contract number: 515876

Beam dynamics

The measurement campaign on the nonlinear transverse dynamics has been continued. As a first application an algorithm for closed orbit correction has been developed and implemented in a new software tool. The new tool enables a fast correction in each lattice cell without affecting the overall closed orbit properties. A method to determine experimentally the effective errors of each lattice cell under the influence of closed orbit deformations has been developed and tested [3].

EXPERIMENT OPERATION

Slow Extraction

First experiments with the goal to reduce beam loss during slow extraction have been carried out. A new machine setting, similar the one proposed for SIS100/300, aiming for a partial compensation of the chromaticity has been calculated and tested. The setting reduces the dependence of the beam angle on the beam momentum at the position of the extraction septum. Thereby, the effective septum thickness as seen by the beam is reduced. First evidence for a reduction of beam loss from typically 15-20 % down to 10 % has been measured.

Bunch Compression

The new MA loaded, short pulse cavity for final compression of ion bunches before extraction, has been commissioned successfully (figure 5). During the Rf tests the desired gap voltage of 40 kV has been reached. The cavity is being prepared for installation in June 2008.

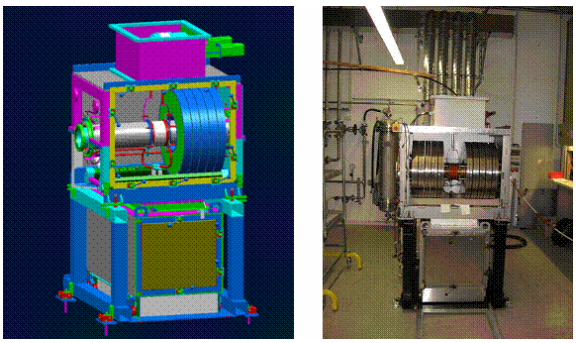

Figure 5: New bunch compression system for the generation of short ion bunches before extraction. The left picture shows a schematic view with the stack of amorphous MA ring cores. The right picture shows the opened cavity in the Rf testing area at GSI.

REFERENCES

[1] C. Omet et. al, Proc. of PAC07, (2007)1416
[2] U. Blell et. al, Proc. of PAC07, (2007)167
[3] A. Parfenova et. al, GSI-ACC-Note-2008-002

UPGRADE OF THE SIS18 INJECTION SYSTEM*

U. Blell, J. Florenkowski, M. Petryk, P. Spiller
GSI, Darmstadt, Germany

Abstract

SIS18 will serve as booster synchrotron for the proposed International Accelerator Facility FAIR [1] at GSI. The aim is to provide high intensity proton and low charge state heavy ion beams of e.g. U^{28+}-ions with a repetition rate of 2.7 – 4 cycles per second. The operation with low charge state heavy ion beams requires modifications of the injection system. At present, the maximum field strength of the electrostatic septum is not sufficient for injection of U^{28+}-beams at the standard energy of 11.4 MeV/u. Furthermore, by means of an increased acceptance, beam loss in the injection channel and corresponding desorption gas production shall be minimized.

THE SIS18 INJECTION SYSTEM

The injection system at the end of the transfer channel consists of an inflector magnet and an electrostatic septum. Both devices and their supply units will be replaced forming a new system as shown in figure 1 [2].

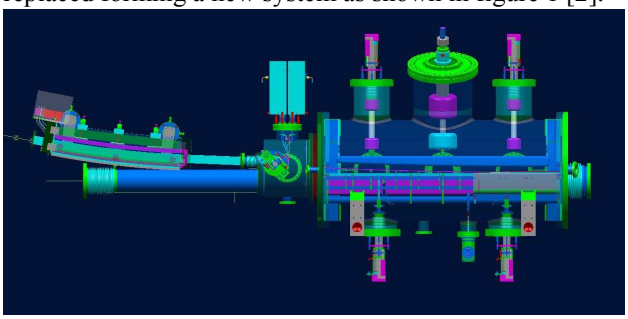

Figure 1: New injection system with curved inflector magnet and 300 kV electrostatic septum.

DESIGN AND IMPROVMENTS OF THE INFLECTOR MAGNET

The existing inflector magnet consists of two straight 4.5°-sections with straight vacuum chambers, while the new inflector is built as a single 9° sector magnet. A new power converter based on modern technical standards has been built to replace the supply unit of the existing magnet. By means of a bent beam pipe, the beam acceptance is increased by a factor of 3. A further design goal was the permanent installation of the heating seal in the inflector magnet. Thereby, the mechanical design of the inflector magnet has been simplified and the service time for the bake-out procedure shortened. The new heating seal provides a bake-out temperature of up to 300° C. The yoke length of the inflector magnet is 0.9 m with an aperture of 78 x 60 mm. The water cooled coils consist of 18 windings with a square cross section of 8 x 8 mm. The operation current at the maximum magnetic rigidity of 4.5 Tm is 2200 A.

DESIGN AND IMPROVEMENTS OF THE ELECTROSTATIC INJECTION SEPTUM

The electrostatic septum provides the final deflection angle of 43 mrad before injection into SIS18. The new electrostatic septum has a larger aperture and can be operated with higher electrical field strengths. In order to reach the required deflection angle, the present 160 kV high voltage power supply will be replaced by a new 300 kV DC power supply unit. The new electrostatic injection septum has a cathode length of 1.5 m. Anode and cathode are adjustable and provide a maximum horizontal channel width of 3.5 cm. The first 1/3 of the anode consists of thin tungsten-rhenium wires which are tightened by 290 springs. In case of damage, the springs will pull out the destroyed wires of the electrical deflection field. The present cathode consists of aluminium, coated with aluminium oxide which allows a maximum electrical field strength of 100 kV/cm at a gap width of 2 cm without significant flashovers during beam operation. The septum is also equipped with clearing electrodes. They are mounted on insulators inside the anode hole and will be supplied with a maximum voltage of –10 kV. The cylindrical UHV chamber of 2000 mm length and 700 mm diameter is made of stainless steel 1.4301. The material is vacuum annealed at 950° C for 3 hours. The completely cleaned and assembled septum unit has been baked out at 240°C and evacuated to the design pressure of 10^{-11}mbar by two Ti-sublimation pumps and an ion sputter triode. In order to minimize beam loss in the injection channel the horizontal beam position and profile shall be controlled directly in front of the injection septum. Therefore, a horizontal beam profile monitor will be installed just at the septum entrance. The existing electrostatic septum is not protected against beam loss in the injection channel. In order to anticipate beam loss on the electrodes, the new septum is equipped with a moveable, water cooled entrance slit.

All components are manufactured and tested and will be installed in the shut down in June 2008.

REFERENCES

[1] FAIR Baseline Technical Report (FBTR), GSI (2006)

[2] U. Blell et.al., "Development of the injection and extraction systems for the upgrade of SIS18, Proc. of the PAC 2007, (2007)167

*Project funded by the European Community
DIRAC-PHASE-1 / SIS18_4 – Injection / Extraction Upgrade
Contract number: 515876

Acceleration of U^{28+}-beams in the SIS18

C. Omet and P. Spiller
GSI, Darmstadt, Germany

Introduction

To prepare the acceleration of highest intensities of intermediate charge state heavy ion beams for the FAIR project, several technical projects have been summarized in the SIS18 upgrade program. The various technical measures of this program are continuously accompanied and verified by machine experiments. Major goal is the reduction of ionization beam loss. The strong dependence of the ionization beam loss on initial systematic loss has been proven. The accelerated number of ions could be increased by reducing the initial system beam loss.

Reduction of Ionization Beam Loss

By the following improvements a considerable reduction of ionization beam loss during U^{28+}-operation has been achieved:
a) precise positioning of the beam in each lattice cell
b) increased pumping speed of the UHV system and
c) fast ramping by means of the new power grid connection.

An algorithm for a precise closed orbit correction has been developed [1] and implemented in the control system [2]. This algorithm provides set values for the local closed orbit correction without affecting the closed orbit as a whole. By means of the new algorithm the beam has been precisely positioned in each lattice cell with special attention to vertical aperture limitations. Thereby it could be avoided that initial beam loss and desorption gas production is generated by scraping of beam tails.

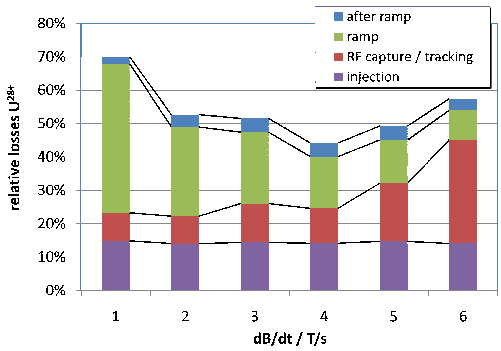

Figure 1: Relative losses during acceleration of U^{28+}.

The former limitation of synchrotron pulse power and correspondingly the ramp rate has been removed by the new 110 kV network connection. Since the cycle time has a major impact on the ionization beam loss, increased ramp rates have been tested at U^{28+}-operation. The SIS18 power converters provide ramp rates of 4 T/s up to 18 Tm and 10 T/s up to 12 Tm. While operation up to 4 T/s is already performed during experiment operation, higher ramp rates require further technical effort. Due to the fact that the existing RF system does not provide sufficient RF voltage, capture and tracking losses are increasing at operation with intermediate charge state heavy ions and higher ramp rates. Beam loss during the capture process and at the beginning of the magnet ramp drive pressure bumps which, as expected, influence significantly the ionization beam loss of U^{28+}-ions (see fig. 1).

The situation with ramp rates higher than 4 T/s will improve as the new h=2 cavity will be available. It is planned to replace all existing magnet chambers by new, NEG coated chambers. A first UHV sector of SIS18 has been equipped with NEG-coated dipole chambers. Thereby the distributed vacuum pumping speed has been increased and the vacuum dynamics further stabilized. The development of the U^{28+}-beam current within the machine cycles over the last machine development runs of 2006 and 2007 is shown in fig. 2. A major improvement has been achieved in 2007 where $6.5 * 10^9$ U^{28+} particles have been extracted. The limitation for reaching higher beam intensities is still the too low pumping speed of the UHV system, as can be seen in [3]. The highest intensity of $7.2 * 10^9$ accelerated particles has been achieved after a 5 s break between the synchrotron cycles. In advance all Ti-Sub Pumps (TSP) in the SIS18 have been used for further enhancement of the vacuum pumping speed.

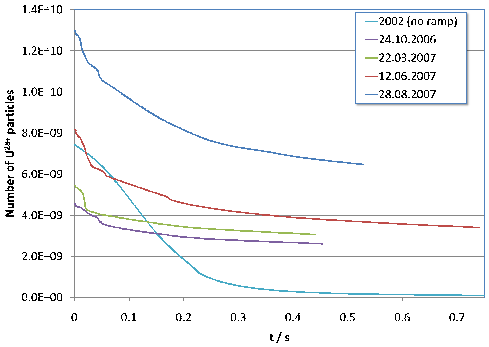

Figure 2: Intensity profiles in different machine cycles with $\dot{B} = 4$ T/s.

References

[1] A. Parfenova, G. Franchetti, B. Franzcak, M. Kirk, and C. Omet. SIS18 closed orbit correction using local bump method. Internal note, GSI, 12 2006.

[2] A. Redelbach. Closed Orbit-Korrektur mit SIST. Internal note, GSI, 8 2007.

[3] C. Omet and P. Spiller. Maschinenexperimente vom 28.08.2007: Schnelle Rampen, Umladungsverluste und dynamisches Vakuum. Internal report, GSI, 10 2007.

Analysis of resonances induced by the SIS-18 electron cooler*

S. Sorge†, O. Boine-Frankenheim, and G. Franchetti, GSI, Darmstadt, Germany

A side effect of the application of an electron cooler in an particle accelerator is its action as a non-linear element of the lattice. This may lead to the excitation of resonances if they are crossed e.g. by the tune spread due to the eigen space charge in the case of a high ion beam current resulting in an increase of the beam emittance [1]. A possible consequence is the reduction of the space charge limit influencing the operation of an accelerator. For that reason, we calculated the resonances driven by the electron space charge field in the cooler installed in the SIS 18 heavy ion synchrotron at GSI Darmstadt. This theoretical study provides the necessary information for dedicated measurements of cooler induced resonances and effects in SIS. For our calculations, we used a numerical model consisting of a rotation matrix representing the ideal lattice together with a non-linear transverse kick element representing the electron cooler. Here, we applied a radial shape of the electron beam having a constant density in the centre and a thin edge region as shown in figure 1 being characteristic for an electron cooler. A radius $b = 22$ mm was chosen for the electron beam. Additionally, an U^{28+} ion beam having a Gaussian profile at the beginning was applied, where $\sigma_{\rm ini} = b$ was assumed.

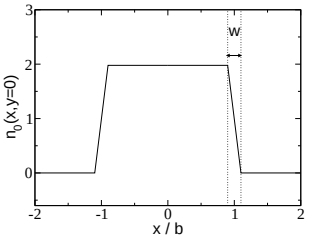

Figure 1: Normalised charge density profile used for the electron beam as provided by the beambeam element of MAD-X as a function of x for $y = 0$. An edge layer with a width $w = 0.01\ b$ was used in the calculations.

To find the positions of the resonances, we observed the relative rms beam width $w_{\rm rel} = \sigma_{\rm fin}/\sigma_{\rm ini}$ depending on the tune values ν_x, ν_y of the rotation matrix.

We explored resonances in the tune range $\nu_x \in [4.05, 4.3]$ and $\nu_y \in [3.2, 3.45]$, what is near the working point $(\nu_x, \nu_y) = (4.2, 3.4)$ [2], and what does not contain a half integer resonance. On the other hand, it was shown in reference [1] within an analytic model, that an electron cooler, with a round electron beam, excites resonances of even order only, where the resonances strength decreases with increasing order. Hence, we searched for resonances of order 4 and 6. The results are shown in figure 2. All resonances found could be identified. Only sum resonances and uncoupled resonances lead to an increased beam width.

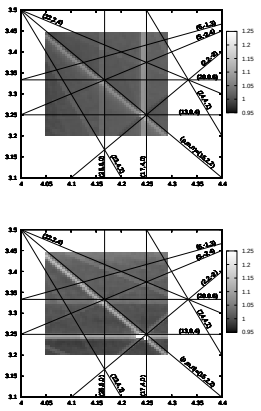

Figure 2: Relative rms beam width in x and y direction , upper and lower picture, respectively, depending on ν_x and ν_y (x and y axis in both figures). The colour scale is within $w_{\rm rel} \leq 1$ (dark grey) and $w_{\rm rel} \geq 1.25$ (white).

On the other hand, there are many resonances driven by the non-linearities of the lattice a real accelerator, see e.g. [3]. In contrast to them, the resonances driven by the electron cooler do not lead to a beam loss, but to an average increase of the beam width of about 20 %. This beam blow up could affect the beam behaviour due to the lattice non-linearities. So, the investigation of the interplay of both sources of resonances in the real SIS would be an important task within an experiment. Here, further theoretical studies are necessary.

The work presented in this report is described in more detail in reference [4].

References

[1] V. Ziemann, "Resonances driven by the electric field of the electron cooler", TSL Note 98-43

[2] B. Franczak, Parameter list of SIS–18, GSI-SIS-TN / 87-13, September 10, 1987

[3] G. Franchetti, P. Schuett, T. Hoffmann, G. Rumolo, and A. Franchi, "Mapping of resonances in SIS18", GSI-Acc-Note-2005-02-001

[4] S. Sorge, O. Boine-Frankenheim, and G. Franchetti, Proc. of COOL, Bad Kreuznach 2007, see http://bel.gsi.de/cool07/PAPER/WEM103.PDF

* Work supported by the European Community RESEARCH INFRASTRUCTURES ACTION under the FP6 programme: Structuring the European Research Area - Specific Support Action - DESIGN STUDY (contract 515873 - DIRACsecondary-Beams)

† S.Sorge@gsi.de

Nonlinear effects induced by closed orbit deformation in SIS18

A. Parfenova, G. Franchetti, I. Hofmann, W. Bayer
GSI, Darmstadt, Germany

For the SIS18 operations as booster for the SIS100 it is necessary to maximize its intensity and minimize the beam loss at nonlinear resonances. The understanding of the beam loss mechanisms needs a full experimental and theoretical beam dynamics study in order to quantify each source of the nonlinear errors in the machine. First results of a novel technique to identified the strength and locations of the nonlinear errors are presented here. Compensation of the resonances is an important issue for the improvement of the machine performance. In the framework of the SIS18 upgrade a measurement on resonance beam loss induced by closed orbit (CO) distortion was carried out. CO errors are relevant for feed down effects of multipoles, which generate unwanted resonances [1]. A static tune scan

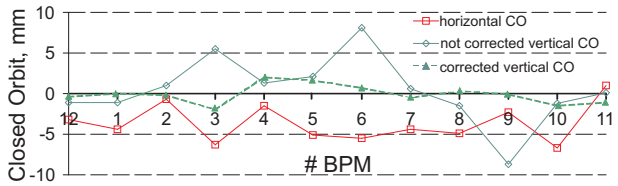

Figure 1: The SIS18 CO measured by POSI [1].

was performed for several working points along the vertical line $Q_x = 4.2$ ($3.2 < Q_y < 3.6$) at injection energy 11.12 MeV/u for a coasting $^{238}U^{73+}$ beam. The multiturn injection was set in order to fill the SIS18 acceptance. An intensity of ≈ 50 μA was used in order to exclude the influence of space charge and image charges on beam loss. For each measurement a dedicated Q_y was chosen and the time evolution of the beam intensity has been recorded by residual gas monitor (RGM). The scan has been performed for corrected [1, 2] and not corrected (artificially distorted) vertical CO produced on top of the corrected orbit by creating three vertical CO bumps in periods [2, 3, 4], [5, 6, 7] and [8, 9, 10]. These orbits are shown on Fig. 1. The local

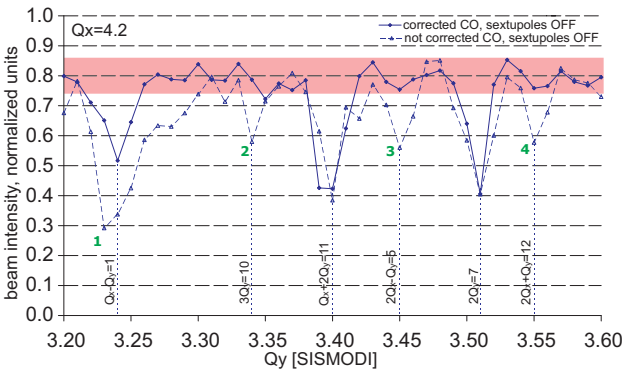

Figure 2: Resonance beam loss 1.1 s after injection.

distortion of the vertical CO keeps the CO at the injection (BPM #12 in Fig. 1) unchanged: this allows us to compare all the tune scans among themselves. The measurement fluctuations of CO on Fig. 1 are of $\pm$ 1 mm. The relative beam loss 1.1 s after injection for the `corrected` and `not corrected` CO is presented in Fig. 2. The intensity baseline for tune off the resonance is centered at 0.8 due to beam life time, which is limited by charge exchange and coulomb scattering processes. The intensity fluctuations around this baseline are plotted as a magenta band. Figure 2 shows the presence of six minima attributed to resonance beam loss. The same six resonances were detected in previous measurements [1]. The dotted vertical lines indicate Q_y at the maximum beam loss. Note that if the **CO is corrected** the resonances `2`, `3` and `4` *either do not exist or are very weak* (see solid line on Fig. 2), if the **CO is not corrected** *additional beam loss occurs* (see dashed line on Fig. 2). For a shorter storage time of 0.3 s and distorted CO the beam loss at the resonances `1`, `2`, `3` and `4` is also present but weaker by $\approx 15 - 20\%$ compared to that for longer storage time 1.1 s [3]. If the chromatic sextupoles are turned `on`, the resonance beam loss increases and a nonlinear vertical tune shift of about -0.02 is introduced.

The measurement technique of nonlinear errors was experimentally confirmed. During the measurements the coherent betatron oscillations were excited by a single Q-kick with the chromaticity corrected. The fractional part of the tune was found from the frequency spectra with a FFT algorithm. The effect of nonlinear tune shift introduced by a given error in one of the sextupoles (S11KS1C) was investigated. The dependence of the fractional part of the horizontal tune on horizontal CO change introduced by the steering magnet (S11MU1A) was measured and used to reconstruct the given sextupole error (strength and polarity). The two different simulated and reconstructed values are presented in Table 1, errors of the order of natural errors are resolved. The reconstruction technique is under development, it can be also applied to reconstruct octupole errors due to multipole feed down effect and, finally, to reconstruct nonlinear errors in the complete machine. The next step of this reconstruction technique is compensation of the sextupolar nonlinear errors (resonances) as a major part of the SIS18 upgrade program.

Table 1: Simulated and measured sextupoles errors.

units	sim. 1	meas. 1	sim. 2	meas. 2
m^{-2}	0.01	0.00994	-0.03	-0.02676

References

[1] A. Parfenova et al., GSI-Acc-Note-2006-05-15.
[2] A. Redelbach, CO-Korrektur mit MIRKO bzw. SIST (2006).
[3] A. Parfenova et al., GSI-Acc-Note-2008-002.

ESR Operation and Development

K. Beckert, C. Dimopoulou, A. Dolinskii, B. Franzke, V. Gostishchev, P. Hülsmann, T. Katayama, S. Litvinov, F. Nolden, P. Petri, U. Popp, G. Schreiber, I. Schurig, M. Steck,[1] and D. Möhl[2]

[1]GSI, Darmstadt, Germany; [2]CERN, Geneva, Switzerland

After very good vacuum conditions in previous years, the operation of the ESR in 2007 was hampered by various problems with the ultrahigh vacuum system. This was particularly distracting, as many experiments with low charge state or low energy beams were scheduled, which are most dependent on good vacuum conditions.

The commissioning of the HITRAP facility was continued with beams of bare ions decelerated to 4 MeV/u and fast extraction of the beam which was re-cooled at the low energy by the electron cooling system. The ESR was also used as a test bed for developments for the FAIR project. Two accumulation schemes which are proposed for the New Experimental Storage Ring (NESR) of the FAIR project were successfully demonstrated. Benchmarking experiments to verify computer simulation tools were continued.

A beam time request for fixed target experiments with low energy bare ions has triggered an ion optical study of the feasibility of slow resonance extraction of decelerated ions from the ESR. Although considered from the beginning of the ESR design, this mode has never been implemented. The design study confirmed that by proper choice of the beam orbit and adjustment of the tune and the chromaticity the existing beam extraction components should allow a slow extraction of bare ions by resonance extraction. The modification of the operating software has been initiated and machine experiments for a demonstration of this type of slow extraction are foreseen in the first quarter of 2008.

1 Operation for Physics Experiments

In a three weeks period the ESR was operated with rare isotope beams of ^{142}Pr and of ^{142}Pm in various charge states for detailed studies of the decay behavior of these ions. At the injection energy of 400 MeV/u a combination of stochastic precooling and final electron cooling was applied. After a total cooling time of about 5 s the ions were cooled to lowest momentum spread with an uncertainty of their revolution frequency below 10^{-6} which allowed detection and observation of the decay of single ions. The observation of single decays allows the determination of the instant of decay with an accuracy of about one second, which is determined by the time for re-cooling the decay product to smallest frequency uncertainty.

The reaction microscope, which was recently installed in the interaction chamber of the internal target, was used in experiments with bare nickel ions at 400 and 30 MeV/u. The ions and electrons emerging from the gas jet after collisions between a fast projectile ion and a target atom are detected in the reaction microscope in coincidence. A pair of Helmholtz coils installed around the target chamber provides a homogeneous magnetic field to guide the low energy electrons. Other experiments at the internal target used decelerated uranium ions in various charge states (92+, 91+, 90+). The injection energy was chosen for maximum production of the required charge state in the stripper foil between SIS and ESR, whereas the energy in the ESR after deceleration was determined by the experiment. Electron cooling after deceleration was mandatory to provide good beam quality for precision experiments and to compensate the heating by the internal target.

Two experiments with low charge states (Li^{1+} and U^{28+}) suffered from the poor vacuum conditions. Due to the beam lifetime of a few seconds these experiments had to be cancelled. After some provisional repair work the conditions for the time dilation experiment with Li^{1*} could be improved, and a beam half life of 15 s was achieved, still a factor of 5 shorter than in the previous year. Although the operation of the ion source and the preparation of lithium ions in the metastable state for the precision spectroscopy is demanding, the feasibility of improving the precision in this experiment by excitation of the metastable ions with two counter propagating laser beams could be finally demonstrated [1].

Decelerated beams of bare ions, neon and nickel, at an energy of 4 MeV/u were provided in two beamtimes scheduled for the commissioning of the HITRAP facility. In order to reduce the total cycle time a deceleration mode with stochastic cooling at the injection energy of 400 MeV/u has been established. The stochastic cooling reduces the cooling time to a few seconds compared to cooling times in excess of 10 s with electron cooling at the injection energy. No degradation of the deceleration efficiency was observed. The accelerating voltage of the electron cooling system needs less variation during the deceleration cycle which simplifies the cycle and reduces its duration by a few seconds. The quality of the decelerated beam is determined by the power of electron cooling at the extraction energy of 4 MeV/u. Results on the beam parameters of the extracted beam, which also provide information on the quality of the cooled beam at low energy, are reported in the HITRAP commissioning report [2]. So far only coasting beams were extracted, but the maximum length of the kicker pulse of 3 μs does not allow to extract more than 75 % of the circulating particles. In order to extract the decelerated beam completely and to provide a short bunch of less than 1μs length for efficient capture in the trap, a system for bunching the beam at harmonic number $h = 1$ after deceleration is in preparation using the modified second ESR cavity.

In preparation of mass measurements in the isochronous mode the ion optical setting of the beam line between SIS, FRS and ESR has been optimized. By improved matching, particularly between FRS and ESR an increase of the number of injected ions by a factor of 10 was demonstrated. This improvement will allow the use of the isochronous mode for rare isotopes with correspondingly lower production rate [3].

At the internal gas target preparations are under way to install a micro-jet target which can produce a hydrogen liquid jet with micrometer diameter. This new set-up should allow an increase of the target thickness for light gases by several orders of magnitude.

2 Machine Development

For the NESR storage ring of the FAIR project two new longitudinal stacking schemes are proposed which use a combination of rf manipulations and electron cooling. By means of these longitudinal stacking techniques it is foreseen to accumulate intense beams of rare isotopes. One scheme uses barrier buckets to confine the circulating ions to a fraction of the circumference and make the empty part of the circumference available for the injection of additional particles. The second scheme uses an rf system operated at harmonic number $h = 1$, which compresses the circulating beam to a fraction of the circumference. By injection of new beam onto the unstable fixed point, the stored beam is not affected by the new injection. A precise timing and short rise and fall times of the injection kicker are crucial for the longitudinal accumulation.

For the experimental verification of the proposed stacking schemes the second ESR rf cavity, which is not needed for standard operation, was modified for broadband operation. A parallel resistance was installed in order to reduce the cavity impedance to 50 Ω. This increased the bandwidth sufficiently to generate barrier pulses with a period of 200 ns, corresponding to a maximum repetition rate of 5 MHz, at the expense of reduced gap voltage. Due to the small momentum spread of the cooled beam the maximum amplitude of the gap voltage of 170 V was sufficient for a first demonstration of both accumulation methods with the same cavity and comparable rf voltages. These accumulation methods also require very accurate synchronization of the pulse of the injection kicker in order not to destroy the stacked beam. Details of the experimental study are described in a separate report [4].

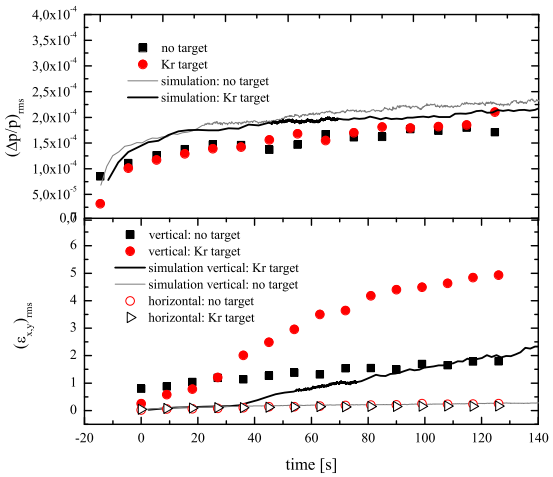

Figure 1: Comparison of measurement and BETACOOL simulation of the longitudinal and transverse heating of a bare nickel beam at 400 MeV/u interacting with a Kr target of 6×10^{12} atoms/cm^2. The initial heating is due to intrabeam scattering, the target is switched on after 30 s.

The experiments aiming at a benchmarking of simulation tools for the prediction of beam parameters in experiments with cooled beams interacting with an internal target were continued. As the results of previous experiments were impaired by the finite dispersion of about 1 m at the target, a new ion optical setting was tested which reduced the dispersion at the target location to less than 10 cm. This could be confirmed by measurements with a horizontal scraper in the target section. An experimental result with a Ni^{28+} beam at 400 MeV/u and the new setting for the dispersion in the target section is shown in Fig. 1. Krypton gas with a thickness of 6×10^{12} atoms/cm^2 was used as target. The measured values are compared to a simulation with the BETACOOL program [5] which is frequently used to predict the parameters of cooled beams. The temporal evolution is well reproduced, but the simulation predicts too small initial emittance of the cold beam.

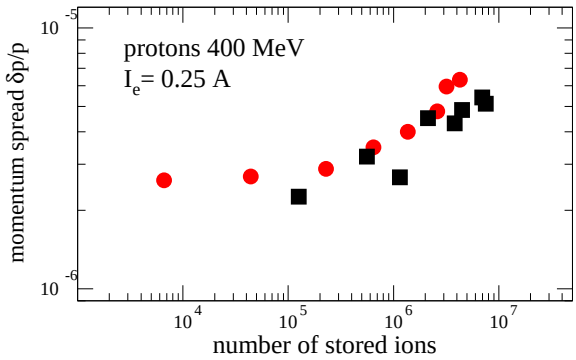

Figure 2: Measurement of the momentum spread (2σ) of a proton beam at 400 MeV cooled with an electron current of 250 mA. By connecting a resonant circuit to the Schottky pick-up (red circles) the sensitivity could be increased by more than one order of magnitude.

In another machine experiment the cooling and detection of protons has been studied. For protons, because of the low charge, the Schottky noise is reduced and therefore protons are useful to find the sensitivity limit of the Schottky noise detection system. The low charge results in much weaker intrabeam scattering, but also in a reduced cooling rate of the electron cooling system. The dependence of the Schottky noise signal on the ion beam intensity was measured in the low intensity regime (Fig. 2), where for highly charged ions an ordering effect was evidenced as a sudden reduction of the momentum spread for less than a few thousand ions. For protons a minimum momentum spread of 2×10^{-6} was found, which saturated below 1×10^5 ion. With the standard set-up for Schottky noise detection the beam signal could not be resolved from the thermal noise for less than 10^5 stored ions. After connecting a resonant circuit to the Schottky pick-up the detection limit could be lowered by one order of magnitude to about 1×10^4 ions. The minimum momentum spread was due to the ripple of the power supply for the main dipole magnets, which were operated at lower current compared to highly charged heavy ions. In order to increase the sensitivity of the Schottky pick-up or alternatively to reduce the required averaging time of the frequency analysis system a new Schottky pick-up operating at higher frequency (a few hundred MHz) is in preparation.

References

[1] C. Novotny et al., contribution to this report.
[2] O. Kester et al., contribution to this report.
[3] S. Litvinov et al., contribution to this report.
[4] C. Dimopoulou et al., contribution to this report.
[5] A.O. Sidorin et al., NIM A 558 (2006) 325.

Accelerator Operation Report

U. Scheeler, D. Wilms
GSI, Darmstadt Germany.

This report describes the operation statistics of the GSI accelerator facility in the year 2007. The presented information is based on the data of the newly implemented GSI electronic operation logbook OLOG [1] which allows an improved evaluation of operation statistics especially for the time-sharing operation mode of the accelerators.

General overview

Table 1: Overall beam time of the accelerator facility

	2007	2006
Integral target time for all experiments	**11064 h**	11527 h
Time for retuning	**90 h**	104 h
Time of interruption	**2584 h**	1906 h
Total beam time	**13738 h**	13559 h

From January till October 2007 four beam time periods were scheduled. The time left was used for shut-down periods to realize an intensive service and upgrade program for the whole facility. Within the beam time periods the SIS has been operated for 5768 hours and the UNILAC for 5831 hours.

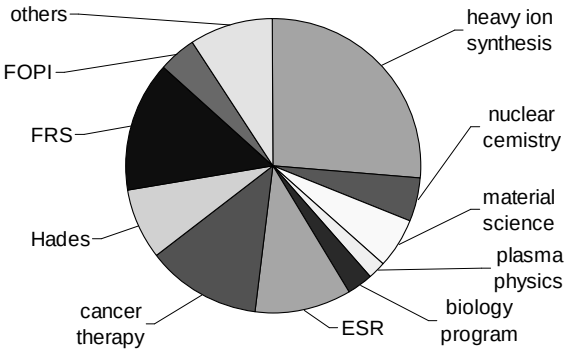

Figure 1: Distribution of target time to the different experiments.

In Table 1 the total beam time of the whole facility is shown. Altogether 11064 hours of beam-on-target-time was successfully delivered to the different physics experiments, especially ^{152}Sm beam to the ESR, light ions to Hades and rare isotopes for the Heavy Ion Program. This amount of total target time is about 450 hours lower compared to 2006. The category 'retuning' shows the time necessary to improve the beam performance during the running experiment. The 'time of interruption' covers the categories ‘accelerator setup’ (840 h), ‘ion source service’ (318 h) and ‘unscheduled down time’ (1426 h). These are all events which lead to a break of the running beam for the corresponding experiment. Altogether these times add up to the 'total beam time', which is higher as the above mentioned operation time of the accelerators due to time sharing operation.

The ratio between target time and total beam time (availability of the facility) for the last two years shows a slight decrease in performance from 85% to 81% which is discussed in the last section. The fraction of target time for each experimental program is shown in figure 1. The details corresponding to UNILAC and SIS beams are given in the next two sections.

UNILAC experiments

The beam time for the UNILAC experiments is shown in Table 2. Altogether 20 different experiments were performed at the UNILAC with 4896 hours of target time. The target time was decreased compared to the value of the year 2006 (5208 hours) mainly because of a longer shut-down period of the UNILAC. The sharing of the beam to the different experiments is shown in figure 1. Main users of the UNILAC beam were the Heavy Ion Program (2801 hours), Materials Science (553 hours), and Nuclear Chemistry Experiments (508 hours).

Table 2: Beam delivered to UNILAC experiments.

	Time	Fraction
Target time for experiments	4896 h	82,6%
Time for retuning	29 h	0,4%
Accelerator setup	361 h	6,1%
Ion source service	172 h	2,9%
Unscheduled down time	473 h	8,0%
Total beam time	5931 h	100%

SIS Experiments

The accelerator has delivered beams to 30 fixed target experiments behind the SIS and to 7 experiments at the ESR. The overall beam time is shown in Table 3. In contrast to the last report the data include UNILAC beam for SIS injection. Hence unscheduled down times rises to 12% and ion source service is integrated in the table. Altogether 6168 hours of target time have been achieved.
The distribution of the beam to different experiments is shown in figure 1. In 2007 the target time for cancer therapy was about 1250 hours and remained nearly constant compared to the year 2006. The target time for the large experiments was about 1700 hours for FRS and about 844

hours for HADES. The target time for ESR has been slightly decreased to about 1200 hours.

Table 3: Beam delivered to SIS/ESR experiments.

	Time	Ratio
Target time for experiments	6168 h	79,0%
Time for retuning	61 h	0,8%
Accelerator setup	479 h	6,1%
Ion source service	146 h	1,9%
Unscheduled down time	953 h	12,2%
Total beam time	7807 h	100%

Accelerator operation

Figure 2 shows the total beam time for all accelerated isotopes during 2007. Over the year 25 different isotopes have been accelerated. The rare isotopes (^{48}Ca, ^{7}Li, ^{64}Ni) were produced by the ECR ion source, which has been operated for 5499 h. This beam was mainly provided to UNILAC experiments. The Penning ion source was mainly used for ^{40}Ar, ^{208}Pb, and ^{129}Xe (4215 hours). The high-current ion source operation lasted for 2930 hours. Especially Uranium beam was delivered from the MEVVA ion source for 553 h.

Table 4: Statistics of all unscheduled down time events

	Time	No. of events
Power supplies	328 h	261
Vacuum and structures	321 h	91
Beam diagnostics	17 h	16
Operation	14 h	23
Safety-/ Interlock system	58 h	44
RF system	153 h	310
Controls	46 h	61
Infrastructure	9 h	6
Others /	43 h	48
Total of unscheduled down time	1084 h	1001

In Table 4 all unscheduled down time events are shown in more detail. As already mentioned, we observed a slight decrease of machine performance of about 5% points for the year 2007 (see Table 1). Besides major failures in the SIS main dipole power supplies, a leakage in the water cooled dipole supply cable and vacuum leaks in the poststripper and the Alvarez sections appeared.

To provide more time for accelerator developments, especially to reach high-intensity beams, each of the four beam period was prolonged by two shifts (56 hours). In total 145 hours of accelerator experiments have been performed at the UNILAC, 181 hours at the SIS, and 84 hours at the ESR. These experiments are typically running with extreme machine settings. This implies a higher break-down risk and time sharing operation is not possible in most cases.

A new category ‘standby time of the experiment’ was introduced to the new logbook. This category was not monitored completely in former years [2] and gives the additional available beam time under the assumption, that all scheduled experiments make full use of the parallel operation opportunities. It includes all kind of breaks of the experiments which are not included in the “time of interruption”, i.e. breaks requested by the experiment, operation of experiments in block mode, or beam interrupts due to beam tuning of experiments running in parallel (Short breaks due to sharing of the beam pulses are not included in this category). Altogether about 5000 hours ‘standby’- time have been collected. For main experiments the ratio between standby time and target time is less then 10%; however, during cancer therapy about 600 hours standby time were obtained due to the fact that patients have been treated only during daytime.

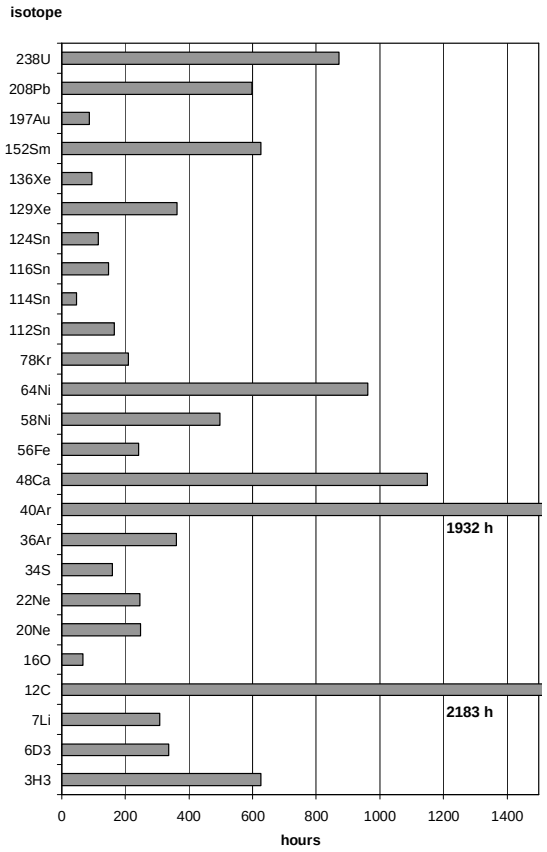

Figure 2: Total beam time for all different ion species.

Besides the evaluation of the beam availability for the experiments which is about 80%, additional monitoring of the standby time shows the degree of time sharing operation of the accelerator. A decrease of standby time leads to more efficient use of operation time. For organizing and scheduling of beam time this should be considered.

References

[1] OLOG GSI operation Logbook
[2] U. Scheeler et al., GSI Scientific Report 2006, 77

HITRAP Commissioning Measurements

L. Dahl, W. Barth, P. Gerhard, F. Herfurth, O. Kester, H.-J. Kluge, S. Koszudowski, C. Kozhuharov, G. Maero, W. Quint, A. Sokolov, G. Vorobjev, D. Winters

GSI, Darmstadt, Germany

Status of the HITRAP Project

The heavy ion trap (HITRAP) will decelerate highly charged ions up to U^{92+}, provided by the GSI accelerator complex at 4 MeV/u, down to 6 keV/u [1,2]. The decelerator contains a double drift buncher (DDB), an IH-type structure and a 4-rod Radio Frequency Quadrupole. The basic working frequency is 108 MHz. Until May 2007 the decelerator was being constructed up to the DDB (Fig.1).

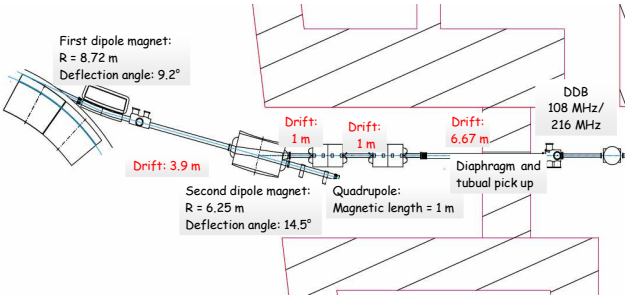

Fig. 1: HITRAP DDB section

Commissioning Measurements

The beam line from the ESR extraction to the HITRAP DDB section contains comprehensive beam diagnostics: Faraday cups, a tubular and two short capacitive pick-ups, three SEM grids and four YAG scintillation screens [3]. A single-shot pepper pot emittance meter [4] was used in the final temporary diagnostic setup containing also a diamond detector for pulse shape measurements.

The first commissioning period in May 2007 served to check the functionality of all components and controls and to transport the $^{64}Ni^{28+}$-beam through the DDB section without buncher operation as a principal acceptance test. The experience was that two additional vertical steering magnets are necessary to improve the beam transmission through a diaphragm mounted to decouple the ESR vacuum of ~10^{-9} Pa from the ~10^{-5} Pa in the HITRAP.

During the second commissioning period in August 2007 with a $^{20}Ne^{10+}$-beam of 2 µA pulse current there was no beam loss measured up to the tubular pick up located behind of the diaphragm. Downstream slight losses occurred due to narrow apertures in the buncher cavities. The capacitive pick-ups located between the two bunchers and behind the second buncher generated signals of the 108 MHz beam bunches (Fig. 2).

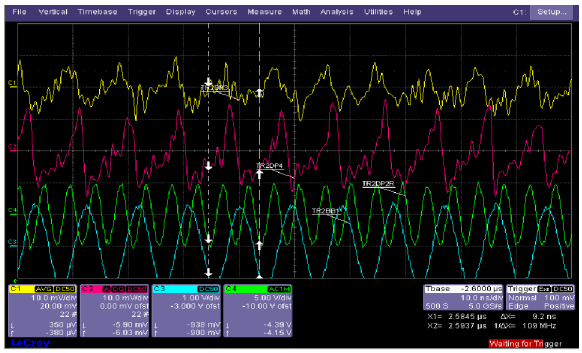

Fig. 2: Upper tracks show the two pick-up signals, lower tracks show rf-signals of 108 and 216 MHz bunchers

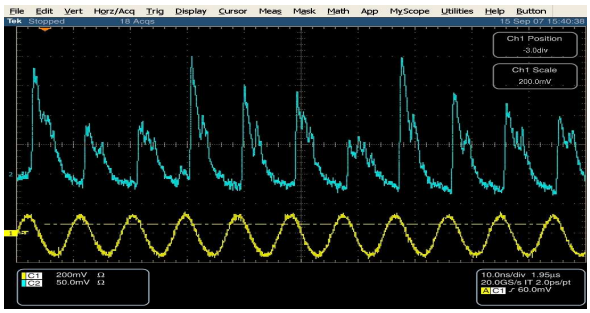

Fig. 3: 108 MHz bunches (upper track) measured with diamond detector and 108 MHz reference signal below

The diamond detector turned out as an excellent diagnostic tool to optimize the bunch length. The extended fall time of the bunch signals (Fig. 3) is an artefact due to amplifier discharge. The transverse emittance was measured by two methods, pepper pot and scintillation screen with quadrupole variation. The results of ε_{xrms}=1.57 and ε_{yrms}=6.69 mm·mrad are in agreement with calculations.

Conclusion

The beam measurements of the HITRAP DDB section confirm the expected performance to meet the parameters for the subsequent IH-decelerator tank, which will be installed in spring 2008.

References

[1] Th. Beier, et. al., HITRAP Technical Design Report, GSI Darmstadt, Germany, Oct. 2003

[2] O. Kester, et. al., The HITRAP decelerator facility GSI, GSI scientific report 2007

[3] P. Forck, et. al., Beam diagnostics for HITRAP, GSI scientific report 2007

[4] J. Pfister, et. al., Single-shot emittance measurements at HLI and HITRAP, GSI scientific report 2007

RF Maintenance & Diagnostics System

H. Klingbeil[1], K.-P. Ningel[1], and M. Kumm[1]
[1]GSI, Darmstadt, Germany

Introduction

In the scope of the FAIR project, several dozens of RF cavity systems will exist. The distances between them will be up to several hundred meters. Therefore, the maintenance effort has to be reduced for each system. Furthermore, monitoring of diagnostics information must be possible without a technician being present locally in the RF supply room.

Some of these tasks are addressed by the 'RF Maintenance & Diagnostics' project. It is dedicated to aspects which are not of interest for the central control system (these will of course be covered separately), but which allow RF personnel to detect and solve specific problems remotely.

Tasks

Modern accelerator RF systems rely on many programmable modules which are, e.g., based on Field Programmable Gate Arrays (FPGAs), Digital Signal Processors (DSPs) or Microcontrollers. This implies some actions which are required from time to time:

- Change of non-volatile operating parameters
- Exchanging firmware (only during shutdown periods)
- Acquisition of data (during machine operation) for offline analysis

These possibilities will be offered by the system under development. For safety reasons, maintenance and diagnostics functionality is separated from the functionality required for accelerator operation.

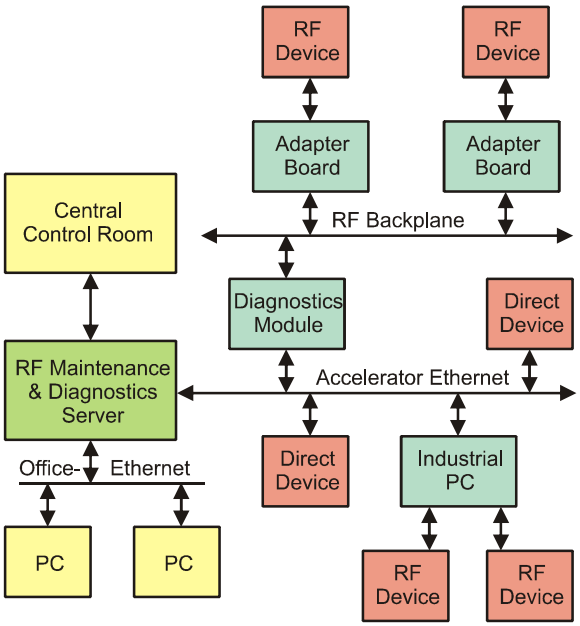

Figure 1: Preliminary Server Software

Server

A central RF diagnostics server will be used which manages all files (parameters and firmware) for the different programmable modules. Due to the large number of cavity RF systems mentioned before, and due to each system having a variety of programmable subsystems and modules, a software architecture had to be created which allows to handle module trees with an arbitrary number of modules in a comfortable way. This development is done by the company 3L Ltd in close collaboration with the GSI RF department.

Figure 1 shows a block diagram of the system under development. A first functional software package is already available. Currently, the focus is on the realization of a stable framework. A comfortable Graphical User Interface (GUI) will be realized later.

Hardware Modules

The above-mentioned server communicates with the hardware modules via Ethernet. Therefore, a so-called diagnostics module is required which forwards the Ethernet telegrams via the standardized RF backplane to the target hardware. The target hardware is connected to the RF backplane using an adapter board which provides a variety of standard interfaces (e.g., JTAG).

Figure 2: Maintenance and Diagnostics Hardware

These three components (diagnostics module, RF backplane, and adapter board) displayed in Fig. 2 (from left to right) are developed by Ubisys Technologies GmbH in close collaboration with the GSI RF department. Special care is taken to guarantee that firmware updates can be resumed after failures (e.g., due to power blackouts). By means of the adapter boards, each module is identified in a unique way to allow error tracking.

References

[1] H. Klingbeil, M. Kumm: 'Diagnostics Requirements of FAIR RF Systems', internal note, 2005.
[2] K.-P. Ningel: 'Specification RF-Maintenance & Diagnostics', internal note, 2008.

Realtime Communication Based on Optical Fibers for the Control of Digital RF Components

M. Kumm[1], T. Guthier[1], S. Sanjari[1], and M. Wess[2]
[1]GSI, Darmstadt, Germany; [2]University of Applied Sciences Fulda, Germany

Overview

The increasing use of digital components in closed-loop RF control systems requires a uniform interface for fast exchange of information between subsystems. The main requirements for such a communication system arise from large distances between the peers (up to several hundreds of meters), high data rates and short and predictable delays. Optical fibers in combination with Field Programmable Gate Arrays (FPGA) have been used to fulfill these demands. These will be used in two main applications: The distribution of parameters for the current acceleration cycle (interface to central control system) and the distribution of digital frequency signals with low latency (inter-DDS communication) as described in the last section.

Implementation

A multimode optical fiber system Agilent (former HP) Versatile Link has been used which has an optical wavelength of 650 nm (visible red light) with data rates up to 125 MBit/s. The use of integrated transmitter/receiver circuits allows a very compact design.

The encoding and decoding to and from a bit serial stream is processed in the FPGA on a multi-purpose FPGA Interface Board (FIB). Due to the requirement of low delays, a simple Manchester code has been implemented since no time consuming synchronization of the clock to the data stream (as with Ethernet) is desired. The decoding of the data stream (up to 50 MBit/s) is realized using a finite state machine (FSM) running at 250 MHz max. Two different links have been implemented to cover all applications, a point-to-point direct link which is used for fast realtime data, and a token ring which can address a large amount of peers with less realtime requirements.

The direct link implementation is very lightweight, since ony two startbits are used to mark the start of a packet. The latency of the point-to-point direct link implementation (including the interface electronic) is 70 ns (plus approximately 5 ns per meter fiber length).

The token ring implementation is a bit more sophisticated. Three startbits, one tokenbit and 8 addressbits are used to detect, occupy and route a packet. The beginning and the end of a packet are marked with an intentional Manchester code violation which is detected from the receiver. This allows different packet sizes on the same token ring for different applications without coding the packet length in the header. The latency for each FIB in the ring is 95 ns (plus approximately 5 ns per meter fiber length).

Applications

RF Control System

The FIB connects the "Modulbus backplane", which is a proprietary interface to the central control system, to those RF devices which are peers in the optical token ring. In the current implementation, up to 256 devices can be connected to the token ring running at 40 MBit/s. Additionally, the GSI timing interface (TIF) is connected to this board to allow switching between different configurations dependent on event and virtual accelerator. The current implementation controls the DSP system for the SIS18 cavity control.

Inter-DDS Communication

For SIS100, a multi-cavity beam phase control system is planned. The beam phase control measures the phase difference of the beam position monitor (BPM) with respect to the cavity RF and corrects the frequency of a Direct Digital Synthesizer (DDS) which is used as master RF oscillator for acceleration [1]. In the existing beam phase control for SIS18, the low-level systems are all installed at the same location. For SIS100, the low level systems are spread over at least three supply rooms which poses a serious problem. A simple coaxial cable between these supply rooms is problematic since temperature drifts and dispersion cause phase shifts in the reference signal. To overcome this problem, the digital Frequency Tuning Word (FTW) of the master DDS is transmitted over the optical direct link to several slave DDS units. The bunch phase timing system (BuTiS) [2] is used to clock the DDS and to synchronize the data. The transmission of a 32 bit FTW via an optical fiber of 1 km length, e.g., takes about 6 μs. The FTW from the master DDS is sent out on each rising clock of the BuTiS time reference of 100 kHz (10 μs period). On the next rising edge this FTW is taken over by both, master and slave DDS. A first implementation has been realized that shows the proof-of-concept.

References

[1] Harald Klingbeil, Bernhard Zipfel, Martin Kumm, and Peter Moritz, A Digital Beam-Phase Control System for Heavy-Ion Synchrotrons, IEEE TRANSACTIONS ON NUCLEAR SCIENCE, VOL. 54, NO. 6, December 2007, p.2604-2610

[2] Peter Moritz, BuTiS - Development of a Bunchphase Timing System, GSI Scientific Report 2006, June 2007, Darmstadt, Germany, p.64

Activities on the SIS18 Vacuum Upgrade *

M.C. Bellachioma[1], M. Bender[2], H. Kollmus[1], A. Krämer[1], J. Kurdal[1], and H. Reich-Sprenger[1]
[1]GSI, Darmstadt, Germany; [2]LMU, München, Germany

For the FAIR project the existing SIS18 will be the injector of the SIS100/300 and the Super-FRS. For this purpose it shall provide 10^{12} U^{28+} ions per second in a 4 Hz mode. One of the issues to achieve this high beam current is the improvement of the machine vacuum. One has to distinguish between the static pressure without beam and the dynamic pressure with beam and losses. Since the beam loss processes by charge exchange are self amplifying the dynamic pressure is amongst others dependent on the static pressure. Here we report on both activities: the realization of a higher distributed pumping speed and the minimization of the beam loss induced desorption.

Static Pressure - NEG coating

To minimize the static pressure pumping speed has to be distributed to locations such as the dipole or quadrupole chambers where lumped pumping is not possible. This is achieved by getter coating of the chambers with the pumping metal compound TiZrV called non-evaporable getter (NEG). A facility for the coating of the bent dipole chambers was set up and commissioned in 2006 [1]. In 2007 16 dipole chambers were coated and 15 of them installed in SIS18. Furthermore, a new facility was built up and commissioned successfully to coat straight vacuum chambers. The setup is similar to the one for the dipoles. It consists of 3 coils, each 1.7 m in length, for different chamber length up to 4.8 m and a diameter of 60 cm. A picture of the facility is shown in figure 1. One quadrupole chamber is already installed in the SIS18 though it was not coated in the GSI facility but at CERN. Nevertheless five beam pipes of a total length of 12 m have been coated in the new facility and installed.
In 2008 it is planned to coat and install the remaining 8 dipole chambers. Furthermore as many quadrupole chambers as can provided from the production will be coated and installed.

Dynamic Pressure - Collimator

In 2007 two beam loss collimators have been installed in the SIS18 (see C. Omet, this report). The aim is to collect charge exchanged beam ions controlled on a dedicated assembly of low desorbing material. In particular it was made out of oxygen-free high-conductivity copper coated with gold and a nickel layer in between as diffusion barrier. The collimators are *in-situ* bakeable to reduce the amount of adsorbats.

* We acknowledge the support of the European Community-Research Infrastructure Action under the FP6 "Structuring the European Research Area" program (DIRACsecondary-Beams, contract number 515873)

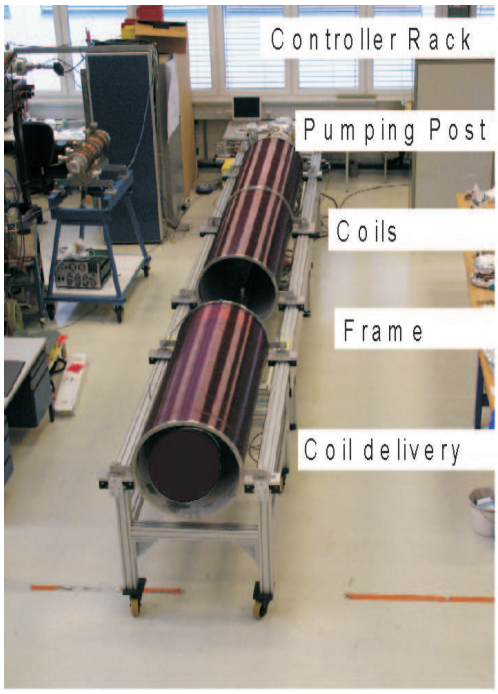

Figure 1: The new facility for the NEG coating of the quadrupole chambers

Furthermore, the collimator chambers consist of NEG coated anti chambers, where the coating was done at GSI. The systems have been installed and the machine experiments are pending.

Quality Control - Experiments

With the UHV ERDA and RBS setup we are able to investigate the quality of the NEG coatings [2]. Properties like the getter stoichiometry, film thickness and activation temperature can be measured. Furthermore, the activation and saturation of the NEG getters can be studied in a very detailed way. First qualitative experiments have been performed to visualize the pumping of CO as carbon and oxygen in a layer depth up to 0.5 μm. We expect to find correlations between the getter composition including the "contamination" with the pumped gas and the number of possible activation cycles of the getter coating. With upcoming experiments it will be possible to quantify possible activation cycles for best pumping performance.

References

[1] M.C. Bellachioma et al., GSI Annual Report 2006, p. 91

[2] M.C. Bellachioma et al., Vacuum 82, 2008, p. 435

Investigation on new Coatings and an in-situ Bake-Out for the SIS18 Beam Loss Collimators *

H. Kollmus[1], M. Bender[2], W. Assmann[2], R. Dörner[3], C. Halfpap[1], B. Kindler[1], A. Krämer[1], B. Lommel[1], and H. Reich-Sprenger[1]

[1]GSI Darmstadt, Germany; [2]LMU München, Germany; [3]Universität Frankfurt, Germany

For an optimal functionality and a high durability of the planned SIS18 beam loss collimators a low ion-induced desorption yield of the collimator material is required. Gold coated copper was found to be the material of choice: copper has a high thermal conductivity, a high specific heat and can be produced with high purity for reasonable prizes. The gold layer prevents the copper from oxidation. The influence of the oxidation on the desorption yield was reported to be significant [1]. But we have also shown that copper and gold diffuse during a typical UHV bake-out cycle [2]. In 2007 we have studied nickel diffusion barriers using Rutherford Backscattering Spectroscopy (RBS). As reported [3] desorption turned out to be predominately a surface effect with a strong link to the bulk properties. Additionally there was always a cleaning observed of the target under ion irradiation. The total amount of desorbed gas corresponds always to roughly one surface monolayer. To observe best cleaning of the target with 1.4 MeV/u Xe ions a flux of a few $1 \cdot 10^{13}$ ions per cm^2 is necessary. Since a beam cleaning of the loss regions in SIS18 is not possible we have tried to minimize the surface coverage by a special bake-out treatment of the target. The idea is to keep the target during UHV bake-out always higher in temperature compared to the environment in order to minimize the readsorption of gas on the surface.

Nickel Diffusion Barrier

To avoid diffusion of gold and copper, which is stimulated by the UHV bake-out procedure, nickel diffusion barriers were investigated using RBS. The measurements were performed with 1.4 MeV/u C ions. Using RBS we gain sensitivity to heavy elements compared to ERDA. Additionally, sensitivity and depth resolution are increased by a comparable heavy projectile like C with the disadvantage to lose any information about low Z target components. Fig. 1 shows the RBS spectra for a nickel-gold coating on copper before and after bake-out. The gold layer thickness is around 400 nm and the nickel layer is about 1 μm. Because of the total layer thickness of 1.4 μm the copper substrate is not detected before bake-out (Fig. 1, blue spectrum) due to the limited penetration depth of the C ions. The red spectrum shows the same sample after bake-out. Essentially the shape of the nickel distribution is changed since copper starts to diffuse across the nickel layer to the sample surface indicated by the dashed line. Additionally, the gold layer is broadened due to the diffusion of gold into nickel. However, the diffusion is strongly reduced compared to samples without diffusion layer [2]. Also complementary ERDA measurement with 1.4 MeV/u Xe ions have shown that under UHV conditions the surface remains as pure gold with sufficient low copper contamination. The desorption yield of this sample was measured to be initially 100 molecules per incoming ion, decreasing to less than 20 after an ion flux of about $1 \cdot 10^{13}$ ions per cm^2.

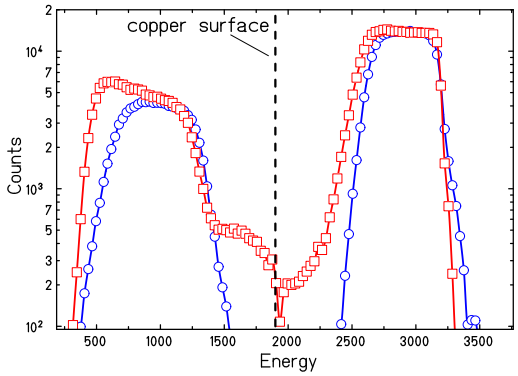

Figure 1: RBS profiles of a gold coated copper with a nickel diffusion barrier before (blue) and after (red) a bake-out for 17h at 250°C and 2.5h at 350°C.

In-situ Bake-Out

Supplementary to gold, rhodium coatings have been investigated. Like gold, rhodium does not oxidize with the advantage that the diffusion with copper is strongly reduced. Additionally we have tested if the initial surface coverage of the samples can be reduced by a special bake-out procedure. Therefore the two rhodium coated copper samples have been prepared identically but one was *in-situ* heated up to 350°C in an UHV environment and the other was kept at room temperature. Afterwards the desorption yields of both samples were measured. For the unbaked sample a desorption yield of around 1000 was observed, whereas the yield of the baked sample was reduced to 260 molecules per ion, resulting in essentially two consequences: First, rhodium is not suitable for a beam loss region due to the high desorption yield. Nevertheless, an *in-situ* bake-out of the loss regions in a good UHV environment can minimize the desorption similar to a cleaning by the ion beam. Therefore, one can expect to reduce the initial desorption of gold coated copper to around 20 molecules per incoming 1.4 MeV/u Xe ion.

References

[1] M. Bender et al., NIM B **256** (2007) p. 387-391
[2] M. Bender et al., GSI Annual Report 2006, p. 94
[3] H. Kollmus et al., Vacuum **82** (2007) p. 402-407

* We acknowledge the support of the European Community-Research Infrastructure Action under the FP6 "Structuring the European Research Area" program (DIRACsecondary-Beams, contract number 515873)

Model Calculations of Ion Induced Desorption Yields *

M. Bender[2], H. Kollmus[1], W. Assmann[2], R. Dörner[3], and H. Reich-Sprenger[1]
[1]GSI, Darmstadt, Germany; [2]LMU, München, Germany; [3]IKF, Frankfurt, Germany

The ion induced desorption is a severe luminosity limitation for low charge state heavy ion accelerators. Thus it was intensively investigated in dedicated experiments during the last years. It was shown that the ion induced desorption is a surface effect with a strong link to the substrate [1]. The overall quantity of desorbed gas during long term irradiation is always in the range of a monolayer (10^{15} cm^{-2}). From the geometrical cross section of the projectile desorption yields of $\eta \geq 100$ molecules per incident ion can not be explained. Therefore we have developed a theoretical model to describe the ion induced desorption as a thermally moderated process using the inelastic Thermal Spike Model.

The inelastic Thermal Spike Model has been developed to explain the processes of track formation and sputtering induced by heavy ions in energy ranges where the electronic energy loss is dominating [2]. First the projectile energy is deposited in the electronic subsystem of a sample. The hot electrons distribute the energy radially away from the ion path within typically 10^{-15} s. Especially in metals the free electrons moderate the energy deposition. After around 10^{-13} s the electronic system heats the lattice by electron-phonon coupling and after 10^{-10} s the sample approaches ambient temperature again.

A computer code to calculate the time dependent radial evolution of the temperature of the electronic system as well as the lattice of metals was developed years ago. We have extended this code to describe the ion induced desorption as a thermally moderated process in terms of

$$\frac{\partial^2 \eta}{\partial r \partial t} = \nu_0(T(r,t)) \cdot \tilde{n}(r,t) \cdot exp\left(-\frac{E_{des}}{k_B \cdot T(r,t)}\right) \quad (1)$$

where $\nu_0(T(r,t))$ is the oscillation frequency of the bound molecules, $\tilde{n}(r,t)$ is the surface coverage and the exponential term the number of the adsorbats that overcome the binding energy given by the Boltzmann distribution. In figure 1 the temperature evolution in space and time of a copper sample after a 1.4 MeV/u Xe impact is shown for the electronic and the lattice system. The influence of the ion impact is even visible in some 10 nm. This transient overheated spot leads to an enhanced thermal desorption shown in figure 2. Here the desorption per time is plotted against the circle segment of a certain radius. The most gas is desorbed from a radius of some nm around the projetiles impact and not from $r = 0$, where the highest temperature is reached but the total surface coverage is the lowest.

Some example values are compared to experimental numbers in the table to give an impression of the results of the calculation. Even the experimentally found (dE/dx)^2-scaling is reproduced by the model.

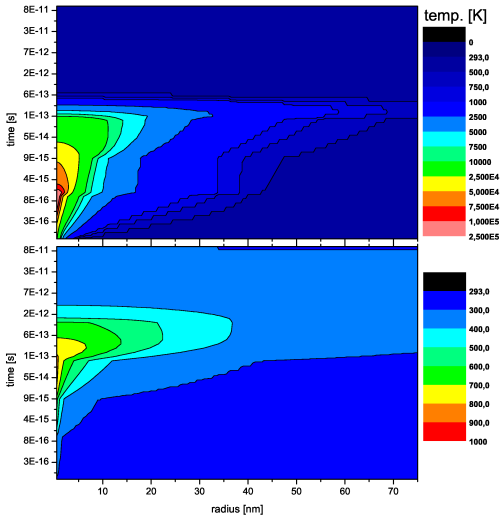

Figure 1: Temperature evolution of the electronic system (top) and the lattice (bottom)

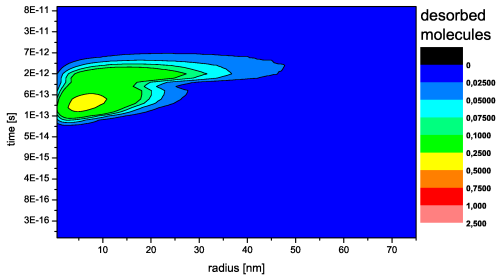

Figure 2: Desorption from one single projectile

Proj. (1.4MeV/u)	Xe	Xe	Xe	C	Pb	Pb (4.2MeV/u)
Target	Cu	Au	Rh	Cu	Cu	Au
Experiment	290	90	1280	10	800	800 (prel.)
Calculation	185	165	3400	5	525	750

In conclusion the extended inelastic Thermal Spike Model is the first approach to calculate ion induced desorption yields in the investigated energy regimes. Like measured in numerously experiments gold and copper show also the lowest desorption yields in the calculation and will thus be used as beam loss collimator materials.

References

[1] H. Kollmus et al., doi:10.1016/j.vacuum.2007.07.062
[2] Z.G. Wang et al., J. Phys.: Condens. Matter **6**, 6733 (1994)

* We acknowledge the support of the European Community-Research Infrastructure Action under the FP6 "Structuring the European Research Area" program (DIRACsecondary-Beams, contract number 515873)

BIF Profile Monitor for the UNILAC - Tests and DAQ Upgrade*

F. Becker[1], R. Haseitl[1], C. Andre[1], P. Forck[1], D.H.H. Hoffmann[1,2], and D. Pfeiffer[1]
[1]GSI Accelerator Beam Diagnostics, Darmstadt, Germany; [2]Technical University, Darmstadt, Germany

BIF experiments at UNILAC

The non-intercepting Beam Induced Fluorescence (BIF) monitor for transverse beam profile measurements was successfully tested for different ion species and energies from 5 to 750 MeV/u at the GSI accelerators [1]. Starting from its first implementation [2] we systematically investigated technical aspects such as the proper choice of optics and gain factors, as well as physical aspects like the dependency of beam energy and ion species on signal amplitude and the signal to background ratio. Investigations of the wavelength spectrum have shown that unwanted profile distortions by 2-step excitation processes have negligible contributions to the total photon yield [3]. At the UNILAC X2 experimental area a pressure dependent measurement was performed. With a regulated needle valve we changed the N_2 residual gas pressure from 10^{-6} to 10^{-3} mbar. Assuming constant beam parameters and within 1.6 σ according the fit function, the signal amplitude increases linearly with the gas pressure, while the profile width remains constant, as shown in Figure 1. Therefore the residual gas pressure can be used as a free parameter to match the required signal strength. Latest simulations of N_2^+ trajectories in the electrical field of the beam show negligible profile distortions, even for highest beam intensities in the upgraded UNILAC. For improved reliability, user-friendly operation and enhancend functional range, the DAQ-system and software are substantially upgraded.

* Work supported by EU, project FP6-CARE-HIPPI

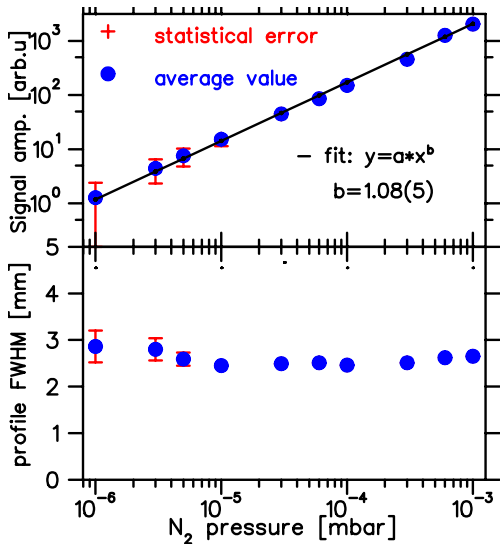

Figure 1: Pressure dependency of signal amplitude and profile width for 10^{10} Ni^{6+} ions per pulse in residual N_2.

Figure 2: National Instruments Compact Vision System & attached Firewire CCD camera and remote controlled iris.

DAQ System and Software

Since BIF shall be established as a standard measurement tool at GSI, a general purpose data acquisition and graphical user interface for CCD cameras is required. The GSI computing infrastructure makes extensive use of the Unix X-Window technology, being able to place the screen output of any software to any monitor in the main control room. For this purpose, a Linux-based software is under development to allow seamless integration into the present system. The firewire cameras are connected to a NI Compact Vision System (CVS) as seen in Figure 2, which is a small embedded system, purpose-built for graphical computing tasks. A broad featured LabVIEW [4] application has been developed for the CVS which receives images from connected cameras, performs image processing steps and holds a data connection via standard Ethernet to a Windows or Linux PC [5]. Available features on the CVS include histogram and projection calculation, image mirroring and rotation, dead pixel correction, image compression, region-of-interest cropping and perspective correction. Detailed performance tests are currently in progress. The CVS and the connected cameras can be controlled from the PC via XML commands. All data from the CVS is received and presented on the PC-side by C++ applications using Qt libraries [6] to provide platform independence for the GUI presentation.

References

[1] P. Forck et al., Proc. DIPAC'05, Lyon, p. 223 (2005).

[2] P. Forck, A. Bank, Proc. EPAC'02, Paris, p. 1885 (2002) and A. Bank, P. Forck, Proc. DIPAC'03, Mainz, p. 137 (2003).

[3] F. Becker, P. Forck, Proc. EPAC'06, Edinb., p. 1013 (2006) and F. Becker, P. Forck, Proc. DIPAC'07, Venice, (2007).

[4] Company National Instruments, www.ni.com

[5] Company Ingenieurbüro HAGEL, www.ib-hagel.de

[6] Company Trolltech, www.trolltech.com

Scintillation Screen Investigations at UNILAC

E. Gütlich, P. Forck, C. Andre, F. Becker, C. Dorn, H. Graf, R. Haseitl, GSI, Darmstadt, Germany

Scintillation screens are widely used since decades for beam profile measurement. Moreover, these screens are an essential part of a pepper-pot ermittance system used for the determination of the width of 'beamlets' created by a plate with many small holes [1, 2]. Within one single macro-pulse, the beam-emittance can be measured. However, there had been doubts concerning the accuracy of the pepper-pot method.

Therefore, we investigated the optical properties of 14 fluorescence materials with different beams delivered by UNILAC. Sensitive scintillation screens, like YAG or phosphor materials show saturation effects for the anticipated high beam currents. Ceramic materials with less light yield, like BN, ZrO_2, ZrO_2 doped with Mg, pure Al_2O_3 and Al_2O_3 doped with Cr ('Chromox') are investigated and compared to Quartz-glass ('Herasil 102') and Quartz-glass doped with Ce ('M382'). At cave X2 a movable target ladder equipped with 6 different screens of diameter 30 mm was installed to allow undisturbed beam observations. The scintillation is detected with a digital CCD camera (AVT-Marlin) equipped with a Firewire interface. The image of each macro-pulse is stored and individually evaluated by a high performance data acquisition system [3].

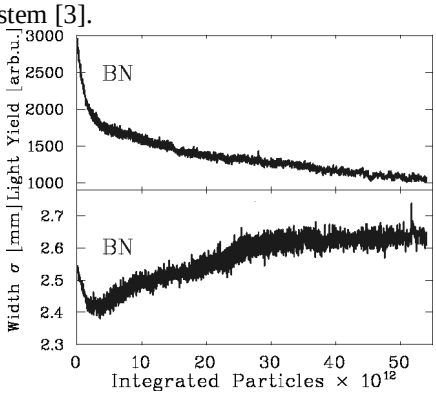

Figure 1: Light yield and beam width σ for BN target irradiated by 1800 macro-pulses of ≈3x10^{10} ppp Ar^{10+} at 11.4 MeV/u.

The various materials are irradiated with Ar^{10+}, Ni^{9+} and U^{28+} beams of energies between 5.5 and 11.4 MeV/u and different beam currents. In Fig. 1 an example is shown for the irradiation with a high current 11.4 MeV/u Ar-beam of about 3x10^{10} particle per pulse (corresponding to 0.5 mA and 100 µs pulse length): The light yield of the BN screen decreases rapidly within the 1800 pulses and the beam width increases significantly. This 10% increase is too small to be detectable with SEM-Grids and is of minor importance for regular beam alignment. However, for the pepper-pot method it results in an overestimation of the emittance value. The increase of the width is due to the irreversible destruction of the screen. As expected from investigations of BN at CERN [4], the previously white surface becomes grey. Similar surface modifications were observed for most ceramic materials with the least changes for ZrO_2 doped with Mg. The investigated Quartz-glass 'Herasil' shows no visible, permanent surface modification

For a lower current of 30 µA and 100 µs length of Ar^{10+} beam at 11.4 MeV/u, the light yield and the beam width for different materials are compared in Fig. 2. As expected, the investigated materials have up to two orders of magnitude different light yield (within 100 µs beam delivery) with 'Chromox' being the most and ZrO_2 the least sensitive material. However, the determined beam width differs in a reproducible manner between the materials: For the given beam parameters Quartz-glass shows about 20% smaller width compared to ZrO_2 doped with Mg.

Presently, we are analysing the data to distinguish between saturation and self-absorbing of scintillation-light. Moreover, the light yield and the determined width depend on the screen temperature, which is significantly increased by the beam impact. Further systematic results for various materials and different ion beams are described in [5] to find an appropriate material for the pepper-pot emittance device.

We acknowledge the valuable discussion with T. Sieber and M. Frauenfeld from MPI-Kernphysik, Heidelberg.

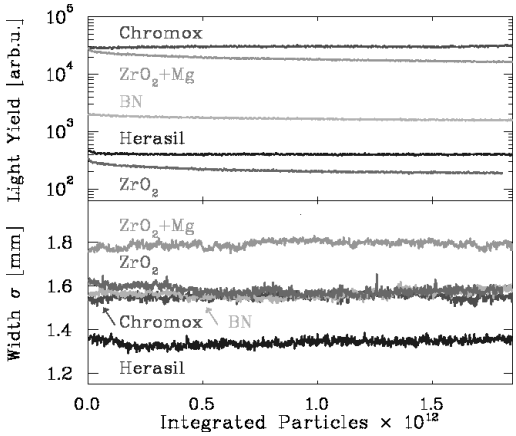

Figure 2: Light yield and beam width for different materials irradiated by 1000 macro-pulses of ≈2x10^{9} ppp Ar^{10+}.

References

[1] T. Hoffmann et al, Proc. Beam Instrum. Workshop AIP 546, p.432 (2000).
[2] J. Pfister et al., this GSI Scientific Report 2007.
[3] F. Becker et al., this GSI Scientific Report 2007.
[4] C. Bal et al., Proc. DIPAC05, p.57 (2005).
[5] E. Gütlich, Diploma Thesis, University of Applied Science Wiesbaden, and E. Gütlich, P. Forck, Proc. Beam Instrum. Workshop 2008, to be published.

Beam Diagnostics for HITRAP

C. Andre, S. Borger, R. Boywitt, L. Dahl, C. Dorn, R. Fischer, P. Forck, H. Graf, M. Hartung, W. Kaufmann, O. Kester, H. Reeg, M. Witthaus, GSI, Darmstadt, Germany

Overview

For the HITRAP beamtime in May and August 2007 [1] several beam-diagnostic devices were launched and used for the first time. The aim of the experiment was to extract the beam from the ESR into HITRAP and to guide it to the pepperpot- and diamond-detectors at the end of the beam-line. Due to the low beam current expected for HTRAP, miscellaneous measurement devices were used to ensure a proper beam detection along the beam-line.

Hardware Setup

The HITRAP beam-line from ESR to the RFQ location is currently equipped with 3 Faraday Cups (FC). A current-amplifier (femto DHPCA-100) is used offering sufficient band-width for the time structure estimation of the extracted pulse length. The amplifier range setting is controlled by LabVIEW. The analogue signals are monitored by a LeCroy 6030A oscilloscope. As for the time-dependent signals from the pick-ups, the oscilloscopes are controlled via remote desktop connection from the main control room.

A capacitive "tubular" pick-up with high-impedance termination is used in front of the first buncher for monitoring the time structure of extracted beam from the ESR After bunching the macro-pulse passes a first "time of flight" measurement section consisting of two successive capacitive pick-ups with 50 Ω termination suited for the 108 MHz bunch frequency. Signals from bunchers and pick-ups are displayed simultaneously and time-correlated by a LeCroy 6100A oscilloscope. The relation between buncher settings, coarse bunch shape and particle energy can be observed and matched in order to adjust the injection into the foreseen IH-Linac stage.

To monitor beam position and profile YAG scintillation screens with 35/70mm diameter are installed in 4 locations and observed by CCD cameras (Marlin F033B, Allied Vision Technology) equipped with an IEEE1394 interface. The data acquisition and the Graphical User Interface were programmed in LabVIEW. The software provides the raw image of the screen with an overlaid grid, as well as scaled projections of the beam in horizontal and vertical direction for each camera.

In addition, three secondary electron emission grid systems (SEM) are installed in the beam-line, operated by the standard control system. The pressure drives of FCs, SEM grids and scintillation screens are controlled by a standard console program via the GSI control system.

Results

In spite of the low HITRAP beam current, all beam diagnostic systems could detect and display adequate beam signals. The upper trace in Fig.1 shows the FC signal of

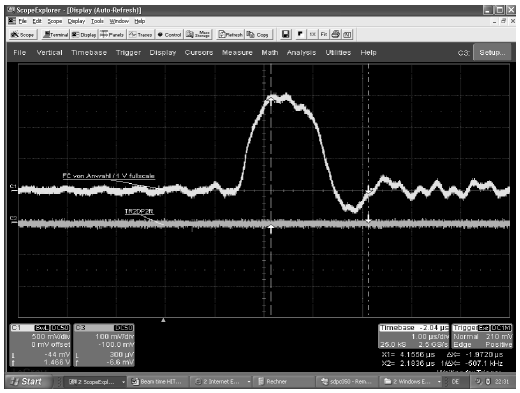

Fig. 1: FC signal (upper trace) recorded with 1 µs/Div and 0.5 µA/Div.

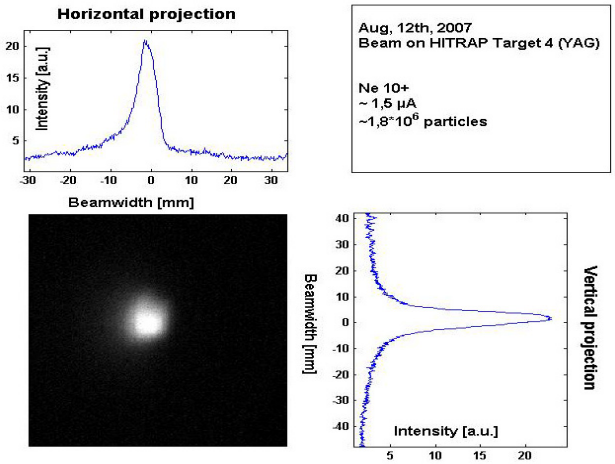

Fig. 2: Scintillation screen; Ne^{10+}, ~$1.8*10^6$ particles

a 1.5 µA Ne^{10+} beam.Fig. 2 shows an image of the scintillation screen and the calculated profiles in x-/y direction. The setup of the optical system and the screens were sensitive enough to acquire reasonable images for each individual shot. The beam profile information in dependence on the quadrupole lens setting have been used to estimate the beam emittance in the HITRAP double drift buncher section (DDB) to approximately $3 \cdot 10^{-6}$ mm mrad at 4 MeV/u.

Outlook

An additional FC, a scintillation screen and a SEM grid will be installed until the next beam time in July 2008 in parallel to the completion of the HITRAP beamline up to the RFQ.

References

[1] O. Kester et al., GSI-Scientific Report 2007.

Transverse Schottky and BTF Measurements in Intense Ion Beams in SIS18

S. Paret[1], V. Kornilov[1], O. Boine-Frankenheim[1], and T. Weiland[2]
[1]GSI, Darmstadt, Germany; [2]TEMF, TU Darmstadt, Germany

The intense beams to be accelerated by SIS18 for FAIR will be affected by collective effects. Due to the low energy in SIS18 the beams will be particularly prone to space charge effects. Since the dynamics of such beams is not fully understood collective effects are subject to our investigation. Here we present transverse Schottky and beam transfer function (BTF) measurements that were performed in February and October 2006 with intense coasting $^{40}Ar^{18+}$ beams in SIS18.

The BTF is defined as the response of a beam to a harmonic excitation and depends on the exciting frequency as well as on the momentum distribution of the ions. From the inverse of the BTF the stability limits of the beam can be evaluated and displayed in the stability diagram [1, 2]. The Schottky noise of the beam is commonly used to measure beam and machine parameters, e. g. the betatron tune.

The transverse ring impedance shifts the coherent betatron frequency of intense beams proportionally to the ion number. Normalizing this shift $\Delta\omega_\beta$ to the rms-width σ of a Schottky band yields a parameter $\chi = \frac{\Delta\omega_\beta}{\sigma}$ as a measure for the strength of collective effects. This parameter depends also on the frequency, the betatron tune and the momentum spread.

The tune shift manifests itself in a shift of the stability

Particles	$\frac{\delta p}{p}$	Q	χ_{est}	χ_{mes}
$7 \cdot 10^9$	$5.6 \cdot 10^{-4}$	3.33	0.60	0.68
$2 \cdot 10^9$	$6.7 \cdot 10^{-4}$	3.27	0.13	0.06

Table 1: Parameters of two beams used in our measurements. The energy was 11.4 MeV/u in both cases.

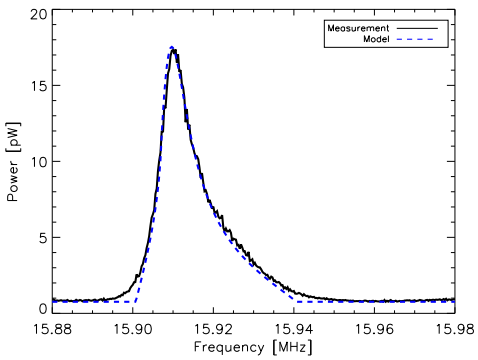

Figure 1: Vertical Schottky spectrum distorted by space charge. The model was fitted to the data assuming a parabolic momentum distribution. Beam parameters are given in the first row in Tab. 1.

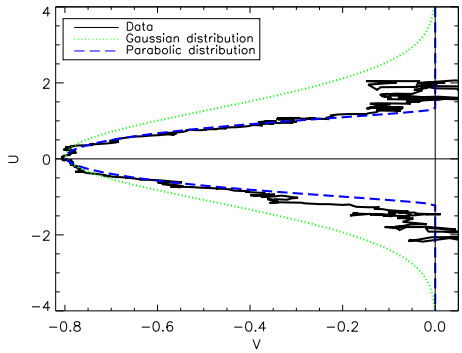

Figure 2: Stability diagram measured vertically at 21 MHz indicating a parabolic momentum distribution. This measurement corresponds to the second row in Tab. 1.

diagram and in a distortion of the BTF's amplitude and the Schottky bands [1, 3] thus allowing the measurement of χ. The adequate modelling of space charge is more complicated, even in the linear model applied here, because it acts incoherently on the beam [4]. Two different models are currently considered.

The largest impedances in the ring, stemming from the the kicker magnets and the resistive wall, could be neglected in our analysis. The impact of space charge χ_{est} was estimated using the momentum spread $\frac{\delta p}{p}$ and tune Q which were obtained from the Schottky measurements and the emittances measured with a rest gas monitor. The experimental value χ_{mes} results from a fit to the data. In Tab. 1 examples for beams used in our experiments are given. A Schottky band remarkably deformed by space charge and a stability diagram are shown in Fig. 1 and Fig. 2, respectively. The measured and estimated values of χ agree roughly.

Our experiments have demonstrated that Schottky noise allows the direct measurement of the space charge parameter. We have also confirmed that the tune can not be read directly from the position of the side bands of intense beams due to the space charge deformation. Further measurements and simulations are planned to answer open questions and to develop these diagnostics for the high-current operation of SIS18 and SIS100.

References

[1] J. Borer et al., IEEE Trans. on Nuclear Science, NS-26 (1979)
[2] V. Kornilov et al., GSI-Acc-Note-2006-12-001 (2006)
[3] S. Chattopadhyay, CERN 84-11 (1984)
[4] K. Y. Ng, FERMILAB-FN-0760-AD (2004)

Integration of an Industrial Motion Controller into the GSI Accelerator Control System

K.Herlo, R. Boywitt, S. Schumacher
GSI, Darmstadt, Germany

As part of the SIS18 upgrade program a new injection septum will be installed. Both septum electrodes can be adjusted by stepping motors. Two motors per plate allow fine adjustment including tilting the plates to some degree. Remote positioning via the accelerator controlsystem is desired to allow fine tuning from the main control room.

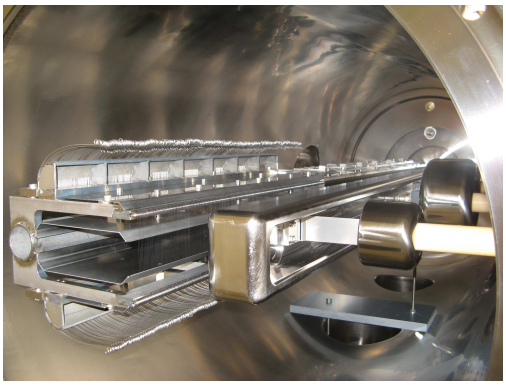

Figure 1: Injection Septum

When moving the motors, only small skew angles are allowed. Too big differences in the positions of both motors of a plate will result in stress on the ceramic bearings which then may brake.

The standard stepping motor controller in the GSI accelerators unfortunaltely can handle only one motor at a time. When used to drive a septum plate, both motors have to be moved alternatively stepwise to always assure small skew angles: A cumbersome and error-prone process.

Presently, the control system's communications middleware is rebuild to overcome the limitation to the original proprietary front-end platform, which is VME CPUs with MIL-Bus device interfaces. A newly develpoped device manager, using CORBA as communication middleware, replaces present day's MOPS, the system software on the VME master controller (see Figure 2). While it allows integration of the existing equiment adaption software, it can be used on any Linux, or Windows computer.

The new controls middleware allowed integration of a commercial stepping motor controller for the septum, Cosylabs [1] MicroIOC-M-Box.

It combines Delta Tau's [2] versatile multi axis stepping motor controller with an embedded CPU, running Linux. The motor controller supports up to eight motors and can drive each of them independently and simultaneously. It allows parallel movement of the septum motors and also provides online checking of the skew angle limitations.

Cosylab upgraded its MicroIOC-M-Box by an extension box, containing power drivers for GSI's stepping motors, which also transmits end switch and position encoder data.

The MicroIOC-M-Box was integrated on network level into the control system, replacing the present GμP/SE VME controllers. The GNU software development system was installed for the MicroIOC CPU, and the external components of the renovated front-end communication layer software, like the OmniORB CORBA ORB, were prepared for the MicroIOC. Then the new front-end controls software, the device manager, could be installed on the M-Box.

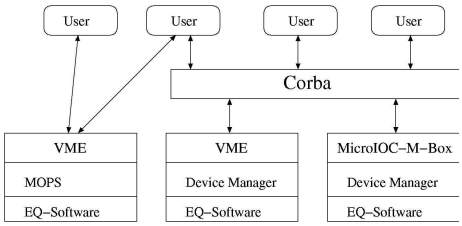

Figure 2: Control system

For presentation of the septum motors, a new specific equipment model was developed. It assures parallel movement of both motors of each plate and allows adjustment of both plates independently. Security checks prevent from large skew angles.

Figure 3: MicroIOC-M-Box-PMAC

The septum motor device can be accessed in the same way as any other device in the accelerator control system. However, being one of the first devices connected by the renovated network communication, it can be accessed directly from Linux, and Windows computers.

The new septum motor control is ready to be installed in the GSI accelerator environment. It is a major step towards a flexible controls environment, allowing to integrate a wide range of equipment hardware.

References

[1] http://cosylab.com
[2] http://www.deltatau.com

First observation of the unbound nuclei ^{12}Li and ^{13}Li *

Yu. Aksyutina[1], H.T. Johansson[1,2], L.V. Chulkov[1,3], H. Simon[1], P. Adrich[1,4], T. Aumann[1], K. Boretzky[1], M.J.G. Borge[5], D. Cortina-Gil[1], U. Datta Pramanik[1], Th.W. Elze[6], H. Emling[1], J. Fernandez-Vasquez[1], C. Forssén[2], H. Geissel[1], M. Hellström[1], K.L. Jones[1], B. Jonson[2], A. Kliemkiewicz[1,4], J.V. Kratz[7], R. Kulessa[4], M. Lantz[2], Y. Leifels[1], E. Lubkiewicz[4], K. Markenroth[2], M. Matos[1], M. Meister[1,2,8], G. Münzenberg[1], F. Nickel[1], T. Nilsson[2], G. Nyman[2], R. Palit[6], M. Pantea[8], V. Pribora[3], R. Reifarth[1,6], A. Richter[8], K. Riisager[9], Ch. Scheidenberger[1], G. Schrieder[8], J. Stroth[1,6], K. Sümmerer[1], O. Tengblad[5], E. Wajda[4], W. Walus[4], and M.V. Zhukov[2]

[1]Gesellschaft für Schwerionenforschung (GSI), D–64291 Darmstadt; [2]Fundamental Fyzik, Chalmers Tekniska Högskola, S–412 96 Göteborg, Schweden; [3]Kurchatov Institute, RU–123182 Moscow, Russia; [4]Instytut Fizyki, Uniwersytet Jagelloński, PL–30-059 Krakau, Polen; [5]Insto. Estructura de la Materia, CSIC, E–28006 Madrid, Spanien; [6]Institut für Kernphysik, Johann-Wolfgang-Goethe-Universität, D–60486 Frankfurt; [7]Institut für Kernchemie, Johannes Gutenberg-Universität, D–55099 Mainz; [8]Institut für Kernphysik, Technische Universität Darmstadt, D–64289 Darmstadt; [9]Institut for Fysik og Astronomi, Aarhus Universitet, DK–8000 Aarhus C, Dänemark

Nucleon knockout reactions using ^{11}Li and ^{14}Be secondary beams at relativistic energies were studied experimentally at the ALADIN-LAND setup. In the ^{10}Li break up channel, the results of earlier experiments using C target are confirmed by new data taken with hydrogen target. The two isotopes ^{12}Li and ^{13}Li are observed for the first time.

Radioactive beams of ^{11}Li and ^{14}Be (280 and 304 MeV/u) were produced by fragmentation of ^{18}O beams (308 and 360 MeV/u) on a thick Be target. Separated through the magnetic field in the FRS, secondary beams were directed to a liquid hydrogen target, situated in front of the large-gap dipole magnet spectrometer ALADIN.

The charge of the reaction fragments was determined by means of their specific energy loss in pin-diodes and in a scintillator time-of-flight wall. Their mass number is obtained analyzing their magnetic rigidity. Neutrons were detected with the large area neutron detector LAND. As all reaction products are identified, their four-momenta are reconstructed and the invariant mass (IM) spectra obtained.

In the one neutron knockout channel from ^{11}Li we observe its unbound ^{10}Li subsystem. The obtained spectrum is very similar to the one from our previous experiment using a C target[1]. After proton removal from ^{14}Be we observe ^{11}Li in coincidence with one or two neutrons.

The corresponding IM spectra (Fig.1) were fitted with a sum of contributions from resonances with Breit-Wigner shapes. For events, where only one neutron is registered in LAND, the lowest lying state, which is assumed to be an *s*-state, is treated as virtual state and its cross-section is described by Eq.[20] of Ref.[2]. One of the free fit parameters, the neutron separation energy in the mother nucleus, can be effectively used as a consistency check for the model. The binding energies obtained for ^{11}Li 0.352(13) MeV and for ^{14}Be 1.40(13) MeV are equal to the known values: 0.376 MeV and 1.36 MeV, respectively.

After one proton removal from the core of the halo nucleus, the energy correlations of the break up fragments are related to the ground state distribution for the projectile. This distribution, without inclusion of any final state interactions, is included [3] as a background contribution in the experimental spectrum for the case when two neutrons are detected in LAND.

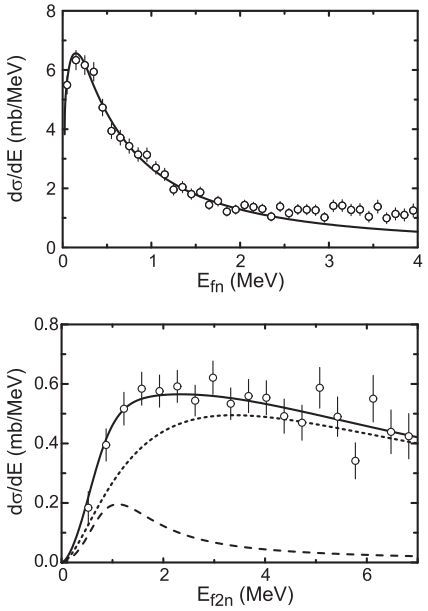

Figure 1: The ^{12}Li IM spectrum (upper panel) is described in terms of a *s*-state with scattering length a= -11(1) fm, while the ^{13}Li IM spectrum (lower panel) is superposition of a correlated background (dotted line) and a broad Breit-Wigner resonance with E=1.47(0.35) MeV and $\Gamma \approx 1 \div 3$ MeV (dashed line)

.

References

[1] H. Simon et al, Nucl. Phys. **A 791** (2007) 267

[2] G.F. Bertsch et al, Phys. Rev. **C 57** (1998) 1366

[3] C. Forssén et al, Nucl. Phys. **A 673** (2000) 143

* Supported by the BMBF No. 06 DA 115, No. 06 OF 838 and No. 06 MZ 864 I and by GSI No. DA RICK, No. OF ELZ, No. MZ KRAK

Discovery of two-proton radioactivity of ^{19}Mg by tracking the decay products*

I. Mukha[†1,2], K. Sümmerer[3], L. Acosta[4], M. A. G. Alvarez[1], E. Casarejos[5], A. Chatillon[3], D. Cortina-Gil[5], J. Espino[1], A. Fomichev[6], J. E. García-Ramos[4], H. Geissel[3], J. Gómez-Camacho[1], L.V. Grigorenko[2,3,6], J. Hoffmann[3], O. Kiselev[3,7], A. Korsheninnikov[2], N. Kurz[3], Yu. Litvinov[3], I. Martel[4], C. Nociforo[3], W. Ott[3], M. Pfützner[8], C. Rodríguez Tajes[5], E. Roeckl[3], M. Stanoiu[3,9], H. Weick[3], and P. J. Woods[10]

[1]Universidad de Sevilla, Spain; [2]RRC "Kurchatov Institute", Moscow, Russia; [3]GSI, Darmstadt, Germany; [4]Universidad de Huelva, Spain; [5]Universidade de Santiago de Compostela, Spain; [6]Joint Institute for Nuclear Research, Dubna, Russia; [7]Johannes Gutenberg Universität, Mainz, Germany; [8]IEP, Warsaw University, Poland; [9]IFIN-HH, Bucharest, Romania; [10]University of Edinburgh, UK

We have observed the two-proton radioactivity of the previously unknown ^{19}Mg ground-state (gs) by tracking the decay products in-flight. Three-body model calculations have predicted this decay to have a half-life between 0.5 and 60 ps with a Q-value ranging from 0.55 to 0.85 MeV [1]. Details of the experiment and the analysis procedure have been published recently [2]. A primary beam of ^{24}Mg was converted into ^{20}Mg and separated in the GSI fragment separator, FRS. The 1n knock-out reaction in a secondary ^{9}Be target placed at the FRS midplane formed ^{19}Mg which decayed in flight into ^{17}Ne and two protons. The trajectories of the decay products were measured by using tracking micro-strip detectors which allowed to reconstruct the 2p-decay vertices and fragment correlations.

Due to the finite vertex-reconstruction resolution, the delayed vertex stemming from a finite life-time of the ^{19}Mg gs decay cannot simply be extracted by gating on breakup events downstream from the target, as indicated in Fig.1a. Instead, the vertex distribution along the beam direction has been simulated by varying the life-time of ^{19}Mg, taking into account the vertex-reconstruction resolution as a function of the 2p-decay Q-value. The dashed line in Fig.1b shows a vertex distribution resulting from prompt decays inside the target; this curve nicely coincides with data from ^{17}Ne+2p events with *large* Q-values, where prompt decay is expected. The data points in Fig.1c finally represent a vertex distribution gated on *low* Q-values corresponding to the ^{19}Mg gs decay. As the dashed curve in Fig.1c shows, a simulation with $T_{1/2} = 0$ does not well represent the data points. An optimum fit is obtained if a finite life-time of 4 ps is used in the simulation; here a 25% contribution of a prompt background has to be taken into account [2]. By plotting the fit probability as a function of half-life, a ^{19}Mg half-life of 4.0(15) ps in the system of ^{19}Mg has been derived, which fits nicely to the predictions of Ref. [1].

Since the proton angular distributions and the p-^{17}Ne relative energies are closely related [2], the Q-value of the 2p-decay of the ^{19}Mg ground-state can be inferred from the measured p–p–^{17}Ne angular correlations. This Q-value amounts to 0.75(5) MeV, again in good agreement with the predictions of the three-body model [1].

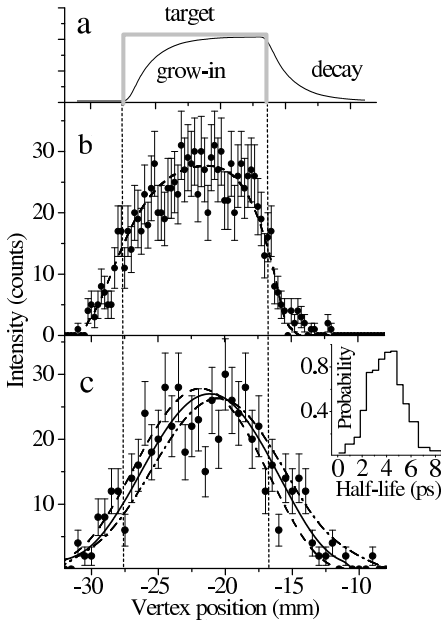

Figure 1: Profiles of the reaction vertices along the beam direction with respect to the closest micro-strip detector. a) Ideal profiles of prompt (grey curve) and delayed (black curve) decays expected in a thick target. b) Vertex distribution of ^{17}Ne+p+p events corresponding to short-lived excited states in ^{19}Mg. The dashed curve shows the Monte Carlo simulation of the detector response for the 2p-decay ^{19}Mg$^{*} \rightarrow ^{17}$Ne+p+p with $T_{1/2}$=0. c) The same as b) but corresponding to the ground state of ^{19}Mg. The dashed curve depicts a simulation of the 2p-decay component with $T_{1/2}$=0. The solid and dash-dotted curves are fits to the data assuming a mixture of 25% of the $T_{1/2}$=0 component and 75% of the radioactivity component with $T_{1/2}$ values of 4 and 8 ps, respectively. The insert shows the probability (as a function of the assumed half-lives) that the simulations match the data. For more details, see Ref. [2].

With the described technique, a search for other 2p-emitters, e. g., ^{30}Ar, ^{34}Ca is feasible at FRS [2].

References

[1] L.V. Grigorenko *et al.*, Nucl. Phys. **A713**, 372 (2003).

[2] I. Mukha *et al.*, Phys. Rev. Lett. **99**, 182501 (2007).

* Work supported by EU, EURONS contract No. EC-I3.

† mukha@us.es

Observation of Non-Exponential Orbital Electron Capture Decays of Hydrogen-Like ^{140}Pr and ^{142}Pm Ions

Yu.A. Litvinov[1,2], F. Bosch[1], H. Geissel[1,2], N. Winckler[1,2], D. Boutin[1,2], H.G. Essel[1], T. Faestermann[3], S. Hess[1], P. Kienle[3,4], R. Knöbel[1,2], C. Kozhuharov[1], J. Kurcewicz[1], L. Maier[3], K. Beckert[1], P. Beller*[1], C. Brandau[1], L. Chen[2], C. Dimopoulou[1], B. Fabian[2], A. Fragner[4], E. Haettner[2], M. Hausmann[5], S.A. Litvinov[1,2], M. Mazzocco[1,6], F. Montes[1,5], A. Musumarra[7,8], C. Nociforo[1], F. Nolden[1], W.R. Plaß[2], A. Prochazka[1], R. Reda[4], R. Reuschl[1], C. Scheidenberger[1,2], M. Steck[1], T. Stöhlker[1,9], S. Torilov[10], M. Trassinelli[1], B. Sun[1,11], H. Weick[1], and M. Winkler[1]

[1]GSI, Darmstadt, Germany; [2]JLU Gießen, Germany; [3]TU München, Germany; [4]SMI Vienna, Austria; [5]MSU East Lansing, U.S.A.; [6]INFN Padova, Italy; [7]INFN Catania, Italy; [8]Universitá di Catania, Italy; [9]RKU Heidelberg, Germany; [10]St. Petersburg University, Russia; [11]Peking University, China

We continued to investigate two-body beta decay of stored, highly-charged ions by single-ion decay spectroscopy at the example of H-like ^{140}Pr and ^{142}Pm ions. For this purpose bunches of $^{140}Pr^{58+}$ and $^{142}Pm^{60+}$ ions, containing on average two parent ions, were produced in the FRS (start of the "clock"), in-flight separated and then injected into the ESR at an energy of 400 MeV per nucleon. Their velocity spread was reduced within 6-10 sec by stochastic and electron cooling to a value of $\Delta v/v \approx 5 \cdot 10^{-7}$.

The 30^{th} harmonics of the revolution frequency of about 2 MHz was measured by the Fourier frequency analysis of the signals induced by the coasting ions at each revolution in pick-up plates. For cooled ions f is uniquely related to the mass-over-charge ratio M/q of the stored ions, which is the basis for the Schottky mass measurements. Thus the ions of interest and their decay products could be unambiguously identified.

The analysis was done by inspection of each spectrum taken as a function of time. Then the time of appearance of a daughter nucleus following the decay of its mother was determined. Only the times of the appearance of the daughter nuclei were considered, which are delayed compared to the decay of the mother ion by about 900±300 msec.

An example of obtained results is shown in Figure 1. The time of the injection into the ESR is within 1 μs the time of the creation of the ions. The data were fitted with the exponential decay function (solid line). It is clear to see that the expected exponential decrease of the EC-decays as a function of time shows a superimposed periodic time modulation (dashed lines). The extracted periods of the modulation are 7.06(8) sec and 7.10(22) sec (laboratory frame) for ^{140}Pr and ^{142}Pm ions, respectively. The details on the experimental setup, data analysis, fit results, and a short discussion of a possible origin of this modulation can be found in Ref. [1].

The observed periodic modulations of the expected exponential decrease still suffer from restricted statistics. However, the "zero hypothesis" of a pure exponential decay can be already rejected according to the χ^2/DoF-values on the 99% confidence level for both investigated nuclear systems [1].

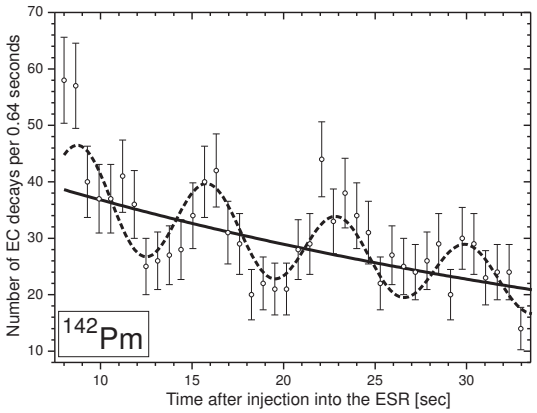

Figure 1: Number of EC-decays of H-like ^{142}Pm ions per 0.64 seconds as a function of the time after the injection into the ring (first 33 seconds). The solid and dashed lines represent the exponential decay fit with and without superimposed cosine function, respectively.

A possible interpretation of the modulations can be due to the properties of the electron neutrino that is generated in the EC-decay as a coherent superposition of at least two mass eigenstates. This possibility is meanwhile extensively discussed in literature [2, 3, 4]. Being different in detail, all the theoretical explanations show that the modulation period - assuming that the modulation is real and is related to the emitted neutrinos - should be sensitive to the nuclear mass. We have to note also critical opinions as e.g. Ref. [5]

References

[1] Yu.A. Litvinov et al., *arXiv:0801.2079 [nucl-ex]*.

[2] H.J. Lipkin, *arXiv:0801.1465 [hep-ph]*.

[3] A. Ivanov, R. Reda, P. Kienle, *arXiv:0801.2121 [nucl-th]*.

[4] M. Faber, *arXiv:0801.3262 [nucl-th]*.

[5] C. Giunti, *arXiv:0801.4639 [hep-ph]*.

* 25.07.2006 deceased

Measurement of the β^+ and orbital electron-capture decay rates in fully-ionized, hydrogen-like, and helium-like ^{140}Pr ions

Yu.A. Litvinov[1,2], F. Bosch[1], H. Geissel[1,2], J. Kurcewicz[1], Z. Patyk[3], N. Winckler[1,2], L. Batist[4], K. Beckert[1], D. Boutin[1,2], C. Brandau[1], L. Chen[2], C. Dimopoulou[1], B. Fabian[2], T. Faestermann[5], A. Fragner[6], L. Grigorenko[7], E. Haettner[2], S. Hess[1], P. Kienle[5,6], R. Knöbel[1,2], C. Kozhuharov[1], S.A. Litvinov[1,2], L. Maier[5], M. Mazzocco[1,8], F. Montes[1,9], G. Münzenberg[1], A. Musumarra[10,11], C. Nociforo[1], F. Nolden[1], M. Pfützner[12], W.R. Plaß[2], A. Prochazka[1], R. Reda[6], R. Reuschl[1], C. Scheidenberger[1,2], M. Steck[1], T. Stöhlker[1,12], S. Torilov[13], M. Trassinelli[1], B. Sun[1,14], H. Weick[1], and M. Winkler[1]

[1]GSI, Darmstadt, Germany; [2]JLU Gießen, Germany; [3]TU München, Germany; [4]NPI St. Petersburg, Russia; [5]TU München, Germany; [6]SMI Vienna, Austria; [7]JINR Dubna, Russia; [8]INFN Padova, Italy; [9]MSU East Lansing, U.S.A.; [10]INFN Catania, Italy; [11]Universitá di Catania, Italy; [12]University Warsaw, Poland; [12]RKU Heidelberg, Germany; [13]St. Petersburg University, Russia; [14]Peking University, China

Radioactive ^{140}Pr ions have been produced via the projectile fragmentation of $\sim 3 \cdot 10^9$ ^{152}Sm ions/spill in a 1 g/cm^2 thick Be target. The fully-ionized, H- and He-like ^{140}Pr ions were separated in-flight with the Bρ-ΔE-Bρ separation method in the FRS and injected into the ESR. In the ESR they were cooled by stochastic and electron cooling to $\delta v/v \approx 5 \cdot 10^{-7}$. The unambiguous identification of cooled ions and their decay products has been done with the time-resolved Schottky Mass Spectrometry [1].

Several decay measurements of ^{140}Pr^{59+}, ^{140}Pr^{58+}, and ^{140}Pr^{57+} ions have been performed which have presented consistent results [2]. The averaged values for the λ_{EC} and λ_{β^+} decay constants are presented in Table 1.

The striking result is - in spite of the fact that the number of orbital electrons is *reduced* from two in ^{140}Pr^{57+} ions to only one in ^{140}Pr^{58+} ions - that the EC-rate *increases* by a factor of 1.49(8) [2]. Moreover, the half-life of H-like ^{140}Pr^{58+} ions ($T_{1/2}$ = ln(2)/λ = 3.04(9) min) is shorter than in the neutral atom ($T_{1/2}$ = 3.39(1) min).

Our result can be explained by taking into account the conservation of total angular momentum of the nucleus-lepton system. In the initial state (i), the total angular momentum $F_i = I_i \pm s$ of a ^{140}Pr nucleus with spin $I_i = 1$ and a single K-electron with spin $s = 1/2$ can have two values $1/2$ and $3/2$ as schematically shown in Fig. 1. In the final state (f), however, there is only one value, $F_f = 1/2$,

Table 1: Measured β^+ and EC decay constants obtained for fully-ionized, H- and He-like ^{140}Pr ions. The values are given in the rest frame of the ions.

Ion	λ_{β^+} $[s^{-1}]$	λ_{EC} $[s^{-1}]$
^{140}Pr^{59+}	0.00158(8)	—
^{140}Pr^{58+}	0.00161(10)	0.00219(6)
^{140}Pr^{57+}	0.00154(11)	0.00147(7)

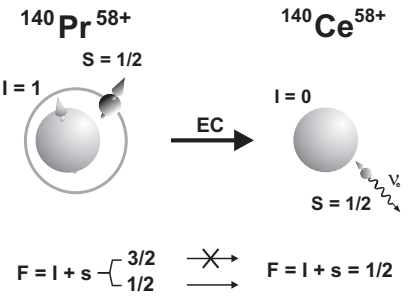

Figure 1: Illustration of the EC decay of the H-like ^{140}Pr^{58+} ions to bare ^{140}Ce^{58+} ions.

which is the sum of the zero angular momentum of the ^{140}Ce nucleus $I_f = 0$ and of the spin $s = 1/2$ of the emitted electron-neutrino. Hence, only transitions from the $F_i = 1/2$ hyperfine state can contribute to the allowed decay. The decay from the $F_i = 3/2$ state would require that the emitted neutrino carries away two units of orbital angular momentum.

A systematic theoretical study of EC decay rates for H- and He-like ions dependent on the nuclear spins can be found in Ref. [3]. In the case of ^{140}Pr only one F_i-state contributes to the decay and the EC-decay rate depends on the ratio of the statistical weights of the transition, i. e. $(2I_i+1)/(2F_i+1)$=3/2, which agrees with our experimental result. Our results were also confirmed within about 3% by detailed calculations in Ref. [4].

References

[1] Yu.A. Litvinov et al., Nucl. Phys. A **756**, 3 (2005).

[2] Yu.A. Litvinov et al., Phys. Rev. Lett. **99** (2007) 262501.

[3] Z. Patyk et al., Phys. Rev. **C 77** (2008) 014306.

[4] A.N. Ivanov, M. Faber, R. Reda, and P. Kienle, Phys. Lett. B, *in press* (2008); *arXiv:nucl-th/0711.3184*.

Discovery of new isotopes and isomers with Schottky Mass Spectrometry in the heavy neutron-rich region

L. Chen[1,2], H. Geissel[1,2], Yu. A. Litvinov[1,2], W. R. Plaß[1,2], C. Scheidenberger[1,2], K. Beckert[1], P. Beller[1], F. Bosch[1], D. Boutin[1,2], I. Cullen[3], B. Franzke[1], M. Hausmann[4], R. Knöbel[1,2], C. Kozhuharov[1], S. A. Litvinov[1,2], Z. Liu[3], F. Montes[4], G. Münzenberg[1], F. Nolden[1], Z. Podolyak[3], M. Shindo[5], M. Steck[1], B. Sun[1], P.M. Walker[3], H. Weick[1], and M. Winkler[1]

[1]GSI Darmstadt; [2]JLU Giessen; [3]Uni. Surrey; [4]MSU East Lansing; [5]Uni. Tokyo

Important progress with the Schottky Mass Spectrometry (SMS)[1, 2] mass and half-life measurements program at GSI has been made in the last year. In our 2004 SMS experiment a large area in the heavy neutron-rich region $82 \leq Z \leq 92$ has been investigated with relativistic ^{238}U projectile fragments at the FRS-ESR facility. The stored fragments in the ESR were cooled by electron cooling and measured with time-resolved SMS. 5 new isotopes (^{236}Ac ^{224}At, ^{221}Po, ^{222}Po and ^{213}Tl) and 6 new isomers (^{230m}Th, ^{234m}Ac, ^{228m}Fr, ^{213m}Bi, ^{214m}Bi and ^{204m}Pb) have been discovered for the first time in this experiment. The masses of 42 isotopes were measured for the first time. The masses of new isotopes and the excitation energies of new isomers were analyzed with the time-resolved SMS method.

Fig.1 and Fig.2 are examples of newly discovered isotopes and isomers. In Fig.1 the Schottky noise signals of the new isotope ^{222}Po is shown. ^{222}Po was identified in the upper plotted injection in Fig.1 while in the lower part another injection without ^{222}Po was plotted for comparison. The measured mass excess of ^{222}Po is 22490(40) keV in this experiment. Note in Fig.1 ^{222}Po, ^{222}At and ^{222}Ra are all single stored ions in ESR. In Fig.2 the pure isomeric

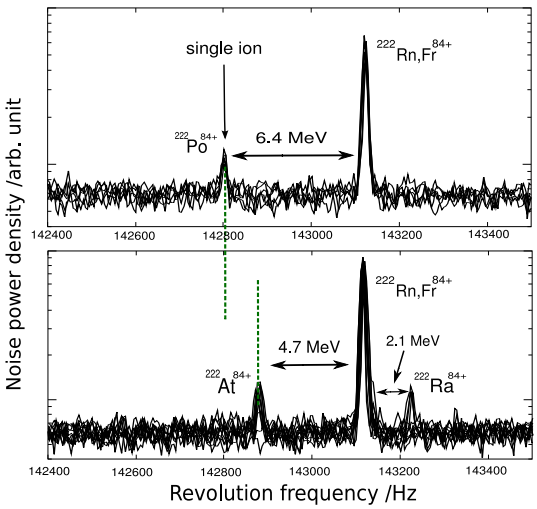

Figure 1: Schottky noise signals where the new isotope ^{222}Po is identified (upper plot). The lower plot shows another injection witout ^{222}Po but with ^{222}At. The strong peak is a mixture of ^{222}Rn and ^{222}Fr.

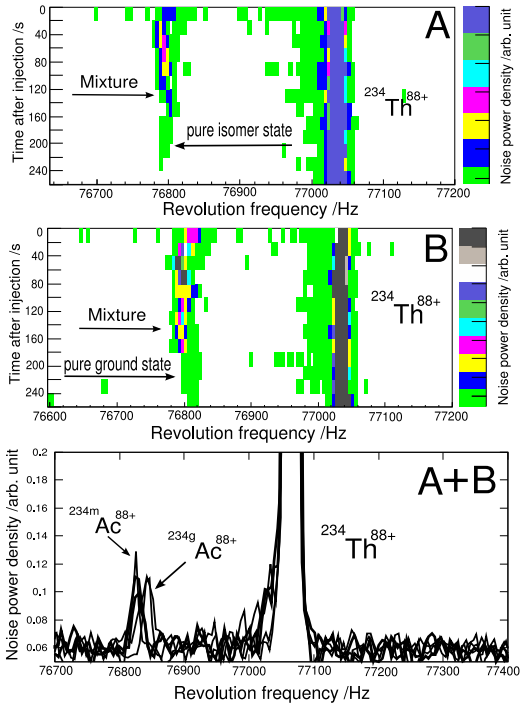

Figure 2: Schottky noise spectra in which the newly identified isomer ^{234m}Ac can be identified. The mixture in the picture means the mixture of ^{234m}Ac and ^{234g}Ac.

state ^{234m}Ac was observed in injection A after the loss of the ground state in ring while in injection B the isomeric state was lost first so the pure ground state was observed afterwards. Both injections in Fig.2 are plotted in the third panel (A+B) to show the small but clear frequency difference between the isomer state and the ground state. Besides the six new identified isomers, there are some isotopes where a long-lived isomeric state is strongly suggested by the observation of mixed ground state and isomeric state, though they can not be identified directly in this experiment. Two examples of those cases are ^{236}Pa and ^{232}Ac.

References

[1] T. Radon, et al. Nucl. Phys. A677 (2000) 75.

[2] Yu.A. Litvinov, et al., Nucl. Phys. A756 (2005) 3.

Isochronous mass measurements of uranium fission products

B. Sun[1,2], R. Knöbel[1,3], H. Geissel[1,3], Yu. A. Litvinov[1,3], K. Beckert[1], F. Bosch[1], D. Boutin[1,3], C. Brandau[1], L. Chen[3], I. Cullen[4], C. Dimopoulou[1], B. Fabian[3], M. Hausmann[5], O. Klepper[1], C. Kozhuharov[1], S. A. Litvinov[1,3], M. Mazzocco[1,6], F. Montes[5], G. Münzenberg[1], A. Musumarra[7,8], S. Nakajima[9], C. Nociforo[1], F. Nolden[1], T. Ohtsubo[10], A. Ozawa[11], Z. Patyk[12], W. R. Plaß[3], C. Scheidenberger[1,3], M. Steck[1], T. Suzuki[9], P. M. Walker[4], H. Weick[1], N. Winckler[1,3], M. Winkler[1], and T. Yamaguchi[9]

[1]GSI, Darmstadt, Germany; [2]Peking University, China; [3]JLU Gießen, Germany; [4]University of Surrey, U.K.; [5]MSU, East Lansing, U.S.A.; [6]INFN Padova, Italy; [7]INFN-LNS Catania, Italy; [8]Universitá di Catania, Italy; [9]Saitama University, Japan; [10]Niigata University, Japan; [11]University of Tsukuba, Japan; [12]SINS, Warsaw, Poland

Masses and lifetimes of fragments characterized by half-lives of a few seconds and more have been accurately measured with time-resolved Schottky mass spectrometery [1]. The access to very short-lived stored nuclei is limited by the duration of the cooling process. This restriction can be circumvented by tuning the storage ring to its transition energy. In this special isochronous ion-optical mode the revolution time is independent on the velocity spread by reason that the faster ions of each isotope are guided on longer trajectories to preserve a constant revolution time [2]. The isochronous condition is strictly fulfilled only for one mass-to-charge (m/q) ratio in a narrow Bρ interval [3].

In IMS experiments by recording the secondary electrons released when the stored ions penetrate a 17 μg/cm^2 carbon foil (coated with CsI) the revolution time is measured with a channel-plate detector at each turn. Recording an isochronous time-of-flight (ToF) spectrum for uranium fission fragments has demonstrated an maximum mass-to-charge ratio of more than 10%. A Bρ cut is possible inside the ESR and in the analysis [4] but can bias the final results of the mass measurements. A better solution is to measure in addition to the revolution time the Bρ of each fragment in front of the ESR. This idea has been realized in a recent experiment where the high resolution of the FRS is used to determine the Bρ of the injected fragments within $1.5 \cdot 10^{-4}$ at the second dispersive focal plane via a modified slit system. The mass resolution achieved with this Bρ tagging is about $5 \cdot 10^5$ (σ value) [3, 5].

The Bρ tagging method has been applied in the last experiment in which we measured the masses of neutron-rich uranium fission products. More than 100 different nuclides have been identified in the time-of-flight spectra. The analysis method employing a correlation matrix approach - developed for the SMS data analysis - has been applied to IMS data for the first time in front of the ESR. In this way we can compensate the broadening of the peaks due to slow drifts of, e.g., magnetic fields of the ESR. Figure 1 shows a comparison of our preliminary mass values and recent values from JYFLTRAP [6, 7, 8] with the values from the AME2003 Atomic Mass Evaluation [9]. One can see that both measurements agree well with each other. Both data sets show similar deviations to the AME2003 which range up to about 1 MeV. Most of the AME data for these nuclei are based on previous β-endpoint measurements.

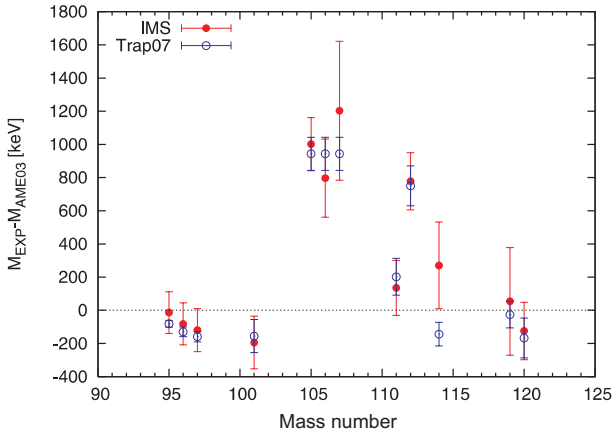

Figure 1: Comparison of our preliminary mass values (full circles) and recent values from JYFLTRAP [6, 7, 8] (empty circles) with the values from the AME2003 Atomic Mass Evaluation [9].

References

[1] L. Chen, et al., GSI Annual Report 2007 (this volume).

[2] M. Hausmann, et al., Nucl. Instr. Meth. A 446 (2000) 569.

[3] H. Geissel, et al., Hyperfine Interactions 173 (2006) 49-54.

[4] M. Matoš, Doctoral Thesis, Universität Gießen.

[5] L. Chen, et al., GSI Annual Report 2005 (2006) 141.

[6] S. Rahaman, et al., Eur. Phys. J. A 32, 87-96 (2007).

[7] U. Hager, et al., Nucl. Phys. A 793 (2007) 20-39.

[8] U. Hager, et al., Phys. Rev. C 75, 064302 (2007).

[9] G. Audi, et al., Nucl. Phys. A 729 (2003) 3.

Energy dependence of the production cross sections of fragmentation residues

E. Casarejos[1], J. Benlliure[1], M. Fernandez[1], L. Gyot[2], P. Napolitani[2], C. Paradela[3], and the S266 collaboration[1,2,3,4,5,6]

[1]USC, Santiago de Compostela, Spain; [2]GSI, Darmstadt, Germany; [3]IPN, Orsay, France; [4]CEA, Saclay, France; [5]GANIL, Caen, France; [6]Yale University, New Haven, CT, USA

This work belongs to a large experimental program performed at GSI during the last years aiming for detailed investigations of the fragmentation/spallation reactions. These reactions are of interest because of their applications, e.g., RIB production, characterizations of spallation sources, ... but also because accurate measurements provide insight into the dynamics of peripheral relativistic heavy-ion collisions. The case of ^{136}Xe resumes the characteristics of the medium mass nuclei. The mechanism involved also are simplified since fission is largely suppressed here, thus concentrating the observation in the particle evaporation channels. The measurement of different targets and energies allowed, in the same experiment, to obtain a large collection of data. These measurements provided a deep systematic study, highlighting the features of the mechanisms implicated in the production of residues around the projectile.

The experiment was performed at the FRS, whose resolving power allows for unambiguous identification of each isotopic species when using an appropriate technique [1]. A ^{136}Xe beam was accelerated by SIS at convenient energies. The residues resulting from the collision flew forwards and were analyzed in-flight at the FRS. The inverse kinematics technique has been demonstrated to be a powerful tool in order to undertake fragmentation/spallation measurements of production cross sections and momenta, and studies of the implicated reaction mechanisms. In Fig. 1 the cross sections measured for isotopes around the projectile are shown, for three different energies. We can observe that the values for the production cross sections of residues far enough of the projectile, Te and lower Z values, are very similar. They are independent of the energy in the broad range of 0.2 to 1.0 AGeV. One expects this result considering an abrasion model describing the reaction [2]. Following the Glauber image at high energies, only the geometry of interacting nuclei plays a role, through the nucleus matter distribution. The energy dependence is kept in the nucleon-nucleon cross sections, but it results almost constant in a broad range of energies.

However we observe clear effects of the energy in Xe and I isotopes, as well as for the charge-exchange channel Cs. The relative amount of cross section of Cs/Xe is 7% at 1AGeV, but more than 30% at 0.2 AGeV. Abrasion models, typically describing high-energy reactions, cannot reproduce those results following the previous ideas: these models can hardly include a charge pick-up channel.

With the help of microscopic codes based in the intranuclear cascade approach, containing the state-of-the-art description of fragmentation reactions [3], we could reproduce realistically our measured results. Studying the influence of specific channels we concluded that the collisions involved in charge-exchange processes are the direct responsible for the energy effects observed. This channel being related to the most peripheral impacts and lowest excitation energies, affects restrictively to those residues very close to the projectile. The mechanisms to induce (p,n) exchanges at these energies are dominated by quasi-elastic processes. The dependence in energy, remarkably in Cs isotopes, but also clear in Xe and I, with increasing production with decreasing energies, is the straight result of the energy dependence of the charge-exchange channels.

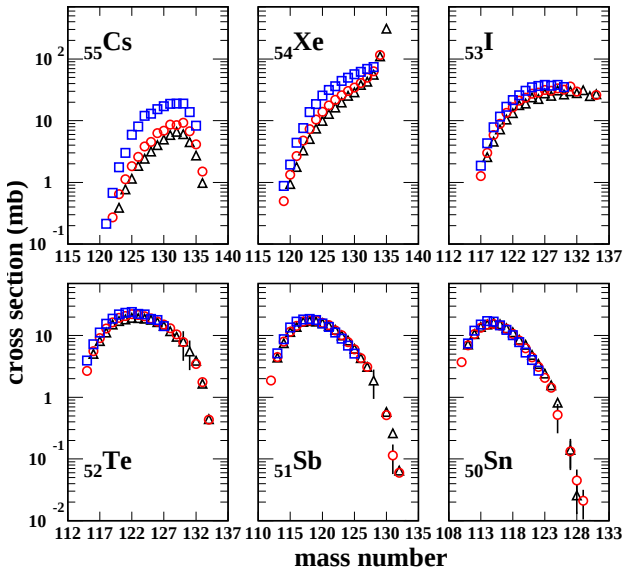

Figure 1: Measured isotopic cross sections of residues of the reaction of ^{136}Xe with ^{48}Ti at 1.0 AGeV(triangles), 0.5 AGeV(circles), and 0.2 AGeV(squares).

We have observed that the abrasion codes are limited in their prediction capabilities for the most peripheral collisions, notably at decreasing energies. The use of microscopic models becomes mandatory in order to obtain realistic cross sections for isotopes around the projectile and remarkably for charge-exchange channels, and related ones. We also note the sensitivity of these kind of data to focus in specific channels which can benchmark the descriptions contained in the models. More challenging applications of these observations are being studied by our collaboration.

[1] http://www-wnt.gsi.de/CHARMS/
[2] J.-J. Gaimard et al., Nucl. Phys. A 531 (1991) 709
[3] A. Boudard et al., Phys. Rev. C 66 044615 (2002)

Production of medium-mass neutron-rich nuclei from fragmentation of ^{132}Sn

D. Pérez Loureiro for the S294 collaboration

U. Santiago (Spain), GSI (Germany), CENBG (France), VINCA (Serbia), U. Warsaw (Poland), CEA (France), U. Yale (USA), U. Helsinki (Finland)

Medium-mass neutron-rich nuclei are important for nuclear structure investigations (e.g. shell evolution with neutron excess) and nuclear astrophysics (e.g. r-process in nucleosynthesis). However, these investigations are limited because of the difficulties in producing medium-mass nuclei with a large neutron excess. The traditional way for producing neutron rich nuclei was fission of actinides [1].

A new idea is to use a two step reaction scheme. Medium-mass neutron-rich isotopes are produced with high intensities as fission fragments. Then, they are used as projectiles in a second step to produce even more neutron-rich nuclei by cold fragmentation. In fact, this two step reaction might be a tool for producing beams of extremely neutron rich isotopes of refractory elements and short lived nuclei in ISOL facilities [2].

In a recent work [3] the feasibility of the two step reaction scheme was investigated by calculating the production cross sections of residual nuclei in this kind of reactions. Two different model calculations were used, EPAX [4], the semiempirical parameterisation for fragmentation cross sections, and the cold fragmentation code COFRA, which is described in ref. [5]. It has been shown that the predictions of both model calculations applied for fragmentation of neutron-rich projectiles differ considerably.

In order to obtain a clear answer for these discrepancies, an experiment was performed at GSI Fragment Separator (FRS) in November 2006. A 950 MeV/u ^{238}U beam with an intensity of 10^9 projectiles per spill impinged onto a a 650 mg/cm^2 Pb target at the entrance of the FRS to produce fission fragments. The forward emitted fission products were isotopically identified by the first section of the FRS by using and improved time-of-flight system and TPC chambers for position and angle measurements. The tracking correction to the time-of-flight allowed for the first time to isotopically separate at the FRS A≈130 fragments with a limited flight path (20 m).

These fully identified fission residues impinged onto a secondary beryllium target (2.6 g/cm^2) located at the intermediate focal plane. The fragmentation residues were also isotopically identified in the second section of the spectrometer using a similar technique but with a longer flight path (36 m). The production cross sections of these fragmentation residues were obtained normalizing the measured yields to the secondary beam current (fission fragments) and the beryllium target thickness.

Figure 1 shows the measured cross sections of residual nuclei produced in the fragmentation of ^{132}Sn with a beryllium target. As expected, this two step reaction scheme leads to the production of very neutron-rich medium-mass fragments. Indeed, we have observed for the first time

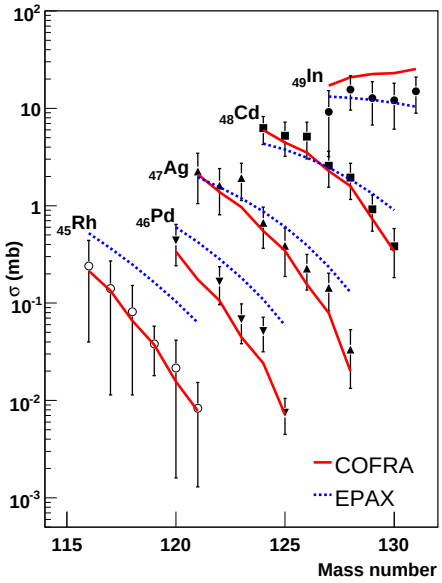

Figure 1: Preliminary production cross sections from fragmentation of residues produced in the fragmentation of ^{132}Sn on ^{9}Be. The data are compared to two model calculations, EPAX (dashed line) and COFRA (solid line).

the production of ^{125}Pd. In this figure we also compare the measured cross sections with the predictions obtained with two model calculations, EPAX and COFRA. As can be seen, the production cross sections of residual nuclei far from projectile are clearly overestimated by EPAX. However the COFRA code based on analytical simplification of the Abrasion Ablation model provides a better description of the data.

In the same experiment, we also measured the direct production cross sections of medium-mass neutron-rich nuclei in ^{238}U fission reactions. The comparison of these cross sections with the ones presented in this report will allow to conclude on the optimum reaction mechanism for the production of extremely neutron-rich medium-mass nuclei.

References

[1] M. Bernas et al., Phys Lett. B, 415 (1997) 111

[2] EURISOL WEB page: `http://www.ganil.fr/eurisol`

[3] K. Hellariutta et al., Eur. Phys. J. A, 17 (2003) 17

[4] K. Sümmerer and B. Blank, Phys. Rev. C 034607 (2000)

[5] J. Benlliure et al., Nucl. Phys. A, 660 (1999) 87

Isomeric state in the r-process waiting point nucleus ^{130}Cd

L. Caceres[1,2], A. Jungclaus[2], M. Górska[1], M. Pfützner[3], S. Pietri[4], E. Werner-Malento[3], H. Grawe[1], K. Langanke[1], G. Martinez-Pinedo[1], F. Nowacki[5], A. Poves[2], J. Quenca[1], D. Rudolph[6], Z. Podolyak[4], P.H. Regan[4], P. Detistov[7], S. Lalkovski[8,7], V. Modamio[2], J. Walker[2], P. Bednarczyk[1,9], P. Doornenbal[1], H. Geissel[1], J. Gerl[1], J. Grębosz[1,9], I. Kojouharov[1], N. Kurz[1], W. Prokopowicz[1], H. Schaffner[1], H.J. Wollersheim[1], K. Andgren[10], J. Benlliure[11], G. Benzoni[12], A.M. Bruce[8], E. Casarejos[11], B. Cederwall[10], F.C.L. Crespi1[2], B. Hadinia[10], M. Hellström[6], R. Hoischen[6,1], G. Ilie1[3], A. Khaplanov[10], M. Kmiecik[9], R. Kumar[14], A. Maj[9], S. Mandal[15], F. Montes[2], S. Myalski[9], G. Simpson1[6], S.J. Steer[4], S. Tashenov[1] and O. Wieland[12]

[1]GSI, Darmstadt, Germany; [2]Universidad Autónoma de Madrid, Spain, [3]IEP, Warsaw University, Poland, [4]University of Surrey, Guildford, UK, [5]IReS, IN2P3-CNRS, Strasbourg, France, [6]Lund University, Sweden, [7]University of Sofia, Bulgaria, [8]University of Brighton, Brighton, UK, [9]The Henryk Niewodniczaski Institute of Nuclear Physics, Cracow, Poland, [10]KTH Stockholm, Sweden, [11]Universidad de Santiago de Compostela, Spain, [12]INFN, University of Milano and INFN sezione di Milano, Italy, [13]Universität zu Köln, Germany, [14] Inter University Accelerator Centre, New Delhi, India, [15]University of Delhi, New Delhi, India, [16]Institut Laue-Langevin, France

The single-particle ordering which underlies the shell structure, and with it the magic numbers in atomic nuclei, may change for nuclei approaching the neutron dripline as caused by the central potential becoming diffuse [1]. As a consequence, shell quenching is expected in very neutron rich nuclei. The region south of the doubly-magic nucleus ^{132}Sn is crucial for stellar nucleosynthesis due to the close relation between the N=82 shell closure and the A~130 peak of the solar r-process abundance distribution. It was shown in the nineties that with the mass models available at that time the assumption of a quenching of the N=82 neutron shell closure leads to a considerable improvement in the global abundance fit in r-process calculations [2]. Recent spectroscopic observations in nuclei close to ^{132}Sn have been interpreted as the first experimental evidence of a quenching of the N=82 shell closure [3] in ^{130}Cd, much closer to ^{132}Sn than predicted by any calculation.

In a GSI experiment performed by the RISING collaboration the identification of isomeric decays in ^{130}Cd was achieved. This is the most neutron-rich N=82 r-process waiting-point nucleus in which gamma-ray transitions have been observed, and at the same time the first r-process waiting-point nucleus in which an isomeric state has been observed. The new results for this nucleus present the most direct information with respect to a possible modification of the N=82 shell gap already close to ^{132}Sn.

Isomer spectroscopy was performed to search for a spin/parity 8^+ seniority isomer in ^{130}Cd [4] with the stretched $g_{9/2}^{-2}$ configuration, based on the expected analogy with the N=50 nucleus ^{98}Cd [5].

The experiment utilized fission and fragmentation reactions in order to optimize the production method.

The ions of interest were separated from other reaction products and identified ion by ion in the GSI FRagment Separator (FRS) [6]. Finally, the ions were implanted in a passive stopper in the final focal plane of the FRS. Gamma-rays were detected by 15 large volume Ge Cluster detectors [7] which surrounded the stopper in a close geometry. In Fig.1 the gamma-ray spectrum is shown with 4 newly identified transitions observed in mutual coincidence. They form a single cascade from the isomeric state to the ground state as shown in the level scheme in Fig1. Our experimental results clearly show that the previously discussed [3] energy of the tentatively assigned 2^+ state in ^{130}Cd was not correct.

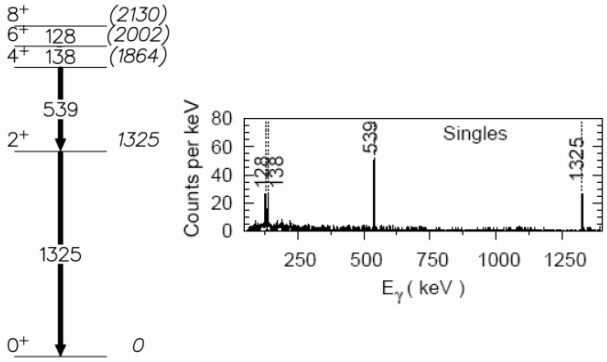

Fig.1 Level scheme and energy spectrum obtained for the isomeric decay in ^{130}Cd.

In [4] the new level scheme for ^{130}Cd is compared to shell model calculations employing modern interactions and assuming the persistence of the N=82 shell gap. The fact that the calculations fully account for the level energies and isomeric half lifes of ^{130}Cd leads to the conclusion that the new experimental results on ^{130}Cd provide no evidence for a N=82 shell quenching in Z=48.

References

[1] J. Dobaczewski, I. Hamamoto, W. Nazarewicz and J.A. Sheik, Phys. Rev. Lett. 72, 981 (1994).
[2] B. Pfeiffer, K.-L. Kratz and F.-K. Thielemann, Z. Phys. A 357, 235 (1997).
[3] T. Kautzsch et al., Eur. Phys. J. A 9, 201 (2000).
[4] A. Jungclaus et al., Phys. Rev. Lett. 99, 132501 (2007)
[5] M. Górska et al., Phys. Rev. Lett. 79, 2415 (1997).
[6] H. Geissel et al., Nucl. Instr. Meth. B 70, 286 (1992).
[7] J. Eberth et al., Nucl. Instr. Meth. A 369, 135 (1996).

‘Mirror Isomers’ in the $1f_{7/2}$ Shell

D. Rudolph[1,2], R. Hoischen[1,2], P. Montuenga[1], M. Hellström[1], S. Pietri[3], Zs. Podolyák[3], P.H. Regan[3], A.B. Garnsworthy[3,4], S.J. Steer[3], F. Becker[2], P. Bednarczyk[5,2], L. Cáceres[2,6], P. Doornenbal[2], J. Gerl[2], M. Górska[2], J. Gręboszˊ[5,2], I. Kojouharov[2], N. Kurz[2], W. Prokopowicz[2,5], H. Schaffner[2], H.J. Wollersheim[2], L.-L. Andersson[1], L. Atanasova[7], D.L. Balabanski[7,8], M.A. Bentley[9], A. Blazhev[10], C. Brandau[2,3], J.R. Brown[9], C. Fahlander[1], E.K. Johansson[1], and A. Jungclaus[6]

[1]Department of Physics, Lund University, S–22100 Lund, Sweden; [2]Gesellschaft für Schwerionenforschung mbH, D–64291 Darmstadt, Germany; [3]Department of Physics, University of Surrey, Guildford, GU2 7XH, UK; [4]WNSL, Yale University, New Haven, CT 06520-8124, USA; [5]The Henryk Niewodniczański Institute of Nuclear Physics (IFJ PAN), PL–31-342 Kraków, Poland; [6]Departamento de Fisica Teórica, Universidad Autonoma de Madrid, E–280 49 Madrid, Spain; [7]Faculty of Physics, University of Sofia, BG–1164 Sofia, Bulgaria; [8]Institute for Nuclear Research and Nuclear Energy, Bulgarian Academy of Sciences, BG-1784 Sofia, Bulgaria; [9]Department of Physics, University of York, York, YO10 5DD, UK; [10]Institut für Kernphysik, Universität zu Köln, D–50937 Köln, Germany

Isomeric states in nuclei near doubly-magic nuclei provide efficient probes of the nuclear interaction active at these cornerstones on the nuclidic chart. Even more profound studies can be performed by comparing the decay characteristics of isobaric analogue states near self-conjugate doubly-magic nuclei. In the region between ^{40}Ca and ^{56}Ni the breaking of isospin symmetry due to the Coulomb force or certain parts of the strong force can be investigated in great detail [1], largely owing to the fact of good confinement of the $\mathcal{N} = 3$ shell, combined with the option of reliable large-scale shell-model calculations [2].

Recently, absolute and relative $E2$ transition rates in $A = 51$, $T_z = \pm 1/2$ nuclei have been used to establish effective charges near ^{56}Ni [3]. Amongst others, these results have been confirmed in a RISING study of 10^+ ‘mirror isomers’ in the $A = 54$, $T_z = \pm 1$ system [4]. From the same RISING experiment it is possible to collect information on the respective exotic partners of additional five cases of isomeric isobaric analogue states: $^{43}_{22}\mathrm{Ti}_{21}$–$^{43}_{21}\mathrm{Sc}_{22}$ (two isomers), $^{45}_{24}\mathrm{Cr}_{21}$–$^{45}_{21}\mathrm{Sc}_{24}$, $^{45}_{23}\mathrm{V}_{22}$–$^{45}_{22}\mathrm{Ti}_{23}$, and $^{53}_{27}\mathrm{Co}_{26}$–$^{53}_{26}\mathrm{Fe}_{27}$. The half-life values of the two isomers in ^{43}Ti and the one in ^{45}V are improved, while the isomeric states in ^{45}Cr and ^{53}Co are observed for the first time.

In the following we focus on the isomer in ^{53}Co. It provides a new class of isomer production, namely ‘in situ’ by means of nuclear reactions of the radioactive fragment beams with a ‘secondary target’, i.e. the ^{9}Be stopper in the center of the highly efficient RISING Ge array. Figs. 1(a) and (b) show γ-ray spectra in correlation with uniquely, i.e. ion-by-ion identified incoming ^{54}Ni and ^{52,53}Co nuclei. The intense 451 keV line belongs to ^{54}Ni [4] and is thus absent in panel (a). Via its decay curve, the 741 keV line can be associated with a rather short-lived, known $T_{1/2} = 63.5(14)$ ns isomeric state in ^{53}Fe. Note that this line is seen in *both* Ni *and* Co correlated spectra. Its yield is in principle equally enhanced in panels (a) and (b) due to the same, short period of correlation with the time zero of implantation. Considering on top that the FRS did not at all allow the transmission of ^{53}Fe fragments in the used setting, the corresponding isomeric states must arise from

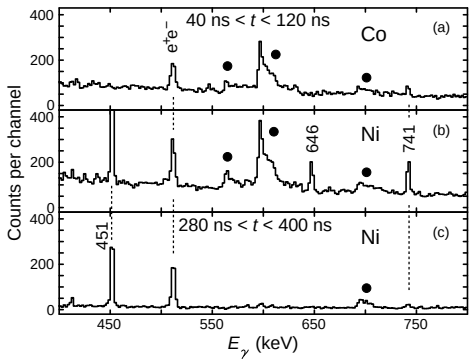

Figure 1: Gamma-ray spectra correlated in time with implanted ^{54}Ni [panels (b) and (c)] and ^{52,53}Co ions [panel (a)]. Peaks of interest are marked with their energy in keV. The structures marked with filled circles arise from $^{\mathrm{nat}}$Ge$(n, n'\gamma)$ background reactions.

nuclear reactions during the stopping process, and it appears easier to produce ^{53}Fe in secondary reactions of Ni compared to Co fragments. Because the new 646 keV line [$T_{1/2} = 14(^{6}_{4})$ ns] is seen only in the Ni-correlated γ-ray spectrum, its isomeric origin has to be a Ni or Co isotope. A more profound exclusion principle and isospin symmetry arguments yield ^{53}Co as the only plausible candidate. The consequences of the result are discussed in Ref. [5].

This work is supported by the European Commission contract no. 506065 (EURONS), the Swedish VR, EPSRC (United Kingdom), the German BMBF, the Polish Ministry of Science and Higher Education, the Bulgarian Science Fund, the Spanish MEC, and the U.S. DOE.

References

[1] M.A. Bentley and S.M. Lenzi, Prog. Part. Nucl. Phys. **59**, 497 (2007).

[2] E. Caurier *et al.*, Rev. Mod. Phys. **77**, 427 (2005).

[3] R. du Rietz *et al.*, Phys. Rev. Lett. **93**, 222501 (2004).

[4] D. Rudolph *et al.*, submitted to Phys. Rev. Lett.

[5] D. Rudolph *et al.*, submitted to Eur. Phys. J. A.

Probing the new shell closure at N=34 by a one neutron knockout reaction*

P. Maierbeck[1], R. Gernhäuser[1], R. Krücken[1], T. Kröll[1], H. Alvarez-Pol[2], F. Aksouh[3], T. Aumann[3], K. Behr[3], E. A. Benjamim[2], J. Benlliure[2], V. Bildstein[1], M. Böhmer[1], K. Boretzky[3], M. J. G. Borge[4], A. Brünle[3], A. Bürger[5,6], M. Caamano[2], E. Casarejos[2], A. Chatillon[3], L. V. Chulkov[3], D. Cortina Gil[2], J. Enders[7], K. Eppinger[1], T. Faestermann[1], J. Friese[1], L. Fabbietti[1], M. Gascon[2], H. Geissel[3], J. Gerl[3], M. Gorska[3], P. G. Hansen†[8], B. Jonson[9], R. Kanungo[3,10], O. Kiselev[3], I. Kojouharov[3], A. Klimkiewicz[3], T. Kurtukian[2], N. Kurz[3], K. Larsson[3,9], T. Le Bleis[3], K. Mahata[3], L. Maier[1], T. Nilsson[7], C. Nociforo[3], G. Nyman[9], C. Pascual-Izarra[4], A. Perea[4], D. Perez[2], A. Prochazka[3,11], C. Rodrigo-Tajes[2], D. Rossi[3,12], H. Schaffner[3], G. Schrieder[7], S. Schwertel[1], H. Simon[3], B. Sitar[11], M. Stanoiu[3], K. Sümmerer[3], O. Tengblad[4], H. Weick[3], and S. Winkler[1]

[1]E12, Physik Department, TU München, Germany; [2]USC, Santiago de Compostela, Spain; [3]GSI, Darmstadt, Germany; [4]CSIC, Madrid, Spain; [5]CEA, Saclay, France; [6]ISKP, Bonn, Germany; [7]TU Darmstadt, Germany; [8]MSU, East Lansing, USA; [9]Chalmers University of Technology, Göteborg, Sweden; [10]St Mary's University, Halifax, Canada; [11]Comenius University, Bratislava, Slovakia; [12]Johannes Gutenberg Universität, Mainz, Germany

The evolution of nuclear structure towards neutron-rich nuclei is in the focus of current theoretical and experimental investigations. Due to the influence of the residual interaction between valence orbitals the shell structure is expected to change locally. E. g. for Calcium isotopes, a new shell closure for neutron number N=34 is predicted [1]. Knockout experiments are a tool to probe the single particle structure of nuclei and therefore to test the theoretical predictions. In a new series of experiments at the Fragment Separator (FRS) at GSI in Darmstadt these reactions will be studied. In April 2006 we performed the first experiment "Single Particle occupancies near ^{54}Ca by single neutron knockout using high resolution γ-spectroscopy" (S277).

A 500 AMeV ^{86}Kr primary beam was fragmented on a 1625 mg/cm^2 ^{9}Be production target. The first two dipole stages of the FRS were used to separate primary fragments and for unique mass and charge identification. The knockout reactions of interest were induced in a secondary target (1720 mg/cm^2 ^{9}Be) placed in the intermediate focus (F2) of the FRS. 24 HPGe detectors of the MINIBALL [2] gamma-ray spectrometer were used to tag reaction channels populating exited states in the residual nucleus, allowing for exclusive measurements. The second half of the FRS provided the identification of the secondary fragments after one-nucleon removal and a precise measurement of their longitudinal momentum. From this distributions the angular momentum of the knocked out nuclei can be determined [3]. With a ^{48}Ca primary beam and the reaction ^{48}Ca$\rightarrow^{47}$Ca the properties of the setup and the methods of analysis have been adjusted with good event statistics.

Due to the high velocity of the fragments ($\beta \approx 0.7$c), a good energy and position calibration is essential for the Doppler correction of the measured γ-rays.

Figure (1) shows the measured gamma spectra of the ^{48}Ca$\rightarrow^{47}$Ca and the ^{56}Ti$\rightarrow^{55}$Ti reactions respectively. The spectra were taken in coincidence with fully identified reaction products. For the Calcium knockout reactions, the transitions at 565 keV, 586 keV are clearly separated from the background, the transition at and 2013 keV is visible. In case of ^{55}Ti there is a strong indication for a new γ transition at E$_\gamma \approx 955$ keV.

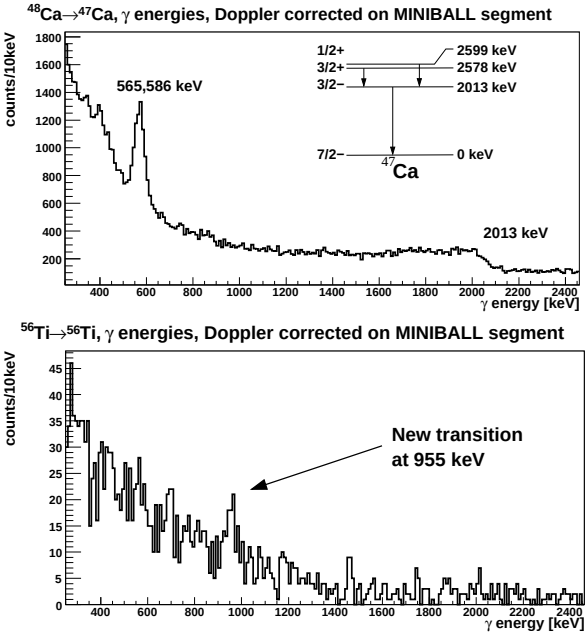

Figure 1: Gamma spectrum after Doppler correction of the ^{48}Ca$\rightarrow^{47}$Ca (upper panel) and of the ^{56}Ti$\rightarrow^{55}$Ti knockout reaction (lower panel)

The analysis of the inclusive and exclusive rection cross sections as well as of the momentum distributions is ongoing. The results will be published soon.

References

[1] M. Honma et al., Phys. Rev. C65, 061301, 2002

[2] J. Eberth et al., Prog. Part. Nucl. Phys. 46, 289 (2001)

[3] D. Cortina-Gil et al., PRL93, 062501, 2004

*Work supported by the BMBF (06MT238), by the DFG cluster of excellence 'Origin and Structure of the Universe' and by the EC through I3-EURONS (RII3-CT-2004-506065)

One-neutron knockout of very neutron-rich Nitrogen isotopes

C. Rodriguez-Tajes for the S245 collaboration[1]

[1]Univ. Santiago de Compostela (Spain), GSI (Germany), TU Munich (Germany), Chalmers (Sweden),Univ. Darmstadt (Germany), TRIUMF (Canada),IEM CSIC (Spain)

The study of exotic nuclei far from the valley of beta stability has attracted in the last decades an enormous interest. Near the neutron dripline the large neutron excess and the low neutron binding energy can lead to dramatic changes in the nuclear structure. This is the case of the so called "halo nuclei" [1, 2, 3, 4] where low binding energies allow the extension of the wave function of one or more nucleons far away from the core region. Halo-states have been extensively investigated using the very well established one-nucleon knockout technique [5]. The experimental signatures of these phenomena are narrow momentum distributions of the emerging fragments after one-neutron knockout, reflecting the large spatial extension of the removed nucleon, and the large one-neutron removal cross sections that represent a complementary source for structure information.

We have recently extended these investigations to very neutron-rich secondary beams, ranging from C to Al. The experiment was performed at the FRS with a primary beam of ^{40}Ar at 700 MeV/nucleon. Different secondary fragments, with Z=6-13, were produced by nuclear fragmentation of the primary beam in a Be target located at the entrance of the FRS. The first half of the FRS was set to transport the secondary fragments up to the intermediate focal plane F2, where one-neutron knockout on a Be target took place. A complete identification of these secondary beams was achieved by measuring the time-of-flight between two plastic detectors and by energy-deposition measurements in an ionization chamber. The second half of the spectrometer was set to the magnetic rigidity of the emerging $^{A-1}$Z breakup fragments. The identification of those fragments was performed in a similar way as for the secondary projectiles.This unambiguous double identification ensures a very clean reaction channel selection.The fragment longitudinal momentum was measured by using Time Projection Chambers. The corresponding one-neutron removal cross-sections (σ_{-1n}) were obtained from the ratio of the number of fragments measured at the final focus and incident projectiles impinging on the knockout target. This ratio was corrected for the acquisition dead time, secondary reactions, spectrometer acceptance and transmission losses, evaluated by help of the Monte-Carlo code MOCADI.

This report focusses on the n-rich nitrogen isotopes, showing the most relevant results in Figure 1. The longitudinal momentum distributions of fragments emerging after one-neutron knockout from different n-rich nitrogen ($^{20-22}$N) secondary beams are depicted on top panels. An important change in the shape of the most n-rich case (^{22}N) can be already observed by simple inspection of the resulting distributions. The bottom panel shows the evolution of the FWHM and (σ_{-1n}) of the measured knockout reactions, with the neutron number. Both observables exhibit a very similar behavior for $^{17-21}$N, whereas ^{22}N is clearly distinguished from the others exhibiting a large cross-section and a narrow fragment momentum distribution. These new

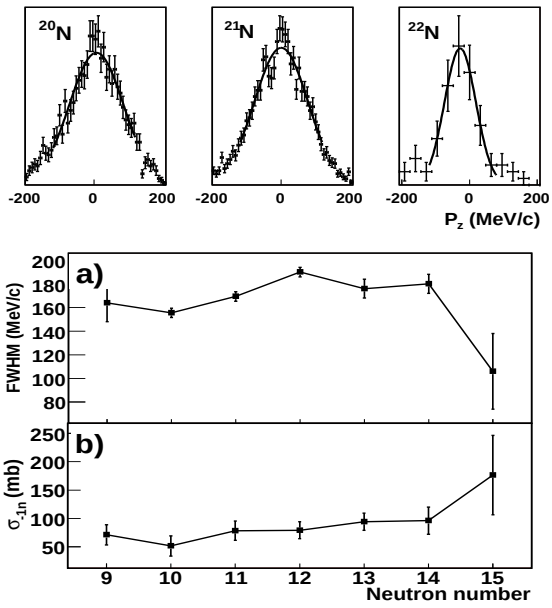

Figure 1: Top panel: Longitudinal momentum distributions of fragments emerging after one-neutron knockout of different n-rich nitrogen ($^{20-22}$N) secondary beams. Bottom panel: (a) shows the FWHM's of the momentum distributions for the full range of nitrogen isotopes studied ($^{17-22}$N), (b) presents the associated (σ_{-1n}) measured.

experimental results, together with the small neutron binding energy of this nuclei (S_n= 1.222 MeV [6]) suggest the idea of a one-neutron halo structure for ^{22}N and will be the subject of detailed analysis.

References

[1] T. Aumann et al., Phys. Rev. Lett 84 (2000) 35

[2] V. Maddalena et al., Phys. Rev. C 63 (2001) 024613

[3] D. Cortina-Gil et al., Phys. Lett. B 529 (2002) 36

[4] B. Jonson, Phys. Rep 289 (2004) 1

[5] P.G. Hansen and J.A. Tostevin, Annu. Rev. Nucl. Part. Sci. 53 (2003) 219

[6] G. Audi,A.H. Wapstra and C. Thibault, Nucl. Phys. A 729 (2003) 337

Spectroscopy of neutron-rich Mg and Al isotopes*

R. Kanungo[1#], A. Prochazka[2,3], C. Nociforo[2], D. Acker[2], T. Aumann[2], K. –H. Behr[2], D. Boutin[3], A. Brünle[2], D. Cortina-Gil[4], B. Davids[5], M. Diakaki[6], F. Farinon[2,3], H. Geissel[2], R. Gernhäuser[7], J. Gerl[2], W. Hueller[2], R. Janik[8], B. Jonson[9], C. Karagiannis[2], B. Kindler[2], R. Knöbel[2,3], R. Krücken[7], M. Lantz[9], H. Lenske[3], Y. Litvinov[2], B. Lommel[2], K. Mahata[2], P. Maierbeck[7], A. Musummara[10], T. Nilsson[8], C. Perro[1], C. Scheidenberger[2], B. Sitar[7], P. Strmen[8], B. Sun[2], I. Szarka[8], I. Tanihata[11], H. Weick[2], M. Winkler[2], I. Wishert[2]

[1]St. Mary's University, Halifax, Canada; [2] GSI, Darmstadt, Germany; [3]University of Giessen, Giessen, Germany,[4]Uiversity of Santiago, Compostela, Spain, [5]TRIUMF, Vancouver, Canada, [6]National Technical University, Athens, Greece, [7]TU München, Munich, Germany, [8]Commenius University, Bratislava, Slovakia, [9]Chalmers Institute of Technology, Goteborg, Sweden, [10]Catania University and LNS-INFN, Catania, Italy, [11]RCNP, Osaka University, Osaka, Japan

The measurements of interaction cross sections and one-neutron removal momentum distributions for neutron-rich Mg and Al isotopes are reported.

The breakdown of N=20 shell closure in neutron-rich nuclei [1-3] points to a change in our conventional concept of nuclear shell structure. The quenching of this shell gap in Mg isotopes has been observed through a large B(E2) value and a reduced excitation energy. Beta decay studies suggest an unexpected ground state spin of $3/2^+$ for ^{33}Mg [4]. There is no spectroscopic investigation determining orbital occupancies in Mg isotopes to elucidate the cause for the disappearance of the N=20 shell gap.

We investigated this by measuring the momentum distribution of the valence neutron in ^{33}Mg and ^{34}Al. The shape of the distribution reflects on the orbital occupied by the neutron. An eikonal model analysis of the measured distribution will provide us the signature of the orbital and the neutron occupation probability. The *rms* radius is yet another way to understand the unusual features due to unexpected orbitals. We therefore measured the interaction cross section of $^{33\text{-}35}$Mg to understand the variation of nuclear size as one moves beyond N=20.

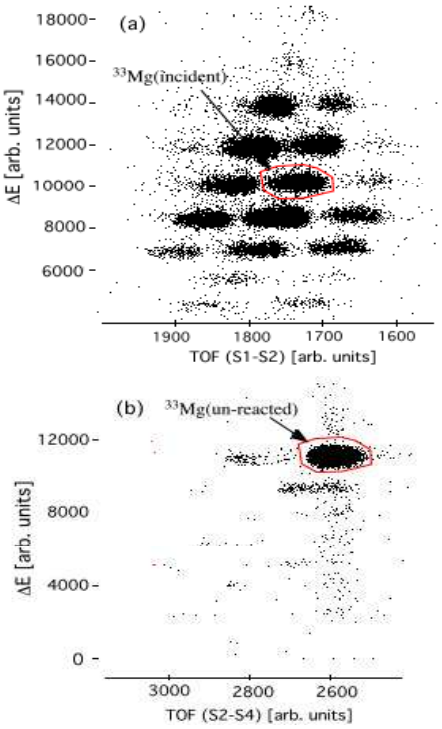

Figure 1: Particle identification for measurement of interaction cross section for ^{33}Mg,

The experiments were performed at the fragment separator FRS at GSI. The desired neutron-rich isotopes were produced by the fragmentation of a ^{48}Ca primary beam (E/A = 1 GeV) with a 6 g/cm^2 Be target. FRS was operated in the dispersion-matched mode. The first part of the separator was used for identification of the incoming beam species. The desired nuclei were identified using Bρ-ΔE-TOF method. Fast plastic scintillators were used for measuring time-of-flight (TOF), and energy loss (ΔE) was measured using multi-sampling ionization chambers. The reaction targets, C and CH_2 were placed at the dispersive mid-plane of FRS. Bρ analysis of the incoming and outgoing particles was possible using tracking chambers, TPC, placed before and after the reaction target.

The interaction cross section will be determined by counting the number of incident ^{33}Mg and number of unreacted ^{33}Mg after the target. Figure 1a shows the ^{33}Mg species identified before the target while the un-reacted ^{33}Mg after the target, is shown in Fig.1b. The momentum distribution after one neutron removal is measured by transporting ^{32}Mg after reaction in the C- target to the final focus. The position distribution of ^{32}Mg at the final focus is proportional to the momentum distribution. The high beam energy, that is presently only achievable at GSI, was chosen to ensure minimum transmission losses in transporting the nuclei after the reaction target to the final focus. This is crucial in order to reliably determine both interaction cross section as well as the high and low momentum ends of the momentum distribution. The data analysis is currently in progress .

References

[1] C. Thibault et al., Phys. Rev. C 12 (1975) 644.
[2] T. Motobayashi et al, Phys. Lett. B 346 (1995) 9.
[3] B.V. Pritychenko et al, Phys. Lett. B 461 (1999) 322.
[4] S. Nummela et al, Phys. Rev. C 64 (2001) 054313

* Work supported by .Alexander von Humboldt Foundation
# ritu@triumf.ca.

Progress in the HypHI project: Hypernuclear Spectroscopy with Induced Reactions by Stable Heavy Ion Beams and Rare Isotope Beams (S319)

T.R. Saito[1,2], P. Achenbach[2], S. Ajimura[3], S. Bianchin[1], O. Borodina[1], T. Fukuda[4], Y. Hayashi[5], T. Hiraiwa[5], J. Hoffmann[1], M. Kavatsyuk[1], N. Kurz[1], O. Lepyoshkina[1], S. Minami[1,2], Y. Mizoi[4], T. Mochizuki[3], M. Moritsu[5], D. Nakajima[1], W. Ott[1], J. Pochodzalla[2], C. Rappold[1], A. Sakaguchi[3], K. Tanida[5], and W. Trautmann[1]

[1]GSI, Darmstadt, Germany; [2]IKP Mainz Univ., Mainz, Germany; [3]Osaka Univ., Osaka, Japan; [4]Osaka Ele.-Comm. Univ., Neyagawa, Japan; [5]Kyoto Univ., Kyoto, Japan

The HypHI project [1] aims to perform precise hypernuclear spectroscopy with induced reactions of stable heavy ion and rare-isotope beams at GSI and FAIR. The international HypHI collaboration currently prepares for the first HypHI experiment which is defined as Phase 0, and the proposal of the HypHI Phase 0 experiment was already approved by the GSI G-PAC 34 in April 2007 [2, 3]. The whole experimental setup of the Phase 0 experiment has been already fully designed based on Monte Carlo simulations [2, 3]. In the Phase 0 experiment, light hypernuclei such as ${}^{3}_{\Lambda}$H, ${}^{4}_{\Lambda}$H and${}^{5}_{\Lambda}$He will be produced by an induced reaction of ^{6}Li beams at 2 A GeV impinged on a carbon target with a thickness of 8 g/cm^2. The experimental setup consists of the ALADiN dipole magnet, a plastic finger hodoscopes for the start of Time-Of-Flight (TOF) measurements (TOF-start), three arrays of scintillating fiber (SciFi) detectors between the target and the ALADiN magnet, two TOF walls (TOF+ and the ALADiN TOF wall) behind the ALADiN magnet, and two drift chambers (one in front of the ALADiN magnet and the other behind it). The trigger system to the data acquisition consists of three levels, the tracking trigger produced by SciFi detectors, the π^- trigger by the ALADiN TOF wall and the $Z = 2$ trigger by TOF+. For the trigger system, a universal trigger module VUPROM has been developed for HypHI with a total I/O channels of 256, an FPGA running at 400 MHz and a DSP at 1 GHz [4]. Details of the proposed Phase 0 experiment can be found in ref. [2].

Two experiments for testing prototype detectors were performed in March and September 2007. In the experiment in March, a cocktail beam of π^+, proton, deuteron and α at a π^+ momentum of 1 GeV/c was delivered and identified in cave A. The experiment in September took place behind the FOPI detector during the FOPI experiment with primary ^{58}Ni beams at 1.9 A GeV and primary ^{12}C beams at 0.85 A GeV. In the latter experiment, $Z = 1 \sim 3$ light fragments were produced and identified by induced reaction of the primary beams in a carbon target with a thickness of 4 g/cm^2 for detector tests. Prototypes of SciFi detectors were tested in both experiments, and the position and energy resolutions were investigated [5, 6]. It is revealed that the observed energy resolution was excellent enough to show clear separation between $Z = 1$ and 2 particles in the SciFi detectors, which is essential to reject background associated in the production of unbound Λ-hyperons with α-particles [5]. Prototype detectors of TOF+ with/without a hole in the center were tested in the experiment in September by observing light fragments. Time and Energy resolution of the the prototypes were measured in the experiment together with cosmic-ray measurements in the laboratory, and observed time and energy resolutions also fulfill the requirement for the Phase 0 experiment [7]. The logic module VUPROM was commissioned in the experiment in September, and it also showed the satisfactory [4]. The principle of the $Z = 2$ trigger was also studied in the experiment in September, and it has been found that the $Z = 2$ trigger is feasible with VUPROMs [4, 8]. Constructions of TOF-start, SciFi detectors and TOF+ will be completed in mid of 2008, and 80 modules of VUPROMs will be produced by spring in 2008. Three drift chambers have been already delivered at GSI from KEK. In 2008, works on all the trigger systems will be completed with another test experiment in cave C planned in July 2008. We currently plan to perform the Phase 0 experiment in the beginning of 2009.

The HypHI collaboration would like to thank to the FOPI collaboration, D. Schardt and H. Iwase for their supports to the two test experiments in cave A and cave B. TRS and his research group at GSI are granted by the Helmholtz Association and GSI as Helmholtz-University Young Investigators Group VH-NG-239 and by DFG research grant SA 1696-1/1.

References

[1] T.R. Saito, *et al.*, Letter Of Intent of "Hypernuclei with Stable Heavy Ion Beam and RI-beam Induced Reactions at GSI (HypHI)". Submitted to GSI EA 30.

[2] T.R. Saito, *et al.*, Proposal of the HypHI Phase 0 experiment submitted to the G-PAC 33 in October 2006.

[3] T.R. Saito, *et al.*, Progress Report on Proposal of the HypHI Phase 0 experiment submitted to the G-PAC 34 in April 2007.

[4] S. Minami *et al.*, in these reports.

[5] D. Nakajima *et al.*, in these reports.

[6] P. Achenbach *et al.*, in these reports.

[7] O. Borodina *et al.*, in these reports.

[8] C. Rappold *et al.*, in these reports.

Nuclear Structure Studies in Fermionic Molecular Dynamics

S. Bacca, H. Feldmeier, and T. Neff
GSI, Darmstadt, Germany

In the Fermionic Molecular Dynamics (FMD) approach many-body wave functions are described by Slater determinants of Gaussian wave-packets localized in phase space. The symmetries of the Hamiltonian are restored by projection on parity, angular and linear momentum. An effective interaction derived from the realistic Argonne V18 interaction by explicit introduction of short-range central and tensor correlations by means of the Unitary Correlation Operator Method (UCOM) is used.

Charge- and Parity-Projected FMD states

The nuclear interaction features a strong tensor force. In the UCOM approach short-range tensor forces are mapped onto the central part of the correlated interaction. But the correlated interaction still has long-range tensor forces. Their strength depends on the range I_θ of the tensor correlation operator [1] that can not be fixed in the two-body system. This long-range tensor forces will induce corresponding correlations in the many-body wave function. In a typical mean-field approach these correlations are difficult to describe. Following an idea by Sugimoto *et al.* [2] we extend the FMD wave functions by allowing for the most general superposition of proton and neutron in the single-particle state. This is motivated by the fact that the long-ranged tensor force is caused by the exchange of the isovector pseudoscalar pion. The many-body state has of course definite charge and parity. Therefore the isospin mixed FMD state is obtained by variation after projection on parity and charge (CPP). We compare the FMD results with exact no-core shell model calculations for the same interaction. We find that CPP wave functions account for a significant part of the tensor correlations [3].

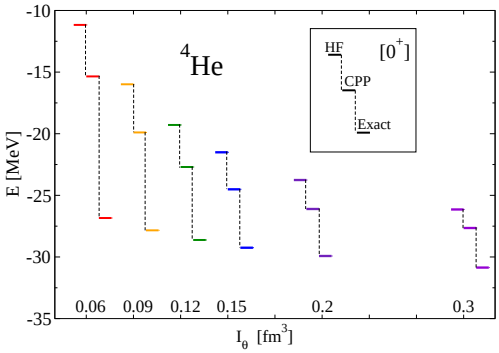

Figure 1: ^{4}He energies calculated within Hartree-Fock (HF) and Charge- and Parity-Projected FMD (CPP) compared with exact results for different ranges of the tensor correlation operator.

Harmonic Oscillator Occupation Numbers

In [4] we studied the structure of ^{12}C with a special emphasis on the first excited 0^+ state, the famous Hoyle state. The Hoyle state is a well pronounced cluster state and has a very large spatial extension. These theoretical predictions could be confirmed by comparison to inelastic electron scattering data exciting the Hoyle state.

Cluster states like the Hoyle state are notoriously difficult to describe in shell model calculations. To obtain a better understanding of this problem we calculated for our FMD wave functions single- and many-particle occupation numbers in the shell model basis. In Fig. 2 we show the decomposition in $N\hbar\Omega$ shell model configurations for the Hoyle state. We find a substantial occupation of about 13% for $0\hbar\Omega$ configurations due to the mixing between cluster and shell model configurations. The rest of the wave function can be understood as a coherent superposition of highly excited (in the shell model picture) configurations. Configurations with more than 50 $\hbar\Omega$ excitations are needed to describe the FMD wave functions. It is therefore not surprising that no-core shell model calculations, where the model space is restricted with todays computers to $8\hbar\Omega$, can not reproduce the Hoyle and other cluster states.

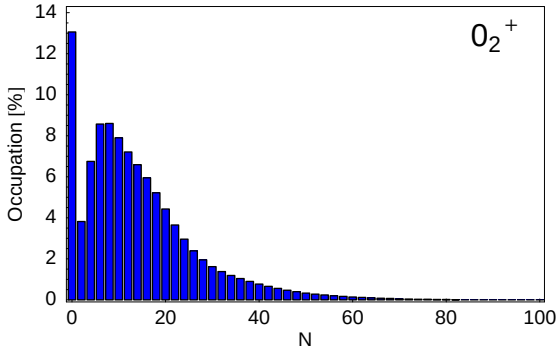

Figure 2: Decomposition of the FMD Hoyle state wave function in ^{12}C in contributions from $N\hbar\Omega$ shell model excitations.

References

[1] R. Roth, H. Hergert, P. Papakonstantinou, T. Neff, H. Feldmeier, Phys. Rev. C**72**, 034002 (2005).

[2] S. Sugimoto, K. Ikeda, H. Toki, Nucl. Phys. **A740**, 77 (2004).

[3] S. Bacca, T. Neff, H. Feldmeier, *in preparation*

[4] M. Chernykh, H. Feldmeier, T. Neff, P. von Neumann-Cosel, A. Richter, Phys. Rev. Lett. **98**, 032501 (2007) .

Nuclear Reactions in Fermionic Molecular Dynamics

H. Feldmeier and T. Neff
GSI, Darmstadt, Germany

In the Fermionic Molecular Dynamics (FMD) approach many-body wave functions are described by Slater determinants of Gaussian wave-packets localized in phase space. The FMD wave functions can therefore describe shell model configurations and states composed of two clusters on the same footing. It is therefore natural to apply the FMD approach also to nuclear reactions. In the asymptotic region the reaction partners are well separated and can be described using basis states built from localized clusters in their respective eigenstates. This is essentially the same approach as followed in the microscopic cluster model. In the interaction region we will add additional FMD configurations. These configurations will mix with the cluster states and allow us to extract cluster spectroscopic factors or asymptotic normalization coefficients.

As a first application of the FMD approach to low energy nuclear reactions we study the radiative capture reaction ^{3}He(α,γ)^{7}Be. At the low energies relevant for astrophysical scenarious the α-particles are captured from the $1/2^+$, $3/2^+$ and $5/2^+$ scattering states into the $3/2^-$ and $1/2^-$ bound states. In a fully microscopic calculation we therefore have to the determine the wave functions of the bound and scattering states with the appropriate boundary conditions. Results for the phase shifts are shown in Fig. 1.

For the cross section we have to evaluate the dipole transition matrix elements that are dominated by the exponential tail of the bound state wave functions. The dipole matrix element is therefore strongly dependend on the binding energy relative to the threshold, and the asymptotic normalization coefficient (ANC). As the cross sections are governed by phase space factors it is essential that the microscopic model has the correct binding energies. The energies will of course depend on the nucleon-nucleon interaction but also on the many-body states used to describe the α and ^{3}He clusters and the ^{7}Be bound states.

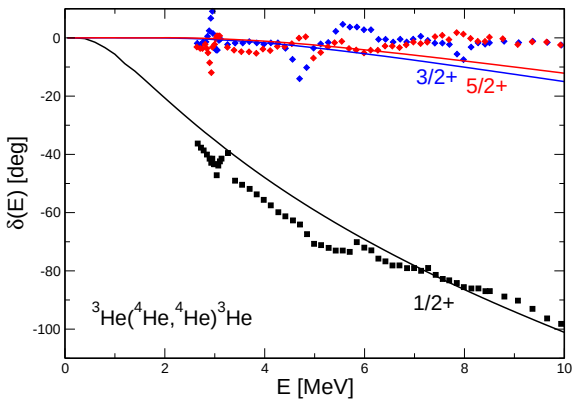

Figure 1: Phase shifts in the positive parity channels for α–^{3}He elastic scattering. In the radiative capture reaction at low energies the α-particles are captured from these states.

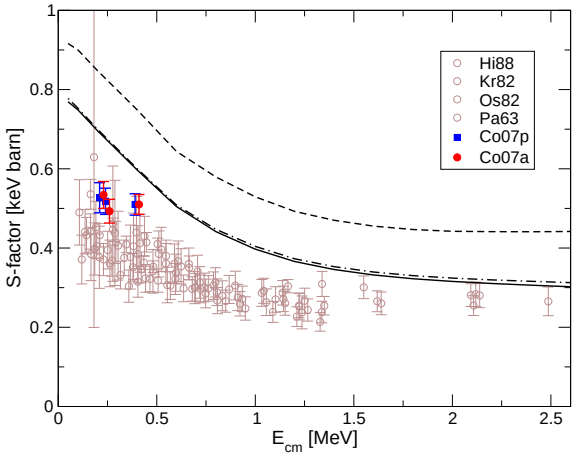

Figure 2: S-factor for the ^{3}He(α,γ)^{7}Be reaction calculated with different FMD wave functions. Experimental data including some new measurements [1] that provide consistent results from direct capture and activation measurements.

To get the correct energies a small fine-tuning of our nucleon-nucleon interaction is necessary for each set of basis states. In Fig. 2 we show results obtained with different basis sets of FMD states. In all calculations the same cluster states are used in the asymptotic regions. To improve the description of the ^{7}Be bound states we first add a single FMD state obtained in a variation after parity projection procedure. In this Hilbert space we obtain the S-factor given by the dashed curve. Next we use FMD states obtained in variation after angular momentum projection on $3/2^-$ and $1/2^-$. With these configurations we obtain the dash-dotted curve. Finally we add states obtained in variation after angular momentum projection on $5/2^-$ and $7/2^-$. With the fine-tuning of the interaction we find an almost identical ANC and the S-factor given by the solid curve does not change much.

The S-factor depends very sensitively on the ANC. It is therefore possible that further improvements in the description of cluster and bound state wave functions might improve the agreement with the experimental cross sections.

References

[1] F. Confortola, *et al.*, Phys. Rev. C **75**, 065803 (2007).

The Unitary Correlation Operator Method from a Similarity Renormalization Group Perspective

H. Hergert and R. Roth
Institut für Kernphysik, TU Darmstadt, Schlossgartenstr. 9, 64289 Darmstadt, Germany

The Unitary Correlation Operator Method (UCOM) (see [1] and references therein), was devised as a means to describe the correlations induced by the short-range repulsion and the tensor force of modern realistic NN interactions by an explicit unitary transformation. One obtains a phase-shift equivalent correlated interaction $\mathrm{V}_{\mathrm{UCOM}}$ which exhibits a dramatically improved convergence behavior in practical calculations, resulting from a pre-diagonalization of the interaction in momentum space, as shown for the ${}^3S_1$ partial wave in Fig. 1.

This observation provides a first heuristic link to the similarity renormalization group (SRG) approach. Following Wegner's formulation of the SRG [2], one can evolve the many-body Hamiltonian towards a band-diagonal structure by solving the flow equation

$$\frac{d\mathrm{H}_\alpha}{d\alpha} = \left[\eta(\alpha), \mathrm{H}_\alpha\right], \quad \mathrm{H}_0 = \mathrm{H}\,, \tag{1}$$

where α denotes the flow parameter. The generator $\eta(\alpha)$ has to be chosen appropriately for practical applications. Bogner et al. [3] have recently employed $\eta(\alpha) = \left[\frac{\mathrm{q}^2}{2\mu}, \mathrm{H}_\alpha\right]$, which aims to diagonalize the two-body Hamiltonian H_α in a basis of eigenstates of the radial and orbital angular momentum operators. When evaluated for a typical NN interaction at the initial point of the flow, the structure of $\eta(0)$ closely resembles the non-trivial generators used in the UCOM transformation [4]. This result connects the SRG flow picture with a physically intuitive picture of central and tensor correlations in a many-body state. Conversely, the flow equation confirms that the UCOM ansatz contains the important generators, and offers guidance for possible improvements or generalizations of the UCOM scheme.

In Fig. 1, we compare the ${}^3S_1$ matrix elements of AV18 to V_{UCOM} and a SRG-evolved interaction V_α (see [4] for details). The large off-diagonal contributions and strongly repulsive diagonal terms of the parent interaction are dramatically suppressed by the UCOM and SRG transformations, and the attractive low-momentum component is enhanced. The $\mathrm{V}_{\mathrm{UCOM}}$ and V_α matrix elements are very similar, the only noticeable difference being the stronger increase of the SRG matrix elements at high momenta when approaching the diagonal. The same agreement is obtained for the matrix elements in the coupled channel ${}^3S_1 - {}^3D_1$.

This is a numerical confirmation of the close relation of the UCOM and SRG approaches, which offers many interesting prospects for future work, particularly on the optimization of the UCOM correlators via the SRG approach and the application of both approaches to the three-nucleon system.

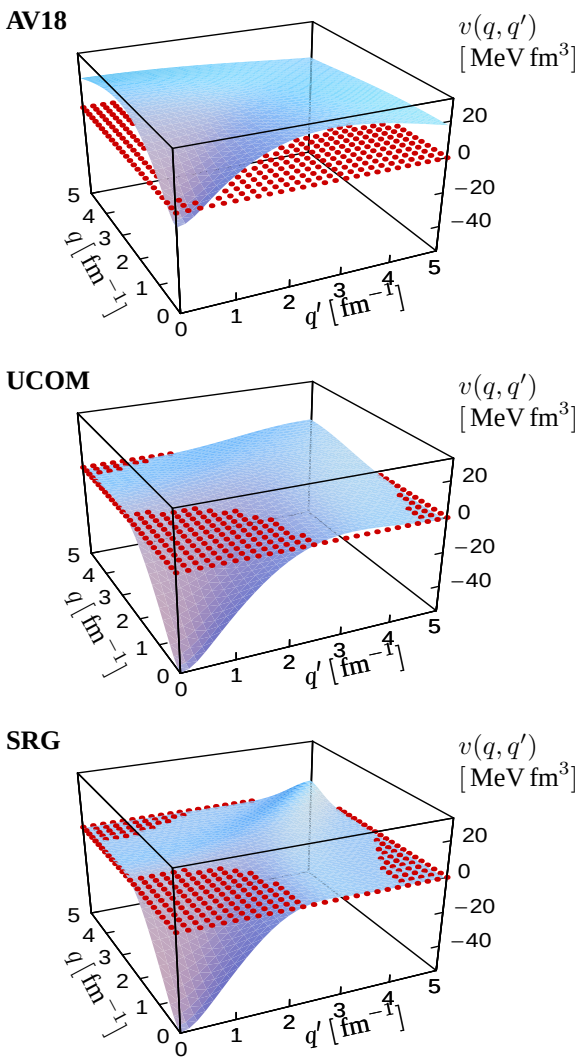

Figure 1: Momentum-space matrix elements in the ${}^3S_1$ partial wave for the AV18 potential (top), $\mathrm{V}_{\mathrm{UCOM}}$ (center), and the SRG-evolved AV18 (bottom).

Work supported by the DFG (SFB 634).

References

[1] R. Roth *et al.*, Phys. Rev. **C72**, 034002 (2005).
[2] F. Wegner, Ann. Phys. (Leipzig) **3**, 77 (1994).
[3] S. K. Bogner *et al.*, Phys. Rev. **C75**, 061001 (2007).
[4] H. Hergert and R. Roth, Phys. Rev. **C75**, 051001 (2007).

Importance Truncated No-Core Shell Model *

R. Roth

Institut für Kernphysik, TU Darmstadt, Schlossgartenstr. 9, 64289 Darmstadt, Germany

One of the most universal tools for the *ab initio* solution of the nuclear many-body problem is the No-Core Shell Model (NCSM). It is widely used for the description of ground states and low-lying excited states of nuclei throughout the p-shell [1]. Apart from energies, detailed spectroscopic information and form-factors can be extracted from the resulting many-body eigenstates. The limitation of converged NCSM calculations to the p-shell results solely from the dimension of the $N_{\max}\hbar\omega$ model space, which grows factorially with the number of particles and the truncation parameter $N_{\max}$. However, for the description of an individual eigenstate, e.g. the ground state, many of the basis states are irrelevant, i.e., their amplitude in the expansion of the eigenstates is extremely small or zero. If these irrelevant states were known beforehand one could restrict the model space to the important basis states and thus reduce the dimension significantly.

Such an *a priori* measure for the importance of individual basis states for the description of a selected target state can be derived within many-body perturbation theory [2]. Starting from an initial approximation of the target state $|\Psi_{\text{ref}}\rangle$, the importance of a basis state $|\Phi_\nu\rangle$ can be estimated through its amplitude in the first-order perturbative expansion of the target state,

$$\kappa_\nu = -\frac{\langle\Phi_\nu|\,\mathrm{H}\,|\Psi_{\text{ref}}\rangle}{\epsilon_\nu - \epsilon_{\text{ref}}}\ .$$

In the framework of multiconfigurational perturbation theory the reference state can already be a superposition of many basis states. Note, however, that the perturbative importance measure entails a $n\mathrm{p}n\mathrm{h}$-hierarchy: assuming a two-body Hamiltonian, only those states that differ form the reference state by a 2p2h excitation at most can have non-zero κ_ν. We therefore use an iterative scheme for the construction of the importance truncated $N_{\max}\hbar\omega$ model space: We start from a simple shell-model Slater determinant as initial reference state and, in the first iteration, construct all 1p1h and 2p2h configurations, keeping only those with $|\kappa_\nu| > \kappa_{\min}$. After solving the eigenvalue problem in this basis, the eigenstate is used as new reference state for the second iteration, which extends the importance truncated model space up to the 4p4h level.

Typically we use as sequence of values for $\kappa_{\min}$ starting from $\kappa_{\min} = 3 \times 10^{-5}$ and extrapolate the energies to $\kappa_{\min} \to 0$, thus recovering the full space. That this scheme is very reliable is demonstrated in Fig. 1, where the importance truncated NCSM results after one and two iteration are compared to the full NCSM (using ANTOINE [4]) for ^{4}He with the $\mathrm{V_{UCOM}}$ interaction [3]. Although the dimension of the model space is reduced by up to two orders of magnitude through the importance truncation, the full NCSM result is reproduced after two iterations to an accuracy of 10 keV for all $N_{\max}$ and $\hbar\omega$. The reduction of the model space dimension becomes more significant for heavier nuclei. For ^{16}O as depicted in Fig. 1, this allows us to go to large $N_{\max}$ whereas the full NCSM is restricted to $N_{\max} \leq 8$. The importance truncated NCSM after two iterations already shows good agreement with the full NCSM results. The effect of configurations up to the 6p6h level can be included either via a third iteration or perturbatively and turns out to be small (cf. Fig. 1).

The importance truncated NCSM combines the intrinsic advantages of the NCSM (translational invariance, variation upper bound) with a computationally efficient and physically motivated truncation scheme that extends its range to medium-heavy nuclei.

References

[1] P. Navrátil et al.; Phys. Rev. Lett. 99, 042501 (2007).

[2] R. Roth, P. Navrátil; Phys. Rev. Lett. 99, 092501 (2007).

[3] R. Roth et al.; Phys. Rev. C 72, 034002 (2005); Phys. Rev. C 73, 044312 (2006); and references therein.

[4] E. Caurier, F. Nowacki; Acta Phys. Polonica 30, 705 (1999).

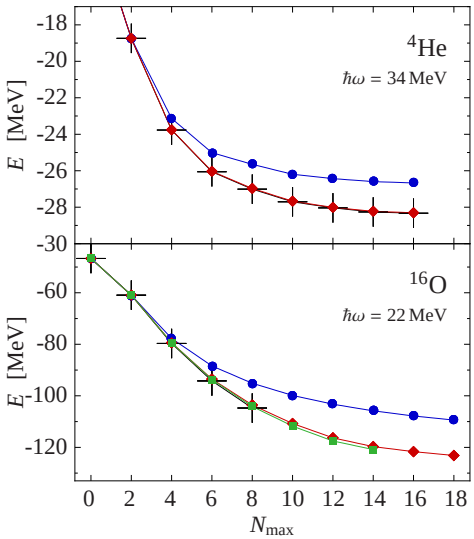

Figure 1: Convergence of the ground state energy of ^{4}He and ^{16}O as function of $N_{\max}$ using the $\mathrm{V_{UCOM}}$ interaction. The crosses indicate full NCSM results. The disks and diamonds depict results of the importance truncated NCSM after one and two iterations, i.e. up to 2p2h and 4p4h configurations, respectively. The squares include a perturbative correction for up to 6p6h configurations.

* Supported by DFG through SFB 634.

Giant Resonances using the UCOM and Second RPA*

P. Papakonstantinou, R. Roth, H. Hergert, and A. Zapp
Institut für Kernphysik, TU Darmstadt, Germany

We aim to describe nuclear collective excitations starting from correlated realistic nucleon-nucleon (NN) interactions. The latter are constructed within the Unitary Correlation Operator Method (UCOM) [1, 2], which explicitly considers short-range correlations in order to properly soften the short-range behaviour of realistic NN potentials. It has been concluded that first-order RPA with a two-body UCOM interaction (UCOM-RPA) is not capable, in general, of reproducing quantitatively the properties of giant resonances (GRs), due to missing higher-order configurations and long-range correlations as well as neglected three-body terms in the Hamiltonian [3, 4]. In this work we go beyond first-order RPA and employ a UCOM interaction, $V_{\rm UCOM}$, in Second RPA (SRPA) [5, 6]. The coupling between ph and $2p2h$ excitations is taken into account. Excitations are built on top of the Hartree-Fock (HF) ground state, as in the usual RPA. The same interaction is used to describe the Hartree-Fock (HF) ground state and the residual interactions. The HF-based formulation of SRPA preserves the sum rules m_0 and m_1 of RPA [5], but not symmetries like translational invariance [7].

We have used the correlated Argonne V18 interaction and we have examined the IS monopole (ISM), IV dipole (IVD) and IS quadrupole (ISQ) response of the nuclei ^{16}O and ^{40}Ca. We present our results in comparison with experimental data in Fig.1. In all cases, the SRPA centroid energies are much lower than the RPA ones. The reason is to a large extent that, within SRPA, the coupling of single-particle states with virtual phonons is implicitly taken into account. This dresses the underlying HF single-particle states with self-energy insertions and brings them closer to each other energetically, thereby lowering the underlying ph energies. It is an important physical effect which cannot be ignored when using completely "undressed" (with respect to long-range correlations) HF states like the ones produced by the $V_{\rm UCOM}$. In this scheme the undressed HF energies are viewed as auxiliary model quantities which should not be directly compared with experiment.

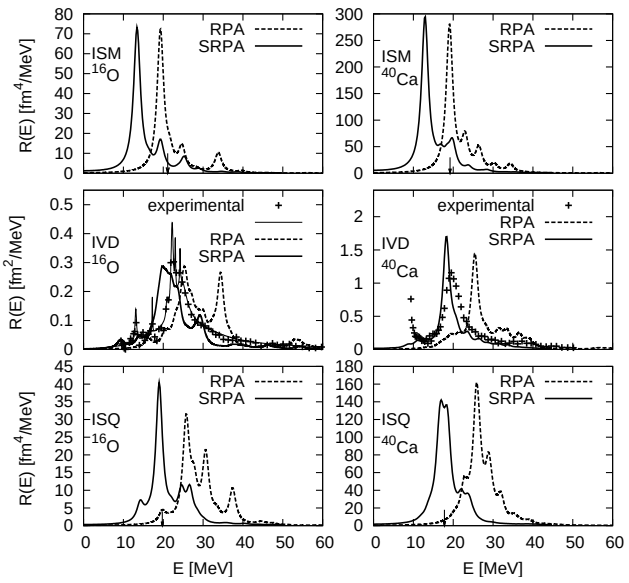

Figure 1: The ISM, IVD, and ISQ strength distributions for ^{16}O and ^{40}Ca compared with experimental data (points) or centroids (arrows) taken from Refs. [8, 9, 10, 11, 12].

We observe that the IV GDR is more realistically reproduced within SRPA than within RPA. Its centroid energy is somewhat underestimated. In the case of the IS GQR, the agreement of the SRPA results with experiment is very good. It appears as though, once coupling to higher-order configurations is taken into account, a realistic effective mass is restored. The energy of the IS GMR is underestimated. This is another indication that there are missing three-body effects and our two-body interaction should be supplemented with a three-body term to describe them.

In short, the UCOM-SRPA emerges as a promising tool for consistent calculations of collective states in closed-shell nuclei. This is an interesting development, given that SRPA can accommodate more physics than RPA (e.g., fragmentation) and provides a more fundamental treatment of the nucleon effective mass. Remaining discrepancies due to the missing three-body terms and self-consistency issues of the present SRPA model should be considered in future work. Up to now we have considered mostly the centroids of GRs, but their decay properties can also be studied within UCOM-SRPA. Heavier nuclei and low-lying states will be a topic for future work as well.

* Supported by the Deutsche Forschungsgemeinschaft, SFB 634.

References

[1] R. Roth et al, Nucl. Phys. **A745**, 3 (2004).
[2] R. Roth et al, Phys. Rev. **C72**, 034002 (2005).
[3] N. Paar et al, Phys. Rev. **C74**, 014318 (2006).
[4] P. Papakonstantinou et al, Phys. Rev. **C75**, 014310 (2007).
[5] C. Yannouleas, Phys. Rev. **C35**, 1159 (1987).
[6] J. Wambach, Rep. Prog. Phys. **51**, 989 (1988).
[7] M. Tohyama and P. Schuck, Eur. Phys. J. **A19**, 203 (2004).
[8] Y.-W. Lui et al, Phys. Rev. **C64**, 064308 (2001).
[9] D. Youngblood et al, Phys. Rev. **C63**, 067301 (2001).
[10] J. Ahrens et al, et al., Nucl. Phys. **A251**, 479 (1975).
[11] S. LeBrun et al, Phys. Rev. **C35**, 2005 (1987).
[12] A. Veyssière et al, H. Beil, Nucl. Phys. **A227**, 513 (1974).

RPA and shell model study of the proton Pygmy resonance

C. Barbieri[1], E. Caurier[2], K. Langanke[1,3], and G. Martínez-Pinedo[1]

[1]GSI, Darmstadt, Germany; [2]Université Louis Pasteur, Strasbourg, France; [3]TU, Darmstadt, Germany

Recent advances in the experimental techniques for radioactive beams have led to the discovery of low-lying dipole strength in neutron rich isotopes which is interpreted as a pygmy dipole resonance (PDR). This new excitation mode is explained as the resonant oscillation of the weakly bound neutron skin against the isospin saturated proton-neutron core. The possibility for a similar excitation for the proton skin has been considered recently in Ref. [1] using a relativistic model and the quasiparticle random phase approximation (QRPA). These calculations suggest that low-lying dipole strength should be observed also in isotopes close to the proton dripline, such as ^{32,34}Ar.

In this work, we study the dipole excitation spectrum of these isotopes by performing both RPA and shell model calculations in a no-core model space [2]. The calculations were performed using the unitary correlator operator method interaction (V_{UCOM}) with a tensor correlation volume of $I_\vartheta = 0.09$ fm^3 [3, 4]. The shell-model calculations included up to 2p2h configurations, and go beyond the RPA approach. It is found that this configuration mixing broadens the pygmy strength slightly and reduces sensibly its strength, as compared to the RPA predictions. The resulting distribution are shown in Figs. 1 and 2.

For ^{32}Ar, enhanced low-lying strength was found at energies up to 12 MeV, which could be identified as proton PDR. The corresponding strength distribution is peaked at about 9 MeV. The RPA approximation predicts about 1.0 e^{2}fm^2 in this energy region. Additional correlations, as accounted for in shell model studies, reduce this strength. Furthermore the pygmy peak is slightly broadened due to a larger number of configurations. By explicitly including up to 2p2h states, the pygmy strength is halved to 0.49 e^{2}fm^2 (see Tab. 1). The results obtained here predict a well defined pygmy peak separated from the IVGDR, in accordance with the previous relativistic QRPA calculations of Paar et al. [1]. Excitations associated with a PDR were also found for ^{34}Ar, which has only two more protons than neutrons. The present calculations place its strength

	^{32}Ar		^{34}Ar	
	$\bar{E}_{pyg}$	$\sum B_{pyg}$(E1)	$\bar{E}_{pyg}$	$\sum B_{pyg}$(E1)
RPA	9.15	1.0	12.7	0.8
SM(2p2h)	8.95	0.49	11.6	0.62

Table 1: Total dipole strength (e^{2}fm^2) and its centroid (MeV) in the Pygmy resonance region, as obtained in RPA and shell model with 2p2h configurations. The dipole distribution was integrated up to 12 MeV of excitation energy for ^{32}Ar and 14 MeV for ^{34}Ar.

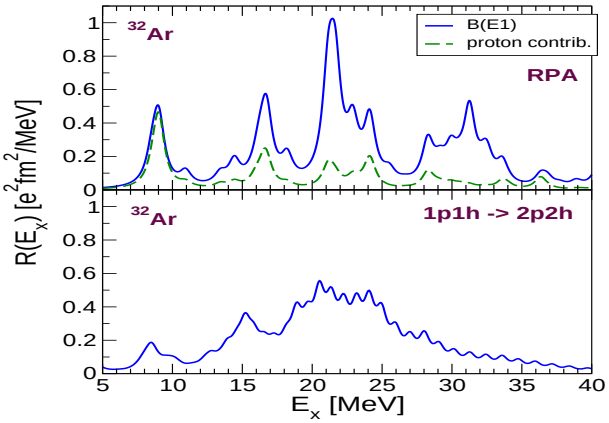

Figure 1: Isovector spectral strength for ^{32}Ar obtained with consistent HF+RPA (top) and the shell model up to 2p2h (bottom) [2]. The dashed line in the RPA plot, shows the contribution coming form proton excitations.

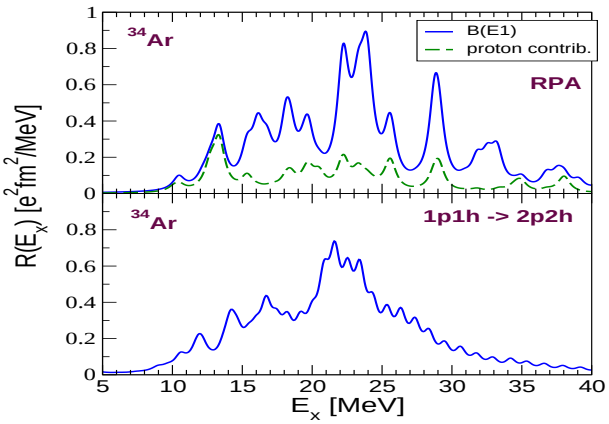

Figure 2: Same as Fig. 1 but for ^{34}Ar.

at energies up to 14 MeV and close to the IVGDR. The total strength found up to this energy is also reduced by shell model calculations, as compared to RPA. However, the mixing with the nearby giant resonance states leads to a rather uniform response without a well defined pygmy peak.

References

[1] N. Paar, D. Vretenar, and P. Ring, Phys. Rev. Lett. 94, 182501 (2005).

[2] C. Barbieri, E. Caurier, K. Langanke, and G. Martínez-Pinedo, Phys. Rev. C (2008), in print.

[3] T. Neff and H. Feldmeier, Nucl. Phys. **A713**, 311 (2003).

[4] R. Roth, H. Hergert, P. Papakonstantinou, T. Neff, and H. Feldmeier, Phys. Rev. C 72, 034002 (2005).

Breaking of the SU(4) symmetry in the pf-shell nuclei

I. Petermann*[1,2], K. Langanke[1,2], G. Martínez-Pinedo[1], and K. Sieja[1]
[1]GSI, Darmstadt, Germany; [2]Institut für Kernphysik, TU Darmstadt, Germany

The SU(4) symmetry is known to be a reasonable concept for p-shell nuclei and is recognizable in sd-shell nuclei. In heavy nuclei it is strongly broken. However, as pointed in [1], the breaking of SU(4) symmetry may be exaggerated in nuclear models which do not consider all, but only certain correlations, e.g. HFB-type and IBM models that only include pairing between like-nucleons. The isovector and isoscalar pairing are both needed to complete SU(4) symmetry in the spin-isospin space. It was noted in [2] that the sizable low-lying strength in GT$_-$ transitions can be a proof of the reminiscence of the SU(4) symmetry and the long searched-for indicator of the proton-neutron pairing. Since the Gamow-Teller operator is one of the SU(4) group generators, it can only connect states belonging to the same group representations. Thus, if one considers an odd-odd $N = Z$ nucleus and its isobar with $N = Z+2$, then the full GT$_-$ strength of the $T = 1, J = 0$ ground state of the isobar should be concentrated in a single daughter state at low excitation energy with $T = 0, J = 1$, if SU(4) were a good symmetry. Of course, the GT resonance is fragmented in real nuclei but the amount of the GT$_-$ strength located at low excitation energy may be a test of how much it is broken. The GT$_-$ strengths were calculated using large scale shell-model approach with KB3G interaction for several pf shell nuclei in Ref. [3]. The agreement of the shell-model calculations with the available experimental data is reasonable. Shell model calculations predicting small GT$_-$ strength at low excitation energies for ^{62}Ge will soon be experimentally tested at GSI. The analysis of the GT strengths confirms former results [1] that in pf nuclei the SU(4) survives only in $N = Z$ nuclei in the beginning of the shell. It was found that the latter gets broken with growing neutron excess and when moving from double-magic to mid-shell nuclei. Obviously, a strong spin-orbit splitting connected to a sizable splitting of the single-particle levels of spin-orbit partners, breaks as well the SU(4) symmetry. The influence of the spin-orbit splitting on the GT$_-$ strengths is shown in Figure 1 where the results of calculations with artificially modified interaction for ^{50}Cr are shown. The lowest part of the Figure corresponds to a calculation with an original force, while in the uppest one the spin-orbit splitting is removed. The middle part of the plot shows the situation between these two cases. As expected, when no spin-orbit splitting is present, the GT$_-$ resonance is concentrated in 90% in a single transition to the first 1^+ state which gets more and more fragmented and shifted to higher energies once the spin-orbit splitting is switched on.

* Supported by the Deutsche Forschungsgemeinschaft through contract SFB 634.

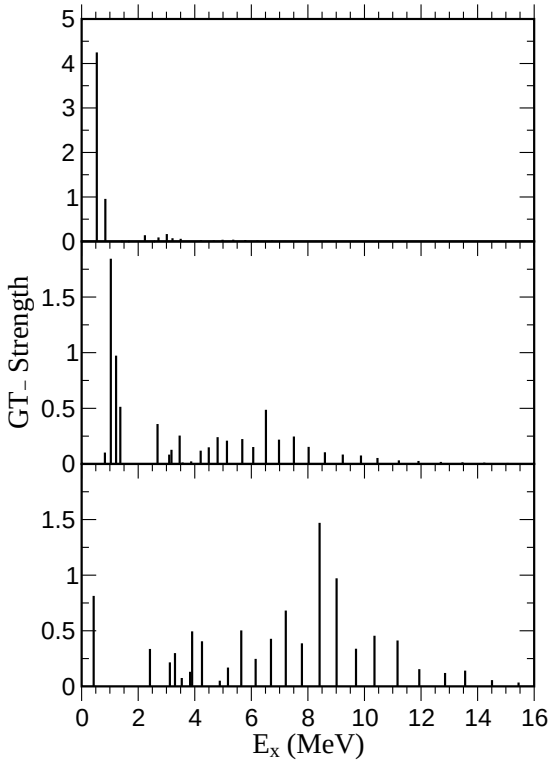

Figure 1: GT$_-$ strength distributions in ^{50}Cr calculated with rescaled KB3G interaction. The lowest panel corresponds to the original KB3G force, the upper to the no spin-orbit splitting limit while the middle part of the Figure shows the situation in between the two cases.

More systematic investigations of the SU(4) symmetry breaking and GT strengths distributions are still under way in pf and $sdpf$ nuclei. The large scale shell model calculations, as a model of reference, can be then compared to the predictions of the SU(4)-Wigner and of the Eliott-Evans SU(4) (i.e. IBM-4) models. The interest is to look into the energies, M1 and E2 electromagnetic transition rates and to GT strengths distributions and to provide a complete picture of GT and magnetic properties of nuclei in the mass $A \sim 50$ region.

References

[1] P. Vogel and W.E. Ormand, Phys. Rev. C **47** (1993) 623.

[2] F. Iachello, *Shell Model and Nuclear Structure*, (World Scientific, Singapore, 1988), p409.

[3] I. Petermann, G. Martínez-Pinedo, K. Langanke, E. Caurier, Eur. Phys. J. A **34**, 319 (2007).

Beta-decay of nuclei near $N = 82, 126$ closed neutron shells *

I.N. Borzov†[1], J.J. Cuenca-García[1], K. Langanke[1], G. Martínez-Pinedo[1], and F. Montes[2]

[1]Gesellschaft für Schwerionenforschung Darmstadt, Planckstr. 1, D-64291 Darmstadt, Germany; [2]National Superconducting Cyclotron Laboratory, Michigan State University, East Lansing, MI 48824, USA

Half-lives of nuclei with magic neutron numbers play an important role in the matter flow of the astrophysical r-process. We have used a self-consistent approach to calculate the half lives of spherical nuclei in the vicinity of the $N = 82$ and 126 neutron shell closures. Our calculations are based on the description of the ground states by the Fayans energy-density functional (DF) [1], while the β-strength-functions for Gamow-Teller and first-forbidden decays are determined in the continuum QRPA approach using the Landau-Migdal spin-isospin NN-interaction augmented by the one-pion and one-rho meson exchange [2]. The DF+CQRPA approach has been proven to give a good description of the ground state and β-decay properties, and magnetic moments of spherical nuclei [1-3].

We have calculated the β half-lives for nuclei with charge numbers $Z = 42 - 49$ and $Z = 72 - 79$ relevant for the r-process path near the neutron shells at $N = 82$ and 126. Fig.1 compares our results with recent data for the

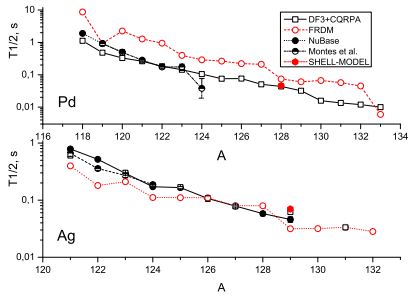

Figure 1: Beta-decay half-lives of Pd, Ag isotopes.

$Z = 46, 47$ isochains [6] and with half lives obtained on the basis of the Finite Range Droplet Model + Gross Theory (FRDM) [4] and the shell model [5]. Our agreement with data is rather good and points to shorter half lives of the N=82 waiting points than predicted by the FRDM approach. The consequences of the improved half-lives have been explored in local r-process calculations using once the standard FRDM half lives and then replacing the FRDM results by the present ones. Most strikingly, our shorter half-lives yield a noticeably larger mass flow to heavier nuclei beyond $N = 82$ (Fig.2).

Recently an experiment at GSI has for the first time determined half-lives of nuclei in the $N \approx 126$ region below the doubly magic ^{208}Pb, which serve as stringent test for model predictions. As is shown in Fig.3 our calculated half-lives are generally in better agreement with the

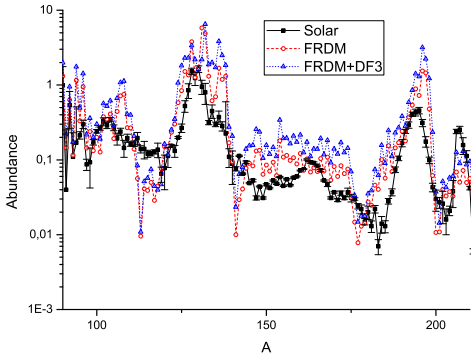

Figure 2: The r-process abundances calculated for two sets of β-half-lives: FRDM [4] and FRDM+DF3 (see text).

data in this mass range than the FRDM predictions. In $N \approx 126$ region, the calculations find significant contributions of first-forbidden transitions to the half-lives which have been either ignored or insufficiently accounted for in previous studies.

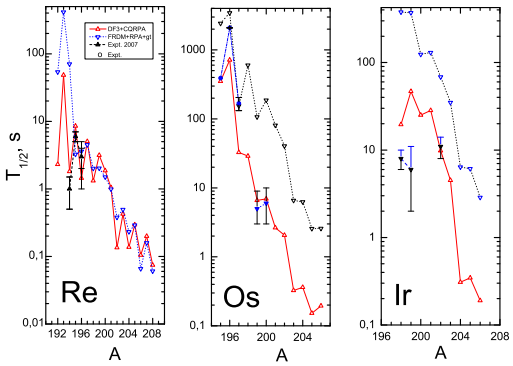

Figure 3: Beta-decay half-lives of Re, Os, Ir isotopes.

References

[1] S.A. Fayans et al., Nucl. Phys. A**676** (2000) 49.

[2] I.N. Borzov, Phys.Rev. C **67** (2003) 025802.

[3] I.N.Borzov et al., Rus.J.Nucl.Phys. **71** (2008) 1-24

[4] P. Moeller et al., Phys.Rev. C **67** (2003) 055802.

[5] J. Cuenca-García et al., Eur.Jour.Phys. A **34** (2007) 99.

[6] F. Montes et al., Phys.Rev. C **73** (2006) 035801.

[7] T. Kurtukian-Nieto, J. Benlliure et al. (2007, submitted)

* Work supported by DFG contract No. 436 RUS 113907/0-1

† i.borzov@gsi.de

Role of phonon coupling in the ^{132}Sn(e,e′) cross sections of PDR excitation *

S. Kamerdzhiev[†1], V. Ponomarev[2], G. Tertychny[1], and the ELISe collaboration[3]

[1]IPPE Obninsk, Russia; [2]IKP TU Darmstadt, Germany; [3]GSI Darmstadt, Germany

The low-lying electric dipole strength near the nucleon separation energy which is often called "Pygmy Dipole Resonance" (PDR) has attracted the interest of several research groups [1-4]. The reason is that the PDR influences strongly the r-process in astrophysics. For example, the inclusion of the PDR increases the elemental r-abundance distributions for nuclei around A = 130 by about two orders of magnitude [4] in comparison with extrapolation of the giant dipole resonance tail.

The only means to predict the PDR properties, especially in unstable nuclei, are microscopic calculations. The modern status of them is similar to that of the giant resonances in the sense that in both cases it is necessary to go beyond the standard RPA or QRPA approaches and to include the interaction of the single particle and collective degrees of freedom, i.e., to add phonon coupling (PC). Because the PDR exhausts only about 1% of the Thomas-Reihe-Kuhn energy weighted sum rule (EWSR) this phenomenon is a challenge for the theory and the modern experimental data should be helpful to clarify the problem. Possibilities of the electron scattering are of great interest in this connection.

Using the Extended Theory of Finite Fermi Systems [5] which takes into account, in addition to the standard RPA, the single-particle continuum and phonon coupling, we have calculated the photoabsorption cross section for ^{132}Sn in a wide energy interval (5.0-35.0) MeV with and without phonon coupling. That was necessary to compare with the recent GSI experiment [2]. We obtained the PDR at about 10 MeV which is enhanced by the phonon coupling. In the (5.0-10.0) MeV interval it exhausts 3.7% of the EWSR. These characteristics are in a reasonable agreement with the experimental data [2], as well as for the GDR data.

We have calculated the transition densities from the E1 strength distributions and found that the PDR in ^{132}Sn has a large isoscalar component while the GDR is a pure isovector mode. This result agrees with the properties of the PDR and GDR in stable nuclei [1].

In Fig.1 we present the calculations of the ^{132}Sn(e,e′) cross sections in the DWBA for the electron energy of 300 MeV calculated with these transition densities (solid and dashed lines). For comparison, we also present the results obtained within the RPA, i.e. without PC (circles and crosses). One notices that the role of the PC for the absolute value of the (e,e′) cross sections is more important for the PDR: while RPA+PC and RPA results almost coincide for the GDR, a difference between them for the PDR is

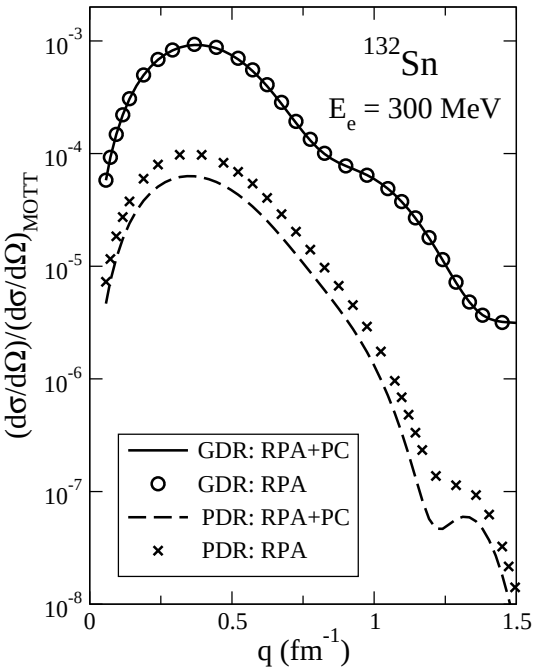

Figure 1: The ^{132}Sn(e,e′) cross section of excitation of the GDR and PDR with and without phonon coupling

a factor of 1.7 at q=0.8 fm^{-1}. The later is due to the considerable difference in the summed E1 strength for the PDR in RPA and RPA+PC calculations. We hope that future experiments will allow to clarify the question and conclude on accuracy of predictions by our approach.

.

.

References

[1] N. Ryezayeva, T. Hartmann, Y. Kalmykov et al., Phys. Rev. Lett. 89, 272502 (2002).

[2] P. Adrich, A. Klimkiewicz, M. Fallot et al., Phys. Rev. Lett. 95, 132501 (2005).

[3] S.Volz, N.Tsoneva, M. Babilon et al., Nucl. Phys. A 779 , 1 (2006).

[4] S. Goriely, Phys. Lett. B460, 138 (1998).

[5] S. Kamerdzhiev, J. Speth, G.Tertychny, Phys. Rep. 393, 1 (2004).

* Work supported by the INTAS grant 03-54-6545, DFG grant SFB-634 and by the RFBR grant 05-02-04005

† kamerdzhiev@ippe.ru

Continuum RPA in the Relativistic Point Coupling Model

J. Daoutidis[1], P. Ring*[1], T. Nikšić[2], and D. Vretenar[2]
[1]Technische Universität München, Germany; [2]University Zagreb, Croatia

Abstract

A computer code is developed to solve the linear response equations in the continuum for the point-coupling Lagrangian of relativistic mean-field (RMF) theory. Satisfying agreement is found with earlier solutions of these equations in a discrete oscillator basis.

The response equations

The response to a dynamic external field is an important tool to investigate the structure of nuclear systems. With the new experimental techniques to investigate nuclei far from stability it has gained renewed interest in recent year. On the theoretical side the random phase approximation in the framework of modern density functional theories is an excellent tool to investigate this response. Covariant density functionals are of special importance, because they provide with a minimal set of phenomenological parameters an excellent description of nuclear properties all over the periodic table [1]. So far, the relativistic RPA and QRPA equations have been solved mostly in a discrete basis [2]. Here the continuum is not treated correctly and one obtains in the first step a discrete spectrum, which has to be smeared out by a Lorentzian. In order to check the validity of this method we developed a program for the solution of the linear response equations in the continuum.

Starting from the energy density of the relativistic point coupling model [3] with the parameter set PC-F1, we solve in a first step the RMF equations on a mesh in r-space. This gives us the static solution of the problem and using the techniques of Ref. [4] it allows us to calculate the free-response $R^0(\mathbf{r}, \mathbf{r}', E)$ in an external field.

In the second step we solve the linear response equation

$$\begin{aligned} R(\mathbf{r}, \mathbf{r}', E) &= R^0(\mathbf{r}, \mathbf{r}', E) \\ &+ \int d^3r'' R^0(\mathbf{r}, \mathbf{r}'', E) V(r'') R(\mathbf{r}'', \mathbf{r}', E) \end{aligned} \quad (1)$$

where the radial dependence of the interaction parameters $V(r)$ is determined by the density dependence of the coupling constants of the point coupling model. In the case of spherical symmetry this is a set of one-dimensional integral equations in the radial coordinate r, which is solved on a mesh by matrix inversion.

The dipole response in ^{90}Zr

In Fig. 1 we show for the nucleus ^{90}Zr the free isovector dipole response (left panels) and compare it with the full response in the right panels. We observe the well known

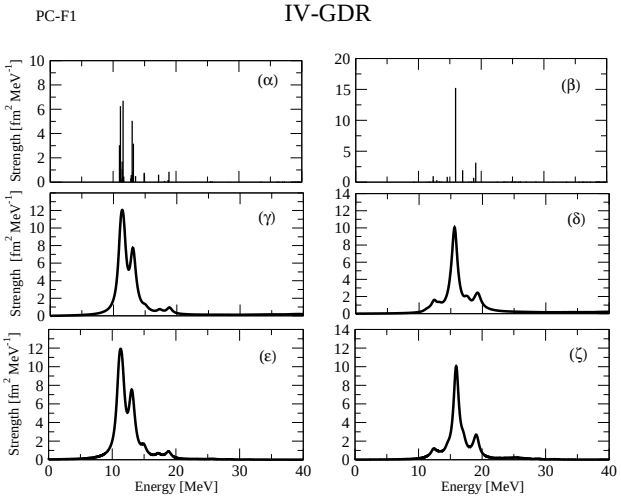

Figure 1: The isovector dipole response in ^{90}Zr as a function of the energy. The left and right panels show the free and the full response.

shift of the IVGDR to higher energies. In the upper two panels we show the results from a discretized calculation in a spherical oscillator basis. In the middle panels we show the same calculations, but now the peaks are smeared out by a Lorentzian curve. In the lower two panels we show the results of a continuum RPA calculation. We find that the discretized calculations smeared with a Lorentzian is in excellent agreement with the full continuum calculation.

Of course, this is a nucleus in the valley of stability and pairing correlations are not taken into account so far. Work is in progress to include pairing correlations and to investigate also nuclei far from stability close to the drip lines.

This work has been supported in part by the Bundesministerium für Bildung und Forschung - project 06 MT 246 and by the DFG cluster of excellence "Origin and Structure of the Universe" (www.universe-cluster.de)

References

[1] D. Vretenar, A. V. Afanasjev, G. A. Lalazissis, and P. Ring, Phys. Rep. **409**, 101 (2005).

[2] T. Nikšić, D. Vretenar, and P. Ring, Phys. Rev. **C72**, 014312 (2005).

[3] T. Bürvenich, D. G. Madland, J. A. Maruhn, and P.-G. Reinhard, Phys. Rev. **C65**, 044308 (2002).

[4] S. Shlomo and G. F. Bertsch, Nucl. Phys. **A243**, 507 (1975).

* ring@ph.tum.de

Low-energy nuclear dynamics within energy density functional theory

E. Litvinova[1], P. Ring[2,3], V. Tselyaev[4], K. Langanke[1], G. Martinez-Pinedo[1], H.P. Loens[1], H. Feldmeier[1], J. Dobaczewski[5], and V. Flambaum[6]

[1]GSI, Darmstadt, Germany; [2]Technische Universität München, Germany; [3]Universidad Autónoma de Madrid, Spain; [4]St. Petersburg State University, Russia; [5]University of Warsaw, Poland; [6]University of New South Wales, Sydney, Australia

Relativistic Quasiparticle Time Blocking Approximation: astrophysical applications

The self-consistent Relativistic Quasiparticle Random Phase Approximation (RQRPA) [1] based on the covariant energy density functional is supplemented with the quasiparticle-phonon coupling (QPC) model within the Quasiparticle Time Blocking Approximation (QTBA) [2]. The relativistic QTBA (RQTBA) being an extension of the model of Ref. [3] for systems with pairing is formulated in terms of the Bethe-Salpeter equation (BSE) in the doubled quasiparticle space. The BSE with an energy-dependent residual two-quasiparticle interaction is solved in the shell-model Dirac basis as well as in the momentum-channel representation. The same NL3 set of the coupling constants generates the Dirac-Hartree-BCS single-quasiparticle spectrum, the static part of the residual two-quasiparticle interaction and the quasiparticle-phonon coupling amplitudes providing a fully consistent description of nuclear excited states.

A quantitative description of electric dipole excitations in the chain of even tin ^{100}Sn – ^{140}Sn and nickel ^{68}Ni - ^{78}Ni isotopes and in the chain of isotones ^{88}Sr, ^{90}Zr, ^{92}Mo is performed within the RQTBA framework. Coupling to collective vibrations results in spectra with a multitude of 2q$\otimes$phonon states providing a noticeable fragmentation of the giant dipole resonance as well as of the soft dipole mode (pygmy resonance). The obtained results for photoabsorption cross sections and for integral contributions of the low-lying strength to the calculated dipole spectra agree very well with the available experimental data, see Fig. 1.

The influence of the pygmy resonance on (n,γ)-reaction cross sections and reaction rates has been investigated within the Hauser-Feshbach model. The (n,γ) cross sections can be strongly enhanced which has a pronounced influence on the r-process abundance distribution.

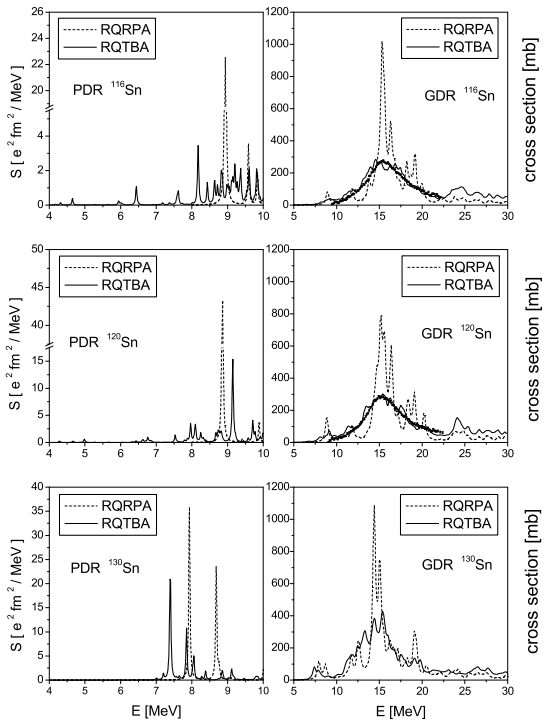

Figure 1: Dipole photoabsorption cross sections in tin isotopes calculated within RQRPA and RQTBA, compared to EXFOR data (right panels), and fine structure of the low-lying strength (left panels).

Enhancement of variation of the fine structure constant in ^{229}Th

A very narrow transition between the ground and the first excited states in ^{229}Th, supposed to be investigated with laser spectroscopy for a laboratory search for the variation of the fundamental constants [4], has been analysed within the HFB method based on the Skyrme density functional [5]. Changes of the energy levels due to a possible variation of the fine structure constant α are expressed through the Coulomb energy by the Hellmann-Feynman theorem. It has been found that the relative change of the transition frequency $\delta\omega/\omega$ is several thousand times greater than the variations $\delta\alpha/\alpha$. The numerical accuracy has been analysed.

References

[1] N. Paar, P. Ring, T. Nikšić, and D. Vretenar, Phys. Rev. **C67**, 034312 (2003).

[2] V. I. Tselyaev, Phys. Rev. **C75**, 024306 (2007).

[3] E. Litvinova, P. Ring, and V. I. Tselyaev, Phys. Rev. **C75**, 064308 (2007).

[4] V.V. Flambaum, Phys. Rev. Lett. **97**, 092502 (2006).

[5] J. Dobaczewski, J. Dudek, Comput. Phys. Commun. **102**, 166 (1997); **102**, 183 (1997).

Parity-dependent nuclear level densities and their influence on Hauser-Feshbach calculations for astrophysical reaction rates

H. P. Loens[1,2], C. Özen[1], K. Langanke[1,2], G. Martínez-Pinedo[1], Y. Kalmykov[2], P. von Neumann-Cosel[2], and A. Richter[2]

[1]GSI, Darmstadt, Germany; [2]Technische Universität Darmstadt, Darmstadt, Germany

The nuclear level density is a crucial input to the so-called statistical or Hauser-Feshbach model [1]. This model describes nuclear reactions via the formation of a compound nucleus. Due to its simplicity and applicability for highly excited nuclei, this model is often used to obtain astrophysical reaction rates for nucleosynthesis modelling. However, for the involved nuclei few data is experimentally known and a theoretical nuclear level density model is needed to describe the nuclear spectrum at higher energies.

Most of the theoretical models are based on a statistical description of the nucleus as a Fermi gas combined with parameter modifications to describe experimental data phenomenologically (see [1]). However, microscopical methods became computationally feasible recently. These microscopical calculations of parity and angular momentum projected nuclear level densities are based upon Shell-Model Monte Carlo (SMMC) [2, 3], Hartree-Fock-Bogolioubov (HFB) plus combinatorial methods [4] or BCS-like methods [5]. All these approaches show a non-uniform parity distribution for most nuclei at low to moderate energies. Moreover, experimental investigations also indicate that for certain nuclei the point of equipartition of parities lies at several MeV [3] (see also fig 1).

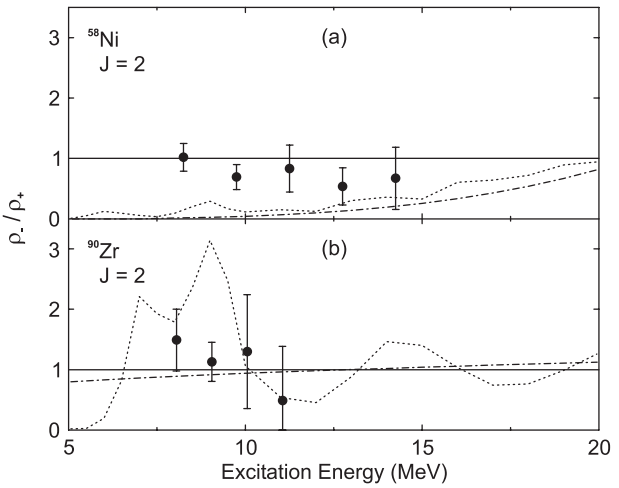

Figure 1: Ratio of experimental (see [3]) parity projected level densities (circles) of **(a)** ^{58}Ni and **(b)** ^{90}Zr compared to a Fermi gas description (solid lines), HFB calculations [4] (dotted lines) and SMMC calculations [3] (dash-dotted lines).

We have extended the statistical model to take a non-uniform parity distribution for the target, compound and residual nucleus into account. This extends previous work [5] - where detailed parity distributions were employed only for the target and residual nuclei - by additionally considering the parity dependence within the compound via the introduction of weighting factors into the summation over the compound quantum numbers (see e.g. [1], p. 289, eq. 3.6). These weighting factors are obtained from microscopical parity-projected level densities given by [4, 5].

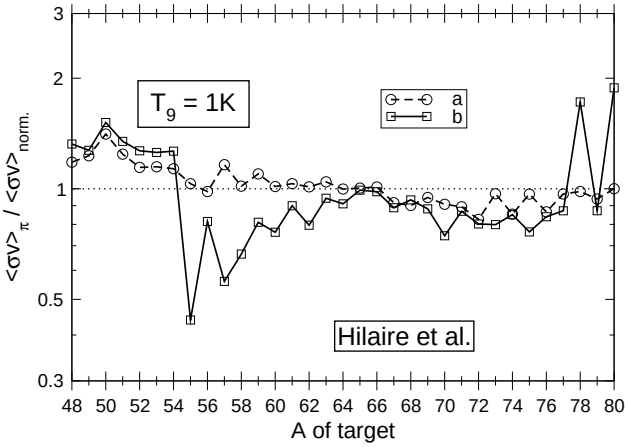

Figure 2: Ratio between (n,γ) reaction rates for nickel isotopes at temperature 1 GK obtained assuming: (a) non-uniform parity distribution for target and residual nucleus, (b) non-uniform parity distribution for target, compound and residual nucleus; and the reaction rate obtained with a uniform parity distribution - the level densities of [4] were used.

With this extended method we calculated a full chain of (n,γ)-reactions on nickel isotopes (see fig. 2). We find large effects on the calculation of astrophysical reaction rates, even larger than the inclusion of non-equipartitioned parities within the target and residual nuclei only. Possible consequences of our treatment on nucleosynthesis calculations will be explored in the future.

References

[1] J.J. Cowan *et al.*, Phys. Rep. **208**, 1 (1991)

[2] C. Özen *et al.*, Phys. Rev. C **75**, 064307 (2007)

[3] Y. Kalmykov *et al.*, Phys. Rev. Lett. **99**, 202502 (2007)

[4] S. Hilaire *et al.*, Nucl. Phys. A **779**, 63 (2006)

[5] D. Mocelj *et al.*, Phys. Rev. C **75**, 045805 (2007)

Separability of compound-nucleus and fragment properties in fission

K.-H. Schmidt[1], A. Kelić[1], and M. V. Ricciardi[1]
[1]GSI, Darmstadt, Germany.

Nuclear fission is a prominent example for the decay of a meta-stable state, in which many properties of the decay process are determined on the out-of-equilibrium descent outside the meta-stable state beyond the barrier. Out-of-equilibrium processes still pose a severe challenge to their theoretical description; thus, the realistic modelling of the fission process is far from being achieved at present times. This is a particular problem at low excitation energies, where the influence of nuclear structure is responsible for individual features, which are specific for each fissionning system. Thus, it is important to study a great variety of systems and to measure as many quantities as possible in order to gain a complete overview on the underlying physics. We have analyzed the large body of experimental data on nuclear fission with a semiempirical ordering scheme based on the macroscopic-microscopic approach and the separability of compound-nucleus (CN) and fragment properties on the fission path [1]. Using this approach we analyse [1] the microscopic corrections to the macroscopic potential from the appearance of fission channels. We applied this procedure to ^{226}Th, ^{239}U, ^{252}Cf, and ^{260}Md as shown in Fig. 1. According to the separability principle [1] it should be possible to trace the microscopic structures deduced in Fig. 1 back to shells in the fragments, which should be the same for all systems. The success of this approach is illustrated in Fig. 1–third row in a schematic way. Obviously, the complex behaviour of shell structure as a function of mass asymmetry of the four systems shown in Fig. 1 can be reproduced already rather well as a superposition of only two shells at N=82 and N=92. Thus, the separability of CN and fragment properties of the system on the fission path seems to be realized to a good approximation and makes the macro-microscopic approach particularly strong in its application to nuclear fission. By deducing the shell effects from the measured fission-fragment nuclide distributions and attributing those to two major shells in the nascent fragments, we arrived at a remarkably realistic reproduction of the microscopic features of fission over the whole range covered by experiment. This approach is also suited for robust extrapolations, e.g. it has already been used to predict nuclide distributions from the fission of neutron-rich nuclei on the astrophysical r-process path [2].

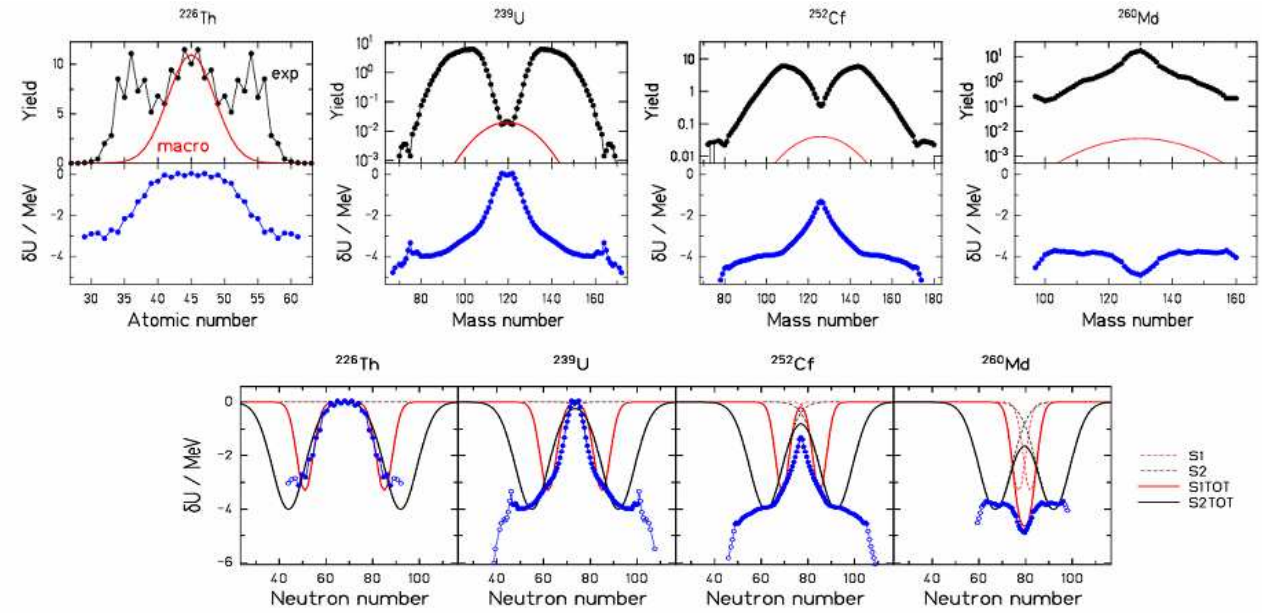

Figure 1: Extraction of the microscopic potential responsible for the nuclear-charge or mass split in fission: The amount the measured yields (data points in upper row) exceed the macroscopic prediction (red lines in upper row) is attributed to the shell-correction energy at saddle. The shell correction energies are displayed as a function of atomic number and mass number, respectively, (second row) and in a projection on neutron number (third row). In the third raw, also the comparison of the empirical shell corrections (points) and the shell correction energies constructed from two neutron shells at N=82 (S1, light lines) and N=92 (S2, dark lines) is shown. For more details and references to the data, see [1].

References

[1] K.-H. Schmidt, A. Kelić and M.V. Ricciardi, arXiv nucl-ex/0711.3967v1.
[2] A. Kelić, N. Zinner , et al., Phys. Lett. B616 (2005) 48

R-process Nucleosynthesis in Type II Supernovae

K. Otsuki[1], A. Arcones[1,2], A. Burrows [3], T. Janka[4], and G. Martínez-Pinedo[1,2]
[1]GSI, Darmstadt, Germany; [2]Institut für Kernphysik, TU Darmstadt, Germany; [3]Princeton, NY, USA;
[4]Max-Planck-Institut für Astrophysik, Garching, Germany

The origin of rapid-neutron capture elements is one of the outstanding problems in nuclear astrophysics. Although core-collapse supernovae are the leading candidate for the astrophysical site of the r-process, there is no definitive conclusion. This is partly because of the poorly understood explosion mechanism in current supernova models. Here, we explore the occurrence of the r-process in two different core-collapse supernova models with different explosion mechanisms.

R-process in Neutrino-Driven Winds

The proto-neutron star, which is formed in a core-collapse supernova, releases neutrinos during its Kelvin-Helmholtz cooling phase. These neutrinos heat up the material of the neutron star surface and carry with them an outflow of baryonic matter that is denoted as neutrino-driven wind.

We have used recent hydrodynamical simulations for neutrino-driven winds [1] together with an r-process nucleosynthesis network in order to study the production of heavy elements in such winds. Although the conditions achieved in the simulations are not favorable for the r-process as the entropy is too low they are useful to study the influence of the wind termination shock, which was found in neutrino-driven wind simulations. These studies allow us to understand the differences between a pure exponential expansion that is normally assumed in parametric calculations and a realistic wind (see Fig. 1)

R-process in New Supernova Model

Burrows et al. (2006) [2] have proposed a new supernova explosion mechanism which is driven by acoustic power generated in the inner core. In their 2D simulation, there are several mass elements with high enough entropy ($S > 500$) and low electron fraction($Y_e < 0.4$) to allow for an r-process to occur. Such environments have not been found in previous r-process studies based in neutrino driven winds. We have studied r-process nucleosynthesis in the 25 $M_\odot$ of reference [2]. In this model, entropies vary in the range of 1.8×10^5 to 9.2, electron fractions are 0.30 to 0.50.

Our network code consists of more than 10000 reactions and 4000 elements. Charged current reactions for seed production and neutron-capture reactions are solved at the same time. The neutron-capture of light elements are also included [3, 4]. We found that r-process in mass elements with entropy between 100 to 1000 generate a large amount of actinide elements. Studies of total ejecta, including contribution from low entropy mass elements, are ongoing.

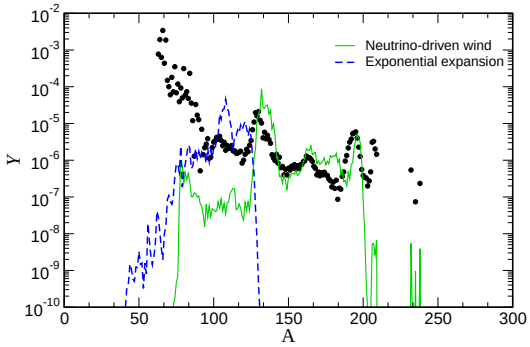

Figure 1: Final abundances for a mass element of a $15M_\odot$ supernova explosion where the entropy was increased by a factor of 2 (solid line). The closed circles indicate scaled solar abundances. The dashed line shows an exponential expansion with similar expansion time scale, entropy and Y_e to the wind expansion.

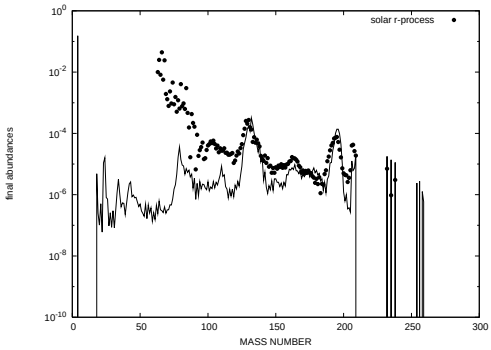

Figure 2: An example of r-process yields with entropy 146 and $Y_e = 0.38$. The closed circles indicate scaled solar r-process abundances.

References

[1] A.Arcones, H.Th.Janka, and L.Scheck, Astron.& Astrophys. 467,1227 (2007)

[2] A. Burrows, E. Livne, L. Dessart, C.D. Ott, and J. Murphy, ApJ 640 (2006) 878

[3] K. Otsuki, G.J. Mathews, and T. Kajino, New Astronomy 8 (2003) 767

[4] T. Sasaqui, T. Kajino, G.J. Mathews, K. Otsuki, and T. Nakamura, ApJ 634 (2005) 1173

Influence of Mass Uncertainties of Exotic Nuclei on the rp- and νp-Process

T. Fleckenstein[1], H. Geissel[1,2], G. Martinez-Pinedo[2], W.R. Plaß[1], H. Schatz[3], and C. Scheidenberger[1,2]

[1]Justus-Liebig-Universität Gießen, Germany; [2]GSI, Darmstadt, Germany; [3]Michigan State University, MI, USA

The impact of mass uncertainties of proton-rich nuclei with A=80-105 on astrophysical observables, e.g. x-ray burst light-curves, production path and final chemical abundance produced in nucleosynthesis (rp- and νp-processes) has been investigated. A database of mass measurements in the mass region A=80-135 since the last atomic-mass evaluation AME 2003 has been created. In addition, extrapolations have been done to hitherto experimentally unknown masses close to the proton dripline. In order to investigate the dependence of nucleosynthesis processes on mass uncertainties, network-codes for nucleosynthesis processes in a type II x-ray burst and for the nucleosynthesis processes in neutrino-driven proton-rich winds of a supernova explosion have been applied. New possible waiting point nuclei have been found in the rp-process, and important key nuclei have been discovered for the νp-process.

In particular, the x-ray burst lightcurve, the final abundances and the production flow have been investigated. In order to investigate the impact of the mass uncertainties of individual isotopes, the mass excess values have been varied by 2σ. These small mass excess changes, result in an impact on the astrophysical results of the network code(Fig.1). The impact on the astrophysical observables has been calculated, via an automatic master-slave-computer-network. The quantified impact have been summed up for the influences on the lightcurve, final ashes and production flow. Thus, the master-slave-network delivers 3 data tables, after a typical calculation time of the 100 CPU-cluster of two weeks. Within this calculation time, the master-slave-network varied up to three nuclides per run and compares all runs, which differ in only one nuclide's mass change. Using this method, it is possible to exclude nuclei, which have no impact on the astrophysical process model at the defined stellar conditions, e.g. temperature, density and entropy. These nuclei have no impact on the process, since no production flow passes these nuclei. Only a few nuclei show severe impact on the astrophysical parameters. Further investigation of these nuclei identified these nuclei as new possible waiting point nuclides (Fig.2). These investigations have been performed for the $rp-$ and the $\nu p-$process. The νp-process shows a different behavior, due to the additional neutron fluxes in the reaction- network. Because of the additional neutrons, the νp-process synthesizes less neutron-deficient than the $rp-$process. A more severe difference to the $rp-$process are the additional (n,p)-reactions, which bridge $\beta-$waiting point nuclei. Therefore the classical waiting point mechanism of the $rp-$process is no longer applicable.

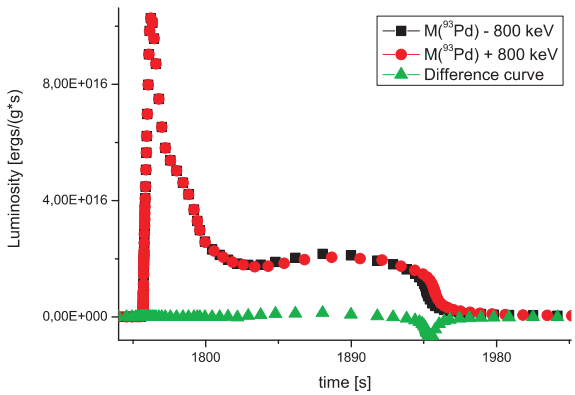

Figure 1: Comparison of two light-curves. The figure shows three curves. The black and the red line are results of the XRB-network calculation. The green one is the difference of both light-curves. Integral I is the area of the difference curve above 0. Integral II is the area below 0. For comparision of different runs, one calculates the absolut sum of both integrals. The second criterion is the maximal amplitude of the difference curve, which is caused by a decreased or increased burntime.

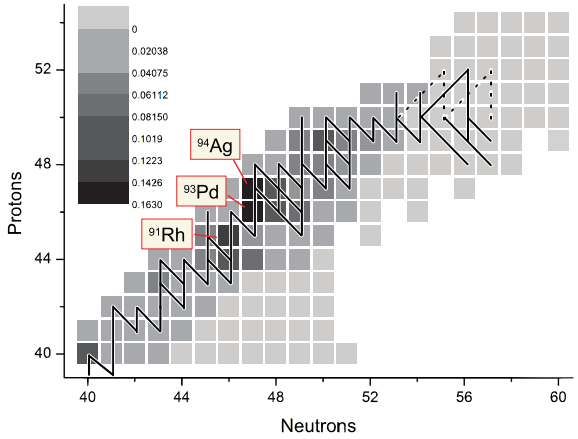

Figure 2: Overview on results of x-ray burst-simulations. Color-coded scale for the impact of mass variations on light-curve, final abundances (ashes) and path of the process. (White means not important, black stands for highest importance). The scale shows the relative impact, normalized to the mean value.

References

[1] Martinez-Pinedo et al.; **arXiv:astro-ph/0608490 v1**; [2006]

[2] Schatz et al.; **Physics Reports 294, 167-263**; [1998]

Light elements and neutrino emission from neutron star

A. Arcones [*1,2], G. Martínez-Pinedo[1], A. Schwenk[3], H.-Th. Janka[4], and K. Langanke[1]

[1]GSI, Darmstadt, Germany; [2]Institut für Kernphysik, TU Darmstadt, Germany; [3]TRIUMF, Vancouver, Canada; [4]Max-Planck-Institut für Astrophysik, Garching, Germany

After core-collapse supernova explosions, neutron stars form and cool down emitting neutrinos, which carry away baryonic matter from the surface of the new-born neutron star. This is known as neutrino-driven wind and it is considered the most promising site for the production of heavy elements via the rapid neutron capture process. We study details on the composition of the matter on the neutron star surface, which could be relevant for the characteristics of the wind.

All currently available calculations of core-collapse supernova explosions assume a composition of neutrons, protons, alpha particles and a representative heavy nucleus. However, the formation of light cluster nuclei with $A = 2, 3$ can take place for the temperature and density conditions present in the outer layers of the neutron star. We explore the impact of the so far neglected light element abundances based on two different equations of state. The virial equation of state [1] includes nuclei with $A \leq 4$ and their interactions. The Nuclear Statistical Equilibrium (NSE) equation of state considers an ensemble of non-interacting nuclei. In Fig. 1 we compare the compositions for the $15M_{\odot}$ model of Ref. [2] at a time of 2s after the explosion has started. The simpler composition commonly used in supernova simulations corresponds to the dashed line of the same figure.

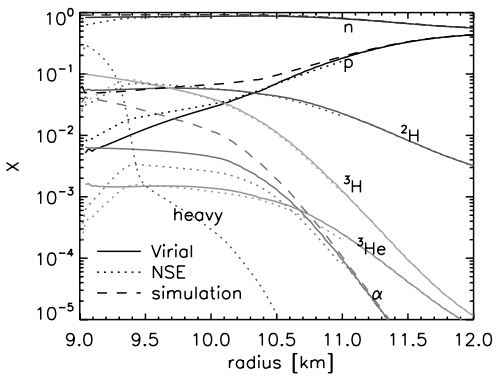

Figure 1: Mass fractions of different elements in the neutron star outer layers.

Once clusters of light elements start to appear most of the protons are bound in light nuclei. Neutrinos coming out from the neutron star interact mainly with neutrons, whose abundances do not change much when cluster formation is considered in the EoS. In contrast, for antineutrinos, which interact mainly with protons, the situation is different as now the interactions occur predominantly with deuterons and tritons. This can affect the properties (spectrum and luminosities) of the neutrinos emitted from the neutron star. To explore this effect we have computed the opacities, defined as $\kappa = \sigma n$ with σ being the cross section and n the number density of particles that interact with neutrinos. The opacities for antineutrino interactions with different elements are shown in Fig. 2. For the radii at which neutrino spectra form ($R_{\nu_e} \approx 9.7$ km and $R_{\bar{\nu}_e} \approx 9.1$ km) the total opacity is clearly dominated by the interaction with deuterons and tritons.

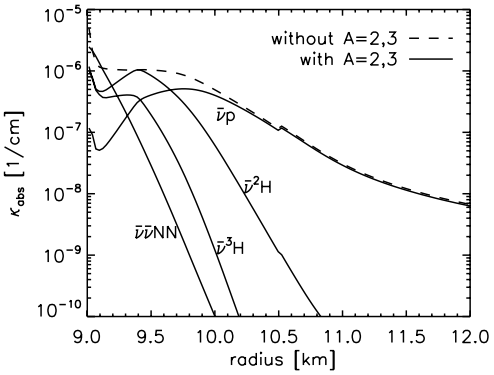

Figure 2: Absorption opacity for electron antineutrinos is shown in the surface of the neutron star 7s after the explosion. The solid lines correspond to calculation done with detail composition, while for the dashed lines only neutrons, protons and alpha particles are considered.

In order to quantify the possible changes full transport calculations are needed. We have, however, estimated that the average antineutrino energy is reduced by about 3% which can have consequences for the neutrino detection on Earth.

References

[1] E.O'Connor, D.Gazit, C.J.Horowitz, A.Schwenk, and N.Barnea, Phys.Rev.C 75, 055803 (2007)

[2] A.Arcones, H.Th.Janka, and L.Scheck, Astron.& Astrophys. 467,1227 (2007)

* supported by the Deutsche Forschungsgemeinschaft through contract SFB634

Dynamic polarization of ^{6}He in the elastic scattering at ^{209}Bi targets*

L. Borowska† [1,2], K. Terenetsky[2], V. Verbitsky[2], and S. Fritzsche[3,4]

[1]University of Kassel; [2]KINR, Kyiv, Ukraine; [3]GSI, Darmstadt; [4]Max-Planck Institute for Nuclear Physics, Heidelberg

The existence of (neutron) halos in light and mid-range nuclei has been one of the most exciting discoveries in nuclear and astrophysics during the last two decades [1]. Today, such neutron halos are well confirmed for various nuclei, including ^{6}He, ^{11}Li, ^{14}Be as well as for several others. Often, these halos are formed by two (or more) loosely attached neutrons which surround a deeply bound core with binding energies of less than 1 MeV, in contrast to the 6-8 MeV of stable nuclei. From the study of halo nuclei one may obtain therefore information not only about the nuclear forces but also on neutron-neutron correlations or (so-called) astrophysical S-factors [2] for describing various nuclear reactions.

Several theoretical model have been suggested in the literature to explain the structure of these halo nuclei. Apart from a number of microscopic (shell) models, emphasis was placed especially on the elastic scattering of halo nuclei in the field of heavy targets at energies below and near to the Coulomb barrier. While, for a pure Coulomb field, the angle-differential scattering cross section of a point-like projectile along a classical (Rutherford) trajectory is known to follow a $1/sin^4(\theta/2)$ dependence, with θ being the scattering angle of the projectile, deviations from this 'law' are expected if the projectile is surrounded by a neutron halo. From this viewpoint, ^{6}He projectile ions can be seen also as a bound $\alpha + 2n$ 'deuteron-like' (nuclear) cluster with mass $m_{\rm d}$, where a charged α core (the 'proton' with mass $m_{\rm p}$ and charge $Z_{\rm p}$) is surrounded by the neutral halo, (the 'neutron' with mass $m_{\rm n}$), and with a binding energy of about $\varepsilon_0 \approx -0.975$ MeV.

To further explore the (shape and) structure of neutron halos, we considered the elastic scattering of ^{6}He in the Coulomb field of ^{209}Bi target within the adiabatic approximation. In this approximation, an equation for the relative motion of the deuteron-like projectile,

$$\left[\frac{\hbar^2\Delta_{\mathbf{r}}}{2\mu} + \varepsilon_0 + \delta V(R) + \frac{Z_p Z_T e^2}{R} - \frac{Z_p Z_T e^2}{r_p} - V_{np}(r)\right]\varphi^+(\mathbf{r},\mathbf{R}) = 0\,, \quad (1)$$

was derived as function of the center-of-mass coordinate R, and where the complex potential $\delta V(R)$ describes both, the polarization as well as breakup of the neutron halo [3]. In fact, the potential $\delta V(R)$ can be constructed free of all parameters (other than those that are needed to describe the scattering process) and, hence, supports a direct solution of the elastic scattering of halo nuclei in the Coulomb field of heavy targets.

* Work supported by GSI under the Project KS-FRI.

† borowska@uni-bonn.de; now at University of Bonn

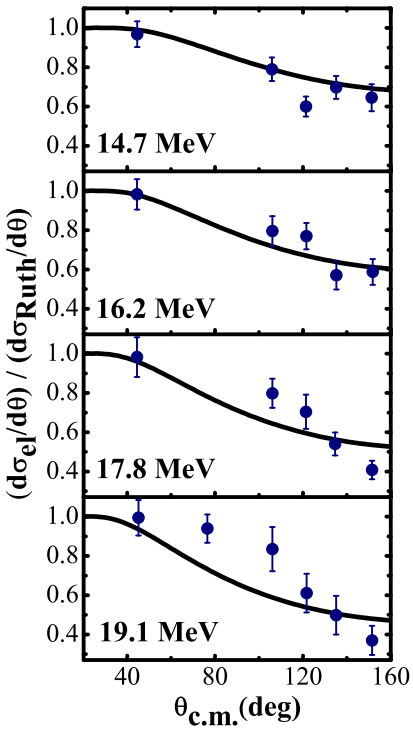

Figure 1: Elastic differential cross-sections for the collision of low-energy ^{6}He ions by ^{209}Bi nuclei as function of the scattering angle θ in the centre-of-mass frame. Comparison is shown for the four collision energies as observed experimentally [4].

Applying a numerical solution of $\delta V(R)$, the differential cross-section for the ^{6}He + ^{209}Bi elastic scattering were calculated at the sub-barrier energies between 14.7 and 19.1 MeV [3]. Figure 1 displays these cross sections and compares them with experiment [4], taken relative to the differential cross sections for a pure Rutherford scattering of a projectile with mass m_d and charge Z_p. The good agreement with experiment therefore makes a *di-neutron* configuration very likely for the ground state of the ^{6}He halo nucleus. No additional parameters were required in the computations in order to explain the deviations from Rutherford's scattering cross sections.

References

[1] I. Tanihata *et al.*, Phys. Rev. Lett. 55 (1985) 2676.

[2] W. Liu *et al.*, Nucl. Phys. A 758 (2005) 110.

[3] L. Borowska, K. Terenetsky, V. Verbitsky and S. Fritzsche, Phys. Rev. C 76 (2007) 034606.

[4] E. F. Aguilera *et al.*, Phys. Rev. Lett. 84 (2000) 5058.

The reaction ^{48}Ca + ^{238}U $\rightarrow$ ^{286}112* studied at the GSI-SHIP

S. Hofmann [*1,2], D. Ackermann [1], S. Antalic [3], H.G. Burkhard[1], V.F. Comas [4], R. Dressler [5], Z. Gan [6], S. Heinz [1], J.A. Heredia [4], F.P. Heßberger [1], J. Khuyagbaatar [1], B. Kindler [1], I. Kojouharov [1], P. Kuusiniemi [7], M. Leino [8], B. Lommel [1], R. Mann [1], G. Münzenberg [†1], K. Nishio [9], A.G. Popeko [10], S. Saro [3], H.J. Schött [1], B. Streicher [3], B. Sulignano [1], J. Uusitalo [8], M. Venhart [3], and A.V. Yeremin [10]

[1] GSI, Darmstadt, Germany; [2] Johann Wolfgang Goethe-Universität, Frankfurt, Germany; [3] Comenius University, Bratislava, Slovakia; [4] InSTEC, Habana, Cuba; [5] PSI, Villigen, Switzerland; [6] IMP, Lanzhou, China; [7] University of Oulu, Finland; [8] University of Jyväskylä, Finland; [9] JAEA, Tokai, Ibaraki, Japan; [10] FLNR, Dubna, Russia

The aim of our recent experiments at the GSI-SHIP was the confirmation of results obtained from the investigation of the reaction ^{48}Ca + ^{238}U $\rightarrow$ ^{286}112* at FLNR in Dubna [1]. Using the Dubna Gas-Filled Recoil Separator (DGFRS), most significant data were measured during the last eight years, which, if confirmed, would represent a great step towards discovery and exploration of the predicted island of superheavy elements (SHEs).

Despite the high level of experimental standards in heavy ion laboratories worldwide, only negative or ambiguous results were obtained in repetition experiments so far [2, 3]. Only recently, a first confirmation of data from the reaction ^{48}Ca + ^{242}Pu $\rightarrow$ ^{290}114* obtained at DGFRS was reported from a chemistry experiment, performed at FLNR in Dubna by an international collaboration [3, 4].

Due to the systematic study at DGFRS using ^{48}Ca beams and various actinide targets, nuclei in a new relatively neutron rich region were produced and assigned to elements from rutherfordium to element 116 and even element 118. On the basis of α decay chains and measurement of excitation functions, the produced isotopes are now consistently assigned, after correction of the number of emitted neutrons with respect to earlier experiments [5].

In particular, for the production of the isotope ^{283}112 in the reaction ^{48}Ca + ^{238}U via a 3n evaporation channel, a maximum cross-section of 2.5 pb was reported [1]. The decay properties were α emission with $T_{1/2}$ = 3.8 s and E_α = 9.54 MeV. A 90 % branching for spontaneous fission (SF) and a half-life of 0.20 s was obtained for the daughter nucleus ^{279}Ds. In two cases out of twenty, including the production of ^{283}112 via α decay from heavier elements, the decay chains continued down to ^{271}Sg or ^{267}Rf, where they ended by SF. The objective of our experiment was the reproduction of the data obtained by direct production.

Our study of the reaction ^{48}Ca + ^{238}U $\rightarrow$ ^{286}112* was performed in three parts. Part 1 took place from April 6 to June 9, 2005, part 2 from October 4 to 30, 2006, and part 3 from January 19 to February 14, 2007. Details of the irradiations and results are given in [6].

A total of four events was detected, which we assigned to a heavy nucleus produced in the reaction. One was observed in part 1 of the experiment, three in part 3. Two events consisted of an implanted evaporation residue, subsequent α decay and SF. In the other two cases no α particle was detected before SF.

The two decay chains including the α decays fully confirm the data that were previously assigned to the isotope ^{283}112 in experiments at FLNR. The two other events are consistent with a previously unknown 50 % SF branch of this isotope.

The important properties which so far can be deduced from the study of SHEs at DGFRS [1] are that the half-lives of isotopes increase, when the predicted spherical closed shell N = 184 is approached. The trend of shell-correction energies for nuclei along the measured decay chains reveals a monotonic decrease of the (negative) shell correction energies with increasing neutron number. No discontinuity is observed, when the proton number 114 is crossed at neutron numbers 172 to 176. This result could mean that proton number 114 as a closed shell or subshell has less influence on the stability of SHEs than the closed neutron shell at N = 184.

Future experimental work will take this aspect into account. The aim will be to reach N = 184, which is possible in various reactions using actinide targets and the neutron richest, but still stable projectiles. These reactions lead into a region of elements as heavy as Z = 120 and beyond, where reduced fusion probability must be expected. If, however, the subshell closure at Z = 120 has a stronger influence on the stability of SHEs than the subshell closure at Z = 114, as predicted by certain nuclear mean field models [7], then it could turn out that isotopes near Z = 120 and N = 184 possess increased stability and may become accessible to experimental studies.

References

[1] Yu.Ts. Oganessian: J. Phys. **G 34** (2007) R165.

[2] K.E. Gregorich et al., Phys. Rev. **C 72** (2005) 014605.

[3] R. Eichler et al., Nucl. Phys. **A 787** (2007) 373c.

[4] R. Eichler et al., Nature **447** (2007) 72.

[5] Yu. Ts. Oganessian et al., Phys. Rev. **C 69** (2004) 054607.

[6] S. Hofmann et al., Eur. Phys. J. **A 32** (2007) 251.

[7] K. Rutz et al., Phys. Rev. **C 56** (1997) 238.

* email: S.Hofmann@gsi.de

† *Present address:* D-31199 Diekholzen, Germany

Calculated decay properties of Z = 120 isotopes

A. Sobiczewski[1,2] and S. Hofmann[2,3]

[1]Soltan Institute for Nuclear Studies, Hoża 69, PL-00-681 Warsaw, Poland; [2]GSI, Darmstadt, Germany; [3]Institute für Kernphysik, Johann Wolfgang Goethe-Universität, D-60438 Frankfurt, Germany

This contribution concerns a planned experiment of the synthesis of element 120 in the reaction ^{64}Ni+ ^{238}U at the GSI-SHIP. The use of ^{238}U as a target is a continuation of the recent experiment in which the nucleus ^{283}112 has been synthesized [1].

The objective of our contribution is a prediction of the properties of nuclei which may be produced in this experiment. We assume that, similar to previous reactions with actinide targets [2], the compound nucleus will emit 4 or 3 neutrons, leading to the final nuclei ^{298}120 or ^{299}120, respectively. Three measurable quantities, characteristic for these two nuclei and for a few nuclei which could be produced by α decay, are analyzed. These quantities are α-transition energy, $Q^{\rm t}_{\alpha}$, α-decay half-life, T_{α}, and spontaneous-fission half-life, $T_{\rm sf}$. As one can expect α decay of these nuclei, the main attention is given to this decay mode.

The results are shown in Table 1. Three variants of the transition energy are given. Two of them, TF [3] and MM [4], are obtained within macroscopic-microscopic models which well describe masses of heavy nuclei. The third variant, AWT [5], is an extrapolation of a systematics of experimental masses. For even-even nuclei, $Q^{\rm t}_{\alpha}$ is equal to the decay energy, Q_{α} (g.s. to g.s. transition, where g.s. denotes the ground state). For even-odd nuclei, this energy is decreased by the average excitation energy of a neutron quasiparticle state, $\bar{E}_{\rm n}$ = 0.171 MeV, to which the decay is expected to go [6]. One can see that the MM and TF results for $Q^{\rm t}_{\alpha}$ differ only little from each other for the heaviest nuclei with Z = 120, while they differ by more than 1 MeV for lighter ones with Z = 114. The AWT results are close to the MM ones.

The α-decay half-life, T_{α}, is calculated from $Q^{\rm t}_{\alpha}$ by a phenomenological formula proposed recently in [6]. One can see that T_{α} calculated for the nucleus ^{298}120 is very small. It is close to the detection limit of around 1 μs. The half-life of the odd-A isotope, ^{299}120, is larger by a factor of 5. The differences between the three variants of T_{α} directly reflect the differences between the corresponding $Q^{\rm t}_{\alpha}$ discussed above.

The fission half-life $T_{\rm sf}$ is taken from [7, 8]. It is calculated only for even-even nuclei. One can see that $T_{\rm sf}$ is larger than T_{α} for the nuclei with Z = 120, 118, and 116, supporting the expectation that α decay should be observed for these nuclei. For the nucleus ^{286}114, $T_{\rm sf}$ is larger than T_{α} obtained in the MM and AWT cases, while it is smaller than T_{α} in the TF case.

Concluding, one can say that α decay of the considered nuclei may be expected, rather than spontaneous fission. However, the estimated T_{α} of the nucleus ^{298}120 is very small, close to the limit of being observable. The half-life of the odd-A isotope ^{299}120 is only about 5 times longer. The calculations indicate that the observation of the α decay of any of these two nuclei would imply the observation of at least two other α decays of the descendant nuclei.

References

[1] S. Hofmann et al., Eur. Phys. J. A 32 (2007) 251.

[2] Yu.Ts. Oganessian, J. Phys. G 34 (2007) R165.

[3] W.D. Myers and W.J. Świątecki, Nucl. Phys. A 601 (1996) 141.

[4] I. Muntian et al, Phys. At. Nucl. 66 (2003) 1015.

[5] G. Audi, A.H. Wapstra and C. Thibault, Nucl. Phys. A 729 (2003) 337.

[6] A. Parkhomenko and A. Sobiczewski, Acta Phys. Pol. B 36 (2005) 3095.

[7] R. Smolańczuk et al., Phys. Rev. C 52 (1995) 1871.

[8] R. Smolańczuk, Phys. Rev. C 56 (1997) 812.

Table 1: Values of the energies $Q^{\rm t}_{\alpha}$ and the half-lives T_{α} and $T_{\rm sf}$.

Z	A	$Q^{\rm t}_{\alpha}$/MeV			T_{α}			$T_{\rm sf}$
		MM	TF	AWT	MM	TF	AWT	
120	298	13.44	13.58		2.9 μs	1.6 μs		27 ms [8]
120	299	13.06	13.16		15 μs	9.8 μs		
118	294	12.11	12.51		390 μs	56 μs		22 ms [8]
118	295	12.05	12.25		520 μs	200 μs		
116	290	11.08	11.34	11.30	23 ms	5.5 ms	6.8 ms	12 min [8]
116	291	10.74	11.16	10.83	160 ms	15 ms	93 ms	
114	286	10.86	9.61	10.70	19 ms	43 s	48 ms	1.5 s [7]
114	287	10.39	9.36	10.27	300 ms	240 s	620 ms	

The new Isotope ^{271}Hs Observed in the ^{26}Mg(^{248}Cm,3n) Reaction

J. Dvorak[1], Z. Dvorakova[1], R. Krücken[1], F. Nebel[1], R. Perego[1], R. Schuber[1], A. Semchenkov[1, 2], A. Türler[1], B. Wierczinski[1], A. Yakushev[1], W. Brüchle[2], Ch. E. Düllmann[2, 3, 4], E. Jäger[2], M. Schädel[2], B. Schausten[2], E. Schimpf[2], M. Chelnokov[5], V. Gorshkov[5], A. Kuznetsov[5], A. Yeremin[5], K. Eberhardt[6], P. Thörle[6], Y. Nagame[7], K. Nishio[7], Z. Qin[2, 8], and M. Wegrzecki[9]

[1]TU Munich, Garching, Germany; [2]GSI, Darmstadt, Germany; [3]LBNL, Berkeley, CA, USA; [4]UC, Berkeley, CA, USA; [5]JINR, Dubna, Russia; [6]U Mainz, Germany; [7]JAEA, Tokai-mura, Japan; [8]IMP, Lanzhou, China; [9]ITE, Warsaw, Poland

Heavy-ion hot-fusion reactions with actinide targets have been extensively used to produce relatively neutron-rich superheavy elements (SHE), i.e. elements with atomic numbers $Z \geq 104$. In these reactions surviving SHE nuclei are usually formed after evaporation of four or more neutrons. Consequently, up to now only 4*n* and 5*n* evaporation channels have been exploited in the synthesis of SHE with beams up to $Z = 16$. Lower x*n* channels were not studied, probably due to the fact that the magnitude of the 3*n* channel was decreasing rapidly in the sequence of carbon, nitrogen, and oxygen induced reactions. This has commonly been interpreted as the vanishing of the 3*n* channel with increasing atomic number of the projectile. In this work, we report the successful search for the 3*n* evaporation channel product of the hot fusion reaction ^{26}Mg + ^{248}Cm the new isotope ^{271}Hs.

Hassium nuclei were produced in the reaction ^{248}Cm(^{26}Mg, x*n*)$^{274-x}$Hs at the UNILAC at GSI and isolated using the efficient on-line chemical separation and detection system COMPACT [1]. In two runs Hs isotopes were produced at 5 different beam energies from 130 to 150 MeV in the centre of the target (see Table 1). In the first run [1], the unique chain No. 14 observed at a beam energy of 136 MeV could be attributed neither to the decay of ^{269}Hs nor to ^{270}Hs. The first α-particle had an energy of 9.30 MeV, followed after 149.2 s by an α-particle with an energy of 8.20 MeV. The chain was terminated by fission after another 12 s. It was proposed that this decay chain originates from the decay of ^{271}Hs. In the second run we observed four more chains at beam energies of 130 MeV (3 events) and 140 MeV (1 event) with unique decay properties different from ^{269,270}Hs.

Table 1. Decay chains of ^{271}Hs observed in this work at beam energy E_{Lab}. In detector numbers, #, , t stands for "top detector" and b for "bottom detector".

E_{Lab}, (MeV)	$E_{\alpha 1}$,(^{271}Hs) (MeV) (#)	Δt_1, (s)	$E_{\alpha 2/SF}$,(^{267}Sg) (MeV) (#)	Δt_2, (s)	E_{SF},(^{263}Rf) (MeV) (#)
130	9.16(24t)	142	26/--(25b/--)		
130	9.02(16b)	30.4	89/68(15t/15b)		
130	9.23(20t)	264	15/83(20t/19b)		
136*	9.30(7t)	149	8.20(7t)	12	89/95(7t/7b)
136*	9.10(14t)	96	80/90(14t/13b)		
140	9.14(12t)	47.9	69/--(12t/--)		

* events from [2], see text for details.

All these additional events are characterized by a first α-particle with an energy > 9 MeV and were terminated by SF with long lifetimes. Three of these chains were detected at 130 MeV beam energy. This is below the expected maximum of the 4*n* channel and far below the energy where significant contribution of the 5n channel is expected. The decay chain No. 10 in [2] was tentatively attributed to the decay of ^{269}Hs, assuming that the α-particle from the decay of ^{265}Sg is missing. This α-SF chain was detected at 136 MeV beam energy, about 10 MeV below the maximum of the 5*n* channel. The α-particle energy was 9.10 MeV and SF followed after 96 s, similar to chains observed in the second run mostly at 130 MeV. It is very unlikely (0.03%) to always miss the second α-particle (Sg decay) in five decay chains observed at lower beam energies. Therefore, all these six chains were attributed to the new isotope ^{271}Hs produced in the 3*n* evaporation channel. Taking into account the long α-decay life-time for ^{267}Sg detected in the chain mentioned before, which is consistent with the relatively low energy of the detected α-particle, partial SF and α-decay half-lives may become sufficiently similar that branching into both decay modes can be observed.

In total we have observed 26 nuclear decay chains from Hs isotopes assigned to ^{269}Hs (5*n*), ^{270}Hs (4*n*), and ^{271}Hs (3*n*) with the decay properties summarized in Table 2. The measured cross section for the 3*n* channel is unexpectedly high, similar to that of the 4*n* and 5*n* channels [2]. This is in strong contrast to expectations based on the idea of a "vanishing" 3*n* channel in hot fusion reactions with increasing projectile atomic number.

Table 2. Decay properties of Hs isotopes.

Nuclei	Half-life	E_α, (MeV)[#]
^{269}Hs	--	8.95 ± 0.05
	4 s[†]	9.13 ± 0.05
^{270}Hs	23 s[†]	8.88 ± 0.05
^{271}Hs	4 s[†]	9.13 ± 0.05
	--	9.30 ± 0.05

[#]Most probable energy considering the peak shape as measured in a calibration run.

[†]Half-life calculated from E_α values of the most probable transitions using the formalism of Ref. [3].

References

[1] J. Dvorak *et al*., Phys. Rev. Lett. **97**, 242501 (2006).
[2] J. Dvorak *et al*., GSI Sci. Rep. 2007, this issue.
[3] A. Parkhomenko and A. Sobiczewski, Acta Phys. Pol. B **36**, 3095 (2005).

* Work supported by BMBF (06MT247I)

Cross Section Measurements of the Reaction ^{26}Mg(^{248}Cm,xn) $^{274-x}$Hs*

J. Dvorak[1], Z. Dvorakova[1], R. Krücken[1], F. Nebel[1], R. Perego[1], R. Schuber[1], A. Semchenkov[1, 2], A. Türler[1], B. Wierczinski[1], A. Yakushev[1], W. Brüchle[2], Ch. E. Düllmann[2, 3, 4], E. Jäger[2], M. Schädel[2], B. Schausten[2], E. Schimpf[2], M. Chelnokov[5], V. Gorshkov[5], A. Kuznetsov[5], A. Yeremin[5], K. Eberhardt[6], P. Thörle[6], Y. Nagame[7], K. Nishio[7], Z. Qin[2, 8], and M. Wegrzecki[9]

[1]TU Munich, Garching, Germany; [2]GSI, Darmstadt, Germany; [3]LBNL, Berkeley, CA, USA; [4]UC, Berkeley, CA, USA; [5]JINR, Dubna, Russia; [6]U Mainz, Germany; [7]JAEA, Tokai-mura, Japan; [8]IMP, Lanzhou, China; [9]ITE, Warsaw, Poland

The studies of complete fusion reactions leading to production of superheavy elements (SHE) with $Z \geq 108$ is extremely difficult due to very low production cross sections. Excitation function measurements of evaporation residues from a fusion reaction together with measurements of the fusion – fission cross section provide important experimental information for understanding the process of compound nucleus (CN) formation and its survival in the competition between fission and neutron evaporation. In this work, we report excitation function measurements of the reaction ^{26}Mg + ^{248}Cm leading to element 108, hassium.

Hassium nuclei were produced in the reaction ^{248}Cm(^{26}Mg, x*n*)$^{274-x}$Hs at the linear accelerator UNILAC at GSI, where five beam energies were applied in two experimental campaigns. During the first run [1], two beam energies were applied – 145 and 136 MeV in the middle of the target (E^* = 49 and 40 MeV). These correspond to the calculated maxima [2] of the cross sections for the 5*n* and 4*n* evaporation channel, respectively. In the 4*n* evaporation channel the doubly magic nucleus ^{270}Hs has been produced in the 4*n* evaporation channel for the first time. The same irradiation setup and the same efficient on-line chemical separation and detection system COMPACT has been used in a 2nd run to isolate Hs-isotopes [3]. Three additional beam energies were investigated – 150, 140, and 130 MeV in the middle of the target (E^* = 53, 44, and 35 MeV). In total 26 decay chains from three different Hs isotopes were observed: ^{269}Hs, ^{270}Hs, and ^{271}Hs, produced via 5*n*, 4*n* and 3*n*, respectively [1,3]. Beam integrals and the number of Hs nuclei observed at the five investigated beam energies are presented in Table 1.

Table 1. Irradiation conditions and number of detected Hs decay chains produced in the complete fusion reaction ^{248}Cm(^{26}Mg, x*n*)$^{274-x}$Hs.

E_{Lab}, MeV	Irradiation time, h	Beam integral particles,	3*n* ^{271}Hs	4*n* ^{270}Hs	5*n* ^{269}Hs
130	91	$1.71 \cdot 10^{18}$	0	0	3
136	120	$2.02 \cdot 10^{18}$	2	4	1
140	158	$2.55 \cdot 10^{18}$	1	2	3
145	139	$1.46 \cdot 10^{18}$	0	1	7
150	91	$1.43 \cdot 10^{18}$	0	0	2

Based on the assignment of these chains, the cross sections for the 3*n*, 4*n*, and 5*n* evaporation channels of the reaction ^{248}Cm(^{26}Mg, x*n*)$^{274-x}$Hs were evaluated. Figure 1 shows the measured cross sections together with results from HIVAP [2] calculations. The most likely attribution was used for two chains where no unambiguous attribution of the decay chains was possible. The cross section values varied within the error limits when an alternative attribution was applied. Decay losses during transport to the detection system (about 3 s), were not considered in the cross section calculations.

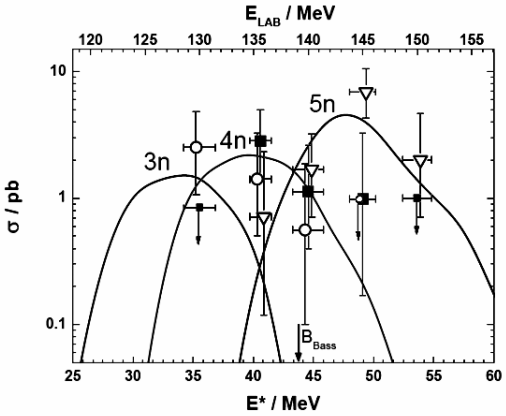

Figure 1: Comparison of production cross sections measured for the reaction ^{248}Cm(^{26}Mg,5-3*n*)$^{269-271}$Hs (symbols) along with excitation functions calculated with HIVAP (lines) [2]. Error bars represent 68% confidence intervals.

Strikingly high cross sections are observed for the 3*n* channel at energies well below the Bass fusion barrier. This indicates that most probably the fusion barrier for favourable collision of deformed nuclei is lower than the conventionally used "Bass barrier" [4] and that multi-dimensional fusion models [5] need to be applied. The observation of the 3*n* channel with cross sections at the same level as the 4*n* and 5*n* channel in the hot fusion reaction ^{26}Mg+^{248}Cm indicates the possible discovery of new neutron-rich transactinide nuclei using relatively light heavy-ion beams of the most neutron-rich stable isotopes and actinide targets.

References

[1] J. Dvorak *et al*., Phys. Rev. Lett. **97**, 242501 (2006).
[2] W. Reisdorf and M. Schädel, Z. Phys. A 343, 47 (1992).
[3] J. Dvorak *et al*., GSI Sci. Rep. 2007, this issue.
[4] R. Bass, Nucl. Phys. A 231, 45 (1974).
[5] K. Nishio *et al*., Phys. Rev. Lett. 93 162701 (2004).

* Work supported by BMBF (06MT247I)

Identification of an Isomeric State in ^{253}Fm

F.P. Heßberger[1], S. Antalic[2], D. Ackermann[1], M. Block[1], S. Heinz[1], B. Kindler[1], J. Khuyagbaatar[1], B. Lommel[1], R. Mann[1], Š. Šaro[2], S. Hofmann[1,3]

[1]GSI, Darmstadt, Germany; [2]Comenius University, Bratislava, Slovakia, [3]Johann Wolfgang Goethe Universität, Frankfurt am Main, Germany

Due to higher available beam intensities and development of more sensitive detector systems in combination with recoil separators, a breakthrough in nuclear structure investigations of heavy actinide and transactinide ($Z \geq 100$) nuclei has been achieved during the past decade [1]. So far, experimental techniques concentrated on measurements of γ-rays or conversion electrons (CE) in prompt or delayed coincidence with implanted nuclei or α-particles. Another important source for information on nuclear structure is the investigation of β^--, β^+- or EC-decay, which has been applied in the past for numerous nuclei up to $Z = 100$. In contrast to α-decay, in these processes no particles are emitted having energies characteristic for a specific isotope. Therefore mass separated samples are required. Recoil separators are in general not laid out for such a separation. However, in complete fusion reactions leading to heaviest nuclei only very few evaporation channels are open at a specific bombarding energy, but a broad 'cocktail' of isotopes can be produced by decay of the primary reaction product. So identification of the atomic number Z seems to be more important. It can be achieved by measuring the characteristic X-rays. Such EC studies can be performed by the technique of CE-X-ray-γ coincidences. Registration of CE is required due to high γ-background in the focal plane of the separator.

As a first test case we investigated the decay of excited levels in ^{253}Fm, produced by ^{253}No −EC→ ^{253}Md −EC→ ^{253}Fm. The primary product was synthesized in the reaction ^{207}Pb(^{48}Ca,2n)^{253}No.

Fig. 1a) shows the γ-spectrum observed in coincidence with CE and $K_{\alpha 1,2}$ X-rays of fermium (within our coincidence time window of the data acquisition system of 10 μs), while in fig. 2 the time distribution Δt(CE-γ) is plotted as a function of E_γ for γ-rays in coincidence with $K_{\alpha 1,2}$ X-rays of fermium. Evidently the transition of E_γ = 187.5 keV appears before the 'prompt' peak, i.e. it populates a nuclear level having a life-time larger than the time resolution of the CE-γ-coincidences. From the time distribution we extracted the half-life of the correponding level as $T_{1/2}$ = (0.5±0.3) μs. For the K X-rays also part of the decays is observed before the CE, while all other γ-lines appear within the 'prompt' peak.

More information on the decay of this isomeric level is obtained from γ-γ coincidences. Evidently the transitions at 150.2 keV (fig. 1b) and 187.5 keV (fig. 1c) are in coincidence with each other, while the line at 76.1 keV is observed only in coincidence with the 187.5 keV line.

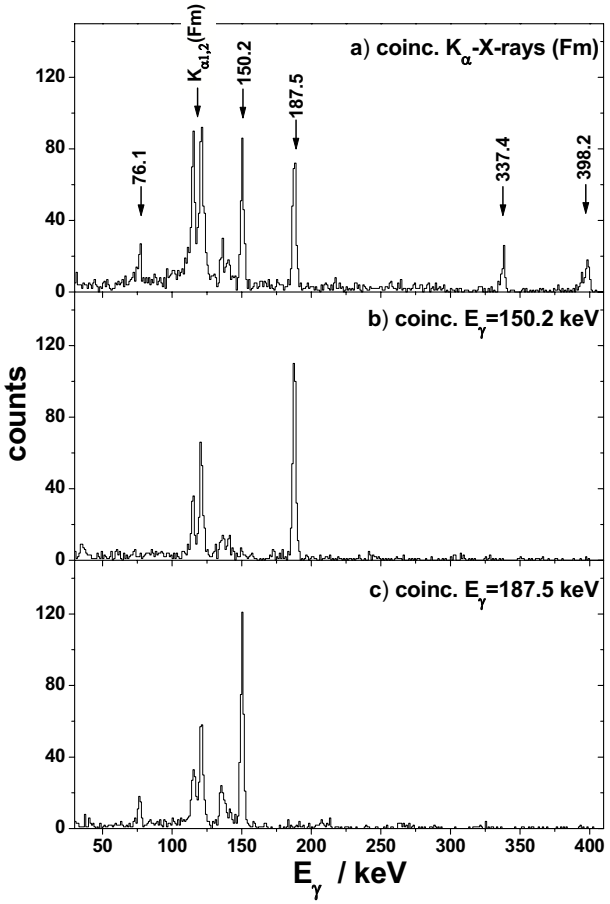

Fig. 1: CE- γ-γ coincidence spectra from EC decay of ^{253}Md −EC→ ^{253}Fm using a fourfold segmented VEGA type clover detector; a) γ rays in coincidence with CE and K_α X-rays of fermium; b,c) γ rays in coincidence with CE and 150.2 keV (b) or 187.5 keV (c) γ-ray transitions.

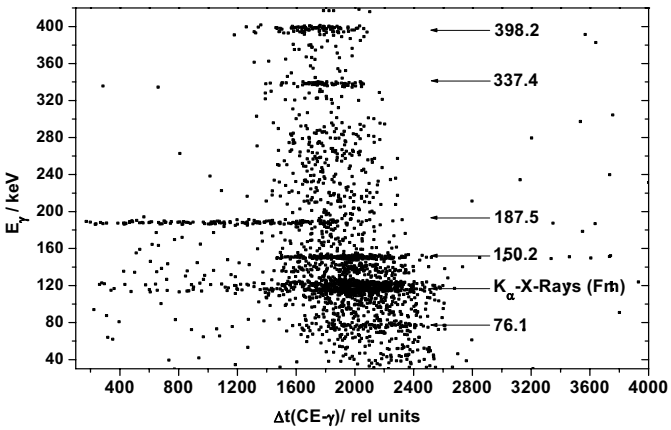

Fig. 2: Two dimensional plot of γ-ray energies versus time difference between the emission of a γ ray and emission of a CE. The slight dependence of the time on the energy in the prompt peak is due to a shift of the trigger times of the γ and CE signals at low energies.

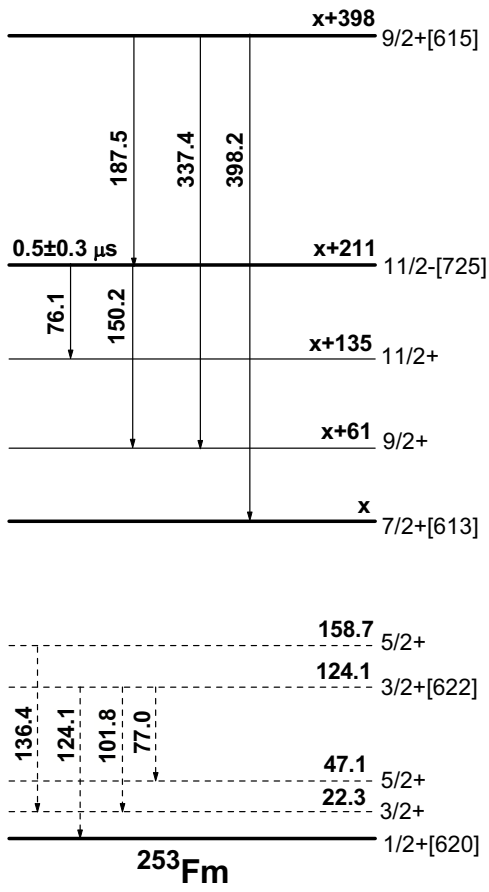

Fig. 3: Partial level scheme of ^{253}Fm as derived from our experiment (full lines) and that of Asai et al. [5] (dashed lines)

A preliminary partial decay scheme is sketched in fig. 3. The isomer is attributed to the $11/2^-[725]$ level which is isomeric also in the neighbouring isotone ^{251}Cf (E^* = 370.39 keV, $T_{1/2}$ = 1.3 μs) [2]. In analogy to ^{251}Cf [2] the strongest transitions depopulating the isomeric level are assumed as the decays into the $11/2^+$ and $9/2^+$ members of the rotational band built up on the Nilsson level $7/2^+[613]$; we attribute the lines at 150.2 keV ($11/2^- \rightarrow 9/2^-$) and 76.1 keV ($11/2^- \rightarrow 9/2^-$) to them since their energy difference of ΔE = 74.1 keV is nearly identical to that of the corresponding levels in ^{251}Cf (ΔE = 73.1 keV).

Since the sum intensity of the 150.2 keV and 76.1 keV -lines is close to that of the 187.5 keV line, and there is no indication for a second intense line feeding the isomer, we conclude that the 187.5 keV is only weakly converted and thus probably has the same multipolarity (E1) as the 150.2 keV and 76.1 keV transitions. So a possible state feeding the isomer is the $9/2^+[615]$ Nilsson level. The 337.4 keV transition represents the sum 150.2 keV + 187.5 keV. Since it appears almost exclusively in the 'prompt' peak (see fig. 2) it is rather interpreted as the direct transition $9/2^+[615] \rightarrow 9/2^+$, bypassing the isomer, than as the result of summing of the two γs in one Clover segment.

The γ-line at 398.2 keV can only be assigned tentatively. The energy difference ΔE = (398.2-337.4) keV = 60.8 keV is close the energy difference of 60.0 keV between the $9/2^+$ level and the $7/2^+[613]$ band head in ^{251}Cf. So the 398.2 keV line may be attributed to the $9/2^+[615] \rightarrow 7/2^+[613]$ transition.

The further deexcitation of the $7/2^+[613]$ level is not established so far. No further intense γ-lines were observed. It was also found that K X-rays measured in coincidence with 150.2 keV γ's have a similar time distribution as the 187.5 keV γ's, i.e. they essentially stem from processes preceding the feeding of the isomer. In other words, K-conversion does not seem to play a significant role in the decay of the $7/2^+[613]$ level towards the ground-state. Therefore these transitions must be strongly L converted, i.e. either they have E2 character, or, if we assume them as M1 transitions, they must have energies below the K-binding energy in fermium (E_B = 149.2 keV).

Some estimate on the excitation energy of the isomeric level can be made on the basis of the CE energies. The average energies of CE's in coincidence with the 150.2 keV or the 187.5 keV transitions are nearly the same and about 180 keV. So the $11/2^-[725]$ level can be expected at around $E^* \approx$ (300-350) keV, i.e. at a somewhat lower value than in ^{251}Cf, where it is placed at 370.39 keV. Indeed a decrease of the $11/2^-[725]$ level in E^* with increasing proton number is expected from theory [3] for N=153 isotones. In ^{257}Rf it was assigned to an isomeric state ($T_{1/2} \approx 4$ s) at $E^* \approx 70$ keV [4] decaying by α-emission.

Low lying levels in ^{253}Fm have been recently investigated by Asai et al. [5] on the basis of measuring CE and γs in coincidence with α-decays of ^{257}No. The γ-transitions and their assignments are shown as dashed lines in fig. 3. They identified a low lying $3/2^+[622]$ Nilsson level at E^* = 124.1 keV. None of the γ-lines reported by them have been observed so far in our experiment, indicating that the $3/2^+[622]$ level (or the $5/2^+$ member of its rotational band) is not populated by the decay of the isomeric state. A reason could be, that according to the energy estimations for the isomer, the $7/2^+[613]$ level might be quite close or even lower than the $3/2^+[622]$ level. So the $7/2^+[613]$ level (and possibly members of the rotational band built up on it) might decay directly into the ground state rotational band. More sensitive measurements are necessary to clarify the situation.

References

[1] M. Leino, F.P. Heßberger, Annu. Rev. Nucl. Part. Sci. 54, 175 (2004)
[2] R.B. Firestone et al. (eds.), Table of Isotopes, 8th. Edition (1996)
[3] A. Parkhomenko, A. Sobiczewski, Acta Phys. Pol. B 36, 3115 (2005)
[4] B.Streicher, PHD, Comenius Univ. Bratislava (2006)
[5] M. Asai et al., PRL 95, 102502 (2005)

Search for shell effects and long interaction times in U+U collisions

S. Heinz[1], C. Golabek[2], W.Mittig[2], A.C.C. Villari[2] and the E511 collaboration
[1]GSI, Darmstadt, Germany; [2]GANIL, Caen, France

At the VAMOS spectrometer of GANIL we investigated shell effects and nuclear interaction times in the very heavy di-nuclear system U+U. We expect the following signatures:

a) If shell effects appear they should be most pronounced at moderate excitation energies. In this case we would expect an asymmetric break-up (quasi-fission) of the di-nuclear system with preferential emission of one fragment close to the doubly magic nucleus ^{208}Pb.

b) We expect a correlation between the nuclear interaction time, the number of exchanged nucleons during the contact period and the dissipation of kinetic energy. The longest interaction times should appear in collisions with a large number of exchanged nucleons.

The experiments have been performed at five different beam energies around the Coulomb barrier (6.09 to 7.35×A MeV). The spectrometer was covering scattering angles of 35°±7°, corresponding to 56°−84° and 96°−124° in the centre of mass frame. For beam energies beyond 6.9×A MeV we found a broad bump in the mass region 190<A<230 which originates from deep inelastic and quasi-fission products. The maximum yield of these products was observed at the highest investigated beam energy of 7.35×A MeV [1].

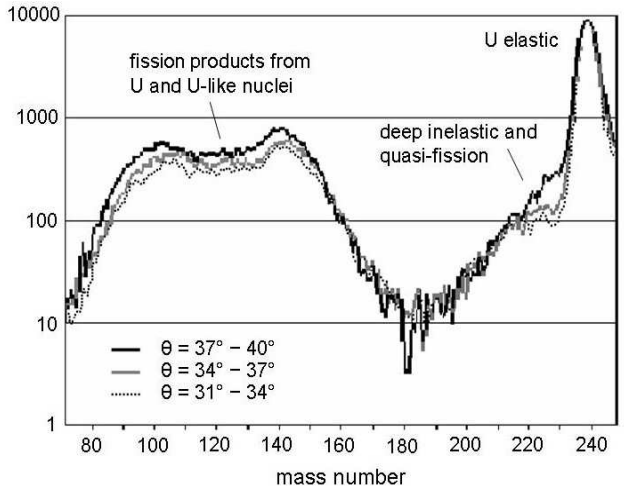

Figure 1: Mass spectra from the collision system U+U at 7.35×A MeV for different scattering angle ranges.

Figure 1 displays the mass spectra for three different scattering angle ranges. The mass distributions for the events containing the most central collisions (θ=31°−37°) differ clearly from the spectrum for θ=37°−40° in the mass range 215<A<230: the fragment yield drops only slightly for A<230 and shows a sudden drop around A=215. Such behaviour is predicted in [2] if the closed shells in ^{208}Pb determine the break-up of the di-nuclear system. According to calculations in [2] the potential energy at the nuclear contact point has a minimum at A=208. For masses below A=208 the potential energy increases steeply. This leads to a drop in the yield for masses A<208 and, hence, to a "shoulder" in the mass spectrum at A=208. If the break-up is not determined by the Pb shells, one would expect an exponential decrease in the yield for nuclei lighter than uranium. In order to clarify if shell effects are reflected in the spectrum of fig. 1, further experiments at beam energies above 7.35×A MeV will be performed, since we expect, that at higher excitation energies the influence of the Pb shells should disappear.

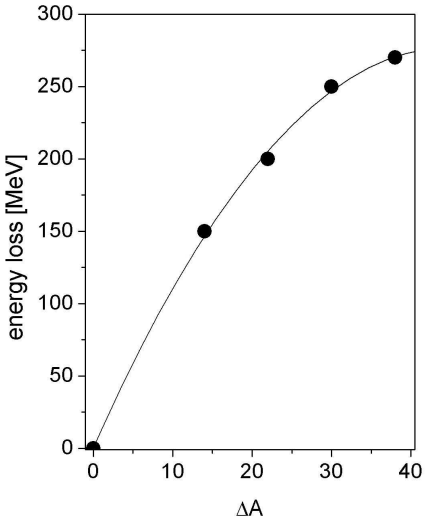

Figure 2: Kinetic energy loss as a function of the number of transferred nucleons ΔA.

The kinetic energy loss as a function of the number of transferred nucleons ΔA is shown in fig. 2. A transfer of up to 50 mass and 20 charge units was found. We expect that the longest interaction times are correlated with the largest observed values for ΔA. From our experiment we cannot deduce absolute values for the interaction times. Presently only a comparison with theory is possible. The calculations in [2] result in interaction times of 5×10^{-21} – 2×10^{-20} s for events leading to reaction products with A≤204 correlated with a kinetic energy loss of ≥200 MeV. If we only assume "simple" diffusion, i..e without regarding shell effects, the interaction time T_{int} is correlated with the number of transferred nucleons via $\Delta A=\lambda_0 T_{int}$. The nucleon flow rate is given in [3] as $\lambda_0=10^{22}$ s^{-1}. Thus, for ΔA=50 we obtain an interaction time of 5×10^{-21} s.

References

[1] S. Heinz et al, GSI Sci. Rep. 2006, p.136.
[2] V.I. Zagrebaev et al, Phys. Rev. C73 (2006) 03160.
[3] C. Riedel et al, Z. Phys. A290 (1979) 47-55.

Production cross-sections of the isotopes ^{213}Th and ^{214}Th

J. Khuyagbaatar[1], S. Hofmann[1], F.P. Heβberger[1], D.Ackermann[1], S. Antalic[2], H.G. Burkhard[1], S. Heinz[1], B. Kindler[1], A.F. Lisetskiy[3], B. Lommel[1], R. Mann[1], K. Nishio[4], H.J. Schött[1] and B. Sulignano[1]

[1]GSI, Darmstadt, Germany, [2]Comenius University, Bratislava, Slovakia, [3]University of Arizona, USA, [4]Japan Atomic Energy Agency (JAEA), Tokai, Japan

The thorium isotopes have been produced in the fusion-evaporation reaction ^{164}Dy(^{54}Cr,xn)$^{218-x}$Th at SHIP. So far unknown isomeric states located at 1180 and 2181 keV have been found in ^{213}Th and ^{214}Th, respectively. They decay via γ-emission with $T_{1/2}$=(1.24±0.12) μs (^{214}Th) and $T_{1/2}$=(1.4±0.4) μs (^{213}Th) [1].

The cross-sections for the production of the isotopes ^{214}Th and ^{213}Th cannot be obtained individually for each isotope, because their ground-state properties (α energies and half-lives) are almost identical. The measured values for the sum of both isotopes obtained in our experiment are (3.50±0.03) μb at 47 MeV and (1.95±0.05) μb at 55 MeV of excitation energy. These values include direct production of the ground-states and feeding by decay of the isomers. The error bars represent statistical fluctuations only. Systematic errors could modify the values up to a factor of two, however, at a constant ratio.

The cross-sections for production of the isomeric states in ^{214}Th (8^+) and ^{213}Th ($13/2^+$) were deduced individually using the measured intensities of the γ lines at 623 (^{214m}Th) and 381 keV (^{213m}Th), respectively. The obtained values are given in the line marked by σ_m in table 1. These values were calculated using the absolute coincidence efficiencies between the evaporation residues and γ's. The decay of these short lived isomers during their flight time of 1.5μs through SHIP has been considered.

Table 1. Measured and calculated cross-sections (given in μb) for the production of ^{214}Th and ^{213}Th at the two excitation energies E*. Cross-sections, marked by the indexes H1 and H2 are results from HIVAP calculations using the parameter sets of [2] and [3], respectively. See text for detail.

	^{214}Th	^{214}Th	^{213}Th	^{213}Th
E* / MeV	47	55	47	55
σH1	8.3	3.3	0.04	0.8
σH2	4.5	0.25	0.05	0.38
σ_m	1.2±0.3	0.3±0.1	0.16±0.11	0.5±0.3
$\sigma_{m+g.s.}$	3.48	1.0	0.02	1.0
$\sigma_{g.s.}$	2.3	0.7	-	0.5
$\sigma_m/\sigma_{g.s.}$	0.5	0.4	-	1.0

For both excitation energies the summed cross-sections measured for the ground-state α decay are considerably higher than the cross-sections for the production of the isomers, which indicates a rather large direct population of the ground-states in the reaction.

We performed HIVAP calculations in order to estimate the production of ^{213}Th and ^{214}Th. We used the standard parameter set as given in ref [2] as well as a modified one which was adapted to reproduce cross-sections measured in the region of neutron deficient thorium and uranium nuclei [3]. Data from both calculations, marked by the indexes H1 and H2, respectively, are given in table 1.

Obviously, the maxima of the 4n and 5n channels are shifted to lower excitation energies using the H2 calculations. However, in both cases the cross-section for ^{214}Th is largest and the one for ^{213}Th almost negligible at 47 MeV excitation energy. Comparable cross sections for the production of both isotopes are obtained at 55 MeV of excitation energy in the case of H2. In accordance with the calculations we attributed a major part (3.48 μb) of the total cross-section measured at 47 MeV of excitation energy to the production of ^{214}Th and the smaller rest of 0.02 μb to ^{213}Th. The 1.95 μb cross-section measured at 55 MeV was shared in equal parts between ^{213}Th and ^{214}Th. These values are given in the line marked by $\sigma_{m+g.s.}$. The cross-sections for the direct production of the ground-states in the reaction are obtained by subtracting the cross-sections obtained for the isomeric states. The values are given in the line marked by $\sigma_{g.s.}$. Due to the small absolute values and large uncertainties in the case of ^{213}Th at 47 MeV of excitation energy, no data could be obtained there.

Finally, we used the cross-sections for calculating the isomeric ratios $\sigma_m/\sigma_{g.s.}$ The values are given in the last row of table 1. Taking into account the uncertainties of the procedure, reasonable values were obtained. The ratios are nearly equal at the two excitation energies for the production of ^{214}Th. Such a behaviour, namely a constant isomeric ratio, is expected on the higher energy side of the excitation function. In the case of ^{213}Th at 55 MeV of excitation energy we obtained an isomeric ratio which is a factor of 2 higher than that of ^{214}Th.

References

[1] J. Khuyagbaatar et al., accepted for publication in EPJ A.
[2] W. Reisdorf, Z. Phys. A 300, 227. 1981.
[3] K. Nishio et al., Phys. Rev. C 62, 014602. 2000.

Electron-capture delayed fission in ^{194}At

A.N. Andreyev[1,7,8], S. Antalic[2], D. Ackermann[3], L. Bianco[4], S. Franchoo[5], S. Heinz[3], F.P. Heßberger[3], S. Hofmann[3,9], M. Huyse[1], I. Kojouharov[3], B. Kindler[3], B. Lommel[3], R. Mann[3], K. Nishio[6], R.D. Page[4], J. Ressler[7], P. Sapple[4], S. Saro[2], B. Sulignano[3], J. Thomson[4], P. Van Duppen[1], and M. Venhart[2]

[1]Instituut voor Kern- en Stralingsfysica, K.U.Leuven, University of Leuven, Belgium; [2]Department of Nuclear Physics and Biophysics, Comenius University, Bratislava, Slovakia; [3]Gesellschaft fur Schwerionenforschung, Darmstadt, Germany; [4]Oliver Lodge Laboratory, University of Liverpool, Liverpool, UK; [5]IPN Orsay, France; [6]Advanced Science Research Center, Japan Atomic Energy Agency, Tokai, Japan; [7]Dept. of Chemistry, Simon Fraser University, Burnaby BC Canada ; [8]TRIUMF, Vancouver BC, Canada; [9]Physikalisches Institut, J.W. Goethe-Universität, Frankfurt, Germany

Beta-delayed fission (βDF), and in particular, electron-capture delayed fission (ECDF), is a rare nuclear decay process (only a dozen of cases are known so far) in which a very neutron-rich or neutron-deficient parent nucleus first undergoes beta decay, populating excited states in the daughter nucleus. If the energies of these states are comparable to or higher than the fission barrier of the daughter nuclide, then fission may happen from this state in competition with gamma decay towards the ground state. The beta-delayed fission is believed to play an important role in the astrophysical r-process phenomena, such as production of heavy elements and cosmochronometers, termination of the r-process and "fission recycling" [1].

We report on the first identification of the electron-capture delayed fission in the neutron-deficient isotope ^{194}At produced in the complete fusion reaction ^{141}Pr(^{56}Fe,3n)^{194}At at the velocity filter SHIP. The typical intensity of the pulsed (5 ms "beam ON" / 15 ms "beam OFF") ^{56}Fe beam was $\sim$600 pnA. The data were taken at several beam energies, covering the energy range of the 2n-4n evaporation channels.

Fig.1a shows the energy spectrum of all events registered in the PSSD at the focal plane of SHIP. The following four groups of events are seen in the spectrum: i) the highest energy group (E_{PSSD} $\sim$220-240 MeV) corresponds to the "full" energy ^{56}Fe projectiles "leaking" through the SHIP with a low intensity ($<$0.4 Hz); ii) the broadly distributed lower-energy scattered ^{56}Fe ions (E_{PSSD} $<$200 MeV); iii) the At-Bi recoil nuclei produced in the xn, pxn and α,xn channels of the reaction (E_{PSSD} $\sim$20 MeV); iv) β and α decays of reaction products (E_{PSSD} $<$8 MeV). In this spectrum, the fission fragments with the expected energy of about 50-150 MeV are hidden under the tail of scattered ^{56}Fe ions. To remove the beam-related events which hamper the observation of fission events, the data registered only during the 15 ms "beam OFF" time interval are shown in Fig. 1b. The 66 events with the energy of E_{PSSD} $\sim$60-160 MeV cannot be due to scattered beam particles and we assign them to fission fragments from the daughter nucleus ^{194}Po resulting after EC decay of ^{194}At. This conclusion is based on a number of arguments. First of all, the excitation

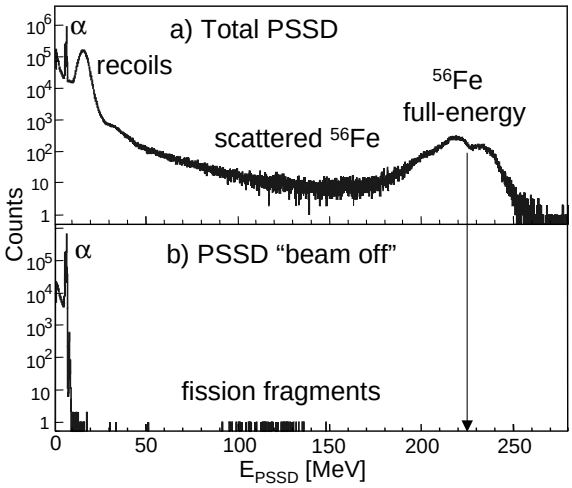

Figure 1: a) Total energy spectrum in the PSSD. b) The same as a), but within the 15 ms "beam OFF" interval.

function for these events has the same shape and the same beam energy dependence as the excitation function for the α decays of ^{194}At. Secondly, the half-life value for these fission events, deduced from the recoil-fission correlation analysis, is in a good agreement with the α-decay half-life of ^{194}At. Thirdly, approximately half of these events are double-fold events, in which the coincident signals have been measured in the PSSD and in the backward Si detectors of the SHIP detection system [2]. Finally, in contrast to the beam-related background, most of these events were observed in coincidence with γ decays registered in the Ge detector, which is expected for fission fragments due to their high gamma multiplicity. The preliminary estimate of the probability for the ECDF in ^{194}At is P_{ECDF} $\sim$0.01, which is one of the highest values known so far. The detailed analysis is in progress [3].

References

[1] I. V. Panov *et al.*, Nucl. Phys. A **747**, 633 (2005).

[2] S. Hofmann *et al.*, Eur. Phys. J., A **32**, 251 (2007).

[3] A.N. Andreyev *et al.*, in preparation (2008)

Towards mass measurements of nobelium isotopes with SHIPTRAP*

M. Block[1], D. Ackermann[1], K. Blaum[1,2], A. Chaudhuri[3], M. Dworschak[1], S. Eliseev[1], R. Ferrer[2], E. Haettner[4], F. Herfurth[1], F.P. Heßberger[1], S. Hofmann[1], J. Ketelaer[2], H.-J. Kluge[1], A. Martín[1], G. Marx[3], M. Mazzocco[1], J. Neumayr[5], Y. Novikov[6], W.R. Plaß[4], S. Rahaman[7], C. Rauth[1], D. Rodríguez[8], L. Schweikhard[3], C. Scheidenberger[1,4], P.G. Thirolf[5], G. Vorobjev[1], and C. Weber[7]

[1]GSI, Darmstadt, Germany; [2]Johannes Gutenberg-Universität, Mainz, Germany; [3]Ernst Moritz Arndt-Universität, Greifswald, Germany; [4]Justus Liebig-Universität, Giessen, Germany; [5]Ludwig Maximilians-Universität, München, Germany; [6]St. Petersburg Nuclear Physics Institute, Gatchina, Russia; [7]University of Jyväskylä, Finnland; [8]Universidad de Huelva, Spain

The Penning trap mass spectrometer SHIPTRAP, schematically shown in Figure 1, is set up behind the velocity filter SHIP for high-precision mass measurements of rare isotopes produced in fusion-evaporation reactions. The reaction products enter a gas cell [1, 2] with an energy of a few hundred keV/u through a thin window and are slowed down and thermalized in ultra-high purity helium at a pressure of about 50 mbar. Depending on the ionization potential of the element singly or doubly charged ions are extracted by a combination of RF and DC electric fields and gas flow through a nozzle. The extraction radiofrequency quadrupole (RFQ) operated as ion guide transports the ions to an RFQ cooler and buncher where a low-emittance bunched ion-beam is formed. These short ion bunches are injected into a double Penning trap system consisting of two cylindrical traps inside a 7-T superconducting solenoid. In the first trap (purification trap) isobars are separated with a mass resolving power of up to 100,000. In the second trap (measurement trap) the cyclotron frequency $\omega_c = qB/m$ of the mass-selected ions is measured from which the mass can be determined. Recently, an improved pumping barrier that separates both traps has been installed. The use of a different sealing and a reduction of the inner diameter to 1.5 mm has led to a significant improvement of the vacuum in the measurement trap.

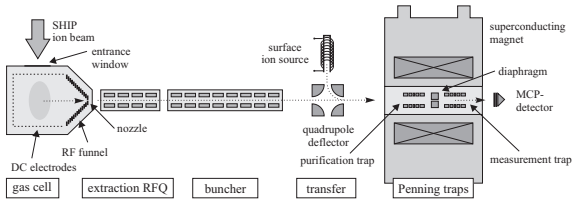

Figure 1: Schematic overview of the SHIPTRAP setup.

SHIPTRAP has been used for high-precision mass measurements of more than fifty rare isotopes since October 2005 [3, 4]. Among the nuclides whose masses have been measured for the first time were ^{144,145}Ho and ^{147,148}Tm that were found to be proton-unbound. From their mass values the proton separation energies for Ho and Tm were accurately derived and used to establish the location of the proton drip line for holmium [5].

Fusion reactions are presently the only competitive production technique to reach the proton drip line for heavy nuclei. Another region that can be exclusively accessed with fusion reactions are the elements above fermium ($Z = 100$). The masses of these nuclides have so far either been determined indirectly from nuclides with known masses using Q_α values or from extrapolations of systematic trends [6]. While the extrapolated mass values have uncertainties of more than 100 keV, the masses obtained from Q_α values are known to ≈10–40 keV but the uncertainties accumulate along the chain. In addition, only some of the nuclides are connected to the region of known masses.

With SHIPTRAP direct mass measurements of transuranium nuclides can be performed. The present reach of SHIPTRAP allows us to perform mass measurements on rare isotopes with a rate of trapped ions of above 0.01 ions per second which for efficiencies of about 1% correspond to a rate of 1 ion per second entering the gas cell. For a primary beam current of 1 particle μA this is equivalent to a production cross section of about 1 μb so that mass measurements of nobelium isotopes around the deformed shell gap at $N = 152$ become feasible.

In August 2007, ^{254}No was produced at SHIP and delivered to SHIPTRAP with a rate of about 4 ions per second. ^{254}No ions were extracted from the gas cell, accumulated in the RFQ cooler and buncher and detected on a silicon detector situated about 1 m downstream of the buncher. From the alpha decay a rate of about 1 ion per 30 seconds was determined. By fast switching of a deflector in front of the silicon detector a time-of-flight mass gate was applied to allow only ions of a certain A/q to reach the detector. The observed activity was consistent with a dominant fraction of ^{254}No^{2+} ions being extracted from the gas cell. The rate of extracted ions will be sufficient for a mass measurement that is planned to be performed in 2008.

References

[1] J.B. Neumayr et al., Nucl. Instr. Meth. B 244 (2006) 489.

[2] S. Eliseev et al., Nucl. Instr. Meth. B 258 (2007) 479.

[3] C. Rauth et al., Eur. Phys. J. ST 150 (2007) 329.

[4] A. Martín et al., Eur. Phys. J. A (2008) in press.

[5] C. Rauth et al., Phys. Rev. Lett. 100 (2008) 012501.

[6] G. Audi et al., Nucl. Phys. A 729 (2003) 3.

* Work supported by EU, contract No. 506065., HGF, contract number VH-NG-033 and VH-NG-037, and BMBF contact number 06GI185I

Resonance ionization spectroscopy on ^{155}Yb and ^{254}No at SHIP

H. Backe[1], P. Kunz[1], W. Lauth[1], M. Laatiaoui[2], M. Sewtz[2], D. Ackermann[3], M. Block[3], F. Herfurth[3], F. P. Heßberger[3], S. Hofmann[3], R. Mann[3], H.J. Kluge[3], and Ch. Rauth[3]

[1]Kernphysik, Univ. Mainz, Germany; [2]Department f. Physik, LMU München, Germany; [3]GSI, Darmstadt, Germany

For the investigation of the completely unknown atomic level structure of the element nobelium a novel experimental procedure has been developed. It is based on Radiation Detected Resonance Ionization Spectroscopy (RADRIS) which had to be improved and modified to accommodate the prerequisites at SHIP. It can be applied to elements like nobelium produced at rates of a few ions per second. The ionized fraction of the fusion product beam from SHIP, is stopped in an argon buffer gas cell, collected onto a tantalum catcher filament from which the radioactive species are re-evaporated as atoms. Then the atoms are resonantly ionized with laser beams and the ions subsequently transported by electrical fields to a semiconductor PIPS detector which detects the resonance ionization by the α decay of the fusion product. This method yields significant efficiency gains compared with earlier attempts to perform resonance ionization directly on the neutral part of the stopped fusion products.

Test experiments were performed with the isotope ^{155}Yb, which is supposed to have an atomic level structure similar to nobelium. It was produced by the fusion reaction ^{107}Ag(^{52}Cr,p3n)^{155}Yb. For the on-line resonance ionization of ^{155}Yb a periodic measurement sequence was applied. During an accumulation period the incoming fusion product ions are guided to a catcher filament by suitable electrical fields. After the beam is turned off the electrical fields are changed so that ions created in the buffer gas close to the filament are transported to an α detector. Then the catcher filament is heated by a short current pulse. The evaporated atoms are ionized by laser beams which are activated at the same time. The laser ions are transported to the detector where their α-energy spectrum is recorded. The resonance ionization of ^{155}Yb was performed with a two-step excitation scheme (λ_1 = 398.9 nm, λ_2 = 399.6 nm).

Laser scans were performed for both excitation steps. For this, α-energy spectra were recorded for different laser frequencies. Higher α activities were detected when the laser frequency was in resonance with the atomic level. Thus, resonance enhancement factors between 20 and 30 were observed, see Fig. 1. This result demonstrates that the detection of atomic levels in fusion products from SHIP with the RADRIS method is possible. A total RIS efficiency of ϵ_{RIS}^{tot} = 0.8 % has been determined under consideration of all experimental parameters [1].

After successful completion of this test experiment, the search for atomic levels in nobelium has been started in a recent beam time last summer. We sought for the $5f^{14}7s7p\ ^1\mathrm{P}_1$ term which was predicted by a Multi-

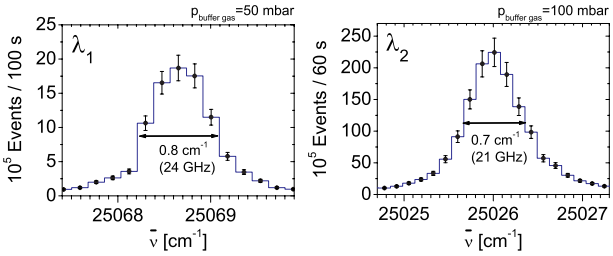

Figure 1: Atomic resonance lines of a two-step excitation scheme in the form of ^{155}Yb α decay rate.

Configuration-Dirac-Fock calculation at 27070 cm^{-1} and with an intermediate Hamiltonian coupled cluster method at 30108 cm^{-1}. The error of these calculations was estimated to be in the order of several hundred cm^{-1}. In a two-step excitation scheme the expected atomic level was probed with tunable lasers. The laser light for the first step was provided with dye lasers with a bandwidth of $\approx$ 0.2 cm^{-1} and an optical-parametric oscillator (OPO) with a bandwidth of $\approx$ 4 cm^{-1}, the non-resonant second step into the continuum with the light of Nd:YAG or Excimer lasers. Their high pulse energies in the range of 60 mJ should be sufficient to saturate also the second step. With a RIS efficiency of 0.8 % and a nobelium production rate by the ^{208}Pb(^{48}Ca,2n)^{254}No reaction of 17/s a count rate of 0.14 events/s is expected at resonance under optimal conditions [1]. A measuring time of 44 s was chosen per step which would result in a number of 6 events at resonance. At a background count rate of $7 \cdot 10^{-4}$/s this number was considered to be sufficient in order to find the resonance. However, in a wavenumber scan from 25800 to 30800 cm^{-1} no resonance was found. A number of reasons could be responsible for this negative result among which are (i) that the resonance has been overlooked due to fluctuations as a result of the low statistics, (ii) that the resonance is not located in the scan interval, or (iii) that the tantalum filament was poisoned by argon buffer gas impurities during the course of the experiment. The latter would have the consequence that the nobelium atoms could not anymore be re-evaporated at the experimentally determined evaporation temperature of $(1200 \pm 100)^\circ$C.

References

[1] H. Backe, P. Kunz, W. Lauth, A. Dretzke, R. Horn, T. Kolb, M. Laatiaoui, M. Sewtz, D. Ackermann, M. Block et al., European Physical Journal D **45**(1), 99 (2007)

Status of the TASCA Commissioning Program*

M. Schädel[1,#], D. Ackermann[1], W. Brüchle[1], Ch.E. Düllmann[1], J. Dvorak[2], K. Eberhardt[3], J. Even[3], A. Gorshkov[2], R. Gräger[2], K.E. Gregorich[4], F.P. Heßberger[1], A. Hübner[1], E. Jäger[1], J. Khuyagbaatar[1], B. Kindler[1], J.V. Kratz[3], D. Liebe[3], B. Lommel[1], J.P. Omtvedt[5], K. Opel[5], A. Sabelnikov[5], F. Samadani[5], B. Schausten[1], R. Schuber[2], E. Schimpf[1], A. Semchenkov[1,2,5], J. Steiner[1], J. Szerypo[6], A. Türler[2], and A. Yakushev[2] for the TASCA Collaboration

[1]GSI, Darmstadt, Germany; [2]Technical University München, Garching, Germany; [3]University of Mainz, Mainz, Germany; [4]LBNL, Berkeley, CA, U.S.A.; [5]University of Oslo, Oslo, Norway; [6]LMU München, Garching, Germany

The **T**rans**A**ctinide **S**eparator and **C**hemistry **A**pparatus, **TASCA**, project [1] is focusing on the separation and investigation of neutron-rich transactinide nuclides produced in actinide target based reactions. The envisioned research program includes both chemical investigations of transactinide or superheavy elements after preseparation with the gas-filled separator and physics motivated nuclear structure and nuclear reaction studies.

The central device of TASCA is a gas-filled separator in a DQQ configuration. It can be operated in the "High Transmission Mode" (HTM, DQ_hQ_v) and in the "Small Image Mode" (SIM, DQ_vQ_h); see Refs. [1-4] for more details. The separator was installed at the UNILAC beam line X8 and, after having all crucial parts of the control system [5] running, an extensive commissioning program was carried out in 2007. This report briefly summarizes the nuclear reactions applied and the most important parameters studied. A few examples are discussed in a very exemplary way. In addition, recent target developments and the progress in the coupling of chemistry set-ups will be outlined. The first chemical study behind TASCA is described in a separate contribution [6].

All nuclear reactions applied are listed in Table 1 together with the mode of TASCA operation (HTM=H, SIM=S) and the separator gas. Also indicated are experiments aimed to test or apply a recoil transfer chamber (RTC) in addition to measurements performed with a focal plane detector (FPD). As the standard FPD we used a (8x3.6) cm^2 large position-sensitive 16-strip silicon detector. Some experiments were devoted to test prototype double-sided silicon strip detectors (DSSSD) which are planned to be used in future experiments with superheavy elements (SHE).

To understand TASCA as a separator and to build up a solid data base providing good predictive power concerning separator operation for future SHE experiments, we investigated the following most important parameters: (i) the magnetic rigidity of reaction products between Z=76, Os, and Z=102, No, produced at different recoil velocities, and the corresponding best settings of the dipole magnet, (ii) the quadrupole focusing, which is especially relevant for the SIM, (iii) the target thickness dependence of the separator transmission - strongly depending on the asymmetry of the nuclear reaction -, and (iv) the optimum gas pressure with respect to focusing and to transmission - being quite different in the HTM and in the SIM. The analysis of a huge amount of data from these experiments is in progress, and it is important to realize that most of the above mentioned parameters influence each other.

Table 1: Nuclear reactions applied in TASCA commissioning experiments; see text for details.

Beam	Target	Product	Mode	Gas	RTC
^{22}Ne	^{nat}Ta	$^{198m-199}$Bi	H + S	He	
	^{179}Au	^{215}Ac	H + S	He	
	^{238}U	^{255}No	H + S	He	
^{30}Si	no	^{30}Si	H + S	Vac	
	^{181}Ta	$^{205-206}$Fr	H	He	
^{40}Ar	^{nat}Ce	^{173,175}Os	H	He	yes
	^{144}Sm	$^{180-182}$Hg	H + S	He	yes
	^{nat}Gd, ^{152}Gd	$^{194-196}$Pb, ^{188}Pb	H + S	He	yes
	^{nat}Lu	^{210}Ac	H + S	He, N_2	
	^{208}Pb	^{245}Fm	H + S	He	yes
	^{232}Th, ^{238}U	targettest, background	H	He	
^{48}Ca	^{144}Sm	^{188}Pb	H + S	He	
	^{206}Pb	^{252}No	H + S	He	
	^{208}Pb	^{254}No	H	He, H_2	
^{54}Cr	^{nat}Gd	$^{209-210}$Ra	H + S		

Always as a first step, the best dipole setting was found in HTM by centring the product distribution with a typical width of ≈ 6 cm on the FPD. A magnetic rigidity range from 1.5 to 2.2 Tm was covered in those experiments. The quadrupole focusing was found to be insensitive to small quadrupole current changes in the HTM while it reacts very sensitively in the SIM. Optimized SIM settings were determined to obtain maximum rates and narrow distributions of ≈ 1.5 cm FWHM.

The target thickness dependence of the transmission was extensively studied in the reactions ^{22}Ne + ^{197}Au (55, 130, 255, 580 µg/cm^2) and ^{40}Ar + ^{144}Sm (75, 190, 380, 930 µg/cm^2) in both modes. A comparison of these data with model calculations [7] will allow selecting an optimum target thickness with the highest product rate for all the envisioned nuclear reactions.

Many experiments were devoted to find the optimum He pressure and to determine the response to pressure changes. For this we checked the spatial distribution and the total rate of the products in the FPD. While a pressure of about 1 mbar is generally best in the HTM, a signifi-

* Work supported by BMBF (06MT247I, 06MT248, 06MZ223I) and GSI-F&E (MT/TÜR, MZJVKR)

m.schaedel@gsi.de

cantly lower pressure in the 0.2 to 0.5 mbar range gives optimum results in the SIM. A more detailed investigation of the pressure dependence is under way.

One of the most interesting but least understood parameter in the operation of gas-filled separators is the gas filling. In addition to He as our standard gas, we did first test experiments with H_2, N_2, and mixtures of He and N_2. In the ^{40}Ar + ^{nat}Lu reaction we probed the influence of small amounts of N_2 in He on the magnetic rigidity and tested the pressure dependence in pure N_2. From the ^{48}Ca + ^{208}Pb reaction clean α-spectra of ^{254}No and its daughter ^{250}Fm were measured in the HTM with He and H_2 fillings. Figure 1 shows an example obtained with 1.5 mbar H_2.

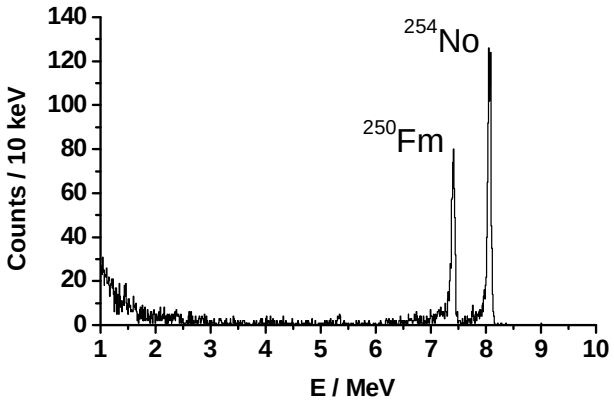

Figure 1: α-spectrum of ^{254}No separated in a 1.5-mbar H_2 gas filling of TASCA. ^{250}Fm is the daughter nucleus.

The ^{22}Ne(^{181}Ta,xn)^{198m,199}Bi reaction was used to check the calculated transmission [7] in the HTM and in the SIM. ^{198m,199}Bi were collected in Al catcher foils directly behind the target (used as the 100% reference value) and in the focal plane. Subsequent γ-ray spectroscopic measurements of these foils allowed determining the transmission and, from a measurement of segments, the spatial product distribution in the focal plane. Very good agreement was found between theoretically calculated transmissions and distributions and the measured ones.

Target development and testing with ^{40}Ar beams of up to 2 μA(particle) continued and concentrated on metallic Th and U targets on 2 μm Ti backings. In addition, large varieties of ^{144}Sm, ^{179}Au and ^{206,208}Pb targets were prepared and used for intense parameter studies at TASCA. Preparations towards new transuranium targets were concentrating on ^{244}Pu. In this ongoing program, considerable progress has been achieved recently.

Commissioning experiments for the RTCs [8], which were built for both two ion-optical modes, focused on finding best conditions for transporting preseparated nuclides to sites where chemistry experiments are envisaged to take place, i.e., a position inside X8 as well as in the nearby radiochemistry laboratory. Suitable nuclides were produced with ^{40}Ar beams, e.g., α-decaying 25-s ^{188}Pb and 4-s ^{245}Fm as well as longer-lived Os, Hg, and Pb isotopes that were identified with γ-ray spectroscopy.

Yields of preseparated Pb isotopes, transported with a He/KCl gas-jet to the chemistry laboratory, were measured as a function of parameters like (i) the thickness of degrader foils installed in front of the RTC window, (ii) the RTC depth, (iii) the pressure inside the RTC, and (iv) the gas-flow rate. Maximum yields of about 65% were obtained for transport to the radiochemistry laboratory through a 10-m long PE capillary at He flow rates of 2.5 L/min at a pressure of 1.2 bar in the RTC.

The product range in the He-filled RTC was measured by inserting catcher foils to positions with different distances from the RTC window. The measured ranges in He turned out to be larger than the values predicted by SRIM calculations, even though the energy loss in the Mylar degrader foil and window agrees well with such calculations. This was confirmed in measurements of EVRs in the FPD after passing through degrader foils.

Preseparated ^{188}Pb was measured after transport into ROMA [9]. Clean α-spectra and high yields allowed determining the half-life of (23.4±0.4) s with better precision than the literature value of (24.2±1.0) [10]. Furthermore experiments were performed where ^{245}Fm was transported into ROMA; see Figure 2. They prove that the TASCA-RTC system is ready for experiments with SHE.

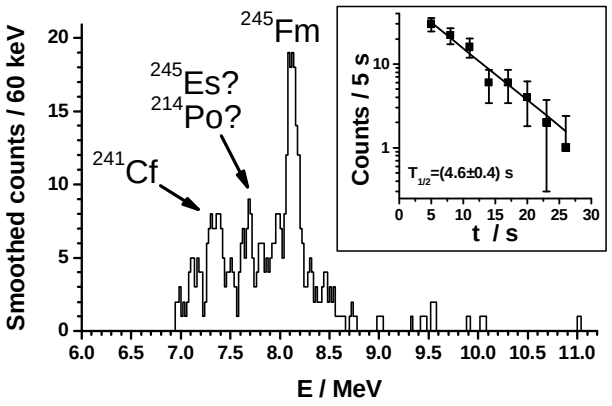

Figure 2: α-spectrum of ^{245}Fm. The insert shows the decay curve for α-particles with 8.05 MeV < E_α < 8.25 MeV.

References

[1] M. Schädel *et al.*, GSI Sci. Rep. 2005, GSI Report 2006-1, 2006, p. 262, and http://www.gsi.de/TASCA
[2] A. Semchenkov *et al.*, GSI Sci. Rep. 2004, GSI Report 2005-1, 2005, p. 332.
[3] M. Schädel, Eur. Phys. J. D 45 (2007) 67.
[4] A. Semchenkov *et al.*, Proceedings EMIS '07, Nucl. Instr. Meth. B, submitted.
[5] E. Jäger *et al.*, GSI Sci. Rep. 2005, GSI Report 2006-1, 2006, p. 263.
[6] J. Even *et al.*, this report.
[7] K.E. Gregorich *et al.*, GSI Sci. Rep. 2006, GSI Report 2007-1, 2007, p. 144.
[8] Ch.E. Düllmann *et al.*, GSI Sci. Rep. 2006, GSI Report 2007-1, 2007, p. 146.
[9] K. Sümmerer *et al.*, GSI Sci. Rep. 1983, GSI Report 84-1, 1984, p. 246.
[10] R.B. Firestone and V.S. Shirley (Eds)., Table of Isotopes, 8th edition, Vol. II

First successful chemistry-experiment behind TASCA –Electrodeposition of Os*

J. Even[1,2,#], W. Brüchle[3], R.A. Buda[1], Ch.E. Düllmann[3], K. Eberhardt[1], E. Jäger[3], H. Jungclas[2], J.V. Kratz[1], J. Khuyagbaatar[3], D. Liebe[1], M. Mendel[1], M. Schädel[3], B. Schausten[3], E. Schimpf[3], A. Semchenkov[3,4], A. Türler[4], V. Vicente Vilas[1], N. Wiehl[1], T. Wunderlich[1], A. Yakushev[4]

[1]Institut für Kernchemie, Johannes-Gutenberg-Universität Mainz, Germany; [2]Fachbereich Chemie, Philipps-Universität Marburg, Germany; [3]GSI, Darmstadt, Germany, [4]Institut für Radiochemie, Technische Universität München, Germany

Underpotential deposition has been shown by Hummrich [1] to be a suitable method for studying the chemical behaviour of the transactinides. For such investigations, the nuclide should have a half-life of at least 10 s. Thus, ^{270}Hs ($T_{1/2}$~22 s [2]) is a good candidate for electrochemical experiments. This report describes the first electrodeposition of short-lived isotopes of osmium, the lighter homologous element of hassium.

Os was produced in the reaction ^{nat}Ce(^{40}Ar,xn). The first experiments took place in cave X1 without preseparation. The reaction products were transported via a He/KCl-jet from the recoil chamber, which was directly behind the target, to a direct catch (DC) apparatus and to the Automated Liquid Online Heavy Element Apparatus (ALOHA). DC samples were collected on glass fibre filters which were measured by γ-spectroscopy. No γ-lines of Os isotopes were visible in the spectra due to the high background of transfer products (see figure 1, top), which clearly demonstrates the need for a physical preseparation [3] for such chemistry experiments. Behind TASCA [4], ^{177}Os and ^{176}Os were seen as the main products (see figure 1, bottom).

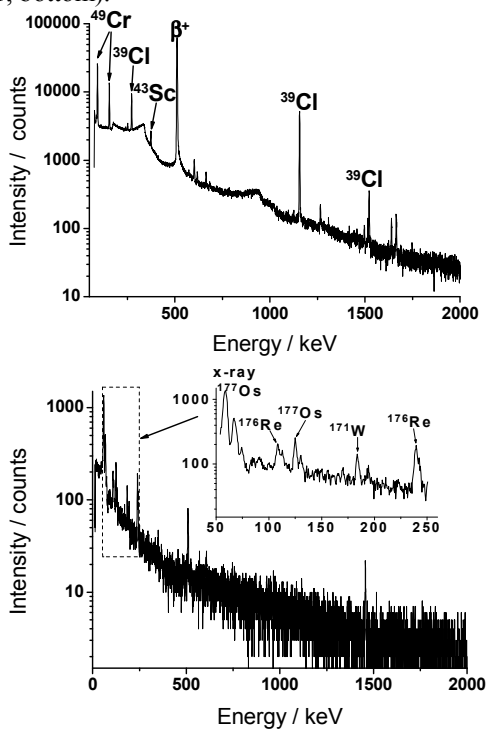

Figure 1: Comparison of the γ-spectra of a sample produced at X1 (top) and at TASCA (bottom).

For the electrochemical studies, the KCl aerosol particles were transported from the HTM-RTC [5] to the radiochemistry laboratory and were deposited on a Ta plate in ALOHA [1]. After 2 min collection time, the sample was dissolved and flushed into the electrolytic cell with 1 ml 0.1 M HCl delivered by a syringe pump. After running the electrolysis for 2 min, the electrodes were measured with a γ detector. The electrolysis was repeated at various potentials vs. an Ag/AgCl reference electrode. Measurements with different electrode materials (Pd, Ni, and palladinated Ni) were performed. The data were analysed according to [6] as shown in figure 2. The $E_{50\%}$-values, i.e., the potential, at which a deposition yield of 50% was observed, were +81 mV for Pd, +67 mV for palladinated Ni, and +10 mV for Ni, with uncertainties of ±50 mV.

To gain information about the deposition kinetics, the electrode potential was kept constant at -800 mV vs. an Ag/AgCl electrode and the electrolysis duration were varied. At room temperature and non-optimal stirring conditions, half of the osmium was deposited on Pd electrodes within (48±10) s and on Ni electrodes within (54±10) s.

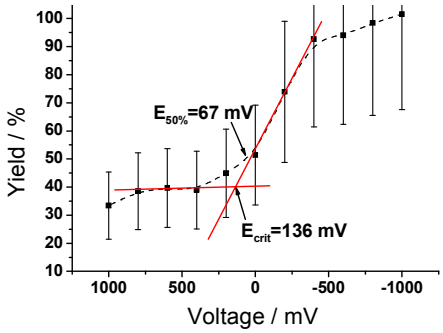

Figure 2: The critical potential on a palladinated Ni-electrode (the dashed line is drawn to guide the eye).

In another experiment with higher beam energy α-decaying ^{172,173}Os were produced and deposited on the Pd electrodes. Due to the small α-branch and the short half-lives (~20 s), only a few counts were detected. It could be shown, however, that it is possible to detect such short-lived nuclides by α spectrometry with an automated electrolytic cell after preseparation with TASCA.

References

[1] H. Hummrich, Doctoral thesis, U. Mainz, 2006.
[2] J. Dvorak et al., Phys. Rev. Lett. **97** (2006) 242501.
[3] Ch.E. Düllmann, Eur. Phys. J. D **45** (2007) 75.
[4] M. Schädel et al., this report.
[5] Ch.E. Düllmann et al., GSI Sci. Rep. 2006, p. 146.
[6] F. Joliot, J. Chim. Phys. **27**, 119 (1930).

* Work supported by BMBF (06MZ223I) and GSI-F&E (MZJVKR)
# evenj@uni-mainz.de

Adsorption Behaviour of HsO_4

A. Yakushev[1], J. Dvorak[1], Z. Dvorakova[1], R. Krücken[1], F. Nebel[1], R. Perego[1], R. Schuber[1], A. Semchenkov[1, 2], A. Türler[1], B. Wierczinski[1], W. Brüchle[2], Ch. E. Düllmann[2, 3, 4], E. Jäger[2], V. Pershina[2], M. Schädel[2], B. Schausten[2], E. Schimpf[2], M. Chelnokov[5], V. Gorshkov[5], A. Kuznetsov[5], A. Yeremin[5], K. Eberhardt[6], P. Thörle[6], Y. Nagame[7], K. Nishio[7], Z. Qin[2, 8], and M. Wegrzecki[9]

[1]TU Munich, Garching, Germany; [2]GSI, Darmstadt, Germany; [3]LBNL, Berkeley, CA, USA; [4]UC, Berkeley, CA, USA; [5]JINR, Dubna, Russia; [6]U Mainz, Germany; [7]JAEA, Tokai-mura, Japan; [8]IMP, Lanzhou, China; [9]ITE, Warsaw, Poland

Element 108, hassium, has been chemically identified for the first time by Ch. E. Düllmann *et al.* as a member of group 8 of the periodic table. A lower volatility of HsO_4 ($-\Delta H_{ads}$ = 46 ± 2 kJ/mol) compared to OsO_4 ($-\Delta H_{ads}$ = 39 ± 1 kJ/mol) has been observed [1]. Both extrapolations of ΔH_{ads} from RuO_4 and OsO_4 [2] and relativistic quantum chemical calculations with the use of the physisorption model [3,4] have shown that adsorption of HsO_4 on inert surfaces should almost be equal to that of OsO_4. The experimentally measured values are in disagreement, though not large, of only 6-7 kJ/mol.

Here we report results of two experiments aimed at synthesizing of new Hs isotopes performed recently at GSI. Two new Hs isotopes, $^{270, 271}$Hs and their daughters were successfully synthesized in the 4n and 3n evaporation channel, respectively, of the complete fusion reaction ^{26}Mg(^{248}Cm, xn)$^{274-xn}$Hs [5,6]. Hs atoms were separated by chemical means as HsO_4 and detected using the new detector setup COMPACT [5]. Products of the nuclear reactions recoiled from the target and were thermalized in a carrier gas (He/O_2 mixture with 10% O_2, 1.5 or 1.8 l/min) at 1.1 bar in the recoil chamber (RC) heated to 400°C. Oxidation started presumably in the RC and was completed on a quartz wool plug at 650°C. This plug also served as a filter for aerosol particles and non-volatile products. The separation factor from non-volatile species was >10^6. Species volatile at room temperature like HsO_4, OsO_4, At, or Rn were transported by the gas flow through a 8-m long PTFE™ capillary to the detection system. Two panels made from Invar™ with 32 PIPS diodes on each panel were combined into a gas tight channel with a narrow gap of 0.5 mm. The exit end of the detector was cooled to –160°C, whereas the entrance was kept at room temperature. The active surface of the diodes was covered with a thin layer of gold (first run) or aluminium (second run). The nearly 4π detection geometry yielded a detection efficiency of more than 80%. The distribution of 26 detected Hs chains along the detector is shown in Fig. 1 in comparison with the deposition peak of $^{172,173}OsO_4$. Using a Monte Carlo model of mobile adsorption [7] the adsorption enthalpy values have been evaluated as $-\Delta H_{ads}(HsO_4)$ = 51 ± 5 kJ/mol and $-\Delta H_{ads}$ (OsO_4) = 42 ± 2 kJ/mol, respectively. The $-\Delta H_{ads}(HsO_4)$ is slightly higher than observed in [1] and the distribution of the Hs events is rather wide. This fact can be explained by the higher gas flow velocity in the detector channel and the gently sloping temperature gradient in the first half of the detector.

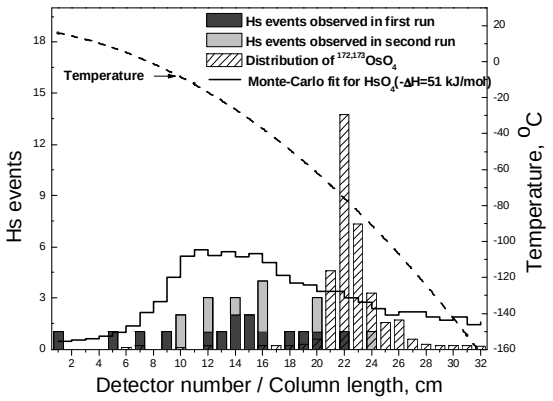

Fig.1. Distribution of HsO_4 and OsO_4 along the detector.

The calculation of the adsorption energy of the Van der Waals interaction of HsO_4 with a surface is sensitive to many parameters. Some of them, such as the ionization potential or the polarizability, can be obtained from accurate electronic structure calculations [3,4]. But it is very difficult to calculate another important parameter – the distance between a molecule and a surface. We propose to use for this parameter a half of the distance between atoms or molecules in molecular crystals. Using these distances in the calculations, the experimental values for adsorption and sublimation enthalpies of noble gases and non-polar molecules, like CH_4, CF_4, SF_6, or RuO_4 and OsO_4 are well reproduced. The intermolecular distance in tetroxide crystals correlates with the bond length between metal and oxygen atoms, which can be calculated theoretically for HsO_4.

Thus, we confirm here an observed earlier lower volatility of HsO_4 compared to OsO_4. This disagreement with the theory caused performance of the new calculations at a higher level of accuracy [8].

References

[1] Ch. E. Düllmann *et al.*, Nature, 418 (2002) 859.
[2] Ch. E. Düllmann *et al.*, J. Phys. Chem. B 106 (2002) 6679.
[3] V. Pershina *et al.*, J. Chem. Phys. 115 (2001) 792.
[4] V. Pershina *et al.*, J. Chem. Phys. 122 (2005) 124301.
[5] J. Dvorak *et al*,. Phys. Rev. Lett. 97, 242501 (2006).
[6] J. Dvorak *et al.*, GSI Sci. Rep. 2007, this issue.
[7] I. Zvara, Radiochim. Acta **38**, 95 (1985).
[8] V. Pershina and J. Anton, GSI Sci. Rep. 2007, this issue

* Work supported by BMBF (06MT247I)

Spin-Polarized 4c-DFT Calculations of the Electronic Structures and Properties of MO_4 (M = Ru, Os, and Hs) and Prediction of Physisorption

V. Pershina[1] and J. Anton[2]
[1]GSI, Darmstadt, Germany; [2]University of Kassel, Kassel, Germany

Volatility of group 8 tetroxides, MO_4 (M = Ru, Os, and Hs) has been a subject of interest of both experimental and theoretical research. Theoretically, very similar electronic structures and properties including volatilities were predicted on the basis of fully relativistic, four-component, density functional theory (4c-DFT) calculations [1,2]. Using a model of physisorption, it was shown that adsorption of HsO_4 on inert surfaces should almost be equal to that of OsO_4. Similar conclusions were obtained using extrapolation in group 8 [3]. Two similar types of experiments have, however, demonstrated that HsO_4 is about 6-7 kJ/mol stronger adsorbed on inert surfaces than OsO_4 [4,5]. In order to understand the reason for this (modest) disagreement, we have undertaken this study at a higher level of theory than before.

Thus, in this work, we have newly calculated the electronic structures of MO_4 (M = Ru, Os, and Hs) using our new version of the 4c-DFT method, which takes into account also magnetic effects [6]. The method implies the solution of the Kohn-Sham equations which in the non-collinear approximation have the form

$$\left\{\vec{t}+V^N+\tilde{V}^H+\frac{\delta E^{xc}[\rho,\vec{m}]}{\delta\rho}-\mu_B\beta\vec{\Sigma}\frac{\delta E^{xc}[\rho,\vec{m}]}{\delta\vec{m}}\right\}\phi_i=\varepsilon_i\phi_i \quad (1)$$

where ρ is electronic and m is magnetization densities. The wavefunctions ϕ are four-component Dirac spinors.

We have also dramatically increased the basis sets, which are now 5p,5d,4f,6s6p,5f for Ru; 6p,6d,5f,7s7p,7d for Os and 7p,7d,6f,8s8p,5g for Hs. These improvements allowed us to reach very high accuracy of the calculated polarizabilities, α, in almost perfect agreement with experiment for RuO_4 and OsO_4 [7] (Table 1). The present calculations have demonstrated a remarkable increase in $\alpha(HsO_4)$ in comparison with the earlier calculations due to a more complete inclusion of correlation effects, as well as improvements in the code.

The geometry (bond lengths, R_e) has been newly optimized in the present calculations. The obtained spectroscopic properties – ionization potentials (IP), α, vibrational frequencies (w_e) and R_e- are given in Table 1. They show very good agreement with the measured values for RuO_4 and OsO_4.

The dispersion interaction energies of the MO_4 molecules with quartz were calculated using the equation [1,2]

$$E(x)=-\frac{3}{16}\left(\frac{\varepsilon-1}{\varepsilon+2}\right)\frac{\alpha_{mol}}{\left(\frac{1}{IP_{slab}}+\frac{1}{IP_{mol}}\right)x^3} \quad (2)$$

Table 1. Calculated IP (in eV), polarizabilities, α (in a.u.), vibrational frequences, w_e (in cm^{-1}), bond lengths, R_e (in a.u.), molecule-surface distances x (in a.u.) and energies of physisorption, $-\Delta H_{ads}$ on quartz (in kJ/mol) for MO_4 (M = Ru, Os, and Hs).

Property	RuO_4	OsO_4	HsO_4	Ref.
IP	12.25	12.35	12.28	calc. [2]
	12.19	12.35	-	exp. [7]
α	58.07	55.28	65.995	this
	58.64	55.13	-	exp. [7]
w_e	1215	1284	1413	this
	-	965	-	exp.
R_e	1.712	1.719	1.779	this
	1.706	1.711	-	exp. [7]
x	2.228	2.23	2.25	this
$-\Delta H_{ads}$	40.23	39	46.5	this
	-	39±1	46±2	exp. [4]

The molecule-surface distances x have been newly estimated (Table 1) using the calculated R_e and assuming that the T_d molecules touch the surface by their facets.

The newly calculated ΔH_{ads} (Table 1) are in perfect agreement with the experimental results [4]. Thus, there is, indeed, a reversal of the trend in group 8 from Os to Hs not only in atomic properties such as IP or α, but also in the interaction energies with the surrounding, which are defined by those properties in a complex way (eq. 2). A reversal of the trend in ΔH_{ads} in group 8 takes its origin from the behaviour of the d-valence atomic orbitals (see Fig. 1 in Ref. [2]).

Thus, both experiments [4,5] and theory have finally agreed on the reversal of the trend in ΔH_{ads} in group 8, which could not be predicted on the basis of the extrapolation in the group. This remarkable example shows that in the case of weak interactions (van der Waals), very accurate calculations with electron correlation at the best level should be performed for the heaviest elements.

References

[1] V. Pershina *et al*. J. Chem. Phys. 115 (2001) 792.
[2] V. Pershina *et al*. J. Chem. Phys. 122 (2005) 124301.
[3] Ch. E. Düllmann *et al*. J. Phys. Chem. B 106 (2002) 6679.
[4] Ch. E. Düllmann *et al*. Nature, 418 (2002) 859 .
[5] A. Yakushev *et al*. GSI Annual Report 2007, this issue.
[6] J. Anton *et al*. Phys. Rev. A 69 (2004) 012505.
[7] CRC Handbook of Chemistry and Physics, 86th edition, ed. D. R. Lide (2005).

Prediction of the Adsorption Behaviour of Pb and Element 114 on Inert Surfaces from *ab initio* Dirac-Coulomb Atomic Calculations

V. Pershina[1], A. Borschevsky[2], E. Eliav[2], and U. Kaldor[2]
[1]GSI, Darmstadt, Germany; [2]Tel Aviv University, Israel

For the chemical identification of the heaviest elements, like 112 and 114, which are of current interest, predictions of their adsorption behaviour on various surfaces used in the experiments are essential. Recently, we have predicted adsorption of element 114 and its homolog Pb on metal surfaces on the basis of the fully relativistic density functional theory calculations of intermetallic compounds [1]. Inert surfaces such as quartz or Teflon can also be used, as well as ice can be formed in the chromatography column at very low temperatures. Information about the interaction of the heaviest elements with inert surfaces is also valuable for designing their transport from the target to the experimental set up. Thus, in this work, we predict the adsorption behaviour of element 114 and its homolog Pb on inert surfaces on the basis of very accurate results of *ab initio* calculations of their atomic properties.

The electronic structure calculations were performed using the DIRAC package [2]. In the Dirac-Coulomb (DC) *ab initio* method, the many-electron relativistic Dirac-Coulomb Hamiltonian

$$H_{DC} = \sum_i h_D + \sum_{i<j} 1/r_{ij} \qquad (1)$$

is employed, where

$$h_D = c\vec{\alpha}\cdot\vec{p} + \beta c^2 + V_{nuc}\,. \qquad (2)$$

The atomic orbitals are four-component spinors

$$\phi_{nk} = \begin{pmatrix} P_{nk}(r) \\ Q_{nk}(r) \end{pmatrix}, \qquad (3)$$

where $P_{nk}(r)$ and $Q_{nk}(r)$ are the large and small component, respectively. The Faegri uncontracted 26s24p18d13f5g2h basis set was used for both elements [3]. Electron correlation was taken into account at various levels of theory including the highest, the Coupled Cluster Single Double (Triple) excitations, CCSD(T), for which the current results are presented.

The calculations of polarizability (α) were performed with the use of the finite field method. The DC CCSD(T) results for α are given in Table 1 along with the ionization potentials (IP) of Pb and element 114 calculated at best using the Dirac-Coulomb-Breit Fock-Space CC (DCB FSCC) method [4]. The van der Walls radii (R_{vdW}) were determined from a linear correlation with $R_{max}(np_{1/2})$-atomic orbitals of the group 14 elements. The adsorption enthalpies, ΔH_{ads}, were calculated using a model of physisorption given by eq. (8) of Ref. [5].

Table 1. Atomic properties of Pb and element 114: ionization potentials, IP (in eV), polarizabilities, α (in a.u.), van der Walls radii, R_{vdW} (in a.u.) and energies of physisorption, $-\Delta H_{ads}$ on quartz (q), ice (i) and Teflon (T) (in kJ/mol).

Property	Pb	Meth.	Ref.	114	Meth.	Ref.
IP	7.349	DCB	[4]	8.539	DCB	[4]
	7.417	exp.	[6]			
α	46.96	DC	this	30.59	DC	this
	45.89	exp.	[6]			
R_{vdW}	4.06	corr.	this	3.94	corr.	this
	4.16	exp.	[6]			
$-\Delta H_{ads}$ (q)	27.34	calc.	this	20.97	calc.	this
$-\Delta H_{ads}$ (i)	26.29	calc.	this	20.20	calc.	this
$-\Delta H_{ads}$ (T)	13.65	calc.	this	10.41	calc.	this
	13.0	exp.				

The obtained ΔH_{ads} on quartz and Teflon for all group 14 elements are shown in Fig. 1 revealing a reversal of the trend from Sn on. The very low $\Delta H_{ads}(114)$ on inert materials guarantees its transport to the chemistry set up.

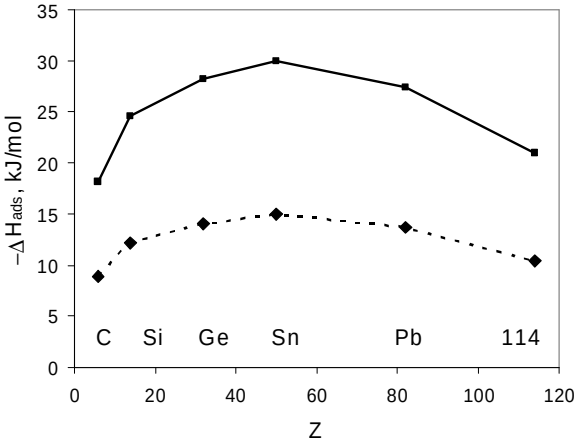

Fig. 1. Calculated dispersion interaction energies (enthalpies of adsorption, $-\Delta H_{ads}$) of group 14 elements with quartz (solid line) and Teflon (dashed line).

References

[1] V. Pershina, J. Anton, and B. Fricke, J. Chem. Phys. 127, (2007) 134310.
[2] DIRAC 04, written by H. J. Ja. Jensen *et al.* (2004).
[3] K. Faegri, Theor. Chim. Acta 105 (2001) 252 .
[4] A. Landau *et al*. J. Chem. Phys. 114 (2001) 2977.
[5] V. Pershina *et al*. J. Chem. Phys. 122 (2005) 124301.
[6] CRC Handbook of Chemistry and Physics, 86th edition, ed. D. R. Lide (2005).

Fully Relativistic *ab initio* Dirac-Coulomb Calculations of Atomic Properties of Rn and Element 118

A. Borschevsky[1], E. Eliav[1], U. Kaldor[1], and V. Pershina[2]
[1]Tel Aviv University, Israel; [2]GSI, Darmstadt, Germany

Experiments on the production of elements 112-116 in Dubna, Russia, have proven the existence of the enhanced stability of their neutron-rich isotopes. Furthermore, the existence of element 118 has been demonstrated using the ^{48}Ca beam and the ^{249}Cf target [1]. The produced ^{294}118 isotope has half-life $T_\alpha=0.89^{+1.07}_{-0.31}$ ms in agreement with the theoretical predictions and decays into ^{286}114 or ^{282}112, which undergo spontaneous fission,.

Chemical identification of element 118 is a matter of the near future. Predictions of its chemical properties, especially those important for gas-phase chromatography experiments [2] are, therefore, needed. Very accurate calculations can nowadays be performed using fully relativistic methods and algorithms. Thus, in this work we predict atomic properties of element 118 and its homolog Rn on the basis of *ab initio* Dirac-Coulomb (DC) calculations using the DIRAC package [3]. In the DC *ab initio* method, the many-electron relativistic Dirac-Coulomb Hamiltonian

$$H_{DC} = \sum_i h_D + \sum_{i<j} 1/r_{ij} \qquad (1)$$

is employed, where

$$h_D = c\vec{\alpha}\cdot\vec{p} + \beta c^2 + V_{nuc}\,. \qquad (2)$$

The atomic orbitals are four-component spinors

$$\phi_{nk} = \begin{pmatrix} P_{nk}(r) \\ Q_{nk}(r) \end{pmatrix}, \qquad (3)$$

where $P_{nk}(r)$ and $Q_{nk}(r)$ are large and small component, respectively. The Faegri uncontracted 26s24p18d13f5g2h basis set was used for Rn and element 118 [4]. The electron correlation was taken into account at various levels of theory - Moller-Plesset (MP2) and Coupled Cluster Single Double (Triple) excitations [CCSD(T)]. The Hartree-Fock (HF) values were also obtained for comparison in order to elucidate the influence of correlation.

The calculations of polarizability (α) were performed with the use of the finite field method. The strengths of the field were chosen as 0.0001, 0.001 and 0.01 a.u. The results are summarized in Table 1. The obtained DC CCSD(T) values are in very good agreement with experiment for Rn [5] and much better than those calculated in Ref. [6] using the MOLFDIR code. The latter values are not accurate due to the small basis sets used. The α(118) is larger than α of the other gases due to the relativistic expansion of the outer $7p_{3/2}$ atomic orbitals (AOs).

Table I. Polarizabilities α (in a.u.) for Rn and element 118 calculated at different levels of correlation.

Atom	α				Ref.
	HF	MP2	CCSD	CCSD(T)	
Rn	34.99	34.96	34.78	35.04	present
	29.22	28.48	28.61	28.61	calc. [6]
	-	-	-	35.766	exp. [5]
118	50.01	44.45	46.64	46.33	present
	54.46	49.47	52.50	52.43	calc. [6]

We also give here estimates of atomic, or van der Walls radii (R_{vdW}) of element 118. They were determined using a correlation between the maximum of the radial charge density of the outer valence $np_{3/2}$ AOs [7] and known R_{vdW} (Fig. 1). The obtained $R_{vdW}(118)$ is larger than R_{vdW} of the other gases due to the same reason an that for α.

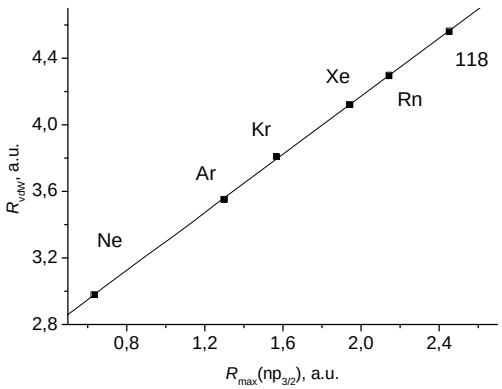

Fig. 1. Correlation between $R_{max}(np_{3/2})$ and R_{vdW} for the rare gases. The obtained value for $R_{vdW}(118)$ = 4.55 a.u.

The calculated properties can be used for further predictions of adsorption behaviour of these elements on various surfaces.

References

[1] Yu. Ts. Oganessia *et al*. Phys. Rev. C 74 (2006) 044602.
[2] H. W. Gäggeler, A. Türler, In: Chemistry of Superheavy Elements, ed. M. Schädel, Kluwer, 2003.
[3] DIRAC 04, written by H.J. Ja. Jensen *et al*. (2004).
[4] K. Faegri, Theor. Chim. Acta 105 (2001) 252 .
[5] CRC Handbook of Chemistry and Physics, 86th edition, ed. D. R. Lide (2005).
[6] C. Nash, J. Phys. Chem. 109 (2005) 3493.
[7] J. P. Desclaux, At. Data Nucl Data Tables, 12 (1973) 311.

Calculation of the low-lying level structure of trans-einsteinium elements*

S. Fritzsche[1,2], C. Z. Dong[3], T. Radtke[2], and A. Uvarov[4]

[1]GSI, Darmstadt; [2]University of Kassel; [3]Northwest Normal University, Lanzhou, China; [4]Max-Planck Institute for Nuclear Physics, Heidelberg

Spectroscopic investigations on the super-heavy elements (SHE) are of fundamental interest in understanding the nuclear, atomic and chemical properties of isotopes near to the border of the nuclear chart. For the trans-einsteinium elements, of course, many of these case studies were initiated and performed in order to predict the properties of yet undiscovered isotopes and in the hope of finding an 'island of stability'. Until today, however, the atomic spectroscopy of SHE with charge numbers $Z \gtrsim 100$ has remained a challenge [1] because these elements need to be produced in nuclear fusion reactions with rates of sometimes only a few atoms per week [2]. From the viewpoint of theory, the study of SHE has attracted great interest because of the rapid increase in relativistic and quantum–electrodynamical (QED) effects and the difficulty in extrapolating the atomic and chemical properties of these elements, such as ionization potentials, electron affinities or the formation of chemical complexes.

There are several difficulties in calculating the level structure of SHE which do not occur for low– and medium–Z elements or are less pronouced there. Apart from (i) QED corrections that cannot be treated in full detail for the heavy elements [3], (ii) the low-lying level structure of these elements is more often than not determined by a number of overlapping and nearly degenerate configurations. This 'overlap' becomes particularly important for the lanthanides and actinides with their open $nf-$shells $(n = 4, 5)$, but it also occurs for elements with a nominal rather simple ground configuration, such as the $7s^2 7p$ configuration of atomic lawrencium. In addition, further complexity arises (iii) from the large *number of electrons* which have to be treated explicitly in any *ab-initio* theory. These difficulties enforces one to go up to the limits of what is computational feasible today. — In order to support also the computation of properties other than atomic level energies, the multiconfiguration Dirac-Fock method was applied for studying the low-lying level structure and absorption rates of nobelium and lawrencium. In this method, the atomic states are approximated by a superposition of configuration state functions of the same symmetry

$$\psi_\alpha(PJM) = \sum_{r=1}^{n_c} c_r(\alpha)\ |\gamma_r PJM\rangle\ , \qquad (1)$$

and are optimized on the basis of the (many-electron) Dirac-Coulomb Hamiltonian, $H_{\rm DC}$ [4].

Nobelium (Z=102) and lawrencium (Z=103) are presently the two most prominent candidates to measure some of their atomic levels for elements with $Z \gtrsim 100$. For nobelium, in particular, an experiment is currently prepared at GSI to find the $^3P_1$ and (perhaps) further resonances between about 20,000 and 30,000 cm^{-1} [5]. In these *on–line* measurements, the isotope ^{254}No is to be produced at the GSI UNILAC by the reaction ^{208}Pb(^{48}Ca,2n)^{254}No with rather a large cross section $\sigma = (3.4 \pm 0.4)$b and separated by the SHIP from the ^{48}Ca projectiles beam. The $5f^{14}7s^2$ ground configuration of nobelium renders this element an ideal candidate to test the predictions from various semi-empirical and *ab-initio* theories.

For lawrencium, in addition, detailed computations have been carried out for the 30 lowest odd- and even-parity levels with total angular momenta $J = 1/2, ..., 9/2$, by applying medium- to large-scale wave function expansions. The results of these calulations are summarized in Table 1 of Ref. [6] that displays the (level) designation, symmetry, excitation energies and absorption rates of these levels with regard to the $7s^2 7p\ ^2P^o_{1/2}$ ground state. In contrast to the $5d\,6s^2\ ^2D^o_{3/2}$ ground state of the homologous element lutetium (Z=71), the $5f^{14}7s^2 7p\ ^2P^o_{1/2}$ ground state of lawrencium was confirmed recently by very extensive computations [7]. Although lawrencium has only three valence electrons in the $7s^2 7p$ ground configuration, strong admixtures of several (odd-parity) configurations were found, for which one of the $7s$ and $7p$ electrons are 'excited' into the $6d$, $7d$, $8s$ and $8p$ subshells. For many of these levels, an accuracy of ~ 1200 cm^{-1} was estimated, and it was found that about 15 of these levels fall into the spectroscopically relevant region.

We therefore hope that our computations will facilitate the set-up of forthcoming experiments and the identification of new levels. Moreover, by providing a rather large number of excitation energies, a critical test on the 'quality' of present-day predictions becomes possible — if these levels will be confirmed or discarded by future measurements.

References

[1] M. Sewtz *et al.*, Phys. Rev. Lett. 90 (2003) 163002.

[2] S. Hofmann and G. Münzenberg, Rev. Mod. Phys. 72 (2000) 733.

[3] S. Fritzsche, Eur. Phys. J. D33 (2005) 15.

[4] F. A. Parpia *et al.*, Comput. Phys. Commun. 94 (1996) 249.

[5] H. Backe and M. Sewtz, private communication (2005).

[6] S. Fritzsche *et al.*, Eur. Phys. J. D45 (2007) 107.

[7] Y. Zou and C. F. Fischer, Phys. Rev. Lett. 88 (2002) 183001.

* Work supported by BMBF under contract No. 06KS203.

Friction in abrasion

A. Bacquias[1], V. Föhr[1], D. Henzlova[2], V. Henzl[2], A. Kelic[1], S. Lukic[1], M. V. Ricciardi[1], K.-H. Schmidt[1]

[1]GSI, Darmstadt, Germany; [2]MSU, East Lansing, Michigan, U.S.A

In very peripheral nucleus-nucleus collisions at energies well above the Fermi-energy regime friction phenomena set in. Friction appears as a consequence of interactions between the projectile and target matter in the overlapping region, and leads to a conversion of relative kinetic energy into excitation energy of projectile and target spectators. Due to this loss in kinetic energy, the velocity of spectator residues is slightly shifted towards the velocity of the reaction partner, i.e. projectile residues are slowed done. As for very peripheral collisions the interaction between the projectile and target matter in the overlapping region depends on in-medium nucleon-nucleon cross sections, the magnitude of the friction gives valuable information on the in-medium nucleon-nucleon cross section [1]: By comparing momentum distributions of spectator residues measured in high-resolution experiments with different theoretical predictions one can obtain the value of the in-medium nucleon-nucleon cross section needed to reproduce experimental data. However, this information was not readily accessible up to now. The reason is that in high-resolution experiments one obtains momenta of final fragments, i.e. after the evaporation of several particles, as a function of the mass or nuclear charge of the residue, while theoretical models describe only the first interaction stage of the collision, i.e. before the evaporation, and the momenta are given as a function of the impact parameter. As high-resolution experiments are not compatible with the full acceptance, until now there was no information on the impact parameter from such type of experiments, and, consequently, a direct comparison between the experiment and the theory was not possible. To overcome this limitation, we have introduced a method that can provide the momenta of the spectators as a function of the impact parameter. Using this method we are able to directly compare high-resolution experimental data to the predictions of theoretical models, and thus get new insight into friction.

In the present work, we profit from the experimental information on the cross sections and the velocity distributions of all nuclides obtained in an experiment at the fragment separator (FRS) of GSI in the reaction ^{136}Xe + Pb [2]. In addition, we exploit the correlation between the impact parameter and the mass of the heaviest residue in a reaction, which is well established for peripheral nuclear collisions [3]. A Glauber calculation [4] on the differential reaction cross section as a function of impact parameter is used to establish a correlation between the residue mass and the impact parameter and finally to find the desired correlation between the spectator velocity and the impact parameter. We apply this correlation down to mass A=40, as the nuclei with A < ~40 produced in the reaction ^{136}Xe+Pb can arise from processes where multifragmentation and emission of intermediate-mass fragments play an important role. In these cases, more than one residue with comparable masses can be produced in one event, leading to the non-unique correlation between the residue mass and the impact parameter.

In figure 1 we present the average measured longitudinal velocity of the fragments in projectile frame as a function of impact parameter obtained using the above-mentioned procedure. For the present work, only data down to the impact parameter of ~11 fm are of interest; nevertheless, for the completeness, we show the whole set of data for which we have extracted the impact parameter. We have also made preliminary calculations with different theoretical models (QMD [5] and ISABEL [6]) or empirical parameterizations (Morrissey [7]). More detailed comparisons are under way.

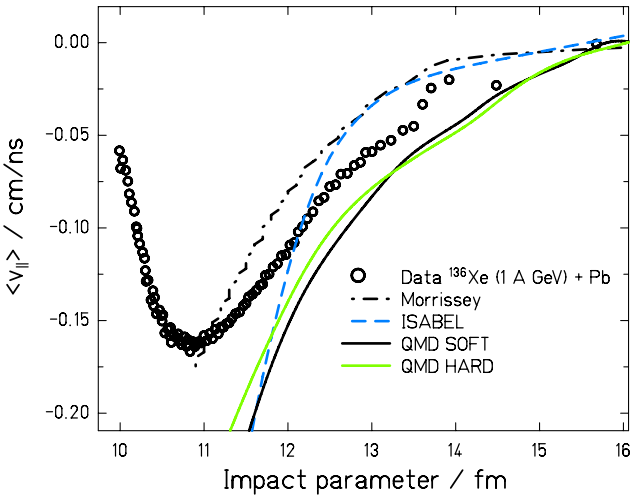

Figure 1: Average fragment velocities from Xe+Pb experiment in the Xe-beam frame (1000 A MeV) plotted against the impact parameter (dots). Full lines show the corresponding result from QMD calculation. Dashed line shows velocities according to ISABEL model. Morrissey systematic is shown with dash-dotted line.

References

[1] P. Danielewicz, *Acta Phys. Pol. B* **33** (2002) 45.
[2] D. Henzlova et al, *arXiv:0801.3110v1* [nucl-ex].
[3] A. Schüttauf, *PhD thesis*, Univ. of Frankfurt 1996.
[4] R. J. Glauber, *Phys. Rev.* **100** (1955) 242.
[5] J. Aichelin, *Phys. Rep.* **202** (1991) 233.
[6] Y. Yariv, Z. Fraenkel, *Phys. Rev. C* **20** (1979) 2227.
[7] D.J. Morrissey, *Phys. Rev. C* **39** (1989) 460.

Experimental study of the influence of the projectile type on residual nuclide distribution in spallation reactions*

S. Lukić[1, #] for the CHARMS collaboration
[1]GSI, Darmstadt, Germany

Nuclear reactions induced by relativistic particle beams have been widely studied in the context of applications like Accelerator Driven Systems, or Radioactive Ion Beam (RIB) production. One of the most important questions for applications is that of the optimal reaction system to deliver the desired final result. In the context of RIB production, one is concerned by the respective influences of the beam particle type and its total energy on the final fragment distribution. To the first order, one can expect the total energy to be the key factor determining the distribution of prefragments. The projectile type can, however, determine some of the parameters of the initial stage of reaction, such as the initial single-particle collision velocity, and the geometry of the collision. In presence of single-particle reaction mechanisms characterized by a certain threshold, these parameters could affect the scope of mechanisms involved at the initial stage, and thus influence fine details of the final distribution.

This question arose during a recent study of additional projectile types for the EURISOL project [1]. It is our aim here to provide at least a partial answer to it, based on available experimental data on a light nucleus (Fe) measured at the GSI Fragment Separator (FRS) in inverse kinematics. For this purpose, a set of raw data on the reaction Fe+d at 500 A MeV was analyzed for the first time, in order to be compared with previously published data on the reaction Fe+p at 1000 A MeV [2,3]. These two reactions are characterized by the same total collision energy, but a different type of the light reaction partner. They were measured under essentially the same conditions in one experiment at the FRS.

The experimental setup was described in detail in refs. [2,3]. For the deuteron run, a 200 mg/cm^2 liquid deuteron target was used.

It was possible to analyze the data for fragments as light as lithium, thanks to fragment energy-loss information coming from scintillators, which complemented energy-loss data from MUSIC ionisation chambers. The obtained nuclide production cross sections are shown using colour plot over the relevant region of the chart of the nuclides in Fig. 1.

The comparison with data from the reaction Fe+p at 1000 A MeV [2,3] shows a surprising level of agreement both in magnitude and shape of the isotopic distributions for all analyzed elements down to oxygen (Fig. 2). This leads us to a conclusion that the total collision energy is indeed the decisive parameter that determines even the finest experimentally available details on fragment-production cross-sections.

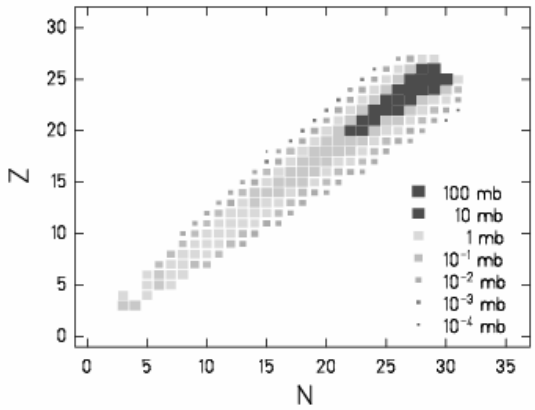

Figure 1: Nuclide production cross sections in the reaction Fe+d at 500 A MeV, measured at the FRS, GSI.

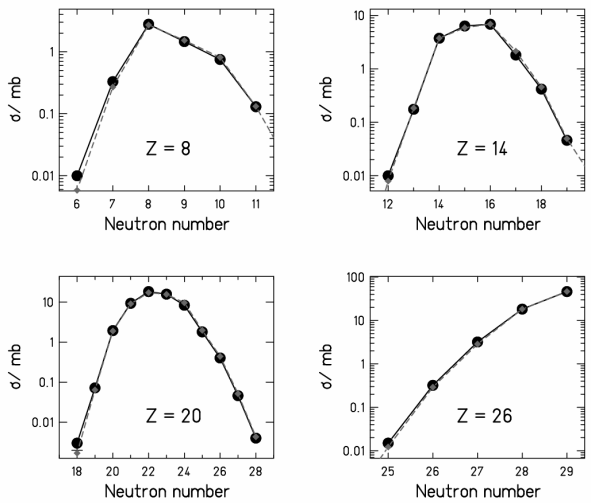

Figure 2: Comparison of production distributions for several isotopic chains in the reactions Fe+d at 500 A MeV(squares) and Fe+p at 1000 A MeV [2,3] (dots).

References

[1] K.-H. Schmidt et al., Phys. Rev. Special Topics AB 10 (2007) 14701.
[2] P. Napolitani et al., Phys. Rev. C70 (2004) 054607.
[3] C. Vilagrassa, PhD thesis, Univ. Paris XI, France, Dec. 2003. http://www-w2k.gsi.de/charms/theses.htm

* We acknowledge the financial support of the European Community under the FP6 "Research Infrastructure Action - Structuring the European Research Area" EURISOL DS Project Contract no. 515768 RIDS. The EC is not liable of any use that can be made on the information contained herein.

#Present affiliation: University of Karlsruhe (TH), Forschungszentrum Karlsruhe, Germany. Strahinja.Lukic@ik.fzk.de

Nuclear-fission studies with exotic beams: analysis of fission channels

C. Böckstiegel[1], S. Steinhäuser[1], K.-H. Schmidt[2], H.-G. Clerc[1], A. Grewe[1], A. Heinz[1], M. de Jong[1], A. R. Junghans[2], J. Müller[1], and B. Voss[2]
[1]IK, TU Darmstadt, Germany; [2] GSI, Darmstadt, Germany.

The present work reports on a systematic study of fission-fragment element yields in the fission of 70 neutron-deficient actinides and pre-actinides between ^{205}At and ^{234}U within the concept of independent fission channels [1]. The fission channels are characterized by several parameters, e.g. the average mass or charge split, the mass or charge width, and the mean total kinetic energy, respectively the elongation of the scission configuration. We extract the values of these parameters for three fission channels from the measured data of 15 nuclides [2] which show features of multi-modal fission.

The experiment was performed at GSI Darmstadt: Relativistic secondary projectiles were produced via fragmentation of a 1 *A* GeV primary beam of ^{238}U and identified in *A* and *Z* by the fragment separator FRS. Details of the experimental technique are given elsewhere [2].

In Fig. 1, we compare the parameters of the independent fission channels, determined in the present work, with the body of previously available data. This allows a systematic view on the variation of position (<*A*>) and width (σ) of the standard I (S1) and standard II (S2) channels, on the width of the super-long (SL) channel and on the relative yields of these three channels as a function of *Z* and *A* of the fissioning system. The data are restricted to spontaneous fission and to initial excitation energies up to a few MeV above the fission barrier. The widths of the S1 and S2 fission channels show fluctuations, which are appreciably larger than the reported statistical uncertainties of the fits. No systematic trend can safely be deduced over the whole mass range. One may only conclude that the width of the S1 fission channel amounts to about 3.5 mass units, while the width of the S2 fission channel is appreciably larger with about 5 mass units. The width of the SL fission channel is rather well determined for the light systems of the present experiment, for which the symmetric fission component dominates, to about 10 mass units over a large mass range, see ref. [2]. Thus, the SL fission channel is much broader than the S1 and S2 fission channels. The values deduced previously for heavier systems fluctuate enormously. These fluctuations are probably explained by the tiny yield of the super-long channel for the heavier systems.

The positions of the S1 and S2 fission channels show a systematic variation as a function of mass number for a given element. This trend is clearly seen for all elements, in spite of some fluctuations. The average slope of the isotopic trend seems to be slightly larger than 0.5. This means that the positions of the S1 and S2 fission channels vary in neutron number and are rather *stable in proton number*. The relative yield of the symmetric SL fission channel shows an exponential decrease with increasing mass number. For systems with $A > 234$, the yield of this channel becomes so low that it could not be determined any more. At the same time, the complementary yield of the lumped asymmetric component increases with increasing mass. Deducing a systematic trend in the competition between the S1 and the S2 fission channels requires a more detailed analysis [3].

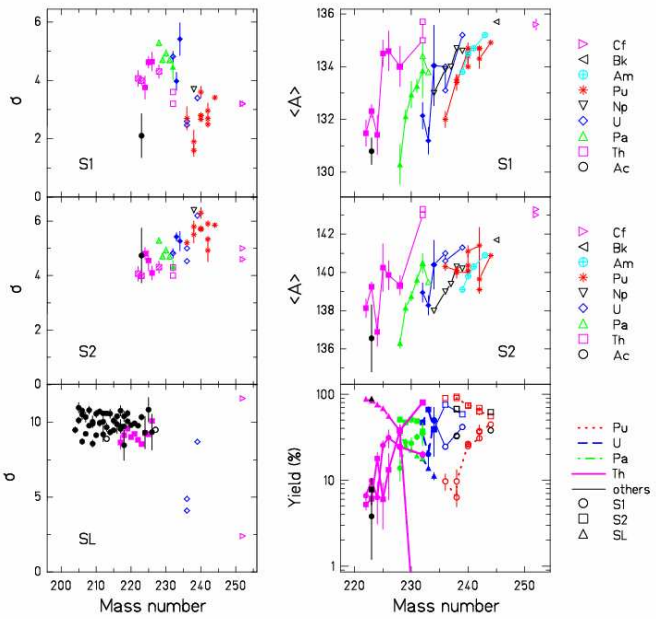

Figure 1: Global view on the parameters of the three independent fission channels standard I (S1), standard II (S2) and super long (SL). The results of the present work (full symbols) are compared with other available experimental data (open symbols) (see ref. [3] for references to other data). All data are given in mass numbers. Values measured in nuclear charge were converted to mass numbers using the unchanged-charge density assumption and neglecting neutron evaporation.

To conclude, the body of data presently available is consistent with the assumption that the parameters of the independent fission channels vary in a smooth and consistent way. Surprisingly, the position of the asymmetric fission channels is found to be constant in atomic number over all systems. More details are given in ref. [3].

References

[1] U. Brosa, S. Grossmann, A. Müller, Phys. Rep. 197 (1990) 167
[2] K.-H. Schmidt et al, Nucl. Phys. A 665 (2000) 221.
[3] C. Böckstiegel et al, Nucl. Phys. A *in press*.

Bimodality in spectator fragmentation

W. Trautmann[1] and the ALADiN Collaboration[1]
[1]GSI, Darmstadt, Germany

This work has been motivated by the presently ongoing discussion of whether bimodality in the thermodynamic sense can be observed in fragmentation reactions and whether one can argue in favour of its providing direct evidence for the first-order character of the nuclear liquid-gas phase transition [1]. Bimodality occurs if non-negligible surface interactions at the phase boundary lead to a convex entropy function in the transition region. Canonical sampling near the transition temperature will then produce two distinct event classes with large differences in the order parameter of the transition [2, 3].

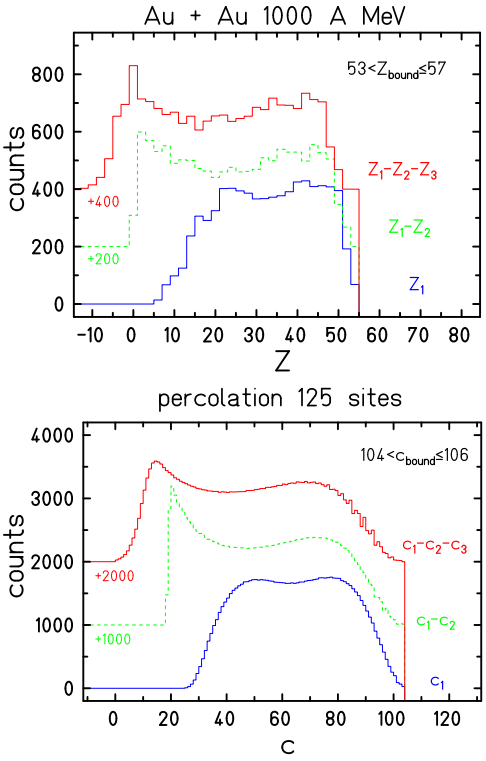

Figure 1: Distributions of the largest atomic number Z_1 (cluster c_1) of a partition and of the two and three cluster differences for ^{197}Au + ^{197}Au at 1000 A MeV (top) and for cubic percolation on a 5^3 lattice (bottom) for the indicated bins of $Z_{\rm bound}$ ($c_{\rm bound}$).

Bimodality has, e.g., been observed in solid-liquid transitions of clusters of Na atoms [4]. In these experiments, the clusters were thermalized in a heat bath of helium gas and excited with photons from a laser beam. Corresponding experiments in nuclear fragmentation face the difficulty that the temperature cannot be similarly predetermined and that a canonical sampling is thus not possible.

A second argument, as will be shown here, follows from the similarity of the observed fragment charge distributions and correlations in the transition region with percolation phenomena [5]. The percolation phase transition is considered to be of second order [6]. Phenomena equally observed in percolation can thus not be used as indicators of a first-order transition.

The experimental data used for this comparison were obtained by the ALADIN collaboration in measurements using ^{197}Au projectiles of 1000 MeV per nucleon delivered by the heavy-ion synchrotron SIS at GSI [7]. The ALADIN spectrometer was used to detect and identify the products of the projectile-spectator decay following collisions with ^{197}Au target nuclei.

In these reactions, the transition from evaporation-like processes to multifragmentation occurs at values $Z_{\rm bound} \approx 55$ of the variable $Z_{\rm bound}$ used for sorting the data according to impact parameter [7]. The distributions of the largest atomic number Z_1 observed in a partition as well as those of the two-fragment and three-fragment differences $Z_1 - Z_2$ and $Z_1 - Z_2 - Z_3$ for a narrow interval in this transition region are given in Fig. 1 (top panel). They are rather wide and exhibit a two-humped structure.

Very similar distributions have been obtained with calculations performed with a cubic-bond-percolation model for various lattice sizes. The results for a 5^3 lattice show the same two-humped structure and resemble the fragmentation data in many respects (Fig. 1, bottom panel), including the widths which are maximum in the transition region, both for the data and for the calculations.

For larger lattices, the distributions are still double-humped but much narrower. The bond parameter $p_{\rm bimod}$ at which the bimodal structure is most pronounced is smaller and closer to the critical value. The observed variation with the lattice size is systematic and confirms that the law of finite-size scaling is obeyed by $p_{\rm bimod}$ [5].

References

[1] M. Pichon et al., Nucl. Phys. A **779** (2006) 267.

[2] D.H.E. Gross, Eur. Phys. J. A **30** (2006) 293.

[3] Ph. Chomaz and F. Gulminelli, Eur. Phys. J. A **30** (2006) 317.

[4] M. Schmidt et al., Phys. Rev. Lett. **86** (2001) 1191.

[5] W. Trautmann et al., in *Proceedings of the XLV International Winter Meeting on Nuclear Physics*, Bormio, Italy, ed. by I. Iori and A. Tarantola, Ricerca Scientifica ed Educazione Permanente Suppl., vol. **127**, Milano, 2007, p. 205, preprint arXiv:0705.0678(nucl-ex), (2007).

[6] D. Stauffer and A. Aharony, *Introduction to percolation theory*, Taylor and Francis, London, 1992.

[7] A. Schüttauf et al., Nucl. Phys. A **607** (1996) 457.

Isoscaling in spectator fragmentation at relativistic energies*

S. Bianchin[1], J. Łukasik[1,2], C. Sfienti[1], W. Trautmann[1], and the ALADiN2000 Collaboration[1]
[1]GSI, Darmstadt, Germany; [2]IFJ-PAN, Kraków, Poland

The phenomenon of isoscaling is receiving considerable interest because of its relation with the symmetry term in statistical [1] and dynamical [2] descriptions of fragmentation reactions. As reported recently, the symmetry term coefficient γ in the liquid-drop description of the nascent fragments appears to be decreasing from the standard value $\gamma = 25$ MeV for isolated nuclei to about 15 MeV or lower for fragments in the hot environment of multifragmentation processes [3, 4]. Similar results were obtained by other groups [5] and interpreted as caused by fragment modifications [6] at the low-density chemical freeze-out [7].

The present study is based on the data collected recently with the ALADIN spectromer, using primary beams of ^{124}Sn and neutron-poor secondary beams of ^{107}Sn and ^{124}La delivered by the FRS fragment separator, all with 600 A MeV incident energy, and natural Sn targets [8, 9].

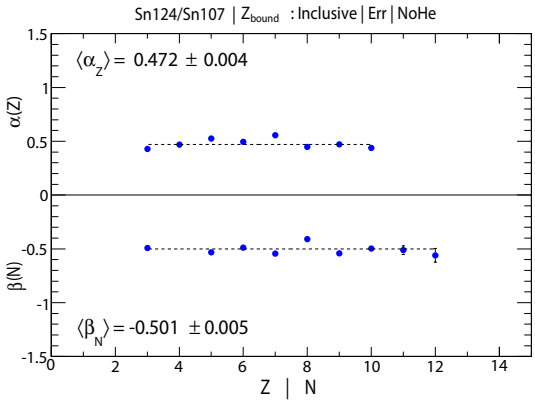

Figure 1: Isoscaling parameters $\alpha(Z)$ and $\beta(N)$ obtained by individually fitting the N and Z dependences of isotopes and isotones, respectively, for inclusive yields from the fragmentation of ^{124}Sn and ^{107}Sn projectiles at 600 A MeV. The lines represent the mean values for isotopes with Z from 3 to 10 and isotones with N from 3 to 12.

Isoscaling refers to the exponential dependence

$$R_{21}(N,Z) = Y_2(N,Z)/Y_1(N,Z) = C \cdot exp(\alpha N + \beta Z)$$

of the yield ratios $R_{21}(N,Z)$, measured in two reactions with differing isotopic compositions, on the neutron number N and proton number Z of the detected products [10]. The quality with which this relation holds has been tested by regarding the behavior of the exponential slopes $\alpha(Z)$ of the yield ratios for individual elements and $\beta(N)$ for individual chains of isotones. As demonstrated in Fig. 1 for the inclusive yields from the ^{124}Sn and ^{107}Sn fragmentations, the deviations from the common mean values are impressively small.

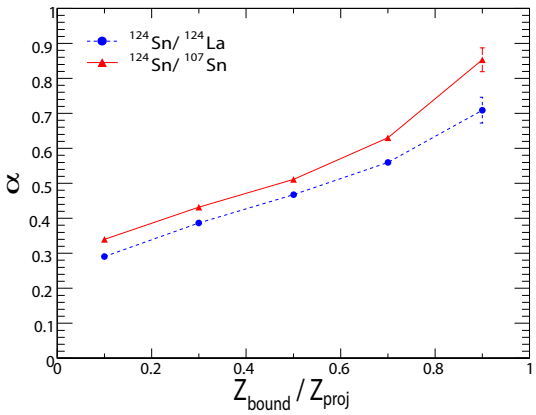

Figure 2: Isoscaling parameter α for the two pairs of reactions with ^{124}Sn/^{124}La and ^{124}Sn/^{107}Sn projectiles as a function of $Z_{\rm bound}$ normalized with respect to $Z_{\rm proj}$.

The rapid drop of the isoscaling parameters with rising fragment production, first observed with INDRA in ^{12}C induced reactions on Sn targets at the same energy [3], has been confirmed (Fig. 2, $Z_{\rm bound}/Z_{\rm proj} > 0.5$) and followed into the region of falling fragment production ($Z_{\rm bound}/Z_{\rm proj} < 0.5$) which was not accessible with the light ^{12}C collision partner. The observed small difference between the two pairs of projectiles reflects the slightly different mean N/Z of the two secondary beams [9, 11].

References

[1] A.S. Botvina, O.V. Lozhkin, W. Trautmann, Phys. Rev. C 65 (2002) 044610.
[2] A. Ono et al., Phys. Rev. C 68 (2003) 051601(R).
[3] A. Le Fèvre et al., GSI Scientific Report 2004, p. 121; Phys. Rev. Lett. 94 (2005) 162701.
[4] W. Trautmann et al., Nucl. Phys. A 787 (2007) 575c.
[5] G. Souliotis et al., Phys. Rev. C 75 (2007) 011601(R).
[6] A.S. Botvina et al., preprint arXiv:0711.3382 [nucl-th].
[7] B.-A. Li and L.-W. Chen, Phys. Rev. C 74 (2006) 034610.
[8] C. Sfienti et al., GSI Scientific Report 2004, p. 122; Nucl. Phys. A 787 (2007) 627c.
[9] S. Bianchin, Ph.D. thesis, Université Louis Pasteur, Strasbourg (2007).
[10] M.B. Tsang et al., Phys. Rev. Lett. 86 (2001) 5023.
[11] J. Łukasik et al., preprint arXiv:0707.0598 [nucl-ex].

* Work supported by the EU, contract No. HPRI-CT-1999-00001.

Isotopic Effects with Stable Beams

J. Łukasik[1,2], W. Trautmann[1], and the INDRA-ALADIN Collaboration
[1]GSI, Darmstadt, Germany; [2]IFJ-PAN, Kraków, Poland

The density dependence of the symmetry term of the nuclear equation of state is currently of high interest both in nuclear physics and astrophysics [1]. Heavy ion collisions between partners with varying neutron-proton asymmetry offer a unique opportunity of studying this problem in the laboratory. Identifying the key observables sensitive to the neutron-proton asymmetry is a basic task here [2, 3]. This contribution presents results of such a sensitivity study performed using the data from the reactions ^{124,129}Xe+^{112,124}Sn at 100 AMeV and ^{124,129}Xe+^{124}Sn at 150 AMeV. The data has been obtained by the INDRA and ALADIN collaborations using the 4π INDRA detector, stable Xe beams from the SIS synchrotron at GSI and isotopically enriched Sn targets.

In Fig. 1, the sensitivity of the directed flow observable (slope of v_1 at midrapidity) to the N/Z variation of the Xe+Sn system is presented for $p, t,^3$He, and α-particles and for three centralities.

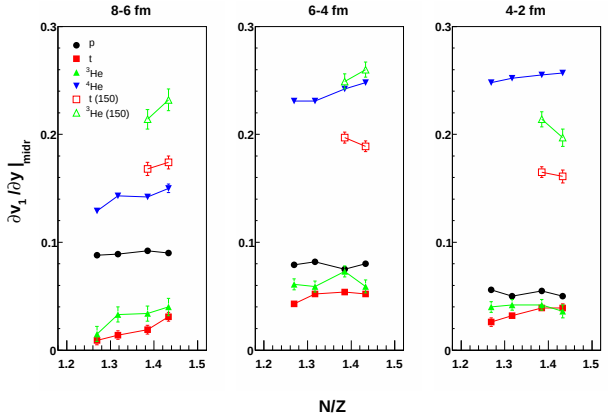

Figure 1: Slope of the v_1 parameter at midrapidity as a function of the N/Z of the colliding system for selected reaction products (symbols) and for three impact parameter bins (panels).

The observed variation in the measured N/Z range is rather small and the trends, except those for α-particles, are not quite well defined and hindered by statistical errors. The sensitivity is even lower in the case of the elliptic flow, v_2, observable, but increases with the increasing $p^{\perp}$ cut (both effects not shown here). The observed few percent increase of the slope of v_1 at midrapidity for α-particles may be possibly used to discriminate between different assumptions about the shape of the symmetry term. What may also encourage further studies, is the observation of the increase of the difference between the flows of the t and ^3He isobars with the increase of the beam energy. Comparisons on the absolute level will require additional corrections [4].

Figure 2 shows the variation of the $t/^3He$ ratio measured at midrapidity as a function of centrality for the reactions at 100 AMeV (left panel) and its variation as a function of the N/Z for the mid-central bin, together with the results for 150 AMeV.

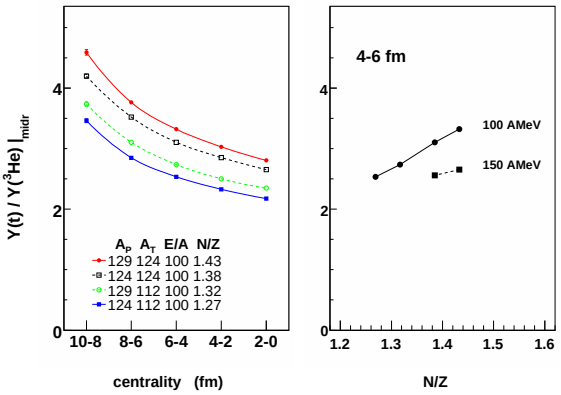

Figure 2: Ratio of the $t/^3$He yields at midrapidity as a function of centrality for the Xe+Sn reactions at 100 AMeV (left panel) and as a function of the N/Z ratio for mid-central collisions (4 fm$<$ b $<$6 fm) at 100 AMeV and at 150 AMeV (right panel).

This observable shows a much cleaner and stronger (about 40%) increase as a function of the N/Z of the system, and possibly, can be used as a reliable discriminator. The models should however disentangle first the influence of the trivial effect of the different neutron content in the system, from the interesting influence of the shape of the symmetry term on the observed variation of the isobar ratio.

Summarizing, the observed isotopic effects on flow observables using the available stable beams are rather small. Improving the discriminating power and reliability of the data will definitely require scanning of larger N/Z intervals ($i.e.$ usage of the radioactive beams), collecting even higher statistics and possibly varying the incident energies. In addition, measurement of the neutrons would allow to avoid model complications due to their inefficiencies in light cluster production.

References

[1] J.M. Lattimer and M. Prakash, Phys. Rep. 333 (2000) 121.
[2] M. Di Toro et al., Eur. Phys. J. A 30 (2006) 153.
[3] Gao-Chan Yong, et al., Phys. Rev. C 74 (2006) 064617.
[4] J. Łukasik, W. Trautmann et al., GSI Scientific Report 2006; A. Andronic, et al., Eur. Phys. J. A 30 (2006) 31.

Isotopic Flow in Xe+Sn Collisions

J. Łukasik[1,2], W. Trautmann[1], and the INDRA-ALADIN Collaboration
[1]GSI, Darmstadt, Germany; [2]IFJ-PAN, Kraków, Poland

The high accuracy that can be achieved in the experimental determination of flow parameters from data collected with advanced 4π detection systems has recently been demonstrated in a combined analysis of INDRA and FOPI data [1]. Excitation functions for directed and elliptic flow in ^{197}Au + ^{197}Au reactions, measured at SIS by the two collaborations [2, 3], were found to agree within 5% to at most 10% in the overlap region 90 to 150 A MeV covered by the two data sets.

Data with this level of precision can be useful for the investigation of presumably small isotopic effects related to the symmetry term in the nuclear equation of state, with the aim to reduce its present uncertainty at densities beyond the saturation density [4, 5]. Identifying the key observables sensitive to the neutron-proton asymmetry is a basic task here which may be achieved by studying collisions between partners with varying neutron-proton asymmetry.

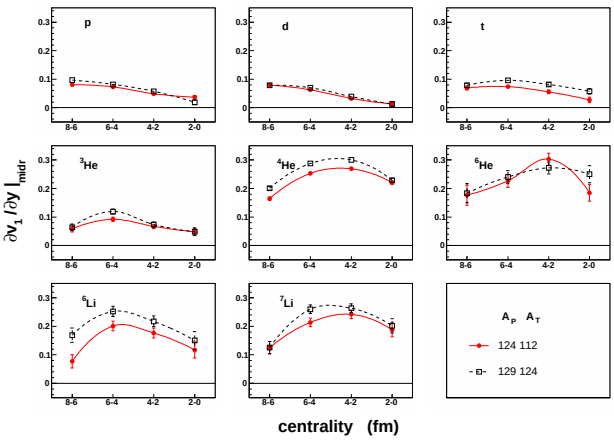

Figure 1: Slopes of directed flow $\partial v_1/\partial y$ at mid-rapidity for eight reaction products with $Z \leq 3$ integrated over $p_t/m > 0.1c$ as a function of centrality for the most neutron rich (open squares, black) and the most neutron poor (dots, red) reaction systems at 100 A MeV.

The present analysis is based on measurements with the INDRA multi-detector using ^{124,129}Xe projectiles of 100 and 150 MeV per nucleon from SIS and isotopically enriched targets of ^{112,124}Sn. Data were taken for all four combinations of projectile and target at 100 A MeV and for the two projectiles and the ^{124}Sn target at 150 A MeV. Examples of the obtained results are shown for two, the most neutron-rich and the most neutron poor, of the four systems studied at 100 A MeV in Figs. 1 and 2. The dependence of the directed flow (slope $\partial v_1/\partial y$ at mid-rapidity) and of the elliptic flow (v_2 at mid-rapidity) are shown for eight reaction products with $Z \leq 3$, selected with the condition $p_t/m > 0.1c$.

The overall behaviour follows the expectations, in particular the dependence on the fragment mass and the impact parameter (see figures) as well as that on the bombarding energy and on p_t (not shown). A possibly isotopic effect is observed for the directed flow which is consistently larger for the more neutron-rich (but with 17 more nucleons also more massive) system. Isotopic effects are practically absent in the elliptic flow (Fig. 2) whose magnitude, however, is rather small at the present bombarding energy near the transition from preferentially in-plane to out-of-plane emissions [1, 2].

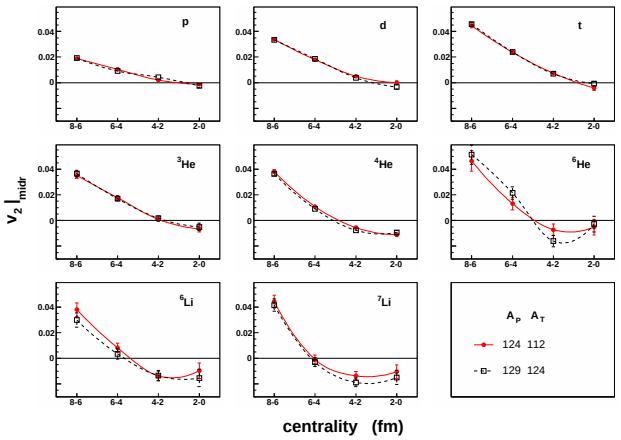

Figure 2: Elliptic flow parameter v_2 at mid-rapidity for eight reaction products with $Z \leq 3$ integrated over $p_t/m > 0.1c$ as a function of centrality for the most neutron rich (open squares, black) and the most neutron poor (dots, red) reaction systems at 100 A MeV.

The displayed data are uncorrected which is sufficient to permit the direct visualization of the magnitude of the isotopic effects. For a comparison with theory, appropriate corrections [1, 6] will have to be applied or, alternatively, simulated events will have to be passed through a filter routine.

References

[1] J. Łukasik, W. Trautmann et al., GSI Scientific Report 2006; A. Andronic et al., Eur. Phys. J. A **30** (2006) 31.

[2] J. Łukasik et al., Phys. Lett. B **608** (2005) 223.

[3] A. Andronic et al., Phys. Lett. B **612** (2005) 173.

[4] M. Di Toro et al., Eur. Phys. J. A **30** (2006) 153.

[5] Gao-Chan Yong et al., Phys. Rev. C **74** (2006) 064617.

[6] J. Łukasik and W. Trautmann, GSI Scientific Report 2005.

N/Z dependence of the nuclear caloric curve*

C. Sfienti[1], S. Bianchin[1], A.S. Botvina[1,2], A. Le Fèvre[1], J. Łukasik[1,3], W. Trautmann[1], and the ALADiN2000 Collaboration[1]

[1]GSI, Darmstadt, Germany; [2]INR-RAS, Moscow, Russia; [2]IFJ-PAN, Kraków, Poland

The systematic data set on isotopic effects in spectator fragmentation collected recently at the GSI laboratory [1] permits investigating the N/Z dependence of the nuclear caloric curve which is of interest for several reasons. It is, for example, a basic assumption of isotopic reaction studies that a variation of the isotopic composition of the system will not change the reaction mechanism as such and that effects related to the asymmetry dependence of the nuclear forces can be isolated in this way [2, 3]. This view is compatible with the observed invariance of the chemical breakup temperatures presented in the following. The interpretation of the breakup temperatures as a manifestation of the limiting temperatures predicted by the Hartree-Fock model [4, 5], on the other hand, is not equally supported.

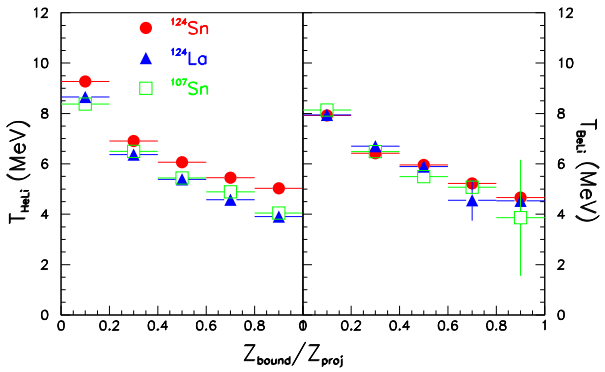

Figure 1: Apparent temperatures $T_{\rm HeLi}$ (left panel) and $T_{\rm BeLi}$ (right panel) as a function of $Z_{\rm bound}/Z_{\rm proj}$ for the three reaction systems produced with ^{107,124}Sn and ^{124}La projectiles. Only statistical errors are displayed.

Two examples of double-isotope temperatures deduced from the isotope yields measured for ^{107,124}Sn and ^{124}La fragmentations at 600 A MeV are shown in Fig. 1 as a function of $Z_{\rm bound}$. Besides the frequently used $T_{\rm HeLi}$, determined from ^{3,4}He and ^{6,7}Li yields, also the results for $T_{\rm BeLi}$ are displayed. For $T_{\rm BeLi}$ the isotope pairs of ^{7,9}Be and ^{6,8}Li are used which each differ by two neutrons. The double difference of their binding energies amounts to 11.3 MeV and is nearly as large as the 13.3 MeV in the $T_{\rm HeLi}$ case. The apparent temperatures are displayed, i.e. no corrections for secondary decays feeding the ground states of these nuclei are applied.

Both temperature observables show the same smooth rise with increasing centrality that was observed earlier in a study of ^{197}Au fragmentations [6]. According to $T_{\rm BeLi}$, the temperatures at the chemical freeze-out are identical for all three reaction systems and have the same dependence on $Z_{\rm bound}$. This is not equally visible in $T_{\rm HeLi}$ which exhibits slightly larger values for the neutron rich case of ^{124}Sn. Inspection of the single isotope ratios shows, however, that the ^{3,4}He ratio represents an exception in that it varies much less than the other ratios with the neutron-richness of the system. This may be explained by the strong population of even-N-even-Z nuclei, evident from the behavior of $<N>/Z$ [1], which suggests that also ^{4}He nuclei are abundantly produced. The effect is stronger in the neutron-poor cases for which the apparent $T_{\rm HeLi}$ is, accordingly, lower. Taking this nuclear-structure effect into account is likely to reduce the difference between the systems also for this thermometer.

The observed invariance of the breakup temperature with the isotopic composition of the system is opposite to what is expected according to the finite-temperature Hartree-Fock calculations of Besprosvany and Levit [4]. The limiting temperatures obtained for the stability of excited nuclei are strongly dependent on the Coulomb pressure generated by the protons they contain. Along isobars, the limiting temperatures decrease rapidly toward the proton-rich side and, along the valley of stability, they decrease with increasing mass because the effect of the increasing Z dominates over that of the decreasing Z/A. For the nuclei studied here, a difference of about 2 MeV is predicted between the limiting temperature of ^{124}Sn and those for the proton rich ^{107}Sn and ^{124}La or for the heavier ^{197}Au [4]. A difference of this magnitude is clearly not seen in the data (Fig. 1). Neither does a comparison with the apparent temperatures measured for ^{197}Au fragmentations (Fig. 7 in ref. [6]) provide evidence for the predicted mass dependence. The temperatures are the same, within errors, when regarded as a function of the scaled quantity $Z_{\rm bound}/Z_{\rm proj}$. This, however, is suggested by the $Z_{\rm bound}$ scaling of fragmentation observables for the case that a comparison of sources of different mass but equal excitation is to be made [7].

References

[1] C. Sfienti et al., GSI Scientific Report 2006, p. 153.
[2] A. Le Fèvre et al., Phys. Rev. Lett. 94 (2005) 162701.
[3] A.S. Botvina et al., Phys. Rev. C 74 (2006) 044609.
[4] J. Besprosvany and S. Levit, Phys. Lett. B 217 (1989) 1.
[5] J.B. Natowitz et al., Phys. Rev. C 52 (1995) R2322.
[6] W. Trautmann et al., Phys. Rev. C 76 (2007) 064606.
[7] A. Schüttauf et al., Nucl. Phys. A 607 (1996) 457.

* Work supported by the EU, contract No. HPRI-CT-1999-00001.

Particle identification with a fibre detector in a p/π^+/d cocktail beam of 3.3 Tm magnetic rigidity at GSI*

P. Achenbach† [1], C. Ayerbe Gayoso[1], M. Kavatsyuk[2], O. Lepyoshkina[2], S. Minami[2], D. Nakajima[2], L. Nungesser[1], J. Pochodzalla[1], C. Rappold[2], and T.R. Saito[2]

[1]Inst. für Kernphysik, Joh. Gutenberg-Universität, Mainz, Germany; [2]GSI, Darmstadt, Germany

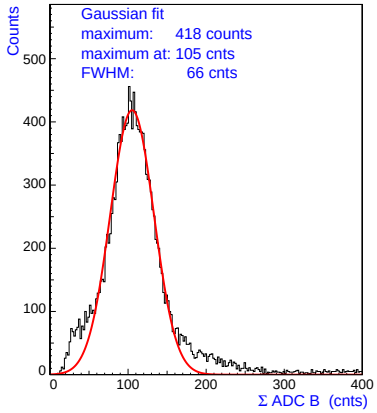

Figure 1: Distributions of the pulse height sum over neighbouring channels of one detection plane. From the Gaussian fit to the data a relative energy resolution $\Delta E/E \sim 60\,\%$ for the protons in the cocktail beam was derived.

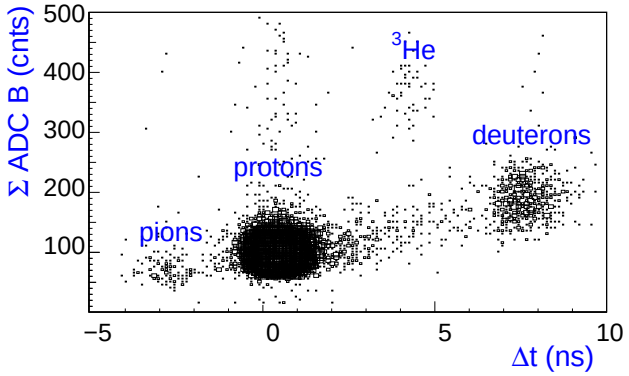

Figure 2: Pulse height sum over neighbouring channels of one detection plane vs. relative time-of-flight of the particles. In the cocktail beam π^+, proton, deuteron, and ^{3}He particles were identified.

The HypHI project is dedicated to hypernuclear spectroscopy with stable heavy ion beams and rare isotope beams at GSI and FAIR [1]. In its first phase it will apply scintillating fibre detectors for tracking and trigger purposes. An analogue fibre set-up is under development at the Institute for Nuclear Physics in Mainz for the KAOS/A1 spectrometer [2].

The performance of a scintillating fibre detector with two detector planes was tested in a ^{12}C beam of 2 AGeV energy and in a p/π^+/d cocktail beam of 3.3 Tm magnetic rigidity with a π^+ momentum of 1 GeV/c at Cave A of GSI. The detector in the beam consisted of 96 read-out channels for three fibre bundles comprising a total of 384 fibres. Four fibres were grouped to one channel and coupled to one pixel of the photodetectors. Two bundles were aligned to a single plane perpendicular to the beam, and one bundle formed a parallel plane directly behind. The trigger was derived from the second plane.

The coordinate detector of the KAOS/A1 spectrometer's electron arm will consist of two vertical planes of fibre arrays, covering an active area of $\sim$1500 $\times$ 500 mm^2, supplemented by one or more horizontal planes. In KAOS/A1, particles will cross the fibre detector with finite angles, compromising the tracking capabilities of a straight detector in which the fibre columns are oriented perpendicular to the detector layers. Accordingly, in fibre arrays of hexagonal packing the slanting columns with 60° inclination were aligned along the beam direction and grouped to common read-out channel.

With a double threshold timing method a time resolution of 310 ps FWHM between two planes of fibres was achieved, leading to a FWHM $\sim 310\,\mathrm{ps}/\sqrt{2} = 220$ ps for a single detector. With minimum ionising particles the resolution decreased to 510 ps. The energy response of the fibre detector was studied in the cocktail beam. Fig. 1 shows the distribution of the pulse height sum over neighbouring channels of one detection plane. From the Gaussian fit to the data a relative variation in the measured energy deposition, $\Delta E/E$, of 60 % was derived for the dominant particle species. Fig. 2 shows the energy loss vs. relative time-of-flight, in which dominant protons and subdominant π^+, deuteron, and ^{3}He particles were identified.

As a summary, it was observed that the prototypes of the fibre detectors showed their capability to measure positions, times, and energy deposits of charged particles fulfilling the requirements for the proposed experiments.

References

[1] T.R Saito et al., "The HypHI project at GSI and FAIR", Proc. of the IX. Intern. Conf. on Hypernuclear and Strange Particle Physics, Joh. Gutenberg-Univ., Mainz, 10–14 Oct. 2006, pp. 171–176, Springer (2007).

[2] P. Achenbach, "Probing hypernuclei at $\overline{\mathrm{P}}$anda and at MAMI-C", Proc. of the IX. Intern. Conf. on Hypernuclear and Strange Particle Physics, Joh. Gutenberg-Univ., Mainz, 10–14 Oct. 2006, pp. 79–84, Springer (2007).

* supported by Helmholtz Association and GSI as Helmholtz-University Young Investigators Group VH-NG-239.

† patrick@kph.uni-mainz.de

Application of the VME Logic Module VULOM as a trajectory trigger for the KAOS/A1 spectrometer

S. Sánchez Majos*, P. Achenbach†, R. Böhm, L. Nungesser, S. Minami, J. Pochodzalla, and T. Saito
Inst. für Kernphysik, Joh. Gutenberg-Universität, Mainz, Germany

KAOS/A1 is a very compact magnetic spectrometer now operated at the electron accelerator MAMI at the Institute for Nuclear Physics in Mainz [1]. It was used (as KaoS) in heavy ion induced experiments at the SIS facility (GSI) in the 1990s [2].

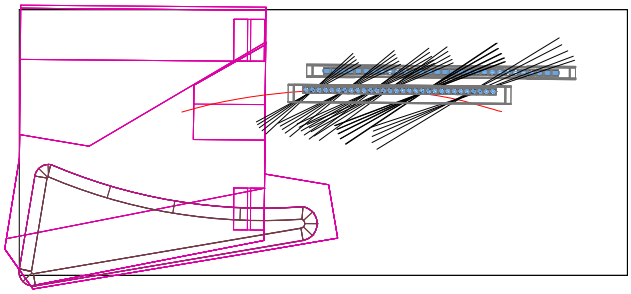

Figure 1: Scheme of the KAOS/A1 platform with pole shoes, magnet yokes, focal plane, and scintillator walls. Kaon trajectories crossing both walls are defining a pattern used for the logic implemented in the VULOM modules.

Fig. 1 shows a schematic view of the kaon arm of the spectrometer. The dipole magnet has a large aperture with large angular acceptance. Particle identification is based on the time-of-flight between target and focal plane. A segmented scintillator wall (F) with 30 paddles read out in both extremes by fast photomultipliers (Hamamatsu $R1828$) is located at the focal plane and measures the arrival time with a resolution of FWHM$=$ 200 ps. A second wall (G) with 30 paddles is used to discriminate events corresponding to valid trajectories. Coincidences of top and bottom PMTs are performed by summing the analogue signals and bringing the output to a constant fraction discriminator with a proper threshold. There are consequently 30 logical signals per wall. In order to cope with the high background rates KAOS/A1 has been equipped with a new trigger system. Particle trajectories shown in Fig. 1 are based on a Geant4 calculation. The correlation between the paddles in both walls extracted from the simulation is the natural input to the trigger. The relatively high complexity of the valid patterns and the intrinsic necessity of a flexible trigger logic for a spectrometer that faces a wide experimental programme demands a programmable logic system. The VME Universal Logic Module VULOM was developed at the Experiment Electronics Department of GSI for general purpose logic operations [3]. The module is equipped with VIRTEX 4 FPGA and ECL front panel inputs (up to 32) and outputs (up to 32). The VHDL code is used for defining the logical function. The compiled program can be loaded into the FPGA via a JTAG connector or directly by means of the VME interface. The program is stored in a dedicated 64 MB flash memory and it is automatically loaded after powering up. Two VULOM units are necessary to cope with 90 valid combinations given by the track conditions.

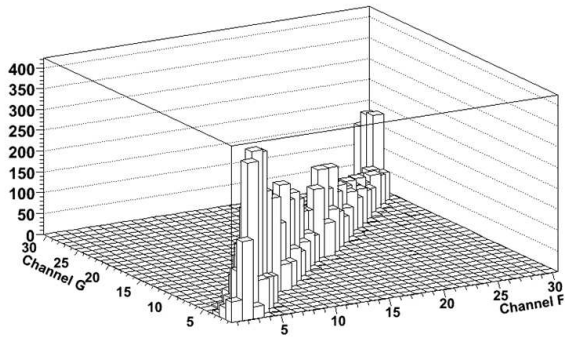

Figure 2: Histogram of paddle hits in both scintillator walls. The logic rejects any event off the diagonal band.

The new trigger system was tested during the first KAOS/A1 beam-time in Nov. 2007. Beam currents up to 10 μA of 855 MeV electrons on a carbon target ($\sim$225 mg/cm^2) were used. Particle identification was carried out successfully and despite the relatively small distance from the target area to the electronics the logic modules did not show any misbehaviour. Fig. 2 shows the number of coincidences for each pair of F and G scintillator paddles. The diagonal band corresponds to the valid trajectories shown in Fig. 1. When the trigger requirement is removed by loading an OR condition of all paddles in the FPGAs the off-diagonal pairs in the plot are generously populated, a sign of the high electromagnetic background. Background suppression depends on the threshold imposed on the summing discriminators. At 500 nA and a sum signal threshold of 30 mV the raw trigger rate changed from 49 kHz to 1 kHz, while at 310 mV the reduction was from 1.7 kHz to 1.4 Hz.

References

[1] P. Achenbach, "Probing hypernuclei at $\overline{\text{P}}$anda and at MAMI-C", Proc. of the IX. Intern. Conf. on Hypernuclear and Strange Particle Physics, Joh. Gutenberg-Univ., Mainz, 10-14 Oct. 2006, pp. 79-84, Berlin and Heidelberg, 2007, Springer.

[2] P. Senger et al. (KaoS Collab.), Nucl. Inst. Meth. in Phys. Res. **A327**, (1993) 393.

[3] S. Minami *et al.*, in these reports.

* sanchez@kph.uni-mainz.de
† patrick@kph.uni-mainz.de

Φ (1020) production in Al+Al collisions at 1.9A GeV beam energy

P. Gasik[1], K. Wiśniewski[1], M .Kirejczyk[1], T. Matulewicz[1], K. Piasecki[1], B. Sikora[1], K. Siwek-Wilczyńska[1], and the FOPI Collaboration[2]

[1]Institute of Experimental Physics, University of Warsaw, Poland; [2]GSI, Darmstadt, Germany

The production of ϕ mesons as carriers of hidden strangeness has been investigated in the K^+K^- decay channel in Al+Al experiment at 1.9A GeV performed by the FOPI Collaboration. ϕ is a neutral, pseudo-vector meson of mass M_ϕ=1.019 GeV/c^2. Because of the relatively long life-time ($c\tau \approx 45$ fm) ϕ mesons produced in heavy-ion collisions decay mostly outside the fireball. Hence, $K^\pm$ mesons that originate from such decays can reach detectors without changing their momenta due to final-state interactions, and ϕ mesons can be identified experimentally by reconstructing invariant masses of the registered K^+K^- pairs. In the upper panel of Fig.1 the invariant mass distribution of kaon-antikaon pairs registered in 3×10^8 collected central Al+Al events is shown. A clear peak, consisting of about 200 counts, centered around the nominal mass of the ϕ meson can be seen. A relatively small background can be quite well reproduced by the event-mixing technique, in which one calculates the invariant masses of K^- and K^+ mesons taken from different events.

The lower panel of Fig. 1 shows the invariant mass spectrum of K^-K^+ pairs after subtraction of the background normalised in the region which is depicted in the upper panel by the shaded area.

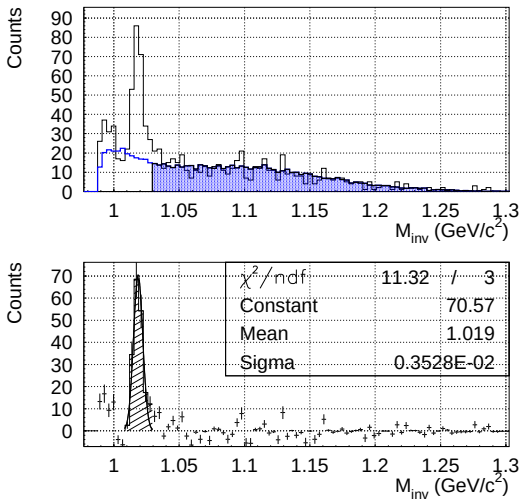

Figure 1: Invariant mass spectrum of K^+K^- pairs. Upper plot shows M_{inv} spectrum with marked, reconstructed background. Lower plot shows M_{inv} after background substraction, with Gaussian fit to the peak corresponding to ϕ meson decays.

After the background subtraction, a Gaussian function is fitted. The centroid is found to be $M_\phi = 1.0188 \pm 0.0004$ GeV/c^2 and the number of reconstructed ϕ mesons $N_\phi = 189 \pm 17 \pm 5$. In order to estimate the ϕ meson detection efficiency, the GEANT-based simulations that include a realistic description of the detector geometry and resolutions were performed. The global reconstruction efficiency depends on assumptions of the input distribution of ϕ mesons in the phase-space that is fed into the simulation software. In this work, a so-called Siemens-Rasmussen thermal distribution with temperature 100 MeV and radial $flow$ velocity of $0.3c$ was used. The background accompanying the ϕ mesons in each event was composed of Al+Al events generated with the IQMD code. In such scenario, the global detection efficiency of ϕ mesons reconstruction turned out to be (1.90 ± 0.02)%. The resulting production probability of ϕ mesons in Al+Al collisions at 1.9A GeV beam energy was estimated to be $P_\phi = (4.9 \pm 1.1) \cdot 10^{-5}$ in the full solid angle.

The present result is about two orders of magnitude smaller than ϕ meson production probability of $(3.6 \pm 3.0) \cdot 10^{-3}$ obtained in [1] in the case of Ni+Ni collisions at 1.9A GeV beam kinetic energy. This huge discrepancy can be attributed partially to the difference in the size of the colliding systems, which could easily account for about 4 times smaller ϕ mesons production probability in the two times smaller Al+Al system. One also should take into account that in the case of the Ni+Ni experiment, only about 23 ϕ mesons were reconstructed in 4.6×10^6 central Ni+Ni collisions, which gives rise to a large statistical uncertainty.

In the next step, the total K^- meson production probability in the Al+Al experiment will be estimated and compared to the ϕ meson yield. The comparison may help to understand the small ϕ-meson production probability measured in the Al+Al system. In this way, the effect of the production and subsequent decays of ϕ meson on the K^- meson production in heavy-ion collisions will be quantified, and the intriguing effect observed in the Ni+Ni system will be verified.

References

[1] A. Mangiarotti et al., Nucl. Phys. **A 714** (2003) 89

Multi-Gap-Resistive-Plate-Chamber (MRPC) time resolution and detection efficiency dependence studies for varying SF_6 concentrations*

I. Deppner[1], M.L. Benabderrahmane[1], M. Ciobanu[1], N. Herrmann[1], A. Reischl[1], Z. Xiao[1], M. Kiš[2], Y. Leifels[2], A. Schüttauf[2], and the FOPI Collaboration[2]

[1]Physikalisches Institut (PI) Universität Heidelberg, Germany; [2]GSI, Darmstadt, Germany

Particle identification utilizing Time-of-Flight (ToF) measurements with RPC detectors is an attractive option since they can work in a magnetic field, can be built with dimensions of m^2(like the FOPI MMRPC [1,2,3]) and have the potential for a very good timing resolution in the order of 50 ps combined with an efficiency above 98 %. To realize these requirements a good understanding of the effects which influence these numbers is needed. Especially, their dependencies on the gas mixture is not known in detail and has to be investigated.

We report on a time resolution and detection efficiency study for an MRPC detector using different gas mixtures. In this study the amount of the quencher (SF_6) has been varied between 0 and 30 %.

In the frame of this work, collaborating between the PI and the GSI, a detector system has been developed with the aim to study the time and efficiency dependence of a MRPC with the required precision. The gas content of the MRPC consisted of three gases with diffrent mixtures: Tetrafluoroethane (65–95 %), SF_6 (30–0) % and Isobutane (5 %).

The system consists of a (4.6×20) cm^2 big 4-Gap-RPC with gaps of 300 μm thickness and two (4×2) cm^2 big scintillators. A schematic view of the setup is shown in figure 1. They are equipped on both sides with fast phototubes (Photonics XP20D0B). The two scintillators are used as a

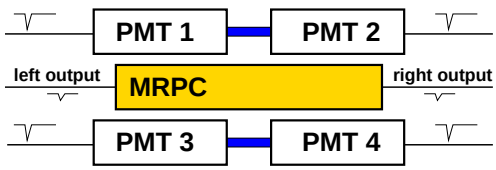

Figure 1: Schematic view of the setup consisting of a RPC and two scintillators. All detectors are read out on both sides.

reference for the time measurement and to trigger the acquisition system. For the data acquisition a system similar to the one used by the FOPI experiment, based on MBS [4], was adopted. The trigger signal was generated by a coincidence of all photomultiplier timing signals and the average time was taken as a reference for the start.

The system was used with cosmic rays and with a π-beam in Cave B. During this test run the high voltage of the MRPC has been ramped from 5.3 kV up to 6.4 kV in steps of 0.1 kV to find the optimal working point. It has been found that the system operates best with an applied high voltage of 6.3 kV, which then was used for the further study of the gas mixture dependence. The photomultiplier system has been found to have a time resolution of 37 ± 2 ps which is sufficient to study the MRPC response.

The results of the test experiment at the GSI complemented with measurements utilizing cosmic radiation are shown in figure 2. The behavior of the time resolution and the detection efficiency versus the quencher gas SF_6 concentration is displayed. As can be seen (fig. 2) a detection

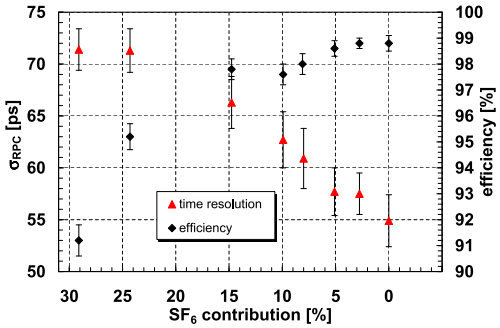

Figure 2: Time resolution and detection efficiency of the RPC versus the SF_6 content in the counting gas for a given high voltage of 6.3 kV.

efficiency above 98 % has been reached for a SF_6 concentrations of ≤ 7.5 %. The effect can be explained by larger avalanches developing in the gap with a smaller content of the quencher gas. Also the dependence of the time resolution can be explained and reaches its best values for smallest quencher gas content.

However, below 3% of the quencher gas so called streamers develop. These comparably big discharges can have detrimental effects on the desired detector performance like for example dark rate and rate capabilities in general.

In general there is a need to go to low content of SF_6 counting gas also for environmental reasons as it is a greenhouse gas. Further studies in terms of other gas mixtures also varying the Isobutane content will be pursued. Additionally, the transition region between avalanche and streamer mode is of great interest and will be investigated.

References

[1] A. Schüttauf et al., Nucl. Inst. and Meth. A **533** (2004) 65-68

[2] A. Schüttauf et al., Nucl. Phys. B **158** (2006) 52-58

[3] M. Ciobanu et al., IEEE Trans Nucl. Sci. **54** (2007) 1201

[4] N. Kurz, H.G. Essel MBS

*Work supported by UE/FP6 HadronPhysics contract nr. RII3-CT-2004-506078 and BMBF 06HD190i

Status of the HADES physics program

The HADES collaboration

Summary

In 2007 the analysis of dielectron spectra from our 2004 ^{12}C+^{12}C run at 1 GeV/u has been finalized. Above the π^0 mass, the measured pair yield is $\sim$7 times larger than the contribution expected from hadron decays after freeze-out. The found invariant-mass and transverse-momentum distributions are fully consistent with the ones measured by the former DLS experiment [1]. The beam-energy dependence of the excess shows a scaling similar to the one of pion production, indicating the important role played by radiation from low-lying baryonic resonances and soft NN collisions. The relevant elementary dielectron production processes were studied separately in dedicated $p+p$ and $d+p$ runs done at a beam energy just below the η meson production threshold ($E_{kin} = 1.25$ GeV/u). It is expected that the direct comparison of the pair spectra from d+p and p+p reactions will allow to constrain the $\Delta \rightarrow Ne^+e^-$ and $N-N$ bremsstrahlung contributions which dominate the intermediate-mass region ($0.15 < M_{ee} < 0.50$ GeV/c^2) of the pair spectrum at this bombarding energy. In particular, the $p-n$ bremsstrahlung process can be studied using $p+n \rightarrow p_{spec}e^+e^-X$ reactions selected by tagging of the forward-going proton spectator p_{spec} in the HADES Forward Wall. Preliminary results from our 2007 $d+p$ run indicate indeed a different shape of the pair yield measured in $p+n$ reactions above the π^0 Dalitz peak, as compared to $p+p$ reactions..

High-statistics spectroscopy of the vector-meson region was started with investigations of Ar+KCl collisions at 1.75 GeV/u in 2005. A dielectron invariant-mass distribution with $\sim 10^5$ signal pairs, showing for the first time a clear ω signal at SIS energies, is presented. The large statistics collected in this experiment also allows to study various rare hadronic probes, like the K^-, K^0 and the $\phi \rightarrow K^+K^-$. The ω meson has furthermore been produced and identified in a dedicated experiment in 2007, using $p+p$ reactions at 3.5 GeV. This measurement provides an important reference for our in-medium studies of vector mesons in HI collisions, as well as in $p+A$ reactions (to be studied in a run scheduled for 2008).

The HADES detector upgrade programme enters its final stage. A full-size prototype of a new high-granularity Time-Of-Flight wall based on RPC technology, including the full chain of analog and digital electronics, has been successfully tested in dedicated in-beam experiments. The data acquisition upgrade aiming at a substantial increase of the HADES data taking speed has also been progressing very well. Based on the successfull development of a multi-purpose Time Read-out Board (TRB), several new components have been developped and tested. Detailed progress reports on these technical activities are given in separate contributions to the present annual report.

C+C collisions at 1 GeV/u

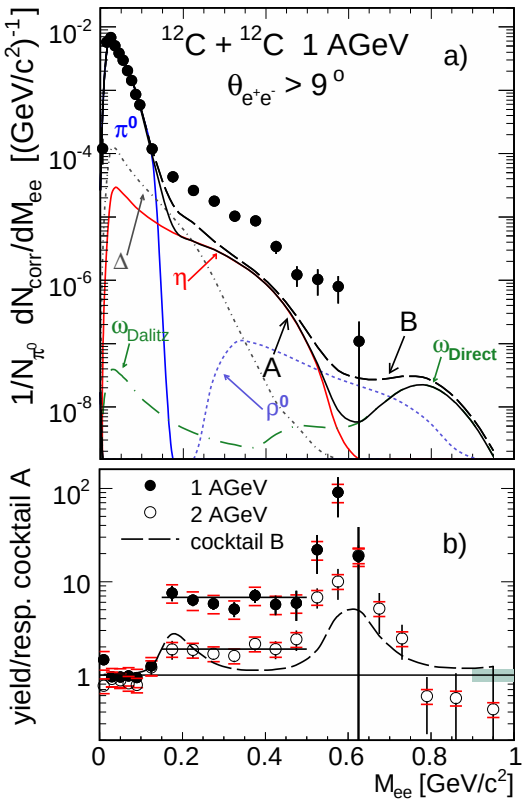

Figure 1: Dielectron yield (corrected for efficiencies) in the HADES acceptance. In panel a), the measured yield is compared to a cocktail calculed from sources assuming vacuum properties only. The cocktail is divided into contributions from mesons with life-times $\tau > \tau_{fireball}$ (full lines, cocktail A) and contributions from short-lived resonances with $\tau \leq \tau_{fireball}$; the sum of all defines cocktail B. Panel b) shows the experimental yield divided by cocktail A for 1 GeV/u (full symbols) and 2 GeV/u (open symbols) data. In addition, the ratio of cocktail B and A for 1 GeV/u data is indicated as dashed line.

The dielectron yield measured in ^{12}C+^{12}C collisions at 1 GeV/u has been corrected for detection and reconstruction inefficiencies, using the same procedure as described in [2, 3]. Fig. 1 shows the resulting e^+e^- invariant-mass distribution of true pairs normalized to the average number of charged pions $N_{\pi^0} = 1/2(N_{\pi^+} + N_{\pi^-})$, as measured in HADES and extrapolated to the full solid angle. The pion multiplicity per participant nucleon found, i.e. $M_\pi/A_{part} = 0.061 \pm 0.009$, agrees well with previous

measurements of charged and neutral pions [4, 5]. The quoted error of 15% is dominated by systematic uncertainties in the pion efficiency correction and the extrapolation procedure. In addition to this overall normalization error, uncertainties caused by the electron-efficiency correction and by the subtraction of the combinatorial background (CB) add up quadratically to point-to-point systematic errors in the pair yield of 22%. They are shown together with the data points.

First we compare our data with a pair cocktail accounting for radiation from long-lived (decaying outside the fireball) mesons only: $\pi^0(\eta) \rightarrow \gamma e^+e^-$, $\omega \rightarrow e^+e^-$ and $\omega \rightarrow \pi^0 e^+e^-$. The π^0 and η Dalitz yields are fixed by published data [4] with respective uncertainties of 10% and 25%. Due to the complete lack of corresponding data on ω production, we apply $m_\perp$ scaling to estimate the (small) multiplicity of this meson [6]. The cocktail calculation has been performed with the PLUTO generator assuming anisotropic meson emission from a Boltzmann-like thermal source (details can be found in [8]). This simulated cocktail is shown in Fig. 1 as solid line. It agrees very well with the data in the π^0 Dalitz region, but for $M_{ee} > 0.15$ GeV/c^2 it strongly underestimates the measured pair yield. This is not surprising, since one expects additional contributions from short-lived resonances, e.g. $\Delta \rightarrow Ne^+e^-$ and $\rho \rightarrow e^+e^-$. Furthermore, as suggested by recent theoretical work [9], at our bombarding energies, "quasi-elastic" (i.e. with no resonance excitation) $p-n$ bremsstrahlung radiation should not be neglected. On the other hand, all of the latter contributions are still subject to large theoretical uncertainties and it is hence not yet possible to construct a reliable complete cocktail. Among others, the following problematic points prevent this: (i) unknown production multiplicities and decay branching ratios of the Δ and, even more so, of all heavier baryon resonances, (ii) treatment of off-shell effects in ρ production, and (iii) correct treatment of bremsstrahlung. Nevertheless, we have made an effort to include in our cocktail in a schematic way pairs from the Δ and ρ decays. For the Δ, we assumed that its contribution scales with the π^0 yield at freeze-out ($N_\Delta = 3/2 N\pi^0$) and that the $\Delta \rightarrow e^+e^-$ differential decay rates of [7] are applicable. To add the ρ meson contribution, we used a similar prescription as for the ω. We modeled this broad resonance as a Breit-Wigner shape, with mass-dependent width $\Gamma(M) = \Gamma_0/M^3$ ($\Gamma_0 = 0.15$ GeV) [7], additionally modified by the m_T scaling accounting for the strongly reduced phase space at low beam energy. The resulting cocktail (B) is shown in Fig. 1 as a long-dashed line. Adding these short-lived contributions increases the simulated yield above 0.15 GeV/c^2 but obviously our second calculation also remains far from reproducing the data. More sophisticated calculations, e.g. based on transport models, are clearly needed.

To better visualize the character of the excess yield, the ratio of data and cocktail A is shown in the bottom of Fig. 1. This ratio is basically unity at low masses, where π^0 Dalitz pairs dominate, but above $M = 0.15$ GeV/c^2 it is large, indicating the onset of processes not accounted for our cocktail A. Fig. 1 also shows the corresponding ratio observed by HADES at 2 GeV/u [2, 3]. It is evident that at 1 GeV/u the overshoot of the data is even much stronger than at 2 GeV/u .

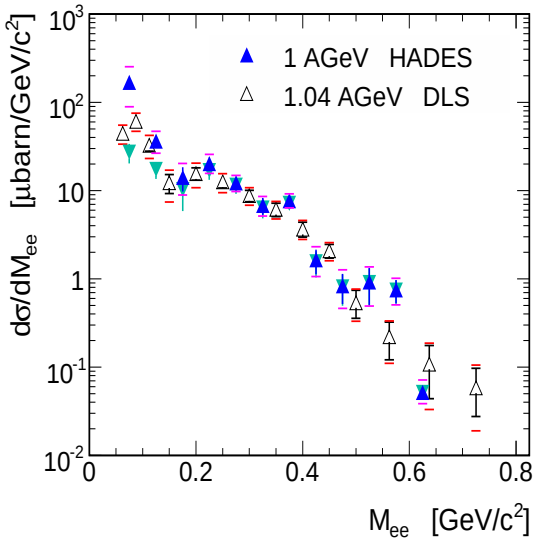

Figure 2: Direct comparison of the dielectron cross sections measured in ^{12}C+^{12}C at 1 GeV/u by HADES and at 1.04 GeV/u by DLS [1]. Invariant-mass distributions are compared within the DLS acceptance. Statistical and systematic errors are shown. Overall normalization errors (not shown) are 20% for the HADES and 30% for the DLS data points. HADES data corresponding to two different fit functions, as discussed in [8], are shown as dark and light triangles, respectively.

In our previous annual report [2] we have used the HADES data measured in 2002 at 2 GeV/u and the DLS data [1] obtained at 1.04 GeV/u to conclude that the excess yield, integrated over the $0.15 < M_{ee} < 0.50$ GeV/c^2 mass range, scales with beam energy like π production. This conclusion can now be verified in a direct comparison of our 1 GeV/u data with the DLS result, both in terms of the integral excess yields and, more differentially, of the respective mass and $P_\perp$ distributions. This is achieved by a mapping of the measured HADES pair yields onto the DLS acceptance, defined in the 3-d space spanned by pair $M_{ee}, P_\perp$ and y. Although the acceptances of both apparatuses do not fully overlap for low-mass, low-$p_\perp$ pairs, in the excess region, the HADES coverage is larger and fully contains the DLS acceptance. Transforming the multiplicities measured by HADES to cross sections, this mapping allows for an almost model-independent comparison of the two data sets (Details can be found in [8]). In Fig. 2 the HADES-mapped invariant-mass distribution is shown together with the DLS result [1]. It is apparent that, within statistical and systematic uncertainties, both measurements are in very good agreement, and in particular in the region of excess yield. The same conclusion is obtained from the comparison of the $P_\perp$ distributions [8].

The confirmation of the – for a long time disputed – DLS results poses again the question of what lies at the origin of the pair excess. In this context, our studies of $p+p$ and $d+p$ reactions are important steps. Indeed, recent calculations in the One Boson Exchange (OBE) framework [9] suggest much larger than heretofore assumed contributions from $p-p$ and, mostly, $p-n$ quasi-elastic bremsstrahlung. Moreover, transport calculations done with the Hadron String Dynamics (HSD) model [10] using a parametrization of bremsstrahlung inspired by the new OBE result seem to be able to match both the HADES and the DLS ^{12}C+^{12}C data. In this situation it is evident that the confrontation of the OBE model calculations with $p+p$ and $d+p$ dilepton data from HADES is mandatory to reach final conclusions on the origin of dileptons at SIS energies.

Status of the ongoing analysis

p+p and d+p experiments

The main motivation to study dielectron production in $p+p$ and $d+p$ reactions at 1.25 GeV/u is to provide a better understanding of pair emission in nucleon-nucleon collisions below the η-meson production threshold. The relevant process involves the nucleon-nucleon interaction mediated by meson exchange and virtual photon emission, either from a nucleon (or excited nucleon resonance) or from the exchanged meson line. Hence, in general, several amplitudes have to be added coherently [9], but in a good approximation one can describe the pair distributions as resulting from the coherent sum of two processes: (i) quasi-elastic bremsstrahlung ($N+N \rightarrow NNe^+e^-$) and (ii) Δ-resonance excitation with its subsequent Dalitz decay ($N+N \rightarrow \Delta N \rightarrow Ne^+e^-$). Both processes appear to be almost equally important for $p-n$ collisions (dominance of the "dipole" radiation), while in $p+p$ reactions the Δ^+ decay plays the major role. Since the Δ^+ resonance also decays strongly into a $p\pi^0$ pair, one can relate its production cross section to the known π^0 production via an isospin relation, $N_{\Delta^+} = 3/2 N_{\pi^0}$ [12] and thus also fix the Dalitz contribution. This argument also holds for Δ production in the $p+n$ reaction, except for the fact that there two Δ isospin states of relevance for lepton production are excited: $\Delta^+ \rightarrow p\pi^0$ and $\Delta^0 \rightarrow n\pi^0$. Furthermore, the isospin dependence of Δ production given by its ratio in $p+p$ and $p+n$ collisions is another important issue. A resonance model [12] assuming isospin symmetry predicts $\sigma(pp \rightarrow p\Delta^+)$ =1/2 $\sigma(pn \rightarrow n(p)\Delta^{+(0)})$. And a slightly smaller (mass-dependent) value is predicted by OBE calculations [9].

In the upper part of Fig. 3 the inclusive invariant-mass distributions of signal and unlike-sign CB pairs are shown, measured in 2006 by HADES in $p+p$ reactions at 1.25 GeV. The signal spectrum contains 39k pairs (with ~ 600 above the π^0 mass) and corresponds to 2.6×10^9 first level triggers (LVL1) demanding at least 3 hits in the HADES TOF/TOFINO wall. The lower part of this figure presents

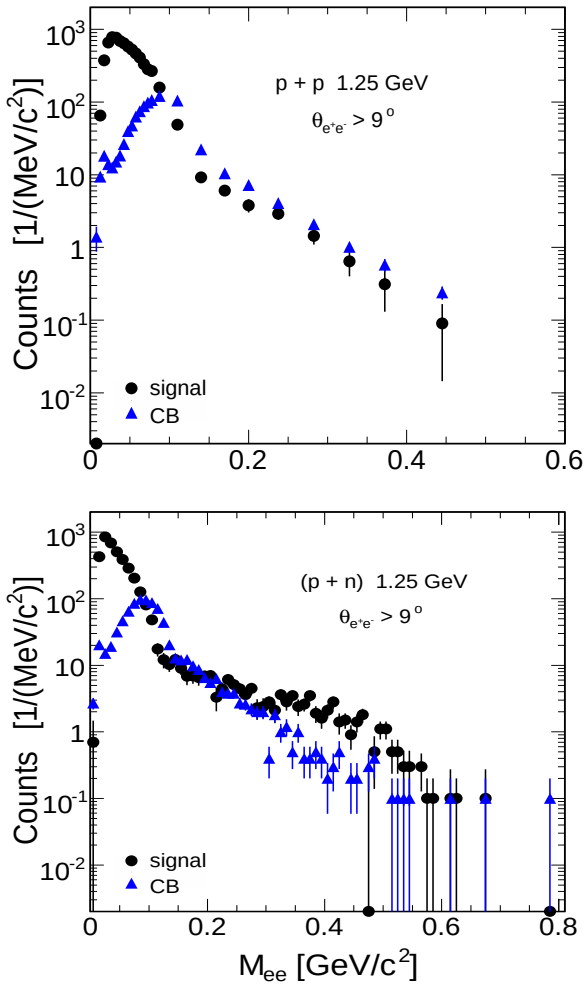

Figure 3: Invariant-mass distributions of signal pairs (dots) and combinatorial background (triangles) in $p+p$ (upper) and $p+n$ (lower) collisions at 1.25 GeV. The latter events were selected from $d+p$ reactions by tagging on a fast proton spectator in the HADES Forward Wall. All distributions are **not** corrected for efficiency and are **not** normalized absolutely.

inclusive dielectron distributions obtained from about 50% of the available statistics of our recent (2007) $d+p$ run at the same kinetic beam energy per nucleon. Here, the total pair statistics amounts to 38k (with ~ 1240 above the π^0 mass); it was obtained with a LVL1 trigger condition demanding at least 2 hits in the TOF/TOFINO and at least 1 charged particle in the Forward Wall, covering the region of $0.5-7^\circ$ polar angles. The latter condition assures detection of the fast forward-going spectator proton from the deuterium projectile, selecting hence mostly $p+n$ reactions. Although both mass distributions have not yet been corrected for reconstruction efficiencies, one clearly notices the stronger yield of the $p+n$ data at masses $M_{ee} > 0.15$ GeV/c^2. This already indicates, as expected, that additional pair sources do exist in $p+n$ collisions. However, besides the already mentioned $p-n$ bremsstrahlung, there is also a non negligible contribution from η-meson Dalitz decays. This is due to the finite Fermi momentum of nu-

cleons ($< p > \simeq 100$ MeV/c) inside the deuterium nucleus which makes possible η production below threshold. Since the relevant momentum distribution is rather well known [11], and since the cross sections of η production in $p+n \to p+n+\eta$, $p+p \to p+p+\eta$, and $p+n \to d+\eta$ are known [13], the corresponding η Dalitz contribution can be estimated and subtracted. Final conclusions, however, can only be drawn after efficiency corrections and an absolute normalization have been made. The normalization will be based on $p-p$, respectively $d-p$ elastic scattering, measured in both runs as well.

1.756 GeV/u ArKCl and 3.5 GeV pp experiments

The main motivation for the Ar+KCl and 3.5 GeV $p+p$ runs was to perform high-resolution spectroscopy of the vector-meson region. Furthermore, an investigation of the medium-heavy Ar+KCl system also allows to study the dependency of the pair excess observed in ^{12}C+^{12}C reactions on the interaction volume and centrality of the collision.

Ar+KCl collisions were measured in September 2005 and provided the largest data sample collected so far by HADES ($\sim$ 7 Tbyte raw data). Thereby 2.2×10^9 LVL1 events were acquired with the condition that at least 16 hits were registered in the TOF/TOFINO, with almost the complete HADES tracking system operational (only 2 outermost MDC chambers were still not mounted). Fig. 4 shows an invariant-mass distribution of the pair signal after CB subtraction. CB was obtained by combining the like-sign and event-mixing techniques as explained in [3]. The signal-to-CB ratio for pairs above the π^0 region amounts to $\sim 1/5$. The presented spectrum is normalized to the number of LVL1 events, but no corrections for pair reconstruction efficiency have been applied yet. Work on efficiency corrections and on the normalization to the measured charged-pion multiplicity are under way. The total number of signal pairs amounts to $\sim$115k. More than 7000 pairs have been measured above the π^0 region; a clear omega signal is visible for the first time at SIS/Bevelac energies.

The interpretation of the pair distribution in the vector-meson region relies very much on the calibration of the tracking system. The quality of the latter has been successfully verified in the reconstruction of narrow hadronic resonances, namely $\Lambda \to p\pi^-$, $K^0_s \to \pi^+\pi^-$, and even $\phi \to K^+K^-$. Studies of strangeness production are of course very interesting for themselves. In particular subthreshold ϕ production is only poorly known at SIS energies. Figure 5 displays the invariant mass of K^+K^- pairs, with a prominent ϕ meson signal visible. The shaded area represents the CB background determined with a mixed-event technique. The successful reconstruction of the ϕ meson was only possible due to particle identification based on a combination of time-of-flight measurement in the TOF detector and track energy-loss determination in all of the four MDC tracking chambers. This technique has already been described in last year's status report [2].

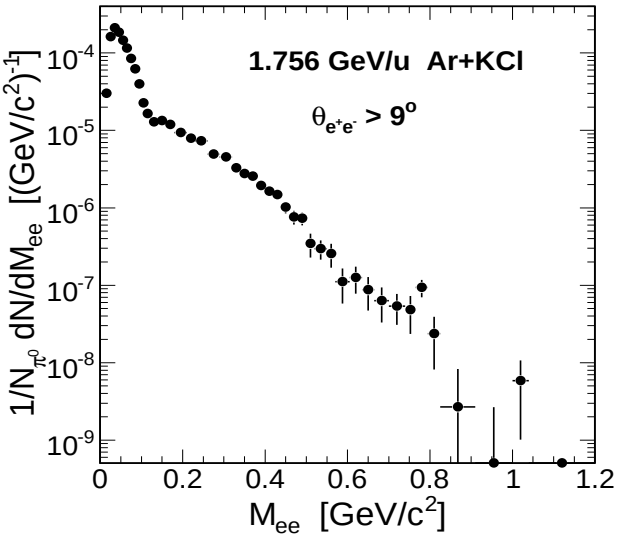

Figure 4: Invariant-mass distribution of signal pairs (after CB subtraction) measured in Ar+KCl collisions at 1.756 GeV/u . The spectrum has been normalized to the number of LVL1 events and pion multiplicity, but is not corrected for the pair reconstruction inefficiency.

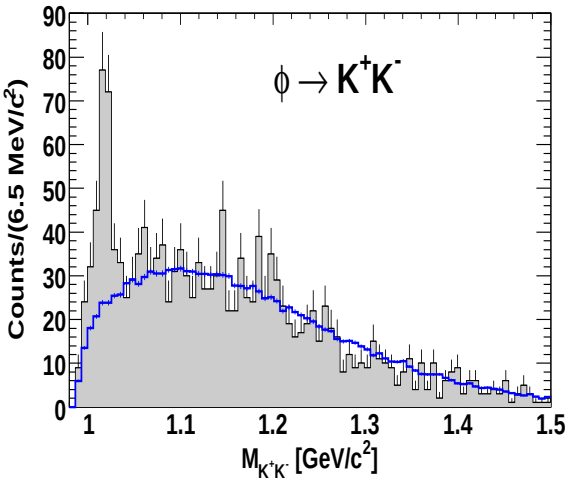

Figure 5: Invariant-mass distribution of K^+K^- pairs measured in Ar+KCl collisions at 1.756 GeV/u . A clear ϕ-meson signal is visible on top of the CB background reconstructed by event-mixing.

Finally, we present very preliminary results from our most recent experimental run, performed with a 3.5 GeV proton beam on a LH_2 target. Using a preliminary on-line calibration of the spectrometer, 70% of the total collected statistics were analyzed in parallel to the data taking. Based on this on-line analysis figure 5 shows the reconstructed invariant-mass distributions of signal pairs (dots) and CB. More than 55k pairs have been obtained in the total mass range and $\sim$7k above the π^0 Dalitz region. A prominent

$\omega \to e^+e^-$ signal is visible with $\sim 3.5\%$ mass resolution. Presently, detailed calibrations of the tracking systems are being performed. Improvements in the particle identification, as well as the tracking resolution are expected to reduce the observed width of the ω peak. The investigation of vector-meson production will be continued with a run measuring $p + A$ collisions at the same beam energy which is scheduled for the second half of 2008. In a four-week running period dielectron production on Be and Nb targets will be studied. This experiment will thus provide information on ω/ρ mass distributions in nuclear matter at normal density and zero temperature. The data already obtained in $p + p$ collisions will thereby serve as an important reference.

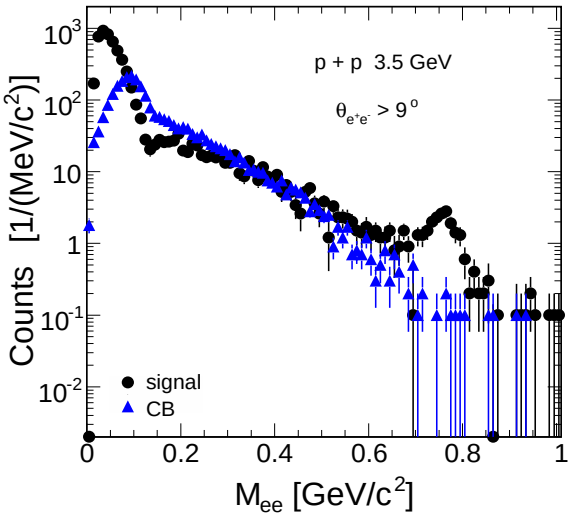

Figure 6: On-line reconstruction of data from our 3.5 GeV $p + p$ run. Shown are invariant-mass distributions of $e + e-$ signal (dots) and CB (triangles) pairs.

The collaboration gratefully acknowledges the support by BMBF grants 06MT238TP5, 06GI146I, 06F-140, 06DR120, and DFG EClust 153 (Germany), by GSI (TM-KRUE, GI/ME3, OF/STR), by grants GA CR 202/00/1668 and GA AS CR IAA1048304 (Czech Republic), by grant KBN 1P03B 056 29 (Poland), by INFN (Italy), by CNRS/IN2P3 (France), by grants MCYT FPA2000-2041-C02-02 and XUGA PGID T02PXIC20605PN (Spain), by grant UCY-10.3.11.12 (Cyprus), by INTAS grant 03-51-3208 and by EU contract RII3-CT-2004-506078, and DIRAC-PHASE-1 contract 515876 .

References

[1] R. J. Porter et al., DLS Collaboration, Phys. Rev. Lett. 79, 1229 (1997).

[2] HADES Collaboration., GSI Scientific Report 2006.

[3] G. Agakichiev et al., HADES Collaboration, Phys. Rev. Lett. 98, 052302 (2007).

[4] R. Averbeck et al., TAPS Collaboration, Z. Phys. A 359, 65 (1997).

[5] C. Sturm et al., KaoS Collaboration, Phys. Rev. Lett. 86, 39 (2001).

[6] E. L. Bratkovskaya, W. Cassing, R. Rapp and J. Wambach, Nucl. Phys. A **634**, 168 (1998).

[7] C. Ernst et al., Phys. Rev. C 58, 447 (1998).

[8] HADES coll., arXiv:0711.4281, submitted to Phys. Lett. B.

[9] L. Kaptari and B. Kampfer, Nucl. Phys. A 764, 338 (2006).

[10] E. L. Bratkovskaya, W. Cassing, arXiv:0712.0635.

[11] M. Lacombe et al., Phys. Lett. B 101(1981) 139.

[12] S. Teis et al., Z. Phys. A 356 (1997) 421.

[13] Cálen et al., Phys.Rev.C 58 (1998) 2667.

[14] W. Cassing and E. L. Bratkovskaya, Phys. Rept. **308**, 65 (1999).

Progress in HADES Tracking and Alignment*

O. Pechenova, V. Pechenov, Sören Lange and W. Kühn for the HADES Collaboration
II Physikalisches Institut, Justus-Liebig-Universität Giessen, Germany

In order to ensure an efficient and accurate operation of the track reconstruction in HADES, we have investigated sources of intrinsic misalignment have developed new approaches for the alignment of HADES tracking detectors.

The effects from time calibration and geometry are distinguished using the drift time deviation variable Δt (calculated time – measured time) and selecting the tracks passed *above* and *below a* wire. The clearances between two parts of the layer in the MDCIII and the MDCIV were detected and defined for each layer. Figure 1 shows the example of such kind of correction for the MDCIV.

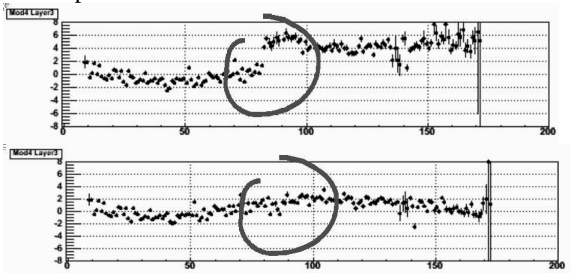

Figure 1: The dependence Δt[ns] vs wire number before (top) and after (bottom) the correction.

Another important reason of misalignment is the shift of the physical centre of a layer. Correction values for each layer were obtained from an iterative procedure using a simultaneous fit for all layers. The procedure converged after 3-4 iterations. Figure 2 illustrates the improvements for different runs after this correction.

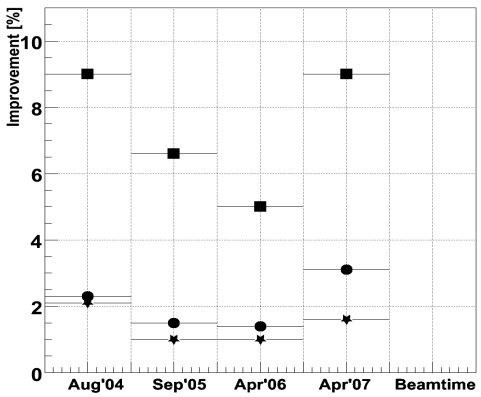

Figure 2: The improvements (%) in the number of fitted tracks (circles), in χ^2/ndf (squares) and in the number of wires per track (stars) for different runs.

The mutual influence of internal and external misalignment was investigated. As a new method, we have used Millepede [1] which solves the linear least square problem for a few hundred alignment parameters. This method is based on a simultaneous fit of track and alignment parameters. Data from different beamtimes, as well as cosmics were used simultaneously for alignment. Software was developed which allows calculating the partial derivatives for all alignment parameters, to fit cosmic tracks passing up to 8 MDC chambers. Moreover, an interface between HYDRA and the Millepede software was implemented. The method was tested using simulated data and was then the applied to real data without magnetic field taken from the 2005–2007 runs. 426 alignment parameters were obtained simultaneously. The influence of misalignment on the reconstruction of individual tracks and pairs from elastic scattering has been estimated. First results are shown in Fig.3 and include the quantity and quality of fitted individual tracks and of pairs from elastic scattering. The number of pairs was increased by 13%-18%.

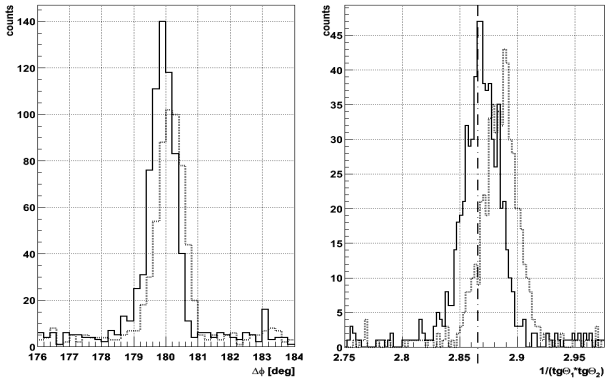

Figure 3. Comparison of the quantity and the quality of pairs from *pp*-elastic scattering before Millepede alignment (dot lines) and after (solid lines).

For the track finder a new method [3] of spike finding on the projection plane was developed and has been used for Ar KCl data analysis. As a result an increased efficiency of the track finder of 5-8% as well as an increased purity of track candidate was observed. On the other hand this method did increase the number of fake tracks. In order to suppress the fake tracks an improved algorithm [4] is under development.

References

[1] http://www.desy.de/~blobel
[2] O.Pechenova, HADES CM XVIII, Cyprus, Oct'07.
[3] V.Pechenov, HADES CM XVIII, Cyprus, Oct'07.
[4] V.Pechenov, HADES Analysis Meeting, GSI, Mar'07.

*Work supported by GSI and BMBF (6GI179)

Λ polarization measurements in Pb+Pb collision

A. Wetzler[1], H. Beck[1], J. Bock[1], C. Blume[1], P. Dinkelaker[1], V. Friese[2], M. Gaździcki[1], C. Höhne[2], D. Kresan[2], B. Lungwitz[1], M. Mitrovski[1], R. Renfordt[1], T. Schuster[1], R. Stock[1], C. Strabel[1], H. Ströbele[1], M. Utvić[1], and the NA49 Collaboration[3]

[1]Fachbereich Physik der Universität Frankfurt, Germany; [2]GSI, Darmstadt, Germany

Polarization relative to the production plane

The production plane is defined by the momentum vectors of the Λ $\vec{V}$ and of the beam $\vec{B}$. The transverse polarization is obtained from the angle θ between the momentum vector of the proton in the Λ rest frame and the normal to the production plane ($\vec{B} \times \vec{V}$). The polarization of the Λ is then: $P_\Lambda = \langle cos\theta \rangle / a \cdot \langle cos^2\theta \rangle$ with $a = 0.642$. The transverse polarization has been observed to be finite in p+p and p+Be collisions. We have analysed the Λ polarization in minimum bias Pb+Pb collisions with respect to the Λ production plane. Fig. 1 shows P_Λ as function of p_t. The NA49 determination of P_Λ (red points) extends up to 2.6 GeV/c. The points are compared to pBe (green points and small error bars)[1] and pp [2] results. The signal is smaller in Pb+Pb collisions than in the more elementary reactions pp and pBe. A differential analysis of P_Λ in terms of centrality shows very similar finite polarizations. Note that the systematic error on P_Λ of 0.15 has the same magnitude as the signal.

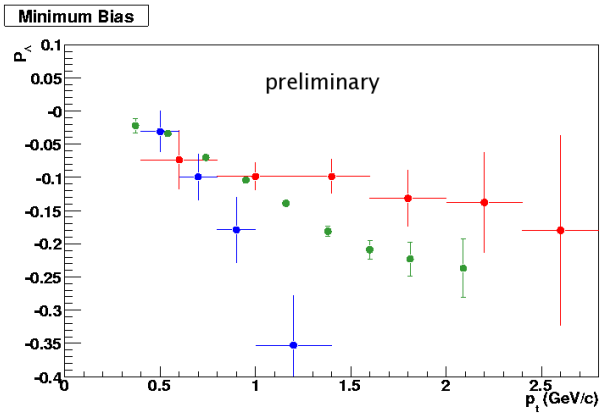

Figure 1: Polarization relative to the production plane of the Λ as function of p_t determined in the rapidity interval $1.4 < y < 2.5$. The red points are minimum bias Pb+Pb, the green points are pBe, and the blue points are pp data.

Polarization relative to the event plane

In a quark-gluon plasma which is produced in a non central nuclear collision the (anti-) quarks can be polarized due to the coupling of the quark spins to the orbital momentum $\vec{L}$ of the system. This polarization might survive hadronization and would thus be observable as a global polarization of the e.g. Λ hyperon [3]. We have measured the global Λ polarization P_Λ in minimum bias Pb+Pb reactions at 158A GeV. The Λ hyperons have been selected in the same way as in [4]. The measurement of P_Λ is based on the following relation: $P_\Lambda = 8/(\pi \cdot a) \cdot (\langle \sin(\phi^*_p - \Psi^{(1)}_{EP}) \rangle) / (R^{(1)}_{EP})$ [5]. In this procedure the direction of $\vec{L}$ is assumed to be normal to the reaction plane. The reaction plane orientation is estimated via a measurement of the first order event plane angle $\Psi^{(1)}_{EP}$ and its resolution $R^{(1)}_{EP}$, as described in [6]. ϕ^*_p is defined as the azimuthal angle of the Λ decay proton 3-momentum in the Λ rest frame. Figure 2 shows the ΛPolarization with respect to the event plane as function of rapidity in the most peripheral events of a minimum bias event sample. A marginal net negative Λ polarization is observed. Its systematic error is still to be determined. The Λ polarization in all other centrality bins is zero. An analysis of midcentral Au+Au collisions done at $\sqrt{s_{NN}}$ = 200 GeV [5] did not reveal a significant polarization signal.

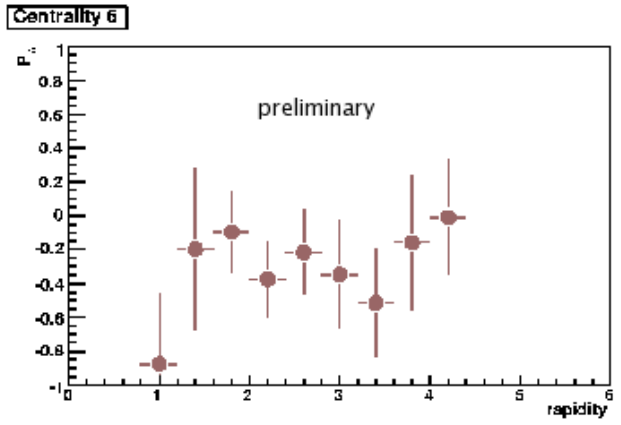

Figure 2: Global Polarization of the Λ as function of rapidity in the most peripheral bin of a minimum bias Pb+Pb sample at 160 GeV per nucleon.The shown error bars represent the stastical spread only.

References

[1] K.J. Heller et al., Phys. Rev. Lett., **41** (1978) 607
[2] P. Chauvet et al., Phys Lett. **B163** (1985)
[3] Z. Liang and X.N. Wang, Phys. Rev. Lett. **94** (2005) 102301.
[4] C. Alt et al. (NA49 coll.), Phys. Rev. **C 75** (2007) 044901
[5] B.I. Abelev (STAR coll.), Phys. Rev. **C 76** (2007) 024915.
[6] C. Alt et al. (NA49 coll.), Phys. Rev. **C 68** (2003) 034903.

Pion freeze-out and two particle correlations in Pb+Au collisions at SPS energies *

S. Schuchmann, H. Appelshäuser, and D. Antończyk for the CERES collaboration
University Frankfurt a.M., Germany

The investigation of momentum correlations of identical bosons yields information about the spatial and temporal evolution of the particle emitting source in heavy ion collisions. A well-established technique to study space-time dimensions in such processes is the Hanbury-Brown Twiss (HBT) interferometry. Measurements of HBT parameters have been reported by several experimental collaborations from AGS to RHIC spanning two orders of magnitude in $\sqrt{s_{NN}}$. The energy dependence may be interpreted in terms of an universal freeze-out scenario [1].

In order to study the subtle variation of HBT parameters over several collision energies [2], the freeze-out volume V_f was introduced [1]. The HBT parameter R_{long} shows a smooth and faster increase from AGS to RHIC energies compared to R_{side} and R_{out}. Therefore it seems reasonable to use this parameter for further investigations of freeze-out properties. R_{out} contains the contribution of the temporal extent of the pion source, hence it is not considered in the calculation. Assuming a density distribution of Gaussian shape and an azimuthal symmetry in central collisions, the freeze-out volume is calculated as

$$V_f = (2\pi)^{\frac{3}{2}} R_{side}^2 R_{long} \tag{1}$$

The parameters R_{side} and R_{long} are determined in the longitudinal co-moving frame (LCMS) defined by the vanishing longitudinal component of the pair momentum. The momentum difference (**q**) in this frame was decomposed into the out, $side$, and $long$ components following the Bertsch-Pratt convention, with q_{long} pointing along the beam, q_{out} along the pair transverse momentum, and q_{side} perpendicular to both of them.

At lower SPS energies a minimum in the excitation function of V_f for heavy colliding systems was observed (Fig.1). This result was explained by the transformation of the reaction system from a baryon- to a pion- dominated system. Taking into account the system composition through the particle multiplicity N in the volume and the total cross section σ of pions with the surrounding medium, it is feasible to access the mean free path of pions λ_f at freeze-out [1]:

$$\lambda_f = \frac{V_f}{N\sigma} = \frac{V_f}{N_N\sigma_{\pi N} + N_\pi\sigma_{\pi\pi}} \tag{2}$$

with

$$N_N = y_{th}\sqrt{2\pi} \cdot \frac{dN_N}{dy}|_{y_{mid}} \tag{3}$$

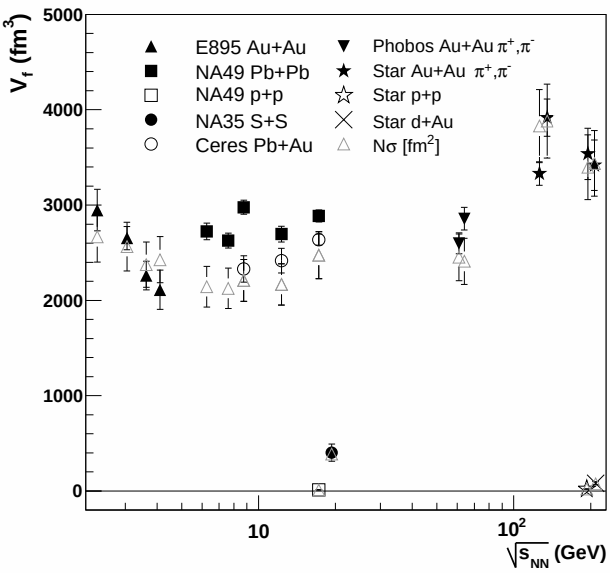

Figure 1: Energy dependence of the freeze-out volume V_f (1) for mean transverse momenta between $\langle k_t \rangle = 0.148$ GeV/c (AGS, SPS) and $\langle\, k_t \rangle = 0.175$ GeV/c (RHIC) around midrapidity. Data are extracted from [1 -13]. Points at the same beam energy are slightly shifted for better visibility.

and

$$N_\pi = y_{th}\sqrt{2\pi} \cdot \frac{dN_{\pi^-}}{dy}|_{y_{mid}}. \tag{4}$$

The calculation is based on the assumption of a thermal equilibrated system at freeze-out with a constant $T_f = 120$ MeV for all beam energies and a thermal rapidity of $y_{th} =$

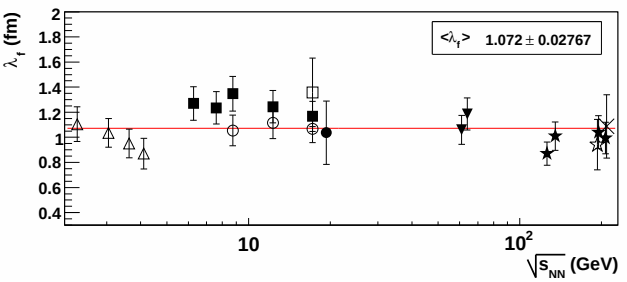

Figure 2: Excitation function of the mean free path λ_f of pions at freeze-out. The line shows a linear fit to the data with $\langle\, \lambda_f \rangle$ as single fit parameter. Caption, see Fig.1.

* Work supported by BMBF and GSI

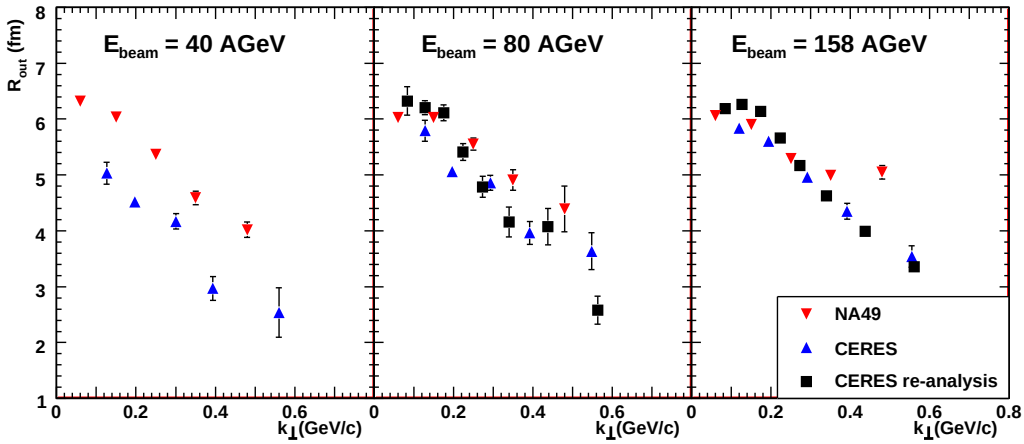

Figure 3: Mean transverse momentum dependence of the R_{out} parameter in central Pb-Pb (NA49) and Pb-Au (CERES) collisions at 40, 80, and 158 AGeV beam energy.

0.87. For the cross sections $\sigma_{\pi N} = 72$ mb, and $\sigma_{\pi\pi} = 13$ mb were used. Within this parametrization the minimum in the excitation function of the freeze-out volume virtually vanishes as it is shown in Fig.2. The data for different colliding nuclei and energies show a remarkable agreement with a common mean free path value of $\sim$1 fm at freeze-out. This seems to support the statement that the particle emitting source is rather opaque than transparent [1]. The opaqueness is parametrized as $\omega = \frac{R}{\lambda_f}$ [16], the ratio of the transverse geometrical radius and the mean free path. If λ_f exceeds the radius considerably ω reaches zero, which characterizes transparent source. As typical geometrical radii are in the range of 7-9 fm, we find $\omega \approx 10$, indicating a rather large opaqueness of the particle emitting source. Indeed, from a theoretical point of view, it stands to reason to challenge an universal kinetic freeze-out temperature for all beam energies. Experimentally however, in the SPS regime systematic uncertainties do not yet allow to derive final conclusions from the measured excitation function of the HBT parameters [2,15]. Especially the R_{out} parameter, which is not involved in the freeze-out volume calculations, reveals discrepancies between preliminary NA49 and CERES analysis (Fig.3). Hence, a reanalysis of the data sets for 40, 80 and 158 AGeV collected in 1999 and 2000, employing an improved calibration scheme of the CERES TPC, is being performed. Until now, the re-analysis of the beam energy data set for 158 and 80 AGeV where accomplished. Preliminary results on the k_t-dependence of the R_{out} parameter are compered to the former CERES [17] and preliminary NA49 [2] results for the centrality between 0-5 % of the geometrical cross section. The slight differences between both experiments in the pair rapidity selection should have minor influence on the R_{out} parameters as presented in [2]. The discrepancies visible between CERES results at the lower transverse momentum can be attributed to the improved understanding of the Coulomb influence on the measured correlation functions. Although, for low k_t bins preliminary results from CERES agree rather well with NA49, there still remains discrepancies for highest k_t range. Re-analysis of 40 AGeV data set will shed some light to understand results of the HBT radii at the SPS energy.

References

[1] D.Adamová et al., PRL 90(2003) 022301

[2] C.Alt et al.(NA49 coll.), nucl-ex/0709.4507v2

[3] B. B. Back et al.(PHOBOS coll.), Phys. Rev. C 73, 031901(R) (2006)

[4] B. B. Back et al.(PHOBOS coll.), Phys. Rev. C 75, 024910 (2007)

[5] Lijuan Ruan (STAR coll.), nucl-ex/0503015

[6] J. Adams et al.(STAR coll.), Phys. Rev. C71, 044906(2005)

[7] S. Adler et al.(PHENIX coll.), Phys. Rev. C 69, 034909 (2004)

[8] Z. Chajecki (STAR coll.), nucl-ex/0511035

[9] Lijuan Ruan PHD Thesis (2004), nucl-ex/0503018

[10] R.Ganz (NA49 coll.), Nucl.Phys. A661 (1999) 448

[11] C. Alt et al. (NA49 coll.), Eur. Phys. J. C 45 (2006)

[12] T. Alber et al.(NA35 coll.), Z. Phys. C 66, 77-88 (1995)

[13] Na35 coll., EPJ C2,643 (1998)

[14] D.Antończyk, PHD Thesis, TU Darmstadt (2006)

[15] Q.Li, M.Bleicher and H.Stöcker, nucl-th/0706209v2

[16] B. Tomasik and U. W. Heinz, nucl-th/9805016

[17] D.Adamová et al. Nucl.Phys. A 714 (2003) 124

Two- and three-particle azimuthal correlations of high-p_t charged hadrons in Pb-Au collisions at 158*A* GeV beam energy*

S. Kniege, H. Appelshäuser, and M. Ploskon, for the CERES collaboration
University Frankfurt, Germany

Energy loss of partons traversing the hot and dense medium in a heavy ion collision can have significant impact on the shape of jets emerging from such collisions. These shapes can be analyzed via azimuthal correlations of a high-p_t trigger particle (T) and associated particles (A) in an event.

Correlation functions (CF) $C_2(\Delta\phi)$ of the difference in the azimuthal angle $\Delta\phi = \phi_T - \phi_A$ are constructed as the normalized ratio of signal- and mixed-event distributions in which trigger- and associated particles are taken from different events. In a two-source approach, correlations arising due to the anisotropy of the source in non-central collisions are subtracted from the measured correlation function. After normalisation to the number of associate pairs per trigger we obtain the conditional yield (CY) $1/N_{\mathrm{T}} \cdot dN^{\mathrm{TA}}/d(\Delta\phi)$ as the number of jet-associated particles per trigger. The analysis is based on $3{\cdot}10^7$ Pb-Au events collected with the CERES-TPC at the CERN-SPS.

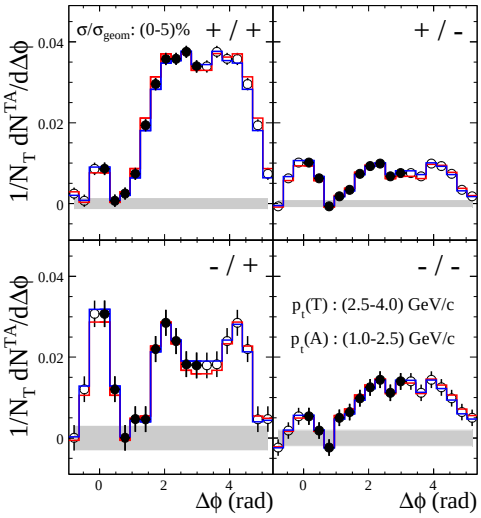

Figure 1: Conditional yield for different charge combinations of the particles (trigger/associated). Systematic uncertainties are indicated (lines, bands).

In Figure 1, the charge dependence of the CY is shown for different charge combinations of trigger- and associated particles for central collisions. The difference in the yields can be understood as to arise from an interplay of initial and final state effects. On the near-side, unlike-sign combinations of trigger- and associated particles dominate the yield. This indicates local charge conservation in the fragmentation process. The ratios of the yields of negative to positive associates agree well with results from PYTHIA simulations for nucleon-nucleon collisions. Hence the yields on the near-side reflect the properties of vacuum fragmentation and support the picture of a surface-biased emission of high p_t-particles in the collisions. On the away-side however, the yield is dominated by positive associates for both, positive- and negative trigger particles. The ratios of the jet-yields correspond to the ratio of negative to positive particles in the associated range. Hence, the jet-yield on the away-side reflects the positive net-charge exess in the bulk medium. This is not reflected by PYTHIA for positive triggers and indicates that on the away-side we observe the bulk medium boosted by partrons traversing it.

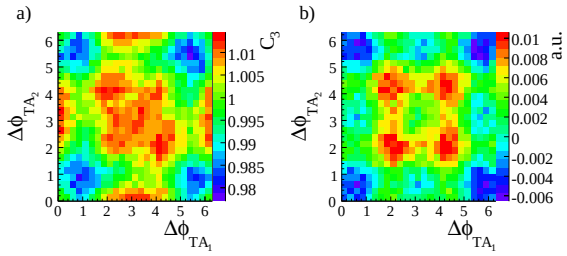

Figure 2: Three-particle CF (a) and jet yield (b) after subtraction of the two-particle correlations (color online).

Another observation is a non-Gaussian shape of the CF on the away-side for central collisions [1]. Different effects like the deflection of jets or mach-cone shock waves [2] can lead to similar shapes on the away-side of the CF. Three-particle correlations as the correlations among two associated particles and a trigger particle can help to disentangle these scenarios. In Figure 2 the three-particle CF (a) as well as the yield (b) after the subtraction of the background components are shown. Clear off-diagonal peaks are visible which indicates cone-like emission of the hadrons. The deflection of jets would result in pairs of associated particles being close by to each other thus populating dominantly the diagonal of the CF.

Summarizing, the yield ratios on the near-side indicate vacuum fragmentation whereas on the away-side the ratios are close to the expectations for the medium. In addition, the away-side exhibits a double-humped structure for central collisions indicating cone-like emission of the particles.

References

[1] M. Ploskon *et al.*, Nucl. Phys. A **783**, 527-530 (2007).

[2] H. Stöcker, Nucl. Phys. A **750**, 121 (2005)

* This work was supported by BMBF and GSI-F&E.

Installation of the Time Projection Chamber into the ALICE experiment

H. Appelshäuser[2], P. Braun-Munzinger[1], J. Castillo[1], U. Frankenfeld[1], C. Garabatos[1], S. Kniege[2], R. Renfordt[2], H.R. Schmidt[1], D.Vranic[1], J. Wiechula[1], and the ALICE collaboration

[1]GSI, Darmstadt, Germany, [2]University of Frankfurt, Frankfurt, Germany

After completion of the commissioning above ground [1] the TPC was moved into the ALICE pit into its parking position in front of the L3 magnet. To verify the soundness of the connections between the readout chambers and the front-end electronics after the transport all sectors were tested once more with a pulser injecting charge into the cathode planes. After all tests were successfully passed the TPC was moved to its final position inside the L3 magnet and all services were installed.

Cooling plant commissioning

In order to remove excess heat from the front-end electronics and to guarantee a temperature stability of $\Delta T<0.1°$ C the TPC is temperature stabilized by a cooling system operating in a "leak less" mode, i.e., the circulating cooling liquid is kept below atmospheric pressure.

The installation of the TPC in its final position within the L3 magnet allowed for the first time to operate the cooling plant together with the TPC. It was found that for some sectors the routing of the cooling lines between the plant and the TPC was such that siphons were formed (with about 1.5 m height). In the attempt to establish flow through these sectors (i.e. push the air out of the system) the pressure had to be raised to a point were it reached or even exceeded atmospheric pressure at the front-end cards. In fig. 1 the pressure development of such a bad sector is shown in comparison to a good sector. In a good sector the maximum pressure to establish flow is about 0.7 – 0.8 bar at the detector side and it drops soon to its steady state level once the air is removed. In a bad sector the flow can only be reached when exceeding the level of safe operation. The problem was solved by rerouting the return lines such that all siphons were avoided. After that the cooling plant worked well according to specs.

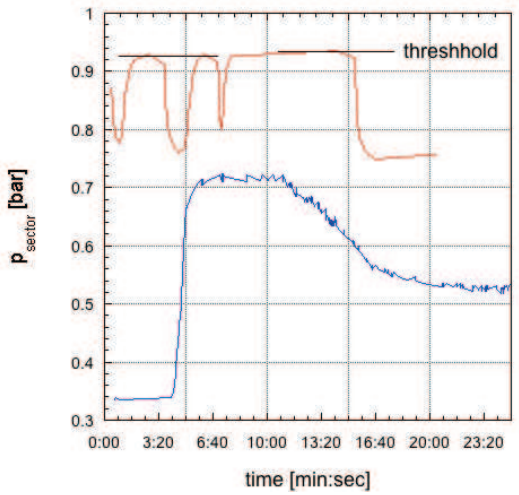

Figure 1: Pressure in the cooling line at the detector side as a function of time of a good sector (bottom, blue) and a bad sector (top, red) showing the effect of siphons in the return line.

Bus bar upgrade

During the testing of the readout and careful monitoring of the voltages at the front-end cards by built-in ADCs it was found that in some partitions of the readout the low voltage showed drops of up to 0.7V. It was traced to imperfect soldering of the high current spring wire sockets into the copper bus bars (fig. 2). Since resoldering seemed

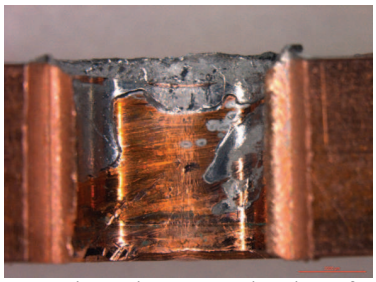

Figure 2: Cut through a copper bus bar after removal of the socket indicating the insufficient distribution of solder.

difficult it was decided to replace the sockets altogether by screws. After this the voltage drops measured were below 20 mV across a sector.

ALICE commissioning run

After installation of the HV (100 kV) system for the drift field, the HV system for the chambers, the low voltage power supplies, the gating and the calibration pulser sys-

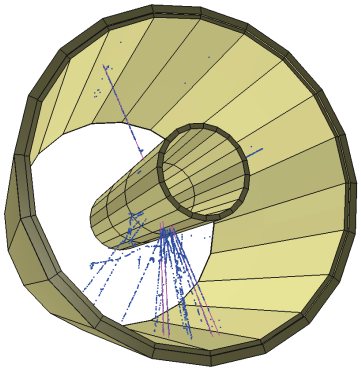

Figure 3: 3D-view of a cosmic event seen in one half of the TPC with all 18 sectors read out.

tems a commissioning run for the ALICE experiment as a whole was performed. In fig. 3 a cosmic event in the TPC is shown. All sectors on the C-side were in operation. In the final step the full readout of the A-side will be established.

References

[1] P. Braun-Munzinger et al., "Commissioning of the ALICE TPC Time Projection Chamber", GSI Annual Report (2006) 226

ALICE High-Level Trigger: Implementation of TRD-specific components *

M. Ploskon[†1], H. Appelshäuser[1], and H. Büsching[1]
[1]Institut für Kernphysik, University of Frankfurt, Germany

HLT-TRD software developments

In order to allow on-line data analysis, calibration and monitoring of the ALICE Transition Radiation Detector (TRD) a number of TRD-specific High Level Trigger (HLT) processing components have been designed and implemented. The TRD processing chain for HLT follows the analysis defined by the off-line algorithms developed within the ALICE analysis framework Aliroot [1]. In order to run the very same off-line algorithms on-line the following publisher-subscriber [1, 2] components wrapping the relevant parts of the off-line software have been implemented:

- **HLT Cluster finder component** (AliHLTTRDClusterizerComponent) handles the raw data input and executes the offline algorithm of cluster finding (AliTRDclusterizer).
- **HLT Tracker component** (AliHLTTRDTrackerComponent) wraps the functionality of the off-line TRD tracking algorithm (AliTRDtracker) taking clusters produced by the cluster finder component as the input.
- **HLT Calibration component** (AliHLTTRDCalibrationComponent) working on the tracks received from the tracker component executes the procedure collecting calibration reference data as implemented by the off-line code. The component delivers accumulated reference data to the HLT File Exchange Server for post processing and insertion into the Offline Condition Data Base (OCDB).
- **HLT Monitoring component** (AliHLTTRDMonitoringComponent) generic monitoring component(s) allowing pre-processing and basic statistical analysis of one of the input data stage (raw, cluster, tracks and calibration reference data).

Design and development of monitoring tools

The monitoring of the TRD data processing on HLT and monitoring of the TRD raw data itself has been designed and implemented within the AliRoot framework. Several dedicated components have been developed among which so called monitoring worker (AliHLTTRDworker) and Graphical User Interface (AliTRDdataGUI) are the core of the monitoring tools. An arbitrary number (as required) of monitoring processes analyze the incoming data from the HLT (TCP dump subscriber components) delivering the resulting histograms (drawable objects) via TCP/IP to the active GUI for inspection and further analysis. The design of the monitoring tools interfaced with the HLT publisher-subscriber infrastructure provide flexible and scalable application for basic and complex monitoring of the detector performance and reconstruction algorithms online. The system allows for monitoring at any level of the HLT processing chain. Moreover, the user interface can be integrated into any application developed within the ROOT framework - into AliEVE (the ALICE visualization tool) particularly.

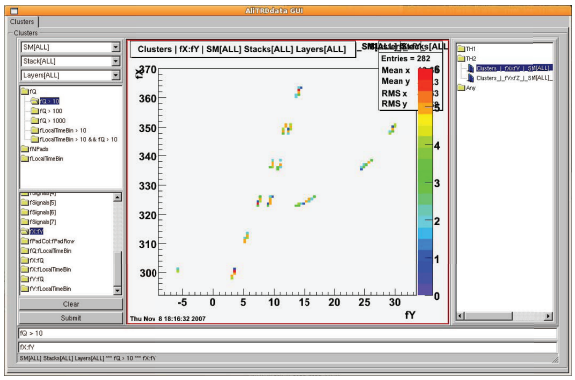

Figure 1: Screen shot of an HLT-TRD event from the test beam run at CERN-PS.

Commissioning and further developments

Most of the above developments have been already deployed and positively verified as fully functional during the TRD test beam experiment (October/November 2007) at CERN-PS. Figure 1 presents a screenshot of the monitoring user interface taken during the test experiment. Further tests have been performed during the Cosmic Ray run of ALICE in December 2007.

Future activity should focus not only on tuning and optimization of the existing software, but also on development and implementation of further analysis components integrating TRD into the global triggering system of HLT.

References

[1] ALICE Collaboration, F. Carminati (ed.) *et al.*, "ALICE: Physics Performance Report, Volume 1", J. Phys. **G30** (2004) 1517.

[2] ALICE Collaboration, T. Alt *et al.*, "Benchmarks and Implementation of the ALICE High Level Trigger", IEEE Trans. Nucl. Sci. **53** (2006) 854.

* Work supported by BMBF, GSI, and H-QM.
† ploskon@ikf.uni-frankfurt.de

Ongoing activities of the ALICE TRD construction at the IKF *

M. Hartig[1], W. Amend[1], K. Antipin[1], H. Appelshäuser[1], C. Blume[1], A. Fick[1], H. Hinke[1], M. Kliemant[1], F. Kramer[1], W. Sommer[1], and A. Wiesenäcker[1]

[1]Institut für Kernphysik Frankfurt, Germany

IN 2004 the *Institut für Kernphysik* at the *Johann Wolfgang Goethe–Universität Frankfurt* took over an active role within the ALICE TRD collaboration. The emphasis of the hardware activities are the production of the TRD readout chambers (ROC) and the integration of the front-end electronic (FEE).

ROC production

The ALICE TRD system [1] is comprised of in total 540 readout chambers in 12 different sizes. The mass production of these chambers is a joint project between JINR Dubna, GSI Darmstadt, NIPNE Bucharest, the University of Heidelberg and the IKF. The IKF is in charge for the production of one type of the ROC. Due to the finally achieved financial support for the production of the entire TRD detector system, the IKF has to produce in total 70 ROCs.

The complete line of production consists of several steps namely the manufacturing of chamber frames with the radiator, the gluing of the pad plane readout board onto the back-panels and the assembly of the two wire planes for the drift and the amplification region. The quality of the production is thoroughly tested and monitored during the whole production cycle. In 2007 the different steps of this production line and the corresponding testing procedures have been well established. An average output of one chamber per two weeks were achieved with a peak production rate of 1 chamber per week. This yields to 33 produced chambers at the end of 2007.

Recently the final leak test of the ROCs was modified to meet concerns about the losses of the expensive Xenon gas during the more than 10 years operation of the ALICE experiment. The original leak test was set up under the assumption that the gas leaks out of a slightly pressurized system and O2 diffusion into a system are the same. However it turned out, that we observed for a significant part of the produced chambers large outward leak of the gas, but only very small inward diffusion of oxygen. This indicates that most of the leaky orifice is extremely long with respect to the mean free path of the gas. As a consequence the setup of the leak test was changed from slight over-pressure to under-pressure inside the ROC. The conductance of the chamber leaks can be directly calculated from the measured Oxygen contamination, the differential pressure and the gas flow. A modification of the sealing improved the gas tightness of the chambers significantly. This new procedure was developed at the GSI detector laboratory and is now established in our general test procedure.

FEE integration and test

In addition to the ROC production the IKF is also responsible for the FEE integration of the TRD. In a first step the different electronic boards are mounted on the ROC namely the readout boards [4], the optical readout interfaces [5] and a board for the detector control system [6]. Afterwards the performance of the whole electronics is checked with 14 different tests. They probe the general functionality of the different components, measure the noise level of the system and test the connectivity of the readout pads. Finally a stress test is performed to check the long term stability of the system. After the cooling system of the electronic is assembled, the tests are repeated a second time. Details of the testing procedure are described in a separate report of A. Fick within this annual report [2] and in [3]

In 2007 we equipped and tested 120 ROCs for TRD super-modules 2 to 5. Within this year the organization of the integration and the tests was optimized considerably. A new laboratory was installed for the assembly of the cooling system. Further a quality assurance of connector boards was added to the production line. With this improvements we achieved a peak production rate of 10 ROCs per week and an average rate of one ROC per day.

To meet the tight time constrains of the ALICE installation schedule we have to make further streamlining. The main focus of this work is to improve the tests and to debug the software. In addition we want to develop a user friendly graphical interface.

References

[1] ALICE TRD, Technical Design Report, CERN/LHCC 2001-021

[2] A. Fick et al., GSI Scientific Report 2007

[3] B. Dönigus, *Assembly and Test of the first Supermodule of the ALICE Transition Radiation Detector*, Diplomarbeit, April 2007

[4] I.Rusanov, J.Stachel, GSI Scientific Report 2005, p.287

[5] V. Lindenstruth et al., GSI Scientific Report 2005, p.289

[6] D. Gottschalk et al., GSI Scientific Report 2004, p.361

* Work supported by BMBF FSP201 and GSI-F&E

Measurement of $B \rightarrow J/\Psi + X$ with the central detectors of ALICE*

W. Sommer†, C. Blume, F. Kramer
for the ALICE-TRD collaboration, Institut für Kernphysik, Universität Frankfurt a.M., Germany

The ALICE experiment is designed to measure a large variety of observables in heavy ion as well as in pp collsions at the CERN LHC. Among these, the measurement of the $b\bar{b}$-production cross section is of high importance in order to understand, e.g., the flavour dependence of jet-quenching phenomena. We present a study on the possibility to detect B-mesons via their decay into $J/\Psi + X$. This requires a good separation of secondary and primary J/Ψs by measuring the topology of the B-meson decay.

Decay topology

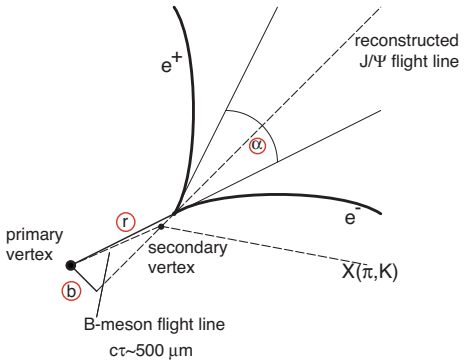

Figure 1: B-meson decay topology. The parameter r allows the separation of primary and secondary J/Ψs.

The lifetime of the B-meson with $c\tau = 500\mu m$ enables its detection via the determination of the secondary decay vertex and its distance to the primary vertex. The decay topology is sketched in figure 1. The B-meson is produced in the primary vertex and decays after a certain distance r with a branching ratio of 1% into a J/Ψ plus hadrons (mainly π or K). The J/Ψ in turn decays with a probability of 6% into an electron and a positron. Since the J/Ψ decays instantaneously the J/Ψ and the B-meson decay vertices are the same. The J/Ψ vertex can be determined via the distance of closest approach (dca) between the tracks of the e^+e^--pair. The electron identification in the ALICE central barrel is achieved with the TRD. Based on the measured kinematics of the e^+e^-pair one can reconstruct the J/Ψ flight path. The study discussed here is based on a detailed simulation of the events and their subsequent reconstruction with the ALICE offline software package AliRoot. This includes the *AliKFParticle* [1] package, which allows an easy identification of the decay topologies.

* supported by BMBF FSP 201 and GSI
† sommer@ikf.uni-frankfurt.de

Impact of the electron energy loss

In the standard ALICE track reconstruction scheme, all particles are tracked as pions. However, since electrons additionally emit Bremsstrahlung, their reconstructed momentum in many cases is lower than their real one. This in turn causes an over-estimation of the parameter r. Therefore a lower cut on the invariant mass of the electron pair at 3 GeV/c^{2}was applied to ensure that none of the leptons underwent a significant energy loss and the vertex information can be seen as reliable. By this cut the total amount of observable J/Ψs is reduced by 35%. Ongoing studies try to improve the electron tracking scheme in order to recover the losses due to Bremsstrahlung.

Results

The distribution of r is shown in figure 2. The summed distribution as well as the distributions for primary and secondary J/Ψs are shown. The relative ratio between the production rates of primary and secondary J/Ψ has been adjusted to the expected ratio of 0.2. From $r > 500\mu m$ on the secondary J/Ψ dominates. Applying a cut at $500\mu m$ results in an efficiency for secondary J/Ψs of 42% and a contamination of the secondary sample with primary J/Ψs of 31%.

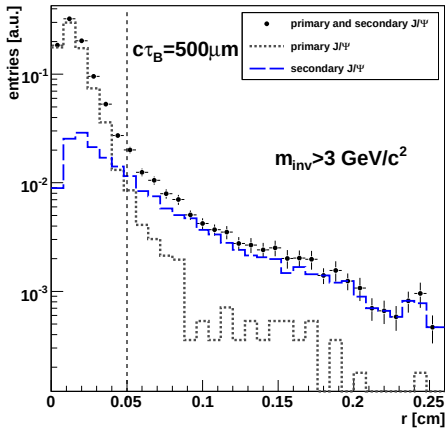

Figure 2: Distance between the primary and secondary vertex r for primary and secondary J/Ψs. The minimal invariant mass for an electron pair was 3 GeV/c^2, to prevent entries from electron pairs with large energy loss.

References

[1] I. Kisel, S. Gorbunov,
www.gsi.de/documents/DOC-2007-May-14-1.pdf

Helmholtz Research School for Quark Matter Studies in Heavy Ion Collisions

H. Büsching[†1] and H. Appelshäuser[2]

[1]FIAS and University of Frankfurt, Germany; [2]Institut für Kernphysik, University of Frankfurt, Germany

The newly founded Helmholtz-Research-School for Quark Matter Studies in Heavy Ion Collisions (H-QM) started its activities with the university winter semester 2006/2007. The Research School under lead management by the Institut für Kernphysik of Johann Wolfgang Goethe-Universität Frankfurt is a joint program of GSI, the University of Frankfurt and the Frankfurt Institute for Advanced Studies (FIAS). Within the framework of a structured PhD education, the Research School aims to specially qualify exceptional PhD candidates from Germany and abroad.

In parallel to their scientific education PhD candidates obtain a specially developed soft skill training to improve their professional qualification for future positions in science and industry. The selected PhD candidates shall become acquainted to the importance of strategic and task sharing collaboration while pursuing a joint, interdisciplinary research project. In addition to educational aspects and the promotion of young scientists H-QM is expected to contribute significantly to the scientific endeavor of GSI. This is facilitated by concentrating the research efforts of a large number of PhD candidates on a common field with interconnected PhD thesis topics. To be attractive for international applicants all events of the school are held in the English language. The new Research School is one of three pioneering programs accepted for special funding by the Helmholtz Association in March 2006. Each school will receive 1.8 million Euro for the next six years from the Initiative and Networking Fund of the Helmholtz Association.

The scientific topic of H-QM is nuclear and hadron physics with a special focus on understanding high energetic heavy ion collisions, both, theoretically and experimentally. The PhD candidates participate in the ALICE-experiment at CERN-LHC, the preparation for FAIR at GSI, or in the quest for theoretical understanding of the experiments. In a first round of applications in 2006 17 participants from eleven different countries have been selected from a pool of more than 200 applications. In 2007 the school reached its current capacity with a total number of 30 participants. In a three year program the participants will be accompanied through their thesis work, allowing two generations of PhD candidates to benefit from the structured PhD approach in the current funding cycle. The candidates will obtain their PhD from the participating joint universities.

The school was officially inaugurated with a symposium at GSI in October 2006 with guests from the Helmholtz Association as well as participating universities. Prof. Berndt Mueller (Duke University/USA) and Prof. Reinhard Stock (Frankfurt) delivered the introductory lectures. The annual program of the Research School includes lectures, specially tailored to the needs of PhD students, weekly colloquia, lecture weeks and soft skill seminars. Further elements of structured PhD education as advisory PhD committees and regular reviews of the current status of the thesis project in presentations and discussions are applied. A PhD committee consists of the PhD candidate, the supervisor, an external supervisor and a mentor. The committee meets twice per year to discuss achievements and future goals for the thesis. All participants and supervisors join once per year for an scientific overview of all H-QM thesis projects in the H-QM Graduate Days, the first of these meetings in 2007 was hosted at Frankfurt.

In April 2007 the first H-QM lecture week was held in Rolandseck in the Rhine valley focusing on particle production in heavy ion collisions and detector types used in heavy ion physics with JProf Dr. Marcus Bleicher (Frankfurt) and Dr. Hans Rudolf Schmidt (GSI). The second lecture week was organized in the Kleinwalsertal in Austria. This time Prof. Dr. Ralf Averbeck (Stony Brook/USA), Dr. Volker Koch (Berkeley/USA) and Prof. Dr. Piotr Salabura (Univ. Krakow/Poland) discussed “Chiral Symmetry” aspects in heavy ion collisions. A very successful first Helmholtz Softskill Program was organized together with the Imperial College London in June 2007 at Easthampsted Park, not far from London. The 4-day joint seminar of all three Helmholtz research schools in Germany increased the sensibility for optimized work relations and the difficulties of working in a team. Interdisciplinary communication and collaboration was practized.

The program of the school is complemented by indivual support for foreign participants on social and bureaucratic issues. In cooperation with FIAS and the Otto-Stern-School at Frankfurt special language courses have been offered for the integration of the international participants. H-QM was able to enable the PhD candidates to actively participate in numerous conferences and workshops, both, national and international. The large number of talks and poster contributions of the PhD candidates at these meetings demonstrate the active research environment at H-QM. The PhD candidates themselves enriched the official program by self organized events as journal clubs or special language exercises.

Additional information on the activities of the Research School is available at:
http://fias.uni-frankfurt.de/helmholtz/index.html

* Work supported by Helmholtz Association

† buschin@ikf.uni-frankfurt.de

The running coupling from the four-gluon vertex in Landau gauge SU(N) Yang-Mills theory *

C. S. Fischer[1,2] and C. Kellermann[1]

[1]Institut fuer Kernphysik, TU Darmstadt, Germany; [2]GSI, Darmstadt, Germany

The running coupling of Yang-Mills theory has been investigated in a number of approaches in recent years [1]. The focus of these studies is the question how to extend our knowledge of the coupling from the perturbative, large momentum region towards small scales of the order of Λ_{QCD}. Perturbation theory alone, plagued by the problem of the Landau pole, is clearly insufficient for this task. In this respect it seems remarkable that the mere improvement of the perturbation series by analyticity constraints leads to a well defined running coupling that freezes out in the infrared.

Infrared fixed points of the couplings of Yang-Mills theory have also been found in two functional approaches to QCD, the functional (or 'exact') renormalization group (FRG) and the framework of Dyson-Schwinger equations (DSEs) [2]. In these approaches nonperturbative running couplings are defined in terms of dressing functions of propagators and dressing functions of the primitively divergent vertices of the theory. In Landau gauge, the couplings from the ghost-gluon vertex, α^{gh-gl}, the three-gluon vertex, α^{3g}, and the four-gluon vertex, α^{4g}, are given by [2]:

$$\alpha^{gh-gl}(p^2) = \frac{g^2}{4\pi} G^2(p^2)\, Z(p^2)\,, \qquad (1)$$

$$\alpha^{3g}(p^2) = \frac{g^2}{4\pi} [\Gamma^{3g}(p^2)]^2\, Z^3(p^2)\,, \qquad (2)$$

$$\alpha^{4g}(p^2) = \frac{g^2}{4\pi} [\Gamma^{4g}(p^2)]\, Z^2(p^2)\,. \qquad (3)$$

Here $g^2/4\pi$ is the coupling at the renormalization point μ^2, whereas $Z(p^2)$ denotes the dressing function of the gluon propagator $D_{\mu\nu}$ and $G(p^2)$ the dressing of the ghost propagator D^G, i.e.

$$D^G(p^2) = -\frac{G(p^2)}{p^2}\,, D_{\mu\nu}(p^2) = \left(\delta_{\mu\nu} - \frac{p_\mu p_\nu}{p^2}\right) \frac{Z(p^2)}{p^2}\,. \qquad (4)$$

The functions Γ^{3g} and Γ^{4g} describe the nonperturbative dressing of the tree-level tensor structures of the three- and four-gluon vertices. In this work we focus on a calculation of $\alpha^{4g}(p^2)$ and compare the result with the previously determined coupling $\alpha^{gh-gl}(p^2)$ [3].

The basic ingredient to the running coupling $\alpha^{4g}(p^2)$ is the dressing function Γ^{4g} of the nonperturbative four-gluon vertex. An evaluation of this dressing together with a corresponding evaluation of the gluon propagator therefore allows to study the running of the coupling with momentum. To this end we employ an approximation scheme of the Dyson-Schwinger equation of the four-gluon vertex described in detail in [4]. Our scheme reproduces the correct asymptotic behavior of the vertex as known from perturbation theory and infrared power counting methods [2].

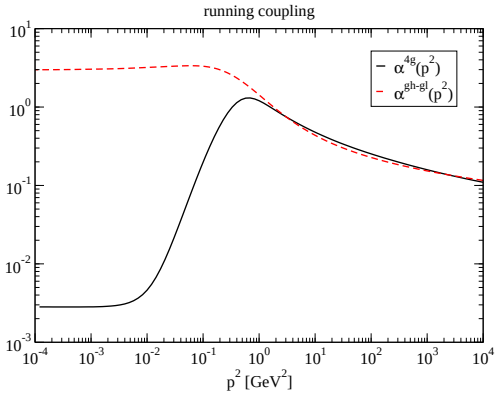

Or result for the coupling is displayed in the figure. The most striking result of our work concerns the running coupling from the four-gluon vertex, built from a combination of vertex dressing and the dressing function of the gluon propagator. Although in the ultraviolet momentum region the coupling agrees nicely with the one from the ghost-gluon vertex (as it should according to gauge invariance), in the infrared we observe strong deviations. Whereas the coupling from the ghost-gluon vertex develops an infrared fixed point at around $\alpha_{gh-gl}(0) \approx 9/N_c$, we find a much smaller fixed point at around $\alpha_{3g}(0) \approx \frac{9\cdot 10^{-3}}{N_c}$ for the coupling from the four-gluon vertex. This finding supports the notion of an infrared effective theory dominated from the Faddeev-Popov determinant proposed in [5]. Furthermore it explains why the structural differences in the Dyson-Schwinger and the functional renormalization group approach are able to obtain the same results in the infrared momentum region.

References

[1] G. M. Prosperi, M. Raciti and C. Simolo, Prog. Part. Nucl. Phys. **58** (2007) 387 [arXiv:hep-ph/0607209].

[2] C. S. Fischer, J. Phys. G **32** (2006) R253 [arXiv:hep-ph/0605173].

[3] C. S. Fischer and R. Alkofer, Phys. Lett. B **536** (2002) 177 [arXiv:hep-ph/0202202].

[4] C. Kellermann and C. S. Fischer, to be submitted to Phys. Rev. D.

[5] D. Zwanziger, Phys. Rev. D **67** (2003) 105001 [arXiv:hep-th/0206053]; Phys. Rev. D **69** (2004) 016002 [arXiv:hep-ph/0303028].

* Work supported by Helmholtz-University Young Investigator Grant VH-NG-332

Radiative and isospin-violating decays of D_s-mesons in the hadrogenesis conjecture

M.F.M. Lutz[1] and M. Soyeur[2]

[1]GSI, Darmstadt, Germany; [2]DAPNIA/SPhN, CEA/Saclay, F-91191 Gif-sur-Yvette Cedex, France

It was argued by Mehen and Springer [1] that the radiative decays of the scalar $D^*_{s0}(2317)^{\pm}$ and the axial vector $D^*_{s1}(2460)^{\pm}$ strongly disfavor a molecule picture in which these states are described as D(D_s)-kaon bound states. We scrutinize this claim by a systematic study of radiative and isospin-violating strong decays of charmed mesons with strangeness in the hadrogenesis conjecture [2].

To establish manifestly gauge invariant results for the electromagnetic decay parameters, we represent massive spin-one particles by antisymmetric tensor fields, rather than by conventional vector fields [3]. Though in general the physics should be independent of the choice of fields, in a non-perturbative approach like coupled-channel dynamics, certain field choices may be superior if they lead to a more transparent realization of the electromagnetic gauge symmetry. The scalar $D^*_{s0}(2317)^{\pm}$ and the axial vector $D^*_{s1}(2460)^{\pm}$ states are generated by coupled-channel dynamics based on the leading order chiral Lagrangian [4, 3]. The formalism developed in [4] is generalized to the tensor field representation of vector states [3]. Chiral correction terms are incorporated systematically in the coupled-channel dynamics [5] and evaluated relying on constraints from large-N_c QCD and from the heavy-quark symmetry [3]. The one-loop contribution to the electromagnetic decay amplitudes of scalar and axial vector states (Fig. 1) are calculated using the chiral Lagrangian, where the role of light vector meson degrees of freedom is explored. It is emphasized that conclusive results on the radiative decay properties require a consistent computation of decay modes into pseudoscalar and vector particles in the final state and a systematic implementation of the chiral symmetry of QCD. This is done in Ref. [3] for the first time.

The main findings of our work [3] are

- The hadronic isospin-violating decay widths of the $D^*_{s0}(2317)$ and $D^*_{s1}(2460)$ states are predicted to be 140 keV. Chiral correction terms are important contributions to the decay widths.

- The invariant $\eta\, D^*$ invariant mass distribution shows a signal of a member of an exotic axial vector sextet characterized by a mass of 2568 MeV and a width of 18 MeV. While that state decouples from the πD^* spectrum, its heavy-quark partner induces a narrow dip (2 MeV wide) at a mass of 2410 MeV in the $\pi\, D$ mass distribution.

- The parameters of the radiative decays $D^*_{s0}(2317) \to \gamma\, D^*_s$ and $D^*_{s1}(2460) \to \gamma\, D_s, \gamma\, D^*_s$ and $D^*_{s1}(2460) \to \gamma\, D^*_{s0}(2317)$ were computed in the hadrogenesis conjecture. We find that the ηD_s and $\eta\, D^*_s$ channels contribute significantly. The results are compatible with all empirical constraints once one gauge-invariant contact term is considered to be more important than expected from a naive naturalness assumption. The decay parameters are subject to a cancellation mechanism, which makes a prediction of their precise values unreliable at the moment.

- When considering light vector mesons as explicit degrees of freedom, radiative decay parameters compatible with the empirical constraints, can be obtained without invoking subleading contact terms. We predict that the $D^*_{s0}(2317)$ and $D^*_{s1}(2460)$ have small coupling strength to the K^*D^* and $\phi\, D^*_s$ channels. Nevertheless, such channels play a decisive role in the radiative decay processes.

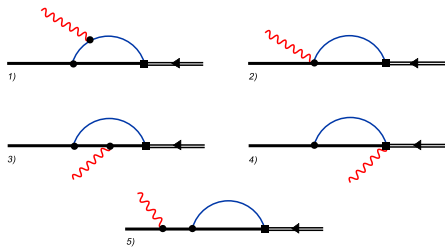

Figure 1: Diagrams contributing to the decay amplitude of a scalar or axial vector molecule. Solid lines represent the propagation of the pseudo-scalar or vector mesons, where the thin lines stand for the light mesons and the thick lines for the heavy mesons. The wavy line is the photon.

Our results do not support the general claim by Mehen and Springer [1] that the radiative decay properties of the $D^*_{s0}(2317)$ and $D^*_{s1}(2460)$ disfavor a molecular interpretation of these states.

References

[1] T. Mehen and R.P. Springer, Phys. Rev. **D 70** (2004) 074014.

[2] M.F.M. Lutz and E.E. Kolomeitsev, Found. Phys. **31** (2001) 1671; M.F.M. Lutz, GSI-Habil-2002-1; M.F.M. Lutz and E.E. Kolomeitsev, Nucl. Phys. **A 700** (2002) 193; M.F.M. Lutz, Gy. Wolf und B. Friman, Nucl. Phys. **A 706** (2002) 431.

[3] M.F.M. Lutz and M. Soyeur, arXiv:0710.1545 [hep-ph].

[4] E.E. Kolomeitsev and M.F.M. Lutz, Phys. Lett. **B 582** (2004) 39.

[5] J. Hofmann and M.F.M. Lutz, Nucl. Phys. **A 733** (2004) 142.

Antikaons and hyperons in nuclear matter with saturation

M.F.M. Lutz[1], C.L. Korpa[2], and M. Möller[3]

[1,2]GSI, Darmstadt, Germany; [2]Department of Theoretical Physics, University of Pecs, Ifjusag u. 6, 7624 Pecs, Hungary

We evaluate the antikaon and hyperon spectral functions in a self-consistent and covariant many-body approach [1]. The computation is based on coupled-channel dynamics derived from the chiral SU(3) Lagrangian [2] and extends our previous study [3]. A novel subtraction scheme is developed that avoids kinematical singularities and medium-induced power divergencies all together. Scalar and vector mean fields are used to model nuclear binding and saturation. Already at nuclear saturation density the impact of the latter on the antikaon spectral function, that becomes significantly more narrow at small momenta, is important. Attractive mass shifts of about 30 and 40 MeV are predicted for the $\Lambda(1405)$ and $\Sigma(1385)$ resonances. Once scalar and vector mean fields for the nucleon are switched on the $\Lambda(1520)$ resonances dissolves almost completely in nuclear matter at saturation density.

Most striking are our explorative results of strangeness properties at twice nuclear saturation density. For such systems it is difficult to establish firm results due to large uncertainties in the values the scalar and vector mean fields of the nucleon take. Also there is no empirical constraint on the hyperon ground-state properties at such densities. Effects not considered in this work, like pion dressing or short-range correlation effects on the hyperon ground states, need to be addressed *and* controlled.

We assume degenerate scalar and vector mean fields

$$|\Sigma_S| = |\Sigma_V| = 500\,\mathrm{MeV} \qquad \text{at} \qquad \rho = 2\,\rho_0\,, \qquad (1)$$

and give the $\Lambda(1115)$ an 'intrinsic' repulsive mean field of 100 MeV at twice saturation density. The latter was chosen such that the in-medium mass of the $\Lambda(1115)$ after self consistency is pulled down by 25 MeV with respect to its free-space value. We deem this as a conservative estimate. At saturation density we used a repulsive 'intrinsic' shift of 36 MeV only, which lead to a mass shift of 30 MeV. The fact that we need such large repulsive 'intrinsic' mass shifts for the $\Lambda(1115)$ reflects a significant cancellation of repulsive mean-field type effects and exchange-type effects implied by the strong coupling of the $\Lambda(1115)$ to the $\bar{K}N$ channel.

In Fig. 1 the resulting antikaon spectral distribution is shown. An intriguing effect is revealed. At small antikaon energies the spectral distributions develops significant strength in a narrow peak at around 70 MeV. The peak remains narrow and pronounced for finite antikaon momenta $0\ \mathrm{MeV} < |\vec{q}| < 200\ \mathrm{MeV}$. This is in contrast to the antikaon spectral distribution at saturation density. The corresponding structure has very little weight and is dissolved much more quickly as the antikaon starts to move through the matter bulk. The physical origin of that peak is readily understood: it reflects the coupling of the antikaon to

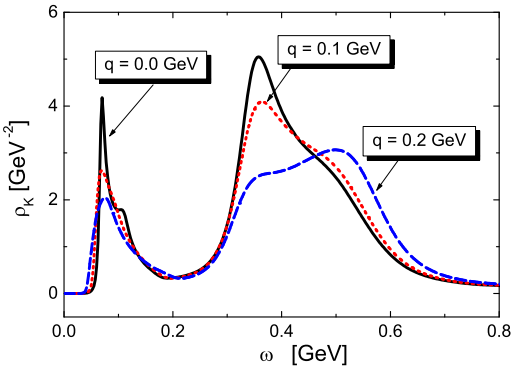

Figure 1: Antikaon spectral distribution as a function of energy ω and momentum $\vec{q}$ at twice nuclear saturation density.

a $\Lambda(1115)$ nucleon-hole state. We emphasize that the soft antikaon mode sits at 70 MeV, even though the $\Lambda(1115)$ effective mass was adjusted to be 30 MeV below its free-space limit at the considered density $2\,\rho_0$. In the low-density limit the soft mode has energy $m_\Lambda - m_N \simeq 175$ MeV, a value significantly larger than the 70 MeV seen in Fig. 1. This illustrates that the $\Lambda(1115)$ nucleon-hole state turns highly collective.

Our observation may have important consequences for the study of finite nuclear systems with strangeness. Given a finite and compressed nucleus A it shows that the two states $A\,\Lambda\,N^{-1}$ and $A\,\bar{K}$ interact strongly with each other by strangeness-exchange forces. The final $A\,\Lambda\,N^{-1}$ state is pulled down to smaller energies by a significant level-level repulsion of the two states. We thus arrive at the conclusion that deeply bound and narrow kaonic nuclei may exist as suggested by Akaishi and Yamazaki [4], however, based on a different mechanism. For instance an α nucleus offered a strangeness quanta may further shrink in size as a consequence of the soft antikaon mode as seen in Fig. 1. Depending on the details the lowest state formed may have higher nuclear densities than the one of the α particle.

References

[1] M.F.M. Lutz, C.L. Korpa and M. Möller, arXiv:0707.1283 [nucl-th].

[2] M.F.M. Lutz and E.E. Kolomeitsev, Nucl. Phys. **700** (2002) 193.

[3] M.F.M. Lutz and C.L. Korpa, Nucl. Phys. **700** (2002) 309.

[4] Y. Akaishi and T. Yamazaki, Phys. Rev. **C 65** (2002) 044005.

In-medium chiral condensate beyond linear density approximation

N. Kaiser, P. de Homont, and W. Weise
Physik-Department, TU München, D-85747 Garching, Germany

The quark condensate $|\langle 0|\bar{q}q|0\rangle|$ is an order parameter of spontaneous chiral symmetry breaking in QCD. With increasing temperature and baryon density it decreases. For low T this effect can be systematically calculated in ChPT and the estimate $T_c \simeq 190\,\mathrm{MeV}$ for the critical temperature has been found. This is remarkably consistent with $T_c = (192 \pm 8)\,\mathrm{MeV}$ [1] obtained in QCD lattice simulations (modulo still persisting disputes between different lattice groups [2]).

The density dependence of the quark condensate can be extracted by exploiting the Feynman-Hellmann theorem with respect to the quark mass term $m_q\,\bar{q}q$. The leading linear term in the density ρ introduces the nucleon sigma-term $\sigma_N = \langle N|m_q\,\bar{q}q|N\rangle = m_q\,\partial M_N/\partial m_q = (45 \pm 8)\,\mathrm{MeV}$. Corrections beyond it arise from the NN-interactions. Because of the Goldstone boson nature of the pion, $m_\pi^2 \sim m_q$, the pion-exchange dynamics in nuclear matter plays a particularly important role. Altogether, one has for the ratio of the in-medium to the vacuum chiral quark condensate:

$$\frac{\langle\bar{q}q\rangle(\rho)}{\langle 0|\bar{q}q|0\rangle} = 1 - \frac{\rho}{f_\pi^2}\left\{\frac{\sigma_N}{m_\pi^2}\left(1 - \frac{3k_f^2}{10M_N^2}\right) + D(k_f)\right\}, \quad (1)$$

where interaction contributions are collected in the function

$$D(k_f) = \frac{1}{2m_\pi}\frac{\partial\bar{E}(k_f)}{\partial m_\pi}\,, \quad (2)$$

defined as the derivative of the interaction energy per particle $\bar{E}(k_f)$ with respect to m_π^2. Our calculation [3] treats systematically the effects from one-pion exchange (with m_π-dependent vertex corrections), iterated 1π-exchange, and irreducible 2π-exchange with no, single and double $\Delta(1232)$-isobar excitations including Pauli-blocking corrections up to three-loop order. It is furthermore necessary to estimate the quark mass dependence of an NN-contact term which encodes short-distance dynamics. Employing recent computations of the NN-potential in lattice QCD [4] at different pion masses we find that the contact term has a negligible influence on the in-medium chiral condensate.

Fig. 1 shows the condensate ratio in the density region $0 \le \rho \le 0.36\,\mathrm{fm}^{-3}$ for three different values of the pion mass, $m_\pi = (0,\,70,\,135)\,\mathrm{MeV}$. One observes a very strong and non-linear dependence of the "dropping" condensate on the actual value of the pion mass m_π. In the chiral limit, $m_\pi = 0$, chiral symmetry seems to be restored already at about $1.5\rho_0$. This much faster decrease is caused primarily by the fact that the ratio:

$$\frac{\sigma_N}{m_\pi^2} = -4c_1 - \frac{9g_A^2 m_\pi}{64\pi f_\pi^2} + \frac{3c_1 m_\pi^2}{2\pi^2 f_\pi^2}\ln\frac{m_\pi}{\lambda} + \frac{9g_A^2}{(4\pi f_\pi)^2} \times\left\{\Delta\ln\frac{m_\pi}{2\Delta} + \sqrt{\Delta^2 - m_\pi^2}\ln\frac{\Delta + \sqrt{\Delta^2 - m_\pi^2}}{m_\pi}\right\}, \quad (3)$$

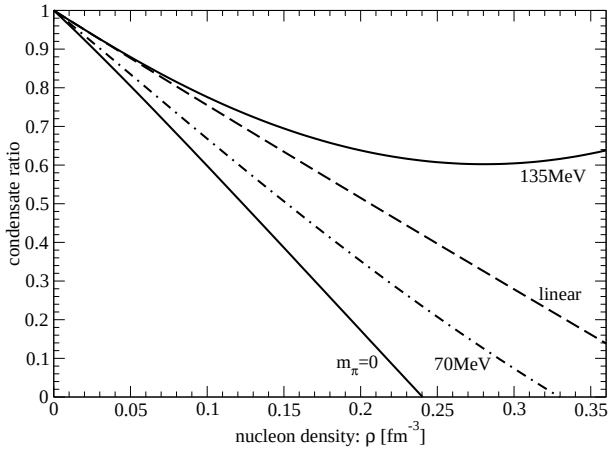

Figure 1: Ratio of in-medium to vacuum chiral condensate versus density ρ for three different values of the pion mass.

is about 1.5 times larger in the chiral limit than at the physical point. By contrast, for the physical pion mass $m_\pi = 135\,\mathrm{MeV}$, the in-medium condensate stabilizes at about 60% of its vacuum value above that same density. In comparison to other works [5, 6] we find more pronounced deviations from the linear density approximation above ρ_0.

The non-linear density dependence of the chiral condensate is driven by 1π- and 2π-exchange processes at long and intermediate range for which the adequate framework is in-medium ChPT. In particular, the explicit treatment of 2π-exchange with virtual $\Delta(1232)$-excitation is mandatory for controlling the pion mass dependence of the energy per nucleon. The strong variation of the condensate with changing m_π, as seen in Fig. 1, points to the delicate interplay of spontaneous and explicit chiral symmetry breaking in fine-tuning the nuclear many-body problem. If the pion were a strictly massless Goldstone boson, chiral symmetry restoration would occur at a density so low that a description of nuclei in terms of nucleons and mesons would not be justified. The non-zero quark mass m_q of about $5\,\mathrm{MeV}$ turns out to be essential in order to stabilize the system.

References

[1] M. Cheng et al., Phys. Rev. D74 (2006) 054507.

[2] Y. Aoki et al., Phys. Lett. B643 (2006) 46.

[3] N. Kaiser, P. de Homont and W. Weise, Phys. Rev. C (2008) in print; nucl-th/0711.3154; and references therein.

[4] N. Ishii et al., Phys. Rev. Lett. 99 (2007) 022001.

[5] M. Lutz et al., Phys. Lett. B474 (2000) 7.

[6] O. Plohl and C. Fuchs, Nucl. Phys. A798 (2008) 75.

Neutrino emission due to Cooper pair recombination in neutron stars*

E.E. Kolomeitsev[1] and D.N. Voskresensky[1,2]
[1]GSI, Darmstadt, Germany; [2]MEPhI, Moscow, Russia

Reactions with Cooper pair breaking and formations (PBF) in superfluid nuclear matter [1] are an intensive source of neutrino pairs and an important ingredient of all modern numerical simulations of neutron star cooling [2]. Consequential is the importance of the recent claim [3, 4] that due to the Ward-identity constraints for the weak vector current the PBF reactions are strongly suppressed by the factor $R(\mathrm{nPFB}) \simeq (1\text{–}5)\cdot 10^{-3}$ for neutron pairs and $R(\mathrm{pPFB}) \simeq 10^{-6}$ for proton pairs.

Using Larkin-Migdal-Leggett formalism for superfluid Fermi liquid [5] we re-calculate neutrino emissivity of nPBF anf pPBF processes for the case of $1S_0$ pairing. Both normal and anomalous vertex corrections are included. We explicitly demonstrate that the Fermi liquid renormalization [5] respects the Ward identity and vector current conservation. Our final estimations of neutron and proton PBF emissivities differ from those in [3, 4].

Neutrino emissivity is given by $\varepsilon_{\nu\bar\nu} = \frac{G^2}{8}\int \frac{d\vec q_1}{(2\pi)^3\,2\,\omega_1}\frac{d\vec q_2}{(2\pi)^3\,2\,\omega_2}\,\omega\, f_{\mathrm B}(\omega)\,2\,\Im\chi(q)$, where G is the weak Fermi constant, $q = (\omega,\vec q) = q_1 + q_2$, $q_{1,2} = (\omega_{1,2},\vec q_{1,2})$ are 4-momenta of outgoing neutrino and antineutrino, $f_{\mathrm B}$ are Bose occupation factors, and $\Im\chi$ is the imaginary part of the susceptibility of the nucleon matter to weak interactions. The susceptibility χ is presented as the sum of diagrams

$-i\,\chi =$ 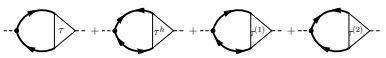

where additional summation over the lepton spins is assumed. The right-hand-side vertices $\hat\tau$, $\hat\tau^h$, $\hat\tau^{(1)}$ and $\hat\tau^{(2)}$ are the full vertices determined by the following equations

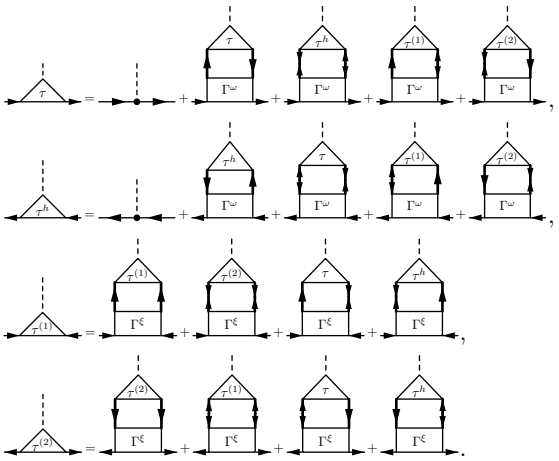

Here the blocks correspond to effective interactions in the particle-particle (Γ^ξ) and the particle-hole (Γ^ω) channels, respectively.

* Work supported by DFG project 436 RUS 113/558/0-3

For the neutron PBF emissivity on the vector current we obtain $\epsilon^{\mathrm{nPFB}}_{\nu\nu,V} = \gamma_V^2\,\frac{4}{81}v^4_{\mathrm{F},n}\,\epsilon^{(0n)}_{\nu\nu}$, where $\epsilon^{(0n)}_{\nu\nu} = 4\rho_n\,G^2\Delta_n^7\,I(\Delta_n/T)/15\,\pi^3$, with $I(z) = \int_1^\infty \mathrm{d}y\,y^5(y^2-1)^{-1/2}e^{-2zy}$ is the old standard result for nPBF emissivity obtained in [1]. Here $\gamma_V \sim 1$ is the nucleon-nucleon correlation factor depending on the scalar Landau-Migdal parameter [2], ρ_n is the neutron density of states on the Fermi surface, $v_{\mathrm{F},n}$ is the neutron Fermi velocity, and Δ_n denotes the neutron-neutron pairing gap.

For the neutron PBF emissivity on the axial-vector current we find $\epsilon^{\mathrm{nPBF}}_{\nu\nu,A} = \gamma_A^2\,g_A^2\,\frac{6}{7}v^2_{\mathrm{F},n}\,\epsilon^{(0n)}_{\nu\nu}$, where γ_A is the correlation factor depending on the spin-isospin Landau-Migdal parameter. The resulting emissivity is the sum $\epsilon^{\mathrm{nPBF}}_{\nu\nu} = \epsilon^{\mathrm{nPBF}}_{\nu\nu,V} + \epsilon^{\mathrm{nPBF}}_{\nu\nu,A}$. The axial-vector contribution, being $\propto v_{\mathrm F}^2$, is the dominant contribution. The ratio of the emissivity of the neutron PFB obtained here to the emissivity calculated in [1], where main contribution was due to the vector current, is then $R(\mathrm{nPFB}) = \epsilon^{\mathrm{nPBF}}_{\nu\nu}/\epsilon^{(0n)}_{\nu\nu} \simeq \frac{6}{7}\gamma^2(g_{nn})g_A^{*2}\,v^2_{\mathrm{F},n}$. For densities $n \sim n_0 = 0.16$ fm^{-3} we estimate $R(\mathrm{nPFB}) \simeq 0.15\text{–}0.25$. For $n \sim 2n_0$ the ratio $R(\mathrm{nPFB})$ increases up to 0.3–0.5.

The bare vector coupling for protons, $c_V^2 \simeq 0.004$, is much smaller than that for neutrons. Electrons present in neutron star matter in the same concentrations as protons induce, however, in-medium renormalization of the coupling due to the process

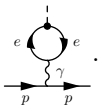

Taking the latter into accound we can estimate the ratio of nPBF and pPBF processes as $\epsilon^{\mathrm{pPBF}}_{\nu\nu}/\epsilon^{\mathrm{nPBF}}_{\nu\nu} \simeq \epsilon^{\mathrm{pPBF}}_{\nu\nu,A}/\epsilon^{\mathrm{nPBF}}_{\nu\nu,A} \sim x_p^{4/3}(\Delta_p/\Delta_n)^{13/2}e^{(\Delta_p-\Delta_n)/T}$, where x_p is proton concentration. Thus, a suppression factor $\sim 10^{-6}$ for the emissivity of the proton PBF process quoted in [3] is misleading.

Our results strongly support conclusion of Refs. [2] about the essential role the medium effects play in neutron star cooling and about the necessity of their consistent treatment in numerical realization of cooling scenarios.

References

[1] G. Flowers *et al.*, Ap. J. 205 (1976) 541.
[2] D.N. Voskresensky, Lect. Notes Phys. 578 (2001) 467.
[3] L.B. Leinson and A. Perez, Phys. Lett. B 638 (2006) 114.
[4] A. Sedrakian *et al.*, Phys. Rev. C76 (2007) 055805.
[5] A.I. Larkin and A.B. Migdal, Sov. Phys. JETP 17 (1963) 1146; A.J. Leggett, Phys. Rev. A 140 (1965) 1869.

Vector mesons in a hot pion gas

F. Riek[1,2] and J. Knoll[1,3]

[1]GSI, Darmstadt, Germany; [2]FIAS, Frankfurt, Germany; [3]University of Heidelberg, Germany

Previous selfconsistent approximation studies [1, 2] for the description of hadrons in hot and dense matter were extended along several lines [3, 4]. These concern the inclusion of the real parts of all polarisation functions by appropriately subtracted dispersion relations and of RPA-type π-ρ – meson correlations, which also lead to corresponding vertex corrections. Thus we arrive at a system of coupled Dyson equations

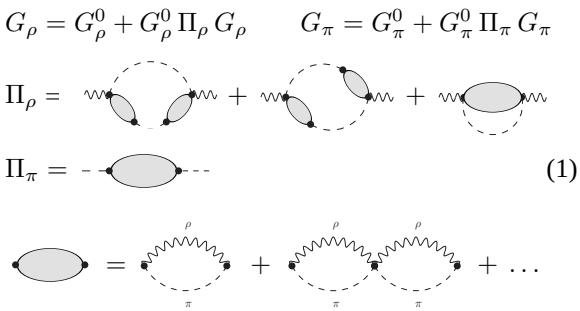

for the propagators G_ρ and G_π depending on the corresponding self-energies Π_ρ and Π_π.

Alongside we improved the method [1, 2, 5] to restore the four-transversality of the vector meson polarisation tensor, such that notoriously appearing spurious modes as in [5] are avoided.

In Fig. 1 we show the dependence of the pion spectral function on the temperature of the system. At zero temperature we have the normal pion pole and in addition a continuum contribution due to the coupling to $\rho\,\pi$-states. At finite temperature the separation between these two contributions vanishes. In addition we obtain strength bellow the vacuum on-shell pion due to scattering processes. In Fig. 2 we show the results for the ρ-meson width as resulting from our calculations at various temperatures. Displayed is the total width and the three partial processes[1]included in the model. We learn that due to the selfconsistent interplay between pion and ρ-meson the width in the $\pi\,\pi$-channel is a bit reduced at large temperatures as compared to the vacuum because pion strength is shifted towards larger masses (see Fig. 1) which effectively suppresses the phasespace for the ρ-meson decay. The other processes[1], $\rho \rightarrow \omega\,\pi$ and $\rho \rightarrow \rho\,\pi\,\pi$, become only important for rather high temperatures as compared to the two pion decay. Generally we conclude from our considerations that in a purely mesonic system also the inclusion of self-consistent effects and vertex corrections does not lead to a significant increase the width of the ρ-meson to a level which could explain the experimental dilepton yields [6] recently observed. Therfore baryonic effects are absolutely essential.

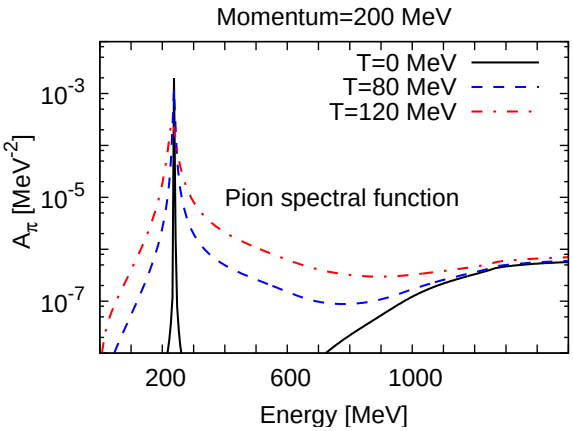

Figure 1: Pion spectral function depending on the temperature.

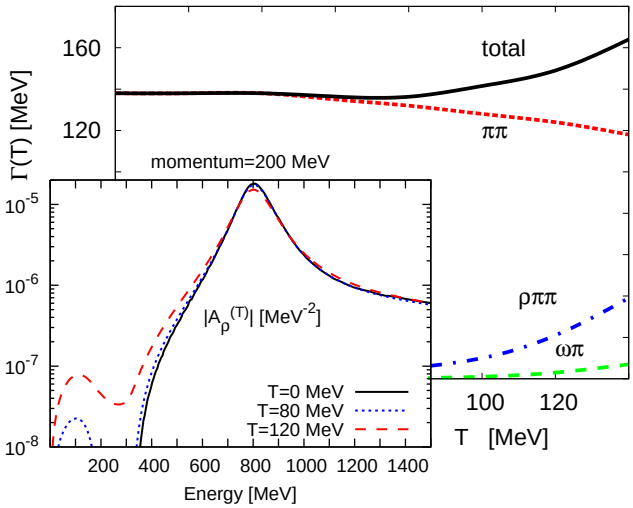

Figure 2: Transversal width of the ρ-meson depending on the temperature and the corresponding spectral function.

References

[1] H. van Hees and J. Knoll, Nucl. Phys. **A683**, 369 (2000).

[2] F. Riek and J. Knoll, Nucl. Phys. **A740**, 287 (2004).

[3] F. Riek, Phd Thesis, December 2007, http://elib.tu-darmstadt.de/diss/000925

[4] F. Riek, H. van Hees, and J. Knoll, Phys. Rev. C **75**, 059801 (2007).

[5] J. Ruppert and T. Renk, Phys. Rev. C **71**, 064903 (2005); Erratum-ibid.C75:059901 (2007)

[6] R. Arnaldi *et al.*, Phys. Rev. Lett. **96**, 162302 (2006).

[1]We included the ω-meson along the same lines as the ρ-meson [3].

Three-body effects in the linear-density approximation

S. Leupold[1,2]

[1]Institut für Theoretische Physik, Universität Giessen, Germany; [2]GSI, Darmstadt, Germany

It is shown that within thermal many-body theory three-body effects appear already in the linear-density approximation for the self-energy of a resonance, if the latter governs the production of particles as a doorway state. This sheds light on the question which aspects of an in-medium spectrum one can hope to describe by traditional transport theory based on two-body reactions of asymptotic states and which features are beyond that setup (note that resonance transport is not addressed here, for further details see [1]). Instead of a general framework I focus directly on an illustrative example, namely the production of dileptons in high-energy heavy-ion collisions. I assume further for simplicity that all dileptons are produced via a ρ-meson (doorway state, vector meson dominance). The key quantity is the spectral function of the considered doorway state:

$$\mathcal{A} = -\mathrm{Im}\frac{1}{q^2 - m_\rho^2 - \Pi} = \frac{-\mathrm{Im}\Pi}{|q^2 - m_\rho^2 - \Pi|^2}\,, \quad (1)$$

with the self-energy Π. In the following, I will study a nucleon-rich medium (density ϱ_N). The self-energy of the ρ is approximated by its two-pion vacuum contribution and an in-medium contribution given by a baryon-resonance nucleon-hole excitation. Using the ρ-N scattering amplitude T one gets in the linear-density approximation

$$\Pi(q) \approx \Pi_{2\pi}(q) + \Pi_{N^* N^{-1}}(q) \approx \Pi_{\mathrm{vac}}(q) + \varrho_N\, T(q)\,. \quad (2)$$

The baryon resonance in turn is assumed to have two decay branches: the ρ-nucleon branch and a pion-nucleon branch. I will further assume that the latter is the dominant one. It is interesting to observe that the linear-density approximation *for the self-energy* (2) enters the spectral function in the denominator. Hence the linear-density effects are iterated to arbitrary high orders. This ensures unitarity [2]. On the other hand, to explore which elementary scattering reactions are covered by (1,2) it is useful to expand (1) up to linear order in ϱ_N. As a first step I will detail the intuitive two-body collision part covered by (1,2). If one replaces on the right hand side of (1) the self-energy in the numerator by (2) and in the denominator by its vacuum part, one gets

$$\mathcal{A} \to \frac{-\mathrm{Im}\Pi_{\mathrm{vac}}}{|q^2 - m_\rho^2 - \Pi_{\mathrm{vac}}|^2} + \frac{-\varrho_N \mathrm{Im}T}{|q^2 - m_\rho^2 - \Pi_{\mathrm{vac}}|^2}\,. \quad (3)$$

I have assumed that the imaginary part of the scattering amplitude is governed by the process $N + \rho \to N^* \to N + \pi$. Therefore the processes on the right hand side of (3) translate via detailed balance to the following dilepton production processes: The first process corresponds $\pi + \pi \to \rho \to$ dileptons whereas the second relates to $N + \pi \to N^* \to N + \rho \to N +$ dileptons. These are the standard two-body production processes (with vacuum cross sections!) which one expects. Such processes can easily be included in a Boltzmann-type transport approach to dilepton production. However, the formulae (1,2) contain more. A *systematic* linear-density expansion reveals additional terms:

$$\mathcal{A} \approx \mathcal{A}_{\mathrm{vac}} - \varrho_N \mathrm{Im}\left[\left(\frac{1}{q^2 - m_\rho^2 - \Pi_{\mathrm{vac}}}\right)^2 T\right]\,. \quad (4)$$

Their graphical interpretation is depicted in Fig. 1. Obviously, subtle interferences with three-body interactions come into play. In addition, disconnected diagrams have to be subtracted which precludes a simple probabalistic interpretation. In Fig. 2 I compare the respective contribution to

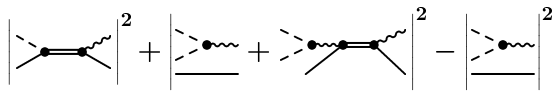

Figure 1: Graphical interpretation of the in-medium part of (4). Dashed/wavy lines denote pions/ρ-mesons, full/double lines nucleons/baryon resonances.

the dilepton production from the right hand sides of (1,3,4). In particular one sees that the in-medium depletion of the ρ-meson peak is not covered, if only two-body reactions are included in a virial expansion or a transport approach. This calls for in-medium cross sections or resonance transport.

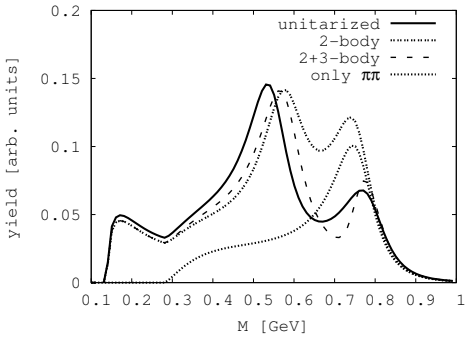

Figure 2: Full line: dilepton production from (1); dash-dotted: from (3); dashed: from (4); dotted: from pions.

References

[1] S. Leupold, *Trivial and non-trivial in-medium effects*, talk given at the "Discussion Forum: What do we learn from dilepton measurements in heavy-ion collisions?", Feb. 27, 2007, GSI, Darmstadt, http://www.gsi.de/documents/DOC-2007-Mar-19-1.pdf.

[2] J. Knoll, Prog. Part. Nucl. Phys. **42** (1999) 177.

Effects of mesonic correlations in the QCD phase transition*

D. Blaschke[1,2], M. Buballa[3], A. E. Radzhabov[2], and M. K. Volkov[2]
[1]University of Wroclaw, Poland; [2]JINR Dubna, Russia; [3]TU Darmstadt, Germany

The so-called PNJL model is an effective model of low-energy QCD, which is capable of describing the chiral as well as the deconfinement transitions (see, e.g., [1]). The model generalizes the well-known Nambu–Jona-Lasinio (NJL) model for the chiral quark dynamics by coupling it to the Polyakov loop, which serves as an order parameter of the deconfinement transition. To a large extent, this removes one of the most disturbing features of the original NJL model, namely the pressure contribution of unconfined quarks in the hadronic phase. In spite of its simplicity a remarkable agreement with the results of lattice QCD thermodynamics has been obtained within this model [1]. However, after successfully removing (most of) the unphysical quark degrees of freedom from the confined phase, the PNJL model treated in mean-field approximation does not contain *any* degree of freedom in this regime. Obviously, this is a rather poor description of the hadronic phase at finite T where mesons are expected to become relevant.

To get a more realistic picture we have therefore extended the model beyond the mean-field approximation and included mesonic correlations [2]. To that end we used a non-local version of the PNJL model and performed a systematic $1/N_c$ expansion of the thermodynamic potential up to next-to-leading order. While the leading order contributions correspond to the mean-field approximation, the next-to-leading order terms describe the mesonic fluctuations. Diagrammatically the latter are given by the ring sum of quark-antiquark polarization loops in the pion and sigma channels.

Our results for the pressure p, divided by the Stefan-Boltzmann limit p_{SB}, are displayed in Fig. 1. For comparison we also show the mean-field result and the mean-field plus pion contribution as well as the result for an ideal pion and sigma gas with the masses fixed at their vacuum values. We find that at low temperatures the mean-field (i.e., quark) contribution is suppressed and the pressure can be well described by a free pion gas. On the other hand, for $T > 1.5\ T_c$ the mesonic contributions are negligible and the quark-gluon mean-field dominates the pressure.

In Fig. 2 we show a comparison with lattice calculations [3, 4]. If we take unphysically large and temperature dependent current quark masses $m_c = 0.4T$, similar the lattice, the meson effects are suppressed (dotted line).

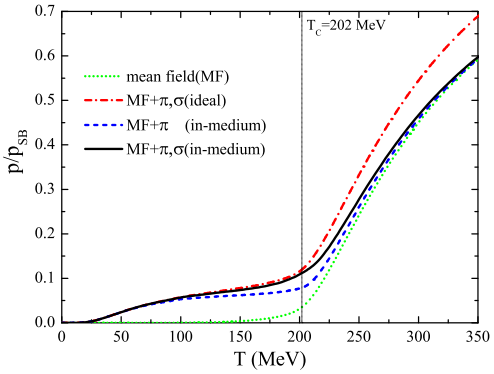

Figure 1: Scaled pressure p/p_{SB} in the nonlocal PNJL model with the physical pion mass: mean field contribution (dotted line), mean field + pion (dashed line), mean field + pion + sigma (solid line). The dash-dotted line denotes the scaled pressure of an ideal pion + sigma gas with fixed masses.

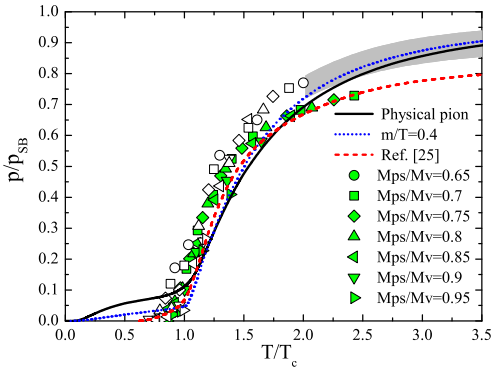

Figure 2: Scaled pressure p/p_{SB} as a function of T/T_c: non-local PNJL model with physical pion mass (solid line) and with $m_c/T = 0.4$ (dotted line). Dashed line: Lattice data for two-flavor QCD with staggered quarks [3]. The shaded region is an estimated continuum extrapolation of these data for massless QCD [3]. Points: Lattice data for two-flavor QCD with Wilson-type quarks [4] for $N_t = 6$ (open symbols) and $N_t = 4$ (filled symbols). The data for the pressure [4] have been divided by the Stefan-Boltzmann limit for $N_t = 6$ and $N_t = 4$, respectively, as given in Ref. [4].

References

[1] C. Ratti, M. A. Thaler and W. Weise, Phys. Rev. D **73**, 014019 (2006).

[2] D. Blaschke, M. Buballa, A. E. Radzhabov and M. K. Volkov, arXiv:0705.0384 [hep-ph].

[3] F. Karsch, E. Laermann and A. Peikert, Phys. Lett. B 478 (2000) 447.

[4] A. Ali Khan *et al.* [CP-PACS collaboration], Phys. Rev. D 64 (2001) 074510.

* Work supported by the Heisenberg-Landau programme, by the Russian Foundation for Basic Research, by BMBF and by the Polish Ministry of Science and Higher Education

Level crossing of particle-hole and mesonic modes in eta mesic nuclei

D. Jido[1], E.E. Kolomeitsev[2], H. Nagahiro[3], and S. Hirenzaki[4]

[1]YITP, Kyoto, Japan; [2]GSI, Darmstadt, Germany; [3]RCNP, Osaka, Japan; [4]Nara Women's University, Nara, Japan

The prominent feature of the η meson is that it couples dominantly to the $N^*(1535)$ (S_{11}) resonance at threshold energies. The low-momentum η meson would then mainly excite N^*–nucleon-hole (N^*-h) states in nuclear matter. Therefore the η meson nuclear dynamics is sensitive to modifications of nucleon and N^* properties in medium. If some medium effects and/or a density increase bring the N^*-h state down below the eta state, so that $m_\eta > m^*_{N^*}(\rho) - m_N * (\rho)$, the optical potential of the eta meson becomes repulsive [1]. Thus it is not sufficient to treat the η meson in a nucleus in terms of an energy-independent optical potential. In our study we describe the eta mode with the frequency ω and the momentum $\vec{k}$ propagating in nuclear medium with the density ρ by the Green's function $G_\eta(\omega, k; \rho) = 1/(\omega^2 - k^2 - m_\eta^2 - \Pi_\eta(\omega, k, \rho))$ with the polarization operator

$$\Pi_\eta(\omega, k; \rho) = \frac{g^2\,\rho\,\left(2\,\omega_R(k;\rho) - i\,\Gamma_{N^*}/2\right)}{[\omega - \omega_R(k;\rho) + i\,\Gamma_{N^*}/2]\,[\omega + \omega_R(k;\rho)]}\,.$$

The coupling constant $g \simeq 2$ follows from the $N^* \to \eta N$ decay width. We denote $\omega_R(k;\rho) = m^*_{N^*}(\rho) - m^*_N(\rho) + k^2/(2m^*_{N^*}(\rho))$. Our final results do not depend on details of the mechanism of the N and N^* mass reduction. In practice we use the chiral doublet model [2] for the medium modification of the N and N^* masses. In this model, the mass difference of the nucleon and N^* is related to the chiral condensate. Assuming its linear decrease with the nuclear density we use $m^*_{N^*}(\rho) - m^*_N(\rho) = (m_{N^*} - m_N)(1 - C\,\rho/\rho_0)$ with $C = 0.2$ [1] and ρ_0 being the nuclear saturation density. The imaginary part of the N^* self-energy is determined by the pionic decay, $N^* \to \pi N$, and the two-body absorption, $N^*N \to \pi NN$, calculated in [1, 3]. In

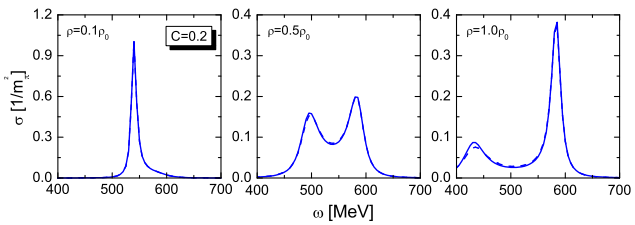

Figure 1: The η meson spectral density in nuclear matter densities.

Fig. 1 the spectral density of eta meson in nuclear matter $\sigma(\omega, k; \rho) = -\Im\, G_\eta(\omega, k; \rho)/\pi$ is shown for several values of the nucleon density at the vanishing momentum. At low density ($\sim 0.1\rho_0$) there is one peak, which corresponds to the eta mesonic mode. At higher densities a two-peak structure emerges associated with the particle-hole and mesonic modes. We study how these structures in the spectral function could reveal themselves in the finite nuclear systems and in η production reactions. We search for poles of the η-nucleus scattering amplitude on the complex energy plane by solving the Lippmann-Schwinger equation $\Psi(p) - \int_0^\infty dp' \frac{v_L(p,p';\omega)\,p'^{\,2}}{\omega^2 - m_\eta^2 - p'^{\,2} + i\epsilon}\Psi(p') = 0$, where Ψ is the wave function of the eta meson. The energy dependent potential is determined by the eta self-energy Π_η evaluated in the local density approximation: $v_L(p, p'; \omega) = \frac{2}{\pi}\int_0^\infty \mathrm{d}r\, r^2\, \Pi_\eta(\omega, 0; \rho(r)) j_L(p\,r)\, j_L(p'\,r)$. We put $k = 0$ since we consider slow eta excitations created for the recoilless kinematic conditions. For the spatial distribution of the nucleon density, $\rho(r)$, we use the 2-parameter Fermi distribution. We calculate the non-relativistic binding energy $E = (\omega^2 - m_\eta^2)/(2\,m_\eta)$ for ^{11}B, $L = 0$ and $C = 0.2$. On the first Riemann sheet we find two poles at $(-88.53 - i\,11.54)$ MeV and $(-74.13 - i\,15.00)$ MeV, which correspond to the deepest bound η state and its first radial excitation, respectively. On the same sheet there is a pole at $(6.40 - i\,0.46)$ MeV standing for a virtual state. On the second Riemann sheet there is a resonance state at $(61.02 - i\,25.82)$ MeV. The formation spectra of the eta meson in the (γ, p) reaction with the ^{12}C target calculated within the in-medium Green's function method [4] are shown in Fig. 2 for the photon energy $E_\gamma = 950$ MeV. The missing mass spectrum calculated with $C = 0.2$ has

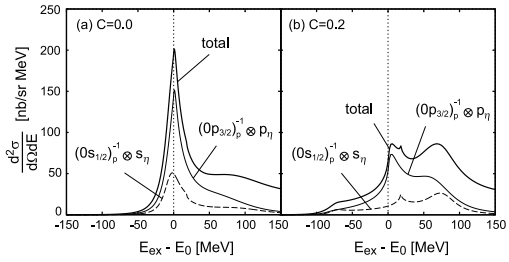

Figure 2: η formation spectra in $^{12}\mathrm{C}(\gamma, p)^{12}\mathrm{B}$ reaction.

richer structure than the one obtained with $C = 0$, when no level crossing takes place. The spectra with $C = 0.2$ has two bumps: a relatively clear peak at 80 MeV and a small bump at -80 MeV. They can be interpret as a manifestation of the resonance and bound states discussed above.

References

[1] H. Nagahiro *et al.*, Phys. Rev. C **68** (2003) 035205.

[2] D. Jido *et al.*, Prog. Theor. Phys. **106** (2001) 873.

[3] H. Kim *et al.*, Nucl. Phys. A **640** (1998) 77.

[4] O. Morimatsu and K. Yazaki, Prog. Part. Nucl. Phys. **33** (1994) 679.

The chiral and deconfinement transitions: PNJL model beyond mean field *

S. Rößner[1], T. Hell[1], C. Ratti[2], and W. Weise[1]

[1]Physik-Department, Technische Universität München; [2]Physics Department, SUNY, Stony Brook

The Polyakov loop extended Nambu and Jona-Lasinio model (PNJL model) in a mean field framework shows astonishingly good agreement with lattice QCD calculations. In particular the coincidence of chiral and deconfinement crossover transitions seen in both lattice QCD and in the PNJL model (see Fig. 1) is a feature that needs to be better understood.

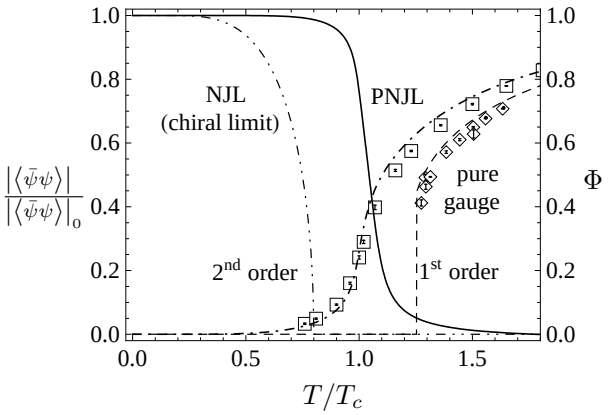

Figure 1: Combining aspects of confinement (Polyakov loop Φ) and spontaneous chiral symmetry breaking (condensate $\langle\bar{\psi}\psi\rangle$) results in a joint crossover in the PNJL model [1, 2, 3]. The lattice results [4] shown here also show this feature. (From Ref. [3])

In Ref. [3] we have presented a way to calculate corrections beyond mean field, resolving issues related to the complex fermion determinant in the PNJL model. This is achieved by means of a perturbative approach establishing a systematically ordered series of correction terms. We define the unperturbed model by the Taylor expansion up to second order in the fields of the real part of the bosonized effective action of the NJL model[1] plus the effective Polyakov loop potential[2]. The first term in such a Taylor expansion defines the mean field limit. Higher orders (beyond mean field) are treated using perturbative techniques. As a prominent example the thermal expectation values of the Polyakov loop $\langle\Phi\rangle$ and its conjugate $\langle\Phi^*\rangle$ are investigated here. Due to corrections beyond mean field the quantity $\langle\Phi\rangle - \langle\Phi^*\rangle$ assumes non-vanishing values once the quark chemical potential is non-zero.

Further important corrections to mean field theory are those generated by collective quark-antiquark excitations. Such collective modes model the effects of light mesons in this framework. In the 2-flavour NJL-model these excitations correspond to the pion and the σ-boson. Due to the small mass of the pion as a pseudo Goldstone mode the resulting corrections of the effective potential are typically larger than corrections related to Polyakov loop induced confinement. In comparison with the mean field (Hartree) pressure such corrections are small (see Fig. 2), supporting the overall picture and conclusions in Ref. [1]. Pionic contributions to the pressure are important, however, below T_c, as seen in Fig. 2.

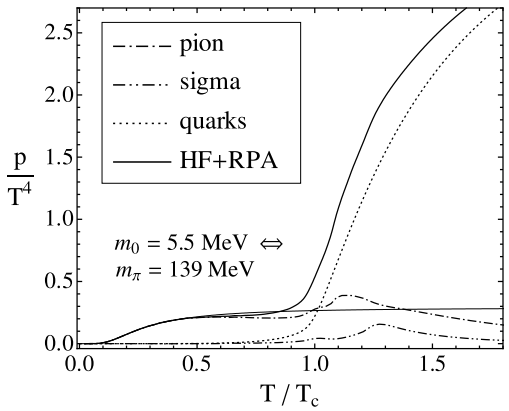

Figure 2: Corrections to the pressure due to dynamic light meson fluctuations (dash-dotted and dash-dot-dotted) plotted together with the mean field (Hartree) pressure (dotted). The thin solid line indicates the pressure of a free meson gas. (From Ref. [3])

On-going investigations involve non-local effective Lagrangians allowing to access temperatures and chemical potentials above the PNJL cutoff scale. At high momentum scales, where the applicability of the present model stops, non-local models are able to make contact with perturbative QCD.

References

[1] S. Rößner, C. Ratti and W. Weise, Phys. Rev. D **75**, 034007 (2007) [arXiv:hep-ph/0609281].

[2] C. Ratti, S. Rößner and W. Weise, Phys. Lett. B **649**, 57 (2007) [arXiv:hep-ph/0701091].

[3] S. Rößner, T. Hell, C. Ratti and W. Weise, arXiv:0712.3152 [hep-ph], and refs. therein.

[4] O. Kaczmarek, F. Zantow, Phys. Rev. D **71**, 114510 (2005) [arXiv:hep-lat/0503017].

* Work supported in part by BMBF, GSI, INFN, the DFG excellence cluster "Origin and Structure of the Universe" and by the Elitenetzwerk Bayern.

[1]The NJL parameters, current quark mass m_0, 4-quark coupling G and 3-momentum cutoff Λ are adjusted such that this part of the model reproduces physical pion properties.

[2]The Polyakov loop potential is parametrised such that is fulfils constraints imposed by the $\mathrm{SU}(3)_\mathrm{c}$ gauge symmetry of QCD. Its parameters are fixed such that pure glue lattice QCD results are reproduced.

The chiral critical surface of the three flavor quark-meson model

M. Wagner*[1], B.-J. Schaefer[2], and J. Wambach[1,3]

[1]Institut für Kernphysik, TU Darmstadt; [2]Institut für Physik, Karl-Franzens-Universität Graz, Austria; [3]GSI, Darmstadt

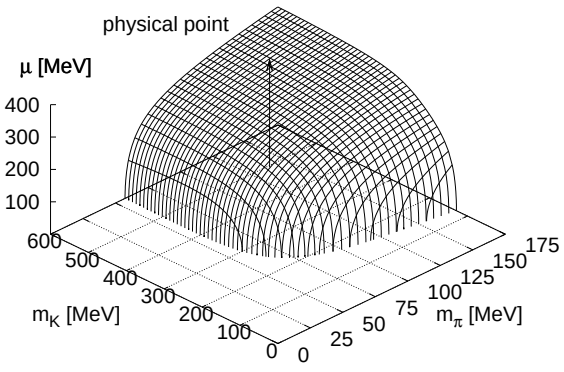

Figure 1: The chiral critical surface with $U(1)_A$ anomaly in the (m_π, m_K) plane.

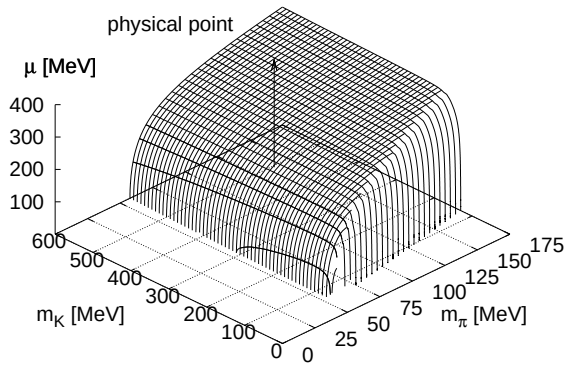

Figure 2: Similar to Fig. 1 but without $U(1)_A$ anomaly.

The question of the existence of a critical endpoint (CEP) in the phase diagram of Quantum Chromodynamics (QCD) is not yet settled. This issue is and will be investigated in current (e.g. RHIC, BNL) and future experiments (e.g. FAIR). These experiments provide access to different regions in the QCD phase diagram in the plane of temperature (T) and baryon chemical potential (μ_B). Lattice calculations can be trusted well at zero chemical potential. For three quark flavors the chiral phase transition is found to be a rapid crossover [1], while the precise value of the critical temperature is still under debate (see e.g. [2]). At finite chemical potential lattice methods suffer from the fermion-sign problem. There exist several methods that try to access at least the region at small chemical potential [2]. Some results with these methods put the existence of a critical endpoint into question [3].

Our investigation in an effective three flavor quark-meson model is carried out in a mean-field approximation. In this approximation the integration over the mesonic degrees of freedom is omitted and the fields are replaced by their constant expectation values. In this way mesonic fluctuations are neglected while the fermionic fluctuations are included. The parameters of the model with and without explicit $U(1)_A$ symmetry breaking respectively are fitted to the known pseudoscalar masses $(m_\pi, m_K, m_\eta^2 + m_{\eta'}^2)$, the scalar sigma mass m_σ and decay constants (f_π, f_K) at the physical point. The Yukawa coupling has been fixed to reproduce a light quark mass of $m_{u,d} = 300$ MeV.

The chiral critical surface is calculated as a function of the pion and kaon masses. To tune these values we varied the strength of the explicit chiral symmetry breaking in the strange and non-strange directions while all other parameters were kept fixed to their values at the physical point.

In Figs. 1 and 2 the chiral critical surface is shown for $m_\sigma = 800\,\text{MeV}$. The standard scenario in which the surface bends towards higher masses is confirmed for both cases. For low pion and kaon masses the phase transition is complete of first order. In the chiral limit this is also expect from universality arguments. Without explicit $U(1)_A$ symmetry breaking the shape of the surface only weakly depends on both masses. This is an effect of the missing anomaly breaking term, which introduces a coupling of the strange and non-strange fields in the grand canonical potential.

A similar investigation with comparable results has been done by Kovacs et al. [4] in a different approximation.

Within the three flavor quark-meson model we have confirmed the existence of a CEP and calculated the chiral critical surface in mean-field approximation. It is known that fluctuations modify both, the position and the size of the critical region [5]. It is therefore natural to go beyond mean-field approximation. This is planed using Renormailzation Group techniques.

References

[1] Y. Aoki, G. Endrodi, Z. Fodor, S. D. Katz, and K. K. Szabo, Nature **443**, 675 (2006).

[2] O. Philipsen, `arXiv:0708.1293 [hep-lat]`,

[3] P. de Forcrand, S. Kim, and O. Philipsen, `arXiv:0711.0262 [hep-lat]`,

[4] P. Kovacs and Z. Szep, Phys. Rev. **D75**, 025015 (2006).

[5] B.-J. Schaefer and J. Wambach, Phys. Rev. **D75**, 085015 (2007).

* mathias.wagner@physik.tu-darmstadt.de

The Phase Structure of the Polyakov-Quark-Meson Model

B.-J. Schaefer*[1], J.M. Pawlowski[2], and J. Wambach[3,4]

[1]Universität Graz, Austria; [2]Universität Heidelberg, Germany; [3]TU Darmstadt; [4]GSI, Darmstadt, Germany

In the heavy-quark limit of QCD the Polyakov loop expectation value serves as an order parameter for the confinement-deconfinement phase transition. A thermodynamic potential for the Polyakov loop can be constructed where the parameters are fitted to precise finite-temperature lattice data for the equation of state in the heavy-quark limit. A first-order confinement-deconfinement phase transition at the critical temperature $T_0 = 270$ MeV is found.

In the limit of vanishing quark masses, QCD exhibits an exact chiral symmetry. An effective realization of this symmetry and its breaking is provided by the quark-meson model.

The combination of both aspects of QCD through the coupling of the light chiral quarks to the Polyakov loop field results in the Polyakov-loop extended quark-meson (PQM) model which has the benefit of renormalizability and a simpler linkage to full QCD compared to other effective Polyakov-loop extended models. In the PQM model the relation between the deconfinement and chiral phase transition can be explored (for more details and references see [1]). The thermodynamic potential and the resulting phase structure is calculated in the mean-field approximation.

Even at the mean-field level there remain open issues: the Polyakov loop potential is fixed at vanishing chemical potential. In this case, the expectation value of the Polyakov loop operator, Φ and that of its adjoint, $\bar{\Phi}$ are linked by complex conjugation. This relation is lost at finite chemical potential and the effective potential depends on two independent variables $\Phi, \bar{\Phi}$. Moreover, the flavor and density dependence of the pure Yang-Mills potential has not been explored as yet. By using perturbative RG arguments as well as physical consistency arguments we extract the qualitative behaviour in the fully coupled system in this work.

In pure Yang-Mills theory the mean values are given by the minima of the effective Polyakov loop potential. Here a polynomial expansion in Φ and $\bar{\Phi}$ of the potential up to quartic terms has been used. This leads to an effective potential in terms of the moduli $|\Phi|$ and $|\bar{\Phi}|$ those expansion coefficients are fixed to lattice data. All coefficients are temperature-independent except the one, b_2, of the quadratic terms which is a function of the ratio T_0/T.

Moreover, the coefficient b_2 genuinely depends on the running coupling which is also changed in the presence of dynamical quarks. In our approximation to the Polyakov loop potential the inclusion of quarks then only leads to a modification of the expansion b_2. By means of RG arguments this effect can be modeled by changing the critical temperature T_0 into an N_f-dependent one, i.e. $T_0 \to T_0(N_f)$, cf. Tab. 1.

N_f	0	1	2	$2+1$	3
T_0 [MeV]	270	240	208	187	178

Table 1: Critical Polyakov loop temperature T_0 for N_f massless flavors.

The critical temperatures shown in Tab. 1 agree with lattice results. Moreover, the chiral crossover temperature also agrees with T_0.

In the presence of a finite chemical potential the running coupling is not only N_f- but also μ-dependent. Consequently, this leads to a T_0 with an additional μ-dependence.

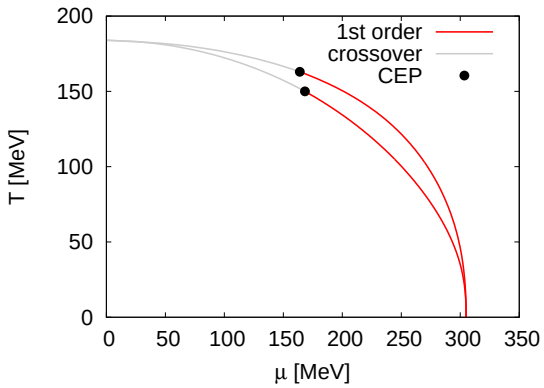

Figure 1: Chiral phase diagrams for the two-flavor PQM model . Upper curve for a μ-independent Polyakov loop potential and lower curve with μ-dependent corrections. The critical endpoints (CEP) are located at $(T_c, \mu_c) = (163, 164)$ MeV (upper case) and at $(150, 168)$ MeV (lower case).

In Fig. 1 the chiral phase diagram obtained for a μ-independent $T_0(N_f)$ (upper curve) and for a μ-dependent $T_0(N_f, \mu)$ (lower curve) is shown.

For a μ-independent $T_0(N_f)$ the corresponding confinement-deconfinement transition line is above the chiral one and for an RG improved $T_0(N_f, \mu)$ the confinement-deconfinement transition temperatures coincides with the chiral one.

References

[1] B.-J. Schaefer, J. M. Pawlowski, and J. Wambach, Phys. Rev. **D76**, 074023 (2007).

* bernd-jochen.schaefer@uni-graz.at

Density fluctuations in the presence of spinodal instabilities

B. Friman[1], C. Sasaki[1], and K. Redlich[2]

[1]GSI, Darmstadt, Germany; [2]Institute of Theoretical Physics, University of Wrocław, Poland

One of the central questions addressed in the context of QCD is the phase structure and the phase diagram of strongly interacting matter at finite temperature and baryon number density. Based on calculations in effective models and in the Lattice Gauge Theory one finds that for physical values of the quark masses the transition at high temperature and low net baryon number density is continuous [1, 2, 3]. In the opposite limit of low temperature and large density the QCD phase transition is expected to be first order. This suggests that the phase diagram exhibits a critical end point (CEP), where the first order chiral transition of QCD terminates [1, 2]. Modifications in the magnitude of fluctuations or the corresponding susceptibilities have been suggested as a possible method to probe the QCD phase diagram related with deconfinement and chiral symmetry restoration [1, 2]. The fluctuations of baryon number and electric charge diverge at the critical end point, while they are finite along the cross over and first order phase boundaries. Consequently, singular fluctuations of baryon number and electric charge as well as a non monotonic behavior of these fluctuations as functions of the collision energy in heavy ion collisions have been proposed as possible signals for the QCD critical end point [1, 4]. However, the finiteness of the fluctuations along the first order transition depend on the assumption that this transition appears in equilibrium [2].

A first order phase transition is intimately linked with the existence of a convex anomaly in the thermodynamic pressure, which can be uncovered in non-equilibrium systems. There is an interval of energy density or baryon number density where the derivative of the pressure with respect to volume is positive. This anomalous behavior characterizes a region of instability in the temperature-density, (T, n_q)-plane. This region is bounded by the spinodal lines, where the pressure derivative with respect to volume vanishes. The derivative taken at constant temperature define the isothermal spinodal lines.

In Fig. 1 we show the evolution of the net quark number fluctuations $\chi_{\mu\mu}$ in the (T, n_q)–plane as obtained in the Nambu–Jona-Lasinio (NJL) model [2]. When entering the coexistence region, there is a singularity in $\chi_{\mu\mu}$ that appears when crossing the isothermal spinodal lines, where the fluctuations diverge and the susceptibility changes sign. Between the spinodal lines, the susceptibility is negative[1]. This implies an instability with respect to fluctuations of the baryon number when crossing the boundary between the chirally symmetric and broken phases. In the case of an equilibrium first order phase transition, the density fluctuations do not diverge. Thus, in equilibrium the fluctuations

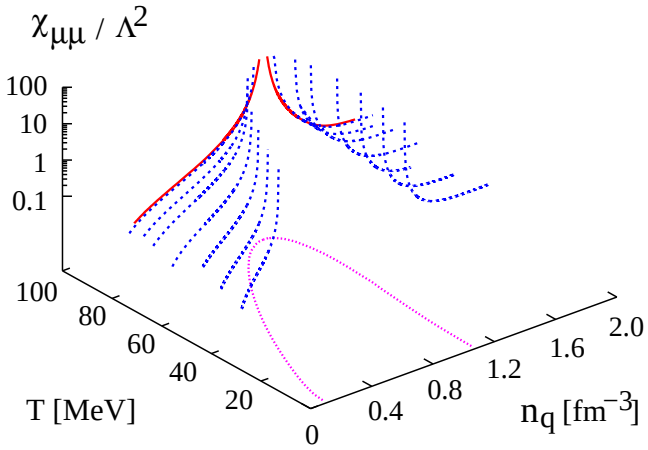

Figure 1: The net quark number susceptibility $\chi_{\mu\mu}/\Lambda^2$ in the stable and meta stable regions, as a function of the quark number density n_q and temperature T. The full line corresponds to the critical temperature T_c at the CEP and the dashed lines to the temperatures 30, 40, 50, 60, 70, 75 and 80 MeV. The dotted line shows the projection of the isothermal spinodal onto the (T, n_q) plane.

increase as one approaches the CEP along the first order transition and decrease again in the cross over region. This led to the prediction of a non-monotonous behavior of the fluctuations with increasing beam energy as a signal for the existence of a CEP [1, 4]. We stress that this is relevant only for the idealized situation where the first order phase transition takes place in equilibrium. In the more realistic non-equilibrium system one expects large fluctuations in a broad region of the phase diagram, i.e., over a broader range of beam energies, due to the spinodal instabilities. In fact, the signal from the first-order transition may be much stronger than that from the CEP [2]. Consequently, in the presence of spinodal phase separation, large fluctuations of baryon or electric charge densities can signal a first order phase transition [2] in the QCD medium.

[1]The negative branches of $\chi_{\mu\mu}$ are not shown in Fig. 1

References

[1] M. Stephanov, Acta Phys.Polon. B **35**, 2939 (2004).

[2] C. Sasaki, B. Friman and K. Redlich, Phys. Rev. Lett. **99**, 232301 (2007).

[3] C. R. Allton *et al.*, Phys. Rev. D **71**, 054508 (2005).

[4] C. Sasaki, B. Friman and K. Redlich, Phys. Rev. D **75**, 074013 (2007).

Hadronization in parton-hadron-string dynamics (PHSD) *

W. Cassing[1], E. L. Bratkovskaya[2], F. Frömel[1], and Yong-Zhong Xing[1]
[1]Univ. of Giessen, Germany; [2]FIAS, Frankfurt, Germany

The dynamics of ultra-relativistic nucleus-nucleus collisions at Super-Proton-Synchrotron (SPS), Relativistic-Heavy-Ion-Collider (RHIC) or future FAIR energies are of fundamental interest with respect to the properties of hadronic/partonic systems at high energy densities. Here we address the transition from partonic to hadronic matter within the Parton-Hadron-String-Dynamics (PHSD) transport model. This novel transport approach is an extension of the familiar Hadron-String-Dynamics (HSD) model [1] and includes additionally an early partonic phase with an equation of state from lattice QCD and quasi-particle properties for massive quarks, antiquarks and gluons that have been obtained from fits to lattice results [2]. The partons are treated as quasi-particles with finite spectral width [3] and propagated off-shell with strict flavor current conservation employing partonic mean fields that are determined in the Dynamical QuasiParticle Model (DQPM) [4]. On the partonic side elastic and inelastic interactions are included ($qq \leftrightarrow qq$, $\bar{q}\bar{q} \leftrightarrow \bar{q}\bar{q}$, $gg \leftrightarrow gg$, $gg \leftrightarrow g$, $q\bar{q} \leftrightarrow g$ etc.) exploiting 'detailed-balance' with cross sections extracted in Refs. [2, 4]. The transition from partonic to hadronic degrees of freedom is described by the fusion of off-shell partons (e.g. $q + \bar{q} \leftrightarrow M$ or $q + q + q \leftrightarrow B$) to color neutral mesonic (M) or baryonic (B) resonances of finite width (or strings) fulfilling energy and momentum conservation as well as flavor current conservation. The respective matrix element in either direction is a function of the local parton density ρ_p (or energy density ϵ) and is determined by the effective interaction in the DQPM [4] which turns strongly attractive below $\rho_p \approx 2.2 fm^{-3}$ to bind the dynamical partons to composite hadrons. On the hadronic side PHSD treats explicitly the familiar baryon octet and decouplet and selected higher resonances as well as their antiparticles. On the meson side it includes the pseudoscalar and vector meson nonets as well as some higher meson resonances (a_1 etc.). Hadrons of even higher masses (> 1.5 GeV in case of baryons and > 1.3 GeV in case of mesons) are treated as 'strings' that reflect the continuum excitation spectrum of mesons or baryons and decay to the known hadrons within HSD [1].

The present report addresses the expansion dynamics of a partonic fireball at initial temperature $T = 1.7 T_c$ (T_c= 0.185 MeV) with quasiparticle properties determined by the DQPM (in line with lattice QCD) [4] at finite quark chemical potential μ_q. The initial distribution in coordinate space is taken as an ellipsoid with an axis ratio a_y^2/a_x^2 = 2 in order to allow for the built-up of elliptic flow (as in semi-central nucleus-nucleus collisions at relativistic energies). Note that the dynamical evolution of the system is entirely described by the transport dynamics in PHSD! The time evolution of the quark(+antiquark), the gluon as well as meson and baryon(+antibaryon) number is shown in Fig. 1 (for μ_q = 0) as a function of time and indicates the gradual transition from partons to hadrons. The latter emerge first at the surface of the partonic fireball and then hadronization proceeds further to the fireball center. The hadronic decomposition is dominantly determined via parton fusion to mesonic or baryonic strings and their hadronic decays. Since on average the number of hadrons from the string decays is larger than the initial number of fusing partons the hadronization process leads to an increase of the total entropy. Furthermore, the particle ratios K/π, N/π, Λ/π etc. follow the microcanonical statistics of string decays and thus lead to approximately 'thermal' hadron abundancies (in line with the statistical hadronization picture of Braun-Munzinger and Stachel [5]). When applying the grandcanonical statistical model the various particle ratios lead to a 'freeze-out' temperature $T_f \approx 160 - 170$ MeV.

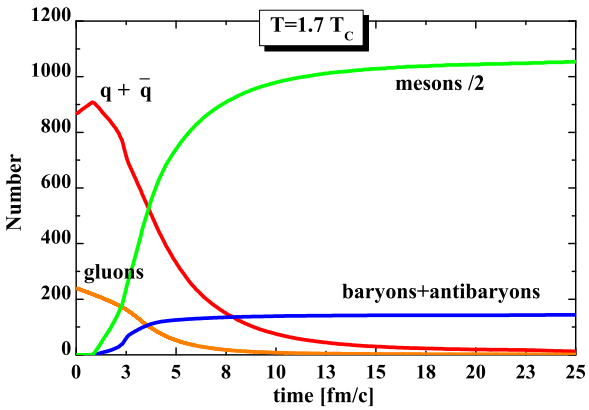

Figure 1: Time evolution in the parton, meson and baryon number for an exploding partonic fireball at initial temperature $T = 1.7\, T_c$.

References

[1] W. Cassing, E. L. Bratkovskaya, Phys. Rep. 308 (1999) 65.

[2] A. Peshier, W. Cassing, Phys. Rev. Lett. 94 (2005) 172301.

[3] F. Frömel, S. Leupold, Phys. Rev. C 76 (2007) 035207.

[4] W. Cassing, Nucl. Phys. A 791 (2007) 365; *ibid.* A 795 (2007) 70.

[5] P. Braun-Munzinger *et al.*, Phys. Lett. B 365 (1996) 1; *ibid.* B 465 (1999) 15; *ibid.* B 518 (2001) 41.

* Work supported by GSI and BMBF

Evidence for non-hadronic interactions of charm in heavy-ion collisions*

O. Linnyk[†1], E. L. Bratkovskaya[1], W. Cassing[2], and H. Stöcker[1,3]

[1]Frankfurt Institute for Advanced Studies, Frankfurt am Main, Germany; [2]Institut für Theoretische Physik, Universität Giessen, Giessen, Germany; [3]GSI, Darmstadt, Germany

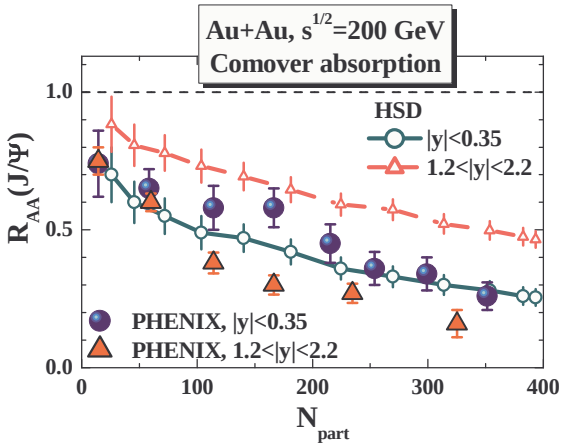

Figure 1: The J/Ψ nuclear modification factor R_{AA} in comparison to the data [2] for midrapidity (circles) and forward rapidity (triangles) in the purely hadronic 'comover' scenario, see [3] for details.

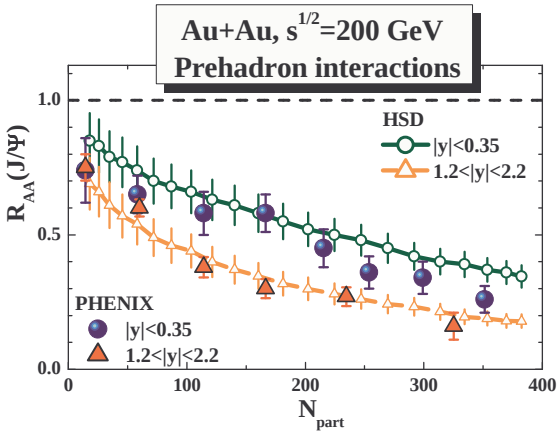

Figure 2: The HSD results for the hadronic 'comover' scenario including additionally pre-hadronic interactions of charm as compared to the data from [2].

An investigation of the formation and suppression dynamics of J/Ψ, χ_c and Ψ' mesons opens the possibility to address fundamental questions about the properties of the state of matter at high temperature and density. Up to date, a simultaneous description of the seemingly energy-independent suppression of J/Ψ together with its narrow rapidity distribution and a strong elliptic flow v_2 of charmed hadrons - as found at the Relativistic-Heavy-Ion-Collider (RHIC) - has presented a challenge to microscopic theories. Employing the Hadron-String-Dynamics (HSD) approach [1], we study a wide range of charm observables for energies from about 20 A·GeV - relevant for the FAIR facility - up to top RHIC energies.

The essential new result of our investigation is that (at top RHIC energies) we find evidence for strong interactions of charm with the pre-hadronic medium. In particular, pre-hadronic interactions (of unformed hadrons) with charm lead to dramatically different rapidity distributions for J/Ψ's and consequently to a substantially modified ratio $R_{AA}^{forward}(J/\Psi)$ to $R_{AA}^{mid}(J/\Psi)$ compared to earlier calculations/predictions.

Further results of our microscopic transport study may be stated as follows:

- The J/Ψ suppression in d+Au collisions at $\sqrt{s}$ = 200 GeV is compatible with the charmonium absorption on nuclei as observed at SPS energies in p+A reactions.
- The Ψ' to J/Ψ ratio is found to be crucial in disentangling different charmonium absorption scenarios. This result essentially emerges from the early dissociation of Ψ' above the critical energy density $\epsilon_c \approx 1$ GeV/fm^3 in the 'QGP melting scenario' whereas the Ψ' in the 'comover model' survives to higher energy densities.
- The collective flow of charm in the HSD transport appears compatible with the SPS data while it is substantially underestimated at top RHIC energies both in the standard hadronic comover scenario and when including interactions of charm with pre-hadronic states.

The open problem - and future challenge - is to incorporate explicit partonic degrees of freedom in the description of relativistic nucleus-nucleus collisions and their transition to hadronic states in a microscopic transport approach. On the experimental side further differential spectra of charmonia and open charm mesons then will constrain the transport properties of charm in the early non-hadronic phase of nucleus-nucleus collisions at RHIC (and possibly at SPS or even FAIR energies).

* Work supported by BMBF

† linnyk@fias.uni-frankfurt.de

References

[1] W. Cassing and E. L. Bratkovskaya, Phys. Rept. **308** (1999) 65.

[2] A. Adare *et al.* [PHENIX Collaboration], Phys. Rev. Lett. **98**, 232301 (2007).

[3] O. Linnyk, E. L. Bratkovskaya, W. Cassing and H. Stoecker, Phys. Rev. C **76**, 041901 (2007).

Multiplicity Fluctuations in Nucleus-Nucleus Collisions: Dependence on Energy and Atomic Number

V.P. Konchakovski[1,2], B. Lungwitz[3], M.I. Gorenstein[2,4], and E.L. Bratkovskaya[4]

[1]Helmholtz Research School, Frankfurt, Germany; [2]Bogolyubov Institute for Theoretical Physics, Kiev, Ukraine; [3]Institut für Kernphysik, University of Frankfurt, Frankfurt, Germany; [4]Frankfurt Institute for Advanced Studies, Frankfurt, Germany

The event-by-event fluctuations in high energy nucleus-nucleus (A+A) collisions are expected to be closely related to the transitions between different phases of QCD matter. Nucleus-nucleus collisions in the SPS energy region are expected to be a suitable tool for a search of critical point signatures [1].

An ambitious experimental program for the search of the QCD critical point has been started by the NA61 Collaboration at the SPS [2]. The program includes a variation in the atomic number A of the colliding nuclei as well as an energy scan. This allows to scan the phase diagram in the plane of temperature T and baryon chemical potential μ_B near the critical point as argued in Ref. [2]. One expects to 'locate' the position of the critical point by studying fluctuations. High statistics multiplicity fluctuation data will be taken for p+p, C+C, S+S and In+In collisions at bombarding energies of E_{lab}=10, 20, 30, 40, 80, and 158 AGeV.

We study the energy and system size dependence of event-by-event multiplicity fluctuations within the microscopic transport approaches HSD and UrQMD. Our study thus is in full correspondence to the experimental program of the NA61 Collaboration [2].

To minimize the event-by-event fluctuations of the number of nucleon participants the NA61 Collaboration fix number of projectile participants N_P^{proj}. In each sample with $N_P^{proj} = const$ the number of target participants, N_P^{targ}, fluctuates with the scaled variance

$$\omega_P^{targ} = \frac{\langle (N_P^{targ})^2 \rangle - \langle N_P^{targ} \rangle^2}{\langle N_P^{targ} \rangle}$$

The fluctuations of N_P^{targ} are quite strong for peripheral reactions and small for the most central collisions (Fig. 1, top). Thus, one can get rid of target participants fluctuations by considering only most central collisions [3, 4].

We consider the centrality selection procedure by fixing the number of projectile participants N_P^{proj}. This corresponds to the real situation of $A + A$ collisions in fixed target experiments. We select 1% most central collisions which correspond to the largest values of N_P^{proj}.

For the 1% most central $A+A$ collision events - selected by the largest values of N_P^{proj} - the HSD multiplicity fluctuations are shown in Fig. 1, bottom.

The smooth energy and atomic number dependence for the multiplicity fluctuations obtained in HSD without explicit phase transition demonstrate that the expected enhanced fluctuations - attributed to the critical point and phase transition - can be observed experimentally on the top of a monotonic and smooth 'background'. Our findings are essential for the optimal choice of collision systems for the experimental search for the QCD critical point.

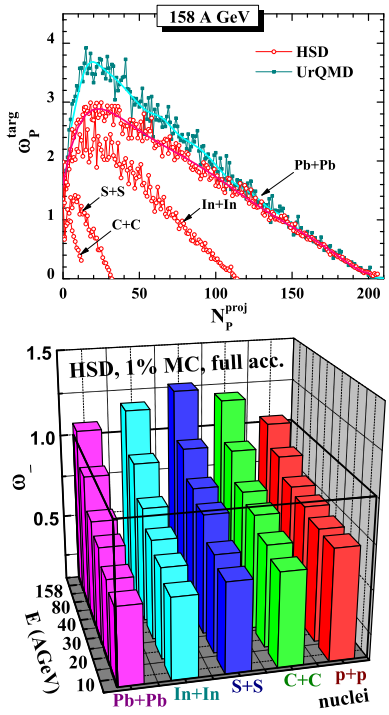

Figure 1: *Top:* the HSD simulations of ω_P^{targ} as a function of N_P^{proj} are shown for In+In, S+S, and C+C collisions at E_{lab}=158 AGeV. The HSD and UrQMD results for Pb+Pb collisions are taken from Ref. [3]. *Bottom:* the HSD results for ω_- in A+A and p+p collisions for the full 4π acceptance. The 1% most central C+C, S+S, In+In, and Pb+Pb collisions at E_{lab}=10, 20, 30, 40, 80, 158 AGeV are selected by choosing the largest value of N_P^{proj}.

References

[1] M.A. Stephanov, K. Rajagopal, and E.V. Shuryak, Phys. Rev. Lett. **81**, 4816 (1998); Phys. Rev. D **60**, 114028 (1999); M.A. Stephanov, Acta Phys. Polon. B **35**, 2939 (2004).

[2] M. Gazdzicki *et al.* [NA61 Collaboration], PoS C**POD2006**, 016 (2006), [arXiv:nucl-ex/0612007].

[3] V.P. Konchakovski, M.I. Gorenstein, E.L. Bratkovskaya, and H. Stoecker, Phys. Rev. C **73**, 034902 (2006).

[4] V.P. Konchakovski, B. Lungwitz, M.I. Gorenstein and E.L. Bratkovskaya, arXiv:0712.2044 [nucl-th].

Importance of three-body collisions in transport theory

A. Larionov[1,2,3], O. Buss[1], K. Gallmeister[1], and U. Mosel[1]

[1]Institut für Theoretische Physik, Universität Giessen, Germany; [2]Frankfurt Institute for Advanced Studies, J.W. Goethe-Universität Frankfurt, Germany; [3]Russian Research Center Kurchatov Institute, Moscow, Russia

Transport theory, based on binary collisions and on the propagation of particles in a selfconsistent mean field, is a very useful tool in understanding heavy-ion collisions in the energy region from the Fermi energies ($E_{\rm lab} \sim 30$ A MeV) up to relativistic energies ($E_{\rm lab} \sim 2$ A GeV). There are, however, systematic deviations from experimental data on pion and kaon production at $E_{\rm lab} > 2$ A GeV: The pion multiplicity is systematically overpredicted, while the slopes of the K^+ transverse mass spectra are too steep in the transport calculations. This suggests that the transport models do not produce enough thermalization. One possible explanation is that non-hadronic degrees of freedom are missing. Exploring more mundane explanations we study whether hadronic many-body collisions — usually missed in the current transport calculations at high energies — could serve as an additional source of the thermalization (see [1] for details and further references).

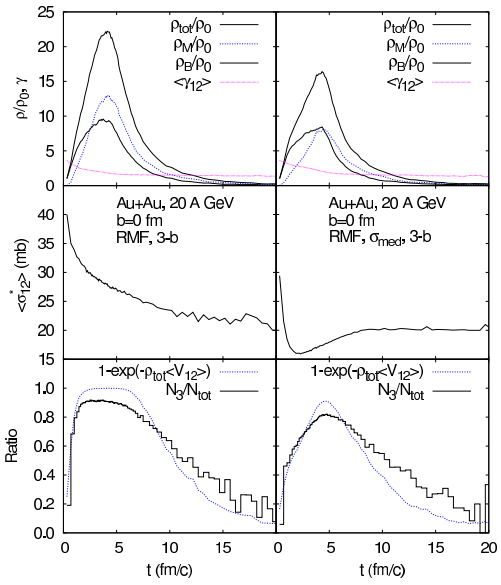

Figure 1: Top panels: Time dependence of total (baryon plus meson) density (thick solid lines), meson density (dashed lines), baryon density (thin solid lines) and γ-factor averaged over colliding pairs (dotted lines). Middle panels: Cross section averaged over colliding pairs. Bottom panels: Ratio of three-body and total (two- plus three-body) collision frequencies (solid histograms) and analytic estimate (dashed lines). Calculations are done with RMF including three-body collisions with vacuum (left) and in-medium (right) cross sections. See [1] for more details.

Fig. 1 highlights the importance of three-body collisions: At the time when the density of colliding particles is highest, three-body collisions by far overwhelm the two-body collisions. As a consequence also the transverse mass spectra in particular of kaons are influenced as can be seen in Fig. 2. We include three-body effects together with a relativistic mean field approach (RMF) and a proper in-medium modification of the collision cross sections. The latter is suggested due to the screening effects which naturally emerge in a very dense system. We conclude that the m_t spectra and also other observables can be reasonably well described, once three-body collisions are included into our GiBUU transport approach [1].

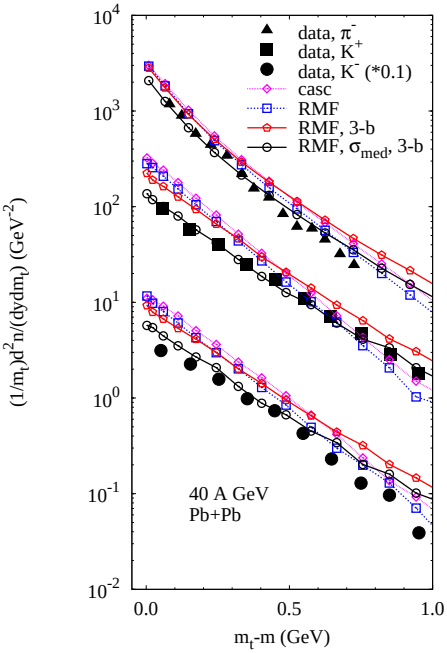

Figure 2: π^-, K^+ and K^- transverse mass spectra at midrapidity from central ($b \leq 4$ fm) Pb+Pb collisions at 40 A GeV. The rapidity region is $|y - y_{NN}| < 0.2$ for π^- and $|y - y_{NN}| < 0.1$ for $K^{\pm}$. Line coding: Binary cascade calculation — dotted lines with open rombuses; RMF calculation including binary collisions only and vacuum cross sections — dashed lines with open boxes; RMF including three-body collisions with vacuum cross sections — solid lines with open pentagons; RMF with three-body collisions and in-medium cross sections —- solid lines with open circles.

References

[1] A. B. Larionov, O. Buss, K. Gallmeister and U. Mosel, Phys. Rev. C 76 (2007) 044909.

Study of diamond surfaces and metalizations for detector applications*

R. Lovrincic and A. Pucci
Kirchhoff-Institut für Physik der Universität Heidelberg

We investigated the metal-diamond interface formation and the growth of chromium thin films as contact material on diamonds, which should help to improve single-crystal diamond (SCD) particle detectors.

As shown previously [1], we are able to derive information about metal film conductivity by means of infrared spectroscopy (IRS) and analysing the data with a Drude type dielectric function. In this manner we learned that Cr films deposited on diamond substrates at room temperature under ultra high vacuum (UHV) conditions exhibit a significantly lower electronic conductivity than bulk Cr, indicating a defect rich layer. For the next step towards understanding the physics of the Cr-diamond interface we investigated the annealing of Cr on SCD with IRS. In case of polycrystalline diamond (PCD), annealing at 900 K for 10 minutes is reported to result in the formation of a 1 nm thick chromium carbide (Cr_3C_2) interlayer, and therby lowering the specific contact resistance by roughly two orders of magnitude [2]. A similar annealing procedure is being used for Cr on SCDs as well, but a proof of carbide formation is lacking.

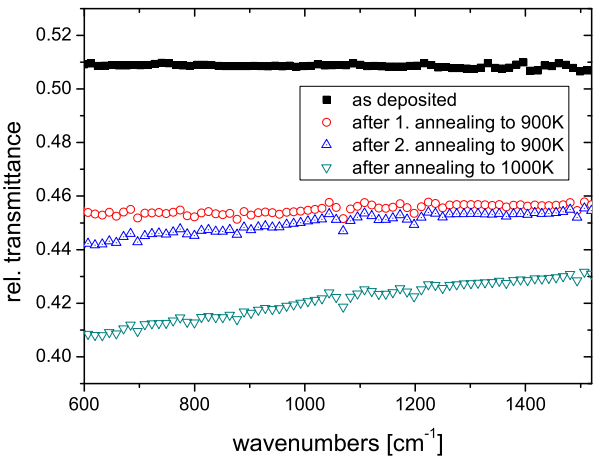

Figure 1: Relative transmittance of a 3.5 nm thick chromium film as deposited and after several annealing steps measured at 300 K. The measurement range is at the low frequency end constrained by our setup and by the inset of interband transitions at the high frequency end.Reference is the diamond substrate.

After depositing 3.5 nm of Cr on a (100) SCD as described in [1], the sample was twice annealed to 900 K for 10 minutes and then once to 1000 K for 10 minutes in UHV. The growth was monitord by IRS, heating was done by electron bombardment of the sample holder, which is made of molybdenum. A type-K thermocouple connected to the sample holder was used to measure the temperature. During annealing the pressure rose to the range of 10^{-8} mbar.

Figure 1 shows the relative transmission spectra of the as-deposited film and after each annealing step with the bare substrate as reference. Before annealing the film shows a nearly frequency independent transmission indicating an amorphous layer with a very short mean free path of the charge carriers. Analysing this spectrum with a Drude-type dielectric function indeed yields a relaxation rate much higher ($140000\,\mathrm{cm}^{-1}$) than typical values for metals. By exploiting the spectrum after the last annealing step in the same way, the obtained relaxation rate is $2800\,\mathrm{cm}^{-1}$, corresponding to a mean free path of roughly 3 nm. The spectra after annealing do not show vibrational features that would clearly indicate the formation of Cr_3C_2, unlike in the similar case of iron on silicon [3]. Several explanations are possible: first, due to a higher inertness of the SCD surface compared to PCD, the formation of a carbide might be hindered. Second, a high electrical conductivity of Cr_3C_2 would shield vibrational features in the spectra. Third, IRS might not be sensitive enough to detect a 1 nm thin layer of Cr_3C_2, because of weak IR activity. In order to answer this questions, further studies of the system by means of X-ray photo-electron spectroscopy are planned.

The effect of Cr-SCD interface annealing studied by IRS can be explained with a restructering of the Cr film, resulting in a better ordered layer with much higher mean free path of the electrons and hence higher conductivity. The formation of a interstitial chromium carbide layer could not be proved, but cannot be ruled out so far either.

Besides our research on diamond metalizations we investigated diamonds supplied by Element 6 with different surface qualities by means of atomic force microscopy. The aim is to find correlations between diamond surface quality and detector performance and finally decide which quality is needded for satisfying detector performance.

The authors gratefully acknowledge helpful discussions with E. Berdermann.

References

[1] R. Lovrincic and A. Pucci, GSI Scientific Report, p. 197 (2006).

[2] M. Yokoba et al., J. Appl. Phys.**81**, p. 6815 (1997).

[3] G. Fahsold et al., J. Appl. Phys. **91**, p. 145 (2002).

* Work supported by EU, project RII3-CT-2004-506078.

Cooling Force on Ions in a Magnetized Electron Plasma*

H.B. Nersisyan, G. Zwicknagel
Institut für Theoretische Physik, Universität Erlangen, Germany

Electron cooling is a well established method to obtain ion beams of high phase space density or to reduce the kinetic energy of ions in traps. To improve its theoretical understanding we investigated the underlying microscopic physics of the energy transfer in individual ion-electron interactions in the presence of a homogeneous magnetic field. This has been done both by analytic perturbative approaches as well as numerical simulations [1]. These studies finally aim at providing reliable cooling force models which can be used e.g. in the BETACOOL program [2].

There, a major question is the domain of validity of analytic expressions such as those presented in [1] which have been derived by 2nd-order perturbation theory. To that end we considered the energy transfer ΔE_i of an ion to a monoenergetic magnetized electron beam due to binary collisions. As ΔE_i depends on the relative ion-electron velocity v_r, it is more suited here than the cooling force itself which follows from ΔE_i by averaging over the velocity distribution of the electrons, i.e. over v_r. From a comparison with fully numerical (non-perturbative) Classical Trajectory Monte Carlo (CTMC) simulations we find as a quite general rule which is widely independent of the magnetic field strength that the predictions of the perturbative treatment are accurate for $v_r/v_c \gtrsim 5$, with the characteristic velocity $v_c = (|Z|e^2/4\pi\varepsilon_0 m_e\lambda)^{1/2}$, wherein are Z the ion charge, m_e the electron mass and λ the screening length of the effective ion-electron interaction. This observed behavior is demonstrated in Fig. 1 for a few examples of the energy transfer ΔE_i for an ion moving along the magnetic field.

In contrast, for low relative velocities $v_{r\|} \lesssim v_c$ the results obtained from perturbation theory (solid and dotted curves) strongly deviate from the CTMC-simulations. In this regime the latter display a large difference between positive ions (protons) [circles] and negative ions (antiprotons) [triangles, stars] which disappears for high $v_r \gtrsim 5v_c$. Such a difference is completely absent in the 2nd-order perturbative treatment where ΔE_i depends on Z^2 only, see [1].

The cooling forces obtained by the perturbative approach will thus be quite accurate if the low velocity regime only slightly contributes to the v_r-average over ΔE_i. That is, if the typical v_r, given by the maximum of the thermal electron velocity and the ion velocity, are large compared to v_c, as it is usually the case for electron cooling in storage rings. A detailed comparison with cooling force measurements is in progress.

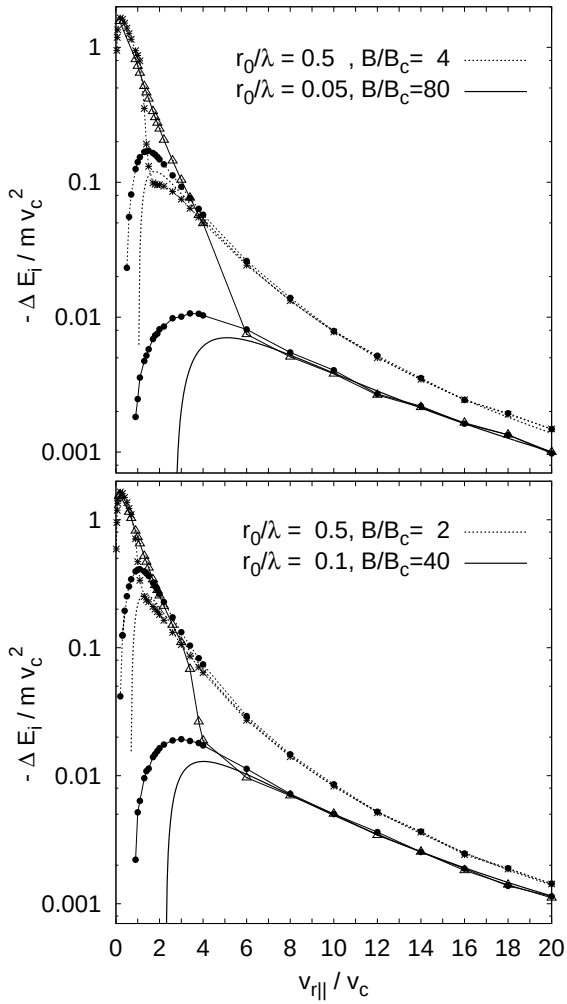

Figure 1: Average energy transfer ΔE_i of an ion moving along the magnetic field and colliding with a monoenergetic electron beam at a relative velocity $v_{r\|}$, different field strengths B and initial cyclotron radii r_0 in units of the screening length λ. Shown are results of CTMC-simulations for positive ions (circles) and negative ions/antiprotons (triangles, stars) and the predictions of the 2nd-order perturbative treatment (solid and dotted curves). Here B is scaled in $B_c = mv_c/e\lambda$ and all velocities in $v_c = (|Z|e^2/4\pi\varepsilon_0 m_e\lambda)^{1/2}$.

References

[1] H. Nersisyan, C. Toepffer, G. Zwicknagel, *Interactions Between Charged Particles in a Magnetic Field* (Springer, Berlin Heidelberg New York 2007)

[2] BETACOOL for the simulation of beam dynamics: http://lepta.jinr.ru/betacool/betacool.htm; A.O. Sidorin *et al.*, NIMA **558**, 325 (2006)

*Work supported by the BMBF (06ER145)

Numerical Simulations of the Calcium Projectile Charge Dependence on the Target Density

S. I. Eisenbarth (Korostiy)[1], O. N. Rosmej[1], V. P. Shevelko[2], D. H. H. Hoffmann[3]
[1]GSI, Darmstadt, Germany, [2]Lebedev Physical Institute, Moscow, Russia, [3]TU-Darmstadt, Germany

In the report we discuss results of numerical simulations of the projectile ion charge dependence on the target density. A five charge state collisional-radiative model has been developed [1], which accounts for collisional and non-collisional processes of the ion population kinetics in heavy ion stopping process and allows predictions of the projectile charge state distribution inside the target. The distribution of the population fractions over the energy levels of the ion Z is described by a system of rate equations for the multilevel kinetics. The model considers the ground and three excited states for each ion from bare till B-like ions. The differential equation for the ion population fraction $P_Z(k)$ of the level k can be written as:

$$\frac{dP_Z(k)}{dt} = \sum_{Z'}\sum_{i} B_{ik} P_{Z'}(i) - B_{kk} P_Z(k) \qquad (1)$$

where the coefficients B_{ik} are the rates of the atomic processes occurring between the level k of the ion Z and the level i of the ion Z' and B_{kk} denotes a sum of the atomic processes, which depopulate the level k of the ion Z.
The ion mean charge is defined as follows:

$$\langle Z \rangle = \sum_{z}\sum_{k} P_Z(k) \cdot Z \qquad (2)$$

Calculations of $P_Z(k)$ and <Z> were carried out for different *Ca*-projectile energies (4.0 - 11.4 MeV/u) and different densities of SiO_2 target. Figure 1 shows the charge state distribution of 6 MeV/u *Ca* ions propagating in SiO_2 of 10^{23} and 10^{19} at/cm^3 target densities. The *Ca* ion mean charge is <Z>=19.1 at solid density and 17.34 at gas density.

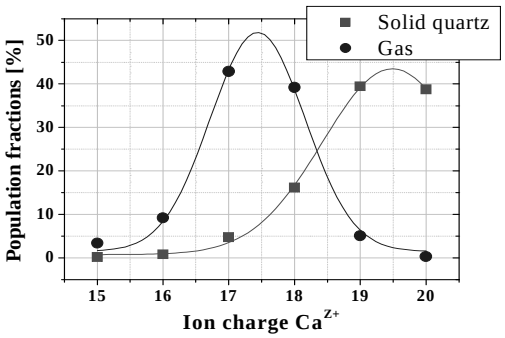

Fig.1 Charge state distribution of 6 MeV/u *Ca* ions propagating in SiO_2 target with densities of 10^{23} at/cm^3 (solid) and 10^{19} at/cm^3 (gas).

The reasons for the dependence of the ion charge state on the target density have been analyzed numerically. Figure 2 shows the total ionization and capture rates in Ca^{+19} versus the target density for two projectile energies.

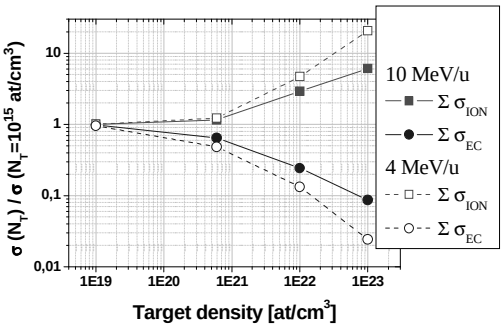

Fig. 2. Calculated total ionization and bound electron capture cross sections of Ca^{19+} ions interacting with SiO_2 as a function of the target density. Total cross sections are normalized to those at a low target density of 10^{15} at/cm^3.

Total ionization rates of ions were defined by:

$$\sigma_{ion}^{total} = P_{n0}\sigma_{ion}(n_0) + P_n^*\sigma_{ion}(n) + .., \qquad (3)$$

Here P_{n0} and P_n^* are the population fractions of the ground and excited states respectively; $\sigma_{ion}(n)$ is the ionization cross section from the level with the principal quantum number n. With growing target density, collisions lead to higher population of the ion excited states P_n^* having low electron binding energies. This results in a strong enhancement of the total ionization cross section. Collision processes lead to the suppression of the capture of the target bound electron to projectile excited states and as a consequence to the reduction of the total bound electron capture rates:

$$\sigma_{EC}^{total} = \sum_{n} \sigma_{EC}(n)/(1+\beta(n)), \qquad (4)$$

Here $\sigma_{EC}(n)$ is the cross section of the bound electron capture to the ion level n, $\beta(n)$ is a quenching factor defined as the ratio of the collisional to radiative rates for depopulation of the ion excited state. $\beta(n)$ is proportional to the target density and strongly depends on the principal quantum number as n^7. Only the electron capture into the ion energy level with low $\beta(n)$ contributes to the charge change process. Growth of the total ionization rates and the suppression of the capture processes at high target densities result in an increase of the ion mean charge.

References:

1. PhD-thesis, Svitlana Korostiy, TU-Darmstadt, 2007

An RFQ Mass Filter for SHIPTRAP*

E. Haettner[1,2], T. Dickel[1], B. Fabian[1,2], T. Fleckenstein[1], H. Geissel[1,2], M. Petrick[1], W. R. Plaß[1], and C. Scheidenberger[1,2]

[1]Justus-Liebig-Universität, Gießen, Germany; [2]GSI, Darmstadt, Germany

At SHIPTRAP, exotic nuclei produced in fusion reactions and separated from the primary beam in the velocity filter SHIP are stopped in a gas-filled stopping cell. The ions are extracted, bunched and transferred to a double Penning trap system, where their masses can be measured. Contaminant ions created in the gas-filled stopping cell and abundantly produced reaction products different from the nuclei of interest can significantly reduce the performance of SHIPTRAP. In order to remove the contaminant ions and thus increase selectivity and efficiency of the experiment, a radio-frequency quadrupole (RFQ) mass filter is being developed. It will also allow for diagnosis and identification of the ions delivered from the stopping cell.

Design Goals. The challenge of constructing a mass filter is to reach a maximum in transmission at a given resolution. At SHIPTRAP a high transmission is of particular importance, in order to avoid losses of the rare exotic ions. Since transmission losses are caused particularly at the entrance and the exit of the mass filter, the mass filter is developed in a matched combination with an RFQ cooler and an RFQ buncher located in front of, and behind the mass filter, respectively. The following causes for transmission losses were examined in detail with help of the simulation programs COMSOL, SIMION [1] and ITSIM [2, 3]:

(i) Collisional losses: In order to cool the ions the RFQ cooler and buncher are operated with buffer gas. This leads to a significant pressure also in the mass filter. Collisions with the rest gas cause a change in the ions' oscillation amplitudes and therewith to transmission losses and deteriorated peak shapes. Computer studies have been used to determine a tolerable upper limit for the residual gas pressure in the mass filter and a lower limit for the buffer gas pressure in the RFQ cooler and buncher and hence the diameter of the apertures between the RFQs.

(ii) Ion entrance: The use of an entrance diaphragm results in field distortions and thus to an expansion of the beam and larger oscillation amplitudes. This causes ion losses on the quadrupole rods and the exit diaphragm. These losses can be minimized by reducing the field distortions. For this purpose a fourfold segmented electrode diaphragm operated with RF voltage was developed. In addition, simulations show that the effect of the field distortions can be reduced by the use of Brubaker lenses [4].

(iii) Ion exit: It is possible to reduce ion losses on the exit diaphragm by operating the instrument in a focusing mode [5]. Ions that are travelling with the same velocity have nodes in their oscillations at the same position (Fig. 1, left). Through an appropriate choice of the DC potentials, the ion velocity can be modified such that a node is present where the mass selective part of the mass filter ends. Hence the ions can be transmitted efficiently through the exit diaphragm. Preliminary simulations show a factor of two difference in transmission between best and worst case. However, the coherence of the ion motion can be disturbed if the ions are not monoenergetic (Fig. 1, right). Despite ion cooling prior to mass separation this is the case (a) if the ions travel through fringing fields, e.g. at the entrance diaphragm of the mass filter, or (b) if the RF amplitude is not the same on all four RF electrodes. Hence special care has to be taken in the design of the mass filter to overcome these effects.

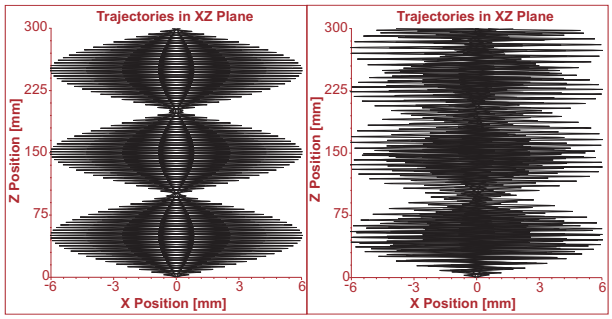

Figure 1: Simulation of ion trajectories in an ideal quadrupole field for a working point with the Mathieu parameter $q = 0.705$ and $a = 0.236$. The ions are monoenergetic with a velocity of 3150m/s (left) and with an velocity spread of $\pm 10\%$ (right). The forward motion occurs in z direction, and oscillations in the x-y plane.

Construction of the Mass Filter. A mass filter with the chosen design parameters is currently under construction. The mass filter will be taken into operation and will be characterized offline in the first half of 2008. A test chamber with an alkali ion source, a Faraday cup and a Channeltron detector has been set up for these measurements. A two-stage RF power supply containing a matched air coil has been constructed, and a control system for the voltages is under development.

References

[1] D.A. Dahl, Int. J. Mass Spectom., 200 (2000) 3.

[2] W.R. Plaß, Dissertation, JLU Gießen, 2001.

[3] G. Wu et al., J. Am. Soc. Mass Spectrom., 17 (2006) 1216.

[4] W.M. Brubaker, Adv. in Mass Spectrom., 4 (1968) 293.

[5] P.H. Dawson, Quadrupole Mass Spectrometry and its Applications, Elsevier, Amsterdam, 1974, 34.

* Work supported by BMBF contract No. 06GI185I.

A Multiple-Reflection Time-of-Flight System for Mass Measurements and Isobaric Separation for SHIPTRAP and the LEB of the Super-FRS at FAIR*

T. Dickel[1], W.R. Plaß[1], U. Czok[1], T. Fleckenstein[1], H. Geissel[1,2], C. Jesch[1,2], M. Petrick[1], K. Reinheimer[1], and C. Scheidenberger[1,2]

[1]Justus-Liebig-Universität, Giessen, Germany; [2]GSI, Darmstadt, Germany

At low-energy radioactive ion beam facilities such as SHIPTRAP and the Low-Energy Branch of the Super-FRS at FAIR, mass measurements and spectroscopy for a broad range of nuclei can be performed. Access to these nuclei is limited by their lifetime and the amount of isobaric contamination. To help to overcome these limitations, a multiple-reflection time-of-flight mass spectrometer (MR-TOF-MS) system has been developed. The system enables mass measurements of nuclei with millisecond half-life and can separate up to 10^7 isobaric ions per second.

The concept of this device has been demonstrated using a setup for offline measurements [1]. Here, the design of a system for online measurements is presented. Fig. 1a shows a schematic overview of the system. The exotic nuclei delivered from a gas-filled stopping cell are guided by curved radiofrequency quadrupoles (RFQs) [2] into the system. They are cooled and bunched in a linear RF trap and injected through a differential pumping section into the time-of-flight analyzer. They travel for a selectable number of turns in the analyzer and are then ejected through an additional reflector to the detector. The detector can be replaced by a Bradbury-Nielsen-Gate. With the gate a desired ion species can be isolated, removing all but the ions of interest. After separation, the ions are captured in an accumulation trap. In order to inject and capture the ions efficiently in the trap, their energy spread is reduced prior to electrostatic deceleration in a novel dynamic energy buncher. After the ions are recaptured they can be made available to experiments downstream of the device.

This system can be operated in three different modes (Fig. 1b-d). If the the analyzer is used in a pass-through mode and with the MCP detector, the system is a broad band mass spectrometer (mass resolving power $> 10^3$), e.g. for diagnostics purposes. If the ions are stored in the analyzer for many turns, the system works as high-resolution mass spectrometer with a mass range of a few percent (mass resolving power up to 10^5) for precision mass measurements. If the detector is replaced by the ion gate the system can be employed as an isobar separator.

Compared to a coaxial setup without post-analyzer reflector, the design shown here has several advantages: (i) The settings of the analyzer are independent of the position of the linear RF trap and the detector or gate, (ii) the settings are independent of the number of turns the ions travel inside the analyzer, (iii) the system can be used as broad-band mass spectrometer, (iv) a compact vertical setup is possible and (v) the number of differential pumping sections is reduced.

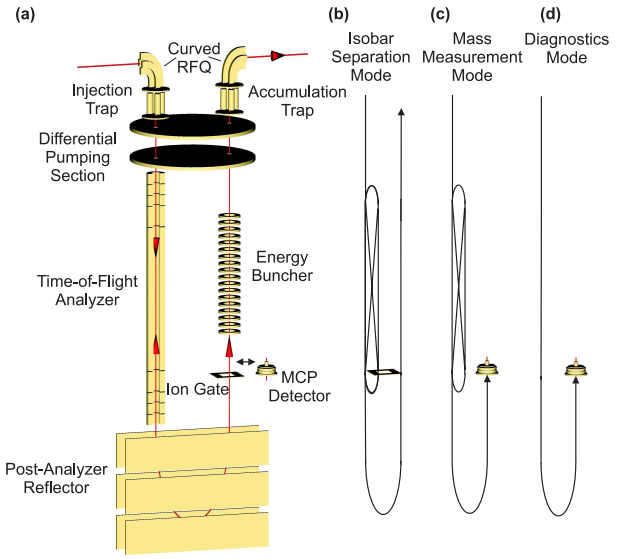

Figure 1: (a) Schematic figure of the MR-TOF-MS system. The main functional elements are shown only, without focusing and deflection electrodes. The overall height of the device is about 2 m. The system can be operated in three different modes, (b) as isobar separator, (c) as high resolution mass spectrometer for direct mass measurements, and (d) as broadband mass spectrometer for diagnostics. In the mode (b) the ion gate is moved into the beam path at the time focus of the device, in the modes (c) and (d) the detector is located in the position of the time focus.

All parts of the system have been simulated and optimized. For the curved RFQ, the linear RF trap [3], the analyzer [1] [4] and the ion gate [4] prototypes have been built. Using the test setup of the linear RF trap it could be shown that ions can be cooled with cooling time constants of less than a millisecond to almost thermal equilibrium. The complete system is currently under construction; online comissioning is scheduled for the first half of 2008.

References

[1] T. Dickel et al., GSI Scientific Report 2005, p. 260.

[2] M. Petrick et al., GSI Scientific Report 2005, p. 39.

[3] W. R. Plaß et al., submitted for publication.

[4] T. Dickel et al., GSI Scientific Report 2006, p. 204.

*Work supported by Helmholtz Association and GSI under contract VH-NG-033, by GSI under contract GIMET2, and by the BMBF under contract 06GI185I

Ion-Optical Matching of the FRS-ESR in the Isochronous Mode

S.A. Litvinov[1,2], H. Weick[1], H. Geissel[1,2], and M. Steck[1]

[1]GSI, Darmstadt, Germany; [2]Justus-Liebig-Universität, Giessen, Germany

Isochronous Mass Spectrometry (IMS) is an experimental technique for direct measurements of short-lived exotic nuclei which has been developed at the FRS-ESR facility at GSI [1]. A bottleneck for the present IMS experiments is the low transmission in the injection channel of the ESR [2]. Further losses occur due to possible an ion-optical mismatch between the FRS [3] and the ESR. Here the results of the first FRS-ESR matching are presented and critical views on the mismatching are shown.

Ion-Optical Calculation

The isochronous optics of the ESR is characterized by the large negative dispersion function in the straight sections ($\sim$ -8 m), whereas the FRS is an achromatic system at the last focal plane in the ring branch. This leads to the large dispersion mismatch. Additionally, there exists a mismatch in the transverse phase space. These all cause incorrect betatron and dispersion motions in the ring, and correspondingly reduces the transverse and longitudinal acceptance. In addition, the transition energy (γ_t) is a function of an integral dispersion and therefore the revolution times are different for the different turns. This motion is illustrated in Fig. 1 for four revolutions in the ESR.

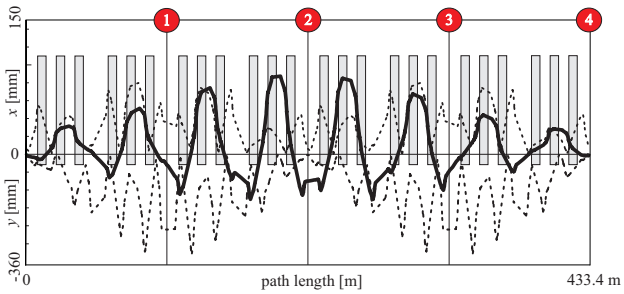

Figure 1: The evolution of the beam envelope in x (upper part) and y (lower part) directions (dashed curves) and the dispersion function (solid curve) with 4 turns in the ESR. The dispersion is shown for a momentum deviation of $+0.2\%$. The dipoles apertures are indicated in the background as boxes.

To perform matching, 11 quadrupoles of the FRS were adjusted. The geometric layout of the injection line into the ESR has been taken into account. The ESR optics was not changed. Also, it was assumed that the beam comes onto the central orbit of the ring, i.e. the orbit shift in the injection septum and the kicker was cancelled. The calculations have been performed with the ion-optical code GICOSY [4]. The calculated setting was successfully used in the FRS-ESR experiment in April 2007.

Transmission Measurement

In the experiment we used a $^{64}Ni^{26+}$ beam with an energy of 497.8 MeV/u from the SIS [5] impinging on a thick 4011 mg/cm^2 beryllium target. The bare 386 MeV/u primary beam was injected into the ring. During the measurements the magnetic rigidity of the ESR was scanned in a wide range and the corresponding transmission of the beam into the ring was measured. It was determined by comparing the SIS and the ESR currents measured with beam transformers. In addition, the number of stored particles has been estimated via integration of the Schottky noise with the on-line FFT (Fast Fourier Transform) analyzer. The results of the measurements for the matched and mismatched FRS-ESR are presented in Fig. 2, where the mismatched case is an injection setting for the ESR in standard mode. The momentum acceptance was defined as a full width at half-maximum (FWHM) and corresponds to 0.33% and 0.5% for the mismatched and matched cases, respectively. The transmission into the ESR for the matched setting in this experiment is larger than for the mismatched one by a factor of about 10. This factor was deduced by the ratio of the corresponding areas in the figure.

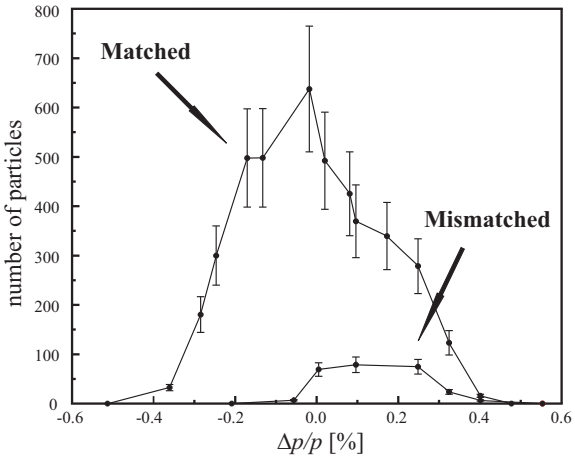

Figure 2: The experimental measured transmission of the ^{64}Ni primary beam in the isochronous ESR as a function of the momentum spread of the ring.

References

[1] M. Hausmann, et al., Nucl. Instr. Meth. A 446, 569 (2000).

[2] B. Franzke, Nucl. Instr. Meth B 24-25, 18 (1987).

[3] H. Geissel, et al., Nucl. Instr. Meth B 70, 286 (1992).

[4] H. Wollnik, et al., AIP Proceedings 177, 74 (1988).

[5] K. Blasche, et al., EPAC Proceedings, 9 (1992).

Characterization and Optimization of a Time-of-Flight Detector for Isochronous Mass Spectrometry at FRS-ESR

B. Fabian[1,2], L. Chen[1,2], T. Dickel[2], H. Geissel[1,2], C. Karagiannis[1], R. Knöbel[1], N. Kuzminchuk[1,2], Y. Litvinov[1], M. Petrick[2], W. R. Plaß[2], C. Scheidenberger[1,2], B. Sun[1], and H. Weick[1]

[1]GSI, Darmstadt, Germany; [2]Justus-Liebig-Universität, Gießen, Germany

Isochronous Mass Spectrometry (IMS) can be used to measure masses of exotic nuclei with lifetimes as short as a few tens of microseconds at the FRS-ESR facility at GSI. For measurement of the ions' revolution frequencies, a time-of-flight detector is used. Secondary electrons released from a thin carbon foil at every passage of the ion through the detector are transported to micro-channel-plates (MCPs) by electric and magnetic fields.

This time-of-flight detector (Fig.1) was characterized in offline experiments and using simulations. The detector efficiency was optimized and tested online with a stable Ni beam. All stages of the detector from the creation of secondary electrons to the detection of the electrons were investigated. The typical number of secondary electrons released per ion can be estimated within an uncertainty of a factor of two using an empirical formula [1]. The formula incorporates the target properties and the electronic stopping power of the ion. Typical average numbers of electrons released from the foil in IMS range from 1 to 10. The transport of the electrons from the foil to the MCPs was calculated for the first time for the real 3D geometry of the detector. The simulation helped to understand the transport of the electrons in the detector and thus to optimize the detection efficiency without sacrificing timing properties. With the optimized settings a larger area of the foil is used, which increases the detection efficiency. The detection efficiency of the MCP in dependence of the average number of secondary electrons impinging on the MCP was also examined. It can be estimated using the open area ratio and the average number of electrons impinging on the MCP. These two parameters will yield the detection efficiency. The intial detection efficiency of the MCP detector for a Ni-projectile was estimated to be about 88%. In addition, saturation effects of the MCPs [2] were examined. The saturation effect is a dead time effect, which occurs because of the long recharge time of the micro channels (1-10ms) compared to the measurement time (400μs). These effects result in a decrease of the gain, the amplitude of the signals and the detection efficiency. In addition the number of ions revolving in the ESR was simulated in a Monte Carlo calculation taking into account the ion optics, the appertures of the ESR and the energy loss in the foil.

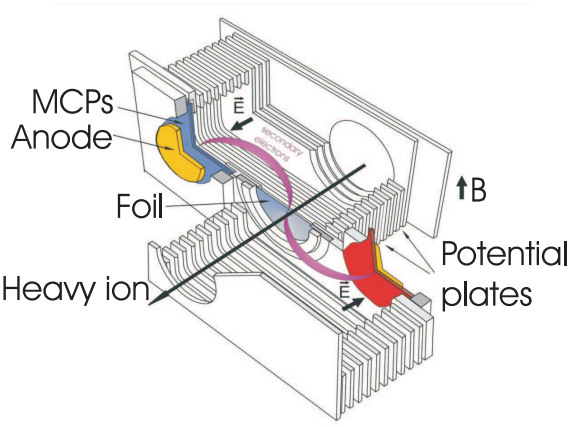

Figure 1: Overview time of flight detector. An ion passing through the foil releases secondary electrons. The electrons are accelerated away from the foil by an electric field created by the potential plates, while a static magnetic field guides them onto a microchannel plate detector.

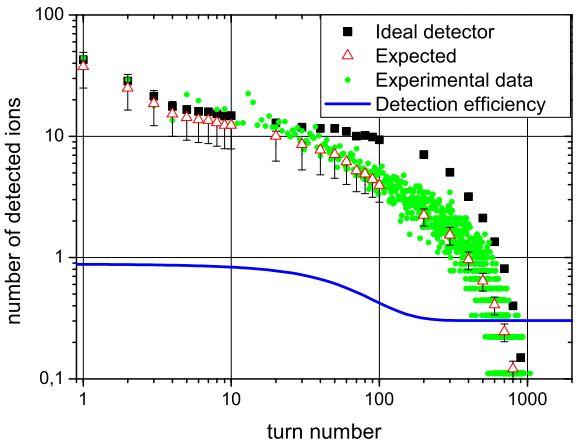

Figure 2: Simulation of the number of the detected ions in dependence of the number of ions' turns in the ESR. The black squares show the performance without dead time effects, while the red empty triangles include the influence of the dead time. The green circles are experimental values measured at the ESR. The blue line shows the temporal developement of the expected detection efficiency.

Taking into account these effects it is possible to describe the behavior of the detection efficiency and the signal amplitude in dependence of the turn number (Fig.2). This knowledge makes it possible to further improve the detector in the ESR and will be used within the ILIMA project to develop a new dual detector system for the CR at FAIR.

References

[1] Rothard et al., Phys, Rev. A 41, (1990) 2521

[2] Fraser et al., Nucl. Instrum. Methods A 306 (1991) 247

Ion Beam Heating of Liquid Jet Li Target for the Super-FRS*

N.A. Tahir[1], V. Kim[2], I.V. Lomonosov[2], A.R. Piriz[3], D.H.H. Hoffmann[4], H. Weick[1], and H. Geissel[1]
[1]GSI, Darmstadt, Germany; [2]IPCP, Chernogolovka, Russia; [3]UCLM, Ciudad Real, Spain; [4]TU Darmstadt, Germany

Survival of the production target over an extended period of time is a very important problem for the Super-FRS. It has been shown [1,2] that a solid graphite target can be used for up to 10^{11} ions per bunch in a fast extraction mode. For higher intensities, one should develop an alternative scheme, for example, a liquid jet metal target. In this contribution we present 3D computer simulations of heating of a liquid Li target and the beam target geometry has been shown in Figure 1.Four different cases for 1 GeV/u uranium bunch with a length = 50 ns have been considered:

Case 1: beam intensity = 10^{12}, σ_x = 2 mm and σ_y = 12 mm.

Case 2: beam intensity = 10^{12}, σ_x = 2 mm and σ_y = 6 mm.

Case 3: beam intensity = 5.0×10^{11}, σ_x = 1 mm and σ_y = 12 mm.

Case 4: beam intensity = 5.0×10^{11}, σ_x = 2 mm and σ_y = 6 mm.

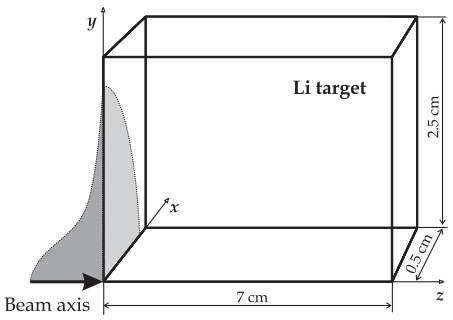

Figure 1: A quarter of the target in plane geometry, length = 7 cm (Z-axis), height = 5 cm (Y-axis), thickness = 1 cm (X-axis), beam is directed along Z-axis.

It is important that the liquid remains safely below the boiling temperature and two-phase liquid-gas region is also avoided. Moreover the liquid should not enter the metastable phase to avoid negative pressures and cavitation.

In Figure 2 we present target temperature at t = 50 ns, immediately after the beam has delivered its total energy for case III. It is seen that the maximum temperature at the beam axis is of the order of 950 K whereas the boiling temperature of Li is 1643 K. The corresponding pressure shown in Figure 3 is about 0.8 GPa.

It is also to be noted that the focal spot area and the beam

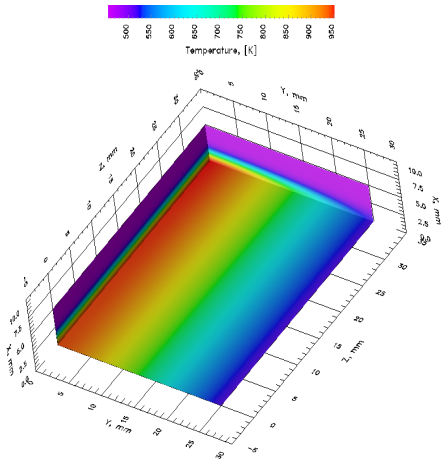

Figure 2: Target temperature at t = 50 ns for case III.

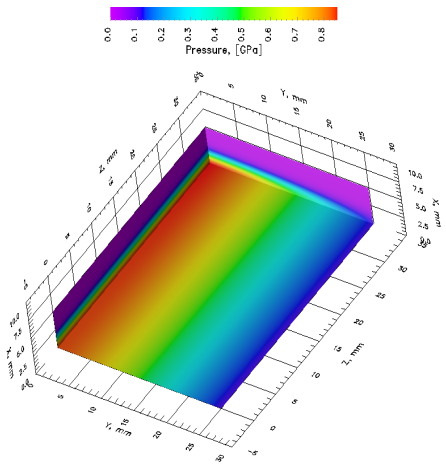

Figure 3: Target pressure at t = 50 ns for case III.

intensity is arranged in such a proportion that the specific energy deposition is same in all the three cases that leads to identical results. In case II, on the other hand, the specific energy deposition is two times higher which results in higher temperature of 1400 K and a pressure of 1.4 GPa. Further details can be found in [3].

References

[1] N.A. Tahir et al., J. Phys. D: Appl. Phys. 38 (2005) 1828..

[2] N.A. Tahir et al., Laser Part. Beams 25 (2007) 523.

[3] N.A. Tahir et al., Laser Part. Beams 25 (2007) 295.

* Work supported by BMBF

Simulations and first tests of slowed down beams project at GSI.*

P. Boutachkov[1], M. Górska[1], J. Gerl[1], H. Geissel[1], I. Kojouharov[1], W. Koenig[1], M.A.G. Alvarez[2], C. Nociforo[1], M. Pomorski[3], W. Prokopowicz[1], H. Schaffner[1], and H. Weick[1]

[1]GSI, Darmstadt, Germany; [2]Seville University, Seville, Spain; [3]Warsaw University, Warsaw, Poland.

The availability of radioactive beams has opened new opportunities for the investigation of exotic nuclei. The NuSTAR HISPEC slowed down beam project [1] at GSI/FAIR aims to produce rare isotopes with energies of 10 MeV/u and less, to be used for spectroscopy and reactions studies. This paper reports on the ongoing feasibility study of slowed down beam production at the GSI FRagment Separator(FRS) facility.

At FRS the nuclei of interest are produced at high energy, they are identified with the standard tracking detectors [2] and slowed down with a thick degrader. Due to the low energy of the slowed down fragments a beam line was constructed after the thick degrader. A position sensitive transmission Time Of Flight (TOF) detector was used to reconstruct the slowed down ions trajectory and velocity on event-by-event basis.

A calculation using EPAX [3] cross sections and ATIMA [4, 5] stopping powers showed that about 80% of the fragments survive the slowing down process. The simulation also predicted that the majority of fragments created due to secondary fragmentation reactions in the degrader have different velocity compared to the ions of interest. Figure 1 shows an example calculation of the yield due to reactions in the degrader when ^{62}Co is slowed down to 10 MeV/u. The square root of the energy per nucleon is proportional to the fragment velocity. Hence, the simulation predicted that ^{62}Co will dominate by three orders of magnitude the ions created due to reactions in the degrader when a TOF gate corresponding to an energy of 10 MeV/u is applied. Based on the simulations only a TOF detector was considered for the first experiments with slowed down beams at the FRS.

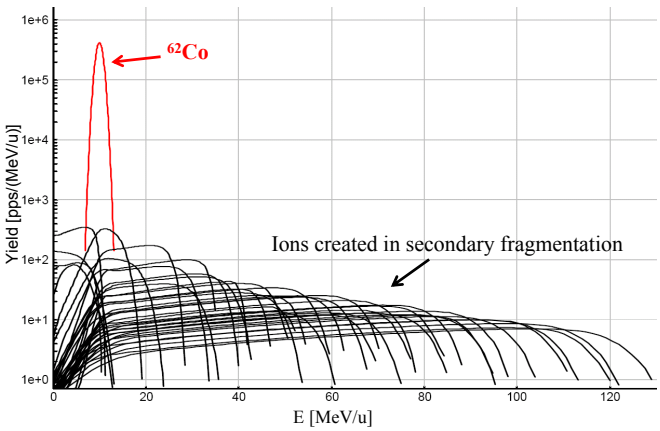

Figure 1: Calculated energy per nucleon distribution of the fragments created when ^{62}Co is slowed down to 10 MeV/u.

* Work supported by EU, EURONS contract No. 91606.

To test the simulations an experiment with a 100 μm scintillator TOF detector and a Si detector positioned after the scintillator was performed in 2007. The Si detector thickness was sufficient to stop 20 MeV/u, ^{62}Co ions. A ^{64}Ni beam was used to create ^{62}Co, which was slowed down to 10 MeV/u. The experiment confirmed the simulated energy and angular straggling. Figure 2 shows the ^{62}Co energy detected with the Si detector as a function of the TOF. A narrow energy distribution around 10 MeV/u was selected with a TOF gate applied to the spectrum shown in the figure. It was observed that the width of the energy distribution is 5 times larger than the expected one. This was attributed to the inhomogeneity of the scintillator detector used in the experiment. Hence, to remove

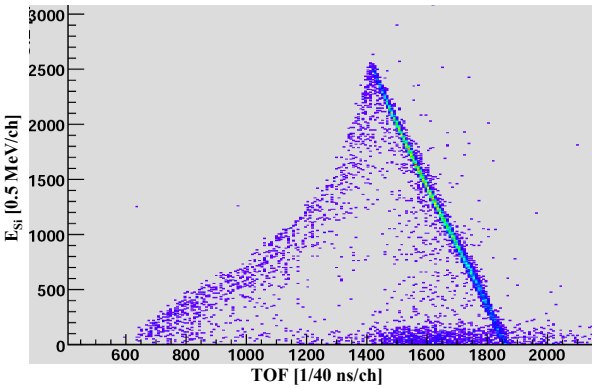

Figure 2: Energy of ^{62}Co deposited in the Si detector versus the TOF measurement with the 100 micron scintillator detector.

the uncertainty due to the energy loss into the TOF detector, a development of fast timing from a large area thin Double Sided Silicon Strip Detector (DSSSD) was initiated. In a follow up test experiment at UNILAC, a 40 μm, 5x5 cm^2 DSSSD detector was tested with pre-amplifiers developed at GSI. A time resolution of 80 ps was obtained, based on the noise level and signal rise time.

Currently there is an on going development of thin TOF detectors to be used at the slowed down setup at FRS. This development will be followed by a proof of principle experiment with slowed down beams.

References

[1] `http://www.gsi.de/nustar/`

[2] H.Geissel, *et al.*, NIM **B70**(1992)286

[3] K.Summerer, *et al.*,PRC **61**(2000)034607

[4] H.Geissel, C.Scheidenberger, NIM **B136**(1998)114

[5] C.Scheidenberger, H.Geissel, NIM **B135**(1998)25

Diamond Detectors for the R^{3}B Experiment *

S. Schwertel[1], M. Böhmer[1], R. Gernhäuser[1], R. Krücken[1], L. Maier[1], and S. Winkler for the R^{3}B collaboration[1]

[1]TU München, Physik-Department E12, Garching

Introduction

For the R^{3}B experiment radiation hard high resolution detectors for tracking and TOF measurement are required. Diamond is an ideal material for such devices.

In detailed test series on small samples we quantified a time resolution to $\sigma\tau \approx 60$ps [1], a detector efficiency of 98 %, a charge collection efficiency of 15 % and a radiation hardness up to a dose of $2.5 \cdot 10^{13}$ ions/cm^2 (^{16}O, 117 MeV) [2].

Detector Layout

The detector substrate material is a 100 μm thick layer of polycrystalline (PC) CVD diamond of size 2.54×2.54 cm^2. The one side used for position measurement is segmented in 128 strips with a pitch of 200 μm and gaps of 20 μm. This is done by metallization with aluminum and lithographic methods. The gaps have to be so small to get full efficiency even if particles hit just inbetween the strips.

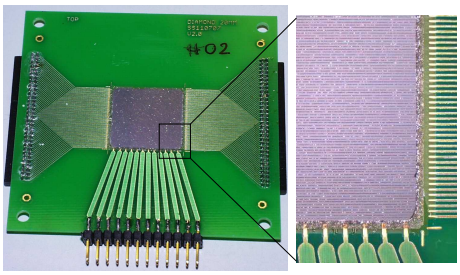

Figure 1: A 1” detector mounted on PCB. The insert shows the micro structures and bond wires.

The back side is used for TOF measurement. It is divided in 16 aluminum strips each with a gap of 50 μm.

Electronics

The back side is read out by 2 GHz broadband preamplifiers followed by an leading edge discriminator and a standard TDC.

For readout of the position side we use new frontend boards based on the APV chip, which was developed for the readout of the silicon microstrip dectors in the CMS tracker at LHC. Each of its 128 channels includes a low noise preamplifier, a shaper and an analogue pipeline with 192 stages and a clock frequency of 40 MHz which allows a deadtime free readout. The linear range is 8 mips corresponding to a typical energy loss signal of a medium mass ($Z < 25$) heavy ion in a layer of 100 μm PC-diamond.

For the digital control of the APV the R^{3}B GTB interface board was modified and equipped with a 12 bit ADC. So we can use existing hard- and software and it is compatible to GSI data acquistion.

Test Experiment

To test a full small size tracking system we used a ^{129}Xe beam of 600 MeV/u and an intensity of 10^5 s^{-1} at the FRS.

A compact stack of two detectors was mounted in air at the FRS middle focus to measure particle positions with respect to each other. Each detector was read out by two APV chips.

Figure 2 shows the position correlation of particles in the two detectors. The intrinsic resolution is in the order of 200 μm. The additional structures shown in figure 2 are related to signal coupling of non neighbouring channels due to the PCB layout.

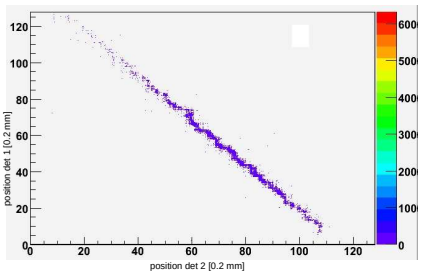

Figure 2: Position correlation of the two detectors

Summary and Outlook

The presented detector tests showed the successful operation of a medium size micro strip diamond detector for heavy ions. The principle of the full readout device was shown as well as the expected position resolution. Current work is focused on simultaneous operation of TOF and position readout where currently resolution suffers from crosstalk.

The first test of a full scale R^{3}B target tracking device (5 $\times$ 5 cm^2) is expected to be performed in 2008.

References

[1] S. Schwertel et al. , “In Beam CVD-Diamond Detectors for Heavy Ions”, Annual report 2005, MLL, Garching

[2] S. Schwertel et al. , “CVD-Diamond Detectors For The HADES Experiment”, This report

*Work supported by EU, EURONS contract No. 506065, BMBF (06MT238), DFG (Exz.-Clust 153-Universe)

Proton tracking in the R^{3}B Experiment

Ch. Wimmer[3], N. Bondar[2], V. Golovtsov[2], M. Heil[1], J. Hoffmann[1] V. Iatsura[2], A. Khanzadeev[2],O.Kiselev[1,4], N. Kurz[1], Ch. Müntz[3], W. Ott[1], E. Roshchin[2], J. Stroth[1, 3], L. Uvarov[2] for the R^{3}B-Collaboration

[1]GSI, Darmstadt, Germany, [2]PNPI, St. Petersburg, Russia, [3]J.-W. Goethe-Universität, Frankfurt, Germany, [4]J. Gutenberg Universität, Mainz, Germany

In 2007 several tests and experiments were performed with the R^{3}B setup located in Cave C. Here, we focus on the new detector system for tracking of break-up protons by means of two drift chambers (DCH) with hexagonal drift cells in both, x and y direction (figure 1). They are used for position tracking of the protons behind the ALADIN magnet. With an active area of 100 x 80 cm^2 the chambers have been designed for efficient detection of minimum-ionizing protons with a spatial resolution of about 200 µm.

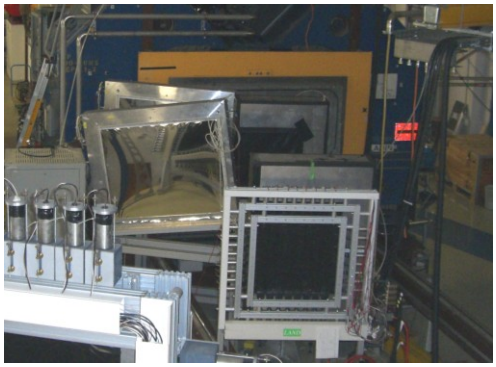

Figure 1: View of DCH installed behind ALADIN in Cave C. The detectors are inclined with respect to each other to avoid ambiguities in tracking.

The 256 channels per chamber (144 in x and 112 in y) are read out via the customized read-out system "Cros3" [1] with 16 front-end boards per DCH providing amplification, discrimination and digitization based on the ASDQ-ASIC chip [2]. This chip also allows measuring the charge via time-over-threshold (ToT). A concentrator board prepares the data on demand of an external trigger. Both, the chambers and the front-end read-out system were developed and built at PNPI in St. Petersburg / Russia. With the support of the GSI electronics department, the readout was successfully integrated in the existing MBS Data Acquisition System. The necessary infrastructure to run the detectors (gas system, support structure, high and low voltage supply) was installed in 2007.

To find tracks of protons dedicated tracking software has been developed. First, the positions of proton hits in the detector plane have to be reconstructed. To obtain the drift length from the drift time, Garfield [3] simulations are conducted. For the momentum reconstruction, this hit information is provided to a tracking routine, which uses additional information from other detectors and the field map of the deflecting magnetic field of the ALADIN magnet.

Commissioning was done with radioactive sources, cosmic rays, p and ^{12}C projectiles to determine the operation point for maximum efficiency. For the ^{12}C test beam two peaks (Figure 2, left) in the ToT (charge) spectrum are visible, one at higher values caused by carbon and one at lower values caused by secondary electrons, nicely demonstrating the capability to detect the energy loss of a particle to support the tracking algorithm and background rejection. From the position correlation of two adjacent drift cells a spatial resolution of 214µm (σ) can be deduced.

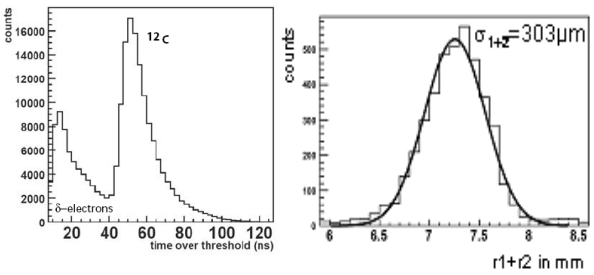

Figure 2, left: Time over threshold distribution (^{12}C test beam); right: Position correlation of two adjacent drift cells, r=distance to wire.

Several production runs have been successfully completed: S223 (^{27}P(γ,p)^{26}Si), S318 (^{17}Ne(γ,2p|p,2p)^{15}O) and S296 (^{12}C(p,2p|pn)).

According to a first analysis of in-beam data the DCH's spatial resolution as well as the cell efficiency (97%) meet requirements for minimal ionizing protons.

References

[1] CROS3: Internal note "CROS3 Readout System", Electronics Department of PNPI, 2001.

[2] ASDQ ASIC: F.M. Newcomer et al., IEEE Transactions on Nuclear Science, Vol. 40, No. 4, 1993.

[3] http://garfield.web.cern.ch/garfield/

Design and Test Results of the R^{3}B/EXL CsI(Tl) Calorimeter Elements*

V. Avdeichikov†[1,2], P. Golubev[1], B. Jakobsson[1], and the NuSTAR Calorimeter Working Group
[1]Lund University, Lund, Sweden; [2]JINR, Dubna, Russia

Five batches of CsI(Tl) crystals, 50 samples in total, supplied by Amcrys Ltd (Khar'kov), St.Gobain Crystals (France) and Lanzhou (China) have been tested with gamma-sources and in a beam of protons by using PD's, two types of APD's and three types of magnetic field insensitive PMT's as readout devices.

The complete R^{3}B/EXL calorimeter/specrometer systems [1] are expected to consist of $\simeq$6000 CsI(Tl) crystals of 7 different shapes in a densely packed geometry. The requirements of spectroscopic quality of crystals are imposed by physics - high efficiency, high energy resolution for 0.1 - 30 MeV γ - rays and for protons up to 200 MeV. The shape of the crystals is defined by the value of the Lorentz boost effect for gammas in 700A MeV reactions [2]. The tested crystals of 10x30 mm^2 (face side), 15x42(back side), and a length of 130 mm will cover the polar angular region of 35° - 130°.

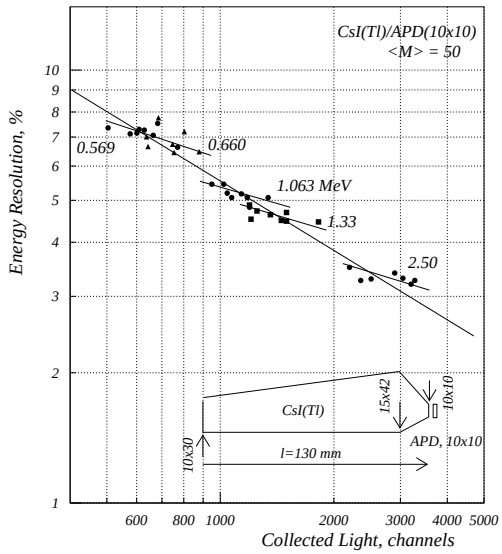

Figure 1: Energy resolution of CsI(Tl)/APD elements of the geometry shown in figure for γ-rays of ^{207}Bi, ^{137}Cs and ^{60}Co. Lines are drawn to guide the eye.

The most important and critical factor for the resolution of long CsI(Tl) crystals arise from the non-uniformity of the light output along the longitudinal axes. To some extent this effect can be amended by the manufacturer during the processing of the primary boule by proper adjustment of the Tl concentration. In addition, we developed a method, based on non-uniform polishing/lapping procedure of the crystal side facets. This method allows to get light output (LO) non-uniformity, defined as $(LO_{max} - LO_{min})/LO_{average}$, on a level better than 0.7%. The method can be applied for mass production of CsI(Tl) crystals with a length up to 150 mm.

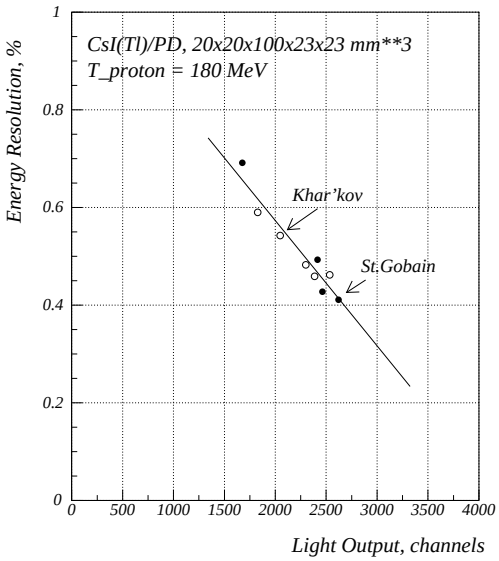

Figure 2: Energy resolution of CsI(Tl)/PD elements for 180 MeV protons. Crystals produced by Amcrys Ltd, Khar'kov (Ukraine) and St.Gobain Crystal (France). The beam energy spread is unknown.

The third batch of 8 crystals, manufactured by Amcrys Ltd, satisfied our requirements on surface treatment, uniformity in Tl doping concentration, light output and energy resolution. Test results for γ-rays (5 energy points) are presented in Fig. 1. The Hamamatsu S86684-1010 APD was used as readout device. The light guide structure is here the extension of crystal itself and it allows to collect 44 - 51% of the primary light on the 10x10mm^2 active area of the APD. The spread of light output from crystal to crystal in one batch is quite high, but this has little influence on the final energy resolution. For an APD of 5x5 mm^2 area the light collection is around 18% which results in 1.3 times worse energy resolution for γ-rays.

Fig. 2 presents test results with the 180 MeV proton beam at TSL, Uppsala, Sweden. In this case, the the energy resolution depends even more strongly on the light output.

References

[1] http://www-win.gsi.de/r3b; http://www-land.gsi.de/exl.

[2] H. Alvarez Pol, http://www.usc.es/genp/r3b.

* Work supported by Swedish Research Council and Swedish Institute.
† Vladimir.Avdeichikov@nuclear.lu.se

A scanner for gamma-ray detectors based on principles of positron tomography

S. Tashenov[1,2], I. Kojouharov[1], T. Engert[1], J. Gerl[1], N. Goel[1] and H. Schaffner[1]
[1]GSI, Darmstadt, Germany; [2]KTH, Stockholm, Sweden.

The rapid development of the novel gamma-ray detectors and detector clusters based on principles of gamma-ray tracking opens new broad perspectives to nuclear spectroscopy. An increase of the efficiency and a gain of the Peak/Total [1] alongside with a possibility for an efficient linear polarimetry and imaging are expected to produce a significant impact on future experiments. The HPGe arrays like AGATA [2], GRETA [3] and DESPEC [4] will determine a new cutting edge of nuclear spectroscopy.

The core principle of these detectors is an application of the pulse shape analysis (PSA) [e.g. 5,6]. Although one may say that this principle is nowadays well established, its verification and steady performance still poses big difficulties and uncertainties. The only reliable solution to its verification is a full 3D scanning of the detectors which experimentally determines pulse shapes from every given position inside the active volume. Easy sounding it turned out to be an extremely lengthy procedure with a timescale of months which may postpone the real experimental application of the PSA and tracking techniques.

As one of the possible ways to speed up this process we proposed and implemented a first detector scanner based on principles of positron emission tomography [7]. An application of the ^{22}Na source emitting pairs of 511 keV gammas in opposite directions allows creating a "collimator-free" scanner where many lines across the detector or even the whole detector is scanned simultaneously, see figure 1.

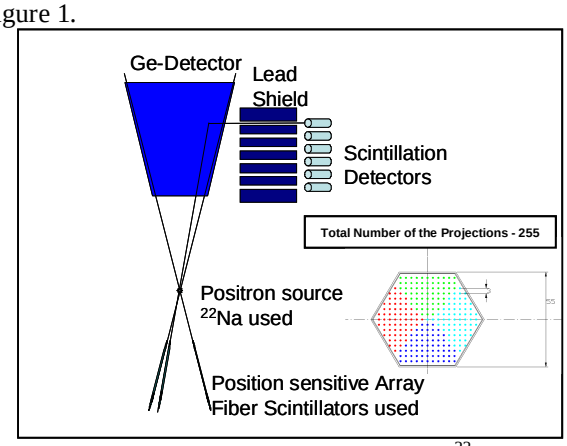

Figure 1: The HPGe scanner based on ^{22}Na source emitting pairs of 511 keV gamma-rays in opposite directions. One of the photons is detected by an array of aligned fiber plastic scintillators arranged in a square matrix covering a hexagonal frontal shape of the AGATA detector. The second Compton scattered gamma is detected by an array of BGO scintillators placed behind 6 round slit collimators.

The 10 cm long and 0.8 mm thick fiber plastic scintillators oriented towards the gamma-ray source are used for registration of 511keV gammas coincident with the HPGe detector. Another photon from the pair being Compton scattered off an electron from the detector material is registered by an array of BGO scintillators placed behind 6 slit collimators. The corresponding 3-fold coincident spectrum registered by the HPGe detector and individual segments shapes obtained are shown on the figure 2. The peak around 250keV corresponds to the meaningful scanning events.

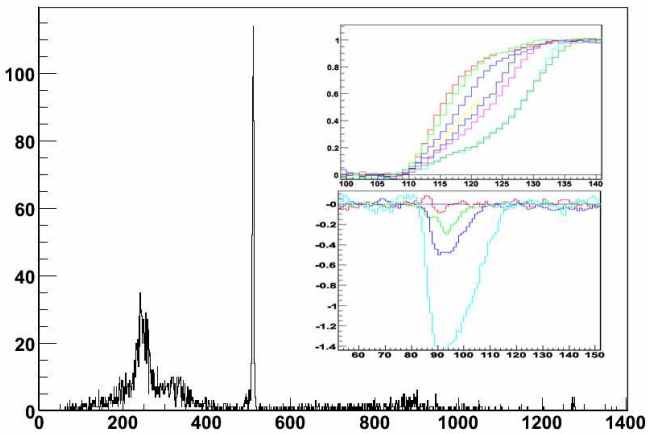

Figure 2: The spectrum of HPGe detector registered in coincidence with the fibers and the BGOs. The broad peak around the energy of 250 keV is attributed to the Compton recoiled electrons. The inset shows typical net charge and mirror signals tagged with 3D positions.

Although a clear capability to obtain the scanning information was demonstrated a low efficiency of the fibers detectors resulted in a scanning 100 slower than originally expected. While the probability to produce Compton scattering in 10 cm plastic is large, the recoiled electrons easily escape from the thin fibers. Apart from that an unintuitive influence of the second gamma-ray line 1274keV hampers clean measurements [7]. The detailed Monte-Carlo studies of a possibility to upgrade the setup to achieve higher scanning speeds are now in progress.

References

[1] S. Tashenov, GSI annual report, this volume
[2] J. Simpson, J. of Phys.: Conf. Ser. 41 (2006) 72-80
[3] I.Y. Lee et al., Nucl. Phys. A 746 (2004) 255c-259c
[4] HISPEC/DESPEC Technical Proposal, (http://www-linux.gsi.de/~wwwnusta/tech_report/09-hispec_despec.pdf) (2005)
[5] E.A. Wulf, et al., IEEE Trans. Nucl. Sci. NS-49 (4 Part 1) (2002) 1876.
[6] K. Vetter, et al., Nucl. Instr. and Meth. A 525 (2004) 322.
[7] I. Kojouharov et al., submitted to IEEE

TANGO – A New Tracking Algorithm for Gamma-Rays

S. Tashenov[1,2], J. Gerl[1]
[1]GSI, Darmstadt, Germany; [2]KTH, Stockholm, Sweden.

The rapidly advancing field of the nuclear spectroscopy into a large extend owes its success to the progress in the development of gamma-ray detectors. A new generation of germanium spectrometers employing principles of gamma-ray tracking like AGATA [1], GRETA [2] and DESPEC [3] are expected to make a significant improvement in the efficiency and the Peak/Total ratio over the presently existing detector clusters such as Euroball and Gammasphere. Despite the obvious advantages, there are still some limitations of the novel gamma-ray tracking technique which is the topic of the present investigations.

The Compton scattering process dominates the photon-matter interaction cross section in the energy region starting from 160 keV till 8 MeV. The principles of gamma-ray tracking employ the energy and momentum conservation relations for Compton scatterings inside the germanium detector. For this purpose a 3D position information for each interaction point is required. It is obtained by the application of the well established technique of the pulse shape analysis (PSA) [4–7].

Despite of the large volumes of the modern germanium detectors, their efficiency is still much lower than 100%. The incomplete absorption of the initial photon energy due to the (multiple) Compton scatterings degrades the efficiency and increases the spectral background (Compton tail). The later causes the low Peak/Total ratio which limits the sensitivity of the detectors to individual gamma-lines. The tracking algorithms which were developed for AGATA and GRETA arrays were not able to improve the Peak/Total ratio despite having all the information on the Compton scatterings in hand [8,9]. In order to overcome this limitation a new gamma-ray tracking algorithm "TANGO" was developed.

The algorithm considers the cases of the full-energy absorption and the escape events separately finding the most appropriate fit for the observed photon track. The fit quality is described in terms of a "Figure of Merit", two of which are calculated assuming these two kinds of events. The algorithms which are based on a single "Figure of Merit" (like MGT [8]) can not properly distinguish between the two possible reasons for a "bad" fit: an incomplete energy deposition (escape) and deviations of the PSA reconstructed positions from the real ones which are larger than the average. In contrast, the TANGO algorithm allows for a much better separation between photo peak and escape events even if the PSA makes errors.

Figure 1 shows the performance of the TANGO algorithm in comparison with the MGT code which was the previous best result. In the case of the low photon multiplicities (e.g. single events) TANGO shows clearly much better performance. With a very little compromise of the efficiency the Peak/Total can be increased till 0.97 comparing to 0.8 for MGT. This corresponds to the decrease of the Compton background by a factor of 7. Such high values for the Peak/Total are unprecedented in germanium gamma-ray spectroscopy and should in near future significantly improve the quality of the spectroscopic information. Further development of the algorithm for the case of large photon multiplicities (e.g. 30) is currently in progress.

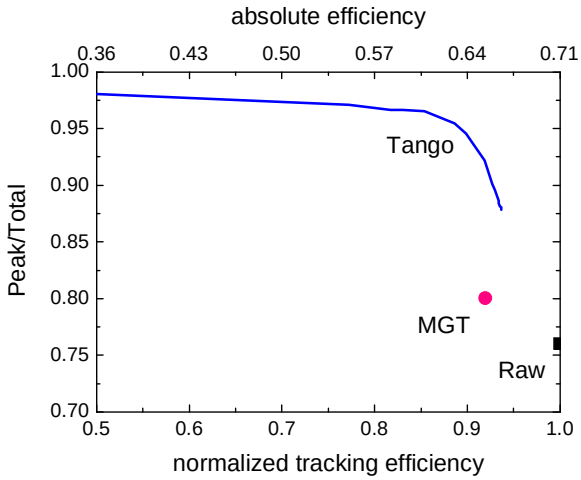

Figure 1: Peak/Total versus the efficiency of the (Raw) observed spectrum and the spectra processed by the new tracking algorithm TANGO and MGT algorithm [8] (previous best result). The germanium shell (AGATA & GRETA) geometry, single (multiplicity 1) photons of the energy 1 MeV and 5 mm position resolution were considered.

References

[1] J. Simpson, J. of Phys.: Conf. Ser. 41 (2006) 72-80
[2] I.Y. Lee et al., Nucl. Phys. A 746 (2004) 255c-259c
[3] HISPEC/DESPEC Technical Proposal, (http://www-linux.gsi.de/~wwwnusta/tech_report/09-hispec_despec.pdf) (2005)
[4] E.A. Wulf, et al., IEEE Trans. Nucl. Sci. NS-49 (4 Part 1) (2002) 1876.
[5] K. Vetter, et al., Nucl. Instr. and Meth. A 525 (2004) 322.
[6] L. Milechina, B. Cederwall, Nucl. Instr. and Meth. A 550 (2005) 278.
[7] A. Olariu, et al., IEEE Trans. Nucl. Sci. NS-53 (3) (2006) 1028.
[8] A. Lopez-Martens et al., Nucl. Instr. Meth. A 533 (2004) 454-466 and private communications
[9] J. Van der Marel and B. Cederwall, Nucl. Instr. Meth. A 477 (2002) 391-396

Trigger study with prototypes of Time-Of-Flight wall for positively charged particles for the HypHI project*

C. Rappold[†1,2], P. Achenbach[3], S. Ajimura[4], S. Bianchin[1], O. Borodina[1], T. Fukuda[5], Y. Hayashi[6], T.Hiraiwa[6], J. Hoffmann[1], M. Kavatsyuk[1], N. Kurz[1], O. Lepyoshkina[1], S. Minami[1,3], S. Mizoi[5], D.Nakajima[1], W. Ott[1], J. Pochodzalla[3], A. Sakaguchi[4], T.R. Saito[1,3], K. Tanida[6], and W. Trautmann[1]

[1]GSI, Darmstadt, Germany; [2]Univ. Louis Pasteur, Strasbourg, France; [3]IKP Mainz Uni., Mainz, Germany; [4] Osaka Uni., Osaka, Japan; [5]Osaka Elect.-Comm. University, Neyagawa, Japan; [6]Kyoto Univ., Kyoto, Japan

The HypHI project aims to study hypernuclei by means of collisions of stable heavy ion and rare-isotope beams on stable target materials [1, 2]. As the first step (Phase 0), the feasibility of hypernuclear spectroscopy with heavy ion beams will be demonstrated with ^{6}Li beam at 2 A GeV impinged on a ^{12}C target by identifying $^{3}_{\Lambda}$H, $^{4}_{\Lambda}$H and $^{5}_{\Lambda}$He hypernuclei [3].

The HypHI collaboration is currently working on preparation of the setup for Phase 0. As discussed in ref. [4], two test experiments were performed in 2007. In the lastest test experiment in cave B, several prototype detectors and newly developed logic modules, VUPROM, which will be used in phase 0 for the trigger system, were tested. In the experiment, light fragments produced by fragmentation reactions of the ^{58}Ni and ^{12}C beams on a carbon target were measured. In the HypHI Phase 0 experiment, the trigger system consists of three simultaneous stages: a tracking trigger for secondary vertexes selections for Λ and hypernuclear decay, a π^- trigger to select π^- with high momenta from the decay of hypernuclei and a Z=2 trigger to select residues of hypernuclear decay. The latter part was implemented and tested during this test experiment [5]. The feasibility of the Z=2 trigger was at first studied by an offline analysis and then thanks to those offline results, the Z=2 trigger part was tested with the VUPROM module. The Z=2 trigger is to select events with Z=2 particle by measuring the pulse width of analog signals from PMTs of each TOF+ bars with a cooperation of updated-type discriminators at the online stage.

Each signal from PMT of the prototype TOF+ bars was fed to the first leading edge discriminator (LED) which provides two outputs, an output corresponding to the leading edge and the second one inverting the first one. Those two outputs were then fed to the second LED, and by making time differency of this second LED output, the pulse width was measured with a TDC. With several beam conditions, several data set were available to analyse the correlation between pulse width and the charge of registered particles.

This correlation of pulse width was studied by using one of the three bars, and particle identification was performed by the other two bars with Time-of-Flight and energy deposit measurements in order to avoid the self-dependence by the particle identification. One of this three bars consists of a hole in the center with a gap of 6 cm. Figure 1 shows the measured pulse width for MIP and alpha particles. It is shown that distributions of measured pulse width are well and clearly separated for those two different particles. As mentioned above, one of the prototype has a hole in the center, which will be used to avoid primary beams in TOF+ wall. In the experiment, the pulse width information was also studied on the influence of this hole, resulting also in the feasibility of the $Z = 2$ trigger with the hole.

The HypHI collaboration would like to thank to the FOPI collaboration for its supports to the test experiments in cave B.

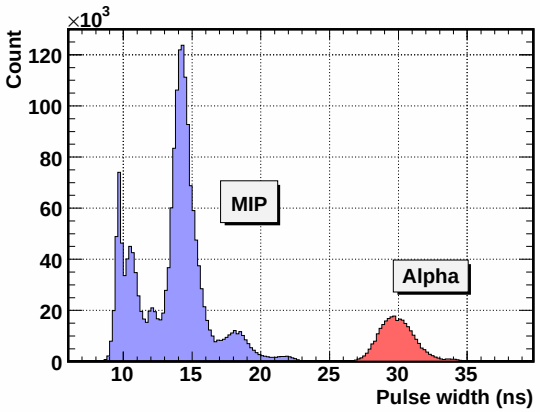

Figure 1: Time-over-threshold of MIP & alpha

References

[1] T.R. Saito *et. al.*, and the HypHI collaboration, in these Scientific Reports.

[2] T.R. Saito *et. al.*, proceedings of HYP2006, October 2006, Mainz, to be published in Eur. Phys. J.

[3] A proposal of the HypHI Phase 0 experiment, the HypHI collaboration, submitted to GSI PAC EA33 with a realization as S319.

[4] T.R Saito *et. al.*, in these reports.

[5] S. Minami *et. al.*, in these reports.

* The HypHI project is granted by the Helmholtz Association and GSI as Helmholtz-University Young Investigators Group VH-NG-239 with Mainz University

† c.rappold@gsi.de

Performance of prototype detectors of a TOF wall for positively charged particles for the HypHI Phase 0 experiment

O. Borodina[1], P. Achenbach[2], S. Ajiamura[3], S. Bianchin[1], T. Fukuda[4], Y. Hayashi[5], T. Hiraiwa[5], J. Hoffmann[1], M. Kavatsyuk[1], N. Kurz[1], O. Lepyoshkina[1], S. Minami[1,2], S. Mizoi[4], T. Mochizuki[3], M. Moritsu[5], D. Nakajima[1], W. Ott[1], J. Pochodzalla[2], C. Rappold[1], T.R. Saito[1,2], A. Sakaguchi[3], K. Tanida[5], and W. Trautmann[1]

[1]GSI, Darmstadt, Germany; [2]IKP Mainz Uni., Mainz, Germany; [3]Osaka Uni., Osaka, Japan; [4]Osaka Ele.-Comm. Uni., Neyagawa, Japan; [5]Kyoto Uni., Kyoto, Japan

The HypHI project [1] aims to study hypernuclei at extreme isospins and to measure directly hypernuclear magnetic moments for the first time. The first experiment aims to demonstrate the feasibility of hypernuclear spectroscopy with heavy ion beams by producing and identifying hydrogen and helium hypernuclei with a Li beam at 2 A GeV impinged on a ^{12}C target. The most promising signals of hypernuclei in the experiment is the existence of a secondary decay vertex well behind the target, which can be identified via measurements of π^- channels of the mesonic decay of hypernuclei of interest.

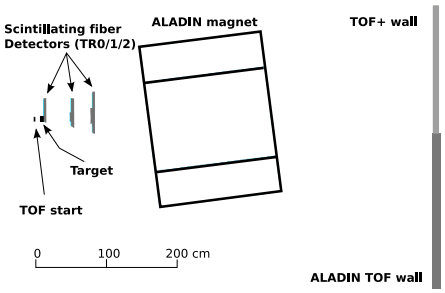

Figure 1: The detector setup for the phase - 0 experiment

Figure 1 shows a setup of the first Phase 0 experiment [2]. Three layers of scintillating fiber detectors (TR0, TR1 and TR2) mounted in front of a large dipole magnet, ALADiN, will be used for tracking particles to reconstruct secondary decay vertices.

Behind the ALADiN magnet, there are two Time-Of-Flight (TOF) walls which measure time and positions of registered particles. One of the TOF walls so called the ALADiN TOF wall already exists and will be used to measure π^-, and the other TOF wall, TOF+, for positively charged particles is under construction. The size of wall is approximately 1×1 m^2 with a centered hole (7.5×6.5cm) for the primary beam [3].

Prototype detectors of TOF+ wall were tested with cosmic rays and in the experiment in cave B by measuring light fragments produced by ^{58}Ni and ^{12}C beams. Prototype detectors tested in the experiment were made of Bicron BC-408 plastic scintillators. The length of the two solid prototypes is 1m and one prototype consists of two bars separated by 6 cm as a hole for primary beams. Scintillating photons are read out by photomultipliers mounted in the both sides of the bars.

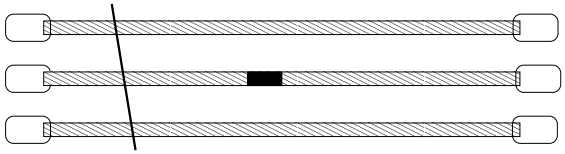

Figure 2: Experimental setup for cosmic ray measurement

Time resolution of the prototypes was measured by cosmic-rays. Three prototype bars were mounted as shown in Figure 2. In the measurement a coincidence of the signals of photomultipliers in the both sides in the first bar was required. A rough estimation of time resolution was obtained with fitting by Gaussian on the time difference histogram between third and fist bars. The time resolution in σ is ~ 340ps.

Detailed analyses were performed with the time walking correction for the leading edge discriminator modules and the position selection. The time walk was corrected with an equation $T = T_0 + a + \frac{b}{\sqrt{q}}$, where T_0 and T are measured and corrected time, while a and b are parameters. The time resolution after the time walking correction is ~ 225ps. To avoid the effect by the different flight distances of propagating photons in the bars, the event selection was made in a small part of bars (10cm). The time resolution with the selection is 150ps.The energy resolution was measured with cosmic-rays by fitting the energy deposit distribution by means of the Landau function, which resulted in an energy resolution of $\sigma_E = 0.5$MeV ($\sim 10\%$) .

The HypHI collaboration would like to thank to the FOPI collaboration for its supports to the test experiments in cave B.

References

[1] T.R. Saito, et al., Letter Of Internet of "Hypernuclei with Stable Heavy Ion Beam and RI-beam Introduced Reaction at GSI (HypHI)". Submitted to GSI EA 30.

[2] A proposal of the HypHI Phase 0 experiment, the HypHI collaboration, submitted to GSI PAC EA33 with a realization as S319.

[3] Rappold, C. et all (2006) Design studies on Time-Of-Flight walls for the HypHI project, GSI Scientific Report 2006, GSI, Darmstadt

The trigger system for hypernuclear spectroscopy with heavy ion beams (HypHI)

S. Minami[1,2], P. Achenbach[2], S. Ajimura[3], S. Bianchin[1], O. Borodina[1], T. Fukuda[4], Y. Hayashi[5], T. Hiraiwa[5], J. Hoffmann[1], M. Kavatsyuk[1], N. Kurz[1], O. Lepyoshkina[1], Y. Mizoi[4], T. Mochizuki[6], M. Moritsu[5], T. Nagae[5], D. Nakajima[7], W. Ott[1], J. Pochodzalla[2], C. Rappold[1,8], A. Sakaguchi[6], T.R. Saito[1], K. Tanida[5], and W. Trautmann[1]

[1]GSI, Darmstadt, Germany; [2]Inst. für Kernphysik, Joh. Gutenberg-Universität, Mainz, Germany ; [3]RCNP, Osaka University, Ibaraki, Japan ; [4]Osaka Electro-Communication Univ., Neyagawa, Japan ; [5]Kyoto University, Kyoto, Japan; [6]Osaka University, Toyonaka, Japan ; [7]Univ. of Tokyo, Bunkyo, Japan ; [8]Univ. Louis Pasteur, Strasbourg, France

The HypHI project aims to study hypernuclei produced as projectile fragments of heavy ion collisions. The first experiment of HypHI, Phase 0, has been designed to identify mesonic decays of the lightest hypernuclei, ${}^{3}_{\Lambda}\mathrm{H} \rightarrow {}^{3}\mathrm{He} + \pi^-$, ${}^{4}_{\Lambda}\mathrm{H} \rightarrow {}^{4}\mathrm{He} + \pi^-$ and ${}^{5}_{\Lambda}\mathrm{He} \rightarrow {}^{4}\mathrm{He} + \mathrm{p} + \pi^-$ produced by collisions of a ^{6}Li beam of 2 *A* GeV and a ^{12}C target [1]. An efficient trigger system is essential because of the expected high reaction rate. The data acquisition (DAQ) system and the electronics used for the experiment constrain the trigger decisions to be reached within 500 nsec with a rate of less than 3 kHz. The detector system of Phase 0 has three layers of scintillating fibre detectors, TR0, TR1 and TR2 behind the target [2]. They are primarily for precise measurements of decay vertices of Λ hypernuclei whose decay path length is about 20 cm in average by assuming a typical lifetime of 0.2 nsec. This feature of decay vertices is also used for the trigger decision by requesting hit patterns on TR0, TR1 and TR2. There are two Time-of-Flight (TOF) walls behind the ALADiN dipole magnet, one for π^- (ALADiN-TOF) and the other for α and proton (TOF+) [3]. The trigger system requests at least one hit with large energy deposit by α at TOF+ and at least one hit at ALADiN-TOF. Trigger rates have been studied by Monte Carlo simulations. The efficiency of ${}^{4}_{\Lambda}\mathrm{H}$ events and the factors of the background reduction are listed in Table 1. For the case of the background, we only use UrQMD outputs [4] as an input to GEANT4 to simulate hadronic reactions in the target. About 40% of the beam is estimated to cause hadronic reactions. The trigger system with 'full trigger' will, therefore, produce triggers with a rate of 0.7 kHz under the condition that the rate of ^{6}Li beam is 10^7 /sec, which fulfills the constraint given by DAQ. It is also shown that the efficiency to select ${}^{4}_{\Lambda}\mathrm{H}$ is kept as high as 7.0%, taking the inefficiency of the detector system into account. The trigger will be made by a newly developed logic module, VUPROM1, a VME 6U module with a PLD, Virtex-4, which is capable to be operated with a clock of 400 MHz frequency [5]. The TOF+ trigger based on time over threshold (TOT) to select α has been tested with the VUPROM1, measuring particles from collisions of a ^{58}Ni beam of 1.9 *A* GeV with a ^{12}C target [6]. Analog signals from TOF+ are fed to comparators and the outputs from the comparators generate TRUE signals while inputs exceed the threshold. The outputs are fed to VUPROM1 to measure TOT with the granularity of 2.5 nsec. TOT is expected to depend on the energy deposit by particles through TOF+. A plot of the energy deposit measured by charge sensitive ADC vs TOT by VUPROM1 is shown in the left panel of Figure 1, and a clear correlation can be observed. The right histogram shows TOT spectra of all events and for events after applying a cut to enhance α. One can observe a peak by α after the cut which is well separated from the proton peak in the ungated spectrum. A large fraction of events without α on TOF+ can be rejected on the trigger level by selecting pulse width of α by VUPROM1.

Table 1: The efficiency for ${}^{4}_{\Lambda}\mathrm{H}$ and reduction factors of the background.

Trigger	${}^{4}_{\Lambda}\mathrm{H}$ Efficiency (%)	Background Reduction (%)
Vertex	14.	1.7
ALADIN-TOF	28.	15.
TOF+	94.	14.
Full trigger	7.0	0.017

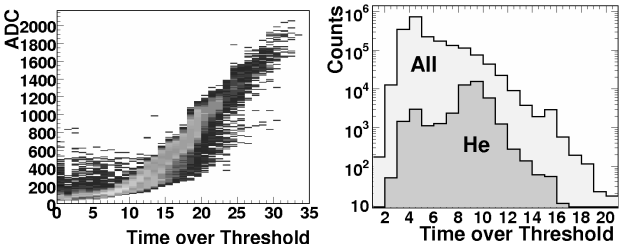

Figure 1: Left) ADC vs TOT by VUPROM1. One channel of VUPROM1 corresponds to 2.5 nsec. Right) TOT with all events and events after applying a cut to enhance α.

References

[1] T.R. Saito *et al.*, Proc. The IX Int. Conf. on Hypernuclear and Strange Particle Physics (HYP2006), Springer-Verlag (2007) 171. ; The HypHI collaboration, A proposal of the HypHI Phase 0 experiment, submitted to GSI PAC (S319).

[2] D. Nakajima *et al.* in these reports.

[3] C. Rappold *et al.* in these reports. ;O. Borodina *et al.* in these reports.

[4] M. Bleicher, *et al.*, J. Phys. G **25** (1999) 1859.

[5] J. Hoffmann *et al.* in these reports.

[6] T.R. Saito *et al.* in these reports.

Scintillating fiber detectors for Phase 0 experiment of HypHI project

D. Nakajima[1,2], P. Achenbach[3], S. Ajimura[4], S. Bianchin[1], O. Borodina[1], T. Fukuda[5], Y. Hayashi[6], T. Hiraiwa[6], J. Hoffmann[1], M. Kavatsyuk[1], N. Kurz[1], O. Lepyoshkina[1], S. Minami[1,3], S. Mizoi[5], M. Moritsu[6], T. Mochizuki[4], T. Nagae[6], W. Ott[1], J. Pochodzalla[3], C. Rappold[1], T. R. Saito[1,3], A.Sakaguchi[4], K. Tanida[6], and W. Trautmann[1]

[1]GSI, Darmstadt, Germany; [2]Univ. of Tokyo, Bunkyo, Japan; [3]IKP Mainz Univ., Mainz, Germany; [4]Osaka Univ., Osaka, Japan; [5]Osaka Ele.-Comm. Univ., Neyagawa, Japan; [6]Kyoto Univ. Kyoto, Japan

The HypHI project at GSI and FAIR aims to perform hypernuclear spectroscopy with stable and unstable heavy ion [1]. Hypernuclear spectroscopy via a heavy ion beam collision is the only way to produce hypernuclei at extreme isospins and to measure magnetic moments of hypernuclei. The first step of the project defined as Phase 0 has been proposed to demonstrate the feasibility of the experimental principle by identifying ${}^{3}_{\Lambda}$H, ${}^{4}_{\Lambda}$H and ${}^{5}_{\Lambda}$He with a 2.0 A GeV ^{6}Li beam impinged on a ^{12}C target [2, 3].

The HypHI collaboration has already completed the design study of the detectors and setup based on Monte Carlo simulations and currently works on the R&D of detectors for Phase 0. The experimental setup consists of the ALADiN magnet, three sets of fiber detectors (TR0, TR1, TR2), TOF wall for negatively charged particle (the ALADiN TOF wall), another TOF wall for positively charged particle (TOF+), and two sets of drift chambers. Three sets of fiber detectors will be used for tracking particles from the target. The most crucial background in Phase 0 could be events with an unbound Λ hyperon associated with the production of a high energy α-particle, because this gives the same final state as the hypernuclear event with a missing proton detection. In events of hydrogen hypernuclear events, there should be no α-particle at TR0 but produced behind TR0 after their decay. Therefore, the hydrogen hypernuclear events can be distinguished from the free-Λ events with an α-particle by selecting $Z = 1$ events at TR0, which requires the energy resolution of TR0 being good enough to separate particles with $Z = 1$ and 2.

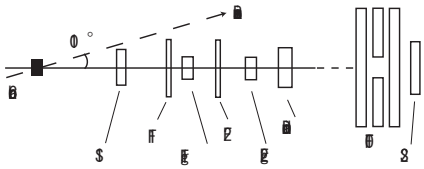

Figure 1: A schematic drawing of the setup

A test experiment has been performed in Cave B in order to test prototypes of the HypHI detectors, and the performance of the two prototypes of fiber detectors(F1, F2) were tested. Figure 1 shows the schematic drawing of the setup of the test experiment. The ^{58}Ni and ^{12}C beams, respectively at 1.9 and 0.85 A GeV, delivered behind the FOPI detector were fragmented into light particles in a ^{12}C target, and these light fragments were used to test prototype detectors. These detectors were placed at an angle of 10 degrees with respect to the primary beam axis to enhance measurements of light fragments. Both of the two fiber detectors, F1 with 4-fiber-layers and F2 with 2-fiber-layers, were mounted between two plastic detectors, a start counter for Time-of-Flight, referred to as S1 in Figure 1, and Fg2. Between F1 and F2, there was an additional plastic detector (Fg1). Figure 2 shows the distribution of the energy deposition of proton, α, and Li particles measured by F1. These spectra show reasonable separations for particles with different charges.

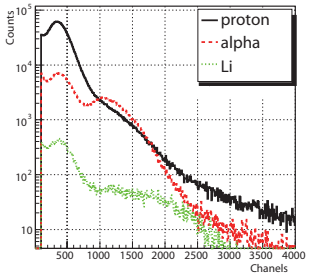

Figure 2: Spectra of the energy deposition for proton, α, and Li measured by fiber detector

The intrinsic time resolution of the fiber detectors was measured in the test experiment and is $\sim$ 1.5 ns in σ for over all the channels.

Since the beam intensity in Phase 0 will be 10^7 ions/s, the fiber detectors should be tolerant to such a high counting rate. Thus the stability of the multianode PMT (Hamamatsu H2760) has been checked under high current in the test experiment. The PMT was mounted in the beamline, and the pulse height and current of the PMT were measured. We observed that PMT was immune to $\sim$ 50 μA/ch. It is expected to be $\sim$ 40 μA/ch by the beam for Phase 0. Therefore, it is implied that the PMT will meet the requirement of Phase 0.

The HypHI collaboration would like to thank to the FOPI collaboration to supports the test experiments in Cave B.

References

[1] T.R. Saito *et al.*, Letter Of Intent of HypHI.

[2] T.R. Saito *et al.*, A proposal of HypHI Phase 0 experiment, submitted to G-PAC 33.

[3] T.R. Saito *et al.*, Progress Report on Proposal of the HypHI Phase 0 experiment submitted to the G-PAC 34.

Position reconstruction in large area scintillating fibre detectors

K. Mahata*[1], H. Johansson[1,2], S. Paschalis[3], H. Simon[1], and T. Aumann[1]

[1]GSI, Darmstadt, Germany; [2]Chalmers Uni. of Tech., Göteborg, Sweden; [3]Uni. of Liverpool, UK

Large area (50×50 cm^2) scintillating fibre detectors are used to detect charged fragments in the reaction studies with relativistic ion beams in the LAND experimental setup at GSI. These detectors are employed to reconstruct the trajectory after a large acceptance dipole magnet (ALADIN) of the heavy fragments from the reactions in order to determine their masses. Each of these detectors consists of about 500 parallel fibres of 1×1 mm^2 cross section allowing for a precise position determination in the dispersive plane. Instead of reading each individual fibre separately, one end of each fibre is coupled to a position sensitive photomultiplier (PSPM), using a specially designed mask. The PSPM has a rectangular anode grid with 18 wires in one direction (u) and 16 wires in the orthogonal direction (v). When an ion passes through one of the fibre, the resultant light induces electrical signals in a few surrounding anode wires. These charge distributions in u and v coordinates, with sub-wire resolution, are used to identify the fibre. Further details about the detectors can be found in Ref. [1].

A new analysis procedure has been developed for position reconstruction in these detectors. It includes gain matching of the PSPM, calibration of the PSPM fibre mask and hit reconstruction.

The measured charge distributions exhibit Gaussian-like shape with about 7 entries each in both u and v. Previously, a weighted mean of the distributions was used for the position information. However, the gain of the PSPM can be position dependent and the signals are amplified using different amplifiers before digitization, which introduces further gain mismatch. In order to overcome the resulting distortions, two inverted parabolas are fitted to the natural logarithm of the measured charge distributions for each hit. Relative gain factors are obtained by minimising the relative residues iteratively. The parabola centroids (u_0, v_0) are used as the hit position in the PSPM.

In a reconstructed image of the PSPM mask (uv plot), each fibre appears as a cluster of points (hits) as shown in Fig. 1. The mean positions $(\bar{u}, \bar{v})$ and the widths of the clusters, representing the fibre location in the PSPM mask, are found out by projecting all the hits onto a 2-dimensional histogram with 1000×1000 bins. After finding the position of all clusters, their neighbours (top, down, left, right) are determined using the distance and angle of the vector connecting them. Using this neighbour information, an integer index pair (*k*, *l*) is assigned to each cluster such that *k* and *l* become column and row indices, respectively. This gives a (*k*, *l*) grid with the corresponding fibre position $(\bar{u}, \bar{v})$ on the PSPM and the position of the fibre in the detector (*x*).

To reconstruct the hits quickly, a lookup table, containing the range of *k* and *l* which can come into play for each unit square in the *uv* coordinate space, is prepared. To reconstruct a hit with coordinate (u_0, v_0), the relevant range of *k* and *l* is first found from the lookup table. Finally, the position is calculated as weighted average of the position of the surrounding clusters (fibres). An exponential probability distribution as a function of distance of the hit from the corresponding cluster has been used to calculate the weights. The width of the distribution, shown in Fig. 1 (inset), corresponds to a individual detector resolution of $\sigma_x \sim 500$ μm.

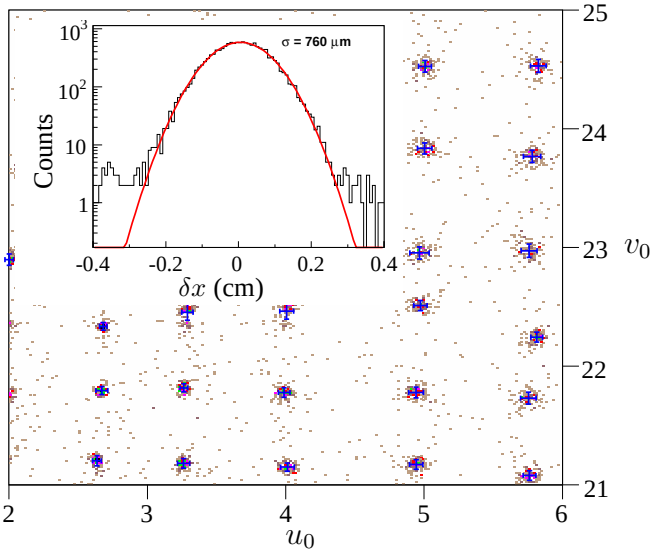

Figure 1: Part of the 2-dimensional (u_0, v_0) histogram for 650A MeV ^{58}Ni ions, used to find the mean position and width of the clusters. The mean positions of the clusters are indicated by crosses. The extents of the crosses correspond to the widths ($\pm\sigma_{u,v}$) of the clusters. Inset shows the difference between the measured position in a third fibre detector and the position extrapolated from two fibre detectors upstream along with a Gaussian fit.

The present procedure allows for a quasi-online calibration for this tracking device. It also allows for a precise determination of the position close to the intrinsic resolution of the detector together with a proper error treatment. Finally, the calibration and the reconstruction procedure has become robust, more precise, easier to use and less time consuming.

References

[1] J. Cub *et al.*, Nucl. Instr. and Meth. A 402 (1998) 67.

* Permanent address: NPD, BARC, Mumbai 400 085, INDIA

Commissioning of the FOPI ToF Barrel *

M. Kiš[1], M. Ciobanu[1,2], P. Gasik[3], N. Herrmann[2], K.D. Hildenbrand [1], T.I. Kang[1,4], P. Koczon[1], Y. Leifels[1], M. Marquardt[1], K. Piasecki[2,3], A. Reischl[2], M.-S. Ryu[1,4], A. Schüttauf[1], J. Weinert[1], N. Zernezki[1], X.Y. Zhang[1], and FOPI Collaboration[1]

[1]GSI,Darmstadt, Germany; [2]Physikalisches Institut, Heidelberg, Germany; [3]University of Warsaw, Warsaw, Poland; [4]Korea University, Seoul, South Korea

During the year 2007 the new ToF Barrel of FOPI was installed and successfully commissioned in a heavy-ion beam production-run experiment. The particular Multi-strip Multi-gap Resistive Plate Counter (MMRPC) design was developed by the FOPI collaboration [1] together with a custom-made front-end electronics [2], while the readout electronics for the detector was developed by the GSI EE department [3].

The MMRPC Barrel (shown in Fig. 1) was commissioned with 26 so-called supermodules (SM) installed, where each SM consists out of a carbon fiber box housing five counters and the readout electronics behind the box. The counters are built from common float glass as

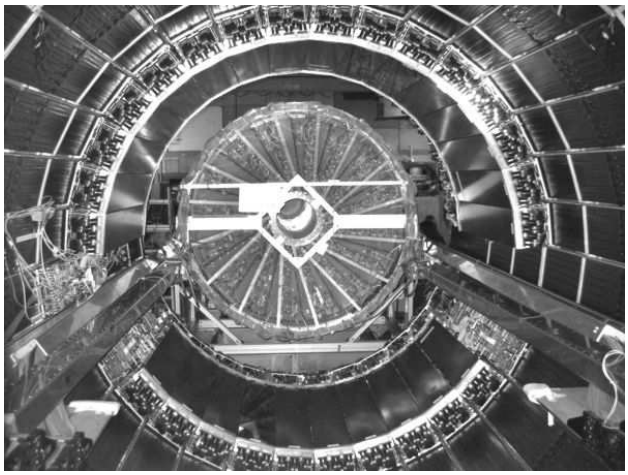

Figure 1: The MMRPC ToF Barrel is mounted inside of the FOPI magnet between the old Plastic ToF Barrel and the Central Drift Chamber (CDC) (moved out of the magnet in this photo).

resistive plate material. Their active volume is divided into 8 gaps of 220 μm and filled with gas mixture of R134a/Isobutane/SF_6 (80:5:15). The active anode area of 4.6 (w) x 90 (l) cm^2 is covered with 16 readout strips. The Barrel covers an active area of about 5 m^2 and polar angles between 36° and 67° in respect to the nominal target position.

We present results obtained in the Ni+Ni (1.92 AGeV) production-run. The ToF resolution $\sigma_{ToF} \leq 100$ ps was determined for the whole system, which includes the START detector as well. The average single-strip time resolution was $\sigma_{t_{ss}} \leq 65$ ps. For the determination of these values only fast pions tracked by the CDC and matched to MMRPC Barrel hits were used. Detection efficiency relative to CDC was about 95%. During the run the dark rate of all counters was well below 0.5 Hz/cm^2 and the whole Barrel was running stable over few weeks.

The obtained ToF resolution allows for a better charged particle identification in comparison to the old Plastic ToF Barrel, in particular K^+ and π^+ can be differentiated up to p $\leq$ 1 GeV/c (see Fig. 2). In the analyzed data set the statistics for K^- is limited. By cutting out slow pions one can intensify the particle separation between kaons and pions, resulting in the clear K^- band shown in Fig. 2. With those results in a very first run FOPI has already reached the design goals of its proposed ToF Barrel upgrade; it is the first system among detectors of similar technology that exhibits such an excellent performance in a running experiment.

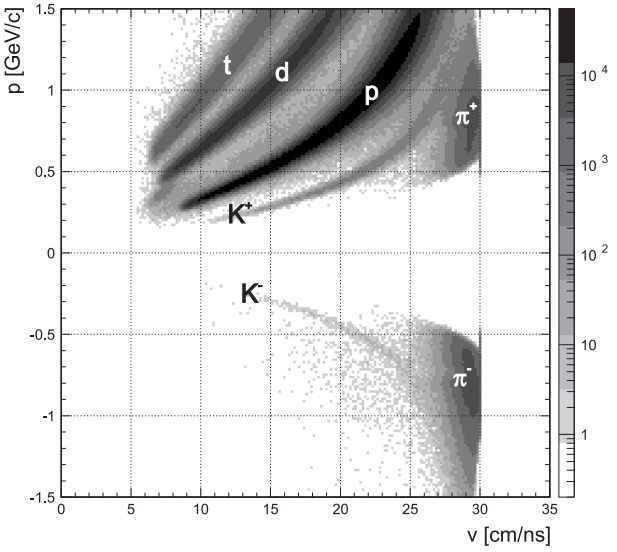

Figure 2: Charged particle identification using momentum measured by the CDC and velocity obtained from the MMRPC Barrel ToF. Note that with the old ToF system, K^- identification was restricted to p $\leq$ 350 MeV/c.

References

[1] A.Schüttauf et. al., Nucl. Phys. B (proc.Supp.) 158 (2006) 52

[2] M. Ciobanu et. al., IEEE Trans. Nucl. Sci. 54 (2007) 1201

[3] K. Koch et al., IEEE Trans. Nucl. Sci. 52 (2005) 745

* Supported by EU/FP6 I3HP contract nr. RII3-CT-2004-506078 and BMBF contract nr. 06HD190i.

A LAAPD based calibration system for FOPIs new MMRPC-barrel *

T.I. Kang[1,3], M. Ciobanu[1,2], M. Kiš[1], A. Schüttauf[1], K.D. Hildenbrand[1], Y.J. Kim[1], P. Koczon[1], Y. Leifels[1], X. Lopez[1], M. Marquard[1], M.S. Ryu[1,3], J.Weinert[1], N. Zernezki[1,2], X. Zhang[1], and the FOPI Collaboration

[1]GSI, Darmstadt, Germany; [2]Universität Heidelberg, Germany; [3]Korea University, Seoul, South Korea

FOPI's new ToF-barrel based on MMRPCs [1] uses a new custom designed readout electronics [2][3] with 4800 independent electronic channels which have to be calibrated in order to reach the envisaged time of flight resolution of $\sigma_{ToF} \leq 100$ ps for the whole system. For this purpose we designed an independent calibration system to determine the relative time and position offsets for all channels.

The design parameters for this system are a time resolution $\sigma_t \leq 500$ ps, insensitivity to magnetic field and a compact size. We decided to use Large Area Avalanche Photodiodes (LAAPD) because of their size and their magnetic field properties (Hamamatsu S8664-55). These LAAPDs were set to a gain of G $\geq$ 50 ($U_{G50} = 370$ V); they have a break-down voltage of $U_B \sim 418$ V. The calibration system itself consists of 2 LAAPDs, mounted at the end faces of a plastic scintillator bar (BC-408), which has a size of 0.8 x 0.8 x 15.5 cm^3. This setup, including the preamplifiers for the LAAPDs, is placed behind an MMRPC-module, orthogonal to the RPC-strips . To amplify the primary LAAPD signal we developed a timing charge sensitive preamplifier (TCSA) [4] with gain G $\sim$ 20 and an excellent timing behavior $\sigma_t \leq 250$ ps. In a second step we use our standard MMRPC-electronics to amplify and digitize the signals [2][3].

The calibration method is based on the idea to use the reaction products during the heavy ion experiment, which pass through the scintillator and the MMRPC to determine the individual time and position offsets for each MMRPC-strip. In a second step it is possible to correct for the walk effect of the MMRPC electronics which uses a leading edge discriminator [3].

We tested this calibration system in October 2007, using a direct proton beam with 1.17 GeV/c at a rate of 1 kHz. Two photo-multipliers with scintillators served as a timing reference ($\sigma_t \leq 40$ ps), the LAAPD system was placed in between them. The main goal of this test was to verify performance, stability and to find the optimal operation regime for the system. For this purpose we varied the applied bias voltage of the LAAPDs and the discriminator threshold of the electronics. As a criterion for the performance we used the time-resolution between the LAAPD system and the reference photo-multipliers. The result of this voltage and threshold scan is shown in Fig 1.

During this test the calibration system was stable and showed, in line with former cosmic-ray measurements, a time resolution of $\sigma_t \leq 353$ ps at the highest bias voltage of $U_b = 408$ V. A decrease of the bias voltage leads to the expected worse timing performance which is due to the lower primary signal in combination with the fixed gain of the TCSA. Nevertheless the time resolution for all voltage settings is below $\sigma_t \leq 510$ ps, which is fully sufficient for all calibration purposes. In addition we were able to choose an optimal voltage between 400 $\leq U_b \leq$405 volt to decrease the current of the LAAPDs to a minimal value and stay well below the break down voltage. The variation of the discriminator threshold at different bias voltages has shown no significant effect on the time resolution.

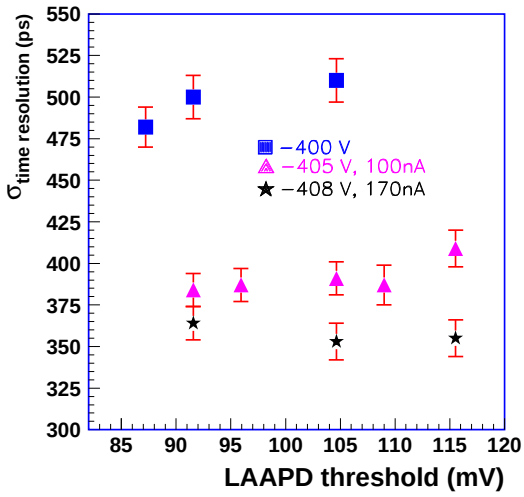

Figure 1: The time resolution of the LAAPD system depending on the discriminator threshold for different bias voltages of the LAAPDs. The best time resolution is reached at a bias voltage of U_b =408 V but a high leakage current for the LAAPDs (170 nA).

From this measurement we can conclude, that the proposed and tested system is fully functional and can be used within FOPI as an independent calibration device for the MMRPCs.

References

[1] A. Schüttauf *et al.*
Nucl. Phy. B (Proc. Suppl.) Vol. 158, pp. 52-55, Aug. 2006.

[2] K.Koch, H.Hardel, R.Schulze, E.Badura and J.Hoffmann
IEEE Trans. on Nucl. Sci., Vol. 52, No. 3, June 2005, 745-747

[3] M.Ciobanu *et al.*
IEEE 2007 Trans. on Nucl. Sci. Vol.54 Nr.4 p.1201

[4] M.Ciobanu *et al.*
Contribution to this annual report

* BMBF

The FOPI GEM-TPC – a precursor prototype for the PANDA-TPC

B. Voss, K. Dermati, J. Hehner, A. Heinz, M. Henske, C.J. Schmidt, S. Schwab,
D. Soyk, U. Tüy, J. Weinert
GSI, Darmstadt, Germany

The Project

In 2007 the construction and building of a medium volume (Ø300mm x 650mm) **T**ime **P**rojection **C**hamber (TPC) based on **G**aseous **E**lectron **M**ultipliers (GEM) as amplification stages has been started. The detector is foreseen to be integrated in several experiments e.g. at ELSA/Bonn, WASA/DESY as well as FOPI/GSI. It serves as a precursor prototype for an even larger TPC (Ø840mm x 1500mm) to be incorporated in PANDA/FAIR as a central tracking device which will be built in the framework of a joint venture project of twelve institutions in Europe.

The Setup

The detector system itself is built completely modular with respect to its components and various functions like supplies, particle detection, amplification, signal mapping and electronic processing (see Fig 1). This minimizes the total risk of a failure in parts of the detector and allows 'stand-alone' operation of all parts as well as the easy exchange and testing at various places in the world. As an additional concept we aim to profit from the cylindrical symmetry of the particle production and identification as much as possible, e.g. by sectioning the 3(4) GEM-layers in an iris-like pattern and subdividing the readout into 46 identical cake-like sectors. The optimum building layout of the pad plane is obtained by ≈ 11700 pads of equal size (≈ 5.9 mm^2) and hexagonal shape. These pads are readout via 46 cards of front-end electronic (FEE) each carrying two N-XYTER [1] chips being capable to handle 128 channels each. Due to the overall power-consumption of ≈ 220 W, a cooling system based on special liquids is foreseen. All necessary media are supplied to and distributed by a common 'media' flange which also carries the field cages and the other flanges and serves to mount the detector. The low and high voltage necessary to operate the FEE (3.3V) and GEMs (≈2kV) and the field cage (≈ 30kV), respectively, is supplied from outside the detector. As an option the high voltage may be generated on site, too. All relevant operational parameters like the flow of the detector gas (e.g. Ne/CO_2) and its pressure, temperatures at various places, supplied voltages etc. are monitored by an adequate sensor system.

The whole detector will be operated inside the magnetic field of the FOPI magnet (see Fig. 2). The 'Spider', a light-weight and still very stiff CFK structure, will serve as a support for the TPC with a weight of roughly 20 kg to be mounted close to the interaction point as well as a platform for additional equipment to be installed upstream of the target. It will be flanged to the outer ring of the vessel of the **C**entral **D**rift **C**hamber (CDC).

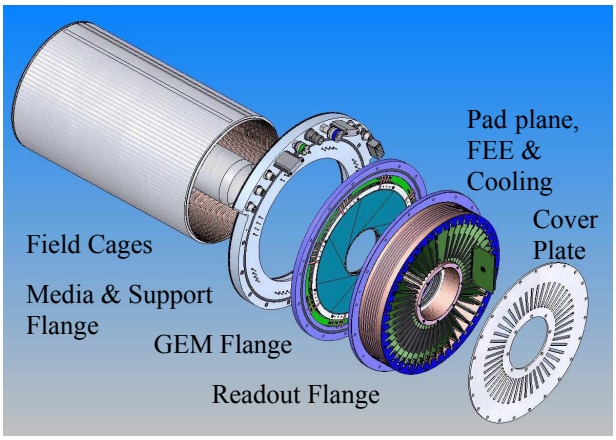

Figure 1: Exploded view of the FOPI GEM-TPC revealing its modular design.

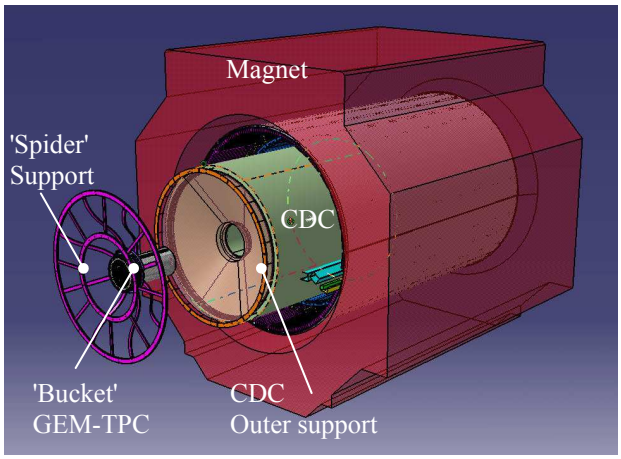

Figure 2: Experimental surrounding at FOPI. The GEM-TPC is mounted on the 'Spider' CFK structure.

Status & Outlook

A first version of the mechanical parts of the detector has been built in order to study different versions of the design in detail. Currently, different scenarios and materials for the support and field defining system of the inner and outer field cage are under investigation, which are based on metallic strip lines on Kapton® (single surface and staggered), PCB strip lines and resistive foils. Moreover, the setup of the production tools and the quality assurance procedures are the central tasks to be performed. It is planned to finalize the detector setup within 2008.

References

[1] Schmidt C.J. et al., GSI Scientific Report 2006, 2007-1, p.238.

A Λ Trigger for the FOPI Detector System *

M. Berger[1], L. Fabbietti[1], O. Hartmann[1], R. Münzer[1], M. Reithner[1], and the FOPI Collaboration
[1]TU München, 85748 Garching

Recently, the search for deeply bound nuclear states with antikaons has attracted large interest. In Ref. [1], the authors claim that the p+p reaction might be a promising tool to produce (K^-pp) nuclear bound states. Such an experiment will be performed using the FOPI detector [2] to detect the final state particles.
The final state of the pp→(K^-pp)K^+ → ΛpK^+ reaction involves Λ hyperons which can be detected using their decay into p + π^- (64% branching ratio). Thus, the FOPI detector will be extended by a Λ trigger system, in order to enrich events containing Λ candidates.
Such a Λ trigger (SIΛVIO – SIlicon Λ Vertexing and Identification Online) built from (double sided) silicon strip detectors is currently under construction. The concept foresees at least two detector layers downstream of the target with distances such that the bulk part of the produced Λs should decay in between the two layers. Fig. 1 illustrates the configuration to be used: the first layer is an annular single sided silicon divided into sectors (left panel), and layer 2 is an arrangement out of eight double sided silicons with rectangular area and strips on both sides. Layer 1 is placed approx. 3 cm behind the target, and layer 2 has a distance of 10 cm from layer 1. The polar angular coverage of the setup from ranges from ≈10° to ≈33°.

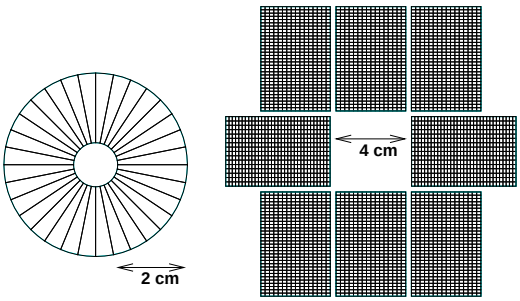

Figure 1: Cut through the two silicon layers. Left: layer 1, right: layer 2. The hole in the middle is left for the beam.

The two layers as shown in Fig. 1 are incorporated into the FOPI simulations environment based on GEANT3.21. The simulations aim to study the acceptance and efficiency of the trigger including all relevant physics processes and finally the reconstruction of the physical signal using the information of all subdetectors. To test the performance of the trigger, the yield of accepted events coming from the signal reaction compared to background events using a transport model (UrQMD) has been evaluated under different trigger conditions. The easiest and probably most practical condition, requesting at least one hit in the first layer and at least one hit more in the second layer, accepts 26% of the signal events and rejects about 96% of the background. Applying other trigger conditions, the background rejection can be improved but on the cost of the accepted signal. Production of δ electrons and small angle scattering are included in the simulation.

A test of the trigger concept has been carried out at GSI in October 2007. A π^-, ($p\pi^+$) beam of 1.17 GeV/c momentum has been focused directly on two consecutive double sided detectors with 40·40 mm^2 area, 1 mm pitch on each side and a thickness of 1 mm. The aim of this measurement was to test the online trigger capability for MIPS and the integration of the trigger into the FOPI DAQ. The readout of the silicon detectors was done using the Mesytec analog electronics which provide a relatively fast information on the number of channels that fire above a given threshold. Such signals are employed to compare the hit multiplicity of two consecutive silicon layers and realize a Λ trigger. During the test experiment, data have been stored for multiplicity triggers equal to 1 or to 2. For a given trigger, the number of MIPS per event are processed offline and divided by the number of triggered events. In Fig. 2 the outcome is plotted as a function of the run number. For an ideal trigger the purity should be 1 or 2 for the multiplicity triggers 1 or 2, respectively. The experimental result is close to this value and the purity of the trigger is estimated to be 94-98%.

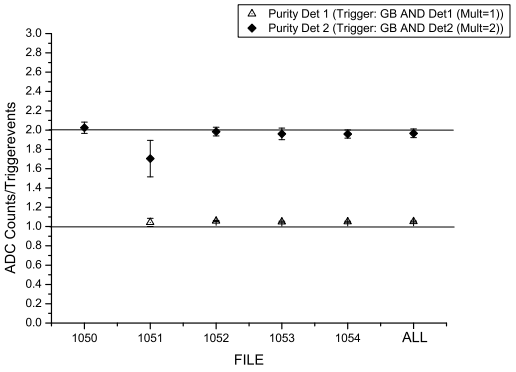

Figure 2: Trigger purity for two different trigger multiplicities as a function of the run number.

References

[1] Yamazaki and Akaishi, Phys.Rev.C 76(2007)045201
[2] http://www.gsi.de/documents/DOC-2007-Mar-168-1.pdf

* Work supported by HGF and DFG-Excellence Cluster Universe

Fibre Optical Interface Based FOPI RPC Acquisition System.

J.Hoffmann, K.Koch, N.Kurz, W.Ott, P.Skott
GSI, Darmstadt, Germany.

A GTB [1] to fibre optic interface "GTBLWL" has been developed for the FOPI RPC detector control and readout and is usable for other GTB data transmissions. The main motivation for this development was galvanic separation of the detectors from readout and trigger electronics to reduce the noise level at the detector. Another advantage of optical data transmission is insensitivity to external interferences.

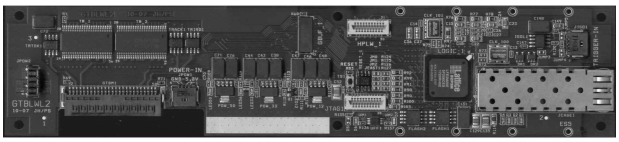

Figure 1: Photograph of GTBLWL board.

The form factor of the GTBLWL PC board was selected for the best fit into the existing FOPI RPC super module [4]. Two GTBLWLs are connected together over 15m fibre optical cables, one of them is connected to detector electronics, the other to the VME DSP module SAM5 [2]. This connection allows bidirectional data transfer. The function of GTBLWL as master or as slave (mounted in super module) is given by FPGA software only.

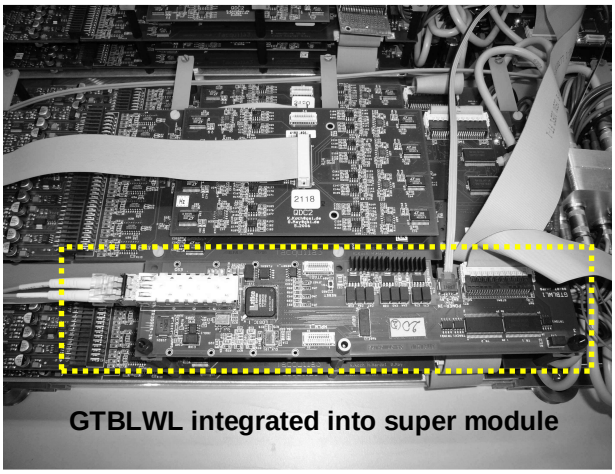

Figure 1: Photograph of GTBLWL board integrated in a super module.

The 2 Gigabit (serialiser/deserialiser) SERDES module is implemented in FPGA. It serializes GTB data and control signals and sent them to the optical link transceiver. Some latency is added to the data stream by the SERDES module. The serial data transfer speed doesn't slow down the GTB data transfer. The laboratory test setup with two GTBLWL interface channels and 40 TACQUILA [3] modules is running for several weeks without errors. The production of 35 modules is already finished.

The final installation at the FOPI experiment will include 15 fibre optic interface pairs reading out 30 super-modules, which correspond to 4800 channels.

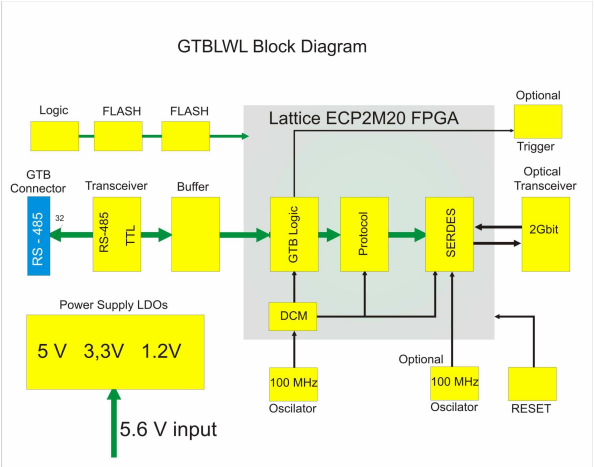

Figure 3: Block diagram of the GTBLWL board.

Once detector electronics is assembled it will be very complex to dismount or remove electronic modules. For that reason the possibility to exchange remotely the FPGA design is implemented. After power up the default design is loaded from first memory. The second FLASH is integrated and can be written over fibre optic connection. With help of special command the content of second FLASH can be loaded into FPGA. In case of problems the old design can be reloaded after switching off and on the power supply.
An optional galvanically isolated trigger circuit is implemented. It requires an additional two wire cable for connecting GTBLWL boards.
All together fifteen GTBLWL pairs are needed for the FOPI RPC setup. 15 master boards will be placed in 19 inch crate equipped with power supply and new developed Europe format adapter boards.

References

[1] www.gsi.de/informationen/wti/ee/elekt_entwicklung/GTB.html
[2] http://www.gsi.de/informationen/wti/ee/elekt_entwicklung/sam5_e.html
[3] http://www.gsi.de/informationen/wti/ee/elekt_entwicklung/tacquila_e.html
[4] http://www.gsi.de/informationen/wti/library/scientificreport2006/PAPERS/INSTRUMENTS-METHODS-24.pdf

Timing Properties of CVD-Diamond Detectors at RelativisticVelocities*

E. Berdermann, M. Ciobanu, M. Kiš, W. Koenig, M. Pomorski and M. Träger
GSI, Darmstadt, Germany

Heavy-Ion Induced Transient Currents (TC)

In order to investigate the behaviour of Single-Crystal CVD-Diamond Detectors (SC-DD) at relativistic ion velocities, we measured original TC Signals (TCS) induced by ^{132}Xe ions of 215AMeV in a SC-DD of a thickness d_D =400µm and a capacitance C_D=0.9pF. At a rate of 1.6kHz, a charge Q_G^{Xe} =1.2*10^8 e-h pairs/ion was generated in the diamond bulk. We present a data discussion according to the theory of Space-Charge Limited Current transients (SCLC) [1], expected for $Q_G > Q_{BI}$, with $Q_{BI} = C_D * V_D$ the bias-induced charge at the electrodes of the sensor.

The ^{132}Xe pulses were recorded with a 1GHz DSO of 10GS/s resolution, connected to the diamond via a high-frequency transmission line of 30m lengths. We compare the shapes of the ^{132}Xe transients with α-signals measured in the laboratory using a broadband amplifier and a 3GHz DSO. Each α-particle generates a charge of Q_G^{α} = 4.2*10^5 e-h pairs within the α-range of 12µm, and represents the 'small-signal case' at 'single-carrier drift'.

Figure 1 shows average ^{132}Xe transients obtained in the bias range 10V≤ $|V_D|$ ≤ 800V (solid and dotted lines) and an average α-signal (dashed line) measured at V_D=800V. Note, the α-amplitude is magnified by an arbitrary factor.

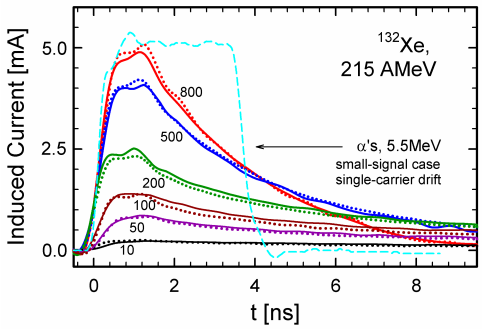

Figure 1: Original TCS obtained in the bias range 10V ≤ $|V_D|$ ≤ 800V from ^{132}Xe ions of 215AMeV (solid and dotted lines). A ^{241}Am-α-transient (dashed line) represents the 'small-signal case' at 'single-carrier drift'. (see text)

The RC_D time constant of the circuit was as short as 45ps at 50Ω impedance. In addition, the bias resistor of 10kΩ ensured a constant voltage on the electrodes at all times, and the measurements were performed in the so-called 'current mode'. The flat top of the α-signal demonstrates the homogeneity of the internal drift field and the absence of trapping and recombination. The right 'kink' indicates the arrival of the leading hole to the backward, grounded electrode and the top width defines the transition time t_{Tr}. In contrary to the prompt signal decay in the 'small-signal case', ^{132}Xe-generated TCS show much longer relaxation time (≈7ns), given by the time needed to expel all space charge from the crystal. Charge expulsion is supported by free carriers present in the neutral detector at thermal equilibrium. Hence, it is faster for low-quality diamond detectors, e.g. for polycrystalline sensors.

The rising slope dI/dt of the ^{132}Xe TCS was maintained at $t_{rt} \leq$ 200ps. The area of pulses recorded at $|V_D| \geq$ 25V were equal to the theoretically predicted charge of Q_G = 19.22pC, indicating a charge-collection efficiency near to unit. The transition time t_{Tr} decreased from t_{Tr}=3ns for the 'small-signal' case to t_{SCLC} = 650ps for the ^{132}Xe transients. This effect was expected, however not only because of the 'dual-carrier drift'. According to the standard SCLC theory, the transit time drops also at 'single-carrier drift' to a constant value $t_{SCLC} = 0.78 * t_{Tr}$ in the transition from the 'small-signal' case to the SCLC case. In our experiment, t_{Tr} saturates for $|V_D| \geq$ 50V, and that is evident to the onset of SCLC for $Q_G^{Xe} \geq$ 45pC (i.e., two ions in a time in the counter). The almost same level of both 'kinks', confirms equal mobility of electrons and holes and the absence of bulk trapping.

Time Resolution for Relativistic Protons

We tested the time resolution of SC-DD using 3.5GeV protons and a new low-capacitance broadband amplifier designed for the diamond start detectors of the HADES spectrometer. Two SC-DD of a thickness d=300µm, equipped with 3mm circular electrodes segmented in four quadrants, were mounted each on an amplifier pcb in order to minimize stray capacitances. Figure 2 shows the time spectrum obtained with two opposite diamond segments aligned in the proton beam. The intrinsic resolution σ ≈ 107ps achieved, is a significant milestone towards the difficult goal of a σ_{MIP}< 100ps. The tail is due to boarder events of longer drift time - an unavoidable experimental drawback in measurements where relativistic particles are used to test sensors smaller than the beam spots.

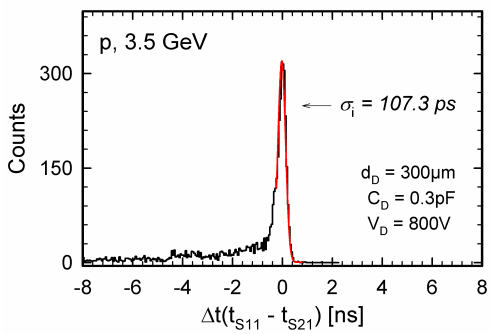

Figure 2: Time resolution of SC-DD for 3.5GeV protons measured with a low-capacitance broadband amplifier.

References

[1] G. Juška *et al.*, Phil. Mag. B 69 (1994) 277

* Work supported by EU, HADRON PHYSICS contract No. 506078.

HADES upgrade: in-beam results from a fully instrumented RPC sextant*

A. Blanco[2], D. Belver[3], P. Cabanelas[3], E. Castro[3], P. Fonte[2,4], A. Gil[5], D. Gonzalez-Diaz[1], T. Heinz[1], W. Koenig[1], C. Muentz[6], M. Palka[1], J. Pietraszko[1], A. Rustamov[1], E. Schwab[1], Y. Sobolev[7], A. Tarantola[6], K. Teilab[6], M. Traxler[1], R. Trebacz[8], S. Yurevich[1], and the HADES-RPC group

[1]GSI, Darmstadt, Germany; [2]LIP, Coimbra, Portugal; [3]USC, Santiago, Spain; [4]ISEC, Coimbra, Portugal; [5]IFIC (CSIC-UV), Valencia, Spain; [6]IKF, Frankfurt, Germany; [7]ASCR, Prague, Czech Republic; [8]JU, Cracow, Poland

With the test of a full sextant the HADES-RPC group made a step forward towards the desired upgrade that will cope with the highest multiplicity collisions from year 2009. The HADES-RPC wall, consisting of 1200 RPC strips with a maximum packing density of 1/(2x15) cm^2, optimizes the number of electronic channels by minimizing the inter-strip cross-talk through adequate shielding. Once the detector concept was validated in a series of tests performed in 2003-2005 [1], [2], [3], [4], the emphasis was put since in ensuring the overall stability of the 400 FEE channels equipping each sextant, at nominal particle loads and under a realistic particle background. As the more salient features of the RPC-FEE and DAQ systems, the following must be mentioned: i) 10x6 DC-DC switching converters, ii) 16x6 MBOs (MotherBOards) providing power regulation and distribution, signal collection, multiplicity trigger, threshold setting/monitoring and temperature, voltage and current sensing, iii) 100x6 DBOs (DaughterBOards) providing 31dB amplification with 2.2 GHz bandwidth, 40 ns built-in dead time and charge-to-ToT conversion, codified in an LVDS output signal (see W. Koenig et al., this report) and iv) 4x6 general purpose TRBs (Trigger and Readout Boards) based on the HPTDC ASIC from CERN (see M. Traxler et al., this report). All modules are custom-made.

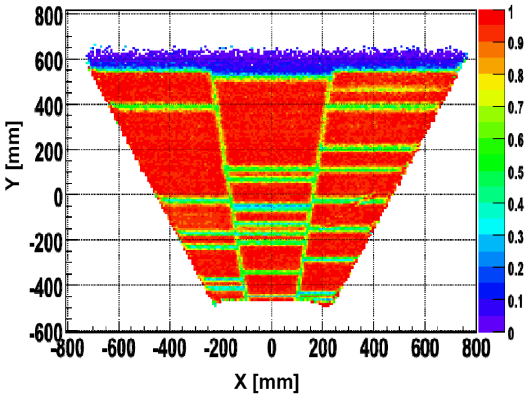

Figure 1: Efficiency of the RPC sextant.

Mid-October 2007, an RPC sextant was instrumented and exposed for one week to secondary particles from reactions of a C beam on Be and Nb targets at 2 GeV/A kinetic energy. Operation of the RPC was performed in conjunction with the tracking chambers (MDCs), the PreSHOWER and the TOF wall (for the reaction trigger). The RPC efficiency was obtained (Fig. 1) by extrapolating each MDC-PreShower track onto the RPC wall and opening a ± 10 cm searching window in Y with respect to the extrapolated position and a ± 10 ns window with respect to the trigger signal. Fig. 1 shows the mechanical division of the sextant in 3 columns per layer (delimited by up-down slanting zones with $\sim 70\%$ efficiency) and the absence of some detector strips (that could be traced back to non-operative DBO channels, already noticed before assembly). A region above 550 mm is also visible where a set of 4 short-MBOs (with only 3 DBOs each) was not instrumented due to technical problems that have been solved meanwhile. Otherwise, efficiency is fairly uniform at an average of 98%. We aim at a reduced failure rate for the final DBO production.

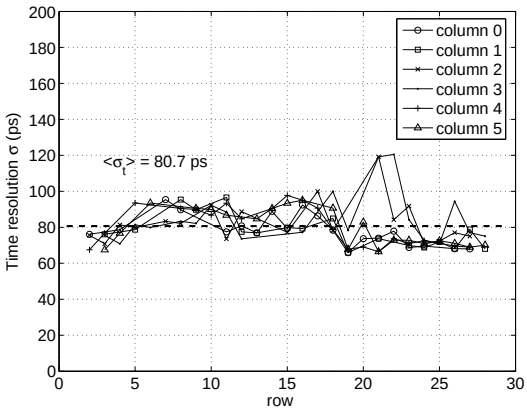

Figure 2: Combined time resolution divided by $\sqrt{2}$ for overlapping strips placed at different columns and rows.

We studied the stability of the system at different comparator thresholds and HV, showing both a comfortable efficiency plateau of ± 20 mV and ± 200 V, respectively. The time resolution of the system was extracted from the time difference between overlapping strips (Fig. 2), yielding 80.7 ps-σ (average) with tails at the level of few percent. In the current analysis the time resolution includes the contribution of particles with different primary ionizations and incident angles. The ongoing differential studies along these variables together with the associated corrections are likely to push the detector performances even further.

References

[1] H. Alvarez-Pol et al, NIM A, 533(2004)79.

[2] H. Alvarez-Pol et al, NIM A, 535(2004)277.

[3] D. Gonzalez-Diaz et al., NIM A, 555(2005)72.

[4] P. Fonte et al., PoS(HEP2005)376.

* supported by EU/FP6 contract 515876 and POCI-FP-81981-2007.

Optimization of the Pion Beam for HADES*

C. Rehm [1], B. Spruck[1], P. Drexler[1], S. Friedrich [1], W. König[2], R. Novotny[1], V. Metag[1]
[1]II. Physikalisches Institut, Universität Gießen, [2] GSI Darmstadt

Previous pion-beam tests revealed several problems in handling the beam. First of all, the π-beam had a halo which lead to a background that disturbed the RICH in a way that the latter could not be run in stable conditions. Furthermore, the focus of the beam showed a strong momentum dependence. Simulations indicated that a way to solve the problems was to introduce an additional quadrupole [1]. Its effect on the beam quality was examined in October 07. During this beam time, primary beam intensitites of about $1.5 \cdot 10^9$ particles per burst were achieved. Such intensities are about a factor 300 below the space-charge limit and a factor 100 below previous experiments. The extraction efficiency was about 50% at a spill length of 1.6 s, with the beam line set to negative polarity. In front of the HADES detector, 10^4 πs with a momentum of 1.17 GeV/c were measured per acceleration cycle. The beam-line with all detectors is shown in Fig1.

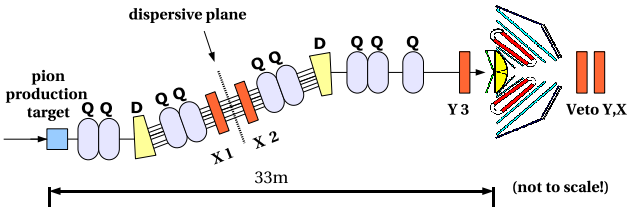

Figure 1: Beam line setup for the pion test beam time with all hodoscopes

In preparation of this test beam-time hodoscopes X1 and X2 were built, consisting of 128 1mm broad and (in beam-direction) 5mm thick scintillatorstrips, which covered an area of 12 $\times$ 12 cm^2 each; both were read out with linear photomultipliers. To reduce the number of channels, two neighbouring strips were read out together, thereby the count rate was distributed over 64 channels and could be kept below 1 MHz per channel.

Fig. 2 shows, as a result, of the test beam-time, the π-beam profile in y-direction, measured in hodoscope Y3, for several angle deviations and deviations from the nominal beam-momentum.

The beam focus is, to first order, momentum-independent. The above given maximal deviations of $\pm 0.3°$ and $\pm 4\%$ are deduced from the difference, resp. the sum, of the space-coordinates, measured in X1 and X2, since those are proportional to the angle and momentum of the particles [2]

* Supported also by EU under RII3-CT-2004-506078 and BMBF 06GI146I

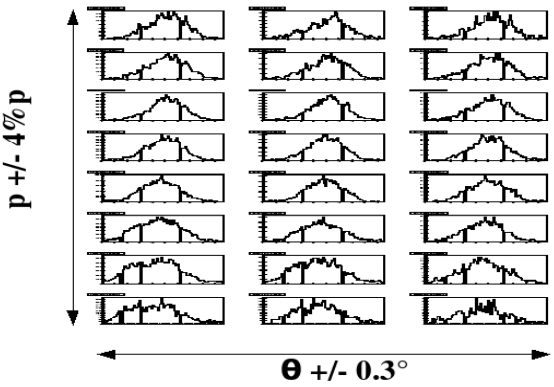

Figure 2: Beam profile in y-direction in hodoscope Y3

An interpolation of the π-trajectories between Y3 and Veto Y showed, in accordance with simulations, that the beam has, in Y-direction, a gaussian shape with a FWHM of 14 mm and only small tails.

Additional information about the focus of the pion beam was gained by reconstructing the tracks of secondary particles. Fig 4 shows the vertices of the secondary particle tracks, derived from the MDC chamber information, reflecting the 3 segments of the Copper focussing target. The ratios of the peak insities are in good agreement with the ratios of the intensity-distribution, in Y-direction, folded with the area of the target (a copper-disc (5mm) and two copper-rings (8 mm, 12 mm diam. resp.) in 20 mm distance, each), i.e. 2:3:5.

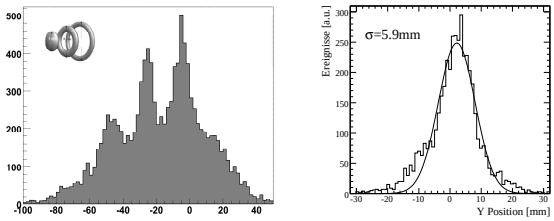

Figure 3: Left Picture:Reconstruction of vertices. The three peaks correspond to the segments of the copper-focussing target. Right picture: π beam profile in y-direction at the HADES target position

References

[1] B. Spruck et.al., GSI Annual Report 2004

[2] Diaz et al, Nuclear Instrumentes Methods in Physics Research (2002)

Design of Antiproton Target for FAIR *

N.A. Tahir[1], V. Kim[2], A. Matveichev[2], A. Shutov[2], A. Ostrik[2], I.V. Lomonosov[2], R. Schmidt[3], M. Brugger[3], K. Knie[1], B. Franzke[1], S. Richter[1], and D. Kraemer[1]

[1]GSI, Darmstadt, Germany; [2]IPCP, Chernogolovka, Russia; [3]CERN, Geneva, Switzerland

Production and collection of antiprotons will be one of the many important experiments that will be done at the FAIR. The SIS100 will deliver a bunched proton beam with, intensity = 2 $\times$ 10^{13} protons, bunch length = 50 ns and particle energy = 29 GeV. The design of a production target that will survive over an extended period of time is a very important and difficult problem.

Figure 1 shows the proposed target geometry which is the same as used previously in the CERN antiproton production experiments. It consists of 6 iridium cylinders, each 1 cm long and having a radius of 2 mm with a small gap of 50 μm between two neighboring pieces. This avoids bending of the target as a result of expansion due to heating. The iridium part is enclosed in a solid graphite casing that is followed by an aluminum cover. The advantage of using graphite is that it has much lower absorption cross section for antiprotons. The dimensions of the different parts of the target are shown in the figure. The proton beam is incident at the left face of the target, the protons generate a shower of secondary particles that deposit their energy in the target. The energy deposition is calculated using the FLUKA code and the results are plotted in Fig. 2. The focal spot size of the beam is characterized with a σ = 1.5 mm in this case. The antiprotons generated in the target will be collected on the right side of the target using a magnetic horn.

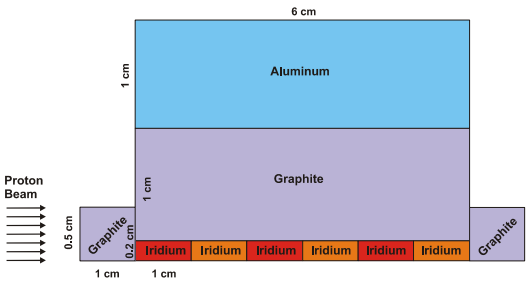

Figure 1: Target initial conditions

Hydrodynamic and thermodynamic response of the target shown in Fig. 1 has been calculated using a a 3D computer code, PIC3D, that includes a semi-empirical equation of state model and elastic-plastic effects. The energy deposition profile shown in Figure 2 is coupled to the 3D code that leads to a maximum energy deposition of 0.17 kJ/g along the beam axis which generates a maximum temperature of 1560 K that is well below the melting temperature of iridium (2700 K). A corresponding maximum pressure of about 9 GPa is generated along the beam axis. The high pressure generates acoustic waves in radial direction that are partly reflected at the graphite–iridium boundary and partly transmitted into the graphite region. This process is repeated when the transmitted wave arrives at the aluminum–graphite boundary. First calculations indicate that the target will survive with the above beam parameters. Since the repetition rate of this experiment will be 0.2 Hz, heat conduction will lead to a substantial cooling of the target during this interval that will avoid heat accumulation.

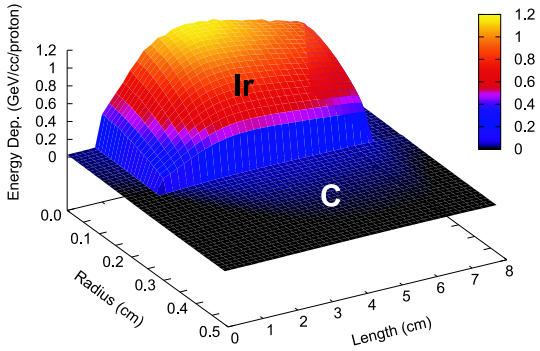

Figure 2: Specific energy deposition by 29 GeV protons in solid graphite and iridium as calculated by FLUKA code.

Figure 3 shows FLUKA calculations of proton energy deposition in a nickel cylinder. It is seen that the level of energy deposition in nickel is significantly lower that in iridium that will lead to a lower temperature and a lower pressure. We are therefore also considering nickel as material for the antiproton production target. A detailed report will be prepared when the final calculations are done.

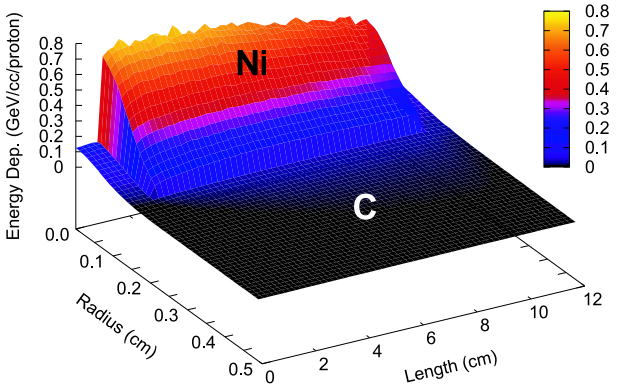

Figure 3: Specific energy deposition by 29 GeV protons in solid graphite and nickel as calculated by FLUKA code.

* Work supported by BMBF

The influence of radiation on the parameters of the APDs of the PANDA-EMC

A. Wilms[1], B. Lewandowski[1], and N. Pitz[2]
[1]GSI, Darmstadt, Germany; [2]IKF, JWGU Frankfurt, Germany

Wavelength dependence of the APD gain

For the application of Avalanche Photodiodes (APDs) as envisaged readout device of the barrel of the electromagnetic calorimeter (EMC) of PANDA several bias voltage dependent measurements have been done so far. Other than the well known determination of the gain-bias characteristic of these devices one main tool for characterization of the APDs is the measurement of the gain dependence on wavelength ($M(\lambda)$). Due to the internal structure of the APDs the internal gain for electron-hole pairs created by photons inside the conversion layer doesn't depend on the wavelength [1]. A decrease of the APD gain indicates the multiplication of electron-hole pairs generated inside the avalanche region of the diode.
To illustrate this fact different gains of an APD were measured by using a monochromator setup providing the needed wavelength variation. The result of this measurement done at a temperature of $T = 20°C$ is shown in the first part of Figure 1 were the values of the gains M = 50, 100, 150, 200, 250, 300 and M = 500 are shown. To guide the eye and to emphazise on the gain constance for lower wavelengths the measured gains were normalized to one gain value at 300 nm (see Fig.1 second plot).

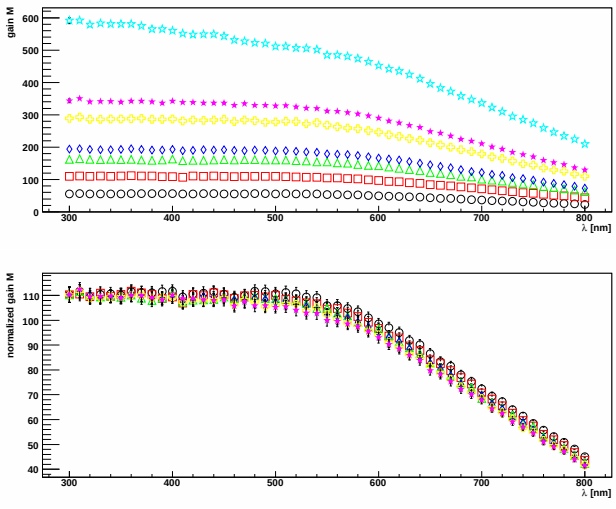

Figure 1: Measurement of $M(\lambda)$ for different gains (above), normalized to one value at 300 nm (below).

It can be clearly seen that the gain values of the APD are constant up to $\lambda \approx 540\,nm$. Therefore no problems with this APD type concerning the wavelength stability of the APD gain in the scintillation light region of the crystals used for the PANDA-EMC barrel part (PWO, $\lambda = 420\,nm$) has been observed.

Change of APD parameters after proton / gamma irradiation

To determine the influence of proton irradiation on the APD parameters several beamtimes at KVI Groningen (the Netherlands) took place by using a 90 MeV proton beam. The APDs were irradiated at a temperature of $T = -25°C$, which is the envisaged operation temperature of the PANDA calorimeter. Afterwards all APD parameters were measured at $T = 20°C$ using the same procedure as used before irradiation. Because of a decrease of the reachable maximum gain by a factor of ≈ 2, only gain values up to $M = 250$ could be measured wavelength dependently. The result of the measurement is shown in Fig.2 and shows occuring radiation damage inside the conversion layer of the diode as well as inside the avalanche region.

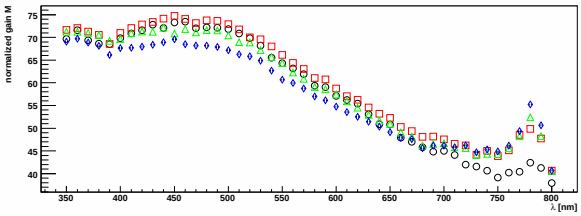

Figure 2: Measurement of normalized $M(\lambda)$ for M=50, 100, 150, 200 and M=250 after proton irradiation.

For evaluating the influence of gamma irradiation on the APDs a beamtime in Giessen took place using a high dose ^{60}Co-source at a temperature of $T = -25°C$. Contrary to our observance in case of proton irradiation no appreciable gain decrease could be observed after gamma irradiation. In Fig.3 can be seen that only the very front part of the conversion layer shows some indication of radiation damage.

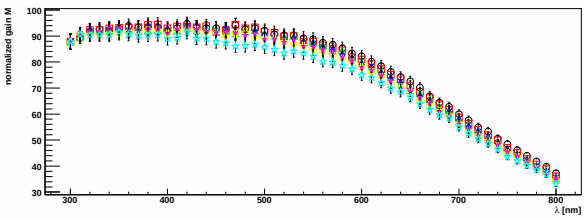

Figure 3: Normalized $M(\lambda)$ for M=50, 100, 150, 200, 250, 300 and M=460 after gamma irradiation.

References

[1] Th. Kirn et al., "Wavelength dependence of Avalanche Photodiode (APD) Parameters", NIM A, Volume 387, Issue 1-2, p. 202-204

High efficiency TRD for CBM in test beam and simulation*

M. Klein-Bösing[1], J. P Wessels[1], M. Petriş[2], M. Petrovici[2], V. Simion[2], and F. Uhlig[3]
[1]Institut für Kernphysik, Münster; [2]NIPNE, Bucharest; [3]GSI, Darmstadt

The CBM (Compressed Baryonic Matter) experiment is designed as a fixed target experiment, in which a TRD shall provide tracking of all charged particles, electron identification and discrimination against a large pion background. In order to fulfill these tasks in the context of high count rates of up to 150 kHz/cm^2 and high particle multiplicities, we constructed TRD prototypes based on a symmetric arrangement of two MWPCs with a common, central pad readout electrode. In this way the anode-cathode gap is small enough to reach the required speed and to reduce space charge effects in a high counting rate environment. At the same time a high conversion efficiency of the transition radiation is obtained due to the duplication of gas volume.

The prototypes have been tested in a beam of electrons, pions and protons with p=1.5 GeV/c and they have shown very good discrimination capability of electrons versus pions which meets the requirements of CBM [1]. The deposited charge spectra have been compared to a simulation in CBMRoot considering this new detector geometry.

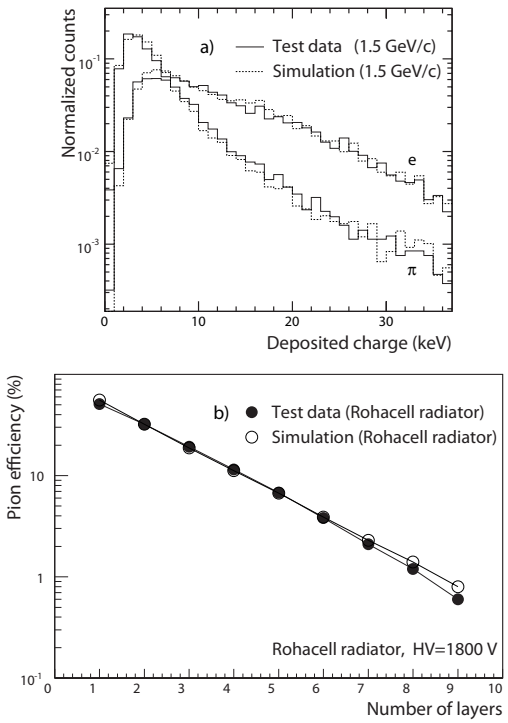

Figure 1: a) Deposited charge for electrons and pions and b) pion efficiency in simulated and test beam data with 5% electron contamination of the pion data sample.

The measured spectra can be described very well by these simulations, see Fig. 1a). With these spectra the misidentification probability for pions can be calculated. This pion efficiency as function of the number of extrapolated detector layers also shows good agreement of simulated and test beam data, see Fig. 1b). In addition, an electron contamination level of 5% of the pion data sample in the test beam could be diagnosed. The pion efficiency of the detector in a pure electron and pion beam is 0.4% for 9 layers TRD.

In the test beam the position resolution of two identical prototypes aligned in a row along the beamline has been determined. The measurement of the coordinate of the avalanche along the wire direction is done by interpolating the pulse height recorded on adjacent readout pads. The intrinsic position resolution of the two prototypes is given by the variance of a Gaussian fitted to the distribution of residuals defined as the distance between the position of the reconstructed clusters in both chambers and a linear fit to the alignment. For the measurement of the rate dependence shown in Fig. 2 a moderate voltage of 1700 V has been chosen, to prevent instabilities of the chambers at high rates. For Xe(90%)CO$_2(10\%)$ the value of the position resolution at moderate intensity is (161 ± 3) μm or 3.2% of the pad width. No significant deterioration of the position resolution is observed up to average particle rates of 200 kHz/cm^2, where it is still much better than the required 200 μm [2].

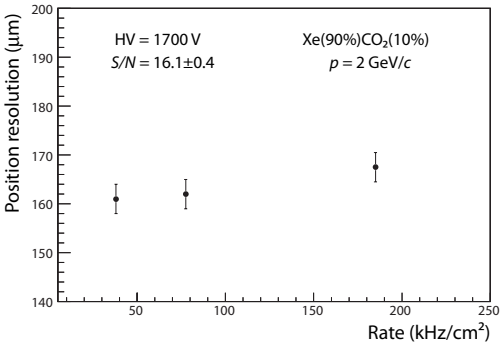

Figure 2: Position resolution as a function of particle rates with HV = 1700 V and $p = 2$ GeV/c, using a Xe(90%)CO$_2(10\%)$ gas mixture.

References

[1] M. Petrovici et al., Nucl. Instr. Meth. Phys. Res. A 579 (2007) 961.

[2] M. Klein-Bösing et al., Nucl. Instr. Meth. Phys. Res. A 585 (2008) 83.

* Work supported by HadronPhysics (I3HP) and BMBF.

Beam tests with an ALICE TRD supermodule

A. Andronic*, GSI, Darmstadt, Germany for the ALICE TRD Collaboration

The Transition Radiation Detector (TRD) of the ALICE experiment at LHC is designed to provide electron/pion identification and tracking of all charged particles [1]. The TRD will supplement the TPC electron/pion identification by a pion rejection factor of the order of 100 at momenta above 1 GeV/c, allowing precision measurements of quarkonia. Sophisticated on-detector electronics [2] is designed to trigger on high-momentum electrons and on jets. The project is now in the production stage, with 2 supermodules installed in the ALICE setup and a few more being prepared for installation before the LHC startup in spring 2008.

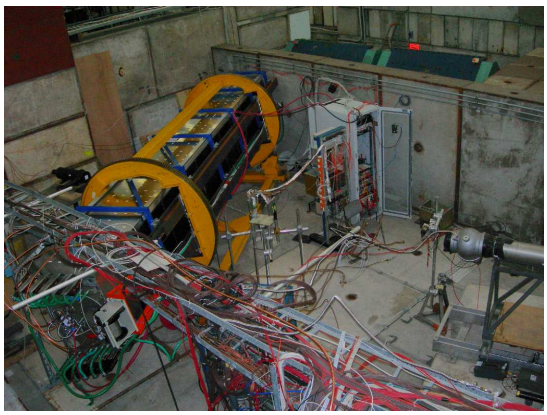

Figure 1: The TRD supermodule installed at the T10 beamline at CERN PS.

A first beam test of a final supermodule (SM) of TRD was performed at the CERN PS accelerator in November 2007, with the aim to provide reference distributions for our particle identification methods [3] as well as to check the overall detector performance. Measurements were carried out in an electron/pion beam with momenta of 1 to 6 GeV/c. Fig. 1 shows a picture of the setup at the beamline. Besides the TRD supermodule, the setup was comprising of: beam trigger scintillators, a Pb-glass calorimeter and a Cherenkov detector for e/π identification and two Si-strip detectors for position reference. The final readout chain of the TRD was used to read 1 stack of the 5 of the SM, both with and without zero suppression.

In Fig. 2 we present the measured average signals as a function of drift time for pions and electrons, for the momentum of 4 GeV/c. The detector signal is spread over about 2 μs. The peak at small drift times originates form the amplification region, while the plateau is from the drift region. For the electrons, the contribution of TR, which is preferentially absorbed at the entrance of the detector (corresponding to large drift times), is evident.

* A.Andronic@gsi.de

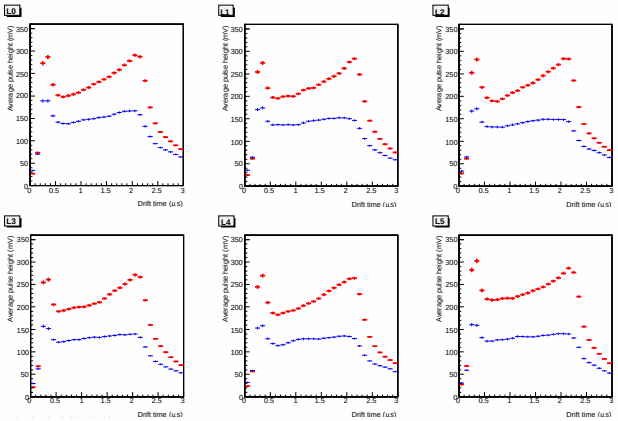

Figure 2: Average pulse heights for the 6 layers, sampled in time bins of 100 ns, for electrons (thicker symbols) and pions of 4 GeV/c.

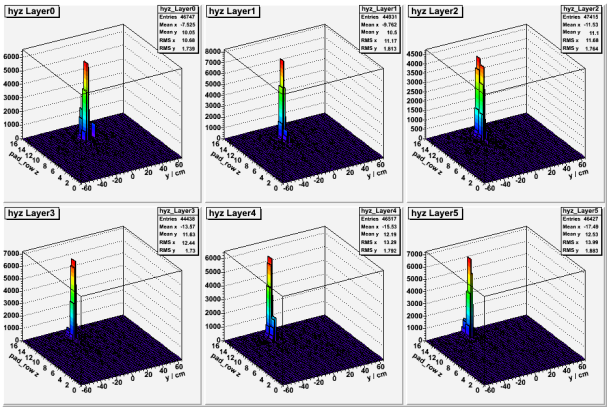

Figure 3: Tracklet distribution over the 6 layers.

In Fig. 3 we illustrate tracklet (track segment within one chamber, reconstructed on-line) performance for the six layers of the TRD. Plotted is the distribution of the found tracklets over the area of the chambers, reflecting the position of the beam incidence.

Data analysis is in progress to estimate the performance for e/π separation and for tracking. The experience during the beamtime will help improve the performance of the detector and of the data readout chain.

References

[1] ALICE Transition Radiation Detector Technical Design Report, ALICE TDR 9, CERN/LHCC 2001-021.

[2] V. Angelov, NIM A 563 (2006) 317.

[3] C. Adler et al., NIM A 552 (2005) 364;
A. Bercuci et al., this Report.

Installation and Commissioning of the ALICE Transition Radiation Detector

K. Oyama[1], A. Andronic[2], R. Bailhache[2], J. de Cuveland[3], T. Dietel[4], B. Dönigus[5,2], D. Emschermann[1], S. Esumi[6], C. Garabatos[2], T. Gunji[7], C. Haltebourg[1], H. Hamagaki[7], M. Hartig[8], N. Heine[4], T. Herold[1], J. Klein[1], M. Kliemant[8], M. Konno[6], D. Krumbhorn[1], M. Kweon[1], V. Lindenstruth[3], C. Lippmann[2], A. Marin[2], J. Mercado[1], F. Rettig[3], D. Sakata[6], M. Sano[6], S. Sano[7], K. Schweda[1], J. Stachel[1], A. Takahara[7], R. Tanabe[6], W. Verhoeven[4], K. Watanabe[6], J. Wessels[4], U. Westerhoff[4], B. Windelband[1], S. Wulff[4], and S. Zimmer[1]

[1]Physikalisches Institut, University of Heidelberg, Germany; [2]GSI, Darmstadt, Germany; [3]KIP, University of Heidelberg, Germany; [4]Institut für Kernphysik, University of Münster, Germany; [5]Helmholtz Research School H-QM, Frankfurt, Germany; [6]Institute of Physics, University of Tsukuba, Japan; [7]Center for Nuclear Study, Faculty of Science, University of Tokyo, Japan; [8]IKF, University of Frankfurt, Germany

The ALICE experiment [1] is dedicated to identify and characterize the quark-gluon plasma created in high-energy Pb-Pb collisions at the LHC. The Transition Radiation Detector (TRD) [2] for ALICE consists of 18 supermodules, each contains 30 drift chambers, surrounding the large volume Time Projection Chamber in the central barrel. TRD identifies electrons at momenta above $p_{\mathrm{T}} = 1$ GeV/c and provides fast trigger capabilities (within 6 μs) for charged particles with high transverse momentum ($p_{\mathrm{T}} > 3$ GeV/c).

The first TRD supermodule was installed in 2006 inside the L3 magnet of ALICE and successfully commissioned [3]. Fig. 1 shows the event display of a cosmic shower event taken in May 2007 by the TRD supermodule positioned at sector 8.

In 2007, the second supermodule was installed at sector 0 and services such as low voltage, high voltage, gas and cooling, network, and optical fibers were connected. All service connections have been tested and the supermodule has been commissioned.

The first global ALICE run with cosmic events took place during a 2 weeks period in December 2007. The two installed TRD supermodules were successfully operated within the ALICE infrastructure including central trigger system, pretrigger [4], global tracking unit [5], and DAQ. Especially, details of the interfaces among supermodules and connection to other parts of the infrastructure were debugged.

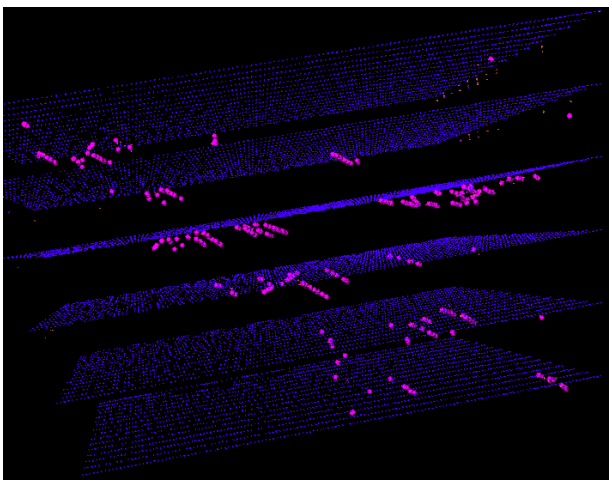

Figure 1: Event display of a cosmic shower event as seen by the TRD supermodule at sector 8.

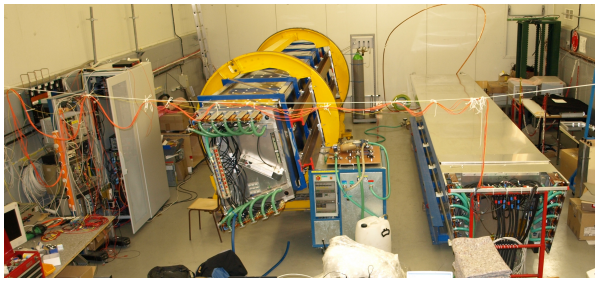

Figure 2: Two supermodules in the clean room for extensive checks prior to their installations.

Meanwhile, two more supermodules arrived from Münster and are now set up in the TRD clean room at point 2 at CERN. Fig. 2 shows both supermodules which are scheduled for installation in sectors 17 and 9. Prior to installation, dedicated tests are performed including comprehensive checks of the readout electronics, HV stability, gas tightness, noise levels and reliability of full operation.

The installation of further supermodules requires careful checks of all services in the cavern and updates of the control software, amongst others. The next global ALICE run with cosmic events is scheduled for March 2008. Afterwards, installation of the two supermodules now sitting in the clean room is foreseen. Presently, the start-up of the LHC is scheduled for summer 2008.

We would like to acknowledge the support by the CERN installation group. This work has been supported by the Federal Ministry of Education and Research under promotional reference 06HD197D and the Helmholtz Association under contract number VH-NG-147.

References

[1] ALICE, http://aliceinfo.cern.ch/

[2] ALICE Collaboration, CERN/LHCC 2001-021, (2001)

[3] C. Lippmann, et al., GSI Scientific Report 2006, 236, (2007)

[4] B. Dönigus et al., GSI Scientific Report 2007, to be published

[5] J. de Cuveland, et al., GSI Scientific Report 2006, 235, (2007)

A gas monitor for the ALICE TRD *

D. Antończyk[1], H. Appelshäuser[1], and D. Wegerle[†1]
[1]IKF, J.W. Goethe University, Frankfurt am Main, Germany

The ALICE TRD [1] is an array of 540 drift chambers which will be operated with 28 m^3 of Xe-CO_2 $[85-15]$ gas. It will provide electron–pion separation for momenta above 1 GeV/c and particle tracking in the high-multiplicity environment of heavy-ion collisions at CERN-LHC. To achieve these goals, accurate pulse–height measurements over the full drift time of about 2 μs are necessary. Therefore, the monitoring of the gas properties, as the gas composition, the drift velocity, and the gas gain, will be an important task. Moreover, the large total volume of the detector and the high cost of xenon makes it mandatory to recirculate the gas mixture used by the detector. The injection of the fresh gas into the system will be limited only to replenish what is lost due to leaks. In addition, air will diffuse into the gas mixture through the same leaks. This will lead to accumulation of nitrogen in the gas mixture and result in the change of the gas properties. The drift velocity monitor, known as GOOFIE, will be then used as an on-line monitor of the gas properties providing also information about concentration of the nitrogen in the gas mixture.

The GOOFIE-type drift velocity monitors were and are still used by many experiments to monitor the electron drift velocity in gas detectors. The well-known principle of operation of this monitor is based on the measurement of the difference in drift time of electrons, produced in the gas by alpha-particle tracks, at two known distances from a so-called pick-up counter [2]. However, the drift monitor has to be adopted to the specific needs of the experiment. The drift region of the ALICE TRD GOOFIE is operated at an unprecedented field strength of 700 V/cm. This requirement limits the total drift length to about 16.15 cm. The latter was found as an optimal ratio between the maximum voltage applicable and the expected monitor resolution. To prevent high electric field in the vicinity of the trigger counters, and to limit the field distortions in the drift channel the voltages of both the anode wire and the cathode tube are taken from the nearest potential strips. To monitor the enclosed gas temperature, two PT1000 sensors were inserted at the top and bottom of the monitor housing, respectively. Moreover, the latter provide the possibility of active cooling of the enclosed gas volume, although this feature has not yet been employed. The pulse-height spectra of the pick-up and trigger counters are recorded as a function of time by a custom made read-out board based on the PASA-ALTRO chain [3]. To avoid any possible fluctuation in the gas composition at this stage a premixed gas mixture of Ar-CO_2 $[70-30]$ was used. The final tests with Xe-CO_2 gas mixture will be taken at CERN facility.

After mentioned modification had been carried out, the system was operated for several days in the SGZ detector laboratory at IKF, Frankfurt, and about 3.2×10^6 events were recorded. Additionally to the pulse-height spectra, each event was stored with an information about the gas temperature, pressure, and current drift voltage. The drift velocity was extracted from the position in time of the 2500 peaks corresponding to the signals coming from both, the near and the far source. It shows a linear correlation with $(\frac{P}{T \cdot U})$ as demonstrated in Fig.1. The ratio P/T is a measure of the gas density and U represents a measure of the drift voltage. The variation of the drift voltage as a function of the gas temperature, makes mandatory to include it into correction procedure. After the subsequent correction, the precision in the drift velocity measurements is 5×10^{-4}.

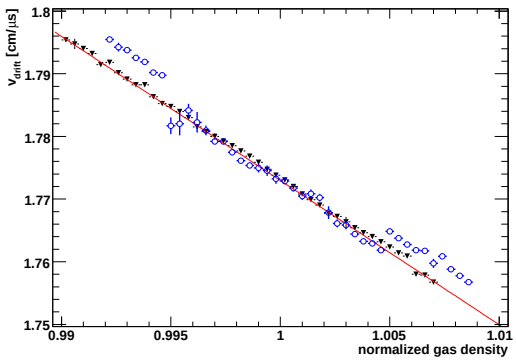

Figure 1: Correlation between the measured drift velocity and the gas density (open points), additionally corrected for variation of the drift field voltage (close points).

In addition to the monitoring of the drift velocity, GOOFIE provides also a precise measurement of the gas gain. Based on a confirmed measurements of both quantities, it will be feasible to extract variation of the gas mixture, including the actual level of the nitrogen contamination.

References

[1] ALICE TRD Technical Design Report, CERN/LHCC 2001-021

[2] D. Antonczyk et al. "A drift velocity monitor for the ALICE TPC", GSI Scientific Report 2004, June 2005 INSMETH-20

[3] L. Musa et al., The ALICE TPC Front End Electronics, Proc. of the IEEE Nuclear Science Symposium, 20-25 Oct. 2003, Portland

* This work is supported by BMBF and GSI
† wegerle@ikf.uni-frankfurt.de

The Pretrigger System for the Transition Radiation Detector in ALICE

B. Dönigus*[1,2], P. Braun-Munzinger[2], O. Busch[3], M. De Gaspari[3], K. Oyama[3], K. Schweda[3], J. Stachel[3], R. Wagner[3], and S. Zimmer[3]

[1]Helmholtz Research School H-QM, Frankfurt, Germany; [2]GSI, Darmstadt, Germany; [3]Physikalisches Institut, University of Heidelberg, Germany

The ALICE Transition Radiation Detector (TRD) [1] identifies electrons in the central barrel with momenta above 1 GeV/c by using their transition radiation emitted when crossing the boundary between materials with different dielectric constants. Furthermore the TRD provides fast (6 μs) triggering capability for high transverse momentum ($\mathrm{p_T} > 3\ \mathrm{GeV/c}$) charged particles.
During data taking, the TRD electronics requires an early wake up signal from the forward detectors and/or the fast time of flight (TOF) detector. This wake up signal is called pretrigger [2].

The delay for the pretrigger is 700 ns from the interaction up to the arrival at the front-end electronics which corresponds to an arrival of the L0 of the central trigger processor (CTP) of above 900 ns. This means the electronics can process 2 presamples, since the electronics uses 100 ns timebins. When a pretrigger arrives at the multi chip modules (MCMs), they start to reconstruct tracklets (the track fragment within one of the six layers of the TRD drift chambers) which are then shipped via an optical link to the global tracking unit (GTU) [3] if no level 0 reject is given within a certain time window. The GTU then starts to combine the tracklets to tracks and identifies electrons with high transverse momentum: a local TRD level 1 trigger accept is issued and sent to the CTP. A scheme of the pretrigger system can be seen in figure 1.

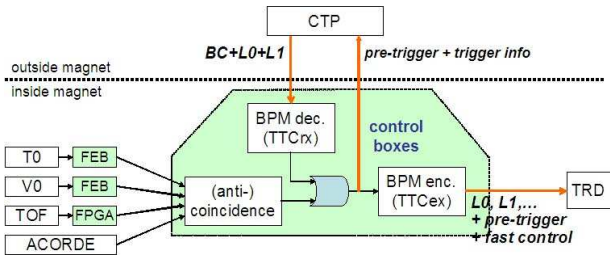

Figure 1: Scheme of the pretrigger system.

The pretrigger system consists of 5 front-end boxes (FEBs) and one control box (CB-A/CB-C) for each detector side and a control box combining the signals from CB-A and CB-C and the TOF (CB-TOF) related trigger decision. The FEBs are programmed via JTAG connection through CB-A/CB-C and are controlled via SCSN. The CBs are controlled via DCS boards which sit on the control box board and are accessible through ethernet.

To meet the strict timing requirements the signals of the forward detectors V0 and T0 are fed into the FEBs of the pretrigger setup and used to perform a trigger decision in the FPGA independently in CB-A/CB-C. The CB-A/CB-C trigger decision is then combined with the trigger decision of the control box for the TOF part of the pretrigger system. A final decision is then taken by another FPGA and in case of a true event the pretrigger is provided to the electronics via TTC fibres and also sent to the CTP of ALICE as the L0 input of the TRD.

For the analysis of the trigger efficiency, the signals from each V0/T0 channel and the signals from each FEB at the level of CB-A/CB-C and CB-TOF are counted, independent of the trigger decision.

The CB-TOF prototype has been installed and has been used to sent pretrigger signals to the TRD electronics in the cosmic run of ALICE in december 2007. The final version of the FEBs connected to the V0 detector are produced and will be installed in march 2008.

The control software which uses the general ALICE TRD DCS hierarchy has to be implemented, the T0 part of the pretrigger has to be produced and the whole pretrigger system has to be installed and commissioned.

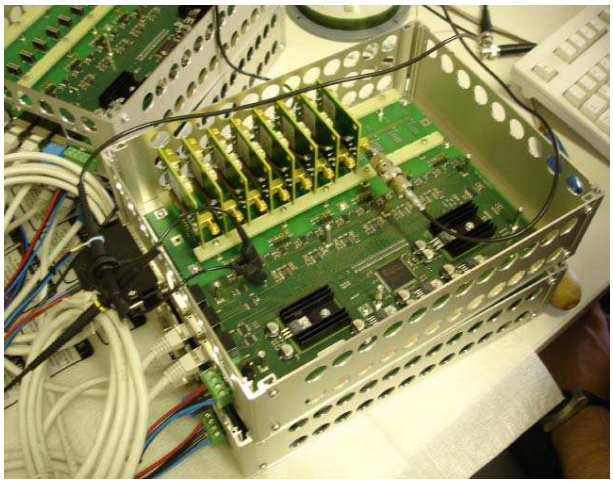

Figure 2: Picture of a FEB tested in the lab at PI Heidelberg.

References

[1] ALICE Collaboration, TRD Technical Design Report, CERN/LHCC 2001-021, (2001)

[2] Pretrigger webpage: https://alice00.physi.uni-heidelberg.de/oyama/PreTrigger/pkwk/index.php

[3] GSI Scientific Report 2006, p. 235, (2007)

* b.doenigus@gsi.de

Mass test of the ALICE TRD front end electronics at IKF*

A. Fick, K. Antipin, H. Appelshäuser, M. Hartig, F. Kramer
for the ALICE collaboration, Institut für Kernphysik, Johann Wolfgang Goethe - Universität Frankfurt a. M., Germany

The Transition Radiation Detector (TRD) [1] is one of the main detector components of the ALICE experiment. It consists of 18 supermodules mounted cylindrical around the beam axis of the LHC. Every supermodule is assembled out of 30 Readout Chambers (ROC) of different types. These ROCs are equipped with front end electronics (FEE) and tested at the Institut für Kernphysik Frankfurt (IKF) [2]. In this report, we briefly describe this testing procedure.

Setup of the test system

In total 14 tests have to be performed for every ROC [3]. The first two aim on the general functionality of every single readout board (ROB) [4]. The shutdown test checks the switching behaviour of the low voltage regulators. The reset test checks the reset line and whether each multichip module (MCM) correctly resets its state to the default one. The next steps of the procedure test the interconnection between the FEE and the readout electronics. The network interface test checks the functionality of the slow control serial network of every ROB. The second test of this sequence is the test of the Optical Readout Interface (ORI) [5]. The bridge test guarantees that a complete readout cycle can be performed even if one of the MCMs is broken. In addition the Laser-ID, a unique identification of every MCM, is validated. Further the three different memories (DMM, DDD and IMM) [6] of the MCMs are tested by read/write cycles. Three different configurations are used to check the read out data for the noise level, for homogeneity of the noise distribution and for non responding ADC - channels of the MCMs. These configurations are:

- no filter configuration with all filters switched off (nf)
- configuration with pedestal subtraction (p)
- configuration with pedestal subtraction, gain correction and tail cancellation (pgt)

In addition to this we use a pulse generator to inject a square wave signal into the cathode wire. This signal is picked up by the pads and transferred to the MCM. A spectrum of a ROB (Figure 1) shows the expected high signal level (red pads). Channels with not connected or not proper conductive pads (green pads) are also visible. With this method bad channels can be identified in an very easy and convenient way.

To finalize the testing procedure every ROC has to perform two long term stress tests. Therefor a trigger signal is sent to the ROC permanently and the status is checked in periods of five minutes. The complete testing procedure is done twice for every readout chamber, once after the FEE is put on the ROC and once after the cooling system is glued on the electronics.

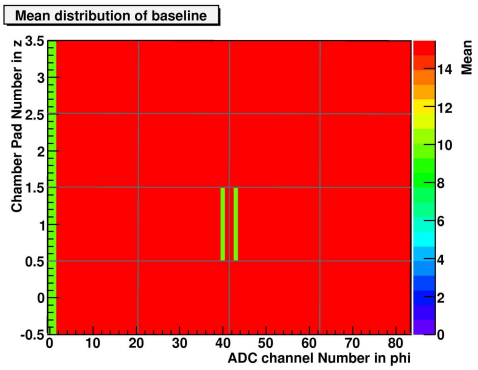

Figure 1: Mean distribution of the basline of a mesurement (p-configuration) with injected pulser signal. Red pads show the expected high signal level, green pads did not pick up the signal and are probably not connected.

Summary and outlook

In 2007 all ROCs of supermodules 2 to 5 (in total 120 ROCs with 912 ROBs) have been equipped with FEE and have been tested successfully. To speed up and to improve the testing procedure, we constantly develop the single components of the tests and transfer them to an easy to handle graphical user interface. This user interface will be based on PVSS, a software platform which is used by all experiments at LHC.

References

[1] ALICE TRD, “Technical Design Report 9”, CERN / LHCC, 2001-021.

[2] M. Kliemant et al., GSI Scientific Report 2006, p.232

[3] B. Dönigus, “Assembly And Test Of The First Supermodule Of The ALICE Transition Radiation Detector”, Diplomarbeit, April 2007

[4] I.Rusanov, J.Stachel, GSI Scientific Report 2005, p.287

[5] V. Lindenstruth et al., GSI Scientific Report 2005, p.289

[6] ALICE TRAP, “User Manual”, CERN, Revision 1.1, 2005-01-03

* Work supported by BMBF and GSI

Revision of the ALICE TRD tracking code

A. Bercuci[1,3], M. Fasel[2], and M. Ivanov[1]

[1]GSI, Darmstadt, Germany; [2]Technische Universitaet, Darmstadt, Germany; [3]On leave from NIPNE, Bucharest, Romania

The algorithm for tracking is the backbone of the reconstruction procedure of the TRD detector of the ALICE experiment at LHC at CERN. Its performance has immediate influence on other reconstruction tasks such as calibration, alignment and particle identification.

The tracking algorithm is designed to work with or without prior estimate of the track position. Thus one can distinguish two main applications: the Stand Alone Tracking (SAT) used in the High Level Trigger (HLT) system of ALICE or to analyze test beam or cosmic rays data and the Standard Tracking (ST) used to reconstruct physics events in the ALICE offline framework.

Standard Tracking

The offline tracking is based on Kalman Filtering (KF) of the data [2]. In the case of TRD, due to the measurement procedure of the charge deposit, clusters' charge and position are correlated over a temporal range of approx $300ns$. Therefore a new approach has to be searched to fulfill the assumption of independence between updating points of the KF based on:
- linear fit of clusters positions in one TRD detector;
- propagate/update track parameters using the fit result.

A tracklet is a linear fit of the clusters attached to one track in one TRD detector (see Fig. 1).

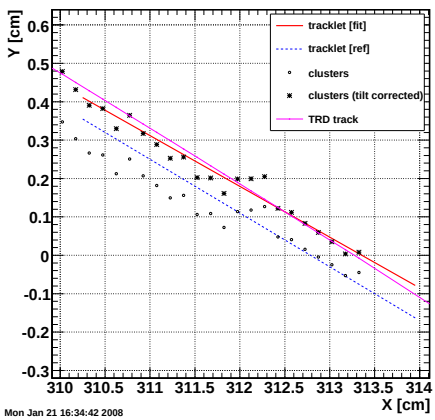

Figure 1: Elements of the tracking algorithm : clusters, tracklets, track and their relation.

The tracklet reconstruction is the center method of the TRD tracking algorithm and it was made common for SAT and ST algorithms. Given a first approximation of the tracklet position and direction one can fit the following residuals to reconstruct the tracklet:

$$\Delta y = y_c - y0 - (dy/dx + h*dz/dx)*(x_c - x_0) + h*(z_c - z_0) \quad (1)$$

where x_c, y_c and z_c are the coordinates of the cluster; x_0, y_0, dy/dx, z_0 and dz/dx are the initial parameters of the tracklet and h is the tangent of the tilting angle. A similar least mean square fit is applied also on the XZ plane. The fit results, y_{fit} and z_{fit}, together with their covariance matrix, are used for track prolongation and update.

Stand Alone Tracking

In the SAT application the Riemann parametrization

$$(x - x_0)^2 + (y - y_0)^2 = R \quad (2)$$

is used to describe track in the XY plane and a linear parameterization in the XZ plane. In order to cope with features of the measured data a new preparatory phase was added in which the overall data content of a TRD stack is analyzed for:
- selecting detectors with potential large number of tracklets;
- defining global positions in detectors for combinatorial search.

After this preparatory phase a Riemann fit (see eq. 2) is performed on the selected data. The values of the fit at reference positions are used to build tracklets for each TRD detector segment.

Motivated by the needs of the HLT system a new organization of data has been introduced such that tracking can be performed in parallel on each of the five stacks of a TRD supermodule.

Although the tracking code is not supposed to access directly the calibration and alignment information (the clusters are calibration and alignment aware) the detector effects have to be propagated correctly to tracking. We add the calibration/alignment awareness of the tracklets for the x_0 calculation, selection of clusters considered in the tracklet fit and dE/dx estimations. A side effect of this development was to use for ST the data structure developed for SAT (stack wise organization).

A special effort was put into the extraction of controlling parameters. This was done in order to render a easily configurable code. The work in the future will be focused on defining sets of such parameters for different physical configurations of the data following the example of the TPC detector.

References

[1] ALICE TRD Technical Design Report, CERN/LHCC 2001-021.

[2] ALICE TPC Technical Design Report, CERN/LHCC 2000-001.

A Bidimensional Method for Particle Identification with the ALICE TRD

A. Bercuci[1,2], A. Andronic[1], and M. Ivanov[1]
[1]GSI, Darmstadt, Germany; [2]On leave from NIPNE, Bucharest, Romania

One of the main objectives of the Transition Radiation Detector (TRD) at LHC at CERN is to provide electron/pion identification for $p_t > 1GeV/c$. The separation of electrons is based on ionization dE/dx and TR production and detection. We have improved the electron identification by better considering the contributions of ionization and TR production on the dE/dx measurements.

The TRD detector design [1] enables up to 30 samples of dE/dx in one module. Due to reconstruction and tracking efficiency a robust estimator for dE/dx has to be introduced. The following effects can affect the dE/dx estimation: missing measurements, cluster sharing between tracks (high multiplicity environment) and drift velocity. The following estimator reflects these requierments: $< dE/dx >_t = 1/n * \sum_{i=t_0}^{t_1} w_i * dE/dx_i$, where t_0 and t_1 are defining slice integration limits of the dE/dx_i measurements in one TRD module, n is the number of measurements in the slice and w_i are weights reflecting cluster sharing and size. The limits t_0 and t_1 are 0 respectively $0.66 * n_{tb}$ for the measurements which contains mainly ionization contributions (dE/dx_{ion}) and $0.66 * n_{tb}$ respectively n_{tb} for those having also TR contribution (dE/dx_{tr}). We are introducing here the calibration awareness by $n_{tb} = N * v_d/\nu$ with N total number of time bins measured, v_d the local drift velocity and ν the sampling frequency.

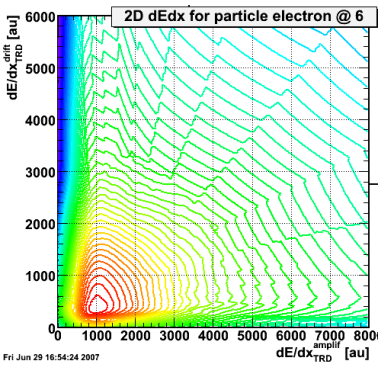

Figure 1: 2D reference distribution of integrated signals in slices for electrons of $2GeV/c$ after smoothing.

In order to account for residual TR contributions in the ionization slice a 2D reference distribution $f(dE/dx_{ion}, dE/dx_{tr})$ has to be constructed. The distribution was constructed by sampling it with simulated data and smoothing it with a specially designed procedure. In order to compress the tails of the Landau like distribution, a log transformation was applied in both components. A 2D parabolic fit was performed on the transformed distribution and an inversion back to the original coordinates were applied. The smoothed distribution for electrons of $2GeV/c$ is shown in Fig. 1.

The Particle IDentification (PID) capabilities of TRD are quantified by the so called *pion efficiency* which represents the percent of pions which are misidentified as electrons at 90% electron identification efficiency. Using a Bayesian approach one can evaluate:

$$P(\pi|dE/dx, p_t) = \frac{P(dE/dx|\pi, p_t) * P_0(\pi, p_t)}{\sum_s P(dE/dx|s, p_t) * P_0(s, p_t)} \quad (1)$$

where $P(dE/dx|\pi, p_t)$ is the smoothed likelihood distribution for π with p_t and $P_0(\pi, p_t)$ is the prior distribution of π. The normalization is performed over the set of particle species $s = e, \pi, \mu, K, p$. For the purpose of showing the intrinsic detector PID capabilities the prior distribution is uniform over all particle species but for physics applications it has to be constructed based on the prior knowledge of particle abundances for a particular physics analysis.

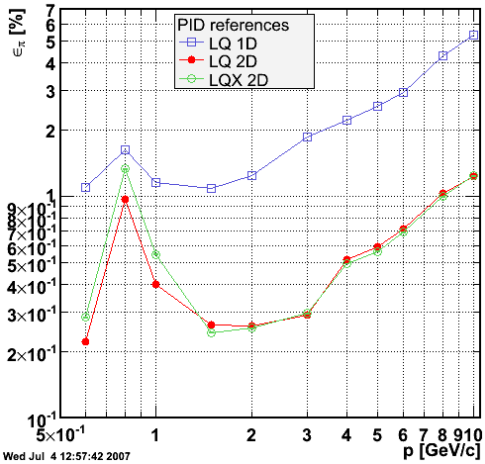

Figure 2: TRD π efficiency as a function of momentum for the new method (LQ 2D) compared with a classical one dimensional likelihood method (LQ 1D).

The modification of π efficiency by better considering TR contribution has yield an improvement factor of 5 (see Fig. 2). The exception is the low momentum range where only a factor 2 was obtained due to the contributions of the K and p dE/dx yields.

References

[1] ALICE TRD Technical Design Report, ALICE TDR 9, CERN/LHCC 2001-021.

A Multidimensional Statistics Package for ALICE Offline Framework

A. Bercuci[1,2] and M. Ivanov[1]

[1]GSI, Darmstadt, Germany; [2]On leave from NIPNE, Bucharest, Romania

AliRoot [1] is the Off-line framework for simulation, reconstruction and analysis for the ALICE experiment at LHC at CERN. Motivated by the developments of the particle identification analysis for the Transition Radiation Detector of ALICE a statistics package was developed for AliRoot for fast access and interpolation of multi dimensional data sets. A special atention in our implementation was given to the computing performances.

k-Dimensional Trees

kD-Trees are space-partitioning data structure for organizing points in a k-dimensional space [2]. In Fig. 1 an example is given for a 2D Gaussian distribution.

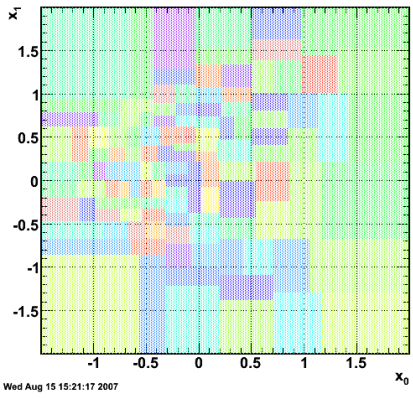

Figure 1: Partitioning of a 2D Gaussian distribution using the kD-Tree. Each rectangle corresponds to a node (generalized bin) of the kD-Tree with fixed number of data points.

In our implementation we minimized and simplified the kD-Tree structure to obtain the maximum performance in terms of CPU and RAM usage. A report on the computing performances can be found at [3].

kD-Trees are useful data structure for searches involving a multidimensional search key e.g. range and nearest neighbour (NN) searches. We have test the NN algorithm on a standard machine[1] for a 3D Gaussian distribution and we obtained an improvement factor of approx. 10 [3] in searching speed compared to the normal loop over data. The improvement is obtained by excluding large ranges of the data space due to kD-Trees organization.

LOESS interpolation

An interpolation subpackage was developed based on the kD-Tree approach following the Locally Weighted Polynomial Regression (LOESS) approach [4]. The LOESS method is based on evaluating the PDF in an arbitrary point by a low-degree polynomial fit to a subset of the data, with explanatory variable values near the point whose response is being estimated. The polynomial is fit using weighted least squares, giving more weight to points near the point whose response is being estimated and less weight to points further away. The traditional weight function used for LOESS is the tri-cube weight $i.e\ w(x_i) = (1 - d^3)^3$ where $d = D(X, x_i)/D_{max}$. Here X and x_i are the coordinates of the evaluation point and explanatory point respectively, $D(\cdot, \cdot)$ is the metric function defined on the data set and $D_{max} = max\{D(X, x_i)\}$. We are using the kD-Tree of the data to construct a pseudo data set defined on the nodes of the kD-Tree for which the relative error of the statistical estimator of the PDF is constant. Consecutively we are using the pseudo data set to estimate the PDF for all points in the data range (see Fig. 2).

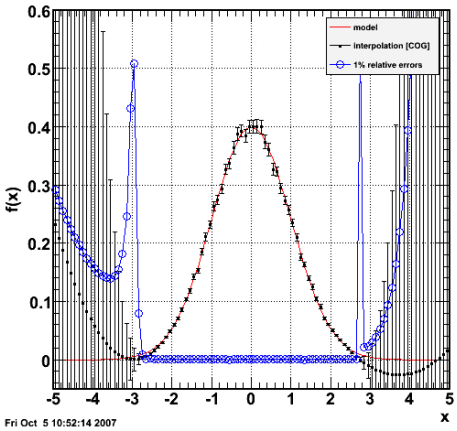

Figure 2: Interpolation of a 1D Gauss model. The evaluation values and the relative uncertainty are displayed.

The PDF evaluations are accompanied by the uncertainty evaluation used to discriminate between interpolation and etrapolation regions. As our method does not contain any assumptions on a general model describing the data the uncertainty of extrapolation are large (see Fig. 2).

References

[1] http://aliceinfo.cern.ch/Offline/.

[2] J.L. Bentley; *Comm. of ACM*, 23(4) (1980) 214.

[3] http://indico.cern.ch/getFile.py/access?contribId=36&sessionId=5&resId=0&materialId=slides&confId=7108.

[4] W.S. Cleveland and S.J. Devlin; *J. Am. Stat. Ass.*, 83 (1988) 596.

[1]Intel(R) Celeron(R) CPU 2.66GHz, 1GB RAM

Measurement of Dose Rate Levels of X-Rays produced at Pre-Accelerator Structures of the GSI UNILAC

G. Fehrenbacher[1], J.G. Festag[1], S. Grosam[1] and K. Vogt[1]
[1]GSI, Darmstadt, Germany

Introduction

The pre-accelerator structure consists of the ion source, a radiofrequency quadrupol RFQ and an Interdigital H-field structure. In these sections x-rays are produced due to high electrical fields in which electrons are unavoidably accelerated during the acceleration process of the ions. During a measurement campaign at these structures the dose rate levels for the produced x-rays were measured by means of passive and active dosemeters.

Method

For the measurements ionization chambers [1] and a new cylindrical dosemeter - based on TL (**T**hermo**L**uminescence) detectors (Harshaw cards type 700) - have been used. The cylinder-dosemeter was developed [2] to measure the ambient dose equivalent H*(10). It is suitable for applications in a wide energy range (from 10 keV to a few MeV) for the detection of photon radiation. The dose response was calculated with Fluka and is given in fig. 1 for the incidence angles 0° and 75° [3].

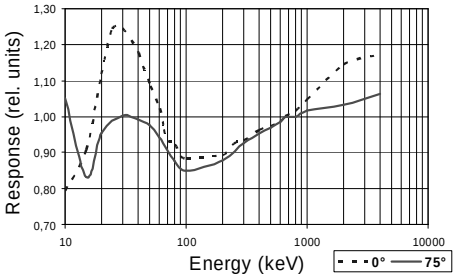

Fig. 1: Dose response of the GSI cylindrical dosemeter for H*(10) measurements.

Results

In fig. 2 the results of the dose rate measurements along the IH-structure are shown for different amplifier voltages with local maxima near the centre of the structure.

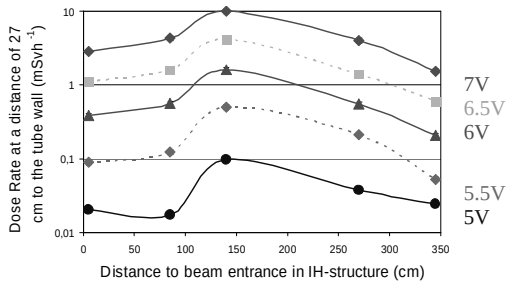

Fig. 2: Dose rate measurements along the IH-structure.

It should be mentioned that the given values of the amplifier voltages are normalized values that are used to adjust the HF-generators. The actual voltages are of the order of several 10 kV for the RFQ - structure and of several MV for the IH - structure.
In fig. 3 the dose rate levels are shown as a function of the amplifier voltage (to be converted in real field strengths in the IH-structure [2]). The following formula describes the dose rate as a function of the amplifier voltage:
$\dot{H} = 10^{\left(a_0 \cdot \sqrt{x - a_1} + a_2\right)}$; the values of the parameters a_0, a_1 and a_2 are given in the table below for different positions at the IH-structure.

Parameter (related to the units V, µSv/h)	2. Half Tank/ South	2.Half Tank/ North	1. Half Tank	End Tank
a_0	2.33	2.325	2.41	2.35
a_1 (threshold voltage)	4.67	4.63	4.52	4.68
a_2	-0.107	-0.232	-0.06	-0.715

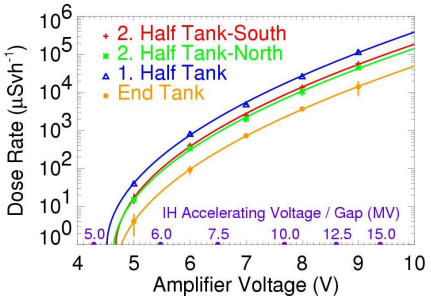

Fig. 3: Dose rate as a function of the amplifier voltage for different positions along the IH-structure.

Summary

Dose rate measurements have been performed at the pre-accelerator structure of the GSI UNILAC. The measurements of the produced x-rays at the IH-structure show that dose rate levels up to the region of Sv/h can occur.

References

[1] Manual of the radiation protection-dose rate meter TOL/E with a ionisation chamber, Berthold/Frieseke GmbH, 1971
[2] S. Grosam, BA Karlsruhe TSW04ST, diploma thesis: „Messungen von Röntgenstrahlungspegeln an der EZR - Ionenquelle und den HLI - Vorbeschleunigerstrukturen des GSI - Ionenbeschleunigers mit Thermolumineszenzdosimetern“, GSI - Safety and Radiation Protection, 30.09.2007.
[3] Fasso A, Ferrari A, Ranft J, and Sala PR. FLUKA: a multi-particle transport code. CERN-2005-10 (2005) INFN/TC_05/11; SLAC-R-773.

Dose assessment for the new experimental area Material Research

G. Freml[1], G. Fehrenbacher[1], Ch. Pöppe[1], and T. Radon[1]
[1]GSI, Darmstadt, Germany

Introduction

Currently the new experimental area "M-Zweig" is built up in the UNILAC experimental hall EH. Three beam line branches will be set up which will mostly be used for material science experiments. The cave is foreseen to be delivered with beam from He to Uranium with maximum energies of 12 MeV/u and maximum intensities of $2 \cdot 10^{11}$ particles per second in the case of Uranium and up to $2 \cdot 10^{12}$ for Argon or lighter beams.

Method of dose rate calculation

Shielding for experimental areas supplied with heavy ion beams for FAIR or experimental areas of SIS 18 are usually calculated by means of Monte-Carlo simulations with the FLUKA-code [1]. In 2004 the transport of heavy ions was added employing the RQMD and the DPMJET models [2,3]. However FLUKA is currently only capable of handling kinetic energies of ions above 100 MeV/u. Future versions of the code will include cross section libraries for the energy range below.

For the present case a work around had to be found to generate proper neutron production. There is only a sparse set of measurements for specific beams, energies, stopping materials and beam intensities to determine dose-rates for these kinds of low energy problems. Based on known physical processes taking place between beam particles and the stopping material like heavy ion fusion and fission processes and neutron emission Back [4] has developed a FORTRAN code for the determination of dose-rates. Based on the results of these formulae for the present case (^{238}U, 12 MeV/u), the distribution of the dose rate around a target was interpolated by a superposition of three built in FLUKA source functions with different energies and distributions.

Shielding design

Due to the three different beam branches three simulations were necessary to determine the overall shielding of the cave. Fig. 1 shows that the highest dose rates outside the shielding are found in the close vicinity of the interaction points and not only simply in forward direction like in thin target problems. Thus the wall thicknesses have to be large close to the interaction points. This explains the discontinuity in the shape of the walls (see panels a and b of Fig. 1). Due to cost reasons it was decided not to use heavy concrete with additional parts of barite or hematite which had resulted in smaller wall thickness. The maximum thickness is foreseen in the forward direction of beam branch 2. The entrance maze has a very simple design as the dose rates in the backward beam directions are quite low. The irregular shape of the already existing floor may need some further shielding with PE-slabs in the cable channels just below the interaction points (see Panel c of Fig.1).

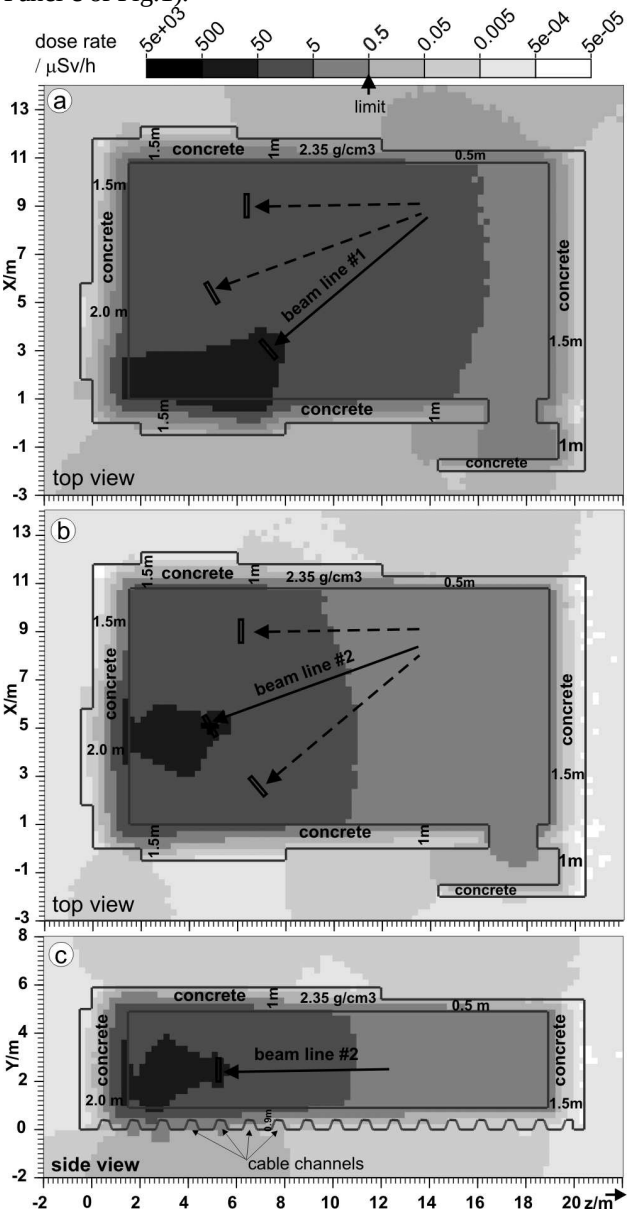

Figure 1: Dose rate distribution of the cave M-Zweig. Panels a) and b) show a top view with beams on target 1 and 2 respectively. Panel c) shows a side view of the dose distribution with the beam on target 2.

References

[1] A. Fassò, A. Ferrari, J. Ranft, and P.R. Sala, CERN-2005-10 (2005), INFN\TC 05\11, SLAC-R-773.
[2] H. Sorge, Physical Review C 52 (1995) 3291-3314.
[3] J. Ranft, Phys. Rev. D 51 (1995) 64.
[4] B. B. Back, Nucl. Instr. and Meth. B74 (1993) 527

Shielding of the Super-FRS pre-separator area*

E. Kozlova[1,2], K. H. Behr[1], G. Fehrenbacher[1], H. Geissel[1,2], T. Radon[1], K. Sümmerer[1], H. Weick[1], M. Winkler[1]
[1]GSI, Darmstadt, Germany; [2]II. Physikalisches Institut, Justus-Liebig Universität Giessen, Germany

Introduction

Progress of the shielding calculation of the Super-FRS is reported here. At least as important as the shielding of the target area is the determination of the shielding in the region of the first dipoles as the part of the primary beam that will not interact in the target will be stopped here. The Monte-Carlo-method with FLUKA [1] used for the shielding assessment here has already been described in reference [2].

Prompt dose

Depending on the thickness of the target the primary beams for the Super-FRS (e.g. 10^{12}uranium/s @ 1.5 GeV/u) will have an interaction rate of about 5% to 50% with the target. The non interacting particles are foreseen to be stopped in specially designed beam catchers. Due to various magnetic rigidities and ion optical settings the primary particles must hit one of six beam catchers in order not to be transported to the main section of the separator with less shielding volume. By a weighted superposition of these different cases, distributions of any scenario can be produced. Fig.1 shows the dose distribution of the most crucial case where the primary beam impinges on the first beam catcher (BC1). Here the interaction probability in the target was 10% whereas the interaction probability is 85% for BC1 and 1% in the other BCs each. The shielding consists of iron blocks (thickness: 2m) and an additional concrete layer of 5m. This combination is believed to be the best compromise between a cost-effective and a compact solution.

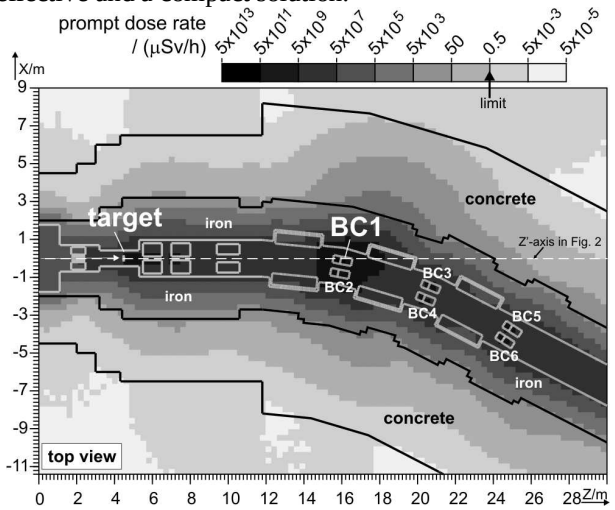

Figure 1: Top view of the prompt dose. The primary beam (^{238}U, 1.5GeV/u, 10^{12}/s) is stopped on beam catcher BC1.

* Work supported by EU, EURONS JRA 'SAFERIB' under contract numbers 515873 and 506065.

Activation and residual dose

With FLUKA sequences of irradiation and cooling times can be employed to score e.g. the residual dose rate at any point in time in a "one-step"-method. As a realistic test scenario four periods of irradiation with a ^{238}U beam of 1.5 GeV/u and an intensity of 10^{12}/s over 90 days with subsequent cooling times of 120 days after each block were assumed (see insert of Fig. 2). Due to the low-Z material the residual dose in the target and the carbon part of the beam catchers is two orders of magnitude less than the residual dose resulting from the second part of the beam catcher (iron, mass 340 kg). The main isotopes that contribute to the residual dose rate of these directly exposed parts after the assumed irradiation sequence are ^{54}Mn, ^{46}Sc, and ^{56}Co. The residual dose rates caused by these longer lived species which have activities of up to 10^{13} Bq range up to 5 Sv/h in the close vicinity of the beam catcher (see Fig. 2). The dose rate on the working platform which was designed for simple maintenance reaches values of a few ten μSv per hour and is thus accessible as a controlled area for hands-on maintenance in the order of minutes. Activated or broken parts like the target etc. can be removed with the help of a transport flask [3]. Therefore the shielding on top of the working platform will be removed and all the inserts can be safely removed together with their plugs into the shielding flask by a crane. The wall thicknesses of the flask amount to roughly 30 cm. and thus will shield against the highly activated iron.

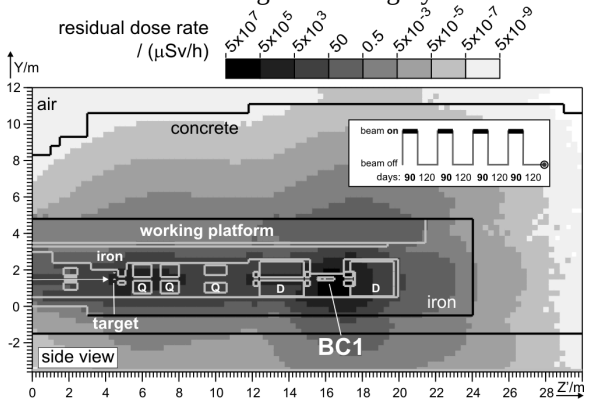

Figure 2: Side view of the residual dose after the time profile which is shown in the insert. The primary beam (1.5GeV/u, 10^{12}/s) is also stopped on beam catcher BC1.

References

[1] www.fluka.org.
[2] G. Fehrenbacher, E. Kozlova, and T. Radon, GSI-Report 2007-1 (2007) p. 75.
[3] E. Kozlova et al., "layout of the Super-FRS target hall", submitted to Nucl. Instr. and Meth. B.

Annual doses in the experimental halls TR, EX, TH

T. Radon[1], G. Fehrenbacher[1], S. Grosam[1], and Ch. Pöppe[1]
[1]GSI, Darmstadt, Germany

Arrangement of the experimental places at GSI into radiation protection areas

According to the German radiation protection ordinance, facilities constituting ionising beams have to be partitioned into several radiation protection areas. The areas in the experimental halls outside the shielding of the caves and accelerators at GSI are declared as surveyed areas. It is obligatory to install these areas if the annual dose can exceed 1mSv per year. It is mandatory to guarantee that the dose in these areas does not exceed 6 mSv per year. If it does, a controlled area has to be set up to which the access is controlled and only possible when wearing a personal licensed dosemeter. The caves and the accelerators are usually controlled areas while the beam is off, and they are prohibited areas when the beam is on, as then the limit of 3 mSv / h is exceeded.

Method of measuring the accelerator induced neutron doses at GSI

The typical doses measured outside the shielding of a particle accelerator in the energy range of several hundred MeV per atomic mass unit is strongly dominated by the neutron component. Depending on the thickness of the shielding the gamma dose originated from the accelerator is between 1% and 10% of the total dose. Thus it would be sufficient to score the neutron dose for a safe operation of the facility. At GSI a detector system based on thermoluminescence which was improved for better response to high energetic neutrons is used since a couple of years [1]. The advantage of the system used here is the total independence of the dose reading on the spill structure of the beams, i.e. there are no dead time effects etc. due to a passive system.

Annual doses in 2007 and future prospects to FAIR operation

Figure 1 shows the SIS and the following experimental areas together with the position of the neutron detectors. It can be seen that the dose values are largest in the vicinity of the SIS extraction area. The three largest dose values are located in an shaft in the shielding close to the extraction of the SIS (6.9 mSv), at the entrance from the area NE4 to NE3 (2.1 mSv) and in the staircase of the experimental area HHT (1.5 mSv). All of these locations belong to at least temporarily controlled areas and may thus reach higher annual doses than 6 mSv. The majority of the measurement positions show values below 0.1 mSv per year. However already with respect to planned intensity upgrades for FAIR the shielding of the SIS has to be reinforced. In addition activation experiments needed e.g. for material tests for FAIR will require at least one adequate shielded experimental area.

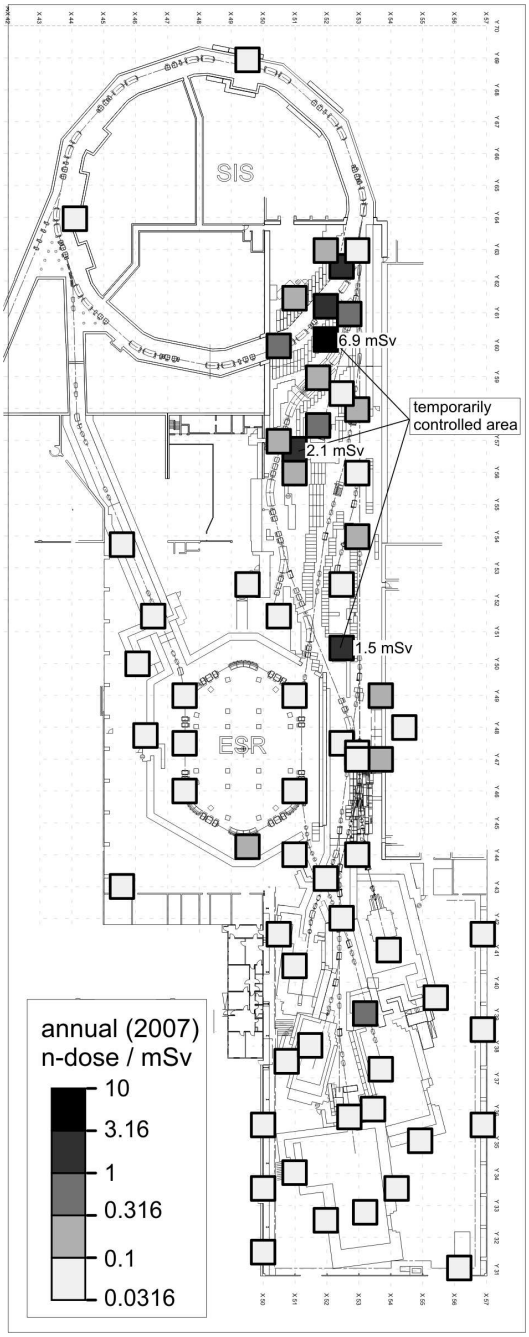

Figure 1: Measurement positions of the annual neutron doses in the experimental halls and their corresponding dose values.

References

[1] G. Fehrenbacher, F. Gutermuth, E. Kozlova, T. Radon, and D. Schardt, GSI-report 2005-1, p. 238.

Activation Experiments on Soil Samples for FAIR

K. Vogt, M. Haida, and G. Fehrenbacher
GSI, Darmstadt, Germany

Introduction

The operation of the new FAIR accelerator facilities will inevitably produce some amount of radioactivity in the surrounding earth and water, mainly caused by neutron radiation.

Although previous experience from the GSI and other accelerators [1] suggests that the resulting radiation exposure to the population will be close to zero, we need to do detailed investigations for the planning of the shielding of the new facilities as well as for the legal approval procedures.

Since the radiation exposure to the population is partially caused by radioactive nuclei produced in the vicinity of the accelerator facilities that are subsequently transported to inhabited regions by groundwater, we need to study not only the total amount of activity that might be produced but also the produced nuclides as well as their transport with groundwater. As a first step in these studies, activation experiments with several earth samples have been performed at the HHD beamdump at SIS 18.

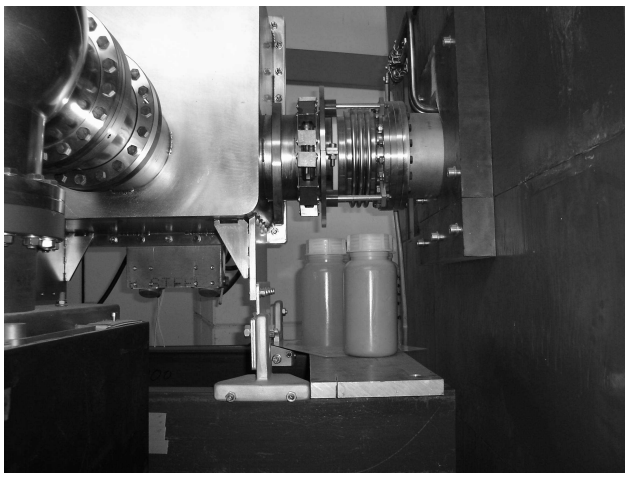

Figure 1: Irradiation of the soil samples.

Method

The earth samples used in this experiment originate from a drilling performed in the area where the new SIS100/300 will be built. Samples have been taken from depths of up to 20 m. Several samples were placed close to the HHD beamdump during machine experiments for about 48 hours, as illustrated in Fig. 1. After the irradiation, the photon spectra emitted by the activated samples were measured using high purity germanium (HPGe) detectors. In addition to these measurements, the activity and the nuclei produced during the irradiation have been calculated using the Monte-Carlo-Code FLUKA [2].

Results

The most prominent lines in the spectra recorded directly after the end of the irradiation originate from the decay of short-lived nuclides, most notably ^{24}Na. For our studies of the long term impact of the FAIR facilities nuclides with longer half-lives are more critical. These can be seen in the spectra recorded several weeks after the irradiation (see Fig. 2).

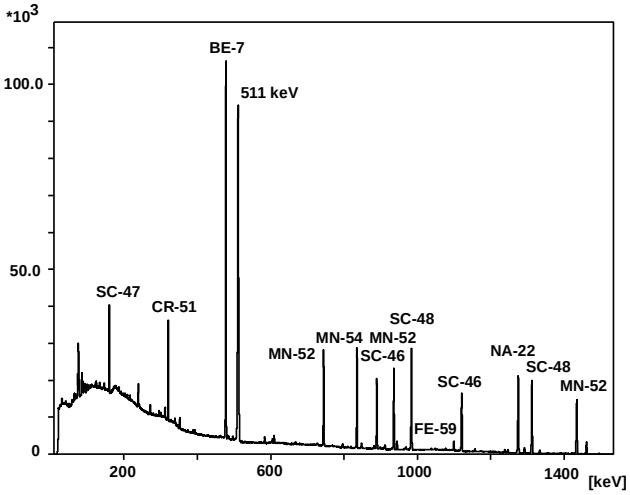

Figure 2: Typical activation spectrum recorded 19 days after the end of the irradiation.

The activities calculated with FLUKA show in general a reasonably good agreement with the measurements considering the large uncertainties involved, although there are rather large deviations for a few nuclides which requires further investigation.

In any case, FLUKA is a useful tool to estimate which nuclides will give the largest contribution to the activity produced by activation of earth and water during the operation of FAIR. The calculations done so far suggest that some of the most important nuclei do not emit any photons that could be detected by the HPGe detectors (e.g. ^{3}H, ^{55}Fe, ^{45}Ca). For the investigation of these nuclei, additional experiments using liquid scintillation spectrometry are needed which are planned for 2008.

References

[1] R. H. Thomas and G. R. Stevenson, Technical Reports Series No. 283, International Atomic Energy Agency (IAEA), Vienna 1988.

[2] A. Fasso, A. Ferrari, J. Ranft, and P.R. Sala, CERN-2005-10 (2005), INFN/TC_05/11, SLAC-R-773.

Development of High Resolution TDC ASICs for CBM-ToF

H. Deppe[1] and H. Flemming[1]
[1]GSI, Darmstadt, Germany

Introduction

The ASIC design group at GSI has evaluated two approaches for an optimal fitting new TDC ASIC for the CBM ToF-detector. The first one for this TDC is a new implementation of a Time to Amplitude Converter (TAC) core developed at GSI [1] in a current CMOS technology. The other one is using a Delay Locked Loop (DLL) to get a very fine time binning for direct time digitisation. Even though the TAC core based TDC achieves a better time resolution the DLL based approach fits better in other requirements so in end of 2007 is was decided to use a DLL based TDC for CBM-ToF.

Table 1: Requirements for the ToF readout electronics

Requirements
time resolution (for digitization) $\leq$ 25 ps
event driven architecture
event rate per channel $\approx$ 50 kHz
time over threshold measurement for walk compensation
$\approx$ 65 000 channels

A Delay Locked Loop based TDC

The principle of a Delay Locked Loop based TDC (Fig. 1) is well known and successfully implemented in many experiments. In a regulated delay line a bunch of clock signals with constant phase shifts are generated. These clock signals are used to clock a hit register to sample the input signal. So in the hit register an image of the input signals time structure is latched. One can get the digital timing information by encoding this image. This architecture is called clock driven.

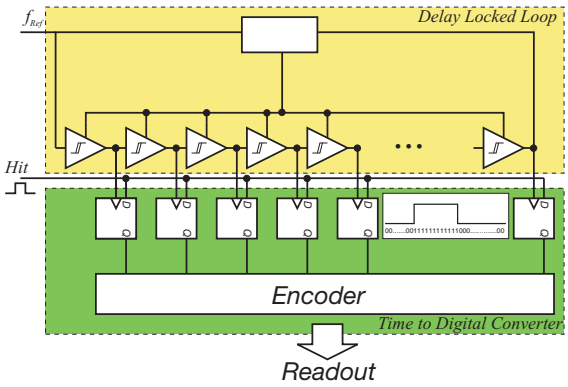

Figure 1: Block diagram of a DLL based TDC

After a first DLL testchip which was allready submitted in 2005 a second chip called *DANTE* was submitted in 2007. Based on the promising results of the first DLL chip *DANTE* was designed to increase the time resolution by using inverting delay cells with a delay of 50 ps in comparison to 100 ps delay cells in the first chip. At the design of this DLL structure the different charge carrier mobility of pmos and nmos transistors had to be compensated very carefully to prevent an odd even structure of the bin sizes. The compensation was very successful which is reflected in good DNL and INL values below $\pm$ 0.5 LSB (DNL) and $\pm$ 0.75 LSB (INL).

The time resolution of the *DANTE* chip in comparison to the first DLL chip is plotted in Fig. 2. The correlated time resolution of $\sigma_{2Ch} = 28.67$ ps leads to an uncorrelated time resolution for the *DANTE* chip of

$$\sigma_{1Ch} = \frac{1}{\sqrt{2}}\sigma_{2Ch} = 20.27 \text{ ps} \quad (1)$$

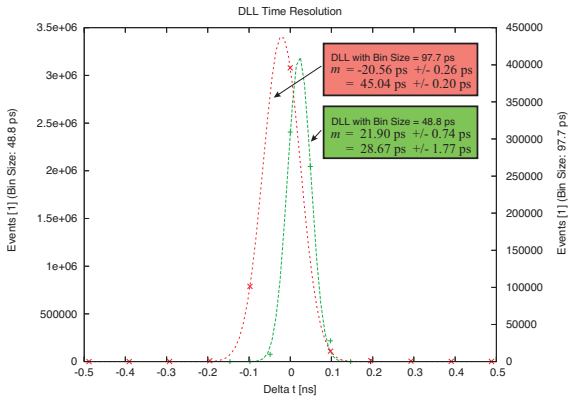

Figure 2: Time Resolution of DLL based TDCs

During 2008 it is planed to design a first prototype of a complete DLL based TDC chip. The aim is to get a multi channel TDC with at least four channels time over threshold measurement capability and a double hit resolution below 3.5 ns. For readout a simple DAQ interface with serial communication will be implemented.

References

[1] K. Koch et.al.: A New Multi Channel Front-End Board for TOF Experiments with Excellent Timing Resolution, GSI Scientific Report 2004, p. 339

Investigation of a High Voltage Lorentz drift based gas discharge switch

M. Iberler, K. Esser, A. Fedjuschenko, Ch. Hock, J. Jacoby, B. Koubeck ,B. Klump, J. Otto, T. Rienecker, A. Schoenlein
J. W. Goethe University Frankfurt, Institut für Angewandte Physik, 60438 Frankfurt

Fast high current and voltage switches are very important tools for pulsed power applications. They have for example applications in accelerator laboratories to drive fast injection- and extraction magnets, beam dumps and in quadrupole lenses.

Basically, there are two complete different principles used to realise a high power switches. One is based on the use of semiconductors, where as the other is based on a triggered breakdown in gases or in vacuum. Now this contribution gives an introduction in a new kind of gas discharge switch, which consists of a coaxial electrode geometry. Initially the inner electrode serves as anode, the outer as cathode. This switch device is called, based on its underlying effect, as Lorentz Drift Switch (LDS) and works usually with a cold cathode.

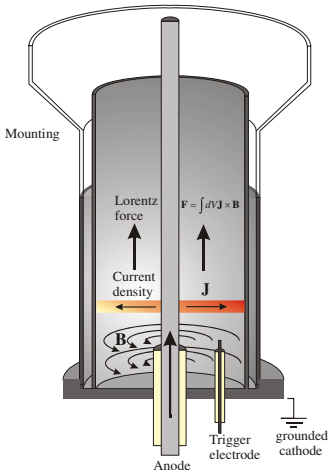

Figure 1: Schematic drawing of the Lorentz Drift Switch.

The Lorentz Drift Switch discharge is a low inductive, fast current, low pressure gas discharge, which works on the left steep branch of a breakdown voltage curve, similarly to the Paschen curve. The Lorentz force which interacts with the discharge is given by:

$$\vec{F} = \int dV\, J \times B \qquad (1)$$

Due to the magneto hydrodynamic motion of the discharge the electrode system has a low electrode erosion and therefore a long life time [1].

With an external triggering a gas breakdown is initiated and forms a conductive plasma sheath and closes the external electric circuit and the capacity begin to discharge. For the first prototype a trigger pin, between the main electrode system was used. To improve the life time of the trigger system a new method associated with a modified electrode system was developed. In the new geometry the trigger system is located outside the main gap in a coaxial hollow cathode.

The ignition of the discharge during the trigger phase occurs over the long distances in the hollow cathode [2]. As trigger system a semiconductor surface trigger was used [3]. For the experimental set up four capacities in parallel with a capacity of 4.4 µF was used for energy storage. The working pressure was adjusted between 10 and 100 Pa.

For first investigations the voltage- and current measurement were performed. Figure 2 shows the current and voltage wave forms of the switch for 2.3kV at a current of more than 6kA. For voltages lower than 2.5kV quenching at the zero point was observed. This characteristic is attributed to a circuit breaker for high voltage and current applications.

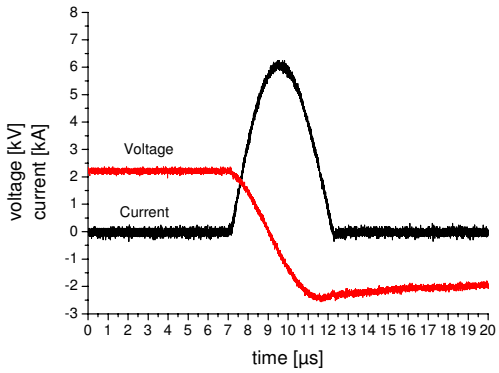

Figure 2: Current- voltage waveforms with current chopping at zero.

For higher voltages a damped oscillation of the current and voltage can be observed.

References

[1] J. Jacoby, C. Bickes, D.H.H. Hoffmann, C. Hofmann, J. Philipps, Experimental Study to Accumulate, Accelerate and Focus a Massive Plasma Beam onto a Target Fusion Engineering and Design 44 (1999) 331.

[2] A. Görtler, “Untersuchungen von gepulsten Oberflächenentladungen an Dielektrika und deren Anwendung zur Triggerung eines Pseudofunkenschalters”, Diplomarbeit, Universität Erlangen-Nürnberg (1986)

[3] M. Iberler, R. Bischoff, K. Frank, I. Petzenhauser, A. Rainer, J. Urban, Fundamental investigation in two flashover-based trigger methods for low-pressure gas discharge switches, IEEE on Plasma Science, Vol 32 (1), 208-214, 2004.

A Tuner for the 350 MHz Superconducting CH-Structure*

A. Bechtold[1], M.Busch[1], H. Liebermann[1], H. Podlech[1], U. Ratzinger[1]
[1]IAP, Universität Frankfurt, Germany.

Abstract

The superconducting CH multi-cell prototype cavity, which has passed a very succesfull power test recently leading to an accelerating gradient of E_a = 7 MV/m, will be equipped with a frequency tuning system [1]. The rf-tuning during operation bases on the principle of a slight elastic deformation at both ends of the tank. This is causing a change in the gap width of the first and last accelerating cell and the accompanying variation of capacity finally results in a frequency shift. The mechanical resonances of the cavity have been investigated experimentally in the environment of an acoustical laboratory at room temperature and within the vertical cryostat at 4 K. Moreover, an active periodic cavity detuning provided by the piezo tuners was implied, while stable superconducting cavity operation was kept by a frequency control loop acting on the rf-frequency oscillator.

Tuner Design

The frequency tuning device comprises two stages: A slow mechanical tuner with a tuning range of $\Delta f_{mech.} = \pm 1$ MHz and a fast piezo tuner operating in an expected range of $\Delta f_{piezo} = \pm 1$ kHz. The piezos will be inserted into the beam pipe, between the inner cold mass containing the helium and the outer room temperature vacuum vessel (fig. 1).

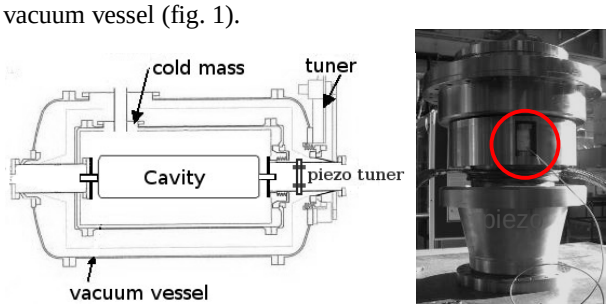

Figure 1: Scheme of the cryostat with tuner positioning on top left. Three piezo elements will be used for the fine tuning.

Microphonics

To avoid instabilities in the control system it is important to care about mechanical resonances of the cavity and their impact on the resonance frequency. Very low resonances can then be damped or pushed to higher frequencies if necessary. We have measured the resonances by using one of the piezos as an actuator stimulating the cavity with either a sinusoidal signal from an acoustic wave generator or with white noise comprising all frequencies between 0 and 100 kHz, alternatively. The response of the cavity was then detected by a microphone at room temperature or by a second piezo used as a detector in the cryostat and was digitally recorded (fig. 2). These wave data were Fourier analyzed subsequently.

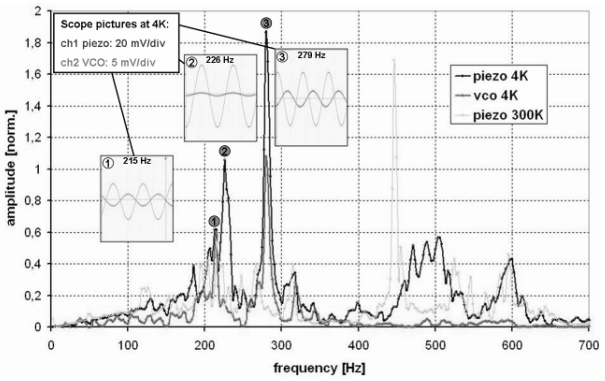

Figure 2: Microphonics at cryogenic temperatures and the impact on the rf-resonance. The VCO (Voltage Controlled Oscillator) signal indicates the action of the control loop to provide stable operation.

Power Test

In former tests the cavity performance was limited. After surface preparation at ACCEL the performance increased significantly (fig. 3) [2].

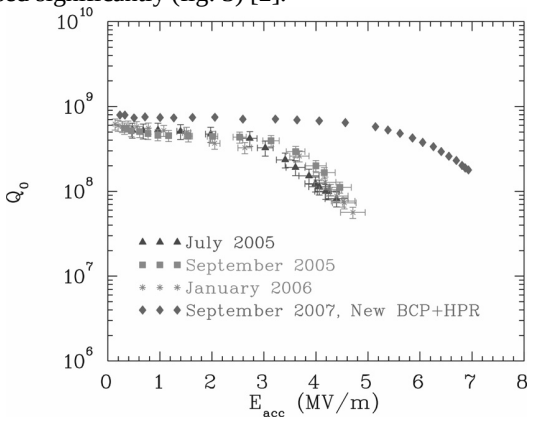

Figure 3: Measured Q-value as a function of accelerating gradient E_a.

References

[1] A. Bechtold, M. Busch, H. Liebermann, H. Podlech, U. Ratzinger, "A tuner for a Superconducting CH-Prototype Cavity", SRF2007, Peking.

[2] H. Podlech, A. Bechtold, M. Busch, H. Klein, H. Liebermann, U. Ratzinger, “Development of the superconducting CH-cavity and Applications to Proton and Ion Acceleration”, SRF2007, Peking.

*project supported by by GSI, BMBF contr. No. 06F134I and EU contr. No. 516520-FI6W

A Successor for the GSI Charge to Frequency Converter Modul

H. Flemming[1]
[1]GSI, Darmstadt, Germany

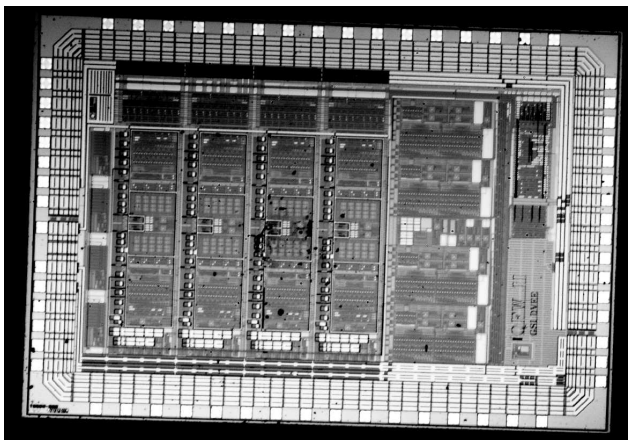

Figure 1: Photograph of the QFW II ASIC. The die size is 4.46 mm by 3.19 mm

Introduction

The GSI charge to frequency converter module originaly designed for the cancer therapy project in 1997 is very successfully implemented in many experiments where charge flow has to be measured over a wide dynamic range.
Since 2004 the ASIC design group of GSI has been developing an application specific integrated circuit (ASIC) which includes the whole converter on one silicon chip[2]. Now a PCB modul based on this ASIC is available which provides four charge to frequency converter channels.

The QFW II ASIC

The QFW II ASIC is the second generation of the charge to frequency converter ASIC development at GSI. A picture of this chip is shown in figure 1. On the left side four converter channels based on a recycling integrator are visible. This functional schema is taken over from the original QFW module[1]. In addition to the first generation described in [2] the QFW II is able to measure positve as well as negative currents.
Right from the converters four 10 bit DACs with a centered bandgap reference are placed which are generating four adjustable reference voltages. Adjacent to this a digital interface for configuration and readout of the internal pulse counters is visible.

The QFW II ASIC is produced in a 350 nm CMOS technology by Austria Mikrosysteme AG (AMS). It is packaged in a 64 pin QFP package and running with a core voltage of 3.3 volts.

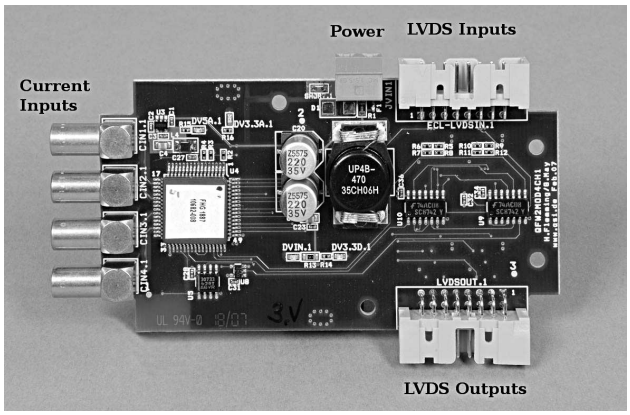

Figure 2: Picture of the charge to frequency converter PCB

The QFW Modul

Due to the very high integration level of the QFW II ASIC less external components are necessary for a ready to use QFW modul. In figure 2 the QFW module is shown. In addition to the QFW II ASIC only some voltage regulators and blocking for power supply as well as LVDS line receivers and drivers for connection to external electronics are needed. The PCB has a size of 54 mm by 100 mm and fits into a standard aluminium injection moulded housing. For power supply a single voltage between 5.2 V and 7 V is sufficient. The main technical parameter are merged in table 1.

	pos. current	neg. current
Leakage Current	300 fA	3.5 pA
Max. Current	13 μA / 130 μA	
Charge resolution	250 fC / 2.5 pC	
Nonlinearity below 1 μA	$< \pm 0.5$ %	

Table 1: Typical parameter of the QFW module

The digital interface of the QFW module is designed to operate with an universal logic module VULOM for configuration and pulse counting which was designed at GSI.

References

[1] EU - Patent: EP 1 031 040 B1, E.Badura, Vorrichtung und Verfahren zum Umwandeln von Ladungsfluss in ein Frequenzsignal

[2] H. Flemming, E. Badura: A high dynamic charge to frequency converter ASIC
GSI Scientific Report 2004

A Charge Sensitive Amplifier for timing and energy measurement (TCSA) *

M.Ciobanu[1,2], M.Kiš[1], A.Schüttauf[1], I.Deppner[2], N.Herrmann[2], K.D.Hildenbrand[1], T.I Kang[1,3], P.Koczon[1], Y.Leifels[1], X.Lopez[1], M.Marquardt[1], A.Reischl[2], M.S.Ryu[1,3], K.Piasecki[2], J.Weinert[1], N.Zernezki[1,2], X.Zhang[1], and the FOPI Collaboration

[1]GSI, Darmstadt, Germany; [2]Universität Heidelberg, Germany; [3]Korea University, Seoul, South Korea

The Time and Charge Sensitive Amplifier (TCSA) has been designed to combine excellent timing properties with a good energy measurement. To reach the best timing properties the time jitter and the noise-to-slope ratio have to be optimized. If we assume a uniform flat distribution of the noise without low or high frequency corners and a spectral density Nd (V^2/Hz) in the frequency band BW(Hz), we get with an amplitude A [1]:

$$\sigma_t \sim 0.44 * \sqrt{Nd}/(A * \sqrt{BW})$$

To decrease the jitter for the timing measurement, the preamplifier has to have low noise and a high bandwidth. As for the energy measurements, the signal to noise ratio

$$S/N = A/(\sqrt{Nd} * \sqrt{BW}).$$

has to be optimized. In this relation, the noise condition is the same as before, but to optimize S/N we should decrease the bandwidth by using an appropriate shaper. We have designed a TCSA which is able to process the signals delivered by fast detectors like Diamonds or LAAPD [2]. In classical CSA designs, one aims at a good stability of the system which affects the timing performance. An alternative is the separation of the time measurement from the main feedback loop which stabilizes the DC biasing of all active elements, and to decrease the dominant pole frequency till the phase reserve becomes large enough to guarantee a stable circuit. At the same time, the time branch must have the maximum bandwidth to reach the timing properties. During our design we aimed at a rise time of $t_R \leq 500ps$ which corresponds to a $BW \geq 0.7GHz$. To achieve this ambitious goal we used for the input stage a BFR998 double gate MOS transistor, which is often used for VHF/UHF preamplifier in TV tuners. They have a low noise characteristics at a 1 GHz bandwidth. Additionally there are two HF-transistors followed by a HF-amplifier. The energy branch uses four medium frequency transistors, a pole-zero cancellation and an output amplifier to shape the signals. With this layout we reached a sensitivity of $S_Q \sim$ 5mV/fC and a gain for the timing branch of about G $\sim$ 20.

Fig.1 displays the measured rise/fall time of the output signal versus the input charge. In the same plot we show the same dependence for the test system alone (pulser and oscilloscope). This contribution can be quadraticly

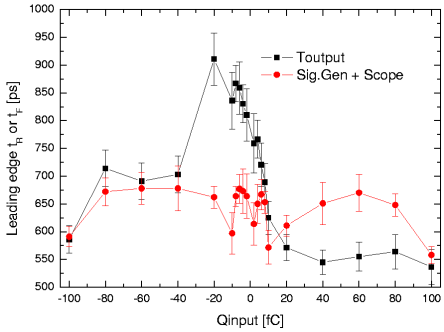

Figure 1: Rise-time measurements depending on the primary signal charge.

subtracted from the measurent, yielding rise times for the TCSA alone of t_R $\leq$500 ps. Using this TCSA for an LAAPD system in the FOPI setup we reached a time resolution for minimum ionizing particles of $\sigma_t \leq$ 353 ps.

In the Fig.2 we show the pulse height spectrum for a 3-line α source measured with a CVD single crystal diamond detector. Due to edge effects of the CVD-detector, the α-lines are broadened. For comparison we show a pulser measurement line, which confirms the very good energy resolution $\frac{\Delta E}{E} \sim$ 0.44 % of the TCSA.

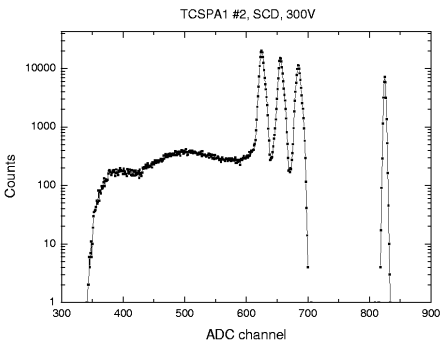

Figure 2: Energy spectrum for a 3-line α-source and a pulser

References

[1] M.Ciobanu et. al.,
IEEE 2007 Trans. on Nucl. Sci. Vol.54 Nr.4 p.1201

[2] T.I. Kang *et al.*
Contribution to this annual report

* work supported by JRA12 of EU/FP6 Hadronphysics (see annex), INTAS Ref.Nr. 03-54-3891 and German BMBF contract 06 HD190I.

High Resolution Double-Hit Timing and Time Over Threshold Measurement Feasibility for the TACQUILA System

K. Koch
GSI, Darmstadt, Germany

Several detector systems, as timing RPCs, have a need for timed double hit resolution at high input rates [1], [2]. For that reason, an expansion card for the high timing resolution system (TACQUILA) has been developed [3]. The enhancement of this system is the opportunity of measuring timed double hits on an input channel and an alternative appointment of the amplitude of the incoming signal by the method of *time over threshold.*

Double Hit Circuitry

Based on fast LVDS cross point switches, level adapters and flip flops, an expansion card for the high timing resolution system (TACQUILA) has been developed (see Fig. 1).

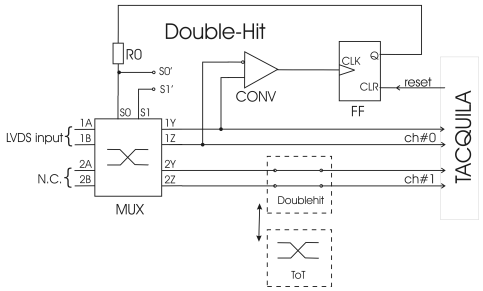

Figure 1: Simplified schematic of the double-hit card

The incoming LVDS timing signal is directed to one input of a fast cross point switch. For the double hit feature in the first time only the first channel is activated (ch#0). After switching the internal path in the MUX unit, the signal is directed to the second output channel (ch#1).

Results

Signals from a pulse generator are fed into a fast comparator board that delivers differential output signals [4]. The double-hit PCB has direct connectivity to that board as well as to the timing measuring system (TACQUILA).

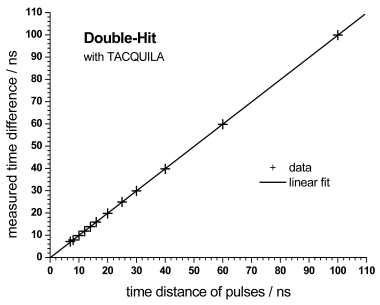

Figure 2: Double-hit measurements

Fig.2 shows the result of double-hit measurements generated with double pulses on one input channel. With a single pulse width of 2ns, the minimum distance between two pulses is obtained to be about 7ns to get separated timing information.

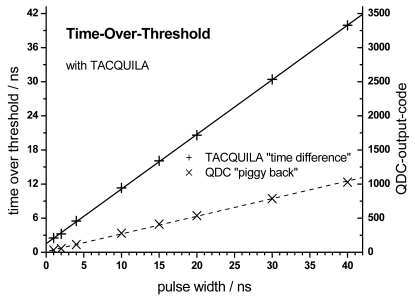

Figure 3: Time over threshold measurements

The results of the time over threshold measurements are depicted in Fig. 3 and show an outstanding linearity of the pulse width (solid line) and are in principal not limited for long pulses. The minimum pulse length is about 1ns. For comparison the data from the simultaneously obtained amplitude measurement with the QDC card of the TACQUILA system is shown (dashed line).

Conclusion

The minimum timing distance between two pulses is about 7ns. The timing resolution between two hits on one channel is about 10ps. For time over threshold measurements, the minimum pulse length is of about 1ns. An outstanding linearity for *double-hit* and *time over threshold* measurements is obtained over a large time scale and is in principal not limited.

References

[1] Upgrading the FOPI Detector system, FOPI-Collaboration, GSI Scientific Report, Darmstadt, Germany, 1998, p177

[2] FAIR Baseline Technical Report, Vol. 1-6, ISBN 3-9811298-0-(2006)

[3] K.Koch et. al., "A New TAC-Based Multichannel Front-End Electronics for TOF Experiments with Very High Time Resolution", IEEE Trans. Nucl. Sci., vol. 52, no. 3, pp. 745-747, June 2005

[4] M.Ciobanu et. al., "A Front-End Electronics Card Comprising a High Gain/High Bandwidth Amplifier and a Fast Discriminator for Time-of-Flight Measurements", IEEE Trans. Nucl. Sci., vol. 54, no. 4, pp. 1201-1206, Aug. 2007

Programmable Trigger Processing Module, VUPROM.

J.Hoffmann, N.Kurz, S.Minami, W.Ott, S.Voltz
GSI, Darmstadt, Germany.

A logic module (VUPROM [1]: **V**me **U**niversal **PRO**cessing **M**odule) for tracking trigger applications at HypHI experiment [2] was developed and tested satisfactorily. The design goal was to implement as many as possible trigger input signals and to process them in a short time period. The eight high density standard connectors (VHDCI) with 32 differential input or output channels each were implemented on the front panel of VUPROM. The four connectors on the VUPROM main board are hard-wired as three inputs and one output. Four piggy-back options allow additional input or output connector combinations. The high speed differential receivers have -4V to +5V common mode input voltage range and input to output delay of 4ns. Receiver outputs are connected directly to XILINX VIRTEX4 FPGA containing over 40K logic cells and running at a clock frequency of up to 400 MHz can be applied to it. Additionally a high performance DSP TMS320C6414

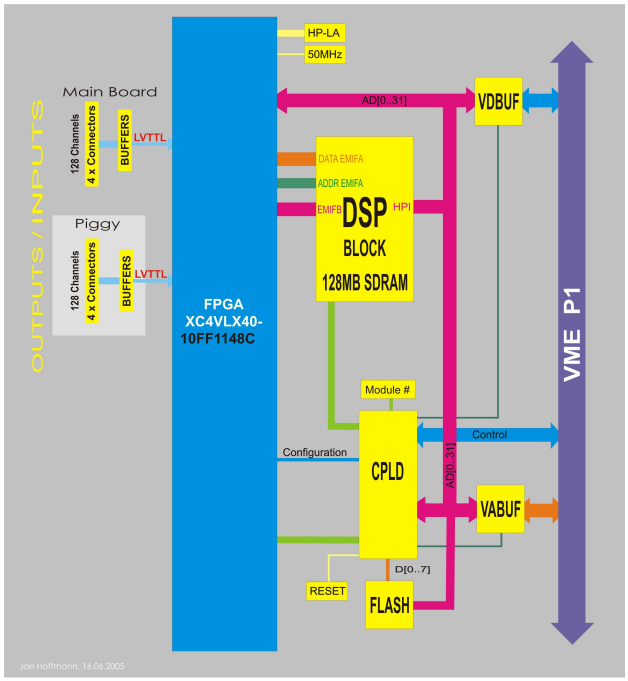

Figure 1: Simplified block diagram of VUPROM.

with 128 Mbytes SDRAM is connected to FPGA. This DSP is intended for complex trigger calculations. The trigger calculation results can be forwarded to front panel output connectors or to the standard VME backplane bus. A 32 times 24 pixel matrix display on the front panel is accessible from the DSP and can be used to show status information of the module. Additionally a standard LEMO® input (TTL and NIM level) and output (TTL or NIM level) are placed at the bottom of the front panel of VUPROM. The function of each of them is free programmable. The FPGA and DSP can be reprogrammed in several different ways. A CPLD with A32/D32 VME interface is implemented to support FLASH memory access and FPGA configuration. A 256 Mbit FLASH allows up to four configuration programmes for the FPGA to be stored in it. The default configuration after power up is from FLASH program one. The other configuration modes can be easy activated over VME command.

A fast static RAM with 256M x 16 bit capacity, for lookup table application is implemented too.

The VME interface design with A32/D32 option is tested successfully. The block transfer option with 32 bit data width can be used too.

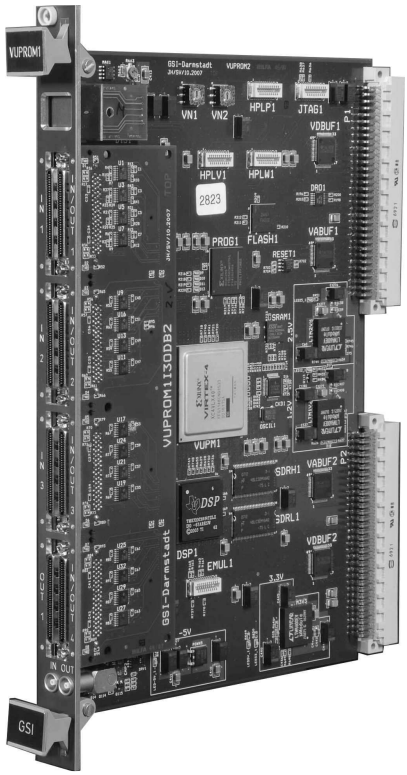

Figure 2: Photograph of VUPROM

References

[1] http://www.gsi.de/informationen/wti/ee/elekt_entwicklung/vuprom1_e.html
[2] http://www.gsi.de/forschung/helmholtz-group/HYPERNuclei/News_HypHI.htm

Level 1 trigger processing by VULOM3 board *

D. Leoni, J. Hoffman, W. Koenig, J. Stroth, M. Traxler
GSI, Darmstadt, Germany

A new HADES Level 1 triggerbox has been implemented using the programmable logic included in a VULOM3 (VME Universal LOgic Module) module. This development will reduce beam time losses caused by the problematic maintenance of the old Level 1 trigger, bringing at the same time better control and monitor capabilities [1].

Firmware architecture

The Level 1 triggerbox collects signals from several HADES detectors, remarkably the upstream diamond detector (Timing Signal), multiplicity in TOF detectors (Physic Triggers) and downstream diamond detector (Veto Signal). The selection process is quite straightforward: every PT pulse enables an acceptance time slot, if a received TS pulse falls inside the time slot and it is not inhibited by VS then an output trigger pulse is issued.

The VULOM3 is an extremely flexible VME module offering up to 32 ECL inputs, 32 ECL outputs and 4 LEMO selectable TTL or NIM connectors. It is equipped with a Xilinx VirtexIV FPGA, on-board SRAM and FLASH memory capable of retaining up to 8 different configurations, making it possible to use the module in a stand-alone setup with an instant-up feature.

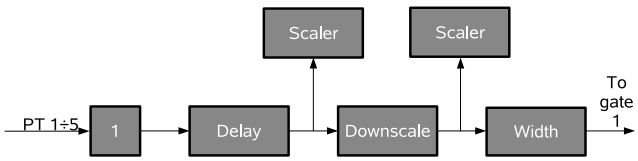

Figure 1: Physic trigger chain block diagram

The firmware architecture is organized into three slightly different chains. The PT chain consists of the following blocks: a sampler, a selectable delay (0-50 ns in 3.3 ns steps), a selectable downscale (up to 2^{16} in power of 2 steps) and a selectable width (3-53 ns in 3.3 ns steps). The delay and width blocks are used to tune the correct timing between PT and TS; in addition there are two 32-bit scalers, before and after the downscale, to provide adequate counting rate capability. A 300 MHz clock is used to synchronize the whole chain: in this application the output jitter is solely determined by the clock period and such a high frequency was chosen to minimize it. The other two chains also have a similar structure: the TS path lacks the downscale and width blocks, the VS path lacks only the downscale block.

* Work supported by EU FP6 grant, contract number 515876 and EU FP6 grant RII3-CT-2004-506078 (JRA1)

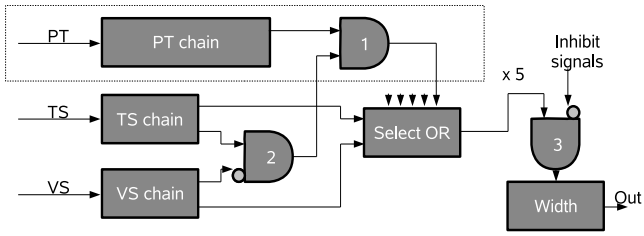

Figure 2: Triggerbox block diagram

A TS pulse entering the triggerbox passes trough the TS chain and arrives to gate 2. Here it can be inhibited by VS, otherwise it proceeds to gate 1. Meanwhile, one or more PT move through the PT chain and stop at gate 1. The TS is used to gate the five PT, and the resulting signals are selectively ORed. After that the output must cross gate 3, where it can be inhibited, and finally exits through a fixed width block. The inhibit signal at gate 3 is obtained from three different sources: a LEMO input, an internal calibration inhibit pulse (1 Hz, 200 µs width) and a high voltage inhibit pulse (spill trigger) with programmable delay and width (0-25 s in 0.1 s steps).

For every trigger issued by the VULOM3 an event packet containing trigger tag and code, latch-state and scaler values is built and sent to the TRB[3] via a dedicated bus. In addition, for the sake of mantaining compatibility with the existing machinery, the triggerbox is equipped with a CTU/DTU trigger bus (replacing the CTU module [2]) and is able to send latch-information as well. Other features include a programmable output pulser (2 MHz - 70 Hz) for testing DAQ, the possibility to create TS on board using a ORed TOF-signal, a sectorwise MDC/TOF coincidence and two multiplexed outputs for timing adjust purposes. Every parameter register can be conveniently set and monitored using the graphical EPICS interface.

The VULOM3 board was successfully tested in October 2007 beam time and it will replace the old triggerbox in the upcoming beam times.

References

[1] J. Hoffman; VULOM3, VME Universal Logic Module, Version 3
http://www.gsi.de/onTEAM/grafik/1130845854/vulom3.pdf

[2] E. Lins; Detector Trigger Unit Technical Manual, HADES-Wiki

[3] M. Traxler, A General Purpose Trigger and Readout Board (TRB) for HADES and FAIR-Experiments, GSI Scientific Report (2006)

Improving the usability of the *CS* Framework

D. Beck, H. Brand, M. Feldmann, M. Kugler, A. Schwinn
GSI, Darmstadt, Germany

The *CS* framework is a LabVIEW based framework for developing event driven, multi-threaded control systems using an object oriented approach. *CS* was upgraded to version 3.1 based on LabVIEW 8.2 and some common application base classes and add-on packages have been added to enhance usability.

CS framework

The *CS* framework is in use since a couple of years at about ten experiments at four institutes. Instead of supporting a maximum number of process variables, the main focus of *CS* is to provide a basis for control systems requiring a high flexibility and performance. A detailed description of *CS* is given in [1]. This text aims at describing the enhancements by the most recent version 3.1.

LabVIEW Libraries

LabVIEW libraries were introduced with version 8.0. They provide a unique namespace and public and private access scope. Private VIs can not be accessed from outside the library. This enables us to hide internal implementation details from the user and therefore to enhance the runtime stability. So, *CS* classes were converted to libraries. Access restriction to protected VIs still depends on convention.

The LabVIEW project explorer eases the navigation in the class hierarchy and building of executable applications and installers.

CS *Application base classes & SCADA*

To enhance the reusability of applications several base classes have been introduced for generic devices, arbitrary function generators, power supplies and motion. Specific sets of events and function are defined that can be overwritten or extended by subclasses. Corresponding GUI classes have been developed as well. Existing device and GUI classes have been adapted to meet the new base classes interface. The base classes provide identical interfaces for certain device types allowing, as an example, for using standardized graphical user interfaces independent of the manufacturer or model of the device.

The Data Logging and Supervisory Control (DSC) module for LabVIEW has been redesigned by National Instruments. Shared Variables are replacing the former Tags. The *DSCInterface* class has been redesigned to use Shared Variables. It was not necessary to modify the interface to DIM [2], it is still the same. The DSC development environment is necessary for the built-in tools for interactive configuration of shared variables, e.g. alarm limits, historical trending as well as OPC binding. Since we prefer to install the runtime environment only for production systems, our own interactive configuration tool was developed.

Fortunately, different *CS* applications, based on *CS* 3.0 or 3.1, can be mixed and work together because both are using DIM as communication layer and a common event data format.

CS *Add-on packages*

The *CSSequencer* package [3] was redesigned with respect to new features of CS 3.1. It provides a generic framework to create, save, load and execute sequences of events with conditions and loops. All events of classes that have inherited from *BaseProcess* class could be used directly. Child classes could also provide special events with dedicated hard wired activities to improve performance.

The *CS-ON-PN* package [4] provides a class library that enables a developer to use Object- or Petri-Net techniques to design and implement its application.

The *CS2JAVA* package [5] allows generating JAVA source that can be imported from UML design tools for documentation or discussions with non LabVIEW experts.

Summary

The *CS* framework has done a major step forward by adding missing features that are required for larger, distributed control systems. The main change is the usage of LabVIEW libraries and new application base classes to enhance reusability. *CS* version 3.1 has been released in December 2007. The control system for FOPI [6] was upgraded and commissioning is planned for early 2008.

References

[1] D. Beck et al., Nucl. Instr. Meth. A 527 (2004) 567-579, http://wiki.gsi.de/cgi-bin/view/CSframework.

[2] C. Gaspar, M. Dönszelmann, Ph. Charpentier, International Conference on Computing in High Energy and Nuclear Physics (Padova, Italy, 1-11 February 2000), http://www.cern.ch/dim.

[3] M. Kugler, "Entwicklung einer Klassenbibliothek zur Erstellung generischer Sequencen im Rahmen des *CS* Frameworks", Diploma-Thesis 2006, Hochschule Darmstadt

[4] A. Schwinn, "Entwicklung von Objekt- und Petri-Netzen im Rahmen eines Kontrollsystems", Diploma-Thesis 2007, Hochschule Darmstadt

[5] M. Feldmann, "Entwicklung einer automatisierten Dokumentation von LabVIEW Quellcode für das Rahmenwerk CS", Bachelor-Thesis 2007, Technische Universität Darmstadt

[6] P.Koczon, "New Slow Control System for FOPI", GSI Scientific Report 2005, page 273

Data Acquisition Backbone Core DABC *

J. Adamczewski[1], H.G. Essel[1], N. Kurz[1], and S. Linev[1]
[1]GSI, Darmstadt, Germany

DABC design

The DABC [1] addresses requirements of FAIR experiments like CBM [2] for detector and data acquisition test beds as well as the need for a general purpose DAQ backbone for experiments in production. The backbone is able to handle any kind of front-end systems and provides event building over fast networks using commodity hard- and software. Especially a mixture of commonly used MBS (daq.gsi.de) based front-ends and others will be needed. Event building based on time stamped data streams gets more common and must be supported.

The DABC software written in C++ runs on standard Linux PCs. A schematic view is shown in Figure 1. Arbitray front-end systems (FES) can be connected to standard Linux PCs (by hardware or network). Application plug-ins for handling the front-ends must be written by the application programmers. More plug-ins may process the data streams. To combine two data input streams on one PC a specific plug-in knowing the data formats is needed. Senders/receivers provided by DABC do the event building over networks like Ethernet or InfiniBand. Behind the receivers the event processing is done by other plug-ins.
The DABC core design has been revised for a better separation from the XDAQ environment [3]. This environment could now be easily replaced by other libraries providing state machines, task controls, and setup/configure mechanisms. The plug-in APIs also have been redesigned to be optimal for general purpose data acquisition applications.

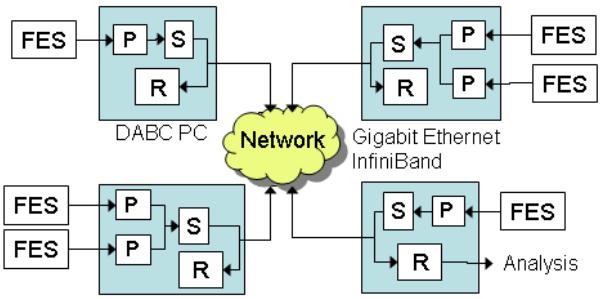

Figure 1: Front-end systems (FES) connected to DABC by application plug-ins (P). Data flow from senders (S) over event building network to receivers (R).

MBS integration

The general purpose DAQ system MBS had to be upgraded to connect MBS front-end systems via TCP to DABC nodes for event building. A new list mode data file format allowing for large files (> 2 GB) and direct event access has been designed and an API library implemented. DIM servers (dim.web.cern.ch) running on the MBS nodes provide control and monitoring by the DABC standard Java GUI. In DABC, MBS plug-ins have been implemented.

Controls and Monitoring

The standard control access to DABC is via DIM. Parameters and commands can be specified in the application plug-ins. A naming convention provides the locations. A generic Java GUI displays all parameters and commands provided by the DIM servers. Special parameters like rates, status, and histograms are visualized as shown in Figure 2.

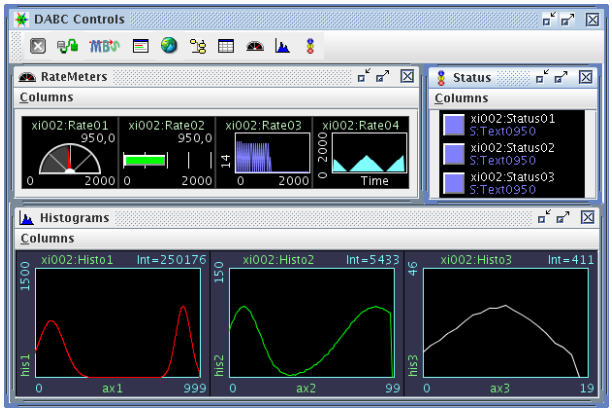

Figure 2: Rate meters, status displays and histograms.

Status and outlook

The new plug-in API description will be published soon. The modifications due to the design review have to be implemented. The MBS plug-ins will be adjusted. The MBS control by DABC GUI must be completed (support for all MBS commands, running standard MBS without DABC). In 2008 DABC will be ready for the test beds as well as for the event building of MBS based DAQ systems. Latest news on wiki.gsi.de/DABC

References

[1] J. Adamczewski, H.G. Essel, N. Kurz, S. Linev, "DataAcquisition Backbone Core DABC", IEEE Trans.on Nucl. Science, Vol.55, No.1, February 2008, to be printed.

[2] "CBM technical status report", GSI, January 2006

[3] J. Adamczewski, H.G. Essel, N. Kurz, S. Linev, "Developments for future DAQ framework DABC", GSI report 2006

* Work supported by EU-RP6 HadronPhysics, RII3-CT-2004-506078

Infiniband performance for Future DAQ *

J. Adamczewski[1], H.G. Essel[1], and S. Linev[1]
[1]GSI, Darmstadt, Germany

Event building performance

High performance DAQ systems are required by the next generation experiments at FAIR like CBM [1] [2]. After combining data from several input channels in the front-end systems the event building is done through standard networks. A bidirectional data rate per node of 1 GByte/s is needed. Several hundred nodes might be necessary to achieve the required total bandwidth. One of the fastest network available today is InfiniBand (IB). Therefore we started, after detailed simulations, investigations in IB performance for event building. First measurement have been done at GSI on a small IB cluster with four nodes [3]. All available software packages for IB have been evaluated. Finally, we selected the **verbs** API of the OpenFabrics Alliance [4]. We measured a single data rate per node of 950 MByte/s in all to all scheme.

Performance scaling

The open question how this scales to over hundred nodes could not be answered at GSI. Therefore we established cooperations with the Forschungszentrum Karlsruhe (FKZ, http://www.campusgrid.de) and the University of Mainz (UM, http://www.zdv.uni-mainz.de/3401.php). In Karsruhe, 23 machines were available, in Mainz 110, all double dual-core Opterons. Karlsruhe has IB switches from QLogic, Mainz from Flextronics. Measurements have been performed with stand alone test programs emulating event building traffic. All nodes work as data sources and data collectors. In round robin mode senders distribute buffers circular to the receivers without synchronization. In synchronized mode the senders follow a time schedule trying to avoid congestions at the receivers. Figure 1 shows the results.

To see the scaling effects, the transfer rates have been normalized to the ones for 5 nodes (FZK) and 10 nodes (UM), respectively. All shown measurements are done with the round robin scheme, FZK 23 and UM 72 also with the synchronization scheme. Below 16K packet size the synchronized mode is rather worse the round robin. With larger packets synchronization gives significant better results. Synchronizing the 23 FZK nodes and the 72 UM nodes gives about 700 MBytes/s. With 110 nodes and packet sizes above 16K the single data rate per node is 500 MByte/s. This is about 50% of the rate measured at the four nodes at GSI. With high number of nodes synchronization gets much more complicated because the switch topology must be taken into account. This works up to 72 nodes, but gets more difficult up to now for 110 nodes. Besides that the 50% are surprisingly good!

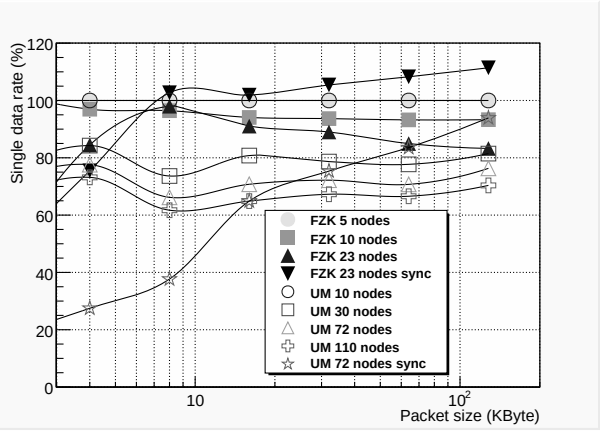

Figure 1: Normalized single data rates.

Event building with DABC

Network event building tests have also performed in a more realistic environment, the data acquisition backbone core DABC [5][6]. On the four GSI machines four threads on each machine generate data wich are combined in another thread, sent over IB to the other nodes for event building. With packet sizes above 32K the single data rate per node is more than 800 MBytes/s.

Summary

More detailed studies are necessary to optimize the traffic on large clusters, because the switch topology becames the critical issue. The data rate achieved up to now with more than hundred nodes is at least 50% of what is required in some years from now. The concept of network event building with very high data rates seems to be feasable.

References

[1] "CBM technical status report", GSI, January 2006

[2] H.G.Essel, "FutureDAQ for CBM: On-line event selection", IEEE TNS Vol.53, No.3, June 2006, pp 677-681

[3] J. Adamczewski, H.G. Essel, S. Linev, "InfiniBand cluster for Future DAQ", GSI report 2006

[4] OpenFabrics Alliance website, http://www.openfabrics.org

[5] J. Adamczewski, H.G. Essel, N. Kurz, S. Linev, "Data Acquisition Backbone Core DABC", IEEE Trans.on Nucl. Science, Vol.55, No.1, February 2008, to be printed.

[6] J. Adamczewski, H.G. Essel, N. Kurz, S. Linev, "Data Acquisition Backbone Core DABC", GSI report 2007

* Work supported by EU-RP6:Hadron Physics, RII3-CT-2004-506078

TRBv2: A Platform for Miscellaneous DAQ/TDC Tasks for HADES and FAIR-Experiments *

M. Traxler[1], I. Fröhlich[2], M. Kajetanowicz[3], J. Michel[4], M. Palka[4], P. Salabura[4], H. Ströbele[2], J. Stroth[2], P. Skott[1], A. Tarantola[2], R. Trebacz[4]

[1]EE, GSI, Darmstadt, Germany, [2]J.-W. Goethe-Universität, Frankfurt, Germany [3]Nowoczesna Elektronika, Krakow, Poland, [4]Jagiellonian University, Krakow, Poland

Introduction

The general-purpose trigger and readout board (TRBv2) with on-board DAQ functionality and extensibility through add on cards has been developed and was used successfully in two beamtimes in the year 2007. The functionality of the TRBv2, already roughly outlined in [1], is described in [2].

Several add on modules, which enhance the functionality/connectivity of the TRBv2, have been developed and commissioned. In this document the functionality of the add ons is described without going into detail of the application in the HADES-experiment, as they are mostly general purpose boards and also of interest for other experiments.

The add on boards built are spanning the full range of medium bandwidth (32 times 250MBit/s) data combining, high bandwidth (2 GBit/s optical links) digital data switching, general purpose IO-boards [1] (LVTTL, LVDS, RS485) up to 96 channel analog to digital converters and 62 channel time and amplitude digitization of fast pulses. The TRBv2 provides as the common base the data transport, slow-control and power-supply for the different applications. Data transport to the add ons and (when applicable) to the FEE, and (optionally) in a high-speed and real-time network is done via a dedicated IP-core (TrbNet) protocol.

MDC-AddOn module

Although built to read out the HADES-MDC-detector, the MDC-AddOn is a generic TRBv2 AddOn which uses ten buses (each with 18 differential RS485 signals and 10 LVTTL signals) to send and receive data, which then is collected and processed on a FPGA. This data is then transported to the TRBv2 and sent via Ethernet to the event builder.

In a second MDC-related project we built a 4 cm x 4.5 cm board, which uses an optical link to transport 250 MBit/s over Polymer Optical Fibres. The board will be used 380 times in the HADES-experiment to readout TDC-information and process it on it's FPGA (35k LUTs). The data will then be received by the MDC-Optical-AddOn (not built up to now), which carries 32 250 MBit/s optical transceivers (OptoLock from Firecomms [3]). The data is then received and combined to events and the TRBv2 manages the data transport to mass storage. This system allows a galvanic isolation and reduces the amount of radiated noise induced into the very sensitive MDC-detectors substantially.

TOF-AddOn

The TOF-AddOn is a 62 channel "Charge to Width" (Q2W) analog FEE, which encodes the time and charge of e.g. photomultiplier signal into a LVDS signal, which is then digitized by the TDC-ASICs on the TRBv2. The time and width information is therefore produced with just two TDC-measurements, no ADC is needed. This Q2W-FEE is an extension of the "Time above Threshold" method [4]. On the TOF-AddOn the NINO-ASIC [5] (8 channel, fast, low power amplifier/discriminator) is used. The individual threshold for the 62 channels are controlled via the TRBv2.

Shower-AddOn

The Shower-AddOn is an 96 channel general purpose ADC board (10 bit, 40/60 MSPS, low noise). The analog inputs are fed in via two high density connectors with 68 pins each. This add on combined with the TRBv2 provides a very high density of ADC channels combined with DAQ and pre-processing power (2 FPGAs + DSP). The PCB is currently in production.

HUB-AddOn

The HUB-AddOn carries 16 SFP slots, which can house up to 3.8 GBit/s SFP-transceivers. It can be used to fan-out trigger information (as a TrbNet-HUB) with a low latency and at the same time work as data combiner which collects the different chunks of data from different sources and forwards the events further up in the DAQ-chain.

References

[1] M. Traxler *et al.*, GSI Scientific Report, 2006, p. 225.

[2] I. Fröhlich *et al.*, "A General Purpose Trigger and Readout Board for HADES and FAIR-Experiments" IEEE Transactions on Nuclear Science, 2008, in print.

[3] http://www.firecomms.com/products-optolock.html.

[4] W. Koenig *et al.*, GSI Scientific Report (2007).

[5] F. Anghinolfi *et al.*, Nucl. Instr. and Meth. in Phys. Res. A 533 (2004) 183187.

* Work supported by EU FP6 grant, contract number 515876 and EU FP6 grant RII3-CT-2004-506078 (JRA1)

GSI IT-Department Activity Report

M. Münch for the GSI IT-Department[1]
[1]GSI, Darmstadt, Germany

Overview

The general scientific activities and infrastructural services of the GSI IT-Department have been briefly described in the "GSI Scientific Report 2006" [1]. A description of special activities and major steps during the year 2007 is given in this report.

Scientific Computing

The simulation and analysis framework FairRoot for the FAIR experiments has been extended in close cooperation with the main users from Panda and CBM. A software development environment for globally distributed teams with an automated build environment, an automated testing tool, an automated code convention checker and a quality control dashboard has been set-up [2]. Other developments, including a generic event display and an external decayer, have been developed in close collaboration with the ROOT team at CERN [3]. An interface between Fluka and FairRoot has been developed to ease the use of Fluka especially for radiation level studies of CBM [4].

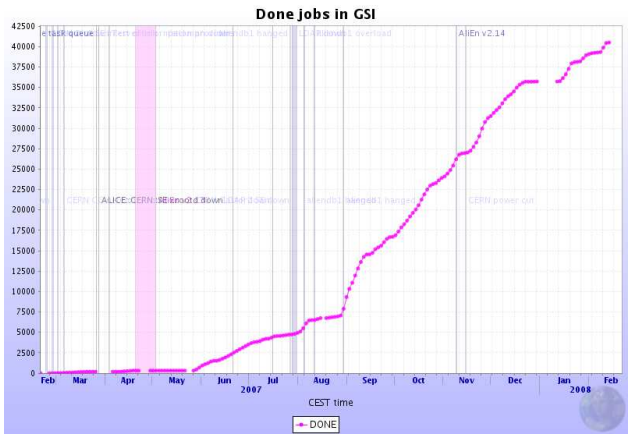

Figure 1: The accumulated number of completed simlation and analysys jobs at the Alice tier 2 centre an GSI. The steep rise marks the increase in available resources and the beginning of the production phase. At the end of 2007, almost 40,000 jobs were completed.

The construction of the Alice tier 2 centre at GSI continued in 2007. Extensive tests of the data transfer to and from GSI and of interactive data analysis have been performed, to investigate the best way to fulfill the requirements of the first year of data taking, which starts in 2008. The Alice tier 2 activities are supported in part by the European Grid project EGEE II and by D-Grid [5].

High Performance Computing and Storage

In order to find a solution for the future data file system for GSI the linux group set up a prototype test cluster with a new generation of cluster file system: Lustre. With Lustre, the data are organized in data objects and meta data. The data objects are dynamically distributed across the servers and the meta data information is organized in a central data base. This concept enables outstanding scalibility and I/O performance.

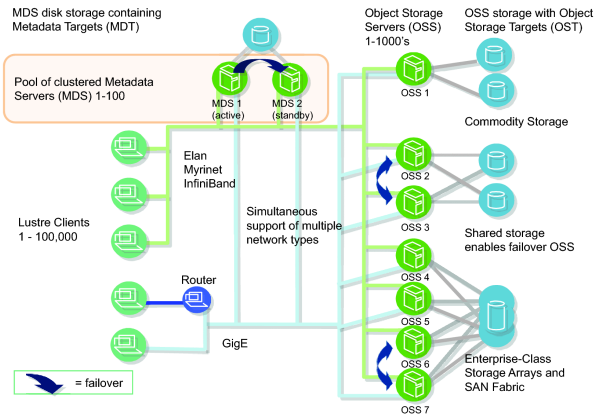

Figure 2: Architecture of the clustre file system "Lustre". The Lustre Clients find a complete directory on the Metadata Servers and access the data on the Object Storage Servers. Only a subset of the shown technologies are currently used at GSI.

The small prototype test cluster reaches an aggregate I/O of more than 1 GByte/s writing/reading to a RAID 5 with a large number of concurrent processes. In our setup, performance of the lustre file system was tested on servers with one and two parallel Gigabit Ethernet connections, finding the transfer rate to and from the file system only limited by the available network bandwidth. It is expected that the larger production cluster will be much faster.

The prototype cluster was already tested sucessfully by the HADES and ALICE group. Lustre is fully compliant to the POSIX standard, so all existing analysis code should continue to run witout any changes necessary. Lustre is also tested to be compatible with gStore - our GSI mass storage system.

However - lustre is very complex. More tests of the desaster recovery strategies and the high availibility setup of the central data base will be necessary. Operation of the full production cluster is expected for spring 2008 with a file system size of about 600 TB and an I/O capacity of

more than 7 Gbyte/s.

In May 2007 the older mass storage interfaces ("adsmcli" and "tsmcli") have been replaced by a new common interface ("gstore"). It provides access to all experiment data at GSI - independent of their location on any ATL or a related cache file system. Since the unification all new experiment data have been archived to the upgraded IBM 3494 tape library, which has a data capacity of 1.6 PB currently. Each of the 6 tape stations has an I/O speed more than 100 MB/s. Currently 0.3 PB of archive space are in use, including 50 TB of doubly stored valuable raw data [6].

Fast and parallel access to gStore is available via 35 TB of read and write cache, providing a bandwidth of up to 1 GB/s.

In 2007 overall nearly 0.6 PB of data have been moved between nearline storage of the compute farms, gStore cache, and gStore archive, which means on average 1.6 TB at each day. gStore is also available for the new Lustre file system.

Office and Desktop Environment

A new file server system, providing additional 3 TB of disk space to the Windows XP desktop workstations, was put into operation as an active-active high availability cluster. Connected to an extendable SAN disk subsystem and making use of the "Veritas Storage Foundation 5.0" file system, the extension of user disk space in terms of hardand software is possible without disrupting the service.

Software licences on almost 1500 client nodes are governed using a central licence management system. Changes in software installations can be tracked and free licenses can be reused, reducing the need for additional purchases.

Central Services

Using Oracle Application Server Technology with Single Sign-On, an LDAP-based user authentication for various web applications has been established. Via role-based user authentication access is granted to various applications, among these the GSI project time recording software (mandatory for every GSI employee), OnTEAM document management server, general security and radiation protection safety courses, accelerator operator's logbook, etc. A new user administration and account database has been created. Processes for an automated exchange of personnel data with the HR department have been established. A new system consisting of a cluster of two Application Servers in an active-active and load-balanced configuration is currently being rolled out.

The establishment of an IT service desk as a single point of contact was making progress in 2007. The launch of the IT trouble ticket system "OTRS" as a particularly important step took place in summer. It allows efficient communication between user and administrator via web interface or via e-mail. The trouble ticket system is the base for tracking and documentaion of requests and incidents. In parallel, organisational changes increased the availability and visibility of the IT support.

IT Infrastructure

Generally, the year 2007 was affected by the quest for additional building infrastructure. The existing computing centre is at its limits in terms of cooling and power supply so no additional computing resources can be put into operation there. Additionally, the storage of all data in one single room is a very risky situation in view of elementary hazards.

In order to improve the situation for the short and medium term, a suitable area in a different building on the campus was started to be used as an extension and backup computing centre. After the first steps in 2007, an area of up to 200 sqm may be converted in the following years. Taking into account the currently increasing activities for the ALICE tier 2 centre and anticipating the needs for FAIR computing, the planning for a new compute centre building was started in 2007.

In the area of networking, a remarkable milestone was the decommissioning of the dated Avaya backbone infrastructure. Four ethernet switches were consolidated into one single Foundry "Big Iron RX16" device, providing connectivity to most of the edge switches throughout the campus and part of the servers in the compute centre.

Also for wireless lan access, state of the art technology using a central controller for all access points was introduced. Based on this, area wide provision of WLAN access will be much easier to implement in the following years.

References

[1] Münch, M.: "GSI IT-Department Activity Report", GSI SR 2006, p. 206

[2] Al-Turany, M.; Bertini, D.; Uhlig, F.: "Improving the Sofware Development Environment in FairRoot", GSI SR 2007

[3] Al-Turany, M.; Bertini, D.; Uhlig, F.: "Status of the FairRoot Simulation and Analysis Framework", GSI SR 2007

[4] Bertini, D.; Paulova, E.: "iFluka: a C++ interface between Fluka and FairRoot", GSI SR 2007

[5] Schwarz, K.; Kreshuk, A.; Malzacher, P.; Manafov, A.; Penso, V.; Preuss, C.; Zynovyev, M.: "Grid Activities at GSI", GSI SR 2007

[6] Göringer, H.; Feyerabend, M.; Sedykh, S.: "The GSI Mass Storage", GSI SR 2007

Grid Activities at GSI*

A. Kreshuk[1], P. Malzacher[1], A. Manafov[1], V. Penso[1], C. Preuss[1], K. Schwarz[1], and M. Zynovyev[1]
[1]GSI, Darmstadt, Germany

Abstract

This article describes the work of the GSI Grid Group with the aim to enlarge and operate an ALICE tier2 centre within the global environment of the LHC Computing Grid and to prototype a possible FAIR grid environment.

ALICE tier2 centre

The current storage philosophy is manyfolded. The complete disk space of 120 TB bought for ALICE in 2007 is mainly distributed over 3 xrootd clusters and 1 lustre test system. The main xrootd cluster based on fileservers serves as strategic or permanent storage and is configured with a single point of entry (redirector) for GSI users and from the Grid. It is configured as a Grid Storage element and globally accessible. All files which are copied there are registered in the AliEn [1] File Catalogue. Additionally a tactical storage cluster has been set up on the local disks of the ALICE worker nodes in the GSI batch farm for data analysis. These data are non permanent and are supposed to stay there only as long as they are needed. Also this second cluster is managed by xrootd and configured as an AliEn Grid Storage. A third and smaller xrootd cluster serves currently the local ALICE community for data storage. Additionally first successful tests have been done with the lustre file system. The GSI dCache installation is maintained as example setup for other ALICE sites. The performance of various storage philosophies (local, remote, xrootd, lustre, ...) is currently being investigated.

With a short interruption in April and May Monte Carlo simulation on the Grid has continued during the whole year. The overall job share of GSI and Forschungszentrum Karlsruhe have been 14.7% of all ALICE jobs worldwide. Meanwhile data analysis of individual users via Grid and PROOF [2] plays an increasing role.

The EGEE project

GSI is participating in EGEE II as partner of the distributed Swiss German Regional Operations Centre (ROC). As lead centre in the sub project ”user training” GSI participated with courses in interactive data analysis in GridKa School 2006 and 2007 and gave a successful gLite user training during an international Grid Workshop in Romania [3]. Also the GSI team continued to contribute to the sub projects COD and GGUS [4].

The Xen infrastructure which hosts currently almost all GSI Grid services has been migrated to the latest version. The main metrics (CPU, memory, network, ...) is being monitored continueously. The GSI Grid group operates now 11 Xen servers with about 40 virtual machines with no technical incident on the server side for a complete year.

D-Grid

Within work package 3 of the HEP community Grid distributed analysis tools are being developed at GSI. Within this context the gLitePROOF package [5] has been released. Herewidth a user can dynamically combine the resources of several Grid centres to create a distributed PROOF cluster for immediate use.

54 more compute nodes have been bought from D-Grid fundings to enlarge the local cluster. They will be equipped with D-Grid middleware and, as the existing machines, be included in the GSI batch farm with proof and xrootd daemons being installed in their system. The configuration has been integrated into the GSI fabric management which is based on FAI . They can be used for local data analysis with PROOF, but also via Grid/batch methods. The interplay between batch and interactive jobs is being investigated.

A Globus Toolkit 4 based interface to the GSI batch farm has been deployed and integrated into the infrastructure.

Preparation for FAIR tier0

PANDA-Grid [6] has been extended to 15 sites and upgraded to the newest AliEn version. The complete Panda framework has been installed on the Grid and the full chain of simulation, digitization, reconstruction, and data analysis has been exercised. First Fast Simulation productions started. Due to the increasing number of users a proper user management has been implemented. CBM and Nustar expressed interest to join so that the synergy effects successfully experienced with FAIRRoot can be extended to the Grid.

References

[1] http://alien.cern.ch

[2] http://root.cern.ch/twiki/bin/view/ROOT/PROOF

[3] ICFA workshop on GRID activities Sinaia, Romania, 2006

[4] P. Malzacher et. al, Grid Activities at GSI, http://www.gsi.de/informationen/wti/library/scientificreport2006/

[5] https://subversion.gsi.de/trac/dgrid/wiki

[6] http://panda-wiki.gsi.de/cgi-bin/view/Computing/PandaGrid

* Work supported by D-Grid (BMBF, Förderkennzeichen 01AK802G), and EGEE-II (European Union under contract number INFSO-RI-031688)

Implementation of a non-linear robust fitting algorithm in AliROOT

A. Kalweit*[1,2] and M. Ivanov[1]

[1]GSI, Darmstadt, Germany; [2]Technische Universität Darmstadt, Darmstadt, Germany

The basic task in the theory of curve fitting is such that n measurements of the variable y_i are made and the function $f(x, a_1, \ldots, a_m)$ is fitted to the data in order to determine the parameters a_i. Usually this is done using a least squares method, namely the a_i are chosen such that the quantity

$$\chi^2 = \sum_{i=0}^{N} \Big(\frac{f(x_i) - y_i}{\sigma_i} \Big)^2 \qquad (1)$$

reaches its global minimum. This method assumes that the distribution of errors is normal [1].

One of the main drawbacks of least squares methods is their instability in case of the presence of outliers (points with an abnormal distance to other values in a sample) in the data. This problem is due to the fact that points are weighted with the square of their distance to the curve. Therefore outliers are usually removed manually by the user. But as a consequence, results are not reproduceable. This can be avoided by the usage of so-called robust algorithms. For fits with functions that are linear in parameters an algorithm which selects the best subset of points is suitable and already existing within the *TLinearFitter* package in *ROOT* [2].

For non-linear functions however, a special toolkit for these purposes was written and added as *AliTMinuitToolkit* to the *AliROOT* framework. The algorithm is based on the so-called HUBER-estimator which leads to a quadratic weighting if the distance of the point is below $k = 2.5\sigma$ and increases linearly afterwards:

$$\begin{aligned} h(x) &= x^2 \ , \ |x| \leq k \\ h(x) &= 2k|x| - k^2 \ , \ |x| > k \ . \end{aligned} \qquad (2)$$

This behavior is illustrated in figure (1). This means, that not the sum of equation (1) is minimized, but

$$\sum_{i=0}^{N} h\Big(\frac{f(x_i) - y_i}{\sigma_i} \Big) \ . \qquad (3)$$

The minimization process is done using the standard *TMinuit* [4] package which was extended by an easy-to-use interface.

Details about non-linear robust fitting and the HUBER-estimator can be found in [3]. The drawback of this method is the need to specify an estimated value for σ already before the fitting procedure.

Figure (2) shows a comparison of robust and non-robust fits to a randomly generated exponential distribution with several corrupted data points.

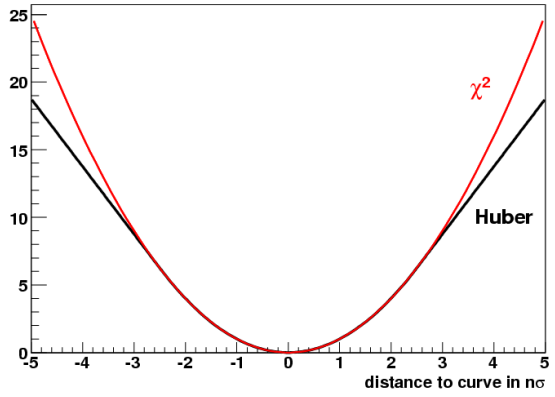

Figure 1: The HUBER-estimator compared to ordinary least squares weighting.

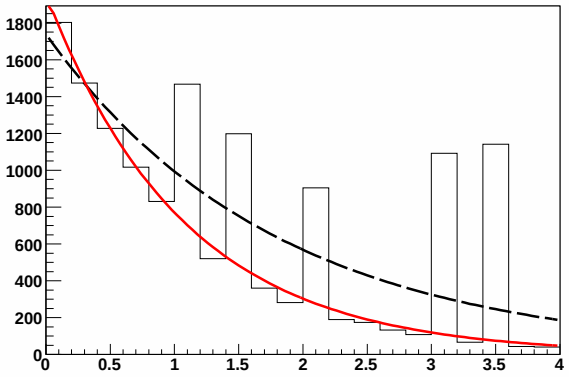

Figure 2: A fitting example with five outliers. The non-robust fit (dashed line) clearly deviates to higher values in contrast to the robust fit (solid line).

References

[1] D. Bates and D. Watts, Nonlinear regression analysis and its applications, Wiley, New York, 1988.

[2] A. Kreshuk, Documentation of the TLinearFitter class in ROOT, http://root.cern.ch/root/html/TLinearFitter.html .

[3] H. Ekblom and K. Madsen, Algorithms for non-linear Huber estimation, BIT Numerical Mathematics 29, 60-76 (1989).

[4] F. James, TMinuit Reference Manual, http://wwwasdoc.web.cern.ch/wwwasdoc/minuit/minmain.htm.

* A.Kalweit@gsi.de

Status of the FairRoot Simulation and Analysis framework

M. Al-Turany[1], D. Bertini[1], and F. Uhlig[1]
[1]GSI, Darmstadt, Germany

Introduction

The FairRoot framework is used for simulation and analysis for CBM and Panda collaborations at the GSI. Among the new developments in 2007 a generic event display, interface to external decayers and an interface for user defined simple phase space decay. Moreover a new mode of the main application has been introduced to enable an easy way for calculating the radiation length in the different materials of the detectors. Further developments concerning the IT infrastructure related to FairRoot are described in separate report in this book.

Event Display

The event display in FairRoot is based on Eve (Event Visualization Environment) package in ROOT [1]. Combined with trajectory visualization in FairRoot [2], the event display can be used directly from macro to display TGeoTracks (MC Tracks) and all sub-classes of CbmPoint and CbmHit, together with detector geometry (see Fig.[1, 2]). The FairEventManager implemented in FairRoot deliver an easy way of making cuts on energy, pt and particle PDG in user events.

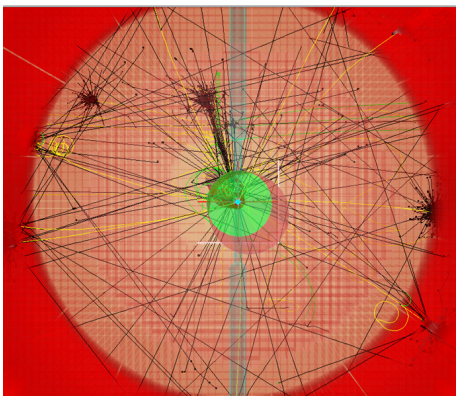

Figure 1: MC tracks and points in PANDA EMC detector.

External decayer

An external decayer (TPythia6Decayer) can be used in place of the concrete Monte Carlo native decay mechanisms only for the specific types of decays defined by the user via a configuration macro. The user can also force certain decay channels to be used instead of decaying according to the branching ratios (default in Pythia). The design allows the use of different decayers at the same time for different particles.

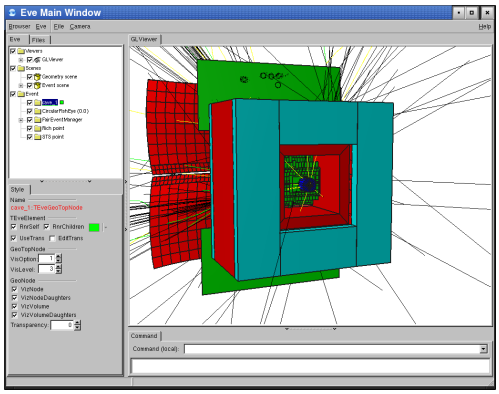

Figure 2: MC tracks and rich points in CBM detector.

Phase space 2 and 3 body decay

The good old GSDK [3] has been interfaced to make it possible for the user to define his own 2 or 3 body decay for certain particles or fragments. The new interface has been also propagated to the ROOT and Geant4vmc authors. In case of Geant3 it is simply a wrapper to the GSDK routine. In Geant4vmc more work has been done on the FairRoot side and the Geant4vmc [4] also to make this transparent for the VMC users and to be able to use this facility without changing the physics list.

Radiation length manager

A new mode for the framework application has been implemented, in this mode the framework register hits in all materials of the detector, for each volume crossed by a particle, two hits are registered, one by entering the volume, the second by existing.

Summary

The development of the FairRoot framework is an on going work, new features are developed in close collaboration with the collaborations using it, ROOT and VMC teams at CERN. Further developments specific to the experiments using FairRoot are described in the experiments sections.

References

[1] http://root.cern.ch/

[2] M.Al-Turany, et al. “CBM Simulation and Analyis Framework”, GSI scintific report 2004, FAIR-EXP-07.

[3] R.Brun, F.Bruyant, M.Maire, A.C.McPherson, P.Zanarini (DD/EE/84-1), May 1986

[4] http://root.cern.ch/root/vmc/

Improving the Software Development Environment in FairRoot

M. Al-Turany[1], D. Bertini[1], and F. Uhlig[1]
[1]GSI, Darmstadt, Germany

Quality Control

One of the challenges of software development for large experiments is to manage the contributions from globally distributed teams. In order to keep the teams synchronized a strong quality control is important.

For a software project this means that it has to be tested on all supported platforms if the project can be build out of the sources, if it runs and in the end if the program delivers the correct results. This tests should be done frequently which results immediately in the necessity to do these checks automatically. If the number of different platform increases it becomes impractical to have installations of all supported platforms at one site. To overcome this problem, the best way is to use a client server architecture, which means to run the quality control at the place where a specific platform is installed and used (client) and only the results are send to a central server responsible for the processing of the data.

The ideal tools for quality control in FairRoot were found with the two programs CMake [2] and Dart2 [3].

Build Environment

Another important point is the question how to create the Makefiles for the different platforms. With increasing number of platforms it becomes unmanageable to write the Makefiles by hand so one needs an automatic way to produce the Makefiles.

CMake is an extensible, open-source system that manages the build process in an operating system and compiler independent manner. Simple configuration files are used to generate standard build files (e.g., Makefiles on Unix and projects/workspaces in Windows MSVC) which are used in the usual way depending on the platform.

Automatic Testing

As part of CMake comes the tool CTest which is used to do all the checks. As first step it automatically updates the local working copy from the SVN repository before it runs the configuration which creates the Makefiles and then builds the project. As last step CTest runs the defined tests and send the all the generated log data to the central Dart2 server. To test the project the same ROOT [4] macros were used as for the normal simulation and reconstruction. The test stage is easily extendable by adding new macros.

With CMake/CTest it is also easy to execute other external programs. For example the class documentation is generated automatically on a daily basis using Doxygen [5].

Rule Checker

For a big software project it is also very important to follow some coding conventions. To test the compliance of the code with this conventions the program RuleChecker [6] is used. The modular code allows to define the rules to be checked in an easy way. This code check is again included in the CMake environment of FairRoot which makes it easy to run the checks and to create in the end a nice web page which can be used by the developers to find violations of the coding conventions.

Dashboard

The second part of the quality control is to collect all the produced information, to process them and as final result to display them in an easy to use fashion. For these tasks the software package Dart2 is used which creates after processing the incoming data as a result linked web pages which display all the gathered information in a so called Dashboard [7]. From here one can access easily the generated Doxygen documentation, the results of the RuleChecker and one has on a daily basis the errors and warnings produced while building the project on the supported platforms together with the results of all the tests.

Summary

In summary a new build framework was implemented for FairRoot which is also used as a tool to produce data for quality control. The build framework CMake is so extensible that also the production of the documentation and the checking of the coding conventions could be included. The results of all the checks are summarized at one location as web page which allows to browse through all the necessary and relevant information.

References

[1] Guide to the Software Engineering Body of Knowledge, 2004 Version SWEBOK A project of the IEEE Computer Society Professional Practices Committee http://www.swebok.org/

[2] http://www.cmake.org

[3] http://na-mic.org/Wiki/index.php/Dart2Summary

[4] http://root.cern.ch

[5] http://www.doxygen.org

[6] Alessandra Potrich, Paolo Tonella, ITC-IRST C++ Code Analysis: an Open Architecture for the Verification of Coding Rules Proceedings of the CHEP 2000, p758-761

[7] http://lxg1417.gsi.de:8081

iFluka : a C++ interface between FairRoot and Fluka

D. Bertini[1] and E. Paulova[1]
[1]GSI, Darmstadt, Germany

Introduction

Fluka [1] is a general purpose tool for calculations of particle transport and interactions with matter. It is mainly used for dosimetry, activation and detector design studies. Fluka provides a high accuracy interaction and propagation of heavy ions (with the DPMJET code[2]) and neutrons down to thermal energies. The package is based on input data cards so that no programming is required by the user. However for more complex application such as the CBM radiation levels studies, user defined routines are necessary. For that purpose, a C++ interface to Fluka has been developped that enable the user to programm those routines using the FairRoot[3] class library.

Design

iFluka is an non intrusive C++ interface to Fluka. It intercepts within the Fluka event loop the call to the user defined fortran routines and forward it to the corresponding C++ functions of the UserAction class. The user can then benefit from all services delivered by the FairRoot framework i.e. generators, field map definition, event by event ntuple-like structure storage containing a complete stack information of transported tracks.

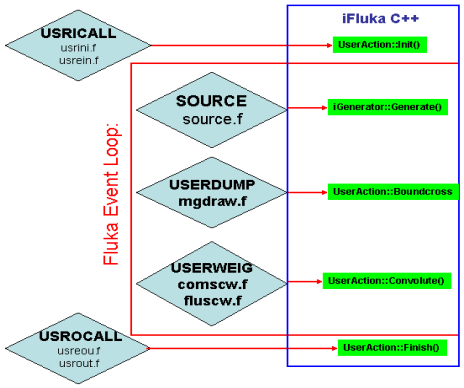

Figure 1: The iFluka design.

Geometry visualization and debugging

The geometry is defined via the standard fluka input data cards using the Combinatorial Geometry (CG) package. Fluka can then be used not only as a fully analogue mode but also in a biased mode which is relevant for radiation studies. Shapes and materials can be displayed via simple Root histograms. Since zooming in and out is activated on the Root canvas, the detection of overlaps and intrusions is easy (figure 2).

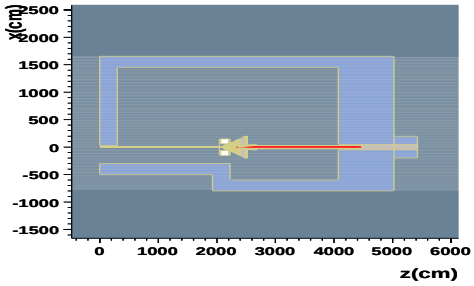

Figure 2: The CBM Cave geometry

Results

iFluka is actually used for the CBM radiation levels studies. One application is to measure accurately the neutrons fluence in the CBM cave in the case of a gold heavy ion transport at 25 GeV/A using the Dual Parton Model [2] and in the case of a modelized central gold on gold collision using UrQmd (figure 3).

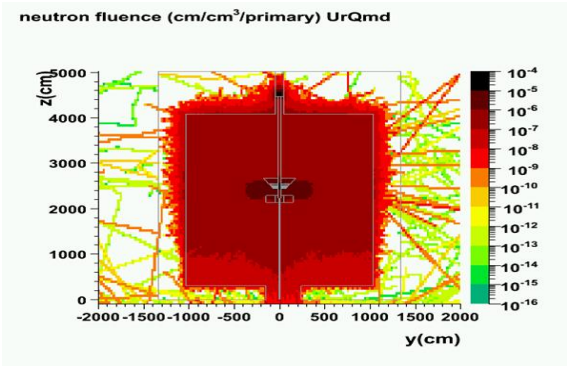

Figure 3: Neutron fluence in CBM cave using UrQmd

References

[1] A. Fasso', A. Ferrari, J. Ranft and P.R. Sala, "FLUKA, a multi-particle transport code", CERN-2005-10(2005),INFN/TC_05/11,SLAC-R-773 FLUKA, and references therein.

[2] S. Roesler, R. Engel and J. Ranft,"The Monte Carlo Event Generator DPMJET-III", SLAC-PUB-8740 (2000)

[3] http://fairroot.gsi.de

The GSI Mass Storage

H.Göringer, M.Feyerabend, S.Sedykh
GSI, Darmstadt, Germany

Overview

The GSI mass storage systems provide safe, reliable, and, if necessary, redundant long term storage of all user and experiment data. Fast and highly parallel access is available for 24 hours a day and 7 days a week.

Backup/Archive functionalities for user data are offered by the commercial Tivoli Storage Manager (**TSM**). Access to the experiment data mass storage (**gStore**) is enabled with GSI made client server systems providing command and programmers interfaces (gstore, RFIO).

gStore is based on automatic tape libraries (ATL) and data mover nodes connected via **S**torage **A**rea **N**etwork (SAN). The data movers provide large read and write disk caches to screen the users as far as possible from tape operations. Tapes and ATLs are also handled by TSM, whereas the interfaces to TSM and to the users as well as the disk cache management are performed by GSI software. Design principles and functionality of gStore are described in more detail in a previous report [1] as well as in a conference talk and paper [2].

Unification adsmcli / tsmcli

In May 2007 the older mass storage interfaces ('adsmcli' and 'tsmcli') have been replaced by a new common interface ('gstore'). The new interface provides access to all experiment data at GSI - independent of their location on any ATL or a related cache file system.

gStore Status and Enhancements

Since the unification all new experiment data have been archived to the upgraded IBM 3494 tape library. Nearly all old data stored on 3590 and LTO2 tape media have been moved to modern tape media in the 3494 ATL. As a result many aged data movers and a TSM server all running on an old Windows system are no longer needed and have been replaced by new Linux data movers and a new AIX TSM server, respectively.

backup/arch data	85 TB	max 140 TB
experiment data	270 TB 3592 22 TB LTO2	max 1.6 PB
13 data movers	disk cache: 36 TB	bandwidth: 600 MB/s to tape 1000 MB/s to cache

Table 1: Status GSI Mass Storage December 2007

gStore is also available for the new Lustre file system which will be made fully available in 2008 as nearline storage for the GSI compute clusters [3].

To follow the increasing user requirements the gStore hardware has been enhanced with 2 new 3592 tapes in the 3494 ATL and with 3 Linux data movers providing additional 20 TB of read and write disk cache.

The current status of the GSI mass storage can be seen in table 1. About 50 TB of valuable raw data are stored twice to prevent from data loss in case of media damage.

Backup Enhancements

A second TSM backup server has been implemented on Linux replacing an aged Windows server. All new backup/archive user data are stored on LTO2 media making the old LTO1 tape library superfluous. If emptied and upgraded with new tapes it could be moved to the 'remote' computing room and used for duplicate long term storage of scientific data.

gStore Usage

As table 2 indicates gStore was heavily used in 2007. The numbers represent the sum of all data movements between tape and cache and between cache and user.

	TB	av. MB/s	no. of files
year 2007	582	18.5	3,116,110
average day	1.6	18.5	8,500
top day	10.6	123	13,270

Table 2:gStore Usage 2007

Future Developments

According to its design gStore is fully scalable in data capacity as well as I/O bandwidth. This has been proved in the past 10 years, where both items have been enhanced by nearly 2 orders of magnitude.

The next challenges on the way to FAIR are the gStore backend to the 200 TB sized Alice Tier2 xrootd file system, currently under test, and the future Hades DAQ, which will be able to send up to 10 data streams, 25 MB/s each, directly to the gStore write cache. All data must be migrated to tape reliably over weeks and undisturbed of the heavy load caused in parallel by the compute farms.

References

[1] H.Göringer et al: The GSI Mass Storage System for Experiment Data, GSI Report 2007-1, p. 210

[2] H.Göringer et al: Experiences with gStore, a scalable Mass Storage System with Tape Backend: Computing in High Energy Physics 2007, Victoria/Canada
http://www-aix.gsi.de/computing/expdv/
gStore-talk-Chep-2007.pdf
related paper, accepted by Journal of Physics:
http://www-aix.gsi.de/computing/expdv/
gStoreChep07JournalofPhysics.pdf

[3] M.Münch et al: GSI IT-Department Activity Report, GSI Report 2008-1

Research programme in atomic physics, plasma physics and materials research

Polarisation of radiative electron capture transitions studied for U^{91+}

S. Hess[1], H. Bräuning[1], U. Spillmann[1], C. Brandau[1], S. Geyer[1], C. Kozhuharov[1], T. Krings[2], A. Kumar[1], R. Märtin[1], R. Reuschl[1], M. Trassinelli[1], S. Trotsenko[1], G. Weber[1], and Th. Stöhlker[1]

[1]GSI, Darmstadt, Germany; [2]Forschungszentrum Jülich, Germany

Only recently the linear polarization of X-rays emitted during the Radiative Electron Capture (REC) in highly charged heavy ions has become accessible experimentally [1,2]. Theoretical investigations show a strong sensitivity of the polarization to details of the process [3]. Here we report on new measurements of the polarization of REC transitions into the K-shell and, for the first time, into the j - sublevels of the L - shell of U^{91+}. A novel Si(Li) Compton polarimeter has been used for the detection of the polarization (the Compton effect is sensitive to the polarization of the incident photon). The experiment has been performed using the internal gas jet of the ESR at GSI. The polarimeter has been positioned at 90° with respect to the ion beam. Molecular hydrogen has been chosen as a target due to several advantages such as a very narrow Compton-profile and therefore small REC linewidths. The Si(Li) polarimeter has an active area of 64 x 64 mm^2 and is surrounded by a guard ring of roughly 7 mm width. The crystal thickness amounts to 6.65 mm and the positive and negative contact electrodes are divided into 32 front- and 32 backside strips, each with a pitch of 2 mm. We made use of the detector's optimal combination of energy and spatial resolution as well as its timing and multihit capability. Figure 1 shows a typical energy spectrum of one of the frontside strips. The investigated REC into the K-shell has an energy of 148 keV in the laboratory frame, while the two different j states of the L-REC are at 51 and 55 keV. For comparison with non-polarized radiation, the non-polarized K-α_2 line is used (see inset of Figure 1), where an isotropic distribution is observed. During the experiment, the frontside strips of the detector were oriented perpendicular to the ion beam. Figure 2 shows a correlation plot where exactly two events in different strips on one side of the detector (multiplicity of 2) have been required. The energies of these two strips are plotted against each other. The energy splitting between the Compton scattered electrons and Compton photons is reflected in the diagonal lines. The spatial distribution of the scattered photons is shown in the insets of Figure 1 for K-α_2 and K-REC. Here, the scattered photons are plotted relative to the location of the Compton interaction. In Figure 3, also the Compton scattering angle ϑ, perpendicular to the detector plane, has been fixed to $90° \pm 5°$ by setting energy conditions corresponding to the kinematical relation between recoil electron energy and scattering angle ϑ. All events in a radius from 6 to 8 mm to the central pixel are plotted. A strong correlation with the Klein - Nishina formula for polarized light can be stated.

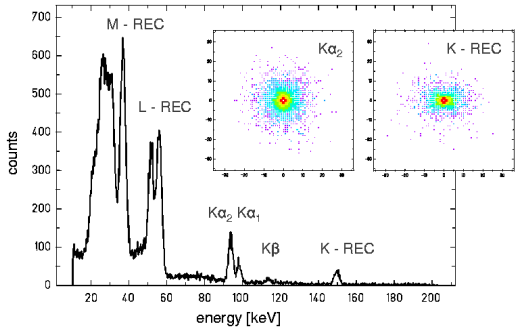

Figure 1: Typical spectrum of a frontside strip and comparison of the Compton images of Kα_2 and K-REC.

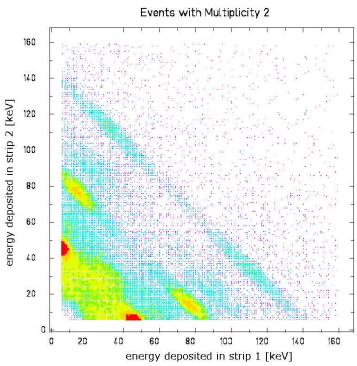

Figure 2: Correlation of events with a multiplicity of 2.

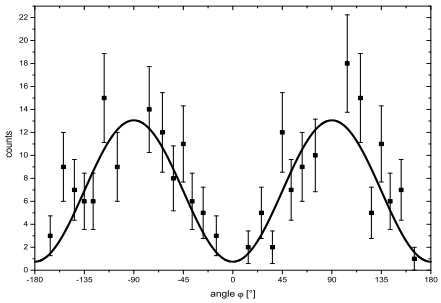

Figure 3: Observed angular distribution for K-REC and the fitted Klein - Nishina formula.

M.T. acknowledges support by the AvH foundation and A.K. by DAAD.

[1] S. Tashenov et al., Phys. Rev. Lett. 97 (2006) 223202
[2] J. Eichler und Th. Stöhlker, Pys. Rep. 439 (2007) 1
[3] A. Surzhykov et al., Phys. Rev. Lett. 94 (2005) 203202

High-accuracy crystal spectroscopy of the n = 2→2 transition in He-like uranium

M. Trassinelli[1,2], A. Kumar[2], R. Märtin[2,3], H.F. Beyer[2], C. Brandau[2], H. Bräuning[2], S. Geyer[2,3], A. Gumberidze[2], P. Indelicato[4], P. Jagodzinski[5], C. Kozhuharov[2], S. Hess[2,3], R. Reuschl[2,3], S. Trotsenko[2,3], G. Weber[2,6], and Th. Stöhlker[2,6]

[1]INSP, CNRS and Université Pierre et Marie Curie-Paris6, F-75015 Paris, France; [2]GSI, D-64291 Darmstadt, Germany; [3]IKF, Johann Wolfgang Goethe-Universität, D-60325 Frankfurt am Main, Germany; [4]Laboratoire Kastler Brossel, CNRS and Université Pierre et Marie Curie-Paris6 and Ecole Normale Supérieure, F-75005 Paris, France; [5]AS, Pl-25509 Kielce, Poland; [6]Physikalisches Institut, Ruprecht-Karls-Universität, D-69120 Heidelberg, Germany

X-ray spectroscopy in heavy few-electron ions allows for sensitive tests of quantum-electrodynamical effects in strong Coulomb fields. Furthermore it opens new perspectives for the study of the simplest many-body systems such as He-like uranium. Recently, accurate measurements were performed for the 1s Lamb shift in H- and He-like uranium ions [1, 2]. In contrast, for the n=2 levels, almost no experimental information is available in high-Z He-like ions. In August 2007, we have obtained the first accurate measurement of the intra-shell $1s2p\,^3P_2 \rightarrow 1s2s\,^3S_1$ transition in He-like uranium using a Bragg spectrometer [3, 4] with a cylindrically bent germanium crystal. The measurement was conducted at the ESR storage ring at GSI. The spectrometer was mounted at the ESR gas-jet target at an observation angle of 90° with respect to the ion beam (see Fig. 1). Excited He-like ions were produced via electron capture in the interaction of the stored H-like beam with a nitrogen gas target.

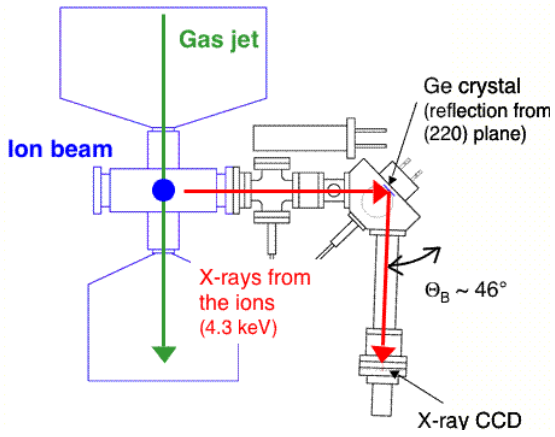

Figure 1: Bragg x-ray spectrometer at the ESR gas-jet target.

In order to reduce systematic uncertainties due to the uncertainty of the observation angle, the accurately measured $1s^22p\,^2P_{3/2} \rightarrow 1s^22s\,^2S_{1/2}$ transition [5] in Li-like uranium (obtained from the interaction of the stored He-like beam with the nitrogen gas-jet target) can be used as a reference (see Fig. 2). In subsequent measurements the ion beam energy (43.55 MeV/u H-like U and 32.60 MeV/u He-like U) was adjusted using the deceleration capabilities of the ESR. Thereby, the Doppler shift was such as to have a transition energy of 4308 eV in the laboratory frame for both cases. Such an energy was chosen to have a Bragg angle of 46.0° where the x-ray lines under investigation appear in the vicinity of the zinc $K\alpha_{1,2}$ lines in second order of diffraction. By repeated recording of the zinc lines, produced by x-ray florescence on a solid target, we were able to monitor the stability of the system.

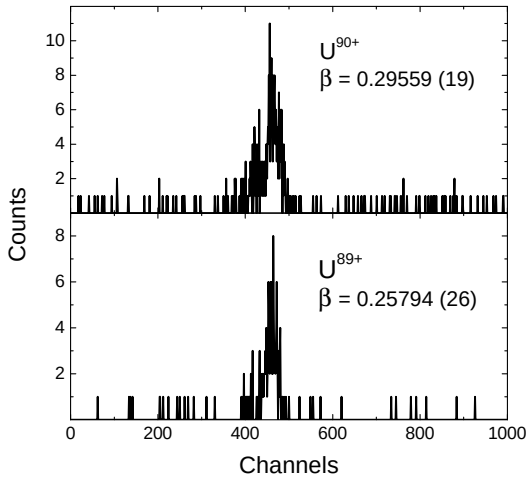

Figure 2: Preliminary x-ray spectra of the $1s2p\,^3P_2 \rightarrow 1s2s\,^3S_1$ He-like (top) and $1s^22p\,^2P_{3/2} \rightarrow 1s^22s\,^2S_{1/2}$ Li-like uranium transitions obtained with the Bragg spectrometer.

In the preliminary data analysis, the expected uncertainty of the transition energy in He-like U is of the order of 0.5 eV, predominantly caused by the counting statistics. This measurement can be significantly improved by increasing the data acquisition time which was limited to about 40 hours in the present experiment.

The support by the A. von Humboldt Foundation (M.T.), the DAAD (A.K., No.: A/05/52927) and by I3 EURONS (EC contract no. 506065) is gratefully acknowledged.

References

[1] A. Gumberidze *et al.*, Phys. Rev. Lett. 92 (2004) 203004.
[2] A. Gumberidze *et al.*, Phys. Rev. Lett. 94 (2005) 223001.
[3] M. Trassinelli *et al.*, GSI Scientific Report 2006, p. 263
[4] M. Trassinelli *et al.*, Can. J. Phys. 85 (2007) 441.
[5] P. Beiersdorfer *et al.*, Phys. Rev. Lett. 71 (1993) 3939.

Development of an X-ray Bragg Spectrometer for Intrashell Transitions in High-Z Few Electron Ions

A. Kumar[1], M. Trassinelli[1,2], R. Märtin [1,3], D. Banas[4], P. Jagodzinski[4], H.F. Beyer[1], and Th. Stöhlker[1,5]

[1]GSI, D-64291 Darmstadt, Germany; [2]INSP, CNRS and Université Pierre et Marie Curie-Paris6, F-75015 Paris, France; [3]IKF, Johann Wolfgang Goethe-Universität, D-60325 Frankfurt am Main, Germany; [4]AS, Pl-25509 Kielce, Poland; [5]Physikalisches Institut, Ruprecht-Karls-Universität, D-69120 Heidelberg, Germany

An x-ray Bragg crystal spectrometer is described, which was used for the first high accuracy measurement of the intra-shell transition $1s2p\,^3P_2 \rightarrow 1s2s\,^3S_1$ of He-like uranium at the ESR storage ring at GSI (see Trassinelli et al. in this report).

The fixed-angle spectrometer operates in the Johann-geometry [1] with a Rowland-circle diameter of 0.8 m. The x-rays are reflected by a cylindrically bent Ge (220) crystal along the dispersion plane and focused on a position sensitive CCD x-ray detector (Fig. 1). The spectrometer's efficiency is about 10^{-6}. Both detection efficiency and wavelength range depend on the size and location of the x-ray source [2]. The wavelength resolution is determined by the crystal's intrinsic rocking curve. Recent measurements have indicated a width of ∼1–2 eV at 8.4 keV.

The back illuminated Charged Coupled Device (DO420; Andor Inc.) consists of an array of 1024×256 square pixels with a dimension of 26×26 μm^2. The chip can be cooled with a Peltier module and an external water cooling system down to -70°C. The quantum efficiency of the detector is larger than 90% for 3 - 4 keV photons [3]. A program written in Fortran 95 and C is used for analyzing the raw data in order to generate energy spectra and the position distribution of the x-rays without and with cluster analysis [4]. Cluster analysis is necessary, because the charge created in the CCD chip substrate by an incoming x-ray can be collected typically by two or more pixels. For a test of the whole spectrometer and further reference an x-ray tube equipped with a molybdenum anode (60 kV and 3.0 kW, water cooled) has been installed. Using a copper and a zinc target, the Kα_1 and Kα_2 fluorescence lines have been measured and used for the characterization of the crystal spectrometer. At the same time, the fine structure of the zinc Kα doublet is being investigated (Fig. 2) and will be compared with the copper lines intensively studied in the past [5].

In addition, a new motion controlled spectrometer [6, 7] is under construction. Different to the instrument presented here, such a spectrometer is capable of observing a wide range of Bragg angles. A LabVIEW program has been written to control the stepping motors to access a wide range of x-ray energies during beam times.

The support by the DAAD (A.K., No.: A/05/52927), the A. von Humboldt Foundation (M.T.) and by I3 EURONS (EC contract no. 506065) is gratefully acknowledged.

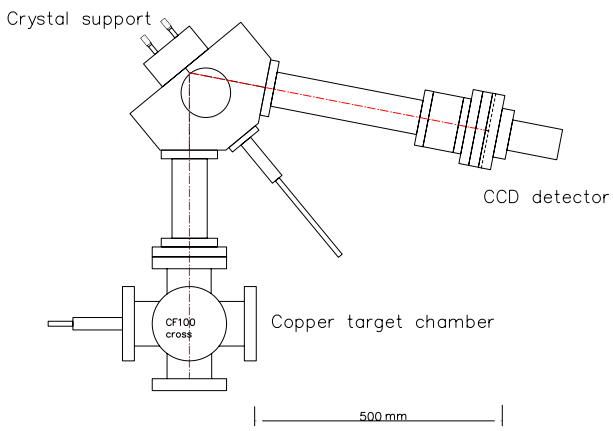

Figure 1: Crystal spectrometer scheme for the measurements of copper Kα doublet at a Bragg angle near 50.5°.

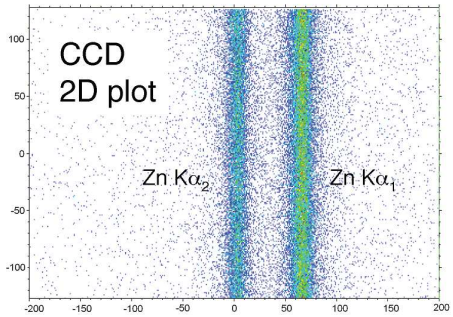

Figure 2: 2D image of the Zn-Kα doublet recorded with a CCD detector coupled to a Johann crystal spectrometer.

References

[1] H.H. Johann, Z. Physik 69 (1931) 185.

[2] H.F. Beyer amd D. Liesen, Nucl. Instr. Meth. A 272 (1988) 895.

[3] F. Zamponi *et al.*, Rev. Sci. Inst. 76 (2005) 116101.

[4] M. Trassinelli *et al.*, GSI Scientific Report 2006, p. 263

[5] M. Deutsch *et al.*, Phys. Rev. A. 51 (1995) 283.

[6] M. Trassinelli *et al.*, Can. J. Phys. 85 (2007) 441.

[7] D. Banas *et al.*, GSI Scientific Report 2005, No. FAIR-APPA-SPARC-06.

Measurement of the spectral shape for two-photon decay in He-like tin

A. Kumar[1], S. Trotsenko[1,2], A.V. Volotka[3], D. Banaś[4], H.F. Beyer[1], H. Bräuning[1], A. Gumberidze[1], S. Hagmann[1,2], S. Hess[1,2], P. Jagodziński[1,5], C. Kozhuharov[1], R. Reuschl[1,2], U. Spillmann[1,2], M. Trassinelli[1,6], G. Weber[1,7], and Th. Stöhlker[1,7]

[1]GSI, Darmstadt, Germany; [2]Institut für Kernphysik, Universität Frankfurt, Germany; [3]Institut für Theoretische Physik, TU Dresden, Germany; [4]Institute of Physics, Świętokrzyska Academy, Kielce, Poland; [5]Department of Physics, University of Technology, Kielce, Poland; [6]Institut des NanoSciences de Paris, Paris, France; [7]Physikalisches Institut, Ruprecht-Karls-Universität Heidelberg, Germany

In heliumlike ions, the (1s2s) $^1S_0$ state can decay to the ground state ($1s^2$) $^1S_0$ via a two-photon (2E1) transition. The energy distribution of the two-photon emission forms a continuous spectrum which has its maximum intensity at half of the transition energy and gradually falls to zero at both endpoints. This continuum energy distribution is determined by the summation over all intermediate bound and continuum states of the transition probabilities. Hence, the spectral shape of the 2E1 decay is sensitive to the entire atomic structure. In heliumlike ions, the nonrelativistic calculations predict an increase in the width of the spectral distribution with atomic nuclear charge Z. Fully relativistic calculations show that at low Z the width behaves similar to the nonrelativistic calculations while at high Z the distribution narrows [1, 2]. Therefore, a measurement of the spectral distribution of the 2E1 decay along the isoelectronic sequence of heliumlike ions uniquely probes our understanding of the interplay between electron-electron correlation and relativistic effects on the structure of the simplest multi-electron atomic system.

The K-shell ionization of Li-like high-Z projectiles occurring in relativistic ion-atom collisions has recently been found to be a highly selective mechanism for populating the 2^1S_0 (2E1: $2^1S_0 \rightarrow 1^1S_0$) and 2^3S_1 (M1: $2^3S_1 \rightarrow 1^1S_0$) states in heliumlike ions and, in particular, this process allows one to measure the undistorted two-photon energy distribution from the decay of the 2^1S_0 state [3, 4, 5]. In this report, we present the first results on the 2E1 decay of the (1s2s) $^1S_0$ state of heliumlike tin (Z=50). The experiment was carried out at the storage ring ESR with 300 MeV/u Li-like tin ions colliding with a nitrogen gas-jet target under single collision conditions. The produced x-rays were detected with a HPGe detector at 35° angle with respect to the beam direction. After the collisions, the singly ionized projectile ions were separated by a dipole magnet and registered by a multi-wire particle detector. For details of the experimental setup we refer to [3, 4].

The x-ray spectra were recorded in coincidence with the up-charged Sn^{48+} ions and only the higher-energy half of the spectrum (Fig. 1a) was used for further analysis. The reason of this is twofold: (1) the symmetric nature of the 2E1 energy distribution was exploited; and, therefore, either of the two halves could provide the Z-dependence information (2) it is clean and independent of the detector efficiency in the present measurement. The intense monoenergetic line in Fig. 1a corresponds to the M1 decay of the 2^3S_1 state. The absence of x-ray lines from the decay of the 2p or higher states ensures that there is no intra/inter-shell excitation occurring simultaneously with the K-shell ionization (cf. [3, 4, 5]). To check the sensitivity on Z, the measured spectral shape for tin is compared with relativistic theoretical calculations [1, 2] for different He-like ions convoluted with the simulation of the detector response function (Fig. 1a). Figure 1b shows the reduced χ^2 of the fit between experimental and theoretical spectral shape using MINUIT. The preliminary results clearly show the best agreement with the relativistic calculations only in the region of correct nuclear charge thus confirming the sensitivity on Z. Detailed data analysis is still in progress.

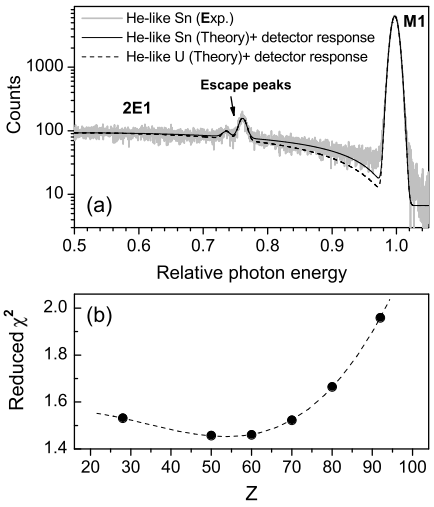

Figure 1: (a) Preliminary comparison of the 2E1 spectral distribution of the measured He-like Sn with that the theoretical He-like Sn and U [1, 2] (convoluted with the simulated detector response function) (b) reduced χ^2 obtained from fig. (a) using the MINUIT minimization code.

The support by the DAAD (A.K., No.: A/05/52927), the A. von Humboldt Foundation (M.T.) and by I3 EURONS (EC contract no. 506065) is gratefully acknowledged.

References

[1] Derevianko and Johnson, Phys. Rev. A 56 (1997) 1288.

[2] A. Volotka, private communication.

[3] J. Rzadkiewicz et al., Phys. Rev. A 74 (2006) 012511.

[4] D. Banas et al., Nucl. Instr. and Meth. B 235 (2005) 326

[5] Th. Stöhlker et al., Phys. Rev. A 58 (1998) 2043.

Ionization of the Projectile in Fast Ion-atom Collisions

M. Nofal[1,2], S. Hagmann[2,3], Th. Stöhlker[2,3], A. Voitkiv[1], B. Najjari[1], A. Surzhykov[1], S. Fritzsche[4], C. Kozhuharov[2], R. Moshammer[1], J. Ullrich[1], A. Gumberidze[2], U. Spillmann[2], R. Reuschl[2], S. Heß[2], S.Trotsenko[2], F. Bosch[2], D. Liesen[2], R. Dörner[3], H. Rothard[5]

[1]Max Planck Institut für Kernphysik, Heidelberg, [2]GSI, Darmstadt, [3]Institut für Kernphysik, Univ. Frankfurt, [4]Institut für Theoretische Physik, Univ. Kassel, [5]CIRIL-Ganil, Caen, France

In relativistic ion-atom collisions electron transfer processes have been at the centre of attention for a variety of reasons, not the least because they are a basic ingredient in relativistic ion accelerator design [1, 2]. Among these transfer processes the electron loss to the projectile continuum appearing as a 0^0-cusp (ELC) merits special consideration. It permits to study in high resolution the dynamics of the ionization for well defined shells of highly charged ionic projectiles with emphasis focusing on continuum states very close to threshold. This provides very sensitive tests of first order theories [3] and has recently received new attention [4].

We have studied forward electron emission in two systems with different projectile Compton profile: U^{88+} + N_2 and Sn^{47+} + N_2 collisions at the supersonic jet-target of the ESR storage ring and report first results for 90AMeV Be-like U^{88+} and 300AMeV Li-like Sn^{47+}. The ELC is identified by measuring coincidences between electrons around $v_e \approx v_{Proj}$ and charge-exchanged projectiles having lost one electron (see Fig 1). Electrons were analyzed with the imaging forward electron spectrometer.

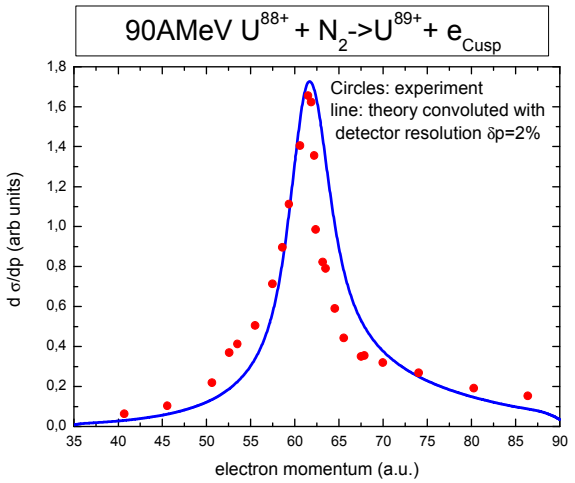

Figure 1: Electron loss to continuum (ELC) cusp measured in 90AMeV U^{88+} + N_2 collisions as function of the electron momentum p_e.

For U^{88+} the theoretical total ionization cross section for 2s ionization of the projectile exceeds the cross section for 1s ionization by more than an order of magnitude; coincident electrons thus may be safely attributed to 2s ionization of the projectile. For U^{88+} the ELC-peak has a longitudinal full width half maximum (FWHM) of 5.6 a.u. of which 1.2 a.u. are instrumental. The peak is nearly symmetric close to the centre but exhibits notable slopes far away from the centre which we tentatively interpret as $2s^2$ – 2pnl excitation with subsequent autoionization.

At higher collision energy and lower binding energies the coincident electrons for incident Sn^{47+} originate from 1s and 2s ionization, unlike in the U case. The ELC peak width for the U^{88+} projectile is longitudinally narrower than for Sn (FWHM=10a.u. for ELC) even though the U(2s) and Sn(1s) Compton profile have nearly comparable width.

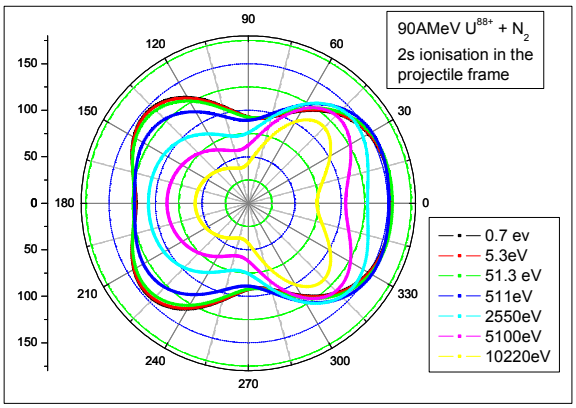

Figure 2: The theoretical DDCS[b/srMeV] for2s ionization of U^{88+} in 90AMeV U^{88+} + N_2 collisions as function of projectile frame emission angle and electron energy.

In order to get more insight into the dynamics of projectile ionization, we performed also theoretical calculations for the double differential ionization cross section DDCS. In Fig.2, we display the DDCS for 2s ionization of U^{88+} at 90AMeV; the emission pattern of the ejected electrons with very low kinetic energy ≤ 50eV is very smooth and exhibits only weakly enhanced humps at about 45^0 and 135^0 in the projectile frame.

In fact, the double-peak structure in Fig 2 reflects the radial behaviour of the 2s wavefunctions since for the ionization of the 1s state (having the same symmetry properties) the DDCS has a single maximum at about 70^0 to 90^0 depending on the continuum electron energy. With increasing electron energy, however, the second peak vanishes and the 2s DDCS exhibits a strong electron emission predominantly in the forward directions.

Support by I3-Eurons (#506065) is gratefully acknowledged.

References

1. H. Gould et al, Phys. Rev. Lett.**52** (1984)180
2. P. Thieberger et al, IEEE Tran. Nuc. Sci. **32** (1985)1767
3. A. Voitkiv, N. Gruen, J. Phys. **B34** (2001) 267
4. A. Surzhykov , S. Fritzsche, J. Phys. **B38** (2005) 2711

Dynamics of Ionization and Charge Transfer Reactions in fast Heavy-Ion Atom Collisions*

K.U. Kühnel[1,#], D. Fischer[1,3], R. Moshammer[1], S. Hagmann[2,5], T. Ferger[1], M. Gudmundsson[3], M. Schäfer[1], N. Nofal[2], C. Dimopoulou[2], M.Steck[2], H. Bräuning[2], C. Brandau[2], C. Kozhuharov[2], Th. Stöhlker[2,7], M. Schöffler[5], T. Zouros[8], G. Lanzano[6], E. de Filippo[6], H. Rothard[4] and J.Ullrich[1]

[1]Max-Planck-Institut für Kernphysik, Heidelberg, Germany; [2]GSI, Darmstadt, Germany, [3]Stockholm University, Sweden, [4]GANIL. Caen, France, [5]IKF, Universität Frankfurt, Germany, [6]INFN, Catania, Italy, [7]KIP, Universität Heidelberg, Germany, [8]University of Crete, Heraklion, Greece

Recently, the first in-ring Reaction Microscope has been installed at the ESR internal gasjet-target to study the dynamics of break-up reactions in collisions of highly charged ions (HCI) with atoms and molecules. It enables measurements of kinematically complete data sets by momentum resolved and coincident detection of all target fragments produced in a single collision [1]. Combined with the ESR, which provides excellent experimental condition w.r.t beam intensity and emittance, it represents the ideal tool to obtain highly differential information on fundamental processes in HCI-atom collisions.

During first experiments we studied single and multiple ionization of He, Ne, and Ar targets as well as electron capture in collisions of 13 AMEV U^{92+} with Ne, the latter for the first time differential with respect to the projectile deflection angle.

In figure 1 (a) the time-of-flight (TOF) spectrum of Ne ions measured in coincidence with single electron capture is shown. The lines correspond to Ne^{7+} to Ne^{10+}, indicating that in addition up to 9 electrons are ionized in the same collision. This can be explained qualitatively because dominantly Ne K-shell electrons are captured at the present high projectile velocity requiring small impact parameters and, thus, most of the target electrons are promoted to the continuum.

The sub-structure of the Ne^{7+} peak reflects the distribution of final state binding energies of the captured electron in the U^{91+} ion. Due to energy and momentum conservation different binding energies result in different momenta for the recoil ion (e.g. [1]) and, thus, in different times-of-flight. Hence, such kind of measurements can be used as a powerful method to obtain precise spectroscopic information of electronic states in HCI [2].

In figure 1 (b) the number of detected recoil ions is plotted as a function of TOF and the horizontal position on the reoil-detector. The position is related to the transverse momentum transfer to the target or the projectile scattering angle. The distribution at X-positions around 32 mm corresponds to random coincidences between charge-changed projectiles and mainly Ne^{1+} ions created in target single-ionization (the cross section for ionization is several orders of magnitude larger than for electron capture). The recoil-ions coincident with electron capture (the vertical lines in the figure) show a much wider position distribution than those created by pure ionization (background). This is again a result of the small impact parameters (leading to large projectile scattering angles) involved in electron transfer collisions.

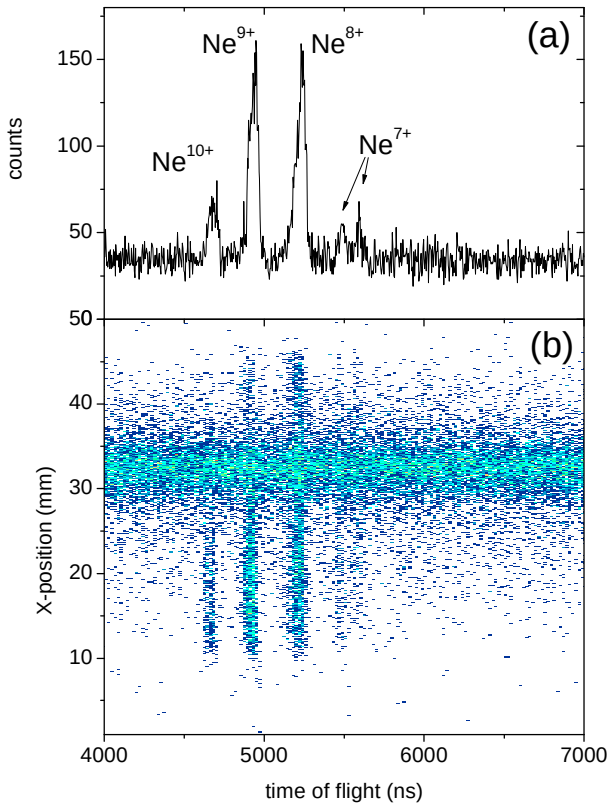

Figure 1: (a) TOF spectrum of Ne ions created in 13 AMeV U^{92+} onto Ne charge transfer reactions. (b) Number of Ne ions as a function of their times-of-flight and position on the detector.

Future experiments are planned to study e.g. radiative and non-radiative charge transfer reactions where also photons are detected in coincidence. Furthermore, simultaneous ionization of target and projectile shall be investigated, to obtain insight into the dynamics of electron emission from HCI's.

References

[1] J. Ullrich et al., Rep. Prog. Phys. **66** (2003), 1463
[2] D. Fischer et al., J. Phys. B **35** (2002, 1369

* Work supported by EU, EURONS contract No. 506065.
#k-u.kuehnel@mpi-hd.mpg.de

Charge Radii from Isotope Shifts in the Dielectronic Recombination of $^{A}Nd^{57+}$

C. Brandau[1], Y.S. Kozhedub[2], Z. Harman[3], C. Kozhuharov[1], V.M. Shabaev[2], A. Müller[4], S. Schippers[4], O.V. Andreev[2], K. Beckert[1], D. Bernhardt[4], F. Bosch[1], S. Böhm[4], F.J. Currell[5], A. Gumberidze[1], J. Jacobi[4], U.D. Jentschura[3], C.H. Keitel[3], H.-J. Kluge[1], P.H. Mokler[3,4], F. Nolden[1], G. Plunien[6], R. Reuschl[1], E.W. Schmidt[4], U. Spillmann[1], Z. Stachura[7], M. Steck[1], Th. Stöhlker[1,8], I.I. Tupitsyn[2], and A. Wolf[3]

[1]GSI Darmstadt; [2]St. Petersburg State University, Russia; [3]MPI-K Heidelberg; [4]Universität Gießen; [5]Queen's University, Belfast, U.K.; [6]TU Dresden; [7]IFJ Kraków, Poland; [8]Universität Heidelberg

The measurement of isotope shifts (IS) in the resonance spectrum of dielectronic recombination (DR) is a novel, precise and very sensitive technique to experimentally determine parameters of nuclear charge distributions of heavy ions. Preliminary experimental results for the two stable isotopes A=142 and A=150 of Li-like $^{A}Nd^{57+}$ were presented previously [1,2]. The experimental data analysis is now finalized and a joint experimental and theoretical paper on the technique, the extracted results for the IS and the derived changes in the mean-square charge radii $^{142,150}\delta\langle r^2\rangle$ is accepted for publication [3]. This joint effort of our experimental DR collaboration and the theory groups from the MPI-K in Heidelberg, from the St. Petersburg State University and from the TU Dresden also triggered further theoretical studies on nuclear size and nuclear deformation contributions in heavy few-electron ions [4,5].

From the isotopic energy displacement of characteristic features in the DR resonance spectra like maxima, minima and inflection points we obtained in total 154 individual IS values for the $2s-2p_{1/2}$ $\Delta n=0$ intra L-shell transition and 45 for the $2s-2p_{3/2}$ excitation. The average ISs are $\delta E^{142,150}(2s-2p_{1/2})$ = 40.2(3)(6) meV and a slightly higher value of $\delta E^{142,150}(2s-2p_{3/2})$ = 42.3(12)(20) meV, respectively. Although statistically not significant it is interesting to see that the experiment reveals the expected small difference between the ISs of the $2s-2p_{1/2}$ and $2s-2p_{3/2}$ intervals. The IS could be determined with a statistical error as low as 0.3 meV only (first parenthesis) and a systematical error of 0.6 meV (second parenthesis). It can be expected that a similar experimental precision can be retained for heavier ions. Since for the studied transitions nuclear size effects scale with large powers of the nuclear charge Z (Z^5 to Z^6), the sensitivity to the nucleus is increased in equal measures for heavier species. A decisive benefit of using few-electron ions for nuclear size and hyperfine studies is that the electronic part (three electrons) can be calculated with high accuracy. As a consequence the interpretation of the data with respect to the nuclear parameters is clear and without ambiguity. For the present case of $2s-2p_j(j=1/2,3/2)$ transitions the derivation of the change in the mean-square charge radii $^{142,150}\delta\langle r^2\rangle$ from the IS data was performed within a full QED treatment (see Table 1) yielding $^{142,150}\delta\langle r^2\rangle$ = -1.36(1)(3) fm^2. This strong increase in the charge radius is predominantly due to the strong deformation of the ^{150}Nd nucleus. The QED corrections to the IS include the sum of one-loop self-energy and vacuum-polarization contributions. The calculation of the nuclear size effect on the transition energies (field shift) comprises one-electron Dirac, electron-correlation, and Breit-interaction contributions. For the mass shift part non relativistic, relativistic, and QED recoil effects were incorporated. An additional small contribution of about 0.3 meV arises from nuclear polarization of the deformed ^{150}Nd nucleus.

Table 1: Individual contributions to the IS of the $2s-2p_{1/2}$ excitation in $^{A}Nd^{57+}$, in meV. For details see main text.

$\delta\langle r^2\rangle$ (fm^2)	Field shift	Mass shift (meV)	QED	NP	Total
1.200	37.2	-1.6	-0.2	-0.3	35.1
1.220	37.9	-1.6	-0.2	-0.3	35.8
1.240	38.5	-1.6	-0.2	-0.3	36.4
1.260	39.1	-1.6	-0.2	-0.3	37.0
1.280	39.7	-1.6	-0.2	-0.3	37.6
1.300	40.3	-1.6	-0.2	-0.3	38.2
1.320	41.0	-1.6	-0.2	-0.3	38.9
1.340	41.6	-1.6	-0.2	-0.3	39.5
1.360	42.2	-1.6	-0.2	-0.3	40.1
1.380	42.8	-1.6	-0.2	-0.3	40.7

The present work underpins the unique features and the new opportunities of the new method. Further experiments with other stable isotopes of the Nd chain and machine experiments towards the realization of DR-IS experiments with unstable isotopes ($^{236}U^{89+}$ and $^{237}U^{89+}$) are approved by the GSI G-PAC. This series of experiments will enable us to proceed further towards the realization of a dedicated experimental set-up at the future storage ring NESR as proposed by us as part of the SPARC program.

[1] C. Brandau, et al., J. Phys. Conf. Ser. **58**, 81 (2007).
[2] C. Brandau, et al., GSI Report 2005, GSI 2006-1, p. 296; GSI Report 2006, GSI 2007-1, p. 249.
[3] C. Brandau, et al., Phys. Rev. Lett., in print.
[4] Y.S. Kozhedub, et al., Phys. Rev. A, in print.
[5] Z. Harman, et al., in preparation.

Laser spectroscopy for the charge radius determination of ^{7,9,10,11}Be

D. Tiedemann[2] , C. Geppert[1], W. Nörtershäuser[1,2] , M. Nothhelfer[2], R. Sanchez[1], F. Schmidt-Kaler[3], M. Zakova[2], C. Zimmermann[4] and the BeTINa collaboration
[1]GSI Darmstadt, [2]University of Mainz, [3] University of Ulm, [4] University of Tübingen

In 1985 Tanihata and coworkers performed scattering experiments with light elements like helium, lithium and beryllium [1,2] and found, completely unexpected, a huge matter radius for some of the isotopes close to the neutron drip line. These so-called halo-nuclei consist of a compact core nucleus and one or more neutrons which are only very weakly bound (<1 MeV separation energy) and have wave functions that extend extremely far away from the core. For the investigation of the interaction of these weakly bound neutrons on the compact core, precision laser spectroscopy is applied. The nuclear charge radius is extracted from the measurements of the isotope shift, which is the sum of the mass and the field shift. For a determination of the charge radius, an accuracy in the order of a few 100 kHz is necessary. This accuracy must be reached in the experimental measurement of the isotopic shift and in the theoretical calculation of the mass shift contribution. The feasibility of this approach has recently been demonstrated for light halo-nuclei ^{6}He [3], ^{8}He [4] and ^{11}Li [5]. While these have two or even four weakly bound halo neutrons, the next heavier halo nucleus ^{11}Be is the archetype of a single-neutron halo nucleus. Since the crucial theoretical prediction of the mass-dependant isotopic shift contribution can only be calculated for atomic systems with up to three electrons, the isotope shift for beryllium has to be measured on Be^{+} ions.

We want to use radioactive beryllium ions that are produced at ISOLDE, CERN, precooled and accumulated in the gas filled RFQ structure at the ISOLTRAP setup. The ions will be transferred into a linear segmented Paul trap, where they will be laser-cooled to less than 7mK to perform precision laser spectroscopy to reach the required accuracy on single ions.

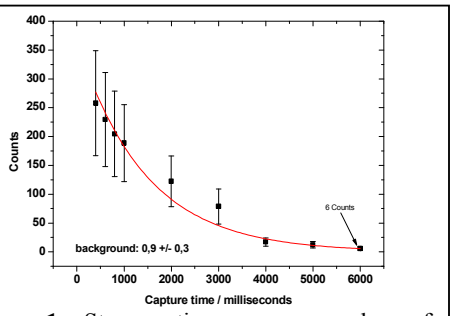

Figure 1: Storage time versus number of extracted ions.

Two main aspects of the experimental apparatus have been developed during 2007. Two designs of RFQ traps have been realized and tested: a circuit board design and a conventional setup with massive rods. The traps were loaded by non-resonant ionization of atoms along the trap axis with a frequency tripled Nd:YAG laser. Due to the lack of an optical detection system, which has been finished just recently, trapping has been verified by extraction from the trap and detection with a channeltron after varying trapping time. No significant ion signal above detector background has been observed with a circuit board design yet, while in the classical Paul trap design storage of several hundred ions could be demonstrated. Figure 1 shows the number of ion counts as a function of the trapping time before the ions were released. A storage time of about 1.5 s can be extracted which is ascribed to collisions of the trapped ions with residual gas (10^{-6} mbar) and the constant flux of neutral atoms from the atom source through the trap axis in this test setup.

For laser cooling and spectroscopy two tuneable

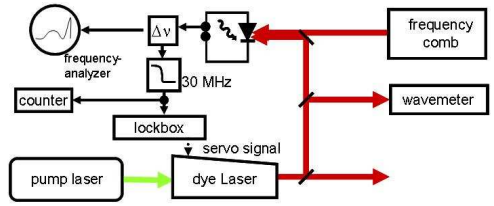

Figure 2: Locking and scanning scheme of the tuneable dye laser.

dye lasers have been set-up and a frequency-lock on a fiber based frequency comb was established (Figure 2). The observed linewidth of 900 kHz is sufficient for the requirements of the beryllium spectroscopy with a natural linewidth of 20 MHz in the 2s-2p transition. Moreover this locking scheme allows for precision tuning of the locked laser, by controlled scanning of the repetition rate of the mode-locked frequency comb.

Further tests of the trap system with optical detection and of the laser system are planned for the first half of 2008. A test of both components at the ISOLDE on-line facility is foreseen later that year.

References

[1] I. Tanihata *et. al.,* PRL **55**, 2676 (1985)
[2] I. Tanihata *et. al,*. Phys. Lett. B **206**, 592 (1988)
[3] L.-B. Wang *et. al.,* PRL **93**, 142501 (2004)
[4] P. Müller *et. al*, PRL **99**, 252501 (2007)
[5] R. Sanchez *et. al.,* PRL **96**, 033002 (2006)

* this work is supported by BMBF Contract Nos. 06MZ215TP6, 06TU263I, 06UL264I and by the Helmholtz Association under Contract VH-NG-148

Absolute Frequency Measurements on the 2S → 3S Transition of ^{7}Li and ^{6}Li*

R. M. Sánchez Alarcón[1], Z. Andjelkovic[2], C. Geppert[1], J. Krämer[2], J. Kluge[1], M. Nothhelfer[2], D. Tiedemann[2], D. F. A Winters[1], M. Zakova[2], and W. Nörtershäuser[1,2]

[1]GSI mbH, Atomphysik, Planckstr. 1, D-64291 Darmstadt, Germany; [2]Institut für Kernchemie, Johannes Gutenberg-Universität Mainz, Fritz-Strassmann-Weg 2, D-55128 Mainz, Germany

Laser spectroscopy plays an important role in the determination of ground state properties of atomic nuclei. Recently this has been again demonstrated by the determination of the nuclear charge radii of the light halo nuclei ^{11}Li [1] and ^{6,8}He [2]. These have been possible thanks to the combination of both, the high resolution of 10^{-5} achieved in the laser spectroscopic isotope shift (IS) measurements and a similar accuracy in atomic theory calculations on the two- and three-electron systems [3]. In the lithium chain, we could provide very accurate numbers for the changes in charge radii between the isotopes. However, absolute charge radius determinations are limited in accuracy by the uncertainty of the reference ^{6,7}Li charge radii, whereas for the helium isotopes the situation is slightly better because the charge radius of ^{4}He is known with higher accuracy. In principle, laser spectroscopy could also be used for a determination of the absolute charge radius as it has been shown in hydrogen [4], provided that the atomic structure calculations of the absolute transition energies can be improved by about an order of magnitude. The calculation of absolute transition energies is still a challenge because of the higher-order mass-independent QED terms, which cancel in isotope shift calculations - since they are mass independent - but contribute fully to the transition energy. Two groups are working on this problem now and try to clearly improve the situation. On the experimental side, transition frequency measurements on these systems are needed with an accuracy of better than about 1 MHz, which is a relative accuracy of a few times 10^{-10}. The recent development of the femto-second frequency comb-device, which links optical and rf frequencies, allows us to determine the transition frequency with the required accuracy.

Therefore, we have measured the $2S \rightarrow 3S$ two-photon transition frequencies of the stable lithium isotopes ^{6,7}Li applying the setup that has been used previously to measure the lithium IS [5] with a laser system that has been adapted for this task. The main modification was that the Titanium-Sapphire (Ti:Sa) laser, which drives the two-photon transition, was phase-locked to a femto-second frequency comb [6] instead of being referenced to an iodine line as previously. Changing the repetition rate of the comb allowed us to sweep the Ti:Sa laser frequency across the resonance line, as it is shown in Fig. 1a. The absolute transition frequency has to be taken as the center of gravity (cg) of the hyperfine components.

Systematics effects, like AC Stark shifts (see Fig. 1b) were studied experimentally. Particularly it was noticed that recorded spectra at high power showed an asymmetry in the line profile that can clearly be observed in Fig. 2a. To understand the profile, simulations were performed that included the lithium atoms crossing through a Gaussian laser field distribution with intensity fluctuations such as they were typical during the experiment. The calculated points shown in Fig. 2 were then fitted with a Lorentzian line profile and the residuals, plotted underneath the peak structure, show a very similar behavior for the fitting of the real as well as of the simulated peaks.

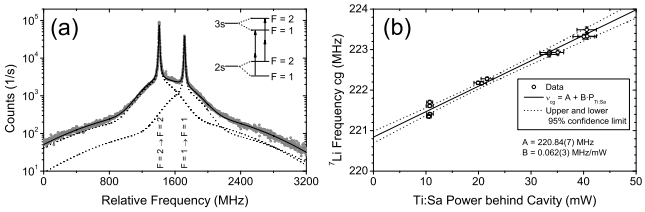

Figure 1: (a) Line shape of the $2S \rightarrow 3S$ atomic transition in ^{7}Li. (b) An AC Stark shift measurement with extrapolation to zero laser intensity.

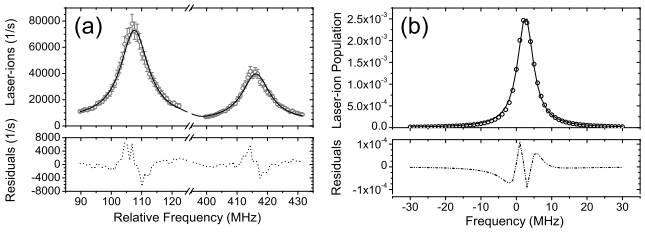

Figure 2: (a) Line profile in the real transition. (b) A simulation reproduces the observed asymmetry quite well.

Final analysis is still ongoing but we expect to improve the accuracy in the transition frequency by about an order of magnitude. Once theory will make the required progress, the absolute field shift contribution in the transition and therefore the total nuclear charge radius could be extracted by pure optical means.

References

[1] R. Sánchez *et al.*, PRL **96**, 033002 (2006).

[2] P. Müller *et al.*, PRL **99**, 252501 (2007).

[3] G. W. F. Drake *et al.* Lect. Notes Phys. **745**, 131 (2008).

[4] T. Udem *et al.* PRL **79**, 2646 (1997).

[5] G. Ewald *et al.*, PRL **93**, 113002 (2004).

[6] http://www.menlosystems.com/fc1500.html

* Work supported by HGF under contract VH-NG-148 and by BMBF under contracts 06MZ215/TP6 and 06TU263I.

Doppler-free spectroscopy of lithium ions at 34% of the speed of light: Toward a test of time dilation

C. Novotny[1], B. Bernhardt[2], D. Bing[3], C. Geppert[4], G. Gwinner[5], T. W. Hänsch[2], R. Holzwarth[2], G. Huber[1], S. Karpuk[1], H.-J. Kluge[4], T. Kühl[4], W. Nörtershäuser[1,4], S. Reinhardt[3], G. Saathoff[2], D. Schwalm[3], M. Steck[3], T. Udem[2], and A. Wolf[3].

[1]Johannes Gutenberg-Universität Mainz, D-55128 Mainz, Germany; [2]Max-Planck-Institut für Quantenoptik, D-85748 Garching, Germany; [3]Max-Planck-Institut für Kernphysik, D-69029 Heidelberg, Germany; [4]Gesellschaft für Schwerionenforschung, D-64291 Darmstadt, Germany; [5]University of Manitoba, Winnipeg, Manitoba, R3T 2N2, Canada

Probing Time Dilation

Time dilation is one of the most fascinating aspects of Special Relativity (SR) as it abolishes the notion of absolute time. It was first observed experimentally by Ives and Stilwell in 1938 [1] on light emitted from moving atoms, using the Doppler effect. Probing time dilation with highest precision is of great interest because any deviation would violate the Einstein relativity principle. New experimental techniques and enhanced measurement methods have increased continuously the sensitivity to hypothetical deviations from the predictions of Special Relativity. Those violations e.g. can be described by a kinematical test theory (MS) [2, 3]. Here the Doppler-shifted frequencies $\nu_{a,p}$ are compared with the rest frequency ν_0 of a moving clock. In SR, these frequencies are given by the relativistic Doppler-formula $\nu_{a,p} = \gamma_{SR}(1\pm\beta)\nu_0$, where the Lorentz factor γ_{SR} appears as a direct consequence of time dilation. The MS test theory parameterizes possible deviations of time dilation by introducing a test parameter α with $\gamma = \gamma_{SR}\,(1 + \alpha\beta^2 + \ldots)$.

Storage Rings and Time Dilation

The best value for the test parameter α has been obtained at the Test Storage Ring at the Max-Planck-Institute für Kernphysik in Heidelberg. An experimental series combines the advantages of precision spectroscopy with superb ion beam quality in storage rings on metastable $^7Li^+$ ions. Combining measurements at two different ion velocities, an upper bound of $|\alpha| < 8.4 \times 10^{-8}$ has been reached [4, 5]. Further improvements of this limit, however, will require higher ion velocities which are possible at the ESR.

Previous experiments had shown the feasibility for testing time dilation at the ESR with an ion velocity of v = 34%c (59MeV/u) [6]. During the latest beam time (2007), the first signal with sub-Doppler linewidth was observed by performing Λ-type spectroscopy on a metastable $^7Li^+$ ion beam.

The laser system used consisted of a frequency-doubled cw Ti:Sa laser (λ_p = 386nm) for the excitation of the ions parallel to the flight direction and a diode laser (λ_a = 780nm) for the excitation in anti-parallel flight direction. Both laser frequencies were measured by secondary frequency standards (e.g. Rb) and wave-meters, respectively. The laser light was guided to the ESR incoupling windows via single-mode polarization-maintaining fibres. The fluorescence signal of the metastable $^7Li^+$ ions was observed by photomultipliers placed along the laser-ion beam interaction zone of the ESR.

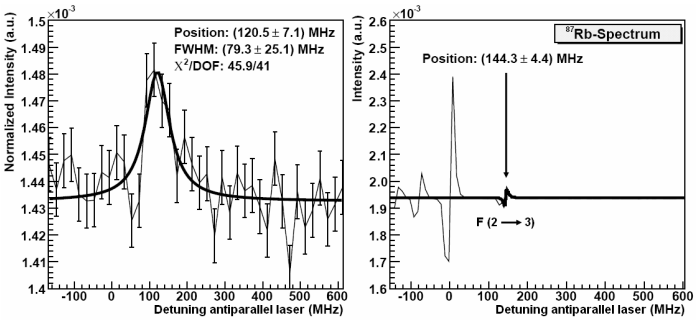

Figure 1: left: Doppler-free signal of the Λ-type spectroscopy. right: Signal from the rubidium reference.

The Doppler-free signal of the Λ-type spectroscopy is shown in Figure 1 and has a FWHM of about 60 MHz in the rest frame of the ions. The Doppler-broadened signal is – for comparison – 9 times wider. This leads, concerning the frequency uncertainties of the lasers, to an upper bound of $|\alpha| < 11 \times 10^{-7}$. The dominant uncertainty in this measurement is the coarse control in frequency compared to the measurements at the TSR ($\Delta\nu_{TSR}/\Delta\nu_{ESR}$ = 1/500) which was due to technical reasons. Nevertheless the upper bound for the test parameter α is only approximately one order of magnitude larger due to the higher sensitivity to α caused by the higher ion velocities. Therefore, reaching and improving, respectively, the recent upper bound is feasible by getting a finer control of the laser frequency.

References

[1] H. E. Ives and G. R. Stilwell, J. Opt. Soc. Am. 28 215-226 (1938)
[2] H. P. Robertson, Rev. Mod. Phys. 21, 378 (1949)
[3] R. Mansouri and R. U. Sexl, Gen. Relativ. Gravit. 8, 497, 515 and 809 (1977)
[4] G. Saathoff *et al.*, Phys. Rev. Lett. 91, 190403-(1-4) (2003)
[5] S. Reinhardt *et al.*, Nature Phys. 3, 861-864 (2007)
[6] C. Novotny *et al.*, Hyperfine Interact. 171, 57-67 (2006)

Investigation of low-energy electrons emitted from solid-state targets in heavy-ion-atom collisions

Natalia Lineva[1], C. Kozhuharov[1], S. Hagmann[1,2], M. Krämer[1], and G. Kraft[1]
[1]GSI Darmstadt, Germany; [2]Institut für Kernphysik, Universität Frankfurt am Main, Germany

Due to inherent difficulties in the detection of low-energy electrons as well as in disentangling the results of multiple collisions and of the superimposed transport mechanisms, most published experiments concentrate so far on electron emission from single collisions in gaseous targets, and the results are scaled with the target density up to the one for fluids and/or solids. For the same reason, the (not so numerous) existing experiments with solid-state targets are usually tailored to study some specific features, as for instance the electron temperature inside the heavy-ion track. For a recent review—it also includes a comprehensive list of the open questions—please confer Rothard and Gervais [1]. Systematic investigations of the energy and angular dependence of low-energy electron emission pertinent to the needs of the radiobiology are rather scarce.

We have performed a series of measurements of low-energy electrons emitted from solid-state targets after bombardment with both electrons as well as with swift heavy ions at UNILAC energies. Based on this, we have developed methods to identify, study, and analyze the problems, which arise from the actual operating conditions that mask the a priori complex and interdependent processes of electron emission and transport; conditions such as target properties and consistence, surfaces, etc. Therefore, we started our investigations with measurements of 1 keV electrons from an electron gun scattered on 4.7 g/cm and 11 g/cm carbon targets by utilizing an electrostatic toroidal spectrometer [2] . We performed numerical simulations with the TRAX Monte Carlo code [3] for a variety of target thicknesses. The results—electron yields in the energy region up to 1 keV—are displayed in Fig. 1 as a function of the polar angle. For all target thicknesses—except for 1 $\mu g/cm^2$—the simulated distributions (small symbols) exhibit the typical behavior of the electron diffusion process. The electrons emitted backwards show the same angular distribution and the same yields; obviously, the back diffusion thickness for 1 keV electrons in carbon is smaller than 2 $\mu g/cm^2$. The diffusion in the forward hemisphere is characterized by the same shape of the angular distribution; here, however, the transmitted intensity decreases with an increasing target thickness. Compared to the simulation, the measured data for 4.7 $\mu g/cm^2$ (big squares) are consistent with the simulation for 3.6 $\mu g/cm^2$, whereas the measured transmission for 11 $\mu g/cm^2$ (big circles) correspond to a simulated thickness slightly larger than 5 $\mu g/cm^2$. Since the target thickness averaged over a larger area is very close to the nominal one, the finding can be explained by large fluctuations of the target thickness (which start with some visible pinholes).

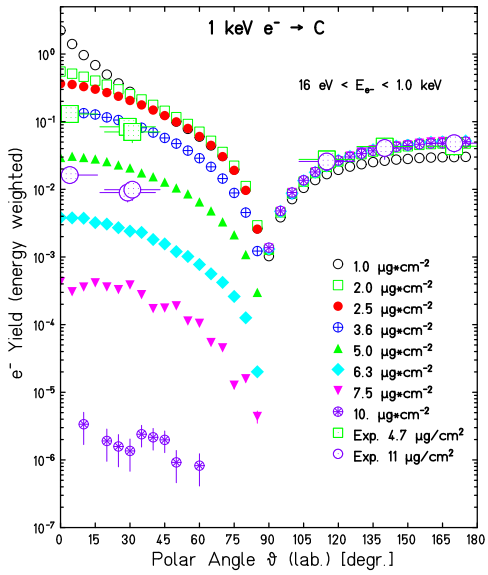

Figure 1: Electron emission yields for 1 keV electron beam impinging on carbon targets as a function of the emission angle. TRAX Monte Carlo simulations (small symbols) are compared to the measured values (big symbols).

We compared the simulated to the measured energy distributions of electrons emitted in selected angular ranges and found a very good agreement of the spectral shapes when we assumed that the effective target thicknesses are 3.6 instead of 4.7 $\mu g/cm^2$ and 5.4 instead of 11 $\mu g/cm^2$. Based on these findings we analyzed the spectra of electrons emitted in collisions of 8.77 MeV protons and 8.77 MeV/u H_3^+ as well as of 3.6 and 11.4 MeV/u carbon ions impinging on a carbon target. We compared the measurement with simple theories and with TRAX simulations. For lower electron energies, the discrepancy between the calculated and measured distributions increases. The measured yields are smaller than the calculated ones, demonstrating that even for targets as thin as 3.6 $\mu g/cm^2$ a large fraction of the low-energy electrons is absorbed in the target. Within the experimental uncertainties the TRAX simulations (*nota bene* based on data from gaseous targets) agree very well with the measurements.

References

[1] H. Rothard, B. Gervais, Kong. Danske Medd. **52** 2006

[2] N. Lineva et al. GSI Annual Report 2006

[3] M. Krämer NIM B **105**, 14 (1995)

Contributions of inner-shell ionization to the Coulomb fragmentation of N_2 in collisions with 3.6 MeV/u Xe^{40+}-ions

U. Werner[1], B. Siegmann[2], and R. Mann[3]

[1]Universität Bielefeld, Fakultät für Physik, Universitätsstr. 25, D-33615 Bielefeld; [2]TU Dortmund, Fakultät für Physik, Otto-Hahn Str. 8, D-44221 Dortmund; [3]Gesellschaft für Schwerionenforschung (GSI), D-64291 Darmstadt

In our previous work we studied the ion-impact induced Coulomb fragmentation of small molecules by a coincidence experiment providing a kinematically complete description of the fragmentation process (see e.g. [1]). Unfortunately, the technique gives no direct information about the ionization process and further details are highly desirable. Especially the importance of inner shell ionization followed by Auger cascades has long been known [2]. In a test experiment we modified our setup to allow at least a crude separation of these processes.

A collimated beam of 3.6 MeV/u Xe^{40+}-ions provided by the UNILAC interacts with a N_2 gas target. The slow ions and electrons generated in the collision process are separated by a homogeneous electric field. The positive ions are accelerated towards the time- and position-sensitive multi-particle detector at one side of the interaction region; electrons are detected by a channeltron at the other side. An additional retarding field in front of the channeltron was included which ensures that only electrons with sufficiently high energies will trigger the spectrometer.

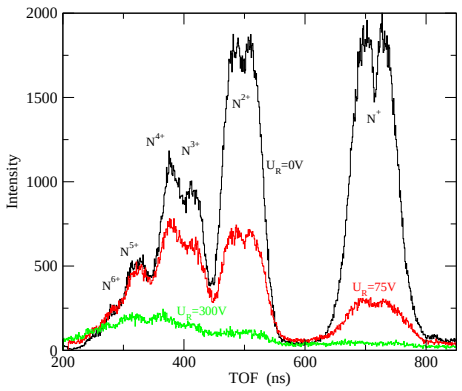

Figure 1: Time of flight spectra of coincident N^{p+}+N^{q+} fragment ions observed in collisions of 3.6 MeV/u Xe^{40+}-ions with N_2. The spectra were obtained for retarding potentials U_R = 0 V, 75 V, and 300 V.

Fig. 1 shows the time of flight spectra of coincident N^{p+}+N^{q+} fragment ions obtained with different retarding potentials U_R. At $U_R = 300$ V K-LL Auger electrons can still overcome the retarding field. These lead to at least doubly ionized atoms and consequently the production of lowly charged ions is suppressed. The measured intensity is quite low since only electrons emitted in a small cone will be detected. For $U_R = 75$ V slower electrons are still effectively discriminated which leads to a significant reduction of the N^+ and N^{2+} intensities. However, the field is not too large for detecting most of the K-LL Auger electrons. Consequently the intensity reduction of the higher charge states is smaller and vanishes for N^{5+}. This behavior clearly demonstrates that inner shell ionization followed by Auger processes is a major mechanism for multiple ionization in molecular fragmentation.

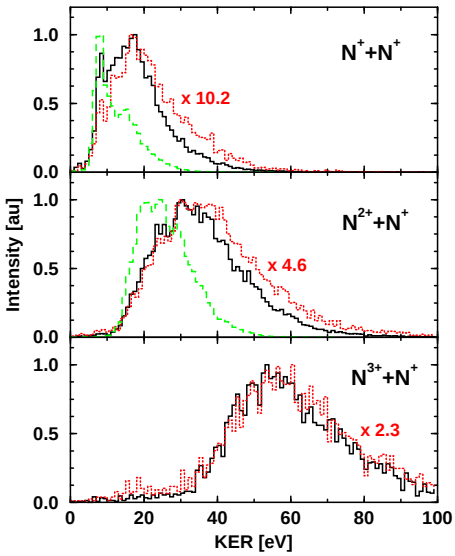

Figure 2: Kinetic energy release (KER) spectra of coincident $N^{q+} + N^+$ fragment ions for retarding potentials of $U_R = 0$V (—) and $U_R = 75$V (- - -). For comparison spectra observed in collisions with 200 keV H^+ without retarding field are shown (– –).

The key question is, how the fragmentation dynamics is influenced by the ionization mechanism. Fig. 2 shows the kinetic energy release of coincident $N^{q+} + N^+$ fragments for $U_R = 0$V and $U_R = 75$V. For $N^+ + N^+$, $N^{2+} + N^+$, and $N^{2+} + N^{2+}$ (not shown) inner shell processes play a minor role and thus the fragmenting molecular ion is in most cases less excited which results in a narrower KER distribution. At higher retardation fields only the "minor" inner shell contribution survives. On average the still observed molecules will be higher excited which is revealed by a broadening at higher energies. For $N^{3+} + N^+$ no such effect occurs which indicates that inner shell ionization dominates here. The same holds true for $N^{3+} + N^{3+}$ and N^{4+}+N^{4+} where furthermore the measured intensities with and without retardation field practically match.

References

[1] B.Siegmann, U. Werner, H.O.Lutz, and R.Mann, J. Phys. **B 35**, 3755 (2002)

[2] R. Mann, H.F. Beyer, and F. Folkman, Phys. Rev. Lett. **46**, 646 (1981)

High-precision mass studies on short-lived nuclides using ISOLTRAP*

M. Kowalska †[1*], D. Beck[2], K. Blaum[2,3], M. Breitenfeldt[4], S. George[2,3], F. Herfurth[2], A. Herlert[1], A. Kellerbauer[5], H.-J. Kluge[2,6], D. Lunney[7], S. Naimi[7], D. Neidherr[2], S. Schwarz[8], and L. Schweikhard[4]

[1]CERN, Geneva, Switzerland; [2]GSI, Darmstadt, Germany; [3]Johannes Gutenberg-Universität, Mainz, Germany; [4]Ernst-Moritz-Arndt-Universität, Greifswald, Germany; [5]MPI für Kernphysik, Heidelberg, Germany; [6]Ruprecht-Karls-Universität, Heidelberg, Germany; [7]CSNSM-IN2P3-CNRS, Orsay, France; [8]NSCL, Michigan State University, East Lansing, USA

The Penning-trap mass spectrometer ISOLTRAP [1], located at the on-line isotope separator ISOLDE at CERN, has recently achieved a number of scientific highlights among others concerning superallowed beta emitters [2], the r-process in nucleosynthesis [3], or nuclear magic numbers [3, 4]. It was shown that with its high performance and the ability to address nuclides with production yields of only a few 100 ions/s and half-lives well below 100 ms, ISOLTRAP is a powerful tool for the investigation of nuclear binding energies.

The ISOLTRAP mass measurements in 2007 addressed nuclides on both sides of beta stability. On the neutron-rich side, the studies of Ag isotopes from 2006 were continued for ground and isomeric states of $^{117,119-121}$Ag. Furthermore, the new Ramsey excitation schemes [2, 5] in presence of isobaric contamination were investigated for In isotopes. On the same side, nuclei close to the doubly magic ^{208}Pb, namely ^{211}Ra and $^{211-213}$Fr, were investigated. Among neutron-deficient nuclides, the studies concentrated on the Cd chain, and masses of $^{99-109}$Cd were measured, with the mass of ^{99}Cd being determined directly for the first time (see Fig. 1).

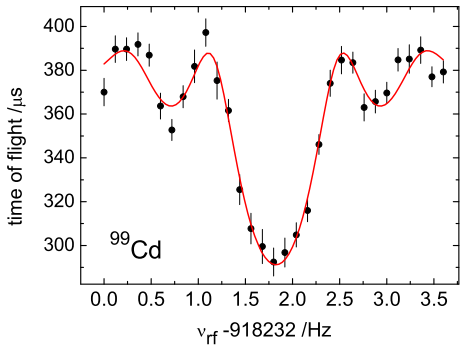

Figure 1: Time-of-flight resonance of ^{99}Cd, whose mass has been determined for the first time directly.

Time was also devoted to technical developments. New alkali and gas ion sources were tested and optimised. First steps were taken for the planned mass measurements on very light nuclides - ^{6,8}He and ^{11,12}Be - for which hydrogen cooling in the ISOLTRAP rfq cooler-buncher will be necessary, replacing helium, which leads to rf-heating for such light ions. A proposal was also accepted by the ISOLDE scientific committee (INTC) to perform mass measurements on ^{138,140}Xe, $^{207-210}$Hg, and $^{223-225}$Rn in order to investigate the proton-neutron interaction [6]. Furthermore, a new project was started which aims at trap-assisted decay spectroscopy, i.e. beta- and gamma-decay studies on pure radioactive beams by using ISOLTRAP as an isobaric, and even isomeric, purifier. The pilot experiment was accepted by the scientific committee, and it will be devoted to decay-studies of neutron-rich Hg and Tl isotopes behind ^{208}Pb [7], where francium contamination is a problem. The studies will give valuable input for the residual interactions in this region, and can lead to the discovery of new isomers, or even isotopes. The production rates for Fr and Tl isotopes were investigated for a UC_x target coupled to a quartz transfer line that transports alkali beams about ten tousend times less efficient. For A=207 a cooling and a time-of-flight resonance were obtained for thallium. Francium was not visible. This has to be compared to a Fr-to-Tl yield ratio of about 100 if a normal transfer line is used (this ratio reaches 10^4 at $A \approx 212$).

Plans for 2008 include an extension of the studies on the neutron-rich side to ^{129,130}Ag and ^{130,131}Cd, which are relevant for the nucleosynthesis r-process. Also, the modifications necessary for studies of halo nuclides ^{6,8}He and ^{11,12}Be will be finalised, and first measurements in this region should take place in the summer. In parallel, two to three beamtimes devoted the newly accepted proposals [6, 7] are planned for summer and autumn 2008.

References

[1] M. Mukherjee *et al.*, Eur. Phys. J. A, accepted.

[2] S. George *et al.*, Phys. Rev. Lett. 98, 162501 (2007).

[3] M. Dworschak *et al.*, Phys. Rev. Lett., accepted.

[4] C. Guenaut *et al.*, Phys. Rev. C 75, 044303 (2007).

[5] S. George *et al.*, Int. J. Mass Spectrom. 264, 110-121 (2007).

[6] D. Beck *et al.*, CERN-INTC-2007-019 (2007).

[7] M. Kowalska *et al.*, CERN-INTC-2007-022 (2007).

* Work supported by BMBF (contracts no. 06MZ215, and 06GF186I), EU (contracts no. HPMT-CT-2000-00197, HPRI-CT-2001-50034, RII3-CT-2004-506065, MC-EIF-42114), and the Helmholtz association (contract no. VH-NG-037).

† kowalska@cern.ch

Mass measurements and collinear laser spectroscopy on neutron-rich and heavy nuclides at the research reactor TRIGA Mainz*

J. Krämer[1], K. Blaum[1,2,3], M. Block[2], K. Eberhardt[1], G. Eitel[1], R. Ferrer[1], Ch. Geppert[1], S. George[1], F. Herfurth[2], J. Ketelaer[1], J. Ketter[1], H.-J. Kluge[2], Sz. Nagy[1], D. Neidherr[1], R. Neugart[1], W. Nörtershäuser[1,2], J. Repp[1], C. Smorra[1], N. Trautmann[1], and C. Weber[4]

[1]University Mainz, Germany; [2]GSI, Darmstadt, Germany; [3]Max-Planck-Institut für Kernphysik, Heidelberg, Germany; [4]University of Jyväskylä, Finland

The TRIGA-SPEC project comprises a Penning trap setup for high-precision mass measurements as well as a beamline for collinear laser spectroscopy on neutron-rich and heavy nuclides at the research reactor TRIGA Mainz. These techniques have been employed for decades at on-line facilities, but to reach regions further away from stability and to improve accuracy, e.g., for fundamental tests of the standard model, a continous effort towards the development of more efficient and more accurate techniques is required. TRIGA-SPEC is devoted as a test bench particularly for the planned MATS [1] and LASPEC [2] facility at FAIR.However, due to the infrastructure at Mainz and the coupling to the research reactor, it provides also the opportunity to perform measurements on heavy trans-actinides as well as short-lived fission products far away from the valley of stability. The data provided will be of high interest for nuclear structure studies. The proposed experimental setup is shown in Fig. 1. Thermal neutron induced fission nuclei will be produced in a target chamber placed near the reactor core and transported towards an ion source via a gas-jet transport system [3].

For first off-line measurements on heavy actinide elements between ^{235}U and ^{249}Cf, a laser desorption ion source has been developed. Ions of heavy elements as well as carbon clusters for mass calibration are produced with a pulsed frequency-doubled Nd:YAG laser with a wavelength of 532 nm and a pulse length of 3-5 ns. The ion-optical transport from the source to the Penning traps was optimized using SIMION 8.0 simulations and the transport efficiency for shooting ions through the traps is estimated to be 80%. For the cylindrical purification trap and the hyperbolical precision trap [4], a 7 T superconducting magnet similar to the one at SHIPTRAP [5] was installed and commissioned. For the very first time the Fourier-Transform Ion Cyclotron Resonance (FTICR) detection method, which was improved to reach single ion sensitivity, will be applied for mass measurements on heavy nuclei. For mass separation of the fission products a 90° dipole mass separator will be used, which reaches a mass energy product of 15 MeVamu. To guide the ions either to the Penning trap or to the collinear laser spectroscopy beamline a 45° electrostatic switchyard was designed and optimized with SIMION 8.0 simulations. For the collinear beamline an alkaline vapour charge exchange cell and an ion deflector with optical viewports to overlap the ion or atom beam with the laser were designed and are currently being manufactured. Collinear spectroscopy needs an accurate determination of the acceleration voltage [6]. Thus, we are going to test a high precision voltage divider with an accuracy of 10^{-5} for voltages up to 60 kV. Additionally, the applicability of a frequency comb for absolute measurements of the transition frequencies will be investigated.

* Work supported by HGF under contracts VH-NG-037 and VH-NG-148

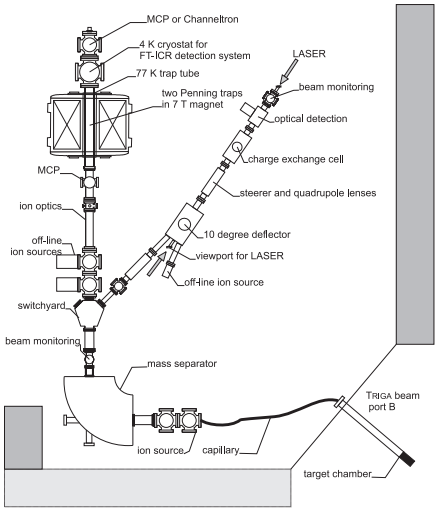

Figure 1: Experimental setup with the mass spectrometry beamline to the left and the laser spectroscopy beamline to the right. Fission products will be transported by a carrier gas to the ion source and subsequently mass separated.

References

[1] K. Blaum, Phys. Rep. **425** (2006) 1

[2] W. Nörtershäuser, P. Campbell, and the LASPEC collaboration, Hyp. Int. **171** (2006) 149.

[3] E. Stender, N. Trautmann, G. Herrmann, Radiochem. Radioanal. Lett. **42** (1980) 291.

[4] C. Weber, K. Blaum, M. Block, R. Ferrer, F. Herfurth, H.-J. Kluge, C. Kozhuharov, G. Marx, M. Mukherjee, W. Quint, S. Rahaman, S. Stahl, the SHIPTRAP collaboration, Eur. Phys. J. A **25** S01 (2005) 25.

[5] S. Rahaman, M. Block, D. Ackermann, D. Beck, A. Chaudhuri, S. Eliseev, H. Geissel, D. Habs, F. Herfurth, F.P. Heberger, et al., Int. J. Mass Spectrom. **251** (2006) 146.

[6] S. L. Kaufmann, Opt. Comm. **17** (1976) 309.

Status of the *g*-factor experiment on highly-charged calcium*

K. Blaum[1,2], H.-J. Kluge[1], W. Quint[†1], B. Schabinger[2], S. Sturm[2], A. Wagner[2], and G. Werth[2]
[1]GSI, Darmstadt, Germany; [2]Institut für Physik, Johannes Gutenberg-Universität, Mainz, Germany

Measurements of the anomalous magnetic moment of the electron bound in hydrogen-like ions with spinless nuclei have proven to be highly-sensitive tests of corresponding calculations based on bound-state quantum electrodynamics (BS-QED). The calculations of the g-factors of the electron bound to hydrogen-like carbon and oxygen and their corresponding measurements performed by the collaboration of GSI and the University of Mainz [1, 2] agreed down to the 9^{th} significant digit.

Presently, a triple-trap Penning-trap experiment on highly-charged calcium is prepared [3, 4], which is expected to yield a precision on the level of 10^{-9} for the electronic g-factor of $^{40,48}Ca^{17,19+}$. This experiment makes use of a cryogenic in-trap electron-beam ion source (EBIS) at $T = 4\,\mathrm{K}$, where the charge breeding of the ions is performed by electron-impact ionization [5].

A new cathode was developed for the EBIS based on a single field emission point (FEP) made from tungsten. The emission of electrons is achieved by applying a voltage between the FEP and an extraction electrode. The electron beam is reflected several hundred times between a reflector and the FEP until it widens up and hits the target, which consists of carbon with a layer of calcium. The electron current on the target is measured by monitoring the voltage drop across the input resistance of an oscilloscope. Atoms from the target get ionized by electron impact and are trapped in the so-called creation trap. After charge breeding the ions are transported either to the analysis trap or the precision trap.

For recording a mass spectrum as shown in figure 1, the electric trap potential is ramped continuously to bring the ions in resonance with the tank circuit. For detection of these ion signals a special device was developed to filter and amplify the signal near the resonance frequency of the tank circuit. This signal is rectified and integrated, yielding the spectral power of the detection signal, which shows peaks of ions with different charge-to-mass ratios.

The spectrum in figure 1 was measured by averaging over several single spectra taken in the precision trap. Assuming that the peak at $U = -10.25$ V corresponds to a charge-to-mass ratio of $\frac{q}{m} = 0.5$, the other peaks can be identified. In this way it was possible to detect mainly several oxygen, nitrogen and carbon ions. The resolution of the spectra is not high enough to discriminate ions with similar charge-to-mass ratios like $^{16}O^{8+}$, $^{14}N^{7+}$ and $^{12}C^{6+}$.

For the high-precision g-factor measurements ultra-

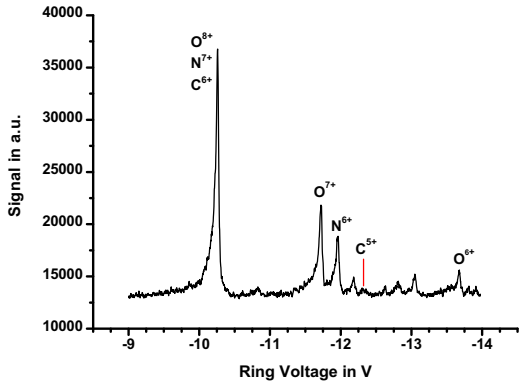

Figure 1: The plot shows a mass spectrum of highly-charged ions recorded in the precision Penning trap. The ions were created using a cryogenic electron beam ion source.

stable voltage sources are needed. To eliminate any possible disturbance, a very stable supply voltage is required, which has to be independent of the electricity network in order to avoid noise and ground loops as well as measurement-time loss due to power cuts. Therefore a battery-based voltage source is being designed. A car battery (12 V) is used to generate the required output voltages ($\pm$15 V, $\pm$5 V), by converting the dc-voltage into ac-voltage, amplifying, commutating and, finally, flattening it again. Each channel is designed for a maximum current of 1,5 A. To control and monitor the voltages as well as the currents a microcontroller, connected to a computer, is used. The $\pm$15 V are almost finished and are tested at the moment. The read-out electronics as well are already working well.

In the future it is planned to study the charge breeding process in detail to create highly-charged calcium ions. After creating single calcium ions the g-factor measurement will be performed.

References

[1] H. Häffner *et al.*, Phys. Rev. Lett. **85**, (2000) 5308.
[2] J. Verdú *et al.*, Phys. Rev. Lett. **92**, (2004) 093002.
[3] M. Vogel *et al.*, Nucl. Instr. Meth. B **235**, (2005) 7-16.
[4] B. Schabinger *et al.*, J. Phys. Conf. Ser. **58**, (2007) 121.
[5] J. Alonso *et al.*, Rev. Sci. Instr., **77**, (2006) 03A901.

* Work supported by the EU, the BMBF, the DFG and the Helmholtz association (VH-NG-037)
† W.Quint@gsi.de

The HITRAP Decelerator Facility GSI

W. Barth[1], M. Bevcic[1], M. Block[1], K. Blaum[1,2], L. Dahl[1], S. Eliseev[1,3], R. Fischer[1], P. Forck[1], G. Gruber[1], F. Herfurth[1], B. Hofmann[1,5], R. Kaminski[1], M. Kaiser[1], O. Kester[*1], H.-J. Kluge[1,4], C. Kozhuharov[1], S. Koszudowski[1,4], G. Maero[1,4], R. Nörenberg[1,5], W. Quint[1,4], U. Ratzinger[5], H. Reich-Sprenger[1], A. Sauer[5], A. Schempp[5], A. Sokolov[1,3],T. Stöhlker[1,4], W. Vinzenz[1], M. Vogel[1], G. Vorobjev[1], D. Winters[1]
[1]GSI Darmstadt, [2]Universität Mainz, [3]University of St. Petersburg, [4]Universität Heidelberg, [5]Universität Frankfurt,

The heavy ion trap facility (HITRAP), which is being built in the re-injection channel between ESR and SIS will provide unique beams of highly charged ions up to bare uranium at very low energies for a large variety of experiments. At the HITRAP facility it is envisaged to decelerate heavy highly charged ions down to energies of the keV-range where they can be captured in a large Penning trap [1]. The HITRAP decelerator linac employs a double drift buncher (DDB) for phase focusing, an interdigital H-type (IH) structure as energy booster and a 4-rod Radio Frequency Quadrupole (RFQ) for final deceleration of the ions down to 6 keV/u.
Additional rf-design simulations of the geometry of the HITRAP IH-structure have been performed to include the geometry changes of the large drift tube which houses the magnetic quadrupole triplet lens. These changes were required to meet the specifications of the lens. The Micro Wave Studio simulations determined rf-parameters of the cavity such as shunt impedance, quality factor and gap voltages. The corresponding rf-parameters of the other cavities have already been measured and are summarized in table 1. Tuning of all cavities has been completed in 2007 and all buncher cavities have been delivered to GSI. In addition the complete set of magnetic quadrupole lenses and steerers of the HITRAP beam line as well as diagnostics systems are now available at GSI. After copper plating the RFQ tank has been shipped to Frankfurt University for assembly and rf-tuning. Alignment of the qudrupole electrodes, adjustment of the voltage flatness and assembly of the de-buncher cavity at the RFQ tank have been completed [2]. Both cavities are shown in fig1.

Table 1: Measured rf-parameters of the linac cavities.

Resonator	length l [m]	Q	R	R/Q	Zeff
DDB 4-gap 108 MHz	0.47	10950	24.30 MOhm	2219	51.70 MOhm/m
DDB 2-gap 216 MHz	0.24	11100	10.32 MOhm	930	43.01 MOhm/m
IH-strucktur	2.61	25800	744.71 MOhm	28865	285.00 MOhm/m
Re-buncher	0.20	3000	2.33 MOhm	777	11.65 MOhm/m
RFQ	1.90	3700	72.63 kOhm	20	138.00 kOhm*m
De-buncher	0.07	2700	1.54 MOhm	570	15.50 MOhm/m

The two cavities of the DDB at the high-energy end of the HITRAP linac have been assembled and installed in the re-injection channel on a huge support structure. The DDB-section has been prepared for a first commissioning beam time in May, which has been complemented with a second beam time in August 2007. The results will be presented in ref. [3].

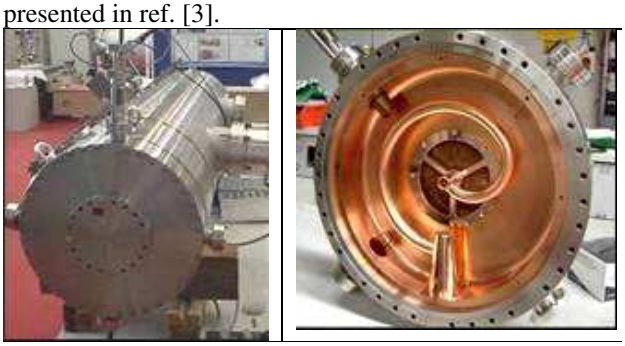

Figure 1: Pictures of the RFQ tank (left) and of the 2-gap spiral de-buncher at the RFQ exit (right)

The hardware of the IH-structure, which comprises the vacuum tank, the drift tube structure and the inner tank triplet lens are completed and rf-measurements of the IH-structure are in preparation (fig.2).

Figure 2: Picture of the IH-structure cavity, prepared for rf-measurements.

[*]O.kester@gsi.de

The HITRAP low energy section

The design, construction and test of the HITRAP low-energy section are performed in parallel to the work on the HITRAP linac. The main component of the low-energy part is the cooler Penning trap. Extensive numerical simulation calculations are under progress in order to determine essential parameter of the electron cooling and resistive cooling process. In particular extraction of the cooled ion cloud and the distribution of the ions at the entrance of the vertical beam line are of further interest for beam transport calculations and the experiments. All essential elements of the trap including the 6T-magnet have been delivered and are operational [4]. The electrode structure, the power supplies and the amplifiers are under construction. The low-energy beam transport line between RFQ and cooler trap has been constructed and delivered to GSI. Baking tests of the vessels have been performed

The vertical beam line (VBL) and the beam lines on top of the re-injection channel will guide the ions from the cooler trap towards the experiments. The beam lines have been designed with respect to particle beam dynamics and vacuum generation. The 3-d CAD design of the complete VBL has been performed and the components are in the call for tender procedure. Two prototypes of the UHV-diagnostic of these beam lines have developed and built by the KVI Groningen and delivered to GSI. Each diagnostic comprises a Faraday cup and a MCP-beam-profile detection, which are mounted on a single stepper motor driven feedthrough.

HITRAP infrastructure and experiments

The required infrastructure of the HITRAP facility in the re-injection channel and on top of the re-injection shielding for the experiments has been installed. Cooling water distribution and electric power distribution are available. The experiment area has been plated with a steel vat, which is required to confine cooling water losses. The platform of the SPECTRAP experiment has been erected and the SC-magnet of SPECTRAP has been installed [5].

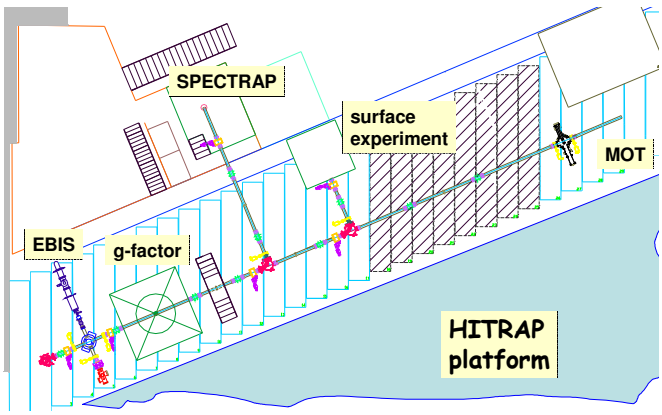

Figure 3: Overview of the HITRAP experiment area.

The SPARC-EBIT which has been purchased in 2007 will be used as test ion source for the HITRAP commissioning [6]. It will be installed at the dedicated position of the EBIS injector of HITRAP. Four experiment stations are foreseen, which cover the needs for the g-factor experiment, SPECTRAP, the surface experiments and a collision experiment using a cold atom target in a MOT. The locations of the different setups are shown in fig.3. The first experiment which is in the assembly and test phase is the surface interaction study. To be able to address the HCI-surface interaction, the deceleration of the HCI to virtually zero energy has been studied numerically. An efficient electron spectrometer has been developed in collaboration of KVI Groningen and TU-Vienna. Spectroscopy of X-rays emitted from hollow atoms created in the surface interaction process will be performed in collaboration with GSI. The surface experiment-setup will be the first HITRAP experiment which will get first beam from HITRAP in 2008.

For a proper tuning of the linac cavities, which comprises the right power level and the settings of the phase delay between the cavities, measurements of beam quality at the exit of the different cavities are required. The measurements of the transverse beam quality have been done via emittance measurements using the GSI emittance meter based on the “single shot pepper pot system” [7]. A pepper pot system based on a micro channel plate is under design, which will be used for emittance measurements in the HITRAP low energy section.

References

[1] T. Beier et al., *HITRAP Technical Design Report*, GSI Darmstadt, 2003, http://www.gsi.de/documents/DOC-2003-Dec-69-2.pdf

[2] B. Hofmann, "Konstruktion und Aufbau einer kompakten RFQ-Spiral-Struktur zum Abbremsen hochgeladener Schwerionenstrahlen für das HITRAP-Projekt der GSI", Dissertation, Universität Frankfurt, Dezember 2007

[3] L. Dahl et al., “HITRAP Commissioning", this report

[4] F. Herfurth et al., „The HITRAP cooler trap", this report

[5] Z. Andjelkovic et al., "Development of the SPECTRAP experiment setup for laser spectroscopy of cold & trapped HCIs", this report

[6] S. Geyer et al., "First tests with the new SPARC-EBIT", this report

[7] J. Pfister et al., "Single-shot emittance measurements at HLI and HITRAP", this report

The HITRAP cooler trap

F. Herfurth*, I. Chiarelli, O. Kester, H.-J. Kluge, S. Koszudowski, C. Kozhuharov, G. Maero, and W. Quint

GSI, Darmstadt, Germany

The HITRAP facility is being constructed in order to decelerate and stop heavy, highly charged ions up to bare uranium. After the production in the GSI accelerator complex, the ions will be decelerated and cooled in the experimental storage ring (ESR) followed by IH and RFQ linear accelerator structures operated in reverse mode [1]. At an energy of 6 keV/u they will be transported to and injected into a Penning trap for cooling and creation of a slow and pulsed ion beam. A 6 T magnetic field, homogeneous over about 0.4 m, ensures the radial confinement during final deceleration and electric potentials up to 18 kV trap the ion bunch longitudinally [2].

The low energy beam line between RFQ and Penning trap is designed with electrostatic einzel lenses operated in acceleration mode to transport the beam with the large divergence of 100 π mm mrad. During 2007 the components of that beam line have been produced. In order to obtain the necessary vacuum below 10^{-13} mbar in the Penning trap two differential pumping barriers are included in the beam line. The vacuum properties of the different elements have been tested in full baking cycles, where the necessary vacuum of $1 \cdot 10^{-10}$ mbar has been reached. The beam line is being assembled.

In order to test the beam line and the cooler trap a UHV compatible test ion source has been prepared. Singly charged helium and hydrogen ions are produced via electron bombardment and accelerated to 5 keV. The such produced ion beam can be electrostatically deflected. This will allow one to scan and measure the acceptance of the low-energy beam-transfer line and the cooler trap. To simulate the injection of an ion bunch that contains 100 000 highly charged ions the test ion source produces $1 \cdot 10^7$ singly charged ions within a pulse of one micro second.

The 27 equally sized and spaced electrodes that form the electric potential needed to store simultaneously electrons and highly charged ions have been designed and are under construction in the GSI Central Workshop. The necessary electric potential has been analyzed in detailed simulations and its qualitative trend on the trap's longitudinal axis is displayed together with the electrode arrangement in fig. 1.

The superconducting, cryogen-free magnet for the trap has been delivered in spring 2007 and was tested to meet the specifications. The magnetic field homogeneity, measured with a NMR probe, is also displayed in fig. 1.

In order to control capture, storage as well as in-trap manipulation for cooling, software components have been built based on the experiment control system CS developed at GSI [3]. A field-programmable gate array (FPGA) card was implemented for the timing of the HITRAP cooler trap

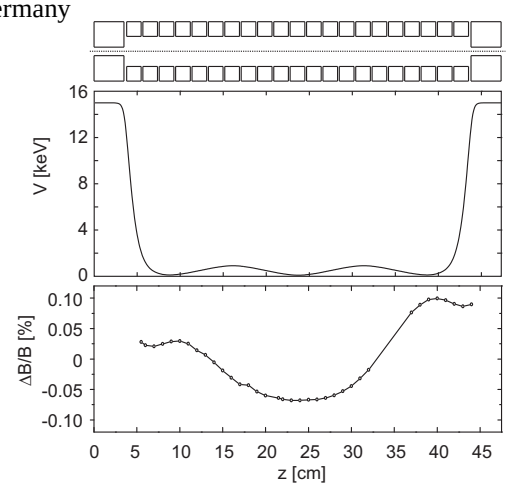

Figure 1: Layout of the cooler Penning trap electrodes. Also displayed is the electrical potential as calculated on axis and the homogeneity of the magnetic field as measured during installation also on the central axis.

processes and is also used at other ion trap installations at GSI (SHIPTRAP) and elsewhere (ISOLTRAP/Geneva, TRIGATRAP/Mainz and MLLTRAP/Munich). The necessary electronic circuitry for read-out of the ion's signals and for resistive cooling has been tested and is being implemented in the specially designed housing that goes into the trap vacuum and will also be cooled to 4 K.

Extensive calculations have been performed in order to find the ion's cloud behavior once stored in the trap. A particle-in-cell (PIC) code has been adapted to the strong magnetic field and is used to observe the development of cloud size and energy during the cooling process [4]. Meanwhile, also the final cooling process, the cooling via image currents induced in the trap electrodes and damped in a resonant circuit, has been implemented. First tests show qualitatively the expected behavior and will now be extended to more quantitative results.

References

[1] O. Kester *et al.*, "Deceleration of highly charged ions for the HITRAP project at GSI", LINAC'06, June 2006, Knoxville, p. 189, http://www.JACoW.org.

[2] F. Herfurth *et al.*, Hyperfine Interact. 173 (2006) 93.

[3] D. Beck *et al.*, Nucl. Instr. Meth. A 527 (2004) 567.

[4] G. Maero *et al.*, "Simulation of cooling mechanisms of highly-charged ions", COOL'07, September 2007, Bad Kreuznach, p. 130, http://www.JACoW.org.

* F.Herfurth@gsi.de

EBIS test ion source for HITRAP and charge breeding*

G. Vorobjev[1#], R.Becker[2], O. Kester[1], J. Pfister[2], A. Sokolov[1], H. Zimmermann[2].
[1]GSI, Darmstadt, Germany; [2]J. W. Goethe-Universität Frankfurt, Germany.

The electron beam ion source MAXEBIS from Frankfurt University has been installed in a test beam setup at GSI to deliver highly charged ions for HITRAP [1] and to serve for charge state breeding experiments. Two ion sources dedicated to the production of singly charged ions for external ion injection have been connected to a so-called multi passage spectrometer (MPS), which is an integral part of the beam line. Recent experiments were dedicated to evaluate the parameters of the ion beam line, i.e. emittance, dependence of the charge state distribution on the confinement time in the electron beam, efficiency of external ion injection and the resolution of the multi passage spectrometer (MPS). Simulations of the beam-line using SIMION 7.0 were performed and additional elements were installed in order to improve the beam parameters for more efficient ion transfer. To simplify downstream focusing the setup has been equipped with new diagnostics and beam optics devices. Investigations of different modes of the ion transmission trough the MPS resulted in better resolution of the analyzing magnet. Figure 1 shows a typical TOF spectrum of charge bred argon ions injected from the sputter gun (solid line) and the rest gas ions without injections (dash line). Clear peaks of charge states of Argon from 12+ to 9+ appear and the rest gas peaks drop down being kicked away by more heavy Argon ions via the cooling process. The amount of charges due to Argon ions as compared to the amount of residual gas ions was estimated to be 10%. The breeding efficiency of the charge state 10+, as derived from the spectra, is 15%, so 10^7 Argon ions have been captured and charge bred.

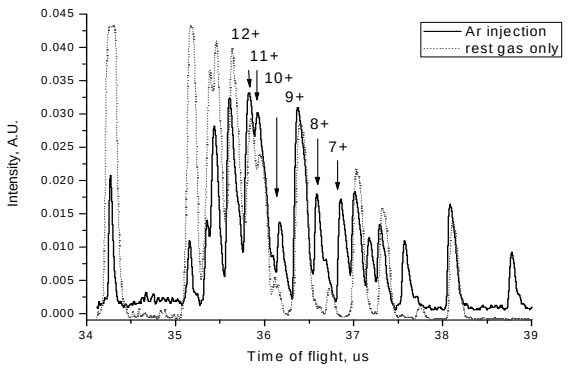

Fig. 1: Argon TOF spectrum from MAXEBIS after 250 ms charge breeding with maximum of charge state 12+.

The emittance of the MAXEBIS ion beam was measured to be 70 mm·mrad, compared to the predicted one of 10 mm·mrad. The picture of the ion beam taken with a CCD camera has shown strong aberrations (Figure 2).

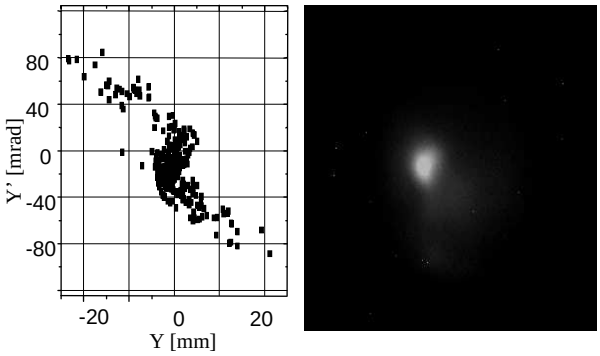

Fig. 2: Ion beam ellipse after passing the complete beam line; simulated – on the left, a measured – on the right.

Due to the complicate running procedure of the cryogenic MAXEBIS a next generation compact Dresden electron beam ion trap (EBIT) [2] has been purchased and installed at GSI and tested. The EBIT will continue the experiments performed so far at the MAXEBIS and is dedicated as SPARC test ion source. Table 1 presents a brief summary of the important parameters for both devices.

For ion – neutral atom collision experiments a Magnesium jet target will being mounted. X-ray spectroscopy for slow ion – fast electron interaction experiments for the study of charge breeding will be used. This will allow the investigation of processes in the ionization chamber, while the ion beam can be used simultaneously in other experiments.

Table 1. Important parameters of the old and new EBIS.

	MAXEBIS	Dresden EBIT
Coil configuration	Solenoid	Helmholtz coils
Temperature, K	4	300
Magnetic field, Tl	5	0.25
Electron current, mA	100	30
Current density, A/cm^2	100	200
Ion beam size, um	200	20
Trap length, cm	80	2
Ion capacity	~ $5*10^9$	~$5*10^7$
Max. electron beam energy, keV	15	15

References

[1] H.-J. Kluge et al. "HITRAP: a facility at GSI for highly charged ions". Advances in Quantum Chemistry, v. 53 pp. 83-98, 2008.
[2] G. Zschornack et al. "Dresden EBIT: Status report and next developments", Review of Scientific Instruments, 77 (2006) 03A904.

* Work supported by EU, EURISOL/DS, RIDS 515768
#g.vorobjev@gsi.de

First tests with the new SPARC-EBIT

S. Geyer[2], O. Kester[1], J. Pfister[2], A. Sokolov[1],
D.F.A. Winters[1], G. Vorobyev[1], Th. Stöhlker[1], G. Zschornack[3]

[1] GSI, Darmstadt, Planckstraße 1, 64291 Darmstadt, Germany
[2] J. W. Goethe-Universität Frankfurt, Max-von-Laue Straße 1, 60438 Frankfurt, Germany
[3] Forschungszentrum Rossendorf, Bautzner Landstraße 128, 01328 Dresden, Germany

The SPARC-EBIT (fig.1) is an Electron Beam Ion Trap (from DREEBIT, Dresden) that will be used for tests and offline measurements, firstly for HITRAP, and later for SPARC (Stored Particle Atomic physics Research Collaboration). In the EBIT the ions are produced by electron impact ionisation of gas atoms by an intense electron beam. The magnetic field of a permanent magnet arrangement focuses the beam and guides it through the ionisation chamber. This design makes the EBIT portable and simple to operate.

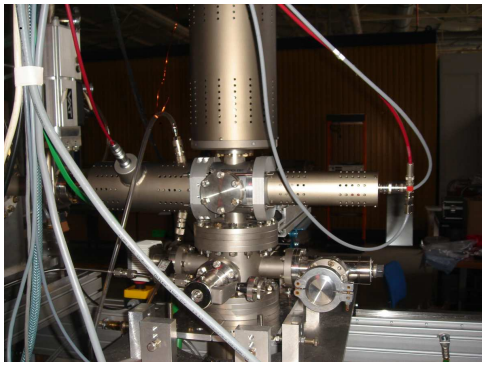

Fig. 1: Photograph of the SPARC-EBIT in the Heckhalle. The electron gun sits on the right hand side, the ions are extracted to the left.

The EBIT-setup is currently being tested in the Heckhalle. When the first tests and experiments have been completed, the SPARC-EBIT will move to the HITRAP [1] beam line, where it will be used as an offline and test ion source. It will also be used to test detectors and perform x-ray experiments using a crystal spectrometer.

Already in December 2007, first x-ray and time-of-flight spectra (TOF) were recorded using the EBIT. For the x-ray measurements a Silicon-pin detector was used, which has a resolution of about 260 eV at ~10keV. In order to fully characterize the new EBIT, experiments were performed with different trapping-times, different gas pressures, and with two gas species (argon and xenon). Fig. 2 shows two of the first raw argon x-ray spectra (*i.e.* no data correction). For longer trapping times, the peaks shift towards higher energies. This was expected, since the average charge state increases with time. This effect was also observed for lower gas pressures. Furthermore, by increasing the gas pressure, charge exchange between atoms and ions is more likely to occur and ionized atoms may recombine.

By extracting the ions from the EBIT in a pulsed mode, TOF-spectra could be obtained. The TOF spectrometer

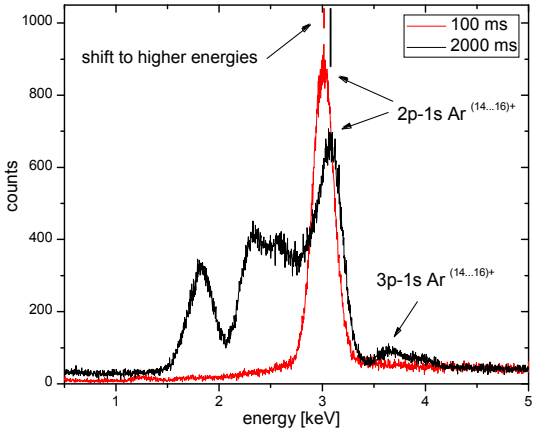

Fig. 2: X-ray spectra with externally injected argon plotted for two different trapping times.

used was built by Weisgerber [2]. Experiments with different pulse times were performed, of which Figure 3 shows an example for argon injection.

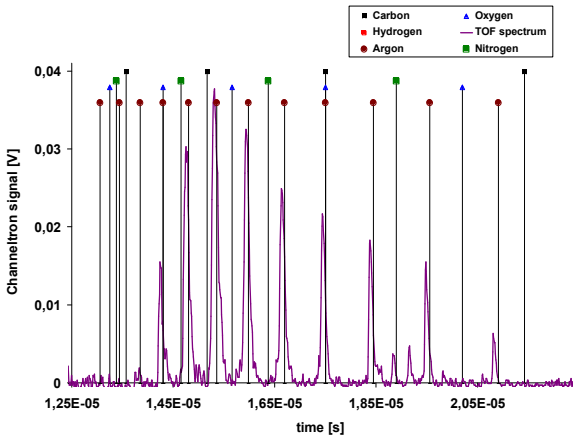

Fig. 3: TOF spectrum obtained with externally injected argon in the EBIT for a trapping time of 1s.

In conclusion, it can be stated that the first tests and experiments were successful. As a next step, a new quadrupole lense will be installed in the EBIT beamline in order to optimise the transport of the extracted ion beams.

References

[1] F. Herfurth et al., *Highly charged ions at rest: The HITRAP project at GSI*, AIP conference proceedings Vol. 793, 2005, p.278

[2] W. Weisgerber, *A time of flight-spectrometer for low-energetic ions*, diploma thesis, University Frankfurt, 1979

Development of the SPECTRAP experimental setup for laser spectroscopy of cold & trapped HCI*

Z. Andjelkovic[1], Ch. Geppert[1,2], J. Krämer[1], W. Nörtershäuser[1,2], M. Vogel[2], V. Hannen[3], Ch. Weinheimer[3], D.F.A. Winters[3], D. Church[4], D. Schneider[5], S. Bharadia[6], D. M. Segal[6], R. Thompson[6], and the HITRAP collaboration[2]

[1]Institut für Kernchemie, Johannes Gutenberg-Universität, Mainz, Germany; [2]Gesellschaft für Schwerionenforschung, Darmstadt, Germany; [3]Westfälische Wilhems-Universität, Münster, Germany; [4]Texas A&M University, USA; [5]Lawrence Berkeley National Laboratory, California, USA; [6]Imperial College London, UK

The new SPECtroscopy TRAP (SPECTRAP) experiment under development within the framework of the HITRAP project will measure ground state hyper-fine splittings in cold, trapped, highly-charged ions (HCI) extracted from the HITRAP facility [1] by means of laser spectroscopy. It is a dedicated cryogenic (Penning) trap, laser and detection system, built in close collaboration with Imperial College London, TU Darmstadt, and the Universities of Münster and Mainz. The cryogenic surrounding allows for efficient cooling of ions during storage, thus opening the possibility for precision experiments with ions nearly at rest. Its optical accessibility (axial and radial) furthermore allows laser cooling, laser excitation and optical detection, making it an ideal tool for laser spectroscopy of HCI [2]. The trap will be operated with a Helmholtz-type superconducting magnet, which was consigned to GSI by Lawrence Berkeley National Laboratory (LBNL), with courtesy of Prof. Dieter Schneider (LBNL) and Prof. Dave Church (Texas A&M University) who are also supporting the project. The system had previously been called RETRAP, and comprised, besides the magnet, a hyperbolic ion trap, ion manipulation and detection components as well as the corresponding electronic and cryogenic components [3].

In March 2007 the RETRAP experimental setup was dismantled at Berkeley (see Fig.1), packed and prepared for shipment to GSI, where it arrived in May 2007. By now a new platform for purposes of the SPECTRAP setup has been constructed next to the re-injection channel, and we have started mounting the newly-arrived equipment on it. At the moment, the magnet as well as the electronic and cryogenic system are being checked and prepared for implementation into the SPECTRAP experiments.

A new open-endcap cylindrical Penning trap [4] has been developed and constructed at Imperial College in London, gold-plated at GSI and assembled. Starting already in 2006, off-line tests of the trap electrode structure were performed at Mainz University [5, 6]. It was operated in radio-frequency mode and loaded from an external argon ion sputter gun. Ar^+ ions were successfully stored for extended periods of time, and the obtained results have shown that the trap operated close to the expected parameters. In the next step, the trap will be mounted into the SPECTRAP magnet, and the work on the mechanical and electronic tasks for the purpose has started.

Figure 1: The RETRAP setup before shipment to GSI

In addition, the first laser system for the planned laser spectroscopy experiments was constructed and tested at Mainz University [6]. It consists of an external cavity diode laser, a reference Fabry-Perot interferometer for frequency locking and the corresponding electronics. Using a red laser diode (670 nm) the system was successfully tested by exciting Li atoms and observing the fluorescence. Future laser systems may include diodes with different wavelengths, ranging from 397 nm (UV) to 1550 nm (IR).

References

[1] T. Beier *et al.*, Nucl. Instr. Meth. Phys. Res. B **235**, 473 (2005)

[2] M. Vogel, D.F.A. Winters, D.M. Segal, R.C. Tompson, Rev. Sci. Ins. **76**, 103102 (2005)

[3] L. Gruber, J.P. Holder, D. Schneider, Physica Scripta **71**, 60 (2005)

[4] G. Gabrielse, L. Haarsma, S.L. Rolston at Int. J. of Mass Spect. and Ion Proc. **88**, 319, (1989)

[5] Jörg Krämer, diploma thesis, Mainz University - Institut für Kernchemie, (March 2007)

[6] Zoran Andjelkovic, diploma thesis, Mainz University - Institut für Kernchemie, (October 2007)

*Work supported by HGF under contract VH-NG-148 and the GSI F&E program.

Single-shot emittance measurements at HLI and HITRAP*

J. Pfister† [1,2], O. Kester[2], L. Dahl[2], T. Hoffmann[2], P. Forck[2], and U. Ratzinger[1]
[1]Institut für Angewandte Physik, J.W. Goethe-Universität Frankfurt, Germany; [2]GSI, Darmstadt, Germany

HITRAP is an ion trap facility which is designed for deceleration and cooling of highly charged ions produced by the GSI-accelerator facilities. The ions are decelerated in the ESR and then ejected at 4 MeV/u. Subsequently they are further decelerated by the HITRAP linac [1]. Since the HITRAP decelerator gets an ion bunch from the ESR every 50-60 seconds, it is necessary during linac commissioning to measure the transverse emittance within a single shot. The pepperpot method is the ideal choice for this task, because the horizontal and vertical emittance are measured at the same time.

The GSI pepperpot emittance meter was built during the late nineties for high current emittance measurements at the UNILAC [2]. The ion beam is shot through a plate with a regular matrix of apertures. The beam spots of the transmitted ions are detected via scintillation on a phosphor screen, which is caught by an cooled CCD camera. Assuming that the aperture holes are points and by knowledge of the distribution of the scintillation on the phosphor one can calculate the transverse emittances only from geometry.

Measurements at the UNILAC revealed problems in the emittance evaluation from pepperpot measurements. The emittance values were always larger than the values determined with the slit grid method. In order to proof the reliability of the pepperpot device, a comparison with the "non-destructive evaluation method" was done at HLI prior to the HITRAP measurements. Measurements were taken with both methods under the same beam conditions. Data evaluation showed that the pepperpot measurements showed approx. 50%–100% bigger emittances than the other method - no matter how the settings of the pepperpot measurements were changed. Single-shot emittance results of HLI were 14.3mm·mrad in horizontal and 13.0mm·mrad in vertical direction compared to the non-destructive evaluation with horizontal 5.9mm·mrad and vertical 10.4mm·mrad. The data analysis of the correct emittance from pepperpot measurements is done by the following scheme. The background is cut in 1% steps of the maximum intensity and the emittance was calculated for each cut. Therewith one gets a curve shown in fig.1 that is linear only in a region, where the real beam is cut. By extrapolation to the 0% cut the real emittance of the ion beam is determined.

The pepperpot system was transfered to the reinjection channel for the first two commissioning beam times of the HITRAP Double Drift Bunchers (DDB). First HITRAP measurements were done with $^{64}Ni^{28+}$. It was found that the resolution of the current pepperpot aperture plate was not sufficient due to ion beam diameter restrictions. For

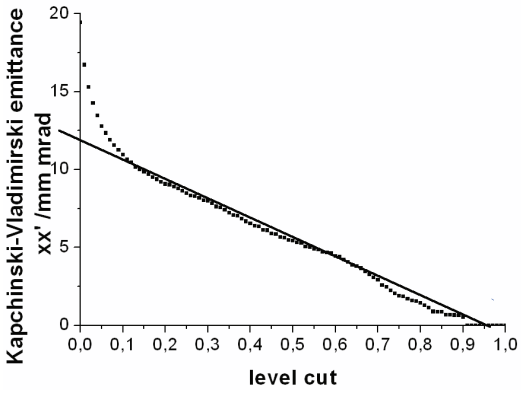

Figure 1: Emittance evaluation through stepwise level cuts for a $^{64}Ni^{28+}$beam at HLI

the second beam time in August the original aperture plate with 2.5mm hole distance was replaced by a 1.6mm one. The change of the pepperpot aperture made a reprogramming of the evaluation software necessary. This process is still going on. Emittances can already be analyzed and ellipses can be printed (see fig.2). Display of the distribution in phase space will be available soon.

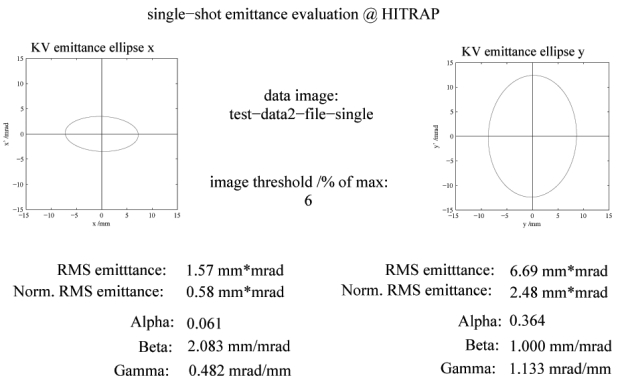

Figure 2: Emittance analysis of the beam from the HITRAP DDB measured with a $^{20}Ne^{10+}$-beam

References

[1] HITRAP webpage of AP division at GSI, `http://www.gsi.de/forschung/ap/projects/hitrap/index_e.html`.

[2] T. Hoffmann et al., "Emittance measurements of high current heavy ion beams using a single shot pepperpot system",AIP Conference Proceedings, November 2000, volume 546, p.432-439.

* Work supported by BMBF contract No. 06 FY160I.
† j.pfister@gsi.de

An ultracold atom target for experiments with highly charged ions at HITRAP*

W. Salzmann[1], I. Blank[1], S. Götz[1], V.G. Hasan[2], R. Hoekstra[2], O. Kester[3], T. Mullins[1], W. Quint[3], A. Sokolov[3], M. Weidemüller[1], and R. Wester[1]

[1]Universität Freiburg, Germany; [2]KVI Groningen, The Netherlands; [3]GSI, Darmstadt, Germany

An ultracold target of rubidium atoms is realized for scattering experiments at the GSI-HITRAP facility. First experiments shall focus on fully kinematically resolved multiple electron-transfer reactions in collisions of many-electron atoms with highly charged ions such as Rb + U^{92+}. Our particular interest in these reactions is the influence of correlation effects in the multi-electron transfer which will be used to investigate the dynamics in quantum mechanical many-particle systems. For precise experiments on such systems, laser cooling represents an excellent possibility to prepare cold targets of many electron atoms.

As thermal motion blurs the momenta of collision products, cooling of targets to lowest temperatures is required. Ideally, control over internal degrees of freedom on the target atoms is provided in order to isolate specific effects, caused by the target atoms electronic properties, such as excitation or orientation. To date such targets of alkali atoms can be prepared by means of laser light for cooling, trapping and electronic manipulation. For multi-electron targets laser cooling represents an alternative to supersonic jets, where comparable momentum resolution cannot be achieved for heavy atom targets.

The Freiburg ultracold target consists of a gas of rubidium atoms which are stored in a magneto-optical trap (MOT) at densities of $10^{11}cm^{-3}$ in a volume of 0.8mm diameter. The temperature of the captured gas is around 100μK which corresponds to momentum uncertainties of individual target atoms of 0.01a.u. The trap captures atoms of the isotope ^{85}Rb with nearly 100% isotope selectivity, and can, if desired, be changed to store ^{87}Rb. Furthermore, the trap operates in a so-called DarkSPOT[1] configuration, which allows 99% of the target atoms to be stored in a single hyperfine state of the electronic ground state. By using optical pumping techniques the electronic configuration of atoms can be controlled with high precision, including their alignment by pumping into a specific m_F magnetic hyperfine state.

For kinematically resolved electron transfer reactions, rubidium recoil ions produced in the collision are momentum analyzed using Recoil-Ion-Momentum Spectroscopy[2] (RIMS). Therefore the setup will be equipped with a special RIMS-spectrometer which provides sufficient access for trapping lasers and allows the detection of recoil ion momenta with high precision[3]. The setup for the ultracold target is fully transportable so it can be implemented into various setups, e.g. the HITRAP facility or the new USR storage ring for antiprotons at FLAIR.

In relation to the planned experiments at HITRAP, we recently performed experiments on double electron transfer in keV Na + O^{6+} collisions using the ultracold Na target at the KVI in Groningen.. The results show two reaction channels which are distinguished by their Q-value, as shown in fig. 1. A dominant peak occurs at small Q-values between 0 and -20eV. It corresponds to the sequential transfer of two electrons into asymmetric final configurations with different principal quantum numbers[4] (3lnl', n>4). A smaller peak at Q-values around -50eV represents the transfer of two electrons into a symmetric configuration 3l3l'. As this transfer occurs simultaneously[4], correlations between the according electrons can be expected to influence its dynamics, which shall be reflected by the dependency of its cross section on the period while the reactants interact, i.e. the reaction energy. The data obtained as a function of energy are currently under analysis and show exciting and also unexpected features.

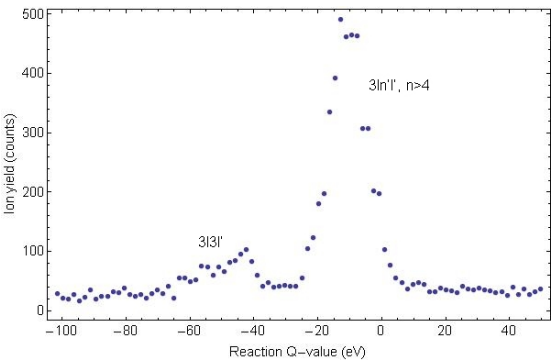

Fig. 1: Q-value spectrum of electron transfer reaction in Na + O^{6+} collisions at 8.6 keV/u. Reaction channels result in a symmetric final configuration (3l3l') and asymmetric configurations (3lnl', n>4)[4] of the two electrons.

Another interesting prospect for ultracold, laser-cooled atoms is the preparation of strongly localized electron targets. These can be created in an elegant manner by excitation of trapped atoms to high lying Rydberg states where electrons are bound by less than 1meV while still being localized at the position of the trap. By using coherent excitation schemes[5], up to 90% of the trapped atoms can be excited, resulting in dense samples of Rydberg atoms which may be used as electron targets e.g. for recombination experiments.

This work is supported by BMBF and the GSI F&E Programme.

[1] W.Ketterle *et al.*, Phys. Rev. Lett. **70**, 2253 (1993)
[2] J. Ullrich *et al.*, Rep. Prog. Phys. **66**, 1463 (2003)
[3] Courtesy of N.Andersen, University of Copenhagen
[4] S.Knoop *et al*. Europhys. Lett. **74**, 992 (2006)
[5] T. Amthor *et al.*, Phys. Rev. Lett. **98**, 023004 (2007).

Hyperfine splitting in highly charged B-like ions *

A. V. Volotka[1], D. A. Glazov[1,2], N. S. Oreshkina[2], G. Plunien[1],
V. M. Shabaev[2], and I. I. Tupitsyn[2]
[1]Technische Universität Dresden, Germany; [2]St. Petersburg State University, Russia

Previous high-precision measurements of the ground-state hyperfine splitting in heavy H-like ions [1-5] intended to probe QED in the strong external electromagnetic field generated by a heavy nucleus. However, accurate calculations (see Ref. [6] and references therein) later revealed that the uncertainty of the predicted splittings, which mainly originates from the nuclear magnetization distribution correction (Bohr-Weisskopf effect), is comparable in magnitude with the QED correction. Accordlingly, a direct identification of QED effects on the hyperfine splitting in heavy H-like ions appeared to be unfeasible. It was shown instead, that this uncertainty can be significantly reduced in a specific difference of the hyperfine splitting values of H- and Li-like ions with the same nucleus [7]. High-precision measurements of the hyperfine splitting in heavy Li-like ions are presently in preparation [8].

The motivation for accurate calculations of the hyperfine splitting in B-like ions is twofold. From one side, high-precision prediction of the hyperfine splitting of B-like Fe may be important for astronomical search [9]. From the other side, the study of the hyperfine splitting in heavy B-like ions can be used to reduce the uncertainty associated with the Bohr-Weisskopf effect in some specific difference of the hyperfine splitting values for B- and Li-like ions or B- and H-like ions. The origin of this reduction is essentially the same as for the related g-factor values [10].

In a recent work [11] we have calculated the ground-state hyperfine splitting of B-like ions. The interelectronic-interaction correction of first order in $1/Z$ is evaluated within a rigorous QED approach. The higher-order terms are calculated employing the large-scale configuration-interaction Dirac-Fock-Sturm method. Table 1 presents the individual contributions and the total theoretical results for the ground-state hyperfine splitting in heavy B-like ions of particular interest. It can be seen that the uncertainties of the total theoretical values are completely determined by the Bohr-Weisskopf effect. These uncertainties can be strongly reduced employing the experimental values for the hyperfine splitting in the corresponding H-like ions. We use the experimental values for the ground state hyperfine splitting, $\Delta E^{(1s)}_{\rm exp} = 1.2159(2)$ eV for H-like ^{207}Pb^{81+} [4] and $\Delta E^{(1s)}_{\rm exp} = 5.0840(8)$ eV for H-like ^{209}Bi^{82+} [1], to extract the Bohr-Weisskopf corrections for the $1s$ state employing the theoretical values for all other contributions from Ref. [6]. Considering different models for the nuclear magnetization distribution, we have found that the ratio of the Bohr-Weisskopf corrections is rather stable, $\varepsilon^{(2p)}_{\rm Pb}/\varepsilon^{(1s)}_{\rm Pb} = 0.287(2)$ for Pb and $\varepsilon^{(2p)}_{\rm Bi}/\varepsilon^{(1s)}_{\rm Bi} = 0.295(2)$ for Bi. It allows us to deduce the following values for B-like ions: $\varepsilon^{(2p)}_{\rm Pb} = 0.0119(2)$ and $\varepsilon^{(2p)}_{\rm Bi} = 0.00437(15)$. The total theoretical values, which include also the modification of the Bohr-Weisskopf effect on the interelectronic-interaction correction, amount to $62.24(2)$ meV for ^{207}Pb^{77+} and $257.84(5)$ meV for ^{209}Bi^{78+}. It should be stressed that the uncertainty of these values is not equal to the sum of the uncertainties of the individual contributions. This is due to the fact, that the total hyperfine splitting value found in this way is sufficiently stable with respect to possible variations of the nuclear parameters. As a result, the most accurate theoretical predictions for the hyperfine splitting values of high-Z boronlike ions have been obtained.

Table 1: Contributions to the ground-state hyperfine splitting of B-like ions, in meV. The total error bars indicated do not include the nuclear magnetic moment uncertainties.

Effect	^{207}Pb^{77+} $\frac{\mu}{\mu_N} = 0.59258$	^{209}Bi^{78+} $\frac{\mu}{\mu_N} = 4.1106$
Dirac value	71.89	296.35
Finite nuclear size	−2.18(1)	−9.84(5)
Bohr-Weisskopf (direct calculation)	−0.84(8)	−0.97(34)
$1/Z$ corr.	−6.82	−28.17
$1/Z^2$ and h.o. corr.	0.24(1)	0.98(3)
QED	−0.06(1)	−0.26(3)
Total	62.23(8)	258.09(35)
Bohr-Weisskopf (from the $1s$ exp.)	−0.83(1)	−1.25(4)
Total	62.24(2)	257.84(5)

References

[1] I. Klaft *et al.*, Phys. Rev. Lett. **73**, 2425 (1994).
[2] J. R. C. López-Urrutia *et al.*, Phys. Rev. Lett. **77**, 826 (1996).
[3] J. R. C. López-Urrutia *et al.*, Phys. Rev. A **57**, 879 (1998).
[4] P. Seelig *et al.*, Phys. Rev. Lett. **81**, 4824 (1998).
[5] P. Beiersdorfer *et al.*, Phys. Rev. A **64**, 032506 (2001).
[6] V. M. Shabaev, Phys. Rep. **356**, 119 (2002).
[7] V. M. Shabaev *et al.*, Phys. Rev. Lett. **86**, 3959 (2001).
[8] D. F. A. Winters *et al.*, Can. J. Phys. **85**, 403 (2007).
[9] R. A. Sunyaev and D. Docenko, Astron. Lett. **33**, 67 (2007).
[10] V. M. Shabaev *et al.*, Phys. Rev. Lett. **96**, 253002 (2006).
[11] N. S. Oreshkina *et al.*, Phys. Lett. A **372**, 675 (2008).

* Work supported by BMBF, DFG, GSI F+E and INTAS-GSI.

Nuclear deformation effect on the binding energies in heavy ions *

Y. S. Kozhedub[1], O. V. Andreev[1], V. M. Shabaev[1], I. I. Tupitsyn[1], C. Brandau[2], C. Kozhuharov[2], G. Plunien[3], and T. Stöhlker[2]

[1]St.Petersburg State University, Russia; [2]GSI, Darmstadt, Germany; [3]Technische Universität Dresden, Germany

The finite-nuclear-size correction to the atomic energy levels is sufficiently well determined by the root-mean-square (rms) radius of the nucleus. The uncertainty due to this correction has usually been estimated by adding (quadratically) two errors, one obtained by varying the rms radius within its error bar, and the other obtained by changing the nuclear charge distribution from the Fermi-type to the homogeneously-charged-sphere model. This rather conservative estimate was sufficient in so far as the total theoretical uncertainty was mainly determined by other contributions. Recent progress made in calculations of higher-order QED-radiative and electron-correlation corrections (see Refs. [1, 2, 3, 4] and references therein) and in view of the current status of precision experiments with heavy few-electron ions [5, 6, 7, 8], however, require a more accurate consideration of the nuclear shape and deformation effects.

We have studied [9] the finite nuclear-size correction in the general case of a deformed nucleus. Approximate analytical formulas for this effect are derived, and direct numerical calculations are performed. In the case of ^{238}U, where the most accurate experimental data were recently reported [6, 7], our study combined with a compilation by Angeli [10] yields a new value for the rms radius $\langle r^2\rangle^{1/2} = 5.8569(33)$ fm. This value is employed to revise the nuclear-size corrections to the binding energies in H- and Li-like uranium. We find that a calculation of the nuclear-size correction for $^{238}U^{91+}$ to a 0.1% accuracy requires to account for the nuclear deformation effect [9]. In Tables 1 and 2 the individual contributions to the $1s$ Lamb shift in $^{238}U^{91+}$ and to the $2p_{1/2} - 2s$ transition energy in $^{238}U^{89+}$ are presented. The presented results differ from the previous compilations [1, 2, 3, 4] by the values of the finite nuclear-size corrections and provide significant improvements of the theoretical predictions for both H- and Li-like uranium. While in Refs. [1, 2, 3, 4] the total theoretical uncertainties were mainly determined by the finite nuclear-size corrections, now they are mainly defined by higher-order QED effects. It can be seen from the tables that our theoretical results agree well within the error bars with the most precise experimental data.

From the analytical and numerical investigations [9] we conclude, that, if the rms radius is known to a rather good accuracy, calculations of the nuclear-size correction should include the nuclear deformation effect.

* Work supported by BMBF, GSI F+E and INTAS-GSI.

Table 1: Individual contributions to the ground-state Lamb shift in $^{238}U^{91+}$, in eV.

Finite nuclear size	198.54(19)
First-order QED	266.45
Second-order QED	-1.26(33)
Nuclear recoil	0.46
Nuclear polarization	-0.20(10)
Total theory	463.99(39)
Experiment, Ref. [6]	460.2(4.6)

Table 2: Individual contributions to the $2p_{1/2} - 2s$ transition energy in $^{238}U^{89+}$, in eV.

One-electron nuclear size	-33.30(3)
One-photon exchange	368.83
One-electron first-order QED	-42.93
Two-photon exchange	-13.37
Screened QED	1.16
One-electron second-order QED	0.22(6)
Three- and more photon effects	0.14(7)
Nuclear recoil	-0.07
Nuclear polarization	0.03(1)
Total theory	280.71(10)
Experiment, Ref. [7]	280.645(15)
Experiment, Ref. [11]	280.59(10)
Experiment, Ref. [5]	280.52(10)

References

[1] V. A. Yerokhin *et al.*, Phys. Rev. Lett. **91**, 073001 (2003).

[2] V. M. Shabaev *et al.*, Int. J. Mass Spectrom. **251**, 109 (2006).

[3] V. A. Yerokhin *et al.*, Phys. Rev. Lett. **97**, 253004 (2006).

[4] V. M. Shabaev *et al.*, AIP Conference Proceedings, **869**, 52 (2007).

[5] C. Brandau *et al.*, Phys. Rev. Lett. **91**, 073202 (2003).

[6] A. Gumberidze *et al.*, Phys. Rev. Lett. **94**, 223001 (2005).

[7] P. Beiersdorfer *et al.*, Phys. Rev. Lett. **95**, 233003 (2005).

[8] C. Brandau *et al.*, Phys. Rev. Lett., in press.

[9] Y. S. Kozhedub *et al.*, submitted to Phys. Rev. A; E-print/physics/0711.4607.

[10] I. Angeli, At. Data Nucl. Data Tables **87**, 185 (2004); revised in 2007, I. Angeli, private communication.

[11] J. Schweppe *et al.*, Phys. Rev. Lett. **66**, 1434 (1991).

Magnetic Moments of Highly Charged Ions: Determination of g-Factors by Double-Resonance Spectroscopy

U.D. Jentschura[1,2], D.L. Moskovkin[3], B. Nikoobakht[1,2], W. Quint[4], V.M. Shabaev[3], and M. Vogel[4,5]

[1]Max-Planck-Institut f. Kernphysik, Heidelberg, Germany; [2]Inst. f. Theor. Physik, Univ. Heidelberg, Germany; [3]Department of Physics, St. Petersburg State University, Russia; [4]GSI, Darmstadt, Germany; [5]Department of Physics, Imperial College London, UK

In the current contribution, we summarize recent experimental-theoretical proposals to obtain access to nuclear properties and/or fundamental constants via double-resonance laser spectroscopy, in combination with trapped hydrogenlike ions. Double-resonant excitation schemes have been discussed at length in the literature, and still, they offer us surprising insight into some well-hidden properties of the ions, as we keep them in a situation of "perpetual check", thus interrogating them in the most revealing way possible with laser and microwave fields.

We here offer proposals for accurate measurements of the g_F factor of a high–Z hydrogenlike ion (nucleus with spin) and of the g_J factor of an electron in the ground state of a low–Z hydrogenlike ion (spinless nucleus).

Thus, in the first proposal, we consider a hydrogenlike ion of high nuclear charge, whose nucleus has a spin, in a magnetic field. In this case, there is the Zeeman splitting of the hyperfine sublevels which needs to be considered in the weak-field regime, i.e. every hyperfine sublevel splits up into individual Zeeman components. The double-resonance scheme in this case involves (i) microwave transitions among the Zeeman sublevels of the hyperfine level, and (ii) laser-induced, optical transitions among the hyperfine levels of the hydrogenlike ion. One transition acts as the probe of the other. The g_F factor of the electron can thus be determined with unprecedented accuracy.

In the second proposal, an ion with low nuclear charge is considered in a bound state, where we suppose that the nucleus is spinless. In this case, the microwave transition is between the ground-state Zeeman components, whose separation is proportional to the electron g_J factor, and the laser-induced, ultra-violet transition is between states of different principal quantum number of the hydrogenlike ion. As compared to the continuous Stern–Gerlach effect, we expect much better statistics and envisage accurate measurements on an accuracy level of 10^{-12} and beyond.

Let us start this brief review with the g_F factor.

The energy of the ground state hyperfine splitting (HFS) in hydrogen-like and lithium-like ions scales with the nuclear charge Z as Z^3 and shifts into the laser-accessible region above $Z \approx 60$. The corresponding upper state lifetime scales as Z^{-9} and thus acceptable fluorescence rates from the magnetic dipole (M1) transitions in the HFS make accurate measurements of the transition by means of laser spectroscopy possible. The $1s$ ground state HFS in hydrogen-like ions has been measured in the following species: $^{165}\mathrm{Ho}^{66+}$, $^{185,187}\mathrm{Re}^{74+}$, $^{203,205}\mathrm{Tl}^{80+}$, $^{207}\mathrm{Pb}^{81+}$ and $^{209}\mathrm{Bi}^{82+}$.

These measurements have either been carried out at the "Experimental Strorage Ring" ESR at the "Gesellschaft für Schwerionenforschung" GSI, Darmstadt, Germany or in an Electon Beam Ion Trap (EBIT). A common experimental limitation to the accuracy for the storage ring measurements is the Doppler width of the transition due to the relativistic velocities of the ions. The measurements performed in an EBIT are not as severely subjected to this effect, but suffer from a low signal-to-noise ratio. The relative precision of these measurements is limited to a value of the order of 10^{-4}.

A novel measurement scheme has been outlined which will allow measurements of the hyperfine frequencies with well-localised particles nearly at rest [1]. This reduces the Doppler width and shift to a level of $\Delta\lambda/\lambda = 10^{-7}$ of the measured transition, which is three orders of magnitude lower than in any previous experiment. An extension of such an experiment using a double-resonance scheme will thus allow precise determinations of g-factors in the ion of interest. This allows sensitive tests of corresponding calculations of the transition energy and lifetime, especially of contributions coming from bound-state QED [2, 3, 4].

The principle of the present laser-microwave double resonance technique is to use fluorescence light from an optical hyperfine transition as a probe for a microwave transition between corresponding Zeeman sublevels which yields the g_F-factor of the electron. Several cases need to be distinguished depending on the values of the nuclear magnetic moment of the ion and details of the HFS. As an example, the case of uranium $^{235}\mathrm{U}^{91+}$ is depicted in figure 1. The inversion of the level scheme does not allow a population of states, but it allows a depopulation of states with extremal m_F, which again can be used for a laser-microwave double resonance experiment:

An initial depopulation of the ($F = 4$, $m_F = 4$) state can be obtained by irradiation of σ^- light at a frequency ω_1. When the depopulation is reached, the corresponding fluorescence including the π-fluorescence light vanishes. When microwave radiation at frequency ω_{MW} comes into resonance with the ($F = 4, m_F = 3 \leftrightarrow 4$) transition as shown in figure 1 the π-fluorescence reappears. Thus, from a scan of the π-fluorescence as a function of ω_{MW} the corresponding g_F-factor can be inferred.

The proposed technique basically is an extension of

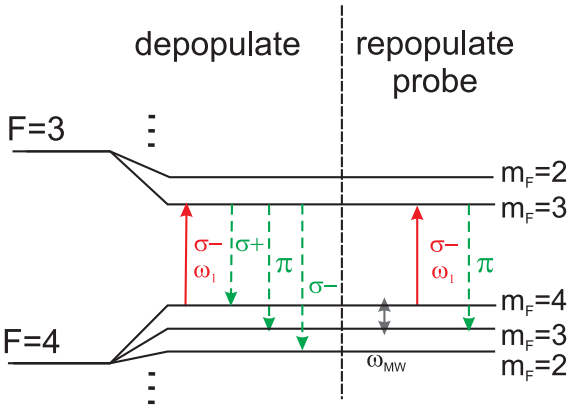

Figure 1: Scheme of the Zeeman-split hyperfine energy levels in the ground state of a hydrogen- like ion with $\mu/\mu_N < 0$ and $I = 7/2$ and the measurement principle for the double-resonance technique. Solid arrows indicate excitation lasers.

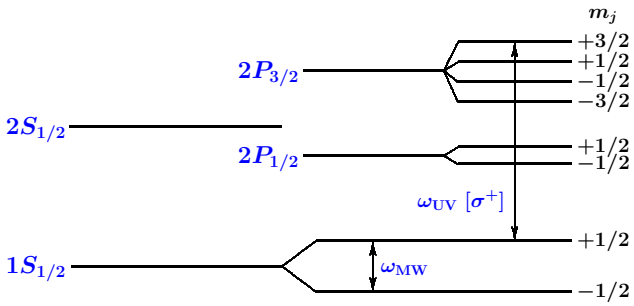

Figure 2: Laser-microwave double-resonance excitation scheme using circularly polarized UV light for excitation of the $1S_{1/2} \Leftrightarrow 2P_{3/2}$ transition and a microwave field for driving the spinflip transition $1S_{1/2}\left(m_j{=}+\frac{1}{2}\right) \Leftrightarrow 1S_{1/2}\left(m_j=-\frac{1}{2}\right)$, in $^4\mathrm{He}^+$. A spinflip among the ground-state Zeeman sublevels is detected by presence/lack of fluorescence for the $1S_{1/2} \Leftrightarrow 2P_{3/2}$ transition.

the HFS laser spectroscopy experiment outlined in [1] to the use of the aforementioned double resoncance techniques. Briefly, a mass and charge-state selected ensemble of cooled and bunched highly-charged ions from the HITRAP facility will be injected into a cryogenic Penning trap designed for laser spectroscopy. During confinement, the ions will remain cooled at a motional temperature of about 4 K, radially compressed by use of a rotating wall technique and excited by a combination of laser and microwave irradiation as discussed. The fluorescence signal will be detected either axially or radially.

Let us continue with the g_J factor.

The bound-electron (Landé) g_j factor for an electron bound in an ion with a spinless nucleus is a constant factor relating the Zeeman energy ΔE in the magnetic field B (directed along the z axis) and the Larmor precession frequency ω_{L} to the magnetic spin projection $m_j = -\frac{1}{2}, \frac{1}{2}$ onto that same z axis. In natural units, we have

$$\Delta E = m_j\,\omega_{\mathrm{L}} = m_j\,g_j\,\mu_{\mathrm{B}}\,B\,, \qquad (1)$$

where $\mu_{\mathrm{B}} = -e/(2m_e)$ is the Bohr magneton, expressed in terms of the electron charge e and the electron mass m_e. Deviations from the Dirac–Breit prediction $g_j(1S) = 2\,(1 + 2\sqrt{1-(Z\alpha)^2})/3$ are due to quantum electrodynamic (QED), nuclear and other effects. The current proposal is based on a Penning trap and is studied here in conjunction with the hydrogen-like helium ion $^4\mathrm{He}^+$, which seems to be well suited for an experimental realization in the near future. The basic excitation scheme is presented in Fig. 2.

In the $^4\mathrm{He}^+$ system, the total angular momentum is equal to the total electron angular momentum J. In the presence of the magnetic field B in the Penning trap, the excited state $2P_{3/2}$ is split into four Zeeman sublevels $\Delta E = m_j\,g_j(2P_{3/2})\,\mu_{\mathrm{B}}\,B$, with $m_j = \pm\frac{1}{2}, \pm\frac{3}{2}$. The Landé g factor of the upper level of the excitation scheme can be obtained easily [5], $g_j(2P_{3/2}) = \frac{4}{3} + \frac{\alpha}{3\pi} - \frac{2}{15}\,(Z\alpha)^2 + \ldots$. A single $^4\mathrm{He}^+$ ion in the Penning trap is prepared in the Zeeman sublevel $m_j = \frac{1}{2}$. Narrow-band ultraviolet (UV) electromagnetic radiation with σ^+ polarization and angular frequency $\omega_{\mathrm{UV}} = 2\pi \times 9.87 \times 10^{15}\,\mathrm{Hz}$ drives the Lyman-α transition $1S_{1/2}\left(m_j{=}+\frac{1}{2}\right) \Leftrightarrow 2P_{3/2}\left(m_j{=}+\frac{3}{2}\right)$, see Fig. 2. This is a closed cycle because decay by emission of a fluorescence photon is only possible to the initial state $1S_{1/2}\,(m_j = +\frac{1}{2})$ (if one ignores one-photon ionization into the continuum). Due to the short lifetime of the upper state, fluorescence intensity of $[2\,\tau(2p_{3/2})]^{-1} \approx 5.01 \times 10^9$ photons/s under saturation conditions makes it possible to detect a single trapped ion with very high sensitivity.

A successful excitation of the spinflip transition results in an instantaneous stop of the fluorescence intensity, because the lower Zeeman level $1S_{1/2}\left(m_j = -\frac{1}{2}\right)$ is not excited by the narrow-band Lyman-α radiation. A quantum jump is thus directly observed with essentially 100% detection efficiency. A second spinflip $1S_{1/2}\left(m_j = -\frac{1}{2}\right) \rightarrow 1S_{1/2}\left(m_j = +\frac{1}{2}\right)$ restores the fluorescence intensity, and the measurement scheme could thus reach very good statistics [5].

This work is supported by the GSI F&E Programme and the EU INTAS Programme.

References

[1] M. Vogel *et al.*, Nucl. Inst. Meth. B **235**, 7 (2005).

[2] V.M. Shabaev, J. Phys. B **27**, 5825 (1994).

[3] V.M. Shabaev *et al.*, Phys. Rev. A **56**, 252 (1997).

[4] D.L. Moskovkin *et al.*, Phys. Rev. A **70**, 032105 (2004).

[5] W. Quint *et al.*, Pis'ma ZhETF **87**, 36 (2008).

Diatomic systems containing antihydrogen *

Vasily Sharipov[1], Leonti Labzowsky[1], and Günter Plunien[2]
[1]St. Petersburg State University, Russia; [2]Technische Universität Dresden, Germany

Experimental success in production of antihydrogen ($\bar{\mathrm{H}}$) atoms [1, 2] has stimulated investigations of atom-$\bar{\mathrm{H}}$ systems. In these experiments the $\bar{\mathrm{H}}$ atoms were produced in Rydberg (highly excited) states. Trapping of antihydrogen atoms in external (electromagnetic) fields will allow for comparative spectroscopic investigation of $\bar{\mathrm{H}}$ atoms as well as their interactions with ordinary matter atoms. Also in regard to future experiments at FLAIR for investigating fundamental interactions it is important to develop an adequate description of excited states of atom-$\bar{\mathrm{H}}$ systems. In this context the need for the account of influences of external electromagnetic fields on spectroscopic properties of H (and $\bar{\mathrm{H}}$) atoms should also be mentioned; a first determination of the limit of accuracy in high-precision spectroscopy experiments has been provided in [3]. A proper description of diatomic matter-antimatter systems has been presented and applied to the hydrogen-antihydrogen ($\mathrm{H}\bar{\mathrm{H}}$) [4], [5] and helium-antihydrogen ($\mathrm{He}\bar{\mathrm{H}}$) quasimolecules [6], respectively. The method of calculation is briefly reported in the following.

Within the adiabatic approximation the potential energy curves and the leptonic part of the wave functions corresponding to different values of the leptonic orbital angular momentum projection Λ onto the internuclear (molecular) axis are calculated employing the Ritz variational principle. Adiabatic corrections to the leptonic potentials are also obtained. Basis functions are constructed as products of explicitly correlated Gaussians and spherical harmonics which describe correctly the motion of leptons with arbitrary orbital angular momentum projection onto the molecular axis. The hadronic part of the wave function for each leptonic level of the hydrogen-antihydrogen and helium-antihydrogen systems is calculated by solving the Schrödinger equation with the obtained leptonic potentials. Corresponding solutions are generated utilizing precise B-spline representations. Employing leptonic and hadronic parts of the wave function and obtained potential curves a complex non-local optical potential in the form proposed in [7] is constructed. This potential describes non-adiabatic effects which can take place in the atom-$\bar{\mathrm{H}}$ system, namely the ejection of the positronium atom. With the calculated wavefunctions the electron-positron and proton-antiproton annihilation rates are computed for a variety of quasimolecular states. The positronium ejection decay rates are also computed for the quasimolecular levels under consideration.

The method described above being applied to the $\mathrm{H}\bar{\mathrm{H}}$ and $\mathrm{He}\bar{\mathrm{H}}$ systems gives the following results: Typical lifetimes of excited states of the $\mathrm{H}\bar{\mathrm{H}}$ quasimolecule (due to hadronic annihilation and Ps atom ejection) lay within the range of about $10^{-13} - 10^{-15}$ sec. What concerns the $\mathrm{He}\bar{\mathrm{H}}$ system the existence of metastable states with a lifetime about few μsec is predicted [6]. These states are characterized by larger values of the leptonic orbital angular momentum projection Λ onto the internuclear axis and arise when the He atom in the ground state and $\bar{\mathrm{H}}$ atom in a Rydberg state interact. It can be seen from Fig. 1 that in this case the positron remains highly excited over the entire range of internuclear distance and therefore, the properties of the $\mathrm{He}\bar{\mathrm{H}}$ quasimolecule in states with large values of Λ are nearly the same as the properties of helium-antiproton system.

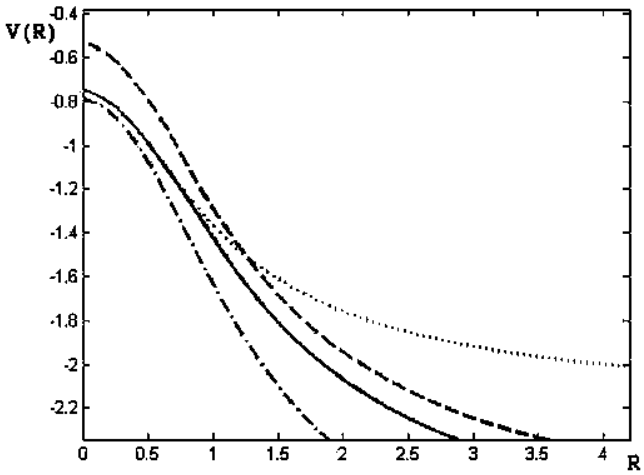

Figure 1: The leptonic potentials for the ground state ($\Lambda = 0$ dash-dotted line) and for excited states ($\Lambda = 1$ solid line, $\Lambda = 30$ dashed line) are plotted versus the internuclear distance R (in atomic units a_0). The potential for the lowest state of the $\mathrm{He}^+\overline{p}$ + unbound Ps system $V_{\mathrm{Ps}}(R)$ (dotted line) is also plotted. The potential $V_1^{\mathrm{lep}}(R)$ approaches $V_{\mathrm{Ps}}(R)$ near the critical internuclear distance $R_{\mathrm{c}} = 0.7a_0$.

References

[1] M. Amoretti *et al.*, Nature **419**, 456 (2002).
[2] G. Gabrielse *et al.*, Phys. Rev. Lett. **89**, 213401 (2002); 233401 (2002).
[3] L. Labzowsky, G. Shedrin, D. Solovyev, and G. Plunien, Phys. Rev. Lett. **98**, 203003 (2007).
[4] V. Sharipov, L. Labzowsky, and G. Plunien, Phys. Rev. A **73**, 052503 (2006).
[5] V. Sharipov, L. Labzowsky, and G. Plunien, Phys. Rev. Lett. **97**, 103005 (2006).
[6] V. Sharipov, L. Labzowsky, and G. Plunien, Phys. Rev. Lett. **98**, 103001 (2007).
[7] B. Zygelman, A. Saenz, P. Froelich, and S. Jonsell, Phys. Rev. A**69**, 042715 (2004).

* Work supported by BMBF, GSI F+E and INTAS-GSI.

Nuclear lifetime prolongation in resonant electron recombination processes

A. Pálffy[1], Z. Harman[1], C. Kozhuharov[2], C. Brandau[2], C. H. Keitel[1], W. Scheid[3], and T. Stöhlker[2,4]

[1]Max-Planck-Institut für Kernphysik, Heidelberg; [2]GSI, Darmstadt, Germany; [3]Justus-Liebig-Universität, Giessen; [4]Ruprecht-Karls-Universität, Heidelberg

The population and lifetime of nuclear excited states are affected by the electronic shells, especially in nuclear processes which directly involve electrons [1]. In particular, the lifetime of low-lying excited nuclear states can be increased by the process of nuclear excitation by electron capture (NEEC) followed by fast x-ray emission (NEECX) in highly-charged heavy ions. In the resonant process of NEEC, the collision of an ion with a free electron leads to resonant capture into an atomic orbital with simultaneous excitation of the nucleus [2]. For some heavy nuclei, NEEC into the K shell is energetically forbidden. In this case, NEEC into the L shell of bare ions will be followed by a stabilizing x-ray decay that suppresses the internal conversion channel and limits the nuclear decay rate to the γ rate, thus modifying the lifetime and population of the nuclear excited state.

We find that NEECX occurring in the fully ionized $^{238}_{92}$U and $^{232}_{90}$Th actinides leads to both lifetime prolongation of the first nuclear excited state and increase of resonance strengths with up to two orders of magnitude compared to the cases where no x-ray stabilization of the system is possible [3]. In Table 1 we present the resonance strength for NEECX followed by γ decay into the excited $2s$, $2p_{1/2}$ and $2p_{3/2}$ atomic states of bare U^{92+} and Th^{90+} with subsequent x-ray decay to the $1s$ atomic ground state. For comparison, the resonance strengths for NEEC into ions with occupied K shell or L subshells followed by γ decay are given, where electronic capture into the ground state prevents subsequent x-ray emission. In Table 2 we present values for the mean lifetimes of the 44.910 keV level of $^{238}_{92}$U and of the 49.369 keV level of $^{232}_{90}$Th for neutral atoms and our theoretical results for H-like, Li-like, B-like and N-like ions formed via NEEC or NEECX.

NEECX into the L shell of bare $^{238}_{92}$U and $^{232}_{90}$Th ions is at present the most promising choice for an experimental verification of NEEC. The prolongation of the nuclear excited state lifetime can be particularly useful in reducing the background signal in a possible NEEC experiment with the studied actinide isotopes. A major difficulty in observing NEEC experimentally arises from background processes, in particular from radiative recombination (RR). For an NEECX experiment in the ESR storage ring using an electron target, the different time scales of RR and NEEC have as a result a spatial separation of the photon emissions. While the RR photons will be emitted instantaneously in the region of the electron target, the radiative decay of the nucleus will occur later, after the ions have already traveled a certain distance in the storage ring. By choosing isotopes with convenient excited-state lifetimes on the order of 10-100 ns, the spatial separation can be determined such that a direct observation of the γ photons following NEEC can be performed with almost complete suppression of the RR background.

In conclusion, our theoretical calculations show that the fast electronic x-ray decay following the resonant capture leads to a substantial increase of the nuclear excited state population and of the resonance strength of NEEC followed by γ decay of the nucleus. The enhancement of the γ photon yield and the convenient nuclear lifetimes of the heavy $^{238}_{92}$U and $^{232}_{90}$Th actinides can be particularly useful for the possible experimental observation of NEEC.

Table 1: Resonance strengths $S_{\rm NEEC}$ and $S_{\rm NEECX}$ for NEEC into He-like ($2s_{1/2}$), Be-like ($2p_{1/2}$) and C-like ($2p_{3/2}$) ions, and NEECX into bare U^{92+} and Th^{90+} ions, respectively, both followed by nuclear γ decay. nl_j denotes the capture orbital.

		He-, Be-, C-like ions	bare ions
^A_ZX	nl_j	$S_{\rm NEEC}$(b eV)	$S_{\rm NEECX}$(b eV)
$^{238}_{92}$U	$2s_{1/2}$	8.8×10^{-3}	5.4×10^{-2}
	$2p_{1/2}$	9.2×10^{-3}	1.58
	$2p_{3/2}$	2.7×10^{-3}	1.16
$^{232}_{90}$Th	$2s_{1/2}$	5.9×10^{-3}	2.0×10^{-2}
	$2p_{1/2}$	7.7×10^{-3}	6.5×10^{-1}
	$2p_{3/2}$	2.6×10^{-3}	5.5×10^{-1}

Table 2: Mean-lives τ of the first nuclear excited states of $^{238}_{92}$U and $^{232}_{90}$Th. τ_0 and τ_γ are the mean lifetimes corresponding to the neutral atom, and the bare ion or H-like ion with the electron in the ground state, respectively. Nuclear mean-lives of Li-like ($2s_{1/2}$), B-like ($2p_{1/2}$) and N-like ($2p_{3/2}$) ions in their electronic ground states are presented in the last column.

	neutral	bare/H-like		Li-, B-, N-like
^A_ZX	τ_0 (ns)	τ_γ (ns)	nl_j	τ_{nl_j} (ns)
$^{238}_{92}$U	0.292	185	$2s_{1/2}$	36.2
			$2p_{1/2}$	1.54
			$2p_{3/2}$	0.67
$^{232}_{90}$Th	0.497	150	$2s_{1/2}$	50.1
			$2p_{1/2}$	2.35
			$2p_{3/2}$	1.04

References

[1] F. Bosch *et al.*, Phys. Rev. Lett 77 (1996) 005190

[2] V.I. Goldanskii and V.A. Namiot, Phys. Lett. 62B (1976) 393, A. Pálffy, W. Scheid and Z. Harman, Phys. Rev. A 73 (2006) 012715

[3] A. Pálffy, Z. Harman, C. Kozhuharov, C. Brandau, C. H. Keitel, W. Scheid and T. Stöhlker, Phys. Lett. B (2008) accepted

Photoionization of He-like ions in the non-relativistic region *

A.I. Mikhailov[1], A.V. Nefiodov[1,2], and G. Plunien[2]

[1]PNPI, 188300 Gatchina, St. Petersburg, Russia; [2]Technische Universität Dresden, D-01062 Dresden, Germany

The single ionization of light atomic systems by photon impact is one of the fundamental processes, which is being persistently investigated during last decades. Although the non-relativistic problem for single photoeffect on H-like atoms was solved analytically a long time ago [1], the further generalization on the case of two-electron targets, such as, for example, the neutral He atom, is a non-trivial task. For theoretical calculations of ionization cross sections, it is usual to employ sophisticated numerical methods dealing with highly correlated wave functions. This allows one to take into account the electron correlations beyond the independent-particle approximation.

In work [2], we have investigated the single ionization of He-like ions by photons with non-relativistic energies ω characterized by $I \le \omega \ll m$, where I is the ionization threshold energy and m is the electron mass ($\hbar = 1$, $c = 1$). The dominant contribution of correlation effects to the cross section is calculated within the framework of non-relativistic perturbation theory. To first order, the problem is reduced to the evaluation of the one-photon exchange diagrams given in Fig. 1. The correlation corrections to the cross section arise due to modification of the binding energy and wave functions of the initial and final states. The cross section for single K-shell photoionization of He-

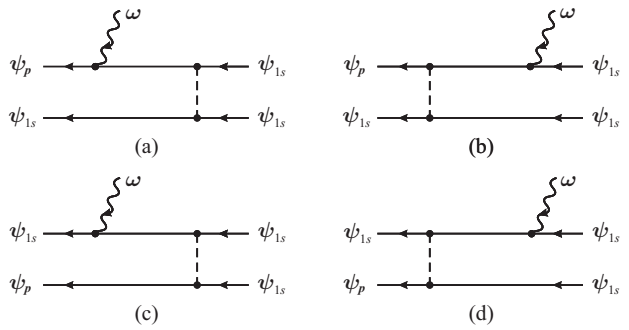

Figure 1: One-photon exchange diagrams.

like ions is given by [2]

$$\sigma^+ = \alpha a_0^2 \frac{2^{10}\pi^2}{3Z^2} \frac{\exp(-4\xi\,\mathrm{cot}^{-1}\,\xi)}{(1+\xi^{-2})^4[1-\exp(-2\pi\xi)]} \times \left\{1 + \left[\frac{\Delta_1}{\varepsilon_\gamma} + a_1(\xi)\right]\frac{1}{Z}\right\}, \quad (1)$$

where $a_0 = 1/(m\alpha)$ is the Bohr radius, $\xi = 1/\sqrt{\varepsilon_p}$, $\varepsilon_p = \varepsilon_\gamma - 1 + \delta_1$, $\delta_1 = \Delta_1/Z$, and $\Delta_1 = 5/4$. The energy of the incoming photon ω and that of the outgoing electron E_p are calibrated by the Coulomb binding energy

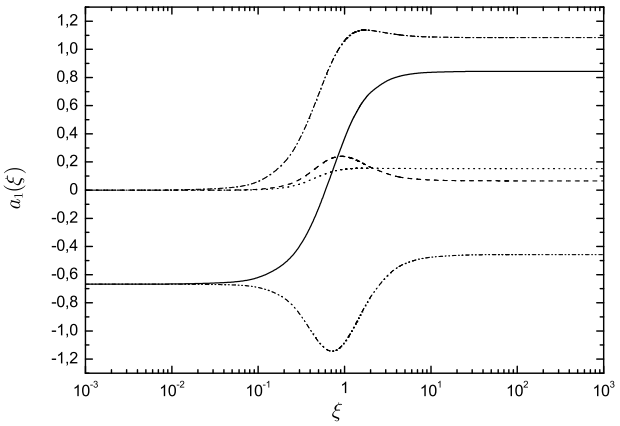

Figure 2: Different contributions to the universal function $a_1(\xi)$ calculated in Coulomb gauge. Contributions of individual diagrams: dash-double dotted line corresponds to Fig. 1(a); dash-dotted line corresponds to Fig. 1(b); dotted line corresponds to Fig. 1(c); dashed line corresponds to Fig. 1(d); solid line, total contribution of all diagrams.

$I = m(\alpha Z)^2/2$ according to $\varepsilon_\gamma = \omega/I$ and $\varepsilon_p = E_p/I$. The quantity $a_1(\xi)$ is a universal function of the dimensionless parameter ξ (see Fig. 2). Equation (1) is valid in the entire non-relativistic domain $1-\delta_1 \le \varepsilon_\gamma \ll 2(\alpha Z)^{-2}$. The function $a_1(\xi)$ describes the "dynamical correlation", originating from the correlated two-electron wave functions both in the initial and final states. Three characteristic domains can be distinguished here, namely, the threshold domain ($\xi \gg 1$), the transition domain ($\xi \simeq 1$), and the high-energy domain ($\xi \ll 1$). If $\xi \le 10^{-1}$ or $\xi \ge 10$, the function $a_1(\xi)$ saturates rapidly approaching the constant limits, while it undergoes significant changes within the range $10^{-1} \le \xi \le 10$. Within the threshold domain, the consistent account of the correlation interaction both in the initial and final states becomes especially crucial.

For some values of the parameter ξ, the correlation term in the square brackets in Eq. (1) vanishes. Accordingly, the cross section (1) coincides with the Coulomb expression. The effect of dynamical suppression of correlations can be also observed in the time-reversed process of the electron capture by hydrogen-like ions.

References

[1] M. Stobbe, Ann. Phys. 7 (1930) 661.

[2] A.I. Mikhailov, A.V. Nefiodov, and G. Plunien, Phys. Lett. A 368 (2007) 391.

* Work supported by BMBF, GSI F+E and INTAS-GSI.

Alignment of heavy, few-electron ions following Coulomb excitation in collisions with light targets *

S. Fritzsche[1,2], A. Surzhykov[2], and T. Stöhlker[1,3]

[1]GSI, Darmstadt; [2]Max–Planck Institute for Nuclear Physics, Heidelberg; [3]Ruprecht-Karls-University Heidelberg

In relativistic ion-atom and ion-electron collisions, different processes are known that lead to the formation of *excited* or *ionized* states of the projectile ions. In their subsequent de-excitation, the ions then often emit one (or several) x-ray photons until the ionic ground state is reached. From the analysis of this 'characteristic' radiation, important information can be obtained about the structure and the population dynamics of highly-charged ions. In previous experiments, emphasis was placed in particular on the angular distribution and linear polarization of the radiation following the *radiative electron capture* (REC) into excited states of bare ions [1, 2]. Beside a rather large number of such REC studies at the GSI storage ring, measurements have been carried out recently also on the Coulomb *excitation* of helium-like uranium ions [3] in order to explore the role of the magnetic interactions in relativistic ion-atom collisions. In these experiments, the alignment measured for the $1s2p_{3/2}$ $J = 1$ level was found to be inconsistent with predictions from a simple one-particle model and, hence, has initiated a more detailed analysis in order to account for the electronic structure of the helium-like projectiles.

In the present work, the semi-classical approximation was applied for studying the alignment of few-electron heavy ions following the Coulomb excitation in collisions with light target nuclei. In this approximation, an excitation of the projectile is caused by the 'Lienard-Wiechert' potential of the target atoms [4]

$$A^\mu \;=\; \sum_{i=1}^{N} \gamma_p \, \frac{\alpha \, Z_T}{r'_i} \, (1, 0, 0, +\beta_p) \,, \qquad (1)$$

as *seen* by the projectile electrons. In this potential, Z_T denotes the charge of the target nucleus, $\gamma_p = (1 - \beta_p^2)^{-1/2}$, and $r'_i = \left[(x_i - b)^2 + y_i^2 + \gamma_p^2 (z_i - v_p t)^2\right]^{1/2}$ is the (time-dependent) distance between the target nucleus and the $i-$th electron of the projectile.

Making use of Eq. (1), a series of multiconfiguration Dirac-Fock computations has been carried out to analyze the alignment of the excited states of high-Z ions [5]. For the K-shell excitation of helium-like uranium ions U^{90+}, for example, Figure 1 displays the alignment parameter $\mathcal{A}_2$ of the $1s2p_{1/2}$ $^3P_1$ and $1s2p_{3/2}$ $^1P_1$ states which can be deduced also experimentally from the angular distribution of the subsequent Kα_2 and Kα_1 x-rays [3]. As seen from this Figure, the alignment $\mathcal{A}_2$ of the $^3P_1$ as well as $^1P_1$ state is large and negative for low energy collisions with $T_p \leq$ 100 MeV/u. This refers to a predominant population of the $M_f = 0$ magnetic substate and therefore to an *alignment*, i.e. an electron density that is directed perpendicular to the beam. In fact, such a result is consistent with the classical picture in which the transferred orbital angular momentum is found perpendicular to the collision direction, that is the $K \rightarrow L$ excitation occurs dominantly due to $M_f = M_i = 0$ transitions. For higher collision energies, in contrast, the relativistic and magnetic effects increase rapidly and the 'classical' picture remains not longer true.

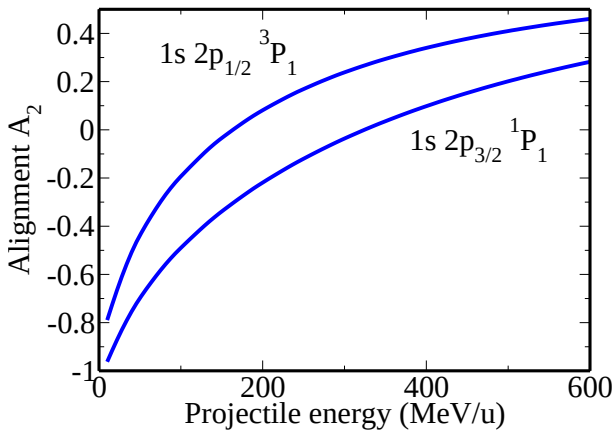

Figure 1: Alignment parameter $\mathcal{A}_2$ of the $1s2p_{1/2}$ $^3P_1$ and $1s2p_{3/2}$ $^1P_1$ levels of helium-like uranium U^{90+} following K–shell excitation.

In conclusion, the alignment of excited states following Coulomb excitation of heavy ions in collisions with light targets strongly depends on the projectile energy [cf. Fig. 1]. Of course, this affects as well the angular distribution and polarization of the (subsequent) radiation. A detailed account of the (level) structure of the few-electron projectile therefore helps to explain the observation but also suggest further investigations concerning the excitation and de-excitation mechanisms in high-Z ions.

* Work supported by GSI under the Project KS-FRI.

References

[1] S. Fritzsche, P. Indelicato, and Th. Stöhlker, J. Phys. B 38 (2005) S707.

[2] J. Eichler and Th. Stöhlker, Phys. Rep. 439 (2007) 1.

[3] A. Gumberidze *et al.*, Hyperfine Int. 146/147 (2003) 133.

[4] D. C. Ionescu and Th. Stöhlker, Phys. Rev. A 67 (2003) 022705.

[5] A. Surzhykov *et al.*, Phys. Rev. A, submitted (2007).

Formation of excited ionic states in relativistic collisions*

A. Surzhykov[1], U. D. Jentschura[1,2], Th. Stöhlker[2,3], and S. Fritzsche[1,3]

[1]Max–Planck Institute for Nuclear Physics, Heidelberg; [2]University of Heidelberg; [3]GSI, Darmstadt

Owing to the recent advances in accelerators and detection techniques, new types of collision experiments have been carried out recently at GSI with high–Z ions and with different target materials. In these experiments, formation (and subsequent decay) of *excited* ionic states were explored in details. Among several other processes, the radiative capture of target electrons into the excited states of few–electron, heavy ions has attracted much interest [1], because it enables one to explore the photon–matter interaction in the largely unexplored domain of relativistic collision energies and strong nuclear fields. Valuable information about the relativistic as well as strong–field phenomena can be obtained, for example, from the magnetic sublevel population of the ionic states as described in terms of the *alignment* parameters $\mathcal{A}_{k0}$ [2]. However, theoretical calculations of these parameters are not a simple task due to the many–electron effects. In order to take these effects into account, we have recently applied the multiconfiguration Dirac–Fock (MCDF) theory for the analysis of radiative electron capture by few–electron, heavy ions. Predictions, based on the MCDF approach, have been found to be in a good agreement with experimental results for the alignment of the $1s_{1/2}\,2p_{3/2}: J = 1, 2$ states of (resulting) helium–like uranium U^{90+} ions [2].

Even though the MCDF method provides an efficient approach for dealing with many–electron effects, it usually leads to rather sophisticated calculations. Instead of the MCDF method, therefore, it is sometimes convenient to apply the effective single–particle approximation if the Pauli principle is properly taken into account [3]. For the high–Z domain, this approximation is well justified because the interelectronic effects are known to be much weaker than the electron–nucleus interaction.

Recently, we have generalized the one–particle approach for studying the REC into excited states of ions with a single valence electron outside of a closed shell [3]. By making use of the standard reduction of the multi–electron matrix element to the one–electron amplitude, we were able to describe all the properties of the electron capture by many–electron ions in terms of their one–electron analogs. For instance, the alignment $\mathcal{A}_{k0}(\alpha_f J_f)$ of the helium–like states $|(n_0 j_0,\, n_b j_b)\, J_f\rangle$ can be expressed in terms of the parameters $\mathcal{A}_{k0}(n_b j_b)$ of the hydrogen–like ions:

$$\mathcal{A}_{k0}(\alpha_f J_f) \;=\; [j_b, J_f]^{1/2} (-1)^{J_f + j_b + j_0} \times \left\{ \begin{array}{ccc} J_f & J_f & k \\ j_b & j_b & j_0 \end{array} \right\} \mathcal{A}_{k0}(n_b j_b)\,. \quad (1)$$

As seen from this equation, the alignment calculations for the single excited states of the two–electron (or even many–electron) ions can be traced back always to the one–electron parameters $\mathcal{A}_{k0}(n_b j_b)$. Since these parameters are tabulated in Ref. [4] for medium– and high–Z ions over a wide range of projectile energies, Eq. (1) provides a fast access to the alignment of few–electron ions as required often for the analysis of electron-capture experiments.

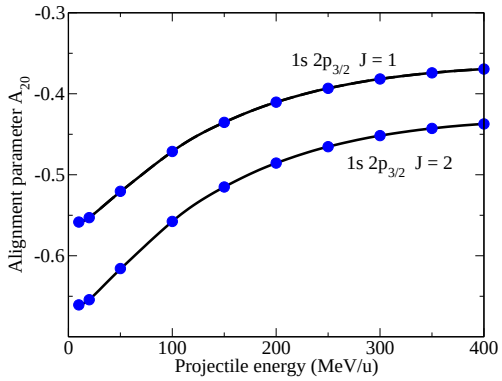

Figure 1: Alignment parameters $\mathcal{A}_{20}$ of the $1s\,2p_{3/2}$ $J = 1, 2$ states of helium–like uranium ions following REC. Results from an effective one–particle model (solid circles) are compared with those from MCDF calculations (—) in Coulomb gauge. From Refs. [2, 3].

In order to check the validity of Eq. (1), detailed calculations were performed for the electron recombination into excited states of some few–electron ions. Figure 1 displays, for example, the parameter $\mathcal{A}_{20}$ of the $1s_{1/2}\,2p_{3/2}$: $J = 1, 2$ states of helium–like uranium ions following REC. This parameter has been calculated within the effective one–particle as well as the MCDF approach for projectile energies in the range $10 \le T_p \le 400$ MeV/u. As can be seen from the figure, results from both approaches deviate by less than 1 %, i.e. well below the accuracy of the present day alignment experiments.

Despite the good applicability of Eq. (1) for the alignment studies with heavy, few–electron ions ions, we have recently reported two cases in which the many–electron effects beyond the Pauli principle and momenta coupling became (relatively) important. These cases concern: (i) the REC by decelerated ions and (ii) the electron recombination into highly–excited ionic states [2, 3].

References

[1] J. Eichler and Th. Stöhlker, Phys. Rep. 439 (2007) 1.

[2] A. Surzhykov *et al.*, Phys. Rev. A 74 (2006) 052710.

[3] A. Surzhykov *et al.*, Eur. Phys. J. D 46 (2008) 36.

[4] J. Eichler *et al.*, Phys. Rev. A **58**, 2128 (1998).

* This work has been supported by the GSI under project KS–FRI.

Ionisation of highly charged relativistic ions by neutral atoms [1]

G. Baur[1], I. Beigman[2], S. V. Shevelko[2], Th. Stöhlker[3], and I. Yu. Tolstikhina[2]

[1]FZ Jülich, Jülich, Germany; [2]P.N. Lebedev Physical Institute, Moscow, Russia; [3]GSI, Darmstadt, Germany

An important issue in the acceleration of U^{28+} at the forthcoming FAIR/GSI facility is the projectile electron loss in the collision with the rest gas atoms (molecules). It can lead to degraded focusing and loss of the beam to the walls. These charge-changed fast ions strike the accelerator container walls and give rise to sputtering and activation of the surface. Evidently, it is important to study the interaction of highly charged heavy ions with neutral (rest gas) targets, for practical as well as theoretical reasons. It is a theoretical challenge to treat the many-electron (relativisic) scattering problem in a realistic nonperturbative way [2].

At high energies some things simplify: higher order effects can be treated in Glauber (eikonal) theory (this will be our next step). Now we will start with a generalisation of the approach used in [4] (LOSS code) to relativistic beam energies (LOSS-R). Relativistic ionisation has been pioneered at Stanford by Anholt and collaborations [5] and it is reviewed in the book by Eichler and Meyerhof [3]. In these works, there are formulae which can be used directly for numerical approaches. However, the electronic wave functions have to be given by relativistic Dirac wave functions. This is appropriate for the inner shells in heavy systems, where relativistic effects have to be taken into account. In [5] K-vacancy production by relativistic projectiles was treated in an analytic way using semirelativistic Darwin wave functions. On the other hand, the outer electrons are most important. For these electronic shells relativistic effects are not important and it may be more convenient to use Schrödinger wave functions. Anylytical solutions are no longer available in this case.

A basic quantity in the LOSS code is the matrix-element F between the initial atomic bound state $|i>$ and the final continuum state $|f>$. It is given by

$$F(q) \equiv < f|e^{iqz}|i > \tag{1}$$

Now a different matrix-element G will appear. It is defined as

$$G(q) \equiv < f|\alpha_x e^{iqz}|i > \tag{2}$$

where α_x is a Dirac matrix.

In terms of these matrix-elements the cross section for ionisation is given by (eq. 6.22 of [3])

$$\frac{d\sigma}{dE} = 8\pi(Z_t\alpha)^2 \int_{q_0}^{\infty} \frac{dq}{q^3}(|F(q)|^2 + \frac{\beta^2(1-q_0^2/q^2)}{(1-\beta^2 q_0^2/q^2)^2}|G(q)|^2) \tag{3}$$

where Z_t is the charge of the target nucleus, $\beta = \frac{v}{c}$ is the projectile velocity and $q_0 = \frac{E_i - E_f}{\hbar v}$. The term involving F tends to a constant for $\gamma \to \infty$ whereas the term term with G rises with $\ln\gamma$. This is the contribution due to the 'equivalent' photons. (Fig. 6.2 of [3] is a good illustration, the 'spin-flip' contribution is also shown there, we neglect it in the following.)

We use an expansion into partial waves. The angular integrations and the necessary spin summations can be done analytically. In the terminology of [6] α_x is an odd operator and we perform a nonrelativistic reduction. Our final formula is

$$\begin{aligned} |G(q)|^2 &= \frac{2\hbar^2}{(mc)^2} \sum_{\lambda\mu l_f} |(l_i+1) f_+(R^d - l_i R) \\ &+ l_i f_-(R^d + (l_i-1)R)|^2 \end{aligned} \tag{4}$$

where we defined two types of radial matrixelements, the one used already in the LOSS code

$$R_{lf\lambda li}(q) \equiv \int_0^{\infty} dr g_{lf} j_\lambda(qr) f_{li} \tag{5}$$

and another one involving the derivative of the radial Schrödinger wave functions:

$$R^d_{lf\lambda li}(q(q) \equiv \int_0^{\infty} dr r g_{lf} j_\lambda(qr) \frac{df_{li}}{dr}. \tag{6}$$

The radial derivative is numerically calculated in a stable way using $\frac{df}{dr} = \int^r \frac{d^2f}{dr^2} dr$ together with the radial Schroedinger equation for $\frac{d^2f}{dr^2}$. The quantity $f_\pm$ is given by

$$f_\pm = \frac{4\pi^{\frac{3}{2}}}{k} i^\lambda Y_{\lambda\mu}(\frac{\pi}{2}, 0) \sqrt{\frac{2l_f+1}{2l_i+1}} \begin{pmatrix} l_f & \lambda & l_i \pm 1 \\ 0 & 0 & 0 \end{pmatrix} \tag{7}$$

Thus all sums over magnetic quantum numbers are done, apart from the sum over multipolarity λ and its projection μ. ($\lambda = 0$ is the dipole term, a monopole contribution does not exist for G, it corresponds to the 'equivalent photon' contribution; on the other hand, the monopole part is contained in the matrix-element F). The code LOSS (see [4]) will be modified using these formulae.

References

[1] INTAS-GSI collaboration INTAS 03-54-4294, to be published.

[2] T.Kirchner, talk at SPARC Working group meeting, GSI,Darmstadt 17-18 July 2007.

[3] J.Eichler, W.E.Meyerhof, Relativistic Atomic Collisions Academic Press 1995.

[4] V.P. Shevelko, I.Yu. Tolstikhina, Th. Stoehlker, NIMB184(2001)294.

[5] R.Anholt, Phys. Rev. A19 (1979)1004

[6] A. Messiah, Quantum Mechanics Vol.2.

Backward scattering of low-energy antiprotons by highly charged and neutral uranium: Coulomb glory *

A. V. Maiorova[1], D. A. Telnov[1], V. M. Shabaev[1], I. I. Tupitsyn[1], G. Plunien[2], and T. Stöhlker[3]
[1]SPbSU, St. Petersburg, Russia; [2]TU Dresden, Dresden, Germany; [3]GSI, Darmstadt, Germany

Investigations of the antiproton scattering by heavy ions at low energies anticipated in the near future with the new GSI facilities can give a unique possibility to observe an interesting phenomenon predicted in Refs. [1, 2] and named the Coulomb glory. The phenomenon consists in a prominent maximum of the differential cross section (DCS) in the backward direction at a certain energy of the incident particle, provided the interaction with a target is represented by the Coulomb attraction of the nucleus screened (partly) by atomic electrons. Note that the pure Rutherford cross section shows a smooth minimum at 180°. Since the expected kinetic energy of the antiproton is as low as a few atomic units, the non-relativistic scattering theory can be employed.

In Ref. [3] we have examined the Coulomb glory in collisions of antiprotons with He-, Ne-, Ni-like, bare, and neutral uranium ($Z = 92$). The ions were chosen to have fully occupied shells with $n = 1$ (U^{90+}), $n = 2$ (U^{82+}), and $n = 3$ (U^{64+}), respectively. The calculations have been performed using both semiclassical and quantum theory. Besides the screening potential due to atomic electrons, the vacuum polarization potential has been taken into account.

The partial wave expansion of the DCS reads

$$\frac{d\sigma}{d\Omega} = \frac{1}{k^2}\left|\frac{\nu}{2\sin^2(\theta/2)}\exp\left(-2i\nu\ln\sin\frac{\theta}{2}\right)\right.$$
$$-\sum_0^\infty (-1)^l(2l+1)\exp(i\delta_l^s)\sin\delta_l^s$$
$$\left.\times\frac{(1-il/\nu)...(1-i/\nu)}{(1+il/\nu)...(1+i/\nu)}P_l(\cos\theta)\right|^2, \qquad (1)$$

where k is the momentum of the antiproton and $\nu = -Z_c m_{\bar{p}}/k$ is the Coulomb parameter (Z_c is the charge of the core). The phase shifts δ_l^s are produced by the short-range corrections to the Coulomb potential of the core; they have been computed with the help of the variable phase method.

To facilitate a comparison between the results at different energies, the differential cross sections have been scaled according to

$$\frac{d\tilde{\sigma}}{d\Omega} = \left(\frac{4E}{Z_c}\right)^2\frac{d\sigma}{d\Omega}. \qquad (2)$$

It has been found that a maximum in the differential cross section at the scattering angle $\theta = 180^\circ$ exists in a wide range of energies of the incident particle. The Coulomb glory can be observed for the energies of the antiproton within the range from 100 eV to 7 keV, depending on the electronic configuration of the ion. In general, the larger the number of electrons, the higher the energy where the effect is strongest. In the case of the Coulomb glory, the differential cross section at $\theta = 180^\circ$ can be much larger than the corresponding background cross section. Actually, the ratio of these two quantities ranges from 4 for He-like uranium to 609 for Ni-like uranium (the results for the latter case are presented in Fig. 1). On the other hand, a maximum of the differential cross section in the backward direction can also be found in the scattering of antiprotons on a bare uranium nucleus. This can be regarded as a manifestation of the screening property of the vacuum-polarization potential in nonrelativistic collisions of heavy particles.

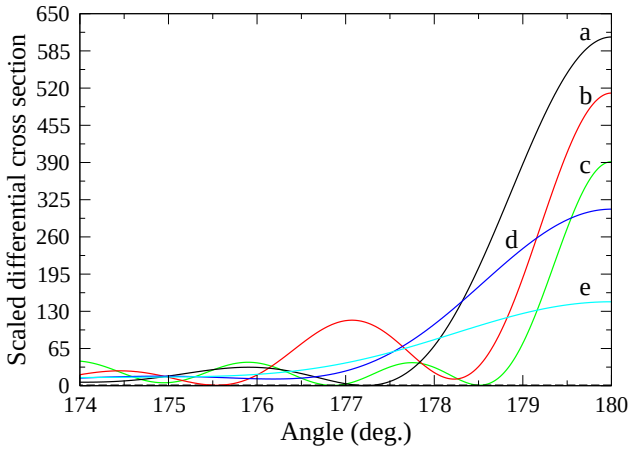

Figure 1: Scaled differential cross section $d\tilde{\sigma}/d\Omega$, defined by Eq. (2), on Ni-like uranium for different energies of the incident antiproton: (a) $E = 2$ keV, (b) $E = 1.5$ keV, (c) $E = 1$ keV, (d) $E = 2.5$ keV, and (e) $E = 3$ keV. The dashed line (close to the 0 line) represents the scaled Rutherford cross section.

References

[1] Yu. N. Demkov, V. N. Ostrovsky, and D. A. Telnov, Zh. Exp. Teor. Fiz., **86**, 442 (1984) [Sov. Phys. – JETP **59**, 257 (1984)].

[2] Yu. N. Demkov and V. N. Ostrovsky, J. Phys. B **34**, L595 (2001).

[3] A. V. Maiorova, D. A. Telnov, V. M. Shabaev, I. I. Tupitsyn, G. Plunien, and T. Stöhlker, Phys. Rev. A **76**, 032709 (2007).

* Work supported by BMBF, GSI F+E and INTAS-GSI.

Energy loss of Ar in a laser-produced C plasma

A. Blažević[1], A. Frank[2], M. Günther[2], K. Harres[2], T. Hessling[1], D.H.H. Hoffmann[1,2], R. Knobloch-Maas[2], F. Nürnberg[2], A. Pelka[2], G. Schaumann[2], A. Schökel[2], M. Schollmeier[2], D. Schuhmacher[2], J. Schütrumpf[2], M. Roth[2]

[1]GSI, Darmstadt, Germany; [2]TU Darmstadt, Germany.

Energy loss measurements of ions penetrating plasmas have become an interesting field of research, especially since the concept of the heavy ion driven Inertial Confinement Fusion had been developed. Earlier experiments of ions interacting with discharge or pinch plasmas [1] showed an increase of the projectile stopping power compared to cold matter. To extend the data base of experimental results to higher plasma densities and temperatures and hence test different theories, the plasma physics group at GSI has devoted its effort to the investigation of the interaction of ions penetrating laser generated hot and dense plasmas ($T_{pl} > 150$ eV, $\rho_{\text{free electrons}} > 10^{20}$ cm^{-3}).

Therefore nhelix [2], a Nd:YAG laser with an energy of up to 100 J, a pulse length of 5 to 15 ns, focused to a large spot of 1 mm diameter, is irradiating a thin (0.5 to 2 µm) carbon foil to produce a carbon plasma. The Unilac ion beam, preferably consisting of Ar ions at an energy of 4 MeV/u, is probing the target. As the ion beam pulse length is several tens of microseconds, consisting of microbunches with a length of 3 ns (FWHM) at a frequency of 108 MHz the target is probed each 9 ns, beginning with cold solid matter over plasma creation, plasma expansion up to vacuum conditions with no target matter in the line of sight of the projectiles. By measuring the time of flight of the ion bunches one gets the energy loss of the projectiles in cold matter, in different plasma conditions during expansion and finally the initial beam energy in one single experiment.

Several improvements in the experimental setup during the last years now lead to successful and reliable results. To generate a more homogeneous plasma for the ion beam a random phase plate was included into the laser beam line creating a homogeneous laser intensity profile over the large focal spot. Additionally the ion beam diameter could be reduced to 0.5 mm by developing a new diamond based semiconductor detector with a high sensitivity and sub nanosecond time resolution. Especially these two improvements led to an increase of the energy resolution of the experimental method to dE/E<1%.

Experiments have been performed with ^{36}Ar projectiles at an energy of 4 MeV/u penetrating a carbon plasma created by irradiating 0.5 to 2 µm thick carbon foils with a laser energy of 50 J. The delay between the laser and a micro bunch could be varied with an accuracy of 1 ns.

Figure 1 shows the measured energy loss data of 4 laser shots on a 0.5 µm thick carbon foils, where the laser-ion delay was shifted always by 2 ns, and a SRIM calculation in cold gas with the same density profile (taken from hydrodynamic simulations).

The triangles show the energy loss data, the solid curves below represent the temporal profile of the laser. As the four carbon foils did not have exactly the same thickness, the energy loss data is normalised to the energy loss in the cold foil (100% corresponds to 1.8 MeV).

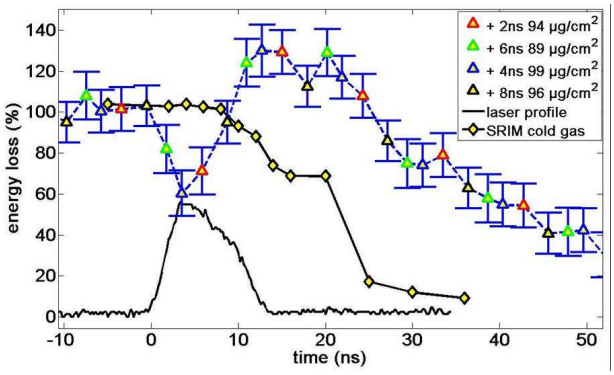

Figure 1: Experimental data on the energy loss of Ar ions at 4 MeV/u penetrating a carbon plasma. The enery loss is scaled to the energy loss in the cold solid foil (1.8 MeV).

The first five triangles represent the energy loss of the projectiles in the cold, solid C foil. Right after the onset of the laser pulse, at the beginning of the plasma creation, the energy loss decreases. The reason for that is not yet understood. We did some experiments (change of the laser irradiation direction, measurement of the transmitted light) to test some possible explanations, but the problem is not yet solved. Few nanoseconds later the energy loss increases again and rises to values above the ones of the cold foil reaching its maximum of 130% at about 13 ns. Considering that at that time the plasma is expanding and the line integral (µg/cm²) is decreasing slowly, the plasma effect (increase of the stopping power in plasma compared to cold matter) is estimated to be about 40-50%. Two mechanisms contribute to this plasma effect:

- an effective energy transfer to the free electron gas (plasmon excitation).
- an increase of the projectile charge state due to a suppression of the electron capture and an increase of the ionization cross sections for the projectile in a fully ionized plasma [3].

References

[1] D.H.H. Hoffmann, Nucl. Instr. and Meth. B, Vol.90, p.1 (1994)

[2] G. Schaumann, M. Roth, and D.H.H. Hoffmann, Laser Part. Beams (2005) 23, p.503-512

[3] A. Frank, this annual report

* Work supported by ISTC 2264

Development of a Monte Carlo code to describe the charge state distribution evolution of argon ions in a carbon plasma

A. Frank[1], A. Blazevic[2], D.H.H. Hoffmann[1], V.V. Vatulin[3], O.A. Vikurnov[3], A. Kunin[3], N. Zhidkov[3], B. Rethfeld[4], and M. Roth[1]

[1]TU Darmstadt; [2]GSI, Darmstadt, Germany; [3]VNIIEF Sarov; [4]TU Kaiserslautern

Introduction

An important field of research of the plasma physics group at GSI is the interaction of heavy ions with laser-produced plasmas. Especially the energy loss of argon in carbon plasmas has been investigated recently ([1]) at Z6 and new precise data has been obtained. A crucial parameter in heavy ion stopping in the intermediate velocity regime is the actual charge state of the projectile ion at every location in the plasma. Therefore a Monte Carlo code describing the charge state evolution of argon ions penetrating a carbon plasma has been developed.

Development

In 2002 cross sections for electron capture, ionization, excitation and decay were obtained from the measurements of charge distributions of argon ions of 4 MeV/u penetrating thin carbon foils at HMI ([2]). Since these measurements concentrated on the non-equilibrium part of the ion charge state evolution, the cross sections can be obtained absolutely from these results. To describe the charge state evolution in carbon foils, the cross sections are calculated by the ETACHA code ([3]). A Monte Carlo method describing projectile charge states in cold matter has been developed in [4] and [5]. This code has now been modified in the following way:

- Calculated density and temperature profiles of the expanding plasma are used as target matter. These simulations have been performed by our colleagues from Sarov.
- In the ionization and in the excitation cross section calculation the target screening is reduced due to the average ionization of the plasma.
- In the mechanical electron capture calculation the target screening is adjusted and the amount of electrons available for recombination is reduced.
- Theoretically calculated cross sections for electron-impact ionization, dielectronic recombination and three-body recombination are added to the code.

Results of calculations

The calculations have been carried out for a carbon foil of 0.5 μm thickness. It is irradiated by a 50 J, 1.064 μm laser pulse with 10 ns FWHM, the same situation as in the energy loss measurements of [1]. The results show a clear increase of the argon mean charge state compared to the average cold gas state (≈ 15.14) as soon as the carbon foil is ionized. When the average ionization of carbon crosses $\bar{Z} = 4$ the recombination cross sections are significantly reduced. If the matter is hot enough, as shown in fig. 2, the resulting mean charge state clearly exceeds even the equilibrium charge of argon in solid carbon (≈ 15.66) since the carbon plasma is now almost completely ionized. The evolution of each argon charge state is presented in fig. 1.
So the results of the simulations support an increased stopping power for larger times compared to the solid state when most of the target has been sufficiently heated. The reason for this is not only the excitation of plasmons but also a higher charge state of the argon ions passing through the plasma.

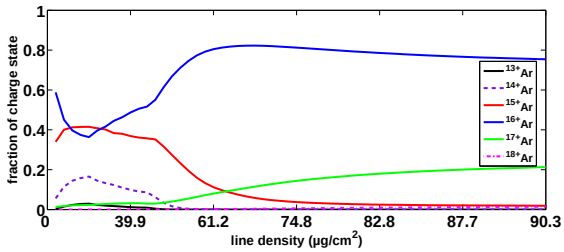

Figure 1: spacial evolution of each argon charge state in a carbon plasma target (9ns after beginning of laser pulse)

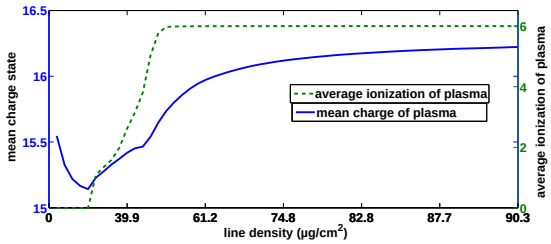

Figure 2: mean charge state of argon (9ns after beginning of laser pulse)

References

[1] A. Blazevic, this annual report

[2] A. Blazevic et.al, Mat.-fys. Meddel. 52:1, p. 109-127 (2006)

[3] J. Rozet et.al, NIM B, v. 107, p. 67-70 (1996)

[4] A. Blazevic et.al, Phys. Rev. A, Vol.61, 032901 (2000)

[5] A. Blazevic et.al, NIM B, v. 190, p. 64-68 (2002)

* supported by ISTC 2264

Experiments with laser heated hohlraum targets

G. Schaumann[1], A. Blažević[2], T. Hessling[1], A. Pelka[1], A. Schökel[1], D. Schumacher[1], and M. Roth[1]
[1]TU-Darmstadt, Germany; [2]GSI, Darmstadt, Germany

One major research activity of the plasma physics group at the Gesellschaft für Schwerionenforschung (GSI) concentrates on the investigation of phenomena concerning the interaction of heavy ions with hot and dense plasma. The laboratory at GSI offers the unique opportunity to measure the charge state distribution and the energy loss of swift heavy ions after they have penetrated a hot and dense plasma [1]. Until now, the plasma has been generated through direct irradiation of a solid density foil target by the high energy laser system *Nhelix*. As the laser with a wavelength of 1064 nm can permeate the plasma up to an electron density of 1/100 of solid state density, the laser energy only heats the surface of the target. Alternatively

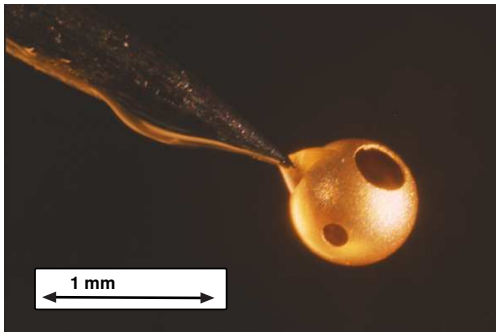

Figure 1: Spherical gold hohlraum (750 μm diameter) with diagnostic port (160 μm) and laser entrance hole (330 μm).

one can utilize a hohlraum target (figure 1) in order to convert the laser energy in thermal radiation which serves as the radiation source to heat the actual plasma target for the ion beam. Laser heated hohlraum targets allow for the production of radiation temperatures with maximum spectral emission in a wavelength range of a few nanometer. This radiation can homogeneously heat the entire volume of a thin foil target. Furthermore, a hohlraum converter is beneficial as it destroys the coherence of the primary laser light. Coherent laser light will always show spatially inhomogeneous heating due to interference patterns, whereas the homogenous radiation field in a cavity with its incoherent thermal radiation does not produce localized intensity peaks due to such interference. Therefore, the concept of indirect heating allows for the production of a spatially homogenous plasma near solid state density.
A lithographic procedure was developed at TU Darmstadt [2] that enables the production of gold hohlraum targets of varied size and shape. First hohlraum experiments have been carried out at GSI with the *Nhelix* laser system and targets of spherical geometry (750 μm diameter, 10 μm wall thickness), which aimed at characterising the temporal profile of the thermal radiation temperature [3]. To measure the radiation temperature profile, a spectrometer with high time resolution was developed and calibrated in terms of absolute intensity units with a deuterium-lamp. While the laser heats the cavity, the rise in temperature was measured with a time resolution $\leq$1 ns up to a maximal radiation temperature of 73 ± 8 eV/kB (85×10^4 C). Figure 2 illustrates the evolution of the temperature until the heating pulse ends at $t = 5$ ns. At later times the temperature is both, undefined in terms that one can not assume a Planckian radiation distribution any more, and technically not measurable, as the source size changes with plasma blowing off the diagnostic port of the holraum.
For this particular Hohlraum geometry, the conversion efficiency (with time resolution) of laser energy to thermal energy of the hohlraum radiation has been derived from the measurements of radiation temperature evolution. With a laser entrance hole of 330 μm and a diagnostic port of 160 μm, the conversion efficiency reaches 74% at the end of the heating pulse. With this converter geometry 14% of the laser energy converted to thermal radiation is available for the heating of a secondary target.

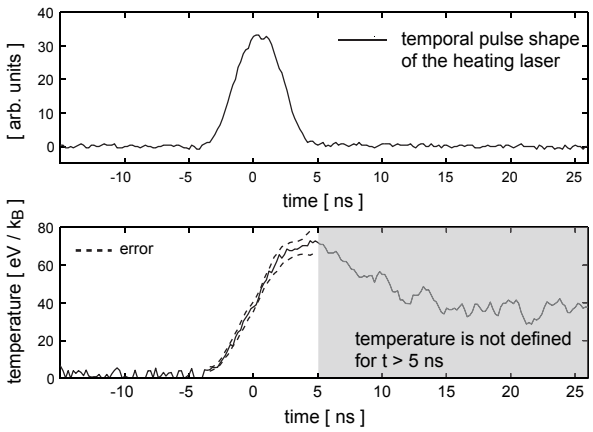

Figure 2: Temporal shape of the *Nhelix* laser pulse (13 J / 532 nm) and of the hohlraum temperature.

References

[1] A. Blažević, this annual report.

[2] T. Hessling, annual report 2006

[3] G. Schaumann, Dissertation TU Darmstadt, 2007

Multiframe interferometry as a diagnostic to measure the free electron density in laser generated plasma

G. Schaumann[1], T. Hessling[1], A. Pelka[1], A. Schökel[1], D. Schumacher[1], and M. Roth[1]
[1]TU-Darmstadt, Germany

The investigation of phenomena concerning the interaction of heavy ions with plasmas is a key research activity of the plasma physics group at the Gesellschaft für Schwerionenforschung (GSI). The laboratory at GSI offers the unique opportunity to measure the charge state distribution and the energy loss of swift heavy ions after they have penetrated a hot and dense plasma [1]. The laser induced plasma expands considerably on a nanosecond timescale, which leads to significant changes of the plasma parameters along the projectile-plasma interaction path. This requires plasma diagnostics sophisticated enough to measure key plasma parameters such as temperature and free electron density with both space and time resolution during the interaction time.

The density of free electrons is an important plasma parameter for the theoretical description of energy loss in ionised matter. An interferometer was developed and constructed to determine the electron density with spatial resolution, and for the first time simultaneously at different times [2]. This diagnostic provides images of the interference pattern with a time difference of 1.5 ns and allows determination of the free electron density up to a maximum density of $3 \times 10^{20}\mathrm{cm}^{-3}$. Figure 1 shows the experimental

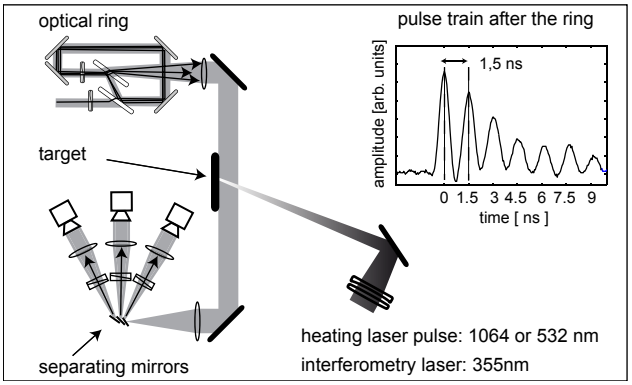

Figure 1: Experimental setup of the multiframe interferometry.

setup of the multiframe interferometry. Before the interaction of the probe beam with the plasma, the pulse of the Nd:YAG laser is frequency tripled, giving a wavelength of 355 nm. This wavelength corresponds to a critical electron density ($n_{ec}[\mathrm{cm}^{-3}] \approx 1 \times 10^{21}/\lambda^2[\mu\mathrm{m}]$) of $8 \times 10^{21}\mathrm{cm}^{-3}$ up to which the probe beam theoretically can permeate the plasma. In practice, the actually measurable maximum electron density is lower and mainly limited by dynamical effects due to the relatively long pulse duration (0.5 ns)

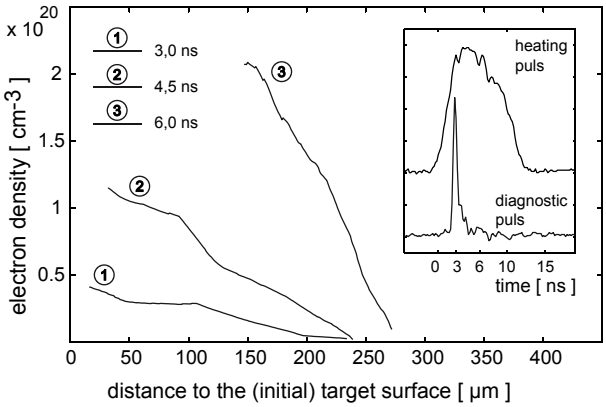

Figure 2: Spatial electron density distribution.

in comparison to the time scale of the plasma expansion. The time resolution of every single image is given by the 0.5 ns (FWHM) pulse duration of the diagnostic laser, while the time in between two frames corresponds to the time of circulation in the optical ring. As the pulse is circulating in the ring a half wave plate gradually turns the polarization direction at each turn and part of the pulse energy is transmitted at the second polarizer. The inset image in figure 1 shows the pulse train generated in the optical ring. In order to be able to separate these pulses spatially, the ring is adjusted so that the subsequent pulses leave the ring under a small angle with respect to each other. At the plasma position the different beams sufficiently superimpose, while in the far field, at the focal position of the first imaging lens, it is possible to separate the subsequent pulses with micro mirrors. A separate Wollaston interferometer [3] for each pulse measures the optical path difference induced by the interaction with the plasma, which allow for the calculation of the free electron density.

Figure 2 illustrates spatial electron density distributions perpendicular to the target surface at the centre of the Gaussian focal spot of the heating laser pulse. The three distributions correspond to the first three pulses and show the time evolution of the free electron density measured at the same experiment, within a single shot of the plasma generating laser.

References

[1] A. Blažević, this annual report.
[2] G. Schaumann, Dissertation TU Darmstadt, 2007
[3] A. Pelka, annual report 2004

Optical diagnostic system for *PHELIX* at *Z6* experimental area*

J. Schütrumpf[1], M. Günther[1], T. Eberl[2], A. Blažević[2], and M. Roth[1]
[1]Technische Universität Darmstadt, Germany; [2]GSI, Darmstadt, Germany

Concept

The *Z6* output sensor is the final *PHELIX* diagnostic prior to the target area *Z6*. During the first months of 2007 ray tracing calculations for the diagnostic system were done and the design was improved in efficiency. The pulse energy of a full system shot is up to 1 kJ with a maximum beam diameter of 280 mm. A test shot compared to a full system shot has a dynamic range of 10^6 in power. The diagnostic consists of broadband attenuation and downscaling optics [1].

Design

The components of the diagnostics are shown in Fig. 1. Digital cameras are used to image near field and far field (Fig. 2) for each *PHELIX* shot. The precision attenuator to adjust the intensity on the digital cameras consists of a half waveplate and two thin film polarizers (TFP). These data are then compared to the main amp sensor in the laserbay of *PHELIX*. A wavefront sensor is installed to measure the aberrations. The alignment was done with a solid state laser. The setup is now ready for secondary alignment with a front end pulse of *PHELIX*.

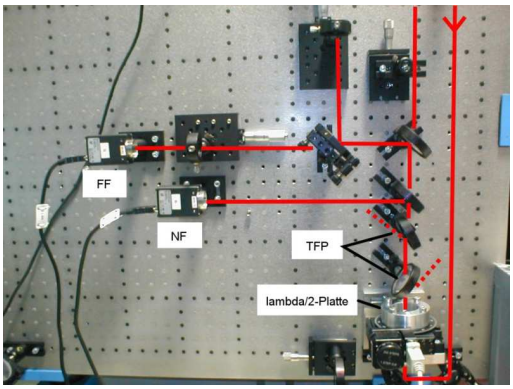

Figure 1: Setup of near field (NF) and far field (FF) imaging. The alignment beam enters from the upper right of the optical table. (for more detail, see [2])

Output sensor aberrations

The primary Seidel coefficients characterize the aberration function and are therefore ideal to quantify the beam quality. The Shack-Hartmann wavefront sensor determines the coefficients by expanding the aberration function in Zernike polynomials [3]. Tab. 1 shows the actual status of the system by specifying distinct aberrations. The

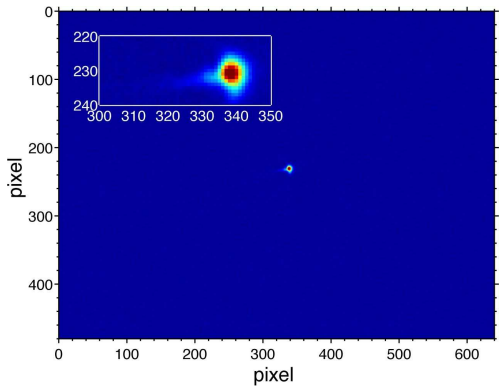

Figure 2: Far field image of the alignment laser. The spot-size is $(45 \pm 5)\,\mu$m in diameter.

Wavefront aberrations of capital importance are reduced to $\lambda/10 - \lambda/500$ by proper adjustment.
Finally no distinct variations to the laser pulse are induced by the output sensor.

Tilt x	-0.039λ
Tilt y	$+0.359\lambda$
Defocus	$+0.541\lambda$
Astigmatism $x^2 - y^2$	-0.060λ
Astigmatism xy	-0.037λ
Coma x	$+0.001\lambda$
Coma y	-0.043λ
Triangular Coma	$+0.000\lambda$
Quadratic Astigmatism	-0.024λ
Spher. Aberration	-0.006λ
5th. spher. Aberration	$+0.000\lambda$

Table 1: Aberrations of the output sensor diagnostics. Values are in units of the used wavelength $\lambda = 1053$ nm.

References

[1] M. GÜNTHER, J. SCHÜTRUMPF, T. EBERL, A. BLAZEVIC and M. ROTH: *The diagnostic for the PHELIX laser at the plasma physics experimental area.* GSI Scientific Report, 2006.

[2] SCHÜTRUMPF, J.: *Charakterisierung eines Hochenergie-Lasersystems am Beispiel PHELIX*. Diplomarbeit, TU Darmstadt, 2007.

[3] M. BORN, E. WOLF and A.B. BHATIA: *Principles of Optics*, Chapter 9, pages 523-525. Cambridge University Press, 7th edition, 1999.

* work supported by VIPBUL

Investigation of Ti K-shell X-rays induced by keV electrons

Y. Zhao[#1, 2], O. N. Rosmej[1], J. Jacoby[3], B. Sicherl[3], A. Mayr[3], D. H. H. Hoffmann[1, 4]
[1]IMP-Lanzhou, China; [2]GSI-Darmstadt, Germany; [3]Frankfurt University, Germany;[4]TU-Darmstadt, Germany.

The development of X-ray diagnostics for investigations of Warm Dense Matter (WDM) is one of the important goals for the FAIR program of the Plasma Physics Department. Due to the high absorption of the radiation in bulk matter, high energetic X-rays such as K-shell radiation of mid- and high Z elements have to be used. K-shell self radiation of highly ionized ions is traditionally used for the diagnostics of high temperature ideal plasma [1]. Strongly non ideal WDM is characterized by a density close to solid density, a temperature of some eV, and a rather low degree of ionization. Self radiation of such plasmas is in the VUV photon energy region and will be trapped in the target. K_α and K_β radiation induced by energetic electrons or protons is a promising toll for WDM diagnostics. The relative intensity of the K_α and K_β characteristic lines as well as the energy gap between them depends on the ionization degree of the heated matter [2]. Experimental K-shell spectra of a Ti target irradiated by 30 mJ, 15 ps, 532 nm, s-polarized laser pulses from a 10 Hz Continuum Leopard-D10 Nd:YAG laser system [3] show this behavior of K_α and K_β radiation. In dense ionized plasma, one has to account for corrections to the ion energy level shifts [4]. In future experiments, an X-ray diagnostic system combining a Si(Li) detector and a crystal spectrometer will be introduced for measurements of the target K-shell radiation.

For this propose the Ti K-shell X-rays induced by keV electrons has been investigated both by a Si(Li) detector and by a Focusing Spectrometer with Spatial Resolution (FSSR) [1]. Electron beams with energy ranging from 1keV to 15keV and with a current of about 100 uA were produced by an electron gun. A Mylar foil with a thickness of 100um was used as the vacuum window, with a transmission of ~55% for Ti K-shell X-rays. For the Si(Li) used in this experiment, a resolution of 160eV and an efficiency of ~93% at 5.9keV has been measured by a standard radioactive source Fe^{55}.

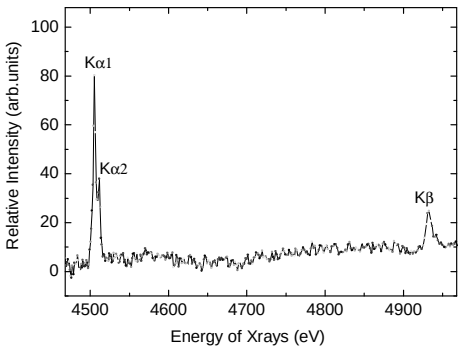

Figure 1: X-ray spectrum in case of 11keV electrons impacting on a Ti target.

The spectral resolution provided by the mica spherically bent crystal spectrometer was better than 3 eV at 4.5 keV photon energy. At the experimental K-shell spectrum shown in fig. 1, Ti - $K_{\alpha 1}$ and - $K_{\alpha 2}$ radiative transitions are well resolved.

In future experiments aimed at the measurement and analysis of the K-shell radiation in WDM, we will combine the advantages of the Si(Li) detector providing absolute yield of the K-shell radiation and those of the FSSR, having high spectral resolution.

On the other hand, knowledge about the dependence of the cross-sections for inner shell ionization by electron impact is important for fundamental research and applications [5]. In experiments, the K-shell X-ray yield dependence on the electron energy has been measured using the Si(Li) detector. Ultra-thin Ti foils with a thickness of 11 and 18 nm were used as a target, K-shell radiation was induced by a mono energetic electron beam. Results are presented in Fig.2. The data in the figure have been normalized to the foil-thickness; and the error bars in the figure only take account of the uncertainty of the beam intensity.

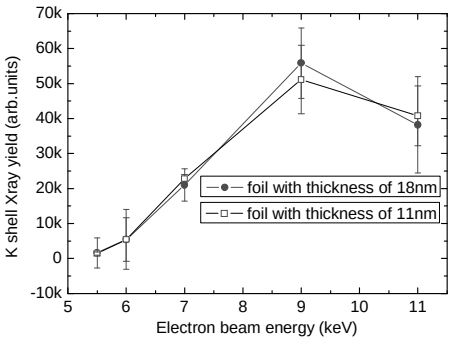

Figure 2: K-shell X-ray yield as the function of electron beam energy.

Theoretically [5], the cross-section of K-shell ionization depends strongly on the electron energy, and the maximum cross-section would take place when the electron beam energy is about twice the K-shell ionization energy (~10keV for Ti). The result shows the case accordingly.

References

[1] A.Ya. Faenov et al, Phys. Scripta, **50**,333 (1994)
[2] E. V. Aglitskii et al , J. Phys. B: At. Mol. Phys **15** (1982), 2001-2008
[3] D. Jung et al, GSI-Scientific report 2007
[4] A. Sengebusch et al, Contr. Plasma Phys.47, (2007)
[5] J.P. Santos et al, J. Phys. B **36** (2003)

Focusing and transport of laser-accelerated protons with quadrupoles

M. Schollmeier[1], M. Geißel[2], K. Flippo[3], S. Becker[4], A.Blažević[5], F. Grüner[4], K. Harres[1], F. Nürnberg[1], P. Rambo[2], U. Schramm[6], J. Schreiber[4], J. Schütrumpf[1], J. Schwarz[2], B. Atherton[2], M. Roth[1], D. Habs[4], and B.M. Hegelich[3,4]

[1]TU, Darmstadt, Germany; [2]SNL, Albuquerque, NM, USA; [3]LANL, Los Alamos, NM, USA; [4]LMU, München, Germany; [5]GSI, Darmstadt, Germany; [6]FZD, Dresden, Germany

The acceleration of MeV-protons and heavier ions by the interaction of an intense laser pulse with a foil target is a well-known phenomenon that has been extensively studied in the last decade. The interaction of a high-energy, high-intensity ($I > 10^{18}$ W/cm^2) laser pulse with a solid target leads to the acceleration of an ion beam in a very robust and reproducible way with up to 10^{13} protons in total. The conversion efficiency of laser energy to proton energy can reach up to 10%, which makes these beams very attractive for applications, e.g. an injection into a synchrotron, which is an experimental scheme of great interest for GSI. However, the beam has a 100% energy spread, is very short on the order of ps, has a divergence up to 40^o half angle and is neutralized by co-moving electrons. All these issues have to be overcome for a real application as an accelerator. There have been attempts to reduce the energy spread [1, 2] by reducing the source size and layer thicknesss that lead to "quasi-monoenergetic" ion beams with poor number of ions and conversion efficiency. Another attempt [3] demonstrated focusing and energy-selection of laser-accelerated protons by irradiating a tiny cylinder behind the target with a secondary, high-intensity laser beam. The cylinder acts as an electrostatic lens and focuses protons with a certain energy. However, this approach currently is not well understood and depends strongly on the interplay of the two laser pulses that makes it difficult for an application.

A solution of these issues is the use of a more traditional ion optical system to catch and transport the beam, e.g. into a buncher section several cm behind the target. This reduces the divergence and removes the electrons. The drift of the beam increases its pulse duration, making it suitable for standard accelerator ion optics. We have used novel permanent magnet mini-quadrupole (PMQ) lenses with a 5 mm aperture developed by LMU in Munich [4], in a demonstration experiment to transport and focus laser-accelerated 15 MeV protons. The quadrupoles as ion optics allowed us to apply standard ion optical codes for the design of the beam line without relying on the laser-plasma interaction.

The initial experiment was carried out at the 250 TW Trident shortpulse laser at Los Alamos National Laboratory and was continued at the 100 TW section of Z-Petawatt at Sandia National Laboratories. Z-Petawatt delivered 40 J laser energy on target and was focused by an off-axis parabolic mirror to a beam spot of 5 μm FWHM. The pulse had an intensity $I > 5 \times 10^{19}$ W/cm^2. The target was a 25 μm thin Cu-foil; the proton beam was diagnosed with a stack of absolutely calibrated radiochromic films (RCF). The resulting spectrum was fit to

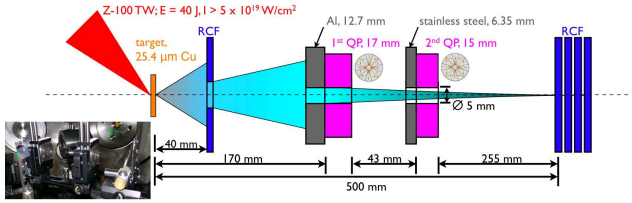

Figure 1: Experimental set-up.

$\mathrm{dN/dE} = \mathrm{N_0(2E\,k_BT)^{-1/2}\,\exp\left[-(2E/k_BT)^{1/2}\right]}$, with the fit parameters $N_0 = 4.9 \times 10^{12}$ and $k_BT = 1.24$ MeV. The maximum energy was 24 MeV and the conversion efficiency for protons over 4 MeV was 1%. Two PMQ's were placed in the target chamber that focused 15 MeV protons in a distance of 50 cm behind the target. The scheme is shown in Fig. 1. Since the PMQ's were originally developed for electrons, their focusing strength is rather weak for the protons and the aperture size is not optimally designed for this beam. However, the 15 MeV protons could be focused to a $(173 \times 286)\,\mu$m focal spot that contained 8×10^5 ions. The intensity distribution is shown in Fig. 2 and contains **100 times more protons/mm^2** as in the case without the magnets. For a magnetic lens system specifically designed for this purpose, even higher numbers can be expected.

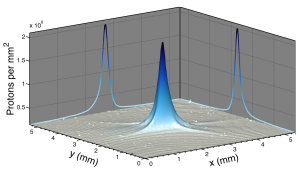

Figure 2: Intensity distribution of focused 15 MeV protons.

In summary we have demonstrated for the first time the transport and focusing of laser-accelerated protons with quadrupole lenses. The proton's divergence was reduced and they were transported over a relatively long distance, where an injection into a buncher section to reduce the energy spread while maintaining the high ion number could take place.

References

[1] B.M. Hegelich *et al.*, Nature **439**, 441 (2006).
[2] H. Schwoerer *et al.*, Nature **439**, 445 (2006).
[3] T. Toncian *et al.*, Science **312**, 412 (2006).
[4] T. Eichner *et al.*, PRST-AB **10**, 082401 (2007).

Enhancement of the beam quality of laser-accelerated protons

K. Harres[1], F. Nürnberg[1], M. Schollmeier[1], A. Blažević[2], D. Carroll[3], M. Quinn[3], P. McKenna[3], K. Markey[4], S. Kar[4], M. Zepf[4], K. Lancester[5], D. Neely[5], O. Lundh[6], C.-G. Wahlström[6], and M. Roth[1]

[1]Technische Universität Darmstadt, Darmstadt, Germany; [2]GSI, Darmstadt, Germany; [3]University of Strathclyde, Glasgow, United Kingdom; [4]Queens University Belfast, Belfast, United Kingdom; [5]CLF, Rutherford Appleton Laboratory, Didcot, United Kingdom; [6]Lund University, Lund, Sweden

The generation of multi-MeV protons produced by the TNSA (target normal sheath acceleration) regime using an ultraintense ($>10^{18}$ W/cm^2) laser as the driver has gained great attention over the last years. It was shown that for most of the interesting applications a better control of the beam parameters is of main interest. Initial success in active manipulation of the spatial energy distribution of the beam by using an ablation ns laser pulse combined with the driver laser was noticeable [1]. Furthermore theoretical studies have shown that it is also possible to shape the spectral energy distribution by use of a double pulse arrangement with two fs pulses [2].

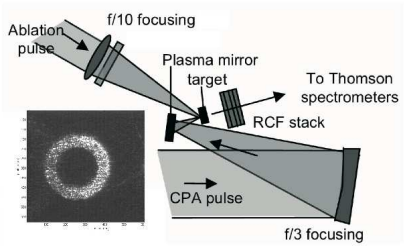

Figure 1: Experimental set up at the Vulcan Petawatt laser facility. The beam is focused using a f/3 off-axis parabolic mirror, with contrast enhancement provided by a plasma mirror. The inset shows the ring of the ablation pulse that is centered around the CPA focus.

We report on further investigations on controlling the beam shape by using an ablation ns laser pulse. All experiments were carried out at the Vulcan-Petawatt laser facility at the Rutherford Appleton Laboratory in Didcot, United Kingdom. The short pulse delivers intensities up to I = 4×10^{20} W/cm^2. To change the spatial energy distribution of the proton beams a ns ablation pulse with intensities I = 10^{11}-10^{13} W/cm^2 was shot on the front surface of the target directly before the short CPA pulse (delay = 0.5-6 ns) to create a long scale pre-plasma that was then heated by the short pulse. Figure 1 shows the experimental set up and one of the focal geometries of the ablation pulse. To produce a homogeneous pre-plasma the focus of the ablation pulse was formed with phase plates to a ring or a disc. The detection of the proton beam was done with stacks of radiochromic films [3] and thomson parabolas [4]. Figure 2 shows the eighth RCFs from two RCF stacks after the irradiation. One from a reference shot with the short pulse only (left), the second one from a shot with the ablation pulse in front (right). It is clearly visible that the spatial distribution of the beam gets more homogeneous. Actually it changes from a more gaussian shape to a more flat top shape [1]. Two proton beam line profiles of the sixth RCFs are shown in figure 3.

Not only that a significant improvement of the beam quality was achieved but also the maximum proton energy was increased by nearly 20 % from 26 MeV to 32 MeV. The short pulse laser energy on the target was 184 J in both cases.

It was shown that the shaping of the proton beam to a more flat top profile is possible, that would be advantageous in applications like proton radiography and imaging.

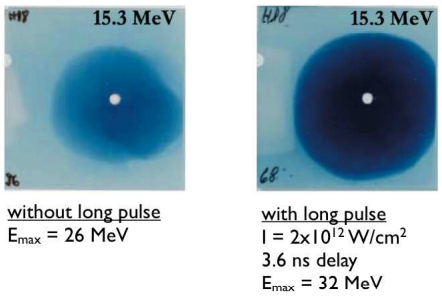

Figure 2: Eighth RCFs from two RCF stacks after the irradiation with the proton beam. The beam produced by the shot with the ablation pulse is much more homogeneous.

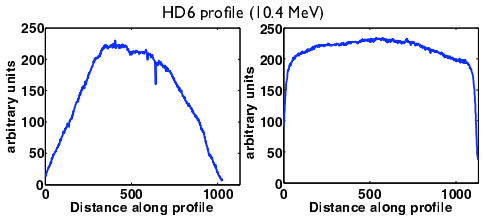

Figure 3: Proton beam line profiles from the sixth RCFs (proton energy 10.4 MeV). The more gaussian shape (left, without long pulse) was changed to a more flat top (right, with long pulse).

References

[1] D.C. Carroll *et al.*, Phys. Rev. E **76**, 065401 (2007)

[2] A.P.L. Robinson *et al.* Plasma Phys. Controlled Fusion **49**, 373 (2007)

[3] F. Nürnberg *et al.*, GSI Scientific report 2006, ISSN: 0174-0814, 280

[4] K. Harres *et al.*, GSI Scientific report 2006, ISSN: 0174-0814, 276

Experimental characterization of picosecond laser interaction with solid targets

D. Jung[1,2], L. A. Gizzi[3], L. Labate[3], D. Neely[1], M. M. Notley[1], P. P. Rajeev[1], M. Roth[2], G. Gregori[1,4]

[1]RAL, Chilton, UK; [2]TU-Darmstadt, Germany; [3]ILIL-IPCF, Pisa, Italy; [4]Clarendon Laboratory, Oxford, UK

Introduction

In this work we present measurements of the interaction of a picosecond laser pulse with a solid target. Time integrated x-ray spectra and pinhole images are compared with collisional radiative and radiation hydrodynamics simulation codes in order to characterize the plasma properties in terms of density and temperature.

Experimental Setup

The experiment was carried out at the Central Laser Facility at the Rutherford Appleton Laboratory (UK). 30 mJ, 15 ps, 532 nm, s-polarized laser pulses from a 10 Hz Continuum Leopard-D10 Nd:YAG laser system were focused on a solid titanium slab (30 x 15 x 3 mm^3) to a spot diameter of ~25 μm at a nominal intensity of 10^{14} W/cm^2. Pulses at fundamental frequency (1064 nm, 70 mJ) are also used in the experiment. A highly orientated pyrolytic graphite (*HOPG*) crystal in 002 orientation [1] coupled to a Fujifilm TR2040 image plate detector [2] measured Ti Kα line emission at 4.51 keV, its satellites, and the Ti Kβ line at 4.93 keV. The overall spectral resolution was E/ΔE~350. An x-ray pinhole camera consisting of four pinholes was used to monitor the radiation temperature. Different filter materials in each pinhole provided spectral information in the energy range up to a few keV. To achieve good signal-to-noise ratio, the signal was integrated over a large number of shots.

Results

The 1D radiation hydrodynamics code HELIOS [4] was used to simulate the titanium plasma. It predicts a maximum radiation temperature of T_r~70 eV and a maximum electron temperature of T_e<150 eV. The mass density is varying from 0.001 to 0.1 g/cm^3 in front of the target. Fig. 1 shows the measured calibrated titanium spectrum at different irradiation intensities and laser wavelength. All spectra were rescaled to equal intensities of the Kα lines. We clearly see that the spectra taken with 532 nm irradiation show a large number of satellites lines up to the Heα line. In contrast, at 1064 nm illumination only the Kα to Kβ lines appear with a few additional satellite lines near the Kα emission. The collisional-radiative code FLYCHK [4] was used to estimate plasma conditions in combination with the experimental data. Best agreement with the experimental data in terms of intensity ratio and line position is obtained by assuming that most of the inner shell emission comes from a plasma with T_e~12 eV and ρ~0.01g/cm^3. While K-shell lines are produced by hot electron collisions, the emission in the 4.55 to 4.75 keV region is associated to thermal ionization of the titanium plasma. Best agreement with the experimental data in terms of satellites is obtained with an electron

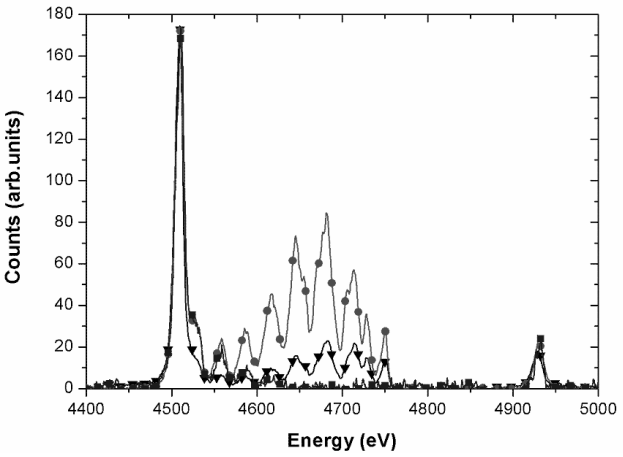

Figure 1: Ti Spectra, 1064 nm @70 mJ (blue/squares), 532 nm @33 mJ (red/circles), 532 nm @13 mJ (black/triangles)

temperature of T_e=180 eV and a density of 0.45 g/cm^3. As the wavelength of the laser is increased we see from Fig. 1 a reduction in the satellite emission. For 1064 nm illumination higher hot electron temperatures and backscatter fractions are predicted [5]. We thus speculate that for the 1064 nm case there is a reduced overall coupling efficiency of the laser energy into thermal heating. The integrated measured emission from each pinhole, F_i, of the multi pinhole camera was used to extract a value for the radiation temperature of the emitting plasma by a χ^2 minimization procedure:

$$\chi^2 = \sum_{i=1}^{3} \frac{\left(F_i - A\int_0^\infty \frac{E^3}{e^{E/k_B T_r} - 1} T_i^F(E) R(E) dE \right)^2}{\sigma_i},$$

where A is a constant, T_i^F the filter's transmission curve, R the detector energy response [3] and σ_i experimental uncertainty in the data. We obtained radiation temperatures T_r between 35eV and 60eV for different irradiation intensities. HELIOS predicted a maximum radiation temperature of 70 eV for an intensity of $4.5x10^{14}$ W/cm^2 which is comparable to the measured values.

References

[1] A. Pak *et al.*, Rev Sci Instrum **75**, 3747 (2004).
[2] J. Miyahara *et al.*, Nucl Instrum Meth A **246**, 572 (1986).
[3] N. Izumi *et al.*, Rev Sci Instrum **77** (2006).
[4] J. J. MacFarlane, I. E. Golovkin, and P. R. Woodruff, J Quant Spectrosc Ra **99**, 381 (2006).
[5] W. L. Kruer, *The physics of laser plasma interactions* (Westview, Boulder, Colo. ; Oxford, 2003).

Low Frequency Inductively Coupled Plasma (LF ICP)

C. Teske, and J. Jacoby
Inst. für Angewandte Physik, J. W. Goethe-Universität, D-60438 Frankfurt am Main, Germany

The topic of inductive coupled plasma (ICP) generation is known as an effective method of producing discharges with electron densities up to $n_e \sim 10^{18}\, m^{-3}$ without the need of electrodes in direct contact with the plasma. It has also been intended to use an ICP as an plasma target for the study of particle beam-plasma interactions.

A low frequency inductively coupled Plasma (LF ICP) has been set up by the plasma physics group and is now under investigation at Frankfurt University [1], [2]. The current device is a pulsed-power operated inductive discharge plasma with pulse duration times of $100\mu s$ to $200\mu s$, operation frequencies of $29kHz$ and pulse energies up to $100J$. Though pulse repetition remained at $1Hz$ for diagnostic purposes, higher repetition rates are no principal problem to the LF ICP.

The experimental setup of the LF ICP consists of a spherical discharge vessel with a diameter of approximately $20cm$ and a discharge volume of $4000ml$, surrounded by four induction coil segments and a capacitor bank. The induction coils are made of massive copper rods with a cross section of $20mm \times 2mm$. Connecting the coil segments in series with the capacitors leads to a series resonant circuit with an inductivity of $2.1\mu H$. The coils are fixed inside a tripod framework made out of insulating material DURATEC and a stainless steel support to guarantee mechanical reliability when high currents in the kA range are applied. It also fixes the coils at a very narrow margin (±0.5mm) to the glass vessel to achieve a maximum coupling efficiency between the primary circuit and the plasma load.

A critical factor of the experiment is the switching of the high currents involved in the low frequency inductive discharge generation and the corresponding high current rise times. Though power semiconductor devices like *thyristors* exist, the current rise time still remains a critical quantity. The maximum current rise time of the experimental device is about $1.8kA/\mu s$ with an applied voltage of $4100V$. For a first proof of principle an *ignitron* switch has been assembled to the primary coil to make the engineering of the LF ICP a less difficult task.

For the application as a plasma stripper the electron density achieved during the discharge generation is of main interest. Therefore a mixture of ArH_2 gas was used to determine the electron density by measuring the Stark broadening of the $H_ß$ emission line. Applying the VCS theory, the time averaged electron density could be determined from the spectroscopic data. According to [3] VCS gives reliable results for the estimated density near $10^{21} m^{-3}$. The resulting electron density achieved during the discharge generation is shown in Fig. 1.

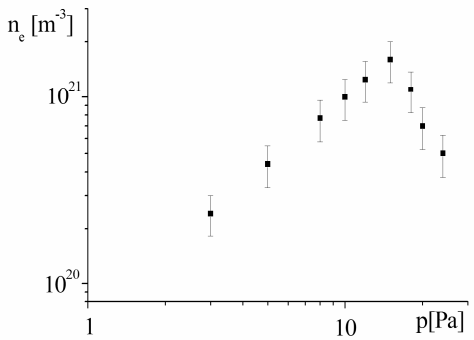

Fig. 1: Time averaged electron density of the LF ICP as a function of the gas pressure

Maximum electron density correlates with the maximum energy transfer efficiency and the maximum line intensity. This is in agreement with the theory of inductive discharge generation which confirms a linear dependence between the electron density and the power density. In terms of achievable electron density the LF ICP is well beyond the limit of $10^{19} m^{-3}$ as the current threshold for RF ICP's.

Compared to its high frequency pendant the LF ICP leads to some promising results in terms of achievable electron density and emitted light spectrum. The maximum electron density achieved with the current experimental setup was in the range of $10^{21} m^{-3}$, which is two orders of magnitude higher than the limit for RF ICP's. The energy transfer efficiency, which is a drawback of many designs, was paramount with 0.8 and still has the potential of improvement. Most of the emitted light was in the blue and violet wavelength with a considerable UV contribution. Referring to the spectroscopic data, there was also evidence for a high fractional ionization.

References

[1] C. Teske und J. Jacoby: *Einrichtung und Verfahren zur Erzeugung eines Plasmas durch niederfrequente induktive Anregung*. Patent Pending: DE 10 2007 039 758.7

[2] C. Teske und J. Jacoby: *Pulsed Low Frequency Inductively Coupled Plasma Generator and Applications*. IEEE Transactions on Plasma Science. Paper submitted 2007.

[3] D. L. Evans, D. P. Aeschliman and R. A. Hill: *Comparison of H_β theory and experiment at electron densities near $10^{15} cm^{-3}$*. Physical Review A, **10**, 6, 1974.

PHELIX – Achievements in 2007

K. Witte[1], V. Bagnoud[1], A. Blazevic[1], S. Borneis[1], C. Bruske[1], J. Caird[2], S. Calderon[3], U. Eisenbarth[1], J. Fils[1,4], S. Götte[1], T. Hahn[1], H.-M. Heuck[1,5], D. H. H. Hoffmann[4], D. Javorkova[1], G. Klappich[1], F. Knobloch[1], Th. Kühl[1,6], M. Kugler[1,7], S. Kunzer[1], M. Kreutz[1], B. LeGarrec[8], T. Merz-Mantwill[1], E. Onkels[1], S. Radau[9], M. Rebscher[1], D. Reemts[1], R. M. Richard[10], M. Roth[1,4], A. Roussel[8], Andreas Tauschwitz[1], Anna Tauschwitz[11], R. Thiel[1], U. Thiemer[1], D. Ursescu[1], U. Wittrock[5], B. Zielbauer[1,12], D. Zimmer[1,6]

[1]GSI Darmstadt; [2]Lawrence Livermore National Laboratory/USA; [3]Pegasus Design, Inc., Pleasanton, Cal./USA; [4]Technische Universität Darmstadt; [5]University of Applied Sciences Münster; [6]Johannes Gutenberg-Universität Mainz; [7]University of Applied Sciences Darmstadt; [8]Commissariat à l'Energie Atomique at Le Barp; [9]ROM Engineering, Inc., Tucson, Arizona/USA; [10]College of Optical Sciences, University of Arizona/USA; [11]University of Frankfurt; [12]Max-Born-Institut Berlin

A large variety of fundamental issues in plasma and atomic physics can be ideally experimentally investigated by the combination of highly charged heavy-ion and powerful laser beams. The GSI is in the worldwide unique position to have both types of beams at its disposal, the two ion beams UNILAC and SIS-18 and the PHELIX (**P**etawatt **H**igh-**E**nergy **L**aser for **H**eavy-**I**on E**x**periments) beam. At the experimental area Z6, the UNILAC ion and PHELIX beams will enable the study of the interaction of MeV ions in hot strongly ionized matter with respect to the energy loss of the ions and their charge-state changes. At the measuring site HHT, SIS-18 and PHELIX will be combined to study equation-of-state and phase transitions in yet unexplored regions of warm dense matter. As to atomic physics, QED in strong fields becomes accessible by the excitation of hydrogen-like uranium ions provided by the SIS-18 beam with a PHELIX driven x-ray laser.

In 2007 PHELIX has become available for laser-plasma experiments in the laser bay. Our major achievements include (a) the demonstration of the projected output energy of 500 J for pulses stretched to 1 ns, (b) the commissioning of the 31.5-cm aperture Faraday isolator (FI), (c) setup of the compressor in the laser bay, (d) improved serrated apertures enabling sharp-edged circular and elliptical fluence profiles of high energy loading, (e) a new stretcher with 1740 grooves/mm adapted to the new MLD (multi-layer dielectric) gratings and allowing a precise and easy control of the pulse duration, (f) larger bandwidth of the stretched pulse enabling shorter durations of the compressed pulse and thereby increasing its power, (g) further improvements of the PHELIX Control System (*PCS*), and (h) the x-ray laser campaign using the complete facility that has confirmed the suitability of PHELIX for state-of-the-art laser-plasma interaction experiments.

(a) Fig. 1 shows the main amplifier (MA) output energy E_{out} versus its input energy E_{in} at constant stored energy in the MA for pulses from the femtosecond front end stretched to 1 ns. The expected linear increase of E_{out} with E_{in} proves that the amplification is entirely in the small-signal gain regime up to the projected output energy of 500 J. Any deviation from linearity would indicate the unwanted appearance of saturation and/or parasitic oscillations. The double-pass gain of ~100 is consistent with the previously measured single-pass gain of ~10.

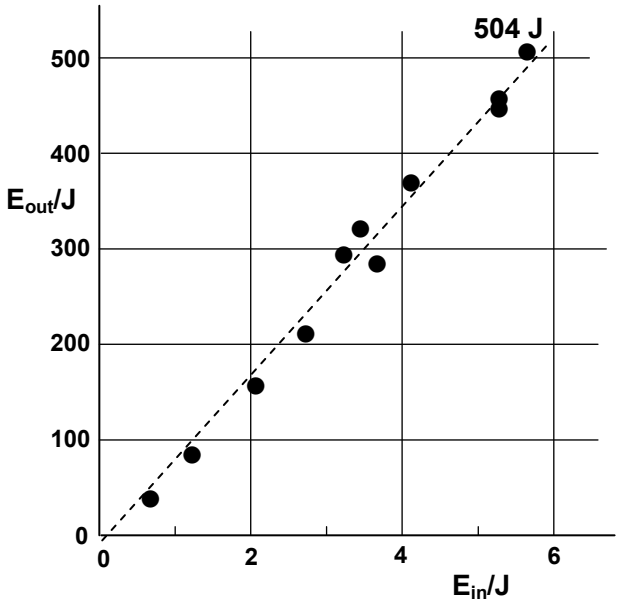

Figure 1: Output energy E_{out} of the main amplifier versus its input energy E_{in}

(b) The 31.5-cm aperture FI serves for the protection of PHELIX from light back-reflected from the target by normal scattering, stimulated Brillouin and/or Raman scattering. The FI consists of two polarizers rotated by 45° versus each other and in-between the 19-mm thick Faraday glass encapsulated by the coil that generates the required magnetic field for about 0.5 milliseconds (pulsed operation). The FI was first commissioned electrically, then synchronized to the laser pulse, and finally optimized with respect to the contrast ratio. The maximal energy of

the back-reflected light tolerated to leak through the FI is 0.1 J. When this value is exceeded, optical components upstream the MA will be damaged. Assuming a pulse with 500 J and a back-reflection from the target not larger than 10%, the minimally allowable contrast ratio is 50/0.1=500. The measured value of 1000 provides some margin for the planned installation of the booster amplifier. A sensitive element in the FI is the Faraday glass whose damage threshold limits the throughput energy to 500 J for a pulse of 1-ns duration and 25-cm diameter while 10-ns pulses allow the operation at 1 kJ.

(c) The compressor has been first commissioned with the multi-layer dielectric (MLD) gratings from Horiba-Jobin-Yvon which span 47cm in the horizontal direction (dispersion) and 33 cm in the vertical direction. The larger MLD gratings from LLNL (80 cm by 40 cm) will be used later. The incidence angle of 72° results in lower alignment and pointing sensitivity. With the small gratings in place, the incident beam profile is horizontally limited to 12 cm. In the vertical direction, the currently used beam extension is 24 cm so that the beam is elliptical. The compressor output energy depends on the pulse duration. The limiting mechanism is the damage threshold of the final grating. For 10- to 50-ps pulses, the maximal throughput energy is 200 J. For the shortest pulses of ~350-fs duration, it is reduced to 120 J.

(d) Serrated apertures (SA) combined with spatial filtering are well proven for the generation of beams with rectangular, squared, circular, or elliptical cross sections. The SA in the PHELIX beam line located between the front end and the preamplifier (see Fig. 2) was formerly fabricated using micro-machining techniques, offering a relatively poor control over the tooth shape. By using micro-lithograhically fabricated SAs, a better control over the tooth shape was achieved. This resulted in steep-edged beam profiles with high-energy loading. The fill factors go up to 0.8. The 12 by 24 cm² elliptical beam could be amplified without any signs of distortion.

(e) The new stretcher was built following the Banks design [1], however with some modifications. The essential new feature is the adjustability of the stretched-pulse duration thereby allowing the operation of the compressor with gratings at a fixed distance. This way the pulse duration can be easily changed from its minimal value of ~400 fs to 20 ps with either positive or negative chirp. The option to choose the sign of the chirp also helps to improve the recompression fidelity by the extinction of unwanted phase contributions occurring upon amplification.

(f) Gain narrowing is the main mechanism in reducing the spectral width of the pulse and thereby also its power. Properly designed Lyot filters can enlarge the spectral width by loss modulation. When the pulse passes the filter, the centre of the spectrum is more suppressed than the wings. Such filters are best incorporated in the low-power section of an amplifier chain where the energy loss is easiest to compensate. In PHELIX a suitable place is in-between the two regenerative amplifiers of the front end. The Lyot filter increases the bandwidth from 5.5 to 12 nm. Due to gain narrowing, the width of 12 nm shrinks to 4.9 nm at the exit of the main amplifier at typical PHELIX operating conditions. Without the Lyot filter, the bandwidth amounts 2.8 nm only. Assuming a constant spectral phase, the Fourier transform of the broader spectrum yields the pulse duration of 340 fs instead of 550 fs.

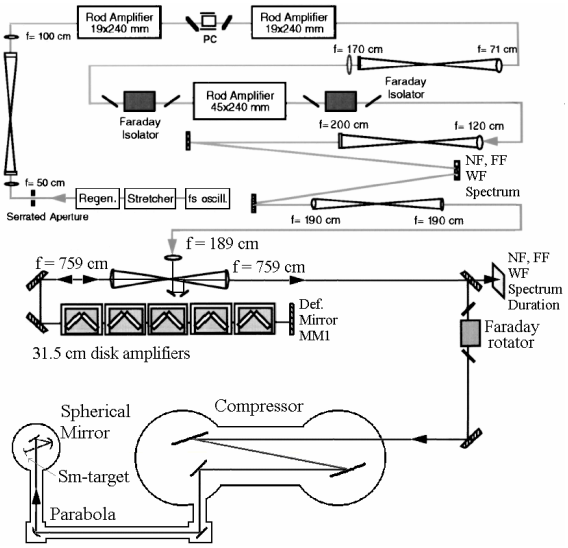

Figure 2: Schematics of PHELIX and the target area. NF near field fluence pattern, FF far field fluence pattern, WF wave front.

(g) As the first user of the control system (*CS)* framework, PHELIX employs the version 3.0 in which the event mechanism is based on DIM (Distributed Information Management) [2]. This eased the PHELIX control system (*PCS*) that is currently running distributed on 14 nodes. About 300 instances of nearly 50 different classes are used within the *PCS*, and roughly 10,000 variables are handled to ensure a safe shot procedure. Incorporation of the beam lines to the experimental areas Z6 and HHT will double the size of the *PCS* that is supposed to go to version 3.1 soon thereby benefiting from the developments available nowadays [3]. The internal distribution of timing signals were renewed in 2007. The hardware includes an interlock in case of a malfunction of the large-aperture FI. The synchronisation with the external experiments will be the next step. The work on the safety system of Z6 made significant progress in 2007. Its connection to the PHELIX interlock system (PILS) which embodies an important milestone will be realized soon.

(h) In December 2007 the PHELIX facility was used in a campaign of 24 full-system shots for the investigation of x-ray laser emission at 6.8 and 7.3 nm from plasma of nickel-like samarium ions employing a new simplified pumping scheme [4] that is particularly suited for the high pump energies needed for x-ray lasers emitting below 10 nm. The scheme was realized by placing a Mach-Zehnder interferometer into the beam line downstream the stretcher (see Fig. 2). It generates two pulses, the pre-pulse and the pump pulse, whose separation in time and intensity ratio can be chosen according to the experimental needs. Typical values are 1 ns and 1:20, respectively. These two pulses were amplified to energies of ~5 J and ~100 J, respectively, recompressed to the duration of 50 to 100 ps, and transported to the target chamber. A low-cost 30-cm diameter, metallic off-axis parabola of good optical quality turned the beam by 90° and directed it to a 20-cm diameter spherical mirror. These two mirrors generated a homogeneously illuminated line focus of 8 mm by 100 µm on the samarium target producing a travelling wave excitation. This pumping scheme ensures perfect on-target overlap of the two pulses which is mandatory for successful x-ray laser experiments and is rather difficult to achieve by beam splitting and subsequent overlapping of the pulses. In addition, any change of the experimental setup needs the realignment of a single beam only. The two samarium lines mentioned above could be clearly identified thus verifying the suitability of the new pumping scheme for x-ray lasers below 10 nm and, in the future, also in the water window. Furthermore, this measuring campaign qualified PHELIX for state-of-the-art laser-plasma interaction experiments.

Beam Line to Z6

The main optical and opto-mechanical components of the Z6 10°-beam line were ordered and delivered in 2007. The setup of the relay telescope and the north and south mirror towers were completed. Particularly noteworthy is the confirmation that the two periscope mirrors for the laser bay mirror tower which have a six-point whiffletree back-support meet all the requirements imposed on them as to wave front distortion (<60 nm peak-to-valley) and thermo-mechanical stability.

Theory

To support the experimental program of PHELIX, the hydro-code CAVEAT is currently extended to include non-linear heat conduction and radiation transport. The new code CAVEAT-TR will enable the in-house simulation of laser heated matter including hohlraum targets that will be used for energy loss experiments in the Z6 target area. While the implementation of heat conduction is finished and successfully tested [5], the implementation of the radiation transport will be completed in time to aid the experimental program at Z6 in 2008.

References

[1] Aberration-free, all reflective laser pulse stretcher, US Patent 5960016, Publication date 28 Sept. 1999.

[2] Enhancing the *CS* Framework for Distributed Control Systems, D. Beck, H. Brand, and S. Götte, GSI Scientific Report 2006, page 214.

[3] Improving the usability of the *CS* framework, D. Beck, H. Brand, M. Feldmann, M. Kugler, and A. Schwinn, GSI Scientific Report 2007 (this publication).

[4] A 180-eV X-Ray Laser Pumped by PHELIX, J. Habib et al., GSI Scientific Report 2007 (this publication).

[5] CAVEAT-TR: A 2D hydrodynamic code with heat conduction and radiation transport. Implementation of the SSI method for heat conduction, M. Basko, J. Maruhn, A. Tauschwitz, GSI Report 2007 -05

A 180 eV X-Ray Laser Pumped by PHELIX

J. Habib[3], S. Kazamias[3], A. Klisnick[3], D. Ros[3], B. Zielbauer[3], D. Zimmer*[1,2], V. Bagnoud[1], U. Eisenbarth[1], D. Javorkova[1], T. Kuehl[1,2], D. Ursescu[4], J. Dunn[5], G. Pert[6], and the PHELIX Team[1]

[1]GSI, Darmstadt, Germany; [2]Johannes Gutenberg-Universität Mainz, Germany; [3]Laserix, Université Paris-Sud 11, Orsay, France; [4]National Institute for Laser, Plasma and Radiation Physics , Bucharest, Romania; [5]Lawrence Livermore National Laboratory, USA; [6]University of York, UK

A number of applications, including imaging of biological specimen and diagnostics of dense plasmas, require coherent X-ray sources exceeding 100 eV photon energy. A main obstacle for such laser sources was the high pump laser energy required for the ionization and the excitation of the lasing transitions. Over the last few years tremendous progress was achieved towards lowering the necessary energy [1]. For this, two pulses of different duration and at different angles of incidence were applied [2]. This is a non-trivial complication, however, for the delivery of high-energy pulses that require the use of large beams. A first experiment using compressed pulses in the range around 50 ps and at energies between 50 J and 100 J at the PHELIX laser therefore incorporated a simplified double pulse scheme recently demonstrated at the PHELIX front-end [3]. In this scheme, a Mach-Zehnder type beam splitting and recombination creates two pulses of identical duration in the front-end of the laser, where the beam diameter is below 5 mm. This double pulse was amplified by the full PHELIX amplifier chain, and recompressed to produce two pulses of 50 ps to 100 ps duration and with a delay of approximately 1 ns. In this scheme, a line focus for both pulses was produced by a single focussing optics consisting of a 300 mm diameter 90-degree off-axis parabola and a 200 mm diameter spherical mirror. (Fig. 1)

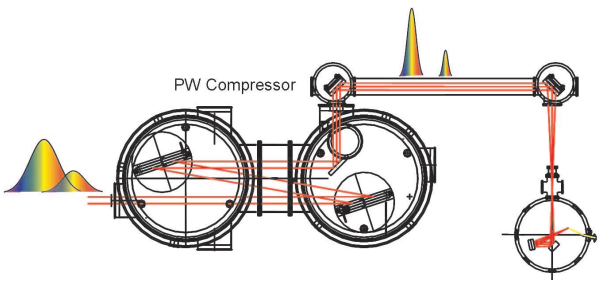

Figure 1: Beam pass of the high energy pumping arrangement. The double-pulse structure before and after compression is illustrated by the inserts above.

A fast photodiode and alternatively a streak camera were used to determine the spacing of the pulses and the relative intensity of possible pre-pulses. The quality and orientation of the line focus were checked with a microscope imaging its shape on a glass diffuser at the final target position. This target was fabricated at the GSI target lab by coating a glass substrate with a film of 2-3 μm of Samarium. The X-ray laser output was analyzed by a 1200 lines/mm flat-filed grating and recorded on an XUV CCD camera. Fig. 2 shows an overlay of the region around the Ni-like Samarium lasing lines at 6.8 nm and 7.3 nm, registered at the second order of the grating, and a reference showing the carbon K-edge at 4.3 nm registered in third order at the same spectrometer settings.

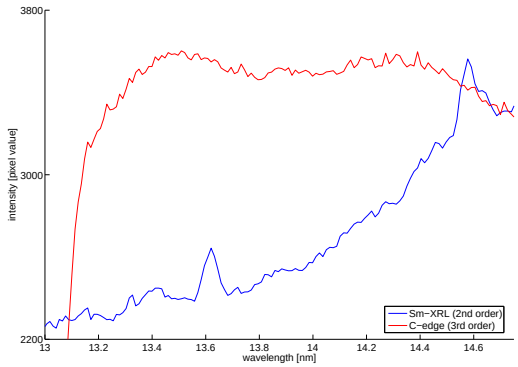

Figure 2: Registered spectrum of the two lasing lines in Ni-like samarium recorded in 2nd order, and a reference spectrum of the carbon K-edge at 4.3 nm recorded in 3rd order of the flat-field grating spectrometer.

The first result demonstrates the feasibility of applying the simplified double pulse scheme for the pumping of high energy X-ray lasers. This opens the way to a wider application of such X-ray sources for dedicated X-ray diagnostics of e.g. ion produced plasmas, as well as a future routine operation at facilities like LASERIX [4]. The work was supported through the Laserlab Europe Integrate Infrastructure Initiative.

References

[1] K. Cassou, et al., Opt.Lett. 32 (2007) 139

[2] T. Kuehl, et al., Laser & Part. Beams 25 (2007) 93

[3] D. Zimmer, et al., To be submitted in 2008, see also this annual report.

[4] S. Kazamias, et al., J.de Physique 138 (2006) 138

* d.zimmer@gsi.de

An improved double-pulse non-normal pumping scheme for transient collisionally excited soft X-ray lasers

D. Zimmer*[1,2], B. Zielbauer[1], V. Bagnoud[1], U. Eisenbarth[1], D. Javorkova[1], T. Kuehl[1,2], and the PHELIX Team[1]

[1]GSI, Darmstadt, Germany; [2]Johannes Gutenberg-Universität Mainz, Germany

An improved pumping scheme for transient collisionally excited soft x-ray lasers is presented. In contrast to usual approaches, where a nanosecond pre-pulse is assumed to provide the optimal plasma preparation and a picosecond pulse performs the final heating- and excitation process, two pulses of equal duration are applied. Both pulses are produced in the front-end of the CPA pump laser. Creating two pulses of equal duration can be well achieved in a Mach-Zehnder geometry. Using the travelling wave focusing geometry from [1] adjustment of the pump optics is straightforward and stable. The two pulses are focused onto the target with the same spherical mirror under non-normal geometry, optimized for efficient traveling wave excitation for the main-pulse. A first experiment [2] was performed on Ni-like palladium (14.7 nm) at less than 500 mJ total pulse energy on the target. This proves that this configuration is at least as efficient as the standard GRIP scheme, providing much simpler and more reliable operation.

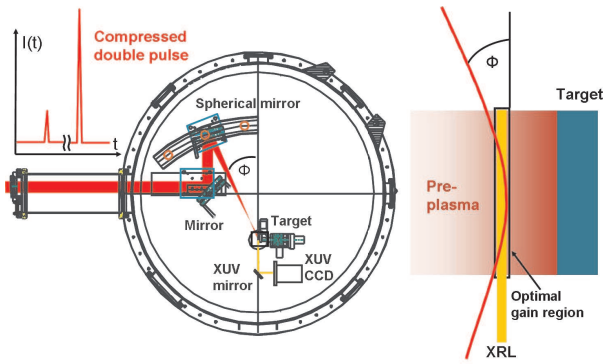

Figure 1: Experimental setup showing the pump laser beam-lines and XRL diagnostics. On the right side the schematic view of the GRIP scheme is given.

The experimental set-up is depicted in fig. 1: We used the focusing system which produces a line focus with an intrinsic travelling wave speed of 1.2 c. The beam from the compressor is deflected by a flat mirror onto a spherical mirror with a focal length of 600 mm which is positioned off the normal incidence. The line focus on the Pd slab target was 50 μm by 5.5 mm FWHM. Both pulses hit the target at the same grazing incidence angle of 29 degrees, a value determined to be the optimal GRIP configuration in the classical scheme [3]. Thereby the electron density at which the energy is absorbed is matched to the optimum pumping density. The insert in fig. 1 shows the effect of the geometry for the absorption of the two pulses on the target. The pre-pulse is - except for a possible weak pre-plasma, produced by the $< 10^{-3}$ pedestal - hitting directly onto the target, creating a plume of plasma expanding with approximately the speed of sound of the metal, around 20 micrometer per nanosecond. The second pulse is refracted in the emerging plasma. An intrinsic improvement comes along with the perfect overlap of both pulses due to the same optical path. This allows an optimized pumping of the gain region. An image of the laser output after 30 cm distance is shown in fig. 2 together with the dependence of the output energy on the duration of the pump pulse. The intensity registered on the CCD camera corresponds to XRL-energies up to 0.3 μJ with less than 700 mJ total pump energy.

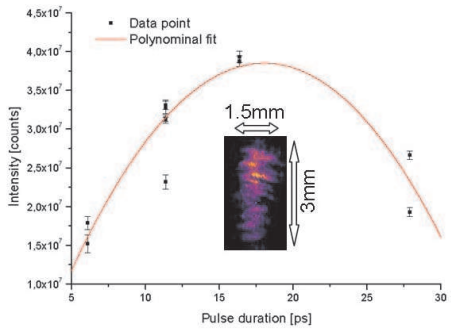

Figure 2: Dependence of the XRL-intensity on the time duration of the pumping pulses with a pulse delay of 1 ns. Insert: XUV camera image showing the XRL beam profile.

The improved double pulse non-normal incidence pumping scheme provides a simplified and efficient way to produce XRL output at close to 100 eV photon energy. In comparison to earlier work using normal incidence on the target, the pumping energy threshold for Pd-XRL emission is strongly reduced from above 1 J to less than 500 mJ. It opens the way to high-repetition-rate XRL's in the 100 eV range and to manageable multi-100 eV XRL sources.

References

[1] P. Neumayer et al., Appl. Phys. B, 78 (2004) 957-959

[2] D. Zimmer, et al., To be submitted in 2008.

[3] B. Zielbauer, thesis, GSI 10/2007

* d.zimmer@gsi.de

Implementation of heat conduction in 2D hydrodynamic code CAVEAT-TR

M.M. Basko*[1], J.A. Maruhn[2], An. Tauschwitz[2], and K. Witte[1]
[1]GSI, Darmstadt, Germany; [2]University of Frankfurt am Main, Germany

Combination of intense laser and ion beams at GSI offers a unique possibility to study matter at high energy densities. The PHELIX laser beam will be used to create hot plasmas by direct target irradiation or using indirect-drive schemes based on radiative hohlraums. A two-dimensional hydrodynamic code including heat conduction and spectral radiation transport is required for preparation and interpretation of experiments involving high-temperature laser plasmas. Here we report on an upgrade of the 2D pure hydrodynamic code CAVEAT [1] developed at LANL to a version which includes thermal conduction. The new version has been named CAVEAT-TR. The implementation of the radiation transport is currently under way.

The original CAVEAT scheme is based on a Godunov-type method and cell-centered values for all principal dynamic variables, one of which is the total energy density. In contrast, a natural principal variable for thermal conduction and radiation transport would be the vertex-centered temperature. The difficulties of combining these two approaches were overcome using the symmetrical semi-implicit (SSI) method [2]. As discussed in [3], the Lagrangian phase of the computation cycle is split into the hydrodynamic step, which remains unaltered from the original CAVEAT version, and the SSI step, which combines heat conduction, radiation and external heating. The SSI terms are evaluated using the SSI-advanced temperatures, which differ from those finally advanced in the Lagrangian step. The arising energy disbalance is corrected at the next time step. Introduction of separate time-step control criteria for the SSI algorithm ensures accuracy and stability of the simulations.

To test the propagation of non-linear heat fronts, we consider a spherically symmetric wave governed by the equation

$$\rho c_V \frac{\partial T}{\partial t} = \frac{1}{r^2}\frac{\partial}{\partial r}\left(r^2 \kappa \frac{\partial T}{\partial r}\right) , \qquad (1)$$

where the conduction coefficient $\kappa = \kappa_0 T^2$. It is assumed that at $t = 0$ a finite amount of energy is instantaneously released in the center at $r = 0$. The solution to this problem is fully analytical. Numerical simulation was performed in the cylindrical r, z coordinates using a 3-block skewed mesh shown in Fig. 1. The results of this simulation are presented in Fig. 2. The temperature profiles along all three line-outs are described to an accuracy of about 0.2%. This demonstrates that the adopted reinterpolation scheme from the cell-centered to the vertex-centered temperatures provides more than sufficient accuracy. The use of cylindrical coordinates does not lead to spurious numerical effects along the z-axis. The calculation needs a relatively large number, $N_{cyc} \gtrsim 10\,000$ of time steps, which is due to the fact that the contrast between the initial central temperature and the "sensitivity" threshold for temperature variations is more than 10 order of magnitude.

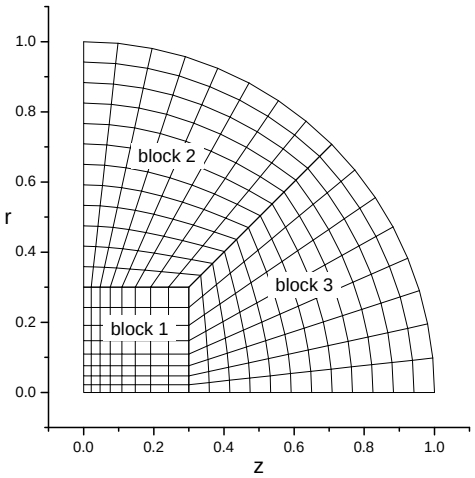

Figure 1: Skewed 3-block mesh.

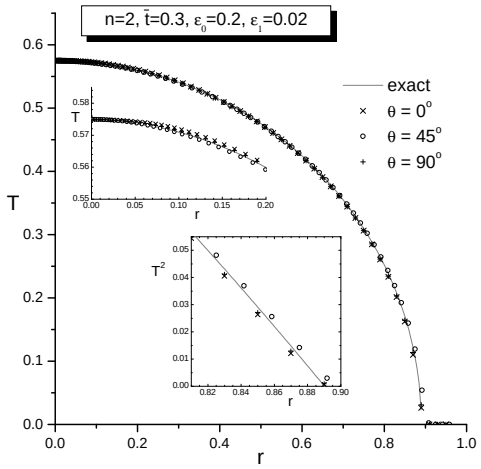

Figure 2: Temperature profiles for the polar angle values θ=0, 45° and 90° compared with the exact solution.

References

[1] F. L. Addessio et al., LA-10613-MS, Rev. 1, UC-905 (Los Alamos, 1992).

[2] E. Livne and A. Glasner, J. Comp. Physics **58** (1985) 59.

[3] M.M. Basko, J.A. Maruhn, An. Tauschwitz, GSI Report 2007-05.

* on leave from ITEP, Moscow

Relativistic critical density increase under a linearly polarized laser pulse*

P. Mulser, TQE: Theoretical Quantum Electronics, TU Darmstadt, Germany

H. Ruhl, Ruhr-Universität Bochum, Germany

A high critical density is important for laser beam propagation into high density samples for uniform heating and efficient energy tramsmission and transport. Its increase under irradiation of intense linearly polarized laser light is analyzed and effects contributing are addressed. It is shown "experimentally" that the concept of a cycle-averaged critical density is meaningful even at relativistic intensities and the corresponding overall Lorentz factor γ is determined and compared with analytical expressions. High γ values are of particular relevance for fast ignition in inertial confinement fusion.

Penetration of the laaser light is determined by the ratio of the laser frequency ω to the plasma frequency $\omega_p = (n_e e^2/\varepsilon_o m_e)^{1/2}$ which depends on the electron mass m_e and the electron density n_e. At high laser intensities the electrons oscillate at MeV energies and become more massive which favours penetration. However, as a consequence of the Lorentz contraction n_e also transforms by the same factor so that one is left with the well-known fact that the plasma frequency is invariant with respect to a Lorentz transformation. Only ω is Doppler shifted in the refractive index $\eta = (1 - \omega_p^2/\omega^2)^{1/2} = (1 - n_e/n_c)^{1/2}$, n_c critical density. At high laser intensities the ions can still be treated as immobile while the electrons move at relativistic velocity. This makes the passage from a monofluid description for low intensities to a two-fluid model necessary with the consequence that Lorentz contraction in n_e has to compete now with the stringent property of quasineutrality of the plasma.

There are essentially four effects which determine the relativistic increase of the critical density from n_c to $n_{cr} = \gamma n_c$: the releativistic electron mass increase from the oscillatory motion (I), the dynamical interplay between Lorentz contraction and restoration of quasineutrality (II), the distortion of the regular electron orbits in presence of the collective plasma electric fields (III), and the electron mass increase due to temperature effects in the MeV range (IV). Effects I and IV act in favour of high γ values, II counteracts and on III nothing is known so far. Due to the violent periodic motion of the electron fluid against the impinging laser beam and its subsequent recession a momentaneous critical density is no longer meaningful and the question of its existence on the laser cycle average arises. With regard to its complexity the problem can be solved only by real (important, however difficult) or numerical experiments.

We decided for the latter. Particle-In-Cell (PIC) simulations were performed with the PSC code [1] for laser intensities $I = 10^s$ W/cm², $s = 18 - 22$ under normal and 45° incidence. The results, averaged over two laser periods at 80 fs, are shown in Fig. 1 (2nd and 4th columns for each intensity at normal and 45° incidence). For supporting the numerical results and perhaps gaining some physical insight, in the absence of any knowledge on phenomenon III , we start from the assumption of regular vacuum-like 8-shape orbits and determine a "theoretical" γ factor from the formula

$$\gamma=[1+ (1 + r)^2a^2/2]^{1/2}, \qquad (1)$$

with ra the reflected normalized wave amplitude. First and 3rd columns in Fig.1 indicate the result for perpendicular and 45° incidence for comparison. We deduce that a cycle-averaged critical density makes sense and that the factor γ of the relativistic increase of the critical density can be fitted reasonably well by

$$\gamma=\{1+ I\lambda^2\ [\mathrm{W/cm^2\mu m^2}]/10^{18}\}^{1/2}\ . \qquad (2)$$

From this fit it can be deduced that quasineutrality of the plasma severely limits the electron density increase due to Lorentz contraction. At high laser intensities the increase of n_c is of great importance in designing and interpreting fast ignition experiments with lasers. For example, at Nd laser intensity $I = 10^{21}$ W/cm² results $\gamma = 30$.

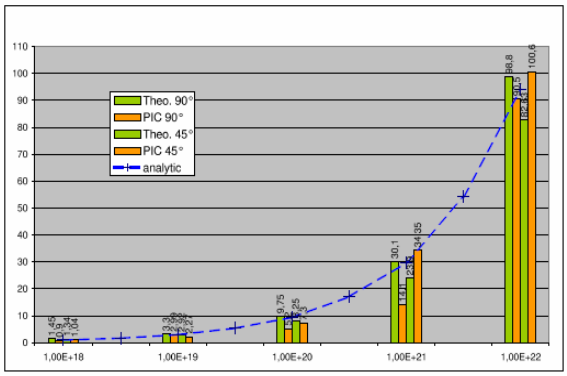

Figure 1: Critical density increase by factor γ as a function of at normal (LHS pairs) and 45° incidence (RHS pairs); dashed line fit from Eq. (2).

References

[1] H. Ruhl, in M. Bonitz et al. (eds) *Introduction to Computational Mehods in Many Body Physics*, ISBN 1- 58949-009-6 (2006).

* Work supported by ILIAS contract with GSI.

Absorption of ultrashort laser pulses in strongly overdense targets

M. Cerchez, R. Jung, J. Osterholz, T. Toncian, and O. Willi, Universität Düsseldorf, Germany
P. Mulser, TQE: Theoretical Quantum Electronics, TU Darmstadt, Germany
H. Ruhl, Institute for Theoretical Physics I, Ruhr-Universität Bochum, Germany

Absorption measurements on solid conducting targets have been performed in s and p polarization with ultrashort, high-contrast Ti:Sa laser pulses at intensities up to 5×10^{16} W/cm² and pulse duration of 8 fs [1]. The particular relevance of these measurements lies in the fact that the extremely short laser pulse interacts with matter close to solid density during the entire pulse duration. A pronounced increase of absorption for p-polarization at increasing angles is observed reaching 77% for an incidence angle of 80°. Simulations performed using a 2-D Particle-In-Cell (PIC) code combined with alternative models allow to isolate a high collisionless absorption component in steep plasma profiles of relative scale lengths $L/\lambda \approx 0.01$. In interpreting the underlying mechanism of this kind of interaction it is found that the model of anharmonic resonance is a favorable candidate.

The experiments have been carried out employing a Ti:Sa laser system operating in CPA mode. It delivers linearly polarized pulses of 100 -120 μJ at 790 nm (central wavelength) and 8 fs duration on target. The pulse contrast ratio was better than 10^5 for times larger than 1 ps before the main pulse and better than 10^8 for times larger than 6 ps. The laser pulse was focused in vacuum onto the target by an f/2.8 off-axis parabola of 108 mm effective focal length to a spot diameter of ≈ 3.2 μm, delivering an average intensity of $(4 - 5) \times 10^{16}$ W/cm². The absorbed energy fraction A was determined as a function of the incidence angle θ and the polarization of the laser radiation. The experimental investigations cover a wide range of θ (10° - 80°) and over 4 orders of magnitude of the laser intensity (5×10^{12} - 5×10^{16} W/cm²). The targets consisted of mirror-flat aluminium layers with a thickness of $\approx$ 300 nm and a roughness of less than 5 nm. The target was placed at the center of an integrating Ulbricht sphere of 10 cm in diameter. The absorbed fraction A is given by $A = 1 - R$, R fraction of light reflected from the target.

The absorption A as a function of angle of incidence is presented in s and p polarization for an intensity, averaged over 10 - 20 shots at each angle, of 5×10^{16} W/cm² . For s polarization, while the angle of incidence is increasing, the absorption drops from 19% at $\theta = 15°$ to 6% at $\theta = 70°$, whereas in p polarization A increases for larger angles and reaches its maximum value of 77% at 80°. The difference $A_p - A_s$ represents a measure of collisionless absorption. The question of how absorption is accomplished when electron-ion collisions become ineffective at high laser intensities has been open for two decades. Numerical simulations with the PSC-PIC code are able to reproduce the experimental values of Fig. 1 for density scale lengths of $L \cong 10$ nm, however they need interpretation. To this aim the MULTI-fs code [2], capable

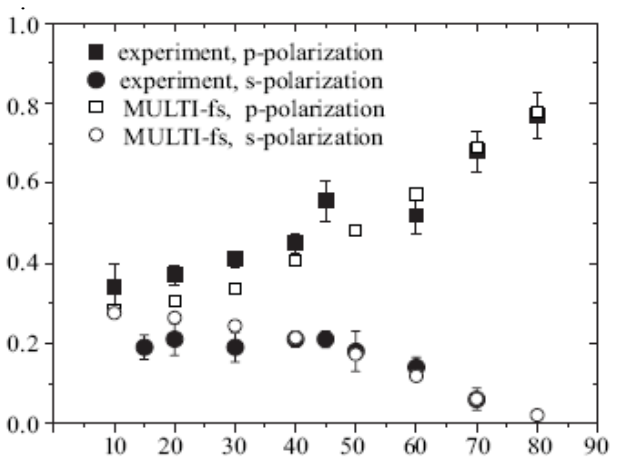

Figure 1: Angular dependence of the absorption A of 8 fs, 790 nm laser pulses by an aluminium target, s (circle filled symbols) and p polarized (squared filled symbols) at an average intensity of 5×10^{16} W/cm². MULTI-fs hydrocode results under the experimental conditions for a plasma profile of L=2 nm are shown by open symbols.

of simulating linear resonance as well as collisional absorption, was used and, as Fig. 1 shows, it reproduces the measurements under realistic conditions. Unfortunately, closer inspection, in particular of the validity of linear resonance absorption, leads to the conclusion that MULTI-fs is not applicable here. Alternatively, satisfactory agreement with the experiment is also found by assuming that all absorption is purely collisional, and by choosing the electron-ion collision frequency properly. In the context here it means unrealistic high values for it, exceding any reasonable estimate by at least a factor of 10. Therefore we developed the new model of anharmonic resonance [3]. A thorough inspection and numerous estimates show that it is the best candidate so far. The measurements of Fig. 1 can be regarded as the first expereimnental proof of [3].

References

[1] Mirela Cerchez et al., Absorption of ultrashort laser pulses in strongly overdense targets; submitted for publication.

[2] K. Eidmann, J. Meyer-ter-Vehn, T. Schlegel, S. Hüller Phys. Rev. E **62**, 1202 (2000).

[3] P. Mulser, D. Bauer and H. Ruhl, *Anharmonic resonance absorption of high-power laser beams*, submitted for publication.

Numerical Modeling of Heavy Ion Induced Stress Waves in Solid Targets*

N.A. Tahir[1], V. Kim[2], A. Shutov[2], I.V. Lomonosov[2], A. Matveichev[2], A. Ostrik[2], A.R. Piriz[3], J.J. Lopez Cela[3], and D.H.H. Hoffmann[4]

[1]GSI, Darmstadt, Germany; [2]IPCP, Chernogolovka, Russia; [3]UCLM, Ciudad Real, Spain; [4]TU Darmstadt, Germany

In August 2007, experiments were carried out at the HHT experimental area to study thermal stress waves induced by uranium beam in targets made of different materials. This work is of importance to development of a solid target for the Super-FRS at FAIR [1]. The following beam and target parameters have been used in these experiments.

Copper Target

The target is cylinder with a length = 7 mm and radius = 5 mm. One face of the cylinder is irradiated with a uranium beam having a particle energy of 400 MeV/u. The beam pulse consists of two bunches, each having a full width at half maximum (FWHM) of 80 ns and the total pule duration is 500 ns. The beam focal spot size (FWHM of the Gaussian power distribution in transverse direction) is assumed to be 0.5 mm. Two different values for beam intensity, N are used.

Case I: N = 5.0 $\times$ 10^7 ions per pulse is considered to study the elastic properties of Cu.

Case II: N = 1.8 $\times$ 10^8 ions per pulse is considered to study the plastic behavior of Cu.

Lead Target

In this case the target is a lead cylinder with a length = 7 mm and radius = 5 mm. Again, one face of the target is irradiated with a uranium beam having a particle energy of 400 MeV/u. The beam pulse consists of two bunches, each having a full width at half maximum (FWHM) of 80 ns and the total pule duration is 500 ns. The beam focal spot size (FWHM of the Gaussian power distribution in transverse direction) is assumed to be 1.0 mm. The following two values for the beam intensity are used.

Case III: N = 2.5 $\times$ 10^7 ions per pulse is considered to study the elastic properties of Pb.

Case IV: N = 5.5 $\times$ 10^7 ions per pulse is considered to study the plastic behavior of Pb.

Tantalum Target

In this set of experiments, tantalum cylinders, each with length and radius = 5 mm are used. The target is facially irradiated with a uranium beam having a particle energy of 400 MeV/u. The beam focal spot size (FWHM of the Gaussian power distribution in transverse direction) is assumed to be 0.5 mm. The following three values for beam intensity, N are used.

Case V: N = 5.0 $\times$ 10^7 ions per pulse is considered to study the elastic properties of Ta. The beam pulse consists of two bunches, each having a full width at half maximum (FWHM) of 80 ns and the total pule duration is 500 ns.

Case VI: N = 1.5 $\times$ 10^8 ions per pulse is considered to study the plastic behavior of Ta. The beam pulse consists of two bunches, each having a full width at half maximum (FWHM) of 80 ns and the total pule duration is 500 ns.

Case VII: N = 4 $\times$ 10^9 ions per pulse is considered to study the material rupture. In this case, the beam pulse consists of four bunches, each having a full width at half maximum (FWHM) of 80 ns and the total pule duration is 1 microsec.

Tungsten Target

For tungsten, we have considered four different cases using cylindrical target, each with length and radius = 5 mm as described below. The targets are facially irradiated with uranium beam having a particle energy of 400 MeV/u.

Case VIII: N = 5 $\times$ 10^7 ions per pulse that is composed of two bunches with the total pule length = 500 ns. The beam spot size (FWHM) = 0.5 mm and this experiment will be performed to study elastic properties of W.

Case IX: N = 1.5 $\times$ 10^8 ions per pulse that again consists of two bunches with the total pule length = 500 ns. The beam spot size (FWHM) = 0.5 mm and this experiment will be carried out to study plasticity in W.

Case X: N = 1.5 $\times$ 10^8 ions per pulse that consists of a single Gaussian bunch that is 250 ns long (FWHM = 80 ns). The beam spot size (FWHM) = 1.0 mm.

Case XI: N = 5.0 $\times$ 10^8 ions per pulse that consists of 4 Gaussian bunches each 250 ns long (FWHM = 80 ns) so that the total pulse length is 1 microsecond. The beam spot size (FWHM) = 1.0 mm. A comparison between simulation results obtained in case X and case XI will show show the effect of beam time structure on the target response.

* Work supported by BMBF

Solid Graphite Target

The following two cases have been considered for graphite target. These experiments will generate physical conditions that will be somewhat similar to those simulated in [1].

Case XII: N = 2.0 $\times$ 10^9 ions per pulse that consists of 5 Gaussian bunches each having a FWHM = 80 ns so that the total pulse length is 1 microsecond. The standard deviation, σ of the spatial power distribution (Gaussian) = 0.5 mm. The target length as well as the radius are 5 mm so the target length is less than the ion range.

Case XIII: N = 4.0 $\times$ 10^9 ions per pulse whereas the rest of the beam parameters are the same as in case XII. The spatial power distribution is a Gaussian with a standard deviation, σ = 2.0 mm. The target length is 15 mm while the radius are 5 mm. In this case the target length is larger than the ion range so that the Bragg peak will lie inside the target.

Using a three-dimensional computer code, PIC3D, we have carried out numerical simulations of beam target interaction. In this contribution we present results for case I, for further details see [2]. The target is longer than the range of the projectile particles and the Bragg peak lies inside the target. The maximum specific energy deposition in this case is of the order 0.24 kJ/g. In Fig. 1 we plot the temperature vs radius at L = 3.5 mm. It is seen that as a result of energy deposition by the first bunch, the temperature increases to a peak value of about 400 K at the center (profile at t = 200 ns) and due to energy deposition by the second bunch, the temperature increases to about 500 K. Fig. 2 shows the corresponding pressure profiles that show propagation of pressure waves in the target. The density does not undergo any significant change in this case. In Fig. 3 we plot the surface pressure at point L = 3.5 mm as a function of time. The surface velocity as a function of time is given in Fig. 4. It is seen that the maximum surface velocity is about 1.5 m/s. The oscillations damp out with time because the material is in elastic regime.

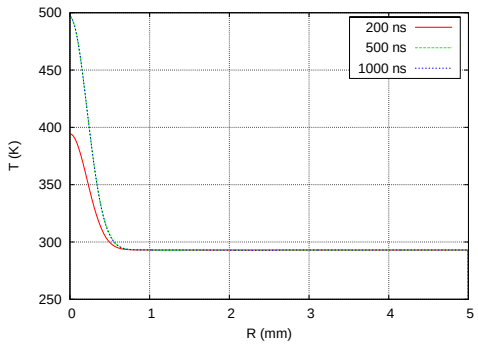

Figure 1: Temperature vs radius: Cu cylinder, L = 7 mm, r = 5 mm, N = 5 $\times$ 10^7 uranium ions, two successive Gaussian bunches (FWHM = 80 ns), pulse duration = 500 ns, spot size (FWHM) = 0.5 mm:

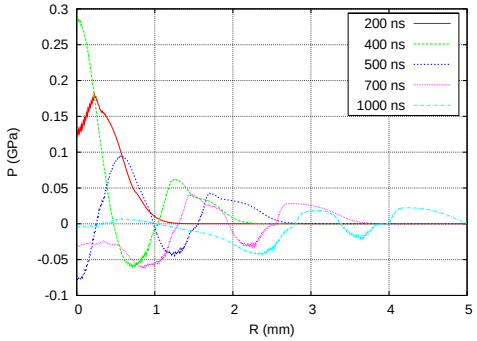

Figure 2: Pressure vs radius for case in Fig. 1

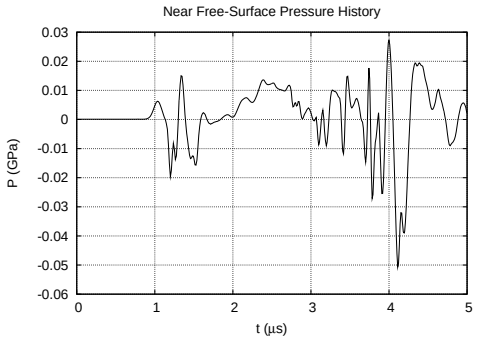

Figure 3: surface pressure vs time for case corressponding to Fig. 1

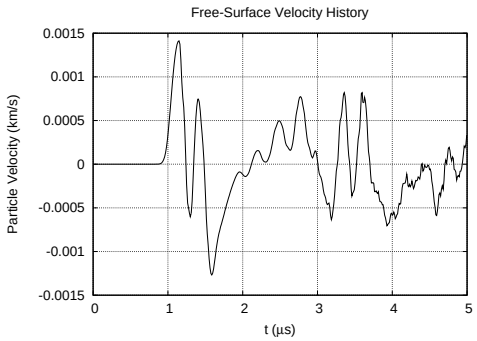

Figure 4: surface velocity vs time for case corressponding to Fig. 1

References

[1] N.A. Tahir et al., J. Phys. D: Appl. Phys. 38 (2005) 1838.

[2] N.A. Tahir et al., Laser Part. Beams 25 (2007) 523.

Gasdynamic issues in transverse beam size measurements*

A. Hug[1,2], D. Varentsov[2], V. Turtikov[3], D.H.H. Hoffmann[1,2], A. Fertman[3], M. Kulish[4], J. Menzel[1], V. Mintsev[4], N. Müller[1], D. Nikolaev[4], B. Sharkov[3], N. Shilkin[4], V. Ternovoi[4], and S. Udrea[1]

[1]TUD, Darmstadt, Germany; [2]GSI, Darmstadt, Germany; [3]ITEP, Moscow, Russia; [4]IPCP, Chernogolovka, Russia

In experiments at the HHT area, intense uranium beams from SIS-18 are focused to a submillimeter-spot to generate high energy density (HED) states in the target material. For this HED physics experiments, as well as for the future HEDgeHOB experiments at FAIR, it is essential to know the beam profile at the focal plane with $(10-50)\,\mu$m accuracy. Due to the high level of energy deposition by the intense beam, any material placed near the focal plane will melt or evaporate. Therefore one needs non-intercepting diagnostics for transverse beam profile measurements.

Position and transverse dimensions of the beam have been measured by recording beam-induced light emission images in the gas-filled target chamber by two fast intensified CCD-cameras, installed perpendicular to the beam axis. However, the interaction with the intense beam may lead to a fast gasdynamic radial expansion of the beam-heated gas, and consequently, modification of the gas radial density distribution during the interaction. This effect is illustrated for Ar and He in Fig. 1, which shows results of corresponding simulations with *VarJET* 2D gasdynamic code[1].

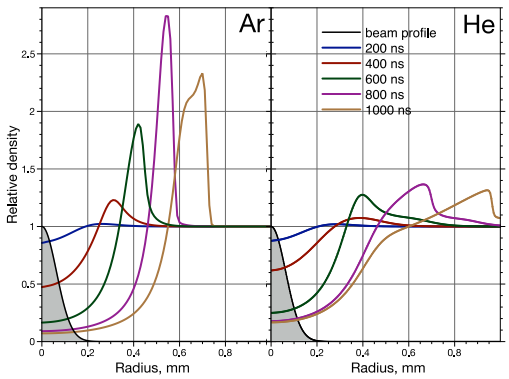

Figure 1: Evolution of radial density profiles of Ar and He due to gasdynamic motion.

The measured transverse light emission profile is a product of the real beam intensity distribution and the gas density profile. Therefore the expansion of the heated gas leads to an increase in the visible beam size. The magnitude of such a "broadening" exclusively due to gasdynamic motion is shown in Fig. 2. The calculations were done for a round gaussian beam with the parameters typical for the HEDP experiments at HHT. It is seen that due to this issue, the visible beam spot size may in the worst case be up to 40% larger than the real one.

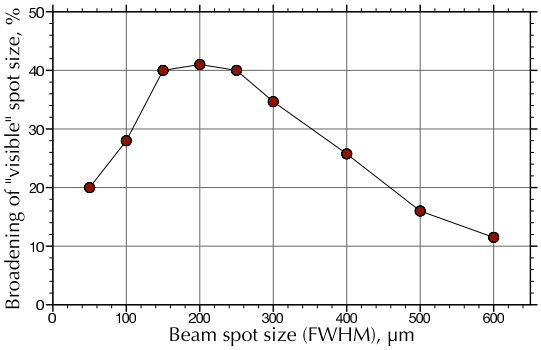

Figure 2: Relative broadening of visible transverse beam dimensions in argon due to gasdynamic motion as a function of real focal spot size.

In order to verify the above simulation results, the laser backlighting system of the HEDP setup at HHT has been modified to provide a possibility for schlieren measurements. The schlieren technique is sensitive to the density gradients in a transparent media. By using a streak camera as a detector, the evolution of the gas radial density gradient during and after the interaction with the beam can be measured.

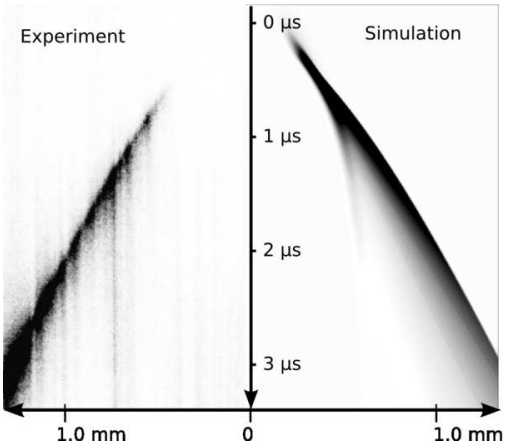

Figure 3: Experimental streak-schlieren image (left) and corresponding simulations (right).

For the first time, shock waves induced by intense heavy ion beam in Ar and He-Ar mixtures at $(100-900)\,$mbar pressures have been detected. Fig. 3 shows a typical streak-schlieren record of a radial shock wave (Ar $900\,$mbar, ^{238}U $2.2\cdot10^9$, $350\,$AMeV, $300\,\mu$m FWHM focal spot size) and the corresponding simulations by the *VarJET* code. Comparison between these measurements and simulations have shown a good quantitative agreement, confirming the importance of the gasdynamic issues for the problem of transverse diagnostics of intense focused heavy ion beams.

*Work supported by GSI-INTAS 03-54-4254, 06-1000012-8707, BMBF 06-DA-118, GSI DA-HOF-1

[1]V.L.Varentsov, D. Varentsov, paper in preparation

Local field corrections vs. Mermin dielectric function on proton stopping in plasmas*

Manuel D. Barriga-Carrasco[1#]
[1]E.T.S.I. Industriales, Universidad de Castilla-La Mancha, 13071, Ciudad Real, Spain.

The energy loss of charged particles in a free electron gas is of considerable interest to actual slowing-down problems. This is a topic of relevance to understand the beam-target interaction in the contexts of particle driven fusion. The energy losses of ions moving in an electron gas can be studied through the stopping power of the medium. Large number of calculations of the stopping power of ions and electrons in plasmas has been carried out using the random phase approximation (RPA) in the dielectric formalism.

The RPA is usually valid for high-velocity projectiles and in the weak coupling limit of an electron gas. But for partially coupled plasmas, which are subject of much interest for current studies of ICF, RPA it is not sufficient and electron collisions have to be taken into account. In this report electron collisions will be treated through two different ways: the Mermin function or the local field corrections (LFC).

Mermin [1] derived an expression for the dielectric function taking account these electron collisions and also preserving the local particle density

$$\varepsilon_{\mathrm{M}}(k,\omega)=1+\frac{(\omega+i\nu)[\varepsilon(k,\omega+i\nu)-1]}{\omega+i\nu\left[\varepsilon(k,\omega+i\nu)-1\right]/[\varepsilon(k,0)-1]},$$

where ε(k,ω) is RPA dielectric function which takes into account the degeneracy of the electron gas [2,3] and ν is the electron collision frequency obtained from [4]. It is easy to see that when ν→0, the Mermin dielectric function reproduces the RPA one.

On the other hand, LFC are included in dielectric function by

$$\varepsilon_{\mathrm{LFC}}(k,\omega)=1-\frac{\left[1-\varepsilon(k,\omega)\right]}{1+\left[1-\varepsilon(k,\omega)\right]G(k,\omega)},$$

where G(k,ω) are the LFC of the electron gas. Mostly static approximations (SLFC), G(k)=G(k,0), have been proposed in the past, as it was considered that greater part of the local field corrections will succeed for the static limit, ω=0, [5]. This latter approximation is used in our calculations.

In the dielectric formalism, the stopping power of an electron gas, defined by its dielectric function, for a swift pointlike ion with charge *Z*, travelling with constant velocity *v* through it, is very well known

$$S_{\mathrm{e}}(v)=\frac{2Z^2}{\pi v^2}\int_0^{\infty}\frac{\mathrm{d}k}{k}\int_0^{kv}\mathrm{d}\omega\,\omega\,\mathrm{Im}\left[\frac{-1}{\varepsilon_x(k,\omega)}\right],$$

expressed in atomic units (a. u.), where $\varepsilon_x(k,\omega)$ denotes any of the former dielectric functions.

Figure 1 shows the stopping power of a T=10 eV and $n_e=10^{23}$ cm^{-3} electron gas as a function of the proton velocity. The solid line represents the stopping power calculated with the RPA dielectric function, ε(k,ω). The dashed line is the one with the Mermin dielectric function, $\varepsilon_M(k,\omega)$, and the dashed dotted line is the one with the LFC dielectric function, $\varepsilon_{LFC}(k,\omega)$.

As it is seen in Fig. 1, LFC produce an enhancement in stopping at velocities smaller than the velocity at maximum but recover rapidly the RPA values after it. On the other hand, Mermin dielectric function also produces a enhancement at velocities smaller than the velocity at maximum but much higher than the one produced by the LFC. Besides, Mermin values decrease significantly below RPA ones at the velocity at maximum and higher velocities. Evidently all of them tend to the Bethe limit at high velocities. Differences between Mermin dielectric function and LFC could achieve 20% at higher velocities than the velocity at maximum.

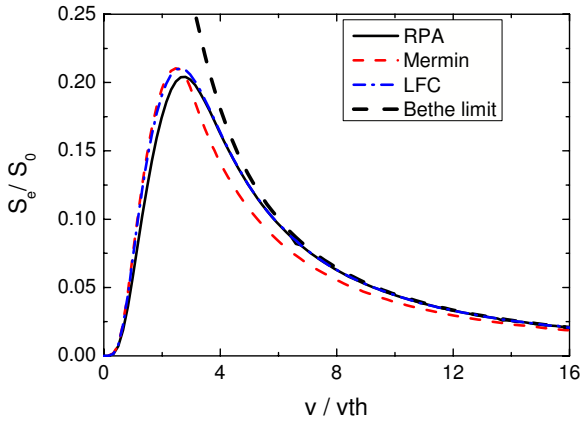

Figure 1: (Color online) Stopping power of a T=10 eV and $n_e=10^{23}$ cm^{-3} electron gas as a function of the proton velocity. Normalized to $S_0=k_F^2$.

References

[1] N. D. Mermin, Phys. Rev. B **1**, 2362 (1970).
[2] N. R. Arista and W. Brandt, Phys. Rev. A **29**, 1471 (1984).
[3] M. D. Barriga-Carrasco, Phys. Rev. E **76**, 016405 (2007).
[4] M. D. Barriga-Carrasco and A. Y. Potekhin, Laser Part. Beams **24**, 553 (2006).
[5] K. Utsumi and S. Ichimaru, Phys. Rev. A **26**, 603 (1982).

* Work supported by Spanish MEC, contract No. FIS2006-05389
#ManuelD.Barriga-Carrasco@uclm.es

High Energy Density Physics Studies Using the CERN SPS*

N.A. Tahir[1], R. Schmidt[2], M. Brugger[2], A. Shutov[3], I.V. Lomonosov[3], A.R. Piriz[4], D.H.H. Hoffmann[5], and C. Deutsch[6]

[1]GSI, Darmstadt, Germany; [2]CERN, Geneva, Switzerland; [3]IPCP, Chernogolovka, Russia; [4]UCLM, Ciudad Real, Spain; [5]TU Darmstadt, Germany; [6]LPGP, Orsay, France

The super proton synchrotron, SPS is used as LHC injector, but also to accelerate and extract protons and ions for fixed target experiments and for producing neutrinos (CNGS). In particular the risks during the fast extraction of LHC and CNGS beams must be considered since any failure during this process can lead to serious equipment damage.When the SPS operates as LHC injector, up to 288 bunches are accelerated, each bunch with about 1.1×10^{11} protons. The bunch length is 0.5 ns and two neighboring bunches are separated by 25 ns so that the duration of the entire beam is about 7 μs. The beam focal spot size (σ) in this case is 0. 88 mm. When the SPS is used as a collider,σ is of the order of 0.06 mm. To assess the damage caused by full impact of the SIS beam we have simulated hydrodynamic and thermodynamic response of solid copper and tungsten cylindrical targets that are facially irradiated by the beam. These simulations have been carried out using a two-dimensional computer code, BIG-2.Three different values for the beam focal spot, namely, with σ = 0.088 mm, 0.28 mm and 0.88 mm have been considered. The energy deposition of 450 GeV protons in the SPS beam has been calculated using the FLUKA code.Figure 1 shows specific energy deposition vs target length along the beam axis for the three values of beam spot size. In Figs. 2–3 we plot the temperature, pressure and density vs target radius at the point of maximum energy deposition along the target length at the end of the pulse.

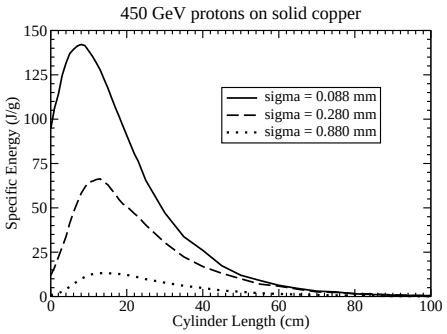

Figure 1: Energy deposited by one SPS bunch in solid Cu

These figures show the maximum temperature in the beam heated region that one achieves at the end of the pulse. The target heating during the initial stages gives rise to a very high pressure that drives a radially outgoing shock which leads to a substantial reduction in density at the target center. This results in lengthening of the range of the protons delivered in subsequent bunches. This important effect must be considered in all safety related issues. For further details see [1].

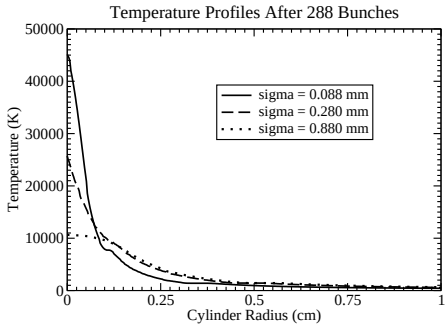

Figure 2: Temperature vs radius in Cu target at t = 7.2 μs.

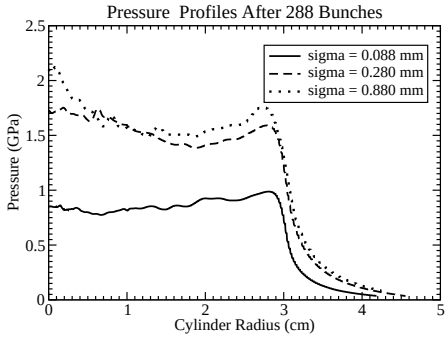

Figure 3: Pressure vs radius in Cu target at t = 7.2 μs.

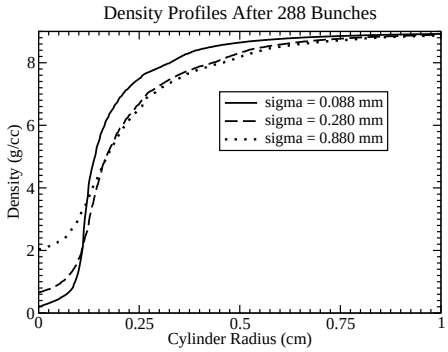

Figure 4: Density vs radius in Cu target at t = 7.2 μs.

References

[1] N.A. Tahir et al.,Laser Part. Beams 25 (2007) 639.

* Work supported by BMBF

Heavy ion driven reactor-size double shell inertial fusion targets*

M.C. Serna Moreno[1,#], N.A. Tahir[2], J.J. López Cela[1], A.R. Piriz[1], and D.H.H. Hoffmann[2]
[1]ETSII, Universidad de Castilla-La Mancha, Spain; [2]GSI, Darmstadt, Germany

Introduction

Inertial Confinement Fusion (ICF) is considered as an alternative to Magnetic Confinement Fusion to achieve controlled thermonuclear fusion. The main goal is to exploit the energy released from thermonuclear fusion reactions to produce electric energy. Heavy ion beams were proposed in 1976 as one of the possible drivers in ICF. The method consists in igniting few milligrams of deuterium-tritium, using small capsules that contain the fuel. Heating the outer part of the target with short pulses of heavy ion beams it is obtained the spherical implosion and compression of the inner part.

For a profitable energy production in power plants using nuclear fusion, it is necessary pulsed operation with few micro-explosions per second and drivers with high efficiency. So, heavy ion beams are a very attractive driver for an ICF power plant because accelerators have high repetition rate (practical accelerators already have repetition rates of 10 to 30 Hz) and high efficiency (efficiencies of 20 to 30 % are obtained, relaxing the need for high target gain). The scheme of a reactor design could be the following:

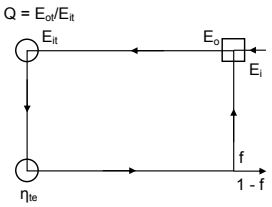

Figure 1: Scheme of a reactor design.

Going around the energy flow loop it is obtained the relation:

$$\eta_d . Q . \eta_{te} . f = 1 \qquad (1)$$

where η_d is the driver efficiency, η_{te} is the thermal to electrical conversion efficiency, f is the recycled fraction of energy, Q is the pellet gain, E_{ot} is the thermonuclear energy output of the pellet and E_{it} is the pellet input energy from the ion beam driver. In a reactor design (fig. 1) it is essential to keep the recirculating fraction of energy as low as possible in order to minimize costs. Then, if $\eta_d \sim 0.25$, $\eta_{te} \sim 0.4$ and $f < 0.25$, the pellet gain Q must be greater than 40.

Many of the central features of any reactor design must depend on the target characteristics, whether single or double shell targets are employed.

Simulations

Implosion, ignition and burn of single and double shell targets have been simulated using a one dimensional Langrangian hydrodynamic code MEDUSA.

Single shell targets

In early 1980's a heavy ion driven reactor study named HIBALL [1] was carried out. HIBALL study considered a single shell multi-layered ICF target [2], [3]. In this work the HIBALL single shell target has been simulated (fig.2). The time history of the input power has been designed to implode the target and achieve the density and temperature profiles in the fuel which are necessary for central ignition. The maximum gain obtained is 179 for an input energy of 4.38 MJ.

Double shell targets

The main advantages of a double shell target are the automatic pulse shaping in the low density gas region (this relaxes constrain on input pulse shape) and the velocity multiplication due to collision of outer heavier shell with the inner lighter shell (this implies that a double shell target can be successfully imploded using lower input power and lower input energy). We are designing a double shell reactor-sized heavy ion driven ICF target (fig.2). This target must be still optimized.

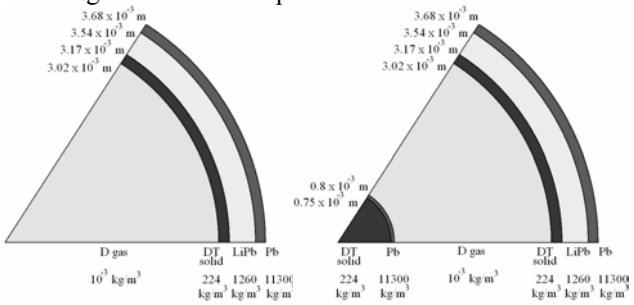

Figure 2: Target initial conditions. Left: single shell target. Right: double shell target.

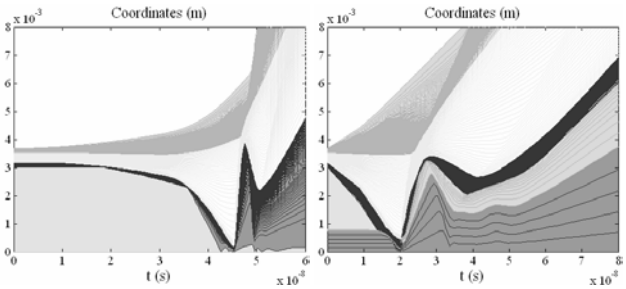

Figure 3: Temporal evolution of the layers of the target. Left: single shell target. Right: double shell target.

References

[1] B. Badger et al., HIBALL Reactor Design Study, UWFDM-450 and KfK 3202 (1981).
[2] N.A. Tahir and K.A. Long, Nucl. Fusion 23, 887 (1983).
[3] N.A. Tahir and K.A. Long, Atomkernenergie / kerntechnik 40, 157 (1982).

* Work supported by JCCM and FSE 2007-2013.
# mariacarmen.serna@uclm.es

Fission Tracks Simulated by Swift Heavy Ions at Crustal Temperatures and Pressures

M. Lang[1,#], J. Lian[1,2], F. Zhang[1], B.W.H. Hendriks[3], C. Trautmann[4], R. Neumann[4], and R.C. Ewing[1]
[1]University of Michigan, Ann Arbor, MI 48109, U.S.A.; [2]Rensselaer Polytechnic Institute, Troy, NY 12180, U.S.A.;
[3]Norges geologiske undersøkelse, Trondheim, Norway; [4]GSI, Darmstadt, Germany.

The fission-track dating technique is an important tool to constrain the history of samples from small archaeological specimens to large geological formations. The method is based on analyzing particle tracks produced by spontaneous fission of ^{238}U nuclei and accumulated over time. In laboratory experiments, fission tracks can be simulated by performing irradiations with energetic heavy ions provided at accelerator facilities [1]. However, a complete realistic simulation of this natural process has never been achieved, because fission tracks also form below the Earth's surface, involving elevated pressure and temperature conditions. Until now, ion-track studies investigated the effects of pressure [2] or temperature [3] separately, but did not address the direct influence of both parameters simultaneously.

In this study, fission-track formation has been simulated, for the first time, under crustal conditions by exposing natural zircon, at a pressure of 7.5 kbar and a temperature of 250 °C to a relativistic heavy ion beam. The irradiation experiment was performed at the ion synchrotron (SIS) using 35-GeV Pb ions of fluence 1×10^{11} ions/cm^2. The experimental approach was similar to the one used in previous high-pressure irradiations [2], where a microscopic sample is pressurized by squeezing two opposing diamond anvils against the sample chamber drilled in a steel gasket and filled with distilled water as pressure-transmitting medium. Sample heating was provided by molybdenum wires wrapped around each diamond.

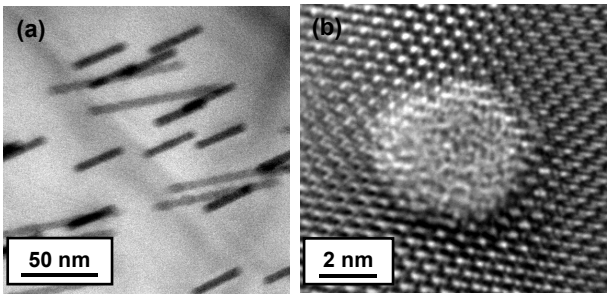

Figure 1: TEM images of zircon irradiated at: (a) elevated pressure (7.5 kbar) and temperature (250 °C), (b) ambient conditions.

After irradiation, pressure and temperature were released and transmission electron microscopy (TEM) was performed on the recovered sample (Fig. 1a). The ion tracks were compared with those obtained in a reference zircon specimen irradiated without pressure and temperature, i.e., at ambient conditions (Fig. 1b). Based on TEM analysis of 250 tracks, a pressure of 7.5 kbar is not sufficient to affect the size and geometry of tracks in zircon. This was evident by comparing the mean diameter of tracks produced under pressure/temperature (Fig. 2a) and ambient conditions (Fig. 2b). Because the track-size distribution is the most crucial parameter used to constrain the thermal history of rock material containing fission tracks, these results are important for the fission track-dating technique.

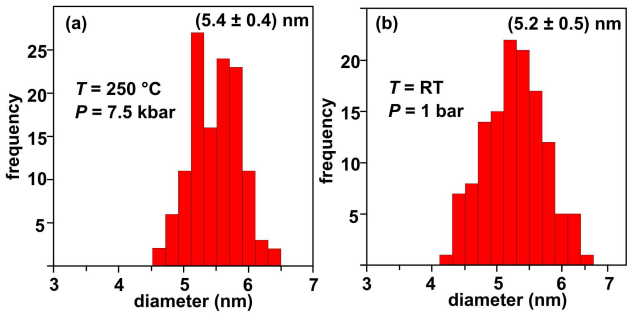

Figure 2: Diameter distribution of ion tracks in zircon produced at (a) 250 °C and 7.5 kbar and (b) room temperature and ambient pressure. The analysis includes in total 250 tracks (data binned in 0.2 nm steps). Both distributions are Gaussian with identical mean values within one σ.

In conclusion, this study clearly demonstrates that the experimental approach of combining pressure, temperature, and ion beams is suitable to simulate fission-track formation in minerals under well constrained thermodynamic conditions of the Earth's crust. Particularly, irradiations at much higher pressure and temperature values may be of interest to test the response of a given material to the simultaneous exposure of these extreme environmental conditions.

Acknowledgement

The authors gratefully acknowledge technical support by Hans Keppler, Wendy Panero, Daniel Reaman, Dieter Schardt, Elko Schubert, and Lars Stixrude. M. L. acknowledges support from the German Science Foundation DFG.

References

[1] S. Miro et al., Nucl. Instr. and Meth. B 227 (2005) 306.
[2] U.A. Glasmacher et al., Phys. Rev. Lett. 96 (2006) 195701.
[3] J. Lian et al., Phys. Rev. B 68 (2003) 134107.

* Work supported by DOE contract No. DE-FG0297ER45656.
# mklang@umich.edu

Structural phase transition in ZrO_2 induced by swift heavy ion irradiation at high pressure

B. Schuster[1,2,*], A. Benyagoub[3], F. Fujara[2], R. Klein[1], M. Lang[4], R. Neumann[1] and C. Trautmann[1]
[1]GSI, Darmstadt, Germany; [2]TU-Darmstadt, Germany, [3]CIMAP Caen, France, [4]University of Michigan U.S.A.

Tracks of nuclear fission fragments in minerals of the Earth's crust and upper mantle are generally used for dating these materials. These samples are mostly gathered from depths where high pressure is predominant. The influence of pressure on track formation is therefore of great interest.

We realized such pressures by means of diamond anvil cells (DAC). A zirconia (ZrO_2) sample was placed in the central aperture (used as sample chamber) of a metal gasket squeezed from opposite sides by two diamond anvils. To ensure hydrostatic pressure, the sample chamber was additionally filled with a pressure medium (methanol:ethanol:water 16:3:1) which solidifies at 14.5 GPa.

The loaded cell was placed in front of the exit window of the SIS beamline in Cave A. To irradiate the sample, the ions require initial energies of ~ 220 MeV/u. The beam passes the Al exit window, the air gap, the first diamond (where most of the energy is deposited), penetrates the sample, and is then stopped in the second diamond. The estimated energy-loss occurring in the sample is around 35 keV/nm.

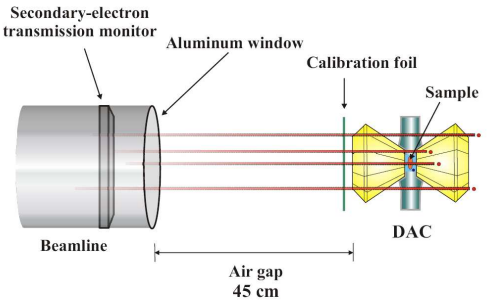

Figure 1: Experimental setup [1].

Zirconia, commonly used in its stabilized form, consists in its pure unstabilized form of a fine white powder with a grain size around 250 nm. It is monoclinic at ambient conditions and has several high-pressure (mostly orthorhombic) as well as two high-temperature (tetragonal and cubic) phases. None of these phases is quenchable to ambient conditions by ordinary means. The pressure applied to the samples during irradiation ranged from 4.3 to 13.6 GPa, and all samples were therefore located in the phase-diagram regime of the first high-pressure phase [2].

The samples were examined with Raman spectroscopy outside as well as inside the cell (through the diamond). Figure 2 displays spectra acquired outside the DAC from different locations of the sample. Spectrum a) resembles that of an unirradiated sample with its most dominant monoclinic peaks at 100, 178, 190, 334, 347, 476, 617, and 640 cm^{-1}. The areas of spectra b) and c) partially changed into the tetragonal phase, whereas the region represented by spectrum d) transformed almost completely into the tetragonal structures with peaks at 145, 260, 462, and 640 cm^{-1}. We note that the tetragonal phase can usually not be stabilized to ambient conditions [3].

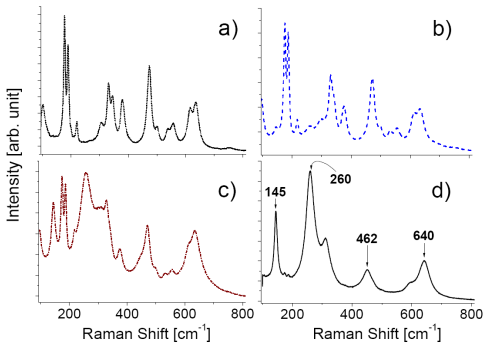

Figure 2: Raman spectra obtained from different locations of ZrO_2 irradiated with Pb ions at a pressure of 10.9 GPa (E_{Sample} = 34.5 MeV/u, fluence = 2.5×10^{11} ions/cm^2).

Ion beam induced formation and stabilization of tetragonal ZrO_2 has been described before [3], but without additional pressure the needed fluence is at least one order of magnitude higher (Fig. 3).

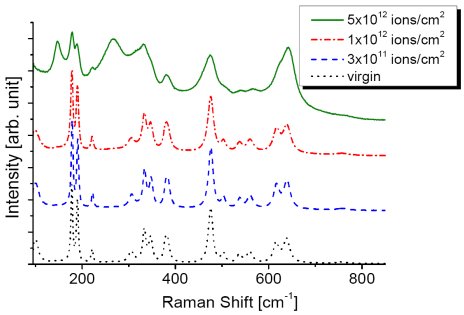

Figure 3: Raman spectra of ZrO_2 irradiated with Pb ions from the UNILAC (E = 11.1 MeV/u). Without applying pressure, the creation of the tetragonal phase requires a fluence of 5×10^{12} ions/cm^2.

Additional reference measurements showed that neither SIS irradiation with about 3×10^{11} Pb-ions/cm^2 behind a diamond nor application of high pressure alone could provoke this transformation.

References

[1] U.A. Glasmacher, M. Lang, Phys. Rev. Lett. **96** (2006) 195701.
[2] O. Ohtaka and D. Andrault, Appl. Crystallography **38** (2005) 727.
[3] A. Benyagoub and F. Levesque, Appl. Phys. Lett. **77** (2000) 3197.

* bea.schuster@gsi.de

Phase transition in boron nitride by ion irradiation under high pressure

R. Klein, B. Schuster, C. Trautmann, and R. Neumann
GSI, Darmstadt, Germany

Introduction

Boron nitride (BN) does not exist as a natural mineral, but can be synthesized in its hexagonal (hBN) and cubic form (cBN). Both phases are stable at ambient conditions and are used in a variety of applications, e.g. as lubricant (hBN) or abrasive (cBN). hBN has a similar layered structure as graphite, whereas cBN is the second-hardest material after diamond with a similar unit cell. There exist at least two other allotropes, namely a rhombohedral (rBN) and a wurtzitic (wBN) structure, which both are metastable at ambient conditions. Wurtzitic and cubic BN have sp^3 bonds, whereas hexagonal as well as rhombohedral BN are sp^2 bonded [1]. At increased temperature ($T \gtrsim 1000$ K) and pressure ($p \gtrsim 9$ GPa), hBN can change into wBN or cBN [2]. The unit cells of hBN and wBN are displayed in Fig. 1.

This study aims at the question how hBN behaves under simultaneous exposure to energetic ions and elevated pressure. In the recent past, phase transitions in solids triggered by swift heavy ions have been demonstrated for some materials under ambient [3] as well as high pressure [4]. Such effects are attributed to beam-induced shock waves and/or thermal spikes.

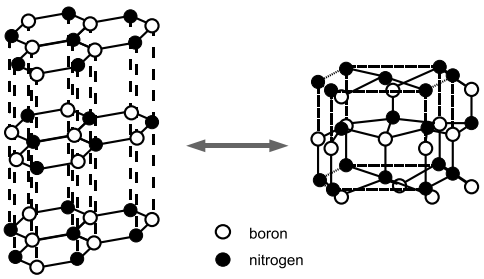

Figure 1: Crystal structure of hexagonal BN (left), and wurtzitic BN (right).

Experimental and results

Powder samples of hBN were mounted in three diamond anvil cells (DAC) and pressurized under non-hydrostatic conditions to circa 6.6, 13.0, and 21.7 GPa. The samples in the DACs were irradiated with 200-MeV/u Pb ions at the SIS beamline in Cave A to a fluence of 4.5×10^{11} ions/cm^2.

In order to obtain data for an ambient-pressure reference, we also irradiated several specimens at the UNILAC (beamline X0) with 11.1-MeV/u Pb ions up to fluences of 5×10^{12} ions/cm^2.

All samples were examined by acquisition of Raman spectra, recorded while keeping the sample under pressure as well as under ambient conditions.

Raman spectra of samples irradiated at 6.6 and 13.0 GPa showed no phase transition or other structural changes, neither when recorded under pressure nor after releasing the pressure. Noticeable alterations occurred only in the sample pressurized to 21.7 GPa. The new phase was observed under pressure and remained after the pressure was released. In the Raman spectrum, the characteristic hBN band at 1365 cm^{-1} decreased significantly. Simultaneously, a new peak appeared at 1086 cm^{-1} (Fig. 2), which we attribute to wBN. At present, x-ray diffractometry is in progress to clarify details of this structural modification. We also plan to apply higher pressures to facilitate phase transitions.

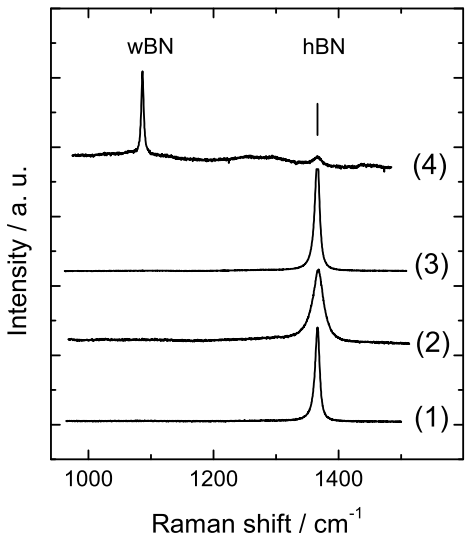

Figure 2: Raman spectra of powder hBN samples recorded under ambient conditions: (1) pristine hBN; (2) hBN pressurized to 22 GPa; (3) hBN irradiated under ambient conditions with 5×10^{11} Pb ions/cm^2; (4) hBN exposed to 4.5×10^{11} Pb ions/cm^2 while pressurized to 21.7 GPa. The energy loss in all samples was circa 20 keV/nm.

References

[1] M. Ueno et al., Phys. Rev. B **45** (1992) 10226
[2] F.P. Bundy, R.H. Wentorf, J. Chem. Phys. **38** (1963) 1144
[3] A. Benyagoub, Nucl. Instr. Meth. B **245** (2006) 225
[4] U.A. Glasmacher et al., Phys. Rev. Lett. **96** (2006) 195701

Raman spectroscopy of heavy ion induced damage in cordierite

Ch. Weikusat [1,2*], U.A. Glasmacher [2], R. Miletich [1], R. Neumann [3], C. Trautmann [3]

[1]Mineralogisches Institut, Universität Heidelberg; [2]Geologisch-Paläontologisches Institut, Universität Heidelberg; [3]GSI, Darmstadt, Germany

The mineral cordierite is a framework silicate with corner-sharing six-membered rings of SiO_4-tetrahedra forming channels along the crystallographic c-axis. During crystal growth, these channels incorporate alkali atoms and various volatiles (e.g. CO_2, H_2O). This feature is applied in petrology to determine the chemical composition of the growth environment [1]. Cordierite is also in use as heat resistant ceramics for various industrial applications.

Small pieces (thickness ~1.7 mm) of natural cordierite single crystals from Madagascar were exposed to Xe ions of 1.465 GeV (11.1 MeV/u) kinetic energy at the UNILAC, applying fluences between 10^8 and 10^{12} ions/cm^2. The penetration depth (90 µm) of the ions and their energy loss (15 keV/nm) at the sample surface were calculated with the SRIM2006 code, assuming the standard chemical composition ($(Mg,Fe^{2+})_2Al_4Si_5O_{18}$) and a density of 2.65 g/cm^3.

Raman spectra of the irradiated crystals were recorded normal to the crystal surface and as point measurements along the ion trajectory (i.e., perpendicular to the irradiated surface) with a stepwidth of 1 µm.

Only the sample irradiated with 10^{12} ions/cm^2 showed severe beam-induced modifications: the colour of the irradiated layer changed from blue to yellowish-brown, and the crystal cracked along the interface between the irradiated and non-irradiated part.

The Raman spectra show distinct band broadening due to radiation induced defects and display significant changes in the volatile composition (Fig. 1).

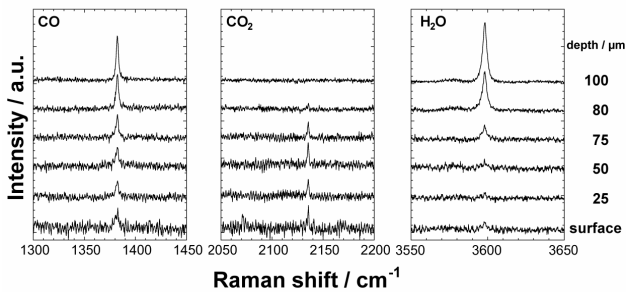

Fig. 1: CO_2, CO and H_2O bands as a function of depth of cordierite irradiated with 10^{12} ions/cm^2.

This has also been observed for natural alpha irradiation of cordierite [2]. The main band of structurally bound CO_2 (1382 cm^{-1}) is reduced and a new band appears at 2135 cm^{-1}, which can be assigned to CO. Also, the band of the H_2O stretching vibration (3598 cm^{-1}) decreased. Figure 2 illustrates the correlation of the band intensity and depth. All spectra taken beyond the calculated ion range are identical to those of the non-irradiated sample.

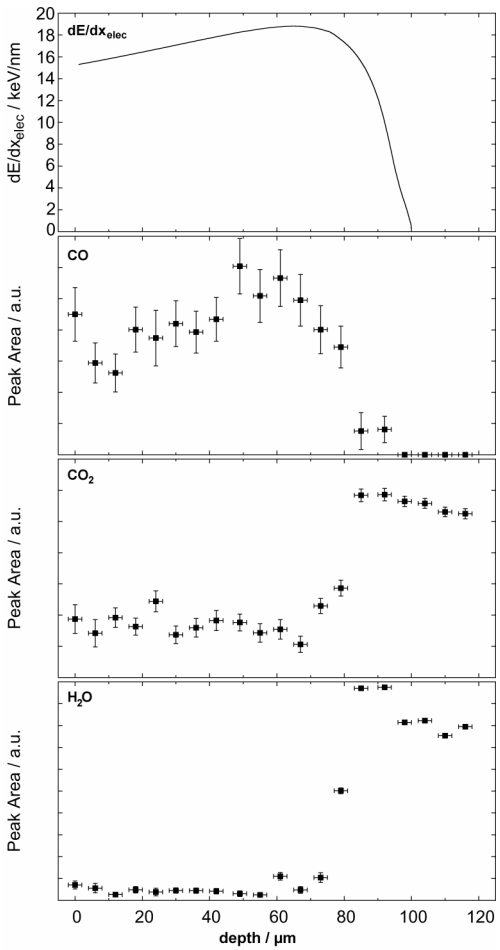

Fig. 2: Electronic energy loss and band areas of CO_2 (1382 cm^{-1}), CO (2135 cm^{-1}), and H_2O (3589 cm^{-1}) versus depth

These observations suggest a radiation induced conversion of CO_2 to CO.

References

[1] B.A. Kolesov, C.A. Geiger, Cordierite II: The role of CO_2 and H_2O, Am. Mineral. 85 (2000) 1265.

[2] L. Nasdala, M. Wildner, R. Wirth, N. Groschopf, D.C. Pal, A. Möller, Alpha particle haloes in chlorite and cordierite, Mineral. Petrol. 86 (2006) 1.

* weikusat@min.uni-heidelberg.de

Spatially resolved characteristics of heavy ion tracks in LiF by static field gradient NMR

H. Stork[1*], A. Hamburger[1], K. Schwartz[2] , F. Fujara[1]
[1]Technische Universität Darmstadt, Institut für Festkörperphysik, [2]Gesellschaft für Schwerionenforschung (GSI), Darmstadt.

Due to the magnetic moments of ^{19}F and ^{7}Li Nuclear Magnetic Resonance (NMR) has been widely used for radiation damage studies in LiF (see [1] and references within). For the first time we employ spatially resolved NMR for studies of heavy ion induced damage. These measurements were accompanied by absorption spectroscopy (VIS and UV). The LiF crystals were irradiated with ^{130}Xe ions at the UNILAC linear accelerator of GSI (energy 1440 MeV, range R = 87.4 µm) with fluences (Φ) from 10^{10} to 10^{12} ions/cm^2.

The spatially resolved ^{19}F-NMR measurements were performed in a specially designed superconducting gradient magnet at a field of 3.73 T and a static field gradient of 74.3 T/m at T = (22 ± 2) °C. A saturation pulse sequence was used for the determination of the spin-lattice relaxation rates T_1^{-1}. For our experiments the thickness of the excited slice was between 6 and 8.5 µm according to a pulse length of 55 and 38 µs.

We measured both the dependence of T_1^{-1} on the fluence in the irradiated regions of the samples (Fig. 1) and on the position l along the ion track (Fig. 2). The change of T_1^{-1} is determined by the main paramagnetic color centers (F centers) in the irradiated LiF [1]. Therefore we measured the concentration of F centers (n_F, cm^{-2}) by optical spectroscopy in all irradiated samples [2].

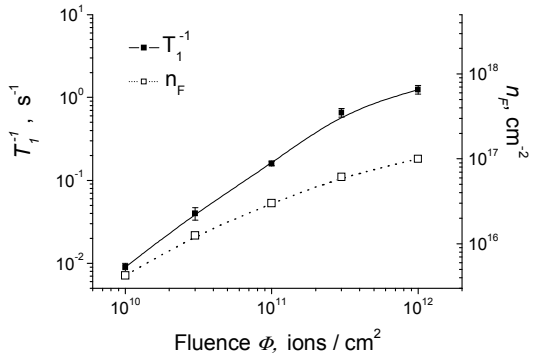

Fig. 1: Irradiation induced changes of T_1^{-1} and the concentration of F centers (n_F, cm^{-2}) on Φ in LiF.

The magnitude of T_1^{-1} and the concentration n_F increases with the fluence (Fig.1). Both T_1^{-1} and n_F have a tendency to saturate at high fluences [2].

We also carried out a NMR measurement along the ion tracks using the high spatial resolution of our NMR method (Fig. 2). The rate T_1^{-1} has a complex dependence on the position l along the tracks, and a strong decrease was observed beyond the ion range ($l > R$). In this region we observed several zones with a different gradient of the relaxation rate demonstrating a non-homogeneous damage structure. The effect is more pronounced for LiF irradiated with high fluences.

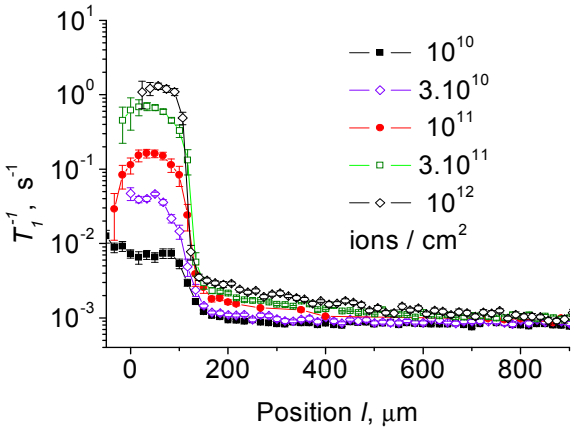

Fig. 2: Position dependent spin-lattice relaxation rates for the ^{130}Xe irradiated LiF crystals for several fluences.

Beyond the ion range, T_1^{-1} is also affected by F centers. In LiF irradiated with Xe ions at $\Phi = 10^{12}$ ions/cm^2, the concentration of F centers in the irradiated part ($l < R$) was $n_F \sim 10^{17}$ cm^{-2} and in the non-irradiated area ($l > R$) only ~ 10^{14} cm^{-2} (the F centers beyond the ion track are probably induced by X-rays from the fast δ electrons in the track) [2]. The decrease of n_F at $l > R$ by three orders of magnitude is in good agreement with the change of the size of T_1^{-1} (Fig. 2). Nevertheless, additional investigations are necessary to clear the damage structure responsible for the behaviour of T_1^{-1} in various zones beyond the track ($l > R$). A special attention must be paid to the influence of the energy loss on color center creation, as well to the ion induced mechanical stress in the irradiated and non-irradiated regions [3].

NMR with high spatial resolution opens up new possibilities for damage studies in heavy ion tracks.

References

[1] T. Klempt, O. Kanert, D. Suter, Phys. Stat. Sol. (b) **236**, 151 (2003).
[2] K. Schwartz, C. Trautmann, A. S. El-Said, R. Neumann, M. Toulemonde, W. Knolle, Phys. Rev. B **70**, 184104 (2004).
[3] I. Manika, J. Maniks, K. Schwartz, C. Trautmann, Nucl. Instr. Meth. B **196,** 299 (2002).
*HolgerStork@physik.tu-darmstadt.de

Velocity Effect on Damage Creation in Ion-Irradiated CeO_2

N. Ishikawa[1], K. Ohhara[1], O. Michikami[2], Y. Ohta[2], M. Lang[3], R. Neumann[4]
[1]JAEA, Tokai, Ibaraki 319-1195, Japan; [2]Iwate Univ., Morioka, Iwate 020-0066, Japan; [3]University of Michigan, Ann Arbor, MI 48109, U.S.A.; [4]GSI, Darmstadt, Germany

Introduction

In various oxide materials, irradiation with high-energy heavy ions creates damage via electronic energy deposition. In the electronic energy loss regime, in most cases, the electronic stopping power, S_e, is the parameter that dominates the damage creation. Some previous studies have shown that also the ion velocity affects the damage creation [1,2]. The ion velocity dependence is important because the velocity significantly influences the process that converts the deposited electronic energy into atomic displacements.

This study is dedicated to the effect of the velocity on damage creation for CeO_2 by irradiating high-energy ions having the same S_e but different velocities.

Experimental

Thin films of CeO_2 were prepared on sapphire substrates by dc sputtering. The film thickness was about 300 nm. The films were irradiated at room temperature with 1.6-GeV Xe from the UNILAC accelerator at GSI, and with 210-MeV Xe and 150-MeV Au from the tandem accelerator at Tokai Research and Development Centre, Japan Atomic Energy Agency (JAEA-Tokai). The incident ions have same the S_e (28-29 keV/nm) but different velocities. The velocities of 1.6-GeV Xe, 210-MeV Xe, and 150-MeV Au are 4.7×10^9, 1.7×10^9, and 1.2×10^9 cm/s, respectively. In order to determine the degradation of the crystal structure, X-ray diffraction (XRD) patterns were recorded before and after the irradiation. In this study, the irradiation-induced change of the (002) diffraction peak is investigated. The electronic stopping power is calculated by the SRIM-2003 code.

Results and Discussion

For all irradiations, the intensity of the (002) XRD peak decreases with increasing fluence. In the range of higher fluence, the intensity decrease tends to saturate. It is known that in most ceramic materials a high-energy heavy ion creates a track along its path. This damage trail has typically a diameter of several nanometers. Inside the track, the solid can be amorphous or have a disordered crystal lattice depending on ion mass, ion energy, and target material. The electron diffraction spots observed in a previous experiment for CeO_2 irradiated with 210-MeV Xe indicated that the crystalline structure is maintained up to 1×10^{13} ions/cm^2 [3]. These findings are confirmed by the present result showing that the XRD intensity decrease stops at about 1×10^{13} ions/cm^2. Both measurements indicate the radiation resistance of CeO_2 at high fluence.

As shown in Fig. 1, the intensity decrease differs for three ion irradiations having the same S_e but different ion velocities. The damage is prominent for slower ions, while it is subtle for faster ions, exhibiting a velocity-dependent damage creation. Velocity-dependent damage behaviour is also found for the change in XRD peak width. These results are qualitatively the same as those found for $Y_3Fe_5O_{12}$ [1] and for $EuBa_2Cu_3O_7$ [2]. The velocity effect can be explained either by the thermal spike model [1] or the Coulomb explosion model [2]. The former model assumes that the ion velocity affects the energy of secondary electrons which determines the radial distribution of deposited energy. The latter model supposes that the ion velocity influences the ionization density which determines the Coulomb repulsive energy of ionized target atoms. In order to clarify which scenario is appropriate, not only qualitative but also quantitative investigations of the velocity effect are necessary.

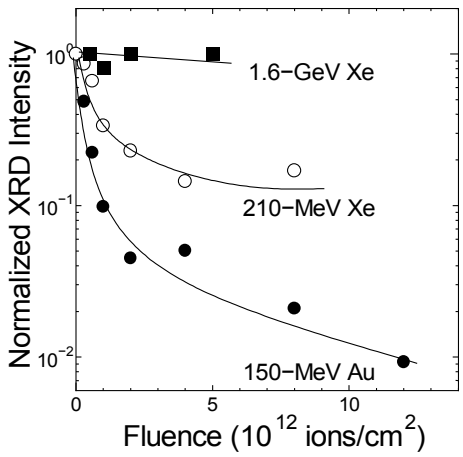

Figure 1: Logarithm of normalized XRD intensity as a function of fluence for the irradiations with 1.6-GeV Xe, 210-MeV Xe, and 150-MeV Au.

References

[1] A. Meftah, F. Brisard, J.M. Costantini, M. Hage-Ali, J. P. Stoquert, F. Studer, and M. Toulemonde, Phys. Rev. B 48 (1993) 920.

[2] N. Ishikawa, A. Iwase, Y. Chimi, O. Michikami, H. Wakana, T. Hashimoto, T. Kambara, C. Müller, and R. Neumann, Nucl. Instr. Meth. B 193 (2002) 278.

[3] T. Sonoda, M. Kinoshita, Y. Chimi, N. Ishikawa, M. Sataka, and A. Iwase, Nucl. Instr. Meth. B 250 (2006) 254.

Low temperature ferromagnetic state induced by GeV ion irradiation in FeRh alloy

A. Iwase[1], Y. Zushi[1], N. Fujita[1] and R. Neumann[2]
[1]Oasaka Prefecture University, Sakai, Osaka, Japan, [2]GSI Darmstadt, Germany.

Fe-50at%Rh alloy is an intermetallic compound which makes the transition from antiferromagnetic to ferromagnetic state near room temperature (RT). Below RT, this alloy is antiferromagnetic down to liquid helium temperature. In this report, we show that irradiation with 1.5-GeV Xe ions induces the ferromagnetic state at 20 K.

Equiatomic compound Fe-50at%Rh sheets of 5x5x0.1mm^3 were irradiated at RT with 11.4 MeV/u (1.5 GeV) Xe ions at the UNILAC linear accelerator of GSI. The fluences were 5x10^{11}, 1x10^{12}, and 2x10^{12} ions/cm^2. The magnetization of irradiated and unirradiated specimens was measured at 20 K as a function of external magnetic field with a SQUID magnetometer, scanning from -6 to +6 kOe with a rate of 250 Oe/min.

Figure 1 displays the magnetization vs. magnetic field for unirradiated and irradiated specimens. The magnetization for the unirradiated sample is nearly proportional to the magnetic field, which shows that the sample is antiferromagnetic at 20 K. For the irradiated specimens, the magnetization shows a steep increase at low field and tends to be saturated at higher field. The shape of the curves for the irradiated specimens implies that the ferromagnetic state is induced in intrinsically antiferromagnetic Fe-50at%Rh at 20 K.

The projected range of 1.5-GeV Xe ions is much smaller than the specimen thickness. Therefore, in irradiated specimens, a ferromagnetic and an antiferromagnetic region coexist. To deduce the ion-induced magnetization, we subtracted the values of magnetization for the unirradiated specimen from those for the irradiated specimens. The result is plotted in Fig. 2. Figure 3 depicts the dependence of the irradiation induced magnetization at 6 kOe on ion fluence. Figures 2 and 3 clearly demonstrate that the irradiation induced magnetization increases monotonically with increasing fluence.

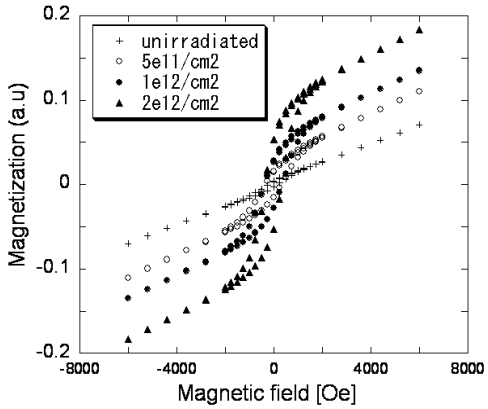

Fig 1: Magnetization vs. magnetic field for unirradiated and 1.5-GeV Xe ion irradiated Fe-50at%Rh

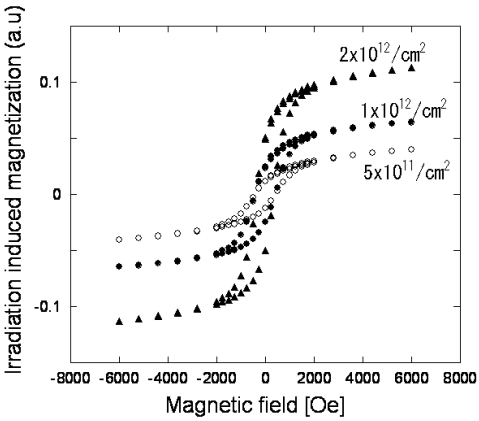

Fig 2: Irradiation-induced magnetization as a function of magnetic field for Fe-50at%Rh specimens

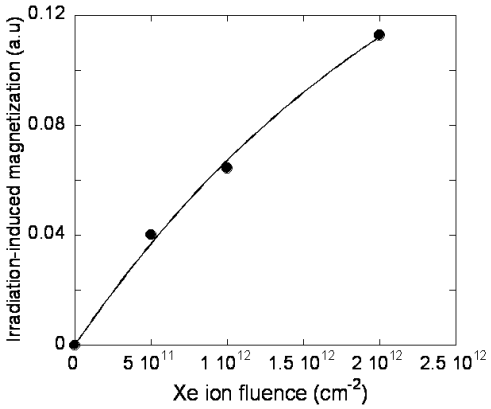

Fig 3: Irradiation-induced magnetization at 6 kOe for Fe-50at%Rh as a function of 1.5-GeV Xe ion fluence

The present result is quite surprising because even a small fluence of GeV ions can change the magnetic state of the alloy. The mechanism of the transition from antiferromagnetic to ferromagnetic state by 1.5-GeV Xe irradiation, however, still remains uncertain. To clarify this mechanism, we irradiated the FeRh specimens with heavy ions of ~100 MeV [1], ~10 MeV [2], and 1.5 GeV. Analyzing the energy dependence of the ion-induced magnetization will enable us to separate the contributions of electronic excitation and elastic collisions to the magnetic transition.

References

[1] Y. Zushi, M. Fukuzumi, Y. Chimi, N. Ishikawa, F. Ono, A. Iwase, Nucl. Instr. Meth. B 256 (2007) 434.
[2] Y. Zushi et al., to be published.

Raman spectroscopy on heavy ion-induced surface modifications of graphite *

M. Tomut [1,2,#], W. Ensinger [3], A. Kelić [1], M. Krause [3], R. Neumann [1], K. Schwartz [1], K.Sümmerer [1], C. Trautmann [1], H. Weick [1], M. Winkler [1]
[1]GSI, Darmstadt, Germany; [2]NIMP, Bucharest, Romania, [3] TU Darmstadt, Germany

Fine-grained isotropic graphite is the material of choice for the production target and the beam catchers at the planned Super-FRS fragment separator at FAIR. Heavy-ion irradiation studies of graphite are needed, as radiation damage will ultimately limit the lifetime of these components. Polycrystalline graphite and highly-oriented pyrolytic graphite (HOPG) were irradiated with energetic ions and subsequently analyzed by Raman spectroscopy as a non-intrusive technique for measuring the degree of structural order and residual stress in the surface layer.

The first-order Raman spectrum is commonly used for the characterization of disordered carbon. It exhibits a graphite (G) peak at 1580 cm^{-1} and a disorder-related (D) peak at 1360 cm^{-1}. The G peak is well defined for HOPG and starts to broaden in materials containing a disordered phase, e.g. irradiated HOPG and polycrystalline graphite (Fig.1). The band position has also been shown to change with stress and temperature [1].

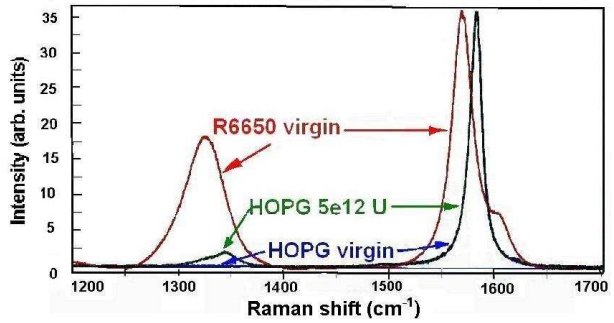

Fig. 1: Raman spectra of pristine HOPG and polycrystalline R6650 graphite and of HOPG irradiated with 5×10^{12} U ions/cm^2.

Samples of 1-mm thick R6650 polycrystalline graphite and HOPG were irradiated at the UNILAC with Ni and U ions of 11.1 MeV/u (range ~ 120 µm).

Figure 2 presents a typical series of spectra, recorded by confocal micro Raman spectroscopy for R6650 graphite irradiated up to a fluence of 5×10^{12} ions/cm^2. The evolution of the G-peak broadening and of the ratio of the D-to-G band intensity with fluence is shown in Tab. 1. The data indicate an annealing effect up to 10^{12} ions/cm^2, followed at higher fluences by increasing disorder and a reduction of the in-plane crystallite size. This modification may become a problem during the bombardment of the graphite target with high-energy ion beams, because such small grains could possibly come off entirely, leading to erosion and roughening.

* Work supported by the European Community under the FP6 DESIGN STUDY (contract 515873 - DIRACsecondary-Beams).
# m.tomut@gsi.de

Fluence (U ions/cm^2)	$FWHM_G$ (cm^{-1})	I_D/I_G	A_D/A_G
pristine	25	0.59	0.98
4×10^{11}	20	0.45	0.89
1×10^{12}	26	0.40	0.76
5×10^{12}	26	0.82	1.33

Table 1: Change of G-band parameters of R6650 graphite for various fluences: band width ($FWHM_G$), relative intensity of D-to-G band (I_D/I_G), and ratio of integrated band intensity (A_D/A_G).

The above mentioned evolution is also accompanied by a change of the residual stress in the surface layer of the irradiated R6650 graphite samples. For fluences up to 10^{12} U ions/cm^2, the G peak slightly shifts towards lower wavenumbers, possibly due to the relaxation of residual stress present in the pristine sample. At 5×10^{12} U ions/cm^2, when the stress fields of the individual tracks start to overlap, compressive stress builds up, as indicated by the positive shift of the G peak. For Ni ions we found that the reversal of the direction of the G-peak shift starts at larger fluences. This is related to the smaller track sizes produced with lighter ions. We observed a similar evolution with fluence for the Raman spectra of HOPG samples. To estimate the residual stress from the peak shift, one needs an appropriate model for the biaxial stress development during irradiation. This model should take into account radiation induced dimensional changes and also possible creep behaviour of graphite.

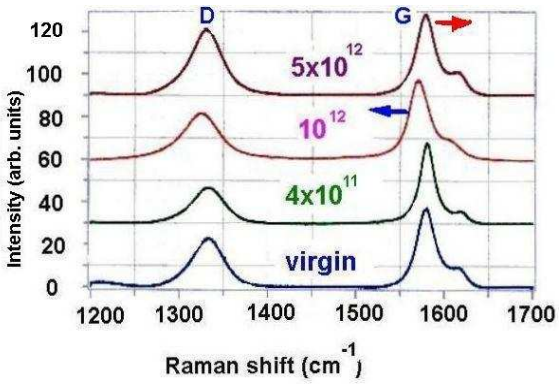

Fig. 2: Sequence of first-order Raman spectra of R6650 graphite irradiated with U ions of different fluences. The arrows show the shift of the G-peak position.

References

[1] C.A. Taylor et al, Thin Sol. Films 429 (2003) 190.

Model for nucleation of dislocation loops in graphite under irradiation with swift heavy ions

M.V. Sorokin[1,*], A.E. Volkov[1], K. Schwartz[2], M. Tomut[2]
[1]RRC Kurchatov Institute, Moscow, Russia; [2]GSI Darmstadt, Germany

Irradiation of highly oriented pyrolytic graphite (HOPG) with swift heavy ions demonstrated that damage of the material is originated by electronic energy loss [1]. To support further analysis of experimental data from Raman spectroscopy, electron microscopy, X-ray scattering, etc., some assumptions about damage structure are necessary. It is reasonable to assume that not only primary Frenkel defects are created directly by irradiation, but also defect aggregates are formed during subsequent kinetics.

In the HOPG lattice, both kinds of point defect (vacancies within hexagonal layers and interstitial atoms between basal planes) are mobile mainly within 2D geometry. Therefore, the initial defect aggregates are presumably the dislocation loops, which can be considered as monolayer disks.

Supersaturated concentration of point defects accompanied by high defect mobilities, resulting from the local temperature increase along the ion trajectories, can lead to homogeneous nucleation. On the other hand, the temperature increase enhances equilibrium point defect concentration (point defect solubility) and therefore reduces the driving force of aggregation. Thus, the temperature dependency of the characteristic nucleation time has a minimum, corresponding to the most favorable nucleation temperature (Fig. 1). The characteristic time can be estimated [2] as:

$$t_c \cong \left(\frac{2}{\pi} \left| \frac{d^2\varphi}{dn^2} \right|_{n=n_c} \right)^{-1/2} \frac{\exp(\varphi(n_c))}{2\pi\nu \exp(-\Phi_m/T)}$$

Here, n is the number of constituent defects in a loop, n_c is a critical nucleus size. The migration energy Φ_m is about 0.1 eV for interstitials and 1.5 eV for vacancies.

The function $\varphi(n)$ is determined by kinetic coefficients and in 2D geometry [2,3] gives:

$$\varphi(n_c) = \frac{\pi\gamma^2\omega}{\ln(1/C_0)T(T_0 - T)}, \quad \left| \frac{d^2\varphi}{dn^2} \right|_{n=n_c} = \frac{\ln^3(1/C_0)}{2\pi\gamma^2\omega} \frac{(T_0 - T)^3}{T}$$

where $T_0 = \Psi/\ln(1/C_0)$. The area occupied by one point defect ω is equal to $(\sqrt{3}/4)a^2 = 0.026$ nm^2. The Gibbs energy for a point defect creation Ψ can be estimated as one half of the energy of three broken sp^2 bonds: $\Psi \cong (3/2)E_b$, where the binding energy is about 2.5 eV. Similarly, the edge tension γ can be estimated from the number of broken bonds per unit length: $\gamma = 0.5E_b/a$.

Generally, the defect concentration C_0 is determined by the irradiation properties, but there is no clear understanding of the defect creation mechanism in graphite irradiated with ions in the electron stopping regime. The highest possible energy transferred from a projectile (with mass M and kinetic energy E) to a target electron corresponds to the head-on collision: $\varepsilon_{\max} = 4m_e E/M$. For the typical UNILAC ion energy of 11.1 MeV/amu, $\varepsilon_{\max}$ amounts to 24 keV, being below the threshold for defect creation in graphite with energetic electrons. A possible explanation of the effect should take into account the high excitation density of swift heavy ions. The ionization of target atoms leads to modifications of the interatomic potential [4], inducing both destruction of chemical bonds and driving forces for atom displacements. An alternative approach assumes rapid energy transfer from the electrons to the lattice (thermal spike) [5] and thermal formation of lattice defects with a threshold much lower than for elastic recoils. Thus, further investigations in this field are required, while C_0 remains a free parameter of the model.

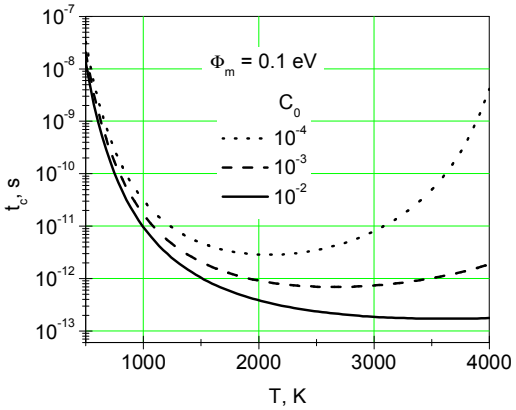

Fig. 1: Characteristic nucleation time of interstitial loops as a function of temperature.

One can conclude that typical temperatures and duration of projectile-induced local heating can create suitable conditions for nucleation of interstitial loops accompanied by the occurrence of less vacancy loops. These loops break the initial plane sequence and therefore create stacking faults, which can be observed experimentally.

References

[1] J. Liu *et al.*, Phys. Rev. **B 64** (2001) 184115.
[2] A.E. Volkov *et al.*, Nucl. Instr. and Meth. **B 209** (2003) 184.
[3] M.V. Sorokin *et al.*, Phys. Rev. **E 72** (2005) 051603.
[4] P. Stampfli, Nucl. Instr. and Meth. **B 107** (1996) 138.
[5] D. Schwen *et al.*, Nucl. Instr. and Meth. **B 256** (2007) 187.

* m40@lab2.ru
This work is supported by INTAS (grant 05-111-5118).

Mechanical degradation of polyimide induced by swift heavy ion irradiation

D. Severin[1#], C. Trautmann[2], and W. Ensinger[1]
[1] University of Technology, Darmstadt, Germany; [2]GSI, Darmstadt, Germany.

In the new superconducting FAIR magnets, polyimide films (Kapton) will be used as insulator. During operation, the material is exposed to high-dose radiation and it has to withstand enormous mechanical forces induced by the magnet field ramping. For better lifetime estimation, this study investigates radiation-induced degradation of the mechanical properties of Kapton by tensile strength measurements.

Foils of 25-µm thick Kapton were irradiated with Ti, Sm, and Au ions of 11.1 MeV/u at a fluence between $1x10^{10}$ and $5x10^{12}$ ions/cm^2. The tensile strength and Young modulus of the samples were measured applying strain on a Zwick tensile tester (model Z020TH) at the Deutsches Kunststoff Institut, Darmstadt. To optimize the irradiation, the samples had a size of 15×30 mm^2 which differs from the DIN norm.

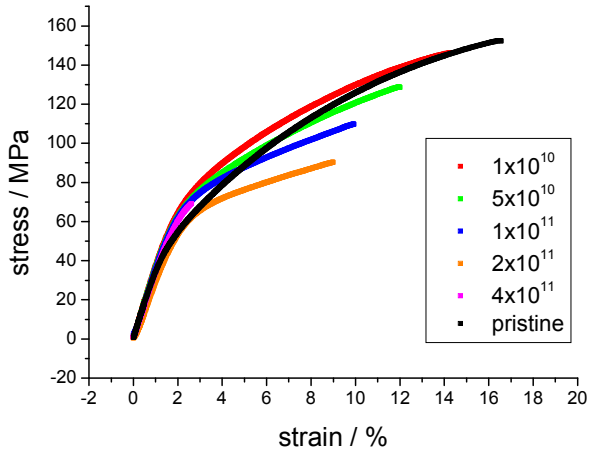

Fig. 1: Stress-strain curves for 25-µm thick Kapton foils before and after irradiation with 11.1 MeV/u Au ions of various fluence.

Figure 1 summarizes for all samples the stress-strain tests results as a function of irradiation dose. The breaking strength (stress at the point of rupture) decreases above a dose of 1 MGy (Fig. 2a). At a fluence of $4×10^{11}$ Au-ions/cm^2, this loss in strength amounts to more than 50%. The breaking strain (maximum elongation at breaking point) follows the same trend (Fig. 2b). The Young modulus, on the other hand, does not change significantly up to 10 MGy, except the slightly larger values of the high-fluence Ti irradiation (Fig. 2c). Obviously ion irradiation in this dose regime does not greatly modify the elastic behaviour of Kapton, but degrades the maximum stress limit. The observed dose limit for the breaking strength and stress coincides well with earlier investigations by infrared and UV/Vis spectroscopy which both indicate pronounced degradation above 1 MGy [1]. This good correlation between optical and mechanical measurements suggests the application of spectroscopic techniques for future dose limit investigations, because they are non-destructive and much easier to perform than tensile strength tests.

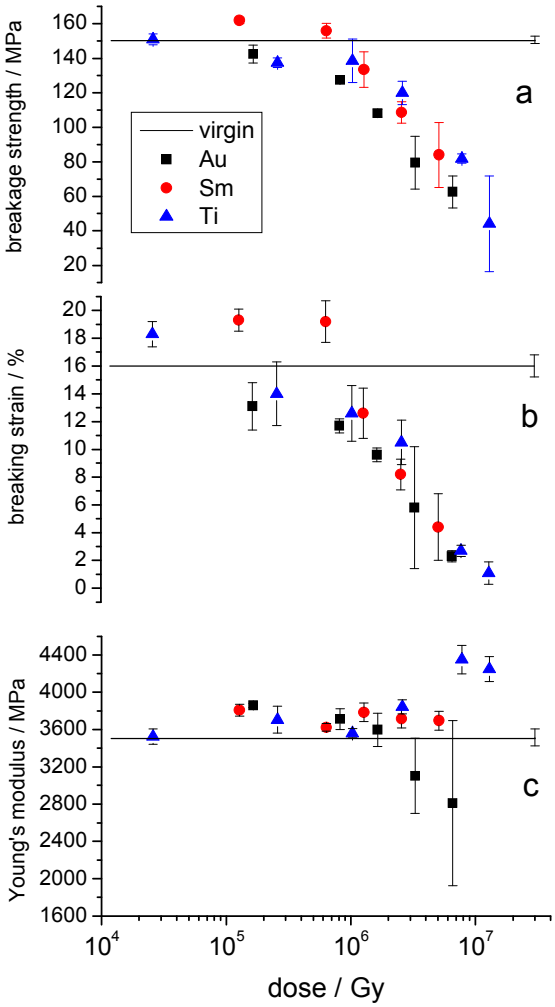

Fig. 2: Tensile strength measurements as a function of irradiation dose for Kapton foils exposed to Ti, Sm, or Au ions (11.1 MeV/u): (a) breaking strength, (b) breaking strain, and (c) Young's modulus.

References

[1] D. Severin, W. Ensinger, R. Neumann, C. Trautmann, G. Walter, I. Alig, S. Dudkin, Nucl. Instr. Meth. B 236 (2005) 456.

contact: d.severin@gsi.de

Degradation of cured polyepoxy under swift heavy ion irradiation

T. Seidl[1], W. Ensinger.[1], R. Neumann[2], D. Severin[1], C. Trautmann[2]
[1]Technische Universität Darmstadt; [2]GSI, Darmstadt,

Glass fibre reinforced plastic (GFRP) is considered as structure support and insulating material for the new superconducting FAIR magnets. GFRP (G11) is a composite material consisting of woven glass fibres (volume fraction ~50 %) and cured polymer resin (e.g. amine-cured epoxy). The material will be exposed to cryogenic temperatures, high radiation levels and dynamic mechanical loads (Lorentzian forces during pulsed operation). Long-term reliability under such extreme conditions is an issue of extreme importance. Although epoxy resin exhibits excellent mechanical and electrical properties, it is probably the weakest component of the GFRP composite because of its rather poor radiation hardness.

This report investigates radiation damage in polyepoxy foils exposed to ions from the UNILAC (Xe and U ions of 11.1 MeV/u, range ~145 µm, fluence 10^{10} – 4×10^{11} ions/cm^2). Since GFRP is only available as thick sheets (≥ 0.5 mm), we synthesised 10-20 µm foils of amine-cured polyepoxy thin enough to be completely penetrated by the ions. The irradiated samples were analyzed by different techniques including infrared and UV/Vis spectroscopy as well as physicochemical methods such as thermogravimetric analysis (TGA).

Fig. 1: Polyepoxy foils exposed to 11.1 MeV/u U ions (2×10^{11} ions/cm^2) suffer from extreme radiation damage including graphitisation and embrittlement.

Depending on the fluence applied, the originally transparent films become brownish and finally black at highest fluence (Fig. 1). This pronounced color change is in general ascribed to the formation of conjugated bonds (chromophore groups) and graphitisation [1]. TGA does not show any significant change of the decomposition temperature, but the residual increases with fluence which is a further indication for graphitisation.

Infrared spectroscopy reveals a decrease of almost all absorption bands of the pristine polyepoxy and a small increase of carbonyl groups.

In the UV/Vis spectra, the absorption edge (originally at ~370 nm) shifts after irradiation to a larger wavelength (Fig. 2). This shift becomes more pronounced with increasing fluence.

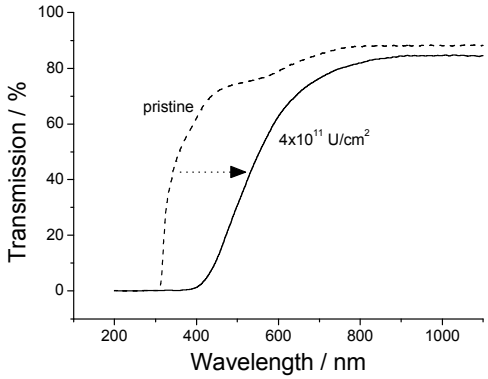

Fig. 2: UV/Vis-spectra of polyepoxy sample before and after irradiation with 4×10^{11} U-ions/cm^2.

Fig. 3 compares these epoxy data to results obtained earlier for Kapton (polyimide) irradiated under similar conditions with various 11.1 MeV/u beams [2, 3]. The shift of the absorption edge is normalized to one, and the different beams are scaled by the dose determined from the fluence and the energy loss. Polyepoxy starts to degrade at ~100 kGy, a critical dose which is about one order of magnitude lower than for Kapton being one of the most radiation hard polymers.

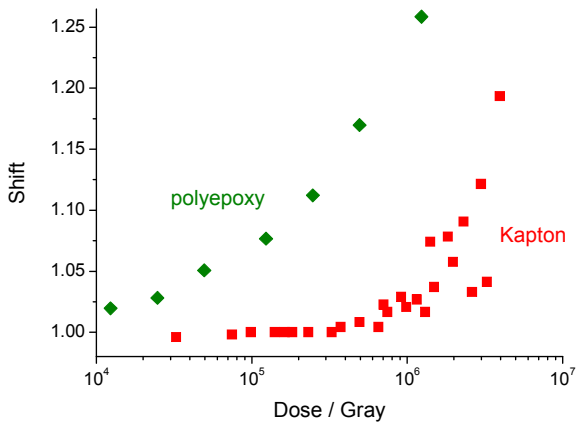

Fig. 3: Normalized shift of the absorption edge as a function of dose for ion-irradiated polyepoxy and Kapton.

Further investigations will focus on macroscopic limits of radiation-damaged epoxy and GFRP material by means of thermal conductivity, electrical (e.g. high voltage tests), and mechanical tests measurements under cryogenic conditions.

References

[1] R.M. Papaléo et al., Phys. Rev. B 53 (1996) 2203.
[2] D. Severin et al., Nucl. Instr. Meth. B 236 (2005) 456.
[3] T. Steckenreiter, E. Balanzat, H. Fuess, C. Trautmann, Nucl. Instr. Meth. B 151 (1999) 161.

Fluence effect on chemical etching of ion tracks in polycarbonate membranes studied by small-angle X-ray scattering

B. Schiedt[1#], P. Apel[2], P. Boeseke[3], T. Cornelius[1], G. Pépy[4], D. Severin[5], M. Toulemonde[6], C. Trautmann[1]

[1]GSI, Darmstadt, Germany; [2]JINR, Dubna, Russia; [3] ESRF, Grenoble, France; [4]Institute of Solid State Physics, Budapest, Hungary; [5]Darmstadt University of Technology, Darmstadt; Germany [6] CIMAP, Caen, France

Ion-track membranes are typically produced by irradiating thin polymer foils with energetic heavy ions having kinetic energies of several hundred MeV. Within a few nanometers around the ion path, the cylindrical damage zone exhibits an increased chemical reactivity compared to the surrounding polymer matrix. Chemical etching allows the creation of extended uniform channels with diameters in the nm to µm range.

Although a large number of studies describe chemical and physical changes of ion-irradiated polymers, there are still numerous open questions on material modifications on the molecular scale and about the nature of the damage as a function of the radial distance from the ion path. In the past, conductivity measurements recorded during the etching process suggested that crosslinking of polymer chains in the track halo slows down the radial etching velocity v_r [1]

Membranes with nanopores of large areal density require high fluences. In such a situation, the haloes of neighbouring tracks can overlap with possible influence on the etching process. We therefore tested the fluence dependence of track etching by irradiating polycarbonate foils with swift heavy ions (Pb) of ~ 11 MeV/u.

To clarify if and at which fluences track overlapping influences radial etching rates, we applied small-angle X-ray scattering (SAXS). Earlier SAXS experiments already demonstrated that track-etched pores in polycarbonate exhibit a narrow size distribution [2], making them ideal candidates for further investigations.

As samples we used 20 µm thick Pokalon foils (LOFO GmbH) and irradiated them with fluences from 10^8 to 3×10^{10} ions/cm^2. Subsequent to UV light exposure (1 h on each side), the irradiated foils were etched in 5 mol/L NaOH at 60 °C. Different pore diameters were obtained by varying the etching time between 1 and 10 min.

The SAXS experiments were performed at the ID01 beam line of the European Synchrotron Research Facility (ESRF). Experimental details are described in [2]. The intensity of the X-rays as a function of the scattering vector shows pronounced oscillations (Fig. 1a), which are a clear indication for cylindrical scattering objects with a very narrow size distribution. Pore diameters were deduced by analysing the oscillation wavelengths [3]. For all fluences, the pore diameter increases linearly as a function of etching time (Fig. 1b), but the radial etch rate v_r (corresponding to the slope of a linear fit to data in Fig. 1b) slightly decreases with for higher fluences (Fig. 1c).

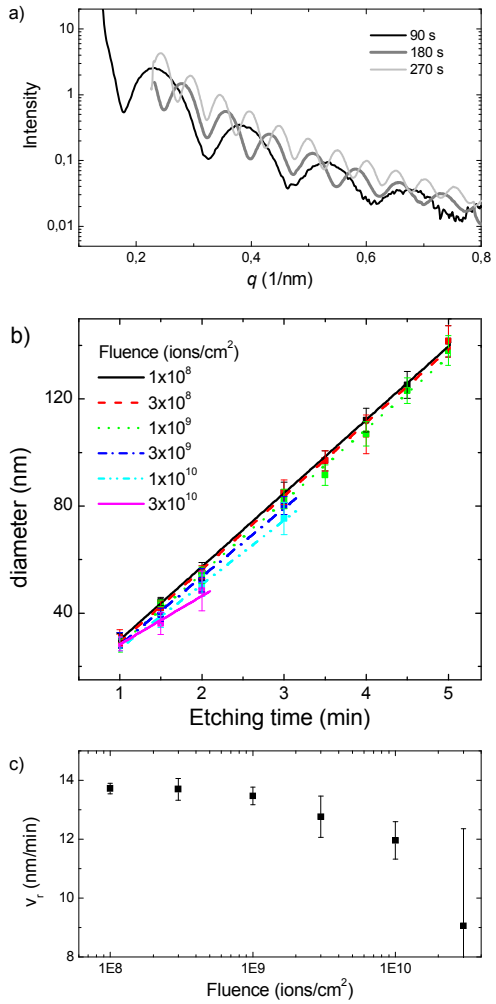

Fig. 1: a) X-ray intensity as a function of the scattering vector *q*, with pore size dependent oscillations for a sample irradiated with 10^9 ions/cm^2 b) pore diameter versus etching time c) average radial etching rate in the range of 10-12 nm/min versus fluence.

Up to 10^9 ions/cm^2, the radial etching rate is almost constant, whereas for higher fluences, v_r is slightly slowed down. We ascribe this effect to the fact that the damaged halo regions around the ion path created by secondary electrons overlap, possibly leading to cross-linked polymer chains which decelerate the etching process.

References

[1] P. Apel et al., Rad. Meas. 31 (1999) 51
[2] G. Pépy et al., J. Appl. Crystallogr. 40 (2007) 388
[3] B. Schiedt, et al., to be submitted to Phys. Rev. B

B.Schiedt@gsi.de

Preparation of anisotropically proton-conductive materials based on poly(vinylidene fluoride) ion track membranes

T. Yamaki[1, #], M. Asano[1], H. Koshikawa[1], Y. Maekawa[1], R. Neumann[2], and K.-O. Voss[2]
[1]Japan Atomic Energy Agency (JAEA), Takasaki, Gunma 370-1292, Japan; [2]GSI, Darmstadt, Germany

Proton exchange membranes (PEMs) for polymer electrolyte fuel cells (PEFCs) have recently been developed by our original techniques of the γ-ray or electron-beam crosslinking and graft polymerization. Our additional main focus is the use of cylindrical damage in polymers produced by bombardment of high-energy ions, that is called a latent track. We are taking the approach using this ion track technology according to two procedures, expecting the preparation of "anisotropically" proton-conductive PEMs. One is ion-track grafting [1], i.e., direct grafting into the activated zone; and the other is the track etching and subsequent chemical modification inside the etched pores. The report in the preceding issue [2] described the former attempt and, therefore, the latter is presented here, including basic characteristics of the resulting PEMs.

A commercially available poly(vinylidene fluoride) (PVDF) film with a thickness of 25 μm was bombarded by swift heavy ions from the TIARA cyclotron of JAEA and the UNILAC linear accelerator of GSI. According to the established procedure [3], track etching was then performed in a 9 M KOH aqueous solution at 80˚C. It should be noted here that irradiation with high-LET GeV beams and preheating treatment of the irradiated films in air accelerated the track etching [4]. The sulfonic acid groups were introduced into the track-etched cylindrical pores of 100 nm diameter (density 3.0×10^9 cm^{-2}) via the γ-ray-induced styrene grafting and subsequent sulfonation.

Figure 1 shows the proton conductivity, σ, in the in-plane and thickness directions for the resulting PEMs whose ion exchange capacity (IEC) was controlled up to 2.2 mmol g^{-1}. The proton transport *only* in the thickness direction, increasing with the IEC, was obtained at < 1.6 mmol g^{-1}. This anisotropic conductivity strongly indicates the formation of one-dimensional straight proton conductive pathways parallel to the ion-beam incident axis.

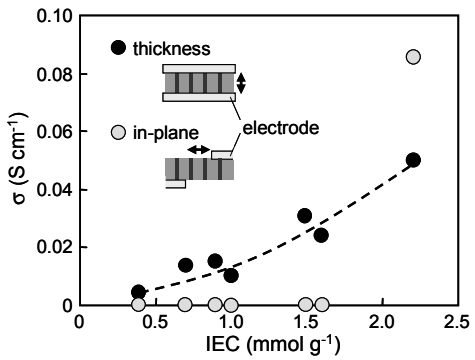

Figure 1: Proton conductivity in the in-plane and thickness directions for the PEMs with different IECs.

A transmission electron microscope (TEM) was used to observe the morphology of proton-conductive, hydrophilic domains in the PEMs. Figure 2 is the representative TEM micrograph of a cross section of the PEM stained by ruthenium tetroxide (RuO_4) vapor. This revealed that the stained lines with about a 100 nm width were arranged almost parallel to the through-thickness direction. Accordingly, it was confirmed that the PEM had a cylindrical electrolyte part with a diameter comparable to the size of the etched pore. In other words, we were able to prepare a novel PEM, which possessed nano-sized proton-conductive pathways extending along the ion projectile as expected.

An interesting result was apparent from the comparison with the properties of the PEMs separately obtained by the usual γ-ray-induced *homogeneous* grafting. The water uptake of the anisotropically conductive PEMs was lower than that of the *homogeneously* grafted PEMs in spite of the same IEC; for example, it decreased from 36% to 23% (up to about two-thirds) at 1.6 mmol g^{-1}. An inert PVDF host without any graft electrolyte chains was found to restrict the swelling of the entire PEM.

Finally, such restricted structure of the new PEM is also expected to reduce methanol transport. In fact, its permeability at controlled IECs was significantly lower than that of a Nafion membrane. It can be concluded, therefore, that our material is applicable for use in a PEFC (especially of the direct methanol type), thus extending the performance beyond the limit of conventional ones.

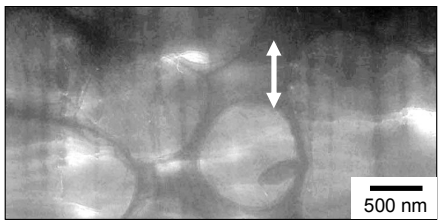

Figure 2: Cross-sectional TEM image of the PEM. The white two-headed arrow indicates the direction perpendicular to the surface, i.e., the thickness direction.

References

[1] N. Betz, Nucl. Instrum. Methods Phys. Res., Sect. B, 105 (1995) 55.
[2] T. Yamaki, A. Hiroki, M. Asano, K.-O. Voss, R. Neumann, and M. Yoshida, GSI Scientific Report 2004, (2005) 260.
[3] Y. Komaki and S. Tsujimura, Science, 199 (1978) 421.
[4] T. Yamaki, R. Rohani, H. Koshikawa, S. Takahashi, S. Hasegawa, M. Asano, K.-O. Voss, R. Neumann, and Y. Maekawa, Kobunshi Ronbunshu (Jpn. J. Polym. Sci. Technol.), in press.

yamaki.tetsuya@jaea.go.jp

Protein biosensing with track-etched single conical nanopores in polyimide

M. Ali[1#], W. Ensinger[1], R. Neumann[2] and B. Schiedt[2, 3, 4]
[1]Technische Universität Darmstadt, Germany; [2]GSI, Darmstadt, Germany and [3]LPN-CNRS, Marcoussis, France;
[4]Université val d'Essonne, Evry, France.

Currently, researchers are deeply involved in the field of nanopore technology due to its wide range of applications. Nanopores have been used for the detection and analysis of a variety of analytes, proteins, small organic molecules and metal ions [1-2]. So it becomes crucial to modify the chemistry of the nanopore walls to achieve desired interactions with molecules of interest.

Single conical nanopores in 12 µm thick polyimide (PI), having carboxyl groups on the surface, were produced by an asymmetric track-etching process [3]. These pores have already been used successfully for the detection of DNA molecules [2] and possess the advantage of a very stable ion current signal. We have recently reported the modification of these pores by EDC/NHS activation [4]. The unmodified and modified pores were characterized by asymmetric *I-V* curves, which originate from their charged surfaces [3].

Here, we demonstrate the attachment of an amino-terminated biological ligand (biotin) to the inner surface of these pores by EDC/PFP coupling chemistry [5]. As a difference to the method reported before, the reactive intermediate pentafluorophenol (PFP) ester is ~10 times more active than the corresponding *N*-hydroxysuccinimide (NHS) ester, which leads to the higher efficiency of the modification reaction.

The carboxyl groups were first activated by an ethanol solution of EDC (0.1 M) and PFP (0.2 M). The reactive intermediate PFP ester (I) was subsequently reacted with either ethylenediamine (EDA) or biotin-amine, leading to an amide bond formation having terminal $-NH_2$ groups (II) and biotin moieties (III) respectively, as shown in the reaction scheme below

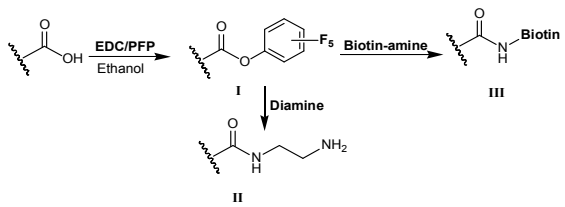

To verify the success of the reaction procedure, the *I-V* curves of unmodified and modified pores with diamine or biotin-amine were measured in 0.1 M KCl at pH 7. Before modification, the pore rectifies the ion current at neutral pH (Fig. 1a), as expected for negative surfaces. After modification with diamine, the rectification as well as the permselectivity is reversed, because at neutral pH the pore walls are positively charged due to the protonation of terminal amino groups.

After functionalization with biotin moieties, a significant change in the *I-V* curves (Fig. 1b) was observed, attributed to the diminution of the pore's surface charge. When the *I-V* curves for the biotinylated conical nanopores were measured in the presence of streptavidin (9 nM), a further decrease in current was observed (Fig. 1b) due to the noncovalent binding of streptavidin with biotin moieties.

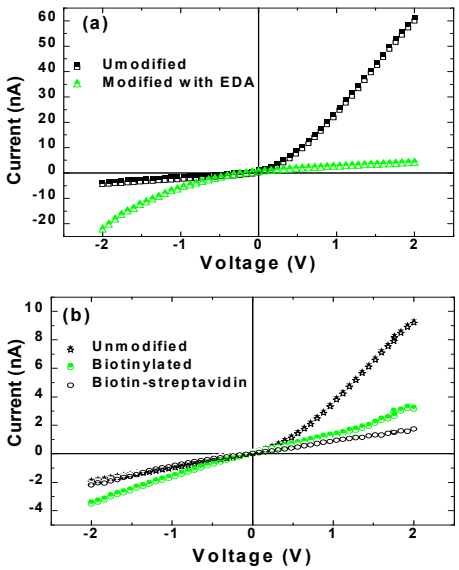

Figure 1: The measured *I-V* curves of a PI pore: Modified with a) ethylenediamine b) biotin and streptavidin.

The biotin-streptavidin system shows a very stable and strong interaction having a dissociation constant of $K_D = 4 * 10^{-14}$ [6]. This additional decrease in current is likely to be caused by a partial blocking of the pore by the streptavidin molecule.

These results explore the possibility to biofunctionalize single conical nanopores in polyimide, opening the way to use nanopores in this material (which have the advantage to exhibit a very stable ion current signal) as a biosensor for protein analytes.

References

[1] H. Bayley and P. S. Cremer, *Nature* 413 (2001) 226
[2] A. Mara, Z. Swiy, C. Trautmann, J. Wan and F. Kamme, *Nano Lett.* 4 (2004) 497
[3] Z. Siwy, D. Dobrev, R. Neumann, C. Trautmann and K. Voss, *Appl. Phys. A*. 76 (2003) 781
[4] M. Ali, B. Schiedt, K. Healy, R. Neumann and W. Ensinger, *Nanotechnology* (2008) In press
[5] J. Lahiri, E. Ostuni and G. I. Whitesides, *Langmuir* 15 (1999) 2055
[6] N. M. Green, *Methods Enzymol*. 184 (1990) 51

M.Ali@gsi.de

NaCl and KCl micro and nanorods grown in ion-track templates*

M. Enculescu[1#], I. Enculescu[1], C. Trautmann[2], R. Neumann[2]
[1] National Institute for Materials Physics, Bucharest, Romania, [2]GSI, Darmstadt, Germany.

Arrays of nanorods, nanotubes and nanowires have potential applications in a wide variety of areas including optoelectronics, data storage, and sensing [1]. Due to their small size and large surface-to-volume ratio, such structures possess unique properties compared to bulk objects. Here we are presenting micro and nanorods grown in etched ion-track templates. This technique has the advantage that the nanowire parameters can be precisely controlled including length, diameter, and geometrical shape as well as areal density. Also the deposition process is versatile because the pores in the template can be filled with many different materials (such as metals, semiconductors, polymers), and by means of various deposition processes, with or without applying a voltage [2, 3].

In this study, we prepared alkali-halide structures with the same method which already successfully demonstrated the growth of KI micro and nanorods [4]. As template material, polycarbonate foils (100 or 30 μm thick) were irradiated with heavy ions (e.g. Pb or U) of 11.1 MeV/u and fluences in the range of 10^5 – 10^8 ions/cm^2. The ion-tracked foils were chemically etched at 50°C in an aqueous solution of 5 M NAOH containing 10% methanol. The resulting pores are cylindrical and have a diameter between several ten nm and a few μm. The etch rate at the above condition is about 2 μm/hour. For the growth of alkali-halide rods, the template floated several days on a saturated NaCl or KCl aqueous solution (ambient temperature). Due to evaporation, crystallization occurs in the solution, on the membrane surface, and inside the pores.

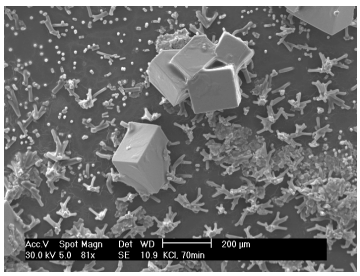

Figure 1: Single crystals of NaCl grown on the surface of an etched ion-track membrane.

Fig. 1 shows the scanning electron micrograph of several NaCl microcrystals grown on the template surface. These larger crystals are generated if the pores are completely filled and the crystal growth on the wire tip of the wire is no longer restricted by the pore geometry. To inspect the NaCl and KCl microrods, the polymer template is dissolved (Fig. 2). During this process some of the structures are quite elastic and bend, but we also observe many broken stumps.

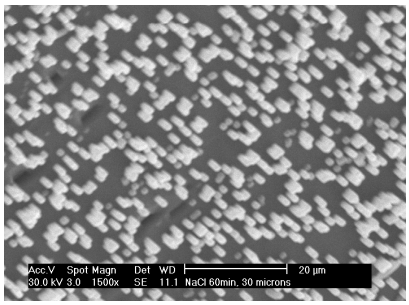

Figure 2: Array of KCl rods grown in the pores of an ion-track template when floating on a saturated KCl solution.

The ends of the rods exhibit facets which is a clear indication that the process has a strong tendency to favour the growth of a single crystal (Fig. 3, left). In some cases, full and hollow types of rod are observed within a given array (Fig. 3, right). The hollow structures appear only for templates with large pore diameters. At present the condition for obtaining this geometry is not very clear, but we assume it is correlated with the growth process being faster at the pore of the walls.

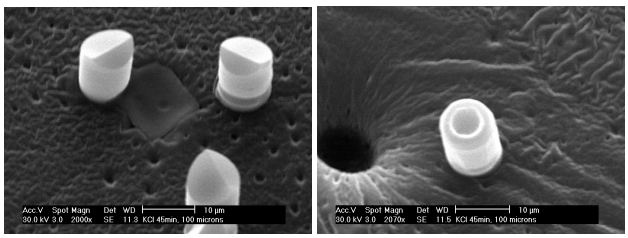

Figure 3: Faceted and hollow KCl rods.

The template method is a versatile approach to the preparation of highly uniform nanostructures. By selecting suitable template parameters, nano and microwires from many different materials can be produced. Here we demonstrated the controlled growth of alkali-halide microrod ensembles which can be directly incorporated into devices and are interesting objects for fabricating micro and nanolasers as recently illustrated for ZnO nanowires [5].

References

[1] Y. Cui, C.M. Lieber; Science 291 (2001) 851.
[2] B. Bercu, I. Enculescu, R. Spohr; Nucl. Instr. Meth. B 225 (2004) 497.
[3] M. Sima, I. Enculescu, A. Ioncea, T. Visan, C Trautmann; Adv. Mat. 6 (2004) 1193.
[4] D. Dobrev, J. Vetter, R. Neumann; Nucl. Instr. Meth. B 146 (1998) 513.
[5] M.H. Huang S. Mao, H. Feick, H. Yan, Y. Wu, H. Kind, E. Weber, R. Russo, P. Yang; Science 292 (2001) 1897.

* Supported by Romanian Ministry of Education and Research, contract No. PNII-IDEI-30/2007.
# mdatcu@infim.ro

Effect of additives on electrochemical deposition of nickel nanowires

E. Matei[1], M. Enculescu[1], M. Sima[1], R. Neumann[2] and I. Enculescu[1]
[1]National Institute for Materials Physics, Magurele, Romania; [2]GSI, Darmstadt, Germany

In the last decade, the deposition of metallic nanowires with magnetic properties proved to be an attractive field due to the wide range of potential applications; one can prepare nanowires with exotic properties, like anisotropic or giant magnetoresistance [1-3], which are suitable as building blocks in the development of devices such as magnetic field sensors or nonvolatile RAM memories.

In this report, we present an improvement in the procedure of nanowire preparation using polycarbonate ion track membranes as templates and electrochemical deposition. Unfortunately, one important drawback of the approach is given by the fact that polycarbonate is hydrophilic. This characteristic makes it difficult to wet the pores with the deposition solution and grow nanowires with high pore filling efficiency. By employing additives in the deposition solution, we succeeded in improving the template wettability and in this way also the efficiency of the nanostructure fabrication process.

The nickel nanowire deposition was performed using a Watts bath, containing nickel sulphate and nickel chloride as nickel ion sources at a working temperature of about 60^{o}C. A comparison between the deposition of nanowires without additives and with polyvinylpyrrolidone (PVP) and gelatin in the deposition bath was made. One can notice a strong correspondence between the three polarization curves (figure 1), the main difference consisting in the shift to larger electronegative potentials of the peak corresponding to nickel deposition for the baths with additives. Also, from the chronoamperemetric curves (figure 2) for deposition in different conditions of potential, it can be noticed that the adequate time for completely filling the pores is different according to the experimental conditions.

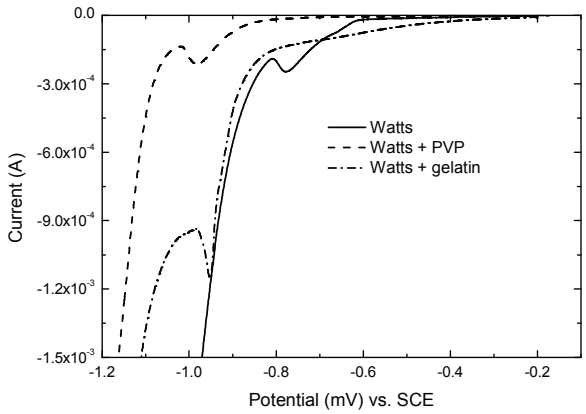

Figure 1: Polarization curves recorded using a Watts bath without additives, and with gelatin and PVP.

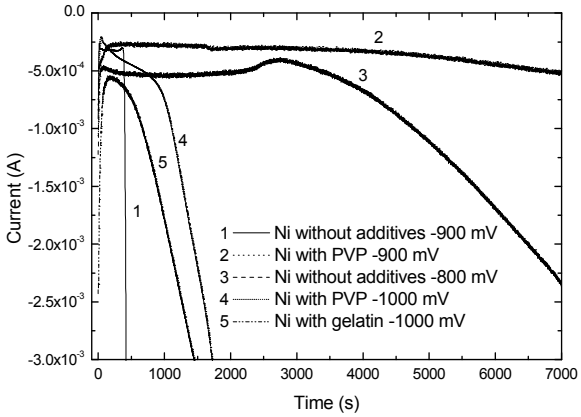

Figure 2: Chronoamperemetric curves for Watts bath without additives, with gelatin, and with PVP, measured potential vs. Saturated Calomel Electrode (SCE).

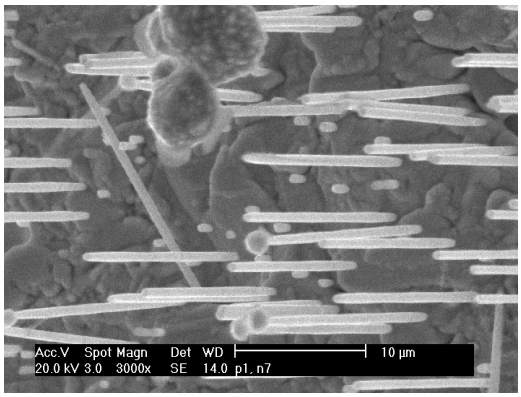

Figure 3: SEM images of a nickel nanowire array deposited from a Watts bath with PVP as additive at a potential of -900 mV vs. SCE.

The use of PVP as an additive in the growth bath gives an increase of pore filling efficiency from 48% up to 80%, allowing the preparation of high-density nanowire arrays. For higher deposition potentials, the efficiency decreases in all cases, possibly due to production of hydrogen at such potentials, enabling the creation of bubbles and that plug the nanopores and stop the deposition.

References

[1] M. Daub, I. Enculescu, R. Neumann, R. Spohr, J.Optoelec. and Adv. Mat. **7** (2005) 865.
[2] L. Piraux, J. M. George, J. F. Despres, C. Leroy, E. Ferain, R. Legras, K. Ounadjela, and A. Fert, Appl. Phys. Lett. **65** (1994) 2484.
[3] Ohgai, T., Hoffer, X., Gravier, L., Wegrowe, J.-E., Ansermet, J. Ph., Nanotechnology **14** (2003) 978.

Surface plasmon resonances of Cu nanowire arrays

J.L. Duan[1,2], T.W. Cornelius[2], J. Liu[1], S. Karim[3], H.J. Yao[1], O. Picht[2], D. Dobrev[2], M. Rauber[4], S. Müller[2], C. Trautmann[2], R. Neumann[2]

[1] Institute of Modern Physics, CAS, China; [2] GSI, Darmstadt, Germany; [3] University of Marburg, Germany; [4] University of Technology Darmstadt, Germany.

In the recent past, considerable attention has been devoted to the optical signature of noble metal (Au, Ag, and Cu) nanostructures in the ultraviolet, visible, and near-infrared spectral ranges, because of their promising applications in optical nanodevices. The optical response of metal nanostructures can be ascribed to surface plasmon resonances (SPR) [1]. In this report, we present our results on SPR of Cu nanowire arrays.

The arrays were produced by filling the nanopores of ion track-etched polycarbonate (PC) templates with Cu. For this purpose, PC foils (Makrofol N, Bayer Leverkusen) of thickness 30 µm were irradiated at the UNILAC linear accelerator with fluences of 10^8 and 5×10^8 ions/cm^2. Prior to chemical etching in 5M NaOH at 50 °C, the foils were illuminated by UV light for 2 hours from each side. Subsequently, Cu nanowires were electrochemically deposited at 50 °C by applying a constant voltage of -200 mV. The electrolyte consisted of 75 g/l $CuSO4\bullet5H_2O$ and 30 g/l H_2SO_4. A thin sputtered Au layer reinforced by an electroplated Cu layer was used as cathode for wire deposition. After removing the cathode, extinction spectra of nanowire arrays embedded in the templates were recorded employing an ultraviolet-visible spectrometer (UV4, UNICAM) under ambient conditions. The direction of light propagation was chosen parallel to the wire axis (i.e. the electric field vector was normal to the wire axis). A track-etched template without wires was used as reference sample.

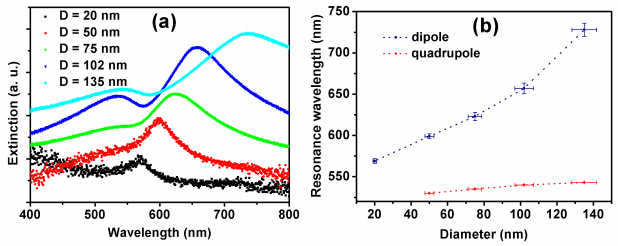

Figure 1: (a) Extinction spectra of Cu nanowire arrays with diameters D = 135, 102, 75, 50, and 20 nm (from top to bottom). (b) Extinction maxima as a function of nanowire diameter.

The spectra of arrays with wire diameters D ranging from 20 to 135 nm and with a fixed wire length L = 30 µm are displayed in Fig. 1a. The wire areal density Φ is 10^8 wires/cm^2 assuming that all pores were filled. For the thinnest wires (D = 20 nm) an isolated SPR peak at 568 nm is clearly observed. Because the electric field vector of the incident light was normal to the long wire axis, this resonance can be attributed to a dipole oscillation of the transverse SPR modes. This assumption is supported by calculations using Gans' theory [1]. As D increases, the dipole peak dramatically shifts to higher wavelengths. Simultaneously, a second peak at shorter wavelengths (530-543 nm) becomes more and more pronounced. Taking the wire geometry into consideration, this peak is likely due to a quadrupole oscillation of transverse SPR. Compared to the dipole resonance, the redshift of the quadrupole peak is less pronounced, as shown in Fig. 1b. The redshifts of both the dipole and quadrupole resonances are similar to theoretical and experimental results obtained for nanoparticles [2]. In Fig. 1b, the wavelength and diameter values are provided with error bars derived from the extinction spectra and scanning electron microscopy images, respectively.

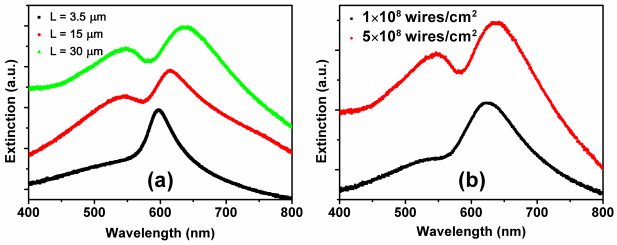

Figure 2: Extinction spectra of arrays of Cu nanowires with (a) lengths L = 30, 15, and 3.5 µm (from top to bottom), diameter D = 75 nm, and areal density $\Phi = 5\times10^8$ wires/cm^2, and (b) L = 30 µm, D = 75 nm, and $\Phi = 5\times10^8$ and 1×10^8 wires/cm^2 (top and bottom, respectively).

Figure 2a illustrates extinction spectra of arrays of 5×10^8 Cu nanowires/cm^2 with D = 75 nm, but each array with different L. With increasing L, the dipole resonance shifts to the red and, simultaneously, the quadrupole peak rises in intensity. A similar behaviour is observed for arrays of wires (D = 75 nm, L = 30 µm) with increasing Φ (Fig. 2b). The surface plasmons of adjacent wires may couple electromagnetically with each other. This coupling increases with rising L and decreasing distance between adjacent wires, i.e., increasing Φ. As is known from studies on nanoparticles, this coupling is effective and could lead to the observed redshift of the SPR. Additionally, since serious phase shifts occur along the wires, the quadrupole oscillation can be excited in longer wires more easily.

In summary, we have demonstrated how surface plasmon resonances of Cu nanowire arrays are controllable via diameter, length, and areal density of the wires.

References

[1] R. Gans, Ann. Phys. 37 (1912) 881

[2] U. Kreibig, M. Vollmer, Optical Properties of Metal Clusters (Springer-Verlag, Berlin Heidelberg, 1995).

Infrared spectroscopic studies of the metallic behaviour of single nanorods

F. Neubrech[1], D. Weber[1], T. Cornelius[2], M. Lopes[3], M. Lamy de la Chapelle[4], R. Neumann[2] and A. Pucci[1, #]

[1]KIP, Heidelberg University, Germany; [2]GSI, Darmstadt, Germany; [3]University of Technology of Troyes (UTT), Troyes, France, [4]Université Paris 13, Paris, France

Using infrared (IR) spectroscopic microscopy we studied resonant light scattering from gold nanorods prepared by electron beam lithography (EBL) as well as from cylindrical gold nanowires prepared by the template method. Rectangular nanorods with diameter in the 100 nm range act as resonant antennae showing significant antenna-like plasmon resonances similar to those of cylindrical nanowires with a higher crystalline quality [1]. The obvious similarity of the IR spectra of both kinds of nanowires shows that differences in their crystallinity have a nearly negligible effect on their antenna behaviour.

Optical properties of antenna-like nanostructures are a field of rapidly increasing interest since their plasmonic resonances are related to strong local electromagnetic field enhancement. Such an amplification, which is particularly strong for gold nanowires in the IR, can be exploited, e.g., for resonance enhanced vibrational spectroscopy and enhanced fluorescence [2].

This report focuses on IR spectroscopic microscopy studies of antenna-like plasmon resonances of single gold nanorods prepared by EBL and their comparison with highly crystalline single gold nanowires. Gold was chosen because of its high chemical stability. Like most metals it shows the Drude-type behaviour in the IR.

Gold nanorods were prepared with EBL on an IR transparent substrate (ZnS) using a 30 kV Hitachi S-3500N scanning electron microscope equipped with a nanometer pattern generation system (NPGS, JC Nabity Lithography Systems). Polymethylmethacrylate (PMMA) was used as a high-resolution resist. After electron beam exposure, the pattern was developed in a 1:3 solution of methylisobutylketone and isopropyl alcohol, and an appropriate amount of gold was evaporated on the sample. For the lift-off process acetone was used. As described in a former publication [3], the cylindrical Au nanowires were prepared by electrochemical deposition in polymeric ion track-etched membranes and transferred onto a ZnS substrate for the IR measurements.

IR spectroscopic microscopy using synchrotron radiation was performed at the synchrotron light source ANKA of the Forschungszentrum Karlsruhe. This technique enables us to locate single nanowires in the visible light mode of the microscope (*Bruker IR scope II*) and to focus the IR radiation on the selected circular area (spot size 8.3 µm). After recording the IR transmittance spectrum of the selected nanowire, a reference spectrum is acquired at a minimum distance of 10 µm from the structure. At least 500 spectra were recorded with a resolution of 8 cm^{-1} in the spectral range between 700 and 7000 cm^{-1} using a FTIR spectrometer (*Bruker IF66v/S*) with a LN_2 cooled mercury cadmium telluride detector.

#pucci@kip.uni-heidelberg.de

We gratefully acknowledge the ANKA company for providing beamtime

The relative transmittance spectra reveal strong fundamental antenna resonances for polarization parallel to the long wire axis.

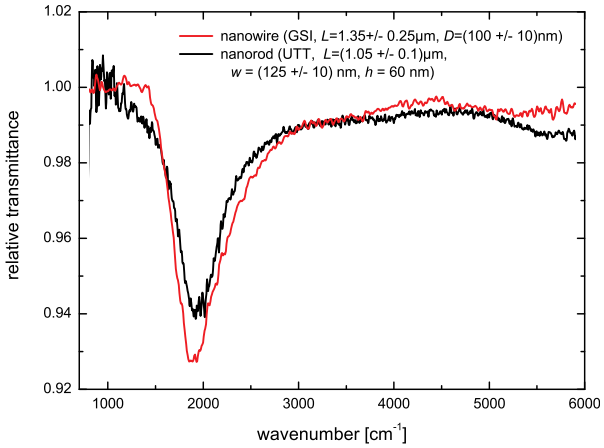

Figure 1: IR spectra of a gold nanorod (on ZnS) prepared by EBL (black line) and an electrochemically prepared cylindrical nanowire (red line) with similar geometric dimensions (length *L*, diameter *D*, width *w*, height *h*).

Figure 1 shows a typical resonant excitation for a cylindrical nanowire (red curve) and a lithographically prepared nanorod (black curve) with rather similar geometric dimensions. The resonance frequencies (minimum of transmittance) are similar, and, surprisingly, resonance width and extinction (as a measure for an average field enhancement [1]) are also nearly the same.

Additional grain boundaries decrease the relaxation rate of free charge carriers. Thus, the IR optical properties of gold are expected to deviate from the ideal metallic behaviour affecting the antenna resonances of the nanowires [2]. A significant influence is anticipated for a 10 times higher relaxation rate in comparison to polycrystalline bulk data. However, we did not find a significant difference of the antenna-like behaviour of highly crystalline gold nanowires and polycrystalline nanorods. Hence, their polycrystalline structure plays a minor role for the plasmonic nanoantenna performance and for applications such as resonance-enhanced vibrational spectroscopy.

References

[1] F. Neubrech et al., Appl. Phys. Lett. 89, 253104 (2006).
[2] A. Pucci, F. Neubrech, J. Aizpurua, T. W. Cornelius, M. Lamy de la Chapelle, in “Nanoscale Science and Technology”, Springer Book Series "Lecture Notes on Nanoscale Science and Technology (LNNST)” ed. Z. Wang, in press (invited book chapter).
[3] S. Karim et al., Appl. Phys. A 84, 403 (2006).

Field emission properties of gold nanowires

A. Dangwal[1], C.S. Pandey[1], G. Müller[1,*], S. Karim[2], T.W. Cornelius[2], and C. Trautmann[2]
[1]Physics Department, University of Wuppertal, Germany; [2]GSI, Darmstadt, Germany

Metallic nanowires (NW) with high length-to-diameter aspect ratios are interesting candidates as field emitters for cold cathode applications. In comparison to carbon nanotubes, the number density, length, and diameter of NW electrochemically grown in etched ion-track templates can be much better controlled. Based on the promising results achieved with gold-coated nickel NW [1], we studied field emission (FE) properties of randomly distributed free-standing gold NW and systematically varied the wire dimensions (Tab. 1). Suitable templates were produced by chemical etching of polycarbonate foils irradiated with various fluences of 11 MeV/u Pb or U ions.

Table 1: Parameters of Au wires as determined from scanning electron microscopy.

sample	density (cm^{-2})	length (µm)	diameter (nm)	aspect ratio
A	~10^6	7.5	257	58
B	~10^7	5.9	250	47
C	7.6×10^6	9.3	254	73
D	3.2×10^6	14.6	265	110
E	7.2×10^6	8.8	121	146

The emission site density and current distribution of all samples were measured with the field emission scanning microscope (FESM). Typically ~5×10^5 emitters/cm^2 were found at maximum fields of 20-40 V/µm. Up to 40 % of the NW on sample A emitted at 33 V/µm, and ~10 % of the partially clustered NW on sample E showed up at 20 V/µm (Fig. 1). Current scans at reduced fields, however, revealed a limited emission uniformity of the NW [2].

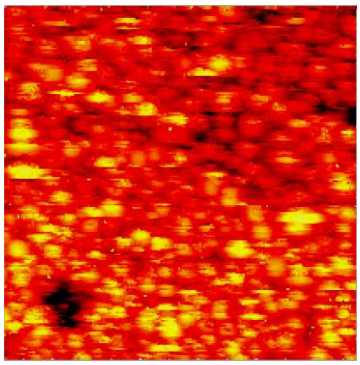

Figure 1: Electric field map required for a current of 2 nA for sample E (W-tip Ø 5 µm, scanned area 0.5×0.5 mm^2).

The local onset field and field enhancement factor β of the Au NW were measured at ~20 spots for each sample. The typical current-field curve (Fig. 2) shows an initial instability and confirms the linear $\ln(I/E^2)$ vs. $1/E$ dependence expected from the Fowler-Nordheim (FN) theory.

* contact: gmueller@uni-wuppertal.de

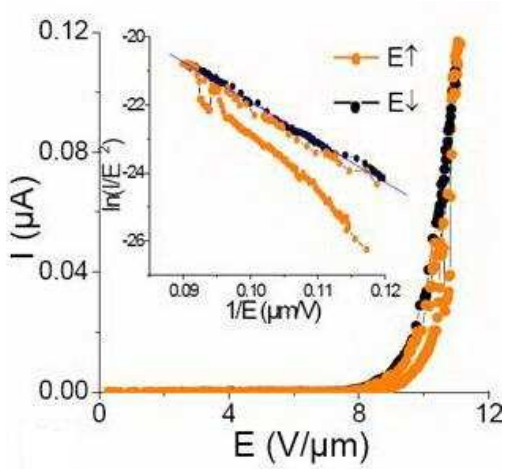

Figure 2: Locally measured current vs. field and FN plot for a single emission site (10 µm resolution) on sample E.

The mean β values deduced from each sample showed the expected correlation with the length (Fig. 3) except for sample E (circled data point) with wires of smaller diameter. The β values were ~5 times larger than the aspect ratio due to sharp tip edges of the NW [3]. The spread of lnβ values was the narrowest for sample E (Fig. 3) and reflects the small size distribution of the NW. Further improvements of the FE homogeneity are envisaged by preparing structured NW arrays.

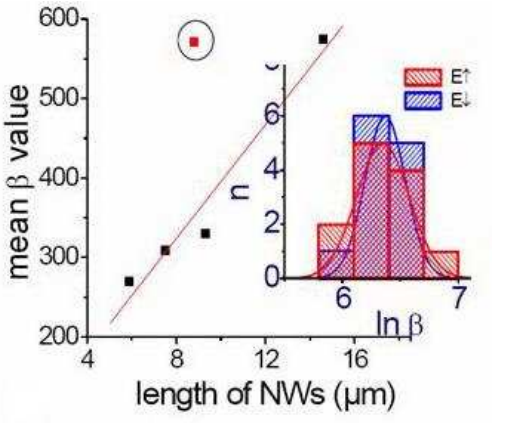

Figure 3: Mean β values vs. length of all NW samples. The inset shows the lnβ distribution found for sample E.

References

[1] A. Dangwal, G. Müller, F. Maurer, J. Brötz, H. Fuess J. Vac. Sci. Technol. B 25 (2007) 586.
[2] A. Dangwal, C.S. Pandey, G. Müller, S. Karim, T.W. Cornelius, C. Trautmann, Techn. Digest IVNC07, Chicago, 2007, IEEE Cat. No. 07TH8951, p. 100.
[3] A. Dangwal, PhD thesis, Univ. of Wuppertal, WUB-DIS 2007-08.

Electrical transport properties of individual gold nanowires

S. Karim[1], W. Ensinger[2], C. Hassel[3], T. W. Cornelius[4], J. L. Duan[5], R. Neumann[4]
[1]Physics Division, PINSTECH, Islamabad, Pakistan; [2]Darmstadt University of Technology, Darmstadt, Germany; [3]Department of physics, University of Duisburg-Essen, Germany; [4]GSI, Darmstadt, Germany; [5]IMP, CAS Lanzhou, P R China

Metallic nanowires are regarded as essential components for the development of nanoelectronic devices. Their electrical resistivity, being one of the most important properties in electrical applications, is the subject of intense theoretical and experimental investigations [1]. When the object size becomes comparable to the electronic mean free path, finite-size effects are expected to occur, leading to additional scattering of the conduction electrons at both the surface [2] and the inner grain boundaries [3]. These scattering processes increase the electrical resistivity.

Here, we present our first results on the resistivity of single cylindrical gold nanowires, electrically contacted by means of electron beam lithography (EBL). In a first step, we prepared ensembles of polycrystalline gold nanowires by electrochemical deposition in etched ion track templates [4]. The wires were freed from the polymeric host by dissolving the matrix in dichloromethane. The solvent was exchanged several times to obtain clean nanowires which were subsequently detached from the bottom support by placing the vessel in an ultrasonic bath. Finally, these polymer-free nanowires were dispersed on a GaAs substrate by spreading some drops of the solution on the wafer.

The GaAs substrate carrying the wires was transferred to a scanning electron microscope (SEM) for contact processing by EBL. In order to fabricate macroscopic bonding pads to one of the wires, which were randomly distributed on the sample, a sufficiently long and well-separated wire was chosen. Based on the contact layout adequate for the selected wire, a polymethylmethacrylate (PMMA) layer was spun onto the substrate and the sample was retransferred into the SEM. Then, the layout was exposed to the electron beam, and the PMMA was developed in a mixture of isopropanol and methylisobutylketone. Subsequently, the gold contacts were deposited by thermal evaporation, and the lift-off process took place in a hot acetone bath leaving the wire contacted with 200-nm thick gold leads. For the electrical measurements, we used a four-point contact geometry by applying currents of typically 1 μA. Temperature dependent measurements were done in a ^{4}He-bath cryostat where the temperature was varied down to few K.

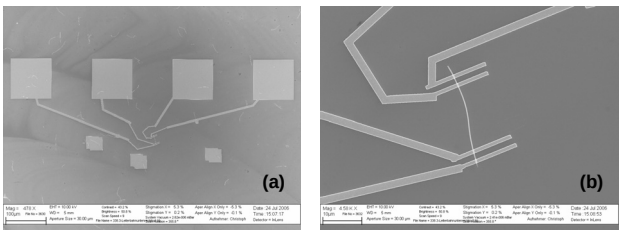

Figure 1: SEM micrographs of (a) low and (b) high magnification of contacted Au nanowire with diameter 80 nm.

Figure 1 (a) depicts the arrangement of four contact pads for electrically connecting a Au wire, while Fig. 1 (b) displays a higher-magnification image. The geometry, length, and diameter of each contacted wire are easily accessible by SEM. The nanowire shape is very important for a correct estimation of the specific electrical resistivity ρ. Figure 2 shows the measured temperature dependence of ρ for a Au wire with diameter 80 nm and length 20 μm in the temperature range of 4–300 K, together with data of bulk gold from [5]. Both wire and bulk show a linear temperature dependence down to ~ 30 K and finally approach a residual value. The wire resistivity amounts to 5.3 and 2.1 μΩ cm at 300 and 4 K, respectively. The ratio of wire-to-bulk resistivity amounts to 2.4 at room temperature and increases with decreasing temperature. The increased nanowire resistivity is attributed to finite-size effects, i.e., additional electron scattering at the wire surface as well as at inner grain boundaries.

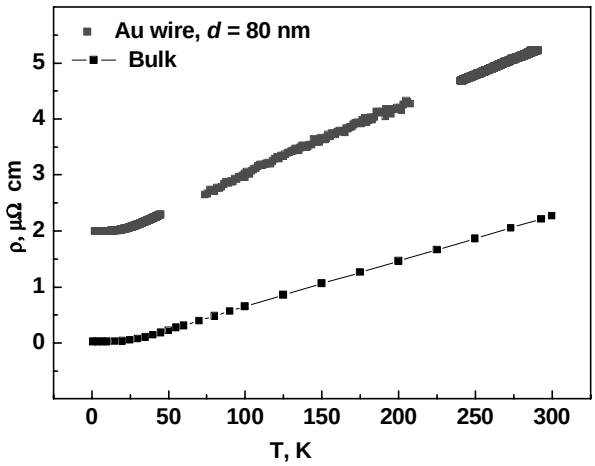

Figure 2: $\rho(T)$ curve of a Au wire of diameter 80 nm together with the values of bulk gold.

In summary, we have successfully employed EBL to contact single gold nanowires and subsequently measured electrical properties at ambient as well as at low temperatures. For a wire of diameter 80 nm, electron scattering from the surface as well as inner grain boundaries becomes significant.

References

[1] G. De Marzi et al., J. Appl. Phys. 96 (2004) 3458
[2] R.B. Dingle, Proc. R. Soc. Ser. A 201 (1950) 545
[3] A.F. Mayadas et al., Phys. Rev. B 1 (1970) 1382
[4] S. Karim et al., Appl. Phys. A 84 (2006) 403
[5] R.A. Matula, J. Phys. Chem. Ref. Data 8 (1979) 1147

Oscillating electrical conductivity in bismuth nanowires

T.W. Cornelius[1], M.E. Toimil-Molares[1], S. Karim[2], R. Neumann[1]
[1]GSI, Darmstadt, Germany; [2]Physics Division, PINSTECH, Nilore Islamabad, Pakistan

In the recent past, extensive studies were performed on nanoscale materials. In particular, bismuth nanowires attracted large interest because of their extraordinary electronic properties and potential application in future thermoelectric devices. When the nanowire diameter becomes comparable to the electronic mean free path l_e and the Fermi wavelength λ_F, finite-size and quantum-size effects (QSE) are expected. Since both parameters are large in Bi ($l_e \sim 100$ nm, $\lambda_F \sim 40$ nm), these effects are anticipated for comparable thick nanowires. QSE cause a splitting of the energy bands in subbands and, thus, a shift of the band edges away from each other [1]. At a critical diameter d_c the band overlap existing in bulk Bi is predicted to disappear, and the wire undergoes a transition from a semimetal to a semiconductor. Due to the subband splitting, the electronic density of states (DOS) at the Fermi level changes (inset of Fig.1).

The electrical conductivity of single Bi nanowires as a function of diameter was investigated. For this purpose, single nanowires were deposited electrochemically in ion track-etched single-pore polycarbonate (PC) membranes. The templates were fabricated by irradiating PC foils with single swift heavy ions at the UNILAC. Subsequently, the foils were etched in 2 mol/l NaOH at 50 °C. After coating one side of the membrane with a conductive layer, the wire was grown electrochemically in the single nanopore. The deposition was continued until a cap was formed on top of the wire. After rinsing and drying the sample, an additional gold layer was sputtered onto the cap for electrically contacting the nanowire and, subsequently, the electrical resistance of the wire was measured [2].

The specific electrical conductivity σ of the nanowires is plotted in Fig. 1 revealing oscillations as a function of wire diameter d. They can be described well by an exponential law corresponding to $\sigma = A + B * \exp(-d/d_c)$ with A and B being fitting parameters where A is related to the wire conductivity. As already mentioned above, QSE causes a splitting of the energy bands in subbands and, thus, a shift of the band edges away from each other. The energy shift can be described by the following expression: $\Delta E \approx N^2 \hbar^2 \pi^2 / (m^* d^2)$ where N is the number of the subband which corresponds to discrete values of the wave vector along the "quantizing" dimensions of the nanowire. Owing to the spike-like DOS for nanowires (see inset of Fig. 1), the kinetic properties of the system will oscillate as a function of d, as long as the carrier gas is degenerate. These oscillations are connected with abrupt changes of the density of states on the Fermi surface as one subband after another passes E_F. According to Farhangfar [3], the periodicity for rectangular nanowires is given by d_c. The exponential behaviour of the oscillations may be explained by the thermal excitation of charge carriers. Only charge carriers close to the Fermi level contribute to the electrical transport. When a subband passes E_F, it is depleted and the charge carriers are transferred to lower states. At room temperature, they are excited thermally to higher subbands so that they participate in the electrical transport. With increasing band gap, i.e., decreasing d, the number of thermally excited carriers decreases and, thus, σ drops. As soon as a lower subband approaches E_F, the charge carrier density recovers and, hence, the conductivity increases to about 3000 S/cm being in agreement with the mean resistivity of 440 μΩ cm (σ = 2272 S/cm) reported in ref. [2]. The whole process occurs repeatedly until the lowest subband passed the Fermi level and the material is transferred into a semiconductor.

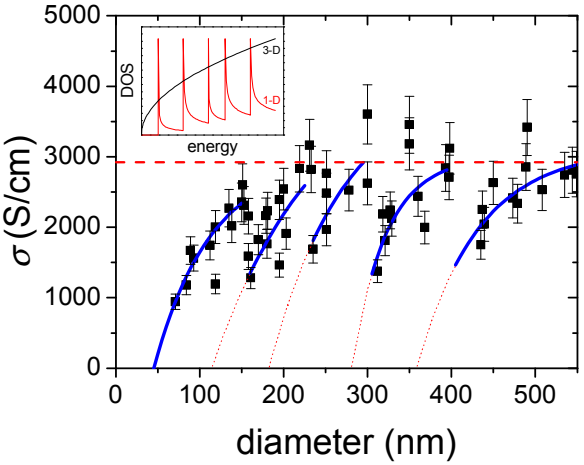

Fig. 1: Specific electrical conductivity of single bismuth nanowires as a function of diameter. The solid and dotted lines represent exponential fits using $\sigma = A + B*\exp(-d/d_c)$ and their interpolation to $\sigma = 0$. The inset shows a schematic of the density of states for three- and one-dimensional materials.

In conclusion, the electrical conductivity as a function of diameter for single bismuth nanowires reveals an oscillatory behaviour. There are reasonable arguments that these sharp periodic alterations originate from a modulation of the density of states at the Fermi level.

References

[1] V.B. Sandormirskiĭ, Sov. Phys. JETP 25 (1967) 101
[2] T.W. Cornelius, M.E. Toimil-Molares, R. Neumann, S. Karim, J. Appl. Phys. 100 (2006) 114307
[3] S. Farhangfar, Phys. Rev. B 74 (2006) 205318

Band Structure and Density of States of Bismuth Nanowires

S. Müller[1], T. W. Cornelius[1], R. Neumann[1], O. Picht[1], and M. Rauber[2]
[1]GSI, Darmstadt, Germany; [2]TU Darmstadt, Germany

The band structure and the density of states $D(E) = 1/V\ dN/dE$ of a material contain important information about transport properties like electrical or thermal conductivity. Here, $D(E)$ of bismuth quantum wires is compared, based on theoretical calculations, to $D(E)$ of bulk bismuth for (110)-textured wires. Due to the large mean free path of charge carriers (100 nm at 300 K) and the large Fermi wavelength of about 40 nm, quantum size effects as well as finite size effects are expected to appear in comparably thick nanowires [1].

The densities of states of a quantum wire with square cross-section were calculated as a function of the edge length d in a first approximation via the Lax two-band model, which takes into account a hole carrier pocket at the T-point of the Brillouin zone and three electron pockets at the L-points L_A, L_B, and L_C. At 77 K, there is a band overlap E_Δ of 38 meV and a direct band gap E_{gap} of 15 meV at the L-point [2] (compare inset of fig. 1 a)). The charge carriers were assumed to be confined normal to the wire direction in a two-dimensional box leading to distinct allowed energy levels. At the T-point these levels are given by

$$E_{ij} = \frac{1}{2}\left(\frac{\pi\hbar}{d}\right)^2\left(\frac{i^2}{m_x^*} + \frac{j^2}{m_y^*}\right). \qquad (1)$$

with arbitrary integer numbers i and j, and effective masses m^* for different directions (the wire axis is the z-axis).

	m_x^*	m_y^*	m_z^*
L_A	0.0015	0.0049	0.2045
$\mathrm{L}_{B,C}$	0.0022	0.0090	0.0778
T	0.0590	0.1593	0.2348

Table 1: Effective masses in units of m_e for $T = 77$ K.

Due to an anisotropic Fermi surface and a strong coupling of electrons at the L-point, the dispersion relation is non-parabolic at this point [3]. Thus, the energy levels at this point have a different form:

$$E_{ij}^{\mathrm{L}} = \frac{1}{2}E_{\mathrm{gap}}\left(\sqrt{1 + 4E_{ij}\cdot E_{\mathrm{gap}}^{-1}} - 1\right). \qquad (2)$$

The densities of states $D^{\mathrm{T}}(E)$ at the T-point and $D^{\mathrm{L}}(E)$ at one L-point are given by

$$D^{\mathrm{T}}(E) = \frac{\sqrt{2m_z^*}}{\pi\hbar\, d^2}\sum_{i,j}\frac{1}{\sqrt{E_\Delta - E_{ij} - E}} \qquad (3)$$

$$D^{\mathrm{L}}(E) = \frac{\sqrt{2m_z^* f(E_{ij}, E_{\mathrm{gap}})}}{\pi\hbar\, d^2}\sum_{i,j}\frac{1}{\sqrt{E - E_{ij}^{\mathrm{L}}}} \qquad (4)$$

with a correction factor $f(E_{ij}, E_{\mathrm{gap}})$. In figure 1a), $D(E)$ is presented for wires with d = 60 nm. The bands overlap like for bulk bismuth, and $D(E)$ of the quantum wire converges towards $D(E)$ of bulk material. However, singularities appear for the nanowires corresponding to quantised energy levels. In figure 1 b), $D(E)$ of a quantum wire with d = 20 nm is shown. Here, the distances between allowed energy levels are larger due to the smaller edge length and the one-dimensional band structure is more pronounced. Furthermore, the computations reveal a band gap, whereas bulk Bi possesses a band overlap. Thus, nanowires of sufficiently small diameters are expected to undergo a transition from semimetal to semiconductor. For (110)-textured wires, the critical edge length, where this transition occurs, was calculated to be 44 nm at 77 K and 15 nm at 300 K. These calculations are in good agreement with [4].

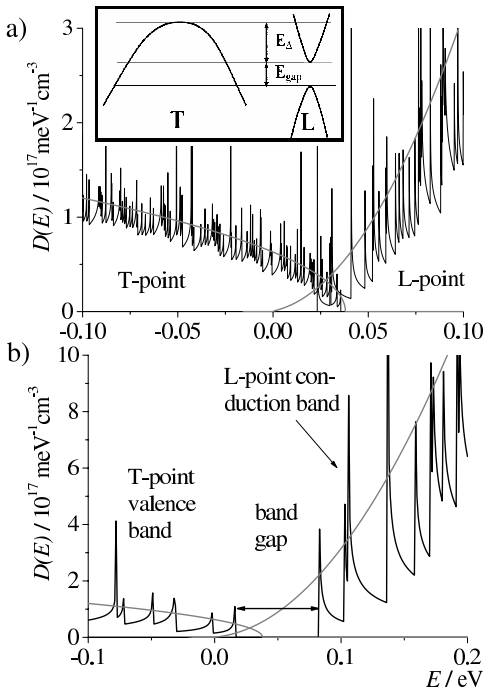

Figure 1: Calculated $D(E)$ of a bismuth quantum wire at 77 K ((110)-textured wire with square cross-section) a) d = 60 nm and b) d = 20 nm. The grey lines represent the calculations for bulk bismuth. The origin of E is the band edge of the L-point conduction band.

References

[1] V. B. Sandomirskiĭ, Sov. Phys. JETP 25 (1967) 101
[2] S. Cronin, PhD thesis, MIT (2002)
[3] B. Lax et al., Physical Review B 6 (1960) 241
[4] Y.-M. Lin et al., Physical Review B 62 (2000) 4610

Microchip construction for Seebeck-effect measurements on bismuth nanowires

M. Schmitt[1], F. Völklein[1], T.W. Cornelius[2], O. Picht[2], S. Müller[2], R. Neumann[2],
[1]FH Wiesbaden, IMtech, Rüsselsheim, Germany; [2]GSI, Darmstadt, Germany;

The characterization of thermoelectric properties of nanoscale materials is a current topic of intensive research. Especially bismuth nanowires are very attractive because of their extraordinary properties and possible applications in thermoelectric devices. For the calculation of the thermoelectric figure of merit $z = \alpha^2\sigma/\lambda$, the Seebeck coefficient α, the electrical conductivity σ and the thermal conductivity λ of the nanowires has to be determined.

The bismuth nanowires under study are fabricated by the template method [1]. Their typical length is in the range of 10 to 20 µm. For the measurement of the Seebeck effect, a temperature difference must be established along the wire axis. For this purpose, a microchip has been designed which is presented in Fig. 1 [2].

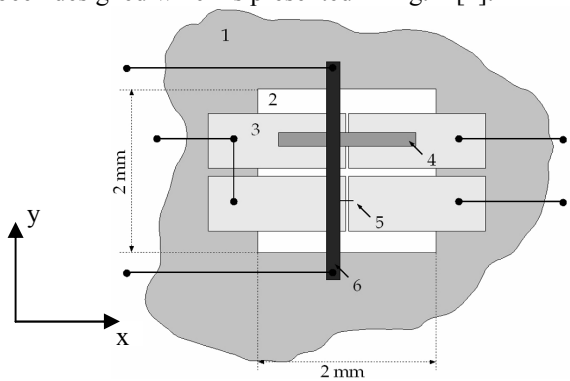

Fig. 1: 1 silicon chip, 2 SiO_xN_y membrane (800 nm), 3 Au contact pads (300nm), 4 bismuth reference film (300 nm), 5 bismuth nanowire, 6 heating film (300 nm).

The chip is realized by using microlithography and micromachining. By anisotropic etching of a (100) Si wafer, an 800 nm thick SiO_xN_y membrane is prepared in the chip center. The low thermal conductivity of the membrane is crucial with respect to the required temperature difference along the nanowire. At its ends the nanowire is electrically connected to thin metal contact pads. The gap between these pads is about 10 to 20 micron. Patterning of the pads is performed by a new method of microscopic exposure of photoresist and a lift-off process. A temperature difference ΔT between the two pairs of contact pads, located on the membrane, is established by a thin film heater. Applying the known Seebeck coefficient of a reference film, ΔT at this gap can be determined. Using ΔT and the measured Seebeck voltage U of the nanowire, its Seebeck coefficient is calculated: $\alpha = U/\Delta T - \alpha_{Au}$, where α_{Au} is the Seebeck coefficient of the Au contact film. Finite element method (FEM) simulations have been carried out to calculate the temperature distribution in the membrane area of the chip. The inset of Fig. 2 shows for a membrane size of 2x2 mm² the temperature increase related to the temperature of the bulk silicon chip, which acts as a heat sink. The FEM results demonstrate an identical temperature difference of 2 K on both gaps. Therefore, ΔT measured with reference film can be assumed as temperature difference at the nanowire. First measurements on microfabricated chips and comparisons with FEM simulations are shown in Fig. 2.

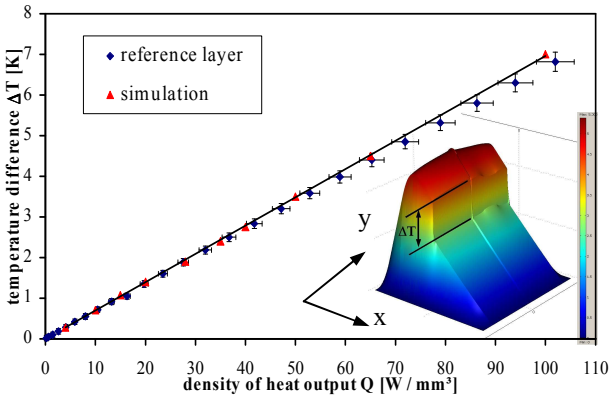

Fig. 2: Temperature difference at the gap between contact pads, measured with Seebeck reference film and values (line), determined by FEM simulation. The inset presents a ΔT = 2 K at the gap between the contact pads for a membrane area of 2x2 mm².

With this measuring set-up, temperature differences of few K between contact pads with a distance of 15 µm have been realized. Measurements of the Seebeck coefficient on Bi nanowires with various diameters are in progress. Fig. 3 displays a Bi nanowire contacted by two Au pads after electrical measurements. The wire is fragmented because of an electrical current of 1 µA used for the experiments.

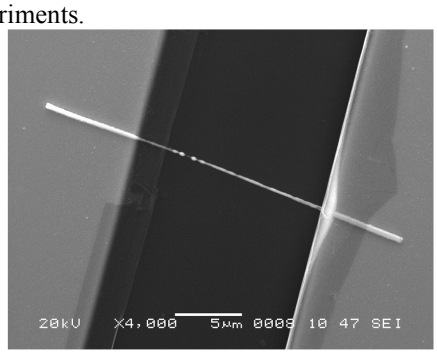

Fig. 3: Bi nanowire connected with Au contact pads; the break is due to a current flow of 1 µA

References

[1] T.W. Cornelius, PhD thesis, Ruperto-Carola University of Heidelberg, 2006.
[2] T.W. Cornelius, F. Völklein, M.E. Toimil Molares, S. Karim, R. Neumann, Proc. European Conf. on Thermoelectrics, Cardiff, 2006.

Closed Pt nanowire arrays as nanostructured microreactors for catalysis

M. Rauber[1], T. W. Cornelius[2], W. Ensinger[1], S. Müller[2], R. Neumann[2], and O. Picht[2]
[1]Darmstadt University of Technology, Darmstadt, Germany; [2]GSI, Darmstadt, Germany

In recent years, the advantages of microstructured devices for chemical reactions have been demonstrated most impressively. The application of microstructured reactors has gained significant importance in chemical synthesis and analysis [1]. The spectrum of chemical conversions, carried out successfully in microstructured reactors, includes many catalytic reactions. Supportless one-dimensional nanostructures were recently recognized as durable catalysts [2]. Due to their low diameter, nanowires provide a very large surface area without the need for a high-surface-area support. Moreover, it is expected that these structures can reduce all degradation pathways discussed for nanoparticles such as Ostwald ripening. To use their full potential in applications, however, nanowires need to be integrated efficiently in different device architectures.

Our approach to a durable catalyst suitable for device integration is based on parallel metal nanostructures. We synthesized closed platinum nanowire arrays (PtNWAs) by template electrodeposition using track-etched polycarbonate (PC) membranes [3]. One side of the irradiated membrane was coated with a conductive Au layer and then electrochemically reinforced by Cu. After etching in NaOH, the wires were grown in the nanopores. The concept of reverse-pulsed plating was adopted to compensate for the slow diffusion-driven transport in high-aspect materials. The deposition was continued until the caps forming on the top of each nanowire coalesced. Finally, an additional metal layer was deposited on the caps to increase the mechanical stability. Afterwards, the polymer matrix was dissolved in dichloromethane.

Fig. 1a shows a schematic of the nanostructured microreactor. The two metal layers are fundamental components since they not only interconnect the wires to an array, but also maintain their parallelism. Furthermore, as an essential structural element, the layers function as a physical barrier, inhibiting effectively mass transport. A closed chamber where reactions can take place is consequently created. Gas- and liquid-phase reactions are feasible. The mechanical stability of the PtNWAs is very high and evidenced impressively by fig. 1b. The cross-sectional view was created by cutting the sample after removing the polymer matrix and imaging by scanning electron microscopy (SEM). The nanowires are still parallel and are barely deformed.

The electrochemical surface area (ECSA) was determined using cyclic voltammetry. In acidic solution, strong interactions (chemisorption) between the electrode surface and H atoms take place for sufficently negative potentials (Fig. 2). Each H atom is covalent-bonded to a Pt atom. Taking into account that this reaction is a charge-transfer process involving one electron, the amount of adsorbed H atoms can be determined. With the surface atom density of the theoretically flat metal the ECSA can be evaluated.

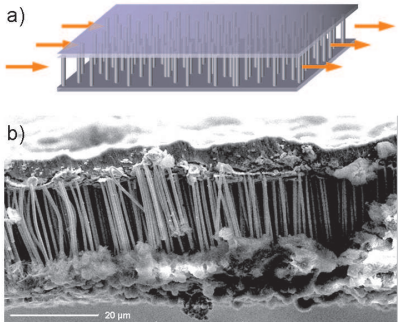

Figure 1: a) Schematic illustration of a nanostructured microreactor. Arrows indicate a flow of gases or liquids. b) SEM image of PtNWA.

As a result, the real surface is four to five times larger than the geometric one which was calculated assuming strictly cylindrical wires. The large ECSA is caused by deviations from a perfectly flat surface. Data obtained by X-ray diffraction confirm that the wires are nanostructered. The estimated grain size using the Scherrer equation was roughly 8 nm.

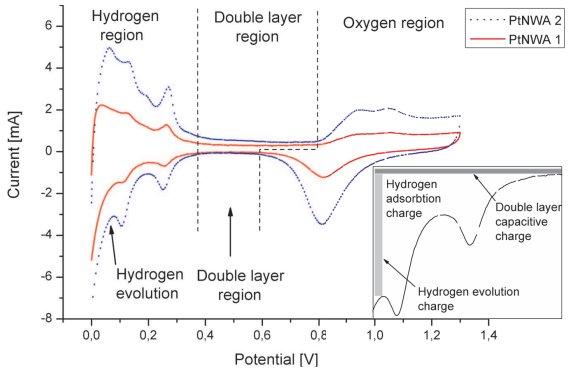

Figure 2: Cyclic voltammetric current potential curves of PtNWAs in contact with acidic solution. The inset shows the different charge contributions in the hydrogen region.

Besides the field of heterogeneous catalysis, further areas of application are imaginable. For instance, nanowires could be functionalized using organic compounds or modified by attaching inorganic nanoparticles. Nanowire arrays may be of great potential in microstructured systems for synthesis and in sensors.

References

[1] K. Jänisch et al., Angew. Chem. Int. Ed. 43 (2004), 406-446
[2] Z. Chen et al., Angew. Chem. 119 (2007), 4138-4141
[3] T. W. Cornelius et al., Nanotechnology 16 (2005), S246-S249

Adaptation of the Ion-Microprobe for the Online-Observation of Radio-Biological Effects*

G. Du, B. E. Fischer, and K.-O. Voss
GSI, Darmstadt, Germany

Introduction

Since 2003 targeted irradiations of living cells with one or a counted number of ions are taking place at the GSI ion microprobe [1]. To evaluate the effect of the irradiation the cells are usually transported to another laboratory and subjected to various treatments. Transient effects, that occur immediately after the ion hit, cannot be observed that way.

Many molecules involved in the reaction of cells to the irradiation event can be visualized using special stains and fluorescence microscopy. Therefore, we have extended the capability of the microprobe during the last two years so that the effect of an ion hit can be followed online with a fluorescence microscope, continuously from 1 second up to an hour after the hit.

As calcium ions are important intermediate messengers in many signal pathways of a cell, in particular in apoptosis, a first application of the new facility was the investigation of calcium-ion production from a precursor molecule as a reaction to an ion hit.

Modification of the Illumination-System

This new facility is an extension of the fluorescence microscopic setup in the big vacuum chamber of the microprobe (Fig. 1). The fluorescence microscope is used together with a PC to recognize, locate and irradiate cell nuclei stained with a fluorescent dye [1].

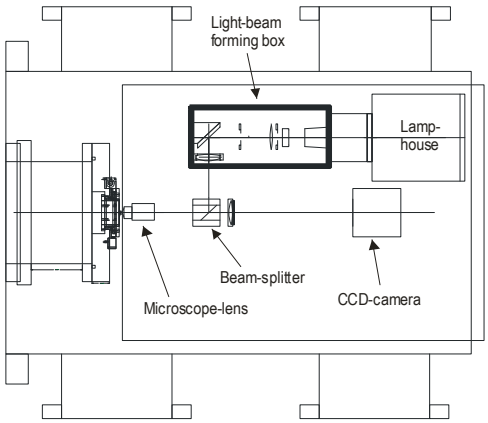

Fig. 1. Fluorescence-microscopic setup at the ion microprobe

Part of this microscope is the light-beam forming box indicated by bold lines. It contains a Koehler illumination system and a manual filter changer. To adapt the illumination system to the new task of exciting various fluorescent dyes in rapid succession, a fast, remotely controlled filter-changer (Fig. 2) has been added, and the manual one has been equipped with a set of wideband neutral density filters to allow the reduction of the light level to the absolute minimum necessary.

To minimize the UV dose applied to the cells still further, a light shutter opens only, when the camera is collecting an image, and the circular iris defining the illuminated area is replaced with an adjustable, rectangular one. This way only the area seen by the CCD-camera is illuminated.

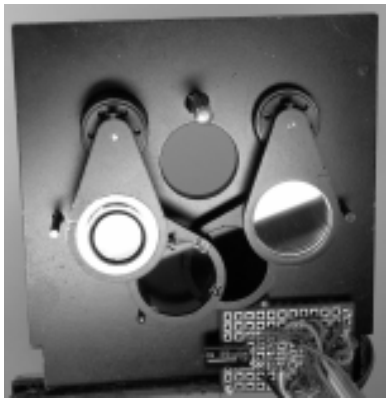

Fig. 2. Filter-changer. Four independent 18 mm diameter filters can swing into the centre position in about 50 ms under remote control. All combinations of these filters can be activated at the same time.

Computer Program to Control the sequence of Events for the New Type of Experiments

The program is written in C++ as a plug-in to the program written for the targeted irradiation of cells by M. Heiß. It contains 3 main sections:

- Observation of the cells before irradiation
- Targeted irradiation of the cells to be investigated
- Observation of the cells after irradiation

The first and last sections contain repeated cycles of taking fluorescence microscopic images excited by UV light at 340 and 380 nm, computing ratio images from image pairs created at 340 and 380 nm, and correcting for background and light level fluctuations.

References

[1] M. Heiß, B.E. Fischer, B. Jakob, C. Fournier, G. Becker, and G. Taucher-Scholz, Radiation Research 165 (2006) 23

* Work supported by EU, MRTN-CT-2003 contract No. 503923.

Research programme biophysics and cancer therapy

Radiation-induced base damage – FPG-sensitive sites in plasmid DNA

K. Psonka[1,2], E. Gudowska-Nowak[1,2], Th. Elsässer[1], and G. Taucher-Scholz[1]
[1]GSI, Darmstadt, Germany; [2]Institute of Physics, Jagiellonian University, Krakow, Poland

Introduction

Radiation-induced damage in DNA depends on the pattern of deposited energy – homogeneous in case of X-rays and very inhomogeneous for charged particles (energy deposited along their tracks in a correlated way). It is accepted that the biological effect, its complexity and severity, induced by low- and high-LET radiation (X-rays and charged particles, respectively) is strongly dependent on the distribution of deposited energy. Damage clustering (spatially correlated lesions) refers to the DNA damage induced in a correlated way by particle radiation due to the localization of deposited dose. Within single clusters, different amounts and types of individual lesions – single- and double-strand breaks (SSB and DSB respectively), base damage (BD) – can occur. Base damage is studied mostly in experiments with post-irradiation treatment of DNA with base excision repair enzymes [1-3].

FPG-sensitive sites in irradiated plasmid DNA

Previously, DSBs induction in ΦX174 irradiated in 20 mM Hepes with X-rays and ions with varying LET was reported [4,5]. Fragmentation of individual DNA molecules as a result of DSBs production was studied using AFM. The data indicated the influence of radiation quality on the spatial location of induced DSBs. Thus, the obtained distributions of produced fragment lengths showed that in case of particle radiation, DSB clustering occured due to an inhomogeneous dose deposition. Since modified bases may contribute to DNA damage induced by irradiation, an experimental effort was undertaken to evaluate the possible contribution of BD to the lesion clustering in plasmid DNA irradiated with ions. FPG (formamidopyrymidine [fapy]-DNA glycosylase) was used for post-irradiation treatment of ΦX174. This repair enzyme produces an incision at the site of damaged bases converting them to a SSB. As a result of the enzyme treatment additional DSBs are also expected to be observed in the case of the proximity of individual lesions (BD and SSB or two BDs). To estimate the contribution of BD to lesions produced in irradiated DNA, plasmid samples (ΦX174 in 20 mM Hepes) were irradiated with 9.5 MeV u^{-1} C, 5.0 MeV u^{-1} Cr, 2.9 MeV u^{-1} Sn or 2.7 MeV u^{-1} Pb ions (LET = 174, 2934, 8409 and 12824 keV μm^{-1}, respectively). As a reference X-rays were used (LET = 2 keV μm^{-1}). Samples incubated with FPG were studied in gel electrophoresis. Irradiation-induced BD was detected as excess yields of SSB/DSB following the conversion of BD to breaks by FPG (see Fig. 1). An increase of linear form of DNA indicating additional DSBs produced is visible after FPG treatment. Conversion of FPG-sensitive sites into breaks is dependent on the projectile's LET.

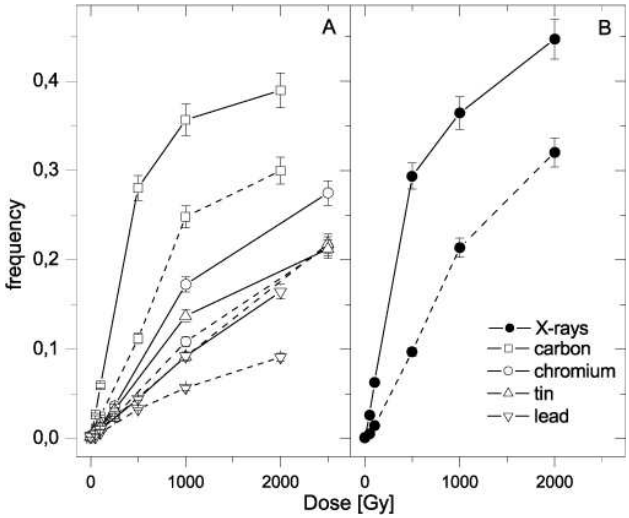

Figure 1: Linear DNA induced by irradiation and by post-irradiation treatment with FPG (dashed and solid line, respectively): A – ions, B – X-rays as a reference.

Clustering of radiation-induced lesions

Although only limited information of breaks yields can be obtained based on the electrophoresis assay, this experiment showed that the lesions in plasmid DNA are produced in form of spatially correlated breaks and altered bases. This was shown by an increase of DSB yields due to FPG action, indicating the association of SSB/DSB with nearby BD (or several BDs). The effect of lesion clustering decreases gradually as the LET of the ion increases. Since BD is mostly an effect of indirect action of radiation through free radicals, this finding may reflect a lower contribution of indirect effect of ions on DNA molecules. Alternatively, clustering of lesions in close proximity may inhibit the enzyme activity resulting in lower rate of BD conversion. BD flanking an SSB or DSB may contribute to the lesion complexity and make the process of DNA repair longer and more difficult.

References

[1] J.P. Pouget et al, Radiat Res, 157 (2002), p. 589
[2] J.R. Milligan et al., Int J Radiat Biol, 76 (2000), p. 1475
[3] M. Hada et al., Radiat Res, 165 (2006), p. 223
[4] K. Psonka et al., GSI Annual Report (2006), p. 340
[5] K. Psonka et al., Adv. Space Res. (2007), 39, p. 1043

Quantification of γH2AX using flow cytometry

J. Topsch, M. Scholz, M. Herrlitz, G. Taucher-Scholz
Biophysics, GSI, Darmstadt, Germany

We are interested in the induction and repair of DNA double strand breaks (dsb) after ionizing radiation using γH2AX as a marker. In addition to the widely applied fluorescence microscopy of immunostained γH2AX foci, we established the flow cytometric detection of γH2AX in our lab. The adaptation of the staining procedure with regard to trypsinization and centrifugation steps was described previously [1]. Here we set out to check the reproducibility of the results obtained by flow cytometry. For this purpose we first irradiated V79 cells with x-rays in four-fold determinations. Secondly we repeated the flow cytometer measurement of the samples after different times. Figure 1 shows the results for V79 cells stained for γH2AX 30 min after x-ray irradiation. The mean fluorescence of gH2AX was obtained by G0/G1 cell cycle phase cells. The square points demonstrate the measurement directly after finishing the staining procedure (fresh) and the circles show the remeasurement on the next day.

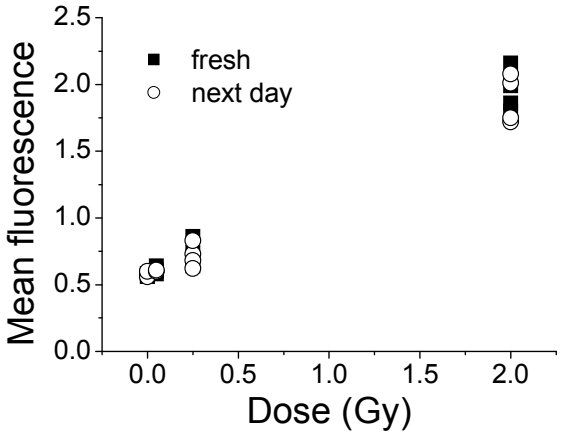

Figure 1: Dose dependency of γH2AX mean fluorescence 30 min after x-ray irradiation of V79 cells in G0/G1 cell cycle phase measured directly and next day after staining.

Figure 2 depicts another x-ray experiment with V79 cells. Here the square points represent again the freshly prepaired samples and the circles now stand for the flow cytometer remeasurement after 14 d. Based on these experiments we conclude that there is a greater variation between the four-fold determined cell probes than between the flow cytometric measurements at different days or weeks. To estimate the fluorescence signal height after heavy ion irradiation we irradiated two different cell lines with up to 30 Gy x-rays. CHO-K1 cells (chinese hamster ovary) showed a linear dose dependency up to 10 Gy followed by a plateau. For human fibroblast cells (AG) we observed a nearly linear dose dependency up to 15 Gy followed by a smooth transition possibly to a plateau at doses above 30 Gy. Flow cytometry delivers clear dose dependent signals over a wide dose range starting at low doses (0,05 Gy for CHO or 0,5 Gy for AG cells) and up to high doses, as measured for 30 Gy x-rays or after heavy ion irradiation (data not shown). In contrast, foci counting with fluorescence microscopy is limited at higher doses (>2 Gy) by overlapping foci [2].

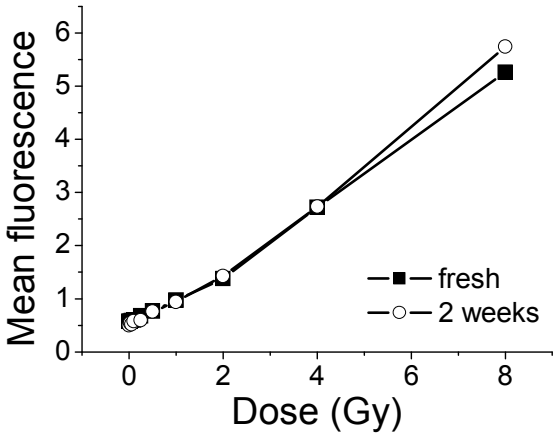

Figure 2: Dose dependency of γH2AX mean fluorescence 30 min after x-ray irradiation of V79 cells in G0/G1 cell cycle phase measured directly and 14d after staining.

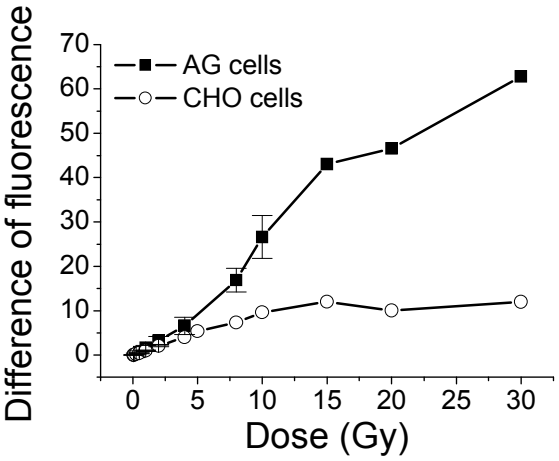

Figure 3: Dose dependency of γH2AX mean fluorescence corrected for unirradiated control 30 min after x-ray irradiation of AG (n=1, up to 10 Gy n=2-4) and CHO (n=1, for low dose range n=2-3) cells in G0/G1 cell cycle phase.

References

[1] J. Topsch *et al.*, GSI Annual Report, 2005.
[2] Y. Schweinfurth, PhD thesis, 2007

Setup of live cell imaging conditions for long term observation of radiation induced DNA damage processing

J. Splinter, G. Becker, Y. Schweinfurth, F Tobias, G. Taucher-Scholz, B. Jakob
[1]GSI Biophysics, Darmstadt, Germany

INTRODUCTION

Live cell imaging (LCI) shows clear advantages in the field of DNA-repair dynamics compared to studies using fixed and immunostained samples which generate only a static view [1]. However, using fluorescently labelled proteins in LCI requires the adequate constructs and transfection of cells. One major point often neglected in this field is the potential perturbation of cellular processes during the observation. One major stress factors is generated by the frequent observation of the cells with fluorescence excitation light under the microscope. This could apply especially in irradiated, pre-damaged cells harbouring the light sensitizer in the vicinity of the DNA. Therefore, it is necessary to establish proper imaging conditions minimizing observation induced artefacts and using additional irradiated controls kept in the dark.

RESULTS AND DISCUSSION

Equipment

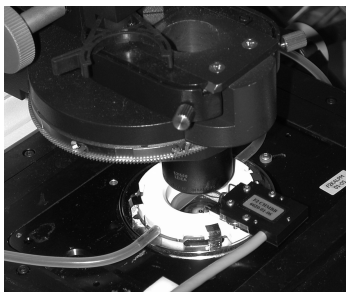

Figure 1: Temperature controlled FCS2 flow chamber

Core of our live cell imaging system is a Leica IRE2 inverted fluorescence microscope equipped with a FCS2 (Bioptec) flow chamber and a PCO Sensicam CCD-camera. The Labview based software was written by G. Böhrnsen and S. Erbes (GSI). It allows the automatic revisiting of stored positions at chosen time intervals, auto focusing and the accumulation of z-stacks. In the FCS2 chamber, cells can be kept healthy with a continuous medium exchange up to at least 48h (data not shown). Nevertheless, utilizing GFP-tagged repair proteins and the fluorescence excitation of the build in mercury lamp leads to the generation of numerous illumination induced DNA damaged sites (indicated by additional bright dots) starting after about 2h observation. In this case, the total illumination time sums up to about 60 s (Fig.2; 2h) This damage can even lead to cell loss at later times (Fig.2; 16h) and restricts the observation frequency.

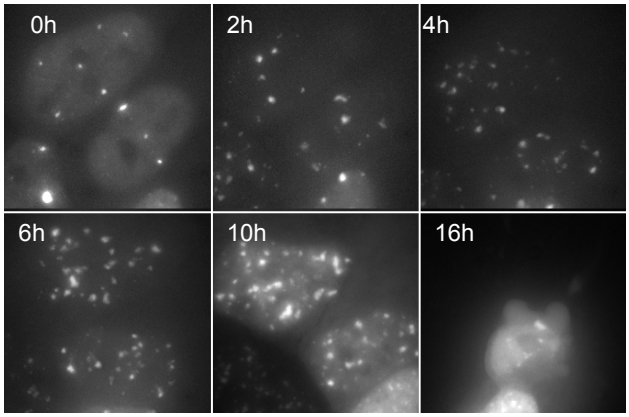

Figure 2: Illumination induced 53BP1-GFP-foci

To minimize this damage enhancing effect in DNA repair experiments, we used additive light filtering (BG38; T0.25ND) to reduce the incident light and limited the amount of acquired images and integration time to the experimental need. Alternatively, a tuneable halogen light source can be built in for fluorescence excitation. Applying these changes, we were able to achieve a substantial decrease of excitation induced DNA-damage at the cost of a slight reduction in image quality and frequency (Fig.3). Our current setup allows us studying the spatiotemporal behaviour of DNA-repair proteins after irradiation of heavy ions over a time course of several hours.

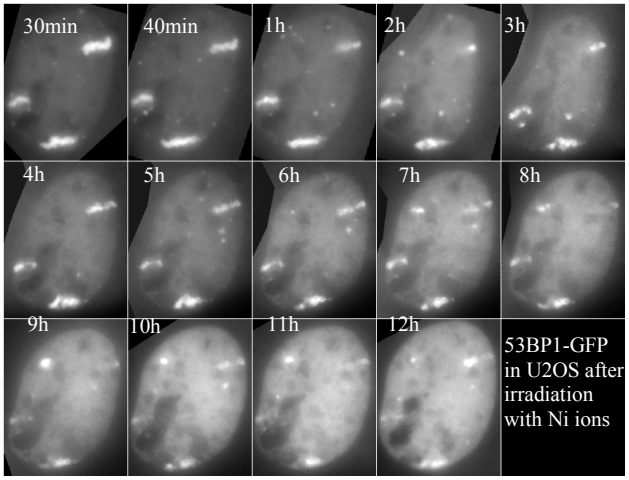

Figure 3: Live cell irradiation experiment using modified imaging conditions

[1] G. Taucher-Scholz and B. Jakob: Ion irradiation as a tool to reveal the spatiotemporal dynamics of DNA damage response processes. In: Genome Integrity, Ed. D.H. Lankenau, (2007) Springer, 453-478.

Comparative Analysis of the DNA Damage Characteristics after Heavy Ion and UV Laser Micro Irradiation

J. Splinter, A.L. Leifke, K. Knoop, B. Jakob and G. Taucher-Scholz
GSI, Darmstadt, Germany

In the last decade an increasing number of reports are published in which UV laser micro irradiation (UVLM) is used as a new tool to generate DNA double-strand breaks (DSBs) in localized regions within single nuclei [1]. Until then only heavy ions (HI) were known for their ability to induce DSBs in strictly localized areas of cell nuclei [2], but compared to UVLM systems the experimental handling is less comfortable. UVLM systems combine high magnification imaging with precise laser irradiation, thus, allowing the observation of early repair proteins in a sub-second timescale and a sub-micrometer resolution [3]. These advantages combined with the low costs compared to HI experiments make UVLM systems a tempting choice in the research field of DNA repair.

Our aim is the characterisation of UVLM systems (λ = 337nm) by the comparison with HI irradiation. This work describes a comparative analysis of the induced DNA damage types after HI and UVLM, respectively.

Results and Discussion

As a basis for the comparative analysis of heavy ion irradiation and UVLM a common parameter of deposited energy is needed. Therefore we adapted a method of laser dosimetry firstly described by Bekker-Jensen et al. [4]. The method defines a laser dose by comparing the number of Replication Protein A (RPA) foci induced by UVLM and X-rays as a reference. In the original assay X-rays up to a dose of 10 Gy were utilised to describe a dose-effect curve which ranges up to the foci yield of the used UVLM system. Using this approach, even after doubling the applied dose up to 20 Gy the obtained dose-effect curve did not reach the high yield of RPA foci which was induced by the UVLM system used here. A further expansion of the dose-effect curve was obtained using heavy ions as reference radiation. Figure 1 shows the resulting dose-effect curve now ranging up to a local dose of 1200 Gy per ion track. Finally, the expansion of the dose-effect curve by using HI data made it possible to define "laser doses" for different values of the laser irradiance (fig. 1). This result was a basis for further comparative studies.

A first comparison was done by the characterisation of the damage types induced by both systems. We used immunocytochemical staining methods and confocal laser scanning microscopy to visualise DSBs and typical UV-induced damages. While we were able to detect DSB damage signals after UVLM (fig. 2), as previously shown [1], we were not able to visualise the induction of the typically UV-induced damages cyclobutane pyrimidine dimers or pyrimidine (6-4) pyrimidone photoproducts. As expected, similar observations were obtained from irradiation with Neon ions (9,6 MeV/u).

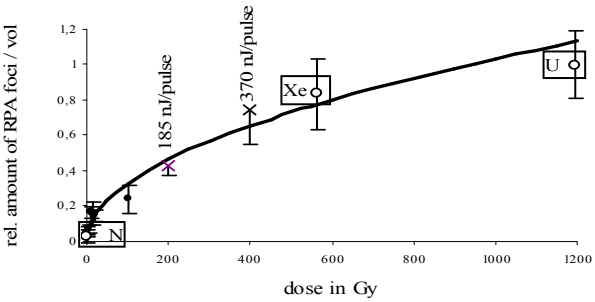

Figure 1: The dose-effect curve shows the relative density of irradiation induced RPA foci after X-ray (black points), HI (white points) and UVLM (crosses).

A difference between UVLM and HI irradiation was found in the induction of the oxidative base damage 8-oxo-7,8-dihydro-2'-deoxyguanosine (8-OHdG). As the depicted nuclei in figure 2 show, in case of an irradiation with Neon ions no 8-OHdG signal could be observed (γH2AX as hit verification), but after UVLM 8-OHdGs are induced. This additional damage implies the activation of the base excision repair (BER) machinery in addition to the DSB related repair pathways.

Our results show that UVLM systems simultaneously induce high amounts of oxidative base damages and DSBs. On this account and due to the better defined mechanism of damage generation and the possibility to measure and calculate the absorbed dose, HI seem to be the preferable tool for the induction of localised DSBs.

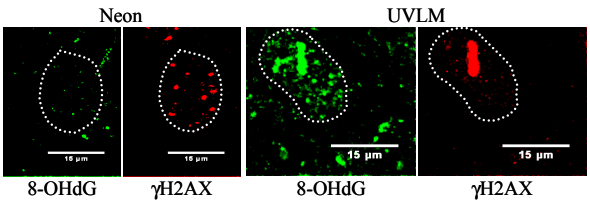

Figure 2: Induction of 8-OHdG and DSBs (γH2AX)

References

[1] E.P. Rogakou et al., Cell Biol. 146 (1999), 905
[2] B. Jakob et al., Radiat. Res. 154 (2000), 398
[3] C. Lukas et al., Nat. Cell Biol. 5 (2003), 255
[4] S. Bekker-Jensen et al., J. Cell Biol. 173 (2006), 195

DNA Damage after High-LET Exposure

M. Ensminger[1], G. Taucher-Scholz[2] M. Löbrich[1], and A. Krempler[1]
[1]Darmstadt University of Technology, Germany; [2]GSI, Darmstadt, Germany

DNA double strand breaks (DSBs) evoked by high-LET particle radiation are more resistant to repair than DNA lesions resulting from irradiation with X-rays or γ-rays. Moreover, the number of residual breaks correlates with the cell killing capacity of high-LET radiation. Due to the increasing importance of heavy ion irradiation for tumor therapy, we aimed at exploring the basis for the impaired repair of high-LET induced breaks. In a first approach, we analyzed the influence of the spatial distribution of DSBs within particle tracks on repair capacity. However, detailed analysis of the repair kinetics in different size ranges of DNA fragments revealed no differences in DSB repair [1]. Owing to the high ionisation density of high-LET particles, it also seemed possible that DSBs resulting from heavy ion irradiation are generally more complex with additional lesions in very close proximity to the DSBs. These breaks would require processing before repair. In this context we recently reported that ATM- and Artemis-deficient cells are specifically defective in the repair of DSBs with slow repair kinetics. Interestingly, the fraction of unrepaired breaks in ATM- and Artemis-deficient cells depends upon the complexity of the DSB ends [2].

To investigate the relationship between LET and complexity of a break, we measured the proportion of those DSBs that require Artemis after various radiation qualities. Stationary G_0-phase primary human fibroblasts were irradiated with X-rays or various ions of different energies. After specific repair times the cells were subjected to pulsed-field gel electrophoresis (PFGE). In addition, γH2AX analysis was used to investigate the repair of individual DSBs after low doses. To determine whether X-rays of different energies would produce varying amounts of complex lesions, we analyzed the repair kinetics of DSBs induced after 2 Gy of 25kV and 125kV X-rays or γ-rays (660keV) in wildtyp (MRC5) and Artemis fibroblasts (F01-240) using γH2AX analysis. For all three radiation qualities DSBs were repaired with identical kinetics in wildtyp cells reaching background levels 24h after irradiation (Fig.1A, left panel). In Artemis cells we observed slower repair kinetics and a repair defect of ~20% (Fig.1A, right panel). However, we could not observe a difference in the remaining DSBs among the three energies. Therefore, the results demonstrate that differences in the energy of X- and γ-rays do not result in varying amounts of complex lesions. We next applied ultra-soft X-rays (carbon K shell radiation, 280eV). The data revealed that the level of unrepaired breaks was significantly elevated (~25%) in Artemis (CJ179) and AT (AT7Bi) cells compared to wildtyp cells (HSF1). These unrepaired DSBs persisted for up to three days (Fig.1B). As the range of Ck-rays is known to be short and a large proportion of the energy is deposited within a very short distance, this supported our notion that high energy deposition within a very short distance results in complex lesions.

Wildtyp (82-6hTert) and Artemis cells (CJ179hTert) were then irradiated with different heavy ions (^{138}Xe, ^{64}Ni, ^{12}C) of varying LET using the UNILAC at the GSI. PFGE analysis revealed that the proportion of unrepaired breaks is significantly elevated in irradiated Artemis cells when compared to wildtyp cells (Fig.1C) after prolonged repair times (24-48h post irradiation). Therefore, our results demonstrate that the high biological effectiveness of high-LET radiation may result from the high proportion of complex DSBs that are repaired with slow kinetics or even stay unrepaired. However, for more conclusive results and for quantification of the proportion of complex lesions in dependence of the LET, more experiments with different ions have to be conducted.

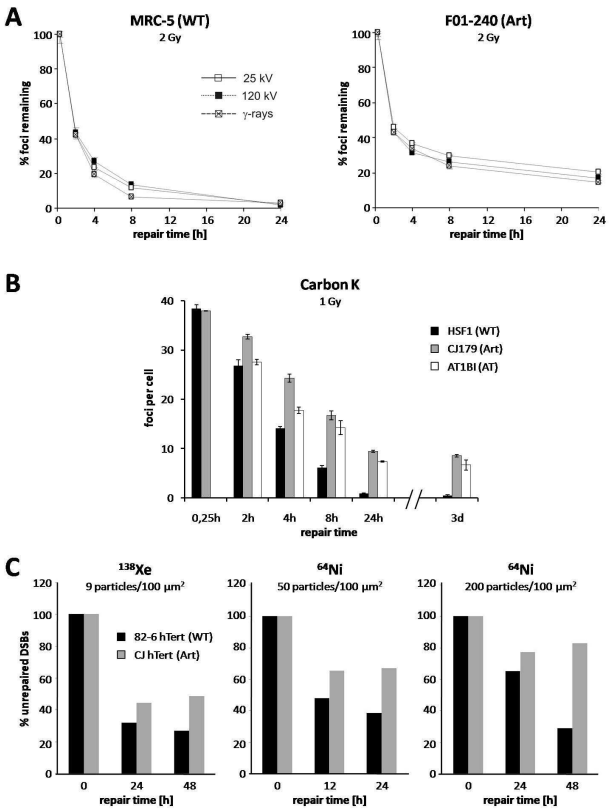

Fig.1: γH2AX analysis in WT and mutant cells after 2 Gy X-rays and γ-rays (A) and 1 Gy carbon K shell radiation (B); PFGE analysis after ^{138}Xe- and ^{64}Ni irradiation (C).

References

[1] A. Fricke, M. Kühne, M. Löbrich, GSI report 2006
[2] E. Riballo, M. Kühne, N. Rief, A. Doherty, et al., Molecular Cell 16 (2005) 715-724

Chromosome aberration rates in peripheral blood lymphocytes of prostate cancer patients and age-matched healthy donors

Hana Hofman-Hüther [1] , Sylvia Ritter[2] and Patricia Virsik-Köpp[3]

[1]Dept. of Radiotherapy and Radiooncology, [2]GSI Darmstadt, [3]Dept. of Environm. Medicine, University of Göttingen, Germany

Spontaneous chromosome aberration rates in peripheral blood lymphocytes obtained from prostate cancer patients before therapy were analyzed in patients treated either with IMRT (intensity-modulated radiation therapy) or with a combination of IMRT and carbon ion boost. Simple exchange-type aberrations (dicentrics and reciprocal translocations) and acentric fragments were analyzed in at least 500 cells for each patient. The analysis was performed using three-color FISH (fluorescent- in situ- hybridization), whereby chromosomes no.1, 2 and 4 were painted. Moreover, the aberration rates were evaluated in lymphocytes from these patients during (in the middle) and after the therapy. Sums of the scored aberrations per cell are shown in fig.1. The first data show that there is a quite variable aberration induction in patients irradiated under the same geometrical conditions. The variability is reported also by other authors (e.g. Lou et al. 2007) and mirrors the variable radiation sensitivity of the individual cancer patients.

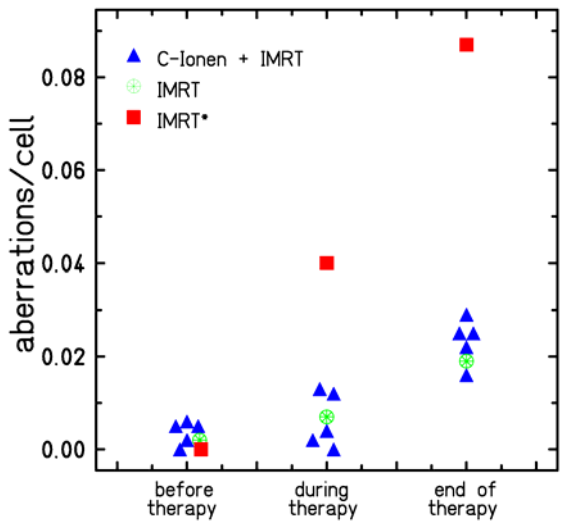

Fig.1. Aberration rates per cell as scored in chromosomes no.1, 2 and 4. These three chromosomes represent about 15% of the genome. Data are shown for patients treated with carbon ion boost plus IMRT or with IMRT only. One patient (outliner, ■) received and IMRT treatment with a larger field. The corresponding rates are thus higher than in the other group.

In parallel with the analysis of aberration rates in prostate cancer patients, we started to analyze spontaneous aberration rates in healthy male donors (age 64 to 92 years), in order to test whether the spontaneous aberration rates in prostate cancer patients are possibly higher than in healthy donors. A difference in these rates would indicate an increased chromosomal instability present in blood lymphocytes of the patients. As can be seen from Table 1, the spontaneous rates in healthy donors are also variable.

Donor	Age	Aberration rate per cell
P-K1	65	**0,004**
P-K2	69	**0,011**
P-K3	65	**0,008**
P-K4	64	**0,005**
P-K5	65	**0,007**
P-K6	65	**0,007**
P-K7	70	**0,009**
P-K8	81	**0,006**
P-K9	82	**0,002**
P-K10	92	**0,000**

Table 1 Spontaneous aberration rates (sums of simple exchanges and acentric fragments) in lymphocytes from older healthy donors.

Our study will be continued for more patients and more healthy donors. In patients, also the aberration rates at later time points, 1 year and later after therapy, will be evaluated. The completed evaluation will be followed by statistical analysis of the patients´ and healthy donors´ data.

In a pilot study using long-term lymphocyte cultures from one healthy donor and one prostate cancer patients, we studied radiation-induced chromosomal instability up to 36 days after irradiation. In the patient, chromosomal instability was significantly higher than in the healthy age-matched donor (data not shown).

References

[1] Lou J et al. (2007), Mutation Res. 617, pp. 104-110

Acknowledgement: The authors thank BMBF for financial support of this study by a grant No. 02S8203 and 02S8497.

Chromosome aberrations in blood lymphocytes of prostate cancer patients *

C. Hartel[1], D. Becker[1], C. Fournier[1], P. Hessel[1], G. Kraft[1], S. Ritter[1], S. Sommer[1], S. Zahnreich[1], E. Nasonova[1,2], P. Virsik-Köpp[3], J. Debus[4], B. Didinger[4], R. Haselmann[4], A. Nikoghosyan[4] and D. Schulz-Ertner[4]

[1]GSI, Darmstadt, Germany; [2]JINR, Dubna, Russia, [3]University Göttingen, Germany, [4]Clinical Radiology, Heidelberg, Germany.

Since 2006 a clinical phase I/II study is carried out treating prostate cancer patients with a combination of C-ion irradiation and IMRT (C-ion treatment at GSI, IMRT in Heidelberg). In parallel to this therapy, a study investigating chromosome aberrations in blood lymphocytes of prostate cancer patients is performed, as described in [1]. Chromosome aberrations in blood lymphocytes are widely used in biological dosimetry as they represent a sensitive marker for ionizing radiation. Since they are unavoidably exposed to radiation during tumor treatment, this study makes it possible to investigate *in vivo* the cytogenetic effects of C-ion radiation and to compare with conventional tumor irradiation.

Patients are irradiated with C-ion boost (6x3GyE) and IMRT (30x2Gy) or solely with IMRT (38x2Gy). Blood samples are drawn from each patient before, during, at the end of and one year after therapy. Lymphocytes are cultured according to standard techniques [2]. Chromosome spreads are prepared and slides are stained using Fluorescence-Plus-Giemsa staining (FPG) and multiplex fluorescence in situ hybridization (mFISH), respectively.

To investigate the individual radiosensitivity, a blood sample from each patient before therapy is irradiated *in vitro* (3Gy X-rays). The results are compared to those of healthy donors (fig. 1). Slight differences in the aberration yield were observed, but no significantly increased radiosensitivity of one patient was found, nor an enhanced sensitivity of all patients compared to healthy donors.

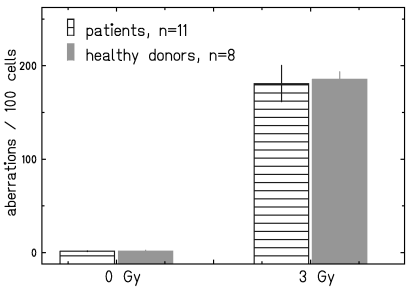

Figure 1: Chromosome aberrations after *in vitro* irradiation of peripheral blood lymphocytes of prostate cancer patients and healthy donors, found using FPG-staining.

The time course of breaks involved in chromosome aberrations found in the blood lymphocytes from patients treated with combined therapy (n=8) or only IMRT (n=1) is given in fig. 2. Results are achieved using mFISH staining which, in contrast to FPG, allows identifying all chromosome breaks involved in chromosome rearrangements. The aberration yield increases during therapy course and decreases slightly during the year after therapy. The response is very similar for both therapy conditions, indicating that under the given exposure conditions C-ions do not induce more damage in the normal tissue than photons. Prostate cancer patients irradiated with a larger field IMRT (not fitting to study conditions) show a higher amount of aberrations (data not shown).

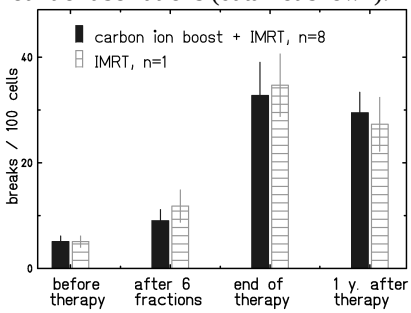

Figure 2: Yield of breaks involved in chromosome aberrations found in prostate cancer patients during therapy course, treated with combined C-ion irradiation and IMRT, or solely IMRT. Results are obtained using mFISH technique.

Interestingly, in one of the patients, a rare event, a multiaberrant cell called a 'rogue cell' was found in an mFISH stained sample (fig. 3). These cells were described in literature (e.g. [3]) and were previously found in our laboratory with FPG technique.

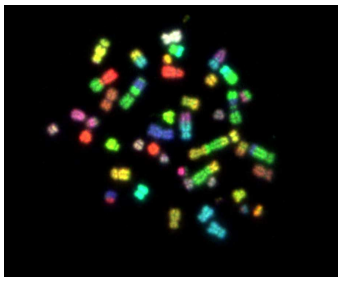

Figure 3: Rogue cell, carrying 4 aberrations with 31 breaks in 25 chromosomes, found in blood lymphocytes of a prostate cancer patient. (mFISH staining, combined colors are shown).

References

[1] S. Ritter *et. al*, GSI Scientific Report 2006, June 2007, p. 348.
[2] IAEA Technical Report Series No 405, 2001.
[3] J.R. Lazutka, Mutation Research 350, 1996, p. 315-329.

* Work supported by BMBF, Bonn, under contract 02S8203 and 02S8497.

Induction of telomerase activity in peripheral blood lymphytes by heavy ion irradiation.

C. Herskind[1], D. Milanovic[1], M. Wang[1], S. Ritter[2], F. Wenz[1]
[1]Dept. of Radiation Oncology, Mannheim Medical Center, University of Heidelberg, Germany. [2] GSI, Darmstadt, Germany

Telomerase is important for elongating and maintaining the telomeres at the end of the chromosomes. Recently, we have shown that telomerase activity is induced in primary human blood lymphocytes after irradiation with clinically relevant doses (2-7 Gy) of x rays in vitro (*1, 2*). This prompted us to test if telomerase activity can also be induced in blood lymphocytes by heavy ion irradiation.

Telomerase appears to play a role in enhancing repair of DNA damage and may increase chromosome stability (*3*). For this reason and because data on the relative biological effectiveness (RBE) of heavy ions is available for chromosome aberration (*4*), we wanted to compare telomerase activity with this end point.

A potential problem is that mitogenic stimulation of lymphocytes with phytohemagglutinin (PHA), necessary for the detection of chromosome damage, induces telomerase activity in its own right. Thus PHA-induced telomerase activity might potentially interfere with induction by radiation. However, we found that telomerase induction by x rays occurred within 1-24 hours after irradiation. By contrast, induction by PHA was observed only at later time points (48-72 hours). Figure 1 shows that mitogenic stimulation with PHA for 12 hours did not increase the telomerase activity. Thus the difference in induction kinetics for the two agents provides a time window for studying radiation-induced telomerase activity without interference from PHA.

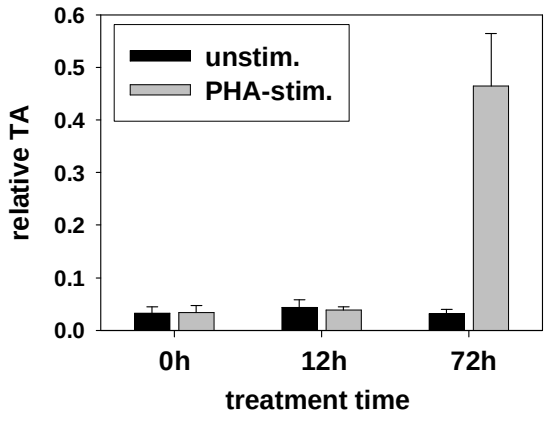

Figure 1: Telomerase activity (TA) in lymphocytes at different time point after mitogenic stimulation with PHA in vitro. Telomerase activity was detected by the Telomere Repeat Amplification Protocol (TRAP) quantified by real-time PCR (*1*). The telomerase activity is shown relative to an external standard (lymphoblastoid cell line, TK6).

The induction of telomerase activity after irradiation with C-ions (spread-out Bragg peak) from the GSI heavy-ion therapy facility is shown Figure 2. A clear induction was seen after a dose of 2 Gy, comparable to the induction by 2-4 Gy of x rays performed in parallel.

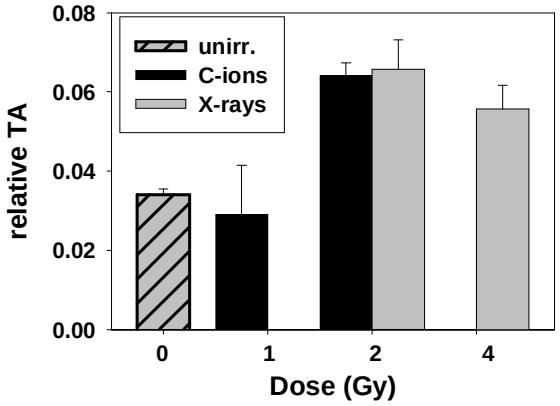

Figure 2: Telomerase activity (TA) in peripheral blood lymphocytes 12 hours after irradiation with C-ions or x rays. Mean values and ranges from two independent experiments are shown. TA is given relative to TK6 cells.

The data do not allow quantitative determination of the RBE, especially since the induction kinetics appeared to be dose dependent (results not shown). However, the data are compatible with a value of RBE in the range 1-2. This is broadly consistent with the RBE value of 1.5-2 for induction of chromosome aberrations in metaphase cells found in these experiments and confirming previously published values (*4*). We conclude that telomerase activity is inducible in primary human lymphocytes by high LET radiation. This might play a role in DNA damage repair and processes leading to chromosome aberrations.

.

Acknowledgement: This study was supported by the BMBF, Bonn (contract no. 02S8203).

References

1. D. Milanovic, P. Maier, F. Wenz, C. Herskind, *Radiat Prot Dosimetry* **122**, 173 (2006).
2. D. Milanovic, P. Maier, M. Wang, F. Wenz, C. Herskind, (submitted).
3. K. H. Shin *et al.*, *Clin Cancer Res* **10**, 2551 (Apr 1, 2004).
4. E. Nasonova, S. Ritter, *Cytogenet Genome Res* **104**, 216 (2004).

Spontaneous level of aneuploidy of chromosomes 7 and X in interphase lymphocytes of two healthy donors of different age *

S. Sommer[1,2], S. Ritter[1], R. Scognamiglio[1,3],
[1]GSI, Darmstadt, Germany; [2]ICHTJ, Warsaw, Poland, [3]Universita Federico II, Napoli, Italy;

Defects in the distribution of chromosomes during mitotic division such as sister chromatid nondisjunction or detachment of kinetochore microtubules at anaphase can give rise to aneuploid cells, for example to a monosomic and a trisomic daughter cell. It is well-known that aneuploidy contributes significantly to carcinogenesis. Also, a relationship between advanced chronological age and increased chromosomal aneuploidy has been reported for humans. In particular hypoploidy increases with age and several studies showed that sex chromosomes are preferentially lost, i.e. the X chromosome in females and the Y chromosome in males [1].

Changes in the copy number of chromosomes can be assessed by means of fluorescence in situ hybridisation (FISH) in both metaphase spreads and interphase cells. However, since the latter technique allows the analysis of large populations within a short time and is able to uncover aneuploidy hidden in non-proliferating cells, it is preferentially used for numerical chromosome studies.

To examine the effect of donor (cell) age as well as radiation exposure on the degree of aneuploidy, we established recently the FISH-technique for the analysis of interphase cells. In a first experiment we measured the spontaneous frequency of aneuploidy for chromosomes 7 and X in interphase lymphocytes of 2 female healthy donors of different age (25 and 50 years old). Peripheral blood was collected by venipuncture. Lymphocytes were isolated, fixed and pancentromeric DNA probes specific for the centromeric regions of chromosomes 7 and X were applied. The probe for chromosomes 7 was labelled with fluorescein isothiocyanate (FITC) (Vysis, France), whereas the probe for chromosomes X was labelled with Spectrum Orange (Cambio, UK).

Fig.1. FISH stained centromeres in human lymphocytes (green: chromosome 7, red: X chromosome). Left: euploid nucleus; middle: triploidy of chromosome X; right: diffused signals of both X chromosome and one chromosome 7.

Centromere signals were evaluated using an Olympus fluorescence microscope equipped with a CCD camera and an image analysis system (ISIS, Metasystems, Germany). At least 500 interphase nuclei were analysed for each donor by two observers. Cells with 2 green (FITC) and 2 red (Spectrum Orange) signals were considered as euploid with respect to chromosome 7 and X, while cells with more or less signals were considered as aneuploid. Also cells with diffused or split signals were scored, while overlapping or mechanically damaged nuclei were excluded from the analysis. Examples are shown in fig. 1.

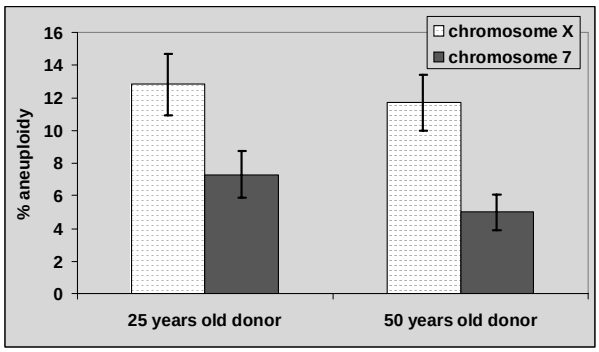

Fig. 2. Percentages of aneuploid lymphocytes in 2 donors of different age. Error bars represent the standard error assuming a Poisson distribution. The yields for both donors were similar (p=0,733). However, there was a significant difference in the level of aneuploidy for chromosome 7 and X (p=0,041).

The levels of aneuploidy found for both chromosomes (fig. 2) were comparable to values reported in the literature [2,3]. In both donors chromosome X showed more aneuploidy than chromosome 7, which is also in line with published data [1]. However, we did not found any age dependence: the level of aneuploidy of chromosome X was similar in both donors (25 and 50 years old). The same was observed for chromosome 7. Furthermore, our preliminary study revealed that in many cell nuclei the signals are difficult to interpret, i.e. signals were diffused or split (fig.1). Possible reasons are differences in the condensation of target DNA and/or a reduced accessibility of target DNA to probe DNA.

These methodological problems as well as the observation that the level of aneuploidy in metaphase spreads is generally significantly lower than in interphase nuclei (own data and [1,2]) suggest that the currently available interphase FISH-technique overestimates the degree of aneuploidy. For more precise measurements refinements of the technique are indispensable.

References

[1] N. Bukvic, Mutation Research 498, 2001, 159-167.
[2] A.B. Mukherjee, Experimental Cell Research 235, 1995, p. 161-169.
[3] O. Reish, Chromosome Research 14, 2006, p. 527-534.

* Work supported by BMBF, Bonn, under contract 02S8203 and 02S8497.

Genetic instability and telomere shortening in normal human fibroblasts after irradiation with X-rays*

S. Zahnreich[1], C. Fournier[1], P. Hessel[1], S. Ritter[1], E. Nasonova[2], L. Melnikova[2], P. Boukamp[3], D. Krunic[3]

[1]GSI, Darmstadt, Germany, [2]JINR, Dubna, Russia, [3]DKFZ, Heidelberg, Germany

Introduction

Former experiments have shown an increased number of non-transmissible chromosomal aberrations in the progeny of normal human fibroblasts after irradiation with X-rays [1, 2]. These *de novo* formed non-transmissible aberrations are an indicator of genomic instability which is considered to be one important step towards carcinogenesis. In parallel experiments we observed accelerated shortening of telomeres in the descendants of normal human fibroblasts [3]. Telomere shortening and dysfunction is believed to play an important role in promoting genomic instability by forming end-to-end fusions of chromosomes and giving rise to further breakage-fusion-bridge cycles. Telomeric fusions are rarely found in normal proliferating cells but frequently observed in virus infected, tumor or senescent cells. This mechanism is, among others, responsible for gene amplification, a phenomenon relevant for carcinogenesis and tumor progression [4].

Materials and Methods

Density inhibited normal human fibroblasts (AG1522) were exposed to 250 kV X-rays (2Gy, 8Gy, 16Gy and a daily fractionated dose of 8x2Gy) and reseeded 24 hours after irradiation. The cells were subcultured every 2 weeks and chromosome samples were prepared according to standard techniques. Unstable aberrations such as dicentrics, rings or breaks were scored regularly after solid Giemsa staining (100 metaphases per time point). For the assessment of telomere length, fluorescence in situ hybridization, 3D image acquisition, deconvolutional microscopy and image processing were performed as described elsewhere [5].

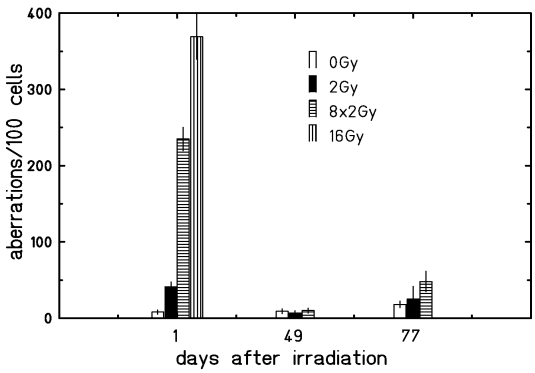

Figure 1: Structural Aberrations scored after solid Giemsa-staining during cultivation and serial passaging over 90 days. Cells irradiated with a single dose of 16 Gy ceased proliferation after 14 days of cultivation.

Results and Conclusion

Figure 1 shows the number of non-transmissible chromosomal aberrations after irradiation of fibroblasts with different doses of Xrays at three representative time points.
A dose dependent increase in unstable aberrations was detected in all populations one day after irradiation. At a later time point (49 days) the level decreased in the progeny of irradiated cells to control level. Shortly before reaching replicative senescence (77 days), the descendants of irradiated cells showed again a higher level of chromosomal aberrations. At this time point, the non-transmissible aberrations consisted mainly of dicentric chromosomes (without acentric fragments) and chromatid type aberrations, both indicating genetic instability.
The telomere length was investigated by measuring the mean telomere signal intensity per nucleus, which is proportional to a mean telomere length of a given cell. Irradiation with 8 Gy of X-rays caused an accelerated shortening of telomeres in the progeny of these cells compared to control cells before reaching senescence (20 % loss of telomeric signal intensity, not shown). The concomitant occurrence of genetic instability and accelerated shortening of the telomeres may indicate a contribution of eroded or structurally impaired telomeres to radiation induced genomic instability. In future studies telomere shortening will be investigated in more detail at early as well as late time points after irradiation.

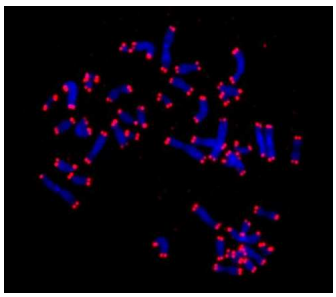

Figure 2: QFISH-Telomere-stained metaphase of normal human fibroblasts (AG1522).

References

[1] Kadhim M. *et al.*, Int. J. Radiat. Biol. 73, 1998, 143 - 148
[2] Fournier C. *et al.*, Radiotherapy and Oncology 83, 2007, 277-282
[3] Krunic D. *et al.*, GSI Annual Report 2006, 345
[4] Riboni R. *et al.*, Cancer Genet Cytogenet 95, 1997, 130-136
[5] Ermler S. *et al.*, Eur. J. Cell Biol. 83, 2004, 681-690

* Work supported by BMBF (Bonn), grant 02S8497

Increase of oxidative stress in normal human fibroblasts after irradiation *

M. Colindres[1,2], C. Fournier[1#], S. Ritter[1], S. Zahnreich[1], H. Decker[2], N. Dencher[3], M. Frenzel[3]
[1]GSI, Darmstadt, Germany; [2]Biophysik, Universität Mainz, Germany, [3]Biochemie,TU Darmstadt, Germany

Introduction

The descendants of irradiated fibroblasts undergo stepwise senescence and differentiation, but genetic instability has also been observed [1]. In the decision of the fate of irradiated cells and their descendents, changes in the cellular redox status play an important role [2]. An accumulation of reactive oxygen species (ROS) in cells following irradiation may lead to secondary cell damage caused by an enhanced oxidation of biomolecules and cell membranes, as already observed during aging [3]. To study alterations in oxidative cellular status, we measured the course of the accumulation of ROS in human fibroblasts up to two weeks after irradiation. The methods for the assessment of the integrity of cell membrane proteins were established by analysing the mitochondrial membrane proteome, i.e. the oxidative phosphorylation (OXPHOS) complexes and HSP60, in unirradiated cells.

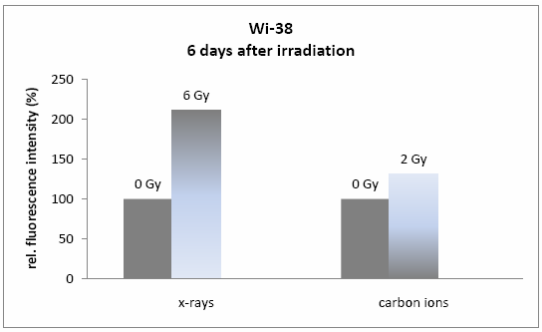

Figure 1: Intracellular accumulation of Reactive Oxygen Species (ROS) in human fetal lung fibroblasts. DCF fluorescence intensities were measured 6 days after exposure to X-rays or 100 MeV/u carbon ions.

Materials and Methods

Confluent fetal human lung fibroblasts (WI-38) were irradiated with X-rays or 100 MeV/u carbon ions (SIS, GSI). At different time points the cells were harvested, and incubated with 25 µM 2´,7´-Dichlorodihydrofluorescein (DCFH-DA; in PBS, 37°C /30 min). DCFH-DA can cross the cell membrane and is trapped in the cell via deacetylation by endogenous esterases to Dichlorodihydrofluorescein (DCFH). DCFH is oxidized by ROS and converted to Dichlorofluorescein (DCF), which fluoresces when excited by 488-nm light [4]. Analysis of the fluorescence was performed by flow cytometry.

After the isolation of mitochondrial membrane proteins from the cells (homogenization, differential centrifugation steps, and digitonin-solubilization of the membrane proteins), the separation was carried out using blue native-PAGE followed by 2D-SDS-PAGE. Protein spots were identified using MALDI mass spectroscopy (MALDI-MS).

Results and conclusions

An increased DCF-fluorescence was detected in irradiated WI-38 cells, persisting for nine days following irradiation and correlating with increasing dose (not shown). The highest response was observed after 6 days for carbon ion as well as for X-ray exposure (fig. 1). This indicates that ionizing radiation causes persistent oxidative stress during the first days after exposure.

The mitochondrial protein pattern of unirradiated WI-38 cells observed was comparable to that of bovine heart mitochondria (fig. 2). Further investigations in irradiated cells will be performed.

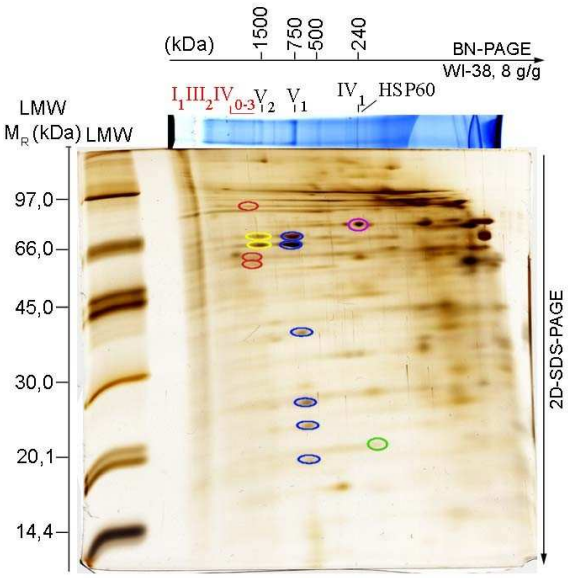

Figure 2: Analysis of solubilized crude mitochondria from WI-38 cells by native PAGE, using in the first dimension a 3-13% polyacrylamid gradient. Protein spots belonging to subunits of OXPHOS complexes [red: supercomplex $I_1III_2IV_{0-3}$; yellow: MF_OF_1ATP synthase dimer; blue: MF_OF_1ATP synthase monomer; green: complex IV (cytochrom c oxidase)] and HSP60 (violet) are indicated (circles).

References

[1] Fournier *et al.*, Radiotherapy and Oncology 83, 2007, 277-282
[2] Valko *et al.*, Int J Biochem Cell Biol. 39, 2007, 44-84.
[3] Dencher *et al.*, Ann. N. Y. Acad. Sci, 2007, 291-298.
[4] Halliwell & Whiteman. British Journal of Pharmacology 142, 2004, 231-255.

* Work supported by BMBF (Bonn), grant 02S8497
# c.fournier@gsi.de

Cell death and cell cycle inhibition induced by carbon ion irradiation in head and neck squamous cell carcinomas *

M. Maalouf[1, 2], C. Fournier[2], G. Alphonse[1], G. Taucher-Scholz[2] and C. Rodriguez-Lafrasse[1]
[1]Laboratory of Molecular and Cellular Radiobiology, EA3738, Lyon, France; [2]GSI, Darmstadt, Germany

Introduction

To date, hadrontherapy has been used successfully to target traditionally difficult-to-operate tumors. However, in some cases among the patients with head and neck squamous cell carcinoma (HNSCC) a local recurrence was observed after the treatment with carbon ions [1]. The reason for a lower control rate of SCC has not been elucidated yet.

The aim of the present study was to investigate the cellular mechanisms of cell death and cell cycle inhibition induced by carbon ions in HNSCC cells. As already reported before, the induction of apoptosis in the radiosensitive SCC61 cells was the main cellular response to carbon ion irradiation. In contrast, the radioresistant SQ20B cells underwent a delayed cell death at 10 days, preceded by a G2 arrest [2]. Here we investigated the mechanisms underlying the cell cycle arrest in SQ20B cells and its relationship to other types of cell death.

Material and methods

A radiosensitive (SCC61) and a radioresistant (SQ20B) HNSCC cell line were irradiated with 9.8 MeV/u carbon ions (GSI). A dose of 10 Gy was chosen for these studies. Senescence-like changes were determined by β-galactosidase (β-gal) activity at pH 6 and protein expression (Western Blot). During 10 days after irradiation, morphological alterations were analyzed microscopically after nuclear DAPI staining. In addition, the proliferation capacity of the cells was studied by BrdU labeling.

Results and discussion

First we examined whether the growth inhibition of SQ20B cells could be related to a mechanism of senescence-like arrest. Figure 1 a, b shows an enhanced β-gal activity of irradiated SQ20B at 10 days.

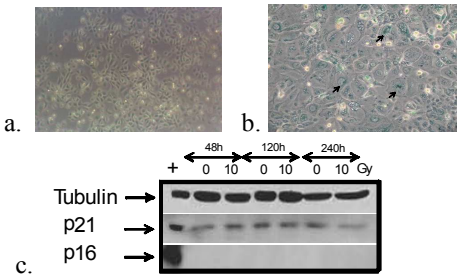

Figure 1: SQ20B cells stained for ß-gal activity 10 days after 0 Gy (a) and 10 Gy (b). Expression of p21 and p16 in SQ20B cells compared to a positive control (+) after carbon ions irradiation (c).

However, no induction or accumulation of senescence related proteins (p21 or p16) was observed (Figure 1c). These observations suggest that the enhanced activity of β-gal detected in SQ20B was more a result of stress rather than an irreversible senescence-like arrest.

At the same time, dramatic morphological alterations were detected in these cells. Figure 2 shows the presence of fragmented or lobulated nuclei in association with micronuclei, characteristics consistent with mitotic catastrophe. The multinucleated cells were detected at 2 days and increased at 5 days after irradiation. In addition, anaphase bridges were observed at 2 days, indicating that the origin of these polyploid cells could be a failed redistribution of the chromosomes.

Notably, none of these morphological alterations was detected in the irradiated SCC61 cells (data not shown).

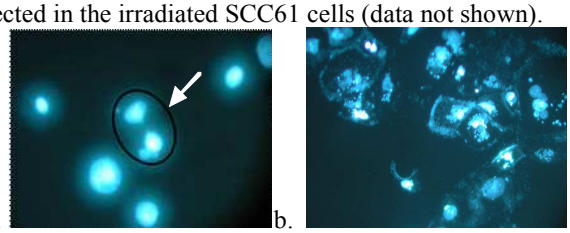

Figure 2: SQ20B cells stained with DAPI at 2 days (a) and 5 days (b) after 10 Gy of carbon ions irradiation.

Although most of SQ20B cells underwent mitotic catastrophe followed by apoptosis, a subpopulation continued to proliferate. Figure 3a shows the increased uptake of BrdU in SQ20B, at 10 days, after carbon ions irradiation. In contrast, no recovery is observed in SCC61 cells (Figure 3b).

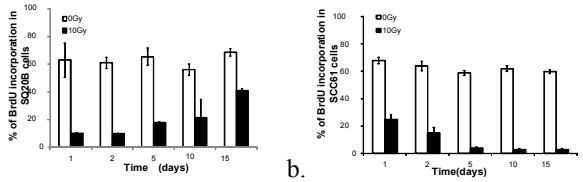

Figure 3: Kinetics of BrdU incorporation in SQ20B (a) and SCC61 (b) following a 10Gy carbon ions irradiation.

Our observations indicate that, despite the high efficiency of carbon ions, a subpopulation of SQ20B cells is able to escape cell death. This might contribute to a potential local recurrence observed among certain HNSCC patients treated by carbon hadrontherapy.

References

[1] JE Mizoe *et al* Int. J. Rad. Oncol. Biol. Phys. 2004, 60: 358-364.
[2] M Maalouf *et al*. Annual GSI report 2006.

* Work supported by EU, EURONS contract No. 506065 and the Verein zur Förderung der Tumortherapie mit schweren Ionen e.V.

Neoplastic Transformation Induced by Carbon Ions*

D.Bettega, †[1], C.Berlusconi[1], P.Calzolari[1], P.Hessel[2], and W.K.Weyrather[2]
[1]Dept.Physics, Univ. of Milan and INFN, Italy; [2]GSI, Darmstadt, Germany

Neoplastic transformation in vitro can be used as an indicator for risk assessment comparing different radiation types. Using CGL1 cells, the irradiation of a tumor volume has been simulated and transformation and induction of micronuclei have been measured with special regard to the entrance channel and the influence of the particle fragments.

After measuring transformation induced by track segment irradiation [1] and a simulated tumor volume with an isodose of 1.5 Gy [2], especially the influence of low doses in the entrance and the effect of the fragments behind the tumor should be elucidated.

Materials and Methods

Experiments were performed using the human hybrid (Hela X skin fibroblast) cell line CGL1 [3]. The measured endpoints were clonogenic survival, transformation induction according to [4] and the frequency of micronuclei in binucleated cells 24 and 48 hours after irradiation. Irradiation was performed in an extended volume with a physical isodose of 0.75 Gy, simulating a tumor in a depth between 60mm and 100mm. Additionally, this dose has been delivered from two opposite ports resulting in a tumor dose of 1.5 Gy (data not shown)

Results and Discussion

Results are shown in figure 1. The effect induced by the entrance dose is comparable to that induced by the fragments behind the tumor for transformation as well as for frequency of micronuclei. This result is in line with the fact that micronuclei formation indicate chromosome damage and that it has been shown that neoplastic transformation of CGL1 cells requires the loss of function of tumor suppressor genes on fibroblasts chromosome 11 and 14 [5].In this very low dose range, this may be mainly the effect of single ions like stopping alpha particles [6].

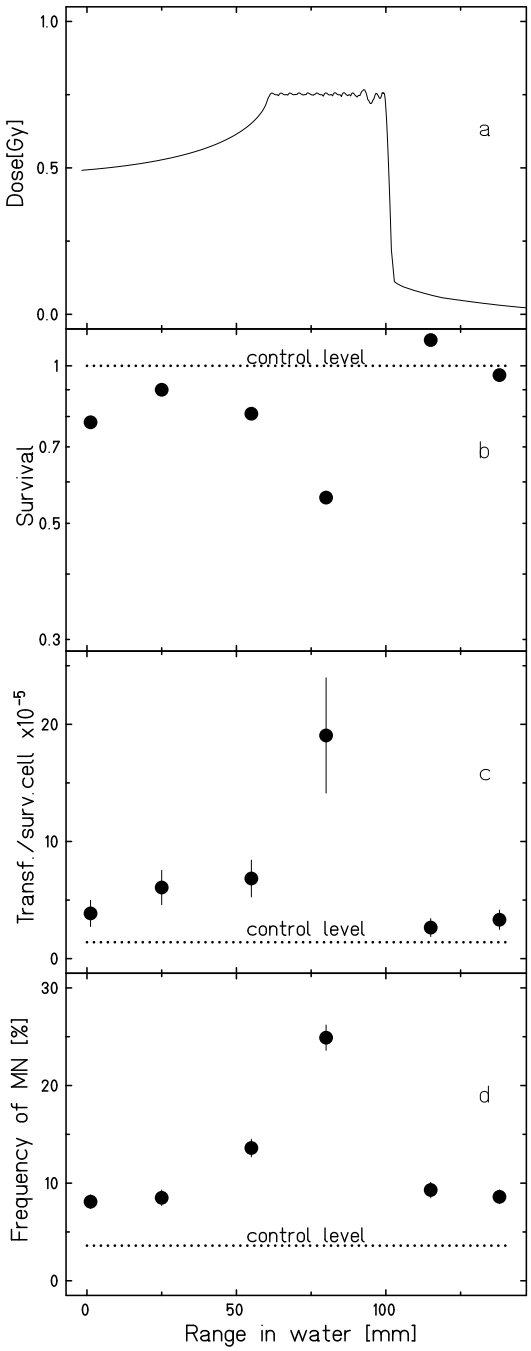

Figure 1:
a) Doseprofile for the irradiated volume
b) Clonogenic survival
c) Transformation frequency per surviving cell
d) Frequency of micronuclei (mean of the values at 24 and 48 hours)

References

[1] Bettega et al., submitted for publication
[2] GSI Scientific Report 2006, 379 (2007)
[3] Stanbridge et al , Science, 215, 252 (1982)
[4] Redpath et al, Radiat. Res. 110, 468 (1987)
[5] Mendonca et al, Radiat. Res. 149, 246 (1998)
[6] Bettega et al, Int.J.Radiat.Biol. 72, 532 (1997)

* Work supported by EU, EURONS contract No. 506065.
† I3-EURONS (European Commission contract no. 506065)

Differentiation potential of hematopoietic stem cells after irradiation with X-rays and high energetic Carbon ions

D. Becker[1,3], C. Fournier[1], S. Ritter[1], R. Marschalek[2],T. Tonn[3]
[1]GSI, Darmstadt, Germany; [2] Faculty of Pharmacology, Johann Wolfgang von Goethe University, Frankfurt, Germany;
[3]Institute for Transfusion Medicine and Immunohaematology, Frankfurt, Germany

The increasing application of heavy ions in radiotherapy is a strong motivation to expand the fundamental research in radiation biology, especially with respect to long term effects in different cell systems. The classical cytogenetic assay to estimate the radiation effect relies only on the measurement of chromosome aberrations in lymphocytes, but a large part of the damaged lymphocytes is eliminated from the population via apoptosis [1]. On the other hand, the occurrence of clonal aberrations has been reported for patients, who had received a chemotherapy years ago [2,3]. Therefore, regarding long term effects after heavy ion therapy, it is important to assess the potential transmission of chromosomal aberrations by hematopoietic stem cells (HSCs) to lymphocytes. HSCs are responsible for the constant renewal of blood. On the other hand they have also the ability to differentiate to a variety of specialized blood cells. As both processes have an impact on a potential transmission of chromosomal aberrations we focused in first experiments on the differentiation of hematopoietic stem cells after irradiation with Carbon ions in comparison to conventional photon irradiation.

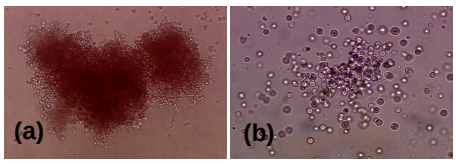

Figure 1: Morphology of colony forming cells in the CFU-Assay (a) erythroid progenitor cells (BFU-E), (b) granulocyte progenitor cells (CFU-G).

Hematopoietic stem and progenitor cells were isolated from the peripheral blood of healthy donors, which were treated with the standard mobilizing agent granulocyte colony-stimulating factor (G-CSF). Low density mononuclear cells were enriched by Ficoll gradient separation and the denser, more mature cell types such as erythrocytes and granulocytes were removed. In a magnetic separation step the cells were stained with a CD34+ antibody coupled with magnetic beads (QBEND/10, mouse IgG1) for 30min at RT (CD34 MicroBead Kit, Miltenyi Biotech). The labelled cells were positively enriched to purities of > 90 % using magnetic columns. The cells were irradiated with X-rays [16mA, 250 kV] or with Carbon ions [100MeV/u, 29keV/µm] at the SIS facility at GSI. To promote proliferation and differentiation of the different hematopoietic lineages cells were cultured in semisolid methylcellulose medium (Methocult, StemCell Technologies, Vancouver) supplemented with the appropriate combinations of cytokines. This so called colony forming unit assay (CFU-Assay) was used to quantify the differentiation potential of mobilised peripheral blood CD34+ cells after irradiation into erythroid, granulocytic, monocyte-macrophage lineages, respectively. The size of the colony allows to distinguish between early and more differentiated progenitors, with early progenitors giving rise to larger burst forming units and more differentiated progenitors to smaller colonies. The colony forming cells were classified and enumerated based on morphological recognition of mature cells by light microscopy (figure 1).

CD34+ enriched stem and progenitor cells were exposed to X-rays or Carbon ions and then cultivated in semisolid medium. After 2 weeks of cultivation, a linear decrease in survival of colony forming units (CFU) following exposure to X-rays (figure 2) was observed. First results showed a similar capacity to form colonies following Carbon ion exposure.

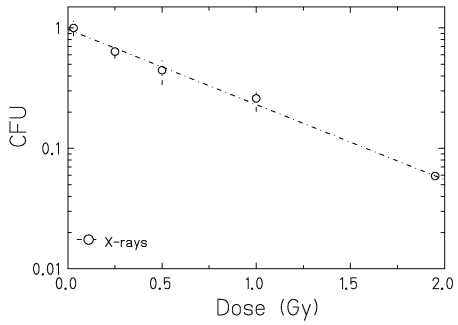

Figure 2: Potential of stem and progenitor cells to form colonies of the erythroid, granulocytic, monocyte-macrophage lineage after irradiation with different doses of X-rays [16mA, 250 kV], assessed by CFU assay

The distribution of the lineage restricted progenitors following either the erythroid, granulocytic, or monocyte-macrophage pathway was changed after irradiation. After exposure to X-rays the amount of erythroid restricted progenitors increased with higher doses concomitantly with a decrease of cells from granulocytic and monocyte-macrophage lineages (not shown). Another difference in the potential of differentiation of irradiated HSCs is given by the increased number of very committed progenitors, giving rise to colony-forming-unit erythrocyte (CFU-E) rather than burst-forming-unit erythrocyte (BFU-E) after irradiation with X-rays. All these differences observed in X-irradiated compared to unirradiated HSCs were also observed following exposure to Carbon ions (not shown). In further experiments chromosomal analysis will be performed [supported by GSI, no. 178].

References

[1] Meijer, A. E. et al (1998), Int. J. R. Biol. 73, 169–177.
[2] Amenomori, T. et al (1985), Int. J. Cell Cloning 3, 133-142.
[3] Littlefield, L. G. et al (1997), Radiat. Res. 148, 135-144.

Radiobiological experiments for heavy ion therapy of prostate cancer

C. von Neubeck[#], Th. Elsässer and W. K. Weyrather
GSI, Darmstadt, Germany;

At GSI the treatment of prostate cancer patients started in 2006 with a combination of carbon boost irradiation and IMRT at Uniklinik Heidelberg. In our study we started to establish an in vitro model for prostate cancer and the surrounding tissue. First the radio-resistance of the used cell lines was determined.

Material and methods

Cell lines

The rat prostate cancer cell line R 3327 AT-1 (R-AT-1) was chosen [1] because this cell line is used in a parallel animal study and will allow an in vivo / in vitro comparison. For the normal tissue, which is co-irradiated during the treatment, the small intestine epithelial cell line of the rats (IEC-6) is an accepted model [2].

Cell survival

For carbon irradiation at SIS and 250 kV X-ray irradiation the cells were seeded in culture flasks and for carbon irradiation at UNILAC in Petri dishes. The cell survival was measured with a colony forming assay. The data were compared with LEM calculations, whose parameters were determined in advance [3].

Results

Cell line characterization

The radio-resistance to 250 kV X-ray of R-AT-1 remained constant over several passages whereas the radio-resistance of IEC-6 increased with progressive passage (data not shown).

RBE after carbon irradiation

The two cell lines were exposed to three different energies corresponding to the treatment situation. 270 MeV/u represents the energy in the entrance channel whereas 100 MeV/u is an ion energy close to the tumour volume and 11.4 MeV/u simulates the energy in the tumour during treatment. Figure 1 shows that R-AT-1 is more radio resistant than IEC-6. All experiments are in good agreement with the LEM calculations. However, the cellular survival in the virtual entrance channel is underestimated whereas the survival in the fictive tumour is lower than predicted by LEM.

The RBE_{α} and RBE_{10} calculations for R-AT-1 were referred to the cumulative X-ray curve whereas these for IEC-6 were standardized on the X-ray curve of a comparable passage. At the end of the particle range the RBE increased (see figure 2). The difference between RBE_{α} and RBE_{10} is larger for R-AT-1 than for IEC-6.

[#]c.vonneubeck@gsi.de

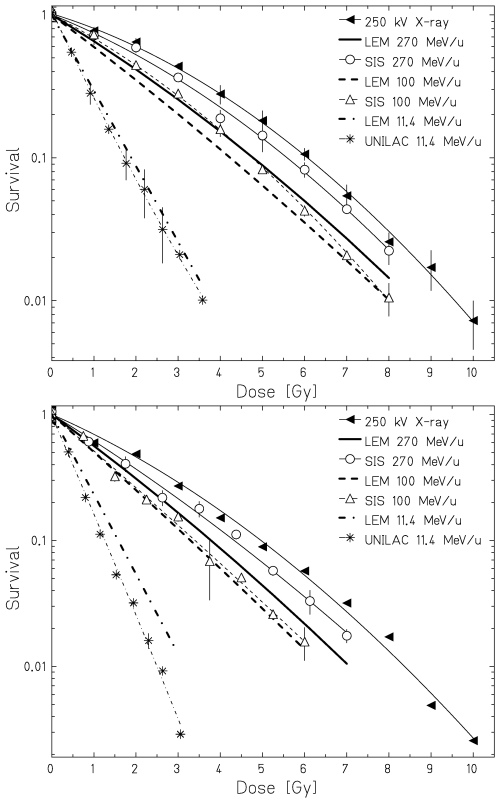

Figure 1: Cell survival after exposure to carbon ions
Upper panel: R-AT-1 *Lower panel: IEC-6*

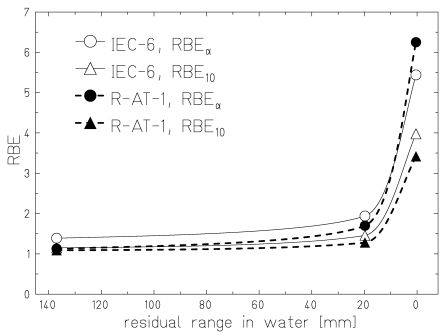

Figure 2: RBE versus residual range in water.

Conclusions

The use of IEC-6 in irradiation experiments is restricted to early passages whereas R-AT-1 shows no age dependent variation in radio sensitivity. For lower energies the RBE varies more for the radio resistant R-AT-1. The RBE of both cell lines is close to 1 for high energies.

References

[1] Isaacs et al. The Prostate 9:261-281 (1986)
[2] Quaroni et al. J. Cell Biology 80:248-265 (1979)
[3] Elsässer and Scholz Radiat. Res. 167:319-329 (2007)

A system for OER measurements

C. Schicker, C. von Neubeck, G. Iancu, U. Kopf, and W.K.Weyrather[#]
GSI, Darmstadt, Germany.

To measure the influence of hypoxia on cell survival after irradiation, a system has been established that enables the irradiation under defined oxygen conditions.

Introduction

Prostate cancers are known to form hypoxic regions. These hypoxic cells are more radio-resistant then well oxygenated tissue and they are often a reason for recurrent tumours in radiotherapy. Furthermore hypoxia enhances malignant progression of the tumour. The ratio of doses under oxic and hypoxic conditions to achieve the same biological effect is called the oxygen enhancement ration (OER). Under normal conditions OER is described as 'dose modifying' i.e. it is constant over the whole dose effect curve. As the OER is strongly LET dependent [1] a system should be developed that enables the irradiation with X-rays and carbon ions for acute hypoxia.

Materials and methods

Cell lines

Chinese hamster ovary cells (CHO-K1) have been primary described by [2]. They were used to establish the OER measurement system. The rat prostate cancer cell line R 3327 AT-1 (R-AT-1) is in vivo and in vitro cultivable [3]. It has been reported that the cell in vivo form hypoxic regions without central necrosis [4].

Both cell lines have been cultivated on a gas-permeable surface which has been fixated on a holder. 24 h after seeding of the CHO cells and 48 h after seeding of the R-AT-1 cells, a second gas-permeable facing is stuck on top of the holder to construct a closed chamber. Fresh medium is injected into the interspaces between the two facings.

Cell survival

For gassing and irradiation the cell carrying holder is inserted into a gas-proof container. Acute hypoxia has been archived by flushing the system before irradiation with 100% nitrogen at room temperature. To simulate the gassing for the oxic cells, cell carrying holders have been upright in a container at room temperature without gassing the system.

Both cell lines were irradiated with 250 kV X-ray and a dose rate of 4 Gy/min. The SIS irradiation has been performed with SOBP carbon ions with a median LET of 100 keV/µm. The cellular survival has been determined with a colony forming assay.

Results

Experiments for survival of CHO-K1 and R-AT-1 have been performed with X-rays and Carbon ions from SIS. For CHO-K1 under acute hypoxia the OER was 2.96 ± 0.053 for X-ray and 1.8 for Carbon. This correlates with literary OER of 2.8 ± 0.2 for X-ray [5]. The OER for R-AT-1 under acute hypoxia was 1.8 for Carbon and 2.7 for X-ray. Plating efficiency of both cell lines has been the same for acute hypoxia and oxic cells.

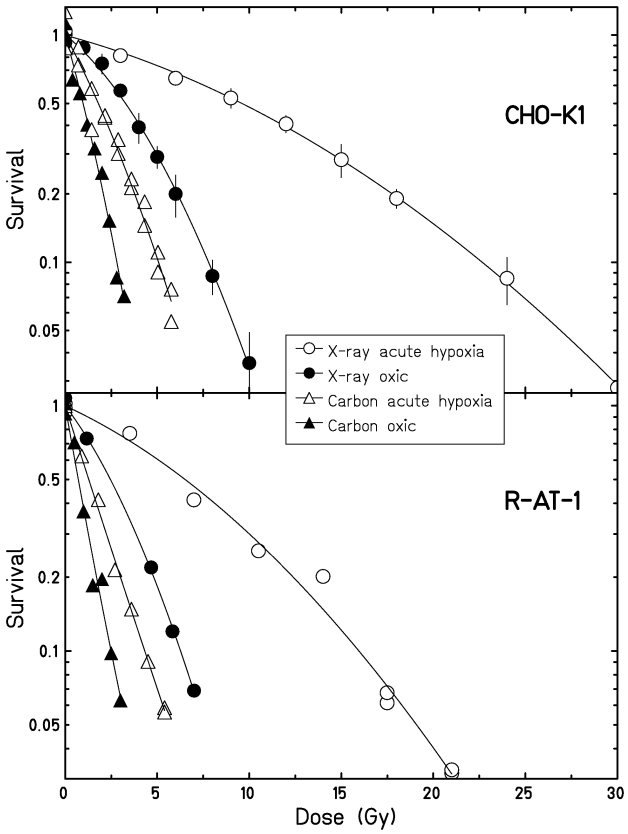

Figure 1: Survival curves of CHO-K1 and R-AT-1 cells under oxic and 1.5 h acute hypoxia after irradiation with 250 kV X-ray and SOPB carbon ions with a median LET of 100 keV/µm.

References

[1] Furusawa et al Radiat. Res. 154, 485-496 (2000)
[2] Puck et al J Exp Med. 108(6):945-56 (1958)
[3] Isaacs et al Prostate 9(3):261-81 (1986)
[4] Bourke et al, Int. J. Radiation Oncology Biol. Phys. 67(4):1179-86 (2007)
[5] Hirayama et al. J Radiat Res (Tokyo) 46(3),325-32 (2005)

Nitric oxide production by macrophages after exposure to ionising radiation*

S.Conrad[1], S.Ritter[2], and K.Nixdorff[1]
[1]Institut für Mikrobiologie und Genetik, Darmstadt; Germany [2] GSI, Darmstadt, Germany

Macrophages are potent elicitors of inflammatory cytokines and nitric oxide (NO). As such, they have been associated with side effects of therapeutic irradiation including pneumonitis and skin fibrosis. While several studies have addressed the effects of X-rays or gamma rays on macrophages, virtually no work has been carried out to date concerning the effects of heavy ion radiation on these cells.

When activated, macrophages which contain inducible nitric oxide synthase (iNOS) produce considerable amounts of NO. NO serves as an antimicrobial agent in the fight against infections, but it also has anti-tumour properties [1]. Furthermore, NO can directly influence the expression of proinflammatory cytokines [2].

In the present report we compared the effects of 250 kV X-rays with those of 9.8 MeV/u carbon ions on NO production in both murine RAW 264.7 macrophages and human monocyte-derived macrophages (MDM) isolated from peripheral blood. Irradiated and non-irradiated macrophages at a density of 1 x 10^6 cells in 24-well culture dishes were stimulated for 24 h with 1 µg/ml lipopolysaccharide (LPS) from *Proteus mirabilis*. Control cultures that were not treated with LPS were included. After the incubation period NO was measured as nitrite in the cell supernatants using a modified Griess reagent [3].

Similar to the results of experiments on TNFα and IL-1β production [4], irradiation of RAW 264.7 macrophages alone with either X-rays or carbon ions was not sufficient to induce the generation of NO by these cells, but a strong NO production was seen after LPS stimulation (Figure 1). Irradiation of LPS-activated cells with X-rays at doses between 0.25 Gy and 2 Gy caused a decrease in NO concentration (Fig. 1A, closed squares), which was consistently seen in repeated experiments. When LPS-activated cells were irradiated with doses of X-rays over 2 Gy, the concentration of NO rose back up to the levels produced by non-irradiated cells, but not higher (Fig. 1A, closed circles). The decrease in NO production after irradiation with low doses of X-rays was not seen in cultures irradiated with carbon ions (Fig. 1B). Indeed, LPS-induced NO production was considerably enhanced in a dosage dependent manner by irradiation with carbon ions. In this case the concentration of NO rose from approximately 30 µM in non-irradiated, LPS-activated macrophages to 140 µM in cells irradiated with 32 Gy carbon ions. Although the figure presents data from one representative experiment, these results were seen consistently in repeated experiments.

While human macrophages do contain the inducible nitric oxide synthase (iNOS) gene, this type of NO cannot be induced in these cells by agonists such as LPS *in vitro*, rather, signals from a complex set of agonists are required [5]. In the present study we were not able to detect NO in human MDM after irradiation with X-rays or carbon ions, also not after stimulation with LPS (data not shown).

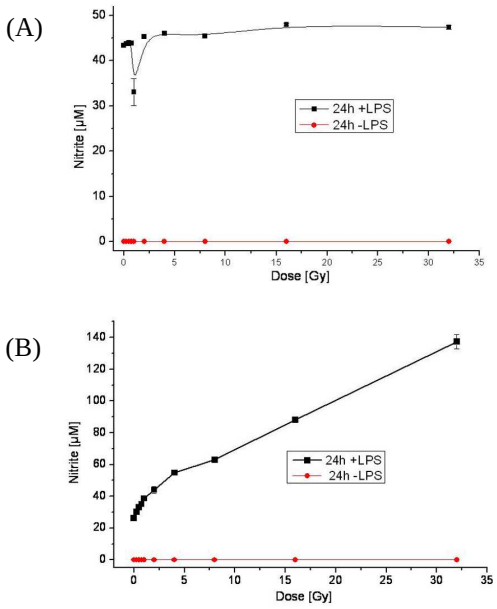

Figure 1. Effects of irradiation on NO production by RAW 264.7 murine macrophages. Cells were irradiated with various doses of 250 kV X-rays (A) or 9.8 MeV/u carbon ions (B).

The question remains as to whether carbon ion irradiation can enhance inducible NO in human macrophages *in vivo* under conditions that might be more favourable to induction. Nevertheless, our results demonstrating greatly enhanced NO production after carbon ion but not after X-ray irradiation in LPS-activated murine macrophages underscore the greater potential of carbon ion irradiation with regard to biological effectiveness.

References

[1] J.M. Tarr, P. Eggleton, P.G. Winward, Current Pharmaceutical Design 12 (2006) 4445-4468
[2] E. Foley, P.H. O'Farrell, Genes and Development 17 (2003) 115-125
[3] J.S. Pollock, U. Forstermann, J.A. Mitchell, T.D. Warner, H.H. Schmidt, M. Nakane, F. Murad, Proceedings of the National Academy of Sciences, U.S.A. 88 (1991) 10480-10484.
[4] S. Conrad, Dissertation TU Darmstadt (2008)
[5] H. Kleinert, A. Pautz, K. Linkker, P.M. Schwarz, European Journal of Pharmacology 500 (/2004) 255-266

*This study was supported by BMBF, grant No. 02S8203

Local Effect Model with an energy-dependent track core

Th. Elsässer and M. Scholz
GSI, Darmstadt, Germany

Introduction

The Local Effect Model (LEM) [1] established at GSI serves as the basis for biological treatment planning in heavy ion therapy and is successfully used in clinical routine [2]. Over the last decade deviations from experimental data have been observed and addressed. However, even with the modified version including cluster effects [3] these deficiencies have not been completely removed. Here, we present a model improvement by application of an energy-dependent minimum radius for the inner part of the radial dose distribution of ion tracks.

Radial dose distribution

The accurate description of the radial dose distribution around ion tracks is a crucial part of the LEM. So far, an amorphous track structure model with a constant minimum radius was used. However, following considerations of [4] a minimum radius r_{min} depending on the particles velocity seems to be more appropriate,

$$r_{min} = r_c \cdot v/c, \tag{1}$$

where v denotes the ion's velocity and c is the speed of light. By comparison with experimental data for the radiation tolerance of the rat spinal cord the best model agreement was found for the parameter r_c=40 nm. The dependence of r_{min} on the specific ion energy is depicted in Fig. 1.

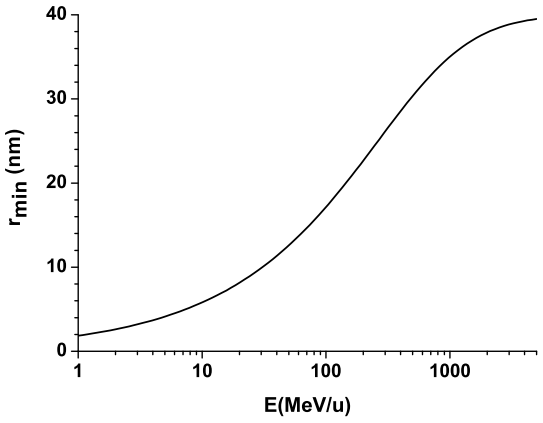

Figure 1: Dependence of the minimum radius r_{min} on the specific energy of the ions

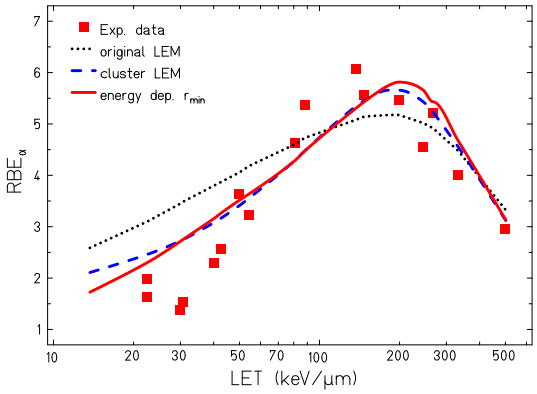

Figure 2: Initial RBE for HSG cells. Experimental data (squares) are compared to the different versions LEM I (dotted line), LEM II (dashed) and LEM III (solid).

Comparison to cell inactivation data

We included the new energy-dependent minimum radius into our calculations of the LEM (LEM III) and compare the simulation results with experimental in vitro data for cell inactivation of human salivary gland (HSG) cells [5]. We find similar results of the initial relative biological effectiveness (RBE) for LET values above 30 keV/μm for the original (LEM I) and cluster version (LEM II) as well as for LEM III. For swifter ions with a lower LET as present in the entrance channel of patient treatments, the RBE predicted for the version with an energy-dependent r_{min} is lower and closer to the experimental data.

Conclusions

We can conclude that the integration of an energy-dependent minimum radius for the radial dose distribution around ion tracks gives better results for low-LET particles. Since we found a similar improvement for a wide range of different cell lines, this new version of the Local Effect Model will further improve the quality of heavy ion treatment planning.

References

[1] M. Scholz et al., Radiat. Environ. Biophys. 36, 59 (1997)

[2] D. Schulz-Ertner et al., Int. J. Radiat. Oncol. Biol. Phys. 67, 171 (2007)

[3] Th. Elsässer and M. Scholz, Radiat. Res. 167, 319 (2007)

[4] A. Mozumder, J. Chem. Phys. 60, 1145 (1974)

[5] Y. Furusawa et al., Radiat. Res. 154, 485 (2000)

Precision Bragg-Curve Measurements for Light-Ion Beams in Water

D. Schardt[1], P. Steidl[1], M. Krämer[1], U. Weber[2], K.Parodi[3], and S. Brons[3]
[1]GSI, Darmstadt, Germany; [2]Rhön-Klinikum AG, Marburg, Germany; [3]HIT, Heidelberg, Germany

Experimental data on unmodified (unmodulated) Bragg curves for a representative set of beam energies are required as an input for the physical model used for treatment planning. A new series of measurements for light-ion beams relevant for tumor therapy applications was completed in 2007 and is presently being analyzed. Previous results of Bragg curve measurements at GSI and HIMAC and comparison with model calculations are discussed in [1].

Bragg curves were recorded for the energy ranges given in table 1 in steps of 25 – 50 MeV/u.

Ion	E [MeV/u]	R_W [cm]
^{1}H	125 – 200	11 – 26
^{3}He	110 – 225	6 – 24
^{7}Li	100 – 240	6 – 28
^{12}C	100 – 400	3 – 27
^{16}O	200 – 400	6 – 21

Table 1: Ions and energy ranges used for Braggcurve measurements. R_W denotes the mean range in water.

Measurements of unmodified Bragg curves require a thin vacuum exit window (Al 100 µm) and transmission chambers [2] with well defined homogeneous thickness. The precision water column used in our measurements is sketched in Fig.1. The actual length of the water column is read-out by an optical linear encoder (Heidenhain) with 1 µm relative accuracy. As an example, measured Bragg curves for protons and ^{12}C with the same range in water are shown in Fig. 2. The peak width is mainly caused by range straggling which scales with $A^{-1/2}$, where A is the mass number of the ions.

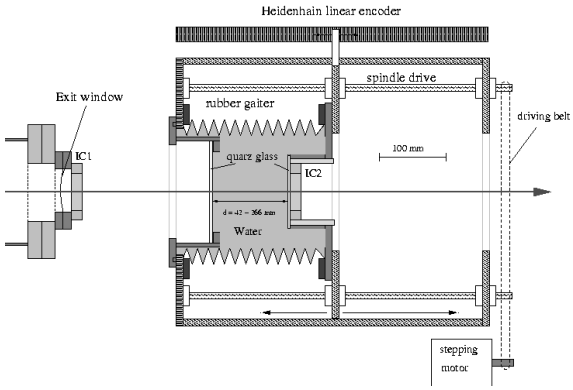

Figure 1: Precision water column for Bragg curve measurements. The ion beam enters from left.

For all materials traversed by the ion beams the water-equivalent thickness was determined by measuring the corresponding shift of the Bragg peak in water. In this way, "absolute" depths in water for the measured Bragg peak positions are obtained. The mean range of the stopping ions is slightly larger. For comparison with stopping power codes, the mean range was determined as the depth in water, where the distal edge of the Bragg peak reaches 82% of the peak value. This value was calculated in [3] for 290 MeV/u ^{12}C ions. We applied it here tentatively to all measured Bragg curves. Comparison with the stopping code ATIMA [4] shows that the calculated ranges are by about 1.4% smaller than those derived from the Bragg peaks. At a range of 27.6 cm for 400 MeV/u ^{12}C ions this corresponds to 3.9 mm deviation. This discrepancy can be explained by a too small value (69 eV) for the mean ionization potential I_W for water used in ATIMA. Changing this value in ATIMA to 78(1) eV gives best reproduction of the experimental data (Fig.3). Similar values were reported in [5] (77 eV) and more recently for proton beams stopping in water (78.4 eV) [6].

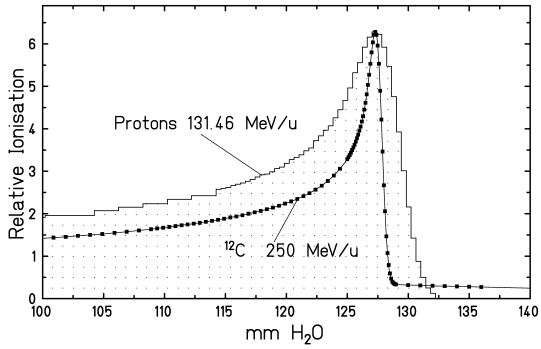

Figure 2: Comparison of measured Bragg curves for protons and ^{12}C ions (normalized to the same peak height).

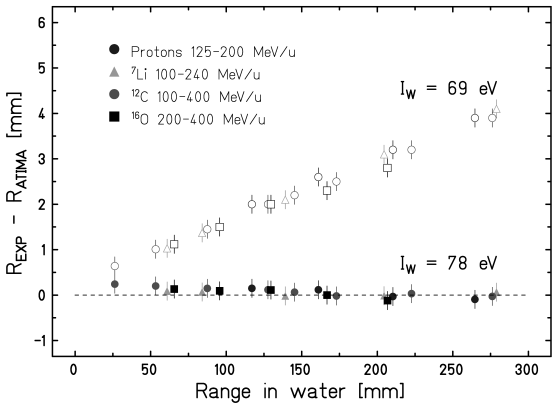

Figure 3: Comparison of ion beam ranges in water from measured Bragg curves with ATIMA [4].

[1] L. Sihver et al., Jpn. J. Med. Phys. 18, 1 (1998)
[2] B. Voss, A. Heinz, H. Risch, GSI Detector Lab
[3] H. Bichsel et al., Rad. Res. 153,208(2003)
[4] ATIMA http://www-linux.gsi.de/~weick/atima/
[5] M. Krämer et al., Phys. med. Biol. 45,3299 (2000)
[6] Y. Kumazaki et al., Rad. Measurem. 42,1683 (2007)

Carbon ions therapy dosimetry with sc-CVD diamond detectors

M. Rębisz, B. Voss, M. Ciobanu, M. Pomorski, M. Kiš, A. Heinz
GSI, Darmstadt, Germany

Introduction

At most particle therapy sites the beam monitoring system has to be calibrated against a standard dosimeter every morning as part of time consuming daily checks (~1 hour) [1]. Trying to improve this situation with respect to accuracy and time consumption, detectors for single particle counting were developed, measuring the total number of particles impinging on a certain area in real time with an efficiency very close to 100 %. Moreover the online determination of the absorbed dose is possible by simultaneously measuring the energy deposition of Heavy Ions (HI) in the detector material together with the number of particles. Investigations on the performance of a beam monitor based on synthetic **s**ingle-**c**rystal diamonds, produced by **C**hemical **V**apour **D**eposition (sc-CVD) operated as single-particle counter for carbon ions at energies of 80 - 430 MeV/u have been performed.

Material & Results

In order to process the signals obtained from the diamond detectors, electronics based on an ASIC (PADI [2]) especially designed for multi-channel applications as well as a 'Time-Charge-Sensitive PreAmplifier' (TCSPA [3]) were applied. Figure 1 shows the counted particle numbers for a ^{12}C ion beam for beam parameters varying with time. For the intensity of 10^8 ions/spill of the carbon beam, using sc-CVD diamond for the online-counting the efficiency of (100±2) % has been proven. Spectra of the deposited energy were registered (see Fig. 2) and a good agreement of the obtained energy resolution with calculations was achieved. An intrinsic precision of the dose measurement better than 3 % was achieved.

Conclusions

A beam monitor based on sc-CVD diamond with a specially developed multi-channel electronic was successfully applied for the dosimetry of therapeutic carbon ion beams. Nevertheless there is still room for improvement of the precision of the measurement which may be realized in the near future with better quality and bigger area detector material delivered by the suppliers. This will result in a more homogeneous response between the detector pixels and will finally also allow the measurement of the geometrical profile of pencil-like carbon beams. A new design of the detector itself with shorter signal transmission lines will decrease the pickup noise and thus smaller signals will be detectable which consequently increases the counting efficiency. Furthermore, in order to cope with the particles fluences of up to several 10^{10} particles/spill for light-ion beam applications one may either adapt the size of the detector pixels and/or perform a rate division using ultra fast pre-scalers e.g., increasing the maximum data rate up to 1.2 GHz in the current setup.

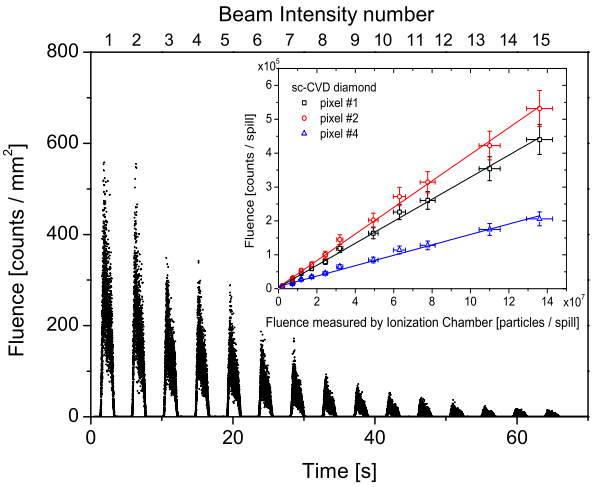

Figure 1: Response of the sc-CVD diamond detector to a static ^{12}C ion beam with an initial energy of 357 MeV/u, constant spot size and varying beam intensity versus time. The insert presents a comparison of the counts obtained from three pixels of the detector as a function of the fluence measured by an ionization chamber (IC). Each pixel is exposed to different parts of the beam spot with approximately 2D-Gaussian shape.

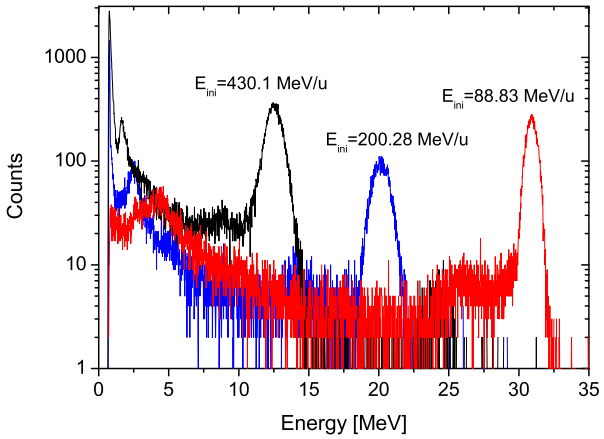

Figure 2: Spectrum for the energy deposited by a therapeutic carbon ion beam with three different initial energies, measured with the sc-CVD diamond detector together with a TCSPA amplifier. The calibration was performed with a mixed nuclide α-source.

References

[1] Karger C.P., Heeg P., Jäkel O., IBIBAM 2007, p. 111.
[2] Ciobanu M., CBM Collaboration Meeting, (2007) https://www.gsi.de/documents/FOLDER-9871170750735.html
[3] Ciobanu M. et. al, GSI Report 2007.

Calculation of primary ionization for a track structure Monte Carlo code - Application of the continuum distorted wave approximation (CDW-EIS)

R. Cunrath[1], O.Belov[2], M. Scholz[1], M. Krämer[1], and Th. Elsässer[1]
[1]GSI, Darmstadt, Germany; [2]JINR, Dubna, Russia

For heavy ion treatment planning, the Local Effect Model (LEM) [1] is applied to determine the biologically equivalent dose. One of its major constituents is the radial dose distribution around stopping ions in water. Presently, a simple amorphous track structure model is used based on experimental data and Monte Carlo simulations. In order to improve this model, possibly by applying results of Monte Carlo simulations directly to the LEM, we investigate the double differential cross sections of primary ionization processes due to ion-target interactions.

CDW-EIS

In the track structure Monte Carlo code TRAX [2], the angular distribution of emitted electrons due to ion-target interaction is calculated according to the classical binary encounter approximation (BEA). It is known that this method yields inaccurate cross sections particularly for large scattering angles. Therefore, we analyzed whether the quantum-mechanical continuum-distorted wave approximation with an initial eikonal state (CDW-EIS) yields better agreement with experimental data. We use the computer code ARGON [3] to calculate the double differential cross sections (DDCS) for the water molecule as target. According to [4] the DDCS of water can be approximated by a linear combination of the DDCS for each molecular orbital with coefficients determined by a population analysis. The corresponding binding energies for gaseous water are 540 eV, 32.2 eV, 18.4 eV, 14.7 eV, and 12.6 eV for the $1a_1, 2a_1, 1b_2, 3a_1$ and $1b_1$ orbital, respectively. For liquid water, different binding energies apply for the $1b_2, 3a_1$ and $1b_1$ orbitals: 16.8 eV, 12.1 eV, and 8.76 eV.

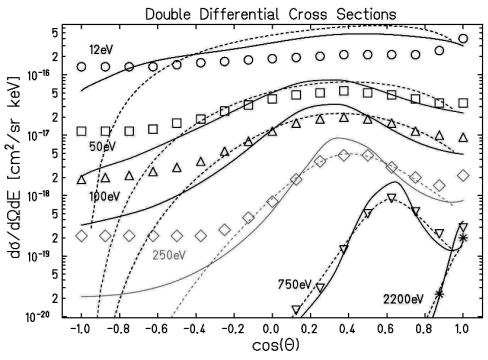

Figure 1: DDCS for 1 MeV protons in gaseous water. Results for CWD-EIS (solid line), BEA (dashed) and corresponding measurements (symbols) for different electron energies.

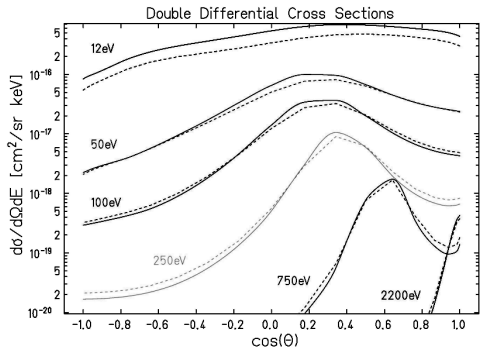

Figure 2: DDCS for 1 MeV protons in gaseous (dashed) and liquid (solid) water.

Comparison with experiments

In Fig. 1, we compare the results for the DDCS of the original BEA and the CDW-EIS to experimental data for 1 MeV protons [5] penetrating gaseous water. In general, a good agreement is found with both approximations. However, for large scattering angles the CDW-EIS coincides better with the measurements. In Fig. 2, we show the DDCS also for liquid water with the binding energies stated above. For low-energy electrons these DDCS are about 50% larger than the gaseous cross sections.

Conclusions

We find that application of the CDW-EIS approximation yields better agreement of the DDCS with experimental data for primary ionization. The implementation of binding energies for the liquid state enables us to include DDCS for liquid water into the track structure code TRAX. In future, the implications of the new description of the DDCS for radials dose distributions relevant for particle therapy will be investigated.

References

[1] M. Scholz et al., Radiat. Environ. Biophys. 36, 59 (1997)

[2] M. Krämer and G. Kraft, Radiat. Environ. Biophys. 33, 91 (1994)

[3] D.M. McSherry et al., Comput. Phys. Commun. 155, 144 (2003)

[4] V. Cobut et al., Radiat. Phys. Chem. 3, 229 (1998)

[5] L.H. Toburen et al., J. Chem. Phys. 66, 5202 (1977), Radiat. Res. 82, 27 (1980)

Minimization-Algorithms for Biological Multiple Field Optimization

M. Horcicka, A. Schmidt, and M. Krämer
GSI, Darmstadt, Germany

Introduction

The software TRiP98 [1, 2, 3] is successfully used for patient treatment planning in the GSI pilot project. A crucial part of the treatment planning is the particle number optimization. The main goal of optimization is to achieve a target dose distribution as close as possible to the prescribed biological dose distribution. Multiple field optimization (MFO) allows a better target conformity and a sparing of organs-at-risk (OAR) by 20-50% in comparison with single field optimization (SFO) [5]. Thus MFO was implemented in TRiP98 and in 2007 the first patients were treated at GSI with MFO plans. In this contribution we examine three numerical algorithms, used to solve the nonlinear optimization problem.

Materials and Methods

To obtain the optimal particle numbers we have to find the minimum of the following function:

$$X^2(\vec{N}) = \sum_{i \in Target} \frac{(D_{pre} - D^i_{bio}(\vec{N}))^2}{\Delta D^2_{pre}}$$

$$+ \sum_{i \in OAR} \frac{(D_{max} - D^i_{bio}(\vec{N}))^2}{\Delta D^2_{max}} \cdot \Theta(D^i_{bio}(\vec{N}) - D_{max})$$

D_{pre} : prescribed dose within the target
D_{max} : maximum dose within OAR
D^i_{bio} : actual biological effective dose at voxel i

Because $D^i_{bio}(\vec{N})$ is nonlinear in $\vec{N}$, we can determine $\vec{N}_{opt} := \nabla X^2(\vec{N}) = 0$ only by numerical methods. We tested the method of steepest descent (GR), conjugated gradients (CG) and the Bortfeld algorithm (BF) [6]. The latter is a modification of Newton's root finding algorithm [4]. The number of voxels i and the dimension of the vector $\vec{N}$ are several ten-thousands. Therefore, iterations are time-consuming and require a lot of memory [6].

Results and Discussion

To characterize the various solutions we consider their convergence behaviour. I.e. on the one hand, how fast the values of $X^2(\vec{N})$ decrease with each iteration and on the other hand, the CPU time for a single iteration. Both we illustrate in figure 1 and figure 2.

The data were taken from the patient plan #135 and performed on a reference device, a single 1.2 GHz Power4 CPU of an IBM p630 server. Other patient plans show a similar behaviour.

During the first iterations the gradient based methods converge fast. At later stages convergence speed slows down. This suggests, that the minimum of $X^2(\vec{N})$ is rather flat. The Bortfeld method converges slow. Due to the evaluation of the second derivative, BF requires the most CPU time. Compared to GR, CG requires more computational effort due to its more complex algorithm.

The results show, that the method of steepest descent has the best numerical properties. In addition, robustness of the GR is satisfactory. Based on these findings we presently prefer the GR.

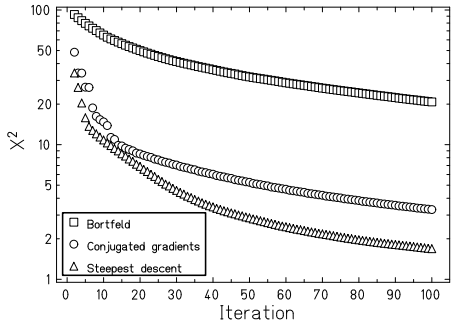

Figure 1: Convergence speed as a function of iterations.

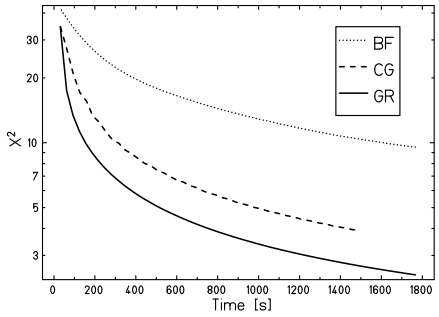

Figure 2: Convergence speed as a function of time.

References

[1] M. Krämer et al, Phys. Med. Biol., 45/11 (2000) 3299.

[2] M. Krämer et al, Phys. Med. Biol., 45/11 (2000) 3319.

[3] O. Jäkel et al, Phys. Med. Biol., 46/4 (2001) 1101.

[4] Th. Bortfeld et al, Phys. Med. Biol., 35/10 (1990) 1423.

[5] A. Schmidt, *Examinations on multiple field optimization in ion therapy*, Dipl.-Thesis, GSI/TU Darmstadt (2006)

[6] M. Krämer et al, *Biological dose optimization with multiple ion fields: Numerical methods*, Submitted to Phys. Med. Biol., (2008)

Treatment Planning for the Carbon Ion Radiotherapy

M.Krämer[1]
[1]GSI, Darmstadt, Germany

In the three therapy beam times 2007 about 50 patients were planned and treated with our treatment planning software, TRiP98, and its development version, TRiP98BEAM. In the past, the standard method was to optimize the biological target dose distribution for the contributing partial fields singly. Due to the enormous effort for the computation of biological effects, only a simple, but still sufficiently accurate dose calculation algorithm could be used for numerical optimization [1]. The recently developed fast approximation of biological effects [2], allowed to introduce more sophisticated dose optimization algorithms into clinical practice. Dose calculation has been refined to reflect the full beam profile (including broadening by multiple scattering, if so desired), which leads to a better coverage of target edges. Dose optimization can now be performed for an (theoretically) arbitrary number of fields simultaneously (multi-field optimization, MFO). The sparing of healthy tissue (organs at risk, OAR) is incorporated and is controlled by specifying constraints, i.e. a maximum OAR dose and weight factors to impose tissue-specific ”penalties”. This new method [3] was repeatedly verified by means of biological dosimetry [4, 5]. Extensive tests were performed to ensure the robustness of the generated plans [6], i.e. the carbon ion fluence maps. Both, particle maps and partial field dose distributions show the required benign behaviour, i.e. contiguous scanner patterns and no steep gradients within the partial fields. To be on the safe side, the scanner patterns obtained with the new algorithms are always recalculated with the standard TRiP98 version for plan assessment. The new methods were cautiously put into clinical operation as early as 2006. Over time, an interesting variant of the MFO evolved: single field optimization with constraints (SFO/constraints). It means, that with the same algorithms as for MFO (but much less computing resources), dose distributions can sometimes be improved already for singly optimized partial fields. This is due to some redundancy inherent in the narrowly overlapping beam spots of the GSI raster scan procedure.

Table 1 shows the ramp-up and run-down, respectively, of the various techniques chosen by the planning crew. Within a year, the novel methods have nearly replaced the classical one, and true MFO is now used in about half of the cases. However, this also depends on the location of OAR relative to the target, MFO is not always beneficial.

Figure 1 shows a sample plan where MFO has a clear benefit in sparing the spinal chord. Figure 2 on the other hand shows a sample plan where MFO has no benefit over SFO/constraints, but both advanced optimization methods yield a better target conformation and significant reduction of maximum dose to the brain stem.

beamtime	classical SFO	SFO/constraints	MFO
0601	15	1	-
0606	17	2	-
0611	1	14	-
0702	-	16	-
0707	1	14	2
0709	1	10	10

Table 1: Number of patients for the various methods.

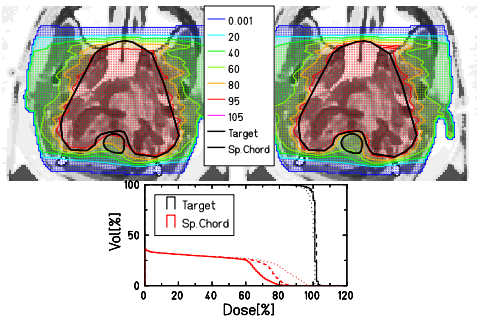

Figure 1: Upper panel: treatment plan for SFO (left), MFO (right). Lower panel: Dose-Volume histograms for SFO/classic (dots), SFO/constraints (dashes), MFO (solid).

References

[1] M.Krämer, M. Scholz, Phys Med Biol. 45 (2000) 3319.
[2] M.Krämer, M. Scholz, Phys Med Biol. 51 (2006) 1959.
[3] M.Krämer et al, submitted to Phys Med Biol. (2008).
[4] A.Schmidt et al, submitted to Phys Med Biol. (2008).
[5] C.v.Neubeck, Diplomarbeit TU Darmstadt (2006).
[6] M.Ellerbrock et al, Int J Rad Oncol Biol Phys. (2008).

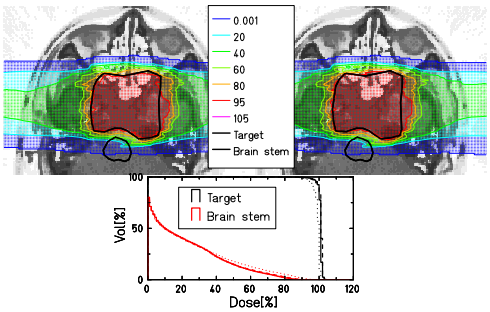

Figure 2: Upper panel: treatment plan for SFO/classic (left), SFO/constraints (right). Lower panel: Dose-Volume histograms for SFO/classic (dots), SFO/constraints (dashes), MFO (solid).

Performance of the DoPET system for ^{12}C irradiation induced β^+-activity

S. Vecchio*[1], K. Parodi[2], and F. Attanasi[1]
[1]Università di Pisa and INFN, Italy; [2]HIT, Heidelberg, Germany

Introduction

The DoPET project (Dosimetry with a Positron Emission Tomograph) funded by INFN aims to realize an in-beam PET system dedicated [1]. The system has been validated through measurements on PMMA phantoms, in the perspective of clinical application in proton therapy monitoring at CATANA. Differences in proton-induced activity distribution down to 1 mm along the proton range have been appreciated [2]. In order to explore a wider range of application of the DoPET prototype, we performed a set of acquistions after ^{12}C irradiations at the hadrontherapy facility at GSI. Preliminary comparison with the results of the in-beam PET available at GSI [3] is reported below.

Figure 1: Experimental configuration for comparison of the two PET systems.

Description of the measurements

Irradiations have been performed on cylindrical PMMA phantoms (7 cm diameter and 7cm length). The cylinder base was oriented orthogonal to the impinging beam. Three monoenergetic configurations have been used for carbon irradiations, as listed in table 1. A squared section of 28 mm side has been adopted. The delivered dose was 60 Gy for each beam configuration, divided as 6 beam repainting of 10 Gy each. The total time required for irradiation spanned from 2 to 6 minutes. The acquisition were started together with the irradiation, and lasted 35 minutes each.

Energy [AMeV]	108.53	112.60	116.57
Range [mm]	21.9	23.6	25.3

Table 1: Beam parameters: range are given in PMMA.

Linear profiles derived from the central slices of reconstructed activities are reported in figure 2: the carbon beam impinges from left. Both tomographs are able to detect the 2mm range shifts. However, the shape of the activity distribution is significantly different. This is due to the different spatial resolution of the two scanners as well as the contribution from ^{15}O, since BASTEI detector starts to acquire β^+ decays during carbon irradiation, in the spill pause, while the DoPET detector is forced to reject all the data before the irradiation end. The latter hypotesis is supported by previous works of the FZD group at GSI[4] and preliminary reconstructions of the BASTEI data after end of irradiation (data not shown). A more detailed data analysis is in progress and will be reported soon.

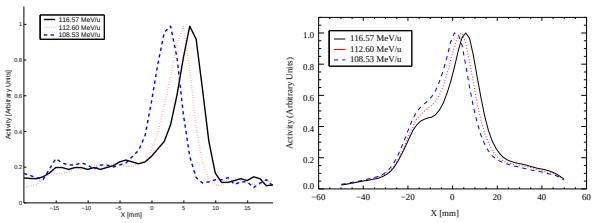

Figure 2: Linear profiles obtained by central slices of the reconstructed images for β^+-activity acquired with DoPET (left) and BASTEI (right) detectors. Phantom entrance surface is at about X = - 20 mm in both reference systems.

Conclusions

DoPET performance appear similar to those of BASTEI detector in terms of detection of deviation from the planned dose distribution, but somewhat worse in terms of activity quantification, since the delayed acquisition start prevents the acquisition of large part of the ^{15}O activity.

References

[1] F. Attanasi et al., LNS Activity Report 2006, p 103
[2] S. Vecchio et al., IEEE NSS Conf. Rec. 2007, NS24-362
[3] Enghardt W et al., Nucl. Instr. Meth. A 525 (2004) 284
[4] Pönisch F et al., Phys. Med. Biol. 49 (2004) 5217

* sara.vecchio@pi.infn.it

Influence of the Time of Flight Information on the Reconstruction of In-Beam PET Data

G.Shakirin[1], P.Crespo[2], and W.Enghardt[1,3]
[1]FZD, Dresden, Germany; [2]now with University of Coimbra, Portugal; [3]Technische Universität Dresden

Introduction

At the experimental heavy ion therapy facility at the GSI Darmstadt an in-beam PET scanner BASTEI is operated for quality assurance monitoring simultaneously to the therapeutic irradiation. Significant improvement in the quality of the images reconstructed using time of flight (TOF) information has recently been reported for usual conditions of nuclear PET (relatively high statistics, full ring geometry of the scanner) [1 - 3]. In order to analyze the advantages for a new in-beam PET system with detectors allowing timing resolution of at least 1.2 ns FWHM, we investigate how the reconstruction of in-beam PET data can profit from the TOF information taking into account specific issues of an in-beam PET system.

Method

The present study is based on a simulation of the β^+-activity distributions from real treatment plans. Firstly, we collect the annihilation points generated via the PosGen Monte Carlo code [4] on the basis of the patient treatment dose distributions. Secondly, the events coming from these annihilation points are simulated and captured with a dual head PET scanner BASTEI. Thirdly, the time difference for each registered event is calculated according to the normal distribution with FWHM of 1.2 ns.

The modification of the 3D MLEM algorithm adapted for the reconstruction of in-beam PET data [5] with the utilization of the TOF information is described by:

$$x_j^{(n+1)} = x_j^{(n)} \frac{1}{\sum_{i'} p_{i'j} a_{i'j}} \sum_i \frac{p_{ij} a_{ij} y_i}{\sum_{j'} p_{ij'} a_{ij'} x_{j'}^{(k)}}, \qquad (1)$$

where $x_j^{(n)}$ is the activity distribution after the n-th iteration, y_i are the measured projections for the i-th channel, a_{ij} are the elements of the system matrix, and p_{ij} are TOF coefficients for i-th channel and j-th voxel. The reconstruction is performed in an image space adapted to the irradiated volume.

Results

We performed reconstructions of the simulated data with MLEM algorithm with and without utilization of the TOF information. Fig. 1 presents results of the reconstruction of the irradiation field located in the head and neck region (clivus chondrosarcoma) (left) and in the pelvic region (prostate carcinoma) (right). It is clearly seen from the ZY and YX slices that elongation of activity along the Y axis (typical for the dual head geometry of the PET scanner) is reduced significantly for TOF reconstructions.

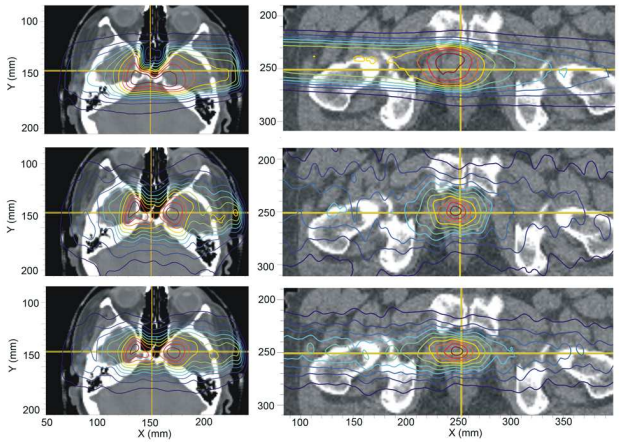

Figure 1: β^+-activity is shown as isolines superimposed with a CT image. First row: the reference distribution of annihilation points. Second row: MLEM reconstruction (50 iterations) without TOF. Third row: MLEM reconstruction (50 iterations) with TOF. Left column: head and and neck field, volume size: 205 x 147 x 131 mm^3, 48000 registered events. Right column: pelvic field, volume size: 416 x 176 x 176 mm^3, 82000 registered events.

The reconstructions of the simulated in-beam PET data performed with TOF information confirm that even for a moderate time resolution of 1.2 ns FWHM there is significant enhancement of the quality of the reconstructed images. In particular, TOF information helps to reduce the elongation effect of the dual head scanner and to reduce the root mean square error by 20 % for the head and neck field and by 36 % for the pelvic field.

References

[1] M. Conti et al. “First experimental results of time-of-flight reconstruction on an LSO PET scanner” Phys. Med. Biol. 50, pp. 4507 – 4526, 2005
[2] W. W. Moses “Time of Flight in PET revisited” IEEE Trans. Nucl. Sci. 50, pp. 1325 – 1330, 2003
[3] C.C. Watson “Image Noise Variance in 3D OSEM Reconstruction of Clinical Time-of-Flight PET”, IEEE NSS MIC 2006, San Diego, M04–5
[4] F. Poenisch et al. "The modeling of positron emitter production and PET imaging during carbon ion therapy", Phys Med. Biol., vol. 49, pp. 5217-5232, 2004
[5] Lauckner K. “Entwicklung eines iterativen 3D Rekonstruktionsverfahrens fuer die Kontrolle der Tumorbehandlung mit Schwerionen mittels der PET” Thesis, Technische Universitaet Dresden, 1999

Results of a 20 minutes decay measurement of a patient irradiation by the in-beam PET scanner

F. Fiedler[1], D. Möckel[1], K. Parodi[2], J. Pawelke[1], F. Pönisch[1,3], M. Priegnitz[1], G. Shakirin[1], and W. Enghardt[1,3]

[1]FZD, Dresden, Germany; [2]HIT, Heidelberg, Germany; [3]OncoRay, TU Dresden, Germany

Introduction

Over the last 10 years, the unique installation of an in-beam PET-scanner at the heavy-ion treatment facility at GSI [1] has demonstrated the benefit of in-beam PET measurements. Additional heavy ion therapy facilities are under construction. Monitoring the irradiation is highly desirable especially for heavy-ion beams, because the beam has the potential to cause excessive damage in the healthy tissue surrounding the tumor. The evaluation of in-beam PET results is based on a comparison between measurement and simulation. Even if all the physical processes of creating and detecting positron emitters are correctly modeled, deviations between measured and simulated β^+-emitter distribution will occur. The predominant reason for that is the blurring as well as the reduction of measured activity via washout. To get realistic estimation of the quantity of washout a decay measurement of 20 minutes was performed over 20 patient treatments, referred to as "fractions".

Methods and Results

The listmode data were taken by the data acquisition system of the in-beam PET camera [1], and spatial subsets were analyzed. We classified the lines of response (LOR) depending on the Hounsfield unit (HU) on the basis of the patient's planning computer tomogram (CT). For each LOR intersecting the irradiated volume, the mean HU ($\overline{\mathrm{HU}}$) and its standard deviation were calculated. The LOR were combined as given in table 1. Since the main positron emitters are well known we fitted the decay curves according to

$$a(t) = a_0 + e^{-t/\tau_{biol}} \left\{ \sum_{i=0}^{2} a_i \, e^{-t/\tau_i} \right\}, i=\{^{11}\mathrm{C},^{15}\mathrm{O},^{10}\mathrm{C}\}$$

where a is the activity, t the measuring time, and τ is the lifespan of the positron emitters. Since we are interested in the quantity of activity which is lost by washout processes, we considered only one biological half-life τ_{biol}, even if this may be a simplification of the real processes [3]. To reduce the statistical error, the data of all 20 treatments were summed up. In figure 1, the anatomical regions corresponding to the LOR subsets are given. A tendency to longer biological half lives in the bone region (right column in fig. 1) than in mixed tissue (middle column in fig. 1), the lowest biological half live was measured, as expected, in soft tissue including the brain (left column in fig. 1), which is well perfused. We expected a dependence of the biological half-life on the number of fractions from previous studies [2]. We selected LOR from 90 to 100 % dose containing at least 10 voxels with 90 % of maximum dose and the remaining LOR with 0 to 90 % of the dose. To reduce the statistical errors, the data from 3 fractions were summed up (i.e. fraction 1 to 3, fraction 2 to 4 etc.) and the biological half lives were fitted. Nevertheless, the standard deviation of the biological half lives is too large for statistically significant result. There seems to be a trend of a decrease of the biological half-life in the high dose area (90 to 100 % of maximum dose), compared to the low dose area as shown in figure 2. A overall fit of the data and the 20 fractions results in a biological half-life of (356 ± 116) s.

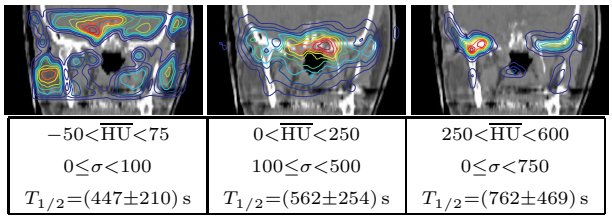

$-50<\overline{\mathrm{HU}}<75$	$0<\overline{\mathrm{HU}}<250$	$250<\overline{\mathrm{HU}}<600$
$0\leq\sigma<100$	$100\leq\sigma<500$	$0\leq\sigma<750$
$T_{1/2}=(447\pm210)$ s	$T_{1/2}=(562\pm254)$ s	$T_{1/2}=(762\pm469)$ s

Figure 1: Backprojection of the subsets of the measured data fulfilling the given $\overline{\mathrm{HU}}$ and σ condition superimposed onto the patient CT. The biological half lives $T_{1/2}$ are given with the standard deviation σ of the fit.

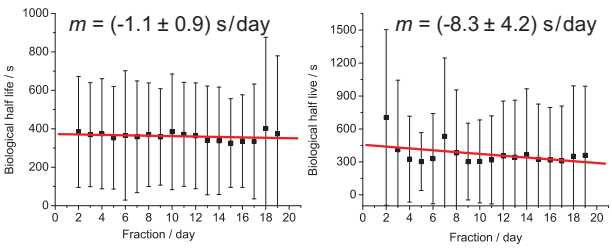

Figure 2: Biological half-life as a function of treatment time. The left figure gives the biological half lives of the $0-90$ % dose region, the rigth the $90-100$ %. The slope of the fit m is given in the figure.

Conclusion

Even with a long decay measurement it is quite difficult to get statistically reliable results. We found a trend of a dependence of the biological half-life on the HU and a decreasing biological half life during the overall treatment time. The half-life seems to be in the order of magnitude of an in-beam PET scan. In future installations, the detection sensitivity should be higher in order to shorten the measuring time, since in longer PET measurements, the washout cannot be neglected.

References

[1] W. Enghardt et al., Nucl. Instr. Meth. A, 525 (2004) 284.
[2] F. Fiedler et al., Acta Oncol. in press.
[3] T. Tomitani et al., Phys. Med. Biol. 48 (2003) 875.

In-beam PET monitoring of phantom irradiation with ^{7}Li-ions

M. Priegnitz[1], D. Möckel[1], K. Parodi[2], F. Fiedler[1], F. Sommerer[3] and W. Enghardt[1,4]
[1]FZ Dresden-Rossendorf, Germany; [2]Heidelberger Ion Therapy Center, Germany; [3]CERN, Switzerland; [4]OncoRay, TU Dresden, Germany.

Introduction

In-beam PET is presently the only possibility of a beamline independent dose delivery monitoring in heavy-ion therapy. It is clinically implemented at the experimental heavy ion treatment facility at GSI Darmstadt. Since 1997 almost 400 patients have been treated there with ^{12}C-ions while monitoring of dose application with in-beam PET has been performed. In the future it is expected to extend tumour irradiation also to other ion species with atomic numbers between 1 (protons) and 8 (oxygen) [1]. Since the application of in-beam PET also for these ions is highly desirable extensive knowledge about the spatial distribution of generated positron emitters is required. Therefore, the β^+-activity induced by ^{7}Li ions has been investigated for the first time at the Gesellschaft für Schwerionenforschung (GSI) Darmstadt.

Materials and Methods

Monoenergetic, pencil-like beams of $^{7}Li^{3+}$ have been stopped completely in targets of polymethyl methacrylate PMMA $(C_5H_8O_2)_n$ (ρ = 1.18 g cm^{-3}), polyethylene PE $(C_2H_4)_n$ (ρ = 0.948 g cm^{-3}), graphite (ρ = 1.8 g cm^{-3}) and water (ρ = 1.0 g cm^{-3}), respectively. To the latter a little amount of gelatine was added, leading to a stoichiometric composition of $H_{66.3}O_{33.1}C_{0.6}$, in order to avoid deterioriation of the β^+-activity distribution by thermal convection. Irradiation was carried out with ^{7}Li ions of energies between 129.1 *A*MeV and 205.3 *A*MeV. The pulsed beam extracted from the heavy ion synchrotron of GSI had a mean average spill duration between 1 s and 2 s, mean pause duration of 2 s and intensities from $3.0 \cdot 10^7$ to $1.9 \cdot 10^8$ ions s^{-1}.

The measurement of ion beam induced β^+-activity was performed by means of the in-beam PET scanner, which is installed at the therapy unit at GSI. It consists of two detector heads of bismuth germanate block detectors from the commercial ECAT EXACT PET Systems (CTI PET Systems Inc. Knoxville, TN, USA) [2]. The targets were placed in the centre of the field of view of the PET scanner and were irradiated 10 min each. PET measurement was performed during the irradiation and further 30 min of decay. By using the backprojection algorithm and including correction of random coincidences, photon attenuation and detection efficiency of the PET scanner, depth profiles of the measured activity are obtained.

Results

During irradiating the targets with ^{7}Li ions positron emitting target fragments are produced through nuclear reactions between incoming ions and nuclei of the target. Photons following the decay of these positron emitters can be detected with the PET camera. The left part of figure 1 shows the depth distribution of the measured activity in a PMMA target with 129.1 *A*MeV ^{7}Li ions. In contrast to carbon ions (figure 1, right) the activity profiles induced by ^{7}Li ions do not show a pronounced maximum at the end of the particle range. This is because the β^+-activity induced by ^{7}Li irradiation is only due to positron emitting target fragments whereas in carbon irradiation also positron emitting projectile fragments contribute to the activity [3].

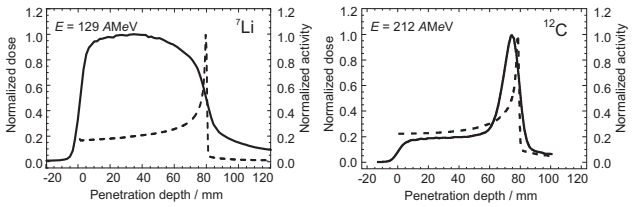

Figure 1: Depth profiles of the reconstructed β^+-activity (solid line) induced by 129.1 *A*MeV ^{7}Li ions (left) and 212.12 *A*MeV ^{12}C ions (right), respectively, in a PMMA-target. The energy of the ions was chosen to get the same range with both ion species. The dashed line indicates the dose distribution.

Figure 2 shows a comparison between measured activity profiles induced by 162.3 *A*MeV ^{7}Li ions in different target material and the respective primary ion ranges. Apparently a correlation between the distal slope of the activity and the primary ion range exists.

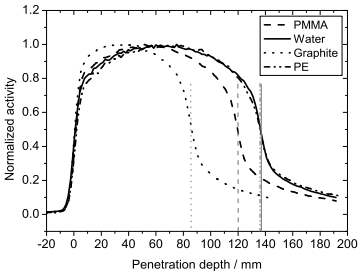

Figure 2: Depth profiles of the measured activity induced by 162.3 *A*MeV ^{7}Li ions in PMMA, water, graphite and PE, respectively. The vertical grey lines indicate the range of the ions in the respective material.

References

[1] J. Kempe, I. Gudowska and A. Brahme, Med. Phys. 34, pp. 183-192, 2007
[2] W. Enghardt, P. Crespo, F. Fiedler *et al.*, Nucl. Instr. Meth. A 525, pp. 284-288, 2004
[3] K. Parodi, W. Enghardt and T. Haberer, Phys. Med. Biol. 47, pp. 21-36, 2002

Initial simulation study of a new method of range adaptation for radiotherapy of moving targets with scanned ion-beams

N. Chaudhri[1], R. Pleskac[1], N. Saito[1], B.Franczak[1],C. Bert[1], A. Schmidt[1], D. Schardt[1] and E. Rietzel[2]
[1]GSI, Darmstadt, Germany; [2]Siemens Medical Solutions, Erlangen, Germany.

In the radiotherapy (RT) of moving targets with scanned ion-beams at GSI we are investigating a new method of fast range adaptation. The method controls an ion-beam depth in a moving target by deflecting the ion-beam on an appropriate thickness of a static wedge shaped energy degrader placed upstream in the ion-optical system. A feasibility study of this method using Monte Carlo simulations are being performed which is based on experimental results.

Introduction

In case of organ motion, methods like gating and tracking are becoming clinical routines in conventional RT. The tracking of the moving target with a scanned ion-beam RT [1] at GSI has been investigated and as a solution a prototype system called 3D online motion compensation (3DOMC) is developed [2]. The system uses a mechanical range shifter which consists of a PMMA double wedge mounted on two linear motors [3]. The range shifter allows a longitudinal motion compensation of ±10mm for a scan field of 8x15 cm^2. 3DOMC system achieves 5mm water equivalent depth compensation in 27ms where the range shifter delay is approximately 17ms [3]. The system time delay would increase for a scan field of 20x20 cm^2 however the required time of the depth compensation is of the order of 10ms which roughly corresponds to an irradiation time of each raster spot of the scanning.

To overcome the problem of slow range adaptation an approach of within a beam-line range adaptation has been considered where range shift is electromagnetically controlled. In the beam-line a magnet deflects an incoming ion-beam on a required thickness of a wedge shaped energy degrader to achieve the required shift corresponding to the position of the moving target. The magnet setting before and after the wedge in the beam-line has to be controlled in a real time. In order to take realistic parameters for the feasibility study we have performed some initial experiments using the therapy beam line at GSI [4].

Based on our experimental results, a simulation has been performed using MOCADI [5]. Mocadi is a Monte Carlo based software which uses a method of ion-optical transfer matrices to calculate a transport of the ion-beam passing through a matter inside the ion-optical system and It takes the energy loss as well the fragment production into account in the calculation.

Simulations

The therapy beam-line at GSI was simulated as an initial feasibility test. The simulated part of the beam-line consists of two dipole magnets and doublet quadrupole magnets [4] and it is set in the achromatic manner. A suitable ion-optical setting and transfer matrices for simulation are obtained using the software MIRKO [6] and GICOSY [7] respectively. A plastic wedge of maximum thickness 30mm and 60mm in length is positioned in between the two dipoles such that the ion-beam on the central axis passes through a wedge thickness of 15mm. Top panel of Figure-1 illustrates the simulated setup.

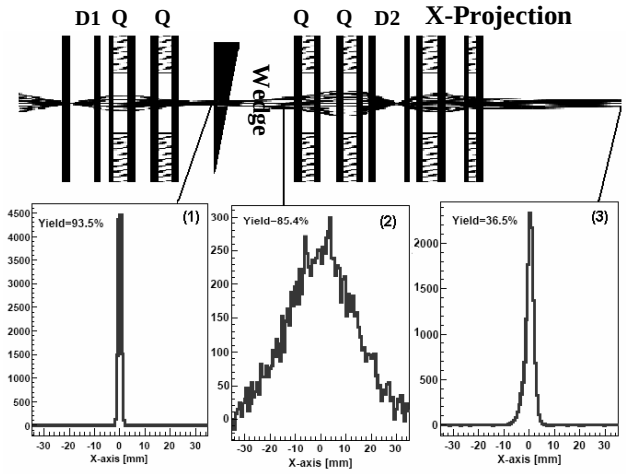

Figure-1: Simulated beam-line (Top). Beam width (bottom) on the x-axis at wedge (1), after the wedge (2) and target position (3).

In the simulation, C^{12} ion-beam with various energies or therapy were set with the primary beam parameter obtained from the experiments [4]. The bottom of Figure-1 shows the ion-beam distribution on x-axis for different position in the beam-line. Optimization of magnet settings and investigation of wedge shape for the design of the new system are currently in progress.

On the base of simulation results the design of the new system, which includes wedge shape and a magnets control system, is foreseen for the further development.

References

[1] C. Bert et al., Med. Phys. 34 (2007) 4768
[2] S. Groezinger, PhD Thesis, TU Darmstadt.
[3] N. Saito et al., This Report.
[4] R. Pleskac et al., This Report.
[5] T. Schwab, PhD Thesis, Universität Giessen, GSI Report 91–10.
[6] MIRKO, http://www-inux.gsi.de/~redelbac/MIRKO/.
[7] GICOSY, http://www-linux.gsi.de/~weick/GICOSY/.

Fast Range Adaptation for Heavy-Ion Therapy of Moving Organs

R. Pleskač[1], N. Chaudhri[1], N. Saito[1], C. Bert[1], A. Schmidt[1], B. Franczak[1], D. Schardt[1], and E. Rietzel[2]

[1]GSI, Darmstadt, Germany; [2]Siemens Medical Solutions, Particle Therapy, Erlangen, Germany

Introduction

At GSI we are presently developing an alternative method for a very fast (in order of few *ms*) range adaptation for radiotherapy of moving organs [1] with scanned ion beams to the existing 3D online motion compensation (3DOMC) [2] system.

The range adaptation can be achieved by deflecting the ion beam (with the energy E_0, see Fig.1) to different positions on a static wedge-shaped energy degrader (corresponding energies E_1 and E_2) in the beam line. Before the beam is delivered to a required point of the moving organ (target) it is first collimated by slits and than deflected by scanning magnets [3]. The entire energy degrader system will consist of one or several degraders mounted on a frame and a step motor which is placing the frame into the beam line.

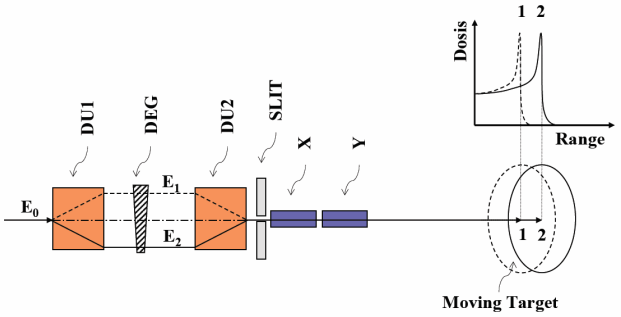

Figure 1: Principle of the fast range (energy) adaptation. Abbreviations: DU – deflection units (e.g. dipoles), DEG – a shaped energy degrader, SLIT – slits or collimator, X and Y – x and y scanning magnets. For the energy of the beam before and behind degrader holds: $E_0 > E_2 > E_1$.

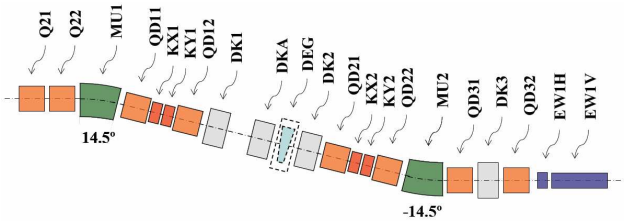

Figure 2: Layout of the trailing part of the therapy beam line (TH4 and HTM). Abbreviations: QD – quadrupole magnets, MU – dipole magnets, KX and KY – horizontal and vertical steerers, DK – diagnostics chambers, DEG – a shaped energy degrader, and EW1H and EW1V – horizontal and vertical energy wobblers (scanning magnets).

Beam Tests and First Results

In 2007 we have performed two experimental tests with the carbon beam at 144 and 357 MeV/u in the existing therapy beam line (see Fig. 2) in order to examine the design of a prototype of the energy degrader system.

In the first experiment we have moved the carbon beam in the horizontal plane relative to the beam axis. The maximum sideward shift of the beam was 35 mm in both directions (see Fig. 3), it means, an active length of the future degrader prototype could be altogether 70 mm.

In the second experiment we have tested two different ion optical settings: we were able to set up both a parallel beam to the beam axis with a beam spot of 5 mm in diameter and a radial beam with a sharp focus of ca. 0,5 mm beam spot in diameter or better on the degrader. The degrader was simulated by existing detectors from the DKA diagnostic chamber: in successive steps we have added an IC, a plastic scintillator and a SEETRAM detector to measure the energy loss and widening of the beam.

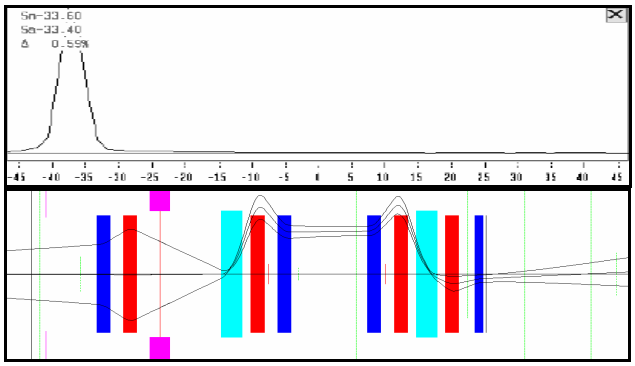

Figure 3: (upper panel) Horizontal profile of the carbon beam measured by a current grid detector placed in the HTMDK1 diagnostic chamber. (lower panel) Corresponding ion optics designed and applied by using the MIRKO Expert program [5]. The beam is shifted sideward relative to beam axis in the area between the last two dipoles HTMMU1 and HTMMU2 (see also Figure 2).

Outlook

The final design of the shaped energy degrader system strongly depends on results of ongoing calculations [4] with the Monte-Carlo code MOCADI [6] concerning the last part of the therapy beam line. The prototype of the energy degrader system can be tested in the beam line under realistic conditions after the end of the patient treatment programme at GSI.

References

[1] C. Bert et al., Med. Phys. 34 (2007) 4768
[2] N. Saito et al., this annual report.
[3] T. Haberer et al.,.NIM A330 (1993) 296-305
[4] N. Chaudhri et al., this annual report.
[5] MIRKO, http://www-linux.gsi.de/~redelbac/MIRKO/.
[6] MOCADI, http://www-linux.gsi.de/~weick/mocadi/.

Gating with scanned carbon beams*

C. Bert[1,#], A. Schmidt[1], U. Scheeler[1], S. Brons[2], P. Moritz[1],
N. Saito[1], N. Chaudhri[1], D. Schardt[1], E. Rietzel[1,3]
[1]GSI, Darmstadt, Germany; [2]HIT, Heidelberg, Germany; [3]Siemens Medical Solutions, Erlangen, Germany

Introduction

In radiation therapy tumor motion requires additional techniques to ensure coverage of the clinical target volume (CTV) with the planned dose. For intra-fractional motion, internal margins, tracking [1], and gating [2] are possible techniques to mitigate the influence of motion.

For scanned beam delivery [3] as it is used in the carbon therapy project of GSI, intra-fractional target motion is more challenging because target motion and scanned beam can interfere with another [4]. This interplay leads to deterioration of the delivered dose distribution and does not allow use of margins to ensure adequate dose coverage of a moving CTV.

In a gated treatment, the dose is delivered synchronized to the breathing motion of the patient in phases with little motion. Target motion is often monitored with an external surrogate such as the height of the chest wall. If the surrogate is within the gating window beam is requested. For synchrotron based particle acceleration as it is used at GSI and NIRS this beam request does not necessarily result in particle delivery because of the pulsed extraction of particles from the synchrotron. Fig. 1 illustrates possible timings for gated beam delivery with a synchrotron.

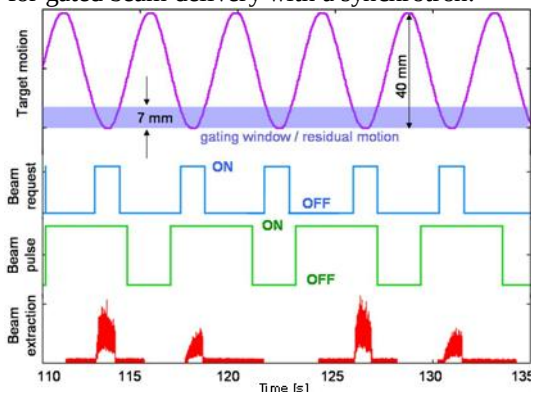

Figure 1: Timing for gated synchrotron-based irradiation

Material and Methods

To allow experiments with gating RF-knock out extraction mode [5] was used which has been implemented experimentally at GSI [6]. A beam of ~18 mm full width at half-maximum (FWHM), a grid spacing of 2 mm between individual beam positions, and gating windows with residual motions from 1-9 mm were used. The treatment plan contained a single iso-energy slice with 8x6 cm^2 lateral extension. As detector, radiographic films were placed on a sliding table. Motion detection was performed with a calibrated CCD camera. The motion signal was analyzed online in a LabVIEW application, gating windows were generated, and communicated to the synchrotron exciter via a digital IO card.

Data were analyzed by visual inspection and by the homogeneity within the film response distribution. The homogeneity H is defined as $H=1-\sigma\mu^{-1}$ with μ mean and σ standard deviation of the film response.

Results

Experimental film responses and corresponding homogeneities are shown in fig. 2 for different gating windows including homogeneity levels. In comparison to the stationary reference irradiation, gated irradiations lead to comparable target dose homogeneity for targets with up to ~7 mm residual motion.

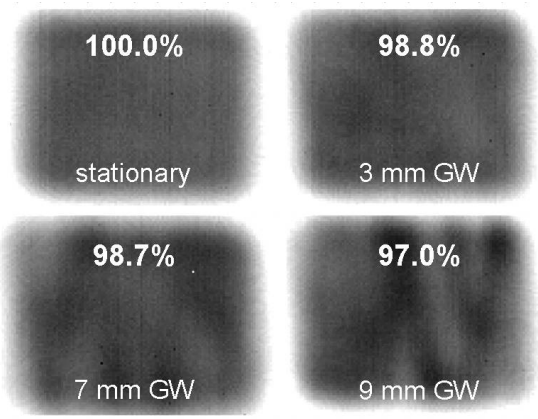

Figure 2: Film response distributions, homogeneities, and gating window sizes for the stationary reference and for gated irradiations with different gating windows. The numbers refer to the homogeneity H within the target area normalized to the stationary result.

Conclusion

Gated beam delivery with scanned carbon ion pencil beams was evaluated experimentally. For pencil beams with ~18 mm FWHM, adequate dose homogeneity was achieved for residual motion of up to 7 mm within the gating window.

References

[1] C. Bert et al. , Med. Phys. 34, 2007, p. 4768
[2] Minohara et al., Int.J.Radiat.Oncol.Biol.Phys. 47, 2000, p. 1097
[3] T. Haberer et al., NIM A330, 1993, p. 296
[4] Phillips et al. Phys. Med. Biol. 37, 1992, p. 223
[5] K. Noda et al., NIMA 374, 1996, p. 269
[6] P. Moritz, http://bel. gsi. de/mk/fg/ko_extr. pdf, 2005

* Work supported by Siemens Medical Solutions, Particle Therapy.
#c.bert@gsi.de

Technical status of the 3DOMC system for therapy of moving tumours

N. Saito[1], C. Bert[1], N. Chaudhri[1], A. Schmidt[1], D. Schardt[1], G.. Kraft[1] and E. Rietzel[2]
[1]GSI, Darmstadt, Germany; [2]Siemens Medical Solutions, Erlangen, Germany

A prototype of the 3D Online Motion Compensation (3DOMC) system for the treatment of moving tumours by scanned ion beams has been developed at GSI. The technical performance of the 3DOMC system was investigated and tested experimentally with scanned carbon ion beams at GSI.

Introduction

Since 1997 cancer patients with localized tumours in the head, neck, and pelvis region were treated at the therapy unit at GSI by applying the rasterscan technique with scanned carbon ion beams [1]. In order to treat moving tumours feasibility studies have been performed, and basic functionality has been proven for lateral and longitudinal compensation separately [2,3,4]. The prototype 3DOMC system employs the raster scanner for lateral target motion compensation and a range shifter to adapt the Bragg peak position longitudinally [2,4]. In 2007 the prototype system was upgraded and integrated in the therapy control system (TCS) at GSI. In this report the technical status of the current 3DOMC system is described.

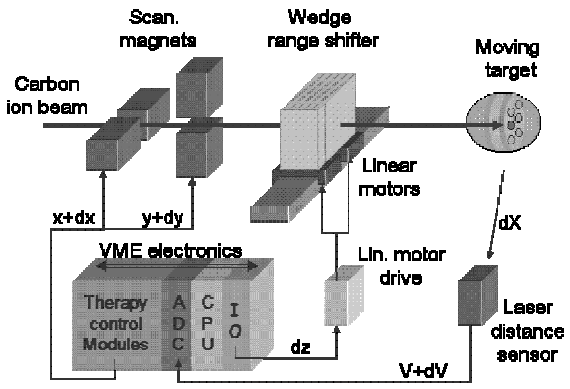

Figure 1: Schematic drawing of the 3DOMC system.

The 3DOMC system

The integrated 3DOMC system consists of three subsystems which are controlled by a CPU installed in the VME crate of TCS. A schematic drawing of the system components and the data flow are shown in fig. 1.

A laser distance sensor is used for target motion detection. The laser sensor (SICK OD 100-35P840) measures distances at a rate of up to 1 kHz with a resolution of 150 µm. The position signal is encoded in analog voltage. An analog-to-digital converter (ADC) in the VME crate is used to transfer the motion information to the TCS.

Lateral beam adaptation to the moving target is performed with the scanning magnets by applying an offset (dx, dy) to the nominal beam positions [2,4]. The previous version of the 3DOMC system used a PC to calculate the offset and sent them to the TCS via TCP/IP or a link bridge [5]. Instead, the current system uses a dedicated CPU located in the TCS's VME crate. This upgrade led to significant improvements of data transfer and stability of the compensations. For the current system the delay time for lateral compensation is negligible (~1ms) and motion prediction is no longer needed [5].

For longitudinal compensation the prototype 3DOMC system employs a range shifter consisting of two sets of Lucite wedges mounted on linear motors [2,4]. In 2007, the two linear motors of the range shifter were upgraded by fast servo linear motors (PASIM SB120) with new digital servo drives (Elmo Tuba A12/230Q). Thereby the acceleration of the motor was improved from 0.6 g to 4.3 g, where g is the standard gravity. In water-equivalent units the 4.3 g acceleration corresponds to a depth compensation rate of 8.0 g. As an example a depth correction of 5 mm water-equivalence takes 16±2 ms with a delay of 11±2 ms by the current range shifter system.

The current 3DOMC system demonstrated an excellent performance of simultaneous lateral and longitudinal motion compensation in real time with carbon ion beams at GSI [6]. As an example, irradiation patterns of radiographic films for stationary exposure compared to uncompensated and compensated moving cases are shown in Fig.2.

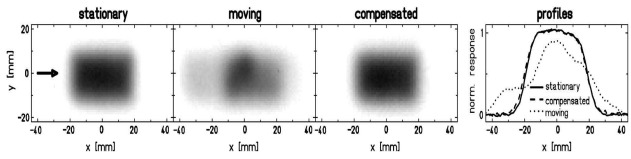

Figure 2: Radiographic film responses and corresponding horizontal profiles at the vertical position indicated by the arrow on the left.

The performance of the 3DOMC system was improved significantly and achieved an excellent functionality as a real time system. Further improvements of the current system and a feasibility study of advanced methods for fast longitudinal compensation are currently in progress.

References

[1] G. Kraft, Nucl. Instr. and Meth. A 454 (2000) 1
[2] S. Grözinger, Ph.D. Thesis, TU Darmstadt (2004)
[3] Q. Li *et al*., Phys. Med. Biol. 49 (2004) 3029
[4] C. Bert, Ph.D. Thesis, TU Darmstadt (2006)
[5] N. Saito et al., GSI Sci. Rep. 2006 (2007) 360
[6] C. Bert et al., Med. Phys. 34 (2007) 4768

Biological dosimetry for motion compensated targets*

A. Schmidt[1], Ch. Bert[1], N. Saito[1], N. Chaudhri[1], G. Iancu[1], D. Schardt[1], and E. Rietzel[1,2]
[1]GSI, Darmstadt, Germany; [2]Siemens Medical Solutions, Erlangen, Germany

Introduction

Since 1997 almost 400 patients with mainly head and neck cancer have been treated successfully with the raster-scan technique [1] at GSI. Due to interplay between scanned beam and organ motion, it is not possible to treat tumor sites influenced by respiratory motion. A potential technique to overcome this problem is tracking [2], where the beam position is adapted to a moving target in 3D based on the measured target position. This work compares measured cell survival to calculated survival in a stationary and a motion compensated irradiation scenario.

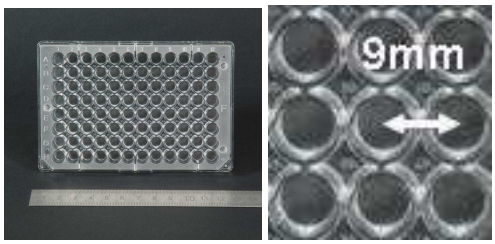

Figure 1: Wellplate (*left*) and expansion (*right*).

Material and Methods

We used chinese hamster ovary cells (CHO) grown in 96-MicroWell™ plates (fig. 1) to allow for survival measurements with a spatial resolution of 9 mm. The plates were put in upright position into a medium filled container under sterile conditions. After irradiation the cells were removed from the plates, counted and reseeded into culture flasks to determine the survival fraction in a colony forming assay. Survival was measured at selected positions only since the cell analyzing procedure is very time consuming and incubator space is limited.

During irradiation the container was placed on a sliding table which sinusoidally moved left-right in beam's eye view (peak-to-peak amplitude: 4 cm; period: 5 s). Because of a stationary ramp shaped absorber placed proximally to the moving container, the table motion not only introduced changes of the lateral target positions but also changes in the radiological depth in comparison to the stationary scenario. The target was a cubic volume of $28 \times 45 \times 23\,\mathrm{mm}^3$ and the irradiation plan was optimized for the stationary scenario to an isoeffective dose of 6 GyE with GSI's treatment planning software TRiP98 [3] using the local effect model taking cluster effects into account [4]. Compensation of the beam positions was performed with the scanner magnets in the lateral beam directions and with an adjustable wedge system to adapt the longitudinal beam position [2, 5]. The measured survival levels of the motion compensated irradiation and the stationary reference irradiation were compared to calculations of the treatment planning software which was recently extended by 4D functionality [6, 7].

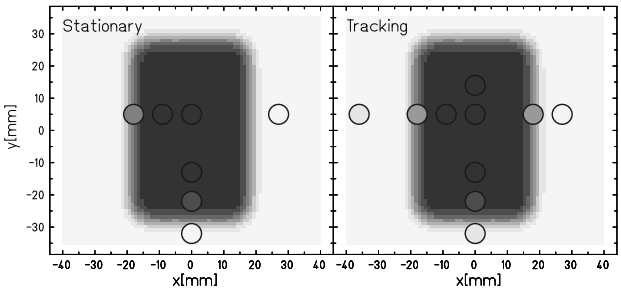

Figure 2: Experimental data of cell survival (circles) in comparison to the calculated survival distribution. High to low survival is coded from light to dark gray, respectively.

Results and Conclusion

Cell survival was measured at 7 and 10 well positions for the stationary reference and the motion compensated irradiation, respectively (see fig. 2). Both, stationary and compensated irradiations confirm the survival levels predicted with our treatment planning software. The relative difference of the measured isoeffective dose to the calculated dose normalized to the target dose is 8 % and 9 % on average for the stationary and the compensated irradiation, respectively. In the target region the relative difference is even lower (6 %).

We presented a setup which allows cell survival measurements for stationary and moving targets with a high spatial resolution. Comparison of the experimental data to calculations reveals good agreement of calculation and measurement.

References

[1] Haberer et al., *NIM* **A330** (1993) 296-305
[2] Bert et al., *Med. Phys.* **34** (2007) 4768-4771
[3] Krämer et al., *PMB* **45** (2000) 3319-3330
[4] Elsässer & Scholz, *Rad. Res.* **167** (2007) 319-329
[5] N.Saito et al., This report.
[6] Bert & Rietzel, *Radiat. Oncol.* **2**:24 (2007)
[7] Schmidt et al., *Med. Phys.* (submitted)

* This work is partially supported by Siemens Medical Solutions, Particle Therapy.

Development of a new raster scan control system for Cave A

P. Steidl and D. Schardt
GSI, Darmstadt, Germany

For future space research experiments in Cave A and in the BIOMAT-Cave of FAIR it is necessary to develop a raster scan system, that performs uniform large-area irradiations for all particles from protons up to uranium and a wide range of energies and intensities. Cave A is still equipped with the prototype of the raster scan system [1] which was upgraded [2] in 2001 by implementing the FactoryLink software which is used for patient treatments in Cave M since 1997.

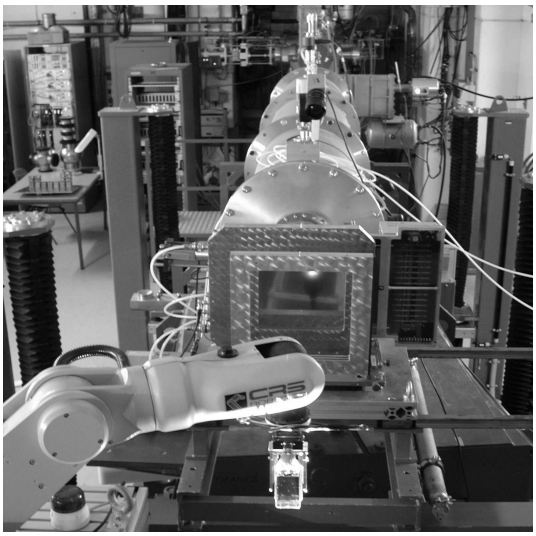

Figure 1: Irradiation of a biological sample using the raster scanner in Cave A

In order to meet the typical requirements of radiobiology and space-related experiments and to facilitate their performance it was decided to replace the FactoryLink software by a LabVIEW program running on a Windows PC. This solution offers the advantage to further employ the existing VME system that has proven to be highly reliable and contains the fast control boards (**S**teuer- und **A**uslese-**M**odul SAM[3]) equipped with DSP processor units. These modules request and abort the beam, control the scanner magnet power supplies and count pulses from the intensity measuring system. Via an optical link bridge the VME crate is controlled by the new LabVIEW control software which runs on a DELL Precision workstation. The E7 (VME-PowerPC) is no longer used for raster scan controlling, it only handles VME arbitration.

The new control software combines all the steps from irradiation planing to processing control in one program whereas several different programs had to be used in the old system. Starting with the input of the main irradiation parameters (projectile, energy, machine number, focus, field size and the desired dose or fluence) the new control software calculates all necessary plan data such as settings of the scanner power supplies or desired pulses per position that represent the precalculated number of particles that shall be delivered to each position.

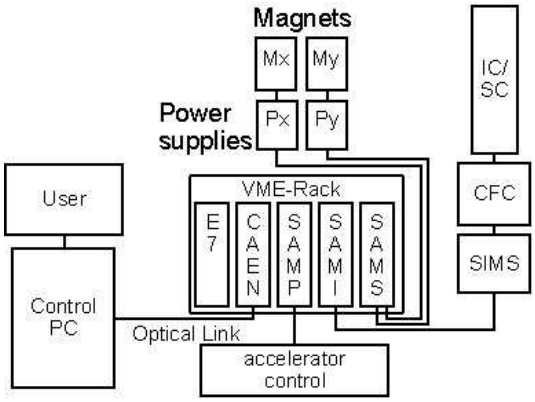

Figure 2: Schematic diagram of the scanner control system

Depending on the desired particle flux the beam intensity is measured by single-ion counting (e.g. scintillation detector), ion chambers (IC) or secondary-electron-monitors (SEM). The electric charge collected by the IC or SEM is fed into a charge-to-frequency converter (CFC) which delivers counting pulses to the scanning control system. Several calibration profiles that perform automatically conversion of actual beam intensity (ions/s) to pulse frequency output of the CFC are provided by the control system to support the user. In addition the beam intensity for optimum performance of the raster scanner is suggested. The maximum tolerable beam intensity is limited by the dynamics of the magnet power supplies.

After initializing the SAMs the plan is loaded and verified and irradiation can be started. The user can define a number of reruns which are executed automatically by the system. Irradiation can be interrupted by the user and taken up again at the last treated raster point. The progress of irradiation is visualized in real time by marking the raster points which have been processed. Optionally the actual beam positions can be measured by a multi-wire proportional chamber and used in a feedback loop for position correction in real time as demonstrated in [2].

References

[1] Th. Haberer et. al. Nucl. Instr. and Meth. 330, 296 (1993)

[2] D. Schardt et. al. GSI Scientific Report 2001, p. 169

[3] J. Hoffmann, Steuerungs- und Auslesemodul - technische Spezifikation, GSI, unpublished

Status Report of the HIT Project

U. Weinrich for the GSI therapy accelerator team

Abstract

Major progress of the Heidelberg ion beam cancer therapy centre took place in 2007. The first turn of the beam in the synchrotron was reached on February, 7th. First beam in a treatment room was achieved on March, 20th. Until December, 16th the beam performance in the first two treatment rooms was pushed to the quality which is required for patient treatment. The LINAC was rendered to clinic for operation responsibility in June. The handing over of the accelerator parts up to three horizontal beam stations to the clinic is actually in preparation.

In parallel to the beam commissioning work the worldwide first gantry for carbon beam was assembled during the year 2007. After finishing the extensive survey and alignment campaign for the gantry components the beam commissioning started in January 2008. The first beam at the isocenter of the gantry was measured on January, 4th. The main focus of the GSI work is now to finalise the beam commissioning for the gantry.

Beam commissioning of the Accelerator

In January 2007 the **M**edium **E**nergy **B**eam **T**ransport line (MEBT), the synchrotron and the **H**igh **E**nergy **B**eam **T**ransport Line (HEBT) were connected to the LINAC. The beam commissioning started in February and already on February, 7th the first turn of the beam was reached in the synchrotron.

Rapidly beam could be captured and accelerated in the synchrotron and the first beam extraction took place on March, 12th. Then the beam was transported further down the HEBT and first beam in the isocenter of the horizontal treatment room 2 could be measured on March, 20th. It should be notred, that the beam diagnostic components for all the accelerator sections had been delivered by GSI. [1]

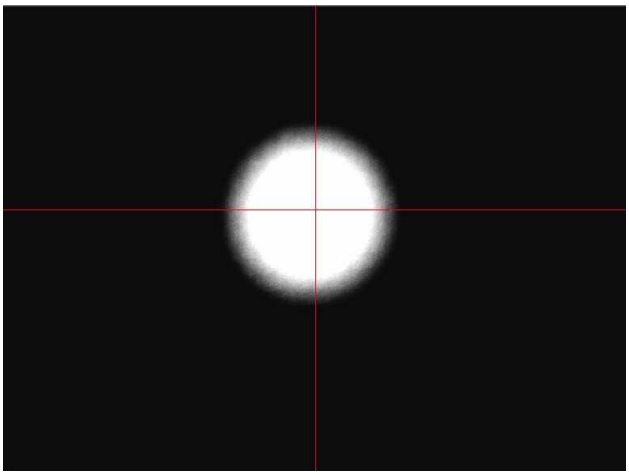

Figure 1: First beam in horizontal place 2 measured with the isocenter diagnostic

All the rest of the year the beam commissioning was needed to push the beam performance to the full requirements needed for patient treatment. A full set of any combination of 255 energies, 10 different intensities and four beam sizes had to be tuned for both carbon and proton beams and for each of the two horizontal treatment rooms. This effort required a significant amount of automatic interpolation features of the accelerator control system. [2]. In addition new operation modes were established, like the spill-interupt process (see Fig. 2).

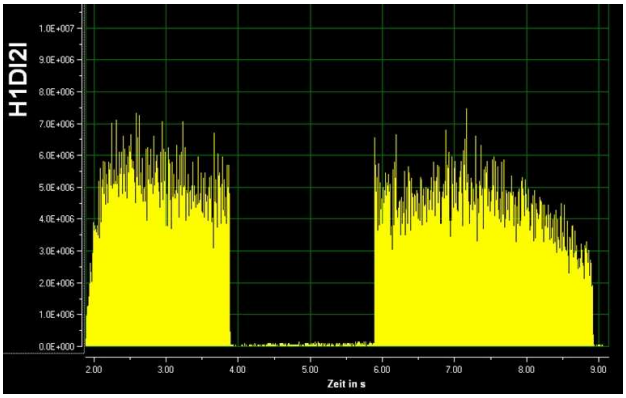

Figure 2: extracted beam with spill-interrupt

From March on the beam was also delivered to the treatment rooms for the commissioning with beam of the treatment technique, which is delivered by the company Siemens Medical Solutions. The accelerator operation for this task was performed by the HIT GmbH, the operating company of the university hospital.

Figure 3: Horizontal treatment place

In June the beam performance tests, the documentation and the training of the operation staff had reached the point that the LINAC could be handed over to the HIT

GmbH for operation. The next step, i.e. to hand over the MEBT, the synchrotron and the HEBT is actually being prepared.
After having reached the full beam performance for patient treatment the remaining commissioning work at the horizontal treatment places is now mainly to be done by the Siemens Medical Solutions. Some GSI experts support with their expertise the clinic in the risk analysis for the accelerator part of the facility.

Progress of the carbon gantry

The main components of the gantry support structure were delivered on January, 19th, 2007. From that date on the assembly of the gantry took place. Delivery and assembly were executed by MT Mechatronics [3]. A major issue was the correct installation and test of the various power and signal cables of the components mounted on the gantry.

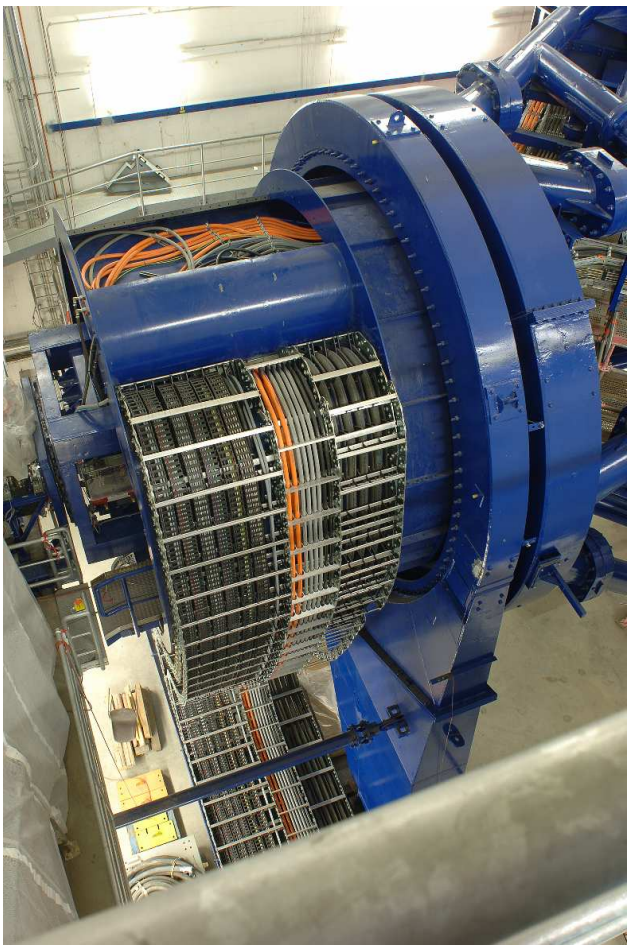

Figure 4: Cable tray for the Gantry

After having assembled the gantry main supporting structure the gantry was ready for its first rotation, which took place on April, 21st.

After having finished the assembly of the beam line components and the cabling work the survey and alignment of the gantry components took place. All relevant beam line components had to be precisely adjusted; their exact position had to be afterwards measured for a number of different Gantry angles. The restricted access to the gantry components led to difficult and rather unusual working conditions.
During the second half of the year also the treatment room of the gantry was fully equipped. Given the size of the gantry most of the patient near equipment including the X-Ray diagnostics will rotate together with the gantry.

In January 2008 the beam commissioning of the QA (Quality Assurance place) and the gantry was started. The transport of Carbon and proton to the isocenter of both stations was reached within one week.

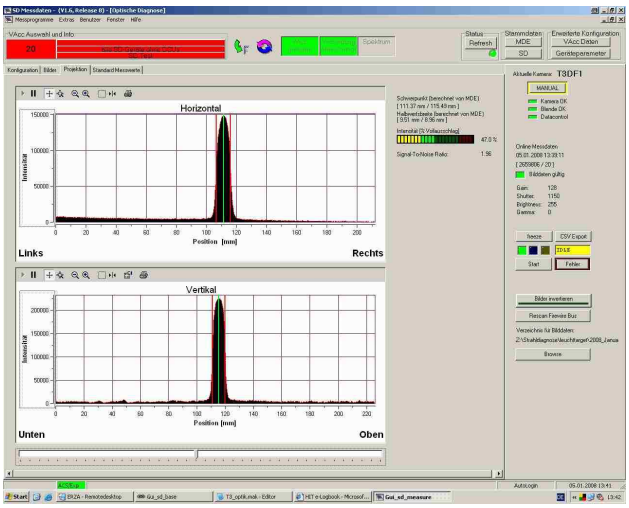

Figure 5: Carbon beam in the isocenter of the gantry patient room

This is the first time world wide that carbon ions can be delivered to an isocenter from many different directions. The main focus of the GSI work during the following months will be to establish the beam performance also to the quality required for patient treatment. Given the fact that the full set has to be achieved for all gantry angles represents a major challenge for this work.

References

[1] M. Schwickert and A. Peters, "DIAGNOSTIC INSTRUMENTATION FOR MEDICAL ACCELERATOR FACILITIES", DIPAC 2007 Venice.
[2] T. Fleck, R. Bär, M. Schwickert, "REQUIREMENTS AND COHERENT REALIZATION OF THE HICAT CONTROL SYSTEM FUNTIONALITY FOR TEST, COMMISSIONING AND OPERATION", ICALEPCS 2007.
[3] Hans-Thomas Zimmerer (MT Mechatronics), "NEW CANCER RADIATION THERAPY FACILITY", December 2007, National Cancer Center Egypt.

HIT Linac upgrade

M. Maier[1], W. Barth[1], A. Orzhekhovskaya[1], B. Schlitt[1], H. Vormann[1], S. Yaramyshev[1], R. Cee[2]
[1]GSI, Darmstadt, Germany, HIT, [2]Heidelberg, Germany

Introduction

During commissioning of the HIT-Linac [1] the maximum achievable transmission was about 20%. The reasons were the poor performance of the ion sources, the field errors of the solenoid matching the beam to the RFQ, the radial matching section of the RFQ itself and the deformed electrodes due to mechanical stress on the tank. Thus a detailed upgrade program was defined and started in 2007 (see Table 1).

Table 1: Timeline of the upgrade program

Apr.-Dec. 2006	Linac commissioning
Aug. 2007	exchange of the solenoid
	Emittance measurements before and behind the new solenoid
Nov. 2007	New RFQ tank copper plated
Dec. 2007	RFQ design of new input radial matcher ready and approved by the HIT company.
Outlook	
until Apr. 08	Machining of the electrodes at NTG
until Jun. 08	Assembly and RF tuning at IAP
Jul. – Sep 08	RFQ test at Danfysik, Denmark

Measurements

In August 2007 the transverse beam emittances were measured for different ion species in front and behind the new solenoid. The main goals were to check the quality of the new solenoid which, according to 3D-field mapping data, has a 16 times smaller field deviation and to approve the final design of a new RFQ Input Radial Matcher (IRM) based on the particle distributions generated from the measured emittance. The improvement of the solenoid could be seen directly in the steering behaviour shown in Figure 1.

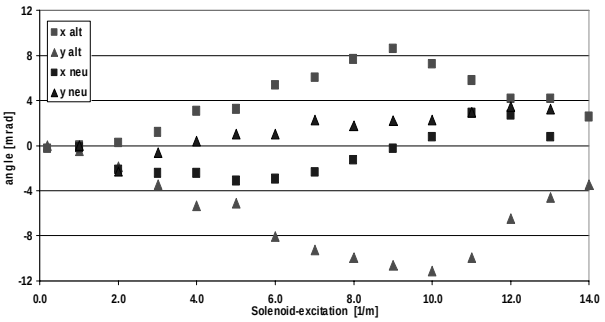

Figure 1: Old (red) and new (blue) solenoid steering

As the HIT-company decided to postpone the necessary ion source upgrade [2]. For this reason it was not possible to measure the beam emittance at the design ion currents. Therefore, the final design of the IRM is based on emittance measurements of the commissioning in 2006 only. (Figure 2).

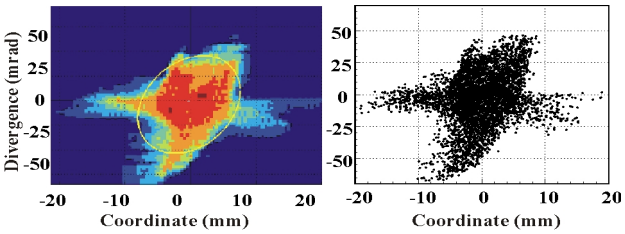

Figure 2: Measurement of the horizontal 200µA C^{4+} beam emittance (left) and the particle distribution (right).

Simulations and Design

The results of the numerous beam dynamics simulation show, that a minor change of the RFQ aperture at the beginning of the electrodes (IRM) leads to an increase of the calculated RFQ transmission from 50% to 75% (Figure 3). The present design of the RFQ electrodes requires a too strong beam convergence at the RFQ entrance.

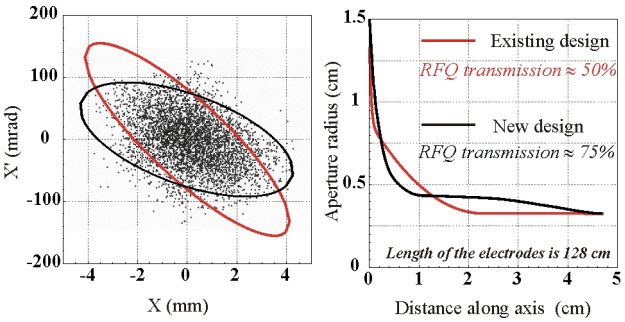

Figure 3 Left: particle distribution at the RFQ entrance; the ellipses represent the acceptance of the present (red) and new RFQ design (black). Right: electrode geometry of the present (red) and new (black) RFQ designs.

Simulations assuming deformed electrodes show that this effect can explain the difference in the measured (~20%) and calculated (~50%) transmission. The new tank, which has to avoid a deformation of the RFQ accelerating channel, has been stiffened and was copper-plated. This new RFQ design will be tested and commissioned with beam at Danfysik, Denmark by autumn 2008.

Acknowledgments

The authors would like to thank the HIT staff for their commitment in the upgrade program.

References

[1] M. Maier et al., LINAC Commissioning for the Heavy Ion Cancer Therapy Facility HIT, An. Rep. 2006, p. 373.
[2] T. Winkelmann, ECR ion source experience at the Heidelberg Ion Beam Therapy Centre, RSI 79, 1 (2008) to be published.

Beam Diagnostics for HIT – Results of Commissioning Phase

A. Reiter, R. Boywitt, C. Dorn, H. Graf, T. Hoffmann, W. Kaufmann, P. Kowina,
C. Müller, H. Reeg, B. Voss, M. Witthaus and M. Schwickert
GSI, Darmstadt, Germany

As part of the GSI duties for the Heidelberg Ion Therapy (HIT), GSI Beam Diagnostics (BD) group acted as contractor for the delivery of beam diagnostic devices. This contract includes production of the mechanical parts (feed-throughs, detectors etc.) as well as installation and commissioning of the 92 different diagnostic devices at the HIT facility and, additionally, integration of the data acquisition into the accelerator control system.

Beam Diagnostic Devices for the HIT Linac and Synchrotron

Between 2004 and 2005 the majority of BD devices was constructed at GSI and had to pass successive factory acceptance tests. Together with the vacuum components that were initially stored at GSI, all BD devices were transported to the HIT facility in spring 2006. During that year the components were installed in the beam lines, while the finished low energy sections with two ECR ion sources were commissioned using the new BD equipment.

In December 2006 the commissioning of the 7 MeV/u Linac, a RFQ followed by an IH Linac, was finished. After the medium energy beam transport section had been commissioned in January 2007, the first beam was injected into the synchrotron in February. The synchrotron is equipped with 6 beam-position monitors (1 BPM per period), 6 mobile beam-loss monitors, 1 AC- and 1 DC-transformer, 1 viewing screen for first turn analysis and 2 pairs of Schottky-pickups. The BPMs were especially designed and matched to the parameters of the HIT synchrotron [1]. The first complete turn of the beam was detected with the fluorescence screen in the diagnostic chamber of period 1, just before re-entry into the injection septum. The AC-transformer senses the current during multi-turn injection, while the DC-transformer monitors the beam intensity during acceleration and extraction phases. To optimize the knock-out extraction a second fluorescence screen is installed just behind the extraction septum inside the septum vacuum chamber.

Beam Diagnostics in the HEBT Section

In the HEBT section 12 additional fluorescence screens are mounted on pneumatic drives for beam alignment during standard operation. Like the synchrotron screens the fluorescence light is digitized by a CCD camera (AVT F033-B Marlin) [2]. The CCD cameras are connected to a FireWire network, partly using optical links to bridge long cable distances.

To determine spill structure and absolute intensity, the beam lines are equipped with 5 scintillators and 13 sandwich detectors, consisting of a pair of a multi-wire proportional chamber (MWPC) and an ionization chamber (IC).

Multi-Wire Proportional Chambers

The multi-wire proportional chambers are part of a combined detector consisting of a MWPC at the front (in beam direction) and an ionization chamber at the back [3]. The detectors are mounted inside a stainless steel cylinder with two 50 µm foil windows that is moved into the beam trajectory by a pneumatic drive. As detector gas serves an Ar/CO_2 (80%/20%) mixture.

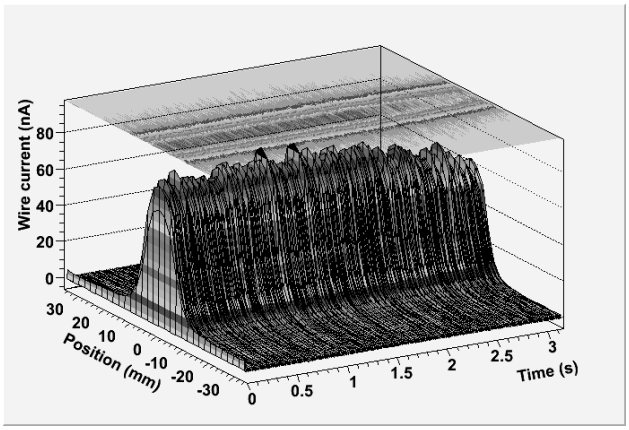

Figure 1: Waterfall plot of vertical beam profiles (slow extraction) measured with sampling rate of 315 Hz

The active area of 70x70 mm^2 is covered in each of the two MWPC planes by 64 wires with a spacing of 1.1 mm. Two adjacent wire signals are summed at the input of a high-resolution integrator circuit with selectable integration time (100 µs to 6 s), multiplexed by a control unit and sequentially digitized by an ADC board.

The control unit operates in two modes. In 'standard-mode' the profiles of several detectors may be recorded once for every trigger signal (usually at the center of the spill). Typically this mode is used to determine the beam axis along straight sections of the HEBT with two MWPCs. The 'fast-mode' allows cyclic measurements of beam profiles within a single spill with one MWPC at a maximum rate of about 850 Hz. Figure 1 presents a fast-mode measurement started at the center of a Carbon spill of 430 MeV/u energy and a repetition rate of 315 Hz. Start and stop trigger can be configured by the operators via programmable timing units. The plot shows the good homogeneity of the transversal spill structure. For more detailed investigations the beam centre-of-mass and beam width (FWHM) are displayed as a function of time in the control system. This functionality is an important tool for machine tuning during optimization of the beam optics, e.g. focus settings at the patient position.

Ionization Chambers

The ionization chambers (IC) are mounted behind the MWPCs and therefore beam intensity and profile can be measured simultaneously. A fast current-to-frequency converter [4] produces a pulse train of NIM signals which is recorded by a multi-channel scaler. Scintillator and beam-loss monitor signals are fed to discriminators and read out by identical scalers in a common DAQ system.

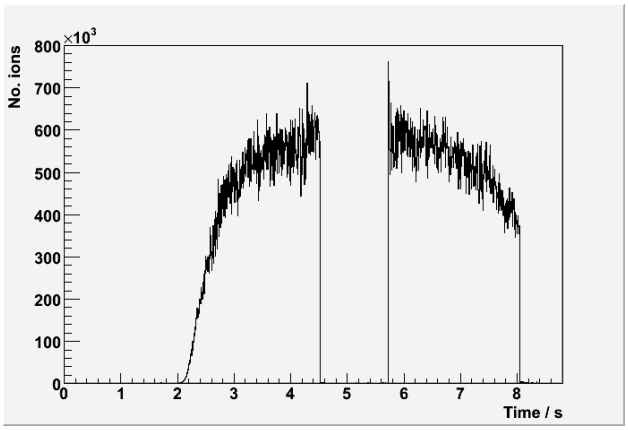

Figure 2: Spill structure with 1 second spill break

The compact PCI scaler boards allow data of all 24 channels to be acquired at 1 kHz (standard) or from up to 3 channels at 10 kHz via DMA access for precision measurements of the spill structure. Based on chamber geometry and energy loss of the ions in the gas mixture, the absolute number of particles can be calculated from the IC count rate. At low intensities this absolute calibration is verified by comparison of IC and scintillator count rates. Figure 2 shows data of a spill-break test recorded at a moderate sampling frequency of 200 Hz. The spill-break is an important functionality of the extraction system that can be triggered directly by the therapy control system. These time-resolved measurements help to optimize the synchrotron extraction in order to produce a nearly uniform spill at a maximum transmission through the HEBT beam lines.

Beam Diagnostics for Horizontal Treatment Places and the Gantry

At the two horizontal treatment places, as well as at the gantry so-called isocenter-diagnostic setups are used to verify position and transversal profile at the isocenter, i.e. the point where the ion beam is applied to the patient. These devices consist of a 300 by 226 mm scintillating screen (P43) monitored by a double Peltier-cooled high-resolution CCD camera [5]. An important advantage is the digitization of the beam profile directly at the beam line, thus minimizing cable noise and image distortions. The whole setup is mounted inside a black metal housing to protect camera and scintillator against external stray light. For the measurements the setup is mounted on the patient robot which moves the screen precisely into the isocenter-position (see fig. 3).

In March 2007 the first beam was reported in the horizontal treatment room and early in 2008 gantry commissioning began.

Figure 3: Robot arm with isocenter-diagnostics at the patient position in front of the beam nozzle (at right)

Figure 4 shows the distribution of the first beam (220 MeV protons) at the gantry exit. For profile measurements at low beam intensities the noise level must be kept as small as possible. The position resolution of this setup is approximately 300 µm per CCD-pixel.

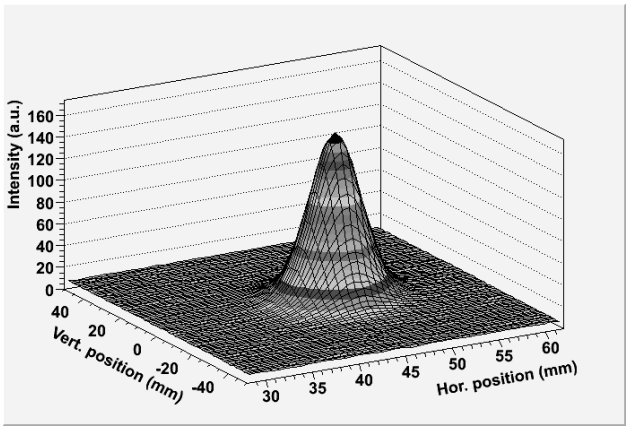

Figure 4: Beam distribution of 220 MeV protons at gantry exit

References

[1] P. Kowina, W. Kaufmann, et al., “Optimisation of ‘shoe-box type’ type beam position monitors using the finite element method”, DIPAC 2005, Lyon
[2] www.alliedvisiontec.de
[3] B. Voss et al., “Beam Monitor for the High-Energy Beam Line of HIT”, GSI Annual report 2005, p. 402
[4] H. Reeg, “A current digitizer for ionisation chambers/ SEMs with high resolution and fast response time”, DIPAC 99, Chester, UK
[5] IEEE1394 Digital CCD camera C4742-80-12AG, User Manual (ver. 1.1), December 2003, Hamamatsu Photonics K.K., Japan

Status of the Linac for the Italian Hadron-Therapy Centre CNAO

B. Schlitt[1], H. Vormann[1], G. Clemente[1], M. Hörr[1], G. Hutter[1], M. Pilz[1], A. Reiter[1], G. Riehl[1], W. Vinzenz[1], E. Feldmeier[2], B. Hofmann[3], U.Ratzinger[3], A. Schempp[3]
[1]GSI, Darmstadt, Germany; [2]HIT, Heidelberg, Germany; [3]IAP, Frankfurt University, Germany

Introduction

The Italian hadron-therapy centre CNAO (Centro Nazionale di Adroterapia Oncologica) [1] is designed for the treatment of tumours with proton and light ion beams and to clinical and radiobiological research. The design consists of two ECR ion sources, a 7 MeV/u injector linac identical to the linac of the Heidelberg ion therapy centre HIT [2][3] and a 400 MeV/u synchrotron. GSI delivers technical support in terms of all linac components [4]: copper-plating, assembly, RF tuning and pre-tests of RFQ, IH-DTL and debuncher (together with IAP, Frankfurt University), pre-assembly of beam line sections with frames, tests of RF amplifiers, linac sub-control system and power supplies. Furthermore, GSI has delivered various beam diagnostics components, to be used along LEBT, linac and MEBT [4][5]. The installation of all linac components on the CNAO site in Pavia as well as the commissioning will be supported.

Status of Linac Components

After successful beam operation of the RFQ at GSI in 2006 [4], the CNAO 200 kW RF amplifier was returned to THOMSON in January 2007. Various additional RF low level tests have been performed with the RFQ in 2007 (verification of the field distribution and investigation of a variable tuner for the integrated drift-tube rebuncher section). High power tests of the RFQ are planned for the RFQ commissioning in Pavia in 2008.

After various pre-assembly work and qualification (fiducialisation) of all linac components at GSI, the RFQ has been sent to Pavia in November 2007 together with the steerer devices, the stripper chamber and vacuum components. All beam diagnostics components were delivered to Pavia in 2007.

First low level RF measurements of the IH-DTL [4] were performed in January 2007. RF tuning was completed in August 2007, profiting from the experiences with the Heidelberg IH-DTL [6]. Vacuum tests have been finished in February 2008.

The debuncher cavity (Fig. 1) was assembled and tuned at IAP until January 2008, based on a new design [7], developed with Micro Wave Studio. Delivery of the IH-linac and the debuncher to Pavia is planned for March 2008.

Several integration tests of the linac sub-control system delivered by ECKELMANN AG into the CNAO accelerator control system were successfully performed at GSI during 2007, including read-out tests of measurement data from beam diagnostic systems delivered by GSI and tests of the timing interface. Installation of the system and commissioning in Pavia is planned for March/April 2008.

Fig. 1: Open debuncher cavity with spiral and drift tube.

Factory acceptance tests of three RF amplifiers for pulse powers of 1400 kW, 200 kW and 4 kW (produced by THOMSON) took place during 2006 and 2007. All three systems were delivered and installed in Pavia in November 2007. Installation of the RF transmission lines and cables in Pavia has been finished in February 2008 by THOMSON. The magnet power supplies from JAEGER were installed and cabled in Pavia by CNAO.

Outlook

During 2007 the accelerator infrastructures (cooling water system, cabling, false floors, etc) have been installed by CNAO as well as the ECR ion sources delivered by PANTECHNIK and major parts of the LEBT. First ion source tests have been performed in May 2007. Linac installation and commissioning has been prepared together with GSI, including the layout of three beam diagnostic test benches for beam commissioning.

Commissioning of LEBT and ion sources as well as of the linac RF system and of the JAEGER power supplies will start soon. Linac installation and commissioning in Pavia is scheduled for the second half of 2008.

We would like to thank our partners from CNAO for the cooperation, as well as our colleagues at GSI for the committed support in all required works.

References

[1] S. Rossi, Proc. EPAC 2006, p. 3631.
[2] M. Maier, B. Schlitt et al., Proc. PAC 2007, p. 2734.
[3] M. Maier, et al., GSI Sci. Rep. 2006, p. 373.
[4] B. Schlitt et al., GSI Sci. Rep. 2006, p. 383.
[5] A. Reiter et al., Proc. EPAC 2006, p. 1028.
[6] G. Clemente et al., GSI Sci. Rep. 2006, p. 376.
[7] E. Feldmeier, private note, 2007.

Annex

Scientific Management

Director: H. Stöcker
Compiled by: S. Bergelt-Brückner, G. Meyer

Publications

FAIR and its experimental program
W. Henning
Proceedings Quark Matter 2006 - The 19th International Conference on Ultra-Relativistic Nucleus-Nucleus Collisions (Shanghai, China, 14-20 November 2006)
Journal of Physics G: Nuclear and Particle Physics, Volume 34, No. 8, August 2007

Black Holes at LHC?
B. Koch, M. Bleicher, and H. Stöcker
[hep-ph/0702187] 9 pp.
Quark Matter 2006, Proceedings of the 19th Int. Conference on
Ultra-Relativistic Nucleus-Nucleus collisions, Shanghai, China, 14-20
November 2006, guest-eds.: Y.-G. Ma, E.-K. Wang, X. Cai, H.-Z. Huang,
X.-N. Wang, and Z.-Y. Zhu
J. Phys. G: Nucl. Part. Phys. 34, S535-S542 (2007)

Early black hole signals at the LHC
B. Koch, M. Bleicher, and H. Stöcker
AIP Conf. Proc. 947, 376-382 (2007)

Charmonium dynamics in Au+Au collisions at ? s = 200 GeV
O. Linnyk, E.L. Bratkovskaya, W. Cassing, and H. Stöcker
[nucl-th/0705.4443]
Phys. Rev. C76, 041901 (R), 4 pp. (2007)

(1+1) Dimensional Hydrodynamics for High-energy Heavy-Ion Collisions
L.M. Satarov, I.N. Mishustin, A.V. Merdeev, H. Stöcker
[hep-ph/0611099] Nov 2006, 43 pp.
Phys. Atomic Nuclei 70 (19), 1773-1796 (2007)

Longitudinal fluid dynamics for ultrarelativistic heavy-ion collisions
L.M. Satarov, I.N. Mishustin, A.V. Merdeev, H.Stöcker
[hep-ph/0606074]
Phys. Rev. C 75, 024903, 10 pp. (2007)

Transport model analysis of the transverse momentum and rapidity
dependence of pion interferometry at SPS energies
Q. Li, M. Bleicher, X. Zhu, and H. Stöcker
[nucl-th/0612030]
J. Phys. G: Nucl. Part. Phys. 34, 537-548 (2007)

Stable TeV Black Hole Remnants at the LHC: Discovery through Di-Jet
suppression, Mono-Jet Emission and a Supersonic Boom in the Quark-Gluon
Plasma
H. Stöcker
[hep-ph/0605062]
Int. J. Mod. Phys. D 16, Nos 2&3, 185-205 (2007)

D anti-D correlations as a sensitive probe for thermalization in high
energy nuclear collisions
X. Zhu, M. Bleicher, S.L. Huang, K. Schweda, H. Stöcker, N. Xu, P. Zhuang
[hep-ph/0604178] (Apr 2006) 4 pp.
Phys. Lett. B 647, 366-370 (2007)

Has the QCD Critical Point Been Signaled by Observations at the BNL
Relativistic Heavy Ion Collider?
R.A. Lacey, N.N. Ajitanand, J.M. Alexander, P. Chung, W.G. Holzmann, M.
Issah, A. Taranenko,
P. Danielewicz, and Horst Stöcker
[nucl-ex/0609025]
Phys. Rev. Lett. 98, 092301, 4 pp. (2007)

Charmonium dynamics in nucleus-nucleus collisions at SPS and FAIR energies
O. Lynnik, E.L. Bratkovskaya, W. Cassing, H. Stöcker
Nucl. Phys. A 786, 183-200 (2007)

Special Issue: International Symposium on Heavy Ion Physics, Frankfurt
am Main, Germany, 3-6 April 2006
eds.: J. Reinhardt & H. Stöcker
Int. J. Mod. Phys. E, 16/3 (Part 1 of 2). World Scientific, April 2007,
vi + 643-936 pp.(2007)

Special Issue: International Symposium on Heavy Ion Physics, Frankfurt
am Main, Germany, 3-6 April 2006
eds.: J. Reinhardt & H. Stöcker
Int. J. Mod. Phys. E, 16/4 (Part 2 of 2). World Scientific, May 2007,
937-1300 pp. (2007)

Equilibration of matter in relativistic heavy-ion collisions
L. Bravina, I. Arsene, M.S. Nilsson, K. Tywoniuk, E. Zabrodin, M.
Bleicher, H. Stöcker, and W. Greiner
Int. J. Mod. Phys. E16, 777-786 (2007)

Complex Structures in Elementary Matter. Proceedings of the
International Symposium on Heavy Ion Physics 2006
J. Reinhardt and H. Stöcker
World Scientific, 676 pp. (2007)

Pion freeze-out as seen through HBT correlations in heavy ion collisions
from FAIR/AGS to RHIC energies
Q. Li, M. Bleicher, and H. Stöcker
[nucl-th/0706.2091]
J. Phys. G: Nucl. Part. Phys. 34, no 9, 2037-2044 (2007)

An Introduction to Mini Black Holes at LHC
H. Stöcker, B. Koch, and M. Bleicher
Proceedings of ISMD 2006, 36th Int. Symp.on Multiparticle Dynamics, 2-8
September 2006, Paraty, Brazil, eds.: Y. Hama, T. Kodama, and F.S. Navarra
Braz. J. Phys. 37, No 2C June 2007, 836-839 (2007)

Mach cones and jet energy loss studies in full (3-1) dimensional ideal
hydrodynamics
B. Betz, K. Paech, D.H. Rischke, and H. Stöcker
Int. J. Mod. Phys. E, 16/7&8 (Part 1 of 2), 1957-1963 (2007)

Signatures for Black Hole production from hadronic observables at the
Large Hadron Collider
Th.J. Humanic, B. Koch, and H. Stöcker
[hep-ph/0607097] Jul 2006, 11 pp.
Special Issue: International Symposium on Heavy Ion Physics (ISHIP
2006), Frankfurt am Main, Germany, 3-6 April 2006
Int. J. Mod. Phys. E, 16/4 (Part 2 of 2), 841-852 (2007)

Has the QCD Critical Point been Signaled by Observations at RHIC?
R.A. Lacey, N.N. Ajitanand, J.M. Alexander, P. Chung, W.G. Holzmann, M.
Issah, A. Taranenko, P. Danielewicz , and H. Stöcker
[nucl-ex/0609025]
Phys. Rev. Lett. 98, 092301-092304 (2007)

In-medium properties of D-mesons at FAIR
L. Tolos, J. Schaffner-Bielich, and H. Stöcker
Dec 2006. 4pp.
To appear in the proceedings of 9th International Conference on
Hypernuclear and Strange Particle Physics (HYP 2006), Mainz, Germany,
10-14 Oct 2006.
[nucl-th/0612077]

(3+1)-Dimensional Hydrodynamic Expansion with a Critical Point from
Realistic Initial Conditions
J. Steinheimer, M. Bleicher, H. Petersen, S. Schramm, H. Stöcker, and D.
Zschiesche
[nucl-th/0710.0332] 8 pp.

MACE -- Mach cones in heavy ion collisions
B. Baeuchle, L. P. Csernai, and H. Stoecker
[nucl-th/0710.1476]

Charmonium dynamics in heavy ion collisions
O. Linnyk, E.L. Bratkovskaya, W. Cassing, and H. Stoecker
[nucl-th/0710.1535]

Parity Doublet Model applied to Neutron Stars
V. Dexheimer, S. Schramm, and H. Stoecker
Proc. Int. Symp. on Exotic States of Nuclear Matter, Catania, Italy,
11-15 Jun 2007
[astrop-ph/0710.3067]

PQCD calculations of elliptic flow and shear viscosity at RHIC
Zhe Xu, C. Greiner, and H. Stöcker
[nucl-th/0711.0961] 4 pp.

Mach cones at central LHC collisions via MACE
B. Bäuchle, H. Stöcker, and L.P: Csernai
Contr. to Workshop on Heavy Ion Collisions at the LHC: Last Call for

Predictions, Geneva, Switzerland, 14 May-8 Jun 2007
[nucl-th/0707.0054] 2 pp.

Strangeness in Relativistic Astrophysics
J. Schaffner-Bielich, S. Schramm, and H. Stöcker
Lectures given at International Conference on Strangeness in quark
Matter (SQM 2007), Levoca, Slovakia, 24-29 Jun 2007
[astro-ph/0711.2639]

Collapse of flow: Probing the order of the phase transition
H. Stöcker
To appear in the Proc. 4th Int. Workshop on Critical Point and Onset
Deconfinement, Darmstadt, Germany, 9-13 Jul 2007
[hep-ph/0710.5089] 12 pp.

Charmed signatures for phase transitions in heavy-ion collisions
Contributed to 4th Int. Workshop on Critical Point and Onset
Deconfinement, Darmstadt, Germany, 9-13 Jul 2007
[nucl-th/0709.2185] 10 pp.

Heavy Ion Collisions at the LHC - Last Call for Predictions
S. Abreu, V. Akkelin, J. Alam, J.L. Albacete, A. Andronic, D. Antonov, F. Arleo, N. Armesto, I.C. Arsene, G.G. Barnafoldi, J. Barrette, B. Bauchle, F. Becattini, B. Betz, M. Bleicher, M. Bluhm, D. Boer, F.W. Bopp, P. Braun-Munzinger, L. Bravina, W. Busza, M. Cacciari, A. Capella, J. Casalderrey-Solana, R. Chatterjee, L.-W. Chen, J. Cleymans, B.A. Cole, Z.Conesa Del Valle, L.P. Csernai, L. Cunqueiro, A. Dainese, J.Dias de Deus H.-T. Ding, M. Djordjevic, H. Drescher, I.M.Dremin A. Dumitru, A. El, R. Engel, D. d'Enterria, K.J. Eskola, G. Fai, E.G. Ferreiro, R.J. Fries, E. Frodermann, H. Fujii, C. Gale, F. Gelis, V.P. Goncalves, V. Greco, C. Greiner, M. Gyulassy, H. van Hees, U. Heinz, H. Honkanen, W.A. Horowitz, E. Iancu, G. Ingelman, J. Jalilian-Marian, S. Jeon, A.B. Kaidalov, B. Kampfer, Z.-B. Kang, Iu.A. Karpenko, G. Kestin, D. Kharzeev, C.M. Ko, Benjamin Koch, B. Kopeliovich, M. Kozlov, I. Kraus, I. Kuznetsova, S.H. Lee, R. Lednicky, J. Letessier, E. Levin, B.-A. Li, Z.-W. Lin, H. Liu, W. Liu, C. Loizides, I.P. Lokhtin, M.V.T. Machado, L.V. Malinina, A.M. Managadze, M.L. Mangano, M. Mannarelli, C. Manuel, G. Martinez, J.G. Milhano, A. Mocsy, D. Molnar, M. Nardi, J.K. Nayak, H. Niemi, H. Oeschler, J.-Y. Ollitrault, G. Paic, C. Pajares, V.S. Pantuev, G. Papp, D. Peressounko, P. Petreczky, S.V. Petrushanko, F. Piccinini, T. Pierog, H.J. Pirner, S. Porteboeuf, I. Potashnikova, G.Y. Qin, J.-W. Qiu, J. Rafelski, K. Rajagopal, J. Ranft, R. Rapp, S.S. Rasanen, J. Rathsman, P. Rau, K. Redlich, T. Renk, A.H. Rezaeian, D. Rischke, S. Roesler, J. Ruppert, P.V. Ruuskanen, C.A. Salgado, S. Sapeta, I. Sarcevic, S. Sarkar, L.I. Sarycheva, I. Schmidt, A.I. Shoshi, B. Sinha, Yu.M. Sinyukov, A.M. Snigirev, D.K. Srivastava, J. Stachel, A. Stasto, H. Stocker, C.Yu. Teplov, R.L. Thews, G. Torrieri, V.Topor Pop, D.N. Triantafyllopoulos, K.L. Tuchin, S. Turbide, K. Tywoniuk, A. Utermann, R. Venugopalan, I. Vitev, R. Vogt, E. Wang, X.N. Wang, K. Werner, E. Wessels, S. Wheaton, S. Wicks, U.A. Wiedemann, G. Wolschin, B.-W. Xiao, Z. Xu, S. Yasui, E. Zabrodin, K. Zapp, B. Zhang, B.-W. Zhang, H. Zhang, D. Zhou
[hep-ph/0711.0974] 185 pp.

Public Talks

Rutgers University, New Jersey, DNP-APS Town Meeting, Jan. 12-14, 2007
W. Henning
FAIR - Brief Description of the Facility
- Experimental Program (Strong Interaction Physics – QCD)

PSI, Villigen, Workshop on Precision Measurements at Low Energies , January 18-19, 2007
W. Henning
Facility for Antiproton and Ion Research
NSAC Town Meeting, Galveston, April 30 – May 2, 2007
W. Henning
Facility for Antiproton and Ion Research

RIKEN, Tokyo, International Nuclear Physics Conference, June 3 – 8, 2007
W. Henning
FAIR – Recent Developments and Status

W. Henning
FAIR – Instrument zur Erforschung der Materie
Jahresempfang des TÜV Hessen
15. März 2007

W. Henning
Strong with some strangeness: past and future perspectives of nuclear physics
Ehrenkolloquium Prof. Dr. Eckhart. Grosse
Forschungszentrum Dresden Rossendorf
23. Juli 2007

H. Stöcker
22.02.- 01.03.07 XXXVIII. Arbeitstreffen Kernphysik in Schleching

H. Stöcker
31.05.-02.06.07 Workshop on Predictions for RHIC at the LHC (at CERN Theory Institute): "Early black hole signals at the LHC"

H. Stöcker
11.06.-16.06.07 7th Latin American Symposium on Nuclear Physics and Applications in Cusco (Qosqo), Peru: "Early black hole signals at the LHC"

H. Stöcker
09.07.-13.07.07 4th International Workshop "Critical Point and Onset of Deconfinement" Darmstadt (GSI): "Collapse and Reappearance of Flow"

Teaching at Universities WS2006/07

Boller, Stöcker
Astrophysik III. Vorlesung, Universität Frankfurt/M.

Schaffner-Bielich, Stöcker
Astrophysikalisches Seminar – Physik des Universums, Seminar, Universität Frankfurt/M.

Dumitru, Greiner, Rischke, Schaffner-Bielich, Schramm, Stöcker
Chiral Models in Nuclear and Particle Physics, Seminar, Universität Frankfurt/M

Boller, Stöcker
Einführung in die Astronomie I, Vorlesung, Universität Frankfurt

Rischke, Bleicher, Dumitru, Greiner, Stöcker
Fluid dynamics for heavy ion collisions, Vorlesung, Universität Frankfurt

Appelshäuser, Bleicher, Blume, Dörner, Dumitru, Greiner, C., Greiner, W., Maruhn, Peters, Ratzinger, Rischke, Schaffner-Bielich, Schmidt-Böcking, Schramm, Stock, Stöcker, Ströbele, Stroth
Interuniversitäres Schwerionenseminar gemeinsam mit der GSI in Darmstadt

Appelshäuser, Bleicher, Blume, Dörner, Dumitru, Greiner, C., Greiner, W., Maruhn, Peters, Rischke, Schaffner-Bielich, Schmidt-Böcking, Schramm, Stock, Stöcker, Ströbele, Stroth
Kolloquium zur Struktur der elementaren Materie und zur Astrophysik

Appelshäuser, Blume, Gyulassy, Stöcker
Relativistic heavy ion physics – Theory and experiment (FIGSS)

Appelshäuser, Bleicher, Blume, Dumitru, Rischke, Schaffner-Bielich, Schramm, Stöcker, Stock, Ströbele, Stroth
Relativistic Nuclear Matter, geminsam mit der GSI und TU in Darmstadt und der Universität Heidelberg, Seminar

Bleicher, Dumitru, Greiner, C., Maruhn, Rischke, Shaffner-Bielich, Schramm, Stöcker
Seminar on the Theory of Elementary Matter (FIGSS)

Deiss, Stöcker
Struktur und Dynamik extragalaktischer Systeme, Vorlesung, Universität Frankfurt

Dumitru, Greiner, C., Rischke, Schaffner-Bielich, Schramm, Stöcker
Chiral Models in Nuclear and Particle Physics, Seminar, Universität Frankfurt

Berger, Greiner, W., Holm, von der Malsburg, Meyer-Hermann, Mishustin, Singer, Solov'yov, Stöcker, Triesch
FIGSS Seminar
Rische, Bleicher, Dumitru, Greiner, C., Stöcker
Fluid dynamics for heavy ion collisions, Seminar, Universität Frankfurt

Deiss, Stöcker,
Innere Struktur und Dynamik der Sterne, Vorlesung, Universität Frankfurt

Berger, Greiner, W., Holm, von der Malsburg, Meyer-Hermann, Mishustin, Singer, Solov'yov, Stöcker, Triesch
Interdisciplinary FIAS Colloquium

Appelshäuser, Bleicher, Blume, Dörner, Dumitru, Greiner, C., Greiner, W., Maruhn, Peters, Ratzinger,

Rischke, Schaffner-Bielich, Schmidt-Böcking, Schramm, Stock, Stöcker, Ströbele, Stroth
Interuniversitäres Schwerionenseminar gemeinsam-mit der GSI in Darmstadt

Appelshäuser, Bleicher, Blume, Dörner, Dumitru, Greiner, C., Greiner, W., Maruhn, Peters, Rischke, Schaffner-Bielich, Schmidt-Böcking, Schramm, Stock, Stöcker, Ströbele, Stroth
Kolloquium zur Struktur der elementaren Materie und zur Astrophysik, Universität Frankfurt

Bleicher, Dumitru, Greiner, C., Maruhn, Rischke, Schaffner-Bielich, Schramm, Stöcker
Seminar on the Theory of Elementary Matter, Universität Frankfurt

Scientific Management: Safety and Radiation Protection

Department leader: G. Fehrenbacher
Compiled by: G. Fehrenbacher

Publications

G. Fehrenbacher, F. Gutermuth, E. Kozlova, T. Radon, T. Aumann, S. Beceiro, T. Le Bleis, K. Boretzky, H. Emling, H. Johansson, O. Kiselev, H. Simon and S. Typel, Measurement of the fluence response of the GSI neutron ball in high-energy neutron fields produced by 500 AMeV and 800 AMeV deuterons, Radiation Protection Dosimetry, Advance Access published May 22, 2007, doi:10.1093/rpd/ncm100.

G. Fehrenbacher1, E. Kozlova, F. Gutermuth, T. Radon, R. Schütz, R. Nolte and R. Böttger, Measurement of the fluence response of the GSI neutron ball dosemeter in the enrgy range from thermal to 19 MeV, Radiation Protection Dosimetry (2007), pp. 1–3, doi:10.1093/rpd/ncm110.

G. Fehrenbacher, Comparison of the shielding design of various carbon ion therapy facilities in the countries Japan, Italy and Germany, 39. Annual Conference of the German-Swiss Association for Radiation Protection and 11th Workshop of Heavy Charged Particles in Biology and Medicine, Heidelberg, 26th-29th September (2007), 16-26.

G. Fehrenbacher F. Gutermuth, T. Radon, Shielding Calculations for the Light Ion Therapy Facility HIT, 39. Annual Conference of the German-Swiss Association for Radiation Protection and 11th Workshop of Heavy Charged Particles in Biology and Medicine, Heidelberg, 26th-29th September (2007), 33-36.

Academic Works

S. GROSAM, Messungen von Röntgenstrahlungspegeln an der EZR - Ionenquelle und den HLI - Vorbeschleunigerstrukturen des GSI - Ionenbeschleunigers mit Thermolumineszenzdosimetern (Diplom, BA), Berufsakademie Karlsruhe, 30.09.2007

Public Talks

G. Fehrenbacher, Strahlenschutz und Sicherheit bei GSI und FAIR , PSI, Villigen, Schweiz, 22.03.07

Georg Fehrenbacher, Sebastian Grosam, Jan Lindenberg: Herausbringen von aktivierten Komponenten aus einem Beschleunigerlabor, 5. Symposium zur Entlassung von radioaktiven Stoffen aus dem Geltungsbereich des Atomgesetzes, Freigabe, Herausgabe, Herausbringen, 29./30. November 2007, Wiesbaden.

FAIR Joint Core Team

Leader: Hans H. Gutbrod

Publications

I. Augustin, Status of the FAIR Project,
Nucl. Instr. and Meth. **B** 261 (2007) 1014 - 1017

I. Augustin, FAIR builds future for ion and antiproton research,
CERN Courier May 2007

I. Augustin, Grundlagenforschung mit FAIR,
Phys. Unserer Zeit 38 (2007), 214 - 215

Public Talks

I. Augustin
FAIR: status of the project
Workshop on Hard QCD with Antiprotons at GSI FAIR,
ECT* Trento (Italy), 16.06.2007

H. Gutbrod
The international Facility for Antiproton and Ion Research – FAIR
Russian Workshop on FAIR
Moscow (Russia), 23.-26.01.2007

H. Gutbrod
The FAIR Project
University Colloquium
Valencia (Spain), 28.03.2007

H. Gutbrod
The multinational Facility for Antiproton and Ion Research – FAIR
Conference on Hadron and Nuclear Physics
Surrey University (U.K.), 02.-05.04.2007

H. Gutbrod
The multinational Facility for Antiproton and Ion Research in Europe
Workshop at Kirchhoff-Institute for Physics
Heidelberg (Germany), 23.04.2007

H. Gutbrod
The FAIR project - A world laboratory for research in Europe
Inauguration of the FAIR Russia Research Center (FRRC)
Moscow (Russia), 18.09.2007

H. Gutbrod
The FAIR project - A world laboratory for research in Europe
International Conference on Nuclear Fragmentation
Kemer (Turkey), 25.09.2007

H. Gutbrod
The FAIR project - A world laboratory for research in Europe
3rd Annual Convocation National Institute of Technology
Durgapur (India), 24.11.2007

Lectures

Th. Beier
Mathematische Ergänzungen zur Quantenmechanik, SS 2007, TU Dresden

Th. Beier
Multipolentwicklung, Legendrepolynome und all das,
WS 2007/8, TU Dresden

Accelerator Division

Division leader: H. Eickhoff
Compiled by: G. Walter

Publications

ACCELERATOR –GSI

1. WoS listed publications

BARTH,W; BAYER,W.; DAHL, L.; GROENING, L.; RICHTER, S.; YARAMYSHEV, S.: Upgrade program of the high current heavy ion UNILAC as an injector for FAIR. Nuclear instruments & methods in physics research, Section A, Accelerators, spectrometers, detectors and associated
equipment / Nucl. Instrum. Methods Phys. Res. Sect. A-Accel. Spectrom. Dect. Assoc. Equip. 577(1-2), 2007: 211–214.

BAYER, W.; EICHHORN, R.; GOPYCH, M.; GRAF, H. D.; HASPER, J.; RICHTER, A.; ZILGES, A.: X-ray spectroscopy - a new method to investigate field emission in superconducting accelerating cavities. Nuclear instruments & methods in physics research, Section A, Accelerators, spectrometers, detectors and associated equipment / Nucl. Instrum. Methods Phys. Res. Sect. A-Accel. Spectrom.
Dect. Assoc. Equip. 575(3), 2007: 321–327.

BELLACHIOMA, M. C.; KURDAL, J.; BENDER, M.; KOLLMUS, H.; KRÄMER, A.; REICH-SPRENGER, H.: Thin film getter coatings for the GSI heavy-ion synchrotron upgrade. Vacuum 82(4), 2007: 435–439.

BENDER, M.; KOLLMUS, H.; ASSMANN, W.: Desorption yields of differently treated copper samples characterized with ERDA. Nuclear instruments & methods in physics research, Section B, Beam interactions with materials and atoms / Nucl. Instrum. Methods Phys. Res. Sect. B-Beam Interact. Mater. Atoms 256(1), 2007: 387–391.

CIAVOLA, G.; GAMMINO, S.; CELONA, L.; CONSOLI, F.; GALLO, G.; MASCALI, D.; PASSARELLO, S.; CAVENAGO, M.; GALATA, A.; SPAEDTKE, P.; TINSCHERT, K.; LANG, R.; KOIVISTO, H.; SUOMINEN, P.; TARVAINEN, O.; BARUE, C.; LECHARTIER, M.; LEROY, R.; BEIJERS, J. P. M.; BRANDENBURG, S.; KREMERS, H. R.; VANROOYEN, D.; KUCHLER, D.; HITZ, D.; SEYFERT, P.; SCHACHTER, L.; DOBRESCU, S.: Status report of the MS-ECRIS construction. High Energy Phys. Nucl. Phys.-Chin. Ed. 31, 2007: 13–17.

HAPE, M.; BECKER, W. J.; RICKEN, W.; PETERS, A.; REEG, H.; SCHLÖRIT, A.: Development and construction of a simulator for high frequency magnetic field measurements. Sens. Lett. 5(1), 2007: 333–336.

KLINGBEIL, H.; ZIPFEL, B.; KUMM, M.; MORITZ, P.: A digital beam-phase control system for heavy-ion synchrotrons. IEEE transactions on nuclear science / IEEE Trans. Nucl. Sci. 54(6), Part 2, 2007: 2604–2610.

KOIVISTO, H.; RONDELIUS, P.; KOPONEN, T.; LAPPALAINEN, P.; ROPPONEN, T.; SAVONEN, M.; SUOMINEN, P.; TARVAINEN, O.; TINSCHERT, K.; CIAVOLA, G.: Development work at JYFL: Plasma potential measurements, electron heating simulations, JYFLMMPS, high temperature ovens. High Energy Phys. Nucl. Phys.-Chin. Ed. 31, 2007: 41–45.

KOLLMUS, H.; BENDER, M.; ASSMANN, W.; KRÄMER, A.; BELLACHIOMA, M. C.; REICH-SPRENGER, H.: Heavy ion-induced desorption investigations using UHV-ERDA. Vacuum 82(4), 2007: 402–407.

LU, Y. R.; RATZINGER, U.; SCHLITT, B.; TIEDE, R.: The general RF tuning for IH-DTL linear accelerators. Nuclear instruments & methods in physics research, Section A, Accelerators, spectrometers, detectors and associated equipment / Nucl. Instrum. Methods Phys. Res. Sect. A-Accel. Spectrom. Dect. Assoc. Equip. 582(2), 2007: 336–344.

NOFAL,M.; HAGMANN, S.; STÖHLKER, T.; JAKUBASSA-AMUNDSEN, D. H.; KOZHUHAROV, C.; WANG, X.; GUMBERIDZE, A.; SPILLMANN, U.; REUSCHL, R.; HESS, S.; TROTSENKO, S.; BANAS, D.; BOSCH, F.; LIESEN, D.; MOSHAMMER, R.; ULLRICH, J.; DORNER, R.; STECK, M.; NOLDEN, F.; BELLER, P.; ROTHARD, H.; BECKERT, K.; FRANCZAK, B.: Radiative electron capture to the continuum and the shortwavelength limit of electron-nucleus Bremsstrahlung in 90A MeV U88+(1s(2)2s(2))+N-2 collisions. Physical review letters / Phys. Rev. Lett. 99(16), 2007: 163201.

RICKEN, W.; BECKER, W. J.; HAPE, M.; PETERS, A.; REEG, H.; SCHLÖRIT, A.: Beam current measurements at a heavy ion accelerator by clip-on ampere-meter.
Sens. Lett. 5(1), 2007: 222–225.

ROTHARD, H.; MOSHAMMER, R.; ULLRICH, J.; KOLLMUS, H.; MANN, R.; HAGMANN, S.; ZOUROS, T. J. M.: Differential multi-electron emission induced by swift highly charged gold ions penetrating carbon foils. Nuclear instruments & methods in physics research, Section B, Beam interactions with materials and atoms / Nucl. Instrum. Methods Phys. Res. Sect. B-Beam Interact. Mater. Atoms 258(1), 2007: 91–95.

SPÄDTKE, P.; LANG, R.; MADER, J.; ROSSBACH, J.; TINSCHERT, K.; STETSON, J.: Ion beam extracted from a 14GHz ECRIS of CAPRICE type. High Energy Phys. Nucl. Phys.-Chin. Ed. 31, 2007: 192–195.

VODEL,W.; NEUBERT, R.; NIETZSCHE, S.; KNAACK, K.; WITTENBURG, K.; PETERS, A.: An LTS-SQUID based measurement tool for characterization of superconductive RF cavities. IEEE transactions on applied superconductivity / IEEE Trans. Appl. Supercond. 17(2), Part 1, 2007: 621–624.

BARTH,W.; BAYER,W.; DAHL, L.; GROENING, L.; RICHTER, S.; YARAMYSHEV, S.: Upgrade program of the high current heavy ion UNILAC as an injector for FAIR. Nuclear instruments & methods in physics research, Section A, Accelerators, spectrometers, detectors and associated equipment / Nucl. Instrum. Methods Phys. Res. Sect. A-Accel. Spectrom. Dect. Assoc. Equip. 577(1-2), 2007: 211–214.
Also part of the programme: FAIR.

BAYER, W.; EICHHORN, R.; GOPYCH, M.; GRAF, H. D.; HASPER, J.; RICHTER, A.; ZILGES, A.: X-ray spectroscopy - a new method to investigate field emission in superconducting accelerating cavities. Nuclear instruments & methods in physics research, Section A, Accelerators, spectrometers, detectors and associated equipment / Nucl. Instrum. Methods Phys. Res. Sect. A-Accel. Spectrom. Dect. Assoc. Equip. 575(3), 2007: 321–327.

BELLACHIOMA, M. C.; KURDAL, J.; BENDER, M.; KOLLMUS, H.; KRÄMER; A.; REICH-SPRENGER, H.: Thin film getter coatings for the GSI heavy-ion synchrotron upgrade. Vacuum 82(4), 2007: 435–439.

BENDER, M.; KOLLMUS, H.; ASSMANN, W.: Desorption yields of differently treated copper samples characterized with ERDA. Nuclear instruments & methods in physics research, Section B, Beam interactions with materials and atoms / Nucl. Instrum. Methods Phys. Res. Sect. B-Beam Interact. Mater. Atoms 256(1), 2007: 387–391.

CIAVOLA, G.; GAMMINO, S.; CELONA, L.; CONSOLI, F.; GALLO, G.; MASCALI, D.; PASSARELLO, S.; CAVENAGO, M.; GALATA, A.; SPAEDTKE, P. EMAIL; TINSCHERT, K.; LANG, R.; KOIVISTO, H.; SUOMINEN, P.; TARVAINEN, O.; BARUE, C.; LECHARTIER, M.; LEROY, R.; BEIJERS, J. P. M.; BRANDENBURG, S.; KREMERS, H. R.; VANROOYEN, D.; KUCHLER, D.; HITZ, D.; SEYFERT, P.; SCHACHTER, L.; DOBRESCU, S.: Status report of the MS-ECRIS construction. High Energy. Phys. Nucl. Phys.-Chin. Ed. 31, 2007: 13–17.

DIMOPOULOU, C.; BECKERT, K.; BELLER, P.; DOLINSKII, A.; LAIER, U.; NOLDEN, F.; SCHREIBER, G.; STECK, M.; YANG, J.: Design of the New Experimental Storage Ring for operation with ions and antiprotons. Phys. Rev. Spec. Top.-Accel. Beams 10(2), 2007: 020101, 8 pages.

KLINGBEIL, H.; ZIPFEL, B.; KUMM, M.; MORITZ, P.: A digital beam-phase control system for heavy-ion synchrotrons. IEEE transactions on nuclear science / IEEE Trans. Nucl. Sci. 54(6), Part 2, 2007: 2604–2610.

MOLVIK, A. W.; KOLLMUS, H.; MAHNER, E.; COVO, M. K.; BELLACHIOMA, M. C.; BENDER, M.; BIENIOSEK, F. M.; HEDLUND, E.; KRÄMER, A; KWAN, J.; MALYSHEV, O. B.; PROST, L.; SEIDL, P. A.; WESTENSKOW, G.; WESTERBERG, L.: Heavy-ion-induced electronic desorption of gas from metals. Physical review letters / Phys. Rev. Lett. 98(6), 2007: 064801.

KOIVISTO, H.; RONDELIUS, P.; KOPONEN, T.; LAPPALAINEN, P.; ROPPONEN, T.; SAVONEN, M.; SUOMINEN, P.; TARVAINEN, O.; TINSCHERT, K.; CIAVOLA, G.: Development work at JYFL: Plasma potential measurements, electron heating simulations, JYFLMMPS, high temperature ovens. High Energy Phys. Nucl. Phys.-Chin. Ed. 31, 2007: 41–45.

SPÄDTKE, P.; LANG, R.; MADER, J.; ROSSBACH, J.; TINSCHERT, K.; STETSON, J.: Ion beam extracted from a 14GHz ECRIS of CAPRICE type. High Energy Phys. Nucl. Phys.-Chin. Ed. 31, 2007: 192–195.

KOLLMUS, H.; BENDER, M.; ASSMANN, W.; KRÄMER, A.; BELLACHIOMA, M. C.; REICH-SPRENGER, H.: Heavy ion-induced desorption investigations using UHV-ERDA. Vacuum 82(4), 2007: 402–407.

VODEL,W.; NEUBERT, R.; NIETZSCHE, S.; KNAACK, K.; WITTENBURG, K.; PETERS, A.: An LTS-SQUID based measurement tool for characteri-

zation of superconductive RF cavities. IEEE transactions on applied superconductivity / IEEE Trans. Appl. Supercond. 17(2), Part

WILFERT, S.; EDELMANN, C.: Inverted magnetron manometer with enhanced operating time. Vacuum 82(4), 2007: 412–419.

2. Other publications

L. Groening, FAIR Newsletter No. 6, The Proton-Linear-Accelerator (p-linac)

L. Groening, FP6/CARE Note, Measurement and Simulation of Transverse Emittance Growth along the Alvarez DTL of the GSI UNILAC

L. Groening, Particle Accelerator Conference, Albuquerque, High Intensity Heavy Ion Beam Emittance Measurements at the GSI UNILAC

L. Groening, Particle Accelerator Conference, Albuquerque, Commissioning of the Linac for the Heidelberg Heavy Ion Cancer Therapy Centre (HIT)

L. Groening, Particle Accelerator Conference, Albuquerque, Development of a Coupled CH-Structure for the GSI Proton Injector

L. Dahl, A. Orzhekhovskaya, S. Yaramyshev GSI-Notiz, Beam dynamics study for the sc solenoid Q5479

A. Orzhekhovskaya, W. Barth, S. Yaramyshev, GSI-Notiz, Numerical investigation of the HIT-RFQ deformation and misaligments of the beam transport line

S. Yaramyshev, A. Orzhekhovskaya, W. Barth, M. Maier, H. Vormann, GSI-Notiz, Beam dynamics study of the new solenoid for HIT linac

A. Orzhekhovskaya, W. Barth, M. Maier, H. Vormann, S. Yaramyshev, Comparison of the beam dynamics simulations and beam emittance measurements for the HIT-LEBT

Stepan Yaramyshev, Comparison of the DYNAMION results, obtained with different Fortran Compilers on different operating systems.

W. Bayer et al., HIGH INTENSITY HEAVY ION BEAM EMITTANCE MEASUREMENTS AT THE GSI UNILAC, Proceedings of PAC07, Albuquerque, New Mexico, USA

M. Maier et al., "Commissioning of the Linac for the Heidelberg Heavy Ion Cancer Therapy Centre (HIT)", Proceedings of PAC07, Albuquerque, New Mexico, USA

Barth, W., Bayer, W., Dahl, L., Groening, L., Richter, S., Yaramyshev, S., Upgrade Program of the High Current Heavy Ion UNILAC as an Injector for FAIR, Nuclear Inst. and Methods in Physics Research, A, 577 (1), p.211-214

M. Maier, W. Barth, W. Bayer, L. Dahl, L. Groening, C. Kleffner, B. Schlitt, K. Tinschert, H. Vormann, S. Yaramyshev, U. Ratzinger, A. Schemp, Commissioning of the Linac for the Heidelberg Heavy Ion Cancer Therapy Centre (HIT), PAC Albuquerque

R. Bär, U. Krause, V. Schaa, W. Schiebel, W. Panschow, P. Schütt (GSI);
"The New FAIR Accelerator Complex at GSI: Project, Controls Challanges and First Steps";
ICALEPCS 2007, Knoxville, USA.

K. Höppner, L. Hechler, K. Herlo, P. Kainberger, U. Krause, S. Matthies (GSI);
"Extended Application Fields for the Renovated GSI Control System";
ICALEPCS 2007, Knoxville, USA.

T. Fleck, R. Bär, M. Schwickert (GSI);
"Requirements and Coherent Realization of the HICAT Control System Functionality for Test, Commissioning and Operation";
ICALEPCS 2007, Knoxville, USA.

T. Fleck, R. Bär, M. Schwickert, U. Weinrich (GSI);
"Experiences with an Industrial Control System: Tracebility of Specifications, Commissioning Support and Conclusions from the HICAT Project";
ICALEPCS 2007, Knoxville, USA.

T. Fleck, R. Bär, M. Schwickert (GSI);
"Status of the Control System of HICAT at an Advanced Stage of Commissioning: Functions, Restrictions and Experiences";
ICALEPCS 2007, Knoxville, USA.

J. Dedic, J. Bobnar, I. Kriznar (Cosylab, Ljubljana, Slovenia), R. Bär, G. Fröhlich, K. Herlo, U. Krause, M. Schwickert (GSI);
"Customizable Motion Control Solution Supporting Large Distances",
ICALEPCS 2007, Knoxville, USA.

K. Höppner (GSI);
"Typesetting tables with LaTeX"; 28th Annual Meeting of the TeX Users Group; 17-20 July 2007, San Diego State University, San Diego, California, USA

Commissioning of the Linac for the Heidelberg Heavy Ion Cancer Therapy Centre (HIT), M. Maier, W. Barth, W. Bayer, L. Dahl, L. Groening, C. Kleffner, B. Schlitt, K. Tinschert, H. Vormann, S. Yaramyshev (GSI, Darmstadt, Germany), U. Ratzinger, A. Schempp (IAP, University of Frankfurt am Main, Germany)

A. Galatis, P. Forck, K. Lang, A. Peters, "First Tests with the SIS18 Digital BPM System" Proc. of the 8th European Workshop on Beam Diagnostics and Instrumentation for Particle Accelerators, Venice (Italy).

T. Giacomini, P. Forck, J. Dietrich (FZ Jülich), D. Liakin (ITEP, Moscow), "The improved IPM design for GSI under test conditions", Proc. of the 8th European Workshop on Beam Diagnostics and Instrumentation for Particle Accelerators, Venice (Italy).

P. Kowina, W. Kaufmann, J. Schölles, "Optimization of the Linear-Cut Beam Position Monitors Based on Finite Element Methods", Proc. of the 8th European Workshop on Beam Diagnostics and Instrumentation for Particle Accelerators, Venice (Italy).

D. Liakin, S. Barabin, A. Orlov (ITEP, Moscow), P. Forck, T. Giacomini, "Test of a Silicon Photomultiplier for Ionization Profile Monitors Application", Proc. of the 8th European Workshop on Beam Diagnostics and Instrumentation for Particle Accelerators, Venice (Italy).

F. Becker, C. Andre, P. Forck, D. Hoffmann, "Beam Induced Fluorescence Monitor for Transverse Profile Determination of 50 MeV/u to 750 MeV/u Heavy Ion Beams", Proc. of the 8th European Workshop on Beam Diagnostics and Instrumentation for Particle Accelerators, Venice (Italy).

M. Schwickert, A. Peters (HIT, Heidelberg), "Beam Diagnostics for Medical Accelerators", Proc. of the 8th European Workshop on Beam Diagnostics and Instrumentation for Particle Accelerators, Venice (Italy).

H. Klingbeil, B. Zipfel, M. Kumm, P. Moritz, IEEE Transactions on Nuclear Science, A Digital Beam-Phase Control System for Heavy-Ion Synchrotrons,Vol. 54, No. 6 Dec. 2007

C. Dimopoulou, K. Beckert, P. Beller, A. Dolinskii, U. Laier, F. Nolden, G. Schreiber, M. Steck, J. Yang Phys. Rev. ST Accel. Beams 10 Design of the New Experimental Storage Ring for operation with ions and antiprotons, Issue 2, Feb. 2007

Public Talks

W. Barth: UNILAC-Hochstromentwicklung

H.Damerau, S.Hancock, C.Rossi, E.Shaposhnikova, J.Tuckmantel, J.-L.Vallet, M.Mehler: 22nd PAC Conference (PAC07) Longitudinal Coupled-Bunch Instabilities In The CERN PS Albuquierque, New Mexico, USA

C. Dimopoulou, B. Franzke, T. Katayama, G. Schreiber, M. Steck, D. Möhl: COOL07 LONGITUDINAL ACCUMULATION OF ION BEAMS IN THE ESR SUPPORTED BY ELECTRON COOLING Bad Kreuznach, Germany

Peter Forck: Layout and Experiences of High Current Beam Diagnostics at GSI, 02.07.2007, IFMIF-Workshop, Madrid (Spain)

Frank Becker: Beam Induced Fluorescence (BIF) Monitor – A Non-Intercepting Transverse Profile Monitor for 5 keV/u to 750 MeV/u Heavy Ion Beams, 09.11.2007, FZ Jülich

F. Becker: Beam Induced Fluorescence Monitor for Transverse Profile Determination of 50 MeV/u to 750 MeV/u Heavy Ion Beams, 21.05.2007, 8th European Workshop on Beam Diagnostics and Instrumentation for Particle Accelerators, Venice (Italy)

F. Becker: The Beam Induced Fluorescence (BIF) Monitor - for Transverse Profile Determination of 5 to 750 MeV/u Heavy Ion Beams, 30.08.2007, Warm Dense Matter Meeting (Heavy Ion and Fusion – LBNL Accel. Div.), Berkeley (USA)

L. Groening: Annual meeting of work package 5 of FP6/CARE/HIPPI activity, Paris, Simulations of Emittance Growth Measurements along the Alvarez DTL

L. Groening: Annual INTAS meeting, Darmstadt, The FAIR Proton Linac

L. Groening: TAC FAIR Accelerators, Darmstadt, The FAIR Proton Linac

L. Groening: Simulation of Emittance Growth for UNILAC, High Current Experiments of the GSI UNILAC using, DYNAMION & PARMILA, Annual Meeting of FP6/CARE/HIPPI activity, Orsay

Piotr Kowina: BPM-Entwicklung für FAIR, 26.04.2007, FZ Jülich

L. Groening: Annual Meeting of FP6/CARE/HIPPI activity, Orsay, Status of the GSI Proton Injector

L. Groening: FAIR Antiproton Workshop, Darmstadt, The FAIR Proton Linac

F. Schwickert: Beam Diagnostics for Medical Accelerators, 23.05.2007, 8th European Workshop on Beam Diagnostics and Instrumentation for Particle Accelerators, Venice (Italy)

M. Schwickert: Beam Diagnostics for HIT and a Glance on FAIR, 20.07.2007, Institut für angewandte Physik, Universität Frankfurt

P.Spädtke, K.Tinschert, R.Lang, J.Mäder, J.Roßbach, J.W.Stetson, L.Celon: Prospects of Ion Beam Extraction and transport Simulations, Internationale Ionenquellenkonferenz, Jeju, Südkorea, 2006

P.Spädtke: Physik der Strahlextraktion aus ECR Ionenquellen, Universität Frankfurt, 21.12.2007

S. Yaramyshev: End to end-simulations – status quo, INTAS meeting, Darmstadt

S. Yaramyshev: Summary of the RFQ-upgrade 2004, INTAS meeting, Darmstadt

S. Yaramyshev: Optimisation of the IRM, INTAS meeting, Darmstadt

S. Yaramyshev: Versatile multiparticle code DYNAMION, INTAS meeting, Darmstadt

S. Yaramyshev: Recent investigations of the HIT front-end, HIT meeting, Darmstadt

S. Yaramyshev: Beam dynamics simulations for the HSI, HSI-Upgrade meeting, GSI, Darmstadt.

S. Yaramyshev: HSI upgrade, GSI meeting

S. Yaramyshev: Beam dynamics study for the HIT front-end and new design of the HIT-RFQ Input Radial Matcher HIT meeting, Heidelberg

FAIR Technical Division

Leader: D. Krämer
Compiled by: S. Richter, P. Karampougiouki

Publications

ACCELERATOR –FAIR

1. WoS listed publications

AL-KHATEEB, A. M.; HASSE, R. W.; BOINE-FRANKENHEIM, O.; DAQA, W. M.; HOFMANN, I.:
Transverse resistive wall impedances and shielding effectiveness for beam pipes of arbitrary wall thickness. Phys. Rev. Spec. Top.-Accel. Beams 10(6), 2007: 064401, 10 pages. Open Access.

BOINE-FRANKENHEIM, O.; CHORNIY, O.:
Stability of coherent synchrotron oscillations with space charge. Phys. Rev. Spec. Top.-Accel. Beams 10(10), 2007: 104202, 10 pages. Open Access.

DIMOPOULOU, C.; BECKERT, K.; BELLER, P.;DOLINSKII, A.; LAIER, U.; NOLDEN, F.; SCHREIBER,G.; STECK, M.; YANG, J.:
Design of the New Experimental Storage Ring for operation with ions and antiprotons. Phys. Rev. Spec. Top.-Accel. Beams 10(2), 2007: 020101, 8 pages. Open Access.

DOLINSKII, A.; LITVINOV, S.; STECK, M.; WEICK, H.:
Study of the mass resolving power in the CR storage ring operated as a TOF spectrometer. Nucl. Instrum. Methods Phys. Res. Sect. A-Accel. Spectrom. Dect. Assoc. Equip. 574(2), 2007: 207–212.

FERTMAN, A.; MUSTAFIN, E.; HINCA, R.; STRASIK, I.; PAVLOVIC, M.; SCHARDT, D.; SOBOLEVSKIY, N.; GOLUBEV, A.; SHARKOV, B.; FEHRENBACHER, G.; HOFMANN, I.; IWASE, H.; KOZOVA, E.; MUSTAFINA, G.:
First results of an experimental study of the residual activity induced by high-energy uranium ions in steel and copper. Nucl. Instrum. Methods Phys. Res. Sect. B-Beam Interact. Mater. Atoms 260(2), 2007: 579–591.

FLOCH, E.; MUSTAFIN, E.; MORITZ, G.; RAMAKERS, H.; GOLUBEV, A.; BOROVLEV, S.; ROGOV, V.; SMIRNOV, G.; TITARENKO, Y.; BATYAEV, V.; KANTSYREV, A.; MARKOV, N.; SMOLYAKOV, A.; HAGEDORN, D.; GHARIB, A.:
Irradiation of bypass diodes up to 2.2E14 Neutron/cm(2) and 1.3 kGy for the FAIR project. IEEE Trans. Appl. Supercond. 17(2), Part 2, 2007: 2462–2465.

GOLUBEV, A. A.; KANTSYREV, A. V.; LUCKJASHIN, V. E.; FERTMAN, A.; KUNIN, A. V.; VATULIN, V. V.; GNUTOV, A. S.; PANOVA, Y. V.; IWASE, H.; MUSTAFIN, E.; SCHARDT, D.; WEYRICH, K.; SOBOLEVSKLY, N. M.; LATYSHEVA, L. N.:
Measurement of the energy deposition profile for U-238 ions with specific energy 500 and 950 MeV/u in stainless steel and copper targets. Nucl. Instrum. Methods Phys. Res. Sect. B-Beam Interact. Mater. Atoms 263(2), 2007: 339–344.

2. Other publications

AIBA, M.; CHANEL, M.; DORDA, U.; GAROBY, R.; KOUTCHOUK, J.-P.; MARTINI, M.; METRAL, E.; PAPAPHILIPPOU, Y.; SCANDALE, W.; ZIMMERMANN, F.; SHILTSEV, V.; FRANCHETTI, G.:
Space-Charge Compensation Options for the LHC Injector Complex. Proc. Of Particle Accelerator Conference Albuquerque, New Mexico, USA 2007. THPAN074.

BENEDETTI, C.; RAMBALDI, S.; TURCHETTI, G.; FRANCHETTI, G.; HOFMANN, I.:
Transverse Self-Consistent Modeling of a 3D Bunch in SIS100 with MICROMAP. Proc. Of Particle Accelerator Conference Albuquerque, New Mexico, USA 2007. THPAN30.

BENEDETTO, E.; RUMOLO, G.; SCHULTE, D.; TOMAS, R.; ZIMMERMANN, F.; FRANCHETTI, G.; OHMI, K.; PIVI, M.; RAUBENHEIMER, T.; FISCHER, W.; SONNAD, K.; VAY, J.-L.:
Modeling Incoherent Electron Cloud Effects. Proc. Of Particle Accelerator Conference Albuquerque, New Mexico, USA 2007. THPAN075.

BLELL, U.; FLORENKOWSKI, J.; KOPF, U.; MÜHLE, C.; PETRYK, M.; PETZENHAUSER, I.; SPILLER; P.:
Development of the injection- and extraction systems for the upgrade of SIS18. Proceedings of the PAC07, 167(2007)

BOINE-FRANKENHEIM, O.; KORNILOV, V.:
3D Simulation of Coherent Instabilities in Long Bunches Induced by the Kicker Impedances in long bunches with space charge. Proc. of PAC 2007, p. 3919

BUSSMANN, M.; HABS, D.; SCHRAMM, U.; BECKERT, K.; BELLER; P.; FRANZKE, B.; KOZHUHAROV, C.; KÜHL, T.; NÖRTERSHÄUSER, W.; NOLDEN, F.; STECK, M.; KARPUK, S.; GEPPERT, C.; NOVOTNY, C.; SAATHOFF, G.; REINHARDT, S.:
Schottky Noise Signal and Momentum Spread for Laser Cooled Beams at Relativistic Energies. Proceedings of COOL 07, Bad Kreuznach, Germany, 10-14.09.2007

DIMOPOULOU, C.; FRANZKE, B.; KATAYAMA, T.; MÖHL, D.; SCHREIBER, G.; STECK, M.:
Longitudinal Accumulation of Ion Beams in the ESR Supported by Electron Cooling. Proceedings of COOL 07, Bad Kreuznach, Germany, 10-14.09.2007

DOLINSKII, A.; NOLDEN, F.; STECK, M.:
Lattice Considerations for the Collector and the Accumulator Ring of the FAIR Project. Proceedings of COOL 07, Bad Kreuznach, Germany, 10-14.09.2007

FRANCHETTI, G.:
Recent Developments in Understanding Beam Loss in High-intensity Synchrotrons. Proc. Of Particle Accelerator Conference Albuquerque, New Mexico, USA 2007. TUZAAB02.

FISCHER, E.; KURNYSHOV, R.; SCHERBAKOV P.;
Analysis of Coupled Electromagnetic-Thermal Effects in Superconducting Accelerator Magnets, Proceedings of EUCAS 2007, Brussels, Belgium, September 2007

FISCHER, E.; KHODZHIBAGIYAN, H.; KOVALENKO, A.:
Full Size Model Magnets for the FAIR SIS100 Synchrotron, Proceedings of MT20, Philadelphia, Pennsylvania, August 2007

GOSTISHCHEV, V.; DIMOPOULOU, C.; DOLINSKII, A.; NOLDEN, F.; STECK, M.:
Internal Target Effects in the ESR Storage Ring with Cooling. Proceedings of COOL 07, Bad Kreuznach, Germany, 10-14.09.2007

HOFMANN, I.; FRANCHETTI, G.:
Scaling Laws for Space Charge Driven Resonances. Proc. Of Particle Accelerator Conference Albuquerque, New Mexico, USA 2007. THPAN017

KATAYAMA, T.; DIMOPOULOU, C.; FRANZKE, B.; KIKUCHI, T.; MÖHL, D.; STECK, M.:
Simulation Study of Ion Beam Accumulation with Moving Barrier Buckets Assisted with Electron Cooling. Proceedings of COOL 07, Bad Kreuznach, Germany, 10-14.09.2007

KORNILOV, V.; BOINE-FRANKENHEIM, O.; HOFMANN,I.:
Stability thresholds for transverse dipole modes with nonlinear space charge. Proc. of PAC 2007, p. 3264

MORITZ, G.:
RAPIDLY-CYCLING SUPERCONDUCTING ACCELERATOR MAGNETS FOR FAIR AT GSI, Proceedings of PAC07, Albuquerque, New Mexiko, USA, June 2007

NOLDEN, F.; DOLINSKII, A.; PESCHKE, C.:
Stochastic Cooling for the FAIR Project. Proceedings of COOL 07, Bad Kreuznach, Germany, 10-14.09.2007

OMET, C.; HOFFMANN, D.H.H.; SPILLER, P.:
FAIR synchrotron operation with low charge state heavy ions. Proceeding of the PAC07, 1416(2007)

OMET, C.; HOFFMANN, D.H.H.; SPILLER, P.:
Poster/Proceeding: FAIR Synchrotron Operation with Low Charge State Heavy Ions, Proceedings of the PAC 07

PARFENOVA, A.S.; FRANCHETTI, G.; HOFMANN, I.; OMET, C., LEE, S.Y.:
Improving the SIS18 Performance by use of the Orbit Response Method. Proc. Of Particle Accelerator Conference Albuquerque, New Mexico, USA 2007. THPAN016.

PESCHKE, C.; NOLDEN, F.:
Pick-Up Electrode System for the CR Stochastic Cooling System. Proceedings of COOL 07, Bad Kreuznach, Germany, 10-14.09.2007

SCHNIZER, P.; SCHNIZER, B.; AKISHIN, P.; FISCHER, E.:
Magnetic field analysisfor superferric accelerator magnets using elliptic multipoles and its adavantages, Proceedings of MT20, Philadelphia, Pennsylvania, USA, August 2007

SCHNIZER, P.; KIESEWETTER, H.R.; MACK, T.; KNAPP, T.; KLOS, F.; MANDERLA, M.; RAUCH, S.; SCHÖNECKER, M.; WERKMANN, R.:
A mole for measuring pulsed superconducting magnets, Proceedings of MT20, Philadelphia, Pennsylvania, USA, August 2007

SCHNIZER, P.; SCHNIZER, B.; AKISHIN, P.; FISCHER, E.:
Measuring Elliptic Apertures using Rotating Coils, Proceedings of IMMW 15, Fermilab, Batavia, IL, USA, Aug. 2007

SCHNIZER, P.:
A mole for measuring pulsed superconducting magnets, Proceedings of IMMW 15, Fermilab, Batavia, IL, USA, Aug. 2007

SCHROEDER, C.; KAUSCHKE, M.:
Kryotechnischer Magnetteststand für FAIR, Proceedings DKV-Tagung, Hannover, Germany, Nov. 2007

SORGE, S.; BOINE-FRANKENHEIM, O.; FRANCHETTI, G.:
Analysis of resonances induced by the SIS-18 electron cooler. Proc. Of COOL 07, Sept. 10-14, 2007, Bad Kreuznach, Germany

SPILLER, P. et al.:
Status of the FAIR SIS100/300 Synchrotron Design. Proceedings of the PAC07, 1419(2007)

STADLMANN, J.; BLASCHE, K.; FRANCZAK, B.; HAGENBRUCK, F.; OMET, C.; RATSCHOW, S.; PYKA, N.; SPILLER, P.J.; KOVALENKO, A.D.:
Ion Optical Layout of the FAIR Synchrotron and Beam Line Systems. PAC 2007: Proceedings

STAFINIAK, A.; FLOCH, E.; HAHNE, P.; HESS, G.; KAUSCHKE, M.; KLOS, F.; MARZOUKI, F.; MORITZ, G.; MUELLER, H.; REBSCHER, M.; SCHNIZER, P.; SCHROEDER, C.; WALTER, G.; WALTER, F.; WELKER, H.;
Commissioning of the Prototype Test Facility for Rapidly-Cycling Superconducting Magnets for FAIR, Proceedings of MT20, Philadelphia, Pennsylvania, August 2007

STECK, M.; BECKERT, K.; BELLER, P.; DIMOPOULOU, C.; NOLDEN, F.:
Limitations to the Observation of Beam Ordering. Proceedings of COOL 07, Bad Kreuznach, Germany, 10-14.09.2007

STECK, M.; DIMOPOULOU, C.; DOLINSKII, A.; NOLDEN, F.:
Rare Isotope Accumulation and Deceleration in the NESR Storage Ring of the FAIR Project. 22th Particle Accelerator Conference (PAC 07), Albuquerque, USA, 25-29.06.2007.

VOLPINI, G.; ALESSANDRIA, F.; BELLOMO, G.; FABBRICATORE, P.; FARINON, S.; KAUGERTS, J.; MORITZ, G.; GAMBARDELLA, U.; WILSON, M. N.:

Low-loss NbTi Rutherford Cable for Application to the SIS-300 Dipole Magnet Prototype, Proceedings of MT20, Philadelphia, Pennsylvania, USA, August 2007

WILLERING, G.P.; VERWEIJ, A.P.; KAUGERTS, J.; TEN KATE, H.H.J.; Stability of NbTi Rutherford Cables Exhibiting Different Contact Resistances, Proceedings of MT20, Philadelphia, Pennsylvania, USA, August 2007

Academic Works

C. PESCHKE
Higher-Order-Mode Dämpfer als Strahllagenmonitore, HuK J.W.Goethe Universitaet, Frankfurt/M 2007

I. PETZENHAUSER
Untersuchungen an mehrstufigen Pseudofunkenschaltern für den Einsatz an den Kickermagneten des SIS100/300 Schwerionensynchrotrons der GSI, FAIR HUK 1, Friedrich-Alexander-Uni Erlangen-Nürnberg in 2007

Invited Talks and Seminar

BLELL, U.; FLORENKOWSKI, J.; KOPF, U.; MUEHLE, C.; PETRYK, M.; PETZENHAUSER, I.; SPILLER, P.:
Development of the injection- and extraction systems for the upgrade of SIS18, Gesellschaft für Schwerionenforschung, Darmstadt, Germany A. Batrakov, S.A. Onischenko, G.E. Ozur, Institute of High Current Electronics SB RAS, Tomsk, Russia

DIMOPOULOU, C.:
The NESR for Atomic Physics: Experiments with Heavy Highly Charged Ions and Deceleration of Antiprotons, 1-4.08.2007, 20th International Seminar on Ion-Atom Collisions (ISIAC07), Ag. Nikolaos, Crete, Greece

DIMOPOULOU, C.:
Longitudinal Stacking and Electron Cooling of Ion Beams in the ESR as a Proof of Principle for FAIR, 20.11.2007, Joint DESY and University of Hamburg Accelerator Physics Seminar

FRANCHETTI, G.:
Recent Developments in Understanding Beam Loss in High-intensity Synchrotrons, PAC 2007, 25.-29. June 2007, Albuquerque, New Mexico, USA

KRAEMER, D.:
Current Status of FAIR-project (invited oral contributions), 22nd PAC 2007, USA, 25.-29.06.07

KRAEMER, D.:
Status of FAIR, Industrie Forum Bukarest, 10.07.2007

KRAEMER, D.:
FAIR – ein internationales Zentrum für Antiprotonen- und Schwerionenforschung, Industrie Forum Wien, 27.03.2007

KRAEMER, D.:
Status of the FAIR-project, 10.-14.09.2007 in Bad Kreuznach, 13.09.2007

MORITZ, G.:
Rapidly-Cycling superconducting accelerator magnets for FAIR at GSI, Proceedings of PAC07, Albuquerque, New Mexiko, USA, June 2007

NOLDEN, F.:
Storage Rings for Radioactive Ion Beams, 24.6.-29.6.2007, 15th International Conference on Electro-Magnetic Isotope Separators and Techniques EMIS 07, Deauville, France

OMET, C.:
Lattice and collimation concept for the FAIR synchrotrons, Workshop CARE-HHH-APD BEAM'07, CERN October 02nd 2007

OMET, C.:
Dynamic vacuum - Collimator technology for suppression and control of desorption gases, Workshop on Materials for Collimators and Beam Absorbers, CERN September 04th 2007

STADLMANN, J.; OMET, C.; SPILLER, P.;
Collimation concepts for beam ions after a charge change 03.09.2007 Workshop on materials and collimators Vortrag Lattice optimization for low charge state heavy ion operation

BOINE-FRANKENHEIM, O.;
Lehrveranstaltung: Beschleunigerphysik, Vorlesung, WS2007/08, TU Darmstadt

BOINE-FRANKENHEIM, O.;
Lehrveranstaltung: Themen aus der Beschleunigerphysik und Technik, Seminar, WS2007/08, TU Darmstadt

Division of Scientific-Technical Infrastructure

Division leader: B. Schönfelder
Compiled by: Badura, Berdermann, Große, Kindler, Malzacher

Publications

GSI as publisher
Series by Library & Documentation

Franzke, Bernhard; Geissel, Hans; Münzenberg, Gottfried:
Mass and Lifetime Measurements of Exotic Nuclei in Storage Rings. GSI Report 2007-6

Basko, Mikhail M.; Maruhn, Joachim A.; Tauschwitz, Anna:
CAVEAT-TR: A 2D hydrodynamic code with heat conduction and radiation transport. I. Implementation of the SSI method for heat conduction. GSI Report 2007-5

Senger, Peter (Ed.):
CBM Progress Report 2006. GSI Report 2007-4

Mulser, Peter; Schlegel, Theodor:
ILIAS Ion and Laser beam Interaction and Application Studies. GSI Report 2007-3

Weyrich, Karin (Ed.):
High Energy Density Physics with Intense Ion and Laser Beams: Annual Report 2006. GSI Report 2007-2

Große, Katrin (Ed.): GSI Scientific Report 2006. GSI Report 2007-1

Riek, F.: Mesonic and Isobar modes in matter [12.12.2007]. GSI Diss 2008-1

Doornenbal, P.: In-beam γ-ray spectroscopy of two-step fragmentation reactions at relativistic energies - The case of ^{36}Ca [23.10.2007]. GSI Diss 2007-9

[not published GSI Diss 2007-08]

Garcia, R. F.: Mass measurements on neutron-deficient nuclides at SHIPTRAP and commissioning of a cryogenic narrow-band FT-ICR mass spectrometer [09.11.2007]. GSI Diss 2007-07

Schiedt, B.: Characterization and Application of Ion Track-Etched Nanopores [16.05.2007]. GSI Diss 2007-6

Beck, T.: Entwicklung einer schnellen Pulsformanalyse für asymmetrische AGATA-Germanium-Detektoren. GSI Diss 2007-5

Nofal, M.: Projectile Continum Electrons and the Short Wavelength Limit of Electron-Nucleus Bremsstrahlung Studied in the Collision of 90 MeV/u U^{88+} with a N_2 Target [28.03.2007]. GSI Diss 2007-4

Hebeler, K.: Renormalization Group Approach to Superfluid Neutron Matter [12.02.2007]. GSI Diss 2007-3

Otamendi, J. A.: Development of an Experiment for Ultrahigh-Precision g-Factor Measurements in a Panning-Trap Setup [07.03.2007]. GSI Diss 2007-2

Korostiy, S.: Spectroscopic investigation of the charge dynamics of heavy ions penetrating solid and gaseous targets [13.11.2006]. GSI Diss 2007-1

Rauth, C.: Direct mass measurements beyond the proton drip-line [07.02.2007]. GSI Diss 2006-12

Eitel, G.: Aufbau eines ortsauflösenden ionennachweisdetektors für die Penningfallen-Massenspektrometrie [20.11.2007]. GSI Dipl 2008-1

Wolf, M: Numerische Modellierung und Bewertung der Umsatzbarkeit eines Kühlers zur Kühlung eines Germanium Detektors [Aug. 2007]. GSI Dipl 2007-10

Maden, I.: Numerische Simulation der physikalischen Eigenschaften eines planaren 3D Germanium Pixeldetektors [Aug. 2007]. GSI Dipl 2007-9

Cunrath, R.: Modellierung von Strahlenschäden für die Therapieplanung [July 2007]. GSI Dipl 2007-8

Schwinn, A.: Entwicklung von Objekt- und Petri-Netzen im Rahmen eines Kontrollsystems. GSI Dipl 2007-07

Zimmer, D. F.: Spektroskopische Diagnose eines Röntgenlaserplasmas [30.05.2007]. GSI Dipl 2007-6

von Neubeck, C.: Aufbau eines 3-dimensionalen Systems zur biologischen Verifikation der Bestrahlungsplanung mit Schwerionen. GSI Dipl 2007-5

Weber, G.: Untersuchungen der Umladungsverluste und Strahllebensdauern gespeicherter U^{28+} Ionen. GSI Dipl 2007-4

Riebel, L.: Untersuchung der optimalen Kühlung eines Germanium Detektors. GSI Dipl 2007-3

Habermann, T. C.: Optimierung des elektrischen Feldes in planaren Germanium Pixeldetektoren. GSI Dipl 2007-2

Kragl, G.: Tumortherapie mit schweren Ionen: Zweidimensionale biologische Dosisverifikation für die Therapie mit ^{12}C und Anpassung des Strahlmodells für ^{3}H. GSI Dipl 2007-1

1. WoS listed publications

ANTALIC, S.; ANDREYEV, A. N.; ACKERMANN, D.; BIANCO, L.; CULLEN, D.; DARBY, I.; FRANCHOO, S.; HEINZ, S.; HEßBERGER, F. P.; HOFMANN, S.; HUYSE, M.; KINDLER, B.; KOJOUHAROV, I.; LEPPANEN, A. P.; LESHER, S. R.; LOMMEL, B.; MANN, R.; MÜNZENBERG, G.; NISHIO, K.; PAGE, R. D.; PAKARINEN, J.; RESSLER, J. J.; SARO, S.; STREICHER, B.; SULIGNANO, B.; THOMSON, J.; VAN DUPPEN, P.; VENHART, M.; WISEMAN, D.; WYSS, R.:
The new isotopes in Po-Rn region. Acta Phys. Pol. B 38(4), 2007: 1557–1560.

BEDNARCZYK, P.; BERDERMANN, E.; GERL, J.; GORSKA, M.; KOJOUHAROV, I.; POMORSKI, M.; REBISZ, M.; VOSS, B.; ACOSTA, L.; BERJILLOS, R.; MARTEL, I.; ALVAREZ, M. A. G.; ESPINO, J. M.; FLORES, J. L.; MUKHA, I.; WOLSKI, R.:
Application of diamond detectors in tracking of heavy ion slowed down radioactive beams. Acta Phys. Pol. B 38(4), 2007: 1293–1296.

BOL, J.; MULLER, S.; BERDERMANN, E.; DE BOER, W.; FURGERI, A.; POMORSKI, M.; SANDER, C.:
Diamond thin film detectors for beam monitoring devices. Phys. Status Solidi A-Appl. Mat. 204(9), 2007: 2997–3003.

DE BOER, W.; BOL, J.; FURGERI, A.; MULLER, S.; SANDER, C.; BERDERMANN, E.; POMORSKI, M.; HUHTINEN, M.:
Radiation hardness of diamond and silicon sensors compared. Phys. Status Solidi A-Appl. Mat. 204(9), 2007: 3004–3010.

GUENAUT, C.; AUDI, G.; BECK, D.; BLAUM, K.; BOLLEN, G.; DELAHAYE, P.; HERFURTH, F.; KELLERBAUER, A.; KLUGE, H. J.; LIBERT, J.; LUNNEY, D.; SCHWARZ, S.; SCHWEIKHARD, L.; YAZIDJIAN, C.:
High-precision mass measurements of nickel, copper, and gallium isotopes and the purported shell closure at N=40. Phys. Rev. C 75(4), 2007: 044303, 12 pages.

HOFMANN, S.; ACKERMANN, D.; ANTALIC, S.; BURKHARD, H. G.; COMAS, V. F.; DRESSLER, R.; GAN, Z.; HEINZ, S.; HEREDIA, J. A.; HEBBERGER,F. P.; KHUYAGBAATAR, J.; KINDLER, B.; KOJOUHAROV, I.; KUUSINIEMI, P.; LEINO, M.; LOMMEL, B.; MANN, R.; MÜNZENBERG, G.; NISHIO,K.; POPEKO, A. G.; SARO,S.; SCHÖTT, H. J.; STREICHER, B.; SULIGNANO, B.; UUSITALO, J.; YEREMIN, A. V.:
Studies of superheavy elements at SHIP. Int. J. Mod. Phys. E-Nucl. Phys. 16(4), 2007: 937–947.

HOFMANN, S.; ACKERMANN, D.; ANTALIC, S.; BURKHARD, H. G.; COMAS, V. F.; DRESSLER, R.; GAN, Z.; HEINZ, S.; HEREDIA, J. A.; HEßBERGER, F. P.; KHUYAGBAATAR, J.; KINDLER, B.; KOJOUHAROV, I.; KUUSINIEMI, P.; LEINO, M.; LOMMEL, B.; MANN, R.; MÜNZENBERG, G.; NISHIO, K.; POPEKO, A. G.; SARO, S.; SCHÖTT, H.J.; STREICHER, B.; SULIGNANO, B.; UUSITALO, J.; VENHART, M.; YEREMIN, A. V.:
The reaction $^{48}Ca+^{238}U$ -> $^{286}112$ studied at the GSI-SHIP. Eur. Phys. J. A 32(3), 2007: 251–260.

KELLERBAUER, A.; AUDI, G.; BECK, D.; BLAUM, K.; BOLLEN, G.; GUENAUT, C.; HERFURTH, F.; HERLERT, A.; KLUGE, H. J.; LUNNEY, D.; SCHWARZ, S.; SCHWEIKHARD, L.; WEBER, C.; YAZIDJIAN, C.:
High-precision masses of neutron-deficient rubidium isotopes using a Penning trap mass spectrometer. Phys. Rev. C 76(4), 2007: 045504, 14 pages.

MARCZEWSKA, B.; KUPRIYANOV, I.; PAL'YANOV, YU.; NOWAK, T:, OLKO, P.; RĘBISZ, M; WALIGÓRSKI; M.P.R.:
A study of radiation dosimeters based on synthetic HPHT diamond. Diamond Relat. Mater. 16, 2007: 191-195.

MORSE, J.; SALOME, M.; BERDERMANN, E.; POMORSKI, M.; CUNNINGHAM, W.; GRANT, J.:
Single crystal CVD diamond as an X-ray beam monitor. Diamond Relat. Mater. 16, 2007: 1049–1052.

OGAWA, H.; GEISSEL, H.; FETTOUHI, A.; FRITZSCHE, S.; PORTILLO, M.; SCHEIDENBERGER, C.; SHEVELKO, V. P.; SURZHYKOV, A.; WEICK, H.; BECKER, F.; BOUTIN, D.; KINDLER, B.; KNOBEL, R. K.; KURCEWICZ, J.; KURCEWICZ, W.; LITVINOV, Y. A.; LOMMEL, B.; MÜNZENBERG, G.; PLASS, W. R.; SAKAMOTO, N.; STADLMANN, J.; TSUCHIDA, H.; WINKLER, M.; YAO, N.:
Gas-solid difference in charge-changing cross sections for bare and H-like nickel ions at 200 MeV/u. Phys. Rev. A75(2), 2007: 020703, 4 pages.

POMORSKI, M.; BERDERMANN, E.; DE BOER, W.; FURGERI, A.; SANDER, C.; MORSE, J.:
Charge transport properties of single crystal CVD-diamond particle detectors. Diamond Relat. Mater. 16, 2007: 1066–1069.

REBISZ, M.; VOSS, B.:
The response of thermally stimulated luminescence in CVD diamonds to heavy charged particles. Sp. Iss. Radiat. Meas. 42, 2007: 628–631.

REBISZ, M.; VOSS, B.; HEINZ, A.; USENKO, E.; POMORSKI, M.:
CVD diamond dosimeters for heavy ion beams. Diamond Relat. Mater. 16(4-7), 2007: 1070–1073.

SCHMIDT, K. H.; KELIC, A.; LUKIC, S.; RICCIARDI, M. V.; VESELSKY, M.:
Benefits of extended capabilities of the driver accelerator for EURISOL. Phys. Rev. Spec.Top.-Accel. Beams 10(1), 2007: 014701, 21 pages.

STREICHER, B.; ANTALIC, S.; SARO, S.; VENHART, M.; HEßBERGER, F. P.; HOFMANN, S.; ACKERMANN, D.; KINDLER, B.; KOJOUHAROV,I.; LOMMEL, B.; MANN, R.; SULIGNANO, B.; KUUSINIEMI, P.:
Alpha-gamma decay studies of ^{261}Sg. Acta Phys. Pol. B 38(4), 2007: 1561–1564.

SULIGNANO, B.; HEINZ, S.; HEßBERGER, F. P.; HOFMANN, S.; ACKERMANN, D.; ANTALIC, S.; KINDLER, B.; KOJOUHAROV, I.; KUUSINIEMI, P.; LOMMEL, B.; MANN, R.; NISHIO, K.; POPEKO, A. G.; SARO, S.; STREICHER, B.; VENHART, M.; YEREMIN, A. V.:
Identification of a K isomer in ^{252}No. Eur. Phys. J. A 33(4), 2007: 327–331.

YAZIDJIAN, C.; AUDI, G.; BECK, D.; BLAUM, K.; GEORGE, S.; GUENAUT, C.; HERFURTH, F.; HERLERT, A.; KELLERBAUER, A.; KLUGE, H. J.; LUNNEY, D.; SCHWEIKHARD, L.:
Evidence for a breakdown of the isobaric multiplet mass equation: A study of the A=35,T=3/2 isospin quartet. Phys. Rev. C 76(2), 2007: 024308, 8 pages.

2. Other publications

D. BECK, H. BRAND
Neues vom CS Framework, HMI-B 616 Berlin, Juli 2007, ISSN 0936-0891, Proc. Frühjahrstagung der Studiengruppe für elektronische Instrumentierung, 26. bis 28. März 2007, Forschungszentrum Dresden Rossendorf

H. BRAND
Kontrollsystemaktivitäten an der GSI, HMI-B 616 Berlin, Juli 2007, ISSN 0936-0891, Proc. Frühjahrstagung der Studiengruppe für elektronische Instrumentierung, 26. bis 28. März 2007, Forschungszentrum Dresden Rossendorf

E. BERDERMANN, M. POMORKSI, A. PULLIA, S. RIBOLDI, M. TRÄGER, H. WEICK, D. BOUTIN, H. GEISSEL, Y. LITVINOV, C. NOCIFORO, K. SÜMMERER, M. WINKLER:
Performance of diamond detectors in a fragmentation experiment. Proceedings. XLV International Winter Meeting on Nuclear Physics, Bormio, Italy, 2007

S. LINEV:
ROOT I/O for SQL databases, CHEP 2006 Proceedings, Mumbai, Presentation, Linev

S. LINEV:
Status of SQL and XML I/O, ROOT workshop, CERN, Presentation

Academic Works

M. FELDMANN
Entwicklung einer automatisierten Dokumentation von LabVIEW Quellcode für das Rahmenwerk CS (Bachelor)
Technische Universität Darmstadt

A. SCHWINN
Entwicklung von Objekt- und Petri-Netzen im Rahmen eines Kontrollsystems (Diplom)
Hochschule Darmstadt

S. SEDIKKI
Study of charmed mesons (D+ -> K pi pi) in CBM experiment. Master, 2007, Strassburg

Academic Teaching

P. MALZACHER
Software Design and Construction (Vorlesung/Übungen), Univ. Frankfurt/M, Wintersemester 2006/7

P. MALZACHER
Introduction to C and C++ (Vorlesung/Übungen), Univ. Frankfurt/M, Wintersemester 2007/8

P. MALZACHER
Software Design and Construction (Vorlesung/Übungen), Univ. Frankfurt/M, Wintersemester 2007/8

Public Talks

E. BERDERMANN for the NoRHDia Collaboration
Performance of diamond detectors in a fragmentation experiment. XLV International Winter Meeting on Nuclear Physics, Bormio, Italy, January 14, 20, 2007

E. BERDERMANN for the NoRHDia Collaboration
Ion spectroscopy – a diamond characterization tool.
18th European Conference on Diamond, Diamond-Like Materials, Carbon Nanotubes, and Nitrides (DIAMOND 2007), Berlin, Germany, September 10,14, 2007

E. BERDERMANN for the NoRHDia Collaboration
CVD-diamond detectors for hadron-physics experiments. University of Augsburg, March 29, 2007

D. BERTINI, M. AL-TURANY, F. UHLIG, I. KÖNIG
FairRoot: FAIR Simulation & Analysis Framework ROOT Workshop, 26-28. March 2007, CERN, Genf

D. BERTINI, M. AL-TURANY, P. MALZACHER, F. UHLIG
FairRoot: the FAIR simulation and analysis framework CHEP 07, 2.-9. September 2007, Victoria, Canada

H. GÖRINGER et al
Experiences with gStore, a scalable Mass Storage System with Tape Backend Computing in High Energy Physics 2007, Victoria/Canada

P. MALZACHER
The German HEP Community Grid (HEPCG), International Symposium on Grid Computing, 26.-29.März 2007, Taipei

P. MALZACHER
End-User Analysis with PROOF, Physics at the Terascale Kick-off Workshop, 4.12.2007, DESY, Hamburg

A. MANAFOV
RGLite plug-in and gLitePROOF package, PROOF on the Grid, CHEP (2007), Victoria, Canada

M. REBISZ:
Diamond detectors for heavy-ion beams dosimetry. IBIBAM, Heidelberg, Germany, September 29, 2007

C. J. SCHMIDT
Test results on the n-XYTER ASIC, a self triggered, sparcifying readout ASIC. Topical Workshop on Electronics for Particle Physics, Prague, Czech Republic, September 3,7, 2007

W. SCHÖN, S. HALLER, C. HUHN
lustre at GSI. HEPIX Fall 2007, St. Louis, 5.11.2007

K. SCHWARZ, A. MANAFOV, P. MALZACHER
RGLite, eine Schnittstelle zwischen ROOT und gLite, DPG Frühjahrstagung (Teilchenphysik), Heidelberg, 2007

K. SCHWARZ, P. MALZACHER, A. MANAFOV
RGLite, an interface between ROOT and gLite -- PROOF on the Grid, CHEP (2007), Victoria, Canada

K. SCHWARZ
GSIAF, "CAF" experience at GSI, PROOF 2007, CERN

Poster presentations

D. BECK, H. BRAND:
Control System Design Using <nop>LabVIEW Object Oriented Programming, Proceedings ICALEPCS 2007, Knoxville, USA

H. BRAND, D. BECK, S. GÖTTE, M. KUGLER,
The PHELIX Control System Based on CS-Framework 3.0, Proceedings ICALEPCS 2007, Knoxville, USA, Poster, Brand

M. RĘBISZ, B.VOSS, Ł. CZOPYK, P. OLKO
1st Poster prize in the category ‘scientific impact’ Investigation of the thermo-luminescence response of diamond to heavy ions. 15th International Conference Solid State Dosimetry, July 8-13, 2007

M. KLOSOWSKI, M. RĘBISZ, Ł. CZOPYK, P. OLKO, B.VOSS, M. WALIGORSKI
TL-efficiency of large-area 2-D detectors to carbon ion beams. 15th International Conference Solid State Dosimetry, July 8-13, 2007

M. RĘBISZ
Participation to the 3rd Summer School on Concepts and Trends in Radiation dosimetry, July 4-7, Delft, The Netherlands

C. J. SCHMIDT for the ALICE-TRD Collaboration
The ALICE Transition Radiation Detector: Chamber manufacturing, system integration and first tracking tests. Vienna Conference on Instrumentation 2007 Vienna, February 19,24, 2007

Research Division: ALICE

Leader: P. Braun-Munzinger
Compiled by: D. Miśkowiec

Publications

PROGRAMME HADRONS & NUCLEI

1. WoS listed publications

D. Antonczyk, D. Miskowiec, Pion-pion and pion-proton correlations: New results from CERES. Braz.J.Phys.37:979-985,2007.

M. Petrovici, et al., A high-efficiency Transition Radiation Detector for high-counting-rate environments. Nucl.Instrum.Meth.A579:961-966,2007.

P. Braun-Munzinger & J.Stachel, The quest for the quark-gluon plasma. Nature 448:302-309,2007.

P. Braun-Munzinger, Quarkonium production in ultra-relativistic nuclear collisions: Suppression versus enhancement. J.Phys.G34:S471-478,2007.

A. Andronic, et al., Statistical hadronization of heavy quarks in ultra-relativistic nucleus-nucleus collisions. Nucl.Phys.A789:334-356,2007.

A. Andronic, et al., Evidence for charmonium generation at the phase boundary in ultra-relativistic nuclear collisions. Phys.Lett.B652:259-261,2007.

J. Petrovic, et al., Radio emission of highly inclined cosmic ray air showers measured with LOPES. Astron.Astrophys.462:389-395,2007.

H. Ulrich, et al., The knee of cosmic rays: News from KASCADE. AIP Conf.Proc.928:31-38,2007.

B. Mitrica, et al., Measurements of cosmic ray muons performed with WILLI detector: Status and perspectives. AIP Conf.Proc.899:131-132,2007, In *Istanbul 2006, Balkan Physical Union* 131-13.

F. Di Pierro, et al., Status of the KASCADE-Grande experiment. Nucl.Phys.Proc.Suppl.165:289-293,2007, In *Catania 2006, Cosmic ray* 289-29.

S. Buitink, et al., Amplified radio emission from cosmic ray air showers in thunderstorms. Astron.Astrophys.467:385-394,2007.

P.G. Isar, et al., Radio Emission in Atmospheric Air Showers: First Measurements with LOPES-30. J.Phys.Conf.Ser.81:012006,2007.

W. Riegler, et al., Gas gain reduction due to space charge in wire chambers. Nucl.Instrum.Meth.A582:469-473,2007.

M.I. Adamovich, et al., Production of V0 pairs in the hyperon experiment WA89. Eur.Phys.J.C52:857-874,2007.

I. Abt, et al., Measurement of D0, D+, D+(s) and D*+ Production in Fixed Target 920-GeV Proton-Nucleus Collisions. Eur.Phys.J.C52:531-542,2007.

I. Abt, et al., Luminosity determination at HERA-B. Nucl.Instrum.Meth.A582:401-412,2007.

M.I. Adamovich, et al., Observation of a resonance in the K(s)p decay channel at a mass of 1765 MeV/c**2. Eur.Phys.J.C50:535-538,2007.

I. Abt, et al., Bottom production cross-section from double muonic decays of b-flavoured hadrons in 920-GeV proton-nucleus collision. Phys.Lett.B650:103-110,2007.

I. Abt, et al., K*0 and phi meson production in proton-nucleus interactions at s**(1/2) = 41.6-GeV. Eur.Phys.J.C50:315-328,2007.

Ch. Hartnack, et al., The nuclear equation of state observed in earthbound experiments. Int.J.Mod.Phys.D16:153-164,2007.

C. Hartnack, et al., On the hadronic equation of state. Int.J.Mod.Phys.E16:753-762,2007.

I. Kraus, et al., Chemical Equilibrium in Collisions of Small Systems. Phys.Rev.C76:064903,2007.

I. Kraus, et al., Do small systems equilibrate chemically? Eur.Phys.J.C49:109-113,2007.

2. Other publications

Academic Works

O. BUSCH
Dielectron Production in Heavy Ion collisions at 158 GeV/c per Nucleon (Ph.D.).
TU Darmstadt, 03.12.2007

Public Talks

A. ANDRONIC

Statistical hadronization of heavy quarks in ultra-relativistic nucleus-nucleus collisions, Colloquium, IKF, Uni Frankfurt, 11-Jan-2007.

Statistical hadronization of charm quarks in ultra-relativistic nucleus-nucleus collisions, XXXVIII Arbeitstreffen Kernphysik - Schleching, 22-Feb-01-Mar-2007.

Statistical hadronization of heavy quarks in ultra-relativistic nucleus-nucleus collisions, Critical Point and Onset of Deconfinement, Darmstadt, 12-Jul-2007.

Statistical hadronization of heavy quarks in ultra-relativistic nucleus-nucleus collisions: from FAIR to LHC, Physics of Compressed Baryonic Matter Symposium, Dresden, 25-Sep-2007.

R. BAILHACHE

Reconstruction of Z0 through his electronic decay channel with the central barrel, Alice Physics Working Group 3, 5-Nov-2007.

A. BERCUCI

Particle identification with the TRD, Alice Physics Working Group 2, 12-Dec-2007.

P.BRAUN-MUNZINGER

Review of models for quarkonium production in ultra-relativistic nuclear collisions, ALICE physics week, Muenster, 13-Feb-2007.

Charmonium, bound state of QCD, probe for QGP, Studienstiftungskolleg, Bochum, March 2007.

Production of open and hidden charm hadrons from SIS to LHC energy, VISIM meeting on charmonia, GSI Darmstadt, 27-Apr-2007.

Hadron production in ultra-relativistic nuclear collisions and the QCD phase boundary, II. Workshop on Collective Dynamics in Ultra-relativistic Nuclear Collisions, Berkeley, Ca, May 2007.

The quest for the quark-gluon plasma, Symposium in Honor of R. Bock's 80th Birthday, GSI Darmstadt, May 2007.

Prediction of thermal hadron production in Pb-Pb collisions at LHC energy, CERN focus week on predictions for LHC, Geneva, May 2007.

Prediction of open and hidden charm production in Pb-Pb collisions at LHC energy, CERN focus week on predictions for LHC, Geneva, May 2007.

Quarkonium production from SIS100 to LHC energy, Workshop on Relativistic Nuclear Physics, Kiev, June 2007.

Charmonium and Open Charm from SIS300 to SPS Energy, VI-SIM workshop on Heavy Ion Perspectives, Bad Liebenzell, 12-Sep-2007.

Charmonium - an exotic bound state, a tool to probe the Quark-Gluon Plasma, Special Session of the Polish Physical Society, Wroclaw, Oct. 2007.

U. FRANKENFELD

Commissioning of the ALICE Time Projection Chamber, Vienna Conference of Instrumentation, 20-Feb-2007.

M. IVANOV

TPC calibration and alignment, Alice Physics Week, Muenster, 16-Feb-2007.

Comparison of V0 finders, Alice Week, Geneva, 3-Jul-2007.

Multidimensional local regression, Alice Week, Geneva, 4-Jul-2007.

A. MARIN

Physics with conversions photons, Alice Physics Week, Muenster, 15-Feb-2007..

Dilepton Measurements with CERES, Critical Point and Onset of Deconfinement, Darmstadt, 12-Jul-2007.

S. MASCIOCCHI

Vertexing for heavy flavour decays in HERA-B and CBM, Alice Physics Working Group 3, 9-Jan-2007.

First tests of a new vertexing package, Alice Week, Geneva, 6-Mar-2007.

Status of the GSi/KIP vertexing package, Alice Physics Working Group 3, 7-May-2007.

The KF vertexing package applied to Lambda_c 3 prong decays, Alice Week, Geneva, 2-Jul-2007.

Update of the KF vertexing package applied to the Lambdac, Alice Physics Working Group 3, 3-Sep-2007.

KF vertexing, Alice Week, Geneva, 1-Oct-2007.

PID in the TRD, Alice Week, Geneva, 1-Oct-2007.

D. MISKOWIEC

Charged particle multiplicity analysis - experience from CERES, Alice Week, Geneva, 6-Mar-2007. .

Correlations and fluctuations from CERES, Critical Point and Onset of Deconfinement, Darmstadt, 10-Jul-2007.

Quark-gluon plasma paradox, Critical Point and Onset of Deconfinement, Darmstadt, 10-Jul-2007.

Freeze-out characterization in Pb+Au collisions at 158 AGeV, Workshop on Particle Correlations and Femtoscopy, Santa Rosa, 1-Aug-2007.

The ALICE experiment, Heavy Ion Perspectives, Bad Liebenzell, 14-Sep-2007.

The ALICE experiment, Hades Summer School, Riezlern, 19-Sep-2007.

The NA45/CERES experiment at the SPS, Hades Summer School, Riezlern, 19-Sep-2007.

H. OESCHLER

Statistical model predictions in pp and PbPb collisions at LHC, Alice Physics Week, Muenster, 13-Feb-2007.

Research: Atomic Physics

Leader: T. Stöhlker
Compiled by: S. Lüttges

Publications

PROGRAMME PNI

1. WoS listed publications

Andreyev, A.H.-J. Kluge:
Exotic lead nuclei get into shape at ISOLDE
CERN Courier October 2007, 19 (2007)
DOI:

Antalic, S., A. N. Andreyev, D. Ackermann, L. Bianco, D. Cullen, I. Darby, S. Franchoo, S. Heinz, F. P. Hessberger, S. Hofmann, M. Huyse, B. Kindler, I. Kojouharov, A. P. Leppanen, S. R. Lesher, B. Lommel, R. Mann, G. Munzenberg, K. Nishio, R. D. Page, J. Pakarinen, J. J. Ressler, S. Saro, B. Streicher, B. Sulignano, J. Thomson, P. Van Duppen, M. Venhart, D. Wiseman, R. Wyss:
The new isotopes in Po-Rn region
Acta Physica Polonica B 38, 1557 (2007)
DOI:

Backe, H., P. Kunz, W. Lauth, A. Dretzke, R. Horn, T. Kolb, M. Laatiaoui, M. Sewtz, D. Ackermann, M. Block, F. Herfurth, F. P. Heßberger, S. Hofmann, R. Mann:
Towards optical spectroscopy of the element nobelium (Z=102) in a buffer gas cell
Eur. Phys. J. D 45, 99 (2007)
DOI: 10.1140/epjd/e2007-00198-1

Banas, D., P. Jagodzinski, M. Pajek, T. Stöhlker, M. Trassinelli, H. F. Beyer, R. Reuschl, U. Spillmann:
Development of a Bragg spectrometer for experiments with highly charged ions at storage rings
J. Phys. Conf. 58, 415 (2007)
DOI: 10.1088/1742-6596/58/1/095

Becker, R., O. Kester, T. Stöhlker:
Simulation of charge breeding for trapped ions
J. Phys. Conf. 58, 443 (2007)
DOI: 10.1088/1742-6596/58/1/102

Becker, U., R. Moshammer, P. Mokler, J. Ullrich:
XXV. International Conference on Photonic, Electronic and Atomic Collisions (Preface)
Institute of Physics (IOP), p. 011001 (2007) (Institute of Physics (IOP) Freiburg, Germany, 2007)
DOI: 10.1088/1742-6596/88/1/011001

Block, M., D. Ackermann, K. Blaum, A. Chaudhuri, Z. Di, S. Eliseev, R. Ferrer, D. Habs, F. Herfurth, F. P. Hessberger, S. Hofmann, H. J. Kluge, G. Maero, A. Martin, G. Marx, M. Mazzocco, M. Mukherjee, J. B. Neumayr, W. R. Plass, W. Quint, S. Rahaman, C. Rauth, D. Rodriguez, C. Scheidenberger, L. Schweikhard, P. G. Thirolf, G. Vorobjev, C. Weber:
Mass measurements of exotic nuclides at SHIPTRAP
American Institute of Physics (AIP), p. 423 (2007) (American Institute of Physics (IOP) Khanty-Mansiysk (Russia), 2007)
DOI: 10.1063/1.2746619

Block, M., D. Ackermann, K. Blaum, A. Chaudhuri, Z. Di, S. Eliseev, R. Ferrer, D. Habs, F. Herfurth, F. P. Heßberger, S. Hofmann, H.-J. Kluge, G. Maero, A. Martín, G. Marx, M. Mazzocco, M. Mukherjee, J. B. Neumayr, W. R. Plaß, W. Quint, S. Rahaman, C. Rauth, D. Rodríguez, C. Scheidenberger, L. Schweikhard, P. G. Thirolf, G. Vorobjev, C. Weber:
Towards direct mass measurements of nobelium at SHIPTRAP
Eur. Phys. J. D 45, 39 (2007)
DOI: 10.1140/epjd/e2007-00189-2

Brandau, C., D. Boutin, H. Geissel, J. Gerl, M. Górska, S. Manikonda, G. Münzenberg, Z. Podolyák,
C. Scheidenberger, H. Weick, M. Winkler, M. Yavor:
Status of the energy-buncher in the low-energy branch of the Super-FRS
Eur. Phys. J. 150, 225 (2007)
DOI: 10.1140/epjst/e2007-00309-2

Brandau, C., C. Kozhuharov, A. Müller, K. Beckert, P. Beller, D. Bernhardt, F. Bosch, S. Böhm, F. J. Currell, A. Gumberidze, Z. Harman, J. Jacobi, P. H. Mokler, F. Nolden, R. Reuschl, S. Schippers, E. W. Schmidt, U. Spillmann, Z. Stachura, M. Steck, T. Stöhlker, A. Wolf:
Photorecombination studies of highly charged ions at the storage ring ESR: a progress report
J. Phys. Conf. 58, 81 (2007)
DOI: 10.1088/1742-6596/58/1/012

Bräuning, H., H. Helm, J. S. Briggs, E. Salzborn:
Double electron transfer in $H^- + H^+$ collisions
Institute of Physics (IOP), p. 012033 (2007) (Institute of Physics (IOP) Freiburg, Germany, 2007)
DOI: 10.1088/1742-6596/88/1/012033

Bushaw, B. A., W. Nörtershäuser, G. W. F. Drake, H.-J. Kluge:
Ionization energy of ^{6,7}Li determined by triple-resonance laser spectroscopy
Phys. Rev. A 75, 052503 (2007)
DOI: 10.1103/PhysRevA.75.052503

Bussmann, M., U. Schramm, D. Habs, M. Steck, T. Kühl, K. Beckert, P. Beller, B. Franzke, W.

Nörtershäuser, C. Geppert, C. Novotny, J. Kluge, F. Nolden, T. Stöhlker, C. Kozhuharov, S. Reinhardt, G. Saathoff, S. Karpuk:
The dynamics of bunched laser-cooled ion beams at relativistic energies
Institute of Physics (IOP), p. 012043 (2007)
(Institute of Physics (IOP) Freiburg, Germany, 2007)
DOI: 10.1088/1742-6596/88/1/012043
Caceres, L. S., M. Gorska, A. Jungclaus, P. H. Regan, A. B. Garnsworthy, S. Pietri, Z. Podolyak, D. Rudolph, S. J. Steer, H. Grawe, D. L. Balabanski, F. Becker, P. Bednarczyk, G. Benzoni, B. Blank, C. Brandau, A. M. Bruce, F. Camera, W. N. Catford, I. J. Cullen, Z. Dombradi, P. Doornenbalal, E. Estevez, H. Geissel, W. Gelletly, J. Gerl, J. Grebosz, A. Heinz, R. Hoischen, G. Ilie, J. Jolie, G. A. Jones, M. Kmiecik, I. Kojouharov, F. G. Kondev, T. Kurtukian-Nieto, N. Kurz, S. Lalkowski, L. Liu, A. Maj, S. Myalsk, F. Montes, M. Pfutzner, W. Prokopowicz, T. Saito, H. Schatfner, S. Schwertel, T. Shizuma, A. J. Simons, S. Tashenov, P. M. Walker, E. Werner-Malento, O. Wielandh, H. J. Wollersheim:
Identification of excited states in the N = Z nucleus Nb-82
Acta Physica Polonica B 38, 1271 (2007)
DOI:
Caliceti, E., M. Meyer-Hermann, P. Ribeca, A. Surzhykov, U. D. Jentschura:
From useful algorithms for slowly convergent series to physical predictions based on divergent perturbative expansions
Phys. Rep. 446, 1 (2007)
DOI: 10.1016/j.physrep.2007.03.003
Cassou, K., S. Kazamias, D. Ros, F. Ple, G. Jamelot, A. Klisnick, O. Lundh, F. Lindau, A. Persson, C. G. Wahstrom, S. de Rossi, D. Joyeux, B. Zielbauer, D. Ursescu, T. Kühl:
Optimization toward a high-average-brightness soft-x-ray laser pumped at grazing incidence
Opt. Lett. 32, 139 (2007)
DOI:
Cederkall, J., A. Ekstrom, C. Fahlander, A. M. Hurst, M. Hjorth-Jensen, F. Ames, A. Banu, P. A. Butler, T. Davinson, U. D. Pramanik, J. Eberth, S. Franchoo, G. Georgiev, M. Gorska, D. Habs, M. Huyse, O. Ivanov, J. Iwanicki, O. Kester, U. Koster, B. A. Marsh, O. Niedermaier, T. Nilsson, P. Reiter, H. Scheit, D. Schwalm, T. Sieber, G. Sletten, I. Stefanescu, J. V. de Walle, P. Van Duppen, N. Warr, D. Weisshaar, F. Wenander:
Sub-barrier Coulomb excitation of ^{110}Sn and its implications for the ^{100}Sn shell closure
Phys. Rev. Lett. 98, 172501 (2007)
DOI: 10.1103/PhysRevLett.98.172501
Chatterjee, S.:
Measurement of the Wavelength of the Lyman-α_1 Transition of $^{208}Pb^{81+}$ Using FOCAL Spectrometers
Dissertation, Ruprechts-Karls-Universität, Heidelberg
Chaudhuri, A., M. Block, S. Eliseev, R. Ferrer, F. Herfurth, A. Martin, G. Marx, M. Mukherjee, C. Rauth, L. Schweikhard, G. Vorobjev:
Carbon-cluster mass calibration at SHIPTRAP
Eur. Phys. J. D 45, 47 (2007)
DOI: 10.1140/epjd/e2007-00001-5
DuBois, R. D., O. de Lucio, M. Thomason, G. Weber, T. Stöhlker, K. Beckert, P. Beller, F. Bosch, C. Brandau, A. Gumberidze, S. Hagmann, C. Kozhuharov, F. Nolden, R. Reuschl, J. Rzadkjewicz, P. Spiller, U. Spillmann, M. Steck, S. Trotsenko:
Beam lifetimes for low-charge-state heavy ions in the GSI storage rings
Nucl. Instrum. Methods Phys. Res., Sect. B 261, 230 (2007)
DOI: 10.1016/j.nimb.2007.03.044
Eichler, J.T. Stöhlker:
Radiative electron capture in relativistic ion-atom collisions and the photoelectric effect in hydrogen-like high-Z systems
Phys. Rep. 439, 1 (2007)
DOI: 10.1016/j.physrep.2006.11.003
Eliseev, S., M. Block, A. Chaudhuri, F. Herfurth, H.-J. Kluge, A. Martin, C. Rauth, G. Vorobjev:
Octupolar Excitation of Ions Stored in a Penning Trap Mass Specrometer - A Study Performed at SHIPTRAP
Int. J. Mass. Spectrom. 262, 45 (2007)
DOI: 10.1016/j.ijms.2006.10.003
Eliseev, S. A., M. Block, A. Chaudhuri, Z. Di, D. Habs, F. Herfurth, H.-J. Kluge, J. B. Neumayr, W. R. Plass, C. Rauth, P. G. Thirolf, G. Vorobjev, Z. Wang:
Extraction efficiency and extraction time of the SHIPTRAP gas-filled stopping cell
Nuclear Instruments & Methods in Physics Research Section B 258, 479 (2007)
DOI: 10.1016/j.nimb.2007.01.291
Ferrer, R., K. Blaum, M. Block, F. Herfurth, J. Ketelaer, S. Nagy, D. Neidherr, C. Weber:
Development of a Fourier-Transform Ion-Cyclotron-Resonance detection for short-lived radionuclides at SHIPTRAP
Eur. Phys. J. 150, 347 (2007)
DOI: 10.1140/epjst/e2007-00342-1
Fritzsche, S., J. Nikkinen, S. M. Huttula, H. Aksela, M. Huttula, S. Aksela:
Interferences in the $3p_4nl$ satellite emission following the excitation of argon across the $2p_{51}$ $_{2}4s$ and $2p_{53/2}3d$ $J = 1$ resonances
Phys. Rev. A 75, 012501 (2007)
DOI: 10.1103/PhysRevA.75.012501
Fritzsche, S., A. Surzhykov, G. Gaigalas:
Interelectronic effects on the photon angular distribution following the radiative electron capture into lithium-like ions
Radiat. Phys. Chem. 76, 612 (2007)
DOI: 10.1016/j.radphyschem.2005.11.038

Fritzsche, S., A. Surzhykov, U. D. Jentschura, T. Stöhlker:
Angular and polarization analysis of x-rays emitted from highly-charged, few-electron ions
Institute of Physics (IOP), p. 012018 (2007)
(Institute of Physics (IOP) Freiburg, Germany, 2007)
DOI: 10.1088/1742-6596/88/1/012018

Geissel, H., Y. A. Litvinov, K. Beckert, P. Beller, F. Bosch, D. Boutin, C. Brandau, L. Chen, M. Hausmann, O. Klepper, R. Knöbel, C. Kozhuharov, J. Kurcewicz, S. A. Litvinov, M. Mazzocco, G. Münzenberg, C. Nociforo, F. Nolden, Z. Patyk, M. Pfützner, W. Plaß, C. Scheidenberger, M. Steck, B. Sun, K. Takahashi, H. Weick, N. Winckler, M. Winkler:
Present and future experiments with stored exotic nuclei at the FRS-ESR facility
Eur. Phys. J. 150, 109 (2007)
DOI: 10.1140/epjst/e2007-00280-x

George, S., S. Baruah, B. Blank, K. Blaum, M. Breitenfeldt, U. Hager, F. Herfurth, A. Herlert, A. Kellerbauer, H.-J. Kluge, M. Kretzschmar, D. Lunney, R. Savreux, S. Schwarz, L. Schweikhard, C. Yazidjian:
Ramsey Method of Separated Oscillatory Fields for High-Precision Penning Trap Mass Spectrometry
Phys. Rev. Lett. 98, 162501 (2007)
DOI: 10.1103/PhysRevLett.98.162501

George, S., K. Blaum, F. Herfurth, A. Herlert, M. Kretzschmar, S. Nagy, S. Schwarz, L. Schweikhard, C. Yazidjian:
The Ramsey method in high-precision mass spectrometry with Penning traps: Experimental results
Int. J. Mass. Spectrom. 264, 110 (2007)
DOI: 10.1016/j.ijms.2007.04.003

George, S., K. Blaum, M. Kretzschmar, L. Schweikhard:
Die Ramsey-Methode in der Präzisions-Massenspektrometrie
Phys. unserer Zeit 38, 163 (2007)
DOI:

Guenaut, C., G. Audi, D. Beck, K. Blaum, G. Bollen, P. Delahaye, F. Herfurth, A. Kellerbauer, H.-J. Kluge, J. Libert, D. Lunney, S. Schwarz, L. Schweikhard, C. Yazidjian:
High-precision mass measurements of nickel, copper, and gallium isotopes and the purported shell closure at N = 40
Phys. Rev. C 75, 044303 (2007)
DOI: 10.1103/PhysRevC.75.044303

Gumberidze, A., T. Stöhlker, D. Banas, K. Beckert, P. Beller, H. F. Beyer, F. Bosch, X. Cai, S. Hagmann, C. Kozhuharov, D. Liesen, F. Nolden, X. Ma, P. H. Mokler, M. Steck, D. Sierpowski, S. Tashenov, A. Warczak, Y. Zou:
Precision tests of QED in strong fields: experiments on hydrogen- and helium-like uranium
J. Phys. Conf. 58, 87 (2007)
DOI: 10.1088/1742-6596/58/1/013

Hagmann, S., M. Nofal, T. Stöhlker, D. H. Jakubassa-Amundsen, C. Kozhuharov, X. Wang, A. Gumberidze, U. Spillmann, R. Reuschl, S. Hess, S. Trotsenko, D. Banas, F. Bosch, D. Liesen, R. Moshammer, J. Ullrich, R. Dörner, M. Steck, F. Nolden, H. Rothard, G. Lanzanó, E. deFilippo:
Radiative electron capture to continuum (RECC) and the short-wavelength limit of electronnucleus
Bremsstrahlung in near-relativistic collisions
Institute of Physics (IOP), p. 012015 (2007)
(Institute of Physics (IOP) Freiburg, Germany, 2007)
DOI: 10.1088/1742-6596/88/1/012015

Hagmann, S., T. Stöhlker, C. Kozhuharov, J. Ullrich, R. Dorner, R. Moshammer, M. Nofal, H. Rothard, U. Spillmann, R. Reuschl, S. Hess, S. Trotsenko, D. Banas, F. Bosch, D. Liesen, M. Steck, C. Dimopoulou, F. Nolden, D. Jakubassa-Amundsen, G. Lanzano, E. deFilippo, X. Wang, B. Wei:
Current and future electron spectroscopy experiments in relativistic storage rings
Nucl. Instrum. Methods Phys. Res., Sect. B 261, 218 (2007)
DOI: 10.1016/j.nimb.2007.03.106

Herlert, A., S. Baruah, K. Blaum, M. Breitenfeldt, P. Delahaye, M. Dworschak, S. George, C. Guénaut, U. Hager, F. Herfurth, A. Kellerbauer, H.-J. Kluge, D. Lunney, R. Savreux, S. Schwarz, L. Schweikhard, C. Yazidjian:
High-precision mass measurements for reliable nuclear astrophysics calculations
Proceedings of Science, p. 1 (2007)
(Proceedings of Science CERN, Geneva, Switzerland, 2007)
DOI:

Hofmann, S., D. Ackermann, S. Antalic, H. Burkhard, V. Comas, R. Dressler, Z. Gan, S. Heinz, J. Heredia, F. Hessberger, J. Khuyagbaatar, B. Kindler, I. Kojouharov, P. Kuusiniemi, M. Leino, B. Lommel, R. Mann, G. Münzenberg, K. Nishio, A. Popeko, S. Saro, H. Schött, B. Streicher, B. Sulignano, J. Uusitalo, M. Venhart, A. Yeremin:
The reaction ^{48}Ca + ^{238}U to ^{286}112* studied at the GSI-SHIP
The European Physical Journal A 32, 251 (2007)
DOI: 10.1140/epja/i2007-10373-x

Hofmann, S., D. Ackermann, S. Antalic, H. G. Burkhard, V. F. Comas, R. Dressler, Z. Gan, S. Heinz, J. A. Heredia, F. P. Hebberger, J. Khuyagbaatar, B. Kindler, I. Kojouharov, P. Kuusiniemi, M. Leino, B. Lommel, R. Mann, G. Menzenberg, K. Nishio, A. G. Popeko, S. Saro, H. J. Schott, B. Streicher, B. Sulignano, J. Uusitalo, A. V. Yeremin:
Studies of superheavy elements at ship
International Journal of Modern Physics E 16, 937 (2007)

DOI: 10.1142/S021830130700640X
Hofmann, S., D. Ackermann, S. Antalic, H. G. Burkhard, V. F. Comas, R. Dressler, Z. Gan, S. Heinz, J. A. Heredia, F. P. Hessberger, J. Khuyagbaatar, B. Kindler, I. Kojouharov, P. Kuusiniemi, M. Leino, B. Lommel, R. Mann, G. Munzenberg, K. Nishio, A. G. Popeko, S. Saro, H. J. Schott, B. Streicher, B. Sulignano, J. Uusitalo, M. Venhart, A. V. Yeremin:
The reaction ^{48}Ca + ^{238}U -> ^{286}112* studied at the GSI-SHIP
Eur. Phys. J. A 32, 251 (2007)
DOI: 10.1140/epja/i2007-10373-x
Ilieva, S., O. Kiselev, H. Emling, P. Egelhof, K. Boretzky, J. P. Meier, H. Simon, K. Mahata, T. Le Bleis, A. Chatillon, F. Aksouh, K. Beckert, P. Beller, C. Kozhuharov, Y. Litvinov, X. C. Le, F. Nolden, M. Steck, T. Stöhlker, G. Ickert, U. Popp, H. Weick, D. Rohe, J. Jourdan, D. Werthmüller, H. Moeini, A. Zalite, S. Paschalis:
Feasibility studies of the EXL setup for FAIR using the GSI storage ring ESR
Eur. Phys. J. 150, 357 (2007)
DOI: 10.1140/epjst/e2007-00345-x
Jänkälä, K., S. Fritzsche, M. Huttula, J. Schulz, S. Urpelainen, S. Heinäsmäki, S. Aksela, H. Aksela:
Many-electron effects in 2p photoionization and Auger decay of atomic aluminium
J. Phys. B 40, 3435 (2007)
DOI: 10.1088/0953-4075/40/17/011
Kabachnik, N. M., S. Fritzsche, A. N. Grum-Grzhimailo, M. Meyer, K. Ueda:
Coherence and correlations in photoinduced Auger and fluorescence cascades in atoms
Phys. Rep. 451, 155 (2007)
DOI: 10.1016/j.physrep.2007.07.005
Kellerbauer, A., G. Audi, D. Beck, K. Blaum, G. Bollen, C. Guénaut, F. Herfurth, A. Herlert, H.-J. Kluge, D. Lunney, S. Schwarz, L. Schweickhard, C. Weber, C. Yazidjian:
High-precision masses of neutron-deficient rubidium isotopes using a Penning trap mass spectrometer
Phys. Rev. C 76, 045504 (2007)
DOI: 10.1103/PhysRevC.76.045504
Kluge, H.-J., W. Quint, D. F. A. Winters:
Atomic physics experiments with trapped an cooled highly charged ions
IOP Conference Series, p. 9 (2007)
(IOP Conference Series Belfast, Northern Ireland, 2007)
DOI: 10.1088/1742-6596/58/1/002
Lanzano, G., E. De Filippo, S. Hagmann, H. Rothard, C. Volant:
Bombarding insulating foils with highly energetic ions
Radiation Effects and Defects in Solids 162, 303 (2007)
DOI: 10.1080/10420150601104908
Lanzano, G., E. De Filippo, S. Hagmann, H. Rothard, C. Volant:
In-flight emission of projectile Auger electrons from highly energetic heavy ions (20 MeV/u < *E* < 100 MeV/u) colliding with carbon foils
Nucl. Instrum. Methods Phys. Res., Sect. B 256, 510 (2007)
DOI: 10.1016/j.nimb.2006.12.099
Lindau, F., O. Lundh, A. Persson, K. Cassou, S. Kazamias, D. Ros, F. Ple, G. Jamelot, A. Klisnick, S. de Rossi, D. Joyeux, B. Zielbauer, D. Ursescu, T. Kühl, C. G. Wahlstrom:
Quantitative study of 10 Hz operation of a soft x-ray laser-energy stability and target considerations
Optics Express 15, 9486 (2007)
DOI:
Litvinov, Y. A., H. Geissel, K. Beckert, P. Beller, F. Bosch, D. Boutin, C. Brandau, L. Chen, I. Cullen, C. Dimopoulou, B. Fabian, M. Hausmann, O. Klepper, R. Knobel, C. Kozhuharov, J. Kurcewicz, S. A. Litvinov, Z. Liu, M. Mazzocco, F. Montes, G. Munzenberg, A. Musumarra, S. Nakajima, C. Nociforo, F. Nolden, T. Ohtsubo, A. Ozawa, Z. Patyk, W. Plass, C. Scheidenberger, M. Steck, B. Sun, T. Suzuki, P. M. Walker, H. Weick, C. Scheidenberger, M. Steck, B. Sun, T. Suzuki, P. M. Walker, H. Weick, N. Winckler, M. Winckler, T. Yamaguchi:
Status of the experimental program on mass measurements of stored exotic nuclei at the FRS-ESR facility
Nucl. Phys. A 787, 315 (2007)
DOI: 10.1016/j.nuclphysa.2006.12.050
Maiorova, A. V., D. A. Telnov, V. M. Shabaev, I. I. Tupitsyn, G. Plunien, T. Stöhlker:
Backward scattering of low-energy antiprotons by highly charged and neutral uranium: Coulomb glory
Phys. Rev. A 76, 032709 (2007)
DOI: 10.1103/PhysRevA.76.032709
Mokler, P. H.:
Concept of a new turbomolecular pump with central opening for free axial access--The Ring turbomolecular pump
Vacuum 82, 408 (2007)
DOI: 10.1016/j.vacuum.2007.05.006
Mokler, P. H.:
Higher Order QED Contributions to the Atomic Structure at Strong Central Fields
Journal of Physics: Conference Series 72, 012014 (2007)
DOI: 10.1088/1742-6596/72/1/012014
Mokler, P. H., X. Ma, E. G. Drukarev, A. I. Mikhailov, I. A. Mikhailov:
Emission characteristics of K cascade photons after radiative electron capture at strong central fields
Journal of Physics: Conference Series 58, 287 (2007)

DOI: 10.1088/1742-6596/58/1/063
Nagy, S., T. Fritioff, I. Bergström, K. Blaum, M. Suhonen, A. Solders, R. Schuch:
High-precision mass measurements for fundamental applications using highly-charged ions with SMILETRAP
J. Phys. Conf. 58, 109 (2007)
DOI: 10.1088/1742-6596/58/1/018
Nofal, M., S. Hagmann, T. Stöhlker, D. H. Jakubassa-Amundsen, C. Kozhuharov, X. Wang, A. Gumberidze, U. Spillmann, R. Reuschl, S. Hess, S. Trotsenko, D. Banas, F. Bosch, D. Liesen, R. Moshammer, J. Ullrich, R. Dörner, M. Steck, F. Nolden, P. Beller, K. Beckert, B. Franczak:
Radiative Elecron Capture to Continuum (RECC) in 90AMeV $U^{88+}(1s^2 2s^2)+N_2$: The Short Wavelength Limit of Electron Nucleus Bremsstrahlung
Journal of Physics Conference Series, p. 307 (2007) (Journal of Physics Conference Series Belfast, Northern Ireland, 2007)
DOI: 10.1088/1742-6596/58/1/068
Nofal, M., S. Hagmann, T. Stöhlker, D. H. Jakubassa-Amundsen, C. Kozhuharov, X. Wang, A. Gumberidze, U. Spillmann, R. Reuschl, S. Hess, S. Trotsenko, D. Banas, F. Bosch, D. Liesen, R. Moshammer, J. Ullrich, R. Dorner, M. Steck, F. Nolden, P. Beller, H. Rothard, K. Beckert, B. Franczak:
Radiative Electron Capture to the Continuum and the Short-Wavelength Limit of Electron-Nucleus Bremsstrahlung in 90*A* MeV U^{88+} ($1s^2 2s^2$) + N_2 Collisions
Phys. Rev. Lett. 99, 163201 (2007)
DOI: 10.1103/PhysRevLett.99.163201
Pietri, S., P. H. Regan, Z. Podolyak, D. Rudolph, M. Gorska, A. Jungclaus, M. Pfutzner, A. B. Garnsworthy, S. J. Steer, L. Caceres, E. Werner-Malento, R. Hoischen, J. Gerl, I. Kojouharov, H. Schaffner, H. J. Wollersheim, F. Becker, P. Bednarczyk, P. Doornenbal, H. Geissel, J. Grebosz, A. Kelic, N. Kurz, F. Montes, W. Prokopowicz, T. Saito, S. Tashenov, A. Heinz, T. Kurtukian-Nieto, G. Benzoni, M. Hellstrom, L. L. Andersson, L. Atanasova, D. L. Balabanski, M. A. Bentley, B. Blank, A. C. Brandau, J. R. Brown, A. M. Bruce, F. Camera, W. N. Catford, I. J. Cullen, Z. Dombradi, E. Estevez, C. Fahlander, W. Gelletly, G. Ilie, E. K. Johansson, J. Jolie, G. A. Jones, M. Kmiecik, F. G. Kondev, S. Lalkovski, Z. Liu, A. Maj, S. Myalski, T. Shizuma, A. J. Simons, S. Schwertel, P. M. Walker, O. Wieland:
First results from the stopped beam isomer rising campaign at GSI
Acta Physica Polonica B 38, 1255 (2007)
DOI:
Pietri, S., P. H. Regan, Z. Podolyak, D. Rudolph, S. Steer, A. B. Garnsworthy, E. Werner-Malento, R. Hoischen, M. Gorska, J. Gerl, H. J. Wollersheim, I. Kojouharov, H. Schaffner, F. Becker, P. Bednarczyk, L. Caceres, P. Doornenbal, H. Geissel, J. Grebosz, A. Kelic, N. Kurz, F. Montes, W. Prokopowicz, T. Saito, S. Tashenov, A. Heinz, M. Pfutzner, T. Kurtukian-Nieto, G. Benzoni, M. Hellstrom, A. Jungclaus, J. Simpson, L. L. Andersson, L. Atanasova, D. Balabanski, M. A. Bentley, A. Blazhev, C. Brandau, J. R. Brown, A. M. Bruce, F. Camera, W. N. Catford, I. J. Cullen, Z. Dombradi, E. Estevez, C. Fahlander, W. Gelletly, G. Ilie, E. K. Johansson, J. Jolie, G. A. Jones, M. Kmiecik, F. G. Kondev, S. Lalkovski, Z. Liu, A. Maj, S. Myalski, T. Shizuma, A. J. Simons, S. Schwertel, P. M. Walker, O. Wieland:
Recent results in fragmentation isomer spectroscopy with rising
Nucl. Instrum. Methods Phys. Res., Sect. B 261, 1079 (2007)
DOI: 10.1016/j.nimb.2007.04.219
Podolyák, Z., S. J. Steer, S. Pietri, E. Werner-Malento, P. H. Regan, D. Rudolph, A. B. Garnsworthy,
R. Hoischen, M. Górska, J. Gerl, H. J. Wollersheim, T. Kurtukian-Nieto, G. Benzoni, F. Becker, P. Bednarczyk, L. Caceres, P. Doornenbal, H. Geissel, J. Gręboszc, A. Kelic, I. Kojouharov, N. Kurz, F. Montes, W. Prokopowicz, T. Saito, H. Schaffner, S. Tashenov, A. Heinz, M. Pfützner, M. Hellström, A. Jungclaus, L. L. Andersson, L. Atanasova, D. L. Balabanski, M. A. Bentley, B. Blank, A. Blazhev, C. Brandau, J. Brown, A. M. Bruce, F. Camera, W. N. Catford, I. J. Cullen, Z. Dombrádi, E. Estevez, C. Fahlander, W. Gelletly, G. Ilie, E. K. Johansson, J. Jolie, G. A. Jones, M. Kmiecik, F. G. Kondev, S. Lalkovski, Z. Liu, A. Maj, S. Myalski, T. Shizuma, A. J. Simons, S. Schwertel, P. M. Walker, O. Wieland, B. A. Brown:
Isomeric decay studies around ^{204}Pt and ^{148}Tb
Eur. Phys. J. 150, 165 (2007)
DOI: 10.1140/epjst/e2007-00294-4
Rauth, C., D. Ackermann, G. Audi, M. Block, A. Chaudhuri, S. Eliseev, F. Herfurth, F. P. Heßberger, S. Hofmann, H. J. Kluge, A. Martín, G. Marx, M. Mukherjee, J. B. Neumayr, W. R. Plaß, S. Rahaman, D. Rodríguez, L. Schweikhard, P. G. Thirolf, G. Vorobjev, C. Weber:
Direct mass measurements around A=146 at SHIPTRAP
Eur. Phys. J. 150, 329 (2007)
DOI: 10.1140/epjst/e2007-00339-8
Regan, P. H., A. B. Garnsworthy, S. Pietri, L. Caceres, M. Gorska, D. Rudolph, Z. Podolyak, S. J. Steer, R. Hoischen, J. Gerl, H. J. Wollersheim, J. Grebosz, H. Schaffner, W. Prokopwicz, I. Kojouharov, F. Becker, P. Bednarczyk, P. Doornenball, H. Geissel, H. Grawe, A. Kelic, N. Kurz, F. Montes, T. Saito, S. Tashenov, E. Werner-Malento, A. Heinz, L. Atanasova, D. Balabanski, G.

Benzoni, B. Blank, A. Blazhev, C. Brandau, A. M. Bruce, F. Camera, I. J. Cullen, M. E. Estevez, C. Fahlander, W. Gelletly, G. Ilie, A. Jungclaus, J. Jolie, T. Kurtukian-Nieto, Z. Liu, M. Kmiecik, A. Maj, S. Myalski, S. Schwertel, T. Shizuma, A. J. Simons, P. M. Walker, O. Wieland:
Isomer spectroscopy using relativistic projectile fragmentation at the N=Z line for A similar to 80 -> 90.
Nucl. Phys. A 787, 491c (2007)
DOI: 10.1016/j.nuclphysa.2006.12.073
Reinhardt, S., B. Bernhardt, C. Geppert, R. Holzwarth, G. Huber, S. Karpuk, N. Miski-Oglu, W. Nörtershäuser, C. Novotny, T. Udem:
Absolute frequency measurements and comparisons in iodine at 735 nm and 772 nm
Opt. Commun. 274, 354 (2007)
DOI: 10.1016/j.optcom.2007.02.050
Reuschl, R., D. Banas, H. F. Beyer, S. Chatterjee, A. Gumberidze, S. Hess, T. Krings, D. Liesen, D. Protic, U. Spillmann, T. Stöhlker, M. Trassinelli, S. Trotsenko, G. Weber, the FOCAL Collaboration:
Recent experimental developments for the Lamb shift investigation in heavy ions
J. Phys. Conf. 58, 407 (2007)
DOI: 10.1088/1742-6596/58/1/093
Rothard, H., R. Moshammer, J. Ullrich, H. Kollmus, R. Mann, S. Hagmann, T. J. M. Zouros:
Differential multi-electron emission induced by swift highly charged gold ions penetrating carbon foils
Nucl. Instrum. Methods Phys. Res., Sect. B 258, 91 (2007)
DOI: 10.1016/j.nimb.2006.12.132
Rudolph, D., S. Pietri, Z. Podolyák, P. H. Regan, A. B. Garnsworthy, R. Hoischen, S. J. Steer, F. Becker, P. Bednarczyk, L. Caceres, P. Doornenbal, H. Geissel, J. Gerl, M. Górska, J. Gręboszb, A. Kelic, I. Kojouharov, N. Kurz, F. Montes, W. Prokopowicz, T. Saito, H. Schaffner, S. Tashenov, E. Werner-Malento, H. J. Wollersheim, L. L. Andersson, L. Atanasova, D. L. Balabanski, M. A. Bentley, G. Benzoni, B. Blank, A. Blazhev, C. Brandau, J. R. Brown, A. M. Bruce, F. Camera, W. N. Catford, I. J. Cullen, Z. Dombrádi, E. Estevez, C. Fahlander, W. Gelletly, A. Heinz, M. Hellström, G. Ilie, E. K. Johansson, J. Jolie, G. A. Jones, A. Jungclaus, M. Kmiecik, F. G. Kondev, T. Kurtukian-Nieto, S. Lalkovski, Z. Liu, A. Maj, S. Myalski, M. Pfützner, T. Shizuma, A. J. Simons, S. Schwertel, P. M. Walker, O. Wieland:
Exciting isomers from the first stopped-beam RISING campaign
Eur. Phys. J. 150, 173 (2007)
DOI: 10.1140/epjst/e2007-00296-2
Rzadkiewicz, J., D. Banas, H. F. Beyer, C. Brandau, C. Z. Dong, S. Fritzsche, A. Gójska, A. Gumberidze, S. Hagmann, C. Kozhuharov, R. Reuschl, U. Spillmann, T. Stöhlker, A. Surzhykov, S. Tashenov, S. Trotsenko:
Study of intra-L shell transitions in Be-like uranium
Journal of Physics: Conference Series 58, 145 (2007)
DOI: 10.1088/1742-6596/58/1/027
Saha, B.S. Fritzsche:
Influence of dense plasma on the low-lying transitions in Be-like ions: relativistic multiconfiguration Dirac-Fock calculation
J. Phys. B 40, 259 (2007)
DOI: 10.1088/0953-4075/40/2/002
Sahoo, B. K., C. Sur, T. Beier, B. P. Das, R. K. Chaudhuri, D. Mukherjee:
Enhanced role of electron correlation in the hyperfine interactions in $^2D_{5/2}$ states in alkaline-earth-metal ions
Phys. Rev. A 75, 042504 (2007)
DOI: 10.1103/PhysRevA.75.042504
Schabinger, B., J. Alonso, K. Blaum, G. Werth, H.-J. Kluge, W. Quint, M. Vogel, S. Stahl:
Towards a *g*-factor determination of the electron bound in highly-charged calcium ions
J. Phys. Conf., p. 121 (2007)
(J. Phys. Conf. Belfast, Northern Ireland, 2007)
DOI: 10.1088/1742-6596/58/1/021
Schneider, D., J. McDonald, B. Zielbauer, D. Ursescu, U. Spillmann, T. Stöhlker, T. Kühl, T. Schenkel, G. Andler, E. Lindroth, R. Schuch:
Electromagnetically confined plasma target for interaction studies with intense laser fields
Nucl. Instrum. Methods Phys. Res., Sect. B 261, 239 (2007)
DOI: 10.1016/j.nimb.2007.03.102
Steer, S. J., Z. Podolyak, S. Pietri, P. H. Regan, D. Rudolph, E. Werner-Malento, A. B. Garnsworthy, R. Hoischen, M. Gorska, J. Gerl, H. J. Wollersheim, F. Becker, P. Bednarczyk, L. Caceres, P. Doornenbal, H. Geissel, J. Grebosz, A. Kelic, N. Kurz, F. Montes, W. Prokopowicz, T. Saito, H. Schaffner, S. Tachenov, A. Heinz, M. Pfuetzner, T. Kurtukian-Nieto, G. Benzoni, A. Jungclaus, D. L. Balabanski, C. Brandau, A. M. Bruce, W. N. Catford, I. J. Cullen, Z. Dombradi, E. Estevez, W. Gelletly, G. Ilie, J. Jolie, G. A. Jones, M. Kmiecik, F. G. Kondev, S. Lalkovski, Z. Liu, A. Maj, S. Myalski, T. Shizuma, S. Schwertel, P. M. Walker, O. Wieland:
Identification of isomeric states 'south' of Pb-208 via projectile fragmentation
Acta Physica Polonica B 38, 1283 (2007)
DOI:
Stöhlker, T., H. F. Beyer, H. Bräuning, A. Bräuning-Demian, C. Brandau, S. Hagmann, C. Kozhuharov, H.-J. Kluge, T. Kühl, D. Liesen, R. Mann, W. Nörtershäuser, W. Quint, U. Schramm, R. Schuch, the SPARC Collaboration:
Atomic physics with highly-charged ions at the future FAIR facility: A status report

Nucl. Instrum. Methods Phys. Res., Sect. B 261, 234 (2007)
DOI: 10.1016/j.nimb.2007.04.168
Stöhlker, T., U. Spillmann, D. Banas, H. F. Beyer, J. C. Dousse, S. Chatterjee, S. Hess, C. Kozhuharov, M. Kavcic, T. Krings, D. Protic, R. Reuschl, J. Szlachetko, S. Tashenov, S. Trotsenko:
A 2D position sensitive germanium detector for spectroscopy and polarimetry of high-energetic x-rays
J. Phys. Conf. 58, 411 (2007)
DOI: 10.1088/1742-6596/58/1/094
Streicher, B., S. Antalic, S. Saro, M. Venhart, F. P. Hessberger, S. Hofmann, D. Ackermann, B. Kindler, I. Kojouharov, B. Lommel, R. Mann, B. Sulignano, P. Kuusiniemi:
Alpha-gamma decay studies of $_{261}$Sg
Acta Physica Polonica B 38, 1561 (2007)
DOI:
Sulignano, B., S. Heinz, F. Heßberger, S. Hofmann, D. Ackermann, S. Antalic, B. Kindler, I. Kojouharov, P. Kuusiniemi, B. Lommel, R. Mann, K. Nishio, A. Popeko, S. Saro, B. Streicher, M. Venhart, A. Yeremin:
Identification of a K isomer in $_{252}$No
The European Physical Journal A 33, 327 (2007)
DOI: 10.1140/epja/i2007-10469-3
Sun, B., Y. A. Litvinov, P. M. Walker, K. Beckert, P. Beller, F. Bosch, D. Boutin, C. Brandau, L. Chen, C. Dimopoulou, H. Geissel, R. Knobel, C. Kozhuharov, J. Kurcewicz, S. A. Litvinov, M. Mazzocco, J. Meng, C. Nociforo, F. Nolden, W. R. Plass, C. Scheidenberger, M. Steck, H. Weick, M. Winkler:
Discovery of a new long-lived isomeric state in $_{125}$Ce
Eur. Phys. J. A 31, 393 (2007)
DOI: 10.1140/epja/i2006-10252-0
Surzhykov, A., U. D. Jentschura, T. Stöhlker, S. Fritzsche:
Effects of configuration interaction on the alignment of beryllium-like ions
J. Phys. Conf. 58, 211 (2007)
DOI: 10.1088/1742-6596/58/1/044
Testa, E., P. N. Abufager, F. Bosch, A. Bräuning-Demian, H. Bräuning, M. Chevallier, C. Cohen, D. Dauvergne, A. Gumberidze, A. L'Hoir, R. Kirsch, C. Kozhuharov, D. Liesen, P. H. Mokler, J. C. Poizat, C. Ray, R. D. Rivarola, J. P. Rozet, T. Stöhlker, S. Toleikis, M. Toulemonde, D. Vernhet, P. Verma:
Using channeling properties for studying the impact-parameter dependence of electron capture by 20-MeV/u uranium ions in a silicon crystal
Phys. Rev. A 76, 062901 (2007)
DOI: 10.1103/PhysRevA.76.062901
Tomaselli, M., T. Kühl, D. Ursescu:
Ab initio calculation of two, three, and four body dynamics
Nucl. Phys. A 790, 246 (2007)
DOI: 10.1016/j.nuclphysa.2007.03.149
Tomaselli, M., T. Kühl, D. Ursescu:
Correlations in the Charge Radii of Complex Systems
American Institute of Physics (AIP), p. 435 (2007) (American Institute of Physics (AIP) Iguazu (Argentina), 2007)
DOI: 10.1063/1.2710619
Tomaselli, M., T. Kühl, D. Ursescu:
Microscopic cluster model for exotic nuclei
Progress in Particle and Nuclear Physics 59, 455 (2007)
DOI: 10.1016/j.ppnp.2007.01.009
Tomaselli, M., T. Kühl, D. Ursescu, S. Fritzsche:
Correlations in many electron systems: theory and applications
Can. J. Phys. 85, 573 (2007)
DOI: 10.1140/epja/i2005-10171-6
Trassinelli, M., D. Banas, H. F. Beyer, P. Jagodzinski, A. Kumar, M. Pajek, T. Stöhlker:
High-accuracy crystal spectroscopy of the n = 2 energy level of helium-like uranium
Can. J. Phys. 85, 441 (2007)
DOI: 10.1139/P07-028
Trassinelli, M.P. Indelicato:
Relativistic calculations of pionic and kaonic atoms' hyperfine structure
Phys. Rev. A 76, 012510 (2007)
DOI: 10.1103/PhysRevA.76.012510
Trotsenko, S., T. Stöhlker, D. Banas, C. Z. Dong, S. Fritzsche, A. Gumberidze, S. Hagmann, S. Hess, P. Indelicato, C. Kozhuharov, M. Nofal, R. Reuschl, J. Rzadkiewicz, U. Spillmann, A. Surzhykov, M. Trassinelli, G. Weber:
Investigation of the Decay Properties of the $1s(2s)_2$ State in Li-Like Uranium
J. Phys. Conf. 58, 141 (2007)
DOI: 10.1088/1742-6596/58/1/026
Van de Walle, J., F. Aksouh, F. Ames, T. Behrens, V. Bildstein, A. Blazhev, J. Cederkall, E. Clement, T. E. Cocolios, T. Davinson, P. Delahaye, J. Eberth, A. Ekstrom, D. V. Fedorov, V. N. Fedosseev, L. M. Fraile, S. Franchoo, R. Gernhauser, G. Georgiev, D. Habs, K. Heyde, G. Huber, M. Huyse, F. Ibrahim, O. Ivanov, J. Iwanicki, J. Jolie, O. Kester, U. Koster, T. Kroll, R. Krucken, M. Lauer, A. F. Lisetskiy, R. Lutter, B. A. Marsh, P. Mayet, O. Niedermaier, T. Nilsson, M. Pantea, O. Perru, R. Raabe, P. Reiter, M. Sawicka, H. Scheit, G. Schrieder, D. Schwalm, M. D. Seliverstov, T. Sieber, G. Sletten, N. Smirnova, M. Stanoiu, I. Stefanescu, J. C. Thomas, J. J. Valiente-Dobon, P. Van Duppen, D. Verney, D. Voulot, N. Warr, D. Weisshaar, F. Wenander, B. H. Wolf, M. Zielinska:
Coulomb Excitation of Neutron-Rich Zn Isotopes: First Observation of the 2_1^+ State in $_{80}$Zn
Phys. Rev. Lett. 99, 142501 (2007)

DOI: 10.1103/PhysRevLett.99.142501
Vogel, M., D. F. A. Winters, H. Ernst, H. Zimmermann, O. Kester:
Scintillation light produced by low-energy beams of highly-charged ions
Nucl. Instrum. Methods Phys. Res., Sect. B 263, 518 (2007)
DOI: 10.1016/j.nimb.2007.06.021
Wang, X.S. Hagmann:
A toroidal sector for the electron branch of a reaction microscope
Meas. Sci. Technol. 18, 161 (2007)
DOI: 10.1088/0957-0233/18/1/020
Weber, G., T. Stöhlker, D. Banas, S. Fritzsche, A. Gumberidze, S. Hagmann, S. Hess, C. Kozhuharov, M. Nofal, U. Popp, R. Reuschl, U. Spillmann, A. Surzhykov, S. Trotsenko:
Radiative processes studied for bare uranium ions in collisions with H_2
J. Phys. Conf. 58, 243 (2007)
DOI: 10.1088/1742-6596/58/1/052
Winkler, M., B. Achenbach, K. H. Behr, M. Berz, D. Boutin, C. Brandau, H. Emling, H. Geissel, H. Iwase, C. Karagiannis, A. Kelic, H. Leibrock, Y. Litvinov, S. Manikonda, J. A. Maruhn, G. Moritz, C. Mühle, G. Münzenberg, C. Nociforo, W. Plass, C. Scheidenberger, H. Simon, K. Sümmerer, M. Svedentsov, N. A. Tahir, A. Tauschwitz, Z. Wang, H. Weick, H. Wollnik, M. Yavor:
The status of the Super-FRS at FAIR
Eur. Phys. J. 150, 263 (2007)
DOI: 10.1140/epjst/e2007-00318-1
Winters, D. F. A., M. Vogel, D. M. Segal, R. C. Thompson, W. Nörtershäuser:
Laser spectroscopy of hyperfine structure in highly charged ions: a test of QED at high fields
Can. J. Phys. 85, 403 (2007)
DOI: 10.1139/P07-023
Yazidjian, C., G. Audi, D. Beck, K. Blaum, S. George, C. Guenaut, F. Herfurth, A. Herlert, A. Kellerbauer, H.-J. Kluge, D. Lunney, L. Schweikhard:
Evidence for a breakdown of the isobaric multiplet mass equation: A study of the $A = 35$, $T = 3$ 2 isospin quartet
Phys. Rev. C 76, 024308 (2007)
DOI: 10.1103/PhysRevC.76.024308

Academic Teaching

K. BLAUM
Laserspektroskopie, Fallen und deren Anwendungen
Universität Mainz, Deutschland, WS06/07 (3 SWS)

K. BLAUM
Seminar zum Fortgeschrittenenpraktikum "Atomphysik",
Universität Mainz, Deutschland, WS06/07 (1 SWS)

K. BLAUM
Übungen zu Laserspektroskopie, Fallen und deren Anwendungen,
Universität Mainz, Deutschland, WS06/07 (1 SWS)

K. BLAUM
Übungen zu Moderne Experimente der Atomphysik,
Universität Mainz, Deutschland, SS07 (1 SWS)

K. BLAUM
Moderne Experimente der Atomphysik,
Universität Mainz, Deutschland, SS07 (3 SWS)

K. BLAUM
Massenspektrometrie und Teilchenfallen, WS07/08,
Universität Mainz, Deutschland, WS07/08 (3 SWS)

K. BLAUM
Übungen zu Massenspektrometrie und Teilchenfallen, WS07/08,
Universität Mainz, Deutschland, WS07/08 (1 SWS)

F. BOSCH
Astronomie und Astrophysik II: Sterne, Galaxien, Universum,
Universität Kassel, Deutschland, SS07

H. BRÄUNING
Atomare Stöße,
Universität Gießen, Deutschland, SS07

H. BRÄUNING
Bau und Physik von Beschleunigern und Synchrotronstrahlungsquellen,
Justus-Liebig Universität, Giessen, WS07/08 (2 SWS)

D. LIESEN
Oberseminar über Atomphysik,
Universität Heidelberg, SS07

D. LIESEN
Gruppenunterricht zur Physik III,
Universität Heidelberg, Deutschland, SS07

D. LIESEN
Oberseminar über Atomphysik,
Universität Heidelberg, WS07/08 (2 SWS)

S. FRITZSCHE
Structure and Dynamics of Atoms and Molecules,
Universität Heidelberg, Philosophenweg 12, WS07/08 (2 SWS)

O. KESTER
Ionenquellen und ihre Anwendung,

J. W. Goethe-Universität Frankfurt, Institut für Angewandte Physik, SS07 (2 SWS)

O. KESTER
Beschleunigerphysik und Ionenquellen,
J. w. Goethe-Universität Frankfurt, WS07/08 (2 SWS)

T. KÜHL
Seminar zum physikalischen Praktikum für Fortgeschrittene I und II,
Universität Mainz, Deutschland, SS07

T. KÜHL
Seminar über Physik dichter Plasmen mit Schwerionen- und Laserstrahlen,
Universität Mainz, Deutschland, SS07

T. KÜHL
Seminar über Physik dichter Plasmen mit Schwerionen- und Laserstrahlen,
Universität Mainz, Deutschland, WS07/08 (3 SWS)

W. NÖRTERSHÄUSER
Moderne Experimente der Atomphysik,
Universität Mainz, Deutschland, SS07

W. NÖRTERSHÄUSER
Übungen zu Moderne Experimente der Atomphysik,
Universität Mainz, Deutschland, SS07

W. NÖRTERSHÄUSER
Physik des Lasers, WS07/08,
Universität Mainz, Deutschland, WS07/08 (3 SWS)

W. NÖRTERSHÄUSER
Übungen zu Physik des Lasers, WS07/08,
Universität Mainz, Deutschland, WS07/08 (1 SWS)

W. QUINT
Seminar für mittlere Semester, Spezielle und Allgemeine Relativitätstheorie: Grundlagen und moderne Experimente,
Universität Heidelberg, Deutschland, SS07

W. QUINT
Quantenelektrodynamik: Moderne Experimente und theoretische Grundlagen,
Universität Heidelberg, WS07/08 (2 SWS)

C. WELSCH
Modern Methods in Atomic and Molecular Physics,
University of Heidelberg, WS07/08 (2 SWS)

C. WELSCH
Physics and Technology of Particle Accelerators,
University of Heidelberg, WS07/08 (2 SWS)

C. WELSCH
Physics with Low-energy Antiprotons, Heidelberg Graduate Days,
University of Heidelberg, WS07/08 (1 SWS)

D. WINTERS
A brief general introduction in atomic physics,
Lecture Series "High-precision atomic physics experiments with stored ions",
Institut für Kernphysik, Westfälische Wilhelms-Universität Münster, SS07

D. WINTERS
The concepts of ion storage (traps and storage rings),
Lecture Series "High-precision atomic physics experiments with stored ions",
Institut für Kernphysik, Westfälische Wilhelms-Universität Münster, SS07

D. WINTERS
Experiments in traps and storage rings (HITRAP, FAIR),
Lecture Series "High-precision atomic physics experiments with stored ions",
Institut für Kernphysik, Westfälische Wilhelms-Universität Münster, SS07

H. ZIMMERMANN
Physik der Vakuumerzeugung,
Universität Frankfurt/Main, Deutschland, SS07

Public Talks

K. BLAUM
High-precision atomic physics experiments with stored and cooled ions in Penning traps for SPARC.
Atomphysik. Topical Workshop of the SPARC Collaboration, Paris (France), 12.02.2007.

K. BLAUM
Präzisionsexperimente mit Penningfallen in der Atom- und Kernphysik.
Atomphysik. Vortragsreihe beim Arbeitstreffen "Kernphysik", Schleching (Austria), 22.02.2007.

K. BLAUM
Penning traps as a versatile tool for fundamental physics research.
Atomphysik. Workshop on electron-capture neutrino mass determination, GSI, Darmstadt (Deutschland), 08.03.2007.

K. BLAUM
High-precision atomic physics experiments with stored and cooled ions in Penning traps.
Atomphysik. DPG Frühjahrstagung Hauptvortrag, Düsseldorf (Deutschland), 20.03.2007.

K. BLAUM
High-accuracy Penning trap mass measurements for nuclear structure and fundamental studies.
Atomphysik. APS April Meeting 2007, Jacksonville (USA), 16.04.2007.

K. BLAUM
Physics of Ion Traps - High-precision experiments with stored and cooled ions in Penning traps.
Atomphysik. Lecture Series on the FANTOM Study Week and Research Symposium 2007, Groningen (Niederlande), 24.04.2007.

K. BLAUM
Precision mass measurements for testing fundamental symmetries.
Atomphysik. International Workshop on Fundamental Symmetries: From nuclei and neutrinos to the Universe, ECT Trento (Italien), 25.06.2007.

K. BLAUM
Die Physik an CERN und ISOLDE.
Atomphysik. Willibald Gymnasium, Eichstätt (Deutschland), 20.07.2007.

K. BLAUM
High-precision Penning trap mass measurements for fundamental studies and symmetries.
Atomphysik. The Fourth Argonne/INT/MSU/JINA RIA Theory Workshop on Rare Isotopes and Fundamental Symmetries, University of Washington (USA), 20.09.2007.

K. BLAUM
High-precision mass measurements with Penning traps for nuclear structure and fundamental studies.
Atomphysik. Symposium on Nuclear Structure, GSI, Darmstadt (Deutschland), 08.10.2007.

M. BLOCK
Transactinide Research with Ion Traps.
Atomphysik. Int. Conference on the Chemistry and Physics of the Transactinide Elements, Davos (Switzerland), 27.09.2007.

C. BRANDAU
Storage Ring Experiments at the Interface of Atomic and Nuclear Physics.
Atomphysik. Workshop on „Next Generation Isomers“, Institute of Physics (IOP), University of Surrey, Guildford (Großbritannien), 02.04.2007.

H. BRÄUNING
Double Electron Transfer in H- - H+ Collisions.
Atomphysik. XXV ICPEAC - 25th International Conference on Photonic, Electronic and Atomic Collisions, Freiburg (Germany), 27.07.2007.

H. BRÄUNING
Ion-Ion Stöße - Ladungstransfer in maßgeschneiderten Stoßsystemen.
Atomphysik. Seminar über Atomphysik, Justus-Liebig Universität, Giessen (Germany), 22.11.2007.

S. FRITZSCHE
Angular and polarization analysis of x-rays emitted from highly-charged heavy ions.
Atomphysik. XXV ICPEAC 2007, Freiburg (Germany), 26.07.2007.

S. FRITZSCHE
Auger electron and x-ray emission from high-Z few-electron ions.
Atomphysik. SPARC Meeting associated to the ISIAC 2007, Agios Nikolaios, Kreta, (Greece) 04.08.2007.

S. FRITZSCHE
Computer algebra: A 'classical' path to explore decoherence and entanglement phenomena in quantum information theory-
Atomphysik. 10th International Workshop on Computer Algebra in Scientific Computing, Bonn (Germany), 17.09.2007.

S. FRITZSCHE
Relativistic effects in heavy and superheavy elements.
Atomphysik. ADAS Workshop on Atomic Data and Structure Analysis, Ringberg Castle, Tegernsee (Germany), 11.10.2007.

S. GEORGE
Advanced measurement techniques in Penning trap mass spectrometry.
Atomphysik. XXXVIII. Arbeitstreffen Kernphysik, Schleching (Deutschland), 24.02.2007.

S. GEORGE
Ultra-Precise Neutrino Oriented Mass Spectrometry at HITRAP.
Atomphysik. NeuMa-Workshop, GSI Darmstadt (Deutschland), 08.03.2007.

S. GEORGE
Mass Measurements on Superallowed Beta-Emitters Using Ramsey's Excitation Method at ISOLTRAP.
Atomphysik. INPC-Konferenz, Tokio (Japan), 05.06.2007.

C. GEPPERT
Laser ion sources: present and future.
Atomphysik. EMIS conference 2007, Deauville (France), 27.06.2007.

A. GUMBERIDZE
Atomic Physics at FAIR: Experimental program of the SPARC Collaboration.
Atomphysik. Meeting of the Theory Working Group of the SPARC Collaboration, GSI, Darmstadt (Deutschland), 17.07.2007.

S. HAGMANN
New Opportunities for Electron- and Ion- Spectroscopy at the NESR Storage Ring.
Atomphysik. Topical Workshop of the SPARC Collaboration, Paris (Frankreich), 12.02.2007.

S. HAGMANN
Electron Spectroscopy at the ESR Heavy Ion Storage Ring: First Results and Future Opportunities.
Atomphysik. The Physics at EBITs and Advanced Research Light Sources (PEARL 2007), Fudan University, Shanghai (China), 08.03.2007.

S. HAGMANN
Radiative Electron Capture to Continuum (RECC) and the Short Wavelength Limit of Electron Nucleus Bremsstrahlung in near-relativistic Collisions.
Atomphysik. XXV ICPEAC - 25th International Conference on Photonic, Electronic and Atomic Collisions, Freiburg (Deutschland) 25.07.2007.

S. HAGMANN
Trends and Future Opportunities in Electron Spectroscopy at Heavy Ion Storage Rings.
Atomphysik. XX International Symposium on Ion-Atom Collisions, Agios Nikolaos, Kreta (Griechenland), 01.08.2007.

F. HERFURTH
Precision Mass Measurements at SHIPTRAP.
Atomphysik. Workshop on Neutrino Mass Determination by Electron Capture - NEUMA07, Darmstadt, (Deutschland) 08.03.2007.

F. HERFURTH
Slow radioactive beams and mass measurements – SHIPTRAP.
Atomphysik. Annual NUSTAR meeting 2007, Darmstadt (Deutschland), 21.03.2007.

F. HERFURTH
Precise Mass Measurements of Rare Nuclei - The Penning Trap Mass Spectrometers ISOLTRAP and SHIPTRAP.
Atomphysik. Nuclear Physics in Astrophysics III, XXI. International Nuclear Physics Divisional Conference of the European Physical Society, Dresden (Deutschland), 29.03.2007.

F. HERFURTH
Precise mass measurements of exotic nuclei - the SHIPTRAP Penning trap mass spectrometer.
Atomphysik. PROCON 07, International Conference on Proton Emitting Nuclei and related topics, Lissabon (Portugal), 22.06.2007.

O. KESTER
Methods for the production of highly charged ions.
Atomphysik. Neuma workshop, GSI Darmstadt (Deutschland), 09.03.2007.

O. KESTER
Review of charge breeding methods and applications.
Atomphysik. International Symposium on EBIS/T, 2007, MPI-K, Heidelberg (Deutschland), 02.08.2007.

O. KESTER
Advanced charge state breeding.
Atomphysik. EURONS / EURISOL-DS town meeting, Helsinki, (Finland) 18.09.2007.

J. KETELAER
FT-ICR detection with single-ion sensitivity for high-precision mass measurements on superheavy elements.
Atomphysik. 40. Jahrestagung der Deutschen Gesellschaft für Massenspektrometrie (11.03.2007 – 14.03.2007), Bremen (Deutschland), 12.03.2007.

J. KETELAER
Eine Waage für einzelne Atome.
Atomphysik. Wissenschaft für alle, GSI, Darmstadt (Deutschland), 07.03.2007.

J. KETELAER
Progress towards mass measurements on single singly charged ions.
Atomphysik. EURONS Trap and Laser Collaboration Meeting (12.04.2007 - 14.04.2007), Saariselkä (Finnland), 00.04.2007.

J. KETELAER
Progress towards mass measurements on single singly charged heavy and superheavy ions.
Atomphysik. ECT* Workshop on Fundamental Symmetries (25.06.2007 - 27.06.2007), Trento (Italien), 00.06.2007.

H.-J. KLUGE
Atomic Physics Goes Online: the Role of ISOLDE in the Past and in the Future.
Atomphysik. ISOLDE Workshop and Users Meeting, CERN, Geneva (Switzerland), 12.02.2007.

H.-J. KLUGE
Gefangen und gekühlt: neue Entwicklungen und Anwendungen der Massenspektrometrie.
Atomphysik. AMOP-Frühjahrstagung 2007 der Deutschen Physikalischen Gesellschaft (DPG), Heinrich-Heine-Universität Düsseldorf, 18.03.2007.

H.-J. KLUGE
Resonance Ionization Mass Spectroscopy for Nuclear Studies.
Atomphysik. Spring Meeting of the American Chemical

Society (ACS), Glenn T. Seaborg Award Symposium, Chicago (USA), 25.03.2007.

S. KREIM
Towards a Direct Measurement of the Proton g-Factor.
Atomphysik. XXXVIII. Arbeitstreffen Kernphysik, Schleching (Deutschland), 24.02.2007.

S. KREIM
Towards a Direct Measurement of the Proton g-Factor.
Atomphysik. FANTOM Workshop, Groningen (Netherlands), 24.05.2007.

A. KUMAR
Selective population of 1s2s states after K-shell ionization of Li-like heavy ions
Atomphysik. 20. ISIAC, Agios Nikolaos, Crete, (Greece), 01.08.2007.

A. KUMAR
High resolution electron spectrometry at NESR
Atomphysik. 20. ISIAC, Agios Nikolaos, Crete, (Greece), 04.08.2007.

S. NAGY
Towards ultra-high precision mass measurements using highly-charged ions in a Penning trap.
Atomphysik. Physics at EBIT and Advanced Research Light sources, PEARL2007 (8-12 March 2007), Fudan University, Shanghai (China), 00.03.2007.

W. NÖRTERSHÄUSER
Halo Nuclei in Laser Light.
Atomphysik. Graduiertenkolleg "Hadrons in vacuum, in Nuclei and Stars", Basel (Schweiz), 09.02.2007.

W. NÖRTERSHÄUSER
From Tests of Fundamental Symmetries to Nuclear Structure - Recent Progress of Laser Spectroscpoy at GSI.
Atomphysik. 3. SPARC Workshop, Paris (Frankreich), 12.02.2007.

W. NÖRTERSHÄUSER
From Present into the Future - Laser Spectroscopy at GSI.
National Laser Conference NLC 07, Vadodara (India), 17.12.2007.

J. PFISTER
Single-shot emittance measurements at BNL Test EBIS.
Atomphysik. X. International Symposium on the Physics and Applications of Electron Beam Ion Sources and Traps, Heidelberg (Germany), 01.08.2007.

W. QUINT
Precision Experiments with Single Particles in Ion Traps for Tests of Fundamental Interactions.
DAMOP Conference, Calgary, Canada, 01.06.2007.

B. SCHABINGER
A miniature EBIT for production of highly charged Ca ions inside a Penning Trap.
Atomphysik. EBIS/T (10th International Symposium on Electron Beam Ion Sources and Traps and Their Applications), Heidelberg (Germany), 03.08.2007.

T. STÖHLKER
Gekühlte Schwerionen - Faszinierende Werkzeuge der Atomphysik.
Atomphysik. PIZZA-Night, Physikalisches Institut, Universität Heidelberg (Deutschland), 18.01.2007.

T. STÖHLKER
The Physics of Highly Charged Heavy Ions Studied at Storage Rings.
Atomphysik. Graduiertenkolleg "Hadrons in Vacuum, in Nuclei and Stars", Basel (Schweiz), 09.02.2007.

T. STÖHLKER
Current Status of SPARC at GSI and FAIR: An Activity Report.
Atomphysik. Topical Workshop of the SPARC Collaboration, Paris (Frankreich), 12.02.2007.

T. STÖHLKER
Atomic Physics with Highly-Charged Heavy and Exotic Ions.
Atomphysik. NUSTAR Annual Meeting, GSI Darmstadt (Deutschland), 22.03.2007.

M. TRASSINELLI
X-ray Spectroscopy of Highly Charged Ions at FAIR
Atomphysik. SPARC Topical Workshop, Paris (France), 13.02.2007.

M. TRASSINELLI
Atomic Physics with Highly Charged Ions at Storage Rings
Kernphysik. 38 Arbeitstreffen, Schleching (Germany), 22.02.2007.

S. ULMER
Towards a direct measurement of the proton g-factor in a cryogenic Penning trap.
Atomphysik. Gruppenseminar Neutronenphysik, Heidelberg (Germany), 05.02.2007.

M. VOGEL
Precise measurements of electronic g-factors as a way to determine the electron's mass.
Atomphysik. 388.Hereaus-Seminar, Bad Honnef (Deutschland), 03.06.2007.

G. WEBER
Radiative processes studied in collisions of bare uranium with a hydrogen gas-target

Atomphysik. General FANTOM Study Week on Particles in Traps: Physics and Technology.
Atomphysik. Groningen (NL), 21.05.2007.

Seminara and Colloquia

K. BLAUM
High-accuracy Penning trap experiments with stored and cooled ions.
Physics Colloquium, Florida State University, Tallahassee, USA, 13.04.2007.

K. BLAUM
Atome auf die Waage gestellt - Präzisionsexperimente mit Penning-Fallen.
Physikalisches Kolloquium, Universität Kassel, Kassel, Deutschland, 26.04.2007.

K. BLAUM
High-accuracy mass measurements with Penning traps.
Nuclear Chemistry Seminar, Universität Mainz, Germany, 07.05.2007.

K. BLAUM
High-accuracy Penning trap experiments with stored and cooled ions.
Kolloquium, GSI, Darmstadt, Deutschland, 22.05.2007.

K. BLAUM
High-precision mass measurements for nuclear structure and fundamental studies.
Physikalisches Kolloquium, Forschungszentrum Rossendorf, Dresden, Deutschland, 12.06.2007.

K. BLAUM
Atome auf die Waage gestellt - Präzisionsmassenmessungen an gespeicherten und gekühlten Ionen in Penning-Fallen.
Physikalisches Kolloquium, Universität Frankfurt/Main, Deutschland, 13.06.2007.

K. BLAUM
Vom Caesar-Code zur Quantenkryptografie.
Abendvortrag, Mainz, Deutschland, 20.06.2007.

K. BLAUM
Atome auf die Waage gestellt - Präzisionsmassenmessungen an gespeicherten und gekühlten Ionen in Penning-Fallen.
Physikalisches Kolloquium, Freie Universität Berlin, Deutschland, 29.06.2007.

K. BLAUM
High-precision experiments with cooled and stored ions in Penning traps.
Paul Scherrer Institut, Villigen, Switzerland, 13.12.2007.

M. BLOCK
Mass measurements of rare isotopes produced by fusion-evaporation reactions at SHIPTRAP.
30th Mazurian Lakes Conference on Physics, Piaski, Poland, 02.09.2007.

M. BLOCK
Transaktiniden-Forschung mit Ionenfallen.
Seminar für Kern- und Radiochemie, Mainz, 12.11.2007.

S. FRITZSCHE
Atomic double slits: Coherence transfer through excitation, ionization and decay processes.
Bothe Colloqium, MPIK Heidelberg, 13.06.2007.

S. FRITZSCHE
Control of entanglement in atomic ionization and decay processes.
Quantum Seminar, Universität Mainz, 21.06.2007.

S. FRITZSCHE
Atomic double slits: Coherence transfer through excitation, ionization and decay processes.
Atomphysik-Seminar, Universität Giessen, 28.06.2007.

S. FRITZSCHE
Atomic calculations for multiple and highly-charged ions.
Plasmaphysik-Seminar, GSI Darmstadt, 10.07.2007.

S. FRITZSCHE
Coherence transfer and entanglement in atomic systems.
Kolloquium für Atom-, Molekül- und Quantenphysik, Universität Heidelberg, Kirchhoff-Institut, 24.10.2007.

S. FRITZSCHE
Simulated x-ray emission from heavy and medium elements: A theoretical tool for plasma diagnostics?
International Workshop on the Theory of Short Pulse Petawatt Laser Plasma Interactions, Lichtenberg Haus, Darmstadt, 16.10.2007.

F. HERFURTH
High precision experiments with Penning traps at GSI.
Maier-Leibnitz-Kolloquium, LMU/TU Munich, Garching, 31.05.2007.

J. KETELAER
Developments for mass spectrometry in Penning traps – towards single ion measurements.
Atomic Physics Seminar, AlbaNova, University Physics Center, Stockholm, Sweden, 03.09.2007.

S. KREIM
Towards a Direct Measurement of the Proton g-Factor.
AP Seminar, GSI, Darmstadt, Deutschland, 11.07.2007.

S. KREIM
Towards the First Direct Measurement of the Proton g-Factor (poster presentation).
ICPEAC, Freiburg, Deutschland, 26.07.2007.

D. NEIDHERR
Development and simulation of a pumping barrier for the Penning trap mass spectrometer SHIPTRAP (poster presentation).
EMIS 2007 (25. - 30.06.2007), Deauville, Frankreich, 00.06.2007.

D. NEIDHERR
Towards high-precision mass values of He, Li and Be at ISOLTRAP/CERN (poster presentation).
EMIS 2007 (25. - 30.06.2007), Deauville, Frankreich, 00.06.2007.

W. NÖRTERSHÄUSER
High-Precision spectroscopy of exotic Nuclei - The nuclear charge radius of Li-11.
NIST Radioactive Group Seminar, Gaithersburg, USA, 08.01.2007.

W. NÖRTERSHÄUSER
Halo nuclei in laser light - The nuclear charge radius of Li-11.
National Superconducting Laboratory NSCL - Nuclear Seminar, Michigan State University, East Lansing, USA, 10.01.2007.

W. NÖRTERSHÄUSER
Halo nuclei in laser light - The nuclear charge radius of Li-11.
Oak Ridge National Laboratory, Physics Division Seminar, Oak Ridge, USA, 11.01.2007.

W. NÖRTERSHÄUSER
Laserspektroskopie hochgeladener Ionen an HITRAP.
Institut für Kernphysik, Westfälische Universität, Münster, Deutschland, 26.01.2007.

W. NÖRTERSHÄUSER
From Present into the Future - Laser Spectroscopy at GSI.
Inter-University Accelerator Center Delhi (India), 20.12.2007.

W. QUINT
The HITRAP-project as a prerequisite for ultra-precise mass measurements.
NEUMA-Workshop, GSI Darmstadt, 00.06.2007.

B. SCHABINGER
Towards a g-factor determination of the electron bound in highly-charged Calcium ions (poster presentation).
ICPEAC 2007 (25 - 31.07.2007), Freiburg, Deutschland, 30.07.2007.

T. STÖHLKER
Die faszinierende Welt starker Felder: Experimente mit hochgeladenen Ionen.
Kolloquium, Universität Heidelberg, 29.06.2007.

T. STÖHLKER
Die faszinierende Welt starker Felder: Experimente mit hochgeladenen Ionen.
Kolloquium, Physikalisches Institut, Universität Heidelberg, Deutschland, 29.06.2007.

T. STÖHLKER
Aktuelle Probleme der Atom- und Molekülphysik.
Universität Heidelberg, 01.12.2007.

T. STÖHLKER
The Physics of Highly Charged Heavy Ions Studied at Storage Rings.
GSI-Studentenprogramm, GSI, 12.07.2007.

S. ULMER
Towards a direct measurement of the proton g-factor in a cryogenic Penning trap.
Gruppenseminar Neutronenphysik, Heidelberg, Germany, 05.02.2007.

S. ULMER
Measurement of the proton g-factor (poster presentation).
ECAMP IX (6 – 11 May 2007), Crete, Greece, 00.05.2007.

C. WELSCH
Low-Energy Antiprotons with FLAIR – on the way to an Attosecond Camera.
PIZZA-night, University of Heidelberg, 25.10.2007.

C. WELSCH
From 20 keV in 3 TeV in 30 Minutes.
Science at KIP, University of Heidelberg, 22.11.2007.

C. WELSCH
The USR at FLAIR – Paving the Way for Fundamental Studies with Antiprotons and Ions.
Cockroft Seminar, Cockroft Institute, UK, 22.11.2007.

C. WELSCH
The Ultra-low Energy Storage Ring - Decelerating Antiprotons to keV Energies.
ANKA Seminar, Forschungszentrum Karlsruhe, 17.12.2007.

Research Division: Biophysics

Leader: G. Kraft
Compiled by: B. Jakob

Awards

D. BECKER
GBS travel award to the GBS-meeting (Mainz)

T. ELSÄSSER
Travel award to the RRS meeting (San Francisco) from the GBS

C. FOURNIER et al.
Poster award at the Wolfsberg conference

F. KNAUF
GBS travel award to the GBS-meeting (Mainz)

G. KRAFT
Ulrich-Hagen-Preis 2007 der Gesellschaft für Biologische Strahlenforschung GBS

K. PSONKA
Christoph-Schmelzer Preis 2007

D. SCHARDT
IBA Europhysics prize 2007

A. SCHMIDT
PTCOG travel award to the China PTCOG meeting

M. SCHOLZ
Honorarprofessur am Shandong Wanjie Medical College und Zibo Wanjie Hospital of China

M. SCHOLZ; M. KRÄMER
Roberts Prize für das am höchten bewertete Paper im Jahr 2006 im Journal "Physics in Medicine and Biology"

Y. SCHWEINFURTH
Young scientist travel award to the RRS meeting (San Francisco) from the Radiation Research Society

J. SPLINTER
GBS travel award to the GBS-meeting (Mainz)

C. VON NEUBECK
GBS travel award to the GBS-meeting (Mainz)

S. ZAHNREICH
GBS travel award to the GBS-meeting (Mainz)

Publications

PROGRAMME HEALTH (Cancer Research)

1. WoS listed publications

AMALDI, U., KRAFT, G., European Developments in Radiotherapy with Beams of Large Radiobiological Effectiveness. Journal of Radiation Research, 48, A27-A41, (2007).

BERT, CH., RIETZEL, E., 4D treatment planning for scanned ion beams. Radiation Oncology, 2, 24, (2007).

BERT, CH., SAITO, N., SCHMIDT, A., CHAUDHRI, N., SCHARDT, D., RIETZEL, E., Target motion tracking with a scanned particle beam. Medical Physics, 34, 4768-4771, (2007).

BREZEANU, M., TAUCHER-SCHOLZ, G., PSONKA, K., TRÄGER, F., HUBENTHAL, F., SFM studies of carbon ion induced damages in plasmid DNA. Journal of Molecular Recognition, 20, 502-507, (2007).

ELSÄSSER, TH., SCHOLZ, M., Cluster Effects within the Local Effect Model. Radiation Research, 167, 319-329, (2007).

FERTMAN, A., MUSTAFIN, E., HINKA, R., STRASÍK, I., PAVLOVIC, M., SCHARDT, D., SOBOLEVSKIY, N.M., GOLUBEV, A.A., SHARKOV, B., FEHRENBACHER, G., HOFMANN, I., IWASE, H., KOZLOVA, E., MUSTAFINA, G., First results of an experimental study of the residual activity induced by high-energy uranium ions in steel and copper. Nuclear Instruments and methods in Physics Research Section B: Beam Interactions with Materials and Atoms, 260, 579-591, (2007).

FOURNIER, C., BECKER, D., WINTER, M., BARBERET, PH., HEISS, M., FISCHER, B., TOPSCH, J., TAUCHER-SCHOLZ, G., Cell Cycle-Related Bystander Responses are not Increased with LET after Heavy-Ion Irradiation. Radiation Research, 167, 194-206, (2007).

FOURNIER, C., WINTER, M., ZAHNREICH, S., NASONOVA, E., MELNIKOVA, L.A., RITTER, S., Interrelation amongst differentiation, senescence and genetic instability in long-term cultures of fibroblasts exposed to different radiation qualities. Radiotherapy and Oncology, 83, 277-282, (2007).

GOETZE, K., SCHOLZ, M., TAUCHER-SCHOLZ, G., MÜLLER-KLIESER, W.K., The impact of conventional and heavy ion irradiation on tumor cell migration in vitro. International Journal of Radiation Biology, 83, 889-896, (2007).

GOLUBEV, A.A., KANTSYREV, A.V., LUCKJASHIN, V.E., FERTMAN, A., KUNIN, A.V., VATULIN, V.V., GNUTOV, A.S., PANOVA, Y.V., IWASE, H., MUSTAFIN, E., SCHARDT, D., WEYRICH, K., SOBOLEVSKIY, N.M.,

LATYSHEVA, L.N., Measurement of the energy deposition profile for 238U ions with specific energy 500 and 950 MeV/u in stainless steel and copper targets. Nuclear Instruments and methods in Physics Research Section B: Beam Interactions with Materials and Atoms, 263, 339-344, (2007).

GUDOWSKA-NOWAK, E., LEE, R., NASONOVA, E., RITTER, S., SCHOLZ, M., Effect of LET and track structure on the statistical distribution of chromosome aberrations. Advances in Space Research, 39, 1070-1075, (2007).

KRAFT, G., Schwere Geschütze gegen den Krebs. Physik Journal, 2, 29-35, (2007).

PSONKA, K., GUDOWSKA-NOWAK, E., BRONS, S., ELSÄSSER, TH., HEISS, M., TAUCHER-SCHOLZ, G., Ionizing radiation-induced fragmentation of plasmid DNA - Atomic force microscopy and biophysical modeling. Advances in Space Research, 39, 1043-1049, (2007).

RIETZEL, E., SCHARDT, D., HABERER, TH., Range accuracy in carbon ion treatment planning based on CT-calibration with real tissue samples. Radiation Oncology, 2, 14, (2007).

SANNITA, W.G., PEACHEY, N.S., STRETTOI, E., BALL, S.L., BELLI, F., BIDOLI, V., CAROZZO, S., CASOLINO, M., DI FINO, L., PICOZZA, P., PIGNATELLI, V., RINALDI, A., SATURNO, M., SCHARDT, D., VAZQUEZ, M., ZACONTE, V., NARICI, L., Electrophysiological responses of the mouse retina to 12C ions. Neuroscience Letters, 416, 231-235, (2007).

SCHARDT, D. for the Heavy-Ion Therapy Collabor, , Tumor therapy with high-energy carbon ion beams. Nuclear Physics A, 787, 633-641, (2007).

SCHOLZ, M., ELSÄSSER, TH., Biophysical Models in Ion Beam Radiotherapy. Advances in Space Research, 40, 1381-1391, (2007).

SCHULZ-ERNTER, D., KARGER, C., FEUERHAKE, A., NIKOGHOSYAN, A., COMBS, S.E., JÄKEL, O., EDLER, L., SCHOLZ, M., DEBUS, J., Effectiveness of carbon ion radiotherapy in the treatment of skull-base chordomas. International journal of radiation oncology, biology, physics, 68, 449-457, (2007).

TENHUMBERG, S., GUDOWSKA-NOWAK, E., NASONOVA, E., RITTER, S., Cell cycle arrest and aberration yield in normal human fibroblasts. II: Effects of 11 MeV u(-1) C ions and 9.9 MeV u(-1) Ni ions. International Journal of Radiation Biology, 83, 501-512, (2007).

TOPSCH, J., SCHOLZ, M., MÜLLER-KLIESER, W.K., Radiobiological Characterization of Human Tumor Cell Multilayers after Conventional and Particle Irradiation. Radiation Research, 167, 645-654, (2007).

UEMATSU, N., WETERINGS, E., YANO, K., MOROTOMI-YANO, K., JAKOB, B., TAUCHER-SCHOLZ, G., MARI, P.O., VAN GENT, D.C., CHEN, B.P., CHEN, D.J., Autophosphorylation of DNA-PKCS regulates its dynamics at DNA double-strand breaks. Journal of Cell Biology, 177, 219-229, (2007).

UZAWA, A., ANDO, K., FURUSAWA, Y., KAGIYA, G., FUJI, H., HATA, M., SAKAE, T., TERUNUMA, T., SCHOLZ, M., RITTER, S., PESCHKE, P., Biological intercomparison using gut crypt survivals for proton and carbon-ion beams. Journal of Radiation Research, 48, A75-A80, (2007).

.

2. Other publications

IWASE, H., GUNZERT-MARX, K., HAETTNER, E., SCHARDT, D., GUTERMUTH, F., KRAEMER, M., KRAFT, G. Experimental and theoretical study of the neutron dose produced by carbon ion therapy beams (NEUDOS10˜ special issue) Radiation Protection Dosimetry, Advance Access published May 23, (2007)

TAUCHER-SCHOLZ, G. , JAKOB, B. Ion Irradiation as a Tool to Reveal the Spatiotemporal Dynamics of DNA Damage Response Processes. In: Genome Integrity, Ed. D.H. Lankenau, Springer, Berlin, Heidelberg, 453-478.(2007)

Academic Works

R CUNRATH
Modellierung von Strahlenschäden für die Therapieplanung.(Diplom)
Julius Maximilians Universität Würzburg (Germany),2007.

F. KNAUF
Rolle der post-translationalen Proteinmodifikation bei der Strahlenreaktion (Diplom).
TU Darmstadt FB Biologie (Germany),.10/2007

G. KRAGL
Tumortherapie mit schweren Ionen: Zweidimensionale biologische Dosisverifikation für die Therapie mit C und Anpassung von Strahleigenschaften für He (Diplom).
TU-Wien Atominstitut der Österreichischen Universitäten (Austria),2007.

G. MARTINO
Microdosimetry measurements for 12C pencil-like beams stopping in water (Diplom).
Universita degli studi di Torino (Italy), Dec. 20, 2007.

S. ZAHNREICH
Spontane und strahleninduzierte Chromosomenschäden und genetische Instabilität in Langzeitkulturen verschiedener humaner Fibroblastenlinien (Diplom).
FH-Darmstadt FB Chemie- und Biotechnologie (Germany) 2007.

M. WINTER
Zelluläre und molekularbiologische Grundlagen der vorzeitigen Alterung humaner Fibroblasten nach Bestrahlung mit Röntgen- und Kohlenstoff-Ionen
TU Darmstadt FB Biologie (Germany),.2007

Public Talks

C. BERT
Ion Beams In Biology And Medicine (IBIBAM) Workshop, Round Table: Treatment of moving organs, Heidelberg (Germany), September 2007

C. BERT
Real-time Motion Adaptive Radiation Therapy Workshop Georgetown University, Washington D.C (USA)., Mai 2007

C. BERT
Seminarreihe *Partikeltherapie*
Universitätsklinikum Gießen und Marburg (Germany), Mai 2007

C. BERT
Medizin-Physik-Seminar,
Deutsches Krebsforschungszentrum, Heidelberg (Germany), Mai 2007

T. ELSÄSSER
Biophysical Modelling of Fragment Distributions of DNA Plasmids after Heavy ion irradiation
International symposium on atomic clusters and collisions (ISACC 2007) Darmstadt (Germany), 23.07.2007

T. ELSÄSSER
Understanding and exploiting the physical and radiobiological qualities of heavy ions
Colloquium at the Institute of Condensed Matter Physics, TU Darmstadt (Germany), 14.05.2007

T. ELSÄSSER
Cluster Effects within the Local Effect Model - Impact on Treatment Planning for Carbon Ion Therapy
Seminar "Medical Physics" at the German Cancer Center (DKFZ) Heidelberg (Germany), 18.04.2007

T. ELSÄSSER
The Local Effect Model - Simulation of the Relative Biological Effectiveness (RBE) for Heavy Ion Treatment Planning
Meeting of the excellence cluster "Munich Center of Advanced Photonics" Munich (Germany), 10.01.2007

T. ELSÄSSER
Dependence of cell survival after carbon irradiation on the alpha/beta-ratio for photon irradiation - Implications of the Local Effect Model
Ion Beams in Medicine and Biology (IBIBAM), Heidelberg (Germany), October 2007

T. ELSÄSSER
Modelling of Track Structure for Heavy Ion Therapy
Heavy Ion Stopping 07 - Experts Meeting, Darmstadt (Germany), October 2007

T. ELSÄSSER
Biophysical Modeling of Fragment Distributions of DNA Plasmids after Photon and Heavy Ion Irradiation
Annual Meeting of the German Society of Radiation Biology (GBS), Mainz, October 2007

C. FOURNIER
Biophysik und Strahlenmedizin
Hochschule Darmstadt / Fb Biotechnologie (Germany), Januar 2007

C. FOURNIER
Fate of human fibroblasts following exposure to low and high LET irradiation: senescence or genetic instability?
IBIBAM, Heidelberg, 25.-29th September, 2007

C. HARTEL
Chromosomenschäden in peripheren Blutlymphozyten von Prostatakarzinompatienten nach Bestrahlung mit IMRT oder kombinierter IMRT / Kohlenstoffionentherapie.
10. Jahrestagung der Gesellschaft für Biologische Strahlenforschung (GBS), Mainz (Germany), 10.-12.10.2007

B. JAKOB
Dynamics of DNA double strand breaks detected by live cell microscopy indicates only limited cluster formation after high LET ionizing radiation
Int. Meeting IBIBAM: Ion Beams in Biology and Medicine, Heidelberg (Germany), 26.09.2007

G. KRAFT
The radiobiology and physical basis of heavy ions tumor therapy
Kolloquium, Univ. Neapel (Italy), 29.01.2007

G. KRAFT
Nine years of heavy ion therapy
Kompetenz Verbund Strahlenforschung, BMU Bonn (Germany), 14.03.2007

G. KRAFT
Krebs Therapie mit Ionen Strahlen
Öffentlicher Abendvortrag der DPG Tagung Giessen, Uni Marburg (Germany), 14.03.2007

G. KRAFT
Schwerionentherapie – Einführung in die Strahlentherapie
Seminar der Uni Marburg (Germany), 20.03.2007

G. KRAFT
Grundlagen der Ionentherapie
Arbeitstagung,VdAK Siegburg (Germany), 22.03.2007

G. KRAFT
Biologische Wirkung von Neutronen
Jahrestagung der Deutschen Physikalischen Gesellschaft und DPG Frühjahrstagung Regensburg (Germany), 28.03.2007

G. KRAFT
Tumor Therapie mit Ionen-Strahlen, Schwerionentherapie an der GSI, Grundlagen, Erfahrungen und Perspektiven, Physikalisches Kolloquium, CAU Kiel (Germany), 24.04.2007

G. KRAFT
Tumor mit Ionen Strahlen
Deutsche Wissenschaftspresse-Konferenz, Bonn (Germany), 14.05.2007

G. KRAFT
Passive degrading of ions and other critical parameter
Joint Symposium on Medical Accelerators, FOTEC, Wiener Neustadt (Austria), 04.06.2007

G. KRAFT
Ionen-Tumortherapie
Kolloquium des Institutes für Physik, Humboldt Universität Berlin (Germany), 05.06.2007

G. KRAFT
Radiobiology of Protons and Carbon Ions
Int. Symposium on Proton, Ions and Neutrons in Radiation Oncology, Munich (Germany), 06.07.2007

G. KRAFT
Ten years of heavy ion therapy - the advantages of carbon beams-
Conference on normal tissue radiation effects, Nevada Cancer Institute,
Las Vegas (USA), 14.07.2007

G. KRAFT
Tumor therapy with heavy ions
Seminar at the Radiotherapy Department of the University of California, San Francisco (USA), 17.07.2007

G. KRAFT
Partikel Therapie – ein innovatives Konzept der Tumortherapie
Capital Market Day, Uni Klinikum Giessen (Germany), 11.09.2007

G. KRAFT
Physikalische und Biologische Grundlagen der Tumortherapie mit schweren Ionen, Warum sie trotzdem funktioniert und was man daraus lernen kann
Preisträger-Vortrag: Gesellschaft für Biologische Strahlenforschung GBS, Mainz (Germany), 12.10.2007

G. KRAFT
Heilen mit Ionen-Strahlen Schwerionentherapie an der GSI Grundlagen, Erfahrungen und Perspektiven
Sat. Morn. Physics, Darmstadt (Germany) 04.11.2007

G. KRAFT
Schwerionen Therapie - ein Zukunftsprojekt
Workshop: Energie in der Tumortherapie, Klinikum Dachau, Schloss Dachau (Germany), 16.11.2007

G. KRAFT
Tumortherapie mit Ionenstrahlen
Kolloquium Physikalische Chemie, Uni Marburg (Germany), 22.11.2007

G. KRAFT
Biophysik und Ionentherapie der GSI
Heidelberger Mediziner Fortbildung (Germany), 23.11.2007

G. KRAFT
Neue Optionen in der Therapie maligner Tumoren – was bringt uns die Partikeltherapie
Workshop: Krebsgesellschaft, Berlin (Germany), 28.11.2007

G. KRAFT
Schwerionentherapie
Mit Teilchen gegen den Krebs
Öffentlicher Abendvortrag, Deutsches Museum, München (Germany), 06.12.2007

M. KRAEMER
Biological treatment planning for ion beams: Status and developments
Ion Beams In Biology And Medicine (IBIBAM),Heidelberg (Germany), September 2007

M. KRAEMER
Bestrahlungsplanung
Seminarreihe Partikeltherapie Universitätsklinikum Gießen und Marburg (Germany), Mai 2007

M. KRAEMER
Swift ions in radiotherapy: treatment planning
Heavy Ion Stopping 07 - Experts Meeting, Darmstadt (Germany), October 2007

S. RITTER
Cytogenetic damage induced in vivo by high and low LET radiation: follow up of radiotherapy patients
IBIBAM, Heidelberg, 25.-29th September, 2007

S. RITTER
Strahleninduzierte genetische Instabilitaet,
219. Sitzung der Strahlenschutzkommission, Dresden (Germaqny), 8.-9.11.07.

N. SAITO
Technical improvements of the 3D-Online Motion Compensation system for scanned ion beam therapy
Int. Meeting IBIBAM: Ion Beams in Biology and Medicine, Heidelberg (Germany), 27.09.2007

D. SCHARDT
Nuclear Fragmentation
Joint Symposoium on Medical Accelerators, Wiener Neustadt (Austria) 04.06.2007

D. SCHARDT
Carbon Ion Therapy at GSI Darmstadt
Int. Workshop IFIMED: Research on Imaging and Accelerators applied to Medicine, Valencia (Spain), 14.06.2007

D. SCHARDT
Precision radiotherapy with ion beams: Physical characterization of the radiation field and novel techniques for in-vivo irradiation monitoring
9th European Conference on Accelerators in Applied Research and Technology (ECAART 9), Firenze (Italy),3.-7.09.2007

D. SCHARDT
Nuclear fragments and fast neutrons in carbon ion radiation therapy
11th HCPBM-Workshop Ion Beams in Biology and Medicine
Heidelberg (Germany), 26.-29.09.2007

D. SCHARDT
Bragg curves of 100-400 MeV/u light ion beams for water
Heavy Ion Stopping 07, Experts Meeting Darmstadt (Germany), 8. – 10.10.2007

D. SCHARDT
Strahlentherapie von Krebstumoren mit schweren Ionen
Kolloquium III. Physikal. Institut, RTWH Aachen (Germany), 26.11.2007

M. SCHOLZ
Biophysikalische Modellierung der Relativen Biologischen Wirksamkeit (RBW) von Ionenstrahlen
Seminar Partikeltherapie, Universität Marburg (Germany), 5.6.2007

M. SCHOLZ
Heavy Ion Tumor Therapy
PTCOG Educational Workshop, Zibo (China), 18.5.2007

M. SCHOLZ
The Increased Biological Effectiveness of Heavy Charged Particle Radiation: From Cell Culture Experiments to Biophysical Modelling
PTCOG Educational Workshop, Zibo (China), 19.5.2007

M. SCHOLZ
Calculation of tumor control probability for non-small cell lung cancer after carbon ion therapy: An application of the Local Effect Model (LEM)
PTCOG 46 Meeting, Zibo (China), 21.5.2007

M. SCHOLZ
The Increased Biological Effectiveness of Ion Beam Radiation: Experimental and Theoretical Aspects
International Symposium "Atomic Cluster Collisions: structure and dynamics from the nuclear to the biological scale", Darmstadt (Germany), July 19 - 23, 2007

M. SCHOLZ
Analyse der Zellmigration mit Hilfe der Videomikroskopie
Workshop ?Quantitative Image Analysis``, Darmstadt (Germany), 15.6.2007

M. SCHOLZ
Biological Aspects of Carbon Ion Therapy
Workshop on Ion Beams in Biology and Medicine, Heidelberg (Germany), 28.9.2007

M. SCHOLZ
Biological Optimization of Carbon Ion Treatment
ESTRO Teaching Course, Heidelberg (Germany), 1.10.2007

M. SCHOLZ
Application of the Local Effect Model (LEM) in Treatment Planning for Carbon Ion Therapy
NIRS International Symposium, Chiba (Japan), 30.11.2007

S. SOMMER
Application of multicolour fluorescence in situ hybridisation for the detection of DNA damage
Congress on: Modern spectroscopy methods in studying structure and function of biopolymeres in biology and medicine, Dubna (Russia), 28.5.-2.6.07

J. SPLINTER
Heavy Ions vs. Laser Microirradiation - Two Systems to Induce Localized DNA Lesions in Living Cells
Int. Meeting IBIBAM: Ion Beams in Biology and Medicine, Heidelberg (Germany), 26.09.2007

J. SPLINTER
Schwerionen und Lasermikrobestrahlung – Zwei Systeme zur Erzeugung lokalisierter DNA Schäden in lebenden Zellen
Nat. Meeting GBS: Gesellschaft für Biologische Strahlenforschung, Mainz (Germany), 11.10.2007

G. TAUCHER-SCHOLZ
Molekulare Strahenbiologie von Protonen und Ionen
Symposium ``Experimentelle Strahlentherapie und Klinische Strahlenbiologie" Dresden (Germany), 02.03.2007

G. TAUCHER-SCHOLZ
Heavy ion-induced production of clustered damage: visualization using plasmid DNA and cells.
.25th Miller Conference on Radiation Chemistry, Buxton (UK), 15.04.2007

G. TAUCHER-SCHOLZ
Strahlenbiologische Grundlagen bei der Tumortherapie mit schweren Ionen
Universität Mainz (Germany),19.06.2007

G. TAUCHER-SCHOLZ
Induction of DNA damage by heavy ions: lesion clustering and localized cellular response
13th International Congress on Radiation Research ,Symposium Track structure physics and chemistry, San Francisco (USA) 08.07.2007

G. TAUCHER-SCHOLZ
Live cell imaging of repair proteins on localized ionizing radiation-induced DNA damage
13th International Congress on Radiation Research
San Francisco (USA) 11.07.2007

G. TAUCHER-SCHOLZ
Physical and molecular basis of the biological effects of charged particle radiation.
ECCO 14 European Cancer Conference
Barcelona (Spain) 25.09.2007.

C. VON NEUBECK
Radiobiologische Experimente für die Schwerionentherapie von Prostatakarzinomen.
10. Jahrestagung der Gesellschaft für Biologische Strahlenforschung (GBS), Mainz (Germany), 10.-12.10.2007

W. WEYRATHER
Latest results on RBE studies
Joint Symposoium on Medical Accelerators, Wiener Neustadt (Austria) 04.06.2007

W. WEYRATHER
Tumortherapie mit Ionenstrahlen
Physikerinnentagung Osnabrueck (Germany) 01.11.2007

W. WEYRATHER
Particle RT
Blockvorlesung im Masterkurs Medical Physics, Uniklinik Mannheim (Germany) 04. 12.2007

W. WEYRATHER
Seminarreihe Partikeltherapie
Universitaetsklinikum Giessen und Marburg (Germany), 17.04.2007

Research Division: CBM

Leader: Peter Senger
Compiled by: Volker Friese

Publications

FAIR-EXPERIMENTS

1. WoS listed publications

J. Adamczewski et al., CBM Collaboration: Data Acquisition backbone Core DABC, J. Phys. Conf. Ser. (2007), in press

V. Ammosov et al., CBM Collaboration: Performance of RPC with low-resistive silicate glass electrodes exposed to an intense continuous electron beam, Nucl. Instr. Meth. A 576 (2007) 391

S. Gorbunov et al., CBM Collaboration: Fast SIMDized Kalman filter based track fit, Comp. Phys. Comm. (2007), in press

J. Heuser, CBM Collaboration: The Compressed Baryonic Matter Experiment at FAIR – Physics of strangeness and charm, status of preparations, J. Phys. G (2007), in press

J. Heuser, CBM Collaboration: Development of a Silicon Tracking and Vertex Detection System for the CBM Experiment at FAIR, Nucl. Instr. Meth. A 582 (2007) 910

C. Höhne et al., CBM Collaboration: Development of a RICH detector for electron identification in CBM, Nucl. Instrum. Phys. A (2007), in press

C. Höhne et al., CBM Collaboration: The CBM experiment at FAIR: exploring the QCD phase diagram at high net baryon densities, Int. J. Mod. Phys. E 16 (2007)

M. Klein-Bösing et al., CBM Collaboration: Position resolution of a high efficiency transition radiation detector for high counting rate environments, Nucl. Instr. Meth. A (2007), in press

A. Laszlo, Z. Fodor and G. Vesztergombi, CBM Collaboration: New results and perspectives on R(AA) measurements below 20 GeV CM-energy at fixed target machines, Int. J. Mod. Phys E 16 (2007) 2516

M. Petrovici et al., CBM Collaboration: A high-efficiency Transition Radiation Detector for high counting rate environments, Nucl. Instr. Meth. A 579 (2007) 961

P. Senger, CBM Collaboration: Compressed Baryonic Matter – Experiments at GSI and FAIR, Phys. Part. Nucl. Lett (2007), in press

The CBM Collaboration, CBM Progress Report 2006, Darmstadt 2007, http://www.gsi.de/documents/DOC-2007-Mar-137.html

PROGRAMME HADRONS & NUCLEI

1. WoS listed publications

P. Senger, Strange particles and neutron stars – Experiments at GSI, Int. J. Mod. Phys. E 16 (2007)

Public Talks

C. Höhne, the CBM experiment at FAIR, XXXVIII. Arbeitstreffen Kernphysik, Schleching, Germany, February 2007

P. Senger, Possible heavy-ion experiments at GSI/FAIR and J-PARC, International Workshop on Nuclear Physics at J-PARC, Tokai, Japan, June 1-2 2007

C. Höhne, Challenges for CBM, Workshop on Electromagnetic Probes of Strongly Interacting matter, Trento, Italy, June 18-22, 2007

T. Galatyuk, Di-electron spectroscopy in CBM, Workshop on Electromagnetic Probes of Strongly Interacting matter, Trento, Italy, June 18-22, 2007

J. Heuser, The Compressed Baryonic Matter experiment at FAIR, International Conference on Strangeness in Quark Matter (SQM2007), Levoca, Slovakia, June 24-29, 2007

A. Kiseleva, Vector meson identification via dimuon measurements at CBM/FAIR, NUCLEUS-2007, Voronezh, Russia, June 25-29, 2007

V. Friese, The CBM Experiment at FAIR, International Workshop on Critical Point and Onset of Deconfinement (CPOD07), Darmstadt, Germany, July 9-13, 2007

P. Senger, What do we learn about dense nuclear matter from heavy-ion collision experiments? XXX Mazurian Lakes Conference on Physics, Piaski, Poland, September 2-9, 2007

C. Schmidt, Test results on the n-XYTER ASIC, Topical Workshop for Electronics in Particle Physics, Prague, Czech Republic, September 3-7, 2007

P. Senger, the CBM Experiment at FAIR, VI-SIM workshop, Bad Liebenzell, Germany, September 12-15, 2007

C. Höhne, Development of a RICH detector for electron identification in CBM, RICH2007 workshop, Trieste, Italy, October 15-20, 2007

Presentations at the Spring Meeting of the German Physical Society, Giessen, Germany, March 12-16, 2007

J. Heuser et al., Development of a Silicon Tracking System for the CBM Experiment at FAIR

C. Höhne et al., The CBM experiment - exploring the QCD phase diagram at high net baryon densities

M. Klein-Bösing et al., Effizienz hochratenfester TRD-Prototypen für CBM

C. Steinle et al., Tracking im Silicon Tracker System des CBM Experiments mittels Hough Transformation

T. Galatyuk et al., Strategy for electron pair reconstruction in CBM

A. Kiseleva et al.,Vector meson identification via dimuon measurements at CBM

D. Gonzalez-Diaz et al., The TOF wall of the CBM experiment at FAIR

S. Gorbunov et al., On-line Event Reconstruction in the CBM Silicon Detector

C. Müntz et al., Bau eines Demonstrators für den Mikro-Vertex Detektor von CBM

K. Solvag et al., Status of the n-XYTER Testing

Research Division: Experimental Nuclear Physics

Leader: Christoph Scheidenberger
Compiled by: Siglind Raiß

Publications

1. WoS listed publications

ANTALIC, S.; ANDREYEV, A. N.; ACKERMANN, D.; BIANCO, L.; CULLEN, D.; DARBY, I.; FRANCHOO, S.; HEINZ, S.; HEßBERGER/HESSBERGER, F. P.; HOFMANN, S.; HUYSE, M.; KINDLER, B.; KOJOUHAROV, I.; LEPPANEN, A. P.; LESHER, S. R.; LOMMEL, B.; MANN, R.; MüNZENBERG/MUNZENBERG, G.; NISHIO, K.; PAGE, R. D.; PAKARINEN, J.; RESSLER, J. J.; SARO, S.; STREICHER, B.; SULIGNANO, B.; THOMSON, J.; VAN DUPPEN, P.; VENHART, M.; WISEMAN, D.; WYSS, R.: The new isotopes in Po-Rn region. Acta physica Polonica B, Particle physics and field theory, nuclear physics, theory of relativity / Acta Phys. Pol. B 38(4), 2007: 1557–1560.

AXIOTIS, M.; LENZI, S. M.; MARGINEAN, N.; NAPOLI, D. R.; UR, C. A.; BRANDOLINI, F.; FARNEA, E.; GADEA, A.; ALGORA, A.; DE ANGELIS, G.; BAZZACCO, D.; BIZZETI, P. G.; BIZZETI-SONA, A.; VON BRENTANO, P.; CAMERON, J. A.; DEWALD, A.; GRAWE, H.; KALFAS, C. A.; LUNARDI, S.; MARTINEZ, T.; PAPADOPOULOS, C. T.; PODOLYAK, Z.; ALVAREZ, C. R.; SANCHEZ-SOLANO, J.; TONEV, D.; VLASTOU, R.: High-spin gamma-ray spectroscopy in Mn-52. Physical review C, Nuclear physics / Phys. Rev. C 76(1), 2007: 014303, 8 pages.

BEDNARCZYK, P.; BERDERMANN, E.; GERL, J.; GORSKA, M.; KOJOUHAROV, I.; POMORSKI, M.; REBISZ, M.; VOSS, B.; ACOSTA, L.; BERJILLOS, R.; MARTEL, I.; ALVAREZ, M. A. G.; ESPINO, J. M.; FLORES, J. L.; MUKHA, I.; WOLSKI, R.: Application of diamond detectors in tracking of heavy ion slowed down radioactive beams. Acta physica Polonica B, Particle physics and field theory, nuclear physics, theory of relativity / Acta Phys. Pol. B 38(4), 2007: 1293–1296.

BLOCK, M.; ACKERMANN, D.; BLAUM, K.; CHAUDHURI, A.; DI, Z.; ELISEEV, S.; FERRER, R.; HABS, D.; HERFURTH, F.; HEßBERGER/HESSBERGER, F. P.; HOFMANN, S.; KLUGE, H. J.; MAERO, G.; MARTIN, A.; MARX, G.; MAZZOCCO, M.; MUKHERJEE, M.; NEUMAYR, J. B.; PLASS, W. R.; QUINT, W.; RAHAMAN, S.; RAUTH, C.; RODRIGUEZ, D.; SCHEIDENBERGER, C.; SCHWEIKHARD, L.; THIROLF, P. G.; VOROBJEV, G.; WEBER, C.: Towards direct mass measurements of nobelium at SHIPTRAP. The European physical journal: D, Atomic, molecular and optical physics / Eur. Phys. J. D 45(1), 2007: 39–45.

BOUTACHKOV, P.; BENCZER-KOLLER, N.; KUMBARTZKI, G. J.; ESCUDEROS, A.; SHARON, Y. Y.; ZAMICK, L.; ROBINSON, S. J. Q.; AI, H.; CHAMBERLAIN, M.; GURDAL, G.; HEINZ, A.; MCCUTCHAN, E. A.; QUIAN, J.; WERNER, V.; WILLIAMS, E.; ALEKSANDROVA, K.; COPOS, C. A.; KOVACHEVA, D. A.; MANCHEV, P.: Sign of the g factor of the 4(1)(+) state in Zn-68. Physical review C, Nuclear physics / Phys. Rev. C 75(2), 2007: 021302, 4 pages.

BRACCO, A.; BENZONI, G.; BLASI, N.; BRAMBILLA, S.; CAMERA, F.; CRESPI, F. C. L.; LEONI, S.; MILLION, B.; MONTANARI, D.; PIGNANELLI, M.; WIELAND, O.; MAJ, A.; BEDNARCZYK, P.; GREBOSZ, J.; KMIECIK, M.; MECZYNSKI, W.; STYCZEN, J.; AUMANN, T.; BANU, A.; BECK, T.; BECKER, F.; CACERES, L.; DOORNENBAL, P.; EMLING, H.; GERL, J.; GEISSEL, H.; GORSKA, M.; KAVATSYUK, O.; KAVATSYUK, M.; KOJOUHAROV, I.; KURZ, N.; LOZEVA, R.; SAITO, N.; SAITO, T.; SHAFFNER, H.; WOLLERSHEIM, H. J.; JOLIE, J.; REITER, P.; WARR, N.; DE ANGELIS, G.; GADEA, A.; NAPOLI, D.; LENZI, S.; LUNARDI, S.; BALABANSKI, D.; LO BIANCO, G.; PETRACHE, C.; SALTARELLI, A.; CASTOLDI, M.; ZUCCHIATTI, A.; WALKER, J.; BURGER, A.: Coulomb excitation of Ni-68 at 600 AMeV. Acta physica Polonica B, Particle physics and field theory, nuclear physics, theory of relativity / Acta Phys. Pol. B 38(4), 2007: 1229–1236.

BRANDAU, C.; BOUTIN, D.; GEISSEL, H.; GERL, J.; GORSKA, M.; MANIKONDA, S.; MüNZENBERG/MUNZENBERG, G.; PODOLYAK, Z.; SCHEIDENBERGER, C.; WEICK, H.; WINKLER, M.; YAVOR, M.: Status of the energy-buncher in the low-energy branch of the Super-FRS. Eur. Phys. J.-Spec. Top. 150, 2007: 225–226.

CACERES, L. S.; GORSKA, M.; JUNGCLAUS, A.;

REGAN, P. H.; GARNSWORTHY, A. B.; PIETRI, S.; PODOLYAK, Z.; RUDOLPH, D.; STEER, S. J.; GRAWE, H.; BALABANSKI, D. L.; BECKER, F.; BEDNARCZYK, P.; BENZONI, G.; BLANK, B.; BRANDAU, C.; BRUCE, A. M.; CAMERA, F.; CATFORD, W. N.; CULLEN, I. J.; DOMBRADI, Z.; DOORNENBALAL, P.; ESTEVEZ, E.; GEISSEL, H.; GELLETLY, W.; GERL, J.; GREBOSZ, J.; HEINZ, A.; HOISCHEN, R.; ILIE, G.; JOLIE, J.; JONES, G. A.; KMIECIK, M.; KOJOUHAROV, I.; KONDEV, F. G.; KURTUKIAN-NIETO, T.; KURZ, N.; LALKOWSKI, S.; LIU, L.; MAJ, A.; MYALSK, S.; MONTES, F.; PFUTZNER, M.; PROKOPOWICZ, W.; SAITO, T.; SCHATFNER, H.; SCHWERTEL, S.; SHIZUMA, T.; SIMONS, A. J.; TASHENOV, S.; WALKER, P. M.; WERNER-MALENTO, E.; WIELANDH, O.; WOLLER-SHEIM, H. J.: Identification of excited states in the N = Z nucleus Nb-82. Acta physica Polonica B, Particle physics and field theory, nuclear physics, theory of relativity / Acta Phys. Pol. B 38(4), 2007: 1271–1275.

CEDERKALL, J.; EKSTROM, A.; FAHLANDER, C.; HURST, A. M.; HJORTH-JENSEN, M.; AMES, F.; BANU, A.; BUTLER, P. A.; DAVINSON, T.; PRAMANIK, U. D.; EBERTH, J.; FRANCHOO, S.; GEORGIEV, G.; GORSKA, M.; HABS, D.; HUYSE, M.; IVANOV, O.; IWANICKI, J.; KESTER, O.; KOSTER, U.; MARSH, B. A.; NIEDERMAIER, O.; NILSSON, T.; REITER, P.; SCHEIT, H.; SCHWALM, D.; SIEBER, T.; SLETTEN, G.; STEFANESCU, I.; DE WALLE, J. V.; VAN DUPPEN, P.; WARR, N.; WEISSHAAR, D.; WENANDER, F.: Sub-barrier Coulomb excitation of Sn-110 and its implications for the Sn-100 shell closure. Physical review letters / Phys. Rev. Lett. 98(17), 2007: 172501, 4 pages.

CLEMENT, E.; GORGEN, A.; KORTEN, W.; BOUCHEZ, E.; CHATILLON, A.; DELAROCHE, J. P.; GIROD, M.; GOUTTE, H.; HURSTEL, A.; LE COZ, Y.; OBERTELLI, A.; PERU, S.; THEISEN, C.; WILSON, J. N.; ZIELIN-SKA, M.; ANDREOIU, C.; BECKER, F.; BUTLER, P. A.; CASANDJIAN, J. M.; CATFORD, W. N.; CZOS-NYKA, T.; DE FRANCE, G.; GERL, J.; HERZBERG, R. D.; IWANICKI, J.; JENKINS, D. G.; JONES, G. D.; NAPIORKOWSKI, P. J.; SLETTEN, G.; TIMIS, C. N.: Shape coexistence in neutron-deficient krypton isotopes. Physical review C, Nuclear physics / Phys. Rev. C 75(5), 2007: 054313, 20 pages.

CUNSOLO, A.; CAPPUZZELLO, F.; CAVALLARO, M.; FOTI, A.; KHOUAJA, A.; ORRIGO, S. E. A.; WINFIELD, J. S.; GASPARINI, L.; LONGO, G.; BORELLO-LEWIN, T.; RODRIGUES, M. R. D.; BARBOSA, M. D. L.; NOCIFORO, C.; PETRASCU, H.: Commissioning of the MAGNEX large-acceptance spectrometer. Eur. Phys. J.-Spec. Top. 150, 2007: 343–346.

DOLINSKII, A.; LITVINOV, S.; STECK, M.; WEICK, H.: Study of the mass resolving power in the CR storage ring operated as a TOF spectrometer. Nuclear instruments & methods in physics research, Section A, Accelerators, spectrometers, detectors and associated equipment / Nucl. Instrum. Methods Phys. Res. Sect. A-Accel. Spectrom. Dect. Assoc. Equip. 574(2), 2007: 207–212.

GARNSWORTHY, A. B.; REGAN, P. H.; PIETRI, S.; RUDOLPH, D.; CACERES, L.; GORSKA, M.; PODOLYAK, Z.; STEER, S. J.; HEINZ, A.; BECKER, F.; BEDNARCZYK, P.; DOORNENBAL, P.; GEISSEL, H.; GERL, J.; GRAWE, H.; GREBOSZ, J.; KELIC, A.; KOJOUHAROV, I.; KURZ, N.; MONTES, F.; PROKOP-WICZ, W.; SAITO, T.; SCHAFFNER, H.; TACHENOV, S.; WERNER-MALENTO, E.; WOLLERSHEIM, H. J.; BENZONI, G.; BLANK, B.; BRANDAU, C.; BRUCE, A. M.; CAMERA, F.; CATFORD, W. N.; CULLEN, I. J.; DOMBRADI, Z.; ESTEVEZ, E.; GELLETLY, W.; HOISCHEN, R.; ILIE, G.; JOLIE, J.; JONES, G. A.; JUNGCLAUS, A.; KMIECIK, M.; KONDEV, F. G.; KURTUKIAN-NIETO, T.; LALKOVSKI, S.; LIU, Z.; MAJ, A.; MYALSKI, S.; PFUTZNER, M.; SHIZUMA, T.; SIMONS, A. J.; SCHWERTEL, S.; WALKER, P. M.; WIELAND, O.: Isomeric states in the light Tc isotopes. Acta physica Polonica B, Particle physics and field theory, nuclear physics, theory of relativity / Acta Phys. Pol. B 38(4), 2007: 1265–1269.

GEISSEL, H.; LITVINOV, Y. A.; BECKERT, K.; BELLER, P.; BOSCH, F.; BOUTIN, D.; BRANDAU, C.; CHEN, L.; HAUSMANN, M.; KLEPPER, O.; KNOBEL, R.; KOZHUHAROV, C.; KURCEWICZ, J.; LITVINOV, S. A.; MAZZOCCO, M.; MüNZENBERG/MUNZENBERG, G.; NOCIFORO, C.; NOLDEN, F.; PATYK, Z.; PFUTZNER, M.; PLASS, W.; SCHEIDENBERGER, C.; STECK, M.; SUN, B.; TAKAHASHI, K.; WEICK, H.; WINCKLER, N.; WINKLER, M.: Present and future experiments with stored exotic nuclei at the FRS-ESR facility. Eur. Phys. J.-Spec. Top. 150, 2007: 109–115.

GERL, J.: Gamma spectroscopy with RIBs from RISING to AGATA. Eur. Phys. J.-Spec. Top. 150, 2007: 353–356.

GORGEN, A.; CLEMENT, E.; KORTEN, W.; BOUCHEZ,

E.; CHATILLON, A.; HURSTEL, A.; LE COZ, Y.; THEISEN, C.; WILSON, J. N.; ZIELINSKA, M.; ANDREOIU, C.; BECKER, F.; BUTLER, P.; CASANDJIAN, J. M.; CATFORD, W. N.; CZOSNYKA, T.; DE FRANCE, G.; GERL, J.; HERZBERG, R. D.; IWANICKI, J.; JENKINS, D. G.; JONES, G. D.; NAPIORKOWSKI, P. J.; SLETTEN, G.; TIMIS, C.: Shape coexistence in Kr-74 and Kr-76. Eur. Phys. J.-Spec. Top. 150, 2007: 117–120.

GORSKA, M.; BANU, A.; BEDNARCZYK, P.; BRACCO, A.; BURGER, A.; CAMERA, F.; CAURIER, E.; DOORNENBAL, P.; GERL, J.; GRAWE, H.; HONMA, M.; HUBEL, H.; JUNGCLAUS, A.; MAJ, A.; NEYENS, G.; NOWACKI, F.; OTSUKA, T.; PFUTZNER, T.; PIETRI, S.; PODOLYAK, Z.; POVES, A.; REGAN, P. H.; REITER, P.; RUDOLPH, D.; WOLLERSHEIM, H. J.; RISING Collaboration: Nuclear structure far off stability - Rising campaigns. Acta physica Polonica B, Particle physics and field theory, nuclear physics, theory of relativity / Acta Phys. Pol. B 38(4), 2007: 1219–1228.

GRAWE, H.; LANGANKE, K.; MARTINEZ-PINEDO, G.: Nuclear structure and astrophysics. Rep. Prog. Phys. 70(9), 2007: 1525–1582.

HAYES, A. B.; CLINE, D.; WU, C. Y.; AI, H.; AMRO, H.; BEAUSANG, C.; CASTEN, R. F.; GERL, J.; HECHT, A. A.; HEINZ, A.; HUA, H.; HUGHES, R.; JANSSENS, R. V. F.; LISTER, C. J.; MACCHIAVELLI, A. O.; MEYER, D. A.; MOORE, E. F.; NAPIORKOWSKI, P.; PARDO, R. C.; SCHLEGEL, C.; SEWERYNIAK, D.; SIMON, M. W.; SREBRNY, J.; TENG, R.; VETTER, K.; WOLLERSHEIM, H. J.: Spin dependence of K mixing, strong configuration mixing, and electromagnetic properties of Hf-178. Physical review C, Nuclear physics / Phys. Rev. C 75(3), 2007: 034308, 27 pages.

HOFMANN, S.; ACKERMANN, D.; ANTALIC, S.; BURKHARD, H. G.; COMAS, V. F.; DRESSLER, R.; GAN, Z.; HEINZ, S.; HEREDIA, J. A.; HEBBERGER, F. P.; KHUYAGBAATAR, J.; KINDLER, B.; KOJOUHAROV, I.; KUUSINIEMI, P.; LEINO, M.; LOMMEL, B.; MANN, R.; MENZENBERG, G.; NISHIO, K.; POPEKO, A. G.; SARO, S.; SCHöTT/SCHOTT, H. J.; STREICHER, B.; SULIGNANO, B.; UUSITALO, J.; YEREMIN, A. V.: Studies of superheavy elements at ship. International journal of modern physics E, Nuclear physics / Int. J. Mod. Phys. E-Nucl. Phys. 16(4), 2007: 937–947.

HOFMANN, S.; ACKERMANN, D.; ANTALIC, S.; BURKHARD, H. G.; COMAS, V. F.; DRESSLER, R.; GAN, Z.; HEINZ, S.; HEREDIA, J. A.; HEßBERGER/HESSBERGER, F. P.; KHUYAGBAATAR, J.; KINDLER, B.; KOJOUHAROV, I.; KUUSINIEMI, P.; LEINO, M.; LOMMEL, B.; MANN, R.; MüNZENBERG/MUNZENBERG, G.; NISHIO, K.; POPEKO, A. G.; SARO, S.; SCHöTT/SCHOTT, H. J.; STREICHER, B.; SULIGNANO, B.; UUSITALO, J.; VENHART, M.; YEREMIN, A. V.: The reaction Ca-48+U-238 -¿(286)112 studied at the GSI-SHIP. The European physical journal A, Hadrons and nuclei / Eur. Phys. J. A 32(3), 2007: 251–260.

ILIEVA, S.; KISELEV, O.; EMLING, H.; EGELHOF, P.; BORETZKY, K.; MEIER, J. P.; SIMON, H.; MAHATA, K.; LE BLEIS, T.; CHATILLON, A.; AKSOUH, F.; BECKERT, K.; BELLER, P.; KOZHUHAROV, C.; LITVINOV, Y.; LE, X. C.; NOLDEN, F.; STECK, M.; STöHLKER/STOHLKER, T.; ICKERT, G.; POPP, U.; WEICK, H.; ROHE, D.; JOURDAN, J.; WERTHMULLER, D.; MOEINI, H.; ZALITE, A.; PASCHALIS, S.: Feasibility studies of the EXL setup for FAIR using the GSI storage ring ESR. Eur. Phys. J.-Spec. Top. 150, 2007: 357–358.

JUNGCLAUS, A.; CACERES, L.; GORSKA, M.; PFUTZNER, M.; PIETRI, S.; WERNER-MALENTO, E.; GRAWE, H.; LANGANKE, K.; MARTINEZ-PINEDO, G.; NOWACKI, F.; POVES, A.; CUENCA-GARCIA, J. J.; RUDOLPH, D.; PODOLYAK, Z.; REGAN, P. H.; DETISTOV, P.; LALKOVSKI, S.; MODAMIO, V.; WALKER, J.; BEDNARCZYK, P.; DOORNENBAL, P.; GEISSEL, H.; GERL, J.; GREBOSZ, J.; KOJOUHAROV, I.; KURZ, N.; PROKOPOWICZ, W.; SCHAFFNER, H.; WOLLERSHEIM, H. J.; ANDGREN, K.; BENLLIURE, J.; BENZONI, G.; BRUCE, A. M.; CASAREJOS, E.; CEDERWALL, B.; CRESPI, F. C. L.; HADINIA, B.; HELLSTROM, M.; HOISCHEN, R.; ILIE, G.; JOLIE, J.; KHAPLANOV, A.; KMIECIK, M.; KUMAR, R.; MAJ, A.; MANDAL, S.; MONTES, F.; MYALSKI, S.; SIMPSON, G. S.; STEER, S. J.; TASHENOV, S.; WIELAND, O.: Observation of isomeric decays in the r-process waiting-point nucleus Cd-130(82). Physical review letters / Phys. Rev. Lett. 99(13), 2007: 132501, 5 pages.

KAVATSYUK, O.; MAZZOCCHI, C.; JANAS, Z.; BANU, A.; BATIST, L.; BECKER, F.; BLAZHEV, A.; BRüCHLE/BRUCHLE, W.; DORING, J.; FAESTERMANN, T.; GORSKA, M.; GRAWE, H.; JUNGCLAUS, A.; KARNY, M.; KAVATSYUK, M.; KLEPPER, O.;

KIRCHNER, R.; LA COMMARA, M.; MIERNIK, K.; MUKHA, I.; PLETTNER, C.; PLOCHOCKI, A.; ROECKL, E.; ROMOLI, M.; RYKACZEWSKI, K.; SCHäDEL/SCHADEL, M.; SCHMIDT, K.; SCHWENGNER, R.; ZYLICZ, J.: Beta decay of Sn-101. The European physical journal A, Hadrons and nuclei / Eur. Phys. J. A 31(3), 2007: 319–325.

KLIMKIEWICZ, A.; ADRICH, P.; BORETZKY, K.; FALLOT, M.; AUMANN, T.; CORTINA-GIL, D.; PRAMANIK, U. D.; ELZE, T. W.; EMLING, H.; GEISSEL, H.; HELLSTROEM, M.; JONES, K. L.; KRATZ, J. V.; KULESSA, R.; LEIFELS, Y.; NOCIFORO, C.; PALIT, R.; SIMON, H.; SUROWKA, G.; SüMMERER/SUMMERER, K.; TYPEL, S.; WALUS, W.: Dipole response of neutron-rich Sn isotopes. Nuclear physics A, Nuclear and hadronic physics / Nucl. Phys. A 788, 2007: 145C–152C.

KLIMKIEWICZ, A.; PAAR, N.; ADRICH, P.; FALLOT, M.; BORETZKY, K.; AUMANN, T.; CORTINA-GIL, D.; PRAMANIK, U. D.; ELZE, T. W.; EMLING, H.; GEISSEL, H.; HELLSTROM, M.; JONES, K. L.; KRATZ, J. V.; KULESSA, R.; NOCIFORO, C.; PALIT, R.; SIMON, H.; SUROWKA, G.; SüMMERER/SUMMERER, K.; VRETENAR, D.; WALUS, W.; LAND CollaborationGSIKO: Nuclear symmetry energy and neutron skins derived from pygmy dipole resonances. Physical review C, Nuclear physics / Phys. Rev. C 76(5), 2007: 051603, 4 pages.

LITVINOV, Y. A.; BOSCH, F.; GEISSEL, H.; KURCEWICZ, J.; PATYK, Z.; WINCKLER, N.; BATIST, L.; BECKERT, K.; BOUTIN, D.; BRANDAU, C.; CHEN, L.; DIMOPOULOU, C.; FABIAN, B.; FAESTERMANN, T.; FRAGNER, A.; GRIGORENKO, L.; HAETTNER, E.; HESS, S.; KIENLE, P.; KNOBEL, R.; KOZHUHAROV, C.; LITVINOV, S. A.; MAIER, L.; MAZZOCCO, M.; MONTES, F.; MüNZENBERG/MUNZENBERG, G.; MUSUMARRA, A.; NOCIFORO, C.; NOLDEN, F.; PFUTZNER, M.; PLASS, W. R.; PROCHAZKA, A.; REDA, R.; REUSCHL, R.; SCHEIDENBERGER, C.; STECK, M.; STöHLKER/STOHLKER, T.; TORILOV, S.; TRASSINELLI, M.; SUN, B.; WEICK, H.; WINKLER, M.: Measurement of the beta(+) and orbital electron-capture decay rates in fully ionized, hydrogenlike, and heliumlike Pr-140 ions. Physical review letters / Phys. Rev. Lett. 99(26), 2007: 262501, 4 pages.

LORENTE, A. S.; ACHENBACH, P.; AGNELLO, M.; BRESSANI, T.; BUFALINO, S.; CEDERWALL, B.; FELICIELLO, A.; FERRO, F.; GERL, J.; IAZZI, F.; KAVATSYUK, M.; KOJOUHAROV, I.; MAJLING, L.; PANTALEO, A.; PALOMBA, M.; POCHODZALLA, J.; RACITI, G.; SAITO, N.; SAITO, T. R.; SCHAFFNER, H.; SFIENTI, C.; SZYMANSKA, K.; TEGNER, P. E.; HyperGamma Collaboration: Performance of HPGe detectors in high magnetic fields. Nuclear instruments & methods in physics research, Section A, Accelerators, spectrometers, detectors and associated equipment / Nucl. Instrum. Methods Phys. Res. Sect. A-Accel. Spectrom. Dect. Assoc. Equip. 573(3), 2007: 410–417.

MAZZOCCO, M.; ACKERMANN, D.; BLOCK, M.; GEISSEL, H.; HEßBERGER/HESSBERGER, F. P.; HOFMANN, S.; IWASA, N.; NISHIO, K.; PLASS, W. R.; SCHEIDENBERGER, C.; WEICK, H.; WINKLER, M.: Extension of the Monte-Carlo code MOCADI to fusion-evaporation reactions. Eur. Phys. J.-Spec. Top. 150, 2007: 363–364.

MUKHA, I.; SüMMERER/SUMMERER, K.; ACOSTA, L.; ALVAREZ, M. A. G.; CASAREJOS, E.; CHATILLON, A.; CORTINA-GIL, D.; ESPINO, J.; FOMICHEV, A.; GARCIA-RAMOS, J. E.; GEISSEL, H.; GOMEZ-CAMACHO, J.; GRIGORENKO, L.; HOFFMANN, J.; KISELEV, O.; KORSHENINNIKOV, A.; KURZ, N.; LITVINOV, Y.; MARTEL, I.; NOCIFORO, C.; OTT, W.; PFUTZNER, M.; RODRIGUEZ-TAJES, C.; ROECKL, E.; STANOIU, M.; WEICK, H.; WOODS, P. J.: Observation of two-proton radioactivity of Mg-19 by tracking the decay products. Physical review letters / Phys. Rev. Lett. 99(18), 2007: 182501, 5 pages.

MYALSKI, S.; KMIECIK, M.; MAJ, A.; REGAN, P. H.; GARNSWORTHY, A. B.; PIETRI, S.; RUDOLPH, D.; PODOLYAK, Z.; STEER, S. J.; BECKER, F.; BEDNARCZYK, P.; GERL, J.; GORSKA, M.; GRAWE, H.; KOJOUHAROV, I.; SCHAFFNER, H.; WOLLERSHEIM, H. J.; PROKOPOWICZ, W.; GREBOSZ, J.; BENZONI, G.; BLANK, B.; BRANDAU, C.; BRUCE, A. M.; CACERES, L.; CAMERA, F.; CATFORD, W. N.; CULLEN, I. J.; DOMBRADI, Z.; DOORNENBAL, P.; ESTEVEZ, E.; GEISSEL, H.; GELLETLY, W.; HEINZ, A.; HOISCHEN, R.; ILIE, G.; JONES, G. A.; JUNGCLAUS, A.; KELIC, A.; KONDEV, F. G.; KURTUKIAN-NIETO, T.; KURZ, N.; LALKOVSKI, S.; LIU, Z.; MONTES, F.; PFUTZNER, M.; SAITO, T.; SHIZUMA, T.; SIMONS, A. J.; SCHWERTEL, S.; TACHENOV, S.; WALKER, P. M.; WERNER-MALENTO, E.; WIELAND, O.: Isomeric ratio for the I-pi=8(+) yrast state in Pd-96 produced in the relativistic fragmentation of Ag-107. Acta physica Polonica B, Particle physics and field theory, nuclear

physics, theory of relativity / Acta Phys. Pol. B 38(4), 2007: 1277–1282.

NEYENS, G.; ATANASOVA, L.; BALABANSKI, D. L.; BECKER, F.; BEDNARCZYK, P.; CACERES, L.; DOORNENBAL, P.; GERL, J.; GORSKA, M.; GREBOSZ, J.; HASS, M.; ILIE, G.; KURZ, N.; KOJOUHAROV, I.; LOZEVA, R.; MAJ, A.; PFUTZNER, M.; PIETRI, S.; PODOLYAK, Z.; PROKOPOWICZ, W.; SAITOH, T. R.; SCHAFFNER, H.; SIMPSON, G.; VERMEULEN, N.; WERNER-MALENTO, E.; WALKER, J.; WOLLERSHEIM, H. J.; BAZZACCO, D.; BENZONI, G.; BLAZHEV, A.; BLASI, N.; BRACCO, A.; BRANDAU, C.; CAMERA, F.; CHAMOLI, S. K.; CHMEL, S.; CRESPI, F. C. L.; DAUGAS, J. M.; DE RYDT, M.; DETISTOV, P.; FAHLANDER, C.; FARNEA, E.; GEORGIEV, G.; GLADNISHKI, K.; HOISCHEN, R.; IONESCU-BUJOR, M.; IORDACHESCU, A.; JOLIE, J.; JUNGCLAUS, A.; KMIECIK, M.; KRASZNAHORKAY, A.; KULESSA, R.; LAKSHMI, S.; LO BIANCO, G.; MALLION, S.; MAZUREK, K.; MECZYNSKI, W.; MONTANARI, D.; MYALSKY, S.; PERRU, O.; RUDOLPH, D.; RUSEV, G.; SALTARELLI, A.; SCHWENGNER, R.; STYCZEN, J.; TURZO, K.; VALIENTE-DOBON, J. J.; WIELAND, O.; ZIEBLINSKI, M.: g factor measurements on relativistic isomeric beams produced by fragmentation and U-fission: The g-rising project at GSI. Acta physica Polonica B, Particle physics and field theory, nuclear physics, theory of relativity / Acta Phys. Pol. B 38(4), 2007: 1237–1247.

OGAWA, H.; GEISSEL, H.; FETTOUHI, A.; FRITZSCHE, S.; PORTILLO, M.; SCHEIDENBERGER, C.; SHEVELKO, V. P.; SURZHYKOV, A.; WEICK, H.; BECKER, F.; BOUTIN, D.; KINDLER, B.; KNOBEL, R. K.; KURCEWICZ, J.; KURCEWICZ, W.; LITVINOV, Y. A.; LOMMEL, B.; MüNZENBERG/MUNZENBERG, G.; PLASS, W. R.; SAKAMOTO, N.; STADLMANN, J.; TSUCHIDA, H.; WINKLER, M.; YAO, N.: Gas-solid difference in charge-changing cross sections for bare and H-like nickel ions at 200 MeV/u. Physical review A, Atomic, molecular, and optical physics / Phys. Rev. A 75(2), 2007: 020703, 4 pages.

PIETRI, S.; REGA, P. H.; PODOLYAK, Z.; JUNGCLAUS, A.; PFUTZNER, M.; RUDOLPH, D.; GARNSWORTHY, A. B.; STEER, S. J.; HOISCHEN, R.; GORSKA, M.; GERL, J.; WOLLERSHEIM, H. J.; KOJOUHAROV, I.; SCHAFFNER, H.; GREBOSZ, J.; BECKER, F.; BEDNARCZYK, P.; CACERES, L.; DOORNENBAL, P.; GEISSEL, H.; KELIC, A.; KURZ, N.; MONTES, F.; PROKOPOWICZ, W.; SAITO, T.; TASHENOV, S.; WERNER-MALENTO, E.; GELLETLY, W.: Experimental details of the Stopped Beam RISING campaign. Eur. Phys. J.-Spec. Top. 150, 2007: 319–320.

PIETRI, S.; REGAN, P. H.; PODOLYAK, Z.; RUDOLPH, D.; GORSKA, M.; JUNGCLAUS, A.; PFUTZNER, M.; GARNSWORTHY, A. B.; STEER, S. J.; CACERES, L.; WERNER-MALENTO, E.; HOISCHEN, R.; GERL, J.; KOJOUHAROV, I.; SCHAFFNER, H.; WOLLERSHEIM, H. J.; BECKER, F.; BEDNARCZYK, P.; DOORNENBAL, P.; GEISSEL, H.; GREBOSZ, J.; KELIC, A.; KURZ, N.; MONTES, F.; PROKOPOWICZ, W.; SAITO, T.; TASHENOV, S.; HEINZ, A.; KURTUKIAN-NIETO, T.; BENZONI, G.; HELLSTROM, M.; ANDERSSON, L. L.; ATANASOVA, L.; BALABANSKI, D. L.; BENTLEY, M. A.; BLANK, B.; BLAZHEV, A.; BRANDAU, C.; BROWN, J. R.; BRUCE, A. M.; CAMERA, F.; CATFORD, W. N.; CULLEN, I. J.; DOMBRADI, Z.; ESTEVEZ, E.; FAHLANDER, C.; GELLETLY, W.; ILIE, G.; JOHANSSON, E. K.; JOLIE, J.; JONES, G. A.; KMIECIK, M.; KONDEV, F. G.; LALKOVSKI, S.; LIU, Z.; MAJ, A.; MYALSKI, S.; SHIZUMA, T.; SIMONS, A. J.; SCHWERTEL, S.; WALKER, P. M.; WIELAND, O.: First results from the stopped beam isomer rising campaign at GSI. Acta physica Polonica B, Particle physics and field theory, nuclear physics, theory of relativity / Acta Phys. Pol. B 38(4), 2007: 1255–1264.

PIETRI, S.; REGAN, P. H.; PODOLYAK, Z.; RUDOLPH, D.; STEER, S.; GARNSWORTHY, A. B.; WERNER-MALENTO, E.; HOISCHEN, R.; GORSKA, M.; GERL, J.; WOLLERSHEIM, H. J.; KOJOUHAROV, I.; SCHAFFNER, H.; BECKER, F.; BEDNARCZYK, P.; CACERES, L.; DOORNENBAL, P.; GEISSEL, H.; GREBOSZ, J.; KELIC, A.; KURZ, N.; MONTES, F.; PROKOPOWICZ, W.; SAITO, T.; TASHENOV, S.; HEINZ, A.; PFUTZNER, M.; KURTUKIAN-NIETO, T.; BENZONI, G.; HELLSTROM, M.; JUNGCLAUS, A.; SIMPSON, J.; ANDERSSON, L. L.; ATANASOVA, L.; BALABANSKI, D.; BENTLEY, M. A.; BLANK, B.; BLAZHEV, A.; BRANDAU, C.; BROWN, J. R.; BRUCE, A. M.; CAMERA, F.; CATFORD, W. N.; CULLEN, I. J.; DOMBRADI, Z.; ESTEVEZ, E.; FAHLANDER, C.; GELLETLY, W.; ILIE, G.; JOHANSSON, E. K.; JOLIE, J.; JONES, G. A.; KMIECIK, M.; KONDEV, F. G.; LALKOVSKI, S.; LIU, Z.; MAJ, A.; MYALSKI, S.; SHIZUMA, T.; SIMONS, A. J.; SCHWERTEL, S.; WALKER, P. M.; WIELAND, O.: Recent results in fragmentation isomer spectroscopy with rising. Nuclear instruments & methods in physics research, Section B, Beam interactions with materials and atoms / Nucl. Instrum. Methods Phys. Res. Sect. B-Beam Interact. Mater. Atoms 261(1-2), 2007: 1079–1083.

PIVOVAROV, Y. L.; GEISSEL, H.; SCHEIDENBERGER, C.: Resonant coherent excitation of relativistic nuclei in aligned crystals: New experimental perspectives at FAIR. Nuclear instruments & methods in physics research, Section B, Beam interactions with materials and atoms / Nucl. Instrum. Methods Phys. Res. Sect. B-Beam Interact. Mater. Atoms 256(1), 2007: 109–113.

PLASS, W. R.; DICKEL, T.; PETRICK, M.; BOUTIN, D.; DI, Z.; FLECKENSTEIN, T.; GEISSEL, H.; JESCH, C.; SCHEIDENBERGER, C.; WANG, Z.: An RF quadrupole-time-of-flight system for isobar-separation and multiplexed low-energy Rare-Isotope Beam experiments. Eur. Phys. J.-Spec. Top. 150, 2007: 367–368.

PODOLYAK, Z.; STEER, S. J.; PIETRI, S.; WERNER-MALENTO, E.; REGAN, P. H.; RUDOLPH, D.; GARNSWORTHY, A. B.; HOISCHEN, R.; GORSKA, M.; GERL, J.; WOLLERSHEIM, H. J.; KURTUKIAN-NIETO, T.; BENZONI, G.; BECKER, F.; BEDNARCZYK, P.; CACERES, L.; DOORNENBAL, P.; GEISSEL, H.; GREBOSZ, J.; KELIC, A.; KOJOUHAROV, I.; KURZ, N.; MONTES, F.; PROKOPOWICZ, W.; SAITO, T.; SCHAFFNER, H.; TASHENOV, S.; HEINZ, A.; PFUTZNER, M.; HELLSTROM, M.; JUNGCLAUS, A.; ANDERSSON, L. L.; ATANASOVA, L.; BALABANSKI, D. L.; BENTLEY, A.; BLANK, B.; BLAZHEV, A.; BRANDAU, C.; BROWN, J.; BRUCE, A. M.; CAMERA, F.; CATFORD, W. N.; CULLEN, I. J.; DOMBRADI, Z.; ESTEVEZ, E.; FAHLANDER, C.; GELLETLY, W.; ILIE, G.; JOHANSSON, E. K.; JOLIE, J.; JONES, G. A.; KMIECIK, M.; KONDEV, F. G.; LALKOVSKI, S.; LIU, Z.; MAJ, A.; MYALSKI, S.; SHIZUMA, T.; SIMONS, A. J.; SCHWERTEL, S.; WALKER, P. M.; WIELAND, O.; BROWN, B. A.: Isomeric decay studies around Pt-204 and Tb-148. Eur. Phys. J.-Spec. Top. 150, 2007: 165–168.

REGAN, P. H.; GARNSWORTHY, A. B.; PIETRI, S.; CACERES, L.; GORSKA, M.; RUDOLPH, D.; PODOLYAK, Z.; STEER, S. J.; HOISCHEN, R.; GERL, J.; WOLLERSHEIM, H. J.; GREBOSZ, J.; SCHAFFNER, H.; PROKOPWICZ, W.; KOJOUHAROV, I.; BECKER, F.; BEDNARCZYK, P.; DOORNENBALL, P.; GEISSEL, H.; GRAWE, H.; KELIC, A.; KURZ, N.; MONTES, F.; SAITO, T.; TASHENOV, S.; WERNER-MALENTO, E.; HEINZ, A.; ATANASOVA, L.; BALABANSKI, D.; BENZONI, G.; BLANK, B.; BLAZHEV, A.; BRANDAU, C.; BRUCE, A. M.; CAMERA, F.; CULLEN, I. J.; ESTEVEZ, M. E.; FAHLANDER, C.; GELLETLY, W.; ILIE, G.; JUNGCLAUS, A.; JOLIE, J.; KURTUKIAN-NIETO, T.; LIU, Z.; KMIECIK, M.; MAJ, A.; MYALSKI, S.; SCHWERTEL, S.; SHIZUMA, T.; SIMONS, A. J.; WALKER, P. M.; WIELAND, O.: Isomer spectroscopy using relativistic projectile fragmentation at the N=Z line for A similar to 80 -¿ 90.. Nuclear physics A, Nuclear and hadronic physics / Nucl. Phys. A 787, 2007: 491C–498C.

ROECKL, E.; MUKHA, I.; BATIST, L.; BLAZHEV, A.; DORING, J.; GRAWE, H.; GRIGORENKOF, L.; HUYSE, M.; JANAS, Z.; KIRCHNER, R.; LA COMMARA, M.; MAZZOCCHI, C.; TABOR, S. L.; VAN DUPPEN, P.: One-proton and two-proton radioactivity of the (21(+)) isomer in 14 Ag. Acta physica Polonica B, Particle physics and field theory, nuclear physics, theory of relativity / Acta Phys. Pol. B 38(4), 2007: 1121–1127.

RUDOLPH, D.; PIETRI, S.; PODOLYAK, Z.; REGAN, P. H.; GARNSWORTHY, A. B.; HOISCHEN, R.; STEER, S. J.; BECKER, F.; BEDNARCZYK, P.; CACERES, L.; DOORNENBAL, P.; GEISSEL, H.; GERL, J.; GORSKA, M.; GREBOSZ, J.; KELIC, A.; KOJOUHAROV, I.; KURZ, N.; MONTES, F.; PROKOPOWICZ, W.; SAITO, T.; SCHAFFNER, H.; TASHENOV, S.; WERNER-MALENTO, E.; WOLLERSHEIM, H. J.; ANDERSSON, L. L.; ATANASOVA, L.; BALABANSKI, D. L.; BENTLEY, M. A.; BENZONI, G.; BLANK, B.; BLAZHEV, A.; BRANDAU, C.; BROWN, J. R.; BRUCE, A. M.; CAMERA, F.; CATFORD, W. N.; CULLEN, I. J.; DOMBRADI, Z.; ESTEVEZ, E.; FAHLANDER, C.; GELLETLY, W.; HEINZ, A.; HELLSTROM, M.; ILIE, G.; JOHANSSON, E. K.; JOLIE, J.; JONES, G. A.; JUNGCLAUS, A.; KMIECIK, M.; KONDEV, F. G.; KURTUKIAN-NIETO, T.; LALKOVSKI, S.; LIU, Z.; MAJ, A.; MYALSKI, S.; PFUTZNER, M.; SHIZUMA, T.; SIMONS, A. J.; SCHWERTEL, S.; WALKER, P. M.; WIELAND, O.: Exciting isomers from the first stopped-beam RISING campaign. Eur. Phys. J.-Spec. Top. 150, 2007: 173–176.

SFIENTI, C.; DE NAPOLI, M.; ADRICH, P.; AUMANN, T.; BACRI, C. O.; BARCZYK, T.; BASSINI, R.; BIANCHIN, S.; BOIANO, C.; BOTVINA, A. S.; BOUDARD, A.; BRZYCHCZYK, J.; CHBIHI, A.; CIBOR, J.; CZECH, B.; DUCRET, J. E.; EMLING, H.; FRANKLAND, J.; HELLSTROM, M.; HENZLOVA, D.; KEZZAR, K.; IMME, G.; IORI, I.; JOHANSSON, H.; LAFRIAKH, A.; LE FèVRE/LE FEVRE, A.; LE GENTIL, E.; LEIFELS, Y.; LYNCH, W. G.; LüHNING/LUHNING, J.; LUKASIK, J.; LYNEN, U.; MAJKA, Z.; MOCKO, M.; MüLLER/MULLER, W. F. J.; MYKULYAK, A.; ORTH, H.; OTTE, A. N.; PALIT, R.; PAWLOWSKI, P.; PULLIA, A.; RACITI, G.; RAPISARDA, E.; SANN, H.; SCHWARZ, C.; SIMON, H.; SüMMERER/SUMMERER,

K.; TRAUTMANN, W.; VOLANT, C.; WALLACE, M.; WEICK, H.; WIECHULA, J.; WIELOCH, A.; ZWIEGLINSKI, B.: Gross properties and isotopic phenomena in spectator fragmentation. Nuclear physics A, Nuclear and hadronic physics / Nucl. Phys. A 787, 2007: 627C–632C.

SIMON, H.; MEISTER, M.; AUMANN, T.; BORGE, M. J. G.; CHULKOV, L. V.; PRAMANIK, U. D.; ELZE, T. W.; EMLING, H.; FORSSEN, C.; GEISSEL, H.; HELLSTROM, M.; JONSON, B.; KRATZ, J.; KULESSA, R.; LEIFELS, Y.; MARKENROTH, K.; MüNZENBERG/MUNZENBERG, G.; NICKEL, F.; NILSSON, T.; NYMAN, G.; RICHTER, A.; RIISAGER, K.; SCHEIDENBERGER, C.; SCHRIEDER, G.; TENGBLAD, O.; ZHUKOV, M. V.: Systematic investigation of the drip-line nuclei Li-11 and Be-14 and their unbound subsystems Li-10 and Be-13. Nuclear physics A, Nuclear and hadronic physics / Nucl. Phys. A 791(3-4), 2007: 267–302.

STEER, S. J.; PODOLYAK, Z.; PIETRI, S.; REGAN, P. H.; RUDOLPH, D.; WERNER-MALENTO, E.; GARNSWORTHY, A. B.; HOISCHEN, R.; GORSKA, M.; GERL, J.; WOLLERSHEIM, H. J.; BECKER, F.; BEDNARCZYK, P.; CACERES, L.; DOORNENBAL, P.; GEISSEL, H.; GREBOSZ, J.; KELIC, A.; KURZ, N.; MONTES, F.; PROKOPOWICZ, W.; SAITO, T.; SCHAFFNER, H.; TACHENOV, S.; HEINZ, A.; PFUETZNER, M.; KURTUKIAN-NIETO, T.; BENZONI, G.; JUNGCLAUS, A.; BALABANSKI, D. L.; BRANDAU, C.; BRUCE, A. M.; CATFORD, W. N.; CULLEN, I. J.; DOMBRADI, Z.; ESTEVEZ, E.; GELLETLY, W.; ILIE, G.; JOLIE, J.; JONES, G. A.; KMIECIK, M.; KONDEV, F. G.; LALKOVSKI, S.; LIU, Z.; MAJ, A.; MYALSKI, S.; SHIZUMA, T.; SCHWERTEL, S.; WALKER, P. M.; WIELAND, O.: Identification of isomeric states śouthóf Pb-208 via projectile fragmentation. Acta physica Polonica B, Particle physics and field theory, nuclear physics, theory of relativity / Acta Phys. Pol. B 38(4), 2007: 1283–1286.

STREICHER, B.; ANTALIC, S.; SARO, S.; VENHART, M.; HEßBERGER/HESSBERGER, F. P.; HOFMANN, S.; ACKERMANN, D.; KINDLER, B.; KOJOUHAROV, I.; LOMMEL, B.; MANN, R.; SULIGNANO, B.; KUUSINIEMI, P.: Alpha-gamma decay studies of (261)Sg. Acta physica Polonica B, Particle physics and field theory, nuclear physics, theory of relativity / Acta Phys. Pol. B 38(4), 2007: 1561–1564.

SULIGNANO, B.; HEINZ, S.; HEßBERGER/HESSBERGER, F. P.; HOFMANN, S.; ACKERMANN, D.; ANTALIC, S.; KINDLER, B.; KOJOUHAROV, I.; KUUSINIEMI, P.; LOMMEL, B.; MANN, R.; NISHIO, K.; POPEKO, A. G.; SARO, S.; STREICHER, B.; VENHART, M.; YEREMIN, A. V.: Identification of a K isomer in No-252. The European physical journal A, Hadrons and nuclei / Eur. Phys. J. A 33(4), 2007: 327–331.

SUN, B.; LITVINOV, Y. A.; WALKER, P. M.; BECKERT, K.; BELLER, P.; BOSCH, F.; BOUTIN, D.; BRANDAU, C.; CHEN, L.; DIMOPOULOU, C.; GEISSEL, H.; KNOBEL, R.; KOZHUNHAROV, C.; KURCEWICZ, J.; LITVINOV, S. A.; MAZZOCCO, M.; MENG, J.; NOCIFORO, C.; NOLDEN, F.; PLASS, W. R.; SCHEIDENBERGER, C.; STECK, M.; WEICK, H.; WINKLER, M.: Discovery of a new long-lived isomeric state in Ce-125. The European physical journal A, Hadrons and nuclei / Eur. Phys. J. A 31(3), 2007: 393–394.

TRAUTMANN, W.; BASSINI, R.; BEGEMANN-BLAICH, M.; FERRERO, A.; FRITZ, S.; GAFFEJAKOV, S. J.; GROSS, C.; IMMEE, G.; IORI, I.; KLEINEVOSS, U.; KUNDE, G. J.; KUNZE, W. D.; LE FèVRE/LE FEVRE, A.; LINDENSTRUTH, V.; LUKASIK, J.; LYNEN, U.; MADDALENA, V.; MAHI, M.; MOHLENKAMP, T.; MORONI, A.; MüLLER/MULLER, W. F. J.; NOCIFORO, C.; OCKER, B.; ODEH, T.; ORTH, H.; PETRUZZELLI, F.; POCHODZALLA, J.; RACITI, G.; RICCOBENE, G.; ROMANO, F. P.; RUBEHN, T.; SAIJA, A.; SANN, H.; SCHNITTKER, M.; SCHUETTAUF, A.; SCHWARZ, C.; SEIDEL, W.; SERFLING, V.; SFIENTI, C.; TRZCINSKI, A.; TUCHOLSKI, A.; VERDE, G.; WORNER, A.; XI, H. F.; ZWIEGLINSKI, B.: Thermal and chemical freeze-out in spectator fragmentation. Physical review C, Nuclear physics / Phys. Rev. C 76(6), 2007: 064606, 13 pages.

WINKLER, M.; ACHENBACH, B.; BEHR, K. H.; BERZ, M.; BOUTIN, D.; BRANDAU, C.; EMLING, H.; GEISSEL, H.; IWASE, H.; KARAGIANNIS, C.; KELIC, A.; LEIBROCK, H.; LITVINOV, Y.; MANIKONDA, S.; MARUHN, J. A.; MORITZ, G.; MüHLE/MUHLE, C.; MüNZENBERG/MUNZENBERG, G.; NOCIFORO, C.; PLASS, W.; SCHEIDENBERGER, C.; SIMON, H.; SüMMERER/SUMMERER, K.; SVEDENTSOV, M.; TAHIR, N. A.; TAUSCHWITZ, A.; WANG, Z.; WEICK, H.; WOLLNIK, H.; YAVOR, M.: The status of the Super-FRS at FAIR. Eur. Phys. J.-Spec. Top. 150, 2007: 263–264.

YAMAGUCHI, T.; SUZUKI, T.; OHNISHI, T.; SüMMERER/SUMMERER, K.; BECKER, F.; FUKUDA, M.; GEISSEL, H.; HOSOI, M.; JANIK, R.; KIMURA, K.; MANDAL, S.; MüNZENBERG/MUNZENBERG, G.; NAKAJIMA, S.; OHTSUBO, T.; OZAWA, A.; PROCHAZKA, A.; SHINDO, M.; SITAR, B.; STRMEN, P.; SUDA, T.; SUGAWARA, K.; SZARKA, I.; TAKI-SAWA, A.; TAKECHI, M.; TANAKA, K.: Nuclear radius systematics of Kr isotopes studied via their interaction cross-sections at relativistic energies. Eur. Phys. J.-Spec. Top. 150, 2007: 197–200.

Academic Works

T. BECK
Entwicklung einer schnellen Pulsformanalyse für asymmetrische AGATA-Germanium-Detektoren (Diss).
Univ. Frankfurt (Germany), 15.7.2007.

P. DOORNENBAL
In-beam γ-ray spectroscopy of two-step fragmentation reactions at relativistic energies – The case of ^{36}Ca (Diss.).
Univ. Köln (Germany), 23.10.2007.

T. FLECKENSTEIN
Influence of Mass Uncertainties of Exotic Nuclei on the p- and nup-Process Model (Diplom).
Univ. Gießen (Germany)

KUZMINCHUK
Study of charge-state distribution and slowing-down of 40-200 MeV/u heavy ions in solids".

Public Talks

B. FABIAN
Characterization and Optimization of a Time-of-Flight Detector for Isochrononous Mass Spectrometry at FRS-ESR
Frühjahrstagung der Deutschen Physikalischen Gesellschaft, Gießen, March 12 – 16, 2007.

L. CACERES
Isomeric Spectroscopy in the N=Z=41 nucleus 82Nb
Frühjahrstagung der Deutschen Physikalischen Gesellschaft, Gießen, March 14, 2007.

L. CHEN ET AL.
Schottky Mass and Half-life Measurements of Neutron-rich Nuclides
Frühjahrstagung der Deutschen Physikalischen Gesellschaft, Gießen, March 12 – 16, 2007.

T. DICKEL ET AL.
Isobaric Separation by a Multiple-Reflection Time-of-Flight Mass Spectrometer
Frühjahrstagung der Deutschen Physikalischen Gesellschaft, Gießen, March 12 – 16, 2007.

J. GERL
Nuclear Structure Results with RISING at GSI and the Future Plans for NUSTAR at FAIR
BARC Mumbay (India), Seminar, 17.4.2007

J. GERL
Gamma-Spectroscopy with RISING
Univ. Bogota (Colombia), Seminar, 11.12.2007

H. GEISSEL
A Versatile High-Resolution Magnetic Spectrometer for Energy Compression and Reaction Studies at the Low-Energy Branch of the Super-FRS
EMIS Conference, Deauville, France, June 2007

H. GEISSEL
Nuclear Decay Measurements of Bare and Few-electron Atoms with the FRS-ESR Facility at High Energies Reveal Novel Properties, FINUSTAR Conference, Crete, September 2007

H. GEISSEL
Precision experiments with relativistic exotic nuclei at GSI
Japanese-German Workshop on Nuclear Structure and Astro-physics, September 2007

H. GEISSEL
Experiments with exotic nuclei at the FRS facility
Seminar at the University Jyväskylä, December 2007

H. GEISSEL
Experiments with Stored Exotic Nuclei (GSI)
VISTAR Workshop, Rußdorf, Österreich, March 2007

M. GORSKA
Structure investigation within RISING
Invited talk Nuclear Physics division, Warsaw University, 03.01.2007

M. GORSKA
"From RISING to HISPEC/DESPEC"
Invited talk Jyvaskyla Users meeting, 01.03.2007

M. GORSKA
"RISING: Rare Isotope Spectroscopic Investigation at GSI"
Frühjahrstagung der Deutschen Physikalischen Gesellschaft, Gießen, Plenary talk, 16.03.2007

M. GORSKA
"Seniority isomers in exotic nuclei"
Surrey Minischool on exotic Nuclei, Invited Lecture, 03.04.2007

M. GORSKA
"Rising stopped beam campaign: results and future plans"
Glasgow University, Invited talk, 08.06.2007

M. GORSKA
"Shell gap below 132Sn based on excited states
in 130Cd and 131In"
ISPUN 2007 Hoi-An, Vietnam, 03.07.2007

M. GORSKA
"Nuclear structure results from the RISING campaign 2006-2007"
Japanese-German Workshop on Nuclear Structure and Astrophysics, Chiemsee, 01.10.2007

O. KLEPPER
Fast Heavy Ions as a Microscope for the Structure of Matter and as Tools in Medicine and Technology
IMP Lanzhou, China, May 2007.

N.A. KUZMINCHUK
Approximate formulae for the mean charge calculation of Ni, Xe, U heavy ions in Be, C, Al, Cu, Ag, Au targets within the energy of 40-200 MeV/u
XXXVII International Conference of charged particles interaction with crystals, Moscou, MSU, 29-31 may, 2007.
Co authors: N.A. Kuzminchuk, Y.L.Pivovarov, C.Scheidenberger, H.Geissel, H.Weick, R.Knoebel, M.Maier.

Approximate formulae for the equilibrium mean charge calculation of Ni, Xe, U heavy ions in Be, C, Al, Cu, Ag, Au targets within the energy of 40-200 MeV/u

IV International conference of students and young researches “Perspectives of fundamental science development”, Tomsk, 15-18 May 2007.

I. KOJOUHAROV
The GSI HPGe Detector Scanner – a sophisticated Device based on PET Technique
IEEE Nuclear science Symposium, Honolulu, USA, October 27-November 2, 2007

I. KOJOUHAROV
GeLab at GSI,
I.Kojouharov, T.Engert, J.Gerl, GammaNet Meeting, Padova, 10-11 May, 2007

Y. LITVINOV
Mass Measurements and Decay Studies in the ESR
ISOLDE Scientific Seminar at CERN
CERN, Geneva, Switzerland, 11 October2007

Y. LITVINOV
Decay Studies with Highly-Charged Ions
3rd Japanese-German EFES(JSPS)-DFG/GSI workshop on Nuclear Structure and Astrophysics
Abtei Frauenwörth im Chiemsee, Germany, September 29 - October 2 2007

Y. LITVINOV
Advanced Atomic Mass Evaluation
Joint EURISOL-EURONS Town Meeting
Helsinki, Finland, Spetember 17-19 2007

Y. LITVINOV
Nuclear Properties far off Stability from Broad-Band Mass and Lifetime Measurements in a Storage Ring (plenary)
International Nuclear Physics Conference INPC 2007
Tokyo, Japan, June 3 – 8 2007

Y. LITVINOV
Beta-decay studies with highly-charged exotic nuclei in the storage ring ESR
International Nuclear Physics Conference INPC 2007
Tokyo, Japan, June 3 – 8 2007

Y. LITVINOV
Advanced Atomic Mass Evaluation (report)
17th Meeting of the Nuclear Structure and decay Data (NSDD) Network
Petersburg Nuclear Physics Institute, St. Petersburg, Russia, June 11-15 2007

Y. LITVINOV
Nuclear Physics in Storage Rings (invited)
38 Arbeitstreffen der Verbundforschung Kernphysik
Schleching, Germany, February 22 – March 02 2007

G. MÜNZENBERG
Ion optics II
ITS LEIF Summer School "Low-energy ion beam techniques", Crete, Greece, May 1st-2nd, 2007,

M. PETRICK ET AL.
Online Test of the Ion Catcher at the FRS at GSI
15th International Conference on Electromagnetic Isotope Separators and Techniques Related to their Applications, Deauville, France, June 24 – 29, 2007.

W.R. PLASS
Direct Mass Measurements of Neutron-deficient Nuclei and their Application to rp- and np-Process Nucleosynthesis
3rd Japanese-German Workshop on Nuclear Structure and Astrophysics, Frauenwörth im Chiemsee, September 29 - October 2, 2007.

W.R. PLASS ET AL.
Multireflektions-Flugzeitmassenspektrometrie, Hauptvortrag,

Spring meeting of the Deutsche Physikalische Gesellschaft, March 19 – 23, 2007.

W.R. PLASS
Physikalisches Kolloquium, Experimente mit gespeicherten Ionen: Grundzustandseigenschaften exotischer Kerne
Ernst-Moritz-Arndt Universität-Greifswald, January 25, 2007.

W.R. PLASS ET AL.
The Low-Energy Branch of the Super-FRS - High-Resolution Spectrometer for Energy Compression and Reaction Studies
15th International Conference on Electromagnetic Isotope Separators and Techniques Related to their Applications, Deauville, France, June 24 – 29, 2007.

W.R. PLASS ET AL.
Isobar Separation by Time-of-Flight Mass Spectrometry
15th International Conference on Electromagnetic Isotope Separators and Techniques Related to their Applications, Deauville, France, June 24 – 29, 2007.

W.R. PLASS ET AL.
A Multiple-Reflection Time-of-Flight Isobar Separator
55th ASMS Conference on Mass Spectrometry and Allied Topics, Indianapolis, IN, USA, June 3 – June 7, 2007.

C. SCHEIDENBERGER
What comes after EURONS?
NUSTAR Annual Meeting 2007, GSI

C. SCHEIDENBERGER
Hallo ist da jemand? Die Entdeckung von extrasolaren Planeten und die Suche nach Leben
Öffentlicher Abendvortrag
VISTARS-07, Russbach (Österreich), 4.-10. März 2007

C. SCHEIDENBERGER
Precision mass measurements of exotic nuclei
Experiment – Theory Intersections in Modern Nuclear Struture
International Workshop at ECT*, Trento (Italy), 23.-27. April 2007

C. SCHEIDENBERGER
Probing exotic nuclei by isochronous and time-resolved Schottky mass spectrometry at FRS-ESR
XXX Mazurian Lakes Conference on Physics: Nuclear Physics and the Fundamental Processes, Piaski (Poland), 2.-9. September 2007

M. WINKLER
Status of the Super-FRS
Annual NuSTAR Meeting, GSI, 21.3.2007

M. WINKLER
The Status of the Super-FRS in-flight Facility at FAIR
EMIS 2007 (15th Int. Conf. on Electromagnetic Isotope Separators), Deauville (Fr), 28.6.2007

M. WINKLER
Super-FRS
FAIR Monthly, GSI (D), 24.7.2007

Vorlesungen

WS 2006/2007

DÜREN, EHRENFRIED, GEISSEL, KOTULLA, KÜHN, LANGE, METAG, NOVOTNY, PLASS, SCHEIDENBERGER, STENZEL
Seminar zu aktuellen Fragestellungen der Hadronen- und Kernphysik, Universität Giessen
ab 7. Semester, 2-stündig, Freitags 14-16 Uhr

GEISSEL, PLASS, SCHEIDENBERGER
Physik exotischer Kerne, Universität Giessen
Seminar, 2 Std. nach Vereinbarung, ab 5. Semester

H. GEISSEL, W. PLASS, C. SCHEIDENBERGER
Grundlagen der Ionenoptik und Massenspektrometrie
Vorlesung, Universität Giessen
2 Std. nach Vereinbarung, ab 5. Semester

SS 2007

H. GEISSEL, W. PLASS, C. SCHEIDENBERGER
Physik exotischer Kerne, Universität Giessen
Vorlesung, 2 Std. nach Vereinbarung, ab 5. Semester

H. GEISSEL, C. SCHEIDENBERGER
Aktuelle Fragestellungen der Schwerionenphysik, Universität Giessen
Seminar, 2 Std. nach Vereinbarung, ab 7. Semester

C. SCHEIDENBERGER
Nuclear structure and nuclear astrophysics
International Summer Student Program 2007 at GSI
Darmstadt (Germany), 15. and 16. August 2007

H. WEICK
Remote-Handling Systems of the In-Flight Fragment Separators FRS at GSI and Super-FRS at FAIR
3rd High-Power Targetry Workshop, September 10-14, 2007, Bad Zurzach, Switzerland

WS 2007/2008

H. GEISSEL, W. PLASS, C. SCHEIDENBERGER
Physik mit schweren Ionen, Universität Giessen
Vorlesung, 2 Std. nach Vereinbarung, ab 5. Semester

DÜREN, EHRENFRIED, GEISSEL, KOTULLA, KÜHN, LANGE, METAG, NOVOTNY, PLASS, SCHEIDENBERGER, STENZEL
Physik an neuen Beschleunigeranlagen, Universität Giessen
Seminar, 2 Std. nach Vereinbarung, ab 7. Semester

Research Division: FOPI

Leader: Y. Leifels
Compiled by: Y. Leifels

Publications

PROGRAMME HADRONS & NUCLEI

1. WoS listed publications

M. Merschmeyer, X. Lopez, N. Bastid, P. Crochet, N. Herrmann et al., FOPI Collaboration: K^0 and Λ Production in Ni+Ni collisions. Phys. Rev. C 76 (2007) 024906 (Open Access)

X. Lopez, N. Herrmann, P. Crochet and the FOPI Collaboration. First sub-threshold measurement of Σ (1385) production in Al+Al collisions at 1.9A GeV. Phys. Rev. C 76 (2007) 052203

X. Lopez and the FOPI collaboration: Isospin dependence of relative yields of K^+ and K^0 mesons at 1.528 AGeV. Phys. Rev. C 75 (2007) 011901

W. Reisdorf and the FOPI collaboration: Systematics of pion emission in heavy ion collisions in the 1A GeV regime. Nucl. Phys. A 781 (2007) 459

2. Other publications

M. Ciobanu et al.: Front-End Electronics Card Comprising a High Gain/High Bandwidth Amplifier and a Fast Discriminator for Time-of-Flight Measurements, Nuclear Science, IEEE Transactions on Volume 54, Issue 4, Part 3, Aug. 2007 Page(s):1201 – 1206.Digital Object Identifier 10.1109/TNS.2007.903186

V.Ammosov, M.Ciobanu et al.: RPC with low-resistive silicate glass electrodes exposed to an intense continuous electron beam at ELBE. Nucl.Instrum.Meth A576 (2007), 331-336

X. Lopez for the FOPI Collaboration: Strangeness production at SIS energies measured with the FOPI detector.Ricera Scientifica ed Educazione Permanente Supplemento 127 (2007) 109

Academic Works

M. L. BENABDERRAHMANE: Titel der Dissertation:. Measurement of K^0 Inclusive Cross Section in Pion-Induced Reactions at 1.15 GeV/c. Univ. Heidelberg (Germany), 18.4.2007

P. VELTEN, Title of the Master thesis: Etude du méson vecteur K(892) dans les collisions Ni + Ni à 1.93 AGeV. IPHC Strasbourg,, June 2007

Y. LEIFELS, Übungsgruppe Physik II, Sommersemester 2007, Univ. Heidelberg

Y. LEIFELS, Übungsgruppe Physik III, Sommersemester 2007/08, Univ. Heidelberg

Public Talks

X. Lopez for the FOPI Collaboration: Heavy ion collisions at SIS energies. Subatech Nantes, France, February 15th, 2007

X. Lopez for the FOPI Collaboration: Heavy ion collisions at SIS energies. IPHC Strasbourg, France, February 9th, 2007

X. Lopez for the FOPI Collaboration: Strangeness production at SIS energies. XLV Conference of the German Physical Society, March 12-16, 2007 (Giessen, Germany)

X. Lopez for the FOPI Collaboration: Heavy ion collisions at SIS energies. IPN Lyon seminar, France, April 6th, 2007

X. Lopez for the FOPI Collaboration: Heavy ion collisions at SIS energies. LPC Clermont-Ferrand seminar, France, April 20th, 2007

X. Lopez for the FOPI Collaboration: Strangeness production at SIS energies. SQM 2007 International Conference on Strangeness in Quark Matter, June 24-29, 2007 (Levoca, Slovakia)

N. Herrmann for the FOPI Collaboration: Strange Hadrons in Dense Baryonic Matter. BARYONS07 International Conference, June 11-15, 2007 (Seoul, Korea

N. Herrmann for the FOPI Collaboration: Strangeness production at SIS energies. CPOD 2007 International Workshop Critical point and the onset of deconfinement, July 9-13,2007 (Darmstadt)

T.I. Kang for the FOPI Collaboration: Time-of-Flight Upgrade with Multi-strip Multi-gap Resistive Plate

Chambers for FOPI Detector. BARYONS07 International Conference, June 11-15, 2007 (Seoul, Korea)

Y.J. Kim for the FOPI Collaboration: Charged Kaon Flow Measurements with FOPI at SIS. Conference of the German Physical Society, March 12-16, 2007 (Gießen, Germany)

M. Kis for the FOPI Collaboration: Upgrade of the FOPI TOF Barrel with MMRPCs. Conference of the German Physical Society, March 12-16, 2007 (Gießen, Germany)

W. Reisdorf: Systematic approach from heavy ion collision observables to the high density Equation of State. IWM 2007, International Workshop on Multifragmentation

Research Division: HADES

Leader: J. Stroth
Compiled by: R. Holzmann

Publications

PROGRAMME HADRONS & NUCLEI

1. WoS listed publications

Agakishiev, G.; Alves, R.; Balanda, A.; Bassini, R.; Bellia, G.; Belver, D.; Belyaev, A.; Blanco, A.; Böhmer, M.; Boiano, C.; Boyard, J. L.; Braun-Munzinger, P.; Cabanelas, P.; Capela, C.; Carolino, N.; Castro, E.; Cavinato, M.; Chernenko, S.; Christ, T.; Destefanis, M.; Díaz, J.; Dohrmann, F.; Dybczak, A.; Eberl, T.; Enghardt, W.; Fateev, O.; Ferreira-Marques, R.; Finocchiaro, P.; Fonte, P.; Friese, J.; Fröhlich, I.; Galatyuk, T.; Garzón, J. A.; Gernhäuser, R.; Gil, A.; Gilardi, C.; Golubeva, M.; González-Díaz, D.; Grosse, E.; Guber, F.; Heidel, K.; Heilmann, M.; Heinz, T.; Hennino, T.; Holzmann, R.; Hutsch, J.; Ierusalimov, A.; Iori, I.; Ivashkin, A.; Jurkovic, M.; Kämpfer, B.; Kajetanowicz, M.; Karavicheva, T.; Kirschner, D.; Koenig, I.; Koenig, W.; Kolb, B. W.; Kotte, R.; Kozuch, A.; Krizek, F.; Krücken, R.; Kühn, W.; Kugler, A.; Kurepin, A. Lang, S.; Lange, J. S.; Lapidus, K.; Lopes, L.; Lorenz, M.; Maier, L.; Mangiarotti, A. Markert, J.; Metag, V.; Micel, J.; Michalska, B.; Morinière, E.; Mousa, J.; Müntz, C.; Naumann, L.; Neves, C.; Novotny, R.; Otwinowski, J.; Pachmayer, Y. C.; Palka, M.; Parpottas, Y.; Pechenov, V.; Pechenova, O.; Pereira, A.; Pérez Cavalcanti, T.; Pietraszko, J.; Przygoda, W.; Rabin, N.; Ramstein, B.; Razin, S.; Reshetin, A.; Riboldi, S.; Rosier, P.; Rustamov, A.; Sadovsky, A.; Sailer, B.; Salabura, P.; Schmah, A.; Schwab, E.; Silva, J.; Smolyankin, V.; Sobiella, M.; Sobolev, Yu.G.; Solovieva, T.; Sousa, C.; Spataro, S.; Spruck, B.; Ströbele, H.; Stroth, J.; Sturm, C.; Sudol, M.; Tarantola, A.; Teilab, K.; Tiflov, V.; Tlusty, P.; Traxler, M.; Trebacz, R.; Troyan, A.; Tsertos, H.; Usenko, E.; Veretenkin, I.; Vieira, M.; Visotski, S.; Wagner, V.; Weber, M.; Wisniowski, M.; Wüstenfeld, J.; Yurevich, S.; Zanevsky, Y.; Zhou, P.; Zumbruch, P.; HADES Collaboration: **Dielectron production in ^{12}C + ^{12}C collisions at 2A GeV with the HADES spectrometer.** Phys. Rev. Lett.. 98 (2007) 052302.

Pietraszko, J; Agakishiev, G.; Alves, R.; Balanda, A.; Bassini, R.; Bellia, G.; Belver, D.; Belyaev, A.; Blanco, A.; Böhmer, M.; Boiano, C.; Boyard, J. L.; Braun-Munzinger, P.; Cabanelas, P.; Capela, C.; Carolino, N.; Castro, E.; Cavinato, M.; Chernenko, S.; Christ, T.; Destefanis, M.; Díaz, J.; Dohrmann, F.; Dybczak, A.; Eberl, T.; Enghardt, W.; Fateev, O.; Ferreira-Marques, R.; Finocchiaro, P.; Fonte, P.; Friese, J.; Fröhlich, I.; Galatyuk, T.; Garzón, J. A.; Gernhäuser, R.; Gil, A.; Gilardi, C.; Golubeva, M.; González-Díaz, D.; Grosse, E.; Guber, F.; Heidel, K.; Heilmann, M.; Heinz, T.; Hennino, T.; Holzmann, R.; Hutsch, J.; Ierusalimov, A.; Iori, I.; Ivashkin, A.; Jurkovic, M.; Kämpfer, B.; Kajetanowicz, M.; Karavicheva, T.; Kirschner, D.; Koenig, I.; Koenig, W.; Kolb, B. W.; Kotte, R.; Kozuch, A.; Krizek, F.; Krücken, R.; Kühn, W.; Kugler, A.; Kurepin, A. Lang, S.; Lange, J. S.; Lapidus, K.; Lopes, L.; Lorenz, M.; Maier, L.; Mangiarotti, A. Markert, J.; Metag, V.; Micel, J.; Michalska, B.; Morinière, E.; Mousa, J.; Müntz, C.; Naumann, L.; Neves, C.; Novotny, R.; Otwinowski, J.; Pachmayer, Y. C.; Palka, M.; Parpottas, Y.; Pechenov, V.; Pechenova, O.; Pereira, A.; Pérez Cavalcanti, T.; Przygoda, W.; Rabin, N.; Ramstein, B.; Razin, S.; Reshetin, A.; Riboldi, S.; Rosier, P.; Rustamov, A.; Sadovsky, A.; Sailer, B.; Salabura, P.; Schmah, A.; Schwab, E.; Silva, J.; Smolyankin, V.; Sobiella, M.; Sobolev, Yu.G.; Solovieva, T.; Sousa, C.; Spataro, S.; Spruck, B.; Ströbele, H.; Stroth, J.; Sturm, C.; Sudol, M.; Tarantola, A.; Teilab, K.; Tiflov, V.; Tlusty, P.; Traxler, M.; Trebacz, R.; Troyan, A.; Tsertos, H.; Usenko, E.; Veretenkin, I.; Vieira, M.; Visotski, S.; Wagner, V.; Weber, M.; Wisniowski, M.; Wüstenfeld, J.; Yurevich, S.; Zanevsky, Y. Zhou, P.; Zumbruch, P.; HADES Collaboration: **Dielectron production in C + C and p + p collisions with HADES.** Int. J. Mod. Phys. A22 (2007) 388 – 396.

Markert, J.; Agakishiev, G.; Alves, R.; Balanda, A.; Bassini, R.; Bellia, G.; Belver, D.; Belyaev, A.; Blanco, A.; Böhmer, M.; Boiano, C.; Boyard, J. L.; Braun-Munzinger, P.; Cabanelas, P.; Capela, C.; Carolino, N.; Castro, E.; Cavinato, M.; Chernenko, S.; Christ, T.; Destefanis, M.; Díaz, J.; Dohrmann, F.; Dybczak, A.; Eberl, T.; Enghardt, W.; Fateev, O.; Ferreira-Marques, R.; Finocchiaro, P.; Fonte, P.; Friese, J.; Fröhlich, I.; Galatyuk, T.; Garzón, J. A.; Gernhäuser, R.; Gil, A.; Gilardi, C.; Golubeva, M.; González-Díaz, D.; Grosse, E.; Guber, F.; Heidel, K.; Heilmann, M.; Heinz, T.; Hennino, T.; Holzmann, R.; Hutsch, J.; Ierusalimov, A.; Iori, I.; Ivashkin, A.; Jurkovic, M.; Kämpfer, B.; Kajetanowicz, M.; Karavicheva, T.; Kirschner, D.; Koenig, I.; Koenig, W.; Kolb, B. W.; Kotte, R.; Kozuch, A.; Krizek, F.; Krücken, R.; Kühn, W.; Kugler, A.; Kurepin, A. Lang, S.; Lange, J. S.; Lapidus, K.; Lopes, L.; Lorenz, M.; Maier, L.; Mangiarotti, J.; Metag, V.; Micel, J.; Michalska, B.; Morinière, E.; Mousa, J.; Müntz, C.; Naumann, L.; Neves, C.; Novotny, R.; Otwinowski, J.; Pachmayer, Y. C.; Palka, M.; Parpottas, Y.; Pechenov, V.; Pechenova, O.; Pereira, A.; Pérez Cavalcanti, T.; Przygoda, W.; Rabin, N.; Ramstein, B.; Razin, S.; Reshetin, A.; Riboldi, S.; Rosier, P.; Rustamov, A.; Sadovsky, A.; Sailer, B.; Salabura, P.; Schmah, A.; Schwab, E.; Silva, J.; Smolyankin, V.; Sobiella, M.; Sobolev, Yu.G.; Solovieva, T.; Sousa, C.; Spataro, S.; Spruck, B.; Ströbele, H.; Stroth, J.; Sturm, C.; Sudol, M.; Tarantola, A.; Teilab, K.; Tiflov, V.;

Tlusty, P.; Traxler, M.; Trebacz, R.; Troyan, A.; Tsertos, H.; Usenko, E.; Veretenkin, I.; Vieira, M.; Visotski, S.; Wagner, V.; Weber, M.; Wisniowski, M.; Wüstenfeld, J.; Yurevich, S.; Zanevsky, Y. Zhou, P.; Zumbruch, P.;HADES Collaboration: **Dielectron production in ^{12}C+^{12}C collisions at 2A GeV with HADES.** J. Phys. G – Nucl. Part. Phys. 34 (2007) S1041 – S1045.

Fröhlich, I.; Agakishiev, G.; Alves, R.; Balanda, A.; Bassini, R.; Bellia, G.; Belver, D.; Belyaev, A.; Blanco, A.; Böhmer, M.; Boiano, C.; Boyard, J. L.; Braun-Munzinger, P.; Cabanelas, P.; Capela, C.; Carolino, N.; Castro, E.; Cavinato, M.; Chernenko, S.; Christ, T.; Destefanis, M.; Díaz, J.; Dohrmann, F.; Dybczak, A.; Eberl, T.; Enghardt, W.; Fateev, O.; Ferreira-Marques, R.; Finocchiaro, P.; Fonte, P.; Friese, J.; Galatyuk, T.; Garzón, J. A.; Gernhäuser, R.; Gil, A.; Gilardi, C.; Golubeva, M.; González-Díaz, D.; Grosse, E.; Guber, F.; Heidel, K.; Heilmann, M.; Heinz, T.; Hennino, T.; Holzmann, R.; Hutsch, J.; Ierusalimov, A.; Iori, I.; Ivashkin, A.; Jurkovic, M.; Kämpfer, B.; Kajetanowicz, M.; Karavicheva, T.; Kirschner, D.; Koenig, I.; Koenig, W.; Kolb, B. W.; Kotte, R.; Kozuch, A.; Krizek, F.; Krücken, R.; Kühn, W.; Kugler, A.; Kurepin, A. Lang, S.; Lange, J. S.; Lapidus, K.; Lopes, L.; Lorenz, M.; Maier, L.; Mangiarotti, A. Markert, J.; Metag, V.; Micel, J.; Michalska, B.; Morinière, E.; Mousa, J.; Müntz, C.; Naumann, L.; Neves, C.; Novotny, R.; Otwinowski, J.; Pachmayer, Y. C.; Palka, M.; Parpottas, Y.; Pechenov, V.; Pechenova, O.; Pereira, A.; Pérez Cavalcanti, T.; Przygoda, W.; Rabin, N.; Ramstein, B.; Razin, S.; Reshetin, A.; Riboldi, S.; Rosier, P.; Rustamov, A.; Sadovsky, A.; Sailer, B.; Salabura, P.; Schmah, A.; Schwab, E.; Silva, J.; Smolyankin, V.; Sobiella, M.; Sobolev, Yu.G.; Solovieva, T.; Sousa, C.; Spataro, S.; Spruck, B.; Ströbele, H.; Stroth, J.; Sturm, C.; Sudol, M.; Tarantola, A.; Teilab, K.; Tiflov, V.; Tlusty, P.; Traxler, M.; Trebacz, R.; Troyan, A.; Tsertos, H.; Usenko, E.; Veretenkin, I.; Vieira, M.; Visotski, S.; Wagner, V.; Weber, M.; Wisniowski, M.; Wüstenfeld, J.; Yurevich, S.; Zanevsky, Y. Zhou, P.; Zumbruch, P.;HADES Collaboration: **Dilepton production in pp and CC collisions with HADES.** Eur. Phys. J. A31 (2007) 831 – 835.

2. Other publications

Przygoda, W. for the HADES Collaboration:
Dielectron production in C+C collisions at 2A GeV with HADES. Nucl. Phys. **A783** (2007) 583c.

Spataro, S. for the HADES Collaboration:
Eta-meson reconstruction in pp reactions at 2.2 GeV with HADES. Int. J. Mod. Phys. **A** 22 (2007) 533.

Christ, T. for the HADES Collaboration:
Dielectron production in C+C at 1A GeV with HADES Int. J. Mod. Phys. **A** 22 (2007) 600.

Eberl, T. for the HADES Collaboration:
Dielectron production in C + C and p + p collisions with HADES. Eur. Phys. J. **C 49** (2007) 261.

ACADEMIC WORKS

Sudol, Malgorzata: **Measurement of low-mass e+e- production in 2 AGeV C-C collisions with HADES.**
Dissertation: J. W. Goethe Univ. Frankfurt/Main (Germany).

Teilab, Khaled: **A new method for the time calibration of the HADES drift chambers.**
Diplom: J. W. Goethe Univ. Frankfurt/Main (Germany).

Tarantola, Attilio: **Development of a system to investigate radiation effects on FPGA devices.**
Master: Univ. Milano (Italy).

Kanaki, Kalliopi; **Study of Lambda hyperon production in C+C collisions at 2 AGeV beam energy with the HADES spectrometer.**
Dissertation: TU Dresden (Germany).

Sadovsky, Alexandre; **Investigation of K+ meson production in C+C collisions at 2 AGeV with HADES.**
Dissertation: TU Dresden (Germany).

Christ, Tassilo; **Identifikation und Analyse von e+e- Paaren in C+C bei 1 AGeV.**
Dissertation: TU München (Germany).

Wójcik, Tomasz; **Investigation of π^0 and η production through dielectron decays in C+C collisions at 2 AGeV with HADES.**
Dissertation: Jagellonian Univ. Cracow (Poland).

LECTURES

Stroth, J.; J. W. Goethe Univ. Frankfurt/Main (Germany)

Salabura, P.; Jagellonian Univ. Cracow (Poland)

Salabura, P.; at H-QM Helmholtz Research School , September 16 – 24, 2007, Kleinwalsertal (Germany)

INVITED TALKS

Holzmann, R.; **Physics with HADES at GSI.** XLV International Winter Meeting on Nuclear Physics, Bormio (Italy), January 15 – 20, 2007.

Salabura, P.; Recent results from HADES.
ECT* workshop on electromagnetic probes, Trento (Italy), June 18 – 24, 2007.

Salabura, P.; **Dielectron production in heavy-ion collisions.**
XXX Mazurian Lakes Conference on Physics, Piaski (Poland), September 2 – 9, 2007.

Research Division: Materials Research

Leader: Reinhard Neumann
Compiled by: Reinhard Neumann

PROGRAMME PNI

1. WoS listed publications

Healy K., Schiedt B., Morrison A.
Solid-state nanopore technologies for nanopore-based DNA analysis
Nanomedicine **2** (2007) 875-897

Enculescu I, Toimil-Molares ME, Zet C, Daub M, Westerburg L, Neumann R, Spohr R
Current perpendicular to plane single-nanowire GMR sensor
Journal of Applied Physics A **86** (2007) 43–48

Haran H, Barak J, David D, Refaeli N, Fischer BE, Voss K-O, Du G, Heiss M
Mapping of single event burnout in power MOSFETs
IEEE Transactions on Nuclear Science **54** (2007) 2488–2494

Cornelius TW, Apel PYu, Schiedt B, Trautmann C, Toimil-Molares ME, Karim S, Neumann R
Investigation of nanopore evolution in ion track-etched polycarbonate membranes
Nuclear Instruments & Methods in Physics Research, Sect. B **265** (2007) 553–557

Man LCT, Apel P, Cheung T, Westerberg L, Yu KN, Zet C, Spohr R
Influence of a surfactant on single ion track etching: Preparing and manipulating cylindrical micro wires
Nuclear Instruments & Methods in Physics Research, Sect. B **265** (2007) 621–625

Fischer BE, Heiß, M
A facility to mass-produce ordered single-hit patterns in continuous 35 mm films
Nuclear Instruments & Methods in Physics Research, Sect. B **260** (2007) 442-444

Lemell C, El-Said AS, Meissl W, Gebeshuber IC, Trautmann C, Toulemonde M, Burgdörfer J, Aumayr F
On the nano-hillock formation induced by slow highly charged ions on insulator surfaces
Solid-State Electronics **51** (2007) 1398–1404

Lushchik A, Lushchik Ch, Schwartz K, Vasil'chenko E, Papaleo R, Sorokin M, Volkov AE, Neumann R, Trautmann C
Creation of nanosize defects in LiF crystals under 5-and 10-MeV Au ion irradiation at room temperature
Physical Review *B* **76** (2007) 054114

Cervera J, Alcaraz A, Schiedt B, Neumann R, Ramírez P
Asymmetric selectivity of synthetic conical nanopores probed by reversal potential measurements
Journal of Physical Chemistry C **111** (2007) 12265-12273

Karim S, Toimil-Molares ME, Ensinger W, Balogh AG, Cornelius TW, Khan EU, Neumann R
Influence of crystallinity on the Rayleigh instability of gold nanowires
Journal of Physics D-Applied Physics **40** (2007) 3767–3770

Sattonnay G, Lahrichi M, Benyagoub A, Costantini JM, Garrido F, Thomé L, Trautmann C
Structural modifications induced by swift heavy ions in cubic stabilized zirconia: An X-ray diffraction investigation
Nuclear Instruments & Methods in Physics Research, Sect. B **257** (2007) 476–479

Nix AK, Schwen D, Ronning C, Krauser J, Trautmann C, Hofsäss H
Electronic properties of graphite-like ion tracks in insulating tetrahedral amorphous carbon

Reviews on Advanced Materials Science **15** (2007) 192-197

Jonckheere R, Enkelmann E, Min M, Trautmann C, Ratschbacher L
Confined fission tracks in ion-irradiated and step-etched prismatic sections of Durango apatite
Chemical Geology **42** (2007) 202-217

Ramírez P, Gómez V, Cervera J, Schiedt B, Mafé S
Ion transport and selectivity in nanopores with spatially inhomogeneous fixed charge distributions
Journal of Chemical Physics **126** (2007) 194703

Pépy G, Boesecke P, Kuklin A, Manceau E, Schiedt B, Siwy Z, Toulemonde M, Trautmann C
Cylindrical nanochannels in ion-track polycarbonate membranes studied by small-angle X-ray scattering
*Journal of Applied Crystallography **40** (2007) 388-392*

El-Said AS, Meissl W, Simon MC, Crespo López-Urrutia JR, Lemell C, Burgdörfer J, Gebeshuber IC, Winter HP, Ullrich J, Trautmann C, Toulemonde M, Aumayr F
Potential energy threshold for nano-hillock formation by impact of slow highly charged ions on a CaF_2(111) surface
Nuclear Instruments & Methods in Physics Research, Sect. B **258** (2007) 167-171

Costantini JM, Trautmann C, Thomé L, Jagielski J, Beuneu F
Swift heavy ion-induced swelling and damage in yttria-stabilized zirconia
Journal of Applied Physics **101** (2007) 073501

Schwartz K, Lang M, Neumann R, Sorokin MV, Trautmann C, Volkov AE, Voss KO
Damage creation in LiF and NaCl crystals irradiated with swift heavy ions at 8 and 300 K
Physica Status Solidi (C) **4** (2007) 1105-1109

Batentschuk M, Winnacker A, Schwartz K, Trautmann C
Storage efficiency of BaFBr:Eu^{2+} image plates irradiated by swift heavy ions
Journal of Luminescence **125** (2007) 40-44

El-Said AS, Aumayr F, Della-Negra S, Neumann R, Schwartz K, Toulemonde M, Trautmann C, Voss KO
Scanning force microscopy of surface damage created by fast C60 cluster ions in CaF_2 and LaF_3 single crystals
Nuclear Instruments & Methods in Physics Research, Sect. B **256** (2007) 313-318

Maurer F, Brötz J, Karim S, Toimil-Molares ME, Trautmann C, Fuess H
Preferred growth orientation of metallic fcc nanowires under direct and alternating electrodeposition conditions
Nanotechnology **18** (2007) 135709

P.I. Gaiduk, C. Trautmann
Tracks in epitaxial $Si_{1-x}Ge_x$ alloy layers: Effect of layer thickness
Nuclear Instruments & Methods in Physics Research, Sect. B **256** (2007) 224-228

Myo Mina, Eva Enkelmanna, Raymond Jonckheere, Christina Trautmann and Lothar Ratschbacher
Measurements of fossil confined fission tracks in ion-irradiated apatite samples with low track densities
Nuclear Instruments & Methods in Physics Research, Sect. B **259** (2007) 943-950

Public Talks

Eingeladene Vorträge bei Konferenzen und wissenschaftl. Institutionen (Invited talks at conferences and other institutions)

Neumann, R.:
Recent results on materials research at GSI.
Japan Atomic Energy Agency (JAEA), Tokai, 14.03.2007.

Neumann, R.:
Materials research at GSI.
RIKEN Nishina Center for Accelerator Based Science, Tokyo-Ikebukuro, 16.03.2007.

Neumann, R.:
Integration und Anwendung von Nanodrähten durch Mikro-Nano-Integration und Mikro-Montage.
Kick-Off-Meeting "Mikro-Nano-Integration" Im Rahmenprogramm "Mikrosysteme 2004-2009"

des BMBF, Fraunhofer-Institut für Zuverlässigkeit und Mikrointegration (IZM), Berlin, 10.05.2007.

Neumann, R.:
Materials research with energetic heavy ions at GSI.
10th German-Vietnamese Seminar, Bonn, 05.06.2007

Neumann, R.:
Materialforschung mit energiereichen Schwerionen bei der GSI.
Seminarvortrag am Institut für Atom- und Molekülphysik, Universität Gießen, 05.07.2007.

Neumann, R.:
Materials research with energetic heavy ions at GSI.
5th German-Korean Seminar, Pyongyang, 23. 10.2007.

Neumann, R.:
Nanodrähte auf der Grundlage von Ionenspuren.
Fachhochschule Kaiserslautern, Standort Zweibrücken, 14.11.2007.

Neumann, R.:
Von Nanodrähten, Zellkernen und Kristallen bei extremen Drücken – Schnelle Ionen als Werkzeug der Materialforschung.
Fachhochschule Kaiserslautern, Standort Zweibrücken, 14.11.2007.

Trautmann, C.:
Materials modifications with MeV-GeV heavy ions: basic aspects and applications,
Institut für Oberflächenmodifizierung, Leipzig, 26.04.2007.

Trautmann, C.:
Materials modifications with MeV-GeV heavy ions; basic aspects and applications,
ITS LEIF meeting, Crete, 05.05.2007

Trautmann, C.:
Materials modifications with MeV-GeV heavy ions. Track formation and sputtering processes in ionic crystals,
Institut für Allgemeine Physik, Technische Universität Wien, 15.05.2007

Trautmann, C.:
Energetic particle flux: swift heavy ions,
DOE Workshop on Materials for Extreme Conditions, Bethesda, Maryland, USA, 11.06.2007

Trautmann, C.:
How energetic heavy ions modify solids: Basic aspects and applications in micro and nanoscience,
Institute of Heavy Ion Physics, Peking University, 07.07.2007

Trautmann, C.:
How energetic heavy ions modify solids: Basic aspects and applications in micro and nanoscience,
Institute of Modern Physics, Lanzhou, 12.07.2007

Trautmann, C.:
Nanostructures produced with energetic heavy ions,
DECHEMA Tagung, Frankfurt, 11.11.2007

Trautmann, C.:
Pressurized solids exposed to swift heavy ions,
Journées thématiques GdR PAMIR, Orsay, 04.12.2007

Trautmann, C.:
Nanostructures produced with energetic heavy ions,
IAEA Consultant's Meeting on Advanced Materials on the Nano-scale synthesized by Radiation-Induced Processes, Vienna, 10.12.2007

Cornelius, T.W.:
Electrical and IR optical properties of bismuth nanowires,
Ruprecht-Karls-University of Heidelberg, Kirchhoff-Institut für Physik (KIP), Heidelberg (Germany), 15.01.2007

Cornelius, T.W.:
Nanowires – from synthesis to application,
University Pierre and Marie Curie, Institut des NanoSciences de Paris (INSP), Paris (France), 21.06.2007

Cornelius, T.W.:
Nanowires – Growth and Characterisation,
Massachusetts Institute of Technology (MIT), Department for Mechanical Engineering, Boston (USA), 24.07.2007

Cornelius, T.W.:

Metal and semimetal nanowires, Pennsylvania State University, Materials Research Institute (MRI), University Park (USA), 01.08.2007

Cornelius, T.W.:
Fabrication and electrical transport properties of bismuth nanowires, Frühjahrstagung der Deutschen Physikalischen Gesellschaft, Regensburg (Germany), 26.03.2007

Schwartz, K.:
Radiation damage creation in solids, Eurasian National University, Department of Applied Physics, Astana, Kazakhstan, 05.06.2007

Schwartz, K.:
Heavy ion induced processes in dielectric materials,
Eurasian National University, Department of Applied Physics, Astana, Kazakhstan, 07.06.2007

Schwartz, K.:
Heavy ion irradiation and nanotechnology, Eurasian National University, Department of Applied Physics, Astana, Kazakhstan, 08.06.2007

Schwartz, K.:
Wechselwirkung von Schwerionen mit Festkörpern und Erzeugung von Strahlenschäden,
TU Darmstadt, Institut für Festkörperphysik, 18.09. 2007

Lehrveranstaltungen

Neumann, R. (WS 2007):
Materialforschung und Nanotechnologie mit energiereicher Strahlung I.
Universität Heidelberg, Vorlesung/lecture.

Neumann, R. (SS 2007):
Materialforschung und Nanotechnologie mit energiereicher Strahlung II.
Universität Heidelberg, Vorlesung/lecture.

Trautmann, C. (WS 2007):
Nanotechnologie; Materialmodifizierung mit energiereichen Schwerionen.
Fachhochschule Rüsselsheim, Vorlesung/lecture.

Cornelius, T.W. (WS 2007):
Nanotechnologie; Herstellung und Charakterisierung von Nanodrähten.
Fachhochschule Rüsselsheim, Vorlesung/lecture.

Academic Works

Schiedt, Birgitta:
Characterization of ion track-etched nanopores. Dissertation:
Universität Heidelberg (2007).

Karim, Shafqat:
Fabrication and characterization of gold nanowires. Dissertation:
Universität Marburg (2007).

Research Division: Nuclear Chemistry

Leader: D. Rudolph
Compiled by: F.P. Heßberger

Abstract

Radiochemically performed excitation function measurements of the reaction $^{248}Cm(^{26}Mg,xn)^{274-x}Hs$ led to the observation of an unexpectedly high 3n cross section and the discovery of the new nuclide ^{271}Hs.

Relativistic quantum-chemical theory predicts that element 112 behaves like a transition element, i.e. homolog Hg, and not like the inert gas Rn upon adsorption on gold surfaces.

Publications

PROGRAMME HADRONS & NUCLEI

1. WoS listed publications

O. KAVATSYUK, C. MAZZOCCHI, Z. JANAS, A. BANU, L. BATIST, F. BECKER, A. BLAZHEV, W. BRÜCHLE, J. DÖRING, T. FAESTERMANN, M. GÓRSKA, H. GRAWE, A. JUNGCLAUS, M. KARNY, M. KAVATSYUK, O. KLEPPER, R. KIRCHNER, M. LA COMMARA, M. MIERNIK, I. MUKHA, C. PLETTNER, A. PŁOCHOCKI, E. ROECKL, M. ROMOLI, K. RYKACZEWSKI, M. SCHÄDEL, K. SCHMIDT, R. SCHWENGNER, J. ZYLICZ:
Beta-decay of ^{101}Sn
Eur. Phys. J. A 31 (2007) 319-325

2. Other publications

PROGRAMME PNI

1. WoS listed publications

M. SCHÄDEL:
Superheavy element chemistry at GSI — status and perspectives
Eur. Phys. J. D. 45 (2007) 67-74

J.P. OMTVEDT, J. ALSTAD, T. BJØRNSTAD, CH.E. DÜLLMANN, K.E. GREGORICH, D.C. HOFFMAN, H. NITSCHE, K. OPEL, D. POLAKOVA, F. SAMADANI, F. SCHULZ, G. SKARNEMARK, L. STAVSETRA, R. SUDOWE , L. ZHENG:
Chemical properties of the transactinide elements studied in liquid phase with SISAK
Eur. Phys. J. D 45 (2007) 91-97

CH.E. DÜLLMANN:
Physical preseparation: a powerful new method for transactinide chemists
Eur. Phys. J. D 45 (2007) 75-80

V. PERSHINA, J. ANTON, T. BASTUG:
Relativistic effects on atomic and molecular properties of the heaviest elements
Eur. Phys. J. D 45 (2007) 87-90

H. HABA, K. TSUKADA, M. ASAI, A. TOYOSHIMA, Y. ISHII, H. TOUME, T. SATO, I. NISHINAKA, T. ICHIKAWA, S. ICHIKAWA, Y. NAGAME, W. SATO, K. MATSUO, Y. KITAMOTO, Y. TASHIRO, A. SHINOHARA, J. SAITO, M. ITO, T. IKEZAWA, M. SAKAMAKI, S. GOTO, H. KUDO, H. KIKUNAGA, M. ARAI, S. KAMATAKI, A. YOKOYAMA, K. AKIYAMA, K. SUEKI, Y. OURA, M. SCHÄDEL, W. BRÜCHLE , J.V. KRATZ:
Extraction behavior of rutherfordium into tributylphosphate from hydrochloric acid
Radiochim. Acta 95, 1-6 (2007)

V. PERSHINA, T. BASTUG, J. ANTON, B. FRICKE:
Theoretical chemistry for chemical identification of the heaviest elements
Nucl. Phys. A 787 (2007) 381c-387c

V. PERSHINA, J. ANTON, B. FRICKE:
Intermetallic compounds of the heaviest elements and their homologs: the electronic structure and bonding of MM', where M = Ge, Sn, Pb and element 114; and M' = Ni, Pd, Pt, Cu, Ag, Au, Sn, Pb and element 114
J. Chem. Phys. 127 (2007) 134310-9

C. SARPE-TUDORAN, B. FRICKE, J. ANTON, V. PERSHINA:
Adsorption of superheavy elements on metal surfaces
J. Chem. Phys. 126, 174702-5 (2007)

2. Other publications

M. SCHÄDEL:
Superheavy Element Chemistry — Achievements and Perspectives
J. Nucl. Radiochem. Sci. 8 (2007) 47-53

CH.E. DÜLLMANN:
Physical preseparation: a powerful new method for transactinide chemists
Proceedings of the 'International Symposium on Exotic Nuclei, EXON 2006'
Khanty-Mansiysk (Russia, west Siberia), July 17-22, 2006
AIP Conf. Proc. 912 (2007) 252- 261

CH.E. DÜLLMANN:
Chemical Investigations of Superheavy Elements – Current Results and New Techniques
Proceedings of the 'Tours Symposium on Nuclear Physics VI, TOURS 2006'

September 5 - 8, 2006, Tours, France
AIP Conf. Proc. 891, 36 (2007) 36-44

W. BRÜCHLE:
Simulation of Elution Curves for Chromatography Columns with a Low Number of Theoretical Plates
Proceedings of the ACS Symposium "Applied Modeling and Computations in Nuclear Science" Washington, DC; Ed. by T.Semkow, S. Jerome, S. Pommé and D.J. Strom, (2006) 269-279

Academic Works

J. DVOŘÁK
Decay properties of nuclei close to Z = 108 and N = 162 (Dissertation)
Technische Universität München (Germany), 12.7.2007

F. HAENSSLER
Chemische Modellstudien und technische Entwicklungen für zukünftige Experimente mit dem Element 114 (Inauguraldissertation)
Philosophisch-naturwissenschaftliche Fakultät der Univ. Bern (Switzerland), 22.3.2007

Public Talks

Ch.E. DÜLLMANN
Heavy Element Chemistry - On the Way to New Compound Classes
Seminar in Inorganic, Analytical, and Physical Chemistry, University of Bern, Department of Chemistry and Biochemistry, Bern (Switzerland), 11.1.2007

A. SEMCHENKOV
TASCA - the new gas-filled separator at the GSI: present status and future plans
Seminar "Radio- und Umweltchemie", PSI, Villigen (Switzerland) 12.1.2007

Ch.E. DÜLLMANN
Experiments on Chemical and Nuclear Properties of Heavy Elements Performed at GSI
16th Research Adjustment Meeting based on "Memorandum of Understanding for the Scientific Cooperation in Research and Development in the Field of Ion Beam Application between the Gesellschaft für Schwerionenforschung mbH (GSI) and the Japan Atomic Energy Agency (JAEA)", Takasaki (Japan), 12.3.2007

M. SCHÄDEL
Bridging the Gap – Nuclear Chemistry Experiments with Superheavy Elements at GSI
Physics Division Seminar, Argonne National Laboratory, Argonne (USA), 23.3.2007

V. PERSHINA
Theoretical chemistry for chemical identification of the heaviest elements
Seminar "Electronic structure and quantum chemistry", FIAS, Frankfurt (Germany), 30.5.2007

Conference/ Workshop Talks

M. SCHÄDEL
Automated Separation Techniques in Superheavy Element Chemistry
American Chemical Society 233rd National Meeting, Chicago (USA), 25.-29.3. 2007

CH.E. DÜLLMANN
Physical Separators for the Heaviest Elements
EMIS 07 - Electromagnetic Isotope Separators and Techniques Related to their Applications, Deauville, (France) June 24.-29.6. 2007

A. SEMCHENKOV
The TransActinide Separator and Chemistry Apparatus (TASCA) at GSI - Optimization of Ion-optical Structure and Magnets Design
EMIS 07 - Electromagnetic Isotope Separators and Techniques Related to their Applications, Deauville (France) June 24.-29.6. 2007

A. SEMCHENKOV
Results from first TASCA commissional experiments
3rd International Conference on the Chemistry and Physics of the Transactinide Elements (TAN 07), Davos (Switzerland), 23.-28.9.2007

M. SCHÄDEL
TASCA – Status and Perspectives
3rd International Conference on the Chemistry and Physics of the Transactinide Elements (TAN 07), Davos (Switzerland), 23.-28.9.2007

CH.E. DÜLLMANN
Toward new compound classes of transactinides - Studies of volatile group 4 element metal complexes with hexafluoroacetylacetone
3rd International Conference on the Chemistry and Physics of the Transactinide Elements (TAN 07), Davos (Switzerland), 23.-28.9.2007

V. PERSHINA
Theoretical predictions of experimental behaviour of elements 112 and heavier
3rd International Conference on the Chemistry and Physics of the Transactinide Elements (TAN 07), Davos (Switzerland), 23.-28.9.2007

V. PERSHINA
Fully relativistic calculations for systems of elements 112 and heavier
Relativistic Effects in Heavy Elements – REHE2007, Ottrott (France), 21.-25.3.2007

Lectures

CH.E. DÜLLMANN
Chemie und Kernchemie der schwersten Elemente
Vorlesung, SS 2007, WS 2007/08
Universität Mainz (Germany)

M. SCHÄDEL
Superschwere Elemente
LehrerInnen Fortbildungsseminar, Albert-Ludwigs-Universität Freiburg , 4.5.2007

CH.E. DÜLLMANN
Relativistische Effekte in der Chemie
LehrerInnen Fortbildungsseminar, Albert-Ludwigs-Universität Freiburg, 9.11.2007

Research Division: Nuclear Reactions and Astrophysics

Leader: Thomas Aumann
Compiled by: M. Valentina Ricciardi

Publications

FAIR-EXPERIMENTS

1. WoS listed publications

ILIEVA S., KISELEV O., EMLING H., EGELHOF P., BORETZKY K., MEIER JP., SIMON H., MAHATA K., LE BLEIS T., CHATILLON A., AKSOUH F., BECKERT K., BELLER P., KOZHUHAROV C., LITVINOV Y., LE XC., NOLDEN F., STECK M., STOHLKER T., ICKERT G., POPP U., WEICK H., ROHE D., JOURDAN J., WERTHMULLER D., MOEINI H., ZALITE A., AND PASCHALIS S.: Feasibility studies of the EXL setup for FAIR using the GSI storage ring ESR. Eur. Phys. Jour. ST 150 (2007) 357

T. AUMANN: Prospects of nuclear structure at the future GSI accelerators. Progr. Part. Nucl. Phys. 59 (2007) 3.

H. SIMON: The ELISe experiment at FAIR. Nucl. Phys. A 787 (2007) 102c.

2. Other publications

==

PROGRAMME HADRONS & NUCLEI

1. WoS listed publications

P. N. NADTOCHY, A. KELIC AND K.-H. SCHMIDT: Fission rate in multi-dimensional Langevin calculations. Phys. Rev. C 75 (2007) 64614

J. PEREIRA, J. BENLLIURE, E. CASAREJOS, P. ARMBRUSTER, M. BERNAS, A. BOUDARD, S. CZAJKOWSKI, T. ENQVIST, R. LEGRAIN, S. LERAY, B. MUSTAPHA, M. PRAVIKOFF, F. REJMUND, K.-H. SCHMIDT, C. STEPHAN, J. TAIEB, L. TASSAN-GOT, C. VOLANT, AND W. WLAZLO: Isotopic production cross sections and recoil velocities of spallation-fission fragments in the reaction ^{238}U(1A GeV)+d. Phys. Rev. C 75 (2007) 14602

J. PEREIRA, P. ARMBRUSTER, J. BENLLIURE AND K.-H. SCHMIDT: Comprehensive analysis of fission-reaction properties in the nuclear spallation of ^{238}U(1 GeV/nucleon) on deuterium. Phys. Rev. C 75 (2007) 44604

C. VILLAGRASA-CANTON, A. BOUDARD, J.-E. DUCRET, B. FERNANDEZ, S. LERAY, C. VOLANT, P. ARMBRUSTER, T. ENQVIST, F. HAMMACHE, K. HELARIUTTA, B. JURADO, M.V. RICCIARDI, K.-H. SCHMIDT, K. SUEMMERER, F. VIVES, O. YORDANOV, L. AUDOUIN, C.-O. BACRI, L. FERRANT, P. NAPOLITANI, F. REJMUND, C. STEPHAN, L. TASSAN-GOT, J. BENLIURE, E. CASAREJOS, M. FENRNADEZ-ORDONEZ, J. PEREIRA, S. CZAJKOWSKI, D. KARAMANIS, M. PRAVIKOFF, J.S. GEORGE, R.A. MEWALDT, N. YANASAK, M. WIEDENBECK, J.J. CONNELL, T. FAESTERMANN, A. HEINZ, A. JUNGHANS: Spallation residues in the reaction ^{56}Fe+p at 0.3A, 0.5A, 0.75A, 1.0A, and 1.5A GeV. Phys. Rev. C 75 (2007) 44603

D. BOILLEY, A. MARCHIX, B, JURADO, K.-H. SCHMIDT: A new formula for the saddle-to-scission time. Eur. Phys. J. A 33 (2007) 47

C. SCHMITT, P.N. NADTOCHY, A. HEINZ, B. JURADO, A. KELIC, K.-H. SCHMIDT: First Experiment on Fission Transients in Highly Fissile Spherical Nuclei Produced by Fragmentation of Radioactive Beams. Phys. Rev. Lett. 99 (2007) 42701

M. MOSCONI, M. HEIL, F. KÄPPELER, A. MENGONI, R. PLAG, K. FUJII, R. GALLINO, G. AERTS, R. TERLIZZI, U. ABBONDANNO, H. ÁLVAREZ-POL, F. ALVAREZ-VELARDE, S. ANDRIAMONJE, J. ANDRZEJEWSKI, P. ASSIMAKOPOULOS, L. AUDOUIN, G. BADUREK, P. BAUMANN, F. BECVÁR, E. BERTHOUMIEUX, S. BISTERZO, F. CALVIÑO, D. CANO-OTT, R. CAPOTE, A. CARRILLO DE ALBORNOZ, P. CENNINI, V. CHEPEL, E. CHIAVERI, N. COLONNA, G. CORTES, A. COUTURE, J. COX, M. DAHLFORS, S. DAVID, I. DILLMAN, R. DOLFINI, C. DOMINGO PARDO, W. DRIDI, I. DURAN, C. ELEFTHERIADIS, M. EMBID-SEGURA, L. FERRANT, A. FERRARI, R. FERREIRA-MARQUES, L. FITZPATRICK, H. FRAISKOELBL, W. FURMAN, I. GONCALVES, E. GONZALEZ-ROMERO, A. GOVERDOVSKI, F. GRAMEGNA, E. GRIESMAYER, C. GUERRERO, F. GUNSING, B. HAAS, R. HAIGHT, A. HERRERA-MARTINEZ, M. IGASHIRA, S. ISAEV, E. JERICHA, Y. KADI, D. KARAMANIS, D. KARADIMOS, M. KERVENO, V. KETLEROV, P. KOEHLER, V. KONOVALOV, E. KOSSIONIDES, M. KRTICKA, C. LAMBOUDIS, H. LEEB, A. LINDOTE, I. LOPES, M. LOZANO, S. LUKIC, J. MARGANIEC, L. MARQUES, S. MARRONE, P. MASTINU, P.M. MILAZZO, C. MOREAU, F. NEVES, H. OBERHUMMER, M. OSHIMA, S. O'BRIEN, J. PANCIN, C. PAPACHRISTODOULOU, C. PAPADOPOULOS, C. PARADELA, N. PATRONIS, A. PAVLIK, P. PAVLOPOULOS, L. PERROT, A. PLOMPEN, A. PLUKIS, A. POCH, C. PRETEL, J. QUESADA, T. RAUSCHER, R. REIFARTH, M. ROSETTI, C. RUBBIA, G. RUDOLF, P. RULLHUSEN, J. SALGADO, L. SARCHIAPONE, I. SAVVIDIS, C. STEPHAN, G. TAGLIENTE, J.L. TAIN, L. TASSAN-GOT, L. TAVORA, G. VANNINI, P. VAZ, A. VENTURA, D. VILLAMARIN, M.C. VINCENTE, V. VLACHOUDIS, R. VLASTOU, F. VOSS, S. WALTER, H. WENDLER, M. WIESCHER AND K. WISSHAK: Neutron reactions and nuclear cosmo-chronology. Progr. Part. Nucl. Phys. 59 (2007) 165

M. HEIL, F. KÄPPELER, E. UBERSEDER, R. GALLINO, M. PIGNATARI: The s process in massive stars. Progr.Part. Nucl. Phys. 59 (2007) 174

N.NENOFF, P. BRINGEL, A. BURGER, S. CHMEL, S. DABABNEH, M. HEIL, H. HUBEL, F. KAPPELER, A. NEUSSER-NEFFGEN, R. PLAG: Indication for hyperdeformed cluster states in 233Th. Eur. Phys. J. A 32 (2007) 165

G. RUGEL, I. DILLMANN, T. FAESTERMANN, M. HEIL, F. KÄPPELER, K. KNIE, G. KORSCHINEK, W. KUTSCHERA, M. POUTIVTSEV, A. WALLNER: Measurement of (n, γ) reaction cross sections at stellar energies for ^{58}Ni and ^{78}Se. Nucl. Instr. Meth. Phys. Res. B 259 (2007) 683

E. UBERSEDER, M. HEIL, F. KÄPPELER, J. GÖRRES, M. WIESCHER: New measurements of the ^{19}F(n, γ)^{20}F cross section and their implications for the stellar reaction rate. Phys. Rev. C 75 (2007) 35801

C. VOCKENHUBER, I. DILLMANN, M. HEIL, F. KAPPELER, N. WINCKLER, W. KUTSCHERA, A. WALLNER, M. BICHLER, S. DABABNEH, S. BISTERZO, R. GALLINO: Stellar (n, γ) cross sections of ^{174}Hf and radioactive ^{182}Hf. Phys. Rev. C 75 (2007) 15804

S. LALKOVSKI, S. ILIEVA, AND A. MINKOVA, N. MINKOV AND T. KUTSAROVA, A. LOPEZ-MARTENS AND A. KORICHI, H. HÜBEL, A. GÖRGEN, A. JANSEN, AND G. SCHÖNWASSER, B. HERSKIND AND M. BERGSTRÖM, ZS. PODOLYÁK: Octupole collectivity in ^{98,100,102}Mo. Phys. Rev. C 75 (2007) 14314

MUKHA, K. SÜMMERER, L. ACOSTA, M. ALVAREZ, E. CASAREJOS, A. CHATILLON, L. CORTINA-GIL, J. ESPINO, A. FOMICHEV, J.E. GARCIA-RAMOS, H. GEISSEL, J. GOMEZ-CAMACHO, L. GRIGORENKO, O. KISELEV, A. KORSHENINNIKOV, N. KURZ, YU. LITVINOV, I. MARTEL, C. NOCIFORO, M. PFUTZNER, C. RODRIGUEZ, E. ROECKL, M. STANOIU, H. WEICK, P. WOODS : Observation of two-proton radioactivity. Phys. Rev. Lett. 99 (2007) 182501

M. CAAMAŃO, D. CORTINA- GIL, W. MITTIG, H. SAVAJOLS, M. CHARTIER, C. E. DEMONCHY, B. FERNÁNDEZ, M. B. GÓMEZ HORNILLOS, A. GILLIBERT, B. JURADO, O. KISELEV, R. LEMMON, A. OBERTELLI, F. REJMUND, M. REJMUND, P. ROUSSEL-CHOMAZ, R. WOLSKI: Resonance State in ^{7}H. Phys. Rev. Lett. 99 (2007) 62502

A.KLIMKIEWICZ, P.ADRICH, K.BORETZKY, M.FALLOT, T.AUMANN, D.CORTINA-GIL, U.DATTA PRAMANIK, TH.W.ELZE, H.EMLING, H.GEISSEL, M.HELLSTROEM, K.L.JONES, J.V.KRATZ, R.KULESSA, Y.LEIFELS, C.NOCIFORO, R.PALIT, H.SIMON, G.SUROWKA, K.SUMMERER, S.TYPEL, W.WALUS: Dipole response of neutron-rich Sn isotopes. Nucl.Phys. A 788 (2007) 145c

A. KLIMKIEWICZ, N. PAAR, P. ADRICH, M. FALLOT, K. BORETZKY, T. AUMANN, D. CORTINA-GIL, U. DATTA PRAMANIK,TH. W. ELZE, H. EMLING, H. GEISSEL, M. HELLSTRÖM, K. L. JONES, J. V. KRATZ, R. KULESSA, C. NOCIFORO, R. PALIT, H. SIMON, G. SUR´OWKA, K. SÜMMERER, D. VRETENAR, AND W. WALUŚ (LAND COLLABORATION): Nuclear symmetry energy and neutron skins derived from pygmy dipole resonances. Phys. Rev. C 76 (2007) 051603(R)

L.POPESCU, C.BAUMER, A.M.VAN DEN BERG, D.FREKERS, D.DE FRENNE, Y.FUJITA, E.W.GREWE, P.HAEFNER, M.N.HARAKEH, M.HUNYADI, M.A.DE HUU, E.JACOBS, H.JOHANSSON, A.KORFF, A.NEGRET, P.VON NEUMANN-COSEL, S.RAKERS, A.RICHTER, N.RYEZAYEVA, A.SHEVCHENKO, H.SIMON, H.J.WORTCHE : Low-lying GT+ strength in ^{64}Co studied via the ^{64}Ni(d, ^{2}He)^{64}Co reaction. Phys.Rev. C 75 (2007) 54312

C.SFIENTI, M.DE NAPOLI, P.ADRICH, T.AUMANN, C.O.BACRI, T.BARCZYK, R.BASSINI, S.BIANCHIN, C.BOIANO, A.S.BOTVINA, A.BOUDARD, J.BRZYCHCZYK, A.CHBIHI, J.CIBOR, B.CZECH, J.-E.DUCRET, H.EMLING, J.FRANKLAND, M.HELLSTROM, D.HENZLOVA, K.KEZZAR, G.IMME, I.IORI, H.JOHANSSON, A.LAFRIAKH, A.LE FEVRE, E.LE GENTIL, Y.LEIFELS, W.G.LYNCH, J.LUHNING, J.LUKASIK, U.LYNEN, Z.MAJKA, M.MOCKO, W.F.J.MULLER, A.MYKULYAK, H.ORTH, A.N.OTTE, R.PALIT, P.PAWLOWSKI, A.PULLIA, G.RACITI, E.RAPISARDA, H.SANN, C.SCHWARZ, H.SIMON, K.SUMMERER, W.TRAUTMANN, C.VOLANT, M.WALLACE, H.WEICK, J.WIECHULA, A.WIELOCH, B.ZWIEGLINSKI : Gross Properties and Isotopic Phenomena in Spectator Fragmentation . Nucl.Phys. A 787 (2007) 627c

H.SIMON, M.MEISTER, T.AUMANN, M.J.G.BORGE, L.V.CHULKOV, U.DATTA PRAMANIK, TH.W.ELZE, H.EMLING, C.FORSSEN, H.GEISSEL, M.HELLSTROM, B.JONSON, J.V.KRATZ, R.KULESSA, Y.LEIFELS, K.MARKENROTH, G.MUNZENBERG, F.NICKEL, T.NILSSON, G.NYMAN, A.RICHTER, K.RIISAGER, C.SCHEIDENBERGER, G.SCHRIEDER, O.TENGBLAD, M.V.ZHUKOV : Systematic investigation of the drip-line nuclei ^{11}Li and ^{14}Be and their unbound subsystems ^{10}Li and ^{13}Be Nucl.Phys. A 791 (2007) 267

A. BRACCO, G. BENZONI, N. BLASI, S. BRAMBILLA, F. CAMERA, F.C.L. CRESPI, S. LEONI, B. MILLION, D. MONTANARI, M. PIGNANELLI, O. WIELAND, A. MAJ, P. BEDNARCZYK, J. GREBOSZ, M. KMIECIK, W. MECZYNSKI, J. STYCZEN, T. AUMANN, A. BANU, T. BECK, F. BECKER, L. CACERES, P. DOORNENBAL, H. EMLING, J. GERL, H. GEISSEL, M. GORSKA, O. KAVATSYUK, M. KAVATSYUK, I. KOJOUHAROV, N. KURZ, R. LOZEVA, N. SAITO, T. SAITO, H. SHAFFNER, H.J. WOLLERSHEIM, J. JOLIE, P. REITER, N. WARR, G. DE ANGELIS, A. GADEA, D. NAPOLI, S. LENZI, S. LUNARDI, D. BALABANSKI, G. LO BIANCO, C. PETRACHE, A. SALTARELLI, M. CASTOLDI, A. ZUCCHIATTI, J. WALKER, A. BUERGER: Coulomb Excitation of ^{68}Ni at 600 A MeV Acta Phys. Polonica B 38 (2007) 1229

T. YAMAGUCHI, T. SUZUKI, T. OHNISHI, K. SUEMMERER, F. BECKER, M. FUKUDA, H. GEISSEL, M. HOSOI, R. JANIK, K. KIMURA, S. MANDAL, G. MUENZENBERG, S. NAKAJIMA, T. OHTSUBO, A. OZAWA, A. PROCHAZKA, M. SHINDO, B. SITAR, P. STRMEN, T. SUDA, K. SUGAWARA, I. SZARKA, A. TAKISAWA, M. TAKECHI, K. TANAKA: Nuclear radius systematics of Kr isotopes studied via their interaction cross-sections at relativistic energies Eur. Phys. Jour. ST 150 (2007) 197

2. Other publications

==

Academic Works

A. KLIMKIEWICZ: Systematic investigation of the dipole response in exotic neutron-rich isotopes in ^{132}Sn mass region.
Dissertation, University of Krakow (Poland) xx.xx.2007

Public Talks (invited talks)

T. AUMANN
R^3B: Reactions with Relativistic Radioactive Beams - Status Report.
Annual NUSTAR Meeting 2007, GSI, Darmstadt, Germany, 21.- 23.03.2007.

T. AUMANN
T.: The dipole response of neutron halos and skins.
Tokyo Institute of Technology, Tokyo, Japan, 03.12.2007

T. AUMANN
Reactions with relativistic radioactive beams: Recent results from GSI and future plans at GSI and FAIR.
The 10th Int. Symp. on Origin of Matter and Evolution of Galaxies (OMEG07), Hokkaido University, Sapporo, Japan, 04-07.12.2007

T. AUMANN
Dipole response of neutron-rich nuclei.
3rd Japanese-German workshop on Nuclear Structure and Astrophysics, Frauenwörth, Chiemsee, Germany, September 29.09-02.10.2007

T. AUMANN
Dipole excitations of neutron-rich nuclei. Workshop 'Exotic Modes of Excitation: from Nuclear Structure to Astrophysics', Trento, Italy, 08.-12.10.2007

T. AUMANN
Experimental Program with Radioactive Beams at FAIR.
Fourth European Summer School on Experimental Nuclear Astrophysics, Santa Tecla, Sicily, Italy, September 26.09-6.10.2007

T. AUMANN
Experiments with High-Energy Radioactive Beams.
6th CNS International Summer School (CISS07), Center of Nuclear Study, University of Tokyo, Japan, 28.08.-01.09.2007

T. AUMANN
Giant resonances in exotic nuclei. Nordic Nuclear Meeting 2007, Gilleleje, Denmark, 12-17.08.2007

T. AUMANN
Experimental Program with Rare-Isotope Beams at FAIR.
International School of Physics "Enrico Fermi", course CLXIX - Nuclear Structure far from Stability: new Physics and new Technology, Varenna, Italy, 17-27.07.2007

T. AUMANN
The dipole response of neutron halos and skins.
The International Symposium on Physics of Unstable Nuclei (ISPUN07), Hoi An, Vietnam, 03-07.2007

K. BORETZKY
Electromagnetic Excitation of Exotic Nuclei: Dipole Strength and Neutron Skins.
International Conference 'Nuclear Physics in Astrophysics III', Dresden, Germany, 26.-31.3.2007

L. CHULKOV
Quasi-free scattering with exotic nuclei.
NUSTAR Seminar, GSI, Darmstadt, Germany, 30.10.2007

P. EGELHOF
Reaction Studies with Radioactive Beams at FAIR: the NuSTAR Projects EXL and R3B.
PNPI Gatchina, St. Petersburg, Russia, 25. 01.2007

P. EGELHOF
Calorimetric Low Temperature Detectors for High Resolution X-Ray Spectroscopy.
SPARC Workshop, Paris, France, 12.-15.02.2007

P. EGELHOF
Bolometers for High-Energy Atomic Cascade Measurements. Workshop on Neutrino Mass Determination by Electron Capture, GSI, Darmstadt, Germany, 08.- 09. 3. 2007

P. EGELHOF
The NuSTAR-Project EXL: Overview and Status. Annual NUSTAR Meeting 2007, GSI, Darmstadt, Germany, 21.-23.03.2007.

P. EGELHOF
Silicon Detectors for the NuSTAR-Project EXL. Workshop on Silicon Detectors for the CBM Experiment
GSI, Darmstadt, Germany, 18. – 20. 04. 2007

P. EGELHOF
Nuclear Structure Studies on Exotic Nuclei with Radioactive Beams – Present Status and Future Perspectives at FAIR.
9th International Spring Seminar on Nuclear Physics, Vico Equense, Italy, 20.- 24. 05. 2007

P. EGELHOF
Exotic Nuclei Studied in Direct Reactions at Low Momentum Transfer – Recent Results and Future Perspectives at FAIR.
International Symposium on Physics of Unstable Nuclei, ISPUN07, Hoi An, Vietnam, 03. – 07. 07. 2007

M. HEIL
Experimentelle Nukleare Astrophysik in Deutschland.
KHuK Jahrestagung, GSI, Darmstadt, Germany, 25.-26.10.2007

M. HEIL
Neutron capture cross section measurements for s-process nucleosynthesis.
International Conference 'Nuclear Physics in Astrophysics III', Dresden, Germany, 26.-31.03.2007

M. HEIL
The (weak) s-process and its relation to explosive nucleosynthesis.

Seminar über aktuelle Themen aus Kosmochemie und Astrophysik, Universität Mainz, 02.07.2007

A. KELIC
Microscopic-macroscopic approach to the nuclear fission process.
Seminar at the Institute of Physics at the University of Basel, Swiss, 18.01.2007

A. KELIC
Microscopic-macroscopic approach to the nuclear fission process.
Seminar at CENBG, Bordeaux, France, 16.02.2007

A. KELIC
Role of the fission in the r-process nucleosynthesis - Needed input.
International Conference 'Nuclear Physics in Astrophysics III', Dresden, Germany, 26.-31.03.2007

A. KELIC
Beam intensities with EURISOL.
EURISOL_EURONS common Town Meeting Helsinki, Finland, 17.-19.09.2007

A. KELIC
The role of fission in the r-process nucleosynthesis - Needed input.
XVII International School on Nuclear Physics, Neutron Physics and Applications, Varna, Bulgaria, 24.- 30.09.2007

M. V. RICCIARDI
Systematic study of spallation reactions in inverse kinematics at the FRS.
Annual NUSTAR Meeting 2007, GSI, Darmstadt, Germany, 21.- 23.03.2007.

M. V. RICCIARDI
High-resolution magnetic spectrometers: an excellent tool to investigate the properties of nuclear matter.
GENCO Award Ceremony, Annual NUSTAR Meeting 2007, GSI, Darmstadt, Germany, 21.- 23.03.2007.

M. V. RICCIARDI
High-resolution experiments on nuclear fragmentation at the FRS at GSI.
International Conference on Nuclear Fragmentation 2007, Kemer (Antalya), Turkey, 24.09.- 01.10. 2007.

K. H. SCHMIDT
New generation of measurements and model developments on nuclide production in spallation reactions.
International Conference on Nuclear Data for Science and Technology, Nice, France, 22.-27.04.2007

K. H. SCHMIDT
Spallation Reactions - Physics and Applications.
XVII International School on Nuclear Physics, Neutron Physics and Applications, Varna, Bulgaria, 24.- 30.09.2007

K. H. SCHMIDT
New Results on Nuclear Fission - Data and Interpretation.
Compound-Nuclear Reactions and Related Topics, Tenaya Lodge at Yosemite National Park, Fish Camp, California (USA), 22. – 26.10.2007

H. SIMON
^{5}H – ^{14}Be: Correlation studies along the dripline.
Advanced Many-Body Methods for Nuclear Structure, ECT, Trento, Italy, 02.– 06.07.2007

H. SIMON
Correlations studies in breakup experiments.
20th European Conference on few Body Problems in Physics, Pisa, Italy, 10.- 14.09.2007

K. SÜMMERER
High-energy Coulomb breakup of proton-dripline nuclei as a tool to study radiative-capture reactions of astrophysical interest.
Int. Conf. on proton-emitting nuclei and related areas (Procon07), Lisbon, Portugal, 17.-23.06.2007

Academic duties

T. AUMANN:
Interdisziplinäre Anwendungen der Atom- und Kernphysik in der Umwelt- und Medizinforschung (Seminar).
Universität Mainz. WS 2006/2007

T. AUMANN
Physik mit Strahlen exotischer Kerne (lecture).
Universität Mainz. SS 2007

P. EGELHOF
Kernphysikalische Aspekte der Astrophysik (lecture).
Universität Mainz. SS 2007

P. EGELHOF und S. ILIEVA
S.: Übungen zur Vorlesung Kernphysikalische Aspekte der Astrophysik (exercises).
Universität Mainz. SS 2007

Research Division: KP3

Leader: K. Peters

Compiled by: K. Götzen

Publications

FAIR -EXPERIMENTS

- L. Schmitt [PANDA Collaboration],
  The PANDA Detector at FAIR,
  Prepared for the 11th Vienna Conference on Instrumentation, Vienna 19.-24.02.2007, Nucl. Instrum. Meth. A **581** (2007) 542.

- K. Korcyl, P. Salabura, L. Schmitt, W. Kühn and J. T. Otwinowski,
  Modelling of the architectural studies for the PANDA DAT system,
  Prepared for the 15th IEEE Realtime Conference, Fermilab, 29.04 - 05.05.2007, to be published in IEEE Trans. Nucl. Sci.

- W. Kühn *et al.*,
  FPGA - Based Compute Nodes for the PANDA - Experiment at FAIR,
  Prepared for the 15th IEEE Realtime Conference, Fermilab, 29.04.-05.05.2007, to be published in IEEE Trans. Nucl. Sci.

- K. Götzen [PANDA Collaboration],
  Fast Simulations for the PANDA Experiment
  in Proceedings of the XLV International Winter Meeting on Nuclear Physics, Bormio, Italy, ed. by I. Iori and A. Tarantola, Ricerca Scientifica ed Educazione Permanente Suppl., vol. **127**, Milano, 2007, p. 291

- K. Götzen [PANDA Collaboration],
  Fast Simulations for the PANDA Experiment at FAIR
  Prepared for the International Conference on Computing in High Energy and Nuclear Physics, Victoria, Canada, 02.-07.09.07, to be published in Journal of Physics, Conference Series

- A.A. Efremov, E.K. Koshurnikov, Y.Y. Lobanov, A.F. Makarov, H. Orth, A.N. issakian, A.S. Vodopianov,
  2 Tesla Superconducting Solenoid for the PANDA Target Spectrometer,
  NIMA **47962** (2007)

PROGRAMME HADRONS & NUCLEI

- K. Zbiri, A. Le Fèvre, J. Aichelin, J. Łukasik, W. Reisdorf, F. Gulminelli, U. Lynen, W.F.J. Müller, H. Orth, C. Schwarz, C. Sfienti, W. Trautmann, K. Turzó, B. Zwiegliński, J.L. Charvet, A. Chbihi, R. Dayras, D. Durand, J.D. Frankland, R. Legrain, N. Le Neindre, O. Lopez, L. Nalpas, M. Parlog, E. Plagnol, M.F. Rivet, E. Rosato, E. Vient, M. Vigilante, C. Volant and J.P. Wieleczko,
  Transition from participant to spectator fragmentation in Au+Au reactions between 60A and 150A MeV
  Phys. Rev. C 75, 034612 (2007).

- W. Trautmann,
  Isotopic effects in multifragmentation and the nuclear equation of state
  Nucl. Phys. A 787, 575c (2007).

- C. Sfienti, M. De Napoli, P. Adrich, T. Aumann, C.O. Bacri, T. Barczyk, R. Bassini, S. Bianchin, C. Boiano, A.S. Botvina, A. Boudard, J. Brzychczyk, A. Chbihi, J. Cibor, B. Czech, J.-É. Ducret, H. Emling, J. Frankland, M. Hellström, D. Henzlova, K. Kezzar, G. Immè, I. Iori, H. Johansson, A. Lafriakh, A. Le Fèvre, E. Le Gentil, Y. Leifels, W.G. Lynch, J. Lühning, J. Łukasik, U. Lynen, Z. Majka, M. Mocko, W.F.J. Müller, A. Mykulyak, H. Orth, A.N. Otte, R. Palit, P. Pawłowski, A. Pullia, G. Raciti, E. Rapisarda, H. Sann, C. Schwarz, H. Simon, K. Sümmerer, W. Trautmann, C. Volant, M. Wallace, H. Weick, J. Wiechula, A. Wieloch and B. Zwiegliński,
  Gross properties and isotopic phenomena in spectator fragmentation
  Nucl. Phys. A 787, 627c (2007).

- N. Le Neindre, E. Bonnet, J.P. Wieleczko, B. Borderie, F. Gulminelli, M.F. Rivet, R. Bougault, A. Chbihi, R. Dayras, J.D. Frankland, E. Galichet, D. Guinet, P. Lautesse, A. Le Fèvre, O. Lopez, J. Łukasik, D. Mercier, J. Moisan, M. Pârlog, E. Rosato, R. Roy, C. Schwarz, C. Sfienti, B. Tamain, W. Trautmann, A. Trzciński, K. Turzó, E. Vient, M. Vigilante, B. Zwiegliński,
  Yield scaling, size hierarchy and fluctuations of observables in fragmentation of excited heavy nuclei
  Nucl. Phys. A 795, 47 (2007).

- W. Trautmann, R. Bassini, M. Begemann-Blaich, A. Ferrero, S. Fritz, S.J. Gaff-Ejakov, C. Groß, G. Immé, I. Iori, U. Kleinevoß, G.J. Kunde, W.D. Kunze, A. Le Fèvre, V. Lindenstruth , J. Łukasik, U. Lynen, V. Maddalena, M. Mahi, T. Möhlenkamp, A. Moroni, W.F.J. Müller, C. Nociforo, B. Ocker, T. Odeh, H. Orth, F. Petruzzelli,

J. Pochodzalla, G. Raciti, G. Riccobene, F.P. Romano, Th. Rubehn, A. Saija, H. Sann, M. Schnittker, A. Schüttauf, C. Schwarz, W. Seidel, V. Serfling, C. Sfienti, A. Trzcinski, A. Tucholski, G. Verde, A. Wörner, Hongfei Xi, and B. Zwiegliński,
Thermal and chemical freeze-out in spectator fragmentation
Phys. Rev. C 76, 064606 (2007).

- W. Trautmann [ALADIN Collaboration],
Bimodality in spectator fragmentation"
in *Proceedings of the XLV International Winter Meeting on Nuclear Physics*, Bormio, Italy, ed. by I. Iori and A. Tarantola, Ricerca Scientifica ed Educazione Permanente Suppl., vol. **127**, Milano, 2007, p. 205, preprint arXiv:0705.0678(nucl-ex), (2007).

- C. Sfienti, M. De Napoli, S. Bianchin, A.S. Botvina, J. Brzychczyk, A. Le Fèvre, J. Łukasik, P. Pawłowski, W. Trautmann, P. Adrich, T. Aumann, C.O. Bacri, T. Barczyk, R. Bassini, C. Boiano, A. Boudard, A. Chbihi, J. Cibor, B. Czech, J.-É. Ducret, H. Emling, J. Frankland, M. Hellström, D. Henzlova, K. Kezzar, G. Immè, I. Iori, H. Johansson, A. Lafriakh, E. Le Gentil, Y. Leifels, W.G. Lynch, J. Lühning, U. Lynen, Z. Majka, M. Mocko, W.F.J. Müller, A. Mykulyak, H. Orth, A.N. Otte, R. Palit, A. Pullia, G. Raciti, E. Rapisarda, H. Sann, C. Schwarz, H. Simon, K. Sümmerer, C. Volant, M. Wallace, H. Weick, J. Wiechula, A. Wieloch and B. Zwiegliński,
Isotopic effects in nuclear reactions at relativistic energies
in *Proceedings of the XLV International Winter Meeting on Nuclear Physics*, Bormio, Italy, ed. by I. Iori and A. Tarantola, Ricerca Scientifica ed Educazione Permanente Suppl., vol. **127**, Milano, 2007, p. 223, preprint arXiv:0704.0227(nucl-ex), (2007).

- S. Bianchin, C. Sfienti, J. Łukasik, A. Le Fèvre, W. Trautmann, P. Adrich, T. Aumann, C.O. Bacri, T. Barczyk, R. Bassini, C. Boiano, A.S. Botvina, A. Boudard, J. Brzychczyk, A. Chbihi, J. Cibor, B. Czech, M. De Napoli, J.-É. Ducret, H. Emling, J. Frankland, M. Hellström, D. Henzlova, K. Kezzar, G. Immè, I. Iori, H. Johansson, A. Lafriakh, E. Le Gentil, Y. Leifels, W.G. Lynch, J. Lühning, U. Lynen, Z. Majka, M. Mocko, W.F.J. Müller, A. Mykulyak, H. Orth, A.N. Otte, R. Palit, P. Pawłowski, A. Pullia, G. Raciti, E. Rapisarda, H. Sann, C. Schwarz, H. Simon, K. Sümmerer, M.B. Tsang, C. Volant, M. Wallace, H. Weick, J. Wiechula, A. Wieloch and B. Zwiegliński,
Mass measurement and isoscaling in ^{124}Sn + Sn and ^{107}Sn + Sn reactions at 600 AMeV
in *Proceedings of the XLV International Winter Meeting on Nuclear Physics*, Bormio, Italy, ed. by I. Iori and A. Tarantola, Ricerca Scientifica ed Educazione Permanente Suppl., vol. **127**, Milano, 2007, p. 233.

- M. Ablikim *et al.* [BES Collaboration],
First observation of J/ψ and $\psi(2S)$ decaying to $nK^0_S\bar{\Lambda}$ +c.c,
Phys. Lett. B **659** (2008) 789 [arXiv:0710.3091 [hep-ex]].

OTHER

- V. Y. Alexakhin *et al.* [COMPASS Collaboration],
The deuteron spin-dependent structure function g1(d) and its first moment,
Phys. Lett. B **647** (2007) 8 [arXiv:hep-ex/0609038].

- E. S. Ageev *et al.* [COMPASS Collaboration],
A new measurement of the Collins and Sivers asymmetries on a transversely polarised deuteron target,
Nucl. Phys. B **765** (2007) 31 [arXiv:hep-ex/0610068].

- E. S. Ageev *et al.* [COMPASS Collaboration],
Spin asymmetry A(1)(d) and the spin-dependent structure function g1(d) of the deuteron at low values of x and Q^2,
Phys. Lett. B **647** (2007) 330 [arXiv:hep-ex/0701014].

- P. Abbon *et al.* [COMPASS Collaboration],
The COMPASS Experiment at CERN,
Nucl. Instrum. Meth. A **577** (2007) 455-518. [arXiv:hep-ex/0703049].

- M. I. Adamovich *et al.* [WA89 Collaboration],
Observation of a resonance in the K(S) p decay channel at a mass of 1765-MeV/c^2,
Eur. Phys. J. C **50** (2007) 535 [arXiv:hep-ex/0702044].

- V. Y. Alexakhin *et al.* [COMPASS Collaboration],
Double spin asymmetry in exclusive ρ^0 muoproduction at COMPASS,
arXiv:0704.1863 [hep-ex].

- B. Aubert *et al.* [BABAR Collaboration],
Exclusive branching fraction measurements of semileptonic tau decays into three charged hadrons, $\tau^- \to \phi\pi^-\nu_\tau$ and $\tau^- \to \phi K^-\nu_\tau$,
Phys. Rev. Lett. **100** (2008) 011801 [arXiv:0707.2981 [hep-ex]].

- B. Aubert *et al.* [BABAR Collaboration],
Measurement of CP asymmetry in $B^0 \to K^0_S\pi^0\pi^0$ decays,
Phys. Rev. D **76** (2007) 071101 [arXiv:hep-ex/0702010].

- B. Aubert *et al.* [BABAR Collaboration],
Measurement of the $B^\pm \to \rho^\pm\pi^0$ branching fraction and direct CP asymmetry,
Phys. Rev. D **75** (2007) 091103 [arXiv:hep-ex/0701035].

- B. Aubert *et al.* [BABAR Collaboration],
  Evidence of a broad structure at an invariant mass of 4.32-GeV/c^2 in the reaction $e^+e^- \to \pi^+\pi^-\psi(2S)$ measured at BaBar,
  Phys. Rev. Lett. **98** (2007) 212001 [arXiv:hep-ex/0610057].

Public Talks

- S. Bianchin
  Mass measurement and isoscaling in ^{124}Sn + Sn and ^{107}Sn + Sn reactions at 600 AMeV.
  XLV International Winter Meeting on Nuclear Physics, Bormio (Italy), 15.-20.01.2007.

- A.S. Botvina
  Production of hypernuclei in multifragmentation of nuclear spectator matter,
  International Simposium "Nuclear Physics at J-PARC", Tokai, Japan, 01.-02.06.2007

- A.S. Botvina
  In-medium properties of nuclear fragments at the liquid-gas phase coexistence,
  International Nuclear Physics Conference (INPC2007), Tokyo, Japan, 03.-08.06.2007

- A.S. Botvina
  In-medium properties of nuclear fragments at the liquid-gas phase coexistence,
  International Workshop on Multifragmentation and Related Topics (IWM2007). Caen, France, 04.-07.11.2007

- K. Götzen
  Fast Simulations for the PANDA Experiment
  XLV International Winter Meeting on Nuclear Physics, Bormio (Italy), 15.-20.01.2007.

- K. Götzen
  Fast Simulations für das PANDA Experiment
  72. Frühjahrstagung der Deutschen Physikalischen Gesellschaft, Gießen, 12.-16.03.2007

- K. Götzen
  Status BEPCII/BESIII
  72. Frühjahrstagung der Deutschen Physikalischen Gesellschaft, Gießen, 12.-16.03.2007

- B. Lewandowski
  Large Area APDs for the PANDA-EMC
  Scint 2007, Winston-Salem (NC USA), 04.-08.06.2007

- J. Łukasik
  Collective flow and isotopic effects at intermediate energies.
  International Conference on Nuclear Fragmentation 2007, Kemer (Turkey), 25.-30.09.2007.

- J. Łukasik
  Collective flow and isotopic effects at intermediate energies.
  International Workshop on Multifragmentation and Related Topics, Caen (France), 04.-07.11.2007.

- H. Nowak
  Entwicklung von großflächigen Avalanche-Photodioden als Auslese für das PANDA EMC
  72. Frühjahrstagung der Deutschen Physikalischen Gesellschaft, Gießen, 12.-16.03.2007

- K. Peters
  EMC@Panda,
  Festkolloquium, Gießen, 7.12.2007

- K. Peters
  Panda - Physics and Beam Requirements,
  pbar@FAIR Workshop, GSI, Darmstadt, 3.12.2007

- K. Peters
  Open and hidden charm physics at PANDA,
  VIQCD Inauguration, FZ Jlich, 30.11.2007

- K. Peters
  Hadronenspektroskopie: Ein Streifzug von Gestern bis Übermorgen,
  Physikalisches Kolloquium, Regensburg, 26.11.2007

- K. Peters
  GSI Project,
  Project X Physics Workshop, FNAL, Batavia, 16. Nov. 2007

- K. Peters
  LAAPDs for the PANDA EMC,
  Nuclear Science Symposium ("NSS") of IEEE Honolulu, 2.11.2007

- K. Peters
  Hadron Physics @ FAIR,
  Seminar, Honolulu, 30.10.2007

- K. Peters
  nextPWA Presentation,
  I3HP2 Town meeting, Frascati, 29.9.2007

- K. Peters
  Spektroskopie mit Antiprotonen,
  Kernphysikalisches Kolloquium, Heidelberg, 22.5.2007

- K. Peters
  The Panda Project @ FAIR,
  Kernphysik Seminar, Bonn, 24.5.2007

- K. Peters
  Significance and Quality Assurance of Spin-Parity Analyses,
  PWA Workshop, IHEP, Beijing, 25.1.2007

- K. Peters
  Potential Problems and Instabilities in Amplitude Analyses,
  PWA Workshop, IHEP, Beijing, 24.1.2007

- G. Schepers
  Particle Identification in the Panda-Experiment@FAIR,
  72. Frühjahrstagung der Deutschen Physikalischen Gesellschaft, Gießen, 12.-16.03.2007

- L. Schmitt
  The PANDA Detector at FAIR
  11th Vienna Conference on Instrumentation, Wien, Östereich, 19.-24.02.2007

- L. Schmitt
  The PANDA Experiment at FAIR,
  SFAIR Consortium Meeting, Chalmers University, Göteborg, Sweden, 12.11.2007

- L. Schmitt
  New Topics and Techniques in Hadron Physics,
  Seminar, Universität Gießen, 19.11.2007

- C. Schwarz
  The Barrel DIRC of the PANDA Experiment
  RICH07, Trieste, Italy, 15.-20.10.2007

- C. Sfienti
  Isotopic effects in nuclear reactions at relativistic energies.
  XLV International Winter Meeting on Nuclear Physics, Bormio (Italy), 15.-20.01.2007.

- C. Sfienti
  Isotopic effects in spectator fragmentation at relativistic energies.
  International Conference on Nuclear Fragmentation 2007, Kemer (Turkey), 25.-30.09.2007.

- C. Sfienti
  Isospin effects in spectator fragmentation at relativistic energies.
  Ganil, Caen (France), 26.10.2007.

- W. Trautmann
  Bimodality in spectator fragmentation.
  XLV International Winter Meeting on Nuclear Physics, Bormio (Italy), 15.-20.01.2007.

- W. Trautmann
  Bimodality in spectator fragmentation.
  International Nuclear Physics Conference, Tokyo (Japan), 03.-08.06.2007.

- W. Trautmann
  Collective flow at intermediate energies.
  International Nuclear Physics Conference, Tokyo (Japan), 03.-08.06.2007.

- W. Trautmann
  N/Z dependence of projectile fragmentation at 600 A MeV.
  International Workshop on Nuclear Dynamics in Heavy-ion Reactions and Neutron Stars, Beijing (China), 10.-14.07.2007.

- W. Trautmann
  Isotopic effects in spectator fragmentation.
  Institute of Modern Physics, Lanzhou (China), 18.07.2007.

- W. Trautmann
  Neutron and proton collective flow and the symmetry energy.
  International Workshop on Multifragmentation and Related Topics, Caen (France), 04.-07.11.2007.

- W. Trautmann
  Phase-space driven expansion in the multifragmentation of spectators at 600 A MeV.
  International Symposium on Complex Systems in Physics and Beyond, Frankfurt am Main, 30.11.2007.

- P. Wieczorek
  Low noise ASIC preamplifier for the PANDA EMC
  72. Frühjahrstagung der Deutschen Physikalischen Gesellschaft, Gießen, 12.-16.03.2007

- A. Wilms
  The electromagnetic calorimeter of the PANDA detector at FAIR/GSI
  Scint 2007, Winston-Salem (NC USA), 04.-08.06.2007

Academic Works

- S. Bianchin
  'Multifragmentation: Rôle de la masse et de l'isospin', (Dissertation)
  Strasbourg, Universität Louis Pasteur (France), 21.09.2007.

Teaching

SS 2007

- H. Appelshäuser, M. Bleicher, M. Blume, Ch. Dörner, A. Dumitru, C. Greiner, W. Greiner, J. A. Maruhn, K. Peters, U. Ratzinger, D.-H. Rischke, J. Schaffner-Bielich, H. Schmidt-Böcking, S. Schramm, R. Stock, H. Stöcker, H. Ströbele, J. Stroth (SS07),
  Interuniversitäres Schwerionenseminar gemeinsam mit der GSI in Darmstadt, JWG Universität Frankfurt, Seminar (2 SWS)

- H. Appelshäuser, M. Bleicher, M. Blume, Ch. Dörner, A. Dumitru, C. Greiner, W. Greiner, J. A. Maruhn, K. Peters, D.-H. Rischke, J. Schaffner-Bielich, H. Schmidt-Böcking, S. Schramm, R. Stock, H. Stöcker, H. Ströbele, J. Stroth (SS07),
  Kolloquium zur Struktur der elementaren Materie und zur Astrophysik, JWG Universität Frankfurt, Seminar (2 SWS)

- H. Appelshäuser, K. Götzen (SS07)
  Übungen zur Vorlesung Kerne und Elementarteilchen, JWG Universität Frankfurt, Übungen (2 SWS)

- Görnitz, Korneck, Trautmann (SS 2007)
  Moderne Physik, JWG Universität Frankfurt, Vorlesung

- H. Orth (SS2007)
  Gruppenunterricht zur Atomphysik, Ruprecht-Karls-Universität Heidelberg, Vorlesung (3 SWS)

- K. Peters (SS07)
  Kernphysik IV, JWG Universität Frankfurt, Vorlesung (2 SWS)

- K. Peters (SS07)
  Panda-Seminar, JWG Universität Frankfurt, Seminar (2 SWS)

- C. Schwarz (SS07)
  Fortgeschrittenen-Praktikum, JWG Universität Frankfurt, Praktikum (8 SWS)

WS 2007/2008

- H. Appelshäuser, M. Bleicher, M. Blume, Ch. Dörner, A. Dumitru, C. Greiner, W. Greiner, J. A. Maruhn, K. Peters, U. Ratzinger, D.-H. Rischke, J. Schaffner-Bielich, H. Schmidt-Böcking, S. Schramm, R. Stock, H. Stöcker, H. Ströbele, J. Stroth (WS07/08),
  Interuniversitäres Schwerionenseminar gemeinsam mit der GSI in Darmstadt, JWG Universität Frankfurt, Seminar (2 SWS)

- H. Appelshäuser, M. Bleicher, M. Blume, Ch. Dörner, A. Dumitru, C. Greiner, W. Greiner, J. A. Maruhn, K. Peters, D.-H. Rischke, J. Schaffner-Bielich, H. Schmidt-Böcking, S. Schramm, R. Stock, H. Stöcker, H. Ströbele, J. Stroth (WS07/08),
  Kolloquium zur Struktur der elementaren Materie und zur Astrophysik, JWG Universität Frankfurt, Seminar (2 SWS)

- H. Orth (WS2007/08)
  Gruppenunterricht zur Kern- und Teilchenphysik, Ruprecht-Karls-Universität Heidelberg, Vorlesung (3 SWS)

- K. Peters (WS07/08)
  Kernphysik I - Grundlagen der Kern- und Teilchenphysik, JWG Universität Frankfurt, Vorlesung (2 SWS)

- K. Peters, K. Götzen (WS07/08)
  Ergänzungen und Übungen zur Vorlesung "Grundlagen der Kern- und Teilchenphysik", Übungen (2 SWS)

- K. Peters (WS07/08)
  Panda-Seminar, JWG Universität Frankfurt, Seminar (2 SWS)

- C. Schwarz (WS07/08)
  Fortgeschrittenen-Praktikum, JWG Universität Frankfurt, Praktikum (8 SWS)

- W. Trautmann (WS 2007/08)
  Kernphysik für Studierende des Lehramtes an Haupt- und Realschulen, JWG Universität Frankfurt, Vorlesung

Research Division: Plasma Physics

Division leader: Thomas Stöhlker
Compiled by: Karin Weyrich

Publications

FAIR-EXPERIMENTS

1. WoS listed publications

N.A. Tahir, V. Kim, I.V. Lomonosov, D.A. Grigoriev, A.R. Piriz, H. Weick, H. Geissel, D.H.H. Hoffmann
High energy density physics problems related to liquid jet lithium target for Super-FRS fast extraction scheme
Laser and Particle Beams 25 (2) (2007) 295-304

N.A. Tahir, P. Spiller, A. Shutov, I.V. Lomonosov, V. Gryaznov, A.R. Piriz, G. Wouchuk, C. Deutsch, V.E. Fortov, D.H.H Hoffmann,.R. Schmidt
HEDgeHOB: High-energy density matter generated by heavy ion beams at the future facility for antiprotons and ion research
Nucl. Instr. Meth. 577 (2007) 238-249

PROGRAMME PNI

1. WoS listed publications

A. Adonin, J. Jacoby, V. Turtikov, A. Fertman, A. Golubev, D.H.H. Hoffmann, A. Ulrich, D. Varentsov, J. Wieser
Laser effect on the 248 nm KrF transition using heavy ion beam pumping.
Nucl. Instr. Meth. A577 (2007) 357-360

Eisenbarth, S., O.N. Rosmej, V.P. Shevelko, A. Blazevic and D.H.H. Hoffmann Numerical simulations of the projectile ion charge difference in solid and gaseous stopping matter
Laser Part. Beams 25 (2007) 601-611

K. Flippo, B.M. Hegelich, B.J. Albright, L. Yin, D.C. Gautier, S. Letzring, M. Schollmeier, J. Schreiber, R. Schulze, J.C. Fernández
Laser-driven ion accelerators: Spectral control, monoenergetic ions and new acceleration mechanisms
Laser and Part. Beams 25 (2007) 3-8

J. Fuchs, Y. Sentoku, E. d'Humieres, T.E. Cowan, J. Cobble, P. Audebert, A. Kemp, A. Nikroo, P. Antici, E. Brambrink, A. Blazevic, E.M. Campbell, J.C. Fernandez, J.- C. Gauthier, M. Geissel, M., Hegelich, S. Karsch, H. Popescu, N. Renard-LeGalloudec, M. Roth, J. Schreiber, R. Stephens, H. Pepin
Comparative spectra and efficiencies of ions laser-accelerated forward from the front and rear surfaces of thin solid foils
Physics of Plasmas 14 (5) (2007) 053105

A.A. Golubev, A.V. Kantsyrev, V.E. Luckjashin, A. Fertman, A.V. Kunin, V.V.Vartulin, A.S. Gnutov, y.V. Panova, H. Iwase, E. Mustafin, D. Schardt, K. Weyrich, N.M. Sobolevskly, L.N. Latisheva.
Measurement of the energy deposition profile for U-238 ions with specific energy 500 and 950 MeV/u in stainless steel and copper targets
NIM B 263 (2) (2007) 339-344

D.H.H Hoffmann,. A. Blazevic, S. Korostiy, P. Ni, S.A. Pikuz, B. Rethfeld, O. Rosmej, M. Roth, N.A. Tahir, S. Udrea, D. Varentsob, K. Weyrich, B.Yu. Sharkod, Y. Maron
Inertial fusion energy issues of intense heavy ion and laser beams interacting with ionized matter studied at GSI-Darmstadt
Nucl. Instr. Meth.A577 (2007) 8-13

D.H.H Hoffmann.
Inertial Fusion Energy on the Horizon
Laser Part. Beams 25 (2007) 511-512

D.H.H Hoffmann, A. Blazevic, O.N. Rosmej, P. Spiller, N.A. Tahir, K. Weyrich, T. Dafni, M. Kuster, P. Ni, M. Roth, S. Udrea, D. Varentsov, J. Jacoby, V. Kain, R. Schmidt, K. Zioutas, V. Mintsev, V.E. Fortov, B. Sharkov
Particle accelerator physics and technology for high energy density physics research
European Physical Journal D44 (2) (2007) 293-300

M. Kuster, H. Brauninger, S. Cebrian, M. Davenport, C. Eleftheriadis, J. Englhauser, H. Fischer, J. Franz, P. Friedrich, R. Hartmann, F.H. Heinsius, D.H.H. Hoffmann, G. Hoffmeister, J.N. Joux, D. Kang, K. Konigsmann, R. Kotthaus, T. Papaevangelou, C. Lasseur, A. Lippitsch, G. Lutz, J. Morales, A. Rodriguez, L. Struder, J. Vogel, K. Zioutas
The x-ray telescope of CAST
New Journal of Physics 9 (2007) Art. No.169

A.R. Piriz, N.A. Tahir, NA, J.J.L.Cela, O.D. Cortazar, M.C.S Moreno, M. Temporal, D.H.H. Hoffmann
Analytical models for the design of the LAPLAS experiment
Contr. Plasma Phys 47 (2007) 213-222

A.R. Piriz, J.J. Cela, M.. Lopez, M.C. Moreno, M.. Serna, O. Cortazar, N.A. Tahir, D.H.H. Hoffmann
A new approach to Rayleigh-Taylor instability: Application to accelerated elastic solids
Nucl. Instr. Meth. A577 (2007) 250-256

B. Rethfeld
Free-electron generation in laser-irradiated dielectrics
Contr Plasma Phys 47 (2007) 360-367

M. Schollmeier, M. Roth, A. Blazevic, E. Brambrink, J.A. Cobble, J.C. Fernandez, K.A. Flippo, D.C. Gautier, D. Habs, K. Harres, B.M. Hegelich, T. Hessling, D.H.H. Hoffmann, S. Letzring, F. Nuernberg, G. Schaumann, J. Schreiber, K. Witte
Laser ion acceleration with micro-grooved targets
Nucl. Instr. and Meth. A577 (2007)186-190

N.A Tahir, V. Kim, A. Matvechev, A. Ostrik, I.V. Lomonosov, A.R. Piriz, J.J. Lopez Cela, D.H.H. Hoffmann
Numerical modeling of heavy ion induced stress waves in solid targets
Laser Part. Beams 25 (2007) 523-540

N.A Tahir, R. Schmidt, M. Brugger, I.V. Lomonosov, A. Shutov, A.R. Piriz, S. Udrea, D.H.H. Hoffmann, C. Deutsch
Prospects of high energy density physics research using the CERN super proton synchrotron (SPS)
Laser Part. Beams 25 (2007) 639-647

N.A Tahir, A.R. Piriz, A. Shutov, I.V. Lomonosov, V. Gryaznov, G. Wouchuk, C. Deutsch, P. Spiller, V.E. Fortov, D.H.H Hoffmann, R.Schmidt
Survey of theoretical work for the proposed HEDgeHOB experimental schemes: HIHEX and LAPLAS
Contrib Plasma Phys. 47 (2007) 223-233

S. Udrea, V. Ternovoi, N. Shilkin, A. Fertman, V.E. Fortov, D.H.H. Hoffmann, A. Hug, M.I. Kulish, V.B. Mintsev, P. Ni, D. Nikolaev, N.A. Tahir, V. Turtikov, D. Varentsov, D. Yuriev
Measurements of electrical resistivity of heavy ion beam produced high energy density matter: Latest results for lead and tungsten
Nucl. Instr. Meth. A 577 (2007) 257-261

D. Varentsov, V.Ya. Ternovoi, M. Kulish, D. Fernengel, A. Fertman, A. Hug, J Menzel, J., P. Ni, D. Nikolaev, N. Shilkin, V. Turtikov, S. Udrea, V.E. Fortov, A.A. Golubev, V.K. Gryaznov, D.H.H. Hoffmann, V. Kim, I.V., Lomonosov, V. Mintsev, B. Yu. Sharkov, A. Shutov, P. Spiller, N.A. Tahir, H. Wahl
High-energy-density physics experiments with intense heavy ion beams
Nucl. Instr. Meth. A 577 (2007) 262-266

K. Weyrich, H. Wahl, A. Golubev, A. Kantsyrev, M. Kulish, S. Dudin, D.H.H. Hoffmann, B. Sharkov, V. Mintsev
Influence of the Gap-target Configuration on the Measured Energy Loss of C-ions in Ar-gas and -plasma
Nucl. Instr. Methods A 577 (2007) 366-370

2. Other publications

S. Andriamonje, S. Aune, S. D. Autiero, K. Barth, A. Belov, B. Beltran, H. Braeuninger, J.M. Carmona, S. Cebrian, J.I. Collar, T. Dafni, M. Davenport, L. Di Lella, C. Eleftheriadis, J. Englhauser, G. Fanourakis, E. Ribas, E. Ferrer, H. Fischer, J. Franz, P. Friedrich, T. Geralis, L.I. Giomataris, S. Gninenko, H. Gomez, M. Hasinoff, F.H. Heinsius, D.H.H., Hoffmann, J. Vogel, K. Zioutas
An improved limit on the axion–photon coupling from the CAST experiment
JCAP (2007) Art. No. 010 April 2007

Academic Works

K. Harres
Charakterisierung eines Hochenergie-Lasersystems am Beispiel PHELIX (Diplom)
Technical University Darmstadt (Germany), 15. 1 .2007

F. Nürnberg
Experimentelle Bestimmung des Energiespektrums von lasererzeugten MeV Ionenstrahlen mit Hilfe einer Thomson- Parabel (Diplom)
Technical University Darmstadt (Germany), 17. 1 .2007

G. Schaumann
Experimente mit lasergeheizten Hohlräumen für die Untersuchung der Wechselwirkung von Schwerionen mit ionisierter Materie (Diss.)
Technical University Darmstadt (Germany), 17. 12. 2007

Public Talks

A. Blazevic
Preparing experiments for the energy loss measurements of ions in dense plasmas
27th International Workshop on Physics of High Energy Density in Matter, Hirschegg (Austria), 29.1-2.2. 2007

A. Blazevic
Experiments on ion stopping in hot and dense plasma at GSI
Workshop on Heavy Ion Stopping (HIS07), Darmstadt (Germany), 8.-10.9.2007

O. Rosmej
Heavy Ion Stopping Process and assotiated K-shell Radiation
Seminarvortrag,Univ. Rostock (Germany), 24.04.2007

O. Rosmej
X-ray spectroscopy in investigation of the heavy ion stopping process
Workshop on Heavy Ion Stopping (HIS07) Darmstadt (Germany), 8.10. 2007

O. Rosmej
Studies od Silicon K-shell Spectra induced by Calcium Projectiles penetrating low density aerogels
Int. Conf. Fundamental Atomic Spectroscopy (FAS), Moscow (Russia), 24.10. 2007

N.A. Tahir
High Energy Density Physics Experiments at GSI
27th International Workshop on Physics of High Energy Density in Matter, Hirschegg (Austria), 29.1-2.2. 2007

N.A Tahir
Warm Dense Matter Studies Using Intense Heavy Ion Beams: The HEDgeHOB Collaboration
International Workshop on Warm Dense Matter (WDM07), Porquerolles (France), 11.-.16.6.2007

N.A. Tahir
Generation of Strongly Correlated Plasmas Using Intense Heavy Ion
Beams at future FAIR Facility at Darmstadt: The HEDgeHOB Collaboration Workshop on Strongly Correlated Plasmas, Bad Honef (Germany), 15-18.7.2007

N.A. Tahir
High Energy Density Matter Studies Using Intense Heavy Ion beams at Future FAIR Facility at Darmstadt: The HEDgeHOB Collaboration
Conf. on Turbulent Mixing and Beyond, Trieste (Italy), 18.-26.8.2007

N.A Tahir
Simulations of Damage Caused to Equipment Due to Full Impact of the LHC Beam at CERN
Workshop on Materials for Collimators and Absorbers Geneva (Switzerland), 3-5.9.2007

N.A. Tahir
High Energy Density Matter Research Using Intense Heavy Ion Beams: The HEDgeHOB Collaboration
Conf. on Inertial Fusion Sciences and Applications (IFSA07),Kobe (Japan), 10-14.9.2007

D. Varentsov
Warm Dense Matter Experiments with Heavy Ion Beams
International Workshop on Warm Dense Matter (WDM07), Porquerolles (France), 11.-.16.6.2007

D. Varentsov
High Energy Density Physics Experiments at GSI
27th International Workshop on Physics of High Energy Density in Matter, Hirschegg (Austria), 29.1-2.2. 2007

D.H.H. Hoffmann
Das CERN Axion Solar Telescope Experiment (CAST) – Axionen, dunkle Materie und einige andere offene Fragen
Vortrag, Universität Rostock (Germany), 18.1.2007

D. H.H. Hoffmann
The CERN Axion Solar Telescope Experiment (CAST) - Axions, Dark Matter and some Open Problems
27th International Workshop on Physics of High Energy Density in Matter, Hirschegg (Austria), 29.1-2.2.2007

D. H.H. Hoffmann
Inertial Fusion and Inertial Fusion Energy
10th International Moscow School of Physics and 35th ITEP Winter School of Physics, Moscow (Russia), 12.-18.2.2007

D. H.H. Hoffmann
High Energy Density Matter Generated by Heavy-Ion Beams, and Application to Fusion Energy
Int. Conf. Frontiers of Plasma Physics and Technology Bangkok (Thailand), 7.3.2007

D. H.H. Hoffmann
High Energy Density Matter Generated by Heavy-Ion Beams, and Application to Fusion Energy
Haereus Workshop on Physics of Dense Plasma, Bad Honnef (Germany),17.7.2007

D. H.H. Hoffmann
Inertial Fusion and Inertial Fusion Energy – Frontiers of Dense Plasma Phsics with Intens Beams and Acclerator Technology
IPP Summer School of Plasma Physics, IPP Garching (Germany), 28.9. 2007

D.H.H. Hoffmann
Heavy Ion Stopping related to High Energy Density Matter States generated by Heavy Ion Beams and Application to Inertial Fusion
Workshop on Heavy Ion Stopping (HIS07), Darmstadt (Germany), 8.10. 2007

D.H.H. Hoffmann
Kernfusion – Die Energie der Zukunft, dunkle Materie und einige andere offene Fragen
Energie Kolloquium, TU Darmstadt Energy Center, Darmstadt (Germany), 2.11.2007

D. H.H. Hoffmann
Das CERN Axion Solar Telescope Experiment (CAST) – Axionen, dunkle Materie und einige andere offene Fragen
Vortrag Physikalisches Kolloquium der Universität Kiel, Kiel (Germany), 27.11. 2007

D. H.H. Hoffmann
Status of High Energy Density Matter Experiments at GSI

Workshop on Physics of Nonideal Plasma, Russian Academy of Sciences, Moscow (Russia), 4.12.2007

D.H.H. Hoffmann
Geheimnisse der Dunklen Materie - Licht und Dunkel im Universum
Vortrag ‚Saturday Morning Physics', TU Darmstadt, Darmstadt (Germany), 15.12.2007

Research Division: SHIP

Leader: S. Hofmann
Compiled by: F.P. Heßberger

Publications

PROGRAMME HADRONS & NUCLEI

1. WoS listed publications

C. RAUTH, D. ACKERMANN, G. AUDI, M. BLOCK, A. CHAUDHURI, S. ELISEEV, F. HERFURTH, F.P. HESSBERGER, S. HOFMANN, H.J. KLUGE, A. MARTIN, G. MARX, M. MUKHERJEE, J.B. NEUMAYR, W.R. PLASS, S. RAHAMAN, D. RODRIGUEZ, L. SCHWEIKHARD, P.G. THIROLF, G. VOROBJEV, C. WEBER:
Direct mass measurements around A=46 at SHIPTRAP.
Eur. Phys. J. - Special Topics 150 (2007) 329-337
Also part of Programme PNI

M. MAZZOCCO, D. ACKERMANN, M. BLOCK, H. GEISSEL, F.P. HESSBERGER, S. HOFMANN, N. IWASA, K. NISHIO, W.R. PLASS, C. SCHEIDENBERGER, H. WEICK, M. WINKLER:
Extension of the Monte-Carlo code MOCADI to fusion-evaporation reactions.
Eur. Phys. J. - Special Topics 150 (2007) 363-364

B. SULIGNANO, S. HEINZ, F.P. HESSBERGER, S. HOFMANN, D. ACKERMANN, S. ANTALIC, B. KINDLER, I. KOJOUHAROV, P. KUUSINIEMI, B. LOMMEL, R. MANN, K. NISHIO, A.G. POPEKO, S. SARO, B. STREICHER, M. VENHART, A.V. YEREMIN:
Identification of a K isomer in in ^{252}No.
Eur. Phys. J A 33 (2007) 327-331

H. BACKE, F.P. HESSBERGER, M. SEWTZ, A. TÜRLER:
Production and properties of the heaviest elements.
Eur. Phys. J. D 45 (2007) 3-15

F.P. HESSBERGER:
GSI experiments on synthesis and nuclear structure investigations of the heaviest nuclei.
Eur. Phys. J. D 45 (2007) 33-37

M. BLOCK, D. ACKERMANN, K. BLAUM, A. CHAUDHURI, Z. Di, S. ELISEEV, R. FERRER, D. HABS, F. HERFURTH, F.P. HESSBERGER, S. HOFMANN, H.-J. KLUGE, G. MAERO, A. MARTIN, G. MARX, M. MAZZOCCO, M. MUKHERJEE, J.B. NEUMAYR, W.R. PLASS, W. QUINT, S. RAHAMAN, C. RAUTH, D. RODRIGUEZ, C. SCHEIDENBERGER, L. SCHWEIKHARD, P.G. THIROLF, G. VOROBJEV, C. WEBER:
Towards direct mass measurements of nobelium at SHIPTRAP.
Eur. Phys. J. D 45 (2007) 39-45
Also part of Programme PNI.

H. BACKE, P. KUNZ, W. LAUTH, A. DRETZKE, R. HORN, T. KOLB, M. LAATIAOUI, M. SEWTZ, D. ACKERMANN, M. BLOCK, F. HERFURTH, F.P. HESSBERGER, S. HOFMANN, R. MANN:
Towards optical spectroscopy of the element nobelium (Z=102) in a buffer gas cell.
Eur. Phys. J. D 45 (2007) 99-106
Also part of Programme PNI.

F.P. HESSBERGER:
Nuclear structure investigations in the region of superheavy nuclei.
Phys. of Atomic Nucl. 70 (2007) 1445-1451

S. HOFMANN, D. ACKERMANN, S. ANTALIC, H.G. BURKHARD, V.F. COMAS, R. DRESSLER, Z. GAN, S. HEINZ, J.A. HEREDIA, F.P. HESSBERGER, J. KHUYAGBAATAR, B. KINDLER, I. KOJOUHAROV, P. KUUSINIEMI, M. LEINO, B. LOMMEL, R. MANN, G. MÜNZENBERG, K. NISHIO, A.G. POPEKO, S. SARO, H.J. SCHÖTT, B. STREICHER, B. SULIGNANO, J. UUSITALO, M. VENHART, A.V. YEREMIN:
The reaction ^{48}Ca + ^{238}U → ^{286}112* studied at the GSI-SHIP.
Eur. Phys. J A 32 (2007) 251-260

S. ANTALIC, A.N. ANDREYEV, D. ACKERMANN, L. BIANCO, D. CULLEN, I. DARBY, S. FRANCHOO, S. HEINZ, F.P. HESSBERGER, S. HOFMANN, M. HUYSE, B. KINDLER, I. KOJOUHAROV, A.P. LEPPÄNEN, S.R. LESHER, B. LOMMEL, R. MANN, G. MÜNZENBERG, K. NISHIO, R.D. PAGE, J. PAKARINEN, J.J. RESSLER, S. SARO, H.J. SCHÖTT, B. STREICHER, B. SULIGNANO, J. THOMSON, P. VAN DUPPEN, M. VENHART, D. WISEMAN, R. WYSS:
The new isotopes Po-Rn region.
Acta Phys. Polonica B 30 (2007) 1557-1560

B. STREICHER, S. ANTALIC, F.P. HESSBERGER, S. HOFMANN, D. ACKERMANN, B. KINDLER, I. KOJOUHAROV, P. KUUSINIEMI, B. LOMMEL, R. MANN, B. SULIGNANO, P. KUUSINIEMI:
Alpha-gamma decay studies of ^{261}Sg.
Acta Phys. Polonica B 38 (2007) 1561-1564

A. CHATILLON, C. THEISEN, E. BOUCHEZ, P.A. BUTLER, E. CLEMENT, O. DORVAUX, S. EECKHAUDT, B.J.P. GALL, A. GÖRGEN, T. GRAHN, P.T. GREENLEES, R.D. HERZBERG, F.P. HESSBERGER, A. HURSTEL, G.D. JONES, P. JONES, R. JULIN, S. JUUTINEN, K. KETTUNEN, F. KHALFALLAH, W. KORTEN, Y. LE COZ, M. LEINO, A.P. LEPPÄNEN, P. NIEMINEN, J. PAKARINEN, J. PERKOWSKI, P. RAHKILA, M. ROUSSEAU, C. SCHOLEY, J. UUSITALO, J.N. WILSON, P. BONCHE, P.H. HEENEN:
Observation of a rotational band in the odd-Z transfermium nucleus ^{251}Md.
Phys. Rev. Lett. 98 (2007) 132503

J. KHUYAGBAATAR, S. HOFMANN, F.P. HESSBERGER, D. ACKERMANN, S. ANTALIC, H.-G. BURKHARD, S. HEINZ, B. KINDLER, A.F. LISETSKY, B. LOMMEL, R. MANN, K. NISHIO, H.J. SCHÖTT, B. SULIGNANO:
Isomeric States in ^{214}Th and ^{213}Th.

Eur. Phys. J. A34 (2007) 355-361

2. Other publications

F.P. HESSBERGER
Experiments on Nuclear Structure and Synthesis of Superheavy Elements at SHIP
Proc. 'Tours Symposium on Nuclear Physics VI' (eds. M.Arnould, M.Lewitowicz, H.Emling, H.Akimune, M.Ohta, H.Utsunomiya, T.Wada, T.Yamagata) Tours (France), 5.-8.9.2006, AIP Conference Proceedings 891 (2007), 10-18

Academic Works

B. SULIGNANO
Search for K isomers in ^{252,254}No and ^{260}Sg and investigation of their nuclear structure. (Dissertation)
Univ. Mainz (Germany), 2.7.2007.

Public Talks

F.P. HESSBERGER
Nuclear Structure Investigations in the Region of Superheavy Nuclei.
Seminar, IReS Strassburg (France), 14.6.2007.

S. HOFMANN
Superschwergewichte - Wie neue Elemente geschmiedet werden.
Kolloquim TU Aachen (Germany), 10.12.2007

Conference/ Workshop Talks

F.P. HESSBERGER
GSI Experiments on Nuclear Structure Investigations of Heaviest Nuclei.
ESNT Workshop on the spectroscopy of transactinide nuclei, CEA/DSM/SPhN Saclay (France), 29.1.-2.2.2007

F.P. HESSBERGER
Probing low lying single particle levels in SHE by alpha-gamma spectroscopy.
3rd Int. Conference on the Chemistry and Physics of the Transactinide Elements (TAN 07), Davos (Switzerland), 23.-28.9.2007

D. ACKERMANN
Superheavy nuclei: self-consistency effects and single-particle degrees of freedom
Nuclear Structure: New Pictures in the Extended Isospin Space (NS07), YITP, Kyoto (Japan), 11.-14.6.2007

D. ACKERMANN
First Day Experiments @ S3 - Transactinde Research @ SPIRAL.
SPIRAL 2 Week, Caen (France), 26.-30.11.2007

D. ACKERMANN
Separators and Spectrometers in Heavy Ion Experiments - State of the Art and Developments.
ESF Workshop on 'The future of stable beams in Nuclear Astrophysics', NRC 'Demokritos', Athens (Greece), 14.-15.12.2007

S. HOFMANN
Study of Superheavy Elements.
Workshop on Nuclear Physics, WONP 2007, Havana (Cuba), 5.-8.2.2007

S. HOFMANN
Overview of SHE Research.
Annual Nustar Meeting, GSI Darmstadt (Germany) 21.-23.3.2007

S. HOFMANN
Synthesis and Decay Properties of the Heaviest Nuclei.
Int. Symp. on Heavy Ion Physics, Dubna (Russia), 24.-26.5.2007

S. HOFMANN
Production and Decay of Superheavy Nuclei.
The Second Int. Symp. "Atomic Cluster Collosions Structure and Dynamics from the Nuclear to the Biological Scale" GSI, Darmstadt (Germany), 19.-23.7.2007

S. HOFMANN
Study of Superheavy Elements at the GSI SHIP.
234th American Chemical Society (ACS) National Meeting, Boston, MA (USA), 19.-23.8.2007

S. HOFMANN
Recent Achievements in the Search for Transactinide Nuclei.
3rd Int. Conference on the Chemistry and Physics of the Transactinide Elements (TAN 07), Davos (Switzerland), 23.-28.9.2007

S. HOFMANN
Study of Superheavy Elements at SHIP.
4th Int. Conf. on Fission and Properties of Neutron-Rich Nuclei, Sanibel Island, Florida (USA), 11.-17.11.2007

Lectures

D. ACKERMANN
An den Grenzen des Periodensystem der chemischen Elemente
Vorlesung, 16. 11. / 7. 12. 2007
Universität Gießen (Germany)

Research Division: Theory

Leaders: K. Langanke/J. Wambach
Compiled by: H. Rinnert

Publications

PROGRAMME HADRONS & NUCLEI

1. WoS listed publications

SONIA BACCA
Photodisintegration of light nuclei for testing a correlated realistic interaction in the continuum
Phys. Rev. C 75, 044001 (2007) (8 pages)

SONIA BACCA, HARTMUTH ARENHOEVEL, NIR BARNEA, WINFRIED LEIDEMANN AND GIUSEPPINA ORLANDINI
Inclusive electron scattering off 4He
Physical Review C 76, 014003 (2007)

BENGT FRIMAN, KAI HEBELER (Darmstadt, GSI) , ACHIM SCHWENK (TRIUMF), LAURA TOLOS (Frankfurt U., FIAS), Neutron matter from low-momentum interactions, In the proceedings of YKIS Seminar on New Frontiers in QCD: Exotic Hadrons and Hadronic Matter, Kyoto, Japan, 20 Nov - 8 Dec 2006, Prog.Theor.Phys.Suppl.168:639-642,2007.
e-Print: arXiv:0704.1404 [nucl-th]

CHIHIRO SASAKI, BENGT FRIMAN (Darmstadt, GSI) , KRZYSZTOF REDLICH (Wroclaw U.), Effective chiral model with Polyakov loops and its application to hot/dense medium. In the Proceedings of YKIS Seminar on New Frontiers in QCD: Exotic Hadrons and Hadronic Matter, Kyoto, Japan, 20 Nov - 8 Dec 2006, Prog.Theor.Phys.Suppl.168:291-294,2007.
e-Print: hep-ph/0703191

K. REDLICH (Wroclaw U. & Darmstadt, GSI) , B. FRIMAN, C. SASAKI (Darmstadt, GSI), QCD phase diagram and charge fluctuations.
In Proceedings of 19th International Conference on Ultra-Relativistic Nucleus-Nucleus Collisions: Quark Matter 2006 (QM2006), Shanghai, China, 14-20 Nov 2006, J.Phys.G34:S437-444,2007.
e-Print: hep-ph/0702296

C. SASAKI, B. FRIMAN (Darmstadt, GSI) , K. REDLICH (Wroclaw U.), Density fluctuations in the presence of spinodal instabilities.
Published in Phys.Rev.Lett.99:232301,2007.
e-Print: hep-ph/0702254

CHIHIRO SASAKI, BENGT FRIMAN (Darmstadt, GSI) , KRZYSZTOF REDLICH (Wroclaw U.), Susceptibilities and the phase structure of an effective chiral model with Polyakov loops,
In proceedings of 19th International Conference on Ultra-Relativistic Nucleus-Nucleus Collisions: Quark Matter 2006 (QM2006), Shanghai, China, 14-20 Nov 2006, International Journal of Modern Physics E16, 2319, 2007
e-Print: hep-ph/0702206

L. TOLOS, B. FRIMAN (Darmstadt, GSI) , A. SCHWENK (TRIUMF & Washington U., Seattle), The Neutron matter equation of state from low-momentum interactions, In the proceedings of Quark Confinement and the Hadron Spectrum 7, Ponta Delgada, Azores, Portugal, 2-7 Sep 2006, AIP Conf.Proc.892:508-510,2007.
e-Print: nucl-th/0611070

C. SASAKI, B. FRIMAN (Darmstadt, GSI) , K. REDLICH (Wroclaw U.), Susceptibilities and the Phase Structure of a Chiral Model with Polyakov Loops, Phys.Rev.D75:074013,2007.
e-Print: hep-ph/0611147

C. SASAKI, B. FRIMAN (Darmstadt, GSI) , K. REDLICH (Darmstadt, GSI & Wroclaw U.), Quark Number Fluctuations in a Chiral Model at Finite Baryon Chemical Potential, Phys.Rev.D75:054026,2007.
e-Print: hep-ph/0611143

K. HEBELER (Darmstadt, GSI) , A. SCHWENK (TRIUMF & Washington U., Seattle) , B. FRIMAN (Darmstadt, GSI), Dependence of the S(0)-1 superfluid pairing gap on nuclear interactions, Phys.Lett.B648:176-180,2007.
e-Print: nucl-th/0611024

M. CHERNYK, H. FELDMEIER, T. NEFF, P. VON NEUMANN-COSEL, AND A. RICHTER
On the Structure of the Hoyle State in 12C Phys. Rev. Lett. 98, 032501 (2007)

L. R. GASQUES, A. V. AFANASJEV, M. BEARD, J. LUBIAN, T. NEFF, M. WIESCHER, AND D. G. YAKOVLEV
Sao Paulo potential as a tool for calculating S factors of fusion reactions in dense stellar matter Phys. Rev. C 76, 045802 (2007)

K. LANGANKE AND G. MARTINEZ-PINEDO
A FAIR chance for supernovae
International Journal of Modern Physics E 16 (2007) 1107

K. LANGANKE, H. FELDMEIER, G. MARTINEZ-PINEDO AND T. NEFF
Astrophysically important nuclear reactions
Progress in Particle and Nuclear Physics 59 (2007) 66

H.-TH. JANKA, K. LANGANKE, A. MAREK, G. MARTINEZ-PINEDO and B. MÜLLER
Theory of Core-Collapse Supernovae
Physics Reports 442 (2007) 38

H. GRAWE, K. LANGANKE AND G. MARTINEZ-PINEDO
Nuclear Structure and Astrophysics
Reports in Progress in Physics 70 (2007) 1525

H. FUJITA, Y. FUJITA, T. ADACHI, A.D. BACHER, G.P.A. BERG, T. BLACK, E. CAURIER, C.C. FOSTER, H. FUJIMURA, K. HARA, K. HARADA, K. HATANAKA, J. JÄNECKE, J. KAMIYA, Y. KANZAKI, K. KATORI, T. KAWABATA, K. LANGANKE, G. MARTINEZ-PINEDO, T.

NORO, D.A. ROBERTS, H. SAKAGUCHI, Y. SHIMBARA, T. SHINADA, E.J. STEPHENSON, H. UENO, T. YAMANAKA, M. YOSHIFUKU and M. YOSOI
Isospin structure of $J^{\pi} = 1^*$ states in ^{58}Ni and ^{58}Cu studied by ^{58}Ni(p,*p'*) and ^{58}Ni(^{3}He,t)^{58}Cu measurements
Physical Review C75 (2007) 034310

A.F. LISETZKY, E. CAURIER, K. LANGANKE, G. MARTINEZ-PINEDO, P. VON NEUMANN-COSEL, F. NOWACKI AND A. RICHTER
Magnetic dipole probes of the *sd* and *pf* shell crossing in the ^{36,38}Ar isotopes
Nuclear Physics A789 (2007) 114

A. BYELIKOV, T. ADACHI, H. FUJITA, K. FUJITA, Y. FUJITA, K. HATANAKA, A. HEGER, Y. KALMYKOV, K. LANGANKE, G. MARTINEZ-PINEDO, K. NAKANISHI, P. VON NEUMANN-COSEL, R. NEVELING, A. RICHTER, N. SAKAMOTO, Y. SAKEMI, A. SHEVCHENKO, Y. SHIMBARA, Y. SHIMIZU, F.D. SMIT, Y. TAMESHIGE, A. TAMII, S.E. WOOSLEY AND M. YOSOI
Neutrino Nucleosynthesis of the Exotic, Odd-Odd Nuclei ^{138}La and ^{180}Ta
Physical Review Letters 98 (2007) 082501

C. SCHOLL, P. PETKOV, V. WERNER, A. LINNEMANN, T. ADACHI, A. DEWALD, A. FITZLER, C. FRANSEN, Y. FUJITA, J. JOLIE, K. LANGANKE, A.F. LISETZKY, G. MARTINEZ-PINEDO, D. M\"UCHER, J.N. ORCE, N. PIETRALLA, N. WARR, K.O. ZELL AND P. VON BRENTANO
New spin assignments in the odd-odd N=Z nucleus ^{42}Sc and the breaking of the ^{40}Ca core
Physical Review C75 (2007) 064321

D. MOCELJ, T. RAUSCHER, G. MARTINEZ-PINEDO, K. LANGANKE, L. PACEARESCU, A. FAESSLER, F.-K. THIELEMANN AND Y. ALHASSID
Large-scale prediction of the parity distribution in the nuclear level density and application to astrophysical reaction rates\
Physical Review C75 (2007) 045805

C. ÖZEN, K. LANGANKE, G. MARTINEZ-PINEDO AND D.J. DEAN
Parity-Projected Shell Model Monte Carlo Level Densities for fp-shell Nuclei
Physical Review C75 (2007) 064307

A. JUNGCLAUS, L. CACERES, M. GORSKA, M. PFÜTZNER, S. PIETRI, E. WERNER-MALENTO, H. GRAWE, K. LANGANKE, G. MARTINEZ-PINEDO, F. NOWACKI, A. POVES, J. CUENCA,
D. RUDOLPH, Z. PODOLYAK, P.H. REGAN, P. DESTINOV, S. LALKOWSKI, V. MODAMIO, J. WALKER, P. BEDNARCZYK, P. DOORNENBAL, H. GEISSEL, J. GERL, J. GREBOSZ, I. KOJOUHAROV, N. KURZ, W. PROKOPOWICZ, H. SCHAFFNER, H.J. WOLLERSHEIM, K. ANDGREN, J. BENLLIURE, G. BENZONI, A.M. BRUCE, E. CASAREJOS, B. CEDERWALL, F.C.L. CRESPI, B. HADINIA, M. HELLSTRÖM, R. HOISCHEN, G. ILIE, J. JOLIE, A. KHAPLANOV, M. KMIECIC, R. KUMAR, A. MAJ, S. MANDAL, F. MONTES, S. MYAKSKI, G. SIMPSON, S.J. STEER, S. TASHENOV AND O. WIELAND
First observation of isomeric decays in the r-process waiting-point nucleus ^{82}Cd
Physical Review Letters 99 (2007) 132501

Y. KALMYKOV, C. \"OZEN, K. LANGANKE, G. MARTINEZ-PINEDO, P. VON NEUMANN-COSEL AND A. RICHTER
Spin- and Parity-Resolved Level Densities from the Fine Structure of Giant Resonances
Physical Review Letters 99 (2007) 202502

J.J. CUENCA-GARCIA, G. MARTINEZ-PINEDO, K. LANGANKE, I.N. BORZOV AND F. NOWACKI
Shell-model half-lives for r-process N=82 nuclei
European Journal of Physics A34 (2007) 99

Y. KALMYKOV, K. LANGANKE, G. MARTINEZ-PINEDO, D. MOCELJ, P. VON NEUMANN-COSEL, I. POLTORATSKA, V.YU. PONOMAREV, A. RICHTER, A. SHEVCHENKO AND J. WAMBACH
Spin- and Parity-Resolved Level Densities from High-Resolution Hadron and Electron Scattering Studies of Giant Resonances
Nuclear Physics A

M.F.M. LUTZ AND M. SOYEUR
Radiative and isospin-violating decays of Ds mesons in the hadrogenesis conjecture
arXiv:0710.1545 [hep-ph]

M.F.M. LUTZ, C.L. KORPA AND M. MOELLER Antikaons and hyperons in nuclear matter with saturation
arXiv:0707.1283 [nucl-th]

M.F.M. LUTZ, C.L. KORPA, A. SEMKE
Self consistency in hadron physics
arXiv:0704.2011 [nucl-th]

E. BRAMBRINK, T. SCHLEGEL, G. MALKA ET AL.
Direct evidence of strongly inhomogeneous energy deposition in target heating with laser-produced ion beams
Phys.Rev.E 75, 065401(R) (2007)

EDS. P. MULSER AND T. SCHLEGEL
"ILIAS - Ion and Laser beam Interaction and Application Studies", GSI Report 2007-03 February

ZHAO-QING FENG, GEN-MING JIN, MING-HUI HUANG ET AL.
Possible way to synthesize superheavy element Z=117, Chin. Phys. Lett. 24 (2007) 2551.

ZHAO-QING FENG, GEN-MING JIN, JUN-QING LI, WERNER SCHEID
Formation of superheavy nuclei in cold fusion reactions,
Phys. Rev. C 76 (2007) 044606.

Academic Works

KAI HEBELER
Renormalization Group Approach to Superfluid Neutron Matter
Dissertation.
Univ. Darmstadt (Germany), 2007

MATTHIAS MÖLLER
Antikaons in infinite nuclear matter and nuclei
Dissertation
Univ. Darmstadt (Germany), 2007.

ALEXANDER SEMKE
Mesonic and Isobar modes in matter
Dissertation
Univ. Darmstadt (Germany), 2007.

Public Talks

C. BARBIERI

University of Barcelona. Jan 31, 2007, "Self-consistent Green's functions approach to nuclear structure"

C. BARBIERI

Berkeley Natl. Lab. May 3, 2007. "Nuclear correlations,Nuclear correlations,from stable to exotic isotopes"

C. BARBIERI

INPC2007, Tokyo. June 2007. POSTER PRESENTED: "Self-consistent Green's function (SCGF) studies of finite nuclei"

C. BARBIERI

ECT* Trento. July 3, 2007. "Self-consistent Green's function (SCGF) studies of finite nuclei"

C. BARBIERI

Chimsee German-Japanese meeting. Sept. 29, 2007. "Pygmy resonance in proton Pygmy resonance in proton rich Argon"

C. BARBIERI

Washington University, St.Louis. Nov. 1, 2007. "Applications of Green's function theory to atoms and nuclei"

C. BARBIERI

INT Seattle. Nov. 7, 2007. "Applications of Green's Function Theory to Atoms and Nuclei"

H.FELDMEIER
"Fermionic Molecular Dynamics - Clusters, Halos, Skins and S-factors"
Invited lecture at International School of Physics "Enrico Fermi" CLXIX, Varenna June 19 – 29; 2007

B. FRIMAN
Theoretical Physics, University of Wroclaw, "Nuclear Matter: a fresh view at an old problem", June 29, 2007

G. MARTINEZ PINEDO
"Nuclear Physics Aspects of supernovae evolution and nucleosynthesis:
The nup-process and the r-process", Physics Department, Technical
University of Munich, January 7, 2007

G. MARTINEZ PINEDO
"Neutrinos and explosive nucleosynthesis", 21st Century COE 6th
Symposium on Neutrino Processes and Stellar Evolution February 7-9,
2007 Sanjo Kaikan, University of Tokyo.

G. MARTINEZ PINEDO
"Nuclear Physics Aspects of supernovae evolution and nucleosynthesis:
nucleosynthesis in neutrino heated matter", in Nuclear Physics in
Astrophysics III, 26 - 31 March 2007, Dresden, Germany

G. MARTINEZ PINEDO
"Nuclear Physics Aspects of supernovae evolution and nucleosynthesis:
Nucleosynthesis of medium and heavy nuclei", seminar at the National
Superconducting Cyclotron Laboratory, Michigan State University, April
11, 2007.

G. MARTINEZ PINEDO
"Nuclear Astrophysics aspects of supernovae evolution and
nucleosynthesis: Explosive nucleosynthesis in core collapse
supernovae", second CARINA Workshop on "Frontier Research in European
Nuclear Astrophysics", Spaulomont, Spa, Belgium, 25 - 28 April 2007.

G. MARTINEZ PINEDO
"Nuclear Physics Aspects of supernovae evolution and nucleosynthesis:
Nucleosynthesis of medium and heavy nuclei" seminar at the
Kernfysisch Versneller Instituut, Groningen, Netherlands, May 8, 2007.

G. MARTINEZ PINEDO
"Nuclear physics aspects of supernova evolution and Nucleosynthesis
heavy elements" lectures given at the Theoretical nuclear physics
school "Exotic Nuclei: New Challenges", Les Houches, (France) May
7-18, 2007

G. MARTINEZ PINEDO
"Weak interaction processes in stars", International Nuclear Physics
Conference, Tokyo, Japan, June 3-8, 2007.

G. MARTINEZ PINEDO

"Many-Body challenges in nuclear astrophysics", International
Conference on "Recent Progress in Many-Body Theories", Barcelona
Spain, July 16-20, 2007.

G. MARTINEZ PINEDO
"Nuclear Physics aspects of supernova evolution and nucleosynthesis:
Nucleosynthesis in neutrino heated ejecta", 3rd Japanese-German
Workshop, Frauenchiemsee, Germany, September 28 to October 2, 2007.

K. LANGANKE
7. 2. Neutrino-nucleus reactions in supernovae, NEPSE07, University of Tokyo, Japan

K. LANGANKE
16.3. Nuclear Astrophysics, Annual Meeting of the Finnish Physical
Society, Tallinn, Estonia

K. LANGANKE
5.5. Supernova and Nuclear Structure, colloquium, Universitaet Frankfurt

K. LANGANKE
16.5. Wir sind alle Sternenstaub - Wissenschaft fuer alle, GSI

K. LANGANKE
21.5. Neutrino-nucleus reactions in supernovae, FRANZ fest, FZ Karlsruhe

K. LANGANKE
23.5. Supernova and Nuclear Structure, colloquium, University of Warsaw, Poland

K. LANGANKE
28.-31.5. Lectures on Nuclear Astrophysics, ECT* School, Trento, Italy

K. LANGANKE
5.7. Supernova and Nuclear Structure, colloquium, Universitaet Muenster

K. LANGANKE
17.-20.7. Lectures on Nuclear Astrophysics, Varenna School, Varenna, Italy

K. LANGANKE
27.7. Weak-Interaction Processes in Nuclear Astrophysics, Nuclear Astrophysics 1957-2007, Caltech, Pasadena, USA

K. LANGANKE
1.8. Radioactive Ion-Beams and Nuclear Astrophysics, TRIUMF, Vancouver, Canada

K. LANGANKE
3.9. Nucleosynthesis - Making the Elements in the Universe, Mazurian Lakes Conference, Piaski, Poland

K. LANGANKE
8.11. Nuclear Astrophysics, FAIR Kick-off meeting, GSI

K. LANGANKE
9.11. Supernova and Nuclear Structure, colloquium, Universitaet Karlsruhe

K. LANGANKE
28.-30.11. Lectures on Nuclear Astrophysics, University of Uppsala, Sweden

K. LANGANKE
30.11. A FAIR Chance for Supernovae, colloquium, University of Uppsala

T. NEFF
Towards microscopic calculations of nuclear reaction rates Nuclear Physics in Astrophysics III, Dresden (Germany)
29.03.07

T. NEFF
Clustering and other exotic phenomena in nuclei Theoretical nuclear physics school "Exotic Nuclei:
New Challenges", Les Houches (France)
07-18.05.07

T. NEFF
Nuclear structure in exotic nuclei
Nuclear Structure: New Pictures in the Extended Isospin Space (NS07), Kyoto (Japan)
12.06.2007

T. NEFF
Fermionic Molecular Dynamics for Nuclear Structure and Reactions
HISS: Nuclear Theory and Astrophysics Applications, Dubna (Russia)
07-17.08.2007

T. NEFF
Shell Structure, Clustering and Halos
Atomic Cluster Collisions: structure and dynamics from the nuclear to the biological scale (ISACC 2007), GSI, Darmstadt (Germany)
19.07.2007

T. NEFF
Nuclear structure and reactions in the Fermionic Molecular Dynamics approach Clusters' 07, Stratford upon Avon (UK)
04.09.2007

T. NEFF
Shells, Clusters and Halos
The 21st Century Center-of-Excellence Program: Exploring New Science by Bridging Particle-Matter Hierarchy, Tohoku Unversity, Sendai (Japan)
13.12.2007

M.F.M.LUTZ
Theoretische Hadronenphysik FAIR from up, down to strange and charm
KHuK Jahrestagung 2007 GSI, 25. Oktober 2007

M.F.M.LUTZ
Hadrogenesis and charmed mesons
11th International Conference on Meson-Nucleon Physics and the Structure of the Nucleon\\ JÜlich, 10.-14. September 2007

M.F.M.LUTZ
Hadrogenesis and charmed mesons "Quarks in Hadrons and Nuclei", Int.
school of nuclear physics
Erice, 16.-24. September 2007

Vorlesungen 2007

B.FRIMAN
Lecturer at the HADES summer school, September 17-23, 2007
Frankfurt-GSI Research School (SS 2007)

B.FRIMAN
QCD: Concepts and Experimental Tests
(Vorlesung 4 Wochenstunden, with P. Braun-Munzinger and S. Leupold)
TU Darmstadt (WS 2007-2008)

B.FRIMAN
Einführung in die Allgemeine Relativitätstheorie
(Vorlesung 3 Wochenstunden)

B.FRIMAN
Quarkonia - Bound states of QCD, Messengers of QGP
(Seminar on "Relativistic Heavy-Ion Physics" zusammen mit P. Braun-Munzinger, H, Oeschler, K. Redlich und J. Wambach)

H.FELDMEIER
WS 2006/07 Informationstheorie und Quantenstatistik, 3+0

H.FELDMEIER
SS 2007 Kernstruktur und nukleare Astrophysik, Seminar 2
WS 2007/08 Theoretische Kernphysik, 3+1

K.LANGANKE
SS 07 Nukleare Astrophysik II
WS 07/08 Nukleare Astrophysik I

M.F.M. LUTZ
TU Darmstadt SS 2007
Einführung in die Quantenfeldtheorie

T.SCHLEGEL
WS 2007/2008 Übungen zum Kurs "Rechenmethoden zur Physik Wintersemester " (Prof. J. Wambach)

PhD, Master, Bachelor, Habilitation and Diploma theses in context of GSI-F+E-contracts

Compiled by K. Große

Andjelkovic, Zoran: **Development and Testing of a Trap and Laser System for Spectroscopy of Highly Charged Ions.** Diplom: Univ. Belgrad.

Austregesilo, Alexander: **Commissioning and performance of a prototype PixelGEM detector for COMPASS.** Diplom: TU München.

Badarch, Urnaa: **Covariant density functional theory for nuclear matter.** Dissertation: JLU Giessen.

Bäuchle, Björn: **Mach cones in heavy ion collisions.** Diplom: Johann Wolfgang Goethe-Universität Frankfurt am Main.

Barchanski, Andreas: **Simulations of Low-Frequency Electromagnetic Fields in the Human Body.** Dissertation: TU Darmstadt.

Bartz, Ulrich: **Aufbau und Untersuchung eines Vielzellendeflektors für ein Funneling-Experiment.** Diplom: J. W. Goethe-Universität Frankfurt am Main.

Bauer, Christopher: **Anwendung der 'Recoil-in-Vacuum'-Methode zur Berechnung der g(2^+_x)-Faktoren von Kernen in der Massenregion um A=130.** Bachelor: TU Darmstadt.

Beller, Jacob: **Rückschlüsse auf die Gestalt schwerer Atomkerne aus gamma-spektroskopischen Daten.** Bachelor: TU Darmstadt.

Bender, Markus: **Untersuchung der Mechanismen schwerioneninduzierter Desorption an beschleunigerrelevanten Materialien.** Dissertation: Univ. Frankfurt.

Bleibel, Johannes: **Untersuchung stark wechselwirkender Materie mittels ultrarelativistischer Schwerionenstöße.** Dissertation: Univ. Tübingen.

Brendel, Lutz: **Untersuchungen zu thermischen Effekten von RFQ-Resonatoren.** Diplom: J. W. Goethe-Universität Frankfurt am Main.

Chaudhuri, Ankur: **Carbon-cluster mass calibration at SHIPTRAP.** Dissertation: Ernst-Moritz-Arndt-Universität Greifswald.

Christ, Tassilo: **Identifikation und Analyse von e^+e^--Paaren in C+C Stößen bei 1 aGeV.** Dissertation: Technische Universität München.

Clemente, Gianluigi: **The Room Temperature CH-DTL and its Application for the FAIR Proton Injector.** Dissertation: J. W. Goethe-Universität Frankfurt am Main.

Costa-Fraga, Rui: **Untersuchung laserinduzierter Plasmen unter Verwendung eines kryogenischen H2 Cluster- und Tröpfchentargets.** Diplom: Frankfurt.

Dangwal, Arti: **Enhanced Field Emission from Metallic Surfaces and Nanowires.** Dissertation: Bergische Universität Wuppertal.

Deppert, Oliver: **Bestimmung der Abklingzeit eines UV Strahlungskonverters.** Bachelor: TU Darmstadt.

Doornenbal, Pieter: **In-beam gamma-ray spectrocopy of two-step fragmentation reactions at relativistic energies – The case of ^{36}Ca.** Dissertation: Universität zu Köln.

Dvorak, Jan: **Decay properties of nuclei close to Z=108 and N=162.** Dissertation: Technische Universität München.

Eitel, Georg: **Aufbau eines ortsauflösenden Ionennachweisdetektors für die Penningfallen-Massenspektrometrie.** Diplom: Johannes Gutenberg-Universität Mainz.

El-Hayek, Youssef: **Zeitaufgelöste Messung der Ionenbunche am GSI-Unilac Beschleuniger.** Bachelor: TU Darmstadt.

Erler, Jochen: **Ein stabilisiertes Paarfunktional.** Diplom: Erlangen.

Fischer, Philipp: **Ein Hochleistungs-RFQ-Beschleuniger für Deuteronen.** Dissertation: J. W. Goethe-Universität Frankfurt am Main.

Frederick Kramer: **Studie zur Messung von Quarkonia mit dem ALICE-TRD und Aufbau eines Teststandes für seine Auslesekammern.** Diplom: J.W. Goethe Universität Frankfurt.

Froehlich, Stefan: **Zum Einfluss von Diskretisierungseffekten und endlichen Volumina auf mesonische Korrelatoren bei hohen Temperaturen.** Diplom: Bielefeld.

Gabor, Christoph: **Untersuchungen zur zerstörungsfreien Emittanzmessung an einem negativen Wasserstoffionenstrahl.** Dissertation: J. W. Goethe-Universität Frankfurt am Main.

Garcia, Rafael Ferrer: **Mass measurements on neutron-deficient nuclides at SHIPTRAP and commissioning of a cryogenic narrow-band FT-ICR mass spectrometer.** Dissertation: Johannes Gutenberg-Universität Mainz.

Gögelein, Peter: **Nuclear Structure for the Crust of Neutron Stars and Exotic Nuclei.** Dissertation: Eberhard Karls Universität Tübingen.

Harres, Knut: **Experimentelle Bestimmung des Energiespektrums von lasererzeugten MeV Ionenstrahlen mit Hilfe einer**

Thomson- Parabel. Diplom: TU Darmstadt.

Hartmann, Frank: **Nichtflüchtige, hardwareeffiziente Realisierung einer Kennlinie auf einem FPGA.** Diplom: Hochschule Fulda.

Haussler, Stephane: **Fluctuations in Ultra-Relativistic Heavy Ion Collisions from Microscopic Descriptions.** Dissertation: Johann Wolfgang Goethe-Universität Frankfurt am Main.

Hebeler, Kai: **Renormalization group approach to superfluid neutron matter.** Dissertation: Universität Darmstadt.

Hempel, Matthias: **Die äußere Kruste kalter Neutronensterne.** Diplom: Frankfurt am Main.

Huber, Tina: **Ion Backflow Studies with a Triple GEM Detector.** Master: TU München.

Kirschner, Daniel Georg: **Level 3 Trigger Algorithm and Hardware Platform for the HADES-Experiment.** Dissertation: Justus-Liebig-Universität Gießen.

Kober, Martin: **Betrachtungen jenseits des Standardmodells der Teilchenphysik. Gravitation unter Einbeziehung zusätzlicher Dimensionen und nichtkommutative Geometrie.** Diplom: Johann Wolfgang Goethe-Universität Frankfurt am Main.

Koch, Benjamin: **Black hole production and graviton emission in models with large extra dimensions.** Dissertation: Johann Wolfgang Goethe-Universität Frankfurt am Main.

Kracke, Holger: **Entwicklung der kryogenen Nachweis-Elektronik zur Bestimmung der axialen Frequenz des Protons in einer Penning-Falle.** Diplom: Johannes Gutenberg-Universität Mainz.

Krämer, Jörg: **Aufbau und Test einer Ionenfalle für die Laserspektroskopie an hochgeladenen Ionen.** Diplom: Johannes Gutenberg-Universität Mainz.

Kraus, Dominik: **Kalibrierung radiochromatischer Filme zur Anwendung in der Laser-Ionenbeschleunigung.** Bachelor: TU Darmstadt.

Ling, Johannes: **Kontaktfreie Messung der Leitfähigkeit Schwerionengetriebener Targets.** Diplom: TU-Darmstadt.

Maier, Ludwig W.: **Speicherringexperiment zum gebundenen Beta-Zerfall vollständig ionisierter ^{207}Tl Kerne.** Dissertation: Technische Universität München.

Malekzadeh, Hossein: **Three Flavor Color Superconductivity.** Dissertation: Frankfurt am Main.

Mitrovski, Michael K.: **Energy and System Size Dependence of Ξ^- and Ξ^+ Production in Relativistic Heavy-Ion Collisions at the CERN-SPS.** Dissertation: J. W. Goethe Universität Frankfurt.

Möller, Matthias: **Antikaons in infinite nuclear matter and nuclei.** Dissertation: Universität Darmstadt.

Möllers, Bernd: **Elektronenkühlung hochgeladener Ionen in Penningfallen.** Dissertation: Universität Erlangen.

Nicmorus, Diana: **Electromagnetic Properties of Light and Heavy Baryons in the Relativistic Quark Model.** Dissertation: Univ. Tübingen.

Nillius, Fabian: **Auf dem Weg zur Speicherung von Antiwasserstoff in einer magnetischen Neutralatomfalle.** Diplom: Johannes Gutenberg-Universität Mainz.

Nörenberg, Ralf: **Aufbau und Test einer COLTRIMS Apparatur zur Untersuchung der Ionisation von metastabilem Helium.** Diplom: Frankfurt.

Nofal, Muaffaq: **Projectile Continuum Electrons in the Short Wavelength Limit of Electron-Nucleus Bremsstrahlung Studied in the Collision of 90 MeV/u U^{88+} with a N_2 Target.** Dissertation: Frankfurt.

Noronha, Jorge: **The Role of Gauge Fields in Color Superconductivity.** Dissertation: Frankfurt am Main.

Nürnberg, Frank: **Vollständige Rekonstruktion und Transportsimulation eines laserbeschleunigten Protonenstrahls unter Verwendung von mikrostrukturierten Targetfolien und radiochromatischen Filmdetektoren.** Diplom: TU Darmstadt.

Nzouekon, Cyrille Joel: **Implementierung einer Kommunikations-Schnittstelle zu einem Flash-Baustein für einen direkten Speicherzugriff auf einem FPGA.** Diplom: Hochschule Fulda.

Ottamendi, Joseba Alonso: **Development of an Experiment for Ultrahigh-Precision g-Factor Measurements in a Penning-Trap Setup.** Dissertation: Johannes Gutenberg-Universität Mainz.

Otten, Anke: **Modellierung des Ausleseprozesses von CR- Bildplatten.** Diplom: TU Darmstadt.

Parganlija, Denis: **Pion-Pion Streuung in einem geeichten chiralen linearen Sigma-Modell.** Diplom: Frankfurt am Main.

Petridis, Nikos: **Anwendung eines kryogenischen Helium-Mikrojets als Target zur laserinduzierten Plasmaerzeugung.** Diplom: Frankfurt.

Petzenhauser, Isfried: **Untersuchungen an mehrstufigen Pseudofunkenschaltern für den Kickermagneten des SIS 100/300 Schwerionensynchrotrons der GSI.** Dissertation: Friedrich-Alexander-Universität Erlangen-Nürnberg.

Rausch, Joachim: **Realisierung einer für FPGA-Architekturen optimierten Kennlinie mittels linearer Interpolation.** Diplom: Hochschule Fulda.

Riek, Felix: **Mesonic and isobar modes in matter.** Dissertation: Universität Darmstadt.

Sailer, Benjamin: **Inklusive e^+e^--Paarproduktion in pp-Reaktionen bei E_kin=2.2 GeV.** Dissertation: Technische Universität München.

Santini, Elvira: **Vector Mesons in Medium and Dilepton Production in Heavy Ion Collisions at Intermediate Energies.** Dissertation: Univ. Tübingen.

Schaumann, Gabriel: **Experimente mit lasergeheizten Hohlräumen für die Wechselwirkung von Schwerionen mit ionisierter Materie.** Dissertation: TU Darmstadt.

Schmid, Mirko von: **Konzeption und Entwicklung segmentierter Detektoren aus Solarzellen zum Nachweis ionisierter Teilchen.** Bachelor: TU Darmstadt.

Schmidt, Roland: **Computer Simulation of a DISC-DIRC Cherenkov Dtector for PANDA.** Diplom: Justus-Liebig-Universität Gießen.

Schneider, Florian: **Construction and test of PixelGEM tracking detectors.** Master: TU München.

Schütrumpf, Jörg: **Charakterisierung eines Hochenergie-Lasersystems am Beispiel PHELIX.** Diplom: TU Darmstadt.

Schuster, Tim: **Production of Neutral Strange Hadrons with High Transverse Momentum in Pb+Pb Collisions at 158AGeV.** Diplom: J. W. Goethe Universität Frankfurt.

Silze, Alexandra: **Ionisationsdynamik im hochdichten Elektronenstrahl einer Dresden EBIS.** Diplom: Technische Universität Dresden.

Skowron, Judith: **Die Empfindlichkeit der in-beam PET-Methode für den Nachweis von Reichweiteabweichungen bei der Ionentherapie.** Master: Technische Universität Dresden.

Stach, Daniel: **Entwicklung und Test von Widerstand-splattenzählern hoher Ratenfestigkeit und Zeitauflösung.** Diplom: HTW Dresden.

Stang, Denise: **Konzeption und Entwicklung eines Abbildungssystems für Laserthomsonstreuung an heißen dichten Plasmen.** Bachelor: TU Darmstadt.

Strabel, Claudia: **Energieabhängigkeit der K0s Produktion in zentralen Pb+Pb Reaktionen.** Diplom: J.W. Goethe Universität Frankfurt.

Teske, Christian: **Erzeugung und Diagnostik eines HF-Plasmas in einem statischen magnetischen Quadrupolfeld.** Dissertation: JWG-Universität Frankfurt.

Thibius, Jan-Paul: **Numerische Berechnungen aus Ionenstrahl-Funneling.** Dissertation: J. W. Goethe-Universität Frankfurt am Main.

Vossberg, Markus: **Wiederaufbau, Inbetriebnahme und Optimierung des Frankfurter Funneling-Experiments.** Diplom: J. W. Goethe-Universität Frankfurt am Main.

Weber, Michael: **Simulationen zum e^+e^- Nachweis mit dem HADES RICH für Projektilenergien bis 15 AGeV.** Diplom: Technische Universität München.

Patents and patent applications

Compiled by: M. Hensel

Granted Patents

P 220
Strahlzuteilungsverfahren für medizinische Teilchenbeschleuniger.
Europa, 07.03.2007.
Naumann, Jakob; Poppensieker, Klaus

P 168
Vorrichtung zur Erzeugung und zum Auswählen von Ionen die in einer Schwerionen-Krebstherapie-Anlage verwendet werden.
Europa, 04.04.2007.
Dahl, Ludwig; Schlitt, Bernhard

P 175
Detector for detecting particle beams and method for the production thereof.
China,Europa, USA. 11.04.2007, 08.08.2007, 25.09.2007.
Berdermann, Eleni; De Boer, Wim

P 158
Ion beam system for irradiating tumour tissues.
China, 18.04.2007.
Kraft, Gerhard

P 163
Verfahren zur Partialdruck-Kalibrierung von Quadrupol-Massenspektrometern und Kalibriereinrichtung dazu.
Deutschland, 26.04.2007.
Rau, Matthias; Jakoby, Wolfgang; Heil, Jürgen; Lauck, Andreas

P 217
Supraconductive cable and method for the production thereof.
Singapur, 30.05.2007.
Fischer, Egbert; Khodghibagiyan, Hamlet; Kovalenko, Alexander; Moritz, Gebhard

P 108
Abgeschirmter Raum für die Ionentherapie mit Abschirmwirkung für Neutronen bis in den Energiebereich GEV.
Europa, 25.07.2007.
Fehrenbacher, Georg; Gutermuth, Frank; Radon, Torsten

P 169
Apparatus for pre-acceleration of ion beams used in a heavy ion beam application system.
Japan, 10.08.2007.
Bechthold, Alexander; Ratziner, Ulrich; Schempp, Alwin; Schlitt, Bernhard

P 177
Verfahren zur Herstellung von Nanostrukturen in Membranen und asymmetrische Membran.
Europa, 26.09.2007.
Siwy, Zuzanna; Dobrev, Dobri; Neumann, Reinhard; Trautmann, Christina; Voss, Kai

P 145
Ionisationskammer für Ionenstrahlen.
Europa, 14.11.2007.
Stelzer, Herbert; Voss, Bernd

P 184
Drucksensorauslösbare Schnellverschlusseinrichtung.
Deutschland, 29.11.2007.
Behr, Karl-Heinz; Jäger, Egon; Mendel, Matthias; Schimpf, Erwin

Patent applications

P 239
Feldemissionsquelle für Elektronen als Feldemissionskathode.
Deutschland, 02.03.2007.
Alonso, Joseba; Blaum, Klaus; Brötz, Joachim; Maurer, Florian; Quint, Wolfgang; Schabinger, Birgit; Trautmann, Christina; Ulmer, Stefan

P 242
Bestimmung von Steuerparametern für eine Bestrahlung eines bewegten Zielvolumens in einem Körper.
Deutschland, 23.03.2007.
Bert, Christoph; Kraft, Gerhard; Rietzel, Eike

P 241
Bestimmung eines Planungsvolumens für eine Bestrahlung eines Körpers.
Deutschland, 23.03.2007.
Bert, Christoph; Kraft, Gerhard; Rietzel, Eike

P 240
Zeit-Amplituden-Konverter-Bauelement.
Deutschland, 08.06.2007.
Deppe, Harald; Flemming, Holger

International and national collaborations *

Compiled by K. Große

The FAIR Collaborations

FAIR: The BIOMAT Collaboration

The High-Energy Irradiation Facility for Biophysics and Materials Research
Spokespersons: M. Durante, Naples (Italy)/Darmstadt (Germany); S. Klaumünzer, Berlin (Germany)

Contributions in this report:
RADIATION-BIOPHYSICS-33

FAIR: The CBM Collaboration

The Condensed Baryonic Matter experiment
<http://www.gsi.de/zukunftsprojekt/experimente/CBM/index_e.html>
Spokesperson: P. Senger Darmstadt (Germany)

Contributions in this report:
FAIR-EXPERIMENTS-02
FAIR-EXPERIMENTS-03
FAIR-EXPERIMENTS-04
FAIR-EXPERIMENTS-05
FAIR-EXPERIMENTS-06
FAIR-EXPERIMENTS-07
FAIR-EXPERIMENTS-08
FAIR-EXPERIMENTS-09
FAIR-EXPERIMENTS-10
FAIR-EXPERIMENTS-11
FAIR-EXPERIMENTS-12
FAIR-EXPERIMENTS-13
FAIR-EXPERIMENTS-14
FAIR-EXPERIMENTS-15
FAIR-EXPERIMENTS-16
FAIR-EXPERIMENTS-17
FAIR-EXPERIMENTS-18
FAIR-EXPERIMENTS-19
FAIR-EXPERIMENTS-20
FAIR-EXPERIMENTS-21
FAIR-EXPERIMENTS-22
FAIR-EXPERIMENTS-23
FAIR-EXPERIMENTS-24
FAIR-EXPERIMENTS-25
INSTRUMENTS-METHODS-30
INSTRUMENTS-METHODS-44
INSTRUMENTS-METHODS-53
INSTRUMENTS-METHODS-54

FAIR: The FLAIR Collaboration

A Facility for Low-energy Antiproton and Ion Research
< http://www-linux.gsi.de/∼flair/>
Spokesperson: E. Widmann (Austria)

Contributions in this report:
ATOMIC-PHYSICS-26
FAIR-EXPERIMENTS-42
FAIR-EXPERIMENTS-43
FAIR-EXPERIMENTS-44
FAIR-EXPERIMENTS-45

FAIR: The HEDgeHOB Collaboration

High Energy Density Matter generated by Heavy iOn Beams
<http://hedgehob.physik.tu-darmstadt.de>
Spokesperson: Hoffmann, D. H. H., Darmstadt (Germany)

Contributions in this report:
FAIR-EXPERIMENTS-38
PLPY-PHELIX-18

The PANDA Collaboration

<http://www.ep1.rub.de/∼panda/auto/_home.htm>
Spokesperson: U. Wiedner, Uppsala (Sweden)
Contributions in this report:

FAIR-EXPERIMENTS-26
FAIR-EXPERIMENTS-27
FAIR-EXPERIMENTS-28
FAIR-EXPERIMENTS-29
FAIR-EXPERIMENTS-30
FAIR-EXPERIMENTS-31
FAIR-EXPERIMENTS-32
FAIR-EXPERIMENTS-33
FAIR-EXPERIMENTS-34
FAIR-EXPERIMENTS-35
FAIR-EXPERIMENTS-36
FAIR-EXPERIMENTS-37
INSTRUMENTS-METHODS-29

* Only listed are colloborations contributed to this report.

FAIR: The NUSTAR Collaboration

International Nuclear Structure and Astrophysics Community GSI
<http://www.gsi.de/forschung/kp/kp2/nustar.html>

As part of FAIR-NUSTAR: The HISPEC Collaboration

High resolution Spectroscopy
Spokesperson: Z. Podolyak, Surrey (United Kingdom)

Contributions in this report:
INSTRUMENTS-METHODS-09
INSTRUMENTS-METHODS-13
INSTRUMENTS-METHODS-14

As part of FAIR-NUSTAR: The R^3B Collaboration

Reactions with Relativistic Radioactive Beams
<http://www-land.gsi.de/r3b/>
Spokesperson: T. Aumann Darmstadt (Germany)

Contributions in this report:
INSTRUMENTS-METHODS-10
INSTRUMENTS-METHODS-11

As part of FAIR-NUSTAR: The ELISe Collaboration

ELectron-Ion Scattering in a Storage Ring (eA collider)
<http://www.gsi.de/zukunftsprojekt/experimente/elise/>
Spokesperson: H. Simon, Darmstadt (Germany)

Contribution in this report:
FAIR-EXPERIMENTS-40
FAIR-EXPERIMENTS-41
NUSTAR-THEORY-09

As part of FAIR-NUSTAR: The EXL Collaboration

Exotic nuclei studied in light-ion induced reactions at the NESR storage ring
<http://ns.ph.liv.ac.uk/∼mc/EXL/collaboration/EXL-collaboration.html>
Spokesperson: M. Chartier, Liverpool (United Kingdom)

Contributions in this report:
INSTRUMENTS-METHODS-12

As part of FAIR-NUSTAR: The ILIMA Collaboration

Contributions in this report:
NUSTAR-THEORY-08

As part of FAIR-NUSTAR: The Super-FRS Collaboration

Contributions in this report:
INSTRUMENTS-METHODS-08
INSTRUMENTS-METHODS-41

FAIR: The SPARC Collaboration

Stored Particles Atomic Physics Collaboration
<http://www.gsi.de/zukunftsprojekt/experimente/sparc/index_e.html>
Spokesperson: R. Schuch, Stockholm (Sweden)

Contributions in this report:
ATOMIC-PHYSICS-02
ATOMIC-PHYSICS-03
ATOMIC-PHYSICS-04
ATOMIC-PHYSICS-19
ATOMIC-PHYSICS-23
ATOMIC-PHYSICS-24
ATOMIC-PHYSICS-28
ATOMIC-PHYSICS-32

FAIR: The WDM Collaboration

Radiative Properties of Warm Dense Matter Produced by Intense Heavy Ion Beams
<http://www.gsi.de/phelix/Experiments/FAIR/WDM/index.html>
Spokesperson: F. B. Rosmej

Contributions in this report:
PLPY-PHELIX-11

FAIR: The FAIR Plasma Physics Collaboration

Contributions in this report:
INSTRUMENTS-METHODS-03
INSTRUMENTS-METHODS-45
PLPY-PHELIX-06

The SIS/ESR/UNILAC Collaborations

The ALADiN 2000 Collaboration

<http://www-kp3.gsi.de/www/kp3/aladinhome.html>
Spokesperson: W. Trautmann, Darmstadt (Germany)

Contributions in this report:
NQMA-EXPERIMENTS-05
NQMA-EXPERIMENTS-06
NQMA-EXPERIMENTS-07
NQMA-EXPERIMENTS-08
NQMA-EXPERIMENTS-09

FAIR: The CHARMS Collaboration

Collaboration for High-Accuracy Experiments on Nuclear Reaction Mechanisms with magnetic Spectrometers
<http://www.gsi.de/charms/>
Spokesperson: Karl-Heinz Schmidt, GSI

Contributions in this report:
NUSTAR-EXPERIMENTS-07
NUSTAR-EXPERIMENTS-08
NQMA-EXPERIMENTS-02
NQMA-EXPERIMENTS-03

The FOPI Collaboration

4π Detector System for Charged Particles
<http://www-fopi.gsi.de/>
Spokesperson: N. Herrmann, Heidelberg (Germany)

Contributions in this report:
NQMA-EXPERIMENTS-12
NQMA-EXPERIMENTS-13
INSTRUMENTS-METHODS-20
INSTRUMENTS-METHODS-21
INSTRUMENTS-METHODS-23
INSTRUMENTS-METHODS-48

The FRS Collaboration

Contributions in this report:

NUSTAR-EXPERIMENTS-05
NUSTAR-EXPERIMENTS-13

The HADES Collaboration

<http://www-hades.gsi.de>
Spokesperson: Salabura, P.

Contributions in this report:
NQMA-EXPERIMENTS-14
NQMA-EXPERIMENTS-15
INSTRUMENTS-METHODS-26
INSTRUMENTS-METHODS-27
INSTRUMENTS-METHODS-51
INSTRUMENTS-METHODS-55

The HITRAP Collaboration

HITRAP - A Facility for Experiments with Heavy Highly Charged Ions and Antiprotons
< http://www.gsi.de/forschung/ap/projects/hitrap/index.html>
Technical Coordinator: O. Kester (GSI), Scientific Coordinator: W. Quint (GSI)

Contributions in this report:
GSI-ACCELERATORS-12
GSI-ACCELERATORS-20
ATOMIC-PHYSICS-15
ATOMIC-PHYSICS-16
ATOMIC-PHYSICS-17
ATOMIC-PHYSICS-18
ATOMIC-PHYSICS-20
ATOMIC-PHYSICS-21
ATOMIC-PHYSICS-22
ATOMIC-PHYSICS-25

The PHELIX Collaboration

Petawatt High-Energy Laser for Heavy Ion Experiments
<http://www.gsi.de/forschung/phelix>
Spokesperson: K. Witte (GSI)

Contributions in this report:
PLPY-PHELIX-12
PLPY-PHELIX-13
PLPY-PHELIX-15
PLPY-PHELIX-16

The LAND-FRS Collaboration

Large Area Neutron time of flight Detector – Fragment Separator
Spokesperson: T. Aumann, Darmstadt (Germany)

Contributions in this report:
INSTRUMENTS-METHODS-19

The NoRDia Collaboration

Novel Radiation Hard CVD Diamond Detectors for Hadron Physics
<http://www-norhdia.gsi.de>
Cordinator at GSI: E. Berdermann.

Contributions in this report:
INSTRUMENTS-METHODS-01
INSTRUMENTS-METHODS-25

The RISING Collaboration

<http://www-linux.gsi.de/EB_at_GSI/index.html>
Spokesperson: H.-J. Wollersheim, GSI, Darmstadt (Germany)
Contributions in this report:
NUSTAR-EXPERIMENTS-09
NUSTAR-EXPERIMENTS-10

The SHIP Collaboration

Separator for Heavy Ion reaction Products
<http:/www.gsi.de/forschung/kp/kp2/ship/>
Spokesperson: S. Hofmann, GSI Contributions in this report:
NUSTAR-SHE-05
NUSTAR-SHE-06
NUSTAR-SHE-07
NUSTAR-SHE-08
NUSTAR-SHE-10

The SHIPTRAP Collaboration

<http://www.gsi.de/forschung/ap/projects/shiptrap/>
Spokesperson: F. Herfurth, Darmstadt (Germany)
Contributions in this report:
NUSTAR-SHE-09
INSTRUMENTS-METHODS-04
INSTRUMENTS-METHODS-05

The TASCA Collaboration

Transactinide Separator and Chemistry Apparatus
<http://www.gsi.de/tasca/>
Spokesperson: M. Schädel, GSI

Contributions in this report:
NUSTAR-SHE-11
NUSTAR-SHE-12

Other collaborations e. g. at external institutions

The ALICE Collaboration

A Large Ion Collider Experiment at CERN LHC
<http://alice.web.cern.ch/Alice/AliceNew/collaboration/>
The collaborations contains 27 countries, 83 institutes, and about 1000 members. Here only the participants of the GSI are listed.
Leader at the GSI: P. Braun-Munzinger

Contributions in this report:
NQMA-EXPERIMENTS-19
INSTRUMENTS-METHODS-58

The ALICE TRD Collaboration

The Transition Radiation Detector of the ALICE experiment at LHC
<http://www-alice.gsi.de/trd>
Project leader: J. Stachel, Heidelberg (Germany)
Contributions in this report:
NQMA-EXPERIMENTS-20
NQMA-EXPERIMENTS-21
NQMA-EXPERIMENTS-22
INSTRUMENTS-METHODS-31
INSTRUMENTS-METHODS-32
INSTRUMENTS-METHODS-33
INSTRUMENTS-METHODS-34
INSTRUMENTS-METHODS-35
INSTRUMENTS-METHODS-36
INSTRUMENTS-METHODS-37
INSTRUMENTS-METHODS-38

The CERES Collaboration

Cherenkov Ring Electron Pair Spectrometer at the CERN SPS
<http://www.physi.uni-heidelberg.de/physi/ceres/>
Spokesperson: J. Stachel, Heidelberg (Germany)

Contributions in this report:
NQMA-EXPERIMENTS-17
NQMA-EXPERIMENTS-18

HIT: The Heidelberg Ionenstrahl-Therapiezentrum Collaboration

Contributions in this report:
EXTERNAL-HIT-01
EXTERNAL-HIT-02
EXTERNAL-HIT-03

The NA49 Collaboration

Large Acceptance Hadron Detector for an Investigation of Pb-induced Reactions at the CERN SPS
<http://na49info.cern.ch/>
Spokesperson: P. Seyboth

Contributions in this report:
NQMA-EXPERIMENTS-16

The ISOLTRAP Collaboration

<http://isoltrap.web.cern.ch/isoltrap>

Contributions in this report:
ATOMIC-PHYSICS-13

Other collaborations:

GSI-ACCELERATORS-02
NUSTAR-EXPERIMENTS-11
INSTRUMENTS-METHODS-15
INSTRUMENTS-METHODS-17
PLPY-PHELIX-09
MATERIALS-06
RADIATION-BIOPHYSICS-10
RADIATION-BIOPHYSICS-14
RADIATION-BIOPHYSICS-23

Connections between contributions to this report and experiment numbers at the GSI accelerators

BIO07 RADIATION-BIOPHYSICS-03
BIO07 RADIATION-BIOPHYSICS-04
BIO14 RADIATION-BIOPHYSICS-11
BIO15 RADIATION-BIOPHYSICS-12
BIO16 RADIATION-BIOPHYSICS-02
E065 ATOMIC-PHYSICS-07
E067 ATOMIC-PHYSICS-10
E070 ATOMIC-PHYSICS-06
E075 ATOMIC-PHYSICS-15
E075 ATOMIC-PHYSICS-16
E075 ATOMIC-PHYSICS-22
E075 ATOMIC-PHYSICS-25
S104 NQMA-EXPERIMENTS-04
S114 NQMA-EXPERIMENTS-05
S185 NQMA-EXPERIMENTS-07
S185 NQMA-EXPERIMENTS-08
S244 NUSTAR-EXPERIMENTS-09
S244 NUSTAR-EXPERIMENTS-10
S245 NUSTAR-EXPERIMENTS-01
S245 NUSTAR-EXPERIMENTS-12
S254 NQMA-EXPERIMENTS-06
S254 NQMA-EXPERIMENTS-09
S266 NUSTAR-EXPERIMENTS-07
S271 NUSTAR-EXPERIMENTS-02
S276 NQMA-EXPERIMENTS-02
S277 NUSTAR-EXPERIMENTS-11
S279 NQMA-EXPERIMENTS-12
S280 INSTRUMENTS-METHODS-25
S294 NUSTAR-EXPERIMENTS-08
S313 NUSTAR-EXPERIMENTS-09
S319 INSTRUMENTS-METHODS-15
S319 INSTRUMENTS-METHODS-16
S319 INSTRUMENTS-METHODS-17
S319 INSTRUMENTS-METHODS-18
S319 NUSTAR-EXPERIMENTS-14
S322 NUSTAR-EXPERIMENTS-13
S325 INSTRUMENTS-METHODS-20
S331 PLPY-PHELIX-18
S333 INSTRUMENTS-METHODS-27
S349 INSTRUMENTS-METHODS-23
SBIO08 RADIATION-BIOPHYSICS-15
SBIO08 RADIATION-BIOPHYSICS-16
SBIO09 RADIATION-BIOPHYSICS-13
SBIO RADIATION-BIOPHYSICS-28
SBIO RADIATION-BIOPHYSICS-33
SMAT MATERIALS-01
SMAT MATERIALS-02
SMAT MATERIALS-03
STHE RADIATION-BIOPHYSICS-19
U165 ATOMIC-PHYSICS-12
U182 NUSTAR-SHE-12
U207 NUSTAR-SHE-10
U217 NUSTAR-SHE-09
U219 NUSTAR-SHE-11
U223 NUSTAR-SHE-01
U224 INSTRUMENTS-METHODS-03
U224 PLPY-PHELIX-06
U225 NUSTAR-SHE-05
U226 PLPY-PHELIX-01
UBIO14 RADIATION-BIOPHYSICS-07
UMAT MATERIALS-04
UMAT MATERIALS-05
UMAT MATERIALS-06
UMAT MATERIALS-07
UMAT MATERIALS-08
UMAT MATERIALS-10
UMAT MATERIALS-11
UMAT MATERIALS-12
UMAT MATERIALS-13
UMAT MATERIALS-15
UMAT MATERIALS-16
UMAT MATERIALS-17
UMAT MATERIALS-18
UMAT MATERIALS-19
UMAT MATERIALS-20
UMAT MATERIALS-21
UMAT MATERIALS-22
UMAT MATERIALS-23
UMAT MATERIALS-24
UMAT MATERIALS-25

GSI Projektträger / KKS

D. Müller

Projektträger des Bundesministeriums für Bildung und Forschung (BMBF)

GSI is the managing institution for the BMBF project funding (so called "Verbundforschung") in the field of "Hadron- and Nuclear Physics". These public funds are foreseen to support research groups at universities in Germany to strengthen their ability to participate in experiments and projects performed at scientific institutions like GSI and CERN which are funded to a significant level from federal resources.

BMBF project funding: 110 running projects with a total budget of 44,1 Mio. € (13,4 Mio. € in 2007).

GSI F&E contracts ("Forschungs- und Entwicklungsvereinbarungen")

Since 1969 GSI has special research and development contracts with German universities to strengthen the collaboration between these universities and GSI. Mainly resources for personnel are provided to enhance the participation of PhD students and young Post-Docs within GSI projects.

GSI F&E Contracts: 97 running projects with a total budget of 12,0 Mio. € (4,1 Mio. € in 2007).

Helmholtz Association "Initiative and Networking Fund (IVF)"

This fund is one of the Helmholtz Association's key instruments in achieving its strategic goals in Research and Innovation. It consists mainly of "Helmholtz Virtual Institutes" (Networks between GSI and University groups) and a programm to promote Young Researchers.

GSI-HGF-IVF: 8 running projects with a total budget of 7,0 Mio. € (1,1 Mio. € in 2007).

EU Framework Programm 6, EURONS

GSI is the managing institution for the European Integrated Infrastructure Initiative (I3) in nuclear structure physics (EURONS). It consists of 44 institutions in 21 countries.

EURONS: 27 projects with a total budget of 14,0 Mio. € (4,2 Mio. € in 2007).

EU projects at GSI

Compiled by R. Simon, M. Pantea, K. Große

FAIR Design Study 'DIRACsecondary-Beams'/FP6 (515873)
<http://www.gsi.de/fair/EU-Design-Study/index.html>
Coordinator: GSI, Darmstadt (Germany)
Project coordinator: J. Eschke
Steering committee: J. Eschke (GSI, chair), H. H. Gutbrod (GSI), W. F. Henning/H. Stöcker (GSI), P. Gianotti (Frascati), R. Krücken (München), R. Maier (FZJ), B. Franzke (GSI), D. Krämer (GSI)
Contact at GSI: J. Eschke, K. Berghöfer, F. Weißbach

Contributions in this report:
FAIR-ACCELERATORS-04
FAIR-ACCELERATORS-08
FAIR-ACCELERATORS-13
FAIR-ACCELERATORS-14
FAIR-ACCELERATORS-15
FAIR-ACCELERATORS-16
FAIR-ACCELERATORS-18
FAIR-ACCELERATORS-25
FAIR-EXPERIMENTS-31
GSI-ACCELERATORS-08
NUSTAR-THEORY-09
INSTRUMENTS-METHODS-12

FAIR Construction 'DIRAC-PHASE 1'/FP6 (515876)
<http://www.gsi.de/fair/EU-Construction/index.html>
Coordinator: GSI, Darmstadt (Germany)
Project coordinator: J. Eschke
Steering committee: J. Eschke (GSI, chair), H. H. Gutbrod (GSI), W. F. Henning/H. Stöcker (GSI), H. Eickhoff (GSI), J.-E. Ducret (CEA), H. Ströbele (U-Frankfurt/M.)
Contact at GSI: J. Eschke, K. Berghöfer, F. Weißbach

Contribution in this report:
FAIR-EXPERIMENTS-26
GSI-ACCELERATORS-06
GSI-ACCELERATORS-15
GSI-ACCELERATORS-16
GSI-ACCELERATORS-17
INSTRUMENTS-METHODS-55

HADRONPHYSICS/FP6 (RII3-CT-2004-506078)
<http://hadronphysics.infn.it/>
Coordinator: INFN Frascati (Italy)
Project coordinator: C. Guaraldo (LNF-INFN)
Management board: M. Anselmino (INFN), B. Erazmus (CNRS/IN2P3, since 1.6.2007), M. Garcon (CEA, since 1.6.2007), T. Johansson (Univ. Uppsala), H. Koch (Univ. Bochum), L. Riccati (INFN), G. Rosner (Univ. Glasgow), P. Senger (GSI, since 19.6.2007), R. Simon (GSI, until 18.6.2007)
Project coordinator at GSI: R. Simon

Contributions in this report:
FAIR-EXPERIMENTS-02
FAIR-EXPERIMENTS-07
FAIR-EXPERIMENTS-08
FAIR-EXPERIMENTS-10
FAIR-EXPERIMENTS-11
FAIR-EXPERIMENTS-12
FAIR-EXPERIMENTS-15
FAIR-EXPERIMENTS-17
FAIR-EXPERIMENTS-18
FAIR-EXPERIMENTS-19
FAIR-EXPERIMENTS-22
FAIR-EXPERIMENTS-23
FAIR-EXPERIMENTS-35
FAIR-EXPERIMENTS-36
NQMA-EXPERIMENTS-13
NQMA-EXPERIMENTS-14
NQMA-EXPERIMENTS-15
NQMA-THEORY-02
NQMA-THEORY-03
INSTRUMENTS-METHODS-20
INSTRUMENTS-METHODS-22
INSTRUMENTS-METHODS-25
INSTRUMENTS-METHODS-29
INSTRUMENTS-METHODS-30
INSTRUMENTS-METHODS-53
INSTRUMENTS-METHODS-54

EURONS/FP6 (RII3-CT-2004-506065)
<http://www.gsi.de/informationen/jofu/EURONS/>
Coordinator: GSI, Darmstadt (Germany)
Project coordinator: A. C. Müller (IN2P3-IPNO), C. Scheidenberger (GSI, deputy coordinator)
Executive board: P. Butler (CERN), P. Van Duppen (U- Leuven), K.-D. Groß (GSI), S. Harissopoulos (NCSR Demokritos), R. Julin (Univ. Jyväskylä), S. Lenzi (INFN Padova)
Contact at GSI: I. Reinhard; M. Pantea

Contributions in this report:
GSI-ACCELERATORS-02
ATOMIC-PHYSICS-05
ATOMIC-PHYSICS-06
ATOMIC-PHYSICS-13
NUSTAR-EXPERIMENTS-02
NUSTAR-EXPERIMENTS-07
NUSTAR-EXPERIMENTS-10
NUSTAR-EXPERIMENTS-11
NUSTAR-EXPERIMENTS-12
NUSTAR-SHE-08
NUSTAR-SHE-09
NUSTAR-SHE-10
INSTRUMENTS-METHODS-09
INSTRUMENTS-METHODS-10

INSTRUMENTS-METHODS-13
INSTRUMENTS-METHODS-14
INSTRUMENTS-METHODS-41

CARE/FP6 (RII3-CT-2003-506395)
<http://esgard.lal.in2p3.fr/Project/Activities/Current/>
Coordinator: CEA Saclay (France)
Project coordinator: R. Aleksan (CEA)
Project coordinator at GSI: H. Eickhoff
Contact at GSI: L. Groening

Contributions in this report:
FAIR-ACCELERATORS-19
FAIR-ACCELERATORS-21
GSI-ACCELERATORS-04
GSI-ACCELERATORS-18
INSTRUMENTS-METHODS-46

EGEE/FP6 (INFSO-RI-508833)
<http://public.eu-egee.org/>
Coordinator: CERN (Switzerland)
Project coordinator: B. Jones (CERN), D. Kranzlmüller (CERN)
Project coordinator at GSI: P. Malzacher
Contact at GSI: P. Malzacher

Contributions in this report:
INSTRUMENTS-METHODS-57

Laserlab/FP6 (RII3-CT-2003-506350)
<http://www.laserlab-europe.net>
Coordinator: Forschungsverbund Berlin (Germany)
Project coordinator: W. Sandner (Berlin)
Project coordinator at GSI: T. Kühl
Contact at GSI: T. Kühl

Contributions in this report:
PLPY-PHELIX-12

EUROTeV/FP6 (011899 RIDS)
<http://www.eurotev.org>
Coordinator: DESY, Hamburg (Germany)
Project coordinator: E. Elsen (DESY)
Project coordinator at GSI: H. Eickhoff
Contact at GSI: P. Schütt

Cellion/FP6 (MRTN-CT-2003-503923)
Network of Excellence
<http://cellion.ifj.edu.pl>
Project coordinator: Z. Stachura (PAN)
Contact at GSI: B. Fischer

EURISOL-Design Study/FP6 (515768 RIDS)
<http://www.eurisol.org>
Coordinator: INFN-LNL (Italy)
Project coordinator: Y. Blumenfeld (IPN-Orsay)
Project coordinator at GSI: K.-H. Schmidt
Contact at GSI: A. Kelic

Contributions in this report:
ATOMIC-PHYSICS-18
NQMA-EXPERIMENTS-03
NUSTAR-EXPERIMENTS-08

EUROTRANS/FP6 (516520 F16W)
<http://nuclear-server.fzk.de/eurotrans/>
Coordinator: FZK, Karlsruhe (Germany)
Project coordinator: J. U. Knebel (NUCLEAR)
Project coordinator at GSI: K.-H. Schmidt
Contact at GSI: A. Kelic

Contributions to other EU projects:
ATOMIC-PHYSICS-25
FAIR-EXPERIMENTS-40
FAIR-EXPERIMENTS-41
INSTRUMENTS-METHODS-03
INSTRUMENTS-METHODS-17
INSTRUMENTS-METHODS-26
INSTRUMENTS-METHODS-35
MATERIALS-25
NUSTAR-THEORY-08
PLPY-PHELIX-06
RADIATION-BIOPHYSICS-10
RADIATION-BIOPHYSICS-12

Workshops, meetings, seminars and talks at the GSI in 2007

Compiled by K. Große

Juha Äystö/University of Jyväskulä: **Precision mass measurements. A new look into structure of exotic nuclei.** GSI Kolloquium, 09.01.2007.

Elena Litvinova / Muenchen: **Covariant theory of particle-vibration coupling and its application.** Theorie-Seminar, 10.01.2007.

Vladimir A. Yerokhin, MPI-K Heidelberg: **Lamb shift in highly charged ions: Recent developments and perspectives.** Atomphysik-Seminar, 10.01.2007.

G. Taucher-Scholz/GSI: **The cellular response to DNA damage: dynamics of repair proteins on heavy ion radiation tracks.** GSI Kolloquium, 16.01.2007.

Peter Sigmund, Department of Physics and Chemistry University of Southern Denmark, Odense: **Some Solved and Unsolved Problems of Heavy Ion Stopping in Matter.** Physik dichter Plasmen mit Schwerionen- und Laserstrahlen, 16.01.2007.

S. Loechner: **Beetle - Ein strahlenharter analoger Auslesechip für das LHCb-Experiment.** IT-EE-Palaver, 16.01.2007.

Theo Schlegel, GSI: **Homogenes Plasmaheizen mit Hohlraumstrahlung, Teil I.** ILIAS-Arbeitsseminar, 16.01.2007.

Andreas Rudolph, ESA Satellitenkontrollzentrum: **Die Weltraummissionen ERS und ENVISAT Erdbeobachtung für und durch Europa.** Wissenschaft für Alle, 17.01.2007.

Gregor Schiwietz, HMI Berlin: **Auger-electron Spectroscopy at the Boarder Line between Atomic and Solid-state Physics.** Atomphysik-Seminar, 17.01.2007.

Tetsuya Yamaki, Japan Atomic Energy Agency (JAEA), Takasaki, Gunma, Japan: **Preparation of Proton Exchange Membranes for Fuel Cell Applications by Ion Track Technology.** Seminar der Materialforschung, 17.01.2007.

C. Lara, S. Boettger, KIP Uni Heidelberg: **SysMES - System Management for embedded Systems.** IT-EE-Palaver, 20.01.2007.

Meeting of the Synergy Group for Front-End Electronics and Data Acquisition. 22.-23.01.2007.

J. Schanko, Fa. Microsoft, Berlin: **2007 Microsoft Office System - Mit weniger Klicks mehr erreichen.** IT-EE-Palaver, 23.01.2007.

Ken Ledingham/University of Strathclyde, Glasgow: **What is the Future for Laser Induced Particle Acceleration and Applications?** GSI Kolloquium, 23.01.2007.

Naeem A.Tahir, GSI Darmstadt: **Studies of Warm Dense Matter Using Intense Beams of Energetic Heavy Ions.** Physik dichter Plasmen mit Schwerionen- und Laserstrahlen, 23.01.2007.

Theo Schlegel, GSI: **Homogenes Plasmaheizen mit Hohlraumstrahlung, Teil II.** ILIAS-Arbeitsseminar, 23.01.2007.

Andreas Wagner, FZ Rossendorf: **Experiments with real photons for nuclear astrophysics.** NuSTAR Seminar, 24.01.2007.

C. Enss, Kirchhoff-Institut für Physik, Univ. Heidelberg: **Entwicklung und Anwendungvon metallischen magnetischen Kalorimetern.** Atomphysik-Seminar, 24.01.2007.

27th International Workshop on High Energy Density in Matter. 28.01.2007.

Franz Käppeler/Forschungszentrum Karlsruhe: **Nuclear Chronometers in Astrophysics Time Scales from Minutes to Cosmic Ages.** GSI Kolloquium, 30.01.2007.

Christian Rauth, GSI: **Precision mass measurements of neutron-deficient radionuclides at SHIPTRAP.** Atomphysik-Seminar, 31.01.2007.

Iris Dillmann, FZ Karlsruhe: **p-process simulations with an updated reaction library.** NuSTAR Seminar, 31.01.2007.

Igor Iosilevskiy, Moscow Institute of Physics and Technology: **HIB heating of porous samples for the study of thermophysics of nuclear materials.** Physik dichter Plasmen mit Schwerionen- und Laserstrahlen, 05.02.2007.

Marek Scholz, Institute of Plasma Physics and Laser Microfusion Warsaw, Poland: **Status and Prospect of MJ Plasma-Focus Experiments.** Physik dichter Plasmen mit Schwerionen- und Laserstrahlen, 06.02.2007.

Norbert Pietralla/TU Darmstadt: **Collective Nuclear States with Mixed Proton-Neutron Symmetry.** GSI Kolloquium, 06.02.2007.

V. Efremov, IHED-RAS, Moskau: **Investigation of porous matter under intense energy fluxes.** ILIAS-Arbeitsseminar, 06.02.2007.

Shyamal Chatterjee, GSI, Darmstadt: **Measurement of the Lyman-1 Transition of $^{208}Pb^{81+}$ using FOCAL Spectrometers.** Atomphysik-Seminar, 07.02.2007.

P. Spädtke, GSI: **Beam Profile Analysis at the ECR Injector Setup.** Beschleuniger-Palaver, 08.02.2007.

Diskussionsthema I: Strahlungstransport und Raytracing;

Strahlungsfelder. Diskussionsthema II: PHELIX-relevante Anregungen von der Hirscheggtagung. ILIAS-Arbeitsseminar, 13.02.2007.

Cesar Domingo Pardo, FZ Karlsruhe: **Neutron capture measurements and stellar nucleosynthesis.** NuSTAR Seminar, 14.02.2007.

Simulation Working Group Meeting. 19.02.2007.

Michael Burchard, Mineralogisches Institut der Universität Heidelberg: **Electronic Structuring on High Pressure Anvils Promises and Problems.** Seminar der Materialforschung, 20.02.2007.

Christian Weinheimer, Univ. Münster: **Low Energy Particle Detection and Low Noise Photon Counting.** Atomphysik-Seminar, 21.02.2007.

Anton Artemyev, St. Petersburg: **Relativistic and QED Effects in teh Spectra of Few-electron Ions.** Atomphysik-Seminar, 22.02.2007.

The Microdosimetric Kinetic Model (MKM) - Is this new biophysical model of cell survival useful for particle therapy? Biophysics Seminar, 22.02.2007.

J.-M. Costantini, CEA/Saclay, France: **Damage and swelling induced in yttria-stabilized zirconia by charged particle irradiations.** Seminar der Materialforschung, 27.02.2007.

P. Malzacher: **Statusbericht HEP D-Grid.** IT-EE-Palaver, 27.02.2007.

V. Basko, ITEP Moskau, zur Zeit GSI: **Self-consistent equations of radiative hydrodynamics.** ILIAS-Arbeitsseminar, 27.02.2007.

What do we learn from dilepton measurements in heavy-ion collisions? CBM Diskussions Forum, 27.02.2007.

9. CBM Collaboration Meeting. 28.02-02.03.2007.

Holger Brand: **3-Day LVOOP Workshop.** GSI-interne Fortbildung, 05.-07.03.2007.

Jens Ketelaer: **Eine Waage für einzelne Atome.** Wissenschaft für Alle, 07.03.2007.

Lucio Rossi/CERN: **The LHC superconducting magnets: the long journey to success.** GSI Kolloquium, 07.03.2007.

Harald Klingbeil, GSI: **RF Control Systems for FAIR.** Beschleuniger-Palaver, 08.03.2007.

Katarzyna Psonka, GSI: **Influence of radiation quality on fragmentation of plasmid DNA: a AFM study.** Biophysics Seminar, 08.03.2007.

Abel Blazevic, GSI: **Ionenstoppen in Laser-geheizten Targets.** ILIAS-Arbeitsseminar, 12.03.2007.

Ivan Mukha, Un. Sevilla: **Two-proton radioactivity of ^{19}Mg probed with microstrip tracking detectors at FRS.** NuSTAR Seminar, 14.03.2007.

Sergei Voloshin: **Quest for flow fluctuations.** Sondersemiar, 14.03.2007.

DESPEC Ge-Array Working Group Meeting. 19.03.2007.

Fission ELISe Meeting. 19.03.2007.

Calorimeter Working Group Meeting. 20.03.2007.

ELISe collaboration Meeting. 20.03.2007.

EXL collaboration board. 20.03.2007.

EXL collaboration council meeting. 20.03.2007.

FAIR Monthly. 20.03.2007.

HISPEC/DESPEC Collaboration Meeting. 20.03.2007.

Joint R3B/EXL collaboration board meeting. 20.03.2007.

R3B collaboration board. 20.03.2007.

NUSTAR Annual Meeting 2007. 21.03.2007.

Matthias Geissel, Sandia National Laboratories, Albuquerque: **Laser Generated High Energy Density Physics and the Status of the Z-Petawatt/ZR Projects at Sandia.** Physik dichter Plasmen mit Schwerionen- und Laserstrahlen, 22.03.2007.

Vacuum Calculations using Monte Carlo Molecular Raytracing. Beschleuniger-Palaver, 22.03.2007.

XX. PANDA Collaboration Meeting. 26.-28.03.2007.

T. Badura: **Praktischer Einstieg in EDMS.** IT-EE-Palaver, 27.03.2007.

ILIAS-Veranstaltung zu Mikhail Baskos 60. Geburtstag. ILIAS-Arbeitsseminar, 27.03.2007.

Dong-O Jeon, ORNL: **The Spallation Neutron Source Commissioning.** Beschleuniger-Palaver, 29.03.2007.

Pavel Apel, Joint Institute for Nuclear Research (JINR), Dubna, Russia: **Recent results on production and application of ion-track etched nanopores.** Seminar der Materialforschung, 03.04.2007.

Peter Mulser, TU Darmstadt: **Stoßabsorption von Laserlicht im Plasma und Bezug zu Ionenstoppen: Modelle, Stand der Dinge, ungelöste Probleme.** ILIAS-Arbeitsseminar, 03.04.2007.

Heinrich Hora, Department of Theoretical Physics, University of New South Wales, Sydney, Australia: **Petawatt-Picosekunden Laserpulse für nichtlineare-Kraft-getriebene Skin-Layer Beschleunigung von Plasmablöcken für Fusion.** Physik dichter

Plasmen mit Schwerionen- und Laserstrahlen, 16.04.2007.

Alexander Pukhov, Heinrich-Heine-Universität Düsseldorf: **Relativistic laser plasmas for particle acceleration and novel radiation sources.** Physik dichter Plasmen mit Schwerionen- und Laserstrahlen, 17.04.2007.

Teodora Baeva, Univ. Düsseldorf: **High harmonic generation from plasma: The theory of relativistic spikes and its experimental confirmation.** ILIAS-Arbeitsseminar, 17.04.2007.

Workshop on Silicon Detector Systems for the CBM Experiment. 18.-20.04.2007.

P. Spiller: **SIS18 upgrade - Auf dem Weg zum FAIR Betrieb.** Beschleuniger-Palaver, 19.04.2007.

Theo Schlegel, GSI: **Bericht über dream beams symposium at MPQ Garching und Workshop on fast ignitor physics in Paris.** ILIAS-Arbeitsseminar, 24.04.2007.

FAIR Monthly. 24.04.2007.

Till Jahnke, IKF Univ. Frankfurt: **Interference and Correlation Effects in Photoionization and Decay of.** Atomphysik-Seminar, 25.04.2007.

Udo Weinrich: **Der Heidelberger Therapiebeschleuniger - Eine GSI Erfolgsstory.** Wissenschaft für Alle, 25.04.2007.

Gudrun Lind-Albrecht, Gasteiner Heilstollen: **Radon and its therapeutic use.** Biophysics Seminar, 27.04.2007.

Workshop on low-mass electron pairs. 27.04.2007.

Paolo Russotto, INFN Laboratori Nazionali del Sud and Dipartimento di Fisica, Universit di Catania: **Dynamical emission of heavy fragments in the ^{112,124}Sn+^{58,64}Ni reactions at 35 AMeV as seen with CHIMERA.** Sonderseminar, 02.05.2007.

Stefan Schippers, Universität Gießen: **The atomic clock $^3P_0 \rightarrow {}^1S_0$ transition in Be-like ^{47}Ti^{18+}: Storage ring measurement of the hyperfine induced transition rate.** Atomphysik-Seminar, 02.05.2007.

Alex Brown, MSU: **New theoretical results for the sd and pf shell nuclei.** NuSTAR Seminar, 03.05.2007.

Eugene Polzik/Niels Bohr Institute, Copenhagen: **Quantum teleportation from light to matter.** GSI Kolloquium, 08.05.2007.

Marius Schollmeier, TU Darmstadt: **Laser-Protonenbeschleunigung mit Linienfoki.** ILIAS-Arbeitsseminar, 08.05.2007.

Stefan Karsch, MPQ: **High-Field Experiments at MPQ and Prospects for PFS and ELI.** Physik dichter Plasmen mit Schwerionen- und Laserstrahlen, 08.05.2007.

Leonti Labzovsky, St. Petersburg: **Ion Beam Polarization at Storage Rings: Production and Preservation.** Atomphysik-Seminar, 09.05.2007.

Teresa Kurtukian-Nieto: **New experimental information on beta-decay halflives of heavy neutron-rich nuclei.** NuSTAR Seminar, 09.05.2007.

A. Plotnikov, GSI: **Radiation damage studies for FAIR.** Beschleuniger-Palaver, 10.05.2007.

J. Splinter: **A pulsed nitrogen laser as a tool for DNA damage induction in vivo and a comparison with DNA damage geometry induced by heavy ions.** Biophysics Seminar, 10.05.2007.

Günther Hasinger/MPI Garching: **The fate of the universe.** GSI Kolloquium, 15.05.2007.

Karl Humer, Vienna University of Technology: **Radiation effects on insulators for fusion magnets.** Seminar der Materialforschung, 15.05.2007.

Katrin Große, Udo Meyer: **GDS GSI Document Server, eine kurze Einführung für Benutzer.** GSI-interne Fortbildung, 15.05.2007.

Kurt Schwartz, GSI: **Color center creation in LiF crystals irradiated with 5- and 10-MeV Au ions: dependence on flux and fluence.** Physik dichter Plasmen mit Schwerionen- und Laserstrahlen, 15.05.2007.

Nonideal femtosecond laser plasmas: modeling and pump-probe experiments. ILIAS-Arbeitsseminar, 15.05.2007.

Beyhan Bastin, LPC Caen: **Collapse of the N=28 shell closure in ^{42}Si.** NuSTAR Seminar, 16.05.2007.

E. Drukarev, St. Petersburg: **TBA.** Theorie-Seminar, 16.05.2007.

Karlheinz Langanke: **GSI-Forschung - Darmstadtium und die Entstehung der Elemente.** Wissenschaft für Alle, 16.05.2007.

Martin Zwierlein, Universität Mainz: **Fermionic Superfluidity with Imbalanced Spin Populations.** Atomphysik-Seminar, 16.05.2007.

P. Moritz, M. Bousonvill, GSI: **BuTiS - A Bunchphase Timing and Synchronization System.** Beschleuniger-Palaver, 16.05.2007.

J. V. Kratz: **First Annual Meeting of the GSI Users' Group.** Sonderseminar, 21.05.2007.

Leonid Dubrovinsky, Universität Bayreuth: **Chemistry at extreme conditions: from geosciences to synthesis of new materials.** Seminar der Materialforschung, 22.05.2007.
Wilfried Nörtershäuser and Klaus Blaum: **Precision at the intersection of atomic and nuclear physics (1) Laser Spectroscopy (2) Mass Measurements.** GSI Kolloquium, 22.05.2007.

FAIR Monthly. 22.05.2007.

C.P. Welsch, CERN, Geneva, Switzerland: **High Dynamic Range Beam Profile Measurements in Particle Accelerators.** Atomphysik-Seminar, 23.05.2007.

Frank Goldenbaum, FZ Jülich: **Evaporation, fission and pre-equilibrium emission in GeV proton-induced spallation reactions.** NuSTAR Seminar, 23.05.2007.

J. Verbaarschot, Stony Brook: **TBA.** Theorie-Seminar, 23.05.2007.

Beam intensity predictions for FAIR: What is behind them. Beschleuniger-Palaver, 24.05.2007.

Llewellyn-Smith/Director UKAEA Culham Division: **The Path to Fusion Power.** GSI Kolloquium, 29.05.2007.

Marco Merkel, Isilon, München: **Clustered Storage vs. klassische NAS Architekturen.** IT-EE-Palaver, 29.05.2007.

Laser-erzeugte stoßfreie elektrostatische Schocks und Ionenbeschleunigung. ILIAS-Arbeitsseminar, 29.05.2007.

Christiane Reinhardt: **Webseiten erstellen und pflegen mit dem CMS onTEAM.** GSI-interne Fortbildung, 30.05.2007.

Daniel Fischer, Stockholm University, Sweden: **Momentum spectroscopy in fast heavy-ion atom collisions.** Atomphysik-Seminar, 30.05.2007.

Valeria Pershina, GSI: **Theoretical chemistry for chemical identification of the heaviest elements.** NuSTAR Seminar, 30.05.2007.

Symposium on the Occasion of Professor Rudolf Bock's 80th Birthday. GSI Kolloquium, 30.05.2007.

Angelina Parfenova, GSI: **Lattice optimization and nonlinear dynamics studies in SIS18.** Beschleuniger-Palaver, 31.05.2007.

Sibaji Raha: **Scaling new heights: National Facility for Astroparticle Physics and Space Science at the gigh altitute station of Bose Institute, India.** Sonderveranstaltung, 31.05.2007.

A. Ipp, Heidelberg: **Non-perturbative renormalization flow at finite temperature.** Theorie-Seminar, 05.06.2007.

Frank Nürnberg, TU Darmstadt: **Space and energy resolved reconstruction of a laser accelerated proton beamusing micro-structured target foils and radiochromic film detectors.** Physik dichter Plasmen mit Schwerionen- und Laserstrahlen, 05.06.2007.

Natalia Borisenko, Lebedev Physical Institute, Moscow: **Application of plastic aerogels for undercritical density laser experiments. Diagnostics and experimental results.** ILIAS-Arbeitsseminar, 05.06.2007.

Wilfried Buchmüller/DESY: **Leptogenesis and Gravitino Dark Matter.** GSI Kolloquium, 05.06.2007.

A. Ipp, Heidelberg: **Non-perturbative renormalization flow at finite temperature.** Theorie-Seminar, 06.06.2007.

Gereon Niedner-Schatteburg, TU Kaiserslautern: **Experiments with atomic and molecular clusters in ion traps.** Atomphysik-Seminar, 06.06.2007.

Lucia-Ana Popescu, KVI: **Investigations with charge-exchange reactions at KVI.** NuSTAR Seminar, 06.06.2007.

M. Al Turany: **Status Fair Root.** IT-EE-Palaver, 12.06.2007.

Maria-Carmen Serna Moreno, ETSII, Universidad de Castilla-La Mancha, Espania: **Rayleigh-Taylor Instability in Accelerated Solids.** Physik dichter Plasmen mit Schwerionen- und Laserstrahlen, 12.06.2007.

Thomson-Streudiagnostik I: Einführung in die Lichtstreuung; Messgrößen. ILIAS-Arbeitsseminar, 12.06.2007.

Atoms and Molecules in Extreme Electromagnetic Fields: From Atto- to Femtoseconds. GSI Kolloquium, 12.06.2007.

Detlev Gotta, Institut für Kernphysik, Forschungszentrum Jülich: **X-rays from pionic and antiprotonic atoms.** Atomphysik-Seminar, 13.06.2007.

Metin Tolan, Universität Dortmund: **Geschüttelt, nicht gerührt! James Bond im Visier der Physik.** Wissenschaft für Alle, 13.06.2007.

Rene Reifarth, GSI and Uni Frankfurt: **Approaches to the s-process with neutrons and protons.** NuSTAR Seminar, 13.06.2007.

V. Flambaum, Sydney: **Variation of fundamental constants in space and time.** Theorie-Seminar, 13.06.2007.

Victor Flambaum, Univ. of New South Wales, Sydney, Australia: **Parity and Time Reversal Violation in Atoms and Test of the Standard Model.** Atomphysik-Seminar, 14.06.2007.

Helmut Dosch/MPI f. Metallforschung Stuttgart: **Ice and Water at Interfaces - New Insights with Synchrotron Light.** GSI Kolloquium, 19.06.2007.

Lichtstreuung im Plasma, Teil II: Quantitative Behandlung der spontanen Lichtstreuung im Plasma; relevante Anwendungen. ILIAS-Arbeitsseminar, 19.06.2007.

FAIR Monthly. 19.06.2007.
Ajay Kumar, GSI Darmstadt: **Measurement of atomic processes in ion-atom collisions via x-ray detection.** Atomphysik-Seminar, 20.06.2007.

Kerstin Schiebel: **Kurierbeiträge erstellen mit dem CMS onTEAM.** GSI-interne Fortbildung, 20.06.2007.

Kerstin Sonnabend, TU Darmstadt: **Nuclear astrophysics with real photons.** NuSTAR Seminar, 20.06.2007.

C. Bert et al.: **Treatment of moving tumors: Status of**

the GSI tracking system. Biophysics Seminar, 21.06.2007.

Isfried Petzenhauser, GSI: **Pseudospark Switches: Modern Accelerator Outdated Switch?** Beschleuniger-Palaver, 21.06.2007.

J. Wilbert, Klinik für Strahlentherapie, Universität Würzburg: **Tracking of thoracic tumours by means of flouroscopy and respiratory signals using a clinical linear accelerator.** Biophysics Seminar, 21.06.2007.

William G. Lynch, Department of Physics and Astronomy and National Superconducting Cyclotron Laboratory, Michigan State University, East Lansing, U.S.A.: **Probing the EOS of neutron rich matter.** Sonderseminar, 21.06.2007.

M. Schollmeier, GSI: **Laser accelerated protons.** Physik dichter Plasmen mit Schwerionen- und Laserstrahlen, 23.06.2007.

Ernst Pernicka/Institut für Ur- und Frühgeschichte Tübingen: **The Sky Disc Of Nebra: Astronomy, Archaeology And Nuclear Methods.** GSI Kolloquium, 26.06.2007.

H. Göringer: **gStore - Experimentdatenhaltung bei GSI.** IT-EE-Palaver, 26.06.2007.

Theo Schlegel, GSI: **Dream beams symposium at MPQ Garching und Workshop on fast ignitor physics in Madrid; Teil II.** ILIAS-Arbeitsseminar, 26.06.2007.

Ralf Plag, GSI and Uni Frankfurt: **From the lowest to the highest count rates with the Karlsruhe 4π BaF_2.** NuSTAR Seminar, 27.06.2007.

Richard Mawhorter, Jet Propulsion Lab. California Inst. of Technology, Pasadena: **Absolute Charge Exchange Cross Sections for Collisions of Highly-Charged Solar Wind Ions with Cometary Gases.** Atomphysik-Seminar, 28.06.2007.

XXI PANDA Collaboration Meeting. 02.-06.07.2007.

G. Pretzler, Universität Düsseldorf: **Laser-Plasmaphysik mit few-cycle-Pulsen.** Physik dichter Plasmen mit Schwerionen- und Laserstrahlen, 03.07.2007.

Dopplereffekt, Lichtdruck und Laser-Plasmainstabilitäten. ILIAS-Arbeitsseminar, 03.07.2007.

Rolf-Dieter Heuer/DESY: **The International Linear Collider: Precision Physics at the Terascale.** GSI Kolloquium, 03.07.2007.

M. Procura / Muenchen: **Nucleon properties: from lattice QCD to the chiral limit.** Theorie-Seminar, 04.07.2007.

Uwe Becker, Fritz-Haber-Institut der MPG, Berlin: **Photoelectron and Ion Spectroscopy of Atoms, Molecules and Fullerenes after Multi-Photon Ionization by FEL Radiation.** Atomphysik-Seminar, 04.07.2007.

4th International Workshop Critical Point and Onset of Deconfinement (CPOD 2007). 09.-13.07.2007.

A. G. Ramm, Kansas State University: **Wave scattering by small impedance particles in a medium.** ILIAS-Arbeitsseminar, 10.07.2007.

Robert Janssens/Argonne National Laboratory: **The Hunt for New Shell Structure in Neutron-Rich Nuclei: Physicsa la Emling.** GSI Kolloquium, 10.07.2007.

Stephan Fritzsche, GSI: **Atomic calculations for multiple and highly-charged ions.** Physik dichter Plasmen mit Schwerionen- und Laserstrahlen, 10.07.2007.

Stephan Oberstedt, EC-JRC, Geel: **Shape isomers - an access to the nuclear energy landscape.** NuSTAR Seminar, 11.07.2007.

Susanne Kreim, Universität Mainz: **Towards a direct measurement of the g-factor of a single isolated (anti)proton in a double Penning trap.** Atomphysik-Seminar, 11.07.2007.

T. Janka / Muenchen: **How do massive stars explode? News on a long-standing problem.** Theorie-Seminar, 11.07.2007.

Christian Stöckl, Laboratory for Laser Energetics (LLE,) Rochester/USA: **Update on the research at the Laboratory for Laser Energetics.** Physik dichter Plasmen mit Schwerionen- und Laserstrahlen, 12.07.2007.

Lokesh C Tribedi, Tata Institute of Fundamental Research, Mumbai, India: **Fast ion collisions with Molecules: Special features.** Atomphysik-Seminar, 12.07.2007.

Ryu Hayano/CERN: **Precision laser spectroscopy of antiprotonic helium atoms - weighing the antiproton.** GSI Kolloquium, 17.07.2007.

Patrick Lau, DLR Köln: **Effects of ionizing radiation on murine osteoblastic cell differentiation and gene expression.** Biophysics Seminar, 18.07.2007.
SGFD working group meeting. 18.-20.07.2007.

ISACC 2007. 19.-23.07.2007.

NUSTAR Board of Representatives Meeting. 23.07.2007.

Toma Toncian, Heinrich-Heine-Universität Düsseldorf: **Laser Triggered Micro Lens for Energy Selection.** ILIAS-Arbeitsseminar, 24.07.2007.

FAIR Monthly. 24.07.2007.

Rolf-Dietmar Herzberg, Liverpool: **K-isomers in transfermium nuclei.** NuSTAR Seminar, 31.07.2007.

T. Pouthier: **Biological applications of the GSI heavy-ion microbeam: Studies on bystander effect.** Biophysics Seminar, 16.08.2007.

FAIR Monthly. 21.08.2007.

Andrzej Bialas, Jagellonian Univ., Krakow: **Wounded nucleons, wounded quarks: an update.** Sonderseminar, 31.08.2007.

Workshop COOL 07. 10.-14.09.2007.

XXII PANDA Collaboration Meeting. 17.-19.09.2007.

F. Uhlig: **CMake.** IT-EE-Palaver, 18.09.2007.

Lionel Prost, FNAL, Batavia, USA: **Operation and Cooling Performance Characterization of FNAL's High Energy Electron Cooler.** Beschleuniger-Palaver, 18.09.2007.

PANDA PID Computing Workshop. 20.-21.09.2007.

M. Schollmeier: **Teilchenbeschleunigung mit Lasern: Bericht von der IFSA2007, 9. 14.9. in Kobe.** ILIAS-Arbeitsseminar, 25.09.2007.

10. CBM Collaboration Meeting. 25.-28.09.2007.

FAIR Monthly. 26.09.2007.

Markus Bender, GSI: **Ion Induced Desorption.** Beschleuniger-Palaver, 27.09.2007.

P. Mulser, TQE-TU Darmstadt: **Trends I in ULIS 2007 (Journal Club).** ILIAS-Arbeitsseminar, 09.10.2007.

Sarah L. Nelson, LBNL: **Cold fusion reactions with the Berkeley gas-filled separator.** NuSTAR Seminar, 10.10.2007.

Laserlab Europe Workshop. 15.10.2007.

Joint R3B-EXL Collaboration Meeting. EXL Collaboration Board. 16.-18.10.2006.

International Symposium on Modern Trends in Nuclear Physics in Honor of Professor Walter F. Henning. 18.10.2007.
Barbara Drossel/TU Darmstadt: **Statistical physics of networks.** GSI Kolloquium, 23.10.2007.

FAIR Monthly. 23.10.2007.

Kritische Nachlese TSPPLPI (Schlegel-Workshop Darmstadt) und ULIS II in Bordeaux (Journal Club). ILIAS-Arbeitsseminar, 23.10.2007.

Dhruba Gupta, VACC Kolkota: **Study of nuclear reactions with rare isotope beams.** NuSTAR Seminar, 25.10.2007.

Jahrestagung des Komitees für Hadronen- und Kernphysik. 25.-26.10.2007.

Dmitriy S. Ivanov, Universität Kaiserslautern: **Atomistic-Continuum Modeling of Surface Modifications and Nanostructuring on Metals and Semiconductors by a short Laser Pulse.** Physik dichter Plasmen mit Schwerionen- und Laserstrahlen, 30.10.2007.

K. Witte, GSI: **PHELIX Science, Status and Roadmap.** ILIAS-Arbeitsseminar, 30.10.2007.

Sami K. Solanki/Max-Planck-Institut für Sonnensystemforschung: **The Sun's magnetic field and global climate change.** GSI Kolloquium, 30.10.2007.

Leonid Chulkov, GSI: **Quasi-free scattering with exotic nuclei.** NuSTAR Seminar, 31.10.2007.

Marek Pfutzner: **Proton-proton correlations in the 2p decay of ^{45}Fe.** NuSTAR Seminar, 31.10.2007.

Zoltan Harman, MPI Heidelberg: **Relativistic Electron Dynamics and Nuclear Properties Explored in Dielectronic and Visible Spectra.** Atomphysik-Seminar, 31.10.2007.

J. Gerl: **NUSTAR Board and Spokespersons Meeting.** 06.11.2007.

FAIR Start Event and International Symposium on the Physics at FAIR. 07.-08.11.2007.

Mirela Cerchez, Universität Düsseldorf: **Absorption of extremely short laser pulses in strongly overdense targets.** ILIAS-Arbeitsseminar, 13.11.2007.

Raphael Granier de Cassagnac, Laboratoire Leprince-Ringuet: **Charming charmonia in the quark gluon plasma.** GSI Kolloquium, 13.11.2007.

S. McCaslin, National Instruments, München: **Multicore Systeme & Skalierbarkeit.** IT-EE-Palaver, 13.11.2007.

Shawn McCaslin, National Instruments: **Algorithm Engineering for Multicore-Systems.** Sonderseminar, 13.11.2007.

W. Barth, P. Hülsmann und U. Ratzinger, Institut für Angewandte Physik, Universität Frankfurt: **Auf dem Weg zu intensiven Strahlpulsen für die Plasmaphysik bei GSI und FAIR.** Physik dichter Plasmen mit Schwerionen- und Laserstrahlen, 13.11.2007.

D. Antonov / Heidelberg: **Jet quenching parameter hat q in the stochastic QCD vacuum with Landau damping.** Theorie-Seminar, 14.11.2007.

J. Schweinzer, MPI für Plasmaphysik, Garching: **Atomic Collision Processes in Plasmas of Asdex Upgrade, Jet and Iter.** Atomphysik-Seminar, 14.11.2007.

Peter von Neumann-Cosel, TU Darmstadt: **Fine structure in the nuclear continuum - Giant resonances, wavelets and scales.** NuSTAR Seminar, 14.11.2007.

Ralph W. Assmann, CERN: **Beam Loss and Collimation at the LHC.** Beschleuniger-Palaver, 15.11.2007.

Anna Tauschwitz, Universität Frankfurt: **Dynamics of tensile pressure in ion-beam heated matter applied to a liquid lithium production target for the Super-FRS at FAIR.** ILIAS-Arbeitsseminar, 20.11.2007.

M. Feyerabend: **Neues vom Tivoli Storage Manager.** IT-EE-Palaver, 20.11.2007.

Matthias Liebendoerfer: **An isotropic diffusion source**

approximation for supernova neutrino transport. Theorie-Seminar, 21.11.2007.

Wolf-Dietrich Zeitz, HMI Berlin: **Observation of Polarized Electronic States at Surface Atoms.** Atomphysik-Seminar, 21.11.2007.

C. Huhn: **Verteiltes Konfigurationsmanagement mit cfengine.** IT-EE-Palaver, 27.11.2007.

K. Witte, GSI/TUD and P. Mulser, TQE-TUD: **ILIAS-Arbeitsseminar.** ILIAS-Arbeitsseminar, 27.11.2007.

Manfred Lindner/MPI Heidelberg: **Neutrinos as Probes of New Physics.** GSI Kolloquium, 27.11.2007.

Zenghu Chang, Kansas State Univ.: **Attosecond pulse generation with a double optical gating.** Physik dichter Plasmen mit Schwerionen- und Laserstrahlen, 27.11.2007.

C. Reinhardt, K. Schiebel: **Schulung der Sekretärinnen - Rund um Office.** GSI-interne Fortbildung, 28.11.2007.

David Boutin, Giessen University: **First direct observation of bound-state beta-decay.** NuSTAR Seminar, 28.11.2007.

Ingo Augustin: **Status des FAIR-Projekts.** Wissenschaft für Alle, 28.11.2007.

Sergiy Trotsenko, GSI Darmstadt: **The Spectral Shape of the Two-photon Decay in He-like Tin.** Atomphysik-Seminar, 28.11.2007.

Christina Dimopoulou, GSI: **Longitudinal Beam Stacking with Electron Cooling at the ESR as a Proof of Prinicple for FAIR.** Beschleuniger-Palaver, 29.11.2007.

Workshop on Antiproton and Experiments at FAIR. 03.-04.12.2007.
Andrea Sengebusch, Universität Rostock: **K-line shift in laser produced dense plasmas.** Physik dichter Plasmen mit Schwerionen- und Laserstrahlen, 04.12.2007.

Mihai Horoi/Central Michigan University: **Correlations in Nuclei: Configuration Interaction, Exponential Convergence Method, Coupled Clusters and Beyond.** Theorie-Seminar, 04.12.2007.

P. Mulser, TQE-TU Darmstadt: **Resonanzabsorption in steilen Dichteprofilen, MULTI und Gültigkeitsbereich der Fresnelformeln.** ILIAS-Arbeitsseminar, 04.12.2007.

Walter Kutschera/Universität Wien: **Science and the Humanities - a Happy Marriage?** GSI Kolloquium, 04.12.2007.

Alexander Voitkiv, MPI Heidelberg: **Relativistic Time Dilatation and the Spectrum of Electrons Emitted by 33 TeV Lead Ions Penetrating Thin Foils.** Atomphysik-Seminar, 05.12.2007.

Vladimir Skokov / Dubna: **Hybrid hydrodynamics: results and open problems.** Theorie-Seminar, 05.12.2007.

M. Kats, ITEP: **New solutions for optimal transport of proton and ion beams to patients.** Beschleuniger-Palaver, 06.12.2007.

XXIII PANDA Collaboration Meeting. 10.-14.12.2007.

H. Paul, Johannes-Kepler-University Linz: **Statistical Analysis of Stopping Power Data and the Gas-Solid Difference.** Physik dichter Plasmen mit Schwerionen- und Laserstrahlen, 11.12.2007.

H.-J. Kull, RWTH Aachen: **Korrelierte Elektron-Ion-Stöße in starken Laserfeldern.** ILIAS-Arbeitsseminar, 11.12.2007.

S. Bosen, M. Kreiten, Fa. AMD: **Die Architektur der AMD Prozessoren.** IT-EE-Palaver, 11.12.2007.

S. Scherer / Mainz: **Higher order terms in effective field theories.** Theorie-Seminar, 12.12.2007.

Uwe Thumm, Kansas State University: **Controlling and imaging the nuclear motion in small molecules with ultrashort laser pulses.** Atomphysik-Seminar, 12.12.2007.

A. Redelbach, GSI: **Recent development of settings generation for SIS18.** Beschleuniger-Palaver, 13.12.2007.

H. Brand, D. Beck: **LVOOP - Object Oriented Programming with LabVIEW.** GSI-interne Fortbildung, 17.-19.12.2007.

Konrad Kleinknecht, Universität Mainz: **Climate change and human energy consumption.** GSI Kolloquium, 18.12.2007.

E. Eppelbaum / Jülich: **The role of the isobar for nuclear forces.** Theorie-Seminar, 19.12.2007.

Fritz Bosch: **Wir sind aus Sternenstaub gemacht... Die kleinen und großen Tricks der Natur bei der Synthese der Elemente in den Sternen.** Wissenschaft für Alle, 19.12.2007.

Experiments performed at the GSI accelerators in 2007

Compiled by Andreas Tauschwitz, beam time coordinator 2007

In all tables 1 shift represents 8 hours of beam delivered to an experiment including necessary accelerator tuning time.

Exp	Short title	Spokesperson	Area	Ion	Shifts main	Shifts parasitic
U068	Bolometric detectors	Egelhof	Z7	^{152}Sm		12
U182	Chemical properties of element 106 and 108	Kratz	X1	^{40}Ar		9
U200	Nuclear struct. of Nobelium and Lawrencium	Hessberger	Y7	^{48}Ca	15	
U207	Optical spectroscopy of Nobelium	Backe	Y7	^{40}Ar, ^{48}Ca	21	
U217	Mass measurements at SHIPTRAP	Block	Y7	^{12}C, ^{36}Ar, ^{40}Ar, ^{48}Ca	45	
U219	TASCA commissioning	Schädel	X8	^{22}Ne, ^{40}Ar, ^{48}Ca	36	23
U221	Test of a CVD diamond detector	Bräuning-Demian	X4, HTA	^{208}Pb, ^{238}U		18
U223	Heavy elements	Hofmann	Y7	^{48}Ca, ^{64}Ni	81	9
U224	X-ray projectile and target radiation	Rosmej	Z6	^{48}Ca		15
U225	Nuclear structure of transfermium isotopes	Hessberger	Y7	^{40}Ar	14	6
U226	Energy loss and charge state distribution	Blasevic	Z6	^{36}Ar, ^{48}Ca		30
U228	Decay properties of fermium isotopes	Khuyagbaatar	Y7	^{40}Ar	66	
U229	Island of strong deformation above Z=82	Andreyev	Y7	^{56}Fe	29	
U230	Investigation of K isomers in 246Fm	Antalic	Y7	^{40}Ar	23	
U233	Fusio reaction 64Ni + 238U => 302/120	Hofmann	Y7	^{64}Ni	99	
U234	g-factors of 2+ states in stable 112,114,116 Sn	Jungclaus	X7	^{112}Sn, ^{114}Sn, ^{116}Sn	18	
UBIO	Biology experiments at UNILAC	Kraft	X6	^{7}Li, ^{12}C, ^{20}Ne, ^{64}Ni, ^{129}Xe, ^{208}Pb, ^{238}U	5	50
UMAT	Material science at UNILAC	Trautmann	X0	^{12}C , ^{36}Ar, ^{40}Ar, ^{64}Ni, ^{129}Xe, ^{208}Pb, ^{238}U	83	9

Exp	Short title	Spokesperson	Area	Ion	Shifts main	Shifts parasitic
FRS000	FRS development	Geissel	FRS	^{12}C, ^{129}Xe, ^{152}Sm	3	12
S104	Investigation of Actinide Nuclei	Schmidt	FRS	^{112}Sn,	3	
S223	Astrophysical reaction rates	Sümmerer	HTC	^{12}C, ^{36}Ar	35	8
S244	GSI FRS &gam. ray spectroscopy campaign	Regan	X7	^{48}Ca		7
S247	Nucleon density in light halo nuclei	Egelhof	HTC	^{12}C	4	
S276	Nuclear mean field precision measurements	Henzl	FRS	^{112}Sn, ^{124}Sn	8	
S280	R&D on synthetic diamond detectors	Berdermann	HTA	^{1}H		14
S296	Quasifree hadronic scattering of exotic nuclei	Lemmon	HTC	^{12}C	27	
S301	Dielectron prod. in pp, dp an AA collisions	Salabura	HAD	^{1}H	83	
S310	g-factors of ismoeric states	Balabanski	FRS	^{64}Ni		15
S312	β-decay lifetimes and β-delayed spectroscopy	Benlliure	FRS	^{40}Ar, ^{208}Pb	18	8
S313	Nuclear dynamical symmetries	Regan	FRS	^{208}Pb	24	4
S316	Isospin symmetry	Fujita	FRS	^{58}Ni	14	
S317	High-intensity effects and beam loss issues	Hofmann	SIS	^{40}Ar	12	
S318	Borromean dripline nucleus 17-Ne	Jonson	HTC	^{20}Ne	25	
S319	HypHI	Saito	HTA	^{12}C	3	
S322	One-neutron removal momentum distribution	Kanungo	FRS	^{48}Ca	28	
S325	Charged Kaon measurements with FOPI	Herrmann	HTB	^{12}C, ^{58}Ni	15,5	24
S326	Proton-Neutron pairing effects	Gadea	FRS	^{78}Kr	14	
S330	100Sn	Faestermann	FRS	^{129}Xe		18
S333	Vector meson production	Salabura	HAD	^{12}C	21	6
S334	Thermal stress waves in graphite	Wilfinger	HHT	^{238}U		10
S338	Strangeness in heavy ion collisions	Herrmann	HTB	^{36}Ar		21
S339	Pion-induced reactions	Matulewicz	HTB	^{12}C	1	
SBIO	Biophysics experiments		HTA, HTM	^{12}C	17,5	
SIST	Radiation safety	Fehrenbacher	HTA	^{12}C	7	
SMAT	Materials research at SIS	Trautmann	HTA	^{208}Pb, ^{238}U	6	21
STHE	Therapy studies	Kraft	HTM, HTA	^{1}H, ^{7}Li, ^{12}C	8,5	
SITH	SchwerIonen Therapie Heidelberg	Haberer	HTA HTM	^{1}H, ^{16}O, ^{12}C	26,75	

E000	ESR development	Steck	ESR	^{1}H, ^{40}Ar, ^{64}Ni, ^{238}U	44	
E028	Tests of calometric detectors	Egelhof	Z7	^{64}Ni		6
E055	Direct mass measurements at FRS-ESR	Scheidenberger	ESR	^{64}Ni	5	
E061	Excited states in He-like uranium	Silver	ESR	^{238}U	15	
E067	Test of time dilatation at the ESR	Karpuk	ESR	^{7}Li	9	
E070	ESR reaction microscope	Fischer	ESR	^{64}Ni	36	
E075	HITRAP decelerator commissioning	Kester	HITRAP	^{20}Ne, ^{64}Ni	39	
E077	Spectroscopy of two-body beta-decays	Litvinov	ESR	^{152}Sm	65	

Statutory organs and scientific advisory committees to GSI

Supervisory Board/Aufsichtsrat:

Dr. B. Vierkorn-Rudolph [chair],
Bundesministerium für Bildung und Forschung, Bonn/Berlin (Germany),
as representative of the Federal Republic of Germany

Ministerialrat Dr. R. Koepke,
Bundesministerium für Bildung und Forschung, Bonn/Berlin (Germany),
as representative of the Federal Republic of Germany

Ministerialdirigent Dr. R. Bernhardt,
Hessisches Ministerium für Wissenschaft und Kunst, Wiesbaden (Germany),
as representative of the State Hessen in Germany

Prof. Dr. R. Klanner,
Universität Hamburg/DESY (Germay),
as representatives of the Scientific Council of the GSI

Scientific Directorate/Wissenschaftliches Direktorium WD:

Prof. Dr. H. Stöcker, [Prof. Dr. W. F. Henning]
Dr. H. Eickhoff, Prof. Dr. K.-H. Langanke, B. Schönfelder, [Dr. A. Kurz]

Division and Department Heads/Bereichs- und Abteilungsleiter:

Dr. T. Aumann, R^3B
Prof. Dr. P. Braun-Munzinger, ALICE
Dr. H. Eickhoff, Accelerator/Beschleunigerbereich
Dr. D. Krämer, FAIR-Technical Division/FAIR Bereich
Prof. Dr. G. Kraft, Biophysics/Biophysik
Prof. Dr. K.-H. Langanke, Research/Forschungsbereich and Theory: Nuclear structure and astrophysics/Theorie: Kernstruktur- und Astrophysik
Dr. Y. Leifels, FOPI
Prof. Dr. F. Maas, Hadron physics/Hadronenphysik
Prof. Dr. R. Neumann, Materials research/Materialforschung
Prof. Dr. K. Peters, PANDA
Prof. Dr. D. Rudolph, Nuclear chemistry/Kernchemie
Prof. Dr. C. Scheidenberger [Prof. Dr. H. Emling], ESR/NESR
B. Schönfelder, Infrastructure/Infrastruktur
Prof. Dr. P. Senger, CBM
Prof. Dr. T. Stöhlker [Prof. Dr. H.-J. Kluge], Atomic physics/Atomphysik
Prof. Dr. T. Stöhlker [Prof. Dr. D. H. H. Hoffmann], Plasma physics/Plasmaphysik
Prof. Dr. J. Stroth, HADES
Prof. Dr. J. Wambach, Theory: QCD and hadron physics/Theorie: QCD und Hadronenphysik
Prof. Dr. K. Witte, PHELIX

Scientific Council/Wissenschaftlicher Rat WR:
<http://www.gsi.de/informationen/users/EAC/wr/>

R. Klanner [chair], Universität Hamburg (Germany); D. von Harrach [vice chair], Johannes-Gutenberg-Universität Mainz (Germany); [N. Holtkamp, Oak Ridge National Laboratory (USA)]; C. Leemann, Thomas Jefferson National Accelerator Facility, Newport News (USA); B. Mueller, Duke University, Durham, North Carolina (USA); [H. Requardt, Siemens AG Medical Solutions, Erlangen (Germany)]; S. Myers, CERN AB, Geneva (Switzerland); T. Roser, BNL, Upton (USA); B. M. Sherrill, Michigan State University, East Lansing (USA); A. Shotter, TRIUMF, Vancouver (Canada); M. Soyeur, DSM/DAPNIA/SPhN, Gif-sur-Yvette (France); R. Sauerbrey, Forschungszentrum Rossendorf, Dresden (Germany); D. Vernhet, Université Paris (France).
Secretary: K.-D. Groß

Scientific Committee/Wissenschaftlicher Ausschuss WA:
<http://www-w2k.gsi.de/wa/scientific_committee.htm>

S. Richter [chair]; H. Simon [vice chair]; A. Bräuning-Demian; T. Cornelius; B. Friman; Y. Leifels; B. Lommel; P. Malzacher; H. Reich-Sprenger; [C. Scheidenberger]; L. Schmitt; M. Scholz; P. Senger; J. Stadlmann; A. Tauschwitz; M. Traxler; D. Varentsov; G. Walter; H. Weick; M. Kreiser (for the Betriebsrat).

Scientific Advisory Committees to GSI

GSI General Programme Advisory Committee G-PAC:
<http://www.gsi.de/informationen/users/EAC/ea/>

J. Aichelin, SUBATECH, Nantes (France); W. Catford, University of Surrey, Guildford (UK); P. Giubellino, INFN Turin, Torino (Italy); R. Hoekstra, KVI Groningen, Groningen (The Netherlands); R. Krücken, Technische Universität München, Physik-Department (Germany); M. Lewitowicz, GANIL, Caen (France); [S. Paul, Technische Universität München, Physik-Department (Germany)]; T. Peitzmann, Utrecht University (The Netherlands); N. Pietralla, Technische Universität Darmstadt, Darmstadt (Germany); H. Schatz, Michigan State University, East Lansing (USA); M. Wada, RIKEN, Saitama (Japan); M. Weidemüller, Universität Freiburg (Germany); E. Widmann, Stefan-Meyer-Institut für subatomare Physik, Österreichische Akademie der Wissenschaften, Vienna (Austria).
Secretary: K. Füssel

GSI Phelix and Plasmaphysics Program Advisory Committee (PPAC):
<http://www.gsi.de/informationen/users/EAC/ppac/>

M. H. R. Hutchinson [Chair], Rutherford Appleton Lab (United Kingdom); S. Jacquemot, LULI, Ecole Polytechnique, Palaiseau (France); G. Logan, LBL Berkeley (USA); T. A. Mehlhorn, Sandia National Laboratories, Albuquerque (USA); R. Sauerbrey, Forschungszentrum Rossendorf, Dresden (Germany); B. Sharkov, Inst. of Theoretical and Experimental Physics Moscow (Russia).
Secretary: K. Füssel

GSI Biophysics & Radio-Biology Program Advisory Committee (Bio-PAC):
<http://www.gsi.de/informationen/users/EAC/bio-pac/>

G. Iliakis [Chair], Institut für Medizinische Strahlenbiologie Universitätsklinikum Essen (Germany); M. Durante, Universita 'Federico II', Napoli (Italy); R. Engenhardt-Cabillic, Klinik für Strahlentherapie Philipps-Universität Marburg Klinikum (Germany); B. Michael, Gray Lab (Cancer Research Trust), Mount-Vernon-Hospital, Northwood (United Kingdom); R. Okayasu, National Institute of Radiological Sciences, Chiba-shi (Japan); E. Pedroni, Paul Scherrer Institut, Villigen (Switzerland).
Secretary: K. Füssel

GSI Materials Research Program Advisory Committee (Mat-PAC):
<http://www.gsi.de/informationen/users/EAC/mat-pac/>

P. Apel, JINR Dubna (Russia); S. Bouffard, CEA-CNRS-ENSICAEN Caen (France); K. Hjort, University of Uppsala (Sweden); W. Wesch, Friedrich Schiller Universittät Jena (Germany). Secretary: K. Füssel

GSI Users' Group Executive Committee (UEC):

<http://www.gsi.de/forschung/usersgroup/index.html>

P. Regan (UK) [Chair-elected]; W. Cassing (Germany); D. Cortina (Spain); D. Dauvergne (France); T. Faestermann (Germany); J. Friese (Germany); U. Glasmacher (Germany), J. Jacoby (Germany); A. Jungclaus (Spain); R. Klein (Germany); J. Kratz (Germany); T. Kühl (Germany); R. Kulessa (Poland); S. Lang (Germany); L. Narici (Italy); M. Petrovici (Romania); P. Salabura (Poland); A. Warczak (Poland).

Scientific Coordination:

Dr. K. D. Groß

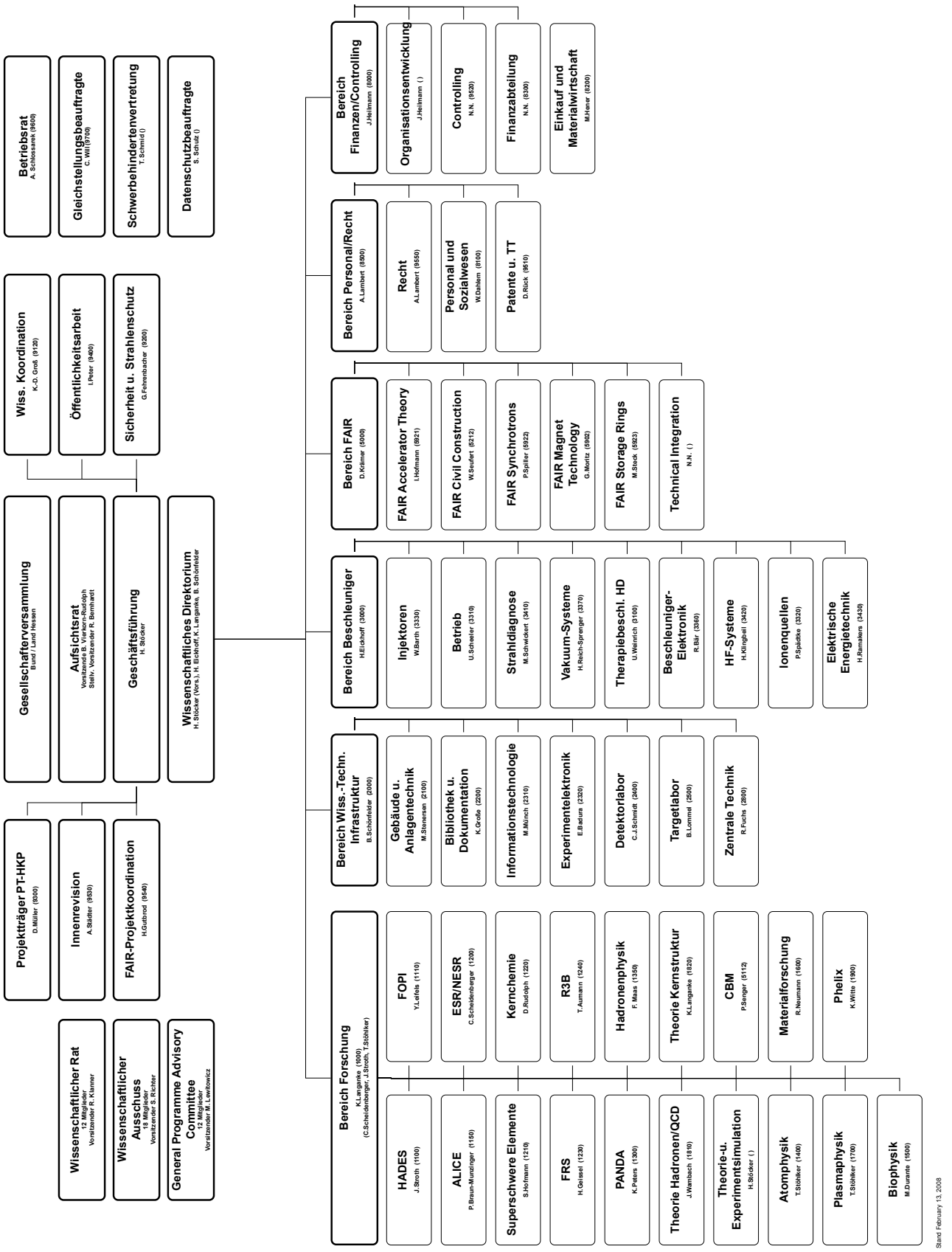
Betriebsrat
A. Schlossarek (9800)
Gleichstellungsbeauftragte
C. Will (9700)
Schwerbehindertenvertretung
T. Schmid ()
Datenschutzbeauftragte
S. Schulz ()
Wiss. Koordination
K.-D. Groß (9120)
Öffentlichkeitsarbeit
I.Peter (9400)
Sicherheit u. Strahlenschutz
G.Fehrenbacher (9200)
Gesellschafterversammlung
Bund / Land Hessen
Aufsichtsrat
Vorsitzende B. Vierkorn-Rudolph
Stellv. Vorsitzender R. Bernhardt
Geschäftsführung
H. Stöcker
Wissenschaftliches Direktorium
H. Stöcker (Vors.), H. Eickhoff, K. Langanke, B. Schönfelder
Projektträger PT-HKP
D.Müller (9300)
Innenrevision
A.Städter (9530)
FAIR-Projektkoordination
H.Gutbrod (9540)
Wissenschaftlicher Rat
12 Mitglieder
Vorsitzender R. Klanner
Wissenschaftlicher Ausschuss
18 Mitglieder
Vorsitzender S. Richter
General Programme Advisory Committee
12 Mitglieder
Vorsitzender M. Lewitowicz
Bereich Finanzen/Controlling
J.Heilmann (8800)
Organisationsentwicklung
J.Heilmann ( )
Controlling
N.N. (8520)
Finanzabteilung
N.N. (8300)
Einkauf und Materialwirtschaft
M.Heiner (8200)
Bereich Personal/Recht
A.Lambert (8500)
Recht
A.Lambert (9550)
Personal und Sozialwesen
W.Dahlem (8100)
Patente u. TT
D.Rück (9510)
Bereich FAIR
D.Krämer (5000)
FAIR Accelerator Theory
I.Hofmann (6021)
FAIR Civil Construction
W.Seufert (6212)
FAIR Synchrotrons
P.Spiller (6922)
FAIR Magnet Technology
G.Moritz (6902)
FAIR Storage Rings
M.Steck (6923)
Technical Integration
N.N. ( )
Bereich Beschleuniger
H.Eickhoff (3000)
Injektoren
W.Barth (3330)
Betrieb
U.Scheeler (3310)
Strahldiagnose
M.Schwickert (3410)
Vakuum-Systeme
H.Reich-Sprenger (3370)
Therapiebeschl. HD
U.Weinrich (3100)
Beschleuniger-Elektronik
R.Bär (3360)
HF-Systeme
H.Klingbeil (3420)
Ionenquellen
P.Spädtke (3320)
Elektrische Energietechnik
H.Ramakers (3430)
Bereich Wiss.-Techn. Infrastruktur
B.Schönfelder (2000)
Gebäude u. Anlagentechnik
M.Stenersen (2100)
Bibliothek u. Dokumentation
K.Große (2200)
Informationstechnologie
M.Münch (2310)
Experimentelektronik
E.Badura (2320)
Detektorlabor
C.J.Schmidt (2400)
Targetlabor
B.Lommel (2500)
Zentrale Technik
R.Fuchs (2800)
Bereich Forschung
K.Langanke (1000)
(C.Scheidenberger, J.Stroth, T.Stöhlker)
FOPI
Y.Leifels (1110)
ESR/NESR
C.Scheidenberger (1200)
Kernchemie
D.Rudolph (1220)
R3B
T.Aumann (1240)
Hadronenphysik
F. Maas (1350)
Theorie Kernstruktur
K.Langanke (1820)
CBM
P.Senger (5112)
Materialforschung
R.Neumann (1600)
Phelix
K.Witte (1900)
HADES
J.Stroth (1100)
ALICE
P.Braun-Munzinger (1150)
Superschwere Elemente
S.Hofmann (1210)
FRS
H.Geissel (1230)
PANDA
K.Peters (1300)
Theorie Hadronen/QCD
J.Wambach (1810)
Theorie-u. Experimentsimulation
H.Stöcker ( )
Atomphysik
T.Stöhlker (1400)
Plasmaphysik
T.Stöhlker (1700)
Biophysik
M.Durante (1500)
Stand February 13, 2008

Facts and Figures

Compiled by J. Heilmann

Gesellschafter/Shareholders since 1969, December 17th

Federal Republic of Germany	90% of budget (and of share capital)
State of Hesse/Land Hessen	10% of budget (and of share capital)

Accelerators

FAIR	Facility for Antiprotons and Ion Research		pre- construction R&D
UNILAC	UNIversal Linear ACcelerator	13 MeV/u for U	in operation since 1976
SIS	Schwer-Ionen-Synchrotron	50–1000 MeV/u for U	in operation since 1989
ESR	Experimental Storage Ring	3–400 MeV/u for U	in operation since 1990

Users of the accelerator complex

In 2007, GSI provided access to 25 experimental areas to more than 1440 scientific users.

GSI Funding in Mio. Euro

research area Structure of Matter	70	
research area Health	3	
special tasks and Helmholtz-ctivities	2	
third party funding	28	
total budget		**103 Mio. Euro**

Personnel 2007 in person years

research area Structure of Matter	384	
FAIR-activities (Structure of Matter)	136	
research area Health	32	
management and management support	72	
scientific and technical infrastructure	210	
personnel involved in projects funded by nat./internat. funding agencies	132	
total personnel		**966 person years**

List of Authors